

Heterodyne dispersive cavity ring-down spectroscopy exploiting eigenmode frequencies for high-fidelity measurements

Agata Cygan, Szymon Wójtewicz, Hubert Józwiak, Grzegorz Kowzan, Nikodem Stolarczyk, Katarzyna Bielska, Piotr Wcisło, Roman Ciuryło, Daniel Lisak

Institute of Physics, Faculty of Physics, Astronomy and Informatics, Nicolaus Copernicus University in Toruń, Grudziadzka 5, 87-100 Torun, Poland

Measuring low light absorption with combined uncertainty $< 1\text{‰}$ is crucial in a wide range of applications. Popular cavity ring-down spectroscopy can provide ultra-high precision, below 0.01‰ , but its accuracy is strongly dependent on the measurement capabilities of the detection system and typically is about 10‰ . Here, we exploit the optical frequency information carried by the ring-down cavity electromagnetic field, not explored in conventional CRDS, for high-fidelity spectroscopy. Instead of measuring only the decaying light intensity, we perform heterodyne detection of ring-downs followed by Fourier analysis to provide exact frequencies of optical cavity modes and a dispersive spectrum of a gas sample from them. This approach is insensitive to inaccuracies in light intensity measurements and eliminates the problem of detector band nonlinearity, the main cause of measurement error in traditional CRDS. Using the CO and HD line intensities as examples, we demonstrate the sub- ‰ accuracy of our method, confirmed by the best *ab initio* results, and the long-term repeatability of our dispersion measurements at 10^{-4} level. Such results have not been achieved in optical spectroscopy before. The high accuracy of the presented method indicates its potential in atmospheric studies, isotope ratio metrology, thermometry, and the establishment of primary gas standards.

The challenge of measuring the shape and intensity of spectral lines with a relative accuracy of 10^{-3} and better is highlighted in numerous scientific, industrial, and metrological applications using sensitive optical spectroscopy. Regarding the effect of global warming, changes in the Earth's climate are expected to impact the capacity of natural repositories of anthropogenic greenhouse gases (GHG), which will generate a feedback response to climate change¹. To predict the evolution of these changes, the location of regional sources and sinks of GHG is essential. Spectroscopic retrieval models must exhibit sensitivity to changes in their concentration at the permille level, necessitating a laboratory spectra accuracy of at least an equivalent magnitude². Any systematic errors are of great concern because they introduce regional bias that imitates sources and sinks of GHG. Particular attention is also required in measurements of the stable isotope ratio, as repeatability is compromised over time due to the aging of reference materials³. A promising approach involves the spectroscopic measurement of the absolute isotope ratio from the ratio of the line intensities of these isotopes. This method has recently demonstrated⁴ a relative combined measurement uncertainty at the sub- ‰ level, showing good agreement with the results obtained from other methods. However, to measure line intensities with such high accuracy, careful calibration of the light intensity detection system is necessary⁵. Accurate measurements of the line intensity ratios are also the basis for the new concept of optical primary thermometry⁶. With the current standard of using first principles to define the units of temperature, pressure, and

number density⁷, optical methods offer promising prospects for realizing new primary gas standards⁸. As molecules interact with electromagnetic radiation, the accurate measurements of the refractive index enable the determination of gas thermodynamic parameters. Cavity-based nitrogen refractometry with a relative precision of 10^{-6} holds the greatest potential for realizing an optical primary pressure standard^{9,10} to date. On the other hand, individual spectral lines, shaped by molecular interactions, provide molecular selectivity for optical gas standards. Progress in the mutual development of line-shape theory and spectroscopic methods¹¹ motivates continuous improvement in *ab initio* accuracies of spectral line intensities^{12,13}, which opens new possibilities for developing gas mixture and pressure standards related to accurate measurement of line intensity.

Many of these applications use cavity ring-down spectroscopy¹⁴ (CRDS) to quantitatively measure trace and weakly absorbing species in the gas phase. Traditional CRDS systems, widely used due to their simplicity, reliability, and calibration-free nature, with inherently high sensitivity and spectral resolution, have been improved with laser and cavity stabilization technologies^{15,16}, and optical frequency combs providing accurate absolute frequency axes¹⁷. Although the best obtained relative precision exceeds 10^{-5} , the determined line intensities can differ by up to several percent between spectrometers due to the limited ability to measure the undistorted ring-down signals^{5,18}. As long as the light is turned off quickly enough, the main factors that limit the accuracy of CRDS are

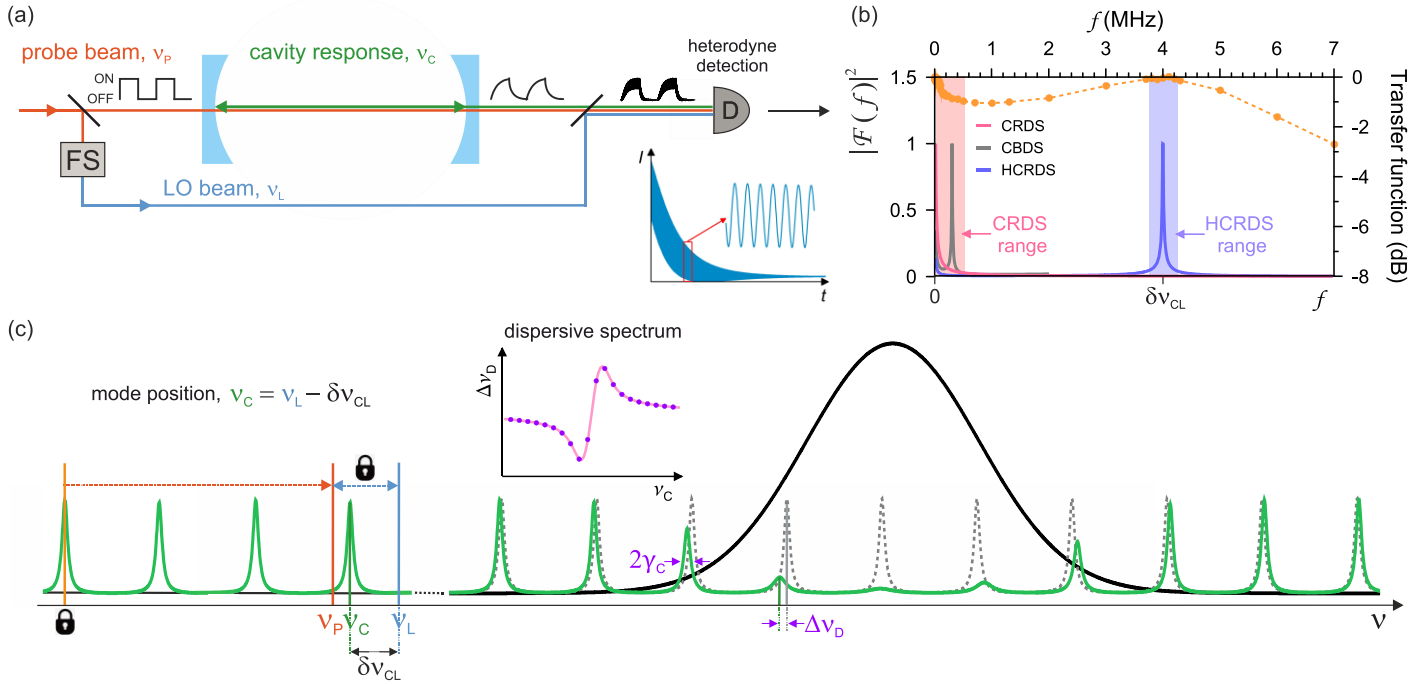


Figure 1 | The principles of HCRDS. **a**, The probe beam excites the optical cavity at arbitrary frequency ν_p close to the cavity resonant frequency, ν_c . The cavity responds at the resonant frequency, ν_c . The LO beam at frequency ν_L is frequency-shifted (FS) relative to the probe beam. After turning off the probe beam, it enables heterodyne detection of ring-down signals with the frequency $\delta\nu_{CL} = \nu_L - \nu_c$. **b**, The power spectrum $|\mathcal{F}(f)|^2$ of the signals obtained by CRDS, CBDS and HCRDS methods. The dots and the dashed line are the measured and fitted shape of the transfer function of the detection system used in CRDS and HCRDS measurements, respectively. The rectangles indicate the range of harmonic components of $|\mathcal{F}(f)|^2$ taken into account in the analysis of the CRDS and HCRDS signals. Fitting the Lorentz profile to the peak at $\delta\nu_{CL}$ provides the width and center of the cavity mode. **c**, In the vicinity of the molecular resonance the cavity modes are shifted by dispersion and broadened by absorption. The probe beam frequency, ν_p , is tuned with steps of FSR by the broadband EOM relative to the locking point while the frequency difference $\nu_L - \nu_p$ is kept constant. For each spectral step ν_c is determined from the measured $\delta\nu_{CL}$. The frequency shifts $\Delta\nu_D(\nu_c)$ between cavity modes disturbed (continuous line) and undisturbed (dashed line) by the molecular line provide the HCRDS dispersion spectrum shown in the inset plot.

the nonlinearity of the amplitude and bandwidth of the detection system, which includes the detector itself, the hardware digitizing ring-downs, and electronic devices along the way. It was recently shown that digitizer nonlinearity can be reduced by the calibration to a metrology-grade reference digitizer⁵. Alternatively, one can measure the dispersion spectrum of the sample obtained from central frequencies of optical cavity modes, the positions of which are shifted within the molecular resonance range^{19,20}. This calibration-free cavity mode dispersion spectroscopy (CMDS) uses only the DC part of the detection band, making it completely insensitive to the nonlinearity of the entire band. Moreover, CMDS is much less sensitive to the amplitude nonlinearity of the detector than traditional CRDS. However, due to the need for point-by-point scanning of each cavity mode profile, the CMDS is much slower than CRDS, which makes it more susceptible to various drifts. We note, however, that the CMDS speed problem can be solved, at the cost of much lower laser-to-cavity coupling efficiency due to the frequency mismatch, by using cavity buildup dispersion spectroscopy (CBDS)²¹, the accuracy of which is similar to CMDS. Both approaches, CRDS and CMDS, discussed above, have recently shown the best results for the line intensity: sub-‰ accuracy in measurements^{12,20} and sub-‰ agreement with *ab initio* results¹².

In this work, we exploit the optical frequency information carried by the ring-down cavity electromagnetic field, not explored in conventional CRDS, for high-fidelity spectroscopic measurements. Instead of measuring only the decaying light intensity, we perform heterodyne detection of ring-downs followed by Fourier analysis not only to reduce noise on the ring-down signals²²⁻²⁴, but mainly to provide exact frequencies of optical cavity modes and a dispersive spectrum of a gas sample from them. We demonstrate that our approach is insensitive to light intensity measurement inaccuracies that constitute a problem for most spectrometers using light

intensity detection. Moreover, it allows the selection of the most linear range of a detector transfer function, thus eliminating the major contribution to the measurement error in the traditional CRDS. We point out that with a small change in configuration, any CRDS system using laser-cavity locking technology can be easily converted into a dispersive CRDS system, providing high accuracy. In other words, dispersive CRDS combines the accuracy of CMDS²⁰ with the speed²⁵ and simplicity of conventional CRDS¹⁴. Using the CO line intensity as an example, we demonstrate the sub-‰ accuracy of our method, confirmed by the best *ab initio* result¹², and the long-term repeatability of our dispersion measurements at 10^{-4} level. For the first time, permille accuracy of the HD line intensity and permille consistency of the HD line intensity and shape with the *ab initio* results are achieved. The showcased high-accuracy examples offer promising insights into the potential application of our method in atmospheric studies^{2,26}, isotope ratio metrology^{4,27}, and the establishment of primary gas standards⁸ and thermometry²⁸.

Results

The principle of heterodyne frequency detection of light decaying from an optical cavity mode

Immediate injection of probe light at the frequency ν_p into a high-finesse optical cavity begins the process of building a field inside the cavity. This always occurs at the local resonant frequency, ν_c , of the cavity²⁹, regardless of the imperfect matching of the laser and cavity own frequency. The conventional CRDS detection system is insensitive to frequency measurement, which results in the incorrect assignment of the determined ring-down time constant, τ , to the laser frequency rather than the cavity resonant frequency. Detection of the light decay relative to a stable, local oscillator (LO) beam with frequency ν_L (Fig. 1a) allows one to extract missing information about the cavity resonance frequency and guarantees the correct

frequency axis of the spectrum. The intensity emerging from the cavity is

$$I_{\text{out}}(t) = I_L + I_C e^{-t/\tau} + 2I_B e^{-t/2\tau} \cos(2\pi \delta\nu_{\text{CL}} t), \quad (1)$$

where the first term is the LO intensity, the second is the exponential decay of the light from the cavity measured by conventional CRDS, and the third is the heterodyne beat, with frequency $\delta\nu_{\text{CL}}$, between the LO and cavity response fields. Further analysis of this signal, in the traditional sense of heterodyne detection, assumes using a band-pass filter to reduce low-frequency technical noise. Similar results provide an analysis of the high-frequency range of the power spectrum (PS) of the signal $I_{\text{out}}(t)$, shown in Fig. 1b (see Methods). Additionally, this approach mitigates the potential heterodyne signal distortion that may arise in certain cases using electrical filters. The Lorentzian peak at frequency $\delta\nu_{\text{CL}}$ provides the position of the cavity mode $\nu_C = \nu_L - \delta\nu_{\text{CL}}$. Moreover, its full width gives the half-width of the cavity mode, $\gamma_C = (4\pi\tau)^{-1}$. High precision of measurements of both quantities is guaranteed by the high stability of the LO frequency ν_L relative to the cavity resonances. We note that the Lorentzian peak at DC frequency does not provide additional information for heterodyne cavity ring-down spectroscopy (HCRDS) presented here. More importantly, this low-frequency range of the PS, used by traditional CRDS, is usually affected by nonlinearities in the detection band. Also, the PS of the build-up signal used by CBDS²¹ may encounter the same problem. Hence, in CBDS, a compromise must be achieved between detuning the laser away from the cavity mode center towards higher beat frequencies and the resulting reduction in the beam power transmitted through the cavity. The HCRDS is insensitive to the detection nonlinearity problems. It allows one to select the optimal $\delta\nu_{\text{CL}}$ frequency so that the measurement of cavity mode parameters coincides with the most linear range of the detector's bandwidth. Moreover, the symmetry of the Lorentz peak ensures that the determined cavity mode position is highly immune to nonlinearities in the light intensity measurement.

Measurement of spectra using heterodyne cavity ring-down spectroscopy

The idea of obtaining dispersion and absorption spectra using the HCRDS method is presented in Fig. 1c. Precise measurement of the position and width of cavity modes requires tight locking of the continuous-wave laser to the cavity. Additionally, to prevent thermal drift of the cavity modes comb, the cavity length is actively stabilized to another laser having long-term stability. The probe laser is split into two beams: one for exciting the cavity mode and the other, LO, serving as a reference for heterodyne detection of light decays. In the implemented approach, both beams are frequency-stepped using a broadband electro-optic modulator (B-EOM) and a microwave driver^{23,28}. Although such a configuration generates a series of sidebands on the laser, the optical cavity acts as a spectral filter, allowing only one of the excitation beam sidebands to resonate with the cavity. Similarly, in the case of heterodyne detection, the limited detection system bandwidth allows the decay beat signal to be observed with only one sideband of the reference beam. The ring-down decays are initiated after the excitation beam is turned off by an acousto-optic modulator (AOM) (see Fig. S1a in the supplementary material). This AOM shifts the probe frequency by almost one cavity's free spectral range (FSR=204.35 MHz) and beyond the cavity resonance to avoid its influence on the ring-down signals measurement and locking the laser to the cavity. The other AOM (see Fig. S1a) shifts the LO beam to set its detuning from the probe, $\nu_L - \nu_p$, constant through the measurement of the entire spectrum. Note that laser tuning in HCRDS systems can also be realized without B-EOM, by relocking the laser to subsequent cavity modes, at the cost of lower tuning speed. This approach would result in absorptive and differential dispersive spectrum¹⁹.

To scan the molecular spectrum, the B-EOM modulation frequency is stepped in increments equal to the FSR. Our maximum

scanning range when using the first-order sideband is ± 20 GHz and can be further multiplied as the sideband order increases. For each frequency step, the single heterodyne ring-down signal is acquired. Frequency scanning through the molecular spectrum is repeated. For each spectrum frequency corresponding to the center of the cavity mode, the power spectra, not the decays themselves, are averaged due to slow phase changes in the collected heterodyne light decays for that frequency. From this information, the positions and widths of the cavity modes are retrieved. Further technical details are provided in Supplementary Section S1.

The cavity mode widths provide the HCRDS absorptive spectrum with absorption coefficient $\alpha(\nu_C) = 4\pi \Delta\nu_C(\nu_C) c^{-1}$, where $\Delta\nu_C = \gamma_C - \gamma_{C,0} = (4\pi)^{-1} cA \text{Re}\{\mathcal{L}(\nu_C)\}$, c is the speed of light, $\gamma_{C,0}$ is the cavity mode half-width in the absence of molecular absorption, A is an area under the spectral line, and $\mathcal{L}(\nu)$ is the normalized complex-valued line-shape function so that $\int \mathcal{L}(\nu) d\nu = 1$. The HCRDS dispersive spectrum is obtained from the frequency shift $\Delta\nu_D(\nu_C)$ between cavity mode positions disturbed and undisturbed by the presence of the molecular resonances. Undisturbed mode positions are fitted as a background of the dispersive spectrum. The dispersive spectrum is given by $\Delta\nu_D(\nu_C) = (4\pi n_0)^{-1} cA \text{Im}\{\mathcal{L}(\nu_C)\}$, where n_0 is a broadband refractive index of the sample. Note that the dispersive cavity mode shift $\Delta\nu_D$ and absorptive cavity mode width $\Delta\nu_C$ are related by the Kramers-Krönig³⁰ relation, which yields $\Delta\nu_D \Delta\nu_C^{-1} = n_0^{-1} \text{Im}\{\mathcal{L}(\nu_C)\} / \text{Re}\{\mathcal{L}(\nu_C)\}$. Accurate measurement of the line area A at a known absorber concentration N_a allows one to determine the line intensity $S = A/N_a$.

HCRDS accuracy tests at the sub-permille level on CO line example

Examples of HCRDS absorption and dispersion spectra of CO transition are shown in Fig. 2a,b. As a benchmark transition we chose one of the most accurately known molecular lines, R(23) from the 3-0 band, the line intensity of which was measured using several techniques with sub-permille accuracy¹². Moreover, because CO is a simple diatomic molecule, its line intensity can be calculated from first principles with high accuracy¹². Fitting the spectra with the quadratic speed-dependent hard-collision profile (qSDHCP)³¹⁻³³, results in the best agreement with the experimental line shape. The lowest standard deviation of the fit residuals achieved for dispersion was 0.14‰, and for absorption was 0.58‰. It should be noted that the qSDHCP is a variant of the currently recommended line-shape model for atmospheric data analysis³⁴, and the demonstrated accuracy of the laboratory dispersion spectrum is an order of magnitude greater than that required for atmospheric studies. In Fig. 2c, CO line intensities recorded using HCRDS are compared with results provided by other techniques implemented here in parallel with HCRDS, as well as with literature data and the *ab initio* calculation. A comparison of HCRDS and CMDS dispersion techniques shows an excellent 0.04‰ agreement with their averaged value. The CO R(23) line intensity, $8.0603(70) \times 10^{-25}$ cm molecule⁻¹, reported here has a sub-‰ relative combined uncertainty. Moreover, a comparison with CMDS data¹² from three years ago demonstrates the long-term repeatability of our dispersion measurements at 2×10^{-4} level. Absorption measurements using HCRDS and cavity mode-width spectroscopy (CMWS)³⁵ provide combined uncertainties similar to dispersive methods. They introduce a small bias in line intensity but within the range of combined uncertainty. This bias is expected because absorption measurements are susceptible to nonlinearity in light-intensity detection. Interestingly, this susceptibility is two orders of magnitude lower for the dispersion techniques (see Methods). Measurement of CO transition by CRDS introduced a large bias, almost 1%, in the line intensity. Furthermore, replacing the optical detector in the detection system produced a different result. Research on the dependence of the line intensity on various configurations of the CRDS detection system has recently been

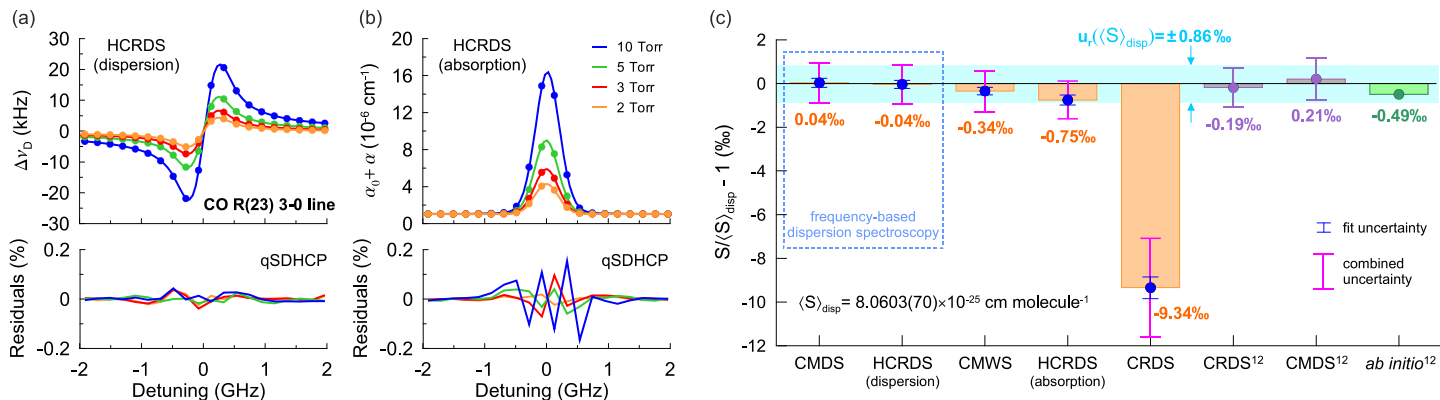


Figure 2 | The accuracy of HCRDS. a,b. Examples of dispersive (a) and absorptive (b) HCRDS spectra. Residuals below correspond to the difference between experimental and fitted qSDHCP line-shape model. The R(23) 3-0 line of CO ($\tilde{\nu}_0 = 6410.879558 \text{ cm}^{-1}$) was measured at temperature 296 K at pressures ranging from 2 to 10 Torr. Each of the spectra presented is an average of 5000 spectral scans, and the signal-to-noise ratio ranges from 1800:1 to 5000:1. Residuals are presented relative to the line profile amplitude at 10 Torr. Typical measurement time for one scan is 60 ms. The offset frequency of 192193.256628 GHz is subtracted from the abscissa. **c.** Comparison of HCRDS results for the intensity of CO R(23) 3-0 line with CMDS, CMWS and CRDS measurement results in this work as well as literature data¹² and *ab initio* calculation¹². The reference line intensity $\langle S \rangle_{\text{disp}}$ is the average of the dispersion measurement results with CMDS and HCRDS. These dispersive measurements provide the relative combined uncertainty of 0.86%. Combined uncertainty includes both type A (fit uncertainty) and type B uncertainties. The large deviation seen for CRDS result is caused by the nonlinearity of the detection bandwidth. The remaining experimental results are in sub-‰ agreement with each other as well as with the best reported data and the *ab initio* results.

carried out⁵. The main reason for the discrepant results obtained with CRDS is the nonlinearity of the detection bandwidth. We found that choosing a linear detector response range in HCRDS can reduce this nonlinearity-related error by over seven orders of magnitude (see Methods). Except for CRDS, all of our CO line intensity results agree with each other in the sub-‰ range. Moreover, our dispersion results agree up to 0.2‰ with the best CO experimental data published to date¹² and up to -0.49‰ with the best *ab initio* calculation of the CO line intensity¹².

Per mille-level accuracy spectroscopy of HD line shape

Dispersive CRDS spectroscopy reveals its potential for the fundamental studies of collisions between hydrogen molecules through accurate measurements of the shape of its spectral lines. In Fig. 3a, we show the HCRDS dispersion spectrum of the P(3) 2-0 HD transition. The qSDHCP does not fully describe the experimental spectrum for this system, which is revealed as a systematic structure on the fit residuals. For lighter molecules such as HD, attention needs to be paid to the proper description of the velocity-changing collisions leading to Dicke narrowing of the line. The speed-dependent billiard-ball profile (SDBBP)³⁶ provides a more physical description of molecular collisions and allows the HD spectrum to be modeled down to random noise in residuals with a standard deviation of 0.6‰. Calculations of SDBBP at low pressures used here require the implementation of an iterative approach³⁷. We note that the selected HD transition, unlike the CO transition, is weaker and not so well isolated from other transitions (Fig. 3b). Our results for the HD line intensity and their comparison with the theory are shown in Fig. 3c. The reference is the line intensity of $3.1793(40) \times 10^{-26} \text{ cm molecule}^{-1}$ obtained from the SDBBP analysis, with a relative combined uncertainty of 1.3‰, in which the line-shape parameters were fixed to *ab initio* values calculated in this work (see Supplementary Section S2). If the line-shape parameters were fitted, SDBBP gave a small deviation of 2.55‰ from the reference line intensity. The results for the qSDHCP show a systematic bias of up to -5.23‰ compared to the reference value due to the incorrect model used to analyze the experimental spectrum. The HD line intensity reported here is one of the most accurate experimental results to date^{38,39}. Moreover, its comparison with *ab initio* calculations of line intensity provided by Ref.⁴⁰ and Ref.⁴¹ gives excellent agreement up to -0.73‰ and 1.79‰, respectively. HCRDS demonstrates the highest accuracy in the experimental study of the molecular shapes of hydrogen lines. For the first time, spectroscopy confirmed both the

ab initio intensity and the *ab initio* shape of the molecular hydrogen line, reaching permille accuracy.

Discussion

The high accuracy of dispersive CRDS makes it an ideal tool for many existing, demanding applications of ultrasensitive optical spectroscopy, where an accurate measurement of the shape and intensity of the molecular line is critical. A very insidious systematic error of the traditional CRDS method may come from the distortion of the detection band that modifies the decay time constant but not the exponential shape of the decay. A recently proposed solution for CRDS is to calibrate its detection system⁵. Although this ultimately provides accuracy similar to the dispersive CRDS presented here, the calibration process can only be performed in a few metrology institutes worldwide. Our dispersive CRDS technique is calibration-free and, in principle, does not require complex modifications to existing frequency-stabilized CRDS systems. More importantly, with the appropriate selection of the linear range of the detection band, this technique is practically insensitive to detection band nonlinearities. Also, its susceptibility to signal amplitude nonlinearity is two orders of magnitude smaller than in traditional CRDS. Moreover, the HCRDS dispersion spectrum is completely measured in frequencies, which allows it to be referenced to atomic frequency standard. This approach will ensure SI-traceability and can significantly facilitate the comparison of inter-laboratory data.

Analyzing the uncertainty budget of the determined line intensities (see Methods), it can be seen that the main contribution comes from pressure measurement and the uncertainty of the sample composition. This provides the unique opportunity to use the dispersive CRDS technique to develop new optical standards for gas composition and pressure based on the measurement of the spectral line intensity. Gas pressure measurement based on the resonant refractive index (i.e., spectroscopic measurement), rather than non-resonant as in current cavity-based refractometry, has the advantage of being much less sensitive to cavity deformation and diffraction effects (Gouy phase shift)⁸. These factors affect the shift of the entire comb of cavity modes, in addition to the pressure-induced changes. Although refractometric measurements of cavity mode positions relative to their vacuum positions pose a challenge, this issue does not affect the measurement of local shifts in cavity modes near molecular resonances. We expect that further development of *ab initio* line intensity calculations will drive progress in this field. A

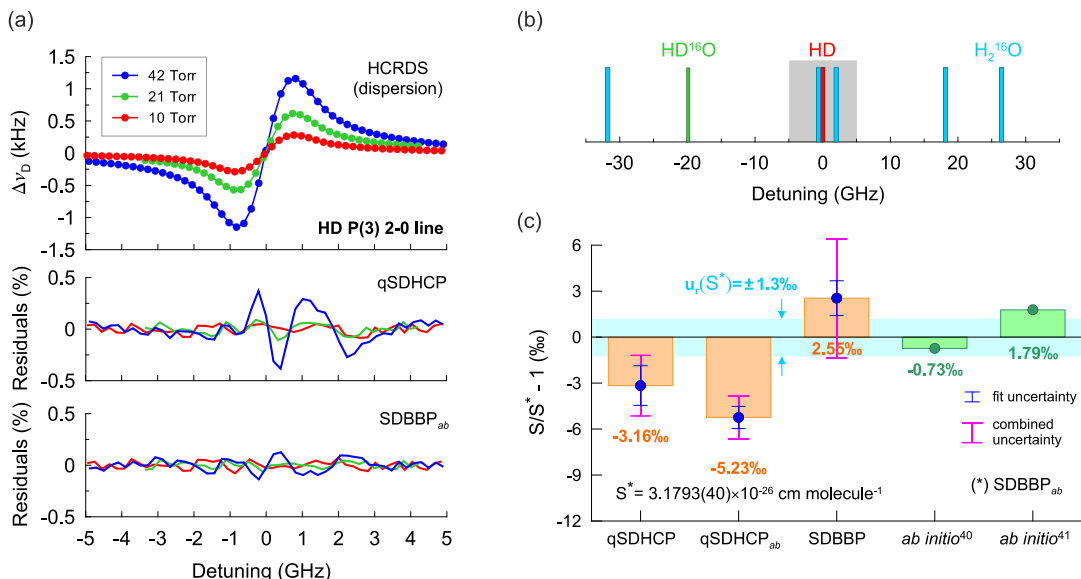


Figure 3 | Permilie-level accuracy spectroscopy of the molecular hydrogen line shape. **a**, The dispersive HCRDS spectrum of the P(3) 2-0 line of HD ($\tilde{\nu}_0 = 6798.7679 \text{ cm}^{-1}$) measured at temperature 296 K at pressures ranging from 10 to 42 Torr. The residuals below correspond to the difference between the experimental model and the fitted line-shape model. In fits qSDHCP and SDBBP_{ab} were used. The subscript *ab* indicates that line-shape parameters such as collisional width and shift, Dicke narrowing and speed dependence of collisional width and shift were set to the *ab initio* values. Each spectrum is an average of 5000-15000 spectral scans, and the signal-to-noise ratio ranges from 700:1 to 2000:1. Residuals are presented relative to the line profile amplitude at 42 Torr. Typical measurement time for one scan is 750 ms. The offset frequency of 203821.934011250 GHz is subtracted from the abscissa. **b**, Transitions in H₂¹⁶O and HD¹⁶O molecules that were included in the analysis of the HD P(3) 2-0 line. The rectangle indicates the spectral range of the HD line measurement. **c**, Line intensity measurement results of the HD spectrum from (a) and their comparison with the *ab initio* results^{40,41}. The reference line intensity S^* corresponds to SDBBP_{ab} analysis with a relative combined uncertainty of 1.23‰. Combined uncertainty includes both type A (fit uncertainty) and type B uncertainties. Results of analysis using qSDHCP, qSDHCP_{ab} and SDBBP are also shown. Permilie agreement with the *ab initio* intensity and shape of the HD line is presented.

significant contribution to the uncertainty budget of line intensity also comes from choosing the correct line-shape model. Accurate dispersive CRDS spectra can help in testing new theoretical models of intermolecular interactions and *ab initio* calculations of line intensities and line-shape parameters. As we have shown, the qSDHCP profile is no longer sufficient to accurately describe the shape of molecular hydrogen lines, and the more physical SDBBP should be used instead. The intensity of the HD line obtained using this model, combining *ab initio* line-shape parameters, agrees excellently with *ab initio*-calculated line intensity. Moreover, the results from Fig. 2c clearly show that agreement between the current most accurate experimental results for CO line intensity is better than their agreement with the most accurate *ab initio* result. Therefore, line intensities determined by our method can serve as a sub-‰ reference used in such important applications as global GHG measurements, studies of the atmosphere of exoplanets or monitoring trace humidity in semiconductor production. Finally, the presented dispersive spectroscopy stimulates an area of research devoted to very accurate *ab initio* calculations of spectral line shapes and their intensities, which have implications for both fundamental science and many applications.

References

1. Fung, I. Y., Doney, S. C., Lindsay, K., John, J. Evolution of carbon sinks in a changing climate. *PNAS* **102**, 11201-11206 (2005).
2. Thompson, D. R. et al. Atmospheric validation of high accuracy CO₂ absorption coefficients for the OCO-2 mission. *J. Quant. Spectrosc. Radiat. Transfer* **113**, 2265-2276 (2012).
3. Coplen, T. B. et al. New guidelines for $\delta^{13}\text{C}$ measurements. *Anal. Chem.* **78**, 2439-2441 (2006).
4. Fleisher, A. J. et al. Absolute $^{13}\text{C}/^{12}\text{C}$ isotope amount ratio for Vienna PeeDee Belemnite from infrared absorption spectroscopy. *Nat. Phys.* **17**, 889-893 (2021).
5. Fleisher, A. J. et al. Twenty-five-fold reduction in measurement uncertainty for a molecular line intensity. *Phys. Rev. Lett.* **123**, 043001 (2019).

6. Amato, L. S. et al. Linestrength ratio spectroscopy as a new primary thermometer for redefined Kelvin dissemination. *New J. Phys.* **21**, 113008 (2019).
7. Stock, M., Davis, R., de Mirandés, E. & Milton, M. J. T. The revision of the SI – the result of three decades of progress in metrology. *Metrologia* **56**, 022001 (2019).
8. Jousten, K. et al. Perspectives for a new realization of the pascal by optical methods. *Metrologia* **54**, S146-S161 (2017).
9. Egan, P. F. et al. Performance of a dual Fabry–Perot cavity refractometer. *Opt. Lett.* **17**, 3945 (2015).
10. Silander, I. et al. Invar-based refractometer for pressure assessments. *Opt. Lett.* **45**, 2652 (2020).
11. Słowiński, M. et al. H₂-He collisions: *Ab initio* theory meets cavity-enhanced spectra. *Phys. Rev. A* **101**, 052705-7 (2020).
12. Bielska, K. et al. Subpromille measurements and calculations of CO (3–0) overtone line intensities. *Phys. Rev. Lett.* **129**, 043002 (2022).
13. Polyansky, O. L. et al. High-accuracy CO₂ line intensities determined from theory and experiment. *Phys. Rev. Lett.* **114**, 243001 (2015).
14. O’Keefe, A. & Deacon, D. A. G. Cavity ringdown optical spectrometer for absorption measurements using pulsed laser sources. *Rev. Sci. Instrum.* **59**, 2544 (1988).
15. Long, D. A. et al. Frequency-stabilized cavity ring-down spectroscopy. *Chem. Phys. Lett.* **536**, 1-8 (2012).
16. Lin, H., Reed, Z. D., Sironneau, V. T. & Hodges, J. T. Cavity ring-down spectrometer for high-fidelity molecular absorption measurements. *J. Quant. Spectrosc. Radiat. Transfer* **161**, 11 (2015).
17. Maddaloni, P. et al. Absolute measurement of the S(0) and S(1) lines in the electric quadrupole fundamental band of D₂ around 3 μm . *J. Chem. Phys.* **133**, 154317 (2010).
18. Wójtewicz S. et al. Line-shape study of self-broadened O₂ transitions measured by Pound-Drever-Hall-locked frequency-stabilized cavity ring-down spectroscopy. *Phys. Rev. A* **84**, 032511 (2011).
19. Cygan, A. et al. One-dimensional frequency-based spectroscopy. *Opt. Express* **23**, 14472 (2015).
20. Cygan, A. et al. High-accuracy and wide dynamic range frequency-based dispersion spectroscopy in an optical cavity. *Opt. Express* **27**, 21810 (2019).
21. Cygan, A. et al. Cavity buildup dispersion spectroscopy. *Comm. Phys.* **4**, 1-9 (2021).
22. Levenson, M. D. et al. Optical heterodyne detection in cavity ring-down spectroscopy. *Chem. Phys. Lett.* **290**, 335-340 (1998).

23. Ye, J. & Hall, J. L. Cavity ringdown heterodyne spectroscopy: High sensitivity with microwatt light power. *Phys. Rev. A* **61**, 061802(R)-4 (2000).
24. He, Y. & Orr, B. J. Rapidly swept, continuous-wave cavity ringdown spectroscopy with optical heterodyne detection: single- and multi-wavelength sensing of gases. *Appl. Phys. B* **75**, 267-280 (2002).
25. Truong, G.-W. et al. Frequency-agile, rapid scanning spectroscopy. *Nat. Photon.* **7**, 532-534 (2013).
26. Miller, C. E. et al. Precision requirements for space-based XCO₂ data. *J. Geophys. Research* **112**, D10314 (2005).
27. Galli, I. et al. Sensing below parts per trillion: radiocarbon-dioxide optical detection. *Phys. Rev. Lett.* **107**, 270802-4 (2011).
28. Gianfrani, L. Linking the thermodynamic temperature to an optical frequency: recent advances in Doppler broadening thermometry. *Phil. Trans. R. Soc. A* **374**, 20150047 (2016).
29. Anderson, D. Z., Frisch, J. C. & Masser, C. S. Mirror reflectometer based on optical decay time. *Appl. Opt.* **23**, 1238 (1984).
30. Peiponen, K.-E. & Saarinen J. J. Generalized Kramers-Kronig relations in nonlinear optical- and THz spectroscopy. *Rep. Prog. Phys.* **72**, 056401 (2009).
31. Lance, B., Blanquet, G., Walrand, J. & Bouanich, P. On the speed-dependent hard collision lineshape models: Application to C₂H₂ perturbed by Xe. *J. Mol. Spectrosc.* **185**, 262-271 (1997).
32. Pine, A. S. Asymmetries and correlations in speed-dependent Dicke-narrowed line shapes of argon-broadened HF. *J. Quant. Spectrosc. Radiat. Transfer* **62**, 397-423 (1999).
33. Ngo, N. H., Lisak, D., Tran, H. & Hartmann, J.-M. An isolated line-shape model to go beyond the Voigt profile in spectroscopic databases and radiative transfer codes. *J. Quant. Spectrosc. Radiat. Transfer* **129**, 89-100 (2013).
34. Tennyson, J. et al. Recommended isolated-line profile for representing high-resolution spectroscopic transitions : IUPAC technical report. *Pure and Applied Chemistry* **86**, 1931-1943 (2014).
35. Cygan, A. et al. Cavity mode-width spectroscopy with widely tunable ultra-narrow laser. *Opt. Express* **21**, 29744 (2013).
36. Ciurylo, R., Shapiro, D. A., Drummond, J. R., May, A. D. Solving the line-shape problem with speed-dependent broadening and shifting and with Dicke narrowing. II. Application. *Phys. Rev. A* **65**, 012502 (2001).
37. Wcislo, P., Cygan, A., Lisak, D. & Ciurylo, R. Iterative approach to the line-shape calculations based on the transport/relaxation equation. *Phys. Rev. A* **88**, 012517-8 (2013).
38. Kassi, S. & Campargue, A. Electric quadrupole and dipole transitions of the first overtone band of HD by CRDS between 1.45 and 1.33 μm . *J. Mol. Spectrosc.* **267**, 36-42 (2011).
39. Kassi, S. & Campargue, A. Electric quadrupole transitions and collision-induced absorption in the region of the first overtone band of H₂ near 1.25 μm . *J. Mol. Spectrosc.* **300**, 55-59 (2014).
40. Pachucki, K., Komasa, J. Electric dipole rovibrational transitions in the HD molecule. *Phys. Rev. A* **78**, 052503 (2008).
41. Jóźwiak, H., Cybulski, H. & Wcislo, P. Positions and intensities of hyperfine components of all rovibrational dipole lines in the HD molecule. *J. Quant. Spectrosc. Radiat. Transfer* **253**, 107171 (2020).

Methods

The influence of light detection nonlinearity on the accuracy of spectral line intensity measurement

In order to gain a comprehensive understanding of how distortions in the ring-down decay signals, induced by the nonlinearity of light intensity detection, impact the accuracy of determined spectral line intensities, it was necessary to initially model the temporal response of the cavity to laser beam deactivation. Subsequently, we simulated conditions close to the experimental ones, in which nonlinear light detection effects modify the measured intensity of the light, which emerges from the cavity.

Immediately injecting light at the frequency ω into the cavity results in a cavity response at the frequency ω_c with temporal inertia described by Γ_c^{-1} . The electric field leaving the cavity is a superposition of the laser and cavity fields:

$$E_{\text{out}}^{\text{ON}}(t) = E_{\text{out}}^0 \frac{\Gamma_c^0}{\Gamma_c - i\delta\omega} (e^{-i\omega t} - e^{-\Gamma_c t} e^{-i\omega_c t}), \quad (2)$$

where $\delta\omega = \omega - \omega_c$ is angular frequency detuning of the laser beam from the cavity mode center, the angular frequency $\Gamma_c = -t_r^{-1} \ln(R e^{-\alpha L})$ relates to the measured cavity mode half width at half maximum $\gamma_c = (2\pi)^{-1} \Gamma_c$, R is reflectance of the cavity mirror, α is the absorption coefficient of the intra-cavity gas sample, $\Gamma_c^0 \approx t_r^{-1} (1 - R)$ is Γ_c for $\alpha = 0$ and $t_r^{-1} = \text{FSR}$. Note that the complex Lorentz function $(\Gamma_c - i\delta\omega)^{-1}$, characterized by α -dependent width Γ_c , relates to the cavity mode shape and quantizes the fraction of the laser field which is transmitted through the cavity when the laser frequency is detuned by $\delta\omega$ away from the cavity mode center. The structure of Eq. (2) indicates the interference pattern with the modulation frequency $\delta\omega$ that will appear on the light transmitted through the cavity in typical cavity-enhanced systems before a steady state is reached²¹.

When the laser beam is turned off at a time t_0 , the process of the intracavity light decay begins. Assuming that the laser field is turned off at the rate of Γ_0 , the field passing through the cavity has a two-part form:

$$E_{\text{out}}^{\text{OFF}}(t) = E_{\text{out}}^0 e^{-i\omega t_0} \Gamma_c^0 \left\{ \frac{1 - (1 - \Gamma_c/\Gamma_0 + i\delta\omega/\Gamma_0) e^{-(\Gamma_c - i\delta\omega)t_0}}{(1 - \Gamma_c/\Gamma_0 + i\delta\omega/\Gamma_0)(\Gamma_c - i\delta\omega)} \times e^{-(\Gamma_c + i\omega_c)(t-t_0)} + \frac{1}{\Gamma_c - \Gamma_0 - i\delta\omega} e^{-(\Gamma_0 + i\omega)(t-t_0)} \right\}, \quad (3)$$

where the first part describes the exponential decay of the cavity mode field with the time-constant Γ_c^{-1} and the second part is the adopted model of the exponential decay of the laser field. The amplitude of the laser field passing through the cavity depends on the detuning $\delta\omega$ of the laser from the center of the cavity mode, the profile of which is defined as before by the complex Lorentz function, but with a width modified to $\Gamma_c - \Gamma_0$. Note that even if initially the laser and cavity are not frequency matched, the ring-down decay is always observed at the cavity mode frequency ω_c . This observation, as well as Eq. (3), are in good agreement with the calculations provided in Ref.⁴². If the laser light is turned off very quickly such that $\Gamma_0 \gg \Gamma_c$ and $\Gamma_0 \gg \delta\omega$, the first term in Eq. (3) dominates and the expression for $E_{\text{out}}^{\text{OFF}}(t)$ can be reduced to a simple single-exponential decay form

$$E_{\text{out}}^{\text{OFF}}(t) = E_{\text{out}}^{\text{ON}}(t_0) e^{-(\Gamma_c + i\omega_c)(t-t_0)}. \quad (4)$$

However, if the laser turn-off rate Γ_0 is relatively small and/or the extinction ratio of the laser field amplitude is low, e.g. 50 dB⁴³, then Eq. (3) clearly shows that the recorded light decay will be distorted as a result of interference at the frequency $\delta\omega$ between the laser and cavity fields. In our CRDS and HCRDS measurements, this situation did not occur because Γ_0 was more than 600 times larger than Γ_c and the extinction ratio of the laser field was ~ 80 dB.

In the HCRDS method, the ring-down decay field described by Eq. (4) is beaten with the laser field of the local oscillator (LO). The field incident on the detector is

$$E_{\text{out}}^{\text{OFF}}(t) = E_{\text{out}}^{\text{ON}}(t_0) e^{-(\Gamma_c + i\omega_c)(t-t_0)} + E_L e^{i\varphi_L} e^{i\omega_L(t-t_0)}, \quad (5)$$

where E_L , ω_L and φ_L are the amplitude, angular frequency, and phase of the LO field. The corresponding light intensity $\sim |E_{\text{out}}^{\text{OFF}}|^2$ is

$$I_{\text{out}}(t) = I_L + I_C e^{-2\Gamma_c t} + 2I_B e^{-\Gamma_c t} \cos(\delta\omega_{\text{CL}} t), \quad (6)$$

where $\delta\omega_{\text{CL}} = \omega_c - \omega_L$ is the beat frequency between the cavity and LO fields. If ω_L is known, the cavity mode position can be easily calculated from the measured value of $\delta\omega_{\text{CL}}$. We note that ω_L needs to be known only on a local frequency axis associated with the cavity modes. Analysis of the Lorentz peak at the frequency $\delta\omega_{\text{CL}}$ in the power spectrum of the light intensity I_{out} provides information about

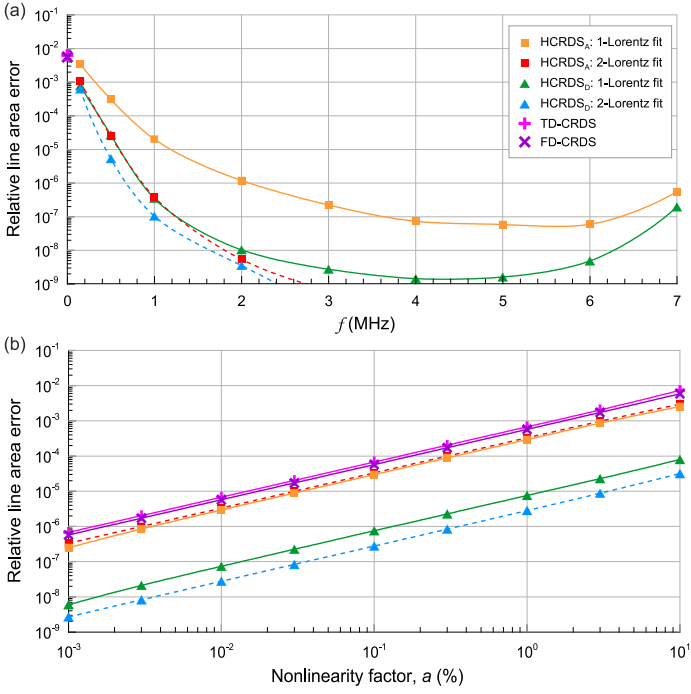


Figure 4 | Nonlinearity of light detection. **a**, The influence of the detection system transfer function, from Fig. 1b, on the accuracy of the line area determined from the simulated absorption and dispersion line profiles in HCRDS and CRDS. The f axis corresponds to the beat frequencies between the LO laser and the cavity response (for CRDS $f = 0$). HCRDS results are presented for both absorption (HCRDS_A) and dispersion (HCRDS_D). Data marked as 1-Lorentz and 2-Lorentz correspond to different models used in the analysis of power spectra of heterodyne ring-downs. Results for traditional CRDS were obtained from both time (TD-CRDS) and frequency (FD-CRDS) domain analysis. **b**, The influence of the nonlinearity of the detection system amplitude on the accuracy of the line area determined from simulated absorption and dispersion line profiles in HCRDS and CRDS. Results for different values of the nonlinearity parameter, a , are presented.

both the dispersion shift of the cavity mode and its absorption broadening.

The transfer function (TF) of the detection system of the spectrometer, described in Supplementary Section S1, was measured as its amplitude response to changes in the beat signal frequency of the detected light. We developed the TF model as a linear combination of complex-valued high-pass and low-pass filter functions. The parameters of this model were selected to reproduce best the experimental shape of the TF shown in Fig. 1b. To test the line intensity accuracy against the nonlinearity of the detection system's bandwidth, the absorption and dispersion profile was simulated with the line intensity and shape parameters corresponding to the R(23) 3-0 CO transition at a pressure of 10 Torr. The light decay signal was simulated using Eq. (6) for each frequency and Fourier transformed. The result was multiplied by our complex-valued TF model and inverse Fourier transformed to reproduce the ring-down decay having a different shape than the original exponential one. The power spectra of the reproduced heterodyne ring-down decays were then analyzed, focusing on the frequency range around the frequency $\delta\omega_{CL}$. Two models, a single Lorentz profile centered on the frequency $\delta\omega_{CL}$ and two Lorentz profiles centered on $\delta\omega_{CL}$ and zero frequencies, were included in the analysis to provide the beat frequency parameter $\delta\omega_{CL}$ (for HCRDS dispersion) and cavity mode width (for HCRDS absorption). Finally, the line area determined from the obtained absorption and dispersion profiles was compared with the simulated value, and the systematic deviation from it was calculated. The entire procedure was repeated for several beat frequencies up to 7 MHz. The results are shown in Fig. 4a. In the same figure, we also present results for

CRDS. The procedure for simulating distorted light decays was similar to that described above for HCRDS, starting with single-exponential decay signals. Their analysis was performed both traditionally in the time domain, determining the time constant, and in the frequency domain using the Lorentz peak of the power spectrum on the zero frequency to determine the cavity mode width. The results for HCRDS are clearly better than those for CRDS for all frequencies in the tested range of $\delta\omega_{CL}$. Note that the greatest advantage of HCRDS over CRDS at the relative accuracy level 10^{-7} is visible for the most linear range of the detection band around the frequency of 4 MHz. Furthermore, dispersive HCRDS, with an accuracy level $> 10^{-9}$, appears to be more accurate than absorptive one. Using the model with simultaneous fitting of two Lorentz profiles further improves the accuracy of the retrieved line intensity, especially in the case of absorption HCRDS.

In tests of the line intensity accuracy in terms of the nonlinearity of the detection system amplitude, the heterodyne ring-down decays simulated using Eq. (6) were multiplied by the nonlinearity function²¹ $y(t) = 1 - a I_{out}(t)/I_{out}^{max}$, where I_{out}^{max} is the maximum amplitude of $I_{out}(t)$ and a is the amplitude nonlinearity parameter in %. As before, the heterodyne ring-down decays were simulated at each frequency in the simulated CO spectrum. Absorption and dispersion profiles were obtained from them and the determined line area was compared with the simulated one. The results are shown in Fig. 4b. In the simulation for HCRDS we chose $\delta\omega_{CL} = 4$ MHz. To analyze the Lorentz peak in the power spectrum, as before, both the single Lorentz profile centered on the frequency $\delta\omega_{CL}$ and two Lorentz profiles centered on $\delta\omega_{CL}$ and 0 frequencies were used. The CRDS results included the decay signal analysis in both time and frequency domains. From Fig. 4b it can be seen that the method of analyzing the light decays in CRDS does not affect the dependence of the line intensity accuracy on a parameter. HCRDS absorption results are similar to CRDS results. However, for dispersive HCRDS we observe a two-order improvement in line intensity accuracy compared to CRDS and absorption HCRDS. This immunity to nonlinear detection is due to the fact, that any deformations of the Lorentz peak amplitude, but symmetrical about its center, will not affect its position. As before, the 2-Lorentz fitting model further improves the line intensity accuracy.

Uncertainty budget for CO and HD line intensities

The intensity of the spectral line can be calculated as $S = A/N_a$, where A is the line area determined from the line shape analysis and N_a is the concentration of absorbers (number of molecules per volume) determined as a κ fraction of the total gas concentration N , $N_a = \kappa N$. Measuring the total pressure p of the gas sample and its temperature T , the total gas concentration N can be determined from the ideal gas law $N = p(k_B T)^{-1}$, where k_B is the Boltzmann constant. As a result we obtain the following formula for the line intensity S measured at temperature T , $S(T) = k_B T A (\kappa p)^{-1}$. Note that the intensity of the line generally depends on the temperature. To take this into account, we define a temperature-dependent function $f_S(T) = \frac{S(T_0)}{S(T)}$, where T_0 is the reference temperature. The final expression for the line intensity determined for the reference temperature T_0 from a spectrum measured at temperature T is

$$S(T_0) = k_B f_S(T) T A (\kappa p)^{-1}. \quad (7)$$

The function $f_S(T)$ can be calculated based on the ratio of total internal partition functions provided by the HITRAN database⁴⁴.

To estimate the combined uncertainty $u(S)$ of the line intensity determined for T_0 , it should be noted that the quantities $f_S(T)$ and T in Eq. (7) are mutually dependent. Hence, the non-zero covariance of these quantities $C_{T,f_S} = \left(\frac{\partial f_S}{\partial T}\right) u^2(T)$ must be taken into account in the calculation of $u(S)$. Assuming that the remaining quantities in Eq. (7) are independent of each other, we found the following formula for

Table 1 | Uncertainty budget for CO line intensity. This table contains the quantities x taken into account when estimating the combined CO line intensity uncertainty using equation (8). Type A standard uncertainties and type B standardized uncertainties of x , and the corresponding combined uncertainties $u(x)$ are given. Uncertainties of the line area, A , are shown for used measurement methods. The combined uncertainty of the line intensity $u(S)$ is given for each method. We also show the value of $u(\langle S \rangle)$ estimated for the mean line intensity $\langle S \rangle$ obtained from the CMDS and HCRDS dispersion measurement results. For each measurement method, the bias of the line intensity from $\langle S \rangle$ is also shown. All values are given in promilles.

Method	Quantity, x	Type A (‰)	Type B (‰)	$u(x)/x$ (‰)	$u(S)/S$ (‰)	$u(\langle S \rangle)/\langle S \rangle$ (‰)	Bias from $\langle S \rangle$ (‰)
	T	< 0.01	0.1	0.1			
	p	0.05	0.62	0.62			
	κ		0.44	0.44			
CMDS	A	0.20	0.32	0.38	0.91	0.86	0.04
HCRDS (dispersion)	A	0.18	0.24	0.30	0.88		-0.04
CMWS	A	0.17	0.39	0.43	0.93		-0.34
HCRDS (absorption)	A	0.23	0.11	0.26	0.87		-0.75
CRDS	A	0.50	2.04	2.10	2.30		-9.34

Table 2 | Uncertainty budget for HD line intensity. This table contains the quantities x taken into account when estimating the combined HD line intensity uncertainty using equation (8). Type A standard uncertainties and type B standardized uncertainties of x , and the corresponding combined uncertainties $u(x)$ are given. Uncertainties of the line area A are shown for the various profiles we used in line shape analysis. The combined uncertainty of the line intensity $u(S)$ is given for each profile. For each profile, the bias of the line intensity from S^* , obtained from SDBBP analysis with *ab initio* values of line-shape parameters, is also shown. All values are given in promilles.

Profile	Quantity, x	Type A (‰)	Type B (‰)	$u(x)/x$ (‰)	$u(S)/S$ (‰)	Bias from S^* (‰)
	T	< 0.01	0.1	0.1		
	p	0.05	0.62	0.62		
	κ		1	1		
SDNGP	A	1.29	0.93	1.59	1.98	-3.16
SDNGP (ab initio)	A	0.72	< 0.01	0.72	1.38	-5.23
SDBBP	A	1.13	3.51	3.69	3.87	2.54
SDBBP* (ab initio)	A	0.36	< 0.01	0.36	1.23	

the square of the relative uncertainty of the line intensity determined for the temperature T_0

$$\frac{u^2(S)}{S^2} \Big|_{T_0} = \left[\frac{1}{T^2} + \frac{1}{f_s^2} \left(\frac{\partial f_s}{\partial T} \right)^2 \right] u^2(T) + \frac{u^2(p)}{p^2} + \frac{u^2(A)}{A^2} + \frac{u^2(\kappa)}{\kappa^2}. \quad (8)$$

This expression was used to estimate the relative combined uncertainties of CO and HD line intensities reported here. The corresponding line intensity uncertainty budgets are presented in Tables 1 and 2. It should be noted that when estimating the combined uncertainty of the CO line intensity, which is the average of the results of the dispersion HCRDS and CMDS methods, only the measurements of A could be treated as independent, while the measurement of T , p , and κ was common to both methods. As a result, the combined uncertainty of the average line intensity $u(\langle S \rangle)$ was

calculated by inserting the relative standard deviation $u(A)/A$ of the mean value of A from both measurement methods into Eq. (8). Let us also note that in the case of HD molecule, the quantity κ is determined not by the isotope composition as it is for CO, but by the purity of the HD sample.

It is worth mentioning how deviations from the ideal gas law affect the line intensity values reported here. We limit ourselves to the first correction in the expanded gas law $p = Nk_B T(1 + B(T)N + C(T)N^2 + \dots)$, where $B(T)$, $C(T)$ are virial coefficients of the second and third order, which reduces the expression for N to the form $N = p(k_B T)^{-1}(1 - pp_n^{-1}T_n T^{-1}V_n^{-1}B(T))$, where p_n , T_n , V_n describe normal conditions. For the measured CO and HD transitions the virial coefficients $B(T)$ determined at a temperature of 296 K are $-8 \text{ cm}^3/\text{mol}$ (Ref.⁴⁵) and $+14 \text{ cm}^3/\text{mol}$ (Ref.⁴⁶), respectively. They correspond to CO and HD line intensity relative corrections of -4.334×10^{-6} and 3.034×10^{-5} , which were calculated for the highest pressures of 10 Torr and 40 Torr, at which the spectra of CO

and HD molecules were measured. These changes are at least two orders of magnitude lower than the accuracy of the determined here line intensities, so they are not included in the uncertainty budget.

References

- Anderson, D. Z., Frisch, J. C. & Masser, C. S. Mirror reflectometer based on optical decay time. *Appl. Opt.* **23**, 1238 (1984).
- Long, D. A., Wójtewicz, S. & Hodges, J. T. Effects of incomplete light extinction in frequency-agile, rapid scanning spectroscopy. *Proc. SPIE* **8726**, 872600 (2013).
- Gordon, I.E. et al. The HITRAN2020 molecular spectroscopic database. *J. Quant. Spectrosc. Radiat. Transfer* **277**, 107949 (2022).
- Bousheheri, A., Bzowski, J., Kestin, J. & Mason, E. A. Equilibrium and transport properties of eleven polyatomic gases at low density. *J. Phys. Chem. Ref. Data* **16**, 445 (1987).
- Garberoglio, G., Jankowski, P., Szalewicz, K. & Harvey, A. H. Second virial coefficients of H₂ and its isotopologues from a six-dimensional potential. *J. Chem. Phys.* **137**, 154308 (2012).

Acknowledgments

A.C., H.J., D.L. were supported by the National Science Centre in Poland through Project No. 2020/39/B/ST2/00719. S.W. was supported by the National Science Centre in Poland through Projects No. 2020/39/B/ST2/00719 and 2021/42/E/ST2/00152. N.S. was supported by the National Science Centre in Poland through Project No. 2019/35/B/ST2/01118. K.B. was supported by the National Science Centre in Poland through Project No. 2018/30/E/ST2/00864. R.C. was supported by the National Science Centre in Poland through Project No. 2021/41/B/ST2/00681. For the purpose of Open Access, the author has applied a CC-BY public copyright licence to any Author Accepted Manuscript (AAM) version arising from this submission. P.W. is funded by the European Union (ERC-2022-STG,H2TRAP,101075678). Views and opinions expressed are however those of the author(s) only and do not necessarily reflect those of the European Union or the European Research Council Executive Agency. Neither the European Union nor the granting authority can be held responsible for them. The research is part of the program of the National Laboratory FAMO in Toruń, Poland.

Author contributions

A.C. and D.L. conceived the idea of eliminating systematic errors in CRDS using heterodyne dispersive cavity ring-down spectroscopy. A.C. and D.L. designed the concept of the research and performed measurements. A.C., S.W., G.K., N.S., K.B., D.L. prepared the experimental setup. A.C., S.W., R.C., D.L. performed data analysis. H.J. and P.W. performed ab initio calculations. A.C. wrote the original draft of the manuscript, and all authors contributed to the final manuscript. A.C. and D.L. coordinated the project.

Competing interests

The authors declare no competing interests.

Additional information

The manuscript contains supplementary material.

Supplementary material

Heterodyne dispersive cavity ring-down spectroscopy exploiting eigenmode frequencies for high-fidelity measurements

Agata Cygan, Szymon Wójtewicz, Hubert Jóźwiak, Grzegorz Kowzan, Nikodem Stolarczyk, Katarzyna Bielska, Piotr Wcisło, Roman Ciuryło, Daniel Lisak

Institute of Physics, Faculty of Physics, Astronomy and Informatics, Nicolaus Copernicus University in Toruń, Grudziadzka 5, 87-100 Torun, Poland

Section S1. HCRDS experiment

A sketch of the experimental system implementing the HCRDS method is shown in Fig. S1a. To measure the shapes of the CO and HD lines, two external cavity diode lasers (*Toptica CTL*) were used, covering the spectral ranges of 1520-1630 nm and 1460-1570 nm, respectively. In each case, the laser beam was divided into two orthogonally polarized beams. An s-polarized beam, phase-modulated at 20 MHz by a narrow-band electro-optic modulator (EOM), was used to lock the laser to the optical cavity using the Pound-Drever-Hall scheme¹. The frequency stability of this lock was at the Hz level. A small portion of the p-polarized laser beam was transmitted via optical fiber to an optical frequency comb system (*Menlo Systems*) to enable continuous measurement of the absolute laser frequency. The main part of the p-polarized beam was further split into two beams - one for excitation of the optical cavity mode and the other for the reference heterodyne detection of light decays from the cavity. Both beams were frequency-stepped using a broad-band electro-optic modulator (B-EOM) and a microwave driver². Although such configuration generates a series of sidebands on the laser, the optical cavity acts as a spectral filter, allowing only one sideband of the excitation beam to resonate with the cavity. Similarly, in the case of heterodyne detection the limited detection system bandwidth allows the observation of the decay of the beat signal with only one sideband of the reference beam. We chose a first-order sideband that enables scanning of the excitation and reference beams in the frequency range of 0.2 – 20 GHz. Note, however, that the scanning range can be further multiplied by choosing a higher-order sideband. The ring-down decays were initiated after turning off the excitation beam by an acousto-optic modulator (AOM) driven by frequency f_A . This AOM also shifts the carrier frequency by almost one free spectral range of the cavity (FSR \approx 204.35 MHz) and beyond the cavity resonance to avoid its influence on the measurement of ring-down signals and locking the laser to the cavity. Another AOM detunes the frequency of the reference beam from the frequency of the excitation beam by a constant value of $\delta\nu_{PL}$ equal to several MHz.

The optical cavity was formed by two high-reflectivity mirrors placed at a distance of \sim 73 cm from each other. The mirrors are dual-wavelength coated to use a separate laser wavelength (1064 nm) to stabilize the cavity length³. This was done with respect to the I_2 -stabilized Nd:YAG laser characterized by long-term frequency stability of 1 kHz. The double-pass acousto-optic modulator system⁴ and phase-sensitive detection were used to generate an error signal in the cavity length locking loop servomechanism. Two sets of cavity mirrors were used for HCRDS measurements - one for the CO molecular system and the other for HD. They were characterized by a reflectance coefficient of 0.999925 and 0.999993, corresponding to full widths at half maximum of the cavity mode of 4.9 kHz and 0.43 kHz, respectively. They lead to cavity finesses of 41900 and 449000 and ring-down time constants of 32 μ s and 350 μ s, respectively. In R(23) 3-0 CO transition measurements, we used a commercial sample of CO with purity of 0.99997, produced by the reaction of water with petrogenic natural gas having an estimated $^{13}\text{C}_{VPDB}$ isotope content of -40‰ with respect to the Vienna PeeDee Belemnite scale⁵. In P(3) 2-0 HD transition measurements, we used a commercial HD sample characterized by a purity of 97.0%. During the measurements, the sample gas pressure was measured in parallel using three manometers (*MKS Baratron 690A* with 10 and 100 Torr full range and *Mensor CPG2500* with 900 Torr full range) with the highest relative combined uncertainty of 6×10^{-4} . The cavity temperature was stabilized at 296 K with a total standard uncertainty of 30 mK. Analog ring-down decays, measured with a DC-coupled photodetector (*New Focus 2053*) with a bandwidth of up to 7 MHz, were digitized with an oscilloscope card characterized by a bandwidth of 100 MHz and 14-bit vertical resolution (*National Instruments PCI-5122*).

To scan the molecular transition the B-EOM modulation frequency was stepped in increments of the FSR. A list of necessary frequencies was prepared and loaded into the microwave generator's memory before each spectrum measurement for fast frequency switching. Then the TTL signal controlled the determination of subsequent frequencies

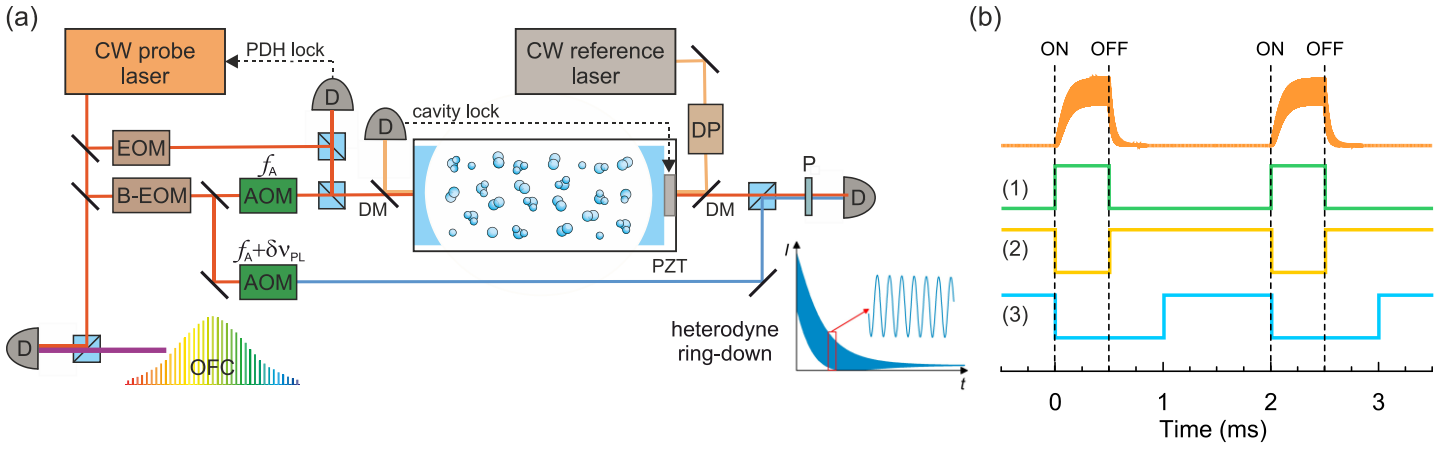


Figure S1 | HCRDS experiment. **a**, A continuous-wave (CW) probe laser is locked to the cavity by the Pound-Drever-Hall (PDH) method. An electro-optic modulator (EOM) modulates the laser light phase to generate the PDH error signal. The cavity length is stabilized with respect to another CW reference laser. The absolute frequency of the laser is measured using the optical frequency comb (OFC). The intracavity gas sample is probed using a single sideband of the broad-band electro-optic modulator (B-EOM) scanning in the microwave range. Acousto-optical modulators (AOM) are used to detune the carrier frequency from the cavity resonance by f_A , and also to detune the local oscillator beam from the probe beam by $\delta\nu_{PL}$. The inset presents an example of a heterodyne ring-down signal. Explanation of abbreviations: D – photodetector, DM – dichroic mirror, PZT – piezo transducer, OFC – optical frequency comb, P – polarizer, DP – double-pass AOM system. **b**, Top: heterodyne response of the cavity to periodic laser power switching. Below: time sequences of TTL signals used in the HCRDS experiment to trigger ring-down signals (1), to start the data acquisition process (2) and to determine the frequency switching time of the microwave generator controlling B-EOM (3).

at the generator output. The time sequences of the TTL signals used in the experiment to control the onset of ring-down signal measurements and data acquisition process and to determine the frequency switching time of the microwave driver are shown in Fig. S1b. The typical TTL signal period was ~ 2 ms for CO measurements and ~ 15 ms for HD measurements. During this time the heterodyne decay signal was acquired, the frequency of the microwave generator was changed, and the cavity was pumped with light at the new frequency. The frequency switching time of the microwave generator was < 1 ms. The size of the frequency list loaded into the microwave generator's memory allowed the entire spectrum to be measured several dozen times without interruption. After collecting the appropriate amount of data, the initial averaging process began. For each frequency in the spectrum, the power spectra, not the decays themselves, were averaged due to slow phase changes in the collected heterodyne light decays for that frequency. From the finally averaged power spectra of heterodyne ring-down signals, information on the positions and widths of cavity modes was obtained, and from them, the absorption and dispersion spectra were obtained. For CO measurements, 5000 spectral scans were collected, while for HD, it was 5000-15000.

Section S2. *Ab initio* calculations of line parameters for the HD molecule

Quantum scattering calculations were performed on the potential energy surface (PES) of the H_2 - H_2 system⁶ within the Born-Oppenheimer (BO) approximation for the separation of electronic and nuclear motion. The PES is six-dimensional, i.e., it depends on the intermolecular distance, \tilde{R} , the three Jacobi angles, θ_1 , θ_2 , and $\varphi = \varphi_1 - \varphi_2$, and the intramolecular distances, r_1 and r_2 (see Ref.⁶ for details). Since the PES is calculated in the BO approximation, it can be used to study all possible combinations of hydrogen isotopologues, provided that the Jacobi angles are transformed accordingly⁷⁻⁹. Here, we used the H_2 - H_2 PES to study HD-HD collisions.

To solve the coupled channels equations, the PES was expanded over bispherical harmonics, $I_{l_1 l_2 l_{12}}(\theta_1, \theta_2, \varphi)$

$$V(\tilde{R}, r_1, r_2, \theta_1, \theta_2, \varphi) = \sum_{l_1 l_2 l_{12}} A_{l_1 l_2 l_{12}}(\tilde{R}, r_1, r_2) I_{l_1 l_2 l_{12}}(\theta_1, \theta_2, \varphi), \quad (6)$$

where the bispherical harmonics are defined as

$$I_{l_1 l_2 l_{12}}(\theta_1, \theta_2, \varphi) = \sqrt{\frac{2l_{12} + 1}{4\pi}} \sum_m C_{m, -m, 0}^{l_1 l_2 l_{12}} Y_{l_1 m}(\theta_1, \varphi_1) Y_{l_2, -m}(\theta_2, \varphi_2). \quad (7)$$

Here, $C_{m, -m, 0}^{l_1 l_2 l_{12}}$ are the Clebsch-Gordan coefficients, and $Y_{lm}(\theta, \varphi)$ denotes the spherical harmonic. Since both collisional partners are heteronuclear, the indices cover both even and odd values, with the restriction that $|l_1 - l_2| \leq l_{12} \leq l_1 + l_2$, and that the sum $l_1 + l_2 + l_{12}$ is an even integer. We note that the expansion terms with odd l_1 and l_2 (which are absent in the

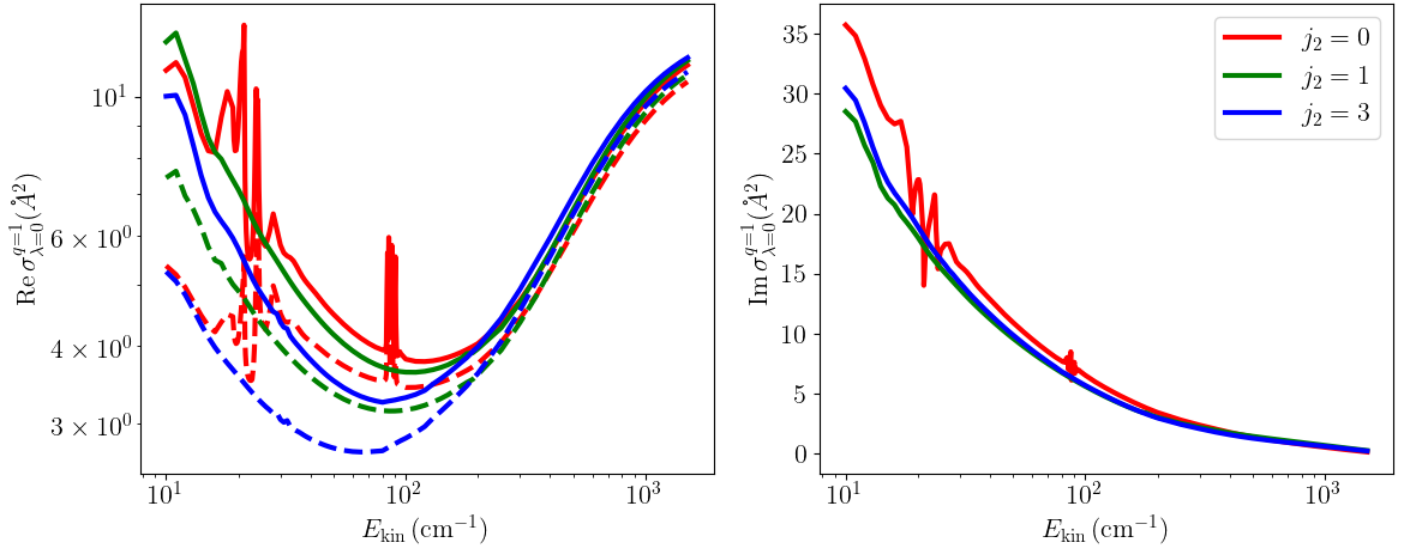


Figure S3 | Generalized spectroscopic cross-sections. Pressure broadening (left panel) and pressure shift (right panel) cross sections of the self-perturbed P(3) 2-0 line in HD, for selected rotational quantum numbers of the perturbing molecule. The dashed lines in the left panel correspond to the inelastic contribution to the pressure broadening cross-section.

expansion of the PES for the $\text{H}_2\text{-H}_2$ system) emerge due to the coordinate transformation (the center-of-mass shift). The sum over l_1, l_2, l_{12} was terminated at the 140th term corresponding to 6,6,12, which ensured the reconstruction of the initial HD-HD PES with a relative root-mean-square error at the level of $1.2 \times 10^{-2} \%$.

The expansion coefficients, $A_{l_1 l_2 l_{12}}(\tilde{R}, r_1, r_2)$, were averaged over the internuclear coordinates, r_1 and r_2 , corresponding to the spectroscopically active and perturbing molecules, respectively. The spectroscopically active molecule may be in the ground ($\nu = 0$) or the second excited ($\nu = 2$) vibrational states, while the perturbing molecule is always in the ground vibrational state (justified for the experimental temperature of 296 K). Thus, the average was performed by integrating the radial coupling terms with the weight corresponding to the squared modulus of the isolated HD wavefunction in the $\nu = 0, j = 3$ and $\nu = 2, j = 2$ rovibrational states (for the average over r_1) and $\nu = 0, j$ (for the average over r_2), where j corresponds to the rotational level of the perturbing HD molecule. The wave functions of isolated HD molecules were obtained by solving the rovibrational Schrödinger equation for the HD molecule with the potential energy curve from Ref.¹⁰ using the Discrete Variable Representation - Finite Basis Representation method.

The close-coupling equations were solved in the body-fixed frame¹¹ using the renormalized Numerov's algorithm for energies in the range $E_{\text{kin}} \in (10, 1500) \text{ cm}^{-1}$ with various steps, to describe the channel-opening effects accurately. At sufficiently large \tilde{R} , the log-derivative matrix was transformed to the space-fixed frame, where boundary conditions were imposed, allowing for the recovery of S-matrix elements. The convergence of the scattering S-matrix is ensured by a proper choice of the integration range, propagator step, the size of the rovibrational basis, and the number of partial waves contributing to each scattering event¹¹. Calculations were performed using the in-house quantum scattering code BIGOS.

The scattering S-matrix elements were used to calculate the generalized spectroscopic cross-sections, $\sigma_{\lambda}^q(\nu_i, j_i, \nu_f, j_f, j_2; E_{\text{kin}})^{11-13}$. Here, q is the tensor rank of the spectral transition operator (for the electric dipole transition considered here, $q=1$), that drives the transition from the $\nu_i = 0, j_i = 3$ to the $\nu_f = 2, j_f = 2$ state in HD. The symbol j_2 denotes the rotational quantum number of the perturbing molecule, and λ is the rank of the velocity tensor. For $\lambda = 0$, the real and imaginary parts of σ correspond to the standard pressure broadening (PBXS) and shift (PSXS) cross sections, respectively. For $\lambda = 1$, the generalized spectroscopic cross section corresponds to the complex Dicke cross section associated with motion narrowing.

Figure S3 presents the pressure broadening (left panel) and pressure shift (right panel) cross-sections for the self-perturbed 2-0 P(3) line in HD. The PBXS for all considered values of j_2 exhibit similar behavior to the one observed in He-perturbed lines of H_2 ¹⁴ and HD¹⁵. First, values of the cross-sections decrease with increasing kinetic energy, then pass through a minimum in the vicinity of $E_{\text{kin}} \approx 100 \text{ cm}^{-1}$, and increase in the high-collision energy regime. The dashed lines in the top left panel of Fig. S3 present the inelastic contribution to collisional broadening, i.e., a half-sum of the total inelastic cross-sections in the initial and final spectroscopic states (see Eq. (10) in Ref.¹⁶). In contrast to He-perturbed HD lines¹⁵, the inelastic contribution to the broadening of self-perturbed HD lines is much more significant, constituting more than 90% of the broadening at kinetic energies larger than 100 cm^{-1} . This is attributed to the presence of inelastic channels absent in atom-molecule collisions, i.e., rotational (de-)excitation of the perturber.

Both the PBXS and PSXS for $j_2 = 0$ exhibit resonant features at kinetic energies in the vicinity of 23 cm^{-1} and 90 cm^{-1} . These features are associated with channel-opening effects: at $E_{\text{kin}} = 22.8690 \text{ cm}^{-1}$, the $(\nu_1, j_1, \nu_2, j_2) \rightarrow (\nu'_1, j'_1, \nu'_2, j'_2) =$

(2,2,0,0) \rightarrow (2,0,0,2) process becomes energetically accessible. This represents a quasi-resonant transfer of rotational quanta $\Delta j = 2$ between HD molecules, with an energy mismatch between the ladders of rotational levels in $v = 0$ and $v = 3$. The second resonant structure is related to the excitation of the perturbing molecule, while the active molecule remains in one of the spectroscopic states (the (0,3,0,0) \rightarrow (0,3,0,1) and (2,2,0,0) \rightarrow (2,2,0,1) transitions).

We averaged the σ_0^1 and σ_1^1 cross-sections over the Maxwell-Boltzmann distribution of relative kinetic energies and summed the resulting values over the relative populations of HD to calculate the six line-shape parameters used in this work in the quadratic speed-dependent hard-collision profile (qSDHCP) and speed-dependent billiard-ball profile (SDBBP):

- the speed-averaged collisional broadening and shift

$$\gamma_0 - i\delta_0 = \frac{1}{2\pi c} \frac{1}{k_B T} \langle v_r \rangle \sum_{j_2} p_{j_2}(T) \int_0^\infty dx e^{-x} \sigma_0^1(j_2; x), \quad (8)$$

- the speed dependences of collisional broadening and shift

$$\gamma_2 - i\delta_2 = \frac{1}{2\pi c} \frac{1}{k_B T} \frac{\langle v_r \rangle \sqrt{M_a}}{2} e^{-y^2} \sum_{j_2} p_{j_2}(T) \int_0^\infty d\bar{x} \left(2\bar{x} \cosh(2\bar{x}y) - \left(\frac{1}{y} + 2y \right) \sinh(2\bar{x}y) \right) \bar{x}^2 e^{-\bar{x}^2} \sigma_0^1(j_2; \bar{x}\bar{v}_p), \quad (9)$$

- the real and imaginary parts of the complex Dicke parameter

$$v_{\text{opt}}^r - i v_{\text{opt}}^i = \frac{1}{2\pi c} \frac{\langle v_r \rangle M_a}{k_B T} \sum_{j_2} p_{j_2}(T) \int_0^\infty dx x e^{-x} \left(\frac{2}{3} x \sigma_1^1 - \sigma_0^1 \right) x^2 e^{-x^2}. \quad (10)$$

Here, $\langle v_r \rangle = \sqrt{8k_B T / \pi \mu}$ is the mean relative speed of the colliding pair at a given temperature, k_B is the Boltzmann constant, μ is the reduced mass of the HD-HD system, and $M_a = m_a / (m_a + m_b)$, $x = E_{\text{kin}} / k_B T$, $\bar{x} = v_r / \bar{v}_p$, $y = \sqrt{m_a / p}$, and m_a and m_p are the masses of the active and perturbing molecules, respectively. For the self-perturbed case considered here, the mass of the perturber (m_p) and the active molecule (m_a) is the same, hence, $M_a = 1/2$. Note that in σ_λ^1 symbols, we kept the quantum numbers related to the spectroscopically active molecule implicit for brevity. The quantity $p_{j_2}(T)$ is the population of the j_2 level at a given temperature

$$p_{j_2}(T) = \frac{(2j_2 + 1) e^{-E_{j_2} / k_B T}}{\sum_{j_2'} (2j_2' + 1) e^{-E_{j_2'} / k_B T}}. \quad (11)$$

Summations over j_2 were truncated at $j_{2\text{max}} = 3$, which covered 97% of the total population of the HD molecule at the experimental temperature. To account for the remaining 3% of the HD population at $T = 296$ K, the cross-sections were extrapolated for $j_2 > 3$ using values for $j_2 = 3$, justified by the lack of significant j_2 -dependence of the cross-sections, as seen in Fig. S3. The final values of the line-shape parameters at 296 K are gathered in Table 1. Uncertainties of line-shape parameters were estimated following the procedure described in Sec. 5 of Ref.¹⁴.

Table 1 | Line-shape parameters calculated for the HD P(3) 2-0 transition. This table contains *ab initio* line-shape parameters (in $10^{-3} \text{ cm}^{-1} \text{ atm}^{-1}$) used in the qSDHCP and SDBBP along with the estimated 1σ standard uncertainties.

γ_0	δ_0	v_{opt}^r	v_{opt}^i	γ_2	δ_2
15.5 ± 1.1	-7.0 ± 1.1	27.5 ± 0.2	-1.0 ± 1.3	4.8 ± 0.4	1.16 ± 0.25

References

1. Drever R. W. P. et al. Laser phase and frequency stabilization using an optical resonator. *Appl. Phys. B* **31**, 97-105 (1983).
2. Truong, G.-W. et al. Frequency-agile, rapid scanning spectroscopy. *Nat. Photon.* **7**, 532-534 (2013).
3. Hodges, J. T., Layer, H. P., Miller, W. W. & Scace, G. E. Frequency-stabilized singlemode cavity ring-down apparatus for high-resolution absorption spectroscopy. *Rev. Sci. Instrum.* **75**, 849-863 (2004).
4. Donley, E. A. et al. Double-pass acousto-optic modulator system. *Rev. Sci. Instrum.* **76**, 063112 (2005).

5. Coplen, T. B. et al. New guidelines for $\delta^{13}\text{C}$ measurements. *Anal. Chem.* **78**, 2439-2441 (2006).
6. Garberoglio, G. et al. Second virial coefficients of H_2 and its isotopologues from a six-dimensional potential. *J. Chem. Phys.* **137**, 154308 (2012).
7. Sultanov, R. A. et al. State-resolved rotational cross sections and thermal rate coefficients for ortho-/para- $\text{H}_2 + \text{HD}$ at low temperatures and $\text{HD} + \text{HD}$ elastic scattering. *Chem. Phys. Lett.* **475**, 175 (2009).
8. Sultanov, R. A. et al. Ultracold collisions between two light indistinguishable diatomic molecules: Elastic and rotational energy transfer in $\text{HD} + \text{HD}$. *Phys. Rev. A* **85**, 052702 (2012).
9. Balakrishnan, N. et al. Rotational Quenching of HD in Collisions with H_2 : Resolving Discrepancies for Low-lying Rotational Transitions. *Astrophys. J.* **866**, 95 (2018).
10. Schwenke, D. W. Calculations of rate constants for the three-body recombination of H_2 in the presence of H_2 . *J. Chem. Phys.* **89**, 2076 (1988).
11. Olejnik, A. et al. Ab initio quantum scattering calculations and a new potential energy surface for the $\text{HCl}(X^1\Sigma^+) - \text{O}_2(X^3\Sigma_g^-)$ system: Collision-induced line shape parameters for O_2 -perturbed R(0) 0-0 line in H^{35}Cl . *J. Chem. Phys.* **159**, 134301 (2023).
12. Monchick, L. and Hunter, L. W. Diatomic-diatom molecular collision integrals for pressure broadening and Dicke narrowing: A generalization of Hess's theory. *J. Chem. Phys.* **85**, 713 (1986).
13. Schäfer, J. and Monchick, L. Line broadening of HD immersed in He and H_2 gas. *Astron. Astrophys.* **265**, 859 (1992).
14. Jóźwiak, H. et al. Ab initio line-shape calculations for the S and O branches of H_2 perturbed by He. *J. Quant. Spectrosc. Radiat. Transf.* **219**, 313 (2018).
15. Stankiewicz, K. et al. Accurate calculations of beyond-Voigt line-shape parameters from first principles for the He-perturbed HD rovibrational lines: A comprehensive dataset in the HITRAN DPL format. *J. Quant. Spectrosc. Radiat. Transf.* **276**, 107911 (2021).
16. Thibault, F. et al. Measurements and calculations of collisional line parameters for Raman lines of CO perturbed by H_2 . *J. Quant. Spectrosc. Radiat. Transf.* **315**, 108874 (2024).

Anodization-free fabrication process for high-quality cross-type Josephson tunnel junctions based on a Nb/Al-AlO_x/Nb trilayer

F Bauer^{1,2}, C Enss^{1,3} and S Kempf^{2,3,1}

¹ Kirchhoff-Institute for Physics, Heidelberg University, Im Neuenheimer Feld 227, D-69120 Heidelberg, Germany

² Institute of Micro- and Nanoelectronic Systems, Karlsruhe Institute of Technology, Hertzstrasse 16, Building 06.41, D-76187 Karlsruhe, Germany

³ Institute for Data Processing and Electronics, Karlsruhe Institute of Technology, Hermann-von-Helmholtz-Platz 1, Building 242, D-76344 Eggenstein-Leopoldshafen, Germany

E-mail: fabienne.bauer@kit.edu

March 2024

Abstract. Josephson tunnel junctions form the basis for various superconducting electronic devices. For this reason, enormous efforts are routinely taken to establish and later on maintain a scalable and reproducible wafer-scale manufacturing process for high-quality Josephson junctions. Here, we present an anodization-free fabrication process for Nb/Al-AlO_x/Nb cross-type Josephson junctions that requires only a small number of process steps and that is intrinsically compatible with wafer-scale fabrication. We show that the fabricated junctions are of very high-quality and, compared to other junction types, exhibit not only a significantly reduced capacitance but also an almost rectangular critical current density profile. Our process hence enables the usage of low capacitance Josephson junctions for superconducting electronic devices such as ultra-low noise dc-SQUIDs, microwave SQUID multiplexers based on non-hysteretic rf-SQUIDs and RFSQ circuits.

Keywords: Josephson tunnel junctions, microfabrication process, Nb/Al-AlO_x/Nb trilayer, subgap leakage, thermal activation theory, unshunted dc-SQUIDs, capacitance measurements.

1. Introduction

Josephson tunnel junctions are key components of any superconducting electronic devices. This includes superconducting quantum bits [1], superconducting quantum interference devices (SQUIDs) [2], rapid single flux quantum (RSFQ) circuits [3, 4], Josephson voltage standards [5], single electron transistors (SETs) [6, 7], Josephson parametric amplifiers [8, 9] or superconductor-insulator-superconductor (SIS) mixers [10, 11]. Most of these devices are based on refractory Josephson tunnel junctions made of an *in-situ* deposited Nb/Al-AlO_x/Nb trilayer, the latter being an excellent choice regarding junction quality, tunability of the critical current density, scalability and run-to-run reproducibility of characteristic junction parameters as well as resilience to thermal cycling. A key requirement for realizing integrated circuits based on these junctions is the availability of a wafer-scale fabrication process. For this reason, research facilities make huge efforts to establish and maintain a fabrication process for high-quality Nb/Al-AlO_x/Nb Josephson tunnel junctions. In some cases, these efforts are further challenged by the need for minimizing the junction capacitance C_{JJ} to allow, for example, improving the energy resolution of SQUIDs [12].

The capacitance $C_{JJ} = C_{\text{int}} + C_{\text{par}}$ of a Josephson tunnel junction is composed of an intrinsic and a parasitic contribution. The intrinsic capacitance C_{int} depends on the material and the dimensions of the tunnel barrier and is determined by barrier thickness d (setting the critical current density) and the junction area A_{JJ} . It scales inversely with the tunnel barrier thickness d . At the same time, the critical current density j_c scales exponentially with the tunnel barrier thickness d . For this reason, reducing the junction area A_{JJ} and simultaneously increasing the critical current density j_c effectively lowers the intrinsic junction capacitance assuming a fixed target value of the critical current I_c . The parasitic capacitance C_{par} is due to overlaps of the superconducting wiring with the junction electrodes that are separated by the wiring insulation. It strongly depends on the fabrication technology, i.e. the type and thickness of insulation layers, the required actual overlap between wiring layers, etc..

In the past, several fabrication processes for Nb/Al-AlO_x/Nb Josephson tunnel junctions have been developed. These are based on reactive ion etching and wet-chemical anodization [13, 14], chemical-mechanical polishing [15, 16], focused ion beam etching [17] or shadow evaporation [18]. Though these processes are used with great success, they either yield junctions with high capacitance or barrier homogeneity as well as alignment accuracy are challenging and potentially cause process faults. Moreover, wet-chemical anodization requires a galvanic connection to ground, necessitating a temporary electrical connection of electrically floating devices such as rf-SQUIDs or qubits to their environment which must be removed in later fabrication steps. This complicates the fabrication process and introduces potential steps for junction damage.

Within this context, we present a variant of a fabrication process for cross-type Josephson tunnel junctions [14, 19, 20] that does not depend on wet-chemical

anodization. Our process is hence particularly suited for fabricating electrically floating superconducting quantum devices. At the same time, the junction capacitance is minimized. Moreover, our process requires only a small number of fabrication steps, is intrinsically compatible with wafer-scale fabrication and yields junctions with very high tunnel barrier homogeneity.

2. Description of fabrication process

Our Josephson tunnel junctions are based on a Nb/Al-AlO_x/Nb trilayer that is *in-situ* sputter-deposited on a thermally oxidized Si substrate. The thickness of the lower Nb base electrode, the Al layer and the upper Nb counter electrode are 100 nm, 7 nm, and 100 nm, respectively. All layers are dc-magnetron sputtered from 3" targets in a high vacuum (HV) sputter system with a base pressure in the order of 10⁻⁶ Pa. During sputtering, the substrate is passively cooled by a thin layer of vacuum grease between substrate and sample holder. Prior to metal deposition, the substrate is pre-cleaned by an rf-driven Ar plasma in the load-lock of the sputtering system. Both Nb layers are sputtered with a rate of 0.63 nm/s at a constant dc-power of 300 W. The pressure of the Ar atmosphere during sputtering is 0.96 Pa to yield Nb free of mechanical stress [21]. The Al film is deposited in an Ar atmosphere with a pressure of 0.72 Pa using a dc-power of 100 W resulting in a deposition rate of 0.31 nm/s. For tunnel barrier formation within the load-lock of the sputtering system, the Al layer is oxidized at room temperature in a static O₂ atmosphere with pressure p_{ox} . The critical current density j_c of the tunnel junctions depends on the total oxygen exposure $p_{\text{ox}}t_{\text{ox}}$ according to $j_c \propto (p_{\text{ox}}t_{\text{ox}})^{-0.64}$ (see figure 1). We typically vary the oxidation time t_{ox} at a fixed value of the oxidation pressure of $p_{\text{ox}} = 4$ kPa.

Figure 2 shows the individual fabrication steps for our cross-type Josephson junctions. After trilayer deposition (see figure 2(a)), a positive, high-resolution UV photoresist (AZ MIR 701 29CP supplied by Microchemicals GmbH) is spin-coated on top of the trilayer and patterned as a narrow stripe using direct laser lithography. The width of this stripe defines one of the lateral dimensions of the final Josephson junction (see below). The resulting photoresist mask is used for etching the entire trilayer stack (see figure 2(b)). Both Nb layers are etched by inductively coupled plasma reactive ion etching (ICP-RIE) using SF₆ and Ar in a mixing ratio of 2:1 at a constant pressure of 2 Pa as process gas. The rf-power and the ICP power are 10 W and 300 W, respectively, resulting in an etch rate of 2.5 nm/s. The Al-AlO_x layer and the thermal oxide of the Si substrate, respectively, act as etch stop for the ICP-RIE processes. The Al-AlO_x layer is wet-chemically etched with an etching solution consisting of phosphoric acid, nitric acid, acetic acid and water that are mixed in a ratio of 16:1:1:2. As will be shown in section 4, wet-chemical etching of the Al layer is key to guarantee a high junction quality when omitting wet-chemical anodization.

The next step is the deposition of a dielectric insulation layer (see figure 2(c)). The

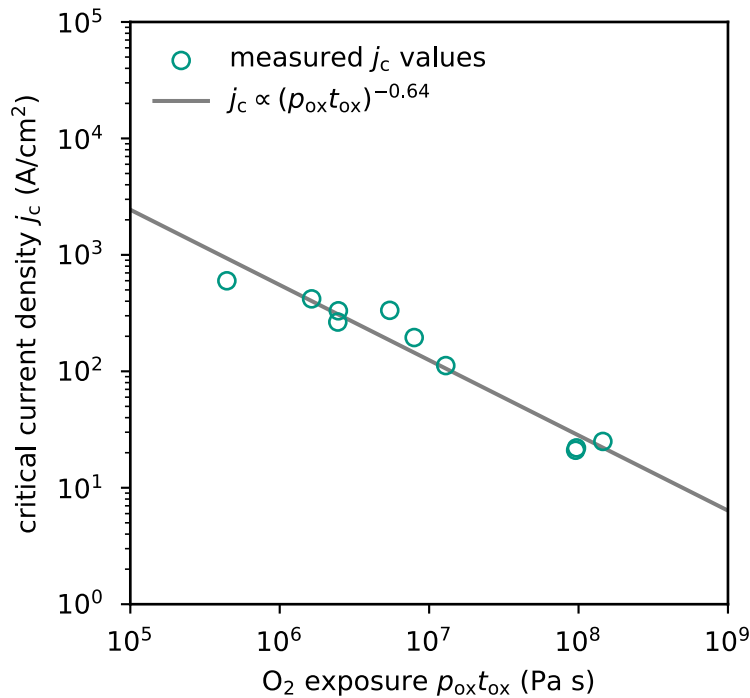


Figure 1: Measured dependence of the critical current density j_c on the oxygen exposure $p_{\text{ox}} t_{\text{ox}}$. The solid line is a fit to the measured data indicating the exponential dependence of the critical current density on the oxygen exposure.

insulation is intended not only to protect the sidewalls of the patterned trilayer stripe, but also to quasi-planarize the layer stack before the deposition of subsequent layers. For deposition, we use the same photoresist mask as for trilayer patterning, i.e. the mask is not removed after the prior etching steps. It is important to note that the photoresist acts as a shadow mask during dc-magnetron sputter deposition, resulting in trenches beside the trilayer stripe. We empirically found that the thickness of the insulation layer at the lowest point of the trenches is only about 50% of the nominally deposited material. For this reason, the thickness of the insulation layer must be at least twice the layer thickness of the Nb base electrode to prevent shorts between the base electrode and subsequent wiring layers. We hence deposit a 220 nm thick SiO₂ layer by rf-magnetron sputtering utilizing a separate HV sputtering system, a gas mixture consisting of 60% Ar and 40% O₂ at a constant pressure of 0.7 Pa as process gas, and an rf-power of 250 W. This results in an overall deposition rate of 1.3 nm/s.

After removal of the photoresist mask (see figure 2(d)), a Nb wiring layer with a thickness of 200 nm is dc-magnetron sputter deposited using a HV sputter system with a base pressure below 6×10^{-6} Pa and a 2" Nb target. The Ar pressure and the dc-power are 0.3 Pa and 70 W, respectively, resulting in a deposition rate of 0.3 nm/s. Prior to the deposition, the surface of the Nb counter electrode (upper Nb layer of the trilayer stripe) is pre-cleaned by Ar ion milling to remove native oxides and hence to ensure a superconducting contact between the counter electrode and the deposited Nb layer.

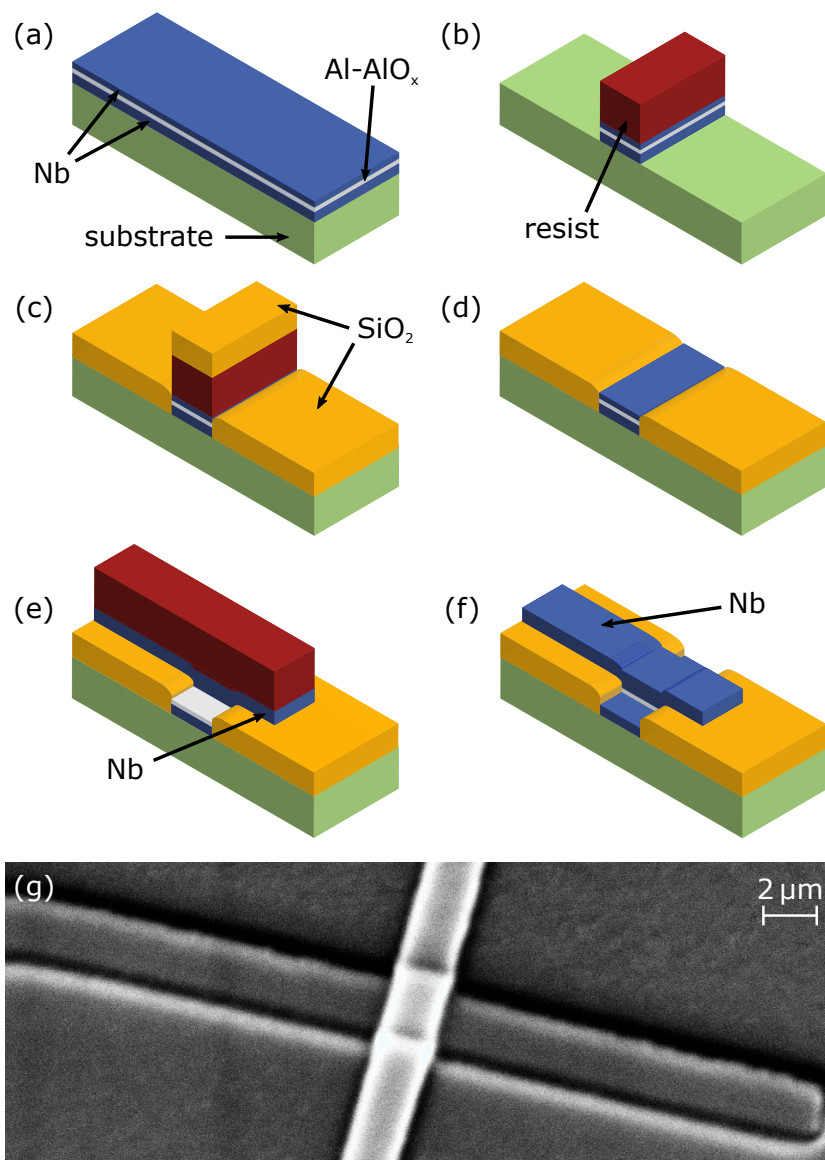


Figure 2: (a)-(f) Schematic overview of the different steps of our fabrication process for cross-type Josephson junctions. Shown are the state of the junction after (a) deposition of the Nb/Al-AlO_x/Nb trilayer, (b) trilayer patterning as a stripe, (c) deposition of the dielectric insulation layer for planarization, (d) removal of the photoresist mask, (e) deposition and patterning of the Nb wiring layer, and (f) removal of the residual Al and photoresist. Dimensions are not to scale. (g) Scanning electron microscope image of a finished cross-type Josephson junction.

This final layer is patterned by structuring a high-resolution UV photoresist (same as for trilayer patterning) as a narrow stripe that is oriented perpendicular to the embedded trilayer stripe and ICP-RIE for Nb etching. The top Nb layer of the trilayer stack is etched within the same etching cycle to define the final size of the counter electrode (see figure 2(e)). By this, we yield rectangular Josephson tunnel junctions from the overlap of the trilayer and Nb wiring stripes. Finally, the residual Al-AlO_x of the trilayer is removed by wet etching to enable later electrical contacts to the Nb base electrode (see figure 2(f)).

It is worth mentioning that the area of our cross-type Josephson junctions is only limited by the resolution of the lithographic tool and not by alignment accuracy. Due to the minimum structure size of our laser lithography tool of 1 μm, we are able to reliably fabricate cross-type junctions with a nominal area of 1 μm × 1 μm, but even sub-micrometer-sized junctions are achievable with the help of e.g. DUV steppers or electron beam lithography. Even though such small junctions require higher values of the critical current density to achieve a target value of the critical current, the total junction capacitance is reduced as the intrinsic capacitance C_{int} linearly decreases with the junction area A while the intrinsic capacitance per unit area C'_{int} only logarithmically increases with the critical current density j_c [22, 23]. In addition, the capacitance of cross-type junctions has a negligible parasitic contribution there are no direct wiring overlaps. Besides that, only two lithographic layers are required during the entire fabrication process. The higher values of the critical current density further lower the time taken to fabricate a batch of cross-type junctions as, according to figure 1, the oxidation time for the formation of the tunnel barrier gets significantly shorter assuming a fixed oxidation pressure.

3. Experimental techniques for junction characterization

Up to now, we have successfully fabricated more than 15 batches of cross-type junctions with linear dimensions varying between 1.0 μm and 4.2 μm using our anodization-free fabrication process. The characteristic figures of merit and hence the quality of fabricated junctions as well as their uniformity across an entire wafer were determined by recording the current-voltage (IV) characteristics (see figure 3 as an example) of a sub-sample of each batch at a temperature of $T = 4.2$ K in a differential four-wire configuration. The utilized measurement set-up comprises low-pass filters at room and cryogenic temperatures to filter external rf interference signals. The dc bias current I is generated by applying a triangular voltage signal V_{gen} with a frequency of 3 Hz to the series connection of all resistors in the input circuit of the set-up. This includes the equivalent resistance $R_{\text{LPF}} = 10.4$ kΩ of both rf-filters as well as the voltage-dependent resistance $R(V) = V/I$ of the Josephson junction to be measured. The actual bias current through the junction hence depends on the voltage drop V across the junction

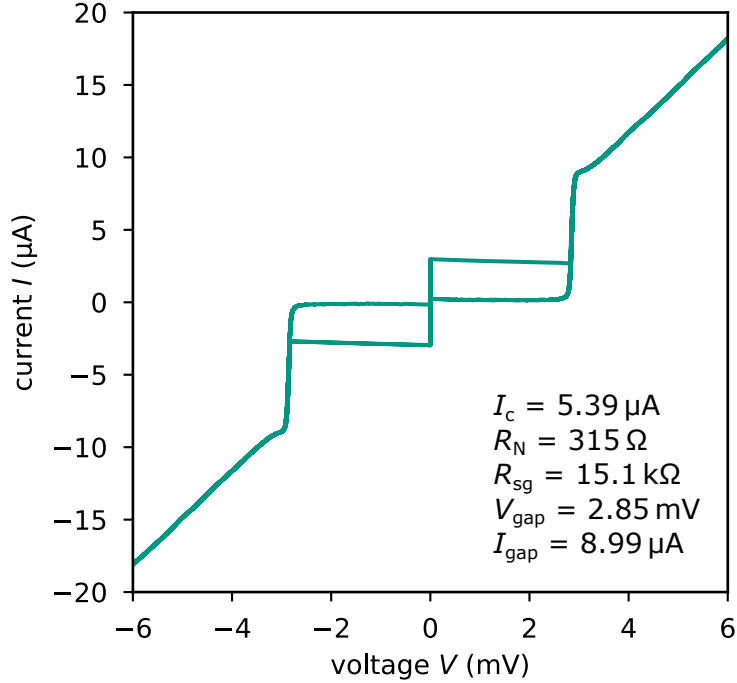


Figure 3: Current-voltage characteristic of one of our cross-type junctions with a target area of $1 \mu\text{m} \times 1 \mu\text{m}$ recorded at a temperature of $T = 4.2 \text{ K}$. All figures of merit except for the critical current I_c were taken directly from the characteristic. The critical current was obtained by the method described in section 3.

and is given by

$$I = \frac{V_{\text{gen}}}{R_{\text{LPF}}} \left(1 - \frac{V}{V_{\text{gen}}} \right). \quad (1)$$

The voltage drop V is measured using a battery-powered differential amplifier. To screen the samples from disturbances induced by variations of magnetic background fields, the cryo-probe is equipped with a mu-metal and a superconducting shield made of Nb.

The quality of each Josephson junction is evaluated by means of different figures of merit, among those the critical current I_c , the normal state resistance R_N , the gap voltage V_{gap} , and the subgap resistance R_{sg} . As conventional, the subgap resistance is determined at a voltage value of $V = 2 \text{ mV}$ in the subgap region. From these quantities, the characteristic resistance ratio R_{sg}/R_N and the $I_c R_N$ product are calculated. The former is a junction area independent figure of merit to quantify subgap leakage, e.g. due to defects or shorts in the tunnel barrier [24, 25]. The latter is a measure for the strength of Cooper pair tunneling that depends on the profile of the electric potential along the tunnel barrier [26].

The critical current I_c of each Josephson junction was determined by its relation $I_c = \kappa I_{\text{gap}}$ [27] to the gap current I_{gap} , the latter corresponding to the amplitude of the quasiparticles' tunneling current at the gap voltage, as the switching current I_{sw} at

$T = 4.2$ K, extracted from IV -characteristics, is always significantly smaller than the true critical current. The deviation between the switching current I_{sw} and the critical current I_c is caused by thermal noise [28, 29]. The recursion formula

$$P(I_{\text{sw}}) = \tau^{-1}(I_{\text{sw}}) \left(\frac{dI}{dt} \right)^{-1} \left[1 - \int_0^{I_{\text{sw}}} P(I) dI \right] \quad (2)$$

describes the related probability of the Josephson junction to escape from the zero-voltage state at a nominal switching current I_{sw} within the interval dI when a bias current I is injected with a sweep rate dI/dt . The temperature dependent escape rate

$$\tau^{-1} = a_{\text{th}} \frac{\omega_0}{2\pi} e^{-E_0/k_{\text{B}}T} \quad (3)$$

is a function of a temperature and damping dependent thermal prefactor a_{th} , the oscillation frequency $\omega_0 = \omega_{\text{p}} [1 - (I/I_c)^2]^{1/4}$ of the Josephson junction with $\omega_{\text{p}} = \sqrt{2\pi I_c / \Phi_0 C_{\text{JJ}}}$ denoting the plasma frequency and the height of the potential barrier E_0 [30]. It can be calculated from the measured switching current distribution $P(I_{\text{sw}})$ of a junction to determine its true critical current I_c by using iterative numerical methods [31]. Figure 4 shows as an example of the measured switching current distribution $P(I_{\text{sw}})$ at $T = 4.2$ K and a fit according to equations 2 and 3 for one of our cross-type junctions with a critical current of $I_c = 38.6$ μA . The dimensionless factor $\kappa = I_c/I_{\text{gap}}$, used to calculate the critical current from the measured gap current, is independent of the junction size and constant for an entire junction batch. It was determined by measuring and evaluating the switching current distribution of some representative junctions from each batch.

In order to investigate the spatial profile of the critical current density j_c along the tunnel barrier, the dependence of the maximum supercurrent $I_{\text{s,max}}$ through the junction on an external magnetic field B_y was measured [32]. For these measurements, the mu-metal shield of our junction characterization set-up was removed and a Helmholtz coil was attached to the sample holder such that the junction was located in the center of the coil. To analyze the measured data (see, for example, figure 11 in section 4), a model of the distribution of the critical current density $j_c(z)$ was generated and the absolute value of the Fourier transform of this model was compared to the measured data.

The specific capacitance C'_{int} of our Josephson junctions was determined by observing Shapiro steps in unshunted dc-SQUIDs [33, 34]. For this, two types of symmetric, unshunted dc-SQUIDs based on cross-type junctions were designed and fabricated. Both variants differ by the junction size (see below). Figure 5 shows a micrograph and the corresponding equivalent circuit model of such a current-biased SQUID comprising $2\mu\text{m} \times 2\mu\text{m}$ -sized cross-type Josephson junctions. The SQUID loop with inductance $L_{\text{s}} = 2(L_1 + L_2)$ is composed of two sections. The upper section with inductance $2L_1$ is patterned from the 200 nm thick Nb wiring layer. In contrast, the lower section with inductance $2L_2$ is formed by the 100 nm thick lower Nb layer of the trilayer stack. Both

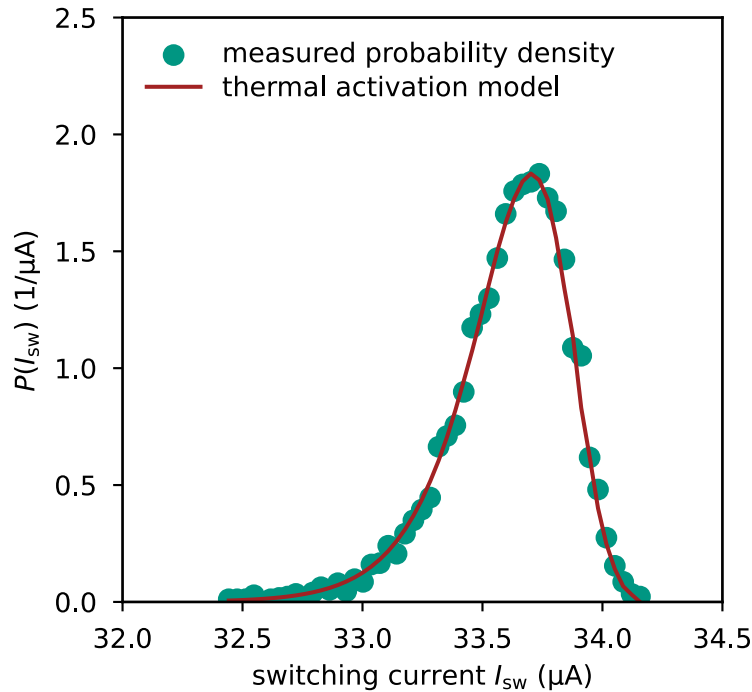


Figure 4: Switching current distribution $P(I_{sw})$ of a $3.4\ \mu\text{m} \times 3.4\ \mu\text{m}$ -sized cross-type junction recorded at a temperature of $T = 4.2\ \text{K}$. For the measurement, the switching current of the junction was measured 5000 times by ramping up the bias current and recording the current values at which the junction switches from the superconducting into the normal conducting state. The solid red line represents a fit for a critical current of $I_c = 38.6\ \mu\text{A}$ according to the thermal activation model represented by equations 2 and 3.

sections are connected via the Josephson junctions. Moreover, feedlines for injecting control currents $I_{ctr,1}$ and $I_{ctr,2}$ are connected to both loop sections at the location of the Josephson junctions. A 400 nm thick Nb ground plane, separated by an insulating SiO_2 layer, was patterned on top of all devices to reduce cross-talk between both loop sections [35]. The resulting parasitic capacitance which is connected in parallel to the capacitance of the two Josephson junctions was estimated to be about 6 fF and corresponds to only 3% of the smallest measured capacitance.

To observe the actual resonance steps in the IV -characteristic, the maximum supercurrent of a respective sample SQUID was suppressed by applying a control current through one of the feedlines. For $\Phi_s = 2L_i I_{ctr,i} = (n + 1/2)\Phi_0$ with $i \in \{1, 2\}$, $n \in \mathbb{Z}$, and Φ_s denoting the magnetic flux threading the SQUID loop, the maximum supercurrent is at its minimum. At the same time, the periodicity $|\Delta I_{ctr,i}| = \Phi_0 / (2L_i)$ of the maximum supercurrent modulation with $\Delta I_{ctr,i}$ being the current difference between two neighboring minima was used to determine the inductance of the SQUID loop [36]. The value of L_s for our unshunted SQUIDs with $2\ \mu\text{m} \times 2\ \mu\text{m}$ -sized junctions was simulated

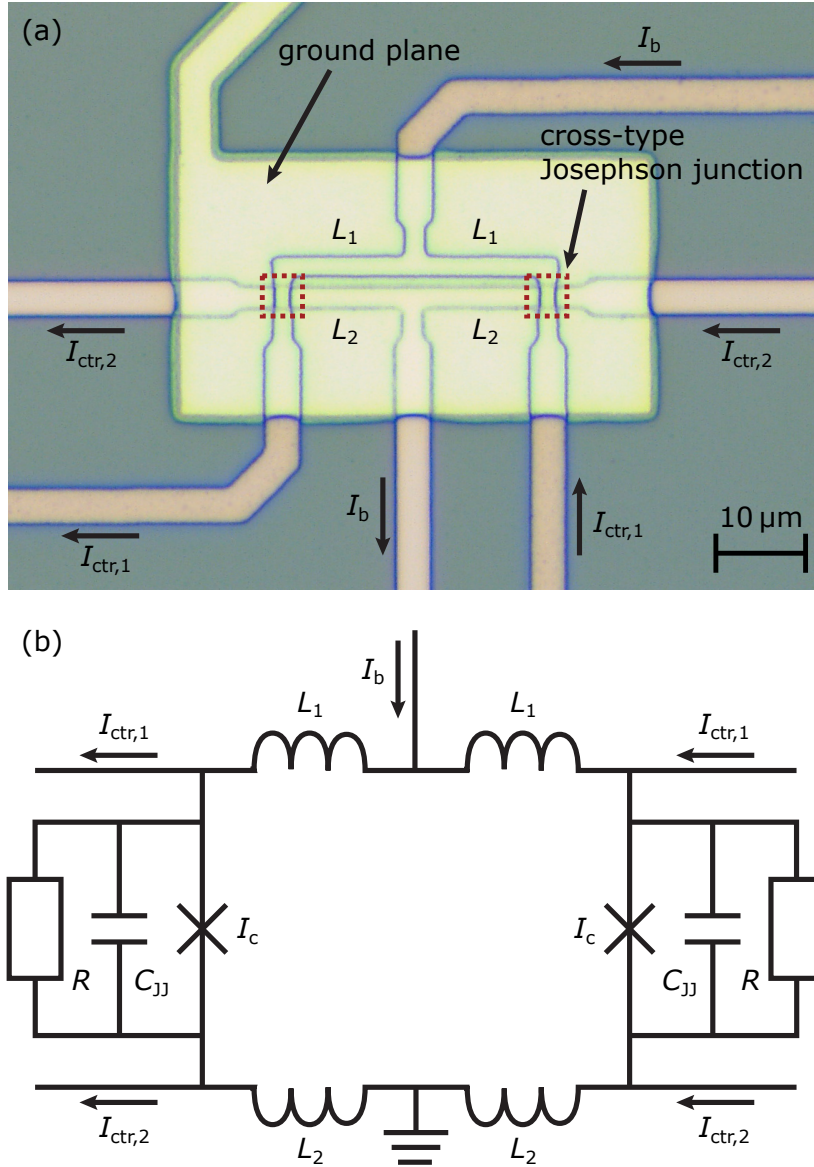


Figure 5: (a) Micrograph and (b) equivalent circuit model of a symmetric, unshunted dc-SQUID based on $2 \mu\text{m} \times 2 \mu\text{m}$ -sized cross-type junctions (framed by dashed red boxes) biased by a current I_b . The SQUID was designed and fabricated to determine the specific capacitance of our Josephson junctions.

to be $L_s = 14.7 \text{ pH}$ using InductEx (numeric simulation software by SUN Magnetics (Pty) Ltd.) and is in perfect agreement with the experimental value of $L_s = 14.0 \text{ pH}$ taking into account possible fabrication induced size and alignment variances. We also fabricated devices with $4 \mu\text{m} \times 4 \mu\text{m}$ -sized cross-type junctions to determine the specific capacitance C'_{int} for junctions with critical current densities $j_c < 100 \text{ A/cm}^2$. Here, the calculated loop inductance is $L_s = 9.6 \text{ pH}$ which is again in good agreement with the experimental value of $L_s = 10.6 \text{ pH}$.

4. Results and discussion

4.1. Sidewall insulation and characteristic resistance ratio

A key factor for the reliable and reproducible fabrication of high-quality cross-type Josephson junctions based on a Nb/Al-AlO_x/Nb trilayer stack is a sufficient galvanic isolation between the base electrode of the junction and a subsequent wiring layer to its top electrode. In our process, this insulation is realized by the quasi-planarizing insulation layer with sufficient thickness to compensate for trenching effects and, even more important, the usage of wet-chemical etching for removing the Al-AlO_x layer during trilayer etching (see figure 2(b)). During the wet etching process, nitric acid oxidizes the Al surface, while phosphoric acid dissolves the native as well as the continuously formed aluminum oxide. Since niobium, similar to aluminum, oxidizes in nitric acid, but niobium oxide does not dissolve in phosphoric acid [37], an oxide layer of a few nm thickness forms on the exposed sidewalls of the patterned Nb/Al-AlO_x stripe and on the surface of the still unstructured lower Nb of the trilayer. This oxide layer serves as a passivation layer. Moreover, compared to plasma induced ion milling no etching residues from redeposited Al atoms [38] appear during wet etching. These residues potentially adhere to the sidewalls of the etched structure forming shorts across the tunnel barrier. Similarly, the passivation layer protects against the formation of shorts originating from potential redeposits during Nb base electrode etching. Overall, the passivation layer formed during wet etching takes on the same task as wet-chemical anodization, however, without the need for a galvanic contact between all patterned trilayer structures.

In order to proof that wet etching of the Al-AlO_x layer using our acidic etching solution in fact substitutes the anodization of the sidewalls of the patterned trilayer stack, we prepared two distinct batches of cross-type junctions. The Nb/Al-AlO_x/Nb trilayer of both batches was sputtered in the same deposition run by placing both substrates side-by-side on the sample holder in the sputter system. For one batch, the Al-AlO_x layer was wet-chemically etched, for the other batch Ar ion milling within the ICP-RIE system was used. For about one half of the Josephson junctions of each batch, the sidewalls were additionally anodized after etching the trilayer stripe.

Figure 6 shows current-voltage characteristics of representative cross-type Josephson junctions for each variant. Irrespective of the actual etching technique, the junctions with anodized sidewalls are of high quality which is indicated by very low subgap leakage. Non-anodized junctions for which the Al-AlO_x was wet-chemically etched are of the same quality and have low subgap leakage. In contrast, the *IV*-characteristics of non-anodized, dry etched cross-type junctions exhibit severe leakage. We attribute this to vertical shorts across the tunnel barrier caused by non-passivated Al and Nb redeposits that are oxidized in case that wet-chemical anodization is subsequently used. We note that the critical current I_c of anodized junctions is about 40% smaller than of non-anodized junctions and attribute this to the reduced junction area due to the thick

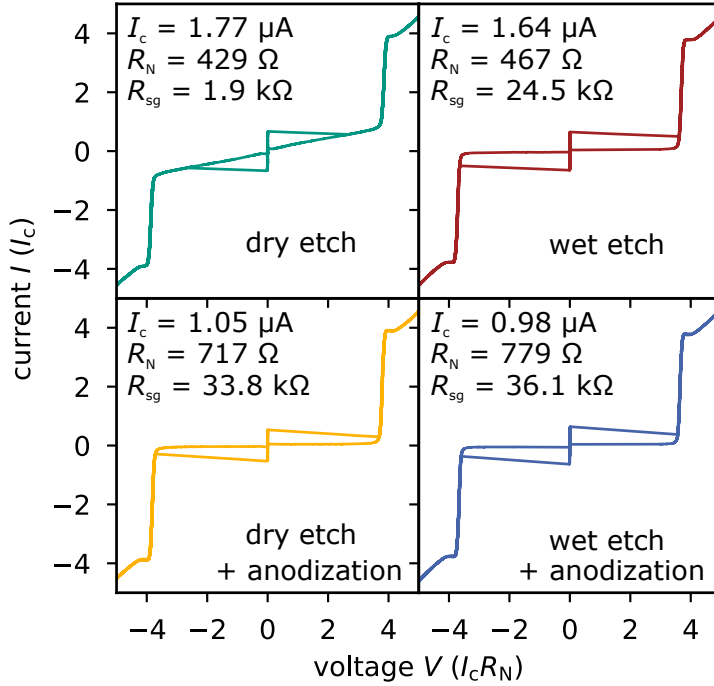


Figure 6: Normalized IV -characteristics of anodized (lower row) and non-anodized (upper row) cross-type junctions with a target area of $A_{\text{target}} = 2.9 \mu\text{m} \times 2.9 \mu\text{m}$ measured at $T = 4.2 \text{ K}$. The Al-AlO_x layer was etched using Ar ion milling in an ICP-RIE system (left column) or using an acidic etching solution based on nitric and phosphoric acid (right column). Note that the current drops to a value below the critical current I_c as the junction jumps into the voltage state due to the voltage dependent junction resistance that is connected in series with the bias resistors (see description of experimental setup in section 3).

oxide layer on the sidewalls caused by anodization.

The number of redeposits that potentially lead to shorts across the tunnel barrier and hence the subgap leakage are expected to increase with the junction width W . Figure 7 displays the dependence of the characteristic resistance ratio R_{sg}/R_N on the width of the quadratic Josephson junctions from the two examined batches and confirms this hypothesis. We observe an increase of spread with increasing junction size for the dry etched junctions with non-anodized sidewalls. Note that the yield of junctions of this variant is only 48 %, i.e. about every second junction has very high subgap leakage or shown an ohmic IV -characteristic. The fact that this large spread is not observed for anodized junctions from the same batch as well as that the yield of all other variants is significantly larger (about 90%) is a clear indication that the leakage originates from the sidewalls and not from the tunnel barrier itself.

The comparison between the non-anodized, wet-chemically etched junctions and the anodized junctions from the same batch as well as the dry etched, anodized junctions

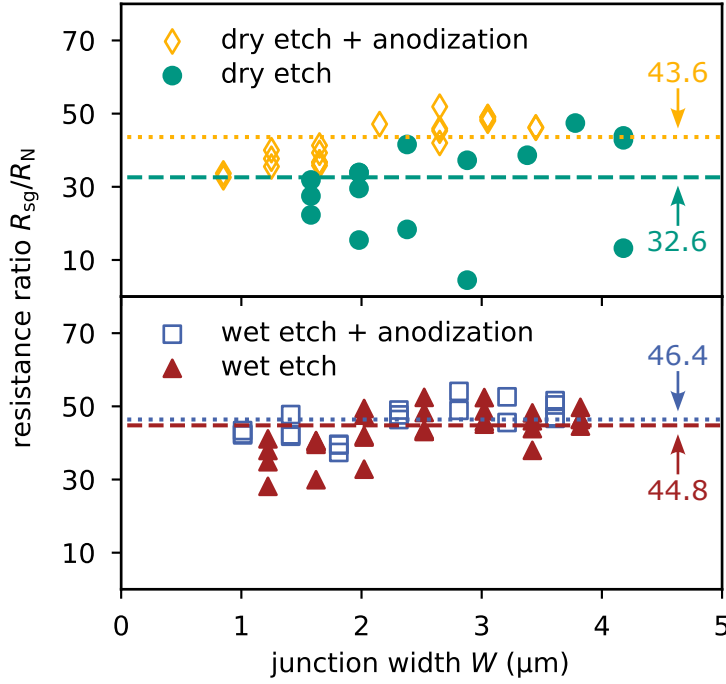


Figure 7: Resistance ratio R_{sg}/R_N versus junction width for quadratic cross-type junctions based on the same Nb/Al-AIO_x/Nb trilayer with anodized (open symbols) and non-anodized (filled symbols) sidewalls, whose Al-AIO_x layer was dry etched (diamonds and circles) or wet etched (squares and triangles). Dotted and dashed horizontal lines mark the mean value for anodized and non-anodized junctions, respectively.

(see figure 7) shows that the use of an acidic etching solution for removing the Al-AIO_x layer indeed replaces wet-chemical anodization of the sidewalls of cross-type Josephson junctions. These three variants show a small spread of the characteristic resistance ratio. The latter tends to get larger the larger the junction is. We attribute this to edge effects that are not caused by redeposits at the sidewalls. Moreover, a direct comparison of the mean characteristic resistance ratios indicates that wet etched, non-anodized junctions show generally lower subgap leakage than dry etched, anodized specimens. This favors the usage of our fabrication process as compared to processes relying on dry etching the Al-AIO_x layer and subsequent wet-chemical anodization.

4.2. Scalability and uniformity of critical current and normal state resistance

For all batches of Josephson junctions that were produced using our anodization-free fabrication process, we checked for the scalability of the critical current I_c and the normal state resistance R_N with respect to the junction area as well as for the uniformity of these parameters within a batch. Figure 8 and figure 9 show as an example the results for a batch with a critical current density of about 600 A/cm². As expected, both, the critical current I_c and the normal state resistance R_N , scale linearly with the effective and the inverse effective junction area, respectively. We note that the effective junction

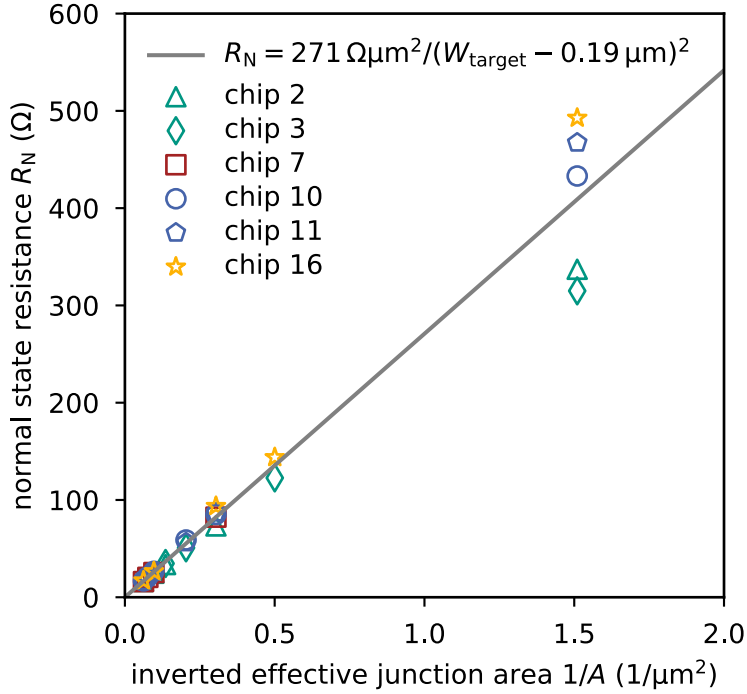


Figure 8: Dependence of the normal state resistance R_N on the inverse of the effective junction area $A = (W_{\text{target}} + \Delta W)^2$ for cross-type junctions from different chips of a single batch produced with our anodization-free fabrication process. The solid line indicates the result of a fit $R_N = \rho_N / (W_{\text{target}} + \Delta W)^2$ of the expected linear dependence and allows to determine that the junction size deviates by only $\Delta W = -0.19 \mu\text{m}$ from the target value.

area A deviates from the target value A_{target} as the lateral junction size deviates by a length ΔW . We determine the deviation by a linear fit $R_N = \rho_N / (W_{\text{target}} + \Delta W)^2$, ρ_N denoting the normal state resistivity, to the data in figure 8 and find that the size of the cross-type junctions of this example batch is on average only $0.19 \mu\text{m}$ smaller than the target value. We attribute this deviation to size variations in the photoresist masks and to a parasitic lateral material loss during etching. Deviations from the linear fit only occur for the smallest junctions with a target area of $A_{\text{target}} = 1 \mu\text{m} \times 1 \mu\text{m}$, for which a potentially location dependent variation of the junction size has the greatest effect.

Besides the scalability of the critical current and the normal state resistance, our cross-type junctions also show a high quality that is reflected, for example, by the high average values of the characteristic resistance ratio $R_{\text{sg}}/R_N > 30$ for small junctions with $W < 2 \mu\text{m}$ and $R_{\text{sg}}/R_N > 40$ for junctions with $W \geq 2 \mu\text{m}$ (compare figure 7) or the value of the gap voltage V_{gap} . For all batches, $V_{\text{gap}} > 2.8 \text{mV}$, i.e. the gap voltage is very close to the value or the energy gap of Nb [39] and the proximity effect due to the Al layer is negligible. We find $\langle R_{\text{sg}}/R_N \rangle = 45.8$ for the example batch displayed in figure 8 and figure 9 and the values for the gap voltage are only statistically distributed with a

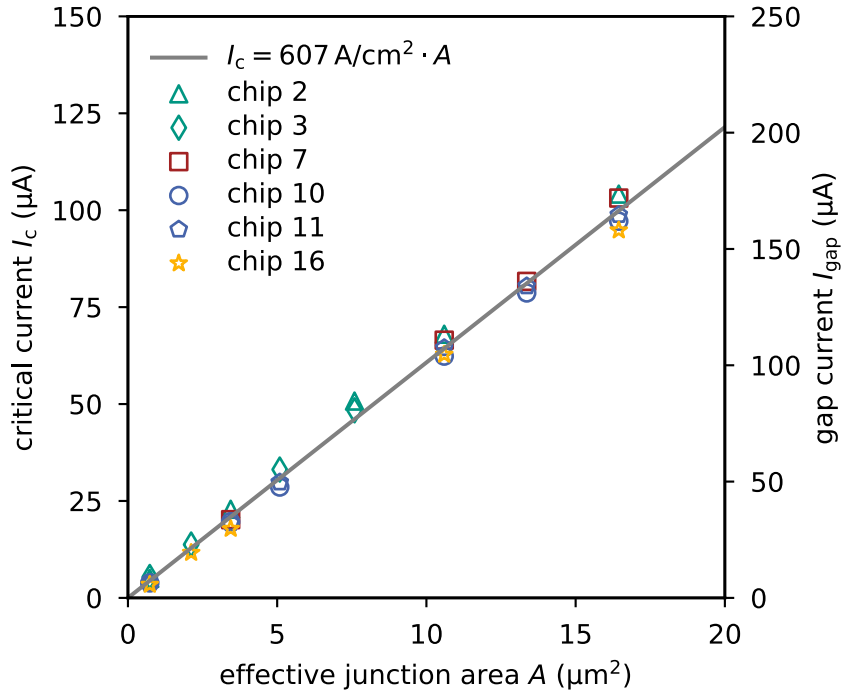


Figure 9: Dependence of the critical current I_c on the effective junction area A for cross-type junctions from different chips of a single batch produced with our anodization-free fabrication process. The solid line indicates the result of a fit $I_c = j_c \cdot A$ of the expected linear dependence and allows to determine the critical current density of this batch to be $j_c = 607 \text{ A/cm}^2$.

standard deviation of $\sigma = 0.01 \text{ mV}$. The $I_c R_N$ product (see figure 10) is independent of junction size and is as high as $I_c R_N = 1.7 \text{ mV}$ for the example batch discussed here. This observation and the almost size independent resistance ratio (see figure 7) indicate that the performance of Nb/Al-AIO_x/Nb Josephson tunnel junctions produced with our cross-type fabrication process is not affected by edge effects caused by the process but rather than by the intrinsic properties of the tunnel barrier that, of course, could be further optimized.

4.3. Profile of the critical current density

The usage of our fabrication process for cross-type Josephson junctions turns out to positively affect the critical current density profile $j_c(z)$ of the tunnel barrier. This can be seen by a comparison between the critical current density distributions shown in figure 11(b) and figure 11(d). Both profiles were generated as models to describe the measured dependencies of the maximum supercurrent $I_{s,\text{max}}(I_B)$ of a $13 \mu\text{m} \times 13 \mu\text{m}$ window-type and a $4.2 \mu\text{m} \times 4.2 \mu\text{m}$ cross-type Josephson junction on the current I_B through the Helmholtz coil of our measurement setup (see section 3). The corresponding plots are shown in figure 11(a) and figure 11(c), respectively. The batch of Nb/Al-AIO_x/Nb window-type junctions was fabricated separately using an anodization-free

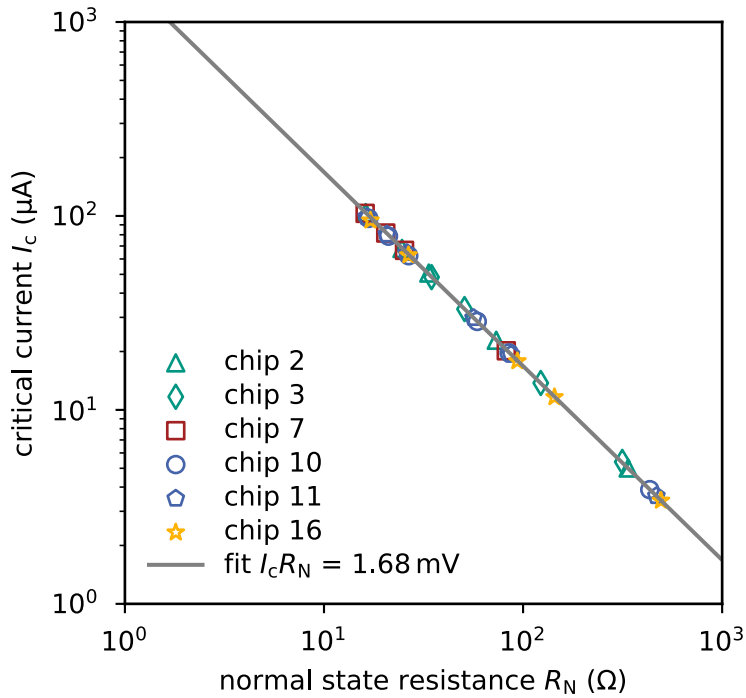


Figure 10: Critical current I_c versus normal resistance R_N for junctions from the same example batch as for figure 8 and figure 9. The solid line represent the result of a fit according to $I_c R_N = \text{const.}$ and allows to determine that the $I_c R_N$ -product takes a value of $I_c R_N = 1.7 \text{ mV}$.

process based on the one described in [40] in which the Al-AlO_x layer was etched by Ar ion milling. The modeled critical current density profile plotted in figure 11(b) is based on two assumptions: 1.) Due to small damages at the edges of the tunnel barrier during dry etching of the Nb top electrode and the Al-AlO_x layer, the flanks of the j_c -profile are not upright but slightly quadratically shaped. 2.) The momentum/energy of the Ar ions during surface cleaning of the top electrode prior to the deposition of the Nb wiring is transferred to the underlying tunnel barrier where it causes damage and thus a reduced critical current density. The area in which this effect occurs is restricted to the size of the window in the insulation layer which is $11 \mu\text{m} \times 11 \mu\text{m}$. The measured magnetic field dependence agrees very well with the modeled $j_c(z)$ -profile. The modeled critical current density profile of the cross-type junction shown in figure 11(d) only assumes small damages at the edges of the tunnel barrier during dry etching of the trilayer stack. It clearly exhibits no indentation and yet describes the measured data in figure 11(c) well. Since there is no insulation window on top of the top electrode for a cross-type Josephson junction, the momentum/energy transfer of the Ar ions should be distributed evenly over the entire tunnel barrier, giving rise to a more homogeneous tunnel barrier.

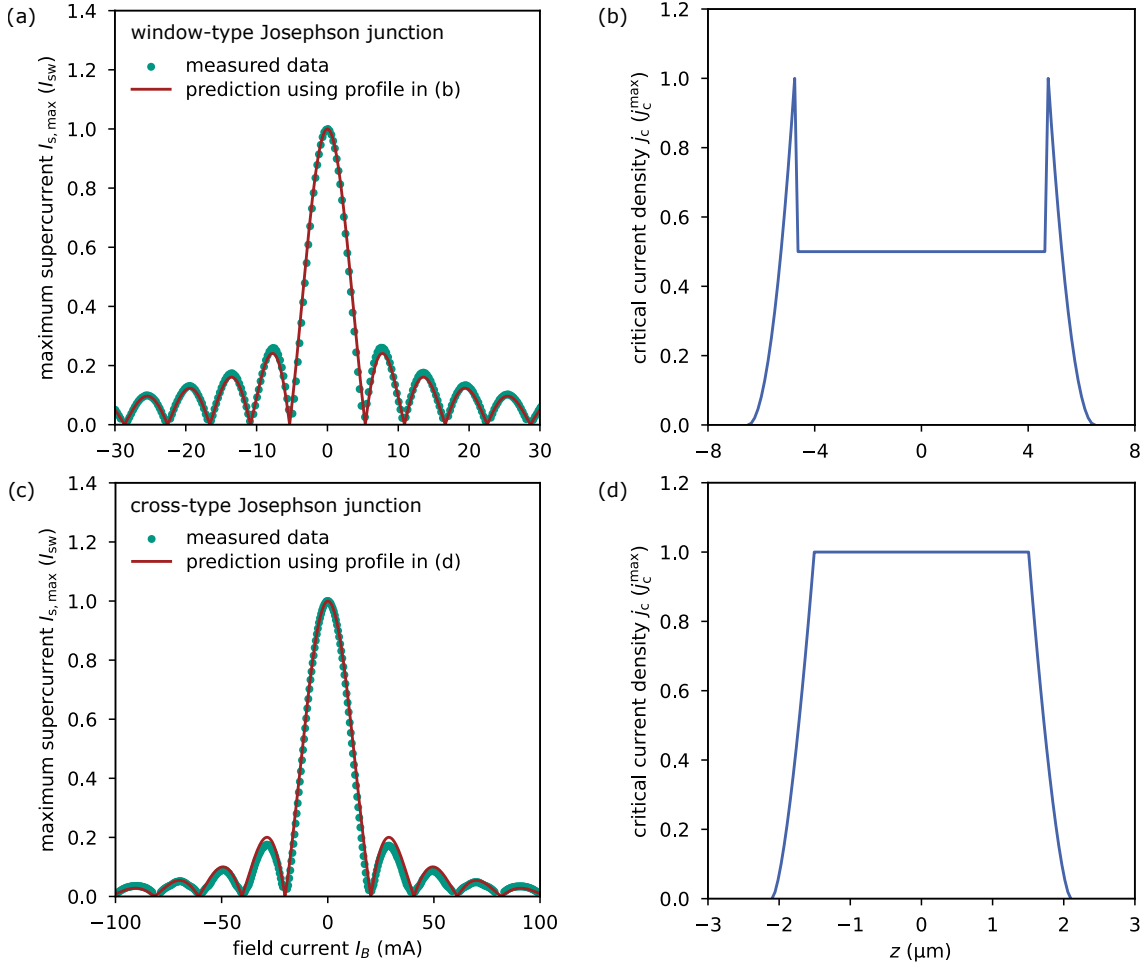


Figure 11: Magnetic field dependence of the normalized maximum supercurrent $I_{s,\max}$ of (a) a $13\ \mu\text{m} \times 13\ \mu\text{m}$ window-type junction and (c) a $4.2\ \mu\text{m} \times 4.2\ \mu\text{m}$ cross-type Josephson junction. For normalization the switching current I_{sw} for zero magnetic field was used. The solid red line corresponds to the predicted magnetic field dependence assuming the corresponding critical current density profile $j_c(z)$ plotted in (b) and (d), respectively.

4.4. Capacitance measurements

We measured the capacitance C_{JJ} of several cross-type Josephson junctions taken from batches with different critical current densities using unshunted dc-SQUIDs as described in section 3. As the parasitic capacitance C_{par} is expected to be negligible due to the missing overlap of wiring layers, the measured values should resemble the intrinsic capacitance related to the tunnel barrier. Figure 12 summarizes the result of our measurements and shows the dependence of the inverse junction capacitance per junction area C'_{JJ} on the critical current density j_c for each measured SQUID. We note that the specific capacitance $C'_{JJ} = C_{JJ}/A$ is derived from the measured capacitance value C_{JJ} as well as the effective junction area A that is determined from fitting the dependence of the normal state resistance on the junction area (see section 4.2). Moreover, figure 13 shows

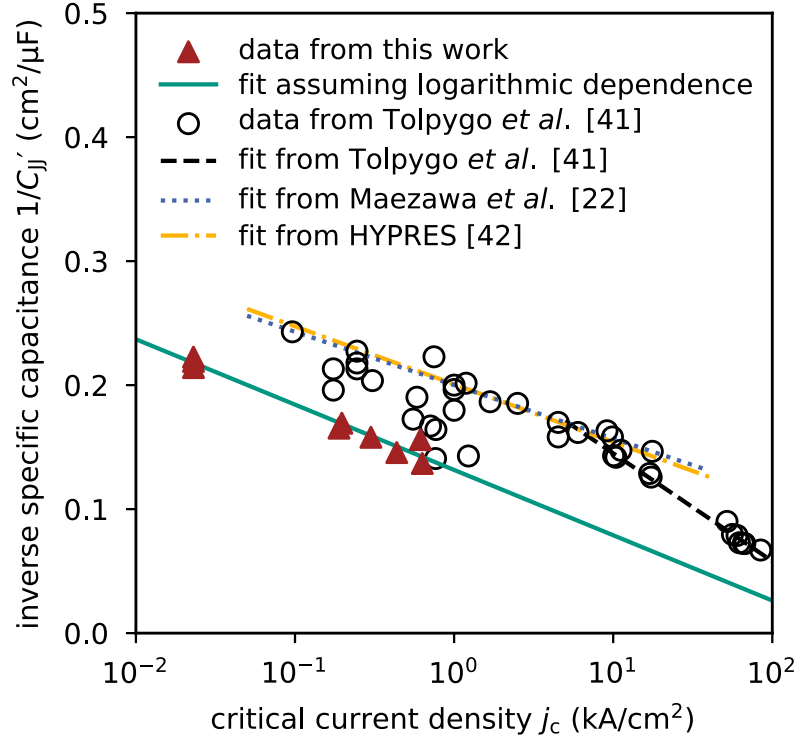


Figure 12: Inverse specific capacitance C'_{JJ} versus critical current density j_c . For our data, each data point represents one characterized unshunted SQUID. The solid green line with $1/C'_{JJ} = 0.132 \text{ cm}^2/\mu\text{F} - 0.053 \text{ cm}^2/\mu\text{F} \log_{10}(j_c \text{ cm}^2/\text{kA})$ represents the result of a fit to the data assuming a logarithmic dependence. The data points and the dashed line in black are from reference [41], the dotted blue line is from reference [22] and the dash-dotted yellow line is from reference [42] for comparison.

an example of a recorded Shapiro step of a current-biased SQUID with an experimentally determined loop inductance of $L_s = 14.0 \text{ pH}$ and a critical current of $I_c = 9.65 \text{ }\mu\text{A}$ of the Josephson junction. The resonance voltage $V_{\text{res}} = 221 \text{ }\mu\text{V}$ for deriving the junction capacitance

$$C_{JJ} = \frac{\Phi_0^2}{2\pi^2 V_{\text{res}}^2 L_s} \quad (4)$$

was determined by fitting the expected shape of the resonance curve to the actual data [43]. The value of the damping parameter $\Gamma = I_c R / V_{\text{res}}$ required for performing this fit was extracted from its relation to the current ratio $I_{\text{res}} / 2I_c$ [44]. For the resonance curve shown in figure 13, $\Gamma = 13.3$. The amplitude of the measured resonance step does not reach the theoretically expected value due to thermal suppression at $T = 4.2 \text{ K}$.

The solid line in figure 12 represent a fit to the data assuming a logarithmic dependence of the specific capacitance on the critical current density [22, 23]. We find

$$\frac{1}{C'_{JJ}} = 0.132 \frac{\text{cm}^2}{\mu\text{F}} - 0.053 \frac{\text{cm}^2}{\mu\text{F}} \log_{10} \left(\frac{j_c}{\text{kA/cm}^2} \right). \quad (5)$$

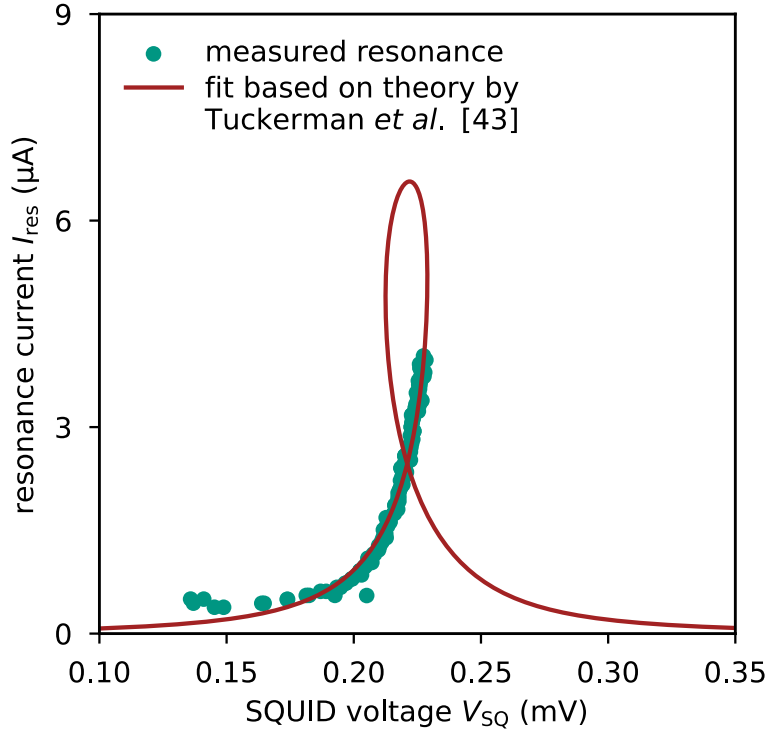


Figure 13: Expected and measured voltage-dependence of the resonance current I_{res} for an unshunted dc-SQUID with inductance $L_s = 14.0$ pH, resonance voltage $V_{\text{res}} = 221$ μV , damping parameter $\Gamma = 13.33$ and junction critical current $I_c = 9.65$ μA . More details are given in the main text.

For comparison, we also display the data and derived functional dependencies of the specific capacitance published in [41] and the references therein. We see that in a critical current density range between approximately 0.01 kA/cm^2 and 10 kA/cm^2 the slope of the functional dependence of our cross-type Josephson junctions is similar to those published by other research groups [22, 42]. Nevertheless, the offset is slightly higher which might be related to different crystal structures of the aluminum oxide barrier.

5. Conclusion

We have developed an anodization-free fabrication process for Nb/Al-AlO_x/Nb cross-type junctions. Our process requires only a small number of fabrication steps and is intrinsically compatible with wafer-scale fabrication. Fabricated junctions are of very high-quality as indicated by the measured values for the subgap to normal state resistance ratio and the $I_c R_N$ product. Compared to other junction types manufactured under the same technical conditions, our cross-type Josephson junctions show not only a significantly reduced specific capacitance but also an almost rectangular critical current density profile. Our process hence enables the usage of low capacitance Josephson

junctions for superconducting electronic devices such as ultra-low noise dc-SQUIDs, microwave SQUID multiplexers based on non-hysteretic rf-SQUIDs, and RFSQ circuits.

Acknowledgments

We would like to thank A Reifenberger, O Kieler and T Wolf for support during device fabrication and characterization. Moreover, we thank A Ferring, C Jakob, M Schmelz, and R Stolz for fruitful discussions. F Bauer acknowledges former financial support by the Helmholtz Graduate School for Hadron and Ion Research (HGS-HIRE of FAIR). The research leading to these results has also received funding from the European Union's Horizon 2020 Research and Innovation Programme, under Grant Agreement No. 824109.

Data Availability Statement

The data that support the findings of this study are available from the corresponding author upon reasonable request.

References

- [1] Clarke J and Wilhelm F K 2008 *Nature* **453** 1031–42 URL <https://doi.org/10.1038/nature07128>
- [2] Fagaly R L 2006 *Review of Scientific Instruments* **77** URL <https://doi.org/10.1063/1.2354545>
- [3] Yohannes D T, Hunt R T, Vivalda J A, Amparo D, Cohen A, Vernik I V and Kirichenko A F 2015 *IEEE Transactions on Applied Superconductivity* **25**(3) 1100405 URL <https://doi.org/10.1109/TASC.2014.2365562>
- [4] Kunert J, Ijsselsteijn R, Il'ichev E, Brandel O, Oelsner G, Anders S, Schultze V, Stolz R and Meyer H G 2017 *Low Temperature Physics* **43**(7) 785 URL <https://doi.org/10.1063/1.4995626>
- [5] Hamilton C A 2000 *Review of Scientific Instruments* **71** URL <https://doi.org/10.1063/1.1289507>
- [6] Blüthner K, Götz M, Krech W, Mühlig H, Wagner T, Fuchs H J, Bluthner K, Gotz M, Muhlig H, Schelle D, Fritzsche L, Nachtmann B and Nowack A 1996 *Journal de Physique IV Proceedings* **111**(C3) 3–163 URL <http://dx.doi.org/10.1051/jp4:1996325>
- [7] Dolata R, Scherer H, Zorin A B and Niemeyer J 2005 *Journal of Applied Physics* **97**(5) URL <https://doi.org/10.1063/1.1855399>
- [8] Bhat A, Meng X, Whiteley S, Jeffery M and Duzer T V 1999 *IEEE Transactions on Applied Superconductivity* **9**(2) 3232–3235 URL <https://doi.org/10.1109/77.783717>
- [9] Aumentado J 2020 *IEEE Microwave Magazine* **21**(8) 45–59 URL <https://doi.org/10.1109/MMM.2020.2993476>
- [10] Rothmel H, Gundlach K H and Voss M 1994 *Le Journal de Physique IV* **04**(C6) 267 URL <https://doi.org/10.1051/jp4:1994643>
- [11] Westig M P, Justen M, Jacobs K, Stutzki J, Schultz M, Schomacker F and Honingh N 2012 *Journal of Applied Physics* **112**(9) 093919 URL <https://doi.org/10.1063/1.4764324>
- [12] Clarke J and Braginski A I (eds) 2004 *The SQUID Handbook: Vol. 1 Fundamentals and Technology of SQUIDs and SQUID Systems* (Wiley-VCH Verlag GmbH & Co. KGaA) ISBN 3527402292
- [13] Gurvitch M, Washington M A and Huggins H A 1983 *Applied Physics Letters* **42**(5) 472 URL <http://aip.scitation.org/doi/10.1063/1.93974>
- [14] Dolata R, Weimann T, Scherer H J and Niemeyer J 1999 *IEEE Transactions on Applied Superconductivity* **9**(2) 3255 URL <https://doi.org/10.1109/77.783723>

- [15] Ketchen M B, Pearson D, Kleinsasser A W, Hu C K, Smyth M, Logan J, Stawiasz K, Baran E, Jaso M, Ross T, Petrillo K, Manny M, Basavaiah S, Brodsky S, Kaplan S B, Gallagher W J and Bhushan M 1991 *Applied Physics Letters* **59**(20) 2609–2611 URL <https://doi.org/10.1063/1.106405>
- [16] Bao Z, Bhushan M, Han S and Lukens J E 1995 *IEEE Transactions on Applied Superconductivity* **5**(2) 2731–2734 URL <https://doi.org/10.1109/77.403155>
- [17] Watanabe M, Nakamura Y and Tsai J S 2004 *Applied Physics Letters* **84**(3) 410–412 URL <https://doi.org/10.1063/1.1640798>
- [18] Harada Y, Haviland D B, Delsing P, Chen C D and Claeson T 1994 *Applied Physics Letters* **65**(5) 636–638 URL <https://doi.org/10.1063/1.112255>
- [19] Dang H and Radparvar M 1991 *IEEE Transactions on Magnetics* **27**(2) 3157 URL <https://doi.org/10.1109/20.133881>
- [20] Anders S, Schmelz M, Fritzsche L, Stolz R, Zakosarenko V, Schönau T and Meyer H G 2009 *Superconductor Science and Technology* **22**(6) 064012 URL <http://dx.doi.org/10.1088/0953-2048/22/6/064012>
- [21] Kaiser C, Meckbach J M, Ilin K S, Lisenfeld J, Schäfer R, Ustinov A V and Siegel M 2011 *Superconductor Science and Technology* **24** URL <http://dx.doi.org/10.1088/0953-2048/24/3/035005>
- [22] Maezawa M, Aoyagi M, Nakagawa H, Kurosawa I, Takada S and Tuckerman A 1995 *Applied Physics Letters* **66**(16) 2134 URL <https://doi.org/10.1063/1.113927>
- [23] Tolpygo S K, Yohannes D, Hunt R T, Vivalda J A, Donnelly D, Amparo D and Kirichenko A F 2007 *IEEE Transactions on Applied Superconductivity* **17**(2) 946 URL <https://doi.org/10.1109/TASC.2007.898571>
- [24] Kuroda K and Yuda M 1988 *Journal of Applied Physics* **63**(7) 2352 URL <https://doi.org/10.1063/1.341051>
- [25] Du J, Charles A D M, Petersson K D and Preston E W 2007 *Superconductor Science and Technology* **20**(11) S350 URL <https://doi.org/10.1088/0953-2048/20/11/S10>
- [26] Likharev K K 1986 *Dynamics of Josephson Junctions and Circuits* (Taylor & Francis) ISBN 9782881240423
- [27] Likharev K K 1979 *Reviews of Modern Physics* **51**(1) 101 URL <https://doi.org/10.1103/RevModPhys.51.101>
- [28] Fulton T A and Dunkleberger L N 1974 *Physical Review B* **9**(11) 4760 URL <https://doi.org/10.1103/PhysRevB.9.4760>
- [29] Danchi W C, Hansen J B, Octavio M, Habbal F and Tinkham M 1984 *Physical Review B* **30** 2503–2516 URL <https://doi.org/10.1103/PhysRevB.30.2503>
- [30] Wallraff A, Lukashenko A, Coqui C, Kemp A, Duty T and Ustinov A V 2003 *Review of Scientific Instruments* **74**(8) 3740 URL <https://doi.org/10.1063/1.1588752>
- [31] Castellano M G, Leoni R, Torrioli G, Chiarello F, Cosmelli C, Costantini A, Diambri-Palazzi G, Carelli P, Cristiano R and Frunzio L 1996 *Journal of Applied Physics* **80**(5) 2922 URL <https://doi.org/10.1063/1.363147>
- [32] Barone A and Paternò G 1982 *Physics and Applications of the Josephson Effect* (John Wiley & Sons, Inc.) ISBN 9783527602780
- [33] Guéret P 1979 *Applied Physics Letters* **35**(11) 889 URL <https://doi.org/10.1063/1.90995>
- [34] Magerlein J H 1981 *IEEE Transactions on Magnetics* **MAG-17**(1) 286 URL <https://doi.org/10.1109/TMAG.1981.1060968>
- [35] Williams T 2017 *EMC for Product Designers* 5th ed (Newnes) ISBN 978-0-08-101016-7
- [36] Henkels W H 1978 *Applied Physics Letters* **32**(12) 829 URL <https://doi.org/10.1063/1.89940>
- [37] Koch C and Rinke T J 2017 *Photolithography: Basics of Microstructuring* 1st ed (MicroChemicals GmbH) ISBN 978-3-9818782-1-9
- [38] Lehmann H W, Krausbauer L and Widmer R 1977 *Journal of Vacuum Science and Technology* **14**(1) 281 URL <https://doi.org/10.1116/1.569140>

- [39] Carbotte J P 1990 *Reviews of Modern Physics* **62**(4) 1027–1157 URL <https://doi.org/10.1103/RevModPhys.62.1027>
- [40] Kempf S, Ferring A, Fleischmann A, Gastaldo L and Enss C 2013 *Superconductor Science and Technology* **26**(6) 065012 URL <http://dx.doi.org/10.1088/0953-2048/26/6/065012>
- [41] Tolpygo S K, Bolkhovsky V, Zarr S, Weir T J, Wynn A, Day A L, Johnson L M and Gouker M A 2017 *IEEE Transactions on Applied Superconductivity* **27**(4) 1100815 URL <https://doi.org/10.1109/TASC.2017.2667403>
- [42] Hypres niobium integrated circuit fabrication, process #03-10-45, design rules, revision #25, 12/12/2012 URL <https://www.hypres.com/wp-content/uploads/2010/11/DesignRules-4.pdf>
- [43] Tuckerman D B and Magerlein J H 1980 *Applied Physics Letters* **37**(2) 241 URL <https://doi.org/10.1063/1.91839>
- [44] Paternò G, Cucolo A M and Modestino G 1985 *Journal of Applied Physics* **57**(5) 1680 URL <https://doi.org/10.1063/1.334437>

Aerosol Jet Printing of High-Temperature Multimodal Sensors for Strain and Temperature Sensing

*Md. Omarsany Bappy, Qiang Jiang, Stephanie Atampugre, and Yanliang Zhang**

Department of Aerospace and Mechanical Engineering, University of Notre Dame, Notre Dame,
Indiana 46556, USA

KEYWORDS: multimodal sensors, thermocouples, nanoparticles, aerosol jet printing, printed sensors, high-temperature applications, health monitoring

ABSTRACT: Integrating multiple sensing capabilities into a single multimodal sensor greatly enhances its applications for in-situ sensing and structural health monitoring. However, the fabrication of multimodal sensors is complicated and limited by the available materials and existing manufacturing methods that often involve complex and expensive fabrication processes. In this study, a high-temperature multimodal sensor is demonstrated by aerosol jet printing of gold and ITO nanoparticle inks. The printed multimodal sensor for concurrent strain and temperature sensing possesses a high gauge factor of 2.54 and thermopower of 55.64 $\mu\text{V}/^\circ\text{C}$ combined with excellent high-temperature thermal stability up to 540 $^\circ\text{C}$. Compared to traditional single-modality sensors, the printed multimodal sensor significantly increases sensing capacity and improves spatial resolution using microscale printed patterns. The study also demonstrates that the strain sensor with integrated thermocouple enables in-situ compensation of the temperature effect on strain sensing, significantly improving strain measurement accuracy at high temperatures. By

combining aerosol jet printing with nanomaterial inks, a wide range of multifunctional devices can be developed for a broad range of emerging applications.

1. INTRODUCTION

In recent years, there has been significant increasing interest in utilizing sensors across a diverse range of applications such as power generation, manufacturing processes, biometric sensing, and structural health monitoring in industries such as aerospace, nuclear, marine, and civil engineering.¹⁻⁵ Increased static or dynamic loads and the widespread adoption of lightweight components necessitate real-time monitoring of strain and temperature on parts with high risks of structural failures.^{6, 7} Multifunctional devices with multiple sensing capabilities have attracted considerable interest in structural health monitoring, in situ sensing, human-machine interfaces, soft robots, and wearable sensing applications.⁸⁻¹⁴

Additive manufacturing has emerged as a very attractive method to print sensors for a broad range of applications.^{15, 16} A variety of materials and methods have been explored to improve the performance of printed sensors for monitoring physical properties such as strain and temperature. For example, printed thermocouples were made using a variety of metals such as Molybdenum silicide vs. Tungsten silicide¹⁷, Indium oxide vs. Indium Tin oxide¹⁸, and Graphene vs. MXene¹⁹. Graphite thin film^{20, 21}, Silver nano particles²², and MXene ink¹⁹ have been widely used in strain sensing applications. Direct printing techniques such as inkjet, aerosol jet, and screen printing have garnered significant attention in recent years due to their ability to transform nanoscale materials directly into functional devices. Significant progress has been achieved in the realm of printed sensors that possess a single modality, such as strain²⁰⁻²⁶, temperature^{2, 27-30}, and pressure³¹⁻³⁴. Nevertheless, the fabrication of multimodal sensors remains a challenge owing to the intricate manufacturing processes and the complexity of decoupling multiple signals.³⁵⁻³⁹ Aerosol jet

printing (AJP) enables direct 3D conformal printing of multimodal sensors onto components with complex geometry, resulting in intimate thermal and mechanical coupling and accurate temperature and strain measurements. A graphene and MXene nano ink-based flexible bimodal sensor by AJP was demonstrated to monitor temperature and detect strain simultaneously up to 150 °C.¹⁹ However, the multimodal sensor for simultaneous measurement of strain and temperature at high temperatures is yet to be explored. Under high-temperature operating conditions, the electrical and mechanical properties of printed sensors can be negatively impacted due to oxidation, fatigue, drifting, thermal deformation, and creep, leading to various challenges.^{6, 40, 41}

Herein, we report an aerosol jet printed high-temperature multimodal sensor for simultaneous strain and temperature measurements. The multimodal sensor is fabricated using ITO and Gold nanoparticles, owing to their exceptional thermal stability, oxidation resistance, and consistent sensing performance at high temperatures. The AJP also makes it possible to print sensors with a high spatial resolution ($\sim 10\ \mu\text{m}$).^{15, 42-46} The printed sensor studied here shows a gauge factor of 2.54 at room temperature, which is around 30% greater than that of typical metal-based strain gauges (e.g., copper-nickel alloy)^{21, 22} with a temperature-sensing thermopower of $55.64\ \mu\text{V}/^\circ\text{C}$.

2. EXPERIMENTAL METHODS

2.1. Sensor Design and Fabrication. The aerosol jet printing method is utilized to print the multimodal sensor in this study. AJP offers the ability to print sensors with fine features, including line widths as small as $\sim 10\ \mu\text{m}$ and film thicknesses $\sim 100\ \text{nm}$, thereby enabling the integration of multiple sensor materials into a compact device. This printing method also allows non-intrusive sensor implementation, featuring intimate thermal contacts and mechanical coupling, leading to highly precise temperature and strain measurements. Furthermore, AJP has the capability to print sensors on not only 2D surfaces but also irregular-shaped components with curved surfaces, such

as valves and welded joints, which are more susceptible to failure and are difficult to attach conventional sensors.

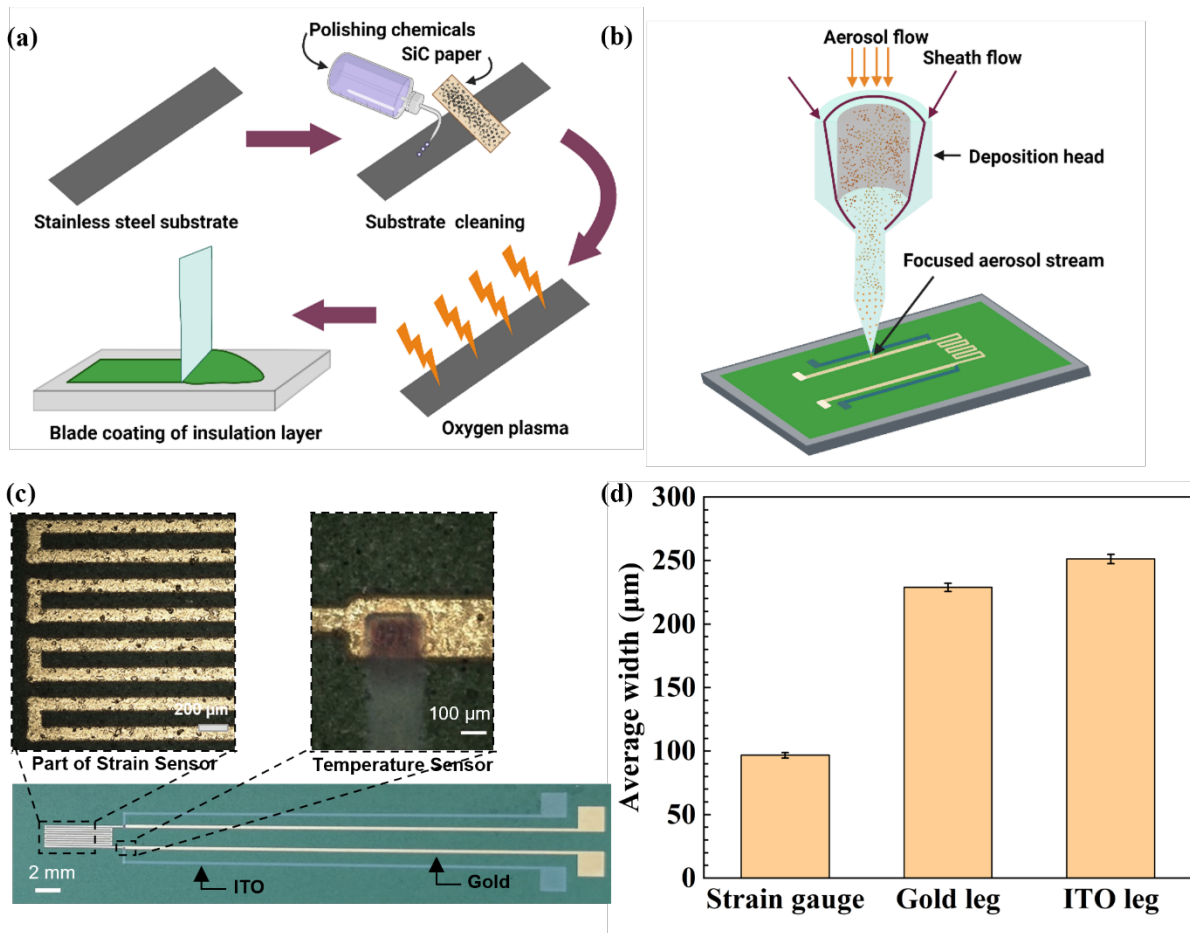


Figure 1. Schematic illustration of a) stainless steel substrate preparation and blade coating of a dielectric layer on the substrate, b) aerosol jet printing of multi-modal sensor on stainless steel substrate (not to scale), c) optical image of the printed sensor consisting of two thermocouples (gold ITO junction) and one strain gauge (gold) along with image viewed at a high magnification of temperature sensor and portion of strain sensor, d) width fluctuation of the printed sensor in distinct regions.

Substrate preparation and the AJP printing process for the multimodal sensor are depicted schematically in Figure 1. To prepare the stainless-steel substrate (154 mm × 26 mm × 0.5 mm)

for printing, it is initially cleaned with isopropyl alcohol and acetone to remove any surface impurities. The surface is then abraded using 200-grit silicon carbide paper to eliminate the possibility of adhesion, such as flaking paint, corrosion, scale, etc. A wet abrasion process is employed using chemical polishing agents and 400-grit silicon carbide paper. Then, the substrate is subjected to a 5-minute oxygen plasma treatment at 100 W (PDC-001-HP, Harrick Plasma, Ithaca, NY) to remove any unwanted foreign particles from the substrate surface. A dielectric layer of HG1 ceramic cement with a thickness of $94.4 \pm 4.8 \mu\text{m}$ (measured by DektakXT, Bruker profilometer, $0.2\mu\text{m}$ stylus radii, and 1 mg stylus force) is applied to the substrate by blade coating to ensure electrical insulation between the sensor and the substrate. The HG1 ceramic cement is then cured through four steps, including air drying for 30 minutes, thermal curing at $200\text{ }^\circ\text{C}$ for 30 minutes, holding at $400\text{ }^\circ\text{C}$ for 30 minutes, and finally, holding at $600\text{ }^\circ\text{C}$ for 30 minutes.

The multimodal sensor is then printed on the cured substrate by an aerosol jet printer (Optomec, Inc., AJ 300 system, Albuquerque, NM). Prior to sensor printing, an AutoCAD file illustrating the sensor design shown in Figure S1 in SI is fed into the printer to create the toolpath for printing. The AJP system includes a deposition head, a programmable motion system, an ultrasonic atomizer, and a pneumatic atomizer. Fabrication of a multimodal strain sensor with integrated thermocouples necessitates using two materials with high-temperature stability and distinct Seebeck coefficients. This study employs gold and ITO nanoparticle inks. The first step is to load the ultrasonic atomizer with a solution containing 2 wt. % gold nanoparticles dissolved in xylene (UTD Au25X, gold nano ink in xylene, UT DotsInc. Champaign IL). The ultrasonic atomizer generates aerosolized ink droplets ranging from 0.5 to 5 microns^{47, 48} to print the strain sensor. The aerosolized ink droplets are collimated into a micro-jet by an annular sheath gas (N_2) that surrounds the entering stream at the transition zone of the printhead. Once the strain sensor is printed using

the gold ink, the ink vial of the ultrasonic atomizer is filled with a 5 wt. % ITO nanoparticle solution (particle size of 18 nm, water solvent, $\geq 99.5\%$ trace metals basis, Sigma Aldrich Co.) to print the ITO electrode. The printed ITO and Gold electrodes form a thermocouple junction (Figure 1c) due to their distinctive Seebeck coefficient. The sensor is constructed by depositing three layers of ink and using multiple lateral passes to create individual electrodes. Real-time pictures of sensor printing at different printing steps are shown in Figure S2. The printing process parameters, such as sheath gas flow rate, carrier gas flow rate, printing speed, standoff distance, ultrasonic power for ink aerosolization and droplet formation, platen temperature are optimized for the gold and ITO inks (Table S1). Following printing, the printed sensors are sintered in a tube furnace at 800 °C for 2 hours in the air to consolidate the printed nanoparticles into a dense, thermally stable, electrically conductive, and mechanically robust structure.

2.2. Calibration Methodology. To evaluate the strain measured by the printed multimodal sensor, the stainless-steel substrate is fixed at one end using a bracket attached to the timing belt of a vertical shaft while the other end is kept free, resembling a cantilever beam (as shown in Figure S3). At first, the sensor is calibrated using a commercial strain sensor (Omega, Precision strain gauges, Resistance 350 Ω , Gauge factor 2.05) and commercial thermocouple (Omega, K-type). The commercial strain gauge is attached to the stainless-steel substrate at exactly the same position as the printed strain gauge and then flexed up to 10 mm in 5 steps using motorized linear movement of a timing belt. The resistance at each deflected position is measured. Strain at different bending positions can be determined from the relative resistance change with respect to resistance at the initial position and gauge factor of the commercial strain gauge using the following equation

$$GF = \frac{\Delta R/R_0}{\varepsilon} \quad (1)$$

where ϵ represents strain, $\Delta R/R_0$ represents the change of resistance with reference to the initial resistance R_0 , and GF is the gauge factor, which represents the sensitivity of the strain sensor. Cantilever beam theory is also applied to calculate the strain experienced by the cantilever beam at each bending position. The theoretical strain calculated from beam theory and strain measured by the commercial strain sensor are compared to ensure the accuracy of calibration methodology. Details of the theoretical calculation of strain is shown in Figure S14. The measured strain is then used to obtain the gauge factor of the printed multimodal sensor. The Seebeck voltage generated at the printed thermocouple junction is also meticulously calibrated using the commercial K-type thermocouple. The DC Seebeck voltage generated at the printed thermocouple was measured up to 550 °C and at the same time the hot and cold junction temperature was measured by the commercial thermocouples. Thus, the generated voltage was calibrated against the known temperature difference between the hot and cold junction.

2.3. Simultaneous Temperature and Strain Measurement Setup. To measure the resistance of the printed strain gauge, a high-frequency alternating current is applied through the printed gold electrodes to the strain gauge, and the resulting AC voltage is measured via the printed ITO electrodes to measure the AC resistance change and determine the strain. At the same time, the DC Seebeck voltage generated at the printed ITO and gold electrode junction is measured to determine the temperature difference between the ITO-gold thermocouple junction and the cold side of the thermocouple. The experimental setup is configured to simultaneously detect strain and temperature as illustrated in Figure S3-4 in the supporting information.

The customized test setup integrates an electric muffle furnace (KSL-1100X-S, 950W, Maximum temperature 1100°C, MTI Corporation) to perform measurements at high temperatures. The system comprises a stepper motor to drive the timing belt, a microcontroller driver to control

the motor, and a base to hold the vertical shaft, to which the timing belt and stainless-steel bracket are attached. A 34970A data acquisition/data logger switch unit is used to measure the Seebeck voltage generated across the gold and ITO junction and the resistance of the strain sensor. The data acquisition unit is controlled by a computer, which is also used to monitor and record data. The sensor is clamped with the bracket, which can move up and down with the linear motion of the timing belt. The movement of the timing belt is precisely regulated at each testing cycle to ensure accurate testing results. The sensor is deflected like a cantilever beam as the tip is placed beneath a ceramic tube attached to the furnace wall, when it moves up strain is induced in it. A rectangular section (30 mm × 12 mm) is cut from the furnace door to insert the sensor inside the furnace and allow up to 10 mm deflection. The furnace door is closed after inserting the sensor inside the furnace and then high-temperature super wool thermal insulation paper is used to minimize heat loss from the cut-away section of the furnace door during high-temperature measurements. Moreover, a cooling water circuit is inserted at the stainless-steel bracket along with the sensor to keep the cold junction of the printed thermocouple at ambient temperature. To ensure thermal stabilization before conducting measurements at high temperatures, the multi-functional sensors undergo annealing at 600°C for 15 hours.

3. RESULTS AND DISCUSSION

3.1. Sensor Morphology. Figure 1c shows an optical image of the sensor and a high-magnification image of the printed thermocouple junction and a part of the strain sensor. The printed sensor consists of two thermocouple junction and one strain gauge. Details of the multimodal sensor design, thermocouple hot junction, cold junction, etc. are shown in Figure S1. The width variation of the printed pattern at different regions of the sensor is measured under an optical microscope (63 locations in each region) and the corresponding average line width along

with the standard deviation is shown in Figure 1d. Detailed line widths at different parts of the printed sensor are shown in Figure S5. The small standard deviation in the width variation indicates the high consistency of microscale additive manufacturing via aerosol jet printing. White light profilometer (Filmetrics, Profilm3D) is used to map the surface topology of the sensor and measure thicknesses at different parts as shown in Figure S6 and Figure S7, which reveals a mean thickness of 3.19 μm along the strain gauge and mean thicknesses of approximately 2.76 μm and 14.31 μm along the gold electrode and the ITO electrode respectively.

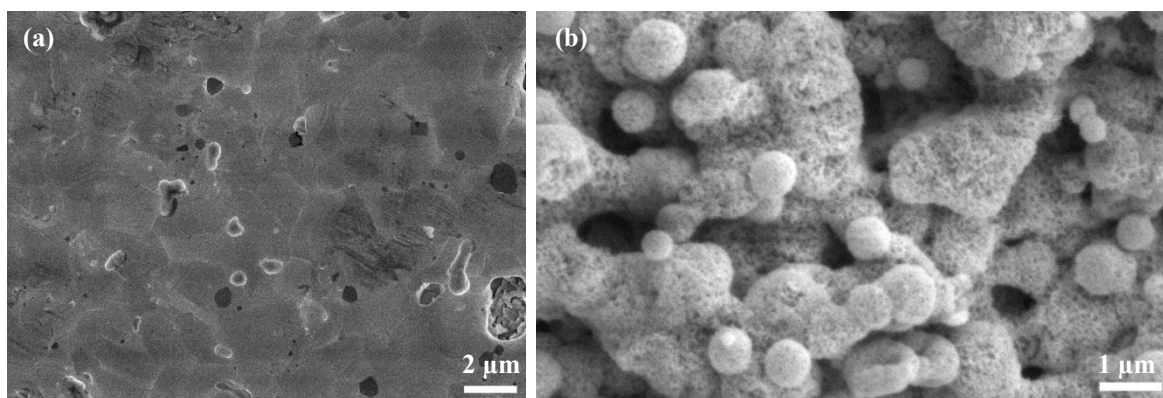


Figure 2. SEM images of the aerosol jet printed gold and ITO films sintered at 800 $^{\circ}\text{C}$, a) morphology of the top surface of the gold film and b) morphology of the top surface of the ITO film.

Figure 2 shows the SEM images of the printed gold and ITO sintered at 800 $^{\circ}\text{C}$. During sintering, the solvents are removed, resulting in porosity, which is then reduced by grain growth and particle coalescing to form well-connected and densified microstructures. The printed gold and ITO under optimized sintering conditions show electrical conductivity of 1.9×10^7 and 1.5×10^4 S/m, respectively. The gold film shows a highly dense microstructure with substantial grain growth because of the relatively high sintering temperature compared to the melting point of the gold nanoparticles, whereas the ITO shows a relatively large porosity as the sintering temperature is well below the melting temperature of ITO. The estimation of porosity is shown in Figure S8.

3.2 Temperature Measurement. The Seebeck voltages produced by the gold/ITO thermocouple junctions are measured at a wide range of temperature differences. The applied temperature gradient determines the thermoelectric voltage, which can be expressed as

$$V = \int_{T_c}^{T_h} S_G(T) - S_{ITO}(T) dT \quad (2)$$

Where S_G and S_{ITO} are the temperature-dependent Seebeck coefficients of gold and ITO electrodes, T_H and T_C represent the hot and cold junction temperatures, respectively. The hot side and cold side thermocouple junctions are shown in Figure S1. Two commercial thermocouples (Omega, K type) are inserted close to hot side and cold side of the sensor to continuously monitor and record the temperature. During measurement, the muffle furnace temperature is increased from ambient to 550 °C with a heating rate of 2.5 °C/min to increase the thermocouple hot junction temperature, and the corresponding Seebeck voltage is recorded. The Seebeck voltage increases linearly with the temperature difference between the hot and cold junctions of the printed thermocouple, as illustrated in Figure 3. The hot junction temperature, cold junction temperature, and generated thermoelectric voltage are shown in Figure S9. The cold junction temperature increases from 22 °C to 30 °C when the hot junction reaches 550 °C. The cold side is maintained as cold as possible using a liquid cold plate as shown in Figure S4. The printed thermocouples generated a maximum Seebeck voltage of 29.8 mV when the hot junction temperature reached 550 °C, with a temperature difference of 520 °C between the hot and cold junctions. The behavior of the printed thermocouple during heating and cooling indicates exactly the same ramp-up and down characteristics, as illustrated in Figure 3a.

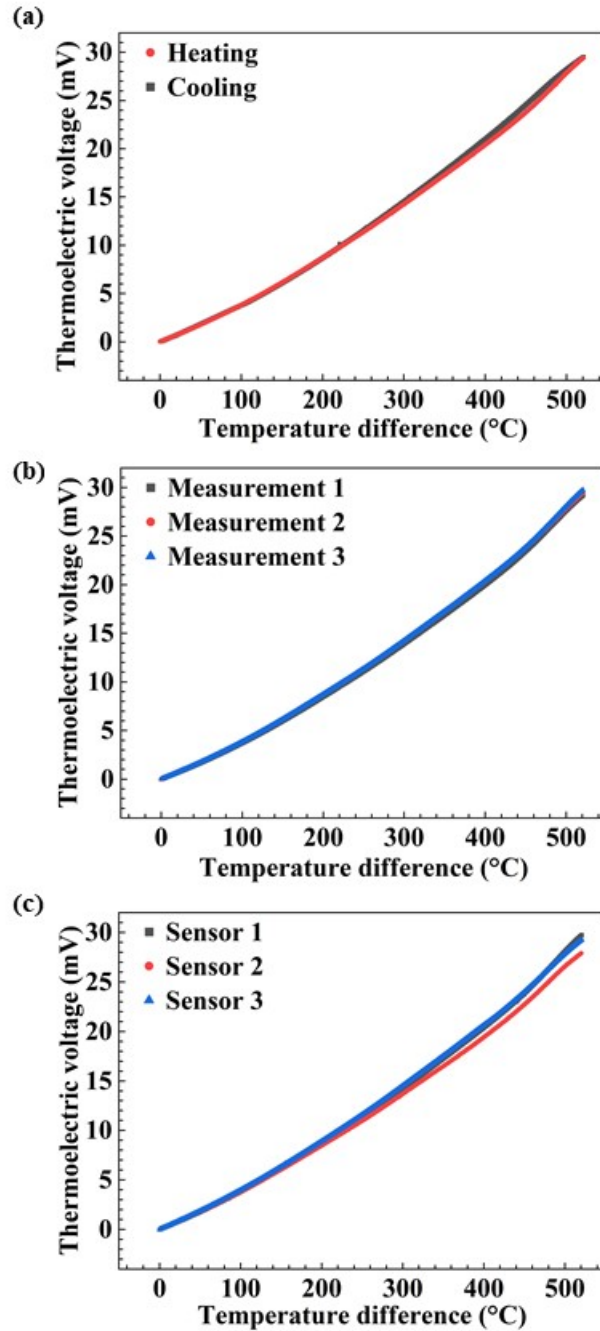


Figure 3. a) Thermoelectric voltage response of the printed gold/ITO thermocouple during heating and cooling cycles, b) stability of the printed thermocouple during three repeated measurements, and c) thermoelectric voltage output vs. temperature for three sensors printed under the same conditions.

For simplicity, only left thermocouple data has been shown in Figure 3 because the hot side temperature was measured near the left thermocouple. However, both the left and right thermocouple shows almost identical Seebeck voltage for same temperature difference as shown in Figure S10. The printed thermocouples show remarkable thermal stability and repeatability during repeated thermal cycling measurements at elevated temperatures up to 550 °C (Figure 3b), revealing high precision in temperature measurement. Moreover, the printed sensor demonstrates excellent reproducibility with three sensors showing an average thermopower of $55.64 \pm 1.5 \mu\text{V}/^\circ\text{C}$ (Figure 3c). The printed thermocouple shows higher thermopower (sensitivity) than other thin film thermocouples reported in the literature (Table S2 in the supporting information).^{2, 19, 49-52} The small variation of the thermopower between the three sensors can be attributed to the measurement error. The slightly variation in commercial thermocouple positions while testing different sensors can cause inaccuracy in exact hot and cold junction temperature measurement.

3.3 Simultaneous Temperature and Strain Measurements at Room Temperature. To obtain an accurate measurement of the strain gauge resistance without including lead wire resistances and contact resistance, the four-wire measurement method is used to measure the resistance of the strain gauge. An alternating current (AC) with a frequency of 5,000 Hz is input to the strain gauge via the gold electrode of the thermocouple, producing an AC resistive voltage that is measured across the ITO electrode. The resistance value of the strain gauge can be determined by the measured voltage and current of the AC signal. The DC Seebeck voltage across the thermocouple is also measured separately to determine temperature without any interference with the AC resistive voltage across the same thermocouple.

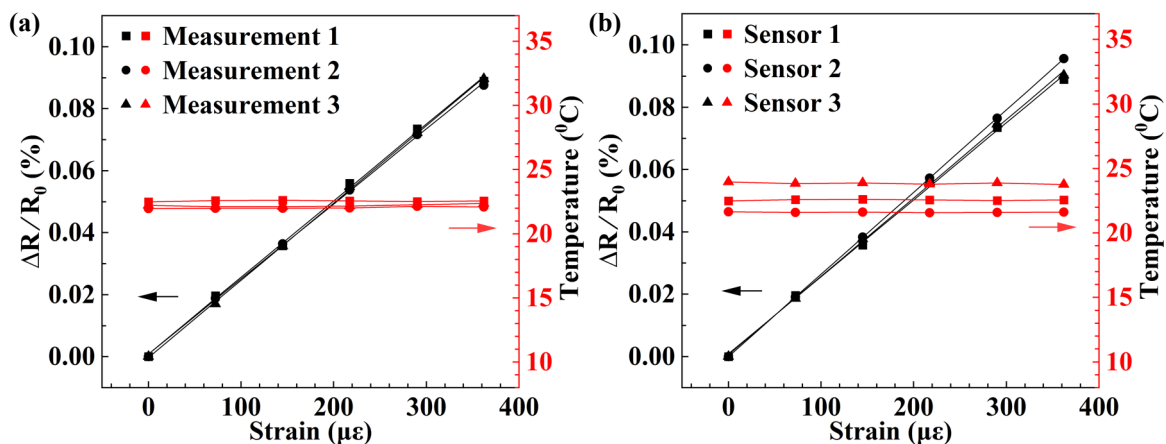


Figure 4. Simultaneous measurements of temperature and strain at ambient temperature, a) for three different measurements of a sensor to show the stability of the printed sensor, and b) for three different sensors.

Concurrent temperature and strain measurement results at room temperature of the printed multimodal sensors are depicted in Figure 4. The resistances of the three strain gauges are 11.95 Ω , 12.0 Ω , and 12.1 Ω at 22 $^{\circ}\text{C}$ ambient temperature. To obtain the response of the strain gauge at different strains, the sensor tip is deflected up to 10 mm in 5 equal steps in a cycle. The change of resistances with repeated bending cycles for a printed sensor is shown in Figure S11 in the SI. Figure 4a shows the relative change of resistance for three repeated measurements of the same sensor at different strains, along with the corresponding temperature, as measured by the multimodal sensor, demonstrating its high repeatability. Figure 4b shows high reproducibility with <3% variations for three different sensors printed under the same conditions. Moreover, the printed strain gauge has a gauge factor of 2.54 ± 0.07 at room temperature, which is about 30% higher than that of most commercial strain sensors with a gauge value of around 2.^{21, 22}

3.4 Performance of the Multimodal Sensor at High Temperature. Concurrent temperature and strain measurement results are illustrated in Figure 5a-d at temperatures 140 $^{\circ}\text{C}$, 285 $^{\circ}\text{C}$, 440

°C, and 540 °C respectively. The signals collected from the sensors were consistent and reliable across all temperature ranges in multiple measurements. The recorded thermoelectric voltage and a corresponding calibration curve of the sensor are utilized to determine the temperature measured by the printed thermocouple which agrees well with the commercial thermocouple.

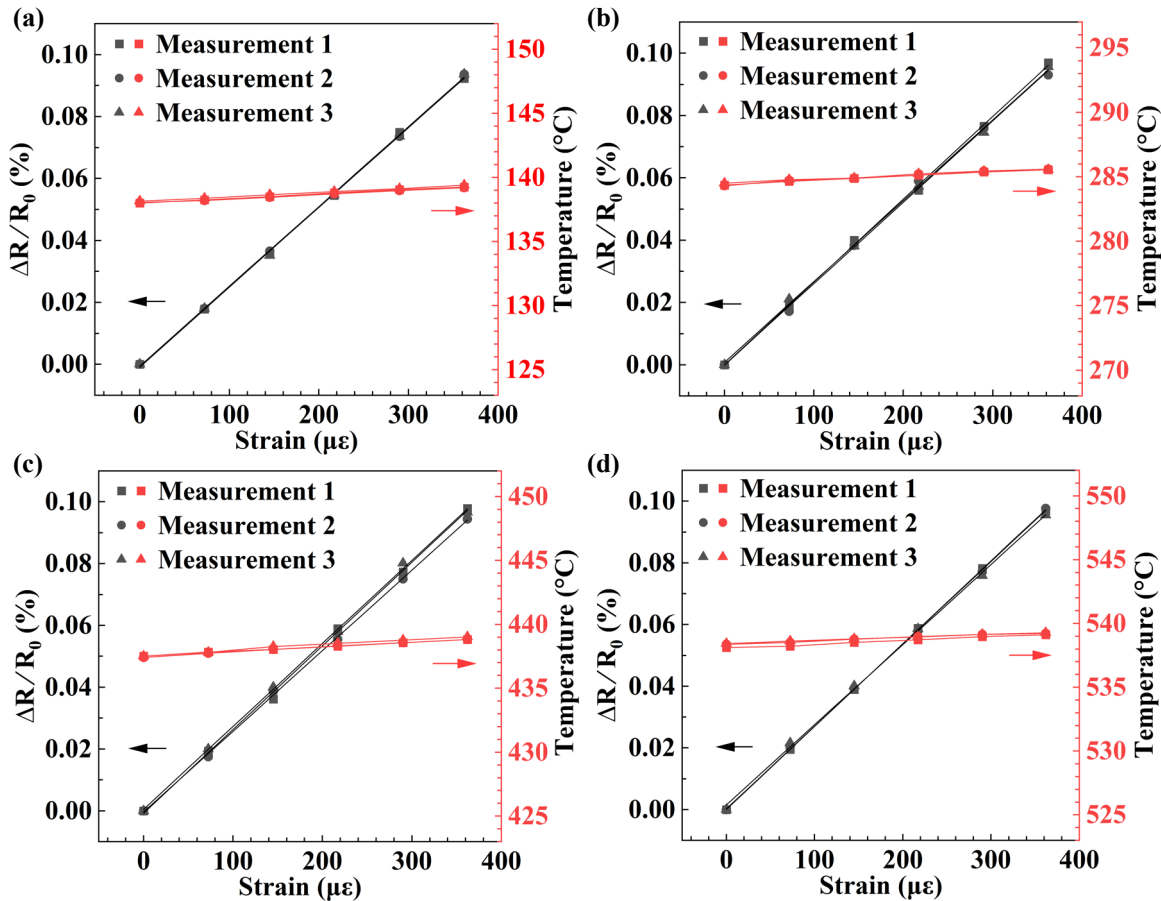


Figure 5. Simultaneous measurement of temperature and strain for three different measurements to show the stability of the multimodal sensor measured at a) 140 °C, b) 285 °C, c) 440 °C, and d) 540 °C.

To measure strain at a certain temperature, at first the temperature of the muffle furnace is stabilized for a long period of time to maintain the test strain gauge completely stable at that specific test environment, and then strain is induced to the strain gauge. Thus, the change of

resistance of the gauge is ensured to be only due to the applied mechanical strain. Multiple measurements are conducted at different strains to assess the stability of the printed sensors. As shown in Figure 5, three black lines show the changes of resistances of same strain gauge in three different measurements and the red lines shows the three different temperature measurements. The repetitive results, as shown in Figure 5, demonstrate the high precision of the printed sensor that does not degrade even at 540 °C. The standard deviation of multiple data points at each strain is very low, indicating identical measurements of resistance changes for a given strain. As shown in Figure S12, the gauge factor of the printed strain gauge varies slightly with temperature. The variation of gauge factor with temperature is around 0.01%/K. The error bar associated with Figure S12 represents the standard deviation of gauge factor of three sensors measured at five different temperatures and indicates excellent repeatability of the three strain gauges, which ensures that the sensor signals can be accurately reproduced at high temperatures. Figure S13 shows that the resistance of the strain gauge increases from 12 Ω to 36 Ω with a temperature coefficient of resistance of 0.0038/°C when the temperature increases from ambient to 542 °C. This highlights the importance of in-situ temperature measurement to decouple the changes in resistance caused by temperature and strain when using resistive-based strain sensors.

4. CONCLUSION

In conclusion, gold and ITO nanoparticle inks were employed to fabricate a multimodal sensor for temperature and strain sensing simultaneously. The highly versatile aerosol jet printing process makes it possible to transform and integrate multiple nanoscale building blocks into a strain sensor with integrated thermocouples, enabling accurate strain measurement without complex temperature compensation methods. The printed multimodal sensor exhibits exceptional high-temperature stability up to 540 °C. The sensor demonstrates a competitive gauge factor of 2.54 at

room temperature and a thermopower of 55.64 $\mu\text{V}/^\circ\text{C}$ over the gold and ITO thermocouple junction. The fully printed multimodal sensors demonstrated in this work open exciting opportunities to directly print and integrate emerging nanoscale materials into multifunctional devices for a broad range of applications.

ASSOCIATED CONTENT

Supporting Information

The Supporting Information is available free of charge on the ACS Publications website.

AUTHOR INFORMATION

Corresponding Author

*Email: yzhang45@nd.edu

Author Contributions

The manuscript was written through contributions of all authors. All authors have given approval to the final version of the manuscript.

Notes

The authors declare no competing financial interest.

ACKNOWLEDGEMENTS

This work was supported by the U.S. Department of Energy under Award No. DE-NE0009138.

REFERENCES

- (1) Fisher, C.; Skolrood, L. N.; Li, K.; Joshi, P. C.; Aytug, T. Aerosol-Jet Printed Sensors for Environmental, Safety, and Health Monitoring: A Review. *Advanced Materials Technologies* **2023**, 2300030.
- (2) Rahman, M. T.; Cheng, C.-Y.; Karagoz, B.; Renn, M.; Schrandt, M.; Gellman, A.; Panat, R. High performance flexible temperature sensors via nanoparticle printing. *ACS Applied Nano Materials* **2019**, 2 (5), 3280-3291.
- (3) Li, H.-N.; Li, D.-S.; Song, G.-B. Recent applications of fiber optic sensors to health monitoring in civil engineering. *Engineering structures* **2004**, 26 (11), 1647-1657.
- (4) Wilson, W. C.; Atkinson, G. M. Passive wireless sensor applications for NASA's extreme aeronautical environments. *IEEE Sensors Journal* **2014**, 14 (11), 3745-3753.
- (5) Phero, T. L.; Fujimoto, K. T.; Khanolkar, A. R.; McMurtrey, M. D.; Johnson, B.; Estrada, D.; Jaques, B.; Novich, K. *Additively Manufactured Strain Sensing for Nuclear Reactor Applications*; Idaho National Laboratory (INL), Idaho Falls, ID (United States), 2023.
- (6) Fichtel, E. J.; McDaniel, A. D. *High temperature strain gage technology for gas turbine engines*; 1994.
- (7) Lei, J.-F.; Will, H. A. Thin-film thermocouples and strain-gauge technologies for engine applications. *Sensors and Actuators A: Physical* **1998**, 65 (2-3), 187-193.
- (8) Kang, H.-K.; Bang, H.-J.; Hong, C.-S.; Kim, C.-G. Simultaneous measurement of strain, temperature and vibration frequency using a fibre optic sensor. *Measurement Science and Technology* **2002**, 13 (8), 1191.
- (9) Xu, K.; Lu, Y.; Takei, K. Multifunctional skin-inspired flexible sensor systems for wearable electronics. *Advanced Materials Technologies* **2019**, 4 (3), 1800628.
- (10) Hou, C.; Wang, H.; Zhang, Q.; Li, Y.; Zhu, M. Highly conductive, flexible, and compressible all-graphene passive electronic skin for sensing human touch. *Advanced Materials* **2014**, 26 (29), 5018-5024.
- (11) Liu, H.; Xiang, H.; Wang, Y.; Li, Z.; Qian, L.; Li, P.; Ma, Y.; Zhou, H.; Huang, W. A flexible multimodal sensor that detects strain, humidity, temperature, and pressure with carbon black and reduced graphene oxide hierarchical composite on paper. *ACS applied materials & interfaces* **2019**, 11 (43), 40613-40619.
- (12) Hua, Q.; Sun, J.; Liu, H.; Bao, R.; Yu, R.; Zhai, J.; Pan, C.; Wang, Z. L. Skin-inspired highly stretchable and conformable matrix networks for multifunctional sensing. *Nature communications* **2018**, 9 (1), 1-11.
- (13) Kim, J.; Lee, M.; Shim, H. J.; Ghaffari, R.; Cho, H. R.; Son, D.; Jung, Y. H.; Soh, M.; Choi, C.; Jung, S. Stretchable silicon nanoribbon electronics for skin prosthesis. *Nature communications* **2014**, 5 (1), 1-11.

- (14) An, B. W.; Heo, S.; Ji, S.; Bien, F.; Park, J.-U. Transparent and flexible fingerprint sensor array with multiplexed detection of tactile pressure and skin temperature. *Nature communications* **2018**, *9* (1), 2458.
- (15) Zeng, M.; Du, Y.; Jiang, Q.; Kempf, N.; Wei, C.; Bimrose, M. V.; Tanvir, A.; Xu, H.; Chen, J.; Kirsch, D. J. High-throughput printing of combinatorial materials from aerosols. *Nature* **2023**, *617* (7960), 292-298.
- (16) Turan, N.; Saeidi-Javash, M.; Chen, J.; Zeng, M.; Zhang, Y.; Go, D. B. Atmospheric pressure and ambient temperature plasma jet sintering of aerosol jet printed silver nanoparticles. *ACS Applied Materials & Interfaces* **2021**, *13* (39), 47244-47251.
- (17) Yakaboylu, G. A.; Pillai, R. C.; Sabolsky, K.; Sabolsky, E. M. MoSi₂-and WSi₂-based embedded ceramic composite thermocouples for high-temperature and harsh-environment sensing. *Sensors and Actuators A: Physical* **2018**, *272*, 139-152.
- (18) Liu, Y.; Ren, W.; Shi, P.; Liu, D.; Zhang, Y.; Liu, M.; Ye, Z.-G.; Jing, W.; Tian, B.; Jiang, Z. A highly thermostable In₂O₃/ITO thin film thermocouple prepared via screen printing for high temperature measurements. *Sensors* **2018**, *18* (4), 958.
- (19) Saeidi-Javash, M.; Du, Y.; Zeng, M.; Wyatt, B. C.; Zhang, B.; Kempf, N.; Anasori, B.; Zhang, Y. All-printed MXene-graphene nanosheet-based bimodal sensors for simultaneous strain and temperature sensing. *ACS Applied Electronic Materials* **2021**, *3* (5), 2341-2348.
- (20) Amjadi, M.; Kyung, K. U.; Park, I.; Sitti, M. Stretchable, skin-mountable, and wearable strain sensors and their potential applications: a review. *Advanced Functional Materials* **2016**, *26* (11), 1678-1698.
- (21) Zhang, Y.; Anderson, N.; Bland, S.; Nutt, S.; Jursich, G.; Joshi, S. All-printed strain sensors: Building blocks of the aircraft structural health monitoring system. *Sensors and Actuators A: Physical* **2017**, *253*, 165-172.
- (22) Rahman, M. T.; Moser, R.; Zbib, H. M.; Ramana, C.; Panat, R. 3D printed high performance strain sensors for high temperature applications. *Journal of Applied Physics* **2018**, *123* (2), 024501.
- (23) Frutiger, A.; Muth, J. T.; Vogt, D. M.; Mengüç, Y.; Campo, A.; Valentine, A. D.; Walsh, C. J.; Lewis, J. A. Capacitive soft strain sensors via multicore-shell fiber printing. *Advanced Materials* **2015**, *27* (15), 2440-2446.
- (24) Muth, J. T.; Vogt, D. M.; Truby, R. L.; Mengüç, Y.; Kolesky, D. B.; Wood, R. J.; Lewis, J. A. Embedded 3D printing of strain sensors within highly stretchable elastomers. *Advanced materials* **2014**, *26* (36), 6307-6312.
- (25) Yamada, T.; Hayamizu, Y.; Yamamoto, Y.; Yomogida, Y.; Izadi-Najafabadi, A.; Futaba, D. N.; Hata, K. A stretchable carbon nanotube strain sensor for human-motion detection. *Nature nanotechnology* **2011**, *6* (5), 296-301.
- (26) Zhao, S.; Li, J.; Cao, D.; Zhang, G.; Li, J.; Li, K.; Yang, Y.; Wang, W.; Jin, Y.; Sun, R. Recent advancements in flexible and stretchable electrodes for electromechanical sensors: strategies, materials, and features. *ACS applied materials & interfaces* **2017**, *9* (14), 12147-12164.

- (27) Dankoco, M.; Tesfay, G.; Bènevent, E.; Bendahan, M. Temperature sensor realized by inkjet printing process on flexible substrate. *Materials Science and Engineering: B* **2016**, *205*, 1-5.
- (28) Katerinopoulou, D.; Zalar, P.; Sweelssen, J.; Kiriakidis, G.; Rentrop, C.; Groen, P.; Gelinck, G. H.; van den Brand, J.; Smits, E. C. Large-area all-printed temperature sensing surfaces using novel composite thermistor materials. *Advanced Electronic Materials* **2019**, *5* (2), 1800605.
- (29) Aliane, A.; Fischer, V.; Galliari, M.; Tournon, L.; Gwoziecki, R.; Serbutoviez, C.; Chartier, I.; Coppard, R. Enhanced printed temperature sensors on flexible substrate. *Microelectronics Journal* **2014**, *45* (12), 1621-1626.
- (30) Harada, S.; Kanao, K.; Yamamoto, Y.; Arie, T.; Akita, S.; Takei, K. Fully printed flexible fingerprint-like three-axis tactile and slip force and temperature sensors for artificial skin. *ACS nano* **2014**, *8* (12), 12851-12857.
- (31) Gong, S.; Schwalb, W.; Wang, Y.; Chen, Y.; Tang, Y.; Si, J.; Shirinzadeh, B.; Cheng, W. A wearable and highly sensitive pressure sensor with ultrathin gold nanowires. *Nature communications* **2014**, *5* (1), 1-8.
- (32) Khan, Y.; Ostfeld, A. E.; Lochner, C. M.; Pierre, A.; Arias, A. C. Monitoring of vital signs with flexible and wearable medical devices. *Advanced materials* **2016**, *28* (22), 4373-4395.
- (33) Lee, S.; Reuveny, A.; Reeder, J.; Lee, S.; Jin, H.; Liu, Q.; Yokota, T.; Sekitani, T.; Isoyama, T.; Abe, Y. A transparent bending-insensitive pressure sensor. *Nature nanotechnology* **2016**, *11* (5), 472-478.
- (34) Mannsfeld, S. C.; Tee, B. C.; Stoltenberg, R. M.; Chen, C. V.; Barman, S.; Muir, B. V.; Sokolov, A. N.; Reese, C.; Bao, Z. Highly sensitive flexible pressure sensors with microstructured rubber dielectric layers. *Nature materials* **2010**, *9* (10), 859-864.
- (35) Won, S. M.; Wang, H.; Kim, B. H.; Lee, K.; Jang, H.; Kwon, K.; Han, M.; Crawford, K. E.; Li, H.; Lee, Y. Multimodal sensing with a three-dimensional piezoresistive structure. *ACS nano* **2019**, *13* (10), 10972-10979.
- (36) Fu, S.; Tao, J.; Wu, W.; Sun, J.; Li, F.; Li, J.; Huo, Z.; Xia, Z.; Bao, R.; Pan, C. Fabrication of large-area bimodal sensors by all-inkjet-printing. *Advanced Materials Technologies* **2019**, *4* (4), 1800703.
- (37) Harada, S.; Honda, W.; Arie, T.; Akita, S.; Takei, K. Fully printed, highly sensitive multifunctional artificial electronic whisker arrays integrated with strain and temperature sensors. *ACS nano* **2014**, *8* (4), 3921-3927.
- (38) Choi, D.; Jang, S.; Kim, J. S.; Kim, H. J.; Kim, D. H.; Kwon, J. Y. A Highly Sensitive Tactile Sensor Using a Pyramid-Plug Structure for Detecting Pressure, Shear Force, and Torsion. *Advanced Materials Technologies* **2019**, *4* (3), 1800284.
- (39) Liu, Y.; Wang, H.; Zhao, W.; Zhang, M.; Qin, H.; Xie, Y. Flexible, stretchable sensors for wearable health monitoring: sensing mechanisms, materials, fabrication strategies and features. *Sensors* **2018**, *18* (2), 645.

- (40) Romanosky, R. R.; Maley, S. M. Harsh environment sensor development for advanced energy systems. In *Micro-and Nanotechnology Sensors, Systems, and Applications V*, 2013; SPIE: Vol. 8725, pp 119-126.
- (41) Watson, J.; Castro, G. A review of high-temperature electronics technology and applications. *Journal of Materials Science: Materials in Electronics* **2015**, *26* (12), 9226-9235. DeepDyve.
- (42) Secor, E. B. Principles of aerosol jet printing. *Flexible and Printed Electronics* **2018**, *3* (3), 035002.
- (43) Zeng, M.; Zavanelli, D.; Chen, J.; Saeidi-Javash, M.; Du, Y.; LeBlanc, S.; Snyder, G. J.; Zhang, Y. Printing thermoelectric inks toward next-generation energy and thermal devices. *Chemical Society Reviews* **2022**, *51* (2), 485-512.
- (44) Du, Y.; Wang, R.; Zeng, M.; Xu, S.; Saeidi-Javash, M.; Wu, W.; Zhang, Y. Hybrid printing of wearable piezoelectric sensors. *Nano Energy* **2021**, *90*, 106522.
- (45) Zeng, M.; Kuang, W.; Khan, I.; Huang, D.; Du, Y.; Saeidi-Javash, M.; Zhang, L.; Cheng, Z.; Hoffman, A. J.; Zhang, Y. Colloidal nanosurfactants for 3D conformal printing of 2D van der Waals materials. *Advanced Materials* **2020**, *32* (39), 2003081.
- (46) Kempf, N.; Zhang, Y. Aerosol jet printed 3 omega sensors for thermal conductivity measurement. *Review of Scientific Instruments* **2021**, *92* (10).
- (47) Feng, J. Q.; Renn, M. J. Aerosol Jet® direct-write for microscale additive manufacturing. *Journal of Micro and Nano-Manufacturing* **2019**, *7* (1).
- (48) Essien, M. Apparatuses and methods for stable aerosol deposition using an aerodynamic lens system. Google Patents: 2018.
- (49) Knoll, M.; Offenzeller, C.; Mayrhofer, B.; Jakoby, B.; Hilber, W. A screen printed thermocouple-array on a flexible substrate for condition monitoring. In *Proceedings*, 2018; MDPI: Vol. 2, p 803.
- (50) Yang, F.; Li, G.; Yang, J.; Wang, Z.; Han, D.; Zheng, F.; Xu, S. Measurement of local temperature increments induced by cultured HepG2 cells with micro-thermocouples in a thermally stabilized system. *Scientific reports* **2017**, *7* (1), 1721.
- (51) Murakami, R.; Kamada, K.; Shoji, Y.; Yokota, Y.; Yoshino, M.; Kurosawa, S.; Ohashi, Y.; Yamaji, A.; Yoshikawa, A. Fabrication of flexible Ir and Ir-Rh wires and application for thermocouple. *Journal of Crystal Growth* **2018**, *487*, 72-77.
- (52) Li, F.; Liu, Y.; Shi, X.; Li, H.; Wang, C.; Zhang, Q.; Ma, R.; Liang, J. Printable and stretchable temperature-strain dual-sensing nanocomposite with high sensitivity and perfect stimulus discriminability. *Nano letters* **2020**, *20* (8), 6176-6184.

Supporting Information

Aerosol Jet Printing of High-Temperature Multimodal Sensors for Strain and Temperature Sensing

*Md. Omarsany Bappy, Qiang Jiang, Stephanie Atampugre, and Yanliang Zhang**

Department of Aerospace and Mechanical Engineering, University of Notre Dame, Notre Dame,
Indiana 46556, USA

*Corresponding author: yzhang45@nd.edu

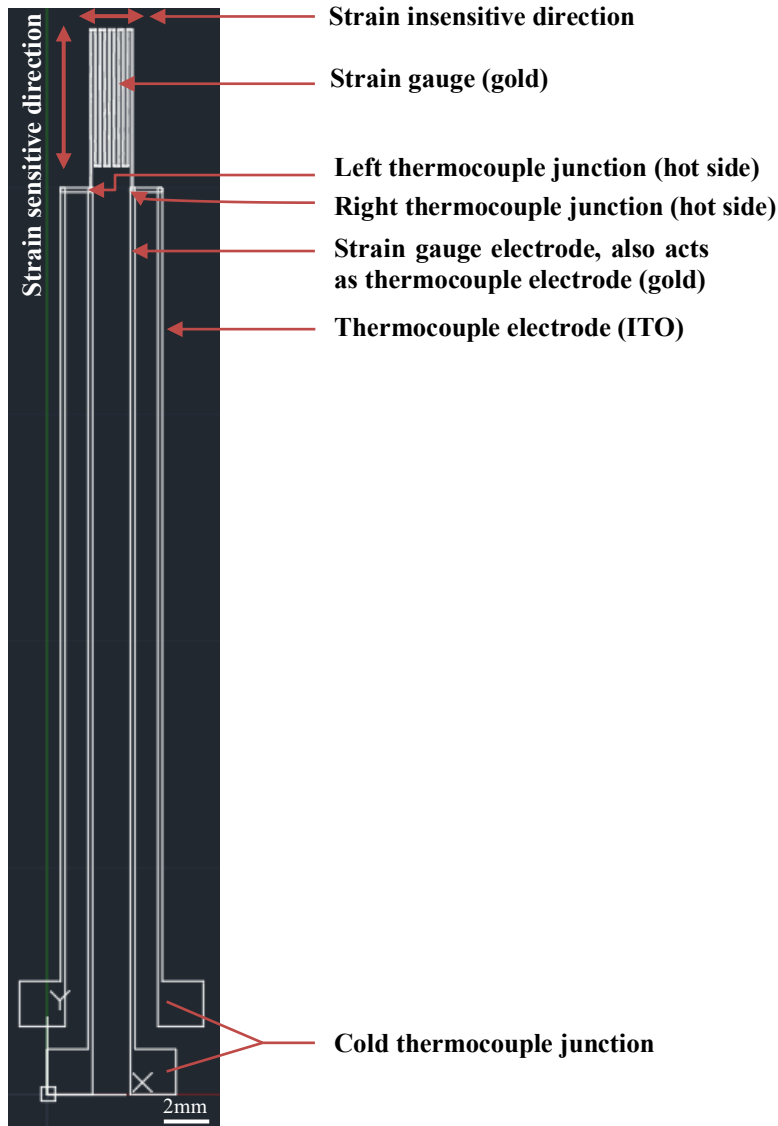


Figure S1. AutoCAD drawing of the printed multimodal sensor. This drawing is fed into the printer before printing the sensor.

The AutoCAD design of the multimodal sensor representing all the different parts along with the associated printed material has been mentioned. The two thermocouples have been named as left and right thermocouples. The hot side, as mentioned in the figure, is kept inside the oven during temperature measurement, and it acts as the hot junction of the thermocouple. On the other hand,

the cold thermocouple junction, as mentioned in the figure, is kept outside the furnace and kept cold by cooling water flow during high-temperature measurement, as shown in Figure S4.

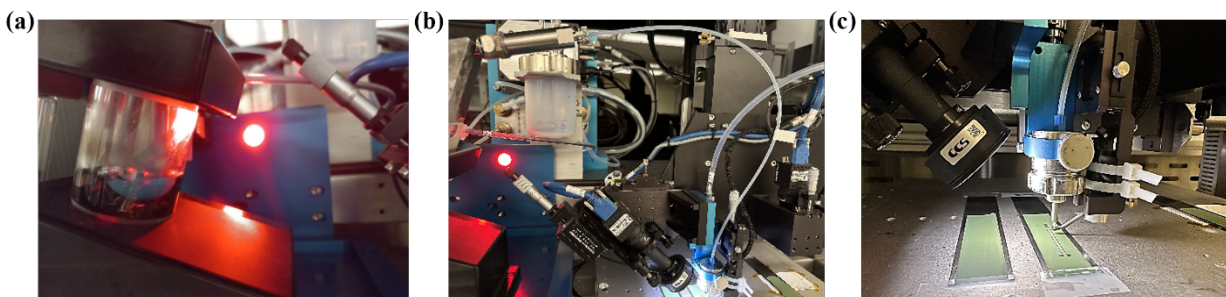


Figure S2. a) Atomization of Gold/ITO nano ink, b) transportation of aerosol droplet particles to the printer head, and c) ink deposition onto the substrate.

At first, 1.2 mL ink is taken in the ink vial and then set into the atomizer. To get the aerosol droplet from the nanoparticle ink, the ultrasonic atomizer current was set at 0.6 A for both gold and ITO. As soon as the atomizer power is turned on, the ink starts aerosolization. A real-time picture of the printing process of the bimodal sensor has been shown in Figure S2, where the atomization of Gold/ITO nano ink, transportation of aerosol droplet particles to the printer head, and finally, the deposition of ink onto the stainless-steel substrate have been captured. When the aerosol droplets start depositing through the nozzle tip, the printed line is taken onto a glass slide and seen under the microscope to check the line width, continuity, and overspray. Then, the printed parameters are optimized based on the perfect continuous line, desired line width, and minimal overspray. After optimization, the sensor AutoCAD file is fed into the printer to print the sensor onto the substrate.

Table S1. Gold and ITO Nanoparticle Ink Printing Parameters

Parameter	Gold	ITO
Nozzle diameter (μm)	200	200
Carrier gas flow rate (sccm)	20	26
Sheath gas flow rate (sccm)	100	60
Number of passes	3	3
Standoff distance (mm)	3	3
Platen temperature ($^{\circ}\text{C}$)	85	85
Chiller temperature ($^{\circ}\text{C}$)	16	16
Printing speed (mm/s)	2	2

The printing parameters can vary depending on the ink viscosity, particle size, solid content, ambient temperature and pressure, etc. That's why, before printing, it's always better to optimize the parameters.

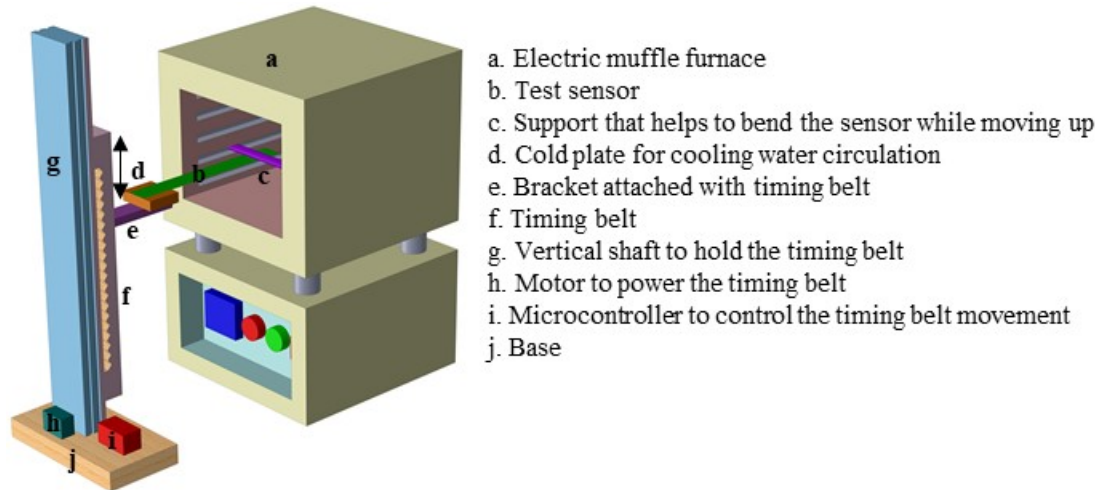


Figure S3. Schematic of the experiment set-up for measuring concurrent temperature and strain at high temperature.

The schematic diagram represents the experimental setup used in this study to test the multimodal sensor. The sensor is fixed on top of the copper cold plate (denoted by ‘d’ in Figure S3) using a clamp to keep the thermocouple cold junction as cool as possible. Water is used as the coolant. The sensor tip is set underneath a ceramic tube (denoted by ‘c’ in Figure S3). When the timing belt moves up, strain is induced into the sensor (acts like a cantilever beam).

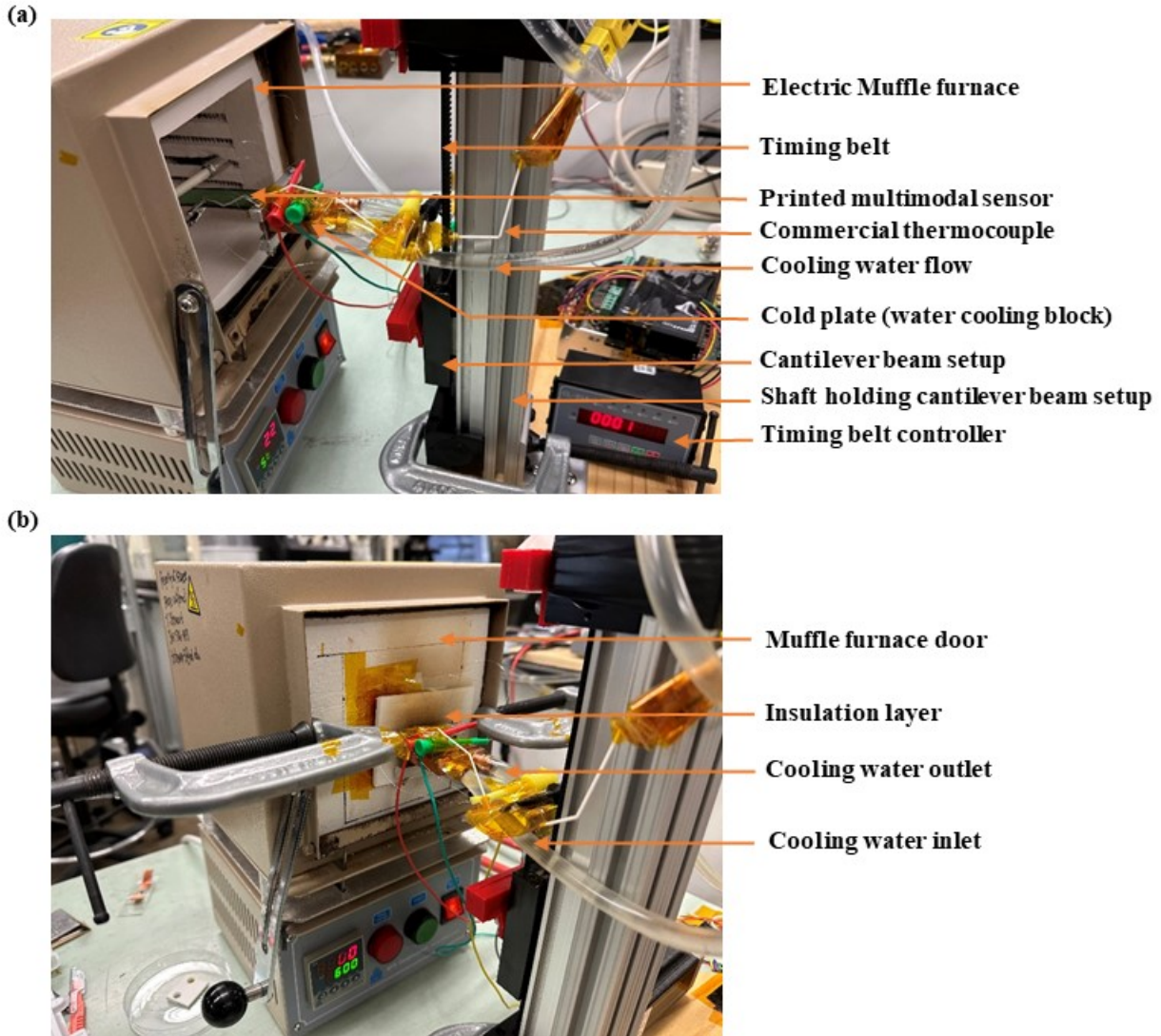


Figure S4. Real-time photo of the experimental setup during measurement at a) room temperature and b) high temperature.

Figure S4 (a) shows the measurement setup of strain testing at room temperature. To test the strain gauge, the timing belt is moved 10 mm upward first in 5 steps. Each step is set to take 3 minutes to get stable resistance data at that strained condition. Then the timing belt is moved 10 mm downward similarly to get the resistance value during straining down. During high-temperature measurements, the cooling water circuit is turned on to maintain the cold junction

temperature as low as possible. The temperature at both the hot side and the cold side is continuously monitored and recorded.

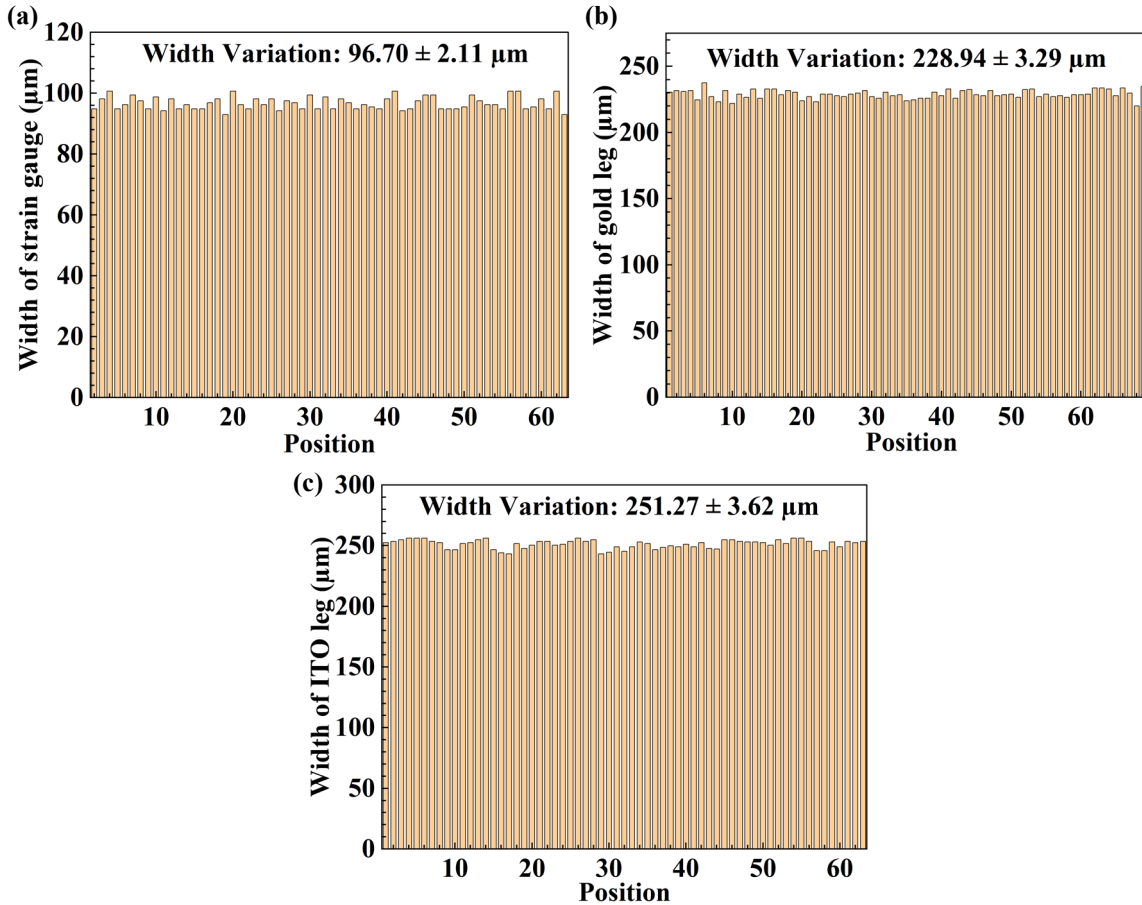


Figure S5. Width variation of the printed multimodal sensor at different regions a) variation of the width along the strain gauge is about $\pm 2.11 \mu\text{m}$ from the mean, i.e., 2.18% from the mean, b) variation of the width along the gold electrode is about $\pm 3.29 \mu\text{m}$ from the mean, i.e., 1.44% from the mean, and c) variation of the width along the ITO electrode is about $\pm 3.62 \mu\text{m}$ from the mean, i.e., 1.44% from the mean, indicating high resolution of the aerosol jet printed sensor.

After printing the sensors, the line width at different parts of the sensors was measured using an optical microscope. The low standard deviation of the printed lines shows the high-quality printing of functional devices by aerosol jet printers.

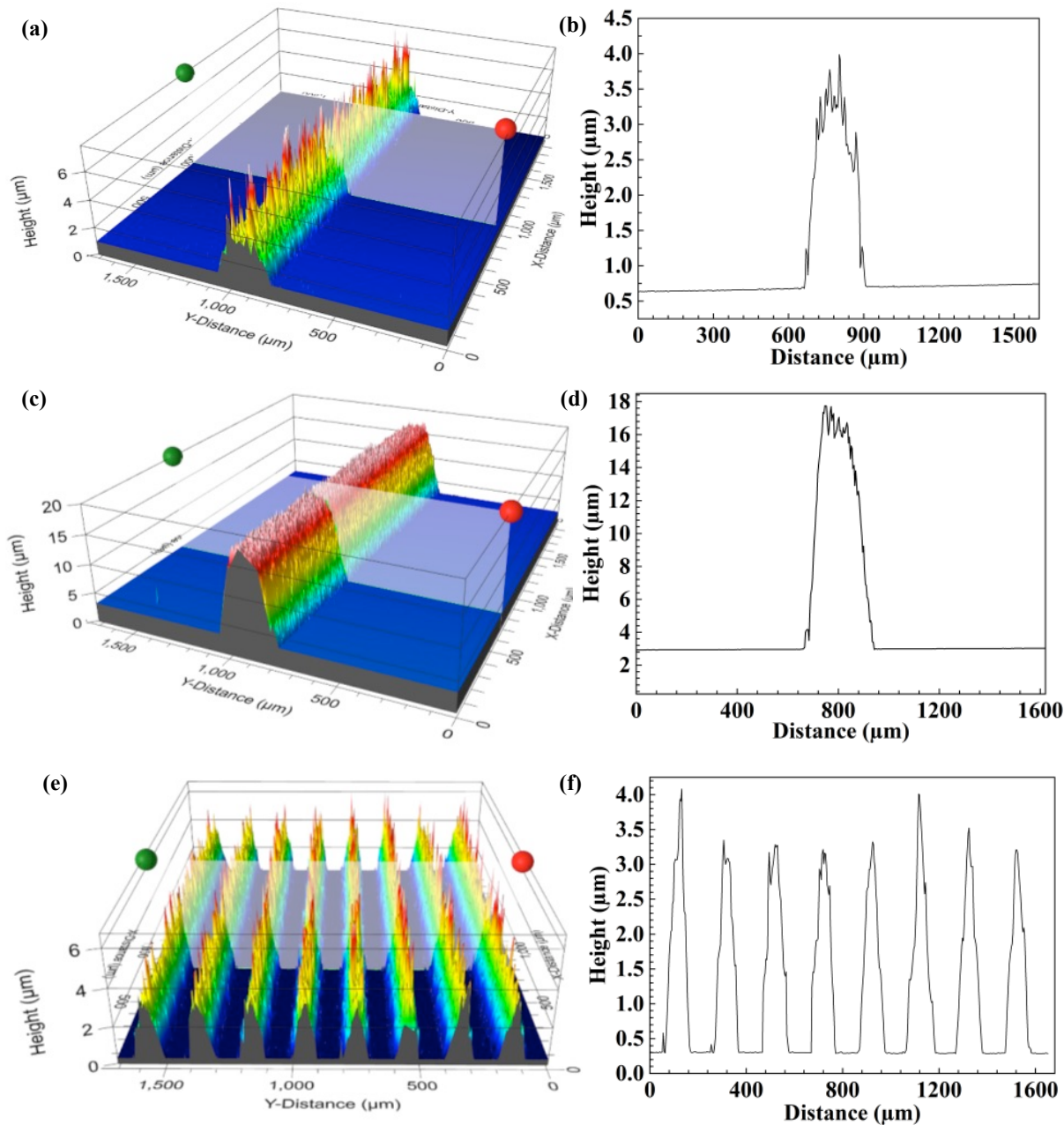


Figure S6. Thickness variation of the aerosol jet printed multimodal sensor at different locations using white light profilometer, a) a typical white light profilometer scan across the printed gold electrode, b) surface topology of the gold electrode, c) white light profilometer scan across the printed ITO electrode, d) surface topology of the ITO electrode, e) white light profilometer scan illuminating the surface topography of a strain sensor along the strain gauge, and f) thickness variation of the printed strain gauge at a certain plane.

Figure S6 shows the 3D scan of the sensor at different parts by using a White light profilometer (Filmetrics, Profilm3D). White light interferometry technology is used by this kind of profilometer to provide quantitative surface topological information. It is a nondestructive, non-contact type of measurement method offering good technology to measure film thickness. The film thickness shown in Figure S6 represents the film thickness across a plane only. Multiple film thicknesses are measured along different planes and then averaged to get the average thickness. Line width variation from bottom to top can also be observed by the profilometer image shown in Figure S6.

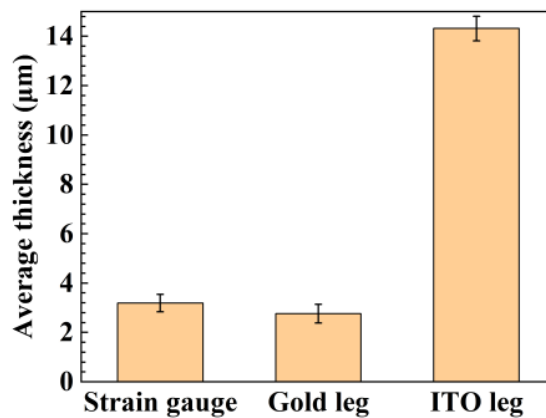


Figure S7. Thickness variation of the aerosol jet printed sensor along different parts.

The variation in film thickness along different parts of the printed multimodal sensor is shown in Figure S7. The average thickness shown in the figure is the average of the thickness taken in 5 different planes and then averaged, and the error bar represents the standard deviation of those 5 film thicknesses.

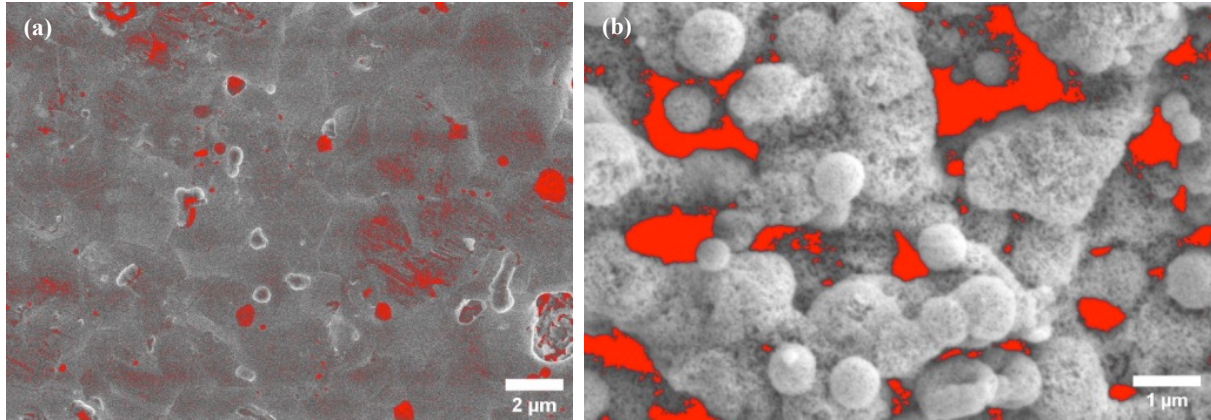


Figure S8. Estimation of porosity of aerosol jet printed (a) gold and (b) ITO sintered at 800°C.

The SEM image of the gold film shows that sintering close to the melting point of gold nanoparticles causes them to coalesce and form larger grains and grain boundaries and relatively dense structures with ~4% porosity. The SEM image of ITO shows a relatively large porosity of ~9% porosity as the sintering temperature is well below the melting temperature of ITO. The porosity has been estimated by ImageJ software.

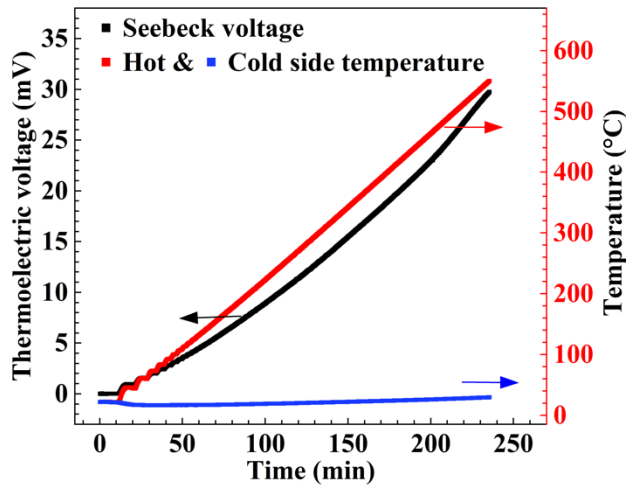


Figure S9. Hot side temperature, cold junction temperature, and corresponding thermoelectric voltage during a temperature measurement test have been shown.

Figure S9 shows the variation of thermoelectric voltage with temperature difference between the hot and cold thermocouple junctions. The hot and cold thermocouple junction temperatures, which were measured using a commercial K-type thermocouple, have been shown separately. Please note that thermoelectric voltage is a function of the temperature difference across the hot and cold junction.

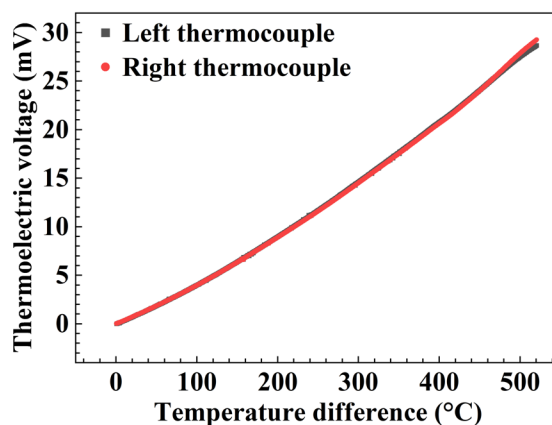


Figure S10. The thermoelectric voltage generated at the two thermocouples has been shown as a function of the temperature difference between the hot and cold junction of the printed sensor.

The Seebeck voltage generated at the left and right thermocouple of a sensor has been shown. During this measurement, the hot side temperature was measured near the left thermocouple. Both the two thermocouples of a single sensor show almost identical thermoelectric voltage across the same temperature difference.

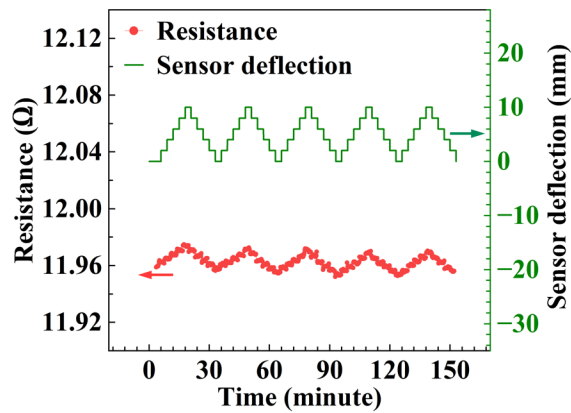


Figure S11. Variation of resistance of a strain gauge at different strains has been demonstrated during real-time monitoring. The sensor has been deflected up to 10 mm in 5 steps; both bending up and down have been performed, as shown by the green lines of the figure, and the corresponding change of resistance of the sensor has been shown.

The strain measurement results of a sensor at room temperature are shown in Figure S11. Initially, the sensor is at zero strain position, and the measurement is started. Then, after some time, the timing belt controller is turned on, and the sensor starts moving up or down according to the preset program. Strain is induced into the sensor as the sensor is bent, and its resistance changes. The resistance of the sensor at each bending position is shown in Figure S11.

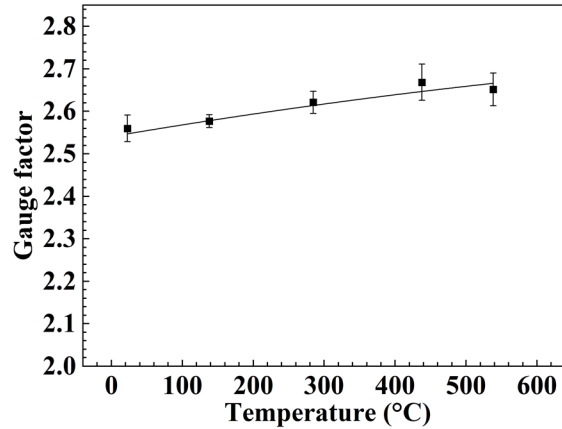


Figure S12. The effect of temperature on the gauge factor of the strain gauge during strain measurement shows a nonlinear fit, and the error bar represents the gauge factor variation at different temperatures.

The gauge factor varies (0.01%/K) with temperature, as shown in Figure S12. To measure the strain at different temperatures precisely, the gauge factor at that temperature should be known. We have tested the sensor at 5 temperatures, and the error bar in Figure S12 shows the standard deviation of the gauge factor of 3 sensors at that test temperature mentioned in Figure S12.

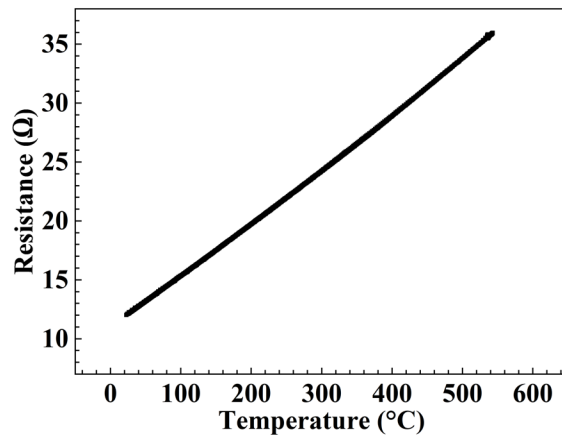


Figure S13. Variation of strain gauge (gold) resistance as a function of temperature. This graph helps to decouple the strain and temperature-sensitive resistance of the strain gauge.

As the temperature of the test sensor is increased from room temperature to 540 °C, the resistance of the printed gauge increases from 12 Ω to 30 Ω due to the metallic nature of gold.

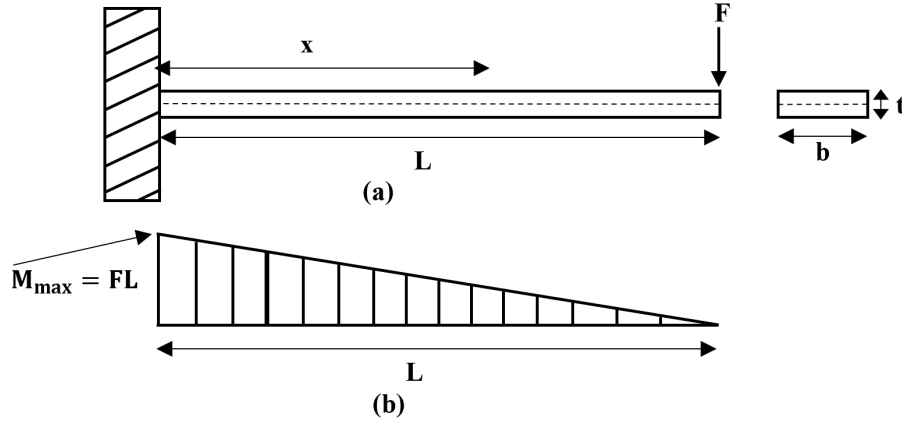


Figure S14. Strain calculation in a cantilever beam. (a) Side view of a cantilever beam. The left side is fixed, and the right side is free. (b) Moment distribution in the cantilever beam.

As mentioned earlier, when the sensor is deflected to induce strain, it acts as a cantilever beam. Here we will deduce the strain equation from Figure S14.

When load ‘F’ is applied at the beam tip, let the beam deflection be δ .

We can write, $\delta = \frac{FL^3}{3EI}$, where, E is Young’s Modulus and I is moment of inertia.

Let’s consider the strain gauge position at ‘x’ from the fixed end. So, the moment at any position of the beam will be $M = F(L - x)$ [considering clockwise moment as positive]

Now the bending stress at the beam is,

$\sigma = \frac{Mc}{I}$, where ‘c’ is the distance from the neutral axis (dotted line in Figure S14 (a))

$$\therefore \sigma = \frac{F(L - x)c}{I} \text{ so, } \frac{F}{I} = \frac{\sigma}{(L - x)c}$$

Now, $\delta = \frac{\sigma}{(L-x)c} \times \frac{L^3}{3E} = \frac{\epsilon \times L^3}{3(L-x)c}$, where strain, $\epsilon = \frac{\sigma}{E}$

$$\therefore \epsilon = \frac{3\delta(L - x)c}{L^3}$$

We print the sensor on top of the surface, so $c = t/2$ for our case. This is the theoretical equation of strain.

Table S2. Comparison of the sensitivity of printed thermocouples manufactured by different techniques

Type	Fabrication Technique	Materials	Temperature Range (°C)	Sensitivity (μV/°C)	Ref.
Thermocouple	Aerosol printing	jet Gold/ITO	20-600	55.64	This work
Thermocouple	Screen printing	Silver/carbon black	25-150	6	1
Thermocouple	Lithography	Palladium/Chromium	~150	21	2
Thermocouple	Aerosol printing	jet Ti3C2Tx MXene/graphene	20-200	53.6	3
Thermocouple	Aerosol printing	jet Cu/Cu-Ni (50:50)	30-232	~43	4
Thermocouple	Screen printing	Carbon-Black inks	50 ΔT	1.1-5.3	5
Thermocouple	Screen printing	In2O3/ITO	1270	44.5	6
Thermocouple	Screen printing	MoSi2/WSi2	1000	25.67	7

REFERENCES

- (1) Knoll, M.; Offenzeller, C.; Mayrhofer, B.; Jakoby, B.; Hilber, W. A screen printed thermocouple-array on a flexible substrate for condition monitoring. In *Proceedings*, 2018; MDPI: Vol. 2, p 803.
- (2) Yang, F.; Li, G.; Yang, J.; Wang, Z.; Han, D.; Zheng, F.; Xu, S. Measurement of local temperature increments induced by cultured HepG2 cells with micro-thermocouples in a thermally stabilized system. *Scientific reports* **2017**, 7 (1), 1721.

(3) Saeidi-Javash, M.; Du, Y.; Zeng, M.; Wyatt, B. C.; Zhang, B.; Kempf, N.; Anasori, B.; Zhang, Y. All-Printed MXene–Graphene Nanosheet-Based Bimodal Sensors for Simultaneous Strain and Temperature Sensing. *ACS Applied Electronic Materials* **2021**, *3* (5), 2341-2348. DOI: 10.1021/acsaelm.1c00218.

(4) Rahman, M. T.; Cheng, C.-Y.; Karagoz, B.; Renn, M.; Schrandt, M.; Gellman, A.; Panat, R. High Performance Flexible Temperature Sensors via Nanoparticle Printing. *ACS Applied Nano Materials* **2019**, *2* (5), 3280-3291. DOI: 10.1021/acsanm.9b00628.

(5) Offenzeller, C.; Knoll, M.; Jakoby, B.; Hilber, W. Screen-printed, pure carbon-black thermocouple fabrication and seebeck coefficients. *Sensors* **2019**, *19* (2), 403.

(6) Liu, Y.; Ren, W.; Shi, P.; Liu, D.; Zhang, Y.; Liu, M.; Ye, Z.-G.; Jing, W.; Tian, B.; Jiang, Z. A highly thermostable In₂O₃/ITO thin film thermocouple prepared via screen printing for high temperature measurements. *Sensors* **2018**, *18* (4), 958.

(7) Yakaboylu, G. A.; Pillai, R. C.; Sabolsky, K.; Sabolsky, E. M. MoSi₂-and WSi₂-based embedded ceramic composite thermocouples for high-temperature and harsh-environment sensing. *Sensors and Actuators A: Physical* **2018**, *272*, 139-152.

First-principle event reconstruction by time-charge readouts for the Taishan Antineutrino Observatory

Xuwei Liu^{a,b,c}, Wei Dou^{a,b,c}, Benda Xu^{a,b,c,d}, Hanwen Wang^e, Guofu Cao^e

^aDepartment of Engineering Physics, Tsinghua University, Beijing, China

^bCenter for High Energy Physics, Tsinghua University, Beijing, China

^cKey Laboratory of Particle & Radiation Imaging (Tsinghua University), Ministry of Education, China

^dKavli Institute for the Physics and Mathematics of the Universe, UTIAS, the University of Tokyo, Tokyo, Japan

^eInstitute of High Energy Physics, Chinese Academy of Sciences, Beijing, China

Abstract

The Taishan Antineutrino Observatory (TAO) is a liquid-scintillator satellite experiment of the Jiangmen Underground Neutrino Observatory (JUNO) to measure the reference reactor neutrino spectrum with sub-percent energy resolution. We use inhomogeneous Poisson process and Tweedie generalized linear model (GLM) to calibrate the detector response and the charge distribution of a SiPM. We develop a pure probabilistic method using time and charge of SiPMs from first principles to reconstruct point-like events in the TAO central detector. Thanks to our precise model and the high photo-coverage and quantum efficiency of the SiPM tiles at TAO, we achieve a vertex position resolution better than 16 mm and an energy resolution of about 2% at 1 MeV, marking the world's best performance of liquid scintillator detectors. Our methodology is applicable to other experiments that utilize PMTs for time and charge readouts.

1. Introduction

The Taishan Antineutrino Observatory (TAO) is a satellite experiment of the Jiangmen Underground Neutrino Observatory (JUNO) [1]. Using 2.8 tons Gadolinium-doped Liquid Scintillator (GdLS) and 4024 Silicon Photomultiplier (SiPM) tiles, TAO will measure the neutrino energy spectrum from a reactor core of the Taishan Nuclear Power Plant 44 m away. It will provide a model-independent reference spectrum with an energy resolution about 2% at 1 MeV. The spectra predicted by reactor flux models disagree with the measured ones by Daya Bay and other reactor antineutrino experiments, due to the incomplete information of decay and fission yields in nuclear database [2]. Thus, the precisely measured spectra of reactor antineutrino would provide more reliable inputs to JUNO for determining the neutrino mass ordering. Such reference spectra can also benchmark the nuclear database. In order to achieve these goals, <1% uncertainty in the physics non-linearity and <0.5% residual non-uniformity are required in TAO, supported by the study of calibration strategy [1].

Many reconstruction methods have been developed for large liquid scintillation and water Cherenkov detectors. Usually, the arrival time of the first photo-electron (PE) and the total integrated charge, collectively referred to as time-charge, in a chunk of PMT/SiPM readout waveforms, are used as substitutes for raw data in the event reconstruction. The time distribution of the first PE is long known to be affected by PE pile-up [3, 4]. KamLAND [5] uses a time-only vertex fitter with heuristic corrections. The Borexino [6] and Super-Kamiokande [7] experiments construct several empirical first-PE time PDFs from calibration and Monte Carlo conditioned by different charges and interpolate during reconstruction. In Ziyuan Li et al. [8]'s study of event reconstruction for JUNO, a rigorous time dependence on the PE counts is used, but they are inaccurately estimated by charge rounding. Guihong Huang et al. [9] improve upon it by relying on both the expectation of PE count and PE count itself. But the time-charge-combined likelihood is a simplified direct product of the two components. Such approximations introduce inherent bias needing to be *ad-hocly* corrected *a posteriori*. Zhen Qian et al. [10] discuss the application of several machine learning models in the reconstruction. The performance of these methods depends on the selection of aggregated features and optimal hyperparameters. Lacking of interpretability, deep learning is still seen as a black box for many applications [11].

To address those difficulties, a fundamental model derived from first principles is necessary, especially for an experiment like TAO with unprecedented energy resolution and vertex reconstruction precision. We use Tweedie generalized linear model (GLM) to calibrate the probabilistic relation of PE count and charge, and to derive an exact joint time-charge PDF from the original light curve at each channel as the predictor to reconstruct the vertex and energy for point-like events. Section 2 discusses the definition and implementation of the detector response for a point-like event in the TAO central detector. Section 4 introduces the dataset used to calibrate the response function and test the reconstruction results. Section 4.1 gives the reconstruction results of position and energy. Section 5 analyses the bias of energy reconstruction and discusses the limitations of our approach.

2. Optical detector model

Fig. 1 shows the schematic of TAO central detector (CD). A spherical acrylic vessel with an inner diameter of 1.8 m is filled with ~ 2.8 tons GdLS. 4024 $50 \times 50 \text{ mm}^2$ SiPM tiles with more than fifty percent photon detection efficiency are installed on the inner surface of copper shell supporting the acrylic vessel. The copper shell is immersed in an linear alkylbenzene (LAB) buffer contained in a cylindrical stainless-steel tank. We focus on the TAO CD and neglect the further details of detector summarized by Hangkun Xu et al. [1] and Abusleme et al. (JUNO collaboration) [2]. TAO detector is under construction. Monte Carlo (MC) simulation is used for assisting in the detector calibration process and evaluating the performance of the reconstruction algorithm (section 4).

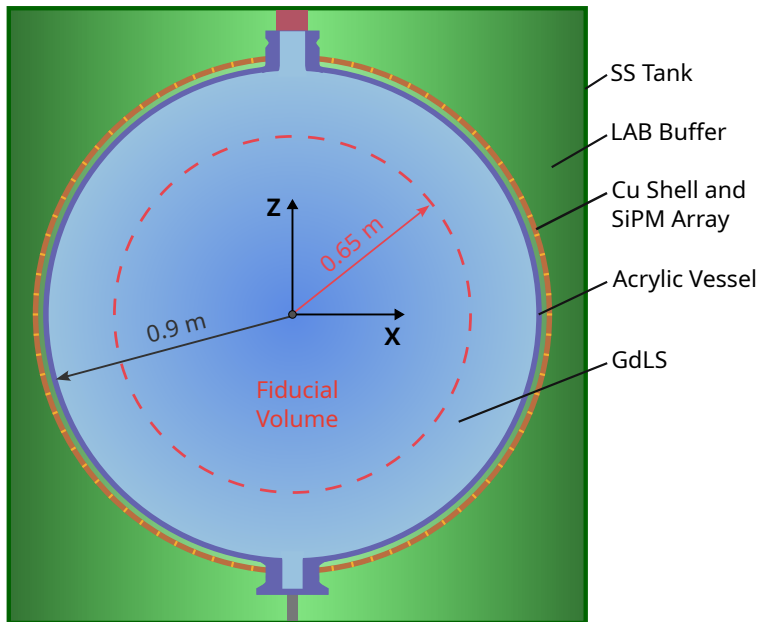


Figure 1: Schematic of the TAO central detector.

The detector response is defined as a map from a point-like event to the time-charge distributions on SiPM tiles. We divide it into two stages. In this section, the first stage of the response function is optical. It maps an event to PE times for a SiPM, which is properly described by an inhomogeneous Poisson point process. We utilize the approach developed by Dou et al. [12] to characterize the optical properties of the detector, including the GdLS time profile and photon transmission in the detector geometry. The second stage is the electronics. It maps the count and times of the PEs in a SiPM to the first-PE time and the total charge, characterizing the properties of the SiPM and analog-to-digital system. We shall discuss it in Section 3.

2.1. Poisson point process

Consider the response function of a point-like event $\delta(\vec{r}, E)$ on j th SiPM, where \vec{r} and E are the vertex and energy of the event. The occurrence of photoelectron (PE) on j th SiPM follows an inhomogeneous Poisson

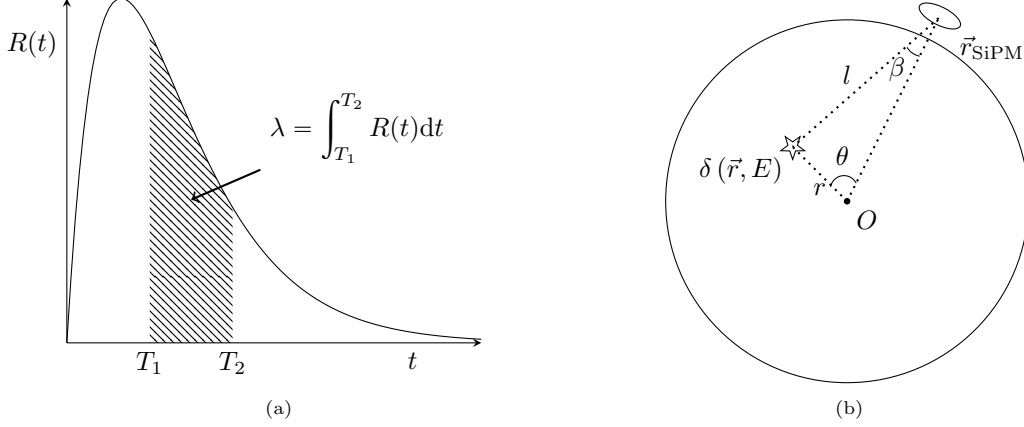


Figure 2: (a) The physical meaning of response function $R(t)$. The PE count in $[T_1, T_2]$ follows Poisson distribution, and the mean PE count is $\lambda = \int_{T_1}^{T_2} R(t)dt$. (b) The schematic diagram of relative positions (r, θ) of event vertex \vec{r} and SiPM \vec{r}_{SiPM} in CD. β is the incident angle on SiPM. l is the distance from vertex to the position of SiPM. The origin of spherical coordinate system O is put at the center of CD. The detector is approximately symmetric rotationally about the $O\text{-}\vec{r}_{\text{SiPM},j}$ axis, thus the relative azimuth ϕ is ignored.

process $R_j(t; \vec{r}, E)$ [13] understood as the expected PE count density at time t . The PE count on j th SiPM within the time interval $[\underline{T}, \bar{T}]$ follows Poisson distribution (Fig. 2a) of expectation

$$\lambda_{j, [\underline{T}, \bar{T}]}(\vec{r}, E) = \int_{\underline{T}}^{\bar{T}} R_j(t; \vec{r}, E) dt. \quad (1)$$

The non-linearity between the number of emitted photons and the kinetic energy of the charged particle is mainly caused by the ionization quenching and Cherenkov radiation [14] that will be discussed in Section 5. The visible energy E is defined as the linear component of $R_j(t; \vec{r}, E)$,

$$R_j(t; \vec{r}, E) = E \cdot R_j(t; \vec{r}), \quad (2)$$

leaving no dependence on E in $R_j(t; \vec{r})$. $R_j(t; \vec{r})$ only encodes the relative difference of the light curve over different \vec{r} . This simplification is the first advantage of Poisson point process as the base model. The second advantage is the ease to incorporate dark noise in Section 3.3. Both results from the linearity of our formulation.

Owing to the good spherical symmetry of TAO CD, in the relative position (r, θ, ϕ) between vertex \vec{r} and position of j th SiPM $\vec{r}_{\text{SiPM},j}$, the azimuth ϕ is irrelevant (Fig. 2b). For i th vertex and j th SiPM, replace $R_j(t; \vec{r}_i)$ with $R(t; r_i, \theta_{ji})$, where

$$r_i = |\vec{r}_i|, \quad \theta_{ji} = \arccos \left(\frac{\vec{r}_i \cdot \vec{r}_{\text{SiPM},j}}{|\vec{r}_i| |\vec{r}_{\text{SiPM},j}|} \right). \quad (3)$$

In TAO, the detector size is much smaller than the scattering or absorption lengths. The variables of $R(t; r, \theta)$ can be separated into time t and position (r, θ) .

2.2. Position part

Zernike polynomials [15] are orthonormal on the unit disk. To characterize the response intensity of different position

$$Z(r, \theta) = \left[\sum_{n=0}^{N_z-1} a_n Z_n(r, \theta) \right]^2, \quad (4)$$

where r is scaled to $[0, 1]$ and Z_n is the n -th order Zernike polynomial. N_z is the maximum order of Zernike polynomial used. Dou et al. [12] introduce Zernike polynomials to characterize the complex total internal reflection and focus. For TAO, since the CD is small and there is no total internal reflection in

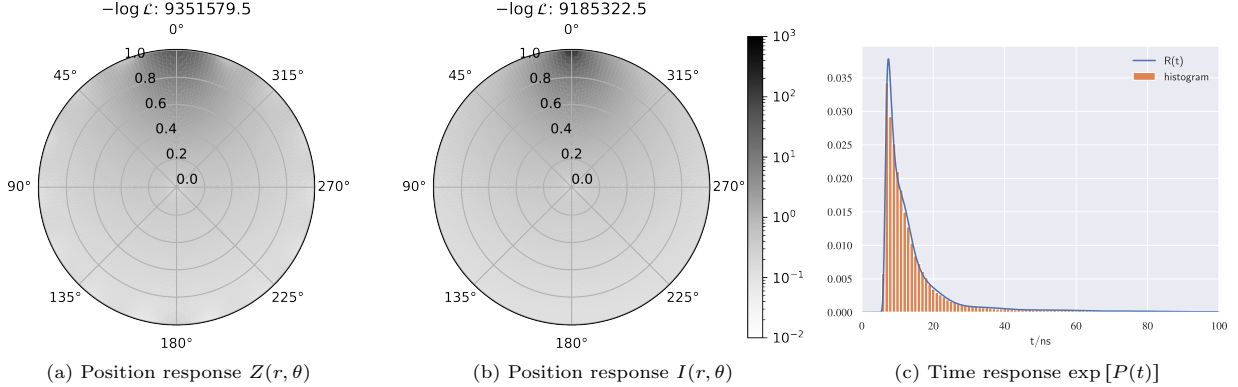


Figure 3: (a) and (b) show the position response in $Z(r, \theta)$ of Zernike polynomials and $I(r, \theta)$ of geometrical construction. The score (log-likelihood of the validation dataset) indicates that the fitting result of the latter is better. (c) shows time response at $r = 0.9$ and $\theta = \pi/2$. We use 40-order Legendre polynomials to fit the histogram of PE time.

CD, it is possible to estimate $Z(r, \theta)$ directly without excessive parameter fitting. The relative intensity is approximately proportional to the solid angle Ω of SiPM measured from vertex and exponential attenuation of distance l from vertex to the position of SiPM,

$$I(r, \theta) \propto \Omega \cdot \exp(-l/l_0) \propto \frac{\cos \beta(r, \theta)}{r^2 + r_{\text{SiPM}}^2 - 2rr_{\text{SiPM}} \cos \theta} \cdot \exp(-l/l_0), \quad (5)$$

where $\beta(r, \theta)$ is the incident angle on SiPM shown in Fig. 2b and l_0 is the attenuation length. To decide which form of the position response to use, we fit the same training dataset with Eqs. (4)(5) and use the same validation dataset introduced in Sec. 2.4 to evaluate them. Fig. 3a and 3b show the fitting result of the position response. The log-likelihoods indicate that compared with a more expressive $Z(r, \theta)$, a specific $I(r, \theta)$ for TAO is more suitable for the description of the position response.

2.3. Time part

We set the event times to 0 without loss of generality. The separation of position and time variables implies that the shape of the time response remains consistent across all SiPM tiles and vertices in the CD. To align the arrival times of photons on different SiPM, we define the time shift t_{shift} as the time of flight from vertex $\delta(\vec{r}, E)$ to the position of SiPM

$$t_{\text{shift}}(r, \theta) = \frac{n_{\text{LS}} l(r, \theta)}{c}, \quad (6)$$

where n_{LS} is the effective refractive index of liquid scintillator considering dispersion, l is the distance from vertex to the position of SiPM and c is the speed of light in vacuum. We use a variant of Ziyuan Li's method [8] to determine n_{LS} . We simulate 10,000 5 MeV electrons located at a fixed point, and get the peak position of hit time distribution for each SiPM. Fig. 4 shows a 2-D histogram of PE hit time and distance $l(r, \theta)$ on 4024 SiPM tiles. The lower edge of histogram corresponds to the first-PE time. It is linearly fitted to extract n_{LS} .

The family of Legendre polynomial [16] is orthonormal on $[-1, 1]$. We scale $(t - t_{\text{shift}})$ to $[-1, 1]$ and express $P(t; r, \theta)$ in Legendre polynomials,

$$P(t; r, \theta) = \exp \left[\sum_{m=0}^{N_p-1} a_m P_m(t - t_{\text{shift}}(r, \theta)) \right], \quad (7)$$

where $P_m(\cdot)$ is the m -th order Legendre polynomial and N_p is the maximum order of Legendre polynomial used. The exponential is to ensure the time part to be nonnegative.

We simulate 100 000 0.5 MeV electrons distributed uniformly in CD, calculate the relative positions for all PE hits in Fig. 2b and fit the coefficients a_m in Eq. (7). The maximum order of Legendre polynomials is determined by an independent validation dataset.

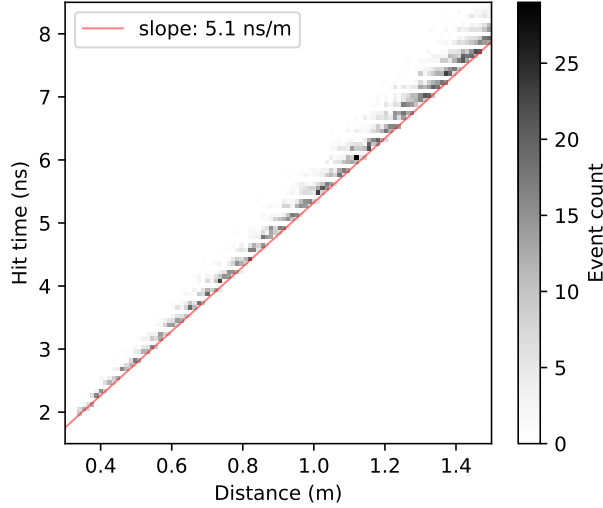


Figure 4: The histogram of hit time and distance. Use a linear equation (red line) to fit the lower edge of the histogram. The reciprocal of slope is the effective light speed.

The optical response function is

$$R(t; r, \theta) = I(r, \theta) \cdot P(t; r, \theta). \quad (8)$$

Fig. 3c shows the $R(t)$ curve at $r = 0.9$ and $\theta = \pi/2$.

2.4. Coefficients fitting and scoring

Electron is an ideal point source in LS because its energy deposition occurs within a radius of a few millimeters [17]. It deposits energy in CD and excites LS molecules. The molecules de-excite and emit scintillation photons, which transmit through the detector and reach the SiPM to produce a PE in part. Those are simulated with GEANT4-based [18] program. In the simulation for coefficients fitting and scoring, 100 000 electrons with energy 0.5 MeV are distributed uniformly in the central detector. The likelihood function

$$\begin{aligned} \log \mathcal{L} &= \log \left\{ \prod_k R_k(t_k; r_k, \theta_{jk}) \prod_{i,j} \exp \left[- \int R_j(t; r_i, \theta_{ji}) dt \right] \right\} \\ &= \underbrace{\sum_k \log R_k(t_k; r_k, \theta_{jk})}_{\text{hit}} - \underbrace{\sum_{i,j} \int R_j(t; r_i, \theta_{ji}) dt}_{\text{nonhit}}, \end{aligned} \quad (9)$$

is used to fit coefficients in Eq. 8 and score them, where i, j and k are indices of the event, SiPM and PE. The nonhit part considers SiPMs without PE, where the hit part includes PE times and corresponding hit SiPMs.

3. Tweedie electronic time-charge likelihood

Tan [19] formulated the PDF of single electron response (SER) charge distribution in a Gaussian $f_N(Q; \mu_Q, \sigma_Q^2)$ and the PE count N_{PE} in Poisson $\pi(\lambda_{\text{PE}})$ where λ_{PE} is the expectation. The charge PDF of SiPM or PMT is:

$$p(Q; \lambda_{\text{PE}}, \mu, \sigma^2) = \sum_{N_{\text{PE}}=0}^{\infty} f_N(Q; N_{\text{PE}}\mu_Q, N_{\text{PE}}\sigma_Q^2) p_{\pi}(N_{\text{PE}}; \lambda_{\text{PE}}) \quad (10)$$

Although widely followed, it makes no physical sense for the Gaussian distribution to allow a negative charge. We follow Kalousis et al. [20] to use a Gamma distribution $\text{Ga}(k, \theta)$ to model the SER charge distribution, where k and θ are the shape and scale parameters. Therefore, the distribution of total charge Q

$$f_{\text{Tw}}(Q; \lambda_{\text{PE}}, k, \theta) = \sum_{N_{\text{PE}}=0}^{\infty} f_{\text{Ga}}(Q; N_{\text{PE}}k, \theta) p_{\pi}(N_{\text{PE}}; \lambda_{\text{PE}}) \quad (11)$$

follows compound Poisson-Gamma distribution. It is a special case of the Tweedie distribution [21] where the Tweedie index parameter ξ satisfies $1 < \xi < 2$ [22]. Tweedie distribution includes the fluctuation of PE count, thus the infinite N_{PE} summation in Eq. (10) is shifted to standard routines [23, 24]. The parameter relationship between Tweedie distribution and its corresponding Poisson and Gamma distribution [25] is:

$$\begin{cases} \lambda = \frac{\mu^{2-\xi}}{\phi(2-\xi)} \\ k = \frac{2-\xi}{\xi-1} \\ \theta = \phi(\xi-1)\mu^{\xi-1} \end{cases} \quad (12)$$

where μ and ϕ are the mean value and dispersion parameters of Tweedie distribution.

3.1. Parameter calibration

Tweedie distributions is a special case of exponential dispersion models (EDM) [26]. Generalized linear model (GLM) [27, 25] is available for Eq. (11) to establish the relationship between the expected PE count λ_{PE} and charge Q . Specifically, we use the following expression of GLM,

$$\begin{cases} Q \sim \text{Tw}(\mu, \phi, \xi) \\ \mu = b\lambda_{\text{PE}} \end{cases} \quad (13)$$

with an identity link function $g(\mu) = \mu$. The intercept of linear predictor is zero. λ_{PE} is predicted by the optical response from Eq. (5) as the input to GLM. According to Eq. (12),

$$\lambda_{\text{PE}}k\theta = \mu \xrightarrow{\mu=b\lambda_{\text{PE}}} b = k\theta = \text{E}[Q|N_{\text{PE}} = 1], \quad (14)$$

the slope b is the expected charge of a single PE.

For simplicity, we ignore the variations of the SiPM-tile Tweedie parameters in the Monte Carlo. In the future we shall calibrate the real detector channel-by-channel. Figs. 5a and 5b show the charge distribution of a selected SiPM for 10,000 1 MeV and 3 MeV electrons located at the center of CD, where λ_{PE} is kept constant. These charges are generated by *electronic simulation* considering dark noise, afterpulse and internal crosstalk [28].

Our electronic simulation includes internal crosstalk, where every PE might induce another PE in the SiPM. It breaks the Poisson assumption in Eq. (11) and necessitates a generalized Poisson [29] suggested by Vinogradov [30], with a probability mass function (PMF) of

$$f_{\text{GP}}(x; \theta, \eta) = \frac{\theta(\theta + \eta x)^{x-1} e^{-\theta - \eta x}}{x!}. \quad (15)$$

Although when the crosstalk rate $\eta \rightarrow 0$ Eq. (15) degenerates back to a Poisson, the extended compound distribution is generally not in the Tweedie family any more. Fortunately, when λ_{PE} is not much larger than 1 and the probability of crosstalk is as low as $\sim 15\%$, the effect is not serious. The Tweedie model of Eq. (11) is validated against a laboratory test of a SiPM sample in Fig. 5c. The data and model exhibits difference at the higher charge tails of the distribution, similar to the Monte Carlo in Fig. 5b. Momentarily, we regard the convenience of Tweedie GLM to surpass the imperfectness of the Poisson assumption, as will be supported by the reconstruction results in Sec. 4. We shall develop regression with the compound of generalized Poisson and Gamma distribution in our future publications.

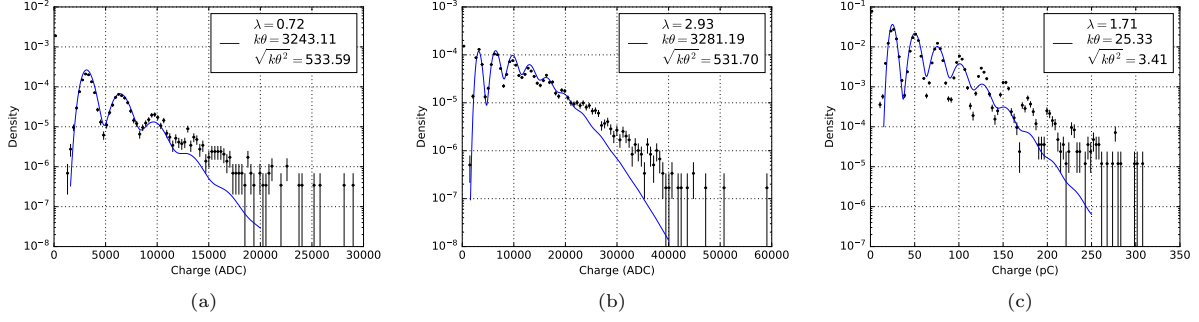


Figure 5: (a) and (b) are charge distributions of a SiPM tile for 10,000 1 MeV and 3 MeV electrons fixed at center of CD (Monte Carlo simulation). (c) is the charge distribution from one channel output of SiPM tile (experimental data). Solid lines are the regression results of Tweedie GLM, where the parameters of Poisson (λ) and Gamma (k and θ) parts are listed. The units of charge are not critical in this research.

3.2. Charge-only reconstruction likelihood

For some small detectors, time readout is usually not important. A charge-only reconstruction likelihood is a direct consequence of the Tweedie distribution in Eq. (11) and the optical model in Eq. (2),

$$L(\vec{r}, E; \{Q_j\}) = \prod_j^{N_{\text{SiPM}}} f_{\text{Tw}}(Q_j; b\lambda_{j, [\underline{T}, \overline{T}]}(\vec{r}, E), \phi, \xi) \quad (16)$$

where $\lambda_{j, [\underline{T}, \overline{T}]}(\vec{r}, E) = E \int_{\underline{T}}^{\overline{T}} R_j(t; \vec{r}) dt$ is the expected PE count in the electronic time window $[\underline{T}, \overline{T}]$ as Eq. (1), and b , ϕ and ξ are calibrated before event reconstruction.

The dark hits from SiPM follows a homogeneous Poisson process of intensity $R_D = 46086 \text{ Hz}$ in our Monte Carlo. It is naturally incorporated into the optical model at Eq. (16) by replacing $ER_j(t)$ with $ER_j(t) + R_D$

$$\lambda_{j, [\underline{T}, \overline{T}]}(\vec{r}, E) = \int_{\underline{T}}^{\overline{T}} (ER_j(t; \vec{r}) + R_D) dt = E \int_{\underline{T}}^{\overline{T}} R_j(t; \vec{r}) dt + R_D \cdot (\overline{T} - \underline{T}) \quad (17)$$

3.3. Time-charge reconstruction likelihood

The time-charge reconstruction is challenging to get correct because of the inter-dependence between the two variables. The charge Q affects first hit time T indirectly via the PE counts, not to be confused with the time-walk [31] which is a time error caused by varying amplitude of pulses and a constant threshold. Conversely, an observed T implies the integrated charge is only contributed by the time window of $[T, \overline{T}]$. It invalidates all the prevents efforts trying to decouple the time-charge reconstruction likelihood into time and charge parts. Instead, we should start from first principles to derive the joint distribution of T and Q .

Consider the following two events. *Event A*: There is no PE or charge in $[\underline{T}, T]$. The charge Q is determined by $\lambda_{\text{PE}, [\underline{T}, \overline{T}]} = \int_{\underline{T}}^{\overline{T}} R(t) dt$; *Event B*: There is no charge in $[\underline{T}, T + \Delta T]$ ($\Delta T > 0$), and Q is determined by $\lambda_{\text{PE}, [T + \Delta T, \overline{T}]} = \int_{T + \Delta T}^{\overline{T}} R(t) dt$. Obviously, $B \subset A$. Fig. 6 shows the probabilities of both events. The set difference $A \setminus B$ has a physical meaning that there is no charge in $[\underline{T}, T]$, and there is a PE

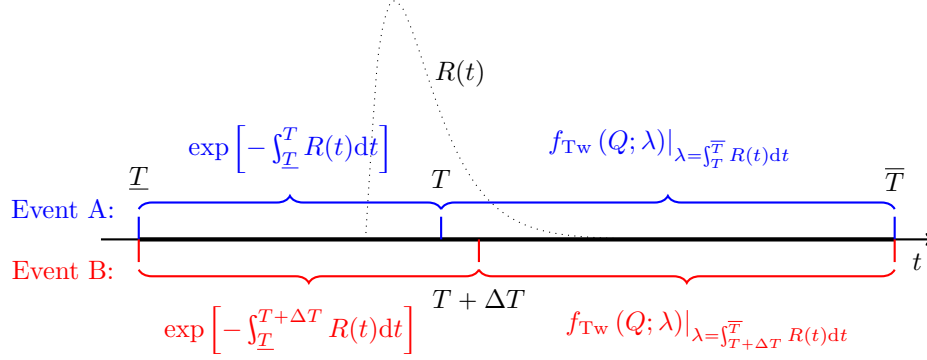


Figure 6: Diagram of response function $R(t)$ (dotted line), event A (blue) and event B (red) along the time axis. Event A contains Event B due to the one-way dimension of object time t and $\Delta T > 0$. The probabilities of each sub events are listed.

in $[T, T + \Delta T]$, and the Q is generated by $\int_{\underline{T}}^{\bar{T}} R(t)dt$. The difference of their probabilities is

$$\begin{aligned}
 f_{TQ}[T, Q; R(t)]\Delta T &= \overbrace{\exp\left[-\int_{\underline{T}}^T R(t)dt\right] f_{Tw}(Q; \lambda)\Big|_{\lambda=\int_{\underline{T}}^T R(t)dt}}^{\text{Event A}} \\
 &\quad - \underbrace{\exp\left[-\int_{\underline{T}}^{T+\Delta T} R(t)dt\right] f_{Tw}(Q; \lambda)\Big|_{\lambda=\int_{\underline{T}}^{T+\Delta T} R(t)dt}}_{\text{Event B}}
 \end{aligned} \tag{18}$$

When $\Delta T \rightarrow 0$,

$$\begin{aligned}
 f_{TQ}[T, Q; R(t)] &= -\frac{\partial}{\partial T} \left\{ \exp\left[-\int_{\underline{T}}^T R(t)dt\right] f_{Tw}(Q; \lambda)\Big|_{\lambda=\int_{\underline{T}}^T R(t)dt} \right\} \\
 &= \exp\left[-\int_{\underline{T}}^T R(t)dt\right] R(T) \left(1 + \frac{\partial}{\partial \lambda}\right) f_{Tw}(Q; \lambda)\Big|_{\lambda=\int_{\underline{T}}^T R(t)dt}
 \end{aligned} \tag{19}$$

Eq. (19) is the joint distribution of charge Q and first hit time T , whose normalization is verified in [Appendix A](#). The reconstruction likelihood is

$$\begin{aligned}
 L(\vec{r}, E, t_0; \{(T_j, Q_j)\}) &= \prod_{\substack{Q_j > 0 \\ \text{hit}}} f_{TQ}[T_j, Q_j; ER_j(t - t_0; \vec{r})] \times \prod_{\substack{Q_j = 0 \\ \text{nonhit}}} p_\pi(0; \lambda_{j, [\underline{T}-t_0, \bar{T}-t_0]}(\vec{r}, E)) \\
 &= \prod_{Q_j > 0} \exp[-\lambda_{j, [\underline{T}-t_0, T_j-t_0]}(\vec{r}, E)] ER_j(T_j - t_0; \vec{r}) \left(1 + \frac{\partial}{\partial \lambda}\right) f_{Tw}(Q_j; \lambda)\Big|_{\lambda=\lambda_{j, [T_j-t_0, \bar{T}-t_0]}(\vec{r}, E)} \\
 &\quad \times \prod_{Q_j = 0} \exp[-\lambda_{j, [\underline{T}-t_0, \bar{T}-t_0]}(\vec{r}, E)]
 \end{aligned} \tag{20}$$

where t_0 is the event time and j is the index of SiPM. Inclusion of dark hits is straightforward by substituting $ER_j(t)$ with $ER_j(t) + R_D$ as Eq. (17).

4. Numerical experiment

We deploy Monte Carlo simulation to fit the coefficients of response function and evaluate the reconstruction. The calibration data will be used to benchmark the reconstruction when available.

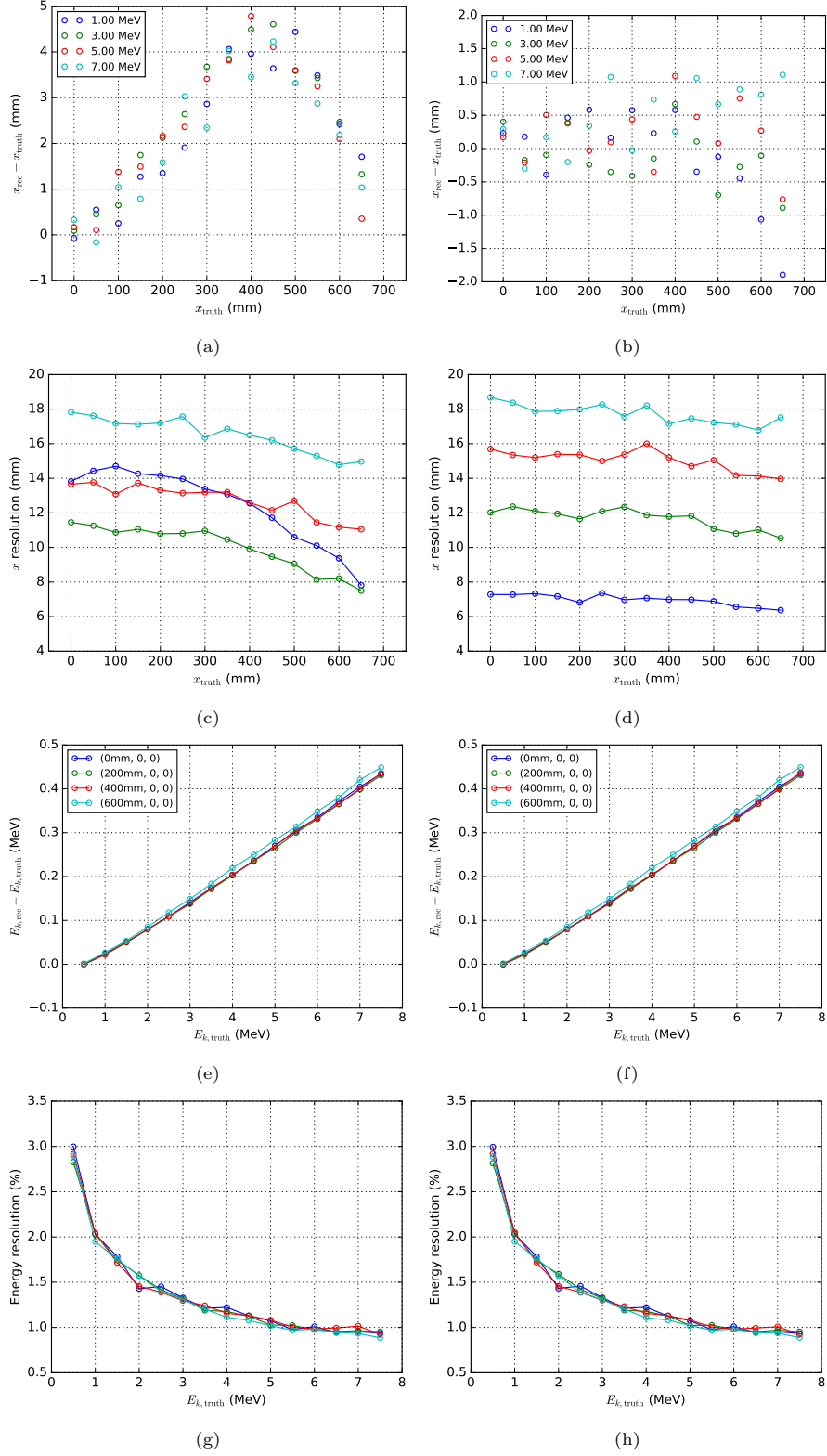


Figure 7: The reconstruction results of vertex (x position) and energy using charge (first column) and first hit time(second column). (a) and (b) show the reconstruction bias and resolution (standard deviation) of x coordinate; (c) and (d) show the reconstruction bias and resolution (relative standard deviation) of kinetic energy.

4.1. Reconstruction results

To evaluate the reconstruction methodologies, electrons with several fixed energies and vertices along x-axis are simulated. The accurate first hit times are extracted from the detector simulation. The transit time spread (TTS) and time delay in electronics have not been considered. Two reconstruction likelihood Eqs. (16) and (20) are used and their results are compared. Compared to the reconstruction with detector simulation, the electronic simulation blurs the number and time of PE, then complex the reconstruction. Table 1 summarizes the simulated datasets.

Table 1: e^- datasets used for calibration of response and evaluation of reconstruction methodology

Usage	Section	Simulation type	Configuration
Optical calibration	2	detector	0.5 MeV e^- uniformly in CD
Electronic calibration	3	detector + electronic	1 MeV and 3 MeV e^- at the detector center
Evaluate reconstruction	4.1	detector + electronic	0.5 ~ 7.5 MeV e^- along the x-axis

4.2. With ADC charge Q

The first column of Fig. 7 shows the reconstruction results using only ADC charge and Eq. (16). Fig. 7a shows the bias of vertex reconstruction along x-axis. The maximum bias in fiducial volume is about 5.0 mm, which occurs around radius of 400 mm. The vertex bias is mainly caused by the approximation of intensity function Eq. (5). For vertex resolution shown in Fig. 7c, the downtrend in low energy range (<3 MeV) and the uptrend in high energy range (>3 MeV) are observed. At low energy, electron deposits its energy in a small volume with a radius of several millimeters. Few photons are produced, which contributes to large reconstruction resolution. At high energy, the electron deposits energy in a larger volume. In this case the electron cannot be considered as a strict point source, which also leads to large resolution.

Fig. 7e shows the bias of energy reconstruction, which is mainly caused by energy non-linearity, as discussed in 5.1. Fig. 7g shows the resolution of energy reconstruction, which verifies the conclusion of 2% energy resolution at 1 MeV. At high energy range (>6 MeV) and detector area outside the fiducial volume, the energy resolution worsens due to energy leakage.

4.3. With ADC charge Q and first hit time T

The second column of Fig. 7 shows the reconstruction results using ADC charge and first hit time. As the radius increases, the bias of vertex reconstruction shown in Fig. 7b also increases, and the maximum bias in FV is about 2.0 mm, which is less than result using only charge. The vertex resolution shown in Fig. 7d is also better than that using charge only, especially for low energy range (<3 MeV). These results indicate that the first hit time plays an important role in reducing the bias and resolution (standard deviation) of vertex reconstruction.

Compared to results using only charge, the energy bias showed in Fig. 7f has no significant difference, which indicates that the energy bias is dominated by the summation of charge for all SiPMs. And the energy resolution showed in Fig. 7h becomes better, especially for high energy range (>6 MeV) and detector area beyond radius 400 mm, with the help of accurate time.

Meanwhile, due to the usage of time in likelihood function Eq. (20), the algorithm can also give the reconstruction result of event time. Figs. 8a and 8b are the bias and resolution of time reconstruction respectively, which shows the same trend over energy, as the reconstruction results of vertex resolution using only charge. The time bias is the difference between reconstructed event time t_0 and the real event time (default zero) in detector simulation. In reality t_0 is affected by trigger time and time delay in cable[8], thus the result of time bias is provided as a reference. The time resolution without considering TTS is less than 0.02 ns. These reasonable results verify the feasibility of reconstruction using first hit time and charge, according to a pure probabilistic model introduced in sec. 2 and 3.2.

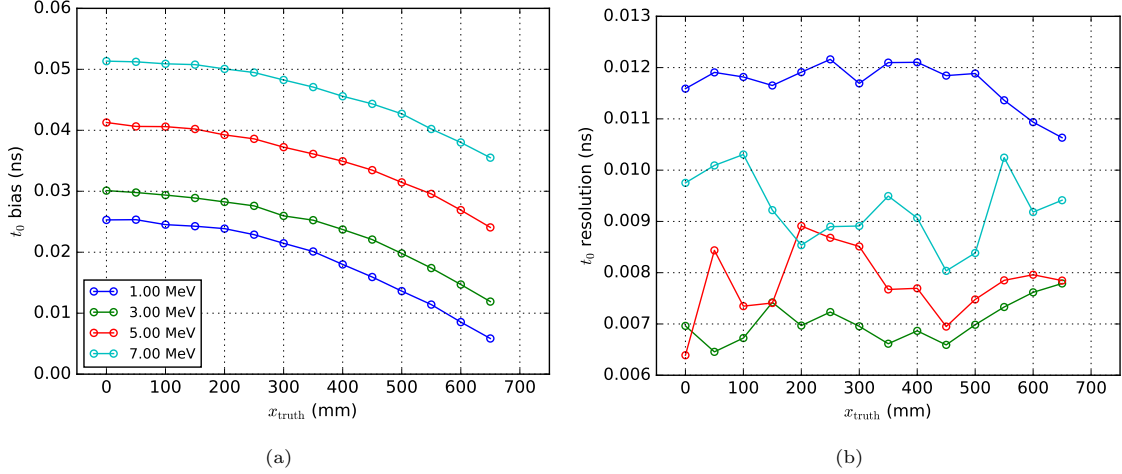


Figure 8: The reconstruction results of time bias (a) and resolution (b), respectively.

5. Discussion

5.1. The effect of non-linearity

The non-linearity between the kinetic energy of charged particles and the number of emitted photons is referred to as the physics non-linearity. As mentioned above, physics non-linearity is mainly caused by ionization quenching and Cherenkov radiation, both of them decrease the PE count received by SiPM. The non-linearity between the sum of PE count and that of the charge on SiPMs is called the electronic non-linearity. These nonlinearities have an influence on the bias of energy reconstruction using charge. In order to quantify the effect, we use the test dataset and fit the pairs of variables (kinetic energy E_k , PE count N_{PE} and charge Q_{ADC}) related to energy with a linear function crossing the origin. Then we calculate the relative residual, which is defined as

$$\text{Rel. res} = \frac{y_{\text{fit}} - y_{\text{measure}}}{y_{\text{measure}}} \times 100\% \quad (21)$$

Specifically, the relative residual of $E_k \rightarrow N_{\text{PE}}$ corresponds to non-linearity caused by ionization quenching and Cherenkov radiation. The relative residual of $N_{\text{PE}} \rightarrow Q_{\text{ADC}}$ shows the non-linearity in electronic simulation, where the effect of dark counts N_{dn} is considered. Figs. 9a and 9b show the relative residual for electron at center of CD. Fig. 9c shows the relative bias of energy reconstruction, which is consistent with energy non-linearity in Figs. 9a and 9b. Notice that the linearity of visible energy in Eq. (2) and response function is calibrated using 0.5 MeV electrons, the energy bias at 0.5 MeV is less than those at other energies. The energy bias can be corrected by the non-linearity calibration studied by Hangkun Xu et al. [1].

5.2. Reconstruction using time and PE count

Ziyuan Li et al. [8] uses the charge to estimate the PE count roughly, according to average charge of one PE on PMT. The construction of nPE map in Guihong Huang's work [9] also has the same problem. Due to the fluctuation of charge for one PE, it is impossible to get an accurate PE count considering only one charge value. Although waveform analysis [32] is helpful to determine the PE count and timing, it is useless for electronic system with time and charge readouts. In Tweedie distribution, the fluctuations of PE count and charge are taken into account inherently and thus there is no problem mentioned above. Nonetheless, the dependency between first hit time T and PE count N is also important. It is the foundation to understand the TQ dependency and reconstruct with T and N . The joint distribution $f_{\text{TN}}[T, N; R(t)]$ can be derived with a similar method discussed in 3.3. Or just simply replace the Tweedie distribution $f_{\text{Tw}}(Q; \lambda)$ in Eq. (19) with the Poisson probability of N

$$p_{\pi}(N; \lambda) = \exp(-\lambda)\lambda^N/N! \quad (22)$$

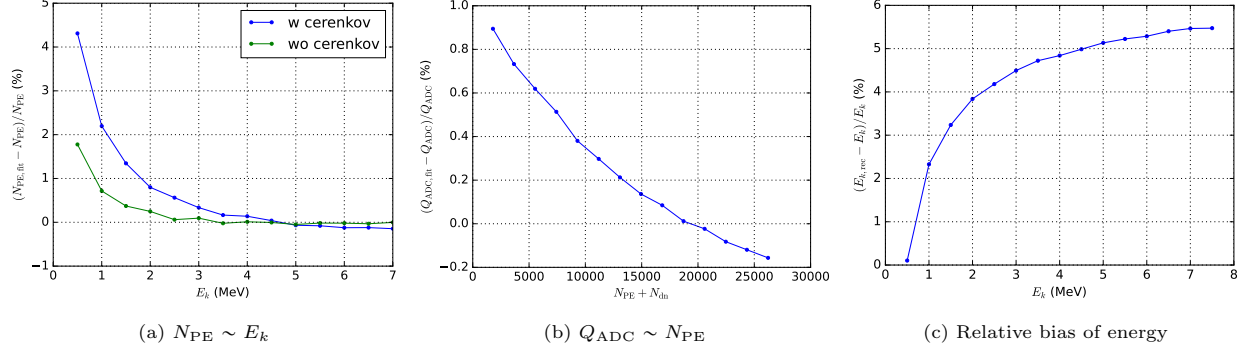


Figure 9: The relative residual between different pairs of variables with/without Cherenkov radiation. The test data are electrons located at center of CD.

and then derive the joint distribution

$$f_{\text{TN}} [T, N; R(t)] = \frac{\exp(-\lambda_{[T, \bar{T}]}) R(T) \lambda_{[T, \bar{T}]}^{N-1}}{(N-1)!} \quad (23)$$

The normalization of Eq. (23) can also be verified. Eq. (23) is so-called first photoelectron timing technique [8], which was also derived by Gioacchino Ranucci [3], later by C. Galbiati and K. McCarty [4]. The form of reconstruction likelihood is similar to Eq. (20):

$$\begin{aligned} L(\vec{r}, E, t_0; \{(T_j, N_j)\}) &= \prod_{\substack{N_j > 0 \\ \text{hit}}} f_{\text{TN}} [T_j, N_j; ER_j(t - t_0; \vec{r})] \times \prod_{\substack{N_j = 0 \\ \text{nonhit}}} p_\pi \left(0; \lambda_{j, [T-t_0, \bar{T}-t_0]}(\vec{r}, E) \right) \\ &= \prod_{N_j > 0} \frac{\exp[-\lambda_{j, [T-t_0, \bar{T}-t_0]}(\vec{r}, E)] ER_j(T_j - t_0; \vec{r}) \lambda_{j, [T-t_0, \bar{T}-t_0]}^{N_j-1}(\vec{r}, E)}{(N_j - 1)!} \\ &\quad \times \prod_{N_j = 0} \exp[-\lambda_{j, [T-t_0, \bar{T}-t_0]}(\vec{r}, E)] \end{aligned} \quad (24)$$

5.3. Application of Tweedie GLM on PMT

Compared to SiPM's charge spectrum, that of PMT has greater variance in Gamma part of Tweedie distribution, and it can also be fitted with Tweedie GLM. Fig. 10 shows a charge spectrum of PMT extracted from Fig. 1 in Kalousis's paper [33] and the fitting result using Tweedie distribution. The charges around the pedestal are not used in the fitting and considered as zero. It indicates that Tweedie GLM is not only suitable for charge distribution of SiPM with low crosstalk, but also for PMT spectrum modeled by Kalousis [33] and Anthony et al. [34].

5.4. Limitations of this methodology

At present, this study is based on Monte Carlo simulation. Electron is used to construct the detector response for point-like event. However, the most common radioactive source used in detector calibration is the γ source, such as ^{137}Cs and ^{60}Co . The γ deposits energy in a volume with a radius of about 10 cm and can not be considered as a point source. Therefore, it is necessary to conceive the calibration methodology of response function using real experimental data. The research from Guihong Huang et al. [9] and Ziyuan Li et al. [8] provides precious experience about the calibration of response function.

To achieve such a good result of vertex reconstruction, the algorithm also needs good time accuracy relative to the change of time response. In this study, we focus on verifying the feasibility of the algorithm, and use the precise value of first hit time in reconstruction and get the upper limit of algorithm. If the time precision or TTS in electronics is comparable to the half-value width of time response curve showed in Fig. 3c, both the bias and resolution of vertex reconstruction will be worse.

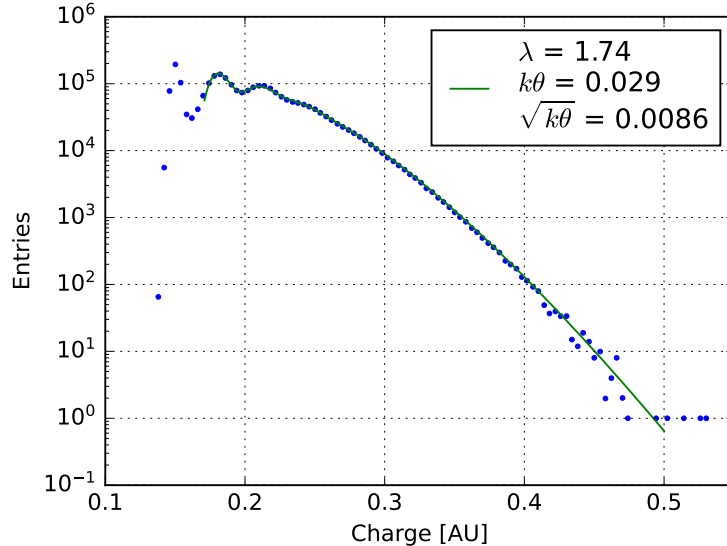


Figure 10: Charge distribution of PMT (blue point) and fitting result using Tweedie distribution (solid line). The first peak is the pedestal and the second one is the single photoelectron peak. The proportion of charge near the pedestal is about 0.175, which is consistent with the fitting results $\exp(-\lambda) \approx 0.176$. The charge spectrum is extracted from Fig. 1 in Kalousis’s paper [33].

Besides, the current charge model does not consider the contribution of external crosstalk. As mentioned in Sec. 3.1, due to the influence of crosstalk, the assumption of Poisson in Tweedie distribution no longer holds true. Tweedie GLM is not suitable to depict the charge distribution of SiPM with high crosstalk ratio. Generally, the Poisson part in compound Poisson Gamma distribution can be replaced by generalized Poisson [35], which is verified to work in V. Chmill [36] and Jack Rolph [37]’s studies. However, it is impossible to regress the parameters of charge distribution with GLM. These limitations will be studied carefully in the future.

6. Conclusion

From first principles, a pure probabilistic methodology is proposed to simultaneously reconstruct vertex, energy and time for point-like events in TAO CD, which is proven to be feasible. In fiducial volume of TAO detector and energy range of reactor neutrinos, a vertex resolution better than 16 mm can be achieved, after considering the dark noise and direct crosstalk of SiPM. This methodology sufficiently utilizes first hit time and charge in reconstruction, which can be used not only for SiPM in TAO detector, but also for other experiments with first hit time and charge readouts, such as 3-inch PMT in JUNO [38] and QBEE electronics in Super Kamiokande [39].

Acknowledgments

We are grateful to Yuyi Wang for proofreading the manuscript. We also thank Yiyang Wu, Jun Weng and Aiqiang Zhang for discussions of reconstruction algorithms and development of SiPM/PMT charge model using Poisson and Gamma distributions.

The idea of first-principle time-charge likelihood originates from the draft *va3* fitter at KamLAND [40]. It grew out of the reconstruction parameter tuning guided by Prof. Itaru Shimizu, and received scrutinization and encouragement from Prof. Jason Detwiler. The corresponding author would like to sincerely appreciate the KamLAND collaboration for education and inspirations on event reconstruction and neutrino physics.

References

- [1] Hangkun Xu et al. Calibration strategy of the JUNO-TAO experiment. *The European Physical Journal C*, 82(12):1112, December 2022.
- [2] Angel Abusleme et al. TAO Conceptual Design Report: A Precision Measurement of the Reactor Antineutrino Spectrum with Sub-percent Energy Resolution. 5 2020.
- [3] Gioacchino Ranucci. An analytical approach to the evaluation of the pulse shape discrimination properties of scintillators. *Nuclear Instruments and Methods in Physics Research Section A: Accelerators, Spectrometers, Detectors and Associated Equipment*, 354(2):389–399, 1995.
- [4] C. Galbiati and K. McCarty. Time and space reconstruction in optical, non-imaging, scintillator-based particle detectors. *Nuclear Instruments and Methods in Physics Research Section A: Accelerators, Spectrometers, Detectors and Associated Equipment*, 568(2):700–709, 2006.
- [5] Mikhail Batygov. *Combined Study of Reactor and Terrestrial Antineutrinos with KamLAND*. PhD thesis, University of Tennessee, Knoxville, 2006.
- [6] G. Bellini et al. Final results of Borexino Phase-I on low-energy solar neutrino spectroscopy. *Phys. Rev. D*, 89:112007, Jun 2014.
- [7] M Jiang et al. Atmospheric neutrino oscillation analysis with improved event reconstruction in Super-Kamiokande IV. *Progress of Theoretical and Experimental Physics*, 2019(5):053F01, 05 2019.
- [8] Zi-Yuan Li et al. Event vertex and time reconstruction in large-volume liquid scintillator detectors. *Nuclear Science and Techniques*, 32:49, 2021.
- [9] Gui-Hong Huang et al. Data-driven simultaneous vertex and energy reconstruction for large liquid scintillator detectors. *Nuclear Science and Techniques*, 34, 2023.
- [10] Zhen Qian et al. Vertex and energy reconstruction in juno with machine learning methods. *Nuclear Instruments and Methods in Physics Research Section A: Accelerators, Spectrometers, Detectors and Associated Equipment*, 1010:165527, 2021.
- [11] Cynthia Rudin. Stop explaining black box machine learning models for high stakes decisions and use interpretable models instead. *Nature machine intelligence*, 1(5):206–215, 2019.
- [12] Wei Dou et al. Reconstruction of point events in liquid-scintillator detectors subjected to total reflection. 2022.
- [13] FABRIZIO GABBIANI and STEVEN J. COX. Chapter 16 - stochastic processes. In FABRIZIO GABBIANI and STEVEN J. COX, editors, *Mathematics for Neuroscientists*, pages 251–266. Academic Press, London, 2010.
- [14] D. Adey et al. A high precision calibration of the nonlinear energy response at daya bay. *Nuclear Instruments and Methods in Physics Research Section A: Accelerators, Spectrometers, Detectors and Associated Equipment*, 940:230–242, 2019.
- [15] Kuo Niu and Chao Tian. Zernike polynomials and their applications. *Journal of Optics*, 24(12):123001, nov 2022.
- [16] George B. Arfken, Hans J. Weber, and Frank E. Harris. Chapter 15 - legendre functions. In George B. Arfken, Hans J. Weber, and Frank E. Harris, editors, *Mathematical Methods for Physicists (Seventh Edition)*, pages 715–772. Academic Press, Boston, seventh edition edition, 2013.
- [17] David Jenkins. *Radiation Detection for Nuclear Physics*. 2053-2563. IOP Publishing, 2020.

- [18] J. Allison, K. Amako, J. Apostolakis, P. Arce, M. Asai, T. Aso, E. Bagli, A. Bagulya, S. Banerjee, G. Barrand, B. R. Beck, A. G. Bogdanov, D. Brandt, J. M. C. Brown, H. Burkhardt, Ph. Canal, D. Cano-Ott, S. Chauvie, K. Cho, G. A. P. Cirrone, G. Cooperman, M. A. Cortés-Giraldo, G. Cosmo, G. Cuttone, G. Depaola, L. Desorgher, X. Dong, A. Dotti, V. D. Elvira, G. Folger, Z. Francis, A. Galoyan, L. Garnier, M. Gayer, K. L. Genser, V. M. Grichine, S. Guatelli, P. Guèye, P. Gumplinger, A. S. Howard, I. Hřivnáčová, S. Hwang, S. Incerti, A. Ivanchenko, V. N. Ivanchenko, F. W. Jones, S. Y. Jun, P. Kaitaniemi, N. Karakatsanis, M. Karamitros, M. Kelsey, A. Kimura, T. Koi, H. Kurashige, A. Lechner, S. B. Lee, F. Longo, M. Maire, D. Mancusi, A. Mantero, E. Mendoza, B. Morgan, K. Murakami, T. Nikitina, L. Pandola, P. Paprocki, J. Perl, I. Petrović, M. G. Pia, W. Pokorski, J. M. Quesada, M. Raine, M. A. Reis, A. Ribon, A. Ristić Fira, F. Romano, G. Russo, G. Santin, T. Sasaki, D. Sawkey, J. I. Shin, I. I. Strakovsky, A. Taborda, S. Tanaka, B. Tomé, T. Toshito, H. N. Tran, P. R. Truscott, L. Urban, V. Uzhinsky, J. M. Verbeke, M. Verderi, B. L. Wendt, H. Wenzel, D. H. Wright, D. M. Wright, T. Yamashita, J. Yarba, and H. Yoshida. Recent developments in Geant4. *Nuclear Instruments and Methods in Physics Research Section A: Accelerators, Spectrometers, Detectors and Associated Equipment*, 835:186–225, November 2016.
- [19] Harry H. Tan. A statistical model of the photomultiplier gain process with applications to optical pulse detection, 1982.
- [20] L.N. Kalousis et al. A fast numerical method for photomultiplier tube calibration. *Journal of Instrumentation*, 15(03):P03023, mar 2020.
- [21] Maurice CK Tweedie et al. An index which distinguishes between some important exponential families. In *Statistics: Applications and new directions: Proc. Indian statistical institute golden Jubilee International conference*, volume 579, pages 579–604, 1984.
- [22] G. K. Smyth. Regression modelling of quantity data with exact zeroes. In *Proceedings of the Second Australia-Japan Workshop on Stochastic Models in Engineering, Technology and Management*, pages 572–580. Technology Management Centre, University of Queensland, 1996.
- [23] Peter K. Dunn and Gordon K. Smyth. Series evaluation of Tweedie exponential dispersion model densities. *Stat Comput*, 15(4):267–280, October 2005.
- [24] Peter K. Dunn and Gordon K. Smyth. Evaluation of Tweedie exponential dispersion model densities by Fourier inversion. *Stat Comput*, 18(1):73–86, March 2008.
- [25] Peter K. Dunn and Gordon K. Smyth. *Generalized Linear Models With Examples in R*. Springer Texts in Statistics. Springer New York, New York, NY, 2018.
- [26] B Jørgensen. Exponential dispersion models (with discussion). *Journal of the Royal Statistical Society B*, 49:127–162, 1987.
- [27] P. McCullagh. *Generalized Linear Models*. Chapman and Hall/CRC, Boca Raton, 2nd edition edition, August 1989.
- [28] Fabio Acerbi and Stefan Gundacker. Understanding and simulating sipms. *Nuclear Instruments and Methods in Physics Research Section A: Accelerators, Spectrometers, Detectors and Associated Equipment*, 926:16–35, 2019. Silicon Photomultipliers: Technology, Characterisation and Applications.
- [29] P.C. Consul and Felix Famoye. Generalized poisson regression model. *Communications in Statistics - Theory and Methods*, 21(1):89–109, 1992.
- [30] S. Vinogradov. Analytical models of probability distribution and excess noise factor of solid state photomultiplier signals with crosstalk. *Nuclear Instruments and Methods in Physics Research Section A: Accelerators, Spectrometers, Detectors and Associated Equipment*, 695:247–251, December 2012.
- [31] Sami Kurtti and Juha T. Kostamovaara. Pulse width time walk compensation method for a pulsed time-of-flight laser rangefinder. *2009 IEEE Instrumentation and Measurement Technology Conference*, pages 1059–1062, 2009.

- [32] D.C. Xu et al. Towards the ultimate pmt waveform analysis for neutrino and dark matter experiments. *Journal of Instrumentation*, 17(06):P06040, jun 2022.
- [33] Leonidas N. Kalousis. An analytical model for photomultiplier tube calibration. *Nuclear Instruments and Methods in Physics Research Section A: Accelerators, Spectrometers, Detectors and Associated Equipment*, 1058:168943, 2024.
- [34] M. Anthony et al. Characterization of photomultiplier tubes with a realistic model through gpu-boosted simulation. *Journal of Instrumentation*, 13(02):T02011, feb 2018.
- [35] S. Vinogradov. Analytical models of probability distribution and excess noise factor of solid state photomultiplier signals with crosstalk. *Nuclear Instruments and Methods in Physics Research Section A: Accelerators, Spectrometers, Detectors and Associated Equipment*, 695:247–251, 2012. New Developments in Photodetection NDIP11.
- [36] V. Chmill et al. On the characterisation of sipms from pulse-height spectra. *Nuclear Instruments and Methods in Physics Research Section A: Accelerators, Spectrometers, Detectors and Associated Equipment*, 854:70–81, 2017.
- [37] Jack Rolph et al. Peakotron: A python module for fitting charge spectra of silicon photomultipliers. *Nuclear Instruments and Methods in Physics Research Section A: Accelerators, Spectrometers, Detectors and Associated Equipment*, 1056:168544, 2023.
- [38] S. Conforti et al. Catiroc: an integrated chip for neutrino experiments using photomultiplier tubes. *Journal of Instrumentation*, 16(05):P05010, may 2021.
- [39] S. Yamada et al. Commissioning of the new electronics and online system for the super-kamiokande experiment. *IEEE Transactions on Nuclear Science*, 57(2):428–432, 2010.
- [40] Benda Xu. *Observation of Geoneutrinos at KamLAND during Reactor Shutdown*. PhD thesis, Tohoku University, Sendai, Japan, 2014.

Appendix A. The normalization of f_{TQ}

To verify the normalization of Eq. (19), first integrate T :

$$\begin{aligned}
\int_{\underline{T}}^{\bar{T}} f_{TQ} [T, Q; R(t)] dT &= - \int_{\lambda_{[\underline{T}, \bar{T}]}}^0 \exp [- (\lambda_{[\underline{T}, \bar{T}]} - \lambda)] \left(1 + \frac{\partial}{\partial \lambda} \right) f_{Tw} (Q; \lambda) d\lambda \\
&= - \int_{\lambda_{[\underline{T}, \bar{T}]}}^0 \frac{\partial}{\partial \lambda} \left\{ \exp [- (\lambda_{[\underline{T}, \bar{T}]} - \lambda)] f_{Tw} (Q; \lambda) \right\} d\lambda \\
&= - \exp [- (\lambda_{[\underline{T}, \bar{T}]} - \lambda)] f_{Tw} (Q; \lambda) \Big|_{\lambda_{[\underline{T}, \bar{T}]}}^0 \\
&= f_{Tw} (Q; \lambda_{[\underline{T}, \bar{T}]})
\end{aligned} \tag{A.1}$$

Eq. (A.1) is the Tweedie PDF used in 3.2. The first line of Eq. (A.1) uses

$$d\lambda = -R(T)dT. \tag{A.2}$$

Then integrate Q , obviously

$$\int f_{Tw} (Q; \lambda_{[\underline{T}, \bar{T}]}) dQ = 1. \tag{A.3}$$

Of course, we can first integrate Q , but notice if Q is zero:

$$f_{Tw} (Q = 0; \lambda_{[\underline{T}, \bar{T}]}) = \exp (-\lambda_{[\underline{T}, \bar{T}]}) \tag{A.4}$$

$$\begin{aligned}
f_T [T; Q \neq 0, R(t)] &= \int f_{TQ} [T, Q; Q \neq 0, R(t)] dQ \\
&= \frac{\int \exp \left[- \int_{\underline{T}}^T R(t) dt \right] R(T) \left(1 + \frac{\partial}{\partial \lambda} \right) f_{Tw} (Q; \lambda) \Big|_{\lambda = \int_{\underline{T}}^T R(t) dt} dQ}{1 - \exp (-\lambda_{[\underline{T}, \bar{T}]})} \\
&= \frac{\exp \left[- \int_{\underline{T}}^T R(t) dt \right] R(T)}{1 - \exp (-\lambda_{[\underline{T}, \bar{T}]})}.
\end{aligned} \tag{A.5}$$

Eq. (A.5) is the distribution of first hit time T . Then integrate T ,

$$\int_{\underline{T}}^{\bar{T}} f_T [T; Q \neq 0, R(t)] dT = \frac{- \int_{\lambda_{[\underline{T}, \bar{T}]}}^0 \exp [- (\lambda_{[\underline{T}, \bar{T}]} - \lambda)] d\lambda}{1 - \exp (-\lambda_{[\underline{T}, \bar{T}]})} = 1. \tag{A.6}$$

Therefore,

$$f_{Tw} (Q = 0; \lambda_{[\underline{T}, \bar{T}]}) + f_{Tw} (Q \neq 0; \lambda_{[\underline{T}, \bar{T}]}) \cdot \int_{T, Q} f_{TQ} [T, Q; Q \neq 0, R(t)] dT dQ = 1. \tag{A.7}$$

¹Long-Distance Signal Propagation in AC-LGAD

C. Bishop, A. Das, J. Ding, M. Gignac, F. Martinez-McKinney, S. M. Mazza, A. Molnar,
N. Nagel, M. Nizam, J. Ott, H. F.-W. Sadrozinski, B. Schumm, A. Seiden, T. Shin,
A. Summerell, M. Wilder, Y. Zhao

SCIPP, Univ. of California Santa Cruz, CA 95064, USA

Abstract– We investigate the signal propagation in AC-LGAD (aka RSD), which are LGAD with a common N^+ layer and segmented AC-coupled readout contacts, by measuring response to IR laser TCT on a large selection of AC-LGAD with strip readout. The interest for this topic derives from the realization that while large charge sharing between neighboring strips is essential for good position resolution, large sharing beyond the next neighbor generates background signals which in general are detrimental to the sensor goal of low occupancy. Using AC-LGAD with strip readout produced by Hamamatsu Photonics (HPK), we evaluate the effects of a variety of sensor properties, including geometrical parameters (strip length, width), process parameters like the N^+ layer resistivity, the coupling capacitance, and the thickness of the bulk on the signal sharing and the position resolution.

PACS: 29.40.Gx, 29.40.Wk, 78.47jc

Keywords: fast silicon sensors; charge multiplication; AC-LGAD strips; charge sharing.

1. Introduction

Low-gain Avalanche Detectors (LGAD) have been recently introduced as fast semiconductor timing sensors [1,2]. In their experimental applications their segmentation is limited to pads with 1 mm pitch by consideration of power and fill-factor. To avoid this restriction which limits the spatial resolution, the AC-LGAD technology (aka Resistive Silicon Detector RSD) [3-5] is under investigation, based on a complete integration of four of the sensor layers in common sheets of the P-type bulk, the P^+ gain layer, the N^+ layer and a dielectric sheet, separating the first three from the segmented metal readout contacts (Fig. 1). A signal originating in the bulk and amplified in the gain layer is then shared between several electronics channels, allowing reconstruction of signal location with a resolution which is a small fraction of the readout pitch. Yet due to the common N^+ layer, the observed signal in AC-LGADs is the sum of the directly induced signal from the moving collected charge on neighboring contacts (shown in red in Fig. 1) and the pick-up of the signal conducted on the N^+ layer common to all contacts (“leakage” shown in yellow).

The relative strength between induced and conducted signal depends on a variety of sensor parameters which we compare in the following study using scanning laser Transient Current Technique (TCT) on strip AC-LGAD produced by HPK : the geometry of the metal readout contacts was varied, as were production details of two common layers (N^+ layer resistivity and dielectric specs) and the bulk thickness. The doping

of the gain layer and the strip pitch were kept constant. This will allow to check the simple assumption that for a large local signal and a small amount of long-distance conducted signal a large N^+ resistivity and a large coupling capacitance are needed.

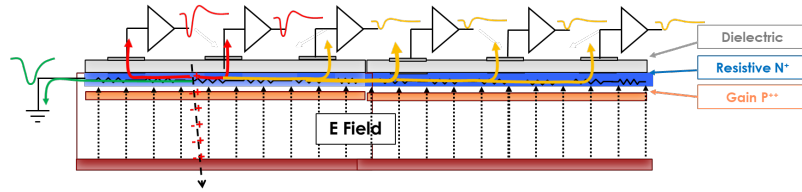


Fig. 1 Cross section of an AC-LGAD showing common sensor layers and the signal shared by neighboring metal contacts.

2. Experimental

2.1 Sensors

The sensors used were fabricated by HPK as part of the US-Japan Collaborative Agreement [6]. Two values for the N^+ sheet resistance and two values for the capacitance of the coupling capacitance were selected, resulting in four basic sensor types as shown in Fig. 2 LEFT.

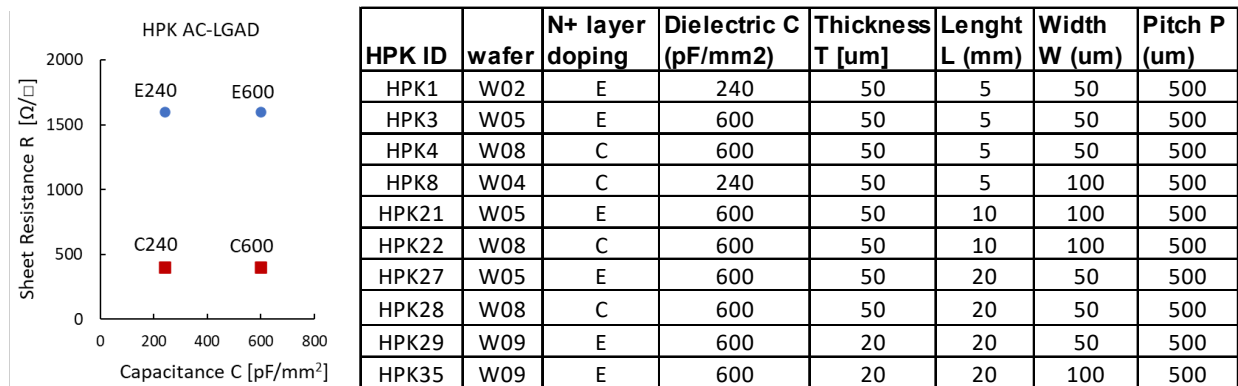


Fig. 2 LEFT: Selected values for the sheet resistance of the N^+ layer and for the capacitance per area of the coupling capacitance. RIGHT: Parameters for the HPK AC-LGAD tested

The detailed sensor layout was then achieved by selecting two thicknesses of the bulk (50 and 20 μm), and for the metal strips, two widths (50 and 100 μm), and three length (5, 10, 20 mm) on a 500 μm pitch as shown in Fig. 2 RIGHT. This way all four of the selection in Fig. 2 are realized and could be compared. It should be pointed out that the actual value of the coupling capacitance varies between 60 pF and 1200 pF.

2.2 IR Laser TCT Measurements

The charge collection measurements using TCT follow the method described in [7]. In short, the sensors are mounted on fast analog amplifier boards with 16 channels and 1 GHz of bandwidth designed at Fermilab (FNAL) [8] and read out by a fast oscilloscope (2 GHz, 20 Gs). Sensors mounted on boards are excited with an infrared (IR) 1064 nm pulsed laser with a pulse temporal width of 400 ps, and a spot of 10-20 μm

width mimicking the response of a MIP in the silicon [9]. The IR laser cannot penetrate the metal strips, therefore the sensor behavior can be characterized only in between metal electrodes.

The read-out board is mounted on X-Y moving stages so the response of the sensor as a function of laser illumination position can be evaluated. Waveforms are averaged to decrease the effect of laser power fluctuations, and a photodiode is used to correct for them. The scans were analyzed using the pulse shape in each position to derive pulse maximum (Pmax) [7]. In addition, the rise time and fall time and the time of arrival were recorded and will be the topic of a later publication.

3. Results and Discussion

3.1 Pulse Height Pmax

An important parameter of the LGAD is the internal gain, which multiplies the generated pulse charge to the level of the collected charge. Yet most of the LGAD investigations of timing or location precision involve the pulse height instead of the charge. The maximum pulse height, Pmax, depends on the bias voltage as shown in Fig. 3. The bias voltages shown values are below the on-set of breakdown. The logarithmic presentation shows the exponential gain dependence to be similar for all sensors, but the data separate along being E-type (purple) or C-type (reddish). Sensors with longer strips require larger bias voltage to reach the same Pmax. Sensors with bulk thickness $T = 20 \mu\text{m}$ and $T = 50 \mu\text{m}$ show essentially the same Pmax range due to different weight fields and rise times. At a noise value of 2 mV , $S/N = 100$ for $P_{\text{max}} = 200 \text{ mV}$.

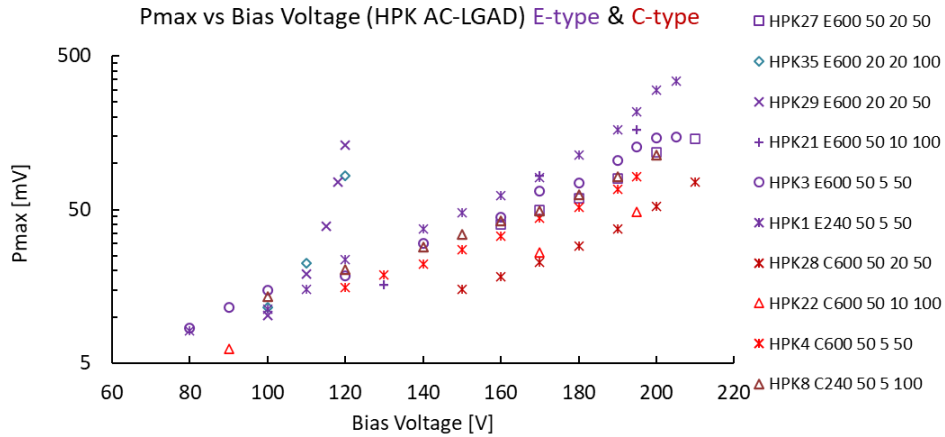


Fig. 3 Bias voltage dependence of the pulse height Pmax for the tested AC-LGADs (Legends : ID#, Type, Thickness T, Strip Length L, Strip Width W)

3.2 Pulse Sharing

The pulse sharing is tested in positional laser (TCT) scans with normalized Pmax as shown in Fig.4, with Fig. 4 LEFT representing the 4 different combinations of N^+ sheet resistance R and dielectric capacitance C indicated in Fig. 2. They all have a length $L = 5 \text{ mm}$ and thickness $T = 50 \mu\text{m}$, and metal width $W = 50 \mu\text{m}$, except for C240, which has $W = 100 \mu\text{m}$. (N.B.: most of the positional scans exhibit increases at the two ends, being attributed to the pick-up from the N^+ layer contact). Different sensors show different signal sharing properties according to the Type used:

- E600 and E240 (high R) have optimal close signal sharing contained within the strip center of the next neighbor, getting reduced to 2 – 3 % “leakage” at long distance, with E600 preferred;
- C600 (low R, high Cap) has large sharing close to and beyond next neighbor, exhibiting long-distance constant “leakage” of the order of 10%;
- C240 (low R, low Cap) has large sharing to the next few neighbors, with the long-distance “leakage” reduced to < 2%.

This large sharing in the C-Type sensors appears to be the root cause for the reduced Pmax compared to E-types shown in Fig. 3.

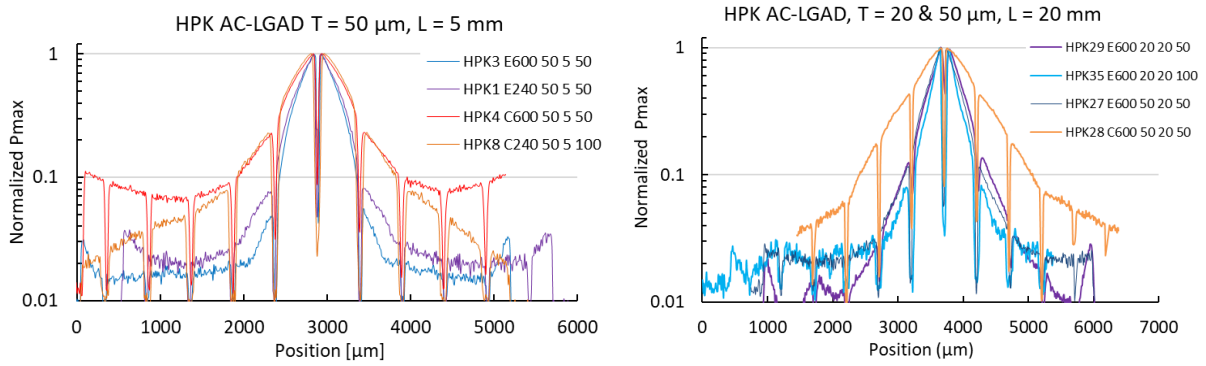


Fig. 4 Normalized Pmax distributions: LEFT of four AC-LGADs with strip length $L = 5$ mm; RIGHT E600 and C600 type sensors with strip length $L = 20$ mm and bulk thickness $T = 20$ & 50 μm , (Legends : ID#, Type, Bulk Thickness T, Strip Length L, Strip Width W).

The strip length influences the sharing to the next neighbor. Fig.4 RIGHT shows the Pmax distributions for sensors with 20 mm length and different bulk thicknesses. The short- and long-distance sharing to the next neighbors is worse for the E600 sensor with strip length $L = 20$ mm than for one with $L = 5$ mm. Yet there is little difference between E240 with strip length $L = 5$ mm having a coupling capacitance of $CC = 60$ pF and E600 with $L = 20$ mm and $CC = 600$ pF. How the sharing changes with the thickness of the bulk T is shown in Fig 4 RIGHT: a thinner E600 sensor with $T = 20$ μm has a better suppression of long-distance sharing than the one with $T = 50$ μm . In addition, the thinner detector with narrow metal width $W = 50$ μm has much less long-range sharing than the one with $W = 100$ μm . As before, the C600 sensor with $T = 50$ shows large sharing diminishing at large distance.

3.3 Position Resolution

The TCT laser scans are being used to evaluate the position resolution across the strips, based on the normalized Pmax distributions between neighboring pairs of strips as shown in Fig. 5 for two AC-LGAD with 5 mm long strips, one a C240 (LEFT) and the other an E600 (RIGHT), respectively. The fraction $Frac$ [7] is defined as

$$Frac = \frac{Pmax(1)}{[Pmax(1) + Pmax(2)]}$$

and shown as function of the position in Fig. 6 LEFT. Both the inter-strip region for Pmax and the Frac distributions are different for E and C Types. The fraction shows a close to linear behavior between deep “notches” at the location of the strip centers, and this region shown in Fig. 6 RIGHT for all 10 sensors is

used to calculate the slope $dFrac/dPos$. The slope of fraction vs. position is very similar separately for E and C sensors, independent of strip length, width and of the bulk thickness T. The linear slope for the C-Type sensors is a factor 1.7 smaller than for the E-Type sensors and covers a much smaller position range, which means that the position resolution needs to be calculated for a large part using the 2nd neighbor.

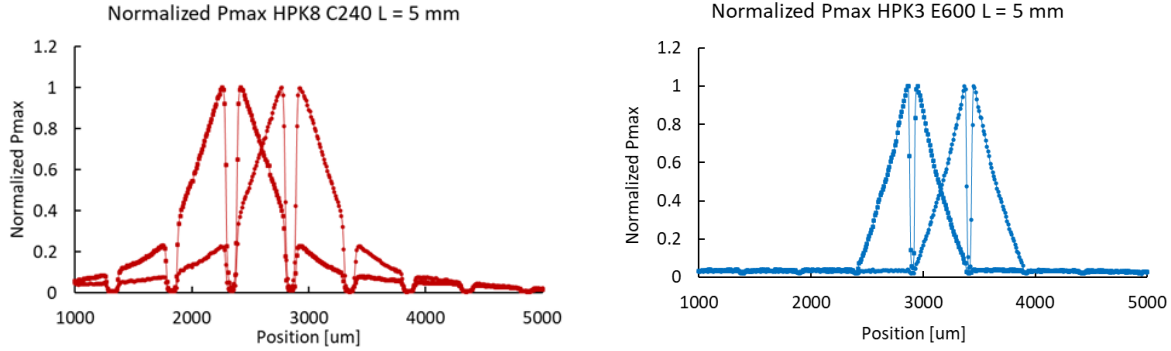


Fig. 5 Normalized Pmax distribution of two neighboring strips of LEFT C240 and RIGHT E600 sensors

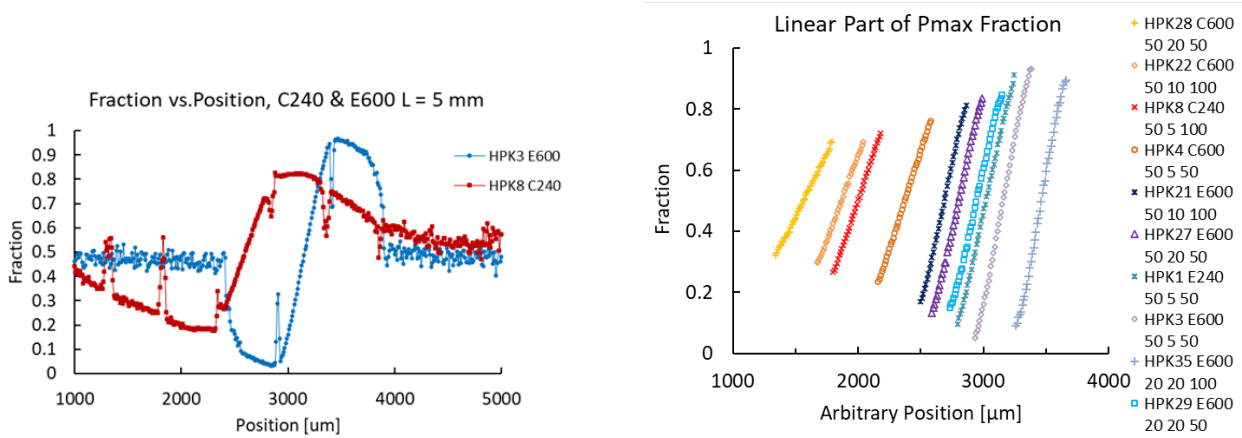


Fig. 6 Position dependence of the fraction: LEFT for the sensors of Fig. 5, RIGHT for all sensors in the region of a linear slope, with two distinct groups in slope (C-Type red/yellow, E-Type blue) (Legends : ID#, Type, Thickness T, Strip Length L, Strip Width W)

The position resolution $\sigma(Pos)$ is calculated from the inverse of the Frac slope $dFrac/dPos$, i.e. $(dPos/dFrac)$ and the signal-to-noise ratio S/N:

$$\sigma(Pos) = \sqrt{2} \left(\frac{dPos}{dFrac} \right) \frac{1}{S/N}$$

and is shown in Fig. 7 as a function of S/N. Like the fraction slope, the predicted resolution falls into two groups depending on the resistance of the N⁺ layer, independent of the coupling capacitance. Again, the advantage of the E-Type sensors is shown by the better position resolution compared to C-Type for the same signal height. For an achievable $S/N \geq 100$ a position resolution of $\sigma(Pos) \leq 8 \mu m$ is reached for the E types independently of strip length, bulk thickness and metal width. There is an outlier, HPK28, which

is a 20 mm long C600 sensor shown in Fig.4 RIGHT where the excessive neighbor sharing causes an inferior position resolution, leading to a reduced Pmax as seen in Fig. 3.

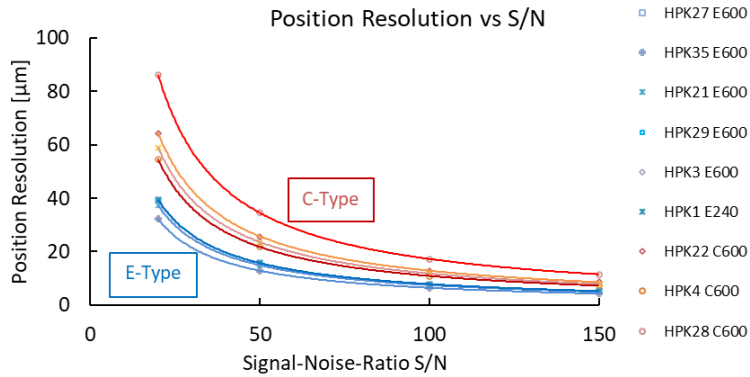


Fig. 7 Projected position resolution vs. signal-to-noise ratio S/N for the 500 um pitch sensors.

4. Conclusions

In AC-LGADs, signal sharing needs to be high between neighboring strips for good position resolution and low for far-distant strips to reduce pick-up noise. Using IR laser TCT, we have investigated the sharing in HPK sensors with variations of the parameters governing the sharing, i.e. the sheet resistance of the N^+ layer and the capacitance of the dielectric. Sensors with different layout of the metal strips were measured. The parameter choice “E600” gives good performance up to a strip length of 20 mm. It combines high sheet resistance of the N^+ layer with large coupling capacitance (thin di-electric layer). It maximizes the pulse height of the signal, leading to lower operating bias voltage, maximizes the amount of next neighbor sharing for good position resolution and reduces the long-distance noise pick-up to the % level. A bulk thickness of 20 μm has the lowest long-distance pick-up. Assuming a realistic signal-to-noise ratio, the high resistance E-type sensor promises an excellent position resolution of about 10 μm on a strip pitch of 500 μm for all tested strip parameters.

5. Acknowledgements

We acknowledge the collaboration with the KEK group (K. Nakamura et al.), the FNAL group (A. Apresyan et al.) and the BNL group (A. Tricoli et al.). H.F.W.S. wants to thank the local organizing committee for the perfect organization and the very pleasant atmosphere of HSTD13.

This work was supported by the United States Department of Energy grant DE-FG02-04ER41286 and by the U.S.-Japan Science and Technology Cooperation Program in High Energy Physics.

6. References

- [1] G. Pellegrini et al., Technology developments and first measurements of Low Gain Avalanche Detectors (LGAD) for high energy physics applications, NIM. A765 (2014) 12 – 16.
- [2] H. F.-W. Sadrozinski et al., Ultra-fast silicon detectors (UFSD), NIM. A730 (2013) 226–231.
- [3] H.F.-W. Sadrozinski, A. Seiden, N. Cartiglia, “4D Tracking with ultra-fast silicon detectors”, Rep. Progr. Phys. 81 (2) (2018).

- [4] M. Mandurrino et al., Demonstration of 200-, 100-, and 50- micron Pitch Resistive AC-Coupled Silicon Detectors (RSD) with 100% Fill-Factor for 4D Particle Tracking, IEEE Electron Device Letters, vol. 40, no. 11, pp. 1780-1783, Nov. 2019.
- [5] M. Tornago et al., Resistive AC-Coupled Silicon Detectors: Principles of operation and first results from a combined analysis of beam test and laser data, NIM 1003 (2021), 165319.
- [6] I. Kita et al., Development of AC-LGAD detector with finer pitch electrodes for high energy physics experiments, May 2023 arXiv:2305.12355v1.
- [7] J. Ott et al., Investigation of signal characteristics and charge sharing in AC-LGADs with laser and test beam measurements, NIM 1045 (2023), 167541.
- [8] R. Heller et al., Characterization of BNL and HPK AC-LGAD sensors with a 120 GeV proton beam, 2022 JINST 17 P05001 [arXiv:2201.07772].
- [9] Particulars, Advanced Measurement Methods, <http://particulars.si/products.php>

A clear case for dust obscuration of the lunar retroreflectors

Sanchit Sabhlok^{a,*}, James B. R. Battat^c, Nicholas R. Colmenares^d, Daniel P. Gonzales^{a,e} and Thomas W. Murphy, Jr.^b

^aDepartment of Physics, University of California San Diego, 9500 Gilman Drive, La Jolla, 92093-0424, CA, USA

^bDepartment of Astronomy and Astrophysics, University of California San Diego, 9500 Gilman Drive, La Jolla, 92093-0424, CA, USA

^cDepartment of Physics and Astronomy, Wellesley College, 106 Central Street, Wellesley, 02481, MA, USA

^dGeodesy and Geophysics Lab, NASA Goddard Space Flight Center, 8800 Greenbelt Rd., Greenbelt, 20771, MD, USA

^eDepartment of Physics, University of Maryland Baltimore County, 1000 Hilltop Circle, Baltimore, 21250, MD, USA

ARTICLE INFO

Keywords:

Eclipses

Moon, surface

Regoliths

ABSTRACT

The passive retroreflector arrays placed on the moon by Apollo 11, 14 and 15 astronauts continue to produce valuable Earth-Moon range measurements that enable high-precision tests of gravitational physics, as well as studies of geo- and selenophysics. The optical throughput of these retroreflectors has declined since their deployment, with an additional signal loss at full moon when the reflectors experience direct solar illumination. We show that the loss in return rate can be attributed to the accumulation of a thin layer of lunar dust on the surfaces of the corner cube retroreflectors. First, a careful analysis of the optical link budget for the Apache Point Observatory Lunar Laser-ranging Operation (APOLLO) experiment reveals that the lunar return rate is 15–20 times smaller than predicted, a deficit that can be explained by a reflector dust covering fraction of ~50%. Second, range measurements taken during a lunar eclipse indicate that the solar illumination of the retroreflectors degrades their throughput by an additional factor of ~15. Finally, a numerical simulation of heat transfer in dust-coated reflectors is able to model the resulting thermal lensing effect, in which thermal gradients in the retroreflectors degrade their far-field diffraction pattern. A comparison of this simulation to eclipse measurements finds a dust coverage fraction of ~50%. Taken together, the link analysis, eclipse observations and thermal modeling support the claim that the retroreflectors are obscured by lunar dust, with both link budget and simulation independently finding the dust fraction to be ~50%.

1. Introduction

The corner cube reflectors (CCRs) placed on the moon by Apollo 11, 14 and 15 astronauts continue to produce scientific output more than 50 years after their deployment. The reflectors were designed to sit passively in the periodic temperature swings of the lunar environment in order to facilitate Lunar Laser Ranging (LLR) measurements. It would be fair to say that these reflectors have greatly outperformed expectations, continuing to operate for more than 50 years after placement. Measurements of the Earth–Moon distance provide precision tests of fundamental physics (e.g. general relativity, Lorentz Invariance, time evolution of fundamental constants), as well as geophysical information and constraints on the composition and dynamics of the lunar interior (Murphy 2013).

The Apache Point Observatory Lunar Laser-ranging Operation (APOLLO) began its science campaign in 2006 (Murphy et al. 2008) with the goal of providing millimeter-accuracy range data to improve constraints on gravitational physics.

When APOLLO started ranging, it became clear that the measured return signal was lower than expected by about a factor of 10 from careful link budget calculations (Murphy et al. 2007). Surprisingly, the signal fell by an additional order of magnitude when the lunar phase was within $\sim 20^\circ$ of full moon (Murphy et al. 2010). Murphy et al. (2010) discussed various scenarios that could lead to the degradation of performance over four decades in the lunar environment, the favored scenario being deposition of dust on the retroreflector surfaces. In a subsequent work, Goodrow and Murphy showed that thermal gradients of a few degrees in a CCR would lead to dramatic suppression of the central intensity of the far-field diffraction pattern (FFDP) Goodrow and Murphy (2012). While this does imply that the return signal from the reflectors would be lowered as a result of a thermal gradient, the paper did not perform any thermal modelling of the CCR under solar illumination.

✉ ssabhlok@ucsd.edu (S. Sabhlok)

ORCID(s): 0000-0002-8780-8226 (S. Sabhlok); 0000-0003-1236-1228 (J.B.R. Battat); 0009-0008-6736-557X (N.R. Colmenares); 0009-0008-0789-2052 (D.P. Gonzales); 0000-0003-1591-6647 (T.W.M. Jr.)

Lunar dust particles must rely on impacts and on electrostatic charges to levitate and transport across the lunar surface due to a lack of atmosphere (Colwell et al. 2007). Evidence for dust levitation was first seen in the western horizon pictures taken by the Surveyor 5, 6 and 7 spacecraft (Criswell 1973, Rennilson and Criswell 1974) shortly after sunset. These images show a distinct glow just above the horizon, indicating forward scattering of the incident solar flux off a levitating dust cloud $< 1\text{m}$ from the ground. These images compliment the reporting of streamers originating from the lunar horizon as seen by the Apollo 17 astronauts from the spacecraft, indicating the presence of levitating dust at scale heights of 5–20 km (McCoy and Criswell 1974, Zook and McCoy 1991). Results from the Lunar Ejecta and Meteorites Experiment (LEAM) placed on the moon by the Apollo 17 astronauts indicated the presence of slow moving dust particles. These particles were not detected uniformly over the course of a lunar day, but peaked strongly around lunar sunrise, with detection rates increasing around 60 hours before sunrise and persisting 30–60 hours after sunrise (Berg et al. 1976). The origin of charge on lunar dust grains can be due to friction between meteorically-agitated dust grains, photoelectric charging from incident solar radiation or charging by the incident solar wind. The impact of solar radiation and wind on the lunar surface creates a plasma sheath over the sunlit and shadowed regions on the surface (Halekas et al. 2011). Experiments have verified that charged dust grains can levitate in such a plasma sheath, allowing for their transport across lunar surfaces (Arnas et al. 2001, Sickafoose et al. 2002).

In this work, we present a three-pronged approach to identify the cause of reflector underperformance and lowered signal during the full moon. Firstly, we perform a detailed link budget analysis in Section 2, supplemented by observations of stars of known magnitudes and by beam scans across the lunar reflectors to carefully analyze the profile of the transmitted laser beam. We then compare these calculations to observed return rates from the moon, and indeed find that the actual return rates are 15–20 times lower than expected. Secondly, in Section 3, we describe results of APOLLO observations during lunar eclipses—especially one in April 2014, under photometric conditions—showing that the return rate improves by more than an order of magnitude soon after a reflector enters the umbral shadow and cools. Section 4 presents results from our custom thermal simulation of a CCR in which we model the expected lunar ranging return rate as a function of solar illumination during a lunar eclipse. We discuss the implications of these results in Section 5, and summarize our results in Section 6.

2. Link Budget

The laser used for APOLLO generates upwards of 10^{17} photons per pulse. Under good conditions, only about one round-trip photon is detected per pulse. A multitude of factors—dominated by divergence—contribute to such a high attrition rate. This section evaluates the link budget, aiming to account for all signal losses along the beam’s round-trip journey from the laser to the detector by way of the moon. We will compare the results of the link equation, Eq. 1, to observations on two high-performance epochs, adjusting some of the parameters to suit changing conditions. The nominal link budget is:

$$N_{\text{detect}} = N_{\text{launch}} \eta_{\text{launch}} \eta_c^2 \eta_r \eta_{\text{NB}} Q \eta_{\text{FOV}} \eta_{\text{refl}} N_{\text{refl}} p_{\text{gauss}} \left(\frac{d}{r\phi} \right)^2 p_{\text{refl}} \left(\frac{D_{\text{eff}}}{r\Phi} \right)^2 \prod_i D_i. \quad (1)$$

Here, the number of photons we expect to detect is denoted as N_{detect} . Table 1 elucidates the meaning of the terms on the right, elaborated in the text.

APOLLO’s laser operates at a wavelength $\lambda = 532\text{ nm}$, and the energy per pulse of the laser is $\sim 0.1\text{ J}$, resulting in $N_{\text{launch}} \approx 2.7 \times 10^{17}$ generated photons per pulse. Transmission losses are accounted later, but we separately address the geometrical loss of the outgoing Gaussian beam due to the secondary mirror obstruction via $\eta_{\text{launch}} = 0.60 \pm 0.03$.

Various transmission and reflective efficiencies associated with specific segments of the photons’ overall path are captured by η factors in Eq. 1. The first efficiency, η_c , is the one-way optical efficiency that is common to both the transmit and receive paths of the APOLLO system—including atmospheric losses. For Apache Point, η_c evaluates to 0.53 ± 0.09 at 532 nm under clear skies and pointing at zenith (three reflections at 0.85 ± 0.05 and 0.87 atmospheric transmission). Because this path is traversed twice—once for the transmitted beam and once for the received signal— η_c appears squared in Eq. 1. The combined term $\eta_c \eta_r \eta_{\text{NB}} Q \approx 0.053$ relates to the total one-way throughput of the receiver/detector, which is experimentally determined as a group in Section 2.2. The η_{FOV} term, nominally computed for a 1.0 arcsec seeing disk, represents the fraction of the point spread function (PSF) captured by the 1.4 arcsec square field of view of the APOLLO receiver, with one corner pixel in the 4×4 array detector unused.

The corner cube reflectors (CCRs) number N_{refl} in the reflector assembly (100 for Apollo 11 and 14; 300 for Apollo 15), have a front-surface reflection loss represented by η_{refl} , and diameter, d .

Table 1

Parameters used in link equation (Eqn. 1). Values for η_r and Q are not determined separately, using the measured amalgam $\eta_c\eta_r\eta_{\text{NB}}Q$ instead. Blank uncertainties are either meaningless or too small to matter. Some parameters are adjusted for specific observations.

Parameter	Description	Value	Uncertainty
N_{launch}	Laser photons per pulse	2.7×10^{17}	0.14×10^{17}
η_{launch}	Central obscuration in uplink	0.60	0.03
η_c	Common-path optical throughput	0.53	0.09
η_r	Receiver efficiency	—	—
η_{NB}	Narrow-band filter transmission	0.99	0.003
Q	Photon detection efficiency	—	—
$\eta_c\eta_r\eta_{\text{NB}}Q$	One-way throughput amalgam	0.053	0.007
η_{FOV}	Limited detector field of view	0.787	adjusted
η_{refl}	Corner cube optical transmission	0.93	0.005
N_{refl}	Number of reflectors in array	100 or 300	—
p_{gauss}	Gaussian profile vs. top-hat	0.693	—
d	Diameter of single corner cube	0.0381 m	—
r	Earth-Moon distance	3.85×10^8 m	adjusted
ϕ	Uplink beam divergence	1.0 "	adjusted
p_{refl}	TIR CCR diffraction vs. top-hat	0.182	—
D_{eff}	Effective telescope aperture	3.26 m	—
Φ	Downlink beam divergence	2.89 "	—
D_i	Adjustments for epoch particulars	Table 2	—

The first squared term in parentheses represents the fraction of the uplink beam reaching a single CCR, according to a top-hat profile having a nominal diameter of $\phi = 1.0$ arcsec (see Section 2.1). For the divergence geometry, the one-way telescope-reflector distance is set to the average Earth–Moon distance of $r = 3.85 \times 10^8$ m. We later correct for the geometry at the epoch of observation via derating terms, D_i . The erroneous top-hat model is then corrected to describe a Gaussian profile more characteristic of atmospheric seeing, whose full-width at half-maximum (FWHM) matches the diameter of the top-hat profile. The correction factor, $p_{\text{gauss}} = \ln 2$, accounts for the reduced central intensity of a Gaussian profile having the same total flux and FWHM as the top-hat (FWHM is $\sqrt{\ln 256}$ times the Gaussian sigma).

The second squared term in parentheses captures geometric loss in the returning beam, whose divergence is also initially treated as a top-hat illumination profile of angular diameter $\Phi = \lambda/d$. This is intercepted by a telescope whose effective diameter is such that the collecting area is $\pi D_{\text{eff}}^2/4$. The top-hat model is then corrected to represent the central intensity of a far-field diffraction pattern arising from total internal reflection (TIR) by the parameter p_{refl} Murphy and Goodrow (2013).

Note that while not appearing explicitly in Table 1, a characteristic uncertainty of 0.05 arcsec is applied for ϕ , which propagates into an uncertainty value for η_{FOV} of 0.03. These uncertainties are applied with the rest in Section 2.4.

2.1. Beam Scan Test: Lunar Beam Profile

In order to assess the uplink divergence, ϕ , we contrive to scan the telescope-fixed laser across the reflector while keeping the detector centered on the reflector. This requires a coordinated move of the receiver's adjustable offset pointing angle to counter the motion of the telescope (and thus outgoing beam). We perform a scan in two dimensions, effectively in a plus-shaped pattern centered on the nominal pointing. As each pixel in the 4×4 detector only spans 0.35 arcsec, very small motions are noticeable.

As such, a scan of this sort is easily thwarted by pointing drift. Moreover, even when maintaining the pointing to the best of our ability, factor-of-two variations in signal on the timescale of tens of seconds are routine, largely due to seeing variations (APOLLO is highly sensitive to seeing, both due to target illumination and overfilling of the small detector). This makes interpreting a beam scan tricky: how much of the variation is due to the pointing offset, how much is variable seeing, and how much is due to variation in other terms in the link budget?

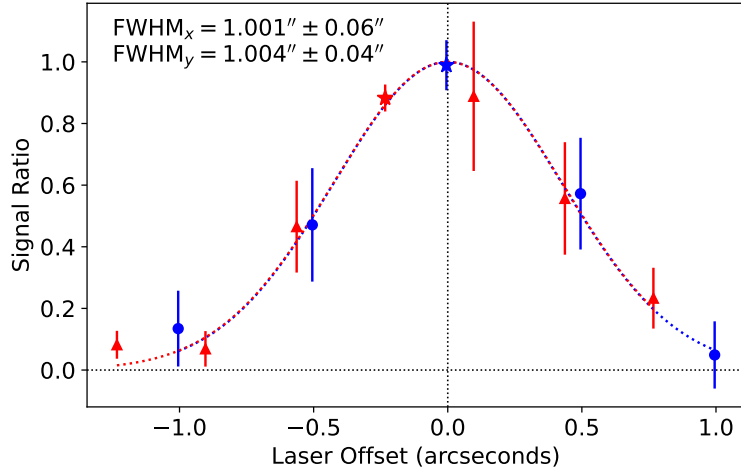


Figure 1: Beam scan results on 2018 February 25 for x (blue circles) and y (red triangles) directions, normalized to the peak. The nominal center positions are denoted by stars. In this case, the FWHM of the Gaussian fits are 1.001 ± 0.06 and 1.004 ± 0.04 arcseconds.

To mitigate this, we execute a pattern of moves that returns to the central position after every offset, thus interleaving central positions between each excursion. During the times pointing at the nominal (central) position, we sometimes adjust the pointing to re-center and maximize signal. Furthermore, we only consider the signal change in the several seconds surrounding the transition from one position to the next, rather than averaging the whole offset result. Each pointing therefore gives two signal ratios: at the beginning of the move, and again at the end.

Fig. 1 shows an example from one epoch, in orthogonal dimensions. Each data point averages the beginning and end ratios for the excursion. Since all measurements are in relation to the return rate at the central position, the result is normalized to the (changing) central value for each paired measurement.

We report here results from beam scans on two epochs. For 2018 February 25, we measure an uplink beam FWHM of 1.00 ± 0.05 arcsec, while on 2018 September 28 we get 1.07 ± 0.19 arcsec. Because the ϕ parameter in Eq. 1 is set to 1.0 arcsec, and squared in the link equation, we apply a derating factor of 0.88 to the latter case (the former needing no correction), as will be summarized in Section 2.3. The distribution of lunar return photons on the receiver array further corroborates—and closely matches—the beam scan results by providing an in-situ characterization of the seeing at the time of observation.

2.2. One-Way Throughput

A number of the terms in Eq. 1 can be simultaneously determined by pointing to a non-variable bright star of known magnitude and spectral type, measuring the photon counts, then comparing to theoretical expectations. We first assess the top-of-atmosphere flux density at 532 nm (in $\text{W m}^{-2} \text{nm}^{-1}$, e.g.) for the spectral type and magnitude, correct for the zenith angle, sum over the effective telescope aperture, multiply by the 2.1 nm bandwidth of the narrow-band filter, and by the effective integration time (typically 500 exposures at 100 ns each), and divide by photon energy to arrive at the number of photons we would detect in the case of no losses. By comparing actual counts, we effectively measure the product $\eta_c \eta_r \eta_{\text{NB}} Q \eta_{\text{FOV}}$.

In practice, we fit a two-dimensional symmetric Gaussian profile to each 50 μs exposure (typically delivering about 1,000 counts across 15 active elements) to determine the theoretical total flux: $2\pi A\sigma^2$, where A is Gaussian amplitude and σ is the standard deviation width parameter—if unconstrained by η_{FOV} . This produces a more stable flux estimate than the variable, jumpy seeing produces in raw terms—since the fraction of light captured in the detector is sensitive to offset and width of the PSF in a way that the total flux is not.

Several such tests on 2019 July 20 under the same detector configuration as for the beam scan epochs resulted in a determination for $\eta_c \eta_r \eta_{\text{NB}} Q$ of 0.053 ± 0.007 . We need only multiply by another factor of η_c to represent a cluster of terms in Eq. 1. The term η_{FOV} can be computed exactly for a centered Gaussian in a 4×4 grid whose pixels are 0.35 arcsec and missing one corner. For example, a Gaussian whose FWHM is 1.0 arcsec delivers 78.7% of its flux

Table 2

Link budget derating factors for the two beam profile experiments.

Cause	Epoch A Value 2018 Feb 25	Derating	Epoch B Value 2018 Sep 28	Derating
Range (r)	3.6008×10^8 m	1.31	3.7724×10^8 m	1.08
Zenith Angle	19.9°	0.98	47.8°	0.87
Angular Offset (libration)	5.7°	0.75	8.13°	0.66
Sun Angle (θ)	-67.3°	0.84	40.8°	0.74
Velocity Aberration	0.946 "	0.762	1.003 "	0.736
Uplink Beam (ϕ)	1.00 "	1.0	1.066 "	0.88
Detector Capture (η_{FOV})	0.90 "	1.05	0.91 "	0.950
Total Derating		0.648		0.282

to such an array, while 1.5 arcsec seeing would result in 50.6%. We use the 1.0 arcsec value in Eq. 1, then correct for conditions in Section 2.3.

2.3. Derating Factors

Some of the parameters in Eq. 1 are not constant, and require adjustment for the time of observation. Moreover, a few additional factors impact the link and need to be considered. These terms appear at the end of Eq. 1 as a product of derating factors. The various derating factors applied in this analysis appear in Table 2.

First, the Earth–Moon distance varies by as much as 13% (full range), and appears to the fourth power in Eq. 1. Based on the distance, r_{obs} , at the time of observation, we apply a “derating” factor (that indeed enhances the link result as often as not) of $(r/r_{\text{obs}})^4$.

The second factor accounts for the fact that we do not operate at zenith pointing, and is provided by the expression $0.87^{2(\sec z - 1)}$. Here, z is the zenith angle of the Moon. The base of 0.87 comes from the atmospheric loss by passing through one atmosphere at 532 nm. The factor of two in the exponent is to account for the beam passing through the atmosphere twice. Finally, we subtract one in the exponent because we already account for one atmosphere of thickness in η_c .

Three other derating factors come from the geometry of the Earth–Moon and Moon–Sun relationships. First, libration of the moon results in an angular offset of the CCR array relative to the Earth–Moon line, producing a reduction of the central irradiance of the far-field diffraction pattern via reduced area and increased diffractive spread. Next, thermal computations by the reflector manufacturer Faller et al. (1972) anticipated modest dependence of reflector behavior on sun angle (θ). Finally, velocity aberration shifts the return far-field diffraction pattern on the surface of the Earth by approximately one arcsecond, so that the telescope sits not at the peak of the pattern, but on the dimmer shoulder. The central lobe of the complex TIR diffraction pattern closely follows that of an Airy pattern from a circular aperture of the CCR’s diameter Murphy and Goodrow (2013). The derating amount is thereby computed using this profile based on the relative tangential velocity at the time of observation—dominated by Earth rotation.

Lastly, atmospheric seeing impacts both the outgoing beam divergence (ϕ), and the fraction of light captured by the detector, η_{FOV} . The latter is calculated according to a Gaussian fit to the lunar return distribution on the 4×4 detector, whose FWHM is given in Table 2, along with the corresponding adjustment relative to the nominal case presented in Table 1. It is reassuring that the FWHM values for the beam scans are not much larger than the FWHM values of the lunar signal on the detector—indicating good beam collimation so that the outgoing beam is essentially seeing-limited. Note that on 2018 September 28, an additional detector element near the center was inoperative, which is why the derating factors are different, despite similar FWHM measures for the two cases.

2.4. Link Assessment and Implied Dust Fraction

The previous sections laid the groundwork for comparing observed lunar return rates to theoretical expectations. Application of Eq. 1 using values in Table 1 and Section 2.2 produces for Apollo 15 a nominal expectation of 19.1 ± 4.8 photons per shot, before derating factors are applied. For the two epochs considered, the derating factors yield approximately 12.4 and 5.4 photons per shot.

On these two nights—the ones for which beam scans were performed, thus obtaining confident optimization of the signal—we assess the photon return rate at the many visits to the central beam position. Because the LLR signal rate is extremely sensitive to telescope pointing and atmospheric seeing (via ϕ and η_{FOV} parameters), we see much variation in central-position rates throughout the roughly ten-minute scan procedure. We therefore take special care in assessing a “reasonable” return rate, looking to identify a consistent “best” central rate that recurs multiple times throughout the scan and that is therefore compatible with the beam divergence assessed over the entire scan period. We believe these “best” rates are more representative of the theoretical link performance of APOLLO, for more meaningful comparison to the link calculation.

The estimated return rates for the two epochs are assessed to be 0.66 and 0.35 photons per shot in February and September of 2018, respectively. The observed rates are therefore well below the theoretical expectations of roughly 12 and 5 photons per shot. The ratios are similar, at 5.2% and 6.7% for the respective epochs. It should be noted that the derating factors produce expectations roughly a factor-of-two different for the two epochs, and that the observed rates are likewise different by approximately the same factor—indicating consistent results.

We therefore conclude that observed return rates are at least an order-of-magnitude lower than expectations, and are unable to account for the difference by careful analysis and experimental characterization. A proposed explanation that runs through this paper, and others before it [Murphy et al. \(2010, 2014\)](#), is that dust accumulation on the front surfaces of the CCRs simultaneously accounts for the link deficit, the additional full-moon deficit, and eclipse response.

Treating the dust as a set of geometrical obstructions, we recognize that the double-pass nature of the CCR makes each dust grain count *twice*, blocking both entering and exiting light paths. If the geometrical covering fraction is f , the probability of passage through the surface is $1 - f$. Independent probabilities for blockage in the two directions means that the probability of round-trip passage is $(1 - f)^2$. This amount of blockage will impact the central intensity of the far-field diffraction pattern (FFDP). Normally, the unobstructed CCR, with front surface area, A , will have a FFDP central intensity proportional to A^2 (effectively, a coherent sum of the electric field over the open aperture, squared for intensity). Since the obstructed CCR has an effective area of $(1 - f)^2 A$, the FFDP central intensity will be reduced by $(1 - f)^4$. This strong dependence on f means that, for instance, a 50% covering fraction results in a sixteen-fold reduction in the FFDP central intensity—which is indeed approximately the factor of signal deficit we deduce. Applied to the signal deficit ratios from the two epochs above, we compute dust fractions of 0.52 and 0.49 for February and September 2018, respectively. The two epochs are therefore telling a very similar story in the context of dust coverage.

We note that infrared observations may be less impacted by dust, as the particles may be less “geometrical” at longer wavelengths. This may be related to the success of recent infrared LLR operations, where reflector performance appears to be better ([Courde et al. 2017](#)). It is also the case the thermal lensing effect explored more below is less impactful at longer wavelengths.

3. Eclipse Observations

To study the effect of solar illumination on ranging throughput, we took advantage of the naturally occurring variation in the solar illumination incident on CCRs during lunar eclipses. During a lunar eclipse, the solar illumination changes from 100% to 0% (shadow) and back to 100% over the course of about five hours as the CCRs enter and then exit the Earth’s umbral shadow. A measurement of the evolution of the lunar return rate during the eclipse provides an independent constraint on the CCR dust coverage fraction, which can be compared to the fractions derived using link budget calculations (Section 2.4) and thermal eclipse simulations (later in Section 4).

We undertook four lunar eclipse ranging campaigns (December 21, 2010; April 15, 2014; September 28, 2015; January 21, 2019). Here, we focus on the 2014 eclipse (MJD 56762 from 5:52 to 10:52 UTC) because photometric sky conditions that night enabled the most reliable study of the throughput of the APOLLO system and lunar retroreflectors. Range measurements were divided into short runs of ~ 150 second duration (3000 laser shots) in order to monitor the evolving lunar return rate as a function of solar illumination of the lunar retroreflectors.

We compare eclipse-night observations to lunar return rates measured during non-eclipse nights, but with the lunar phase within 10 degrees of full moon. In those cases, the median (mean) return rate is 0.02 (0.03) photons per shot, and the maximum is 0.2 photons per shot (see the bottom plot of Fig. 2). During the 2014 eclipse, before the Apollo 11 and 14 reflectors entered the earth’s umbral shadow the median (mean) return rate was also low, at 0.06 (0.08) photons per shot (red histogram in the upper plot of Fig. 2). After the reflectors entered the umbral shadow and began to cool (blue shaded histogram in the upper plot of Fig. 2), the return rate rose as high as 0.77 photons per shot, with a median (mean) value of 0.35 (0.41) photons per shot, which is 17 times higher than the median rate during non-eclipse nights

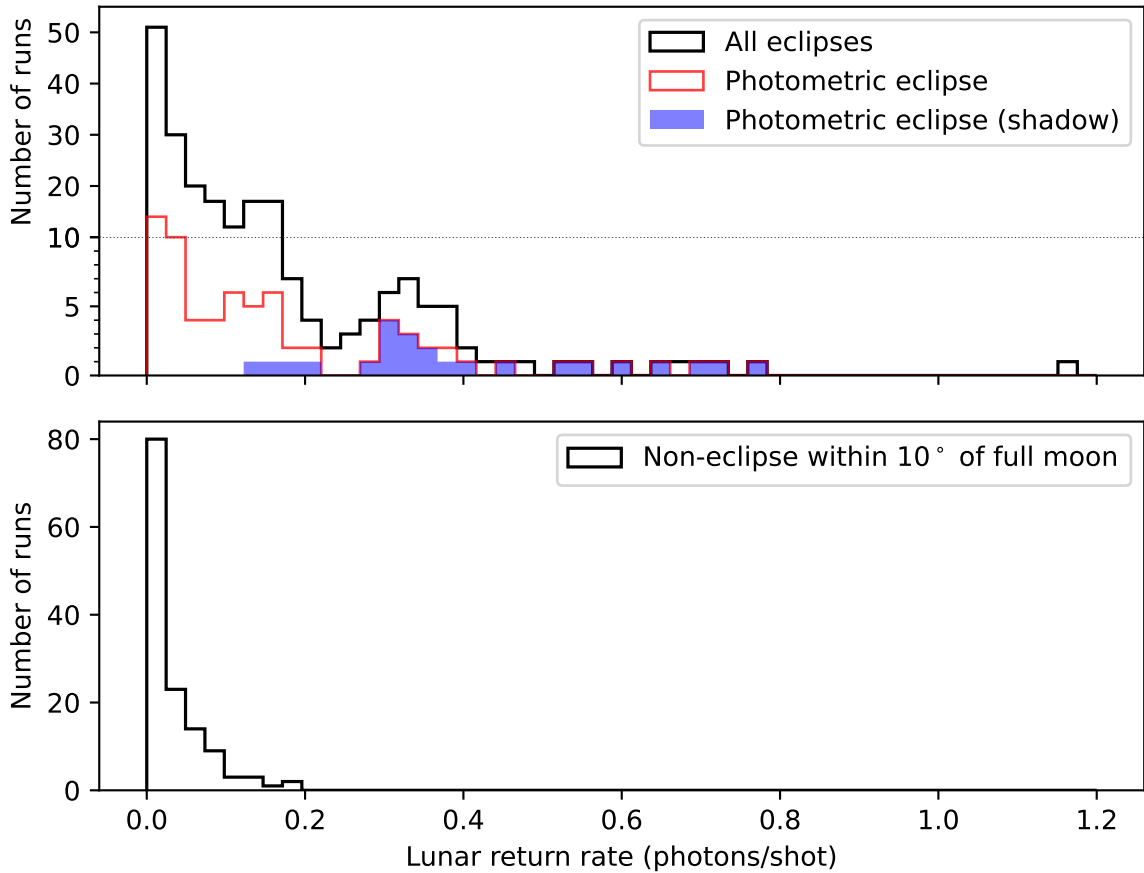


Figure 2: (Top) Histogram of the lunar return rate (photons per shot) during four eclipses (black line), as well as for the photometric eclipse on April 15, 2014 alone (red). Also shown (blue fill) is data from the photometric eclipse when the target reflectors are in full shadow. Note the change of scale on the ordinate indicated by the horizontal dotted line. (Bottom) Lunar return rate histogram when the moon is not in eclipse, but the lunar phase angle is close to full (within 10 degrees). All non-eclipse lunar return rates are less than 0.2 photons per shot. Both histograms aggregate data from all three Apollo reflector arrays (Apollo 11, 14 and 15). The Apollo 11 and 14 rates have been scaled up by a factor of three because those arrays contain three times fewer corner cube reflectors than the Apollo 15 array.

near full moon. The lunar return rate histogram for data from all four eclipses is shown in black in the top plot of Fig. 2, and it tells a consistent story: under overhead solar illumination, the optical throughput of the lunar reflectors degrades by at least an order of magnitude, but when the illumination is suppressed (via a lunar eclipse) and the reflectors cool, the rate increases. As described more fully in Section 4.2, we attribute the rate increase to the cooling of the reflectors when they are in shadow, which in turn reduces the thermal gradients in the CCR and improves the FFDP (and therefore the optical throughput) of the corner cubes.

4. Thermal Modelling of the Corner Cube Retroreflectors

We model the optical response of a CCR under thermal load to estimate the dust coverage fraction for comparison with the degradation estimate from our link budget calculation in Section 2, the eclipse observations in Section 3, and the known degradation of performance during full moon (Murphy et al. 2010). Our simulations were done using a custom code in C developed by our group for this purpose. The simulation has three stages. First, we set up the geometry of the problem, defining the different surfaces, their thermal properties and initial conditions. In the second stage, the code calculates the analytic view factors from all boundary point surface elements to all others and stores them into a

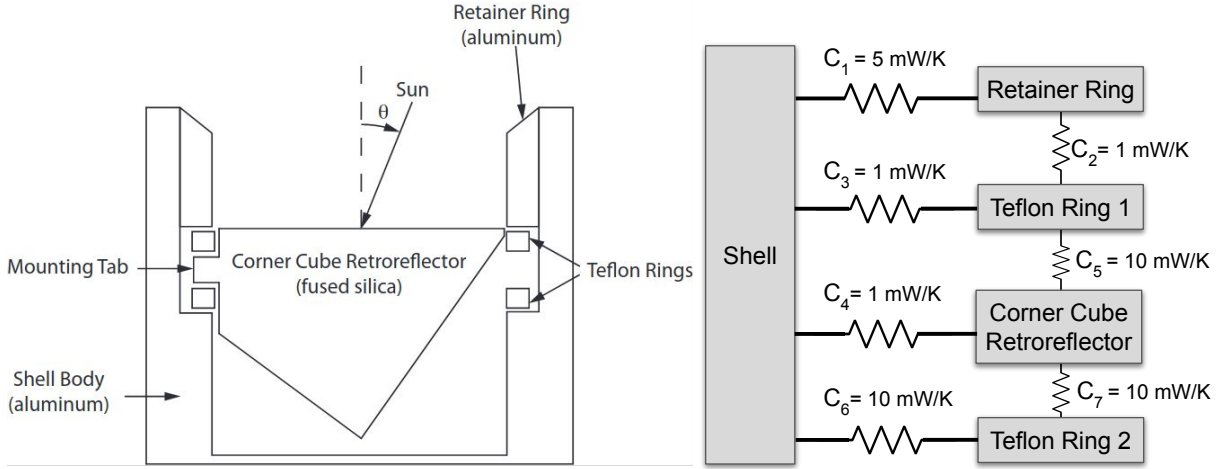


Figure 3: (Left) Schematic diagram defining the geometry of the CCR mounted in the aluminum casing ("shell") via Teflon mounting rings and the retainer ring. (Right) Elements and conductive paths used in our thermal simulation, with specified thermal conductances. The CCR, retainer ring, and the shell radiate heat to space. Solar energy is incident on the top surfaces of the CCR, retainer ring, and shell. The corner cube looks asymmetric from this angle because the tabs are placed at 120 degree intervals around its perimeter, so diametrically opposite sides do not both have tabs.

view factor matrix to be referenced later for radiative heat transfer. Lastly, the code performs conductive and radiative heat transfer, based on the initial conditions for a specified amount of time. The details of the code implementation, including the geometry setup, view factor matrix construction and heat transfer, are described in Appendix A.

A schematic diagram and corresponding thermal model of the mounted CCR is shown in Fig. 3. The fused silica CCR is mounted to an aluminum shell (aluminum 6061-T6), held in place by two teflon rings and an aluminum retainer ring (anodised aluminum 1100). For the CCR, retainer ring and the shell, we have to specify the net absorptivity and emissivity as a result of an impeding dust fraction sitting on the surfaces. To define the net emissivity and absorptivity, we consider a fraction f of the surface to be obscured by lunar dust, with an inherent emissivity ϵ_{dust} and absorptivity α_{dust} . For the shell and the retainer ring, the net emissivity is simply an area-weighted mean of the two emissivities. Effective emissivity and absorptivity for the top of the shell and retainer ring is given by

$$\epsilon_{eff} = (1 - f) \epsilon + f \epsilon_{dust} \quad (2)$$

$$\alpha_{eff} = (1 - f) \alpha + f \alpha_{dust}. \quad (3)$$

The case for the top of the CCR is slightly more complicated by the fact that light can be absorbed by the dust on the way back out of the CCR as well. So the effective absorptivity comes out to be

$$\alpha_{eff,CCR} = [1 - (1 - f)^2] \alpha_{dust}. \quad (4)$$

Our simulation investigates both equilibrium and dynamic modes. First, a constant heat input, modelling the solar flux incident on the moon (1360 W m^{-2}), is used to simulate an equilibrated CCR temperature profile under full-moon illumination conditions. As our interest in this work primarily concerns observations near full moon, we do not consider the possibility of sunlight illuminating the interior of the shell behind the CCR because all incident sunlight is rejected by total internal reflection when the solar illumination is within 17 degrees of normal incidence. The equilibrated temperature profile is then used as a starting point for an eclipse simulation, where the solar flux is varied according to an eclipse illumination profile. The simulation computes the temperature of all elements at each time step, from which the temperature profile of the CCR is extracted.

Given the CCR temperature profile, the path length variations imposed by thermal modification of refractive index within the CCR are calculated, leading to a warped wavefront emerging from the CCR to produce a FFDP—the so-called thermal lensing effect Goodrow and Murphy (2012). The effect is largely driven by the temperature gradient

Table 3
Properties of materials used in the thermal simulation.

Element	Material	Thermal Conductivity $\text{W m}^{-1} \text{K}^{-1}$	Density kg m^{-3}	Heat Capacity $\text{J kg}^{-1} \text{K}^{-1}$	Emissivity	Absorptivity
CCR	Fused Silica	1.38	2200	740	0.87	0.0
Rings 1 & 2	Teflon	0.25	2200	1500	0.8	0.8
Shell	Aluminum 6061-T6	167.0	2700	896	0.025	0.06
Retainer Ring	Anodized Aluminum 1100	222.0	2710	904	0.78	0.32
	Lunar Dust	—	—	—	0.9	0.9

from the surface to the corner of the CCR. The resultant FFDP can then be compared to the case of an isothermal CCR, to quantify the loss in return rate as a percentage. We calculate this loss for the full moon illumination, which can be compared to our measured return rate during full moon observations (Murphy et al. 2010). We also compare the modeled return rate improvement during the eclipse to that observed during the 2014 eclipse. The thermal properties for the different materials used in the simulation are outlined in Table 3.

4.1. Steady-state Simulation Results

To compute the steady-state thermal profile of the CCR in the presence of direct overhead solar illumination (as would be the case during a full moon), we begin the simulation with all elements set to a temperature of 300 K, and assume a solar constant value of 1360 W m^{-2} . We then run the simulation until the average temperature of all four simulated elements (CCR, Teflon rings, retainer rings and shell) stabilize.

The spatial temperature profile of the CCR is extracted and used to generate a FFDP for the CCR. Different values of f result in differing central maximum intensities compared to the isothermal CCR. We find that varying f from 0.5 to 0.65 changes the central maximum intensities of the CCR from $\sim 6\%$ to about $\sim 0.1\%$ of the isothermal case. The peak-to-peak phase difference in the wavefront at a dust fraction of 0.5 is ~ 4.9 radians due to thermal effects. This phase difference across the wavefront results in a diminished central lobe of the FFDP. The former result, at $f = 0.5$, matches the full-moon deficit factor of 10–15 reported in Murphy et al. (2010), and the results from Section 3 and Fig. 7 of this paper.

It is worth briefly discussing the qualitative thermal behavior of the CCR when we simulate equilibrating the geometry for a constant solar flux. As the run is started, a thermal gradient is set up quite rapidly within the CCR, within the first 100 seconds of temporal evolution. The surface of the CCR absorbs heat from incident solar radiation. This creates the thermal gradient in the CCR, with the front face being hotter than the vertex. This thermal gradient is responsible for the reduced intensity in the central maximum of the FFDP. It takes far longer, a few hours, for the system to reach a steady-state temperature. The main cooling channel for the system at this point is the radiative cooling from the CCR front surface, radiating heat to space. We confirmed that the final steady-state temperatures are independent of initial conditions. Since the thermal gradients within the CCR rapidly adjust to the incident solar flux, we expect that during the eclipse simulation, the return rate should quickly improve once the reflector enters the shadow, since the gradients, rather than the absolute temperature, affect the FFDP and therefore the return rate. This is indeed the case as shown in the next subsection.

4.2. Simulation Result Showing Eclipse Profile

We apply our simulation to the case of a lunar eclipse in which the solar illumination incident on the CCRs is modulated by the Earth's shadow. The relative angular sizes of the Earth and Sun as seen from the moon are used to simulate an eclipse profile for different impact parameters for the Earth's center passing in front of the Sun. This is compared to the illumination profile seen at the three different Apollo reflectors Chapront-Touzé and Chapront (1991). The computed illumination profile does not include limb darkening. The impact parameter that best describes the profile for all three reflectors is used as the incident solar flux profile, as shown in Fig. 4. While all reflectors remain under the shadow for different amounts of time, the total time difference between the shortest and longest eclipse times for different reflectors is approximately 6–7 minutes. When comparing to APOLLO observations, this is shorter than the circuit among reflectors, so the impact of different reflectors being under the shadow for different amount of times is minimized. The resultant temperatures for the CCR, teflon rings, the retainer ring and the shell are shown in Fig. 5. Since the FFDP evolution is largely driven by the corner cube gradients, we present the radial and vertical gradients

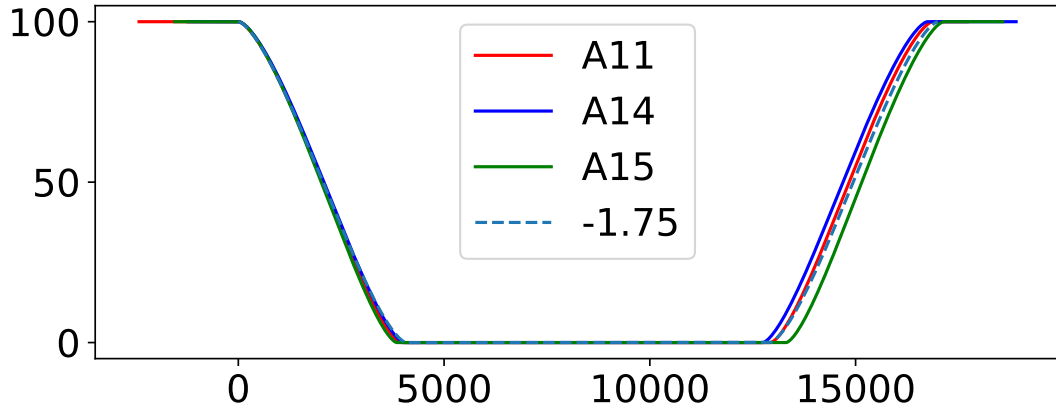


Figure 4: Percentage of maximum solar illumination as a function of time (in seconds) for the three Apollo reflectors Apollo 11 (red), 14 (blue) and 15 (green) for the eclipse on April 15th, 2014, shifted to have the same starting time. The blue dashed curve shows the eclipse profile corresponding to an impact parameter of 1.75 solar angular radii as seen from the moon, which we used in our thermal eclipse simulation since it best approximates the behavior of all three reflectors. Note that these models do not include limb darkening.

within the CCR in Fig. 6. For the radial gradient, due to the trifold symmetry of the corner cube, we consider a radial gradient between the center and a point on the circumference which is a midpoint of one of the “tabs.” We also consider a point on the circumference equidistant from the two nearest tabs for a radial gradient.

The qualitative behavior of the system during the eclipse can be described as follows. Starting from an equilibrated geometry, as the incident solar flux gradually decreases, the amount of heat absorbed by the CCR decreases as well. According to Figure 6, very little radial gradient is initially present, and thus little conduction through the tabs (the chell and CCR being at a similar temperature). Consequently, the CCR loses thermal energy primarily through radiation from the front surface. Before long, the CCR becomes cooler than the shell, so heat conducts into the CCR through the mounting tabs, setting up radial gradients while maintaining a weak vertical gradient as shown in Figures 5 and 6. When the solar flux dwells at zero, the CCR continues to cool, but the gradient is relatively stable, thus resulting in the plateau region in the expected return rate shown in Figure 7. When the reflectors come out of the shadow, solar flux increases so that the CCR starts to absorb more heat and the strong vertical gradient develops again, depressing the expected return rate. Throughout this process, the CCR front surface remains hotter than the vertex, i.e. the gradient maintains the same orientation.

The time dependence of the ratio between the intensity of the central maximum in the FFDP of the CCR during an eclipse with respect to an isothermal corner cube is plotted in Fig. 7, along with the measured return rates from individual Apollo reflectors during the 2014 eclipse. The simulated return rate increases rapidly after the CCR enters the Earth’s shadow, and is correlated with a rapid reduction in the temperature gradient from the back to the front of the CCR as it cools as shown in Fig. 6. As the CCR stays in the shadow, it retains the low vertical gradient compared to steady state illumination during full moon. When the reflectors come out of the shadow, the gradient increases to pre-eclipse levels rapidly, destroying the central maximum in the FFDP resulting in low return rates from the CCR. The simulated ratio between the maximum intensity in the FFDP during the eclipse to the start of eclipse is ~ 7 , as the intensity goes from $\sim 6\%$ to $\sim 42\%$. This is comparable to the observed ratio of median return rate (0.35) during an eclipse with respect to the original rate (0.06), i.e. a factor of 6, as shown in Fig. 7 and reported in Section 4.2. Return rate observations in Fig. 7 show a low return rate prior to eclipse, followed by a rapid rise in the return rate (a factor of ~ 7 in 10000 seconds) after the CCRs enter the umbral shadow.

Our simulation includes only one CCR, and therefore will not capture all elements present in the actual reflector array on the lunar surface. However, our objective is to show that (1) dust reduces the intensity of the central maximum in the FFDP of the CCR and (2) as the incident solar flux on the CCR decreases during the lunar eclipse, the temperature gradient between front face and the vertex rapidly decreases, improving the return rates. Discrepancies between our simulation and the eclipse-night observations are discussed in Section 5.

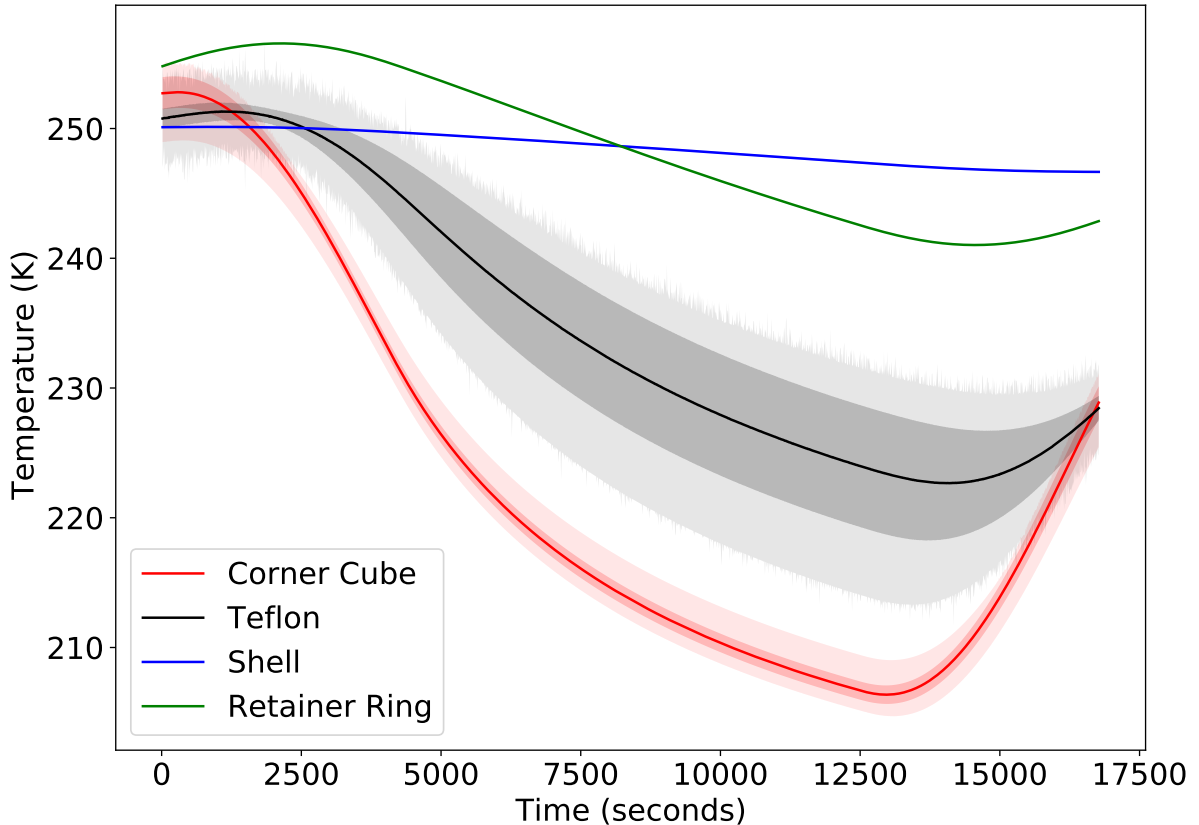


Figure 5: Average temperatures for the CCR, Teflon rings, retainer ring and shell over the course of the simulated eclipse. Dark shading indicates 1σ deviations from the mean, whereas the lighter shading indicates the min-max. The deviations for the shell and the retainer ring are too small to be seen here due to their high thermal conductivity. The range of computed temperatures for the Teflon rings during the simulated eclipse is larger than for the other three elements. This is due to the fact that the temperatures extracted from the simulation average the two Teflon rings that are above and below the CCR. The rings also have slightly different conduction pathways to carry heat from the CCR to the shell or the retainer rings. Some of these pathways have an additional temperature dependence due to the discontinuity in thermal conductance at the Teflon-Retainer Ring and Teflon-shell interface. All of these effects combine to result in a larger range of temperatures for the Teflon rings.

5. Discussion

While the qualitative results from our eclipse simulation are in agreement with the measured return rate during the photometric eclipse night, there are a few details worth expanding on.

5.1. Simulating a Single CCR

We consider the effect of using a single CCR versus an entire array set in a pallet. We model a single dust-obscured CCR to simulate its FFDP, and compare the intensity in the central diffraction maximum to that of an isothermal CCR as an estimate of the expected relative lunar return rate. The thermal and mechanical properties implemented in this simulation have been either taken directly or derived from the description in the original Arthur D. Little Report on the CCR design and performance Arthur D. Little, Inc. (1969). However, our single cylindrical shell and CCR is not likely to track the thermal mass and environmental couplings of the real array, which could result in incorrect temporal behavior. We did not model the changing radiative temperature of the lunar surface, the geometry of coupling, or the blankets in which the arrays are wrapped. We have attempted to approximate some of these factors, but surely these are not perfect.

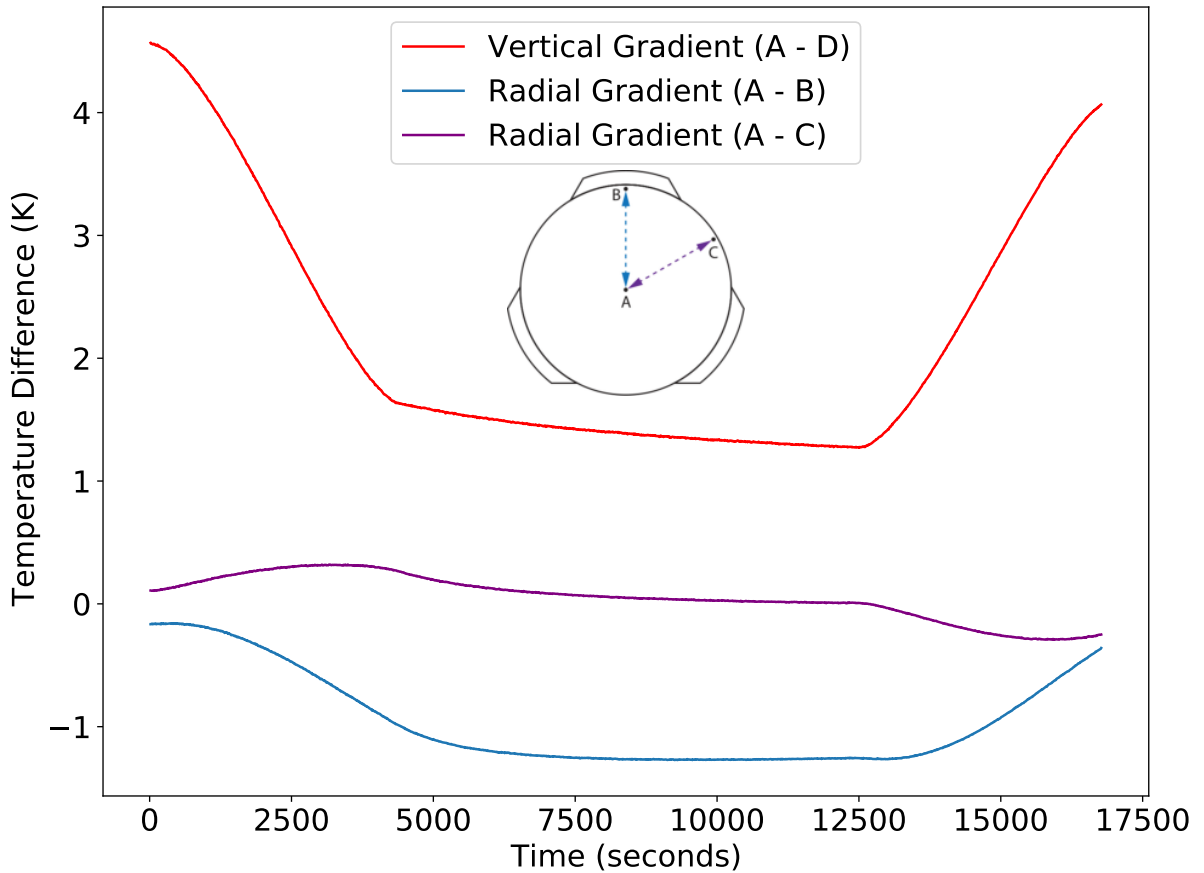


Figure 6: Temperature differences between three pairs of locations on the corner cube as a function of time during an eclipse. Corresponding solar illumination profile is provided in Fig. 4. As the CCR enters the umbral shadow it cools and the vertical temperature gradient drops from ~ 5 K to ~ 2 K, which reduces the thermal lensing and improves the optical throughput. The inset shows the front face of the CCR illustrating locations used for the temperature difference calculations, the center (A), tab midpoint (B) and a point between two tabs along the circumference (C). The dashed lines connecting the points correspond to the gradients shown on the plot. The vertical gradient is calculated by subtracting the temperature of the vertex (D, not shown in inset) from the center of the top surface (A - D). The radial gradient for the top surface is calculated for two points along the top surface circumference, the midpoint of the CCR tabs (A - B), and the midpoint between two tabs (A - C).

5.2. The Effect of Mount Conductances

Our goal was to model the thermal properties of the CCR using the specifications indicated in the ADL design report Arthur D. Little, Inc. (1969). A complication, however, was that the report doesn't describe the individual contact conductances but rather the total conductances through various thermal pathways. The original report uses the term "Mount Conductance" to describe the total heat conductance from outside the shell into the surface and vertex of the corner cube. To convert mount conductance given in the ADL report into contact resistances used in the simulation, we use the fact that the conductance values in ADL report are based on tests using steady state heat flux from the corner cube, through the teflon rings, through the retainer ring into the aluminum array which we have called the "shell" in our simulation. In the simulation, the conductance values for various interfaces between different materials can be tuned, however, the caveat is that the teflon-retainer ring interface is a special case. Since the retainer ring was tightened and then de-rotated by 36° at the time of assembly to prevent any thermal contact, it is likely to approximate a no-contact conductance. If this conductance value has changed since launch, it could only be due to physical contact between the two surfaces, which is likely to change conductance at this interface significantly. Thus, while our simulation can

Dusty lunar retroreflectors

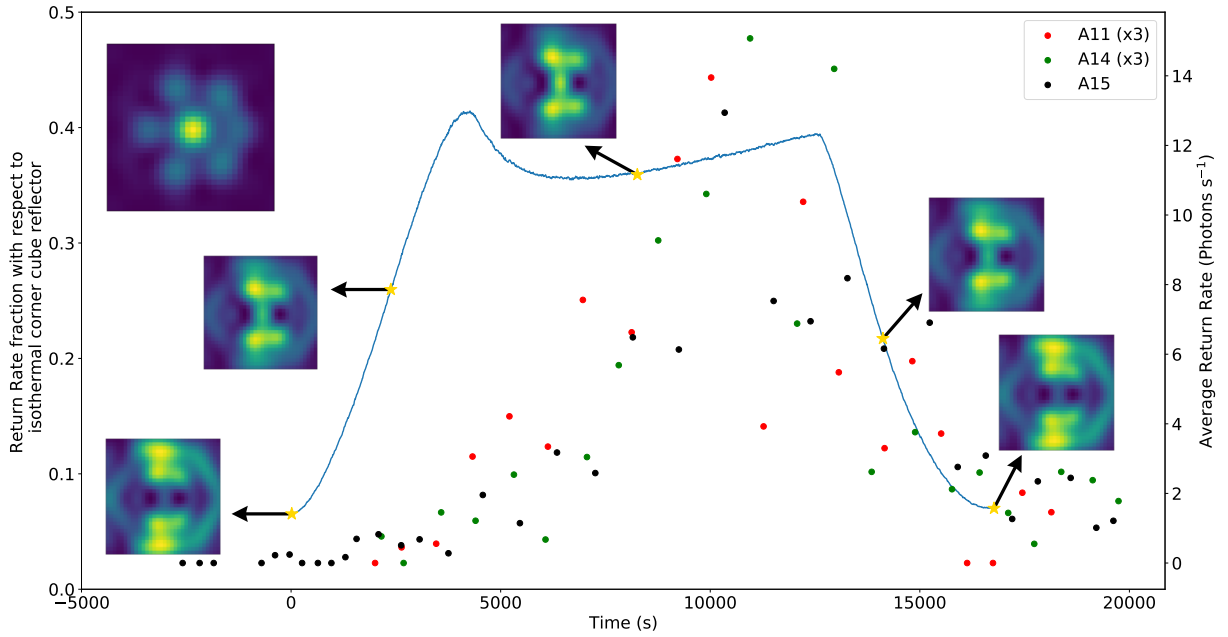


Figure 7: Fraction of light in the central diffraction maximum as compared to an isothermal CCR as a function of time during an eclipse. The measured return rates from the Apollo reflectors are also plotted (right-hand ordinate). Time is relative to when each reflector first enters the Earth shadow, which aligns all reflector time-series with the start of the eclipse simulation. Simulated CCR FFDPs are shown at five representative times during the eclipse. Inset at top left shows the FFDP for an isothermal CCR.

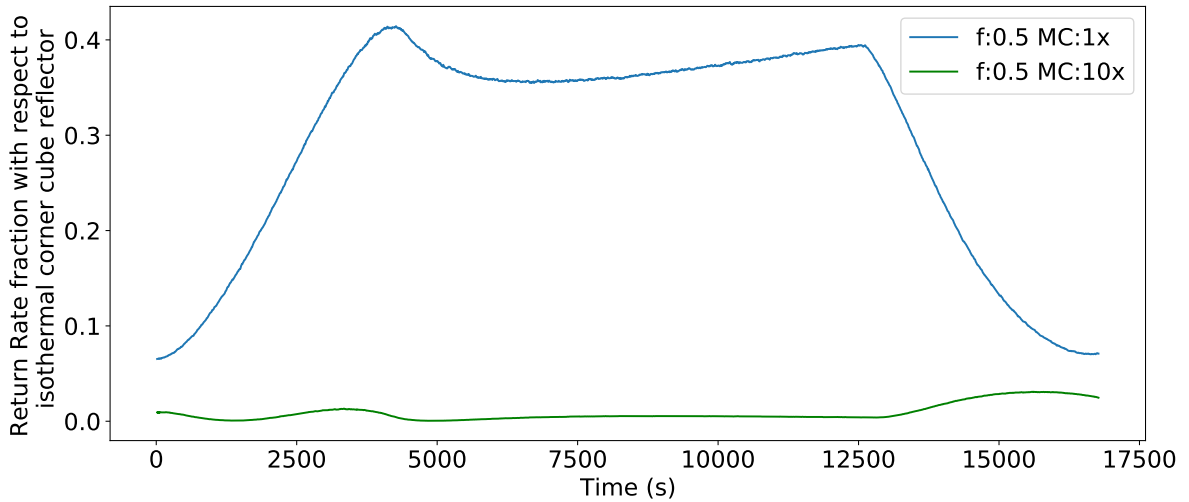


Figure 8: Simulated return rate fractions for the same dust fractions ($f=0.5$), but with the original and rescaled ($\times 10$) mount conductances (MC). The increased mount conductance almost completely depresses the intensity of the central maximum in the FFDP throughout the eclipse, and is therefore disfavored as inconsistent with observations.

change conductance values smoothly, for the real retroreflectors, such a change will be discrete and significant. The computed conductance values for this interface were checked by calculating two extreme cases. First, we calculate the conductance for the case where there was perfect contact between teflon and the retainer ring and then we calculate the case where there is no contact between the retainer ring and the teflon ring and any thermal contact is purely radiative.

Our computed conductance value lies between these two extremes, consistent with the value derived from steady state heat flux assumption based on the ADL report. We calculate that the conductance for perfect contact is approximately a factor of 10 larger than what we calculate for the APOLLO CCRs. Thus, we are satisfied that the conductance values used between the various interfaces are reasonable.

However, to study the possibility that the conductance between the teflon-retainer ring surface has increased drastically, we consider the special case of an eclipse where the mount conductance has increased by a factor of 10 as shown in Fig. 8. The mount conductance values only impact our simulation if they have increased since fabrication, since a decrease would result in smaller gradients in the CCR, in agreement with our simulation and the original predictions and measurements in the ADL report. In order to run a full eclipse simulation, the modified geometry with increased mount conductances is equilibrated. The initial temperature of the shell in this case was found to be higher than the eclipse run presented in Fig. 5, by ~ 20 K. The expected intensity inside the central diffraction maximum is decreased approximately by a factor of 40 during the eclipse compared to the best match simulation with dust fraction of 0.5. Thus, adjusting the mount conductances completely destroys the FFDP.

Thus, given our link budget estimates and steady-state calculation of the dust coverage factor, we find that the mount conductance in our initial estimates based on the ADL report is consistent with the results from both the steady-state dust fraction calculation and the link budget analysis, and unlikely to have changed significantly from launch to present day.

5.3. Comparisons with Infrared LLR Observations

We can use the derived CCR temperatures for the steady state and eclipse simulations, and investigate what happens when an infrared wavelength is used ($\lambda = 1064$ nm). For this calculation, the thermal coefficient of refractive index for fused silica is adjusted for the wavelength 1064 nm (Toyoda and Yabe 1983). In comparison to the steady state performance for the green laser, we find that at 1064 nm, the central intensity in the FFDP is $\sim 60\%$ compared to the case for an isothermal CCR, with a peak-to-peak phase variation of ~ 2.3 radians. This marks a factor of 10 improvement in FFDP in full-moon illumination conditions for an infrared laser compared to the green laser. This agrees with improved results seen by using the infrared laser for LLR at the Grasse laser station when ranging when the lunar phase is within $\pm 18^\circ$ of the full moon. (Courde et al. 2017). Note that this only includes the improved central intensity in the FFDP of the CCR, whereas observations will also depend on other factors such as detector quantum efficiency, atmospheric throughput and laser power, similar to the link budget calculation in Section 2.

5.4. The Effect of Changing Dust Fraction Coverage on the CCRs

Changing the dust fraction changes the equilibrium temperatures of the CCR, as well as the resulting gradients under solar illumination. The expected FFDP for the equilibrium temperature shows that the total intensity inside the central maximum increases as dust fraction is decreased. A smaller dust fraction creates a smaller vertical thermal gradient in the CCR, which improves the return rate of the signal and vice versa. This return rate should become 100% as the total dust fraction goes to zero. Given a dust fraction, the qualitative behavior of the eclipse is very similar to the one presented in Figs. 5 and 8. We find that a dust fraction of 0.5 best matches the eclipse observations.

We also note that the three reflectors Apollo 11, 14 and 15 show remarkably similar improvements during the lunar eclipse. These reflectors are placed at significant distance from each other and were placed over the course of a few years. The similarity indicates that if the dust obscuration is taken as the reason for the degrading performance, then this dust deposition must be uniformly taking place across the surface of the moon. In this case, the dust transport results from the Apollo 17 LEAM experiment (Berg et al. 1976) combined with the experimental observations of dust levitation under a plasma sheath suggests a deposition mechanism (Arnas et al. 2001, Sickafoose et al. 2002, Halekas et al. 2011). The obscuration is likely caused by large particles, as indicated by the LEAM experiment, deposited due to solar wind and radiation during lunar sunrises and sunsets creating a plasma sheath, which transports these dust grains at low altitudes (< 2 m). Thus, our results are consistent with the lunar model of dust transport, where the transport is caused by electrostatic charges on dust particles enabling transport at low altitudes (< 1 m) due to the potential difference created at the time of sunrise.

6. Conclusions

Measurements with the APOLLO ranging system indicate a deficit in the return rate of Apollo lunar retroreflectors by a factor of 16 to 19, with an additional order-of-magnitude loss when the reflectors are under full moon illumination.

We attribute the degraded reflector performance to the accumulation of lunar dust on the reflector surface, which partially blocks lunar ranging laser light and distorts the CCR FFDP by thermal lensing due to absorbed solar radiation near full moon. This conclusion is supported by three independent studies:

1. A detailed link analysis was undertaken, including a measurement of the APOLLO transmit laser beam profile, and the one-way throughput of the telescope optics and the receiver. This study found that the measured lunar return rate was only 6% of the predicted value, corresponding to a dust fraction of ~50%, which in turn results in thermal consequences under solar illumination.
2. Measurements during lunar eclipses reveal that the lunar return rate is highly dependent on solar illumination. For example, during one lunar eclipse on a photometric night, we found that the return rate improved rapidly once the reflectors entered the Earth's shadow, and subsequently degraded when the reflectors exit the shadow. When the reflectors are in shadow during a lunar eclipse, the median return rate is an order of magnitude higher than full-moon non-eclipse observations.
3. We developed a heat transfer model to include conductive and radiative effects and used the simulated temperature profile of the CCR to generate the associated FFDP. We explored two scenarios:
 - (a) Steady-state study: We ran our simulation until we achieved the equilibrium state of the CCRs during full moon solar illumination. In the equilibrium state, the thermal gradient across the CCR degraded the intensity of the FFDP's central lobe by a factor of ~16 compared to an isothermal CCR when a 50% dust fraction was used, in agreement with previous assessments of the full moon deficit Murphy et al. (2010).
 - (b) Time-dependent eclipse study: We then ran the equilibrated CCR setup through an eclipse simulation, roughly matching our observed eclipse conditions. Using the same dust coverage fraction of 50%, the eclipse response improves over the full-moon return rate by a factor of 7, which compares well to the temporal profile observed during the 2014 lunar eclipse.

Taken together, the studies above tell a consistent story: the Apollo 11, 14 and 15 reflector surfaces are partially obscured by dust (~50%), which both reduces their optical throughput by the direct absorption of laser ranging photons, and through thermally induced distortions of the CCR FFDP due to the absorption of solar energy near the full moon phase.

Acknowledgements

We thank Russet J. McMillan for her continued support as APOLLO's operator during observation, and handling of ACS functions during ranging. NRC's research was supported by an appointment to the NASA Postdoctoral Program at the Goddard Space Flight Center, administered by Oak Ridge Associated Universities under contract with NASA. This work is based on access to and observations with the Apache Point Observatory 3.5-meter telescope, which is owned and operated by the Astrophysical Research Consortium. This work was jointly funded by the National Science Foundation (PHY-0602507, PHY-1068879, PHY-1404491, PHY-1708215) and the National Aeronautics and Space Administration (NNG04GD48G, NAG81756, NNX12AE96G, NNX15AC51G, 80NSSC18K0482). JBRB acknowledges the support of the NASA Massachusetts Space Grant (NNX16AH49H).

References

- Arnas, C., Mikikian, M., Doveil, F., 2001. Micro-Sphere Levitation in a Sheath of a Low Pressure Continuous Discharge. *Physica Scripta* Volume T 89, 163–167. doi:10.1238/Physica.Topical.089a00163.
- Arthur D. Little, Inc., 1969. Laser ranging retro-reflector array for the early Apollo scientific experiments package. <http://www.physics.ucsd.edu/tmurphy/apollo/doc/ADL.pdf>. Accessed: 2023-12-20.
- Berg, O.E., Wolf, H., Rhee, J., 1976. Lunar Soil Movement Registered by the Apollo 17 Cosmic Dust Experiment, in: Elsaesser, H., Fechtig, H. (Eds.), *Interplanetary Dust and Zodiacal Light*. volume 48, p. 233. doi:10.1007/3-540-07615-8_486.
- Chapront-Touzé, M., Chapront, J., 1991. Lunar tables and programs from 4000 B.C. to A.D. 8000. Richmond, Va. : Willmann-Bell.
- Colwell, J.E., Batiste, S., Horányi, M., Robertson, S., Sture, S., 2007. Lunar surface: Dust dynamics and regolith mechanics. *Reviews of Geophysics* 45. URL: <http://dx.doi.org/10.1029/2005RG000184>, doi:10.1029/2005rg000184.
- Courde, C., Torre, J.M., Samain, E., Martinot-Lagarde, G., Aimar, M., Albanese, D., Exertier, P., Fienga, A., Maréchal, H., Metris, G., Viot, H., Viswanathan, V., 2017. Lunar laser ranging in infrared at the Grasse laser station. *Astron. Astrophys.* 602, A90. doi:10.1051/0004-6361/201628590, arXiv:1704.06443.
- Criswell, D.R., 1973. Horizon-Glow and the Motion of Lunar Dust, in: Grard, R.J.L. (Ed.), *Photon and Particle Interactions with Surfaces in Space*, p. 545. doi:10.1007/978-94-010-2647-5_36.

- Ehler, J.R., Smith, T.F., 1993. View factors for perpendicular and parallel rectangular plates. *Journal of Thermophysics and Heat Transfer* 7, 173–175.
- Faller, J.E., Alley, C.O., Bender, P.L., Currie, D.G., Dicke, R.H., et al., 1972. Laser Ranging Retroreflector. NASA Apollo 15 Preliminary Science Report, Section 14 SP-289, 14–1.
- Goodrow, S.D., Murphy, T.W., 2012. Effects of thermal gradients on total internal reflection corner cubes. *Applied Optics* 51, 8793. doi:10.1364/AO.51.008793, arXiv:1309.6648.
- Halekas, J.S., Saito, Y., Delory, G.T., Farrell, W.M., 2011. New views of the lunar plasma environment. *Plan. Space Sci* 59, 1681–1694. doi:10.1016/j.pss.2010.08.011.
- McCoy, J.E., Criswell, D.R., 1974. Evidence for a high altitude distribution of lunar dust. *Lunar and Planetary Science Conference Proceedings* 3, 2991–3005.
- Murphy, T.W., 2013. Lunar laser ranging: the millimeter challenge. *Reports on Progress in Physics* 76, 076901. doi:10.1088/0034-4885/76/7/076901, arXiv:1309.6294.
- Murphy, T.W., Goodrow, S.D., 2013. Polarization and far-field diffraction patterns of total internal reflection corner cubes. *Applied Optics* 52, 117. doi:10.1364/AO.52.000117, arXiv:1309.6649.
- Murphy, T.W., McMillan, R.J., Johnson, N.H., Goodrow, S.D., 2014. Lunar Eclipse Observations Reveal Anomalous Thermal Performance of Apollo Reflectors. *Icarus* 231, 183. doi:10.1016/j.icarus.2013.12.006, arXiv:1309.6274.
- Murphy, Jr., T.W., Adelberger, E.G., Battat, J.B.R., Carey, L.N., Hoyle, C.D., LeBlanc, P., Michelsen, E.L., Nordtvedt, K., Orin, A.E., Strasburg, J.D., Stubbs, C.W., Swanson, H.E., Williams, E., 2008. The Apache Point Observatory Lunar Laser-ranging Operation: Instrument Description and First Detections. *Publ. Astron. Soc. Pac.* 120, 20. doi:10.1086/526428, arXiv:0710.0890.
- Murphy, Jr., T.W., Adelberger, E.G., Battat, J.B.R., Hoyle, C.D., McMillan, R.J., Michelsen, E.L., Samad, R., Stubbs, C.W., Swanson, H.E., 2010. Long-term degradation of optical devices on the moon. *Icarus* 208, 31–35. doi:10.1016/j.icarus.2010.02.015, arXiv:1003.0713.
- Murphy, Jr., T.W., Nordtvedt, K., Turyshev, S.G., 2007. The Gravitomagnetic Influence on Gyroscopes and on the Lunar Orbit. *Phys. Rev. Lett.* 98, 071102. doi:10.1103/PhysRevLett.98.071102, arXiv:gr-qc/0702028.
- Rennilson, J.J., Criswell, D.R., 1974. Surveyor Observations of Lunar Horizon-Glow. *Moon* 10, 121–142. doi:10.1007/BF00655715.
- Sickafoose, A.A., Colwell, J.E., Horányi, M., Robertson, S., 2002. Experimental levitation of dust grains in a plasma sheath. *Journal of Geophysical Research (Space Physics)* 107, 1408. doi:10.1029/2002JA009347.
- Toyoda, T., Yabe, M., 1983. The temperature dependence of the refractive indices of fused silica and crystal quartz. *Journal of Physics D Applied Physics* 16, L97–L100. doi:10.1088/0022-3727/16/5/002.
- Zook, H.A., McCoy, J.E., 1991. Large scale lunar horizon glow and a high altitude lunar dust exosphere. *Geophys. Res. Lett.* 18, 2117–2120. doi:10.1029/91GL02235.

A. Thermal Simulation Details

A.1. Setting up the Geometry

Defining the geometry of the problem requires us to define a number of thermal properties for all elements of the 3 dimensional cartesian grid. The CCR are defined in detail in ADL Inc. report (Arthur D. Little, Inc. 1969) and for the purposes of the simulation, we consider the properties defined therein to be a starting point for our simulations. We have a grid of size $51 \times 51 \times 51$ (102 mm \times 102 mm) over which these properties are defined.

While the code as written can be generalized to an arbitrarily shaped cuboid, we work here with cubes for simplicity in view factor calculations later. While we have run the code at different spatial resolutions for testing purposes, all runs for science purposes have been run at a resolution of 2 mm, which makes our simulated box size $102 \times 102 \times 102$ mm. Since the heat transfer is an explicit finite difference scheme, given the material properties used and for ease of comparison for different runs, we have fixed the temporal resolution at 0.005 seconds for all runs. Since the simulation uses cubic voxels, we have oriented the CCR along the (1,1,1) direction, in order to create smooth planes for the sides of the CCRs. While this results in voxelization of the planar surfaces, the effects on heat transfer are minimal. There are two kinds of numerical effects that might occur as a result of voxelization of a planar surface of the CCR. Firstly, the amount of radiative heat transferred between two elements may be slightly inflated due to the increase in surface area as a result of the voxelization. This effect decreases with a decrease in element size, theoretically going to zero as the size of the voxel becomes infinitesimally small. We tested our setup by creating two parallel slabs oriented along the (1,1,1) direction and prescribed a heat flux on one side of one of the slabs, which then radiatively transferred heat to the other slab. Since this is a problem with an analytic solution, we were able to compare our numerical results with the analytic solution and found them to show reasonable agreement with each other. The second effect we need to be careful about is the amount of incident solar flux illuminating each voxel. We tackled this problem by analytically prescribing the heat flux for the entire voxel by multiplying the incident solar flux with the projected area along the (1,1,1) direction.

We first address the assumptions required to simulate a single CCR instead of an entire retroreflector array. The retroreflector array housing the CCRs on the moon is machined out of Aluminum 1100. One of the primary goals of

the design of the reflector array was to provide passive thermal control, since it was understood any thermal gradients would have a significant impact on reflector performance. Thus, the array as a whole was thermally isolated from the lunar environment with multiple blankets, reducing external emissivity to 0.01. Additionally, the CCRs are mounted on Teflon rings and the cavities are recessed into the array to prevent illumination from sunlight unless directly overhead. These designs work well enough that we can treat an individual CCR as a standalone retroreflector for thermal purposes, as we will demonstrate with our simulation. As a result, we have simply replaced the array with an outer layer of aluminum 1100 which we refer to us as the "Shell" in this paper. As we will show, the absence of the remainder of the array has no impact on the thermal performance of the CCR. Thus, our geometry consists of a fused silica CCR, two Teflon rings, the upper aluminum retainer ring and the outer shell. The material properties for these are described in Table 3.

The heat transfer is an explicit finite difference scheme. We first define the array $K_{i,j,k}$, which is total conductance between adjacent cells. So for a cell with indices (i, j, k) and a side length Δx , with thermal conductivity denoted by $\lambda_{i,j,k}$, the conductance with respect to its adjacent cell (i, j, k+1) can be calculated as -

$$K_{i,j,k+1/2} = \frac{\Delta x^2}{\frac{\Delta x}{2k_{i,j,k}} + \frac{\Delta x}{2k_{i,j,k+1}} + R_{i,j,k+1/2}} \quad (5)$$

Where $R_{i,j,k+1/2}$ is the contact resistance between adjacent cells. This is zero for adjacent cells with identical thermal conductivity, i.e. in the bulk of the material. For elements with distinct values of thermal conductivity, we prescribe the value of contact resistance based on the total conductance allowed between the respective surfaces. Based on the results of ADL report, the CCRs were designed to have a prescribed amount of total conductance between materials and the testing of the CCRs tried to constrain the total conductance value. For our purposes, we took the values of total conductance given in the ADL report as starting values. For pairs of material where no value was given, we prescribed the total conductance as follows. We calculated the total conductance in two limiting cases. Firstly, when the two adjacent cells have perfect contact and the total conductance comes purely from the difference in thermal conductivity of the two cells, we can set the value of contact resistance to zero. This gives a minimum conductance value. In the other limit, we assume the two contact surfaces are separated by an infinitesimal distance and the "conductance" is a result of only radiative transfer between the two surfaces. This gives us a temperature dependent total conductance value, assuming the temperature difference between the two surfaces is small compared to the absolute temperature. We then calculate this conductance for the expected temperatures on the lunar surface and get an upper limit for the total conductance. For the actual simulation runs, we end up taking the average of these two conductance values as a starting point. Once we have prescribed the total conductance for a pair of materials, we can then calculate the conductance per element. Knowing the thermal conductivity values, we can then prescribe a value of contact resistance for each element. Thus, prescribing the total conductance between any pair of materials, as designed and tested in the ADL report, gives us a value for the contact resistance between any two elements.

A.2. Constructing the View Factor matrix

Once we have defined our geometry, the code then constructs a view factor matrix. We create a matrix of all boundary point elements and compute the view factors for each pair of surfaces using the analytic expressions from Ehlert and Smith. Since our geometry does not change as a function of time, this is a one time calculation performed at the beginning of a run. It can then be saved and retrieved for a subsequent run. This step of the code takes about 20 minutes to run for the full CCR simulation. We checked our view factor calculations for parallel and plane geometry by constructing two slabs in a parallel and perpendicular configuration. We calculate the view factor matrix, and using the view factor matrix, sum the individual view factors to obtain the total view factor for the slabs, which can then be computed using the same expression for a larger slab. We can also check this against simpler expressions for the special case where the slabs are exactly opposite each other with no relative lateral displacement. We find that the view factors computed are consistent when summed with what we would expect for the pair of larger slabs. We also find the consistency does not depend on the spatial resolution of the geometry, as would be expected for an analytic expression for the view factors.

A.3. Heat Transfer

Given the conductance between adjacent cells, we can calculate the total heat influx into a cell $H_{i,j,k}$ from

$$\begin{aligned} H_{i,j,k} = & K_{i-1/2,j,k} \cdot (T_{i-1,j,k} - T_{i,j,k}) + K_{i+1/2,j,k} \cdot (T_{i+1,j,k} - T_{i,j,k}) \\ & + K_{i,j-1/2,k} \cdot (T_{i,j-1,k} - T_{i,j,k}) + K_{i,j+1/2,k} \cdot (T_{i,j+1,k} - T_{i,j,k}) \\ & + K_{i,j,k-1/2} \cdot (T_{i,j,k-1} - T_{i,j,k}) + K_{i,j,k+1/2} \cdot (T_{i,j,k+1} - T_{i,j,k}). \end{aligned} \quad (6)$$

The change in temperature T in time Δt is given by

$$T_{ijk}^{t+1} = T_{ijk}^t + H_{ijk} \frac{\Delta t}{\Delta x^3 \rho_{i,j,k} C_{i,j,k}}, \quad (7)$$

where $\rho_{i,j,k}$ is the density and $C_{i,j,k}$ is the Specific Heat Capacity for the element (i, j, k) . For every boundary point, we also track the temperature at the center of the external surface. In order to check our heat transfer code, we performed a number of tests. Our general goal was to run simulations with analytic solutions in order to have something concrete to compare to. To test the conduction code, we use a single slab and subject it to an incident flux on one side. We then switch off any radiative effects on the boundaries, thus reducing this to a one-dimensional heat transfer problem with a known solution. We can start the simulation run from an arbitrary temperature and let it run until we have equilibrium. In practice, we started approximately 50° away from the steady state temperature value. We compared the temperatures on the front and back surfaces with the analytically calculated expected temperatures. We found our simulation agreed with the analytic solution to well within 0.5% for the coarsest resolution of 1 cm and to well within 0.1% using the finest resolution of 1 mm. We then tested our radiative heat transfer code by adding a second slab in parallel behind the back face of the first slab, with boundary radiative effects switched off. We had an incident flux on one side of the first slab. Now we can analytically compute 4 temperatures on the front and back surfaces of the two slabs as follows. Assuming the temperatures on the front and back of the first slab are T_1 and T_2 , and that on the front and back of the second slab are T_3 and T_4 , the relevant equations in steady state are

$$Q - \sigma T_1^4 = -k(T_1 - T_2) \quad (8)$$

$$-k(T_1 - T_2) = \sigma T_2^4 - F_{23} \sigma T_3^4 \quad (9)$$

$$F_{23} \sigma T_2^4 - \sigma T_3^4 = -k(T_3 - T_4) \quad (10)$$

$$-k(T_3 - T_4) = \sigma T_4^4, \quad (11)$$

where k is the thermal conductivity of the slab, σ is the Stefan-Boltzmann constant, Q is the incident heat flux per incident area on the front surface and F_{23} is the view factor between the back and front surfaces of slabs 1 and 2 respectively. Solving these sets of equations numerically gives only two real sets of values, only one of which is physical (positive temperatures). We calculated these values and found good agreement between the numerically obtained and the solutions to the analytic equations, with the agreement improving with higher numerical resolution.

Optical-coherence-tomography-based deep-learning scatterer-density estimator using physically accurate noise model

THITIYA SEESAN,¹ PRADIPTA MUKHERJEE,¹ IBRAHIM ABD EL-SADEK,^{1,2} YIHENG LIM,¹ LIDA ZHU,¹ SHUICHI MAKITA,¹ AND YOSHIKI YASUNO^{1,*}

¹*Computational Optics Group, University of Tsukuba, Tsukuba, Ibaraki 305-8573, Japan*

²*Department of Physics, Faculty of Science, Damietta University, New Damietta City 34517, Damietta,*

Egypt

*yoshiaki.yasuno@cog-labs.org

<https://cog-news.blogspot.com/>

Abstract: We demonstrate a deep-learning-based scatterer density estimator (SDE) that processes local speckle patterns of optical coherence tomography (OCT) images and estimates the scatterer density behind each speckle pattern. The SDE is trained using large quantities of numerically simulated OCT images and their associated scatterer densities. The numerical simulation uses a noise model that incorporates the spatial properties of three types of noise, i.e., shot noise, relative-intensity noise, and non-optical noise. The SDE's performance was evaluated numerically and experimentally using two types of scattering phantom and *in vitro* tumor spheroids. The results confirmed that the SDE estimates scatterer densities accurately. The estimation accuracy improved significantly when compared with our previous deep-learning-based SDE, which was trained using numerical speckle patterns generated from a noise model that did not account for the spatial properties of noise.

1. Introduction

Optical coherence tomography (OCT) is a non-invasive imaging modality that is used to provide high-resolution structural information about biological tissues [1–3]. The anatomical images provided by OCT are used widely in clinical diagnosis [4].

In addition to anatomical investigations, OCT-based assessments of the optical properties of tissue have also been studied and have provided useful biomarkers. One commonly investigated optical property of biological tissues is the attenuation coefficient (AC) [5, 6], and the AC is considered to be related to the tissue density. AC measurements are useful in a wide variety of applications, including investigation of tumor spheroid necrosis [7, 8] and distinguishing between normal and cancerous tissues [9–11]. However, AC measurements are strongly influenced by the measurement configuration and conditions, which including the system confocality, the depth position of the focus, and the presence of aberrations [12–14], and these factors can limit the accuracy and reliability of the AC measurements. Although several methods have been proposed to compensate for these effects, they generally require hard-wired assumptions to be made [12] or multiple measurements to be performed [15].

Rather than use the AC to assess biological tissue density, we have proposed a deep-learning based method that estimates the scatterer density of the tissue directly [16–18]. In this work, we denote this method as the scatterer density estimator (SDE). The SDE analyzes the local spatial patterns of an OCT intensity image, i.e., the speckle pattern, using a convolutional neural network (CNN) and then estimates the scatterer density. The CNN was trained using fully numerically simulated OCT speckle patterns that were generated by a simple scalar-optics-based OCT simulator. This approach provides significant amounts of training data, and the data sets reflect the variety of the parameters involved in OCT imaging, including the resolution, the

signal-to-noise ratio (SNR), and the sample scatterer density.

In our previous study [18], we noted that the CNN can estimate two primary quantities: the speckle contrast and the resolution. Hillman *et al.* showed that the local speckle contrast of OCT has a monotonic and negative relationship with the number of scatterers contained within a three-dimensional (3D) resolution volume, which is designated the effective number of scatterers (ENS) [19]. In addition, Kurokawa *et al.* demonstrated that the axial and lateral resolutions of OCT can be estimated based on a local speckle pattern [20]. Therefore, we have anticipated that the CNN will primarily estimate the speckle contrast and the resolutions, and have then estimated the scatterer density based on these quantities.

This previous SDE has provided promising results, but its scatterer density estimation accuracy was limited when it was applied to real experimental data, particularly if the scatterer density or the SNR is low [18]. By considering the possible mechanism for the estimator described above, we hypothesized that the low estimation accuracy for both the speckle contrasts and the resolutions may be limiting factors for the scatterer density. In addition, the estimation accuracy of the scatterer density falls when the SNR is low, i.e., in cases in which the noise forms a significant component of the OCT image. As a result, we hypothesized that our simulation-generated training data (i.e., the speckle patterns) did not actually reflect the physical properties of the noise accurately. This inaccuracy in the noise modeling process may have then caused the inaccuracies in both the speckle contrast and the resolution estimations.

In this paper, we introduce a new physically realistic noise model and demonstrate improved accuracy in the SDE. This new noise model incorporates the spatial properties of the OCT noises including shot noise, relative intensity noise (RIN), and non-optical noise. The accuracy of the SDE is then validated using numerically generated OCT images, along with OCT images of two types of scattering phantoms and *in vitro* tumor spheroids. Our results demonstrate significant improvement in the scatterer density estimation accuracy, particularly under low SNR conditions.

2. Principle

2.1. Neural network-based scatterer density estimator

Our CNN-based SDE estimates the scatterer density from a small spatial pattern of an OCT image, i.e., from a local speckle pattern with an image size of 16×16 pixels. To train the CNN model, we used numerical speckle patterns that were generated by a simple scalar-optics-based OCT simulator, which is designated a “speckle generator.” The speckle generator generates a speckle pattern from an arbitrary parameter set that consists of the scatterer density, the axial and lateral resolutions, and the SNR. The speckle pattern is generated by convolving a 3D scatterer distribution map with a 3D complex point spread function and subsequently adding complex Gaussian noise. The details of the speckle generator are presented in Section 3.1.

In our previous study, the noise was assumed to be fully spatially decorrelated. In other words, the noise signals at the individual pixels are assumed to be fully independent of each other. In the new SDE, we introduce a more physically accurate noise model that accounts for the spatial correlation properties of the noise, as will be described in the next section.

2.2. Noise Model

Similar to our previous noise model, the new noise model has a complex Gaussian distribution, i.e., both the real and imaginary parts of the noise are normally distributed with a zero mean. However, our new noise model accounts for the different spatial correlation properties of the three types of OCT noise, comprising shot noise, RIN, and non-optical noise. These three noise types have different spatial extents, and these differences originated from the different dependencies of these noise types on the light source spectrum.

When the light source spectral intensity is denoted by $S(k)$, the noise within the wavenumber

domain can be described as

$$N_a(k) = c_1 \sqrt{S(k)} N_{\text{sh}}(k) + c_2 S(k) N_{\text{RIN}}(k) + c_3 N_{\text{no}}(k), \quad (1)$$

where k is the wavenumber, and N_{sh} , N_{RIN} , and N_{no} are normally distributed random variables that correspond to the shot noise, the RIN, and the non-optical noise, respectively. All these variables have a zero mean and the same standard deviations, but they are independent of each other. In addition, the constants c_1 , c_2 , and c_3 are proportionality constants.

As the equation shows, the amplitude expectation of the shot noise (i.e., the first term on the right-hand side) is a function of k , and is proportional to the square root of the spectral intensity at each value of k . This is because the shot noise energy, which is the squared power of the amplitude, is proportional to the spectral intensity. Similarly, the amplitude expectation of the RIN (i.e., the second term) is also a function of k , and is also proportional to the spectral intensity. This corresponds to the fact that the RIN energy is proportional to the squared power of the spectral intensity. In contrast, the non-optical noise (i.e., the third term) is independent of the light source spectrum and its amplitude expectation remains constant over the range of k .

The spectral-intensity dependence of the noise causes a spatial correlation of the noise along the depth direction. The noise in the depth domain can be determined by taking the Fourier transform of Eq. (1) as follows

$$\mathcal{F}^{-1} [N_a(z)] = c_1 \mathcal{F}^{-1} \left[\sqrt{S(k)} \right] (z) * N'_{\text{sh}}(z) + c_2 \mathcal{F}^{-1} [S(k)] (z) * N'_{\text{RIN}}(z) + c_3 N'_{\text{no}}(z) \quad (2)$$

where z is the depth and is a Fourier pair of k . $\mathcal{F}^{-1} [\]$ denotes an inverse Fourier transform and $N'_{\text{sh}}(z)$, $N'_{\text{RIN}}(z)$, and $N'_{\text{no}}(z)$ are the Fourier transforms of $N_{\text{sh}}(k)$, $N_{\text{RIN}}(k)$, and $N_{\text{no}}(k)$, respectively. Because $N_{\text{sh}}(k)$, $N_{\text{RIN}}(k)$, and $N_{\text{no}}(k)$ are all normally distributed Gaussian noise, $N'_{\text{sh}}(z)$, $N'_{\text{RIN}}(z)$, and $N'_{\text{no}}(z)$ become normally distributed complex Gaussian noise. As the equation shows, the shot noise is convolved with the Fourier transform of $\sqrt{S(k)}$, and the result is the spatial correlation of the shot noise along the depth direction. Similarly, the RIN is convolved with the Fourier transform of $S(k)$ and this operation also results in a spatial correlation along the depth direction.

Notably, because $\sqrt{S(k)}$ can be wider than $S(k)$, $\mathcal{F}^{-1} \left[\sqrt{S(k)} \right] (z)$ can then be narrower than $\mathcal{F}^{-1} [S(k)] (z)$. This suggests that the spatial correlation distance of the shot noise is shorter than that for the RIN. In contrast to the shot noise and the RIN, i.e., the optical noise types, the non-optical noise (the third term on the right-hand side) shows no spatial correlation. The spatial correlation distances for the three types of noise contained in the new noise model and in the old noise model used in our previous SDE [18] are summarized in Table 1, in addition to the correlation distance of the OCT signal.

In this study, we consider scanning OCT, rather than a full-field OCT. Because each A-line of the scanning OCT is acquired at a different time, none of the three noise types have spatial correlation along the lateral direction. We expect that the different spatial properties of the noises and the OCT signal will be used by the CNN to estimate the speckle contrast and the resolutions accurately. This will then enable more accurate estimation of the scatterer density than our old CNN model, as will be shown in Section 4.

3. Implementation and validation method

3.1. Speckle generation and CNN-model training

The first step in the CNN model training process is the generation of the OCT speckle patterns, i.e., the training datasets. This step is identical to that described in Section 2.1 of [18], with the exception of the noise model. Because the details of this numerical speckle pattern generation

Table 1. Summary of spatial correlation distance characteristics of three noise types and the OCT signal. In the new noise model, each type of noise has different spatial correlation properties, whereas these properties [18] are identical for all noise types in the old noise model.

		New noise model	Old noise model
Shot noise	Lateral	Zero	Zero
	Depth	$\mathcal{F}[\sqrt{S(k)}]$	Zero
RIN	Lateral	Zero	Zero
	Depth	$\mathcal{F}[S(k)]$	Zero
Non-optical noise	Lateral	Zero	Zero
	Depth	Zero	Zero
OCT signal (speckle)	Lateral	Resolution	
	Depth	$\mathcal{F}[S(k)]$	

process have been described elsewhere, we describe the process only briefly here. In this process, we first generate the 3D numerical fields using randomly distributed scatterers. Here, the field has a size of $128 \times 128 \times 128$ pixels ($31.2 \mu\text{m} \times 31.2 \mu\text{m}$ for the lateral directions and $115.8 \mu\text{m}$ for the axial direction), and the pixels with a scatterer have an amplitude of unity but a random phase. This random phase represents the sub-wavelength depth position of the scatterer. The pixels without a scatterer have zero values. The 3D field of scatterers is then convolved with a 3D complex point spread function of the OCT, which is assumed to have a 3D Gaussian distribution and its two lateral resolutions are assumed to be identical. The 3D numerical field is then down-sampled from $128 \times 128 \times 128$ pixels to $16 \times 16 \times 16$ pixels, in keeping with the original physical field size. The pixel size after down-sampling is then $1.95 \mu\text{m}$ for the lateral directions and $7.24 \mu\text{m}$ for the axial direction. After down-sampling of the field, we added the shot noise, the RIN, and the non-optical noise because it follows from the noise model described in Section 2.2.

To train the CNN model, we generated 80,000 3D speckle patterns and then extracted 1,280,000 2D cross-sectional speckle patterns with dimensions of 16×16 pixels. Each 3D speckle pattern was generated with different and randomly selected values for the scatterer density, the resolutions, and the noise energies of the shot noise, the RIN, and the non-optical noise. The axial and lateral resolutions here are independent of each other and range from 3 to $30 \mu\text{m}$. The noise energies for each type of noise are randomly selected as the SNR with respect to each noise type in the range from 0 to 100 dB. The scatterer densities range from 0 to $0.2387 \text{ scatterers}/\mu\text{m}^3$ (0 to $6.5723 \text{ scatterers}/\text{pixel}$).

The CNN consists of three convolutional and max-pooling layer pairs followed by two fully connected layers; this structure is identical to that described in Section 2.2.2 of Ref. [18]. The model was trained to minimize the mean squared error (MSE) between the ground-truth scatterer density values and the network outputs by using the Adam optimizer [21] at a learning rate of 10^{-4} . The batch size of the training was set at 32. Before being input into the model, the input image intensity was normalized into a $[0, 1]$ range. The validation set used for the training consists of 100 2D speckle patterns that were extracted from 100 3D speckle patterns; these patterns were generated independently from the training dataset.

3.2. Evaluation method

The performances of the SDE were validated both numerically and experimentally. The numerical validation used numerically generated OCT speckle patterns, whereas the experimental validations used two types of scattering phantom (comprising Intralipid phantoms and microsphere phantoms) and *in vitro* tumor spheroid samples. For comparison, we also evaluated our previous SDE [18], which is identical to the new SDE with the exception of the noise model used to generate the training dataset. The process details are described in the following sections.

3.2.1. Numerical validation

For the numerical validation, we used 100 2D OCT speckle patterns that were generated using the same method that was used to generate the training dataset. Each of these 100 2D speckle patterns was extracted from different 3D speckle patterns. Therefore, all the 2D speckle patterns are independent of each other and are based on different resolutions, SNR values, and scatterer densities. Note that the noise model used for this generation process is the physically accurate noise model that was described in Section 2.2. Because we know the true density, we can determine the estimation accuracy directly via this numerical validation process.

3.2.2. Validation using scattering phantoms

For the phantom-based experimental validations, we used two scattering phantom types, i.e., Intralipid phantoms and microsphere phantoms.

The Intralipid phantoms are composed of Intralipid solutions with various concentrations of 1%, 2%, 4%, 6%, 8%, and 10% (v/v concentration). These Intralipid solutions are made from a 20% stock solution of Intralipid (IL-20, Sigma-Aldrich I141). Three phantoms were fabricated for each concentration, giving a total of 18 phantoms. Note that these phantoms are identical to the phantoms used in our previous study [18], and the same measurement datasets that were used in the previous study were also reused in this study.

The microsphere phantoms are formed using a mixture of polystyrene microspheres and agarose gel. When compared with the Intralipid droplets, the polystyrene microspheres have well controlled and known sizes and refractive index values, and thus these microspheres are frequently used as phantoms in the biomedical optics field [22]. In our study, the microsphere-based phantom is particularly useful because we can compute the true scatterer densities from the product-specific particle concentrations and diameter in each case.

Six phantoms with volume concentrations of 0.1%, 0.2%, 0.4%, 0.6%, 0.8%, and 1.0% were prepared by mixing 1- μm diameter polystyrene microspheres (89904-10ML-F, Sigma-Aldrich) with the agarose gel (A1296-100G, Sigma-Aldrich). These concentrations corresponded to scatterer densities of 0.0191, 0.0382, 0.0764, 0.1146, 0.1528, and 0.1910 scatterers/ μm^3 , respectively. The scatterer density was computed here using

$$\text{Scatterer density} = \frac{6\sigma}{\pi d^3}, \quad (3)$$

where σ is the volume concentration of the scattering medium and d is the microsphere diameter. The mixture was poured into an acrylic container with a thickness of 1 mm. The container was then refrigerated for 1 h at 5 °C. Note that these phantoms were fabricated by following the protocol described in [23]. Three phantoms were made with each concentration, and thus 18 phantoms were fabricated in total.

Both the Intralipid phantoms and the microsphere phantoms were measured using a swept-source OCT with a probe beam wavelength of 1.3 μm . (The OCT system is described in detail in Section 3.2.5.) For the measurements, we intentionally attenuated the probe beam by applying a variable neutral density (ND) filter to alter the SNR. Each phantom was measured with three different round-trip attenuations, which were 0, -5.4, and -11.8 dB for the Intralipid phantoms,

and 0, -5.6, and 12.0 dB for the microsphere phantoms. The probe power on the sample was 12 mW with 0-dB attenuation.

3.2.3. Human breast cancer spheroid

Tumor spheroids composed of human breast adenocarcinoma (MCF-7 cell line) were used to evaluate the SDEs from a biomedical application perspective. The cells were cultured for 15 days and spheroids with a size of approximately $500 \mu\text{m}$ were formed. The scatterers within the cells are believed to consist of cell nuclei and organelles. For the measurements, each spheroid was extracted from the culturing environment and then placed in a room-temperature culture medium without CO_2 supply.

We performed two types of measurements. The first type involves longitudinal hourly measurements for up to 28 h, where the measurements were performed using a 2D cross-sectional scan protocol. Each cross-sectional image (i.e., B-scan) consists of 512 A-lines. Note that this experiment was performed initially for the study described in Ref. [24], and that the same data set was used in our previous SDE study [18].

The second type is a 3D measurement taken at two longitudinal time points of 0 h and 20 h. A 3D datasets consists of 512×128 A-lines. This measurement was originally performed for the study detailed in Ref. [25].

3.2.4. Statistical analysis

For the numerical validation and the polystyrene microsphere phantom experiment, the agreement between the estimates and the ground truth was evaluated statistically via intraclass correlation (ICC). Here, a higher (i.e., closer to 1.0) ICC indicates a better estimate. This statistical analysis was performed using the `intraclass_corr()` function in the statistics library of Python (Pingouin 0.5.3) in Python 3.7.

3.2.5. OCT devices and measurement protocol

A polarization-sensitive Jones matrix swept-source OCT system [26,27] was used to perform the experimental validations. The probe wavelength was $1.3 \mu\text{m}$ and the measurement speed was 50,000 A-lines/s. The axial resolution and the pixel separation were $14.1 \mu\text{m}$ and $7.24 \mu\text{m}$ (both in the tissue), respectively, while the lateral resolution and the pixel separation were $18.1 \mu\text{m}$ and $1.95 \mu\text{m}$, respectively. Note that the pixel separations were identical to those of the numerically generated speckle patterns. The OCT image used in this study is a coherent composition of multiple polarization channels that is nearly identical to a standard non-polarization-sensitive OCT image.

4. Results

4.1. Numerical validation

Figure 1 shows the numerical validation results, where the estimated scatterer densities are plotted versus the set (ground truth) scatterer densities. The SDE that was trained using the physically accurate noise model (the new SDE, red circles) shows high consistency between the set and estimated scatterer densities. In contrast, the previous SDE [18], which was trained using a spatially-uncorrelated noise model (the old SDE, blue triangles), shows higher variation among the estimates, and the estimated values are also downshifted significantly from the ground truth. The ICCs between the estimates and the ground truth were computed to be 0.975 for the new SDE and 0.722 for the old SDE. The higher ICC of the new SDE is a quantitative demonstration of the superior performance of the new SDE.

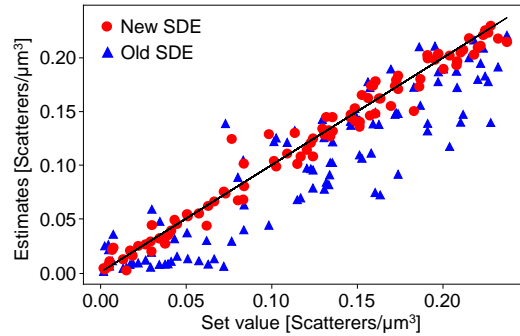


Fig. 1. Numerical validation of the new SDE (red circles) and the old SDE (blue \times). The horizontal and vertical axes correspond to the set scatterer density (the ground truth) and the estimated densities, respectively. The black solid lines represents the perfect estimate. The new SDE gives reasonable estimates, whereas the estimates from the old SDE are downshifted significantly from the ground truth.

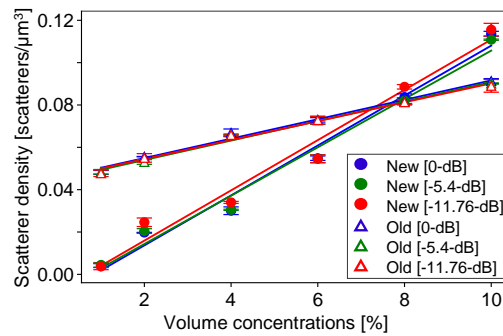


Fig. 2. Scatterer density estimation results for Intralipid phantoms with several volume concentrations and several probe-beam attenuations. The circles and the triangles represent the estimates obtained when using the new and old SDEs, respectively. The colors represent the probe beam attenuations that correspond to the SNR of the OCT image. The error bar shows the standard deviation for three measurements of the three phantoms. Both SDEs show high repeatability (i.e., a small standard deviation in each case) and consistent estimates among the different probe-beam attenuations. However, the old SDE shows a significantly large intercept that indicates the low fidelity of the old SDE, particularly at low concentrations. The lines are linear regression lines computed from the data.

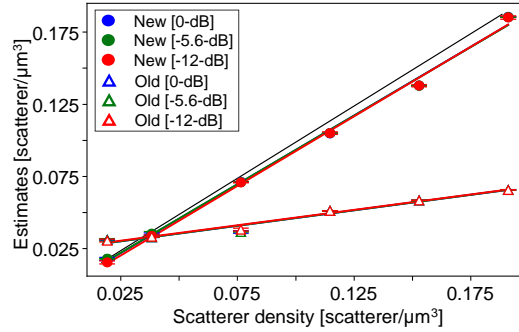


Fig. 3. Scatterer density estimation results for the microsphere phantoms. The vertical axis represents the estimated scatterer density and the horizontal axis represents the theoretically predicted scatterer density as computed from the volume concentration of the phantom using Eq. (3). The error bars represent the standard deviations among the three estimates of the three samples. The black line represents the ideal estimate, while the other lines are linear-regression lines that were computed from the data. The error bars are almost unrecognizable because of the high repeatability of the estimates. The new SDE (circles) provides estimates that are very close to the theoretical predictions (black line). In contrast, the estimate of the old SDE show significant departures from the theoretical predictions. In addition, the estimation results are unaffected by the probe-beam attenuation. Specifically, although the attenuations are represented by different colors, the plots and the regression lines with the different attenuations overlap significantly and are not really distinguishable.

4.2. Intralipid phantom

The results of the Intralipid phantom validation are summarized in Fig. 2. In this figure, the estimated scatterer densities are plotted versus the volume concentrations. The circles and triangles represent the estimates from the new and old SDEs, respectively. The colors of the plots indicate the probe-beam attenuations in each case. Specifically, each color corresponds to a different SNR. The error bars represent the standard deviations among the three measurements of the three phantoms and the lines are linear regression lines that were computed from the data.

Both SDEs showed reasonably small variations (standard deviations) among the phantoms, and showed highly linear relationships between the estimates (on the vertical axis) and the volume concentrations (on the horizontal axis). In addition, the estimated values were not sensitive to probe attenuation. Specifically, both SDEs were unaffected by the SNR of the OCT image. However, the intercept of the old SDE was as high as $0.05 \mu\text{m}^{-3}$ at the 0% volume concentration, whereas that of the new SDE was close to zero ($0.01 \mu\text{m}^{-3}$). Because the scatterer density at the 0% volume concentration might be $0 \mu\text{m}^{-3}$, we can conclude that the new SDE provides significantly better estimation accuracy when compared with the old SDE.

4.3. Polystyrene microsphere phantom

The estimation results for the microsphere phantoms are plotted versus the theoretically computed scatterer density in Fig. 3. The theoretical scatterer density was calculated from the volume concentration of the phantom using Eq. (3). Similar to Fig. 2, the circles and the triangles represent the estimates from the new and old SDEs, respectively, and the colors indicate the probe-beam attenuation levels. The error bars indicate the standard deviations among the three measurements of the three phantoms, but the error bars are nearly invisible here because of the very high measurement repeatability (leading to very small standard deviations). In addition, both SDEs are nearly perfectly independent of the SNRs, as indicated by the fact that the data

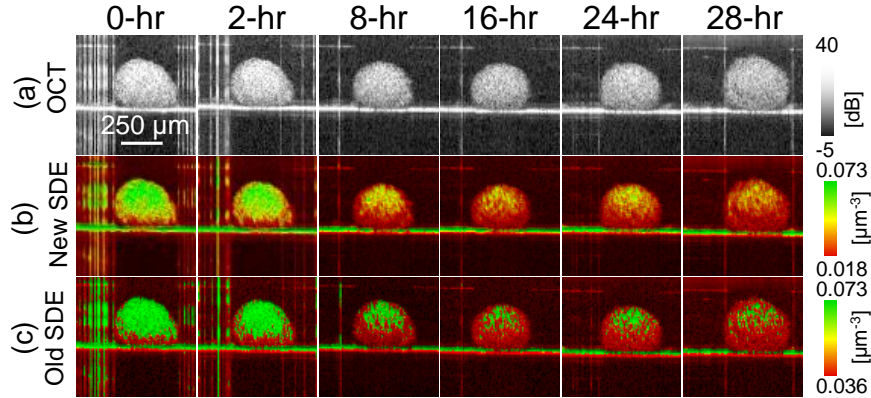


Fig. 4. Time-lapse images of a tumor spheroid. The individual rows show (a) the OCT intensity images, and the scatterer density images obtained by the (b) new and (c) old SDEs. Both SDEs show a reduction in the scatterer density over time.

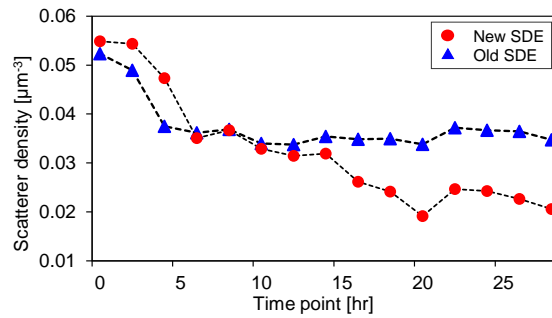


Fig. 5. Mean scatterer density within the spheroid region. Both the new (red circles) and old (blue rectangles) SDEs showed a reduction in the mean scatterer density over time. For the time points after 10 h, the old SDE gives constant scatterer density estimates, whereas the new SDE shows a continuous reduction in the scatterer density. As discussed in Section 5.1, the results from the new SDE are more plausible in this case.

points for the different SNRs are nearly perfectly overlapping each other.

The estimates from both SDEs show highly linear relationships with the theoretically predicted scatterer density. However, the estimates from the old SDE (triangles) show significant departures from the ideal estimation line (i.e., the solid black line). In contrast, the new SDE (circles) shows very close agreement with the theoretical predictions. The ICCs between the estimated values and the theoretical scatterer density values were very high at 0.982 (0-dB attenuation), 0.982 (-5.6-dB attenuation), and 0.981 (-12-dB attenuation) for the new SDE, whereas those for the old SDE were 0.467 (0-dB attenuation), 0.467 (-5.6-dB attenuation), and 0.460 (-11.8-dB attenuation). The higher ICCs indicate the superior performance of the new SDE.

4.4. Tumor spheroids

Figure 4 shows hourly time-lapse images of the MCF-7 spheroid. The individual rows show the OCT B-scans, the scatterer density images obtained using the new SDE, and those obtained

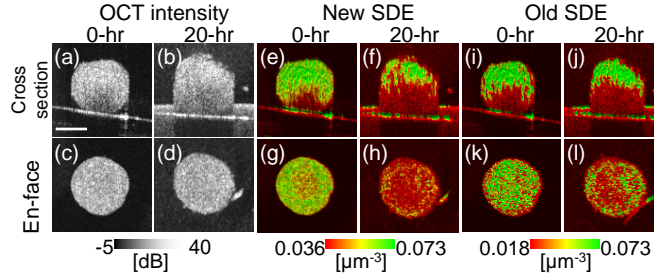


Fig. 6. 3D time-course images of MCF-7 spheroid. (a-d) show OCT intensity images, and (e-h) and (i-l) are scatterer density images acquired when using the new and old estimators, respectively. The first and second rows represent the cross-sectional and *en face* images, respectively. At the zero-hour time point, the OCT intensity did not show a clear structure within the spheroid, whereas the *en face* scatterer density images showed a clear low-density core at their center. In addition, the *en face* scatterer density images showed clear difference between two time points, while this stark contrast was not observed in the *en face* OCT intensity images. The scale bar represents 200 μm

using the old SDE (in order from top to bottom). The color scale (hue) in the scatterer density images represents the estimated scatterer density, while the brightness corresponds to the OCT intensity. Note that the images from the old SDE are identical to those presented in Ref. [18]. In addition, the mean scatterer density was computed within manually segmented spheroid regions and plotted versus time, as shown in Fig. 5. In the figure, the red circles and the blue rectangles correspond to the new and old SDEs, respectively.

Both SDEs showed a reduction in the scatterer density over time, but distinctive differences between the two SDEs can be seen at the later time points after 10 h. At these time points, the new SDE showed a continuous reduction in the scatterer density, whereas the estimates from the old SDE remained constant. The constant estimation from the old SDE may be caused by the relatively large error of low SDE at lower scatterer densities, as shown in the numerical and phantom-based validations presented in Sections 4.1, 4.2, and 4.3. Here, we remind that the low scatterer density may cause a lower OCT signal intensity and thus lead to the higher noise dominance. Therefore, the scatterer density estimation can be more helpful in maintaining the noise model accuracy for the lower scatterer density cases. The continuous reduction in the scatterer density found by the new SDE is more consistent with to our dynamic OCT findings than the results from the old SDE; this will be addressed later in the discussion section (Section 5.1).

Figure 6 shows cross-sectional (first row) and *en face* (second row) images obtained from a volumetric dataset of a tumor spheroid. The *en face* images are the slices acquired around the equator of the spheroid. The left images (a-d) are the OCT intensity images, the middle images (e-h) are the scatterer density images acquired using the new SDE, and the right (i-l) are those acquired when using the old SDE.

The cross-sectional images showed similar appearances to the corresponding images in Fig. 4. However, the *en face* images illustrate that the scatterer density images are more informative than the OCT intensity images. For example, the OCT intensity at zero-hour time point [Fig. 6(c)] only shows a homogeneous appearance. In contrast, the scatterer density image from the new SDE [Fig. 6(g)] revealed that the center region has a lower scatterer density than the peripheral regions. This may be an indication of the well-known necrotic core of MCF-7 spheroids [25, 28, 29].

Notably, the core is not visible when using the old SDE [Fig. 6(k)]. This may occur because the estimator accuracy of the old SDE is too low for the low scatterer density in this case.

The *en face* OCT intensity images at the two time points [Fig. 6(c) and (d)] do not show clear differences, whereas the scatterer density images [Fig. 6(g) versus (h) and Fig. 6(k) versus (l)] show clear reductions in the scatterer density at the late time point (20 h). The reduction in the scatterer density at the later time point is reasonable because the dominant scatterers in these cells are the nuclei and cell organelles, and they are resolved by cell death. Some discussions related to this point can be found in Section 5.1. It should also be noted that the scatterer density from the old SDE at the later time point [Fig. 6(l)] is higher than that obtained from the new SDE [Fig. 6(h)]. This difference also can be attributed to the low accuracy of the old SDE for low scatterer densities.

Additionally, we can see that the scatterer densities of the upper and lower parts of the spheroid are not symmetrical. Specifically, the upper hemisphere shows a higher scatterer density than the lower hemisphere. This issue is discussed in greater detail in Section 5.2.

5. Discussion

5.1. Time course reduction and scatterer density

Both the 2D and 3D spheroid imaging results presented in Section 4.4 showed time-course reductions in the scatterer densities. As shown in Fig. 5, the new SDE indicates a continuous reduction in the scatterer density over 28 h, while the scatterer density estimated using the old SDE becomes constant after 10 hours.

These reductions in the scatterer density can be understood more easily when using dynamic OCT imaging. In our previous paper, the same datasets used in Figs. 4 and 5 were analyzed using two dynamic OCT methods, i.e., the logarithmic intensity variance (LIV) method and the late OCT correlation decay speed (OCDS_l) method. The mean LIV and mean OCDS values within the entire spheroid region were found to be decreasing continuously over 28 hours. These reductions in the dynamic OCT signals indicate the progression of necrosis within the spheroid [25].

The necrotic cell death causes destruction of the nuclei and the cell organelles. Because the nuclei and the organelles are the dominant scatterers within the cell, the progression of the necrosis causes a reduction in the scatterer density.

According to the dynamic OCT analysis, the necrosis has progressed continuously over 28 h; this may also suggest that the reduction in the scatterer density also may progress over this time period. Therefore, the results from the new SDE, which showed a continuous reduction in the scatterer density, are more plausible than the results from the old SDE, in which the scatterer density becomes constant after 10 h.

5.2. Asymmetric appearance of the scatterer density in spheroids

Cross-sectional scatterer density images of the spheroid, where Fig. 4 (b) and (c) show asymmetric appearances between the upper and lower parts of the spheroid. This asymmetry may partially be attributed to the occurrence of multiple scattering in the deeper region of the tissue. Because our speckle generator does not incorporate the multiple scattering effect, the estimation accuracy of the SDE may decrease in the deeper region.

Several possible solutions have been proposed to address this issue. One approach is to apply one of the available multiple-scattering rejection methods [30–33]. Another possible solution is to improve the speckle generator to allow it to account for the multiple scattering effect. Several models and simulation methods have been proposed that can account for multiple scattering [34–38]. Although these current methods are computationally intensive and rather too slow to generate the massive amount of training data required, future investigations of the theoretical model and associated simulation methods may enable development of a speckle

generator that can account for multiple scattering with reasonable computation speeds.

5.3. Computation time of the speckle generator and the SDE

The overall training process of the CNN-based SDE can be split into two sub-processes, i.e., speckle generation and CNN training. The generation of 80,000 3D speckle patterns with dimensions of $16 \times 16 \times 16$ pixels takes approximately 3 hours when using a desktop PC equipped with an Intel Core i7-6900K CPU and a graphics processing unit (GPU; GeForce RTX 3090 Ti, NVIDIA). The main memory of the PC is 128 GB in size, and the GPU has 10752 cores, a 1.86 GHz boost clock, and 24 GB of memory. The speckle generator is written in Python (version 3.7) with a GPU-compatible numerical computation library (CuPy 12.0.0). Notably, the speckle generator is more than 11 times faster than our previous version, which did not use a GPU. Therefore, usage of a GPU is essential when generating large training datasets.

Subsequently, training of the CNN model takes approximately 1 h, where the CNN is written in Python 3.7 with Keras 2.3.1 based on the TensorFlow backend. Therefore, the entire training process takes approximately 4 hours.

Scatterer density estimation of a 512×402 pixel cross-sectional image using a 16×16 pixels sliding window took around 1 minute, and thus the estimation process for a volumetric image that consist of 128 B-scans takes approximately 2 hours.

5.4. Compatibility of the trained model and the scanning protocol

Because the speckle generator generates a speckle pattern with a specific pixel size, each training dataset (i.e., each set of speckle patterns) is specific to a single scan protocol. Therefore, speckle patterns should be generated for each different scan protocol and a specific SDE model should then be trained using these specific speckle patterns.

The other compatibility issue that must be considered is the minimum separation required between adjacent A-lines (i.e., the lateral pixel size). We suspect that our new SDE uses the different lateral spatial properties of the noise and OCT signals to distinguish them, as summarized in Table 1. Specifically, we have assumed that the noise has fully decorrelated between the adjacent A-lines, as described in Section 2.2. However, the OCT signals are mutually correlated along the lateral direction with the correlation distance around the lateral resolution. The different lateral spatial properties of the noise and the OCT may have been used by the SDE model to discriminate the OCT signal from the noise. However, the different lateral extents only become pronounced if the A-line separation is smaller than the lateral resolution. Therefore, the OCT scan protocol to be used with our SDE should have an A-line separation that is smaller than the lateral resolution.

It is also notable that, according to Eq. (2), the RIN may have the same axial extent as the OCT signal. Thus, if the CNN model cannot use the different lateral properties of the signal and the noise, as in the case where the A-line separation is far greater than the lateral resolution, the CNN model cannot discriminate the RIN from the OCT signal. This further emphasizes the need to consider the minimum separation required for the A-lines.

6. Conclusion

In this study, we demonstrated a CNN-based SDE that is trained using speckle patterns generated by a numerical speckle generator. This speckle generator uses a physically realistic noise model that takes the spatial properties of shot noise, RIN, and non-optical noise into account. The SDE was examined using numerically generated OCT speckle patterns along with the experimentally obtained OCT images of two types of scattering phantom and *in vitro* tumor spheroid samples. In these examinations, the SDE's estimation performance was compared with that of our previous CNN-based SDE, which was trained with speckle patterns that did not account for the spatial properties of the noise. All the validation experiments demonstrated the superior estimation

accuracy provided by the new SDE. In particular, the validation using microsphere phantoms demonstrated the excellent agreement of the estimated scatterer density with the ground truth.

In future work, this new SDE can be used in a variety of biomedical application to assess the sub-resolution structural properties of tissues and cells.

Disclosures

T. Seesan, P. Mukherjee, I.A. El-Sadek, Y. Lim, L. Zhu, S. Makita, Y. Yasuno: Sky Technology (F), Nikon (F), Kao Corp. (F), Topcon (F).

Funding

Core Research for Evolutional Science and Technology (JPMJCR2105); Japan Society for the Promotion of Science (21H01836, 22K04962, 22KF0058); Japan Science and Technology Agency (JPMJFS2106); China Scholarship Council (201908130130).

Data, Materials, and Code Availability

Data underlying the results presented in this paper are not publicly available at this time but may be obtained from the authors upon reasonable request.

References

1. D. Huang, E. A. Swanson, C. P. Lin, J. S. Schuman, W. G. Stinson, W. Chang, M. R. Hee, T. Flotte, K. Gregory, C. A. Puliafito, and J. G. Fujimoto, "Optical coherence tomography," *Science* **254**, 1178–1181 (1991).
2. J. G. Fujimoto, C. Pitris, S. A. Boppart, and M. E. Brezinski, "Optical coherence tomography: an emerging technology for biomedical imaging and optical biopsy," *Neoplasia* **2**, 9–25 (2000).
3. J. G. Fujimoto, "Optical coherence tomography for ultrahigh resolution in vivo imaging," *Nat. Biotechnol.* **21**, 1361–1367 (2003).
4. J. Chen and L. Lee, "Clinical applications and new developments of optical coherence tomography: an evidence-based review," *Clin. Exp. Optom.* **90**, 317–335 (2007). PMID: 17697178.
5. S. Liu, "Tissue characterization with depth-resolved attenuation coefficient and backscatter term in intravascular optical coherence tomography images," *J. Biomed. Opt.* **22**, 1 (2017).
6. S. Chang and A. K. Bowden, "Review of methods and applications of attenuation coefficient measurements with optical coherence tomography," *J. Biomed. Opt.* **24**, 1 (2019).
7. Y. Huang, S. Wang, Q. Guo, S. Kessel, I. Rubinoff, L. L.-Y. Chan, P. Li, Y. Liu, J. Qiu, and C. Zhou, "Optical coherence tomography detects necrotic regions and volumetrically quantifies multicellular tumor spheroids," *Cancer Res.* **77**, 6011–6020 (2017).
8. Y. Huang, J. Zou, M. Badar, J. Liu, W. Shi, S. Wang, Q. Guo, X. Wang, S. Kessel, L. L.-Y. Chan, P. Li, Y. Liu, J. Qiu, and C. Zhou, "Longitudinal morphological and physiological monitoring of three-dimensional tumor spheroids using optical coherence tomography," *J. Vis. Exp.* (2020).
9. E. C. C. Cauberg, D. M. de Bruin, D. J. Faber, T. M. de Reijke, M. Visser, J. J. M. C. H. de la Rosette, and T. G. van Leeuwen, "Quantitative measurement of attenuation coefficients of bladder biopsies using optical coherence tomography for grading urothelial carcinoma of the bladder," *J. Biomed. Opt.* **15**, 066013 (2010).
10. Q. Zhao, C. Zhou, H. Wei, Y. He, X. Chai, and Q. Ren, "Ex vivo determination of glucose permeability and optical attenuation coefficient in normal and adenomatous human colon tissues using spectral domain optical coherence tomography," *J. Biomed. Opt.* **17**, 1050041 (2012).
11. B. G. Muller, D. M. de Bruin, M. J. Brandt, W. van den Bos, S. van Huystee, D. J. Faber, D. Savci, P. J. Zondervan, T. M. de Reijke, M. P. Laguna-Pes, T. G. van Leeuwen, and J. J. M. C. H. de la Rosette, "Prostate cancer diagnosis by optical coherence tomography: First results from a needle based optical platform for tissue sampling," *J. Biophotonics* **9**, 490–498 (2016).
12. T. G. van Leeuwen, D. J. Faber, and M. C. Aalders, "Measurement of the axial point spread function in scattering media using single-mode fiber-based optical coherence tomography," *IEEE J. Sel. Top. Quantum Electron.* **9**, 227–233 (2003).
13. S. Stefan, K.-S. Jeong, C. Polucha, N. Tapinos, S. A. Toms, and J. Lee, "Determination of confocal profile and curved focal plane for OCT mapping of the attenuation coefficient," *Biomed. Opt. Express* **9**, 5084 (2018).
14. K. Li, W. Liang, Z. Yang, Y. Liang, and S. Wan, "Robust, accurate depth-resolved attenuation characterization in optical coherence tomography," *Biomed. Opt. Express* **11**, 672 (2020).
15. B. Baumann, C. W. Merkle, R. A. Leitgeb, M. Augustin, A. Wartak, M. Pircher, and C. K. Hitzenberger, "Signal averaging improves signal-to-noise in OCT images: But which approach works best, and when?" *Biomed. Opt. Express* **10**, 5755–5775 (2019).

16. T. Seesan, D. Oida, K. Oikawa, P. Buranasiri, and Y. Yasuno, "Intensity-invariant scatterer density estimation for optical coherence tomography using deep convolutional neural network," *Proc. SPIE, Biomed. Imaging Sens. Conf.* 2020 **11521**, 115210Q (2020).
17. T. Seesan, D. Oida, K. Oikawa, P. Buranasiri, and Y. Yasuno, "Sample and system parameter estimation from local speckle pattern by fully numerically trained deep convolution neural network," *Proc. SPIE, Opt. Coherence Tomogr. Coherence Domain Opt. Methods Biomed.* XXV **11630**, 1163021 (2021).
18. T. Seesan, I. Abd El-Sadek, P. Mukherjee, L. Zhu, K. Oikawa, A. Miyazawa, L. T.-W. Shen, S. Matsusaka, P. Buranasiri, S. Makita, and Y. Yasuno, "Deep convolutional neural network-based scatterer density and resolution estimators in optical coherence tomography," *Biomed. Opt. Express* **13**, 168 (2022).
19. T. R. Hillman, S. G. Adie, V. Seemann, J. J. Armstrong, S. L. Jacques, and D. D. Sampson, "Correlation of static speckle with sample properties in optical coherence tomography," *Opt. Lett.* **31**, 190 (2006).
20. K. Kurokawa, S. Makita, Y.-J. Hong, and Y. Yasuno, "In-plane and out-of-plane tissue micro-displacement measurement by correlation coefficients of optical coherence tomography," *Opt. Lett.* **40**, 2153 (2015).
21. D. P. Kingma and J. Ba, "Adam: a method for stochastic optimization," arXiv:1412.6980 [cs] (2017). ArXiv: 1412.6980.
22. B. W. Pogue and M. S. Patterson, "Review of tissue simulating phantoms for optical spectroscopy, imaging and dosimetry," *J. Biomed. Opt.* **11**, 041102 (2006).
23. A. Mustari, I. Nishidate, M. A. Wares, T. Maeda, S. Kawachi, S. Sato, M. Sato, and Y. Aizu, "Agarose-based Tissue Mimicking Optical Phantoms for Diffuse Reflectance Spectroscopy," *J. Vis. Exp.* p. 57578 (2018).
24. I. Abd El-Sadek, A. Miyazawa, L. Tzu-Wei Shen, S. Makita, S. Fukuda, T. Yamashita, Y. Oka, P. Mukherjee, S. Matsusaka, T. Oshika, H. Kano, and Y. Yasuno, "Optical coherence tomography-based tissue dynamics imaging for longitudinal and drug response evaluation of tumor spheroids," *Biomed. Opt. Express* **11**, 6231 (2020).
25. I. A. El-Sadek, A. Miyazawa, L. T.-W. Shen, S. Makita, P. Mukherjee, A. Lichtenegger, S. Matsusaka, and Y. Yasuno, "Three-dimensional dynamics optical coherence tomography for tumor spheroid evaluation," *Biomed. Opt. Express* **12**, 6844 (2021).
26. E. Li, S. Makita, Y.-J. Hong, D. Kasaragod, and Y. Yasuno, "Three-dimensional multi-contrast imaging of in vivo human skin by Jones matrix optical coherence tomography," *Biomed. Opt. Express* **8**, 1290 (2017).
27. A. Miyazawa, S. Makita, E. Li, K. Yamazaki, M. Kobayashi, S. Sakai, and Y. Yasuno, "Polarization-sensitive optical coherence elastography," *Biomed. Opt. Express* **10**, 5162 (2019).
28. F. Hirschhaeuser, H. Menne, C. Dittfeld, J. West, W. Mueller-Klieser, and L. A. Kunz-Schughart, "Multicellular tumor spheroids: An underestimated tool is catching up again," *J. Biotechnol.* **148**, 3–15 (2010). Organotypic Tissue Culture for Substance Testing.
29. E. C. Costa, A. F. Moreira, D. de Melo-Diogo, V. M. Gaspar, M. P. Carvalho, and I. J. Correia, "3D tumor spheroids: an overview on the tools and techniques used for their analysis," *Biotechnol. Adv.* **34**, 1427–1441 (2016).
30. D. Borycki, M. Hamkało, M. Nowakowski, M. Szkulmowski, and M. Wojtkowski, "Spatiotemporal optical coherence (STOC) manipulation suppresses coherent cross-talk in full-field swept-source optical coherence tomography," *Biomed. Opt. Express* **10**, 2032 (2019).
31. E. Auksorius, D. Borycki, and M. Wojtkowski, "Crosstalk-free volumetric in vivo imaging of a human retina with Fourier-domain full-field optical coherence tomography," *Biomed. Opt. Express* **10**, 6390 (2019).
32. E. Auksorius, D. Borycki, P. Wegrzyn, I. Žičkienė, K. Adomavičius, B. L. Sikorski, and M. Wojtkowski, "Multimode fiber as a tool to reduce cross talk in Fourier-domain full-field optical coherence tomography," *Opt. Lett.* **47**, 838 (2022).
33. L. Zhu, S. Makita, J. Tamaoki, A. Lichtenegger, Y. Lim, Y. Zhu, M. Kobayashi, and Y. Yasuno, "Multi-focus averaging for multiple scattering suppression in optical coherence tomography," *Biomed. Opt. Express* **14**, 4828–4844 (2023).
34. J. M. Schmitt and A. Knüttel, "Model of optical coherence tomography of heterogeneous tissue," *J. Opt. Soc. Am. A* **14**, 1231–1242 (1997).
35. L. Thrane, H. T. Yura, and P. E. Andersen, "Analysis of optical coherence tomography systems based on the extended Huygens–Fresnel principle," *J. Opt. Soc. Am. A* **17**, 484–490 (2000).
36. B. Karamata, P. Lambelet, M. Laubscher, M. Leutenegger, S. Bourquin, and T. Lasser, "Multiple scattering in optical coherence tomography I Investigation and modeling," *J. Opt. Soc. Am. A* **22**, 1369 (2005).
37. P. R. T. Munro, A. Curatolo, and D. D. Sampson, "Full wave model of image formation in optical coherence tomography applicable to general samples," *Opt. Express* **23**, 2541–2556 (2015).
38. P. R. T. Munro, "Three-dimensional full wave model of image formation in optical coherence tomography," *Opt. Express* **24**, 27016–27031 (2016).

Improved Modelling of Detector Response Effects in Phonon-based Crystal Detectors used for Dark Matter Searches

M. J. Wilson,^{1,*} A. Zaytsev,^{1,†} B. von Krosigk,² I. Alkhatib,³ M. Buchanan,³ R. Chen,⁴ M.D. Diamond,³ E. Figueroa-Feliciano,⁴ S.A.S. Harms,³ Z. Hong,³ K.T. Kennard,⁴ N.A. Kurinsky,⁵ R. Mahapatra,⁶ N. Mirabolfathi,⁶ V. Novati,^{4,‡} M. Platt,⁶ R. Ren,³ A. Sattari,³ B. Schmidt,^{4,§} Y. Wang,³ S. Zatschler,^{3,‡} E. Zhang,³ and A. Zuniga³

¹*Institut für Astroteilchenphysik, Karlsruher Institut für Technologie, 76133 Karlsruhe, Germany*

²*Kirchhoff-Institut für Physik, Universität Heidelberg, 69117 Heidelberg, Germany*

³*Department of Physics, University of Toronto, Toronto, ON M5S 1A7, Canada*

⁴*Department of Physics & Astronomy, Northwestern University, Evanston, IL 60208-3112, USA*

⁵*SLAC National Accelerator Laboratory/Kavli Institute for Particle Astrophysics and Cosmology, Menlo Park, CA 94025, USA*

⁶*Department of Physics and Astronomy, and the Mitchell Institute for Fundamental Physics and Astronomy, Texas A&M University, College Station, TX 77843, USA*

(Dated: March 5, 2024)

Various dark matter search experiments employ phonon-based crystal detectors operated at cryogenic temperatures. Some of these detectors, including certain silicon detectors used by the SuperCDMS collaboration, are able to achieve single-charge sensitivity when a voltage bias is applied across the detector. The total amount of phonon energy measured by such a detector is proportional to the number of electron-hole pairs created by the interaction. However, crystal impurities and surface effects can cause propagating charges to either become trapped inside the crystal or create additional unpaired charges, producing non-quantized measured energy as a result. A new analytical model for describing these detector response effects in phonon-based crystal detectors is presented. This model improves upon previous versions by demonstrating how the detector response, and thus the measured energy spectrum, is expected to differ depending on the source of events. We use this model to extract detector response parameters for SuperCDMS HVeV detectors, and illustrate how this robust modelling can help statistically discriminate between sources of events in order to improve the sensitivity of dark matter search experiments.

I. INTRODUCTION

Cryogenic solid-state detectors are used in a number of dark matter (DM) search experiments [1–6]. In these experiments, incoming DM particles are expected to scatter off of the detector nuclei or electrons, creating phonon signals which are measured by high resolution phonon sensors. Resolution on the order of 1 eV is achieved, which allows for reduced energy thresholds and enables the detection of nuclear recoils with energies as low as ~ 10 eV [1–3]. Low-mass DM candidates that produce small interaction energies can be probed via electron recoils by measuring the ionization signal — the number of produced e^-h^+ pairs in the detector [7, 8]. In phonon-based crystal detectors, when a voltage bias is applied across the crystal, the ionization signal is converted into an amplified phonon signal via the Neganov-Trofimov-Luke (NTL) effect [9, 10]. A charge carrier with a charge e accelerated by the electric field scatters off of the crystal lattice and produces NTL phonons with the total energy equal to the work done by the electric field to move the charge through the electric potential difference $\Delta\varphi$:

$$E_{\text{NTL}} = e \Delta\varphi. \quad (1)$$

Normally, when an e^-h^+ pair is created in the crystal, each charge drifts in the electric field all the way to the corresponding electrode on the crystal surface. Together they traverse the entire voltage bias of the detector, so the total energy of the produced NTL phonons is given by:

$$E_{\text{NTL}} = n_{\text{eh}} e V_{\text{bias}}, \quad (2)$$

where n_{eh} is the number of e^-h^+ pairs and V_{bias} is the voltage bias. The total phonon energy produced in an event is then given by:

$$E_{\text{ph}} = E_{\text{dep}} + n_{\text{eh}} e V_{\text{bias}}, \quad (3)$$

where E_{dep} is the energy deposited in the detector by the incoming particle. For a detector with a good phonon energy resolution σ_{res} and a large voltage bias, where $\sigma_{\text{res}} \ll e V_{\text{bias}}$, the spectrum of the phonon energy in Eq. 3 is expected to have quantized peaks corresponding to the integer number of created e^-h^+ pairs. This e^-h^+ -pair quantization is observed in SuperCDMS high-voltage (HV) and HV eV-scale (HVeV) detectors when operated with a voltage bias on the order of 100 V [7, 8, 11].

Due to the presence of impurities in the crystal, non-quantized amount of NTL energy can be produced in an event. We distinguish two categories of effects causing non-quantized NTL energy: charge trapping (CT) and impact ionization (II). In a CT process, a charge carrier gets trapped in an impurity state in the bulk of the crystal. In an II process, a propagating charge ejects (or

* matthew.wilson@kit.edu

† alexander.zaytsev@kit.edu

‡ Presently at LPSC, CNRS, Université Grenoble Alpes, Grenoble, France

§ Presently at IRFU, CEA, Université Paris-Saclay, France

“ionizes”) an additional unpaired charge from a shallow impurity state. Trapped charge carriers and unpaired charge carriers created in an II process terminate or start their trajectories in the bulk of the detector, respectively. As a result, they traverse only a fraction of the voltage bias, producing a non-quantized amount of NTL energy.

A proper modelling of these detector response effects is crucial for DM search analyses. In Section II, we develop an analytical model (the so-called “exponential CTII” model) that describes the NTL energy spectrum for events affected by the CT and II processes. We improve upon the previously used CT and II model introduced in Ref. [12] (the so-called “flat CTII” model) by taking into account the distribution of locations at which the CT and II processes occur. We demonstrate a difference between the NTL energy spectra of events produced on the detector surface and events produced in the detector bulk that can be used for statistical discrimination between surface background and bulk DM events. In Section III, we incorporate the CT and II model into the full detector response model, and take into account additional surface effects that may be relevant to certain calibration data. This modelling is used in Section IV to extract detector response parameters for HVeV detectors.

II. EXPONENTIAL CTII MODEL

The underlying physical assumption of the exponential CTII model is that there are three possible processes that can occur to a charge carrier (an electron or a hole) when it traverses the bulk of the crystal under the influence of an electric field. It can get trapped in an impurity state, it can create a single free electron from an impurity state by promoting it into the conduction band, or it can promote an electron from the valence band to an impurity state, creating a single hole in the valence band. The probabilities for these processes to occur may differ between holes and electrons; therefore we consider in the model a total of six different CT and II processes: electron trapping (“CTe”), hole trapping (“CTh”), creation of a hole by an electron (“IIeh”), creation of an electron by an electron (“IIee”), creation of an electron by a hole (“IIhe”) and creation of a hole by a hole (“IIhh”).

The model assumes that each of the six processes has a small constant probability of occurring at any point of the charge carrier’s trajectory, independent of the location in the bulk of the crystal, of the path already travelled by the charge, and the presence of other charges simultaneously traversing the crystal. Additionally, it is assumed that charges propagate along some z axis that is parallel to a uniform electric field (detectors, including the HVeV detectors used in Refs. [7, 8], are typically designed to have a uniform electric field throughout the bulk). We start by considering that impurities are distributed uniformly throughout the bulk of the crystal, where we let p_i denote the probability for a charge to

undergo a certain process i per unit of distance travelled along the z axis. Here, i refers to the specific CT or II process a charge may undergo (CTe, CTh, IIee, IIeh, IIhe, or IIhh). p_i itself may depend on various factors, including the impurity density and the amount of charge diffusion. If a charge travels a distance Δz in n steps, the total probability of the charge *not* undergoing some CT or II process $\bar{C}_i(\Delta z)$ is $(1 - p_i \Delta z/n)^n$. In the limit of infinitesimally small step sizes, $\bar{C}_i(\Delta z)$ becomes:

$$\begin{aligned} \bar{C}_i(\Delta z) &= \lim_{n \rightarrow \infty} \left(1 - p_i \frac{\Delta z}{n}\right)^n \\ &= e^{-p_i \Delta z} \\ &= e^{-\Delta z/\tau_i}, \end{aligned} \quad (4)$$

where the p_i term in Eq. 4 is replaced with $1/\tau_i$, with τ_i defining the characteristic length of that particular CT or II process. $\bar{C}_i(\Delta z)$ is the complementary cumulative distribution function of the probability density function (PDF) that describes the probability for a charge to travel a distance Δz before a particular CT or II process occurs. This PDF is therefore given by:

$$\begin{aligned} P_i(\Delta z) &= \frac{d}{d(\Delta z)} (1 - \bar{C}_i(\Delta z)) \\ &= \frac{d}{d(\Delta z)} \left(1 - e^{-\Delta z/\tau_i}\right) \\ &= \frac{1}{\tau_i} e^{-\Delta z/\tau_i}. \end{aligned} \quad (5)$$

While these PDFs are described in terms of a distance travelled, the model also imposes the condition that the charges terminate when reaching the crystal surface. That means for a crystal with a thickness Z , the charges are bound between $z = 0$ and $z = Z$. For convenience we choose $Z = 1$, and let z describe the proportion of the crystal thickness rather than a physical distance. The six characteristic lengths τ_i measured in fractions of the crystal thickness are the only fundamental input parameters of the model. We write these characteristic lengths in terms of probabilities f_i defined as:

$$f_i \equiv \int_0^1 P_i(\Delta z) d(\Delta z) = 1 - e^{-1/\tau_i}. \quad (6)$$

Hence f_i is the probability of a particular process occurring if a charge can traverse the entire length of the detector. Equations 5 and 6 are repeated for each of the six processes, and together make up the fundamental building blocks of our exponential CTII model.

The end product of the model is a PDF of the NTL energy produced in an event. This energy is proportional to the distance travelled by the charges along the field lines. We adopt an energy scale E_{neh} such that a unit of E_{neh} is equivalent to the amount of NTL energy produced by a charge that travels a distance equal to the thickness

of the crystal. Using this energy scale, a charge going from $z = 0$ to $z = 1$, as well as an e^-h^+ pair starting at $z = 0.5$ whereby both charges travel a distance $\Delta z = 0.5$, will result in a total energy of $E_{\text{neh}} = 1$. With such units, there is a one-to-one correspondence between the PDFs of the total NTL energy and the total distance travelled by the charges along the electric field.

The exponential CTII model is constructed by finding the analytical solutions for the NTL energy produced by a single e^-h^+ pair for events of three distinct classes. The first are surface events, where a single charge is created at one of the surfaces (i.e. along the $z = 0$ or $z = 1$ plane) and propagates toward the opposite surface; this class of events does not include events created along the lateral surfaces of the crystal. Surface events correspond to laser or LED calibration data, whereby optical photons are absorbed near the $z = 0$ or $z = 1$ surface of the crystal, as well as to charge leakage originating at the crystal surface. The second class of events are single charges produced throughout the bulk of the crystal. These events may correspond to some charge leakage process that happens throughout the detector bulk. The third class of events are bulk- e^-h^+ pairs produced throughout the bulk of the crystal. These events are what is expected for DM interactions. For each class of events, we consider various unique combinations of CT and II processes occurring to the charges, and solve for the probabilities of measuring an energy of E_{neh} given those unique combinations of processes.

Modelling multiple II processes in a single event poses a significant challenge: each additional II process allowed adds an new charge carrier, causing the number of potential combinations of CT and II processes to grow exponentially, and the complexity of each new solution greatly increases. For this reason, we limit the number of solutions to a certain “order” of processes, where the order of a process is defined as follows: for processes of order N , charges that participated or were produced in a primary II process can take part in no more than $(N - 1)$ additional II processes. For surface events and bulk-single-charge events, the solutions for processes up to second order are found, resulting in 28 unique solutions for each event type. For bulk- e^-h^+ -pair events, the solutions for processes up to first order are found, resulting in 16 unique solutions. When solving for these analytical solutions, we assume that any charges existing after the order limit is reached will propagate to a crystal surface with 100% probability. Appendix A provides a detailed description of how these solutions are found, with Appendix A 1, Appendix A 2, and Appendix A 3 adding further details on solving the solutions for each of the three classes of events. The full list of process combinations and the corresponding solutions are catalogued in the supplement documentation and are displayed in Fig. 1. It is immediately apparent how the computed PDFs differ for the different classes of events. Namely, the regions above and below the first e^-h^+ -pair peak are relatively flat for surface events, in contrast to bulk-

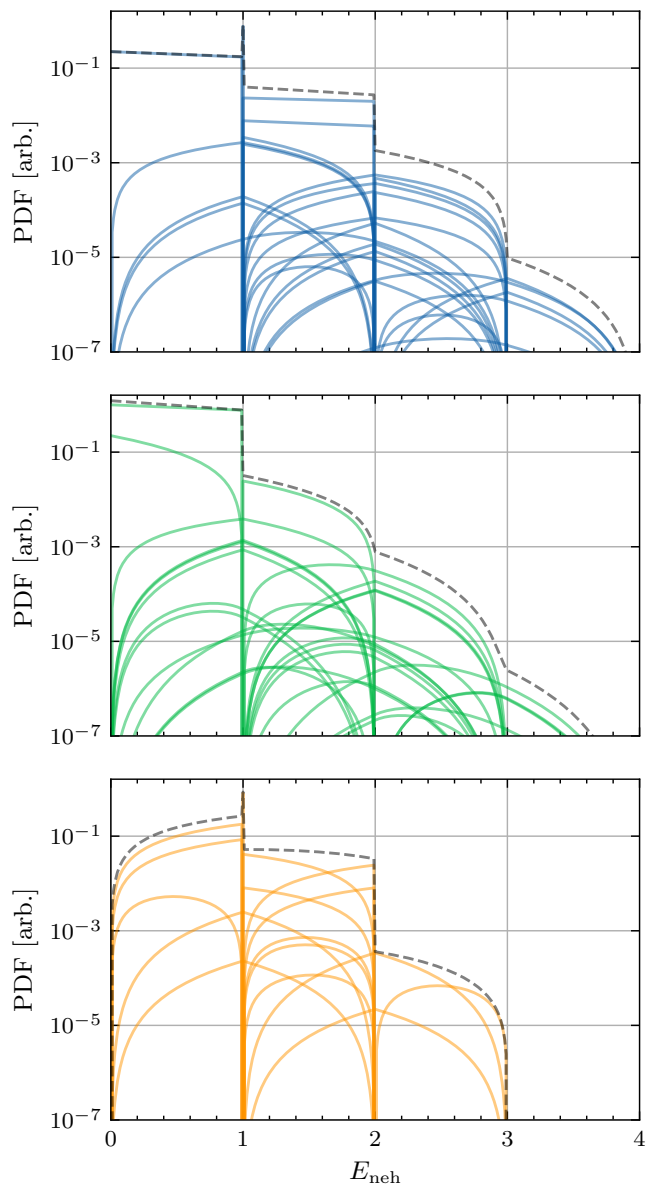


FIG. 1. Analytical solutions in the E_{neh} energy space of the exponential CTII model for single- e^-h^+ -pair events. The unique solutions represented by the solid, coloured curves are found for surface events (top), bulk-single-charge events (middle), and bulk- e^-h^+ -pair events (bottom). This example is shown for arbitrary values of the CT and II parameters: $f_{\text{CTe}} = 20\%$, $f_{\text{CTh}} = 10\%$, $f_{\text{Ilee}} = 1\%$, $f_{\text{IIeh}} = 3\%$, $f_{\text{IIhe}} = 1\%$, and $f_{\text{IIhh}} = 5\%$, and the top and middle plots assume that the initial charge is an electron. The black, dashed curves in each plot are the sums of the analytical solutions for each event type and are examples of $F_{\text{type}}^{(1)}(E_{\text{neh}})$, the one- e^-h^+ -pair PDF.

e^-h^+ -pair events where the PDF in the same regions is more curved. Furthermore, the PDF for bulk-single-charge events does not have a delta function at $E_{\text{neh}} = 1$.

The analytical solutions are found for when there is ini-

tially only a single charge or e^-h^+ pair produced. However large energy depositions in the crystal will often produce multiple charges or e^-h^+ pairs for a single event. Let $F_{\text{type}}^{(1)}(E_{\text{neh}})$ be the probability distribution function for one charge or e^-h^+ pair in the n_{eh} -energy space. The “type” refers to the specific event type to model: either surface events, bulk-single-charge events, or bulk- e^-h^+ -pair events. $F_{\text{type}}^{(1)}(E_{\text{neh}})$ is found by summing the analytical solutions for the given event type, and examples of this function are shown by the black, dashed curves in Fig. 1. Without any additional detector response, the PDF for j e^-h^+ pairs $F_{\text{type}}^{(j)}(E_{\text{neh}})$ is found by convolving $F_{\text{type}}^{(1)}(E_{\text{neh}})$ with itself $(j-1)$ times:

$$F_{\text{type}}^{(j)}(E_{\text{neh}}) = F_{\text{type}}^{(j-1)}(E_{\text{neh}}) * F_{\text{type}}^{(1)}(E_{\text{neh}}). \quad (7)$$

In practice, $F_{\text{type}}^{(j)}(E_{\text{neh}})$ is found using numerical convolution. We can use this to construct the PDF for events that generate multiple e^-h^+ pairs, defined as $H(E_{\text{neh}})$. The solution for $H(E_{\text{neh}})$ up to J e^-h^+ pairs is given by:

$$H(E_{\text{neh}}) = \sum_{j=1}^J a_j \cdot F_{\text{type}}^{(j)}(E_{\text{neh}}), \quad (8)$$

where a_j are the weights associated with producing j e^-h^+ pairs, which are discussed more in Section III. A comparison of the single- and multi- e^-h^+ -pair PDFs for different event types is shown in Fig. 2 for arbitrary CT and II probabilities. Furthermore, the solutions are compared to the PDFs computed using the flat CTII model described in Ref. [12].

The example PDFs from Fig. 2 allow us to make some broad observations about the exponential CTII model. First, while the higher-order processes are significant for the single- e^-h^+ -pair solutions (as seen in the top plot of Fig. 2 above $E_{\text{neh}} = 2$), they generally become less significant or even negligible for multi- e^-h^+ -pair solutions. Second, the type of events being modelled has a significant impact on the shape of the PDFs between the e^-h^+ -pair peaks. Notably, the between-peak shape for the bulk e^-h^+ -pair events differs greatly to that of surface events, as well as that of the flat CTII model which does not differentiate between event types.

III. EXTENDED DETECTOR RESPONSE MODEL

A. Single- and Multi-Hit Solutions

Equation 8 describes the PDF of producing a certain amount of NTL energy for a given event type that generates multiple e^-h^+ pairs, $H(E_{\text{neh}})$, which is derived from the analytical solutions of the exponential CTII model. However $H(E_{\text{neh}})$ can be extended to include other detector response effects that are either measured or expected.

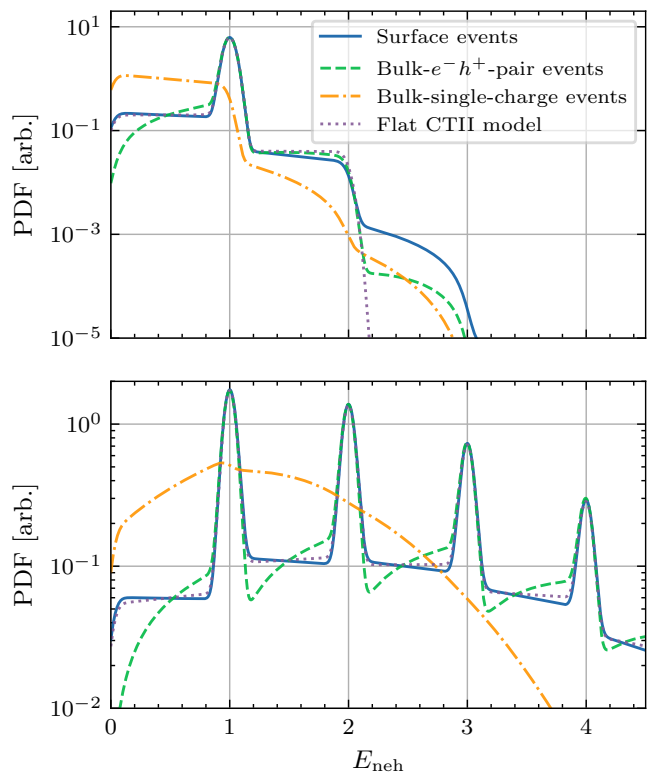


FIG. 2. Example PDFs found for single- e^-h^+ -pair events (top) and multi- e^-h^+ -pair events (bottom). The PDFs are computed for surface events (solid, blue curves), bulk- e^-h^+ -pair events (dashed, green curves), and bulk-single-charge events (dot-dash, orange curves) using the exponential CTII model. For comparison, the PDFs computed using the flat CTII model from Ref. [12] are shown by the dotted, purple curves. These examples are shown for arbitrary CT and II parameters: $f_{CTe} = f_{CTh} = 20\%$ and $f_{IIee} = f_{IIeh} = f_{IIhe} = f_{IIhh} = 2\%$; for the flat CTII model, $f_{CT} = 20\%$ and $f_{II} = 4\%$. Furthermore, the multi- e^-h^+ -pair solutions assume that the e^-h^+ -pair probabilities follow a Poisson distribution with a mean of 2 e^-h^+ pairs. For illustrative purposes, the PDFs are convolved with a Gaussian function with a width of $E_{\text{neh}} = 0.05$ to emulate the detector energy resolution.

These additional effects include ionization probabilities, conversion to the phonon energy scale, and continuous spectra of energy deposition. To start, we define $H^{(1)}$ as the PDF for events resulting from a single interaction of a particle with the crystal, which we call “single-hit” events. Examples of a single-hit event include a single photon absorbed by the crystal, or a single DM particle scattering off of an electron. First we will construct a general formula for $H^{(1)}$, and then subsequently see how this formula is used to model specific interactions from various sources.

The first step to extend the detector response model is to replace the generic weights a_j in Eq. 8 with the probability mass function (PMF) describing the probability of

producing a given amount of ionization. The ionization PMF is specific to the detector material, and is a function of the energy deposited in the detector E_{dep} . Let $p_{\text{eh}}(j | E_{\text{dep}})$ describe the ionization probability of producing j e^-h^+ pairs given E_{dep} . For silicon, results of the ionization yield at low energies can be found in Ref. [13].

Next we need to convert the PDFs to the correct energy scale. As mentioned in Sec. I, event energies are measured by the total phonon energy E_{ph} described by Eq. 3, whereas the $F_{\text{type}}^{(1)}$ functions of the exponential CTII model are described in the n_{eh} -energy space E_{neh} . Using Eq. 3, E_{neh} can be written in terms of E_{ph} as:

$$E_{\text{neh}} = \frac{E_{\text{ph}} - E_{\text{dep}}}{eV_{\text{bias}}}. \quad (9)$$

This change in energy units also changes the overall scaling of the PDFs. To account for this, the PDFs must be scaled by a factor of $|dE_{\text{neh}}/dE_{\text{ph}}| = 1/eV_{\text{bias}}$. Finally, we need to consider the general case where there is a continuum of energy depositions that can occur for a given source of events. This continuum can be described by a *normalized* differential rate spectrum $d\bar{R}/dE_{\text{dep}}(E_{\text{dep}})$, where for a total single-hit event rate of R_{tot} , $d\bar{R}/dE_{\text{dep}}(E_{\text{dep}}) = 1/R_{\text{tot}} \cdot dR/dE_{\text{dep}}(E_{\text{dep}})$. Putting this all together, the extended detector response model for single-hit events in the phonon energy space modelled up to J e^-h^+ pairs is given as:

$$H^{(1)}(E_{\text{ph}}) = \sum_{j=1}^J \left(\int_0^\infty dE_{\text{dep}} p_{\text{eh}}(j | E_{\text{dep}}) \times \frac{F_{\text{type}}^{(j)} \left(\frac{E_{\text{ph}} - E_{\text{dep}}}{eV_{\text{bias}}} \right)}{eV_{\text{bias}}} \frac{d\bar{R}}{dE_{\text{dep}}}(E_{\text{dep}}) \right). \quad (10)$$

Here we assume that J is large enough such that the ionization PMF sums to unity for all E_{dep} . As the $d\bar{R}/dE_{\text{dep}}(E_{\text{dep}})$ function in Eq. 10 is normalized, $H^{(1)}(E_{\text{ph}})$ is describing a PDF for single-hit events from a given source. We also consider so-called ‘‘multi-hit’’ events, which are events generated from simultaneous particle interactions in the detector. In general, the PDF solutions for multi-hit events are found by recursively convolving the single-hit solution from Eq. 10. An example of constructing a multi-hit PDF solution is shown in Section. III A 1.

Up to this point, the detector response model has been described without considering the detector energy resolution σ_{res} . While σ_{res} can be incorporated into the model in different ways, this work assumes that the energy resolution is constant over E_{ph} . Therefore the single-hit model including the energy resolution $H^{(1)}(E_{\text{ph}}, \sigma_{\text{res}})$ can be expressed as:

$$H^{(1)}(E_{\text{ph}}, \sigma_{\text{res}}) = H^{(1)}(E_{\text{ph}}) * G(E_{\text{ph}} | \mu = 0, \sigma_{\text{res}}), \quad (11)$$

where $G(E_{\text{ph}} | \mu = 0, \sigma_{\text{res}})$ is a Gaussian function with a mean $\mu = 0$ and width of σ_{res} . One could also consider,

for example, an energy resolution that depends on n_{eh} . In which case, a Gaussian function with a width equal to the energy resolution at each e^-h^+ -pair peak $\sigma_{\text{res}}^{(j)}$ would be convolved with the corresponding $F_{\text{type}}^{(j)}$ function.

1. Photon-Calibration Events

A typical way to calibrate the energy of HVeV detectors is to use a photon source. Specifically in Refs. [7, 8], a laser source of optical photons was pointed at one of the detector surfaces. The laser was pulsed at some known frequency f_γ , and, depending on the laser intensity, produced an average number of photons per pulse λ that are detected. The probability of a given number of photons per laser event is given by a Poisson distribution with a mean of λ . These photon-calibration events are therefore examples of multi-hit events, where the probability distribution must also account for the probability of the simultaneous absorption of multiple photons in a single event. The differential rate $dR/dE_{\text{ph}}(E_{\text{ph}})$ for photon-calibration events is then given by:

$$\frac{dR}{dE_{\text{ph}}}(E_{\text{ph}}) = f_\gamma \sum_{l=0}^L \text{Pois}(l | \lambda) H^{(l)}(E_{\text{ph}}), \quad (12)$$

where $H^{(l)}(E_{\text{ph}})$ corresponds to the NTL energy produced in an event with $l \leq L$ photons absorbed. $H^{(0)}(E_{\text{ph}})$ corresponds to events with no photons absorbed. Such events may be present in the calibration data if the detector trigger is synchronized with the laser pulses and λ is small. In the simplest scenario, $H^{(0)}(E_{\text{ph}}) = \delta(E_{\text{ph}})$. However the zeroth- e^-h^+ -pair peak can also take a more complex form, like the modified Gaussian noise peak described in Ref. [12]. $H^{(1)}(E_{\text{ph}})$ corresponds to events with one photon absorbed and is generally given by Eq. 10. $H^{(l)}(E_{\text{ph}})$ with $l > 1$ is calculated recursively as $H^{(l)}(E_{\text{ph}}) = H^{(l-1)}(E_{\text{ph}}) * H^{(1)}(E_{\text{ph}})$.

For photon-calibration events, we assume that the photons are absorbed sufficiently close to a detector surface such that these events can effectively be modelled as surface events created along the $z = 0$ or $z = 1$ plane. Furthermore for a spectrum of photon energies E_γ , $d\bar{R}/dE_{\text{dep}} = d\bar{R}/dE_\gamma$. For an LED source, $d\bar{R}/dE_\gamma$ is the normalized energy spectrum of the LED photons. Yet for a laser source like in Refs. [7, 8], the photons are monoenergetic, and therefore $d\bar{R}/dE_{\text{dep}} = \delta(E_{\text{dep}} - E_\gamma)$. Moreover the laser used for the calibration in Refs. [7, 8] produced 1.95 eV photons which, for silicon, always ionize exactly 1 e^-h^+ -pair per absorbed photon [13]. Photons of this energy have an absorption length in silicon of $\mathcal{O}(10 \mu\text{m})$ which, for a detector that is 4 mm thick [8], is sufficiently small to model these events as surface events. For this particular case, Eq. 10 reduces to:

$$H^{(1)}(E_{\text{ph}}) = \frac{F_{\text{surf}}^{(1)} \left(\frac{E_{\text{ph}} - E_\gamma}{eV_{\text{bias}}} \right)}{eV_{\text{bias}}}. \quad (13)$$

Again if we assume a constant energy resolution σ_{res} , Eq. 12 is convolved with a Gaussian function with a mean $\mu = 0$ and a width of σ_{res} in order to compute $dR/dE_{\text{ph}}(E_{\text{ph}})$ with the energy resolution. The distinction between single-hit and multi-hit events displayed here is subtle yet important. For the case of low-energy photon-calibration events, the multi- e^-h^+ -pair peaks observed is not due to multiple e^-h^+ pairs ionized from a single absorbed photon, but rather simultaneously absorbed photons that each ionize a single e^-h^+ pair.

2. Dark Matter Events

For any dark matter search experiment, a detector response model is required to determine the expected signal distribution of a DM candidate in the detector. Therefore Eq. 10 can also be used to compute expected DM signals in HVeV detectors. Unlike photon-calibration events, DM interactions are considered to be single-hit events; generally DM models exclude the possibility of the simultaneous interaction of multiple DM particles with a detector. While the exact signal distribution will depend on the specific DM candidate that is modelled, we will look at examples of two DM candidates commonly searched for using HVeV detectors.

The first candidate is the dark photon that is modelled, for example, in Ref. [14]. In this model, non-relativistic dark photons with a mass $m_{A'}$ constitute all relic dark matter. The interaction rate of dark photon absorption $R_{A'}(m_{A'}, \varepsilon)$ depends on its mass and is proportional to the kinetic mixing parameter ε that couples dark photons to standard model photons. In this model dark photons provide a monoenergetic source of energy deposition equal to its mass such that $d\bar{R}/dE_{\text{dep}} = \delta(E_{\text{dep}} - m_{A'}c^2)$, where c is the speed of light. Substituting this into Eq. 10 and noting that DM interactions are modelled as bulk- e^-h^+ -pair events, the differential rate of dark photon absorption $dR_{A'}/dE_{\text{ph}}(E_{\text{ph}})$ is given by:

$$\begin{aligned} \frac{dR_{A'}}{dE_{\text{ph}}}(E_{\text{ph}}) &= R_{A'}(m_{A'}, \varepsilon)H^{(1)}(E_{\text{ph}}) \\ &= R_{A'}(m_{A'}, \varepsilon) \left(\sum_{j=1}^J p_{\text{eh}}(j | m_{A'}c^2) \times \right. \\ &\quad \left. \frac{1}{eV_{\text{bias}}} F_{\text{bulk-eh}}^{(j)} \left(\frac{E_{\text{ph}} - m_{A'}c^2}{eV_{\text{bias}}} \right) \right). \end{aligned} \quad (14)$$

The second candidate we consider is light DM that elastically scatters off of electrons, as described in Ref. [15]. In this model, the dark matter particle χ with mass m_χ is also assumed to constitute all relic DM, and scattering interactions with electrons are mediated via a dark-sector gauge boson. The total rate of DM-electron scattering interactions $R_\chi(m_\chi, \bar{\sigma}_e)$ is dependent on the DM mass as well as the effective DM-electron scattering cross section $\bar{\sigma}_e$. However, this DM-electron scattering

process produces a spectrum of recoil energies E_r . Specifically in Ref. [15], the recoil spectra are provided as rates over discrete recoil energy bins. Therefore the integral of $d\bar{R}/dE_{\text{dep}}$ in Eq. 10 is replaced by a sum over weights w_k corresponding to the recoil energies $E_r^{(k)}$, where the weights are normalized such that $\sum_k w_k = 1$. The differential rate of DM-electron scattering $dR_\chi/dE_{\text{ph}}(E_{\text{ph}})$ is then given by:

$$\begin{aligned} \frac{dR_\chi}{dE_{\text{ph}}}(E_{\text{ph}}) &= R_\chi(m_\chi, \bar{\sigma}_e)H^{(1)}(E_{\text{ph}}) \\ &= R_\chi(m_\chi, \bar{\sigma}_e) \left(\sum_{j=1}^J \sum_k p_{\text{eh}}(j | E_r^{(k)}) \times \right. \\ &\quad \left. \frac{w_k}{eV_{\text{bias}}} \cdot F_{\text{bulk-eh}}^{(j)} \left(\frac{E_{\text{ph}} - E_r^{(k)}}{eV_{\text{bias}}} \right) \right). \end{aligned} \quad (15)$$

The different rate functions in Eqs. 14 and 15 do not yet include the detector energy resolution. As before we assume that σ_{res} is constant over E_{ph} , and therefore the energy resolution is incorporated by convolving Eqs. 14 and 15 with a Gaussian function with a mean $\mu = 0$ and a width of σ_{res} .

B. Non-ionizing Energy Deposition

The detector response model can be extended further by modelling other phenomena that are observed in the detector. One such phenomenon is the apparent deposition of non-ionizing energy measured together with photon-calibration events. We surmise that this detector response effect occurs in HVeV detectors because of the observed dependence of the e^-h^+ -pair peak positions on λ , the average number of photons per laser or LED pulse [16]. One hypothesis is that some proportion of photons are absorbed directly into the aluminum fins of the phonon sensors. Another hypothesis is that, due to the random initial trajectory of electrons and holes after ionizing, there is some probability that both charges will happen to recombine at the nearest detector surface. This so-called surface trapping effect has been observed in detector simulations using G4CMP [17, 18], and is illustrated in the top plot of Fig. 3. In any case, these hypotheses suppose that some proportion of photons will deposit some non-ionizing energy without generating a typical e^-h^+ pair that undergoes the bulk CT and II processes.

In the case of the hypothesized surface trapping effect, we can include this effect in the model by modifying the single-hit PDF for photon-calibration events described by Eq. 13. Let α be the probability of the created e^-h^+ pair to undergo surface trapping, where $0 \leq \alpha \leq 1$. That means there is a $(1 - \alpha)$ probability that the e^-h^+ pair will propagate through the crystal, undergoing the typical bulk CT and II processes. For photons that undergo surface trapping, the deposited energy will only be the

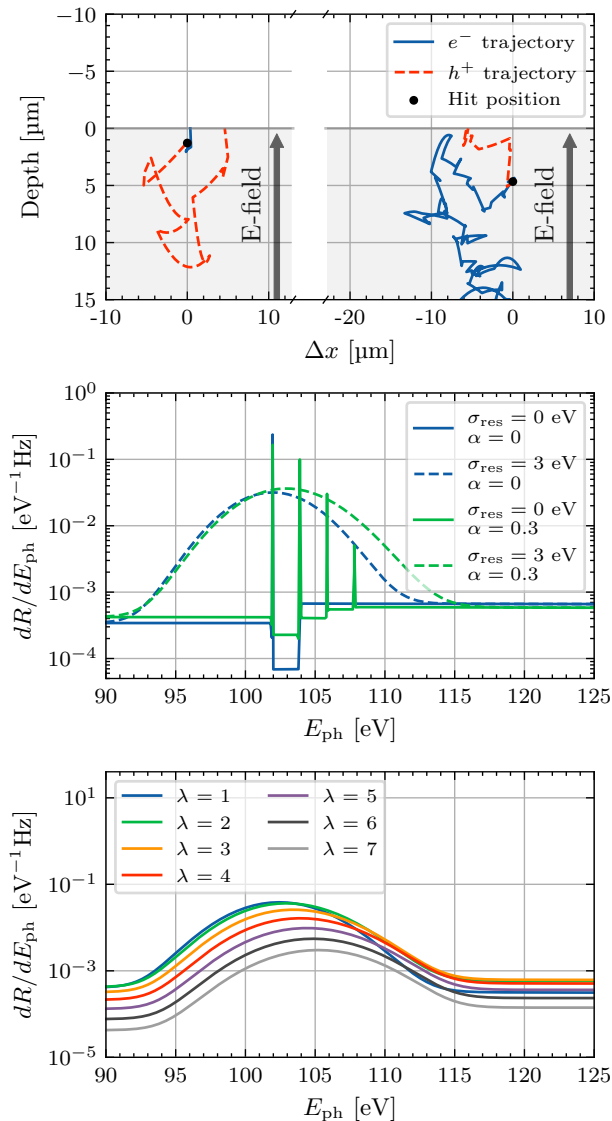


FIG. 3. (top): Illustration of the hypothesized surface trapping effect as observed from simulation data using G4CMP [17, 18]. Two examples are shown of the trajectory of an ionized e^-h^+ pair in terms of the depth below the detector surface and the perpendicular x -coordinate relative to the hit position of the absorbed photon. The right example shows a typical event, where the electron eventually travels in the direction opposing the electric field. The left example shows a surface-trapped event, where the electron recombines with the detector surface before it can turn around. (middle and bottom): Examples of modelling the surface trapping effect using Eq. 16 and 12 with $V_{\text{bias}} = 100$ V, $E_\gamma = 1.95$ eV, $f_\gamma = 1$ Hz, and arbitrary CT and II probabilities. The additional spikes seen in the middle plot demonstrate the contribution of non-ionizing energy deposition when $\alpha > 0$ which, when smeared by the energy resolution, widen and shift the e^-h^+ -pair peaks. This effect also causes a peak position dependence on λ , as demonstrated by the bottom plot with $\alpha = 0.3$.

absorption energy of the photon E_γ . We are then able to

include the surface trapping effect by modifying Eq. 13 in the following way:

$$\begin{aligned}
 H^{(1)}(E_{\text{ph}}) &\rightarrow \alpha\delta(E_{\text{ph}} - E_\gamma) + (1 - \alpha)H^{(1)}(E_{\text{ph}}) \\
 &= \alpha\delta(E_{\text{ph}} - E_\gamma) \\
 &\quad + \frac{(1 - \alpha)}{eV_{\text{bias}}} F_{\text{surf}}^{(1)}\left(\frac{E_{\text{ph}} - E_\gamma}{eV_{\text{bias}}}\right).
 \end{aligned} \tag{16}$$

The multi-hit solution for photon-calibration data with the surface trapping effect is given by Eq. 12, where $H^{(l)}(E_{\text{ph}})$ is found by recursively convolving Eq. 16 with itself. The result of including the surface trapping effect in the detector response model is illustrated in the bottom two plots of Fig. 3. Due to the presence of non-ionizing photons, each peak in the spectrum splits into multiple sub-peaks separated by E_γ , as seen in the middle plot of Fig. 3 before resolution smearing. Each sub-peak corresponds to q ionizing photons and p non-ionizing photons, with the sub-peak location defined as $q \cdot eV_{\text{bias}} + (q + p) \cdot E_\gamma$. Note that a sub-peak corresponding to p and q is part of the function $H^{(q+p)}(E_{\text{ph}})$, rather than of the function $H^{(q)}(E_{\text{ph}})$. Therefore, in order to properly model the sub-structure of the q^{th} e^-h^+ -pair peak, modelling of higher e^-h^+ -pair peaks is required. When normalized, the underlying amplitudes of the sub-peaks in each e^-h^+ -pair peak follow a Poisson distribution of the number of non-ionizing photons with a mean of $\alpha \cdot \lambda$ (see Appendix B for more details). To include all the significant sub-peaks, it is recommended to set the maximum number of modelled peaks (L in Eq. 12) to a number exceeding the number of peaks in the region of interest by the mean number of non-ionizing photons plus at least 3 standard deviations of its distribution, i.e. by $(\alpha \cdot \lambda) + 3 \cdot \sqrt{(\alpha \cdot \lambda)}$.

When the energy resolution is applied, the peak sub-structure from non-ionizing photons gets smeared and appears as a shift and a widening of the e^-h^+ -pair peaks, as shown in the bottom two plots of Fig. 3. When λ increases, there is a greater contribution from non-ionizing photons, resulting in wider peaks that are shifted by a larger amount.

IV. RESULTS

To demonstrate the performance of the exponential CTII and extended detector response model described in Secs. II and III, we fit the model to laser-calibration data acquired from Ref. [8]. Specifically, the model for photon-calibration events described by Eq. 12–13 is fit to laser-calibration datasets from Ref. [8] acquired with $V_{\text{bias}} = 100$ V and $E_\gamma = 1.95$ eV. The individual datasets differ by the laser intensity used during data acquisition, and thus by the value of λ . The fits of the model to two of these datasets are shown in Fig. 4. For simplicity, we reduced the number of parameters in the fits by

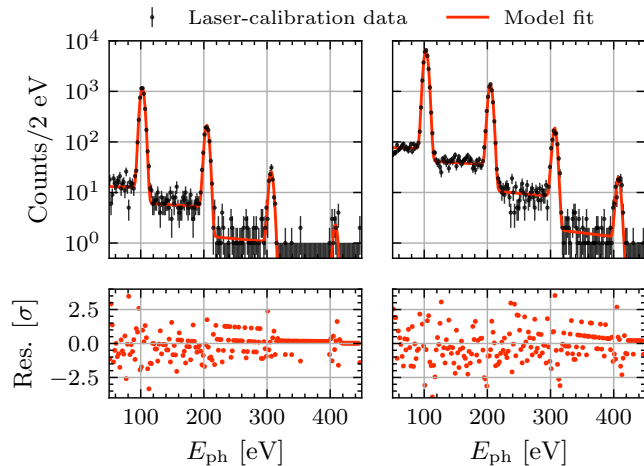


FIG. 4. Results of fitting the exponential CTII and extended detector response model to two laser-calibration datasets from Ref. [8] acquired with $V_{\text{bias}} = 100$ V and $E_{\gamma} = 1.95$ eV. The residuals from the fit results are shown in the bottom plots.

requiring:

$$\begin{aligned} f_{\text{CTe}} &= f_{\text{CTh}} \equiv f_{\text{CT}}, \\ f_{\text{Ilee}} &= f_{\text{Ileh}} = f_{\text{Iihe}} = f_{\text{Iihh}} \equiv \frac{f_{\text{II}}}{2}. \end{aligned} \quad (17)$$

We obtain the best-fit results from the fit to the left (right) laser-calibration dataset in Fig. 4 of $\lambda = 0.41 \pm 0.01$ (0.475 ± 0.005), $\sigma_{\text{res}} = 3.30 \pm 0.04$ eV (3.37 ± 0.02 eV), $f_{\text{CT}} = 11.6 \pm 0.6\%$ ($12.1 \pm 0.3\%$), and $f_{\text{II}} = 0.7 \pm 0.4\%$ ($0.9 \pm 0.2\%$). Within uncertainties, these results are consistent with the results obtained by fitting the flat CTII model from Ref. [12] to the same datasets. The consistency of the results is expected, as the flat CTII model has previously demonstrated that it can accurately describe photon-calibration data [19]. Figure 4 shows that the exponential CTII model is able to obtain equivalent results for this relatively simple scenario. However as will be shown below, the advantages of the model presented in this work become apparent when including additional detector response effects or when modelling different event types.

We can further evaluate the extended detector response model by performing a simultaneous fit of the model to multiple photon-calibration datasets. To do this, the simultaneous fit to multiple datasets is done separately for data acquired from two different experiments. The first are three laser-calibration datasets acquired in Ref. [8]. The second are three LED-calibration datasets acquired at the Northwestern EXperimental Underground Site (NEXUS) at Fermilab (Batavia, IL). This NEXUS facility is located in the NUMI tunnel, which provides an overburden of 225 mwe [20], and hosts a Cryoconcept dry dilution refrigerator. The LED-calibration data reported in this work were acquired by one of four 1-cm-side HVeV detectors that were operated at NEXUS

between May 14th and July 27th, 2022. More information about the experiment design, data acquisition, and data analysis can be found in Ref. [21].

There are several key similarities and differences between laser-calibration datasets acquired in Ref. [8] and the LED-calibration datasets acquired at the NEXUS facility reported in this work. In both cases, the data were acquired using an HVeV detector with an “NF-C” sensor design [11]. Both devices are constituted by a $10 \times 10 \times 4$ mm³ silicon target with two channels of Quasiparticle-trap-assisted Electrothermal-feedback Transition-Edge Sensors [22] (QETs) patterned on the top surface to measure the phonon signal. While the HVeV detector used to acquire the NEXUS data is not the same as the one used in Ref. [8], the substrate from both detectors belong to the same silicon wafer. The means that the impurity levels in both detectors are likely to be similar.

Furthermore, both detectors generated an electric field throughout the bulk of the crystal by applying a high voltage to an aluminum electrode deposited on the detector surface opposite the surface patterned with the QETs; the QET surface of the detectors were kept grounded. In Ref. [8], laser-calibration data were acquired by emitting 1.95 eV photons from a laser onto the center of the QET-face of the detector. In contrast, the LED-calibration data from the NEXUS facility were acquired using a ~ 2 eV LED collimated on the center of the electrode-face of the detector. Yet the data from both detectors were acquired with $V_{\text{bias}} = +100$ V. This means that for the laser-calibration data from Ref. [8], the initial propagating charges are *electrons*, whereas for the LED-calibration data from the NEXUS facility, the initial propagating charges are *holes*. Moreover, because the LED-calibration data from the NEXUS facility illuminated the electrode-face of the detector, any non-ionizing energy deposition due to photon absorption into the aluminum fins of the QETs is expected to be minimal, especially compared to the laser-calibration data from Ref. [8].

We fit the extended model assuming non-ionizing energy deposition caused by surface trapping (Eq. 16) simultaneously to three laser-calibration datasets from Ref. [8] and three LED-calibration datasets from the NEXUS facility, all acquired with $V_{\text{bias}} = 100$ V. Each fit includes the parameters λ_1 , λ_2 , and λ_3 corresponding to the λ value of each dataset, but includes only one value of f_{CT} , f_{II} , σ_{res} , and α for all datasets. For simplicity, we again reduced the number of parameters in the fit by imposing the requirements given by Eq. 17.

In the fit to the data from Ref. [8], we kept the energy of the laser photons fixed at $E_{\gamma} = 1.95$ eV, whereas in the fit to the NEXUS datasets, we allowed the energy of the LED photons to float. Furthermore, a measurement of the LED wavelength spectrum at 4 K found the spread in photon energies to be ~ 0.0012 eV, and therefore we can adequately treat the LED as a monoenergetic source of photons described by Eq. 13. For the

TABLE I. Best-fit results found by fitting the extended model assuming non-ionizing energy deposition caused by surface trapping (Eq.16) simultaneously to multiple datasets. The results in the left column are determined from the fit to three laser-calibration datasets from Ref. [8], and the results in the right column are determined from the fit to three LED-calibration datasets from the NEXUS facility presented in this work. The fit to the NEXUS data also allowed the energy of the LED photons E_γ to float, and included the calibration parameters c_0 , c_1 , and c_2 .

	Laser data (Ref. [8])	LED data (NEXUS)
λ_1	3.18 ± 0.04	2.2 ± 0.1
λ_2	0.66 ± 0.02	4.2 ± 0.2
λ_3	2.90 ± 0.03	5.7 ± 0.2
f_{CT} [%]	13.5 ± 0.2	11.5 ± 0.2
f_{II} [%]	0.4 ± 0.2	$0.0^{+0.3}_{-0.0}$
σ_{res} [eV]	3.41 ± 0.02	2.71 ± 0.06
α [%]	36.9 ± 0.7	41 ± 2
E_γ [eV]	–	2.02 ± 0.07
c_0 [μA]	–	$(1.7 \pm 0.2) \times 10^{-3}$
c_1 [$\mu\text{A}/\text{eV}$]	–	$(9.102 \pm 0.006) \times 10^{-4}$
c_2 [$\mu\text{A}/\text{eV}^2$]	–	$(-242 \pm 7) \times 10^{-10}$

NEXUS datasets, we additionally included parameters to calibrate the data. The calibration converts the pulse amplitude A (in units of μA) of each event to the total phonon energy E_{ph} . The fit includes three calibration parameters c_0 , c_1 , and c_2 that follow the equation:

$$A = c_0 + c_1 \cdot E_{ph} + c_2 \cdot E_{ph}^2, \quad (18)$$

where the quadratic coefficient c_2 is included to account for any saturation effects in the QET sensors that can cause a non-linear response at higher energies [11].

The top and bottom plots of Fig. 5 show the fit results to the datasets from Ref. [8] and the dataset acquired at the NEXUS facility, respectively. The best-fit results of the fit parameters are listed in Tab. I. As the CT and II probabilities of the initial propagating charge have the largest impact on the expected signal for photon-calibration events, we can interpret the values of f_{CT} and f_{II} from the fits to the datasets from Ref. [8] and the datasets acquired at the NEXUS facility as the CT and II probabilities for electrons and holes, respectively. Therefore, these results suggest that for these detectors (that come from the same silicon wafer), the CT probability for electrons may be higher than for holes. By using Eq. 6 and knowing that the thickness of these detectors is 4 mm, the fitted f_{CT} values in Tab. I can be converted to the characteristic lengths of CT, giving 27.6 ± 0.4 mm and 32.7 ± 0.6 mm for electrons and holes, respectively.

In both cases, the fit determined the amount of surface trapping to be $\sim 40\%$. Indeed the inset plots in Fig. 5 that are zoomed-in around the $1 e^-h^+$ -pair peak clearly show the peak position dependence on λ — a feature predicted when assuming surface trapping. Notably, the surface trapping probability found for the NEXUS data (where the LED photons are illuminated on the

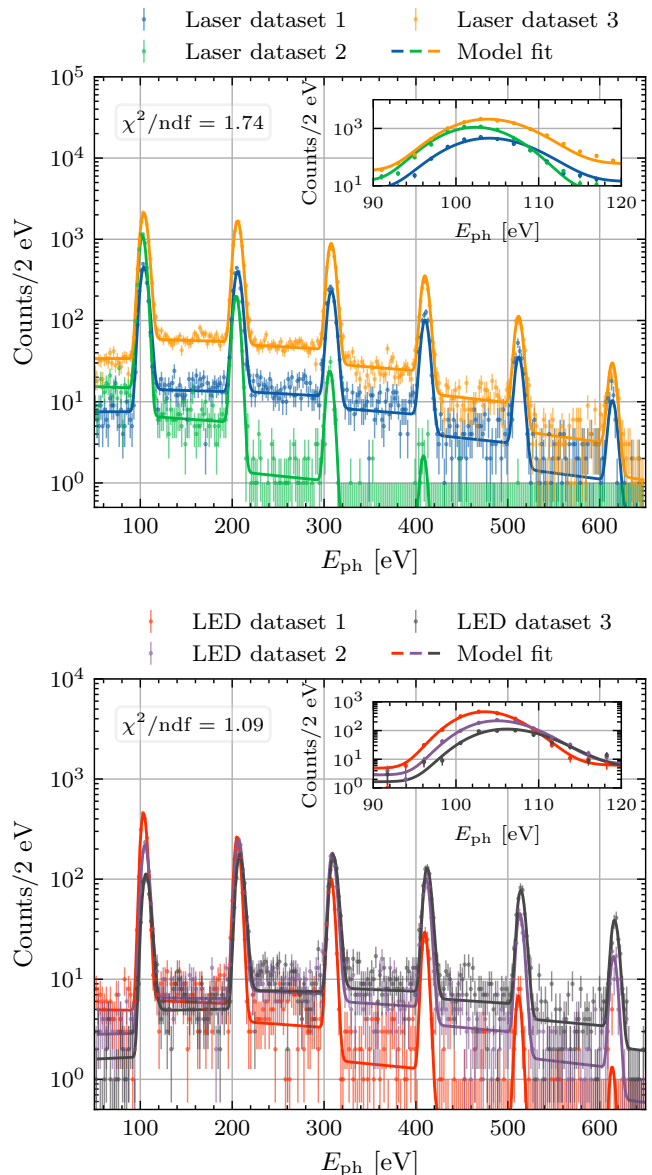


FIG. 5. Results of simultaneous fits of the extended detector response model to three laser-calibration datasets from the HVeV detector in Ref. [8] (top) and three LED datasets acquired from a HVeV detector at the NEXUS facility (bottom). All of the datasets were acquired with $V_{bias} = 100$ V. The model assumes non-ionizing energy deposition caused by surface trapping as described by Eq. 16. The inset plots show the data and fit zoomed-in around the first e^-h^+ -pair peak in order to clearly observe the peak shifts between datasets.

electrode-face of the detector) is slightly higher compared to the data from Ref. [8]. This strongly disfavours the hypothesis that non-ionizing energy deposition occurs due to photons being absorbed directly into the aluminum fins of the QETs. While this result supports the surface trapping hypothesis, we stress that it is just one interpretation of these data. Additional dedicated measurements

are needed to confirm these detector response effects, as well as to understand the differences that these effects have on electrons and holes.

We can additionally demonstrate the differences in the detector response for expected DM signals which, as mentioned in Sec. III A, are modelled as bulk- e^-h^+ -pair events. To do this, we ran simulations using G4CMP [17, 18] of two DM models by generating events within the bulk of a silicon HVeV detector with $V_{\text{bias}} = 100$ V. The first simulated signal is dark photon absorption following Ref. [14] with a dark photon mass $m_{A'} = 10 \text{ eV}/c^2$ and kinetic mixing parameter $\varepsilon = 10^{-12}$, and the second is DM-electron scattering following Ref. [15] with a DM mass $m_\chi = 5 \text{ MeV}/c^2$, effective DM-electron scattering cross section $\bar{\sigma}_e = 10^{-33} \text{ cm}^2$, and a DM form factor of $F_{\text{DM}} = 1$. The total number of events in both simulations were determined assuming an exposure of 6 gram-days, and the ionization PMFs in the simulations are computed using the binomial approach taken in Refs. [7, 8]. Finally, we assumed an energy resolution of $\sigma_{\text{res}} = 3 \text{ eV}$ and the following CT and II probabilities: $f_{\text{CTe}} = f_{\text{CTh}} = 10\%$ and $f_{\text{Ilee}} = f_{\text{Ileh}} = f_{\text{IIhe}} = f_{\text{IIhh}} = 1\%$.

The results of these simulations are shown in Fig. 6, which also shows the expected signal for the two DM models computed using the exponential CTII and extended detector response model from this work following Eqs. 14 and 15. It is important to note that G4CMP-based simulations model CT and II processes using the same PDF described by Eq. 5 and are parameterized using characteristic lengths [17]. The consistency between the solid, orange curves and simulated data shown in Fig. 6 therefore provides a verification of the analytical solutions found for the various CT and II processes modelled. For comparison, Fig. 6 also shows the expected DM signals computed using the flat CTII model from Ref. [12] which, unlike the exponential CTII model, does not distinguish between surface and bulk event types. Differences in the energy spectra for different event sources is evident by comparing Fig. 6 with the energy spectra seen in Figs. 4 and 5. Our modelling expects the signal shape in the between-peak regions to differ for a bulk- e^-h^+ -pair source of events, such as DM, compared to surface events, such as photon-calibration data. The signal shape in the between-peak regions has a lot more curvature for bulk- e^-h^+ -pair events, in contrast to the relatively straight signal shape between the peaks for surface events. This feature is not captured by the flat CTII model, as evident in Fig. 6.

V. DISCUSSION

The exponential CTII model introduced in Sec. II addresses several limitations of the flat CTII model from Ref. [12]. This more robust model adopts a more physically motivated approach to describe CT and II processes in phonon-based crystal detectors. Consequently, it effectively characterizes the detector response across a range

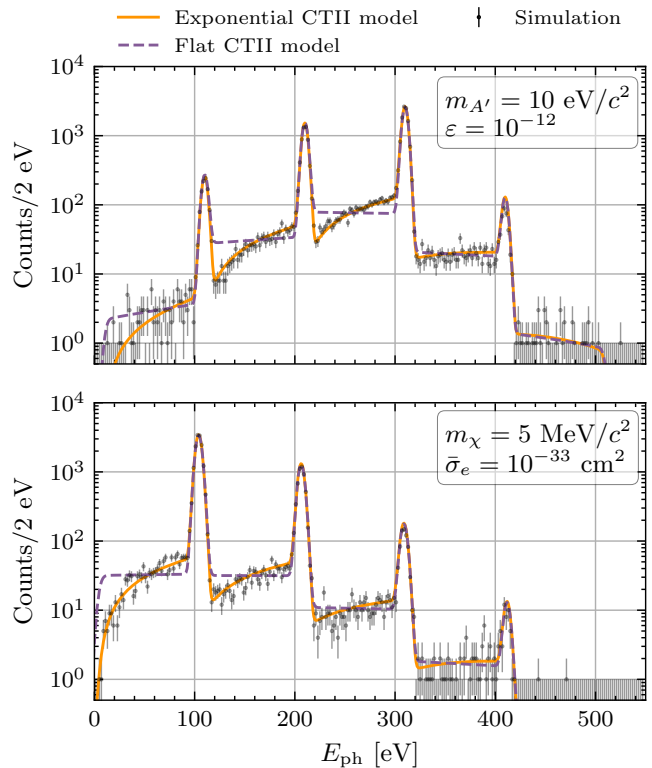


FIG. 6. Simulated data of events generated in the bulk of a silicon HVeV detector with $V_{\text{bias}} = 100$ V for DM signals using G4CMP [17, 18]. The simulations were run for (top) dark photon absorption following Ref. [14] with $m_{A'} = 10 \text{ eV}/c^2$ and $\varepsilon = 10^{-12}$ and (bottom) DM-electron scattering following Ref. [15] with $m_\chi = 5 \text{ MeV}/c^2$, $\bar{\sigma}_e = 10^{-33} \text{ cm}^2$, and $F_{\text{DM}} = 1$. For running the simulations, we assumed an exposure of 6 gram-days, an energy resolution of $\sigma_{\text{res}} = 3 \text{ eV}$ and CT and II probabilities of $f_{\text{CTe}} = f_{\text{CTh}} = 10\%$ and $f_{\text{Ilee}} = f_{\text{Ileh}} = f_{\text{IIhe}} = f_{\text{IIhh}} = 1\%$. The solid, orange curves are the expected signals computed using our model following Eqs. 14 and 15. For comparison, the dashed, purple curves are the expected signals computed using the flat CTII model from Ref. [12].

of event types and allows for the differentiation of CT and II probabilities for electrons and holes. These advantages, coupled with the expanded detector response model detailed in Sec. III, provide a more accurate representation of the detector's response to different sources of events.

The exponential CTII model combined with the extended response model assuming non-ionizing energy deposition caused by surface trapping is shown in Fig. 5 to provide an accurate description of laser-calibration data from Ref. [8] and LED-calibration data acquired from the NEXUS facility reported in this work. While these results are encouraging, we note that this model may not encompass all relevant detector response effects that may occur. Rather, these results motivate using future measurements in order to continue investigating the full extent of these effects. Apart from understanding detector

response effects, the result of the fit to the NEXUS data shown in Fig. 5 and Tab. I additionally demonstrates how the extended detector response model can be utilized to calibrate the detector. Incorporating these additional detector response effects can help to improve the accuracy of the energy calibration.

Furthermore, Fig. 6 illustrates how the signal shape differs for DM models, where the detector response is instead modelled by bulk- e^-h^+ -pair events. Indeed the analytical solutions to the exponential CTII model presented in this work match the spectra of events simulated using G4CMP, whereby CT and II processes are also parameterized using characteristic lengths [17]. The ability of the exponential CTII model to describe different event types provides a large advantage over the flat CTII model from Ref. [12], and can enable statistical discrimination between different background signals and expected DM signals.

Yet it is equally important to outline the limitations of the exponential CTII model. Physically, this model provides no description of the underlying mechanisms of CT or II processes, and simply assumes that there is some probability that these processes occur due to impurities throughout the crystal bulk. The characteristic lengths of these processes, τ_i , could depend not only on the density of impurities, but also on the strength of the electric field, prebiasing history, “baking” history (impurity neutralization by detector irradiation) and temperature [23, 24]. Furthermore, as mentioned in Sec. II, the exponential CTII model limits the analytical solutions to second-order processes for surface and bulk-single-charge events, and first order processes for bulk- e^-h^+ -pair events. This limitation is a practical necessity, as including higher-order processes would exponentially increase the number and the complexity of solutions to solve for. However, the probability of II has been found in measurements to be of the order of 1% [8, 19]. Therefore second- and third-order processes are expected to be extremely subdominant with probabilities $\ll 0.01\%$. Nevertheless, this limitation is quantitatively assessed for each event type in Appendix C.

The bulk CT and II processes modelled in this work are also present in other solid-state DM experiments, including SENSEI and DAMIC-M [25, 26]. These experiments use charge-coupled devices (CCDs) that readout the amount of charge collected at each pixel. As such, charges that become trapped within the bulk of the crystal result in a signal loss. Furthermore, because charge packets are required to move from pixel to pixel, the drift length of charges is typically larger for CCD detectors compared to HVeV detectors. The proposed Oscura experiment aims to account for this signal loss by considering that these trapped charges may be released at a later time and measured as single-electron events [27]. This bulk trapping is distinct from charge transfer inefficiency that occurs in CCD detectors, whereby charges are lost to surrounding pixels as the charge packet is moved from pixel to pixel. As shown in this work, the advantage

of using phonon-based crystal detectors, including HVeV detectors, lies in the ability to exploit the non-quantized e^-h^+ -pair peaks regions on the energy spectrum to extract CT and II parameters as well as to differentiate between different sources of events.

Future plans involve dedicated detector response investigations using HVeV detectors. For example, taking CT and II measurements using crystals of different impurity levels while varying the voltage bias or the amount of prebiasing applied to the crystals can help develop our understanding of the factors that contribute to CT and II. Taking measurements with different voltage polarities will allow us to probe the differences in CT and II processes for electrons and holes. Furthermore, we aim to explore additional detector response effects and phenomena, including sources of non-ionizing energy deposition. While these proposed measurements can be made using a photon-calibration source, finding a source of low-energy, bulk- e^-h^+ -pair events would additionally allow us to investigate the detector response expected for DM signals. The nuclear-recoil ionization yield measurement in Ref. [28] demonstrates a method of producing such events by measuring low-energy neutron recoils off of the nuclei of an HVeV detector. The model presented in this work not only provides a more robust understanding of the detector response effects in phonon-based crystal detectors, but can be utilized to help discriminate between different sources of events in order to improve the sensitivity of DM search experiments.

ACKNOWLEDGMENTS

We would like to thank Francisco Ponce and Chris Stanford for helpful initial discussions about understanding CT and II processes and how to model them. We would further like to thank Michael Kelsey for helpful discussions about G4CMP simulations and Elham Azadbakht for contributions implementing CT and II processes in G4CMP. We also thank Francesco Toschi and Sukeerthi Dharani for comments on a draft version of this manuscript. Funding and support were received from the Deutsche Forschungsgemeinschaft (DFG) under the Emmy Noether Grant No. 420484612, NSERC Canada, the Canada First Excellence Research Fund, the Arthur B. McDonald Institute (Canada), the U.S. Department of Energy (DOE) Office of High Energy Physics, and from the National Science Foundation (NSF). This work was supported in part under NSF Grant No. 2111324. Fermilab is operated by Fermi Research Alliance, LLC, under Contract No. DE-AC02-37407CH11359 with the US Department of Energy, and computing support and resources were provided by SciNet (www.scinethpc.ca), the Digital Research Alliance of Canada (www.alliancecan.ca), and SLAC.

Appendix A: Single- e^-h^+ -Pair Solutions

This appendix provides details on how to find the unique solutions for single- e^-h^+ -pair events. As mentioned in Sec. II, the events are categorized into three distinct classes: surface event, bulk-single-charge events, and bulk- e^-h^+ -pair events. Recall that both propagating electrons and holes have three processes which can occur: charge trapping (“CTe” and “CTh”), creation of a charge of the same kind (“Ilee” and “IIhh”), and creation of a charge of the opposite kind (“Ileh” and “IIhe”). When writing the equation for the probability of a particular scenario occurring, we must consider the probabilities of all possible processes. For example, consider the probability of CT for a propagating electron as a function of Δz , $P_{CTe}(\Delta z)$. The probability of CTe occurring at a distance Δz travelled is the probability of CTe occurring at Δz and Ilee not occurring by Δz and Ileh not occurring by Δz . Using Eqs. 4 and 5, this scenario is described by:

$$\begin{aligned} P_{CTe}(\Delta z) &= \frac{1}{\tau_{CTe}} e^{-\Delta z/\tau_{CTe}} \cdot \bar{C}_{Ilee}(\Delta z) \cdot \bar{C}_{Ileh}(\Delta z) \\ &= \frac{1}{\tau_{CTe}} e^{-\Delta z(1/\tau_{CTe} + 1/\tau_{Ilee} + 1/\tau_{Ileh})} \\ &= \frac{1}{\tau_{CTe}} e^{-\Delta z T_e}, \end{aligned} \quad (\text{A1})$$

where we define

$$T_e \equiv \frac{1}{\tau_{CTe}} + \frac{1}{\tau_{Ilee}} + \frac{1}{\tau_{Ileh}}. \quad (\text{A2})$$

Equivalent equations to Eq. A1 can be found for the other five unique processes and by defining

$$T_h \equiv \frac{1}{\tau_{CTh}} + \frac{1}{\tau_{IIhe}} + \frac{1}{\tau_{IIhh}}. \quad (\text{A3})$$

We also need to consider the probability of a charge propagating a distance Δz without any CT or II process occurring. In this context, it is evaluating the probability of a charge reaching one of the crystal surfaces after travelling a distance Δz . We denote this probability as $P_S(\Delta z)$. For a propagating electron, this probability is given by:

$$\begin{aligned} P_S(\Delta z) &= \bar{C}_{CTe}(\Delta z) \cdot \bar{C}_{Ilee}(\Delta z) \cdot \bar{C}_{Ileh}(\Delta z) \\ &= e^{-\Delta z T_e}. \end{aligned} \quad (\text{A4})$$

Equivalently, the probability for a propagating hole to reach a surface without a CT or II process occurring as a function of Δz is $P_S(\Delta z) = e^{-\Delta z T_h}$. Equation A4 says that if a charge travels the full length of the detector (i.e. $\Delta z = 1$), the probability that it does not undergo a CT or II process is $e^{-T_{e/h}}$.

So far, we have only described probabilities of propagating charges undergoing CT and II processes as a function of the distance travelled. However, detectors do not directly measure the distance charges are able to travel. As mentioned in Sec. II, the NTL energy measured by the detector is proportional to the distance travelled by the charges. In this parameterization, the energy measured due to ionization is therefore equal to the total distance travelled by all propagating charges involved with an event. The probability of measuring some energy E (where E is in n_{eh} -energy space, denoted as E_{neh} in Sec. II) can be described as the sum of probabilities whereby the total distance travelled by all charges z_{tot} is equal to E . While there is no direct constraint on z_{tot} , and thus E , individual charges are constrained by the bounds of the crystal surfaces (i.e. $0 \leq z \leq 1$).

Using the understanding of how the measured energy is related to the distance travelled by the propagating charges, we can start by solving for the almost trivial solutions, which will also create a set of base equations in which all other solutions can be found. We consider the solutions for charges propagating toward the $z = 0$ and $z = 1$ surfaces separately. For a charge travelling toward the $z = 1$ surface that starts at a position z_0 , the total energy that can be measured by the charge is $E = 1 - z_0$. Conversely for a charge travelling toward the $z = 0$ surface that starts at a position z_0 , the total energy that can be measured by the charge is $E = z_0$. Using Eq. A4, we can write the probability distribution for a charge reaching the $z = 0$ and $z = 1$ surfaces as:

$$\begin{aligned} P_{S,q}^0(E, z_0) &= \delta(E - z_0) e^{-z_0 T_q} \\ P_{S,q}^1(E, z_0) &= \delta(E - 1 + z_0) e^{-(1-z_0) T_q}, \end{aligned} \quad (\text{A5})$$

where the subscript $q = (e, h)$ indicates if the charge is an electron or hole, and the superscripts 0 and 1 indicate which surface the charge is travelling toward. Next, we consider the probability distribution of measuring an energy E before some CT or II process occurs. For now, whether the process is CT or II does not matter. These base solutions are found using Eq. A1 as a framework and solved separately for charges propagating toward the $z = 0$ and $z = 1$ surfaces. For charges that undergo some process i and start at a position z_0 , these probability distributions $P_i(E, z_0)$ go as:

$$\begin{aligned} P_i^0(E, z_0) &= \begin{cases} \frac{1}{\tau_i} e^{-E \cdot T_q} & 0 \leq E < z_0 \\ 0 & \text{else,} \end{cases} \\ P_i^1(E, z_0) &= \begin{cases} \frac{1}{\tau_i} e^{-E \cdot T_q} & 0 \leq E < 1 - z_0 \\ 0 & \text{else,} \end{cases} \end{aligned} \quad (\text{A6})$$

where again the superscripts 0 and 1 indicate the direction of propagation.

Some specific solutions can immediately be found from Eq. A6. Specifically when a charge undergoes CT, the charge can no longer propagate and produce more energy or undergo additional processes. Therefore Eq. A6

are also the solutions for the probability distribution of a CT process for a charge starting at a position z_0 . This is decisively not the case for a charge that undergoes II, as both the initial charge and the newly created charge will continue to traverse the crystal and increase the energy measured. Nevertheless, Eqs. A5 and A6 provide the necessary foundation for calculating the probability distribution for any specific scenario. Equipped with the base equations of the probability distributions in energy for propagating charges travelling in either direction with some starting position, we can now analytically solve for the single- e^-h^+ -pair probability distributions corresponding to specific events and scenarios.

1. Surface Events

A surface event starts with the creation of either an e^- or a h^+ at the starting position $z_0 = 0$ or $z_0 = 1$. Knowing the polarity of the voltage bias and the starting position will necessarily decide whether the propagating charge is an e^- or a h^+ . We can reduce the number of solutions to solve for by accounting for the symmetries that exists in this scenario. Firstly, if a solution is found for when an e^- is the initial propagating charge, the solution for when a h^+ is the initial propagating charge can be immediately found by swapping the τ and T parameters. Therefore we need only to keep the distinction between charges that are the same as the initial charge and charges that are the opposite. This is done by replacing the “e” and “h” labels in the τ and T parameters with “s” and “o” labels to indicate the same or opposite charge. Secondly, the solutions should be the same whether the charge is propagating toward the $z = 0$ or $z = 1$ surface. Therefore solutions need only be found for one direction of propagation. However for good practice, the solutions were solved for both directions of propagation and are confirmed to give matching results. Here we will solve some of the solutions for when the initial charge is propagating toward $z = 1$.

We start by defining the probability distribution of the initial starting position of the charges. For surface charges that propagate toward $z = 1$, the probability distribution of the initial starting position $P_{\text{surf}}(z_0)$ trivially goes as:

$$P_{\text{surf}}(z_0) = \delta(z_0). \quad (\text{A7})$$

Next, we can begin to solve for the solutions corresponding to specific scenarios. These probability distributions are indexed as $P_k(E)$, where k iterates through the different solutions. The first, and easiest, solution to solve for is the case where the initial charge reaches the surface without a CT or II process occurring. This probability $P_0(E)$ is found by combining Eqs. A5 and A7.

$$\begin{aligned} P_0(E) &= \int_{-\infty}^{\infty} P_{\text{surf}}(z_0) P_{\text{S},s}^1(E, z_0) dz_0 \\ &= \int_{-\infty}^{\infty} \delta(z_0) \delta(E - 1 + z_0) e^{-(1-z_0)T_s} dz_0 \quad (\text{A8}) \\ &= \delta(E - 1) e^{-T_s} \end{aligned}$$

The solution to $P_0(E)$ is a delta function at $E = 1$ with an amplitude of e^{-T_s} . This makes sense, as a charge travelling from $z = 0$ to $z = 1$ will produce exactly one e^-h^+ -pair worth of energy. Next, we can solve for the solution when the initial charge undergoes CT, $P_1(E)$, which is found by combining Eqs. A6 and A7.

$$\begin{aligned} P_1(E) &= \int_{-\infty}^{\infty} P_{\text{surf}}(z_0) P_{\text{CTs}}^1(E, z_0) dz_0 \\ &= \int_{-\infty}^{\infty} \delta(z_0) P_{\text{CTs}}^1(E, z_0) dz_0 \quad (\text{A9}) \\ &= P_{\text{CTs}}^1(E, 0) \\ &= \begin{cases} \frac{1}{\tau_{\text{CTs}}} e^{-T_s \cdot E} & 0 \leq E < 1 \\ 0 & \text{else} \end{cases} \end{aligned}$$

The next scenario to consider is the case where the initial charge creates a new, like charge, and both the original charge and the new charge happen to reach the surface. We call this probability distribution $P_2(E)$. Let z_{II} be the position where the new charge is created. It is important to remember that the quantity we are interested in is the total distance travelled by all the charges in the scenario. It is helpful to think about the energy gained by each “segment” of charge propagation. In this scenario, there are three such segments: the initial charge that travels from z_0 to z_{II} , and the initial and additional charges that each travel from z_{II} to $z = 1$. It is additionally helpful to think of E as fixed number that constrains the problem. We want to find the combinations of segments that result in E total energy.

Let E_{2a} and E_{2b} be the energy contributions from each of the two charges after II. The combined energy contribution from both charges after II is therefore $E_2 = E_{2a} + E_{2b}$. If E_1 is the energy contribution of the initial charge before II, then the total energy measured will be $E = E_1 + E_2$. We also know that E_1 can be expressed as $z_{\text{II}} - z_0$. Rearranging gives $z_{\text{II}} = E - E_2 + z_0$. What we have done is expressed z_{II} not as a position in the crystal, but rather in terms of energy contributions. The choice of expressing the parameters this way initially seems odd. After all, we already know that E_{2a} and E_{2b} are equal in this scenario. But that is not true for all scenarios, and it turns out that this way of formulating the problem provides a generic framework for solving all of the solutions.

We first need to find the probability that the energy contribution after II is E_2 . This probability is equal to the probability that one charge contributes an energy

of E_{2a} times the probability that the other charge contributes an energy of $E_2 - E_{2a}$, given a starting position of z_{II} and summed over all possibilities of E_{2a} . Expressed in terms of the base equations from Eq. A5 gives:

$$\begin{aligned}
P(E_2) &= \int_{-\infty}^{\infty} dE_{2a} P_{\text{S},\text{s}}^1(E_{2a}, E - E_2 + z_0) \times \\
&\quad P_{\text{S},\text{s}}^1(E_2 - E_{2a}, E - E_2 + z_0) \\
&= \int_{-\infty}^{\infty} dE_{2a} \delta(E_{2a} - 1 + E - E_2 + z_0) \times \\
&\quad \delta(E_2 - E_{2a} - 1 + E - E_2 + z_0) \times \\
&\quad e^{-2(1-E+E_2-z_0)T_s} \\
&= \delta(2E - E_2 - 2 + 2z_0) e^{-2(1-E+E_2-z_0)T_s}.
\end{aligned} \tag{A10}$$

Next, the probability of having a total energy of E for a given starting position z_0 is the probability that the energy contribution after II is E_2 and the energy contribution before II is $E - E_2$. We find this by combining Eqs. A10 and A6, and summing over all possibilities of E_2 .

$$\begin{aligned}
P(E, z_0) &= \int_{-\infty}^{\infty} dE_2 P(E_2) \times P_{\text{IIss}}^1(E - E_2, z_0) \\
&= \int_{E-1+z_0}^E dE_2 \delta(2E - E_2 - 2 + 2z_0) \times \\
&\quad \frac{1}{\tau_{\text{IIss}}} e^{-2(1-E+E_2-z_0)T_s} e^{-(E-E_2)T_s} \\
&= \int_{E-1+z_0}^E dE_2 \delta(2E - E_2 - 2 + 2z_0) \times \\
&\quad \frac{1}{\tau_{\text{IIss}}} e^{-(2-E+E_2-2z_0)T_s} \\
&= \begin{cases} \frac{1}{\tau_{\text{IIss}}} e^{-T_s \cdot E} & 1 - z_0 \leq E < 2(1 - z_0) \\ 0 & \text{else} \end{cases}
\end{aligned} \tag{A11}$$

The final step to find $P_2(E)$ is to integrate over all z_0 .

$$\begin{aligned}
P_2(E) &= \int_{-\infty}^{\infty} P(E, z_0) P_{\text{surf}}(z_0) dz_0 \\
&= \begin{cases} \frac{1}{\tau_{\text{IIss}}} e^{-T_s \cdot E} & 1 \leq E < 2 \\ 0 & \text{else} \end{cases}
\end{aligned} \tag{A12}$$

The next scenario to consider is when the initial charge creates an opposite charge, and both the original and new charge happen to reach the surface. We call this probability distribution $P_3(E)$. Like the previous scenario, the additional charge is created at a position z_{II} , and we need to find the probabilities of each segment of charge propagation. Because of how we formulated the problem, the way to solve for $P_3(E)$ is exactly the same as how to solve

for $P_2(E)$ with just two key substitutions. The II process created an opposite charge, and that opposite charge will propagate toward the $z = 0$ surface. Therefore, one of the $P_{\text{S},\text{s}}^1$ terms in Eq. A10 is replaced with $P_{\text{S},\text{o}}^0$ with the same inputs. And because the process in this scenario is II to an opposite charge, the P_{IIss}^1 term in Eq. A11 is replaced with P_{IIso}^1 , also with the same inputs. Making these substitutions and solving for $P_3(E)$ gives:

$$P_3(E) = \begin{cases} \frac{1}{\tau_{\text{IIso}}} e^{T_o - T_s - T_o \cdot E} & 1 \leq E < 2 \\ 0 & \text{else.} \end{cases} \tag{A13}$$

The solutions for other scenarios can be found by employing the same logic of considering segments of energy contribution, using the correct combination of base equations, and nested integrals. In total, there are 28 solutions found for surface charge events, all of which are catalogued in the supplement documentation. The individual solutions are shown together in the top plot of Fig. 1.

2. Bulk-Single-Charge Events

A single-charge bulk event starts with the creation of either an e^- or h^+ at some starting position z_0 that ranges between $z = 0$ and $z = 1$. As with surface charges, we can use the same symmetry arguments to reduce the number of solutions to solve for. Again, the “e” and “h” labels in the subscripts are replaced with “s” and “o” to indicate charges that are the same and opposite as the initial charge, and solutions are only needed to be found for charges propagating in one direction. For bulk single-charge events, the probability distribution of z_0 is defined as a uniform distribution between $z = 0$ and $z = 1$:

$$P_{\text{bulk}}(z_0) = \begin{cases} 1 & 0 \leq z_0 \leq 1 \\ 0 & \text{else.} \end{cases} \tag{A14}$$

We can again consider the simplest scenarios to solve for $P_0(E)$ (the charge reaches the surface), $P_1(E)$ (the charge undergoes CT), $P_2(E)$ (the charge undergoes II to the same charge and both charges reach the surface), and $P_3(E)$ (the charge undergoes II to the opposite charge and both charges reach the surface). Fortunately, these solutions are mostly solved for in Eqs. A8–A13, except now $P_{\text{surf}}(z_0)$ is replaced with $P_{\text{bulk}}(z_0)$. Making this substitution and solving for the probability distributions gives:

$$\begin{aligned}
P_0(E) &= \begin{cases} e^{-T_s \cdot E} & 0 \leq E < 1 \\ 0 & \text{else,} \end{cases} \\
P_1(E) &= \begin{cases} \frac{1}{\tau_{CTs}} e^{-T_s \cdot E} (1 - E) & 0 \leq E < 1 \\ 0 & \text{else,} \end{cases} \\
P_2(E) &= \begin{cases} \frac{1}{2\tau_{IIs}} e^{-T_s \cdot E} E & 0 \leq E < 1 \\ \frac{1}{2\tau_{IIs}} e^{-T_s \cdot E} (2 - E) & 1 \leq E < 2 \\ 0 & \text{else,} \end{cases} \\
P_3(E) &= \begin{cases} \frac{e^{T_o(1-E)-T_s} - e^{T_s(1-E)-T_o}}{\tau_{IIs}(T_o-T_s)} & 1 \leq E < 2, T_s \neq T_o \\ \frac{1}{\tau_{IIs}} e^{-T_s \cdot E} (2 - E) & 1 \leq E < 2, T_s = T_o \\ 0 & \text{else.} \end{cases} \tag{A15}
\end{aligned}$$

It is evident that the solutions to these problems become complex. One way to determine if these solutions make sense is to examine the boundary conditions. For example, the probability distribution $P_3(E)$ in Eq. A15 ranges from 1–2 e^-h^+ -pairs of energy. If a charge has an initial position of $z = 0$ and immediately creates an opposite charge, the event will produce 1 e^-h^+ -pair of energy. The same is true if the charge has an initial position of $z = 1$ and immediately creates an opposite charge. There is no scenario where this process can produce an energy less than 1 e^-h^+ pair. Furthermore, if the charge has an initial position of $z = 0$ and creates an opposite charge only when it reaches $z = 1$, the event will produce 2 e^-h^+ -pairs of energy. There is likewise no scenario where this process can produce an energy greater than 2 e^-h^+ pairs. The 28 unique solutions found for bulk-single-charge events are catalogued in the supplement documentation, and the individual solutions are shown together in the middle plot of Fig. 1.

3. Bulk- e^-h^+ -Pair Events

A bulk- e^-h^+ -pair event starts with the creation of both an electron and hole at some starting position z_0 that ranges between $z = 0$ and $z = 1$. As with bulk-single-charge events, we assume that z_0 is a uniform distribution between the surfaces of the detector and follows Eq. A14. However unlike the solutions for single charges, the solutions for e^-h^+ -pair events need to keep the distinction between the parameters for electrons and holes. The initial e^- and h^+ will propagate in opposite directions and are treated as independent charges. The only constraint is the initial starting position that they both share. Like with the single-charge events, the solutions will be the same regardless of which direction of propagation is chosen for the charges.

Here we will demonstrate how to find the solutions for the simplest scenarios. Let $P_0(E)$ be the probability that

both the electron and hole reach the surface. We assume the electrons and holes travel toward the $z = 1$ and $z = 0$ surfaces, respectively. As before, the solution can be found by considering the segments of charge propagation in the scenario. If the total energy of the event is E and the electron contributes an energy of E_1 , then the hole must contribute an energy of $E - E_1$. The probability of measuring an energy of E giving a starting position of z_0 is therefore the probability that the electron contributed an energy of E_1 starting at z_0 times the probability that the hole contributed an energy of $E - E_1$ starting at z_0 summed over all possibilities of E_1 . Using the base equations from Eq. A5, this is written as:

$$\begin{aligned}
P(E, z_0) &= \int_{-\infty}^{\infty} P_{S,e}^1(E_1, z_0) P_{S,h}^0(E - E_1, z_0) dE_1 \\
&= \int_{-\infty}^{\infty} \delta(E_1 - 1 + z_0) e^{-(1-z_0)T_e} \times \\
&\quad \delta(E - E_1 - z_0) e^{-z_0 T_h} dE_1 \\
&= \delta(E - 1) e^{-T_e + z_0(T_e - T_h)}. \tag{A16}
\end{aligned}$$

The final step to solve for $P_0(E)$ is to multiply Eq. A16 by Eq. A14 and integrate over all z_0 . However this last step must be considered separately for when $T_e = T_h$ and $T_e \neq T_h$ in order to avoid undefined solutions. For the case where $T_e \neq T_h$, $P_0(E)$ is found to be:

$$\begin{aligned}
P_0(E) &= \int_{-\infty}^{\infty} P(E, z_0) P_{\text{bulk}}(z_0) dz_0 \\
&= \int_0^1 \delta(E - 1) e^{-T_e + z_0(T_e - T_h)} dz_0 \\
&= \frac{1}{T_e - T_h} \delta(E - 1) e^{-T_e} \left[e^{z_0(T_e - T_h)} \right]_0^1 \\
&= \delta(E - 1) \frac{e^{-T_h} - e^{-T_e}}{T_e - T_h}. \tag{A17}
\end{aligned}$$

For the case where $T_e = T_h \equiv T$, $P_0(E)$ is found to be:

$$\begin{aligned}
P_0(E) &= \int_{-\infty}^{\infty} P(E, z_0) P_{\text{bulk}}(z_0) dz_0 \\
&= \int_0^1 \delta(E - 1) e^{-T} dz_0 \\
&= \delta(E - 1) e^{-T}. \tag{A18}
\end{aligned}$$

The next scenario to consider is when the e^- is trapped while the h^+ reaches the surface. Let the probability distribution for this process be $P_1(E)$. As before, E_1 is the energy contribution from the electron, and $E - E_1$ is the energy contribution from the hole. The probability for measuring an energy E given a starting position of z_0 is found in the same way as in Eq. A16, except that for the electron, the appropriate base equation from Eq. A6 is used:

Appendix B: Sub-Peak Distributions due to Non-Ionizing Photons

$$\begin{aligned}
P(E, z_0) &= \int_{-\infty}^{\infty} P_{\text{CTe}}^1(E_1, z_0) P_{\text{S,h}}^0(E - E_1, z_0) dE_1 \\
&= \int_0^{1-z_0} \frac{1}{\tau_{\text{CTe}}} e^{-T_e \cdot E_1} \times \\
&\quad \delta(E - E_1 - z_0) e^{-z_0 T_h} dE_1 \\
&= \begin{cases} \frac{1}{\tau_{\text{CTe}}} e^{-T_e \cdot E + z_0(T_e - T_h)} & z_0 \leq E < 1 \\ 0 & \text{else.} \end{cases} \tag{A19}
\end{aligned}$$

Again we can find $P_1(E)$ by multiplying Eq. A19 with Eq. A14 and integrating over z_0 . For the case where $T_e \neq T_h$, $P_1(E)$ is found to be:

$$\begin{aligned}
P_1(E) &= \int_{-\infty}^{\infty} P(E, z_0) P_{\text{bulk}}(z_0) dz_0 \\
&= \int_0^1 P(E, z_0) dz_0 \\
&= \int_0^E \frac{1}{\tau_{\text{CTe}}} e^{-T_e \cdot E + z_0(T_e - T_h)} dz_0 \tag{A20} \\
&= \frac{1}{\tau_{\text{CTe}}(T_e - T_h)} e^{-T_e \cdot E} \left[e^{z_0(T_e - T_h)} \right]_0^E \\
&= \begin{cases} \frac{e^{-T_h \cdot E} - e^{-T_e \cdot E}}{\tau_{\text{CTe}}(T_e - T_h)} & 0 \leq E < 1 \\ 0 & \text{else.} \end{cases}
\end{aligned}$$

For the case where $T_e = T_h \equiv T$, $P_1(E)$ is found to be:

$$\begin{aligned}
P_1(E) &= \int_{-\infty}^{\infty} P(E, z_0) P_{\text{bulk}}(z_0) dz_0 \\
&= \int_0^1 P(E, z_0) dz_0 \\
&= \int_0^E \frac{1}{\tau_{\text{CTe}}} e^{-T \cdot E} dz_0 \tag{A21} \\
&= \frac{1}{\tau_{\text{CTe}}} e^{-T \cdot E} [z_0]_0^E \\
&= \begin{cases} \frac{e^{-T \cdot E} \cdot E}{\tau_{\text{CTe}}} & 0 \leq E < 1 \\ 0 & \text{else.} \end{cases}
\end{aligned}$$

The solutions for the other scenarios can be found by considering the probabilities for the process that happens to each charge and constraining the energy contribution from each charge to the total measured energy. In total there are 16 unique solutions found for bulk- e^-h^+ -pair events, which are catalogued in the supplement documentation. The individual solutions are shown together in the bottom plot of Fig. 1.

Section IIIB introduced the phenomenon of non-ionizing energy deposition and how the surface trapping effect can be incorporated into the extended detector response model. In this model, the number of photons that hit the detector is given by a Poisson distribution with a mean of λ . Each photon will create an e^-h^+ pair, where there is a probability α that the e^-h^+ pair undergoes surface trapping. Absorbed photons that result in an e^-h^+ -pair that undergoes surface trapping are classified as non-ionizing photons, whereby the deposited energy in the detector will only be the absorption energy of the photon E_γ . This effect results in the formation of a sub-peak structure at each e^-h^+ -pair peak in the energy spectrum, as can be seen in the middle plot of Fig. 3. This appendix provides further details on the distribution of these sub-peak structures and its dependency on λ and α .

Each sub-peak corresponds to q ionizing photons and p non-ionizing photons. The q ionizing photons will produce q e^-h^+ pairs that will propagate through the detector where they may undergo bulk CT and II processes. As will be discussed below, the bulk CT and II processes do not affect the shape of the underlying sub-peak distributions, and thus can be ignored. For the sub-peak distribution of p at the q^{th} e^-h^+ -pair peak, we want to determine the probability $P(p|q)$, simply given as:

$$P(p|q) = \frac{P(q \cap p)}{P(q)}. \tag{B1}$$

To find these probabilities, we must first consider the probabilities of the separate processes. The total number of photons absorbed in the detector is $(p + q)$, and the probability of $(p + q)$ photons hitting the detector is determined from a Poisson distribution with a mean of λ . The probability of having p non-ionizing photons is determined from a binomial distribution with $(p + q)$ trials and a probability of α . Therefore $P(q \cap p)$ is the probability that $(p + q)$ photons hit the detector and p photons are non-ionizing:

$$\begin{aligned}
P(q \cap p) &= \text{Poiss.}((p + q); \lambda) \times \text{Binom.}(p; (p + q), \alpha) \\
&= \frac{\lambda^{(q+p)} e^{-\lambda}}{(q + p)!} \frac{(q + p)!}{p! q!} \alpha^p (1 - \alpha)^q \\
&= \frac{\lambda^{(q+p)} e^{-\lambda}}{p! q!} \alpha^p (1 - \alpha)^q. \tag{B2}
\end{aligned}$$

If the mean number of photons hitting the detector is λ and there is a $(1 - \alpha)$ probability that a photon will be ionizing, then the mean number of ionizing photons hitting the detector is $\lambda \cdot (1 - \alpha)$. Therefore $P(q)$ is determined from a Poisson distribution with a mean of

$\lambda \cdot (1 - \alpha)$:

$$\begin{aligned} P(q) &= \text{Pois.}(q; \lambda(1 - \alpha)) \\ &= \frac{\lambda^q (1 - \alpha)^q e^{-\lambda(1 - \alpha)}}{q!}. \end{aligned} \quad (\text{B3})$$

Likewise, $P(p)$ is determined from a Poisson distribution with a mean of $\lambda \cdot \alpha$:

$$\begin{aligned} P(p) &= \text{Pois.}(p; \lambda \cdot \alpha) \\ &= \frac{\lambda^p \alpha^p e^{-\lambda \cdot \alpha}}{p!}. \end{aligned} \quad (\text{B4})$$

Using Eqs. B2 and B3, Eq. B1 becomes:

$$\begin{aligned} P(p|q) &= \frac{q! \lambda^{(q+p)} e^{-\lambda} \alpha^p (1 - \alpha)^q}{p! q! \lambda^q (1 - \alpha)^q e^{-\lambda(1 - \alpha)}} \\ &= \frac{\lambda^p \alpha^p e^{-\lambda \cdot \alpha}}{p!} \\ &= \text{Pois.}(p; \lambda \cdot \alpha). \end{aligned} \quad (\text{B5})$$

Equation B5 shows that the sub-peak distribution of p for a given q is just the probability of having p non-ionizing photons, which is a Poisson distribution with a mean of $\lambda \cdot \alpha$. Importantly, the sub-peak distribution is *independent* of q , and is therefore the same for each e^-h^+ -pair peak. As shown in Fig. 3, when the resolution smearing is applied, these sub-peak distributions shift the location of the e^-h^+ -pair peaks in the spectrum. The amount that the peaks are shifted by ΔE_{ph} is determined from mean energy of non-ionizing photons at each e^-h^+ -pair peak. As the sub-peak distributions are the same for each peak, the amount that each peak is shifted by is also constant:

$$\Delta E_{\text{ph}} = E_\gamma \cdot \lambda \cdot \alpha. \quad (\text{B6})$$

Lastly, we consider what effect the bulk CT and II processes may have on the sub-peak distributions. For the q^{th} e^-h^+ -pair peak there are q ionizing photons and thus q e^-h^+ pairs that propagate through the detector. The peaks in the sub-peak distribution only arise when all of the primary charges from the e^-h^+ pairs reach the surface without undergoing a CT or II process; otherwise the measured energy will be in a non-quantized region of the spectrum. Appendix A showed that the probability of a charge from a surface event to traverse the detector without undergoing a CT or II process is $e^{-T_{e/h}}$, where $T_{e/h}$ encodes the CT and II probabilities for either the electron or hole. The probability of q charges from a surface event to traverse the detector without undergoing CT or II processes is found from a binomial distribution with q trials and a probability of $e^{-T_{e/h}}$: $\text{Binom.}(q; q, e^{-T_{e/h}}) = e^{-qT_{e/h}}$. Therefore while the overall scaling of the sub-peak distribution depends on q , the shape of the underlying distribution remains constant for each e^-h^+ -pair peak.

Appendix C: Limitations of the Single- e^-h^+ -Pair Solutions

As discussed in Sec. V, the exponential CTII model is limited by the highest order of processes that are modelled. Specifically, solutions for surface events and bulk-single-charge events are found for up to second-order processes, whereas for bulk- e^-h^+ -pair events, solutions are found for up to first-order processes. In order to assess and quantify these limitations, the single- e^-h^+ -pair solutions are compared to simple Monte Carlo (MC) simulations of the CT and II processes. The MC simulations model the CT and II processes using the same initial assumptions as the analytical model: that the probability distributions of CT or II occurring are described by Eq. 5, and where CT and II processes are parameterized by the characteristic lengths τ_i . However unlike the analytical model, the MC simulations are able to include higher-order CT and II processes. In these MC simulations, there are no physical or detector-response processes that are modelled other than CT, II, and generic resolution smearing.

We would like to determine where these higher-order processes become significant such that the analytical model is no longer a suitable description of the MC simulations, and thus of these CT and II processes. There are two main factors that will cause the analytical solutions to deviate from the MC simulations. The first is the total probability of impact ionization, and the second is the total number of events in the simulation. Increasing either the total probability of II or the total number of events will increase the number of events in the MC simulation that undergo higher-order CT or II process that the analytical solutions do not model.

The limitations of the single- e^-h^+ -pair solutions can then be evaluated by using a simple procedure. For each event type, we scanned over the total II probability in the model and the total number of events in the MC simulation. After computing the analytical model and running the simulation for each set of parameters, we performed a Kolmogorov–Smirnov (KS) test to determine if the simulated spectrum is described by the analytical model for a given level of confidence. For simplicity, we define the total II probability of a single charge $f_{\text{II, tot}}$ as $f_{\text{II, tot}} = f_{\text{IIee}} + f_{\text{IIeh}} = f_{\text{IIhe}} + f_{\text{IIhh}}$, where each f_i is equal to $f_{\text{II, tot}}/2$. For surface events and bulk-single-charge events, the tests assume that the initial charge is an electron. Furthermore, each of the solutions and simulations assume a small CT probability of $f_{\text{CTe}} = f_{\text{CTh}} = 1\%$ in order to include all possible processes. The KS tests take the null hypothesis that the MC simulation is described by the same probability distribution as the analytical model, and the results from the tests are subsequently placed into three categories: accepted (failed to reject the null hypothesis at 90% confidence level), rejected the null hypothesis at a 90% confidence level, and rejected the null hypothesis at a 99% confidence level. The results of the KS tests for each event type are shown

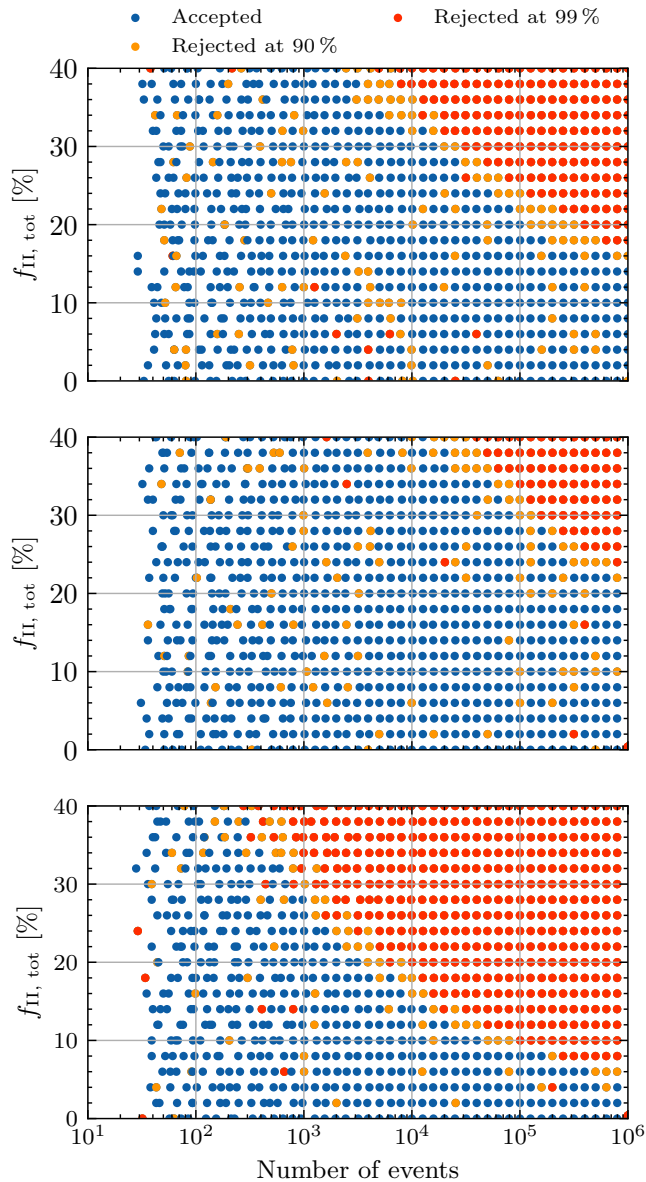


FIG. 7. Results of the KS tests performed using the analytical CT and II solutions and the MC simulations, where each dot corresponds to a test performed for a particular value of the total II probability for a single charge $f_{\text{II, tot}}$ and of the total number of events in the simulation. The tests were performed separately for surface events (top), bulk-single-charge events (middle), and bulk- e^-h^+ -pair events (bottom).

in Fig. 7.

The test results from Fig. 7 clearly illustrate the regions of this parameter space where the analytical solutions of the exponential CTII model deviate from the MC simulations. For reference, measurements of $f_{\text{II, tot}}$ in HVeV detectors have been on the order of 1% [8, 19]. However, these results represent a worst-case scenario for the model, as other parameters can extend the bound-

ary of this limitation. For instance, high CT probabilities will generally lower the probabilities of high-order II processes. Furthermore, these tests were performed using the single- e^-h^+ -pair solutions, whereas modelling the full detector response will often require the multi- e^-h^+ solutions. In many cases, the multi- e^-h^+ solutions will cause the high-order II processes to be subdominant within the total probability distribution, as can be seen by comparing the top and bottom plots of Fig. 2. In these scenarios, the analytical solutions may adequately describe the CT and II processes even for higher II probabilities or for a larger number of events.

- [1] M. F. Albakry *et al.* (SuperCDMS Collaboration), Investigating the sources of low-energy events in a SuperCDMS-HVeV detector, *Phys. Rev. D* **105**, 112006 (2022).
- [2] I. Alkhatib *et al.* (SuperCDMS Collaboration), Light Dark Matter Search with a High-Resolution Athermal Phonon Detector Operated above Ground, *Phys. Rev. Lett.* **127**, 061801 (2021).
- [3] G. Angloher *et al.* (CRESST Collaboration), Results on sub-GeV dark matter from a 10 eV threshold CRESST-III silicon detector, *Phys. Rev. D* **107**, 122003 (2023).
- [4] R. Agnese *et al.* (SuperCDMS Collaboration), Search for low-mass dark matter with CDMSlite using a profile likelihood fit, *Phys. Rev. D* **99**, 062001 (2019).
- [5] A. H. Abdelhameed *et al.* (CRESST Collaboration), First results from the CRESST-III low-mass dark matter program, *Phys. Rev. D* **100**, 102002 (2019).
- [6] E. Armengaud *et al.* (EDELWEISS Collaboration), Searching for low-mass dark matter particles with a massive Ge bolometer operated above ground, *Phys. Rev. D* **99**, 082003 (2019).
- [7] R. Agnese *et al.* (SuperCDMS Collaboration), First Dark Matter Constraints from a SuperCDMS Single-Charge Sensitive Detector, *Phys. Rev. Lett.* **121**, 051301 (2018).
- [8] D. W. Amaral *et al.* (SuperCDMS Collaboration), Constraints on low-mass, relic dark matter candidates from a surface-operated SuperCDMS single-charge sensitive detector, *Phys. Rev. D* **102**, 091101 (2020).
- [9] B. S. Neganov and V. N. Trofimov, Possibility of producing a bulky supersensitive thermal detector at a temperature close to absolute zero, *Sov. J. Exp. Theor. Phys.* **28**, 328 (1978).
- [10] P. N. Luke, Voltage-assisted calorimetric ionization detector, *J. Appl. Phys.* **64**, 6858 (1988).
- [11] R. Ren, C. Bathurst, Y. Y. Chang, R. Chen, C. W. Fink, Z. Hong, N. A. Kurinsky, N. Mast, N. Mishra, V. Novati, *et al.*, Design and characterization of a phonon-mediated cryogenic particle detector with an eV-scale threshold and 100 keV-scale dynamic range, *Phys. Rev. D* **104**, 032010 (2021).
- [12] F. Ponce, W. Page, P. L. Brink, B. Cabrera, M. Cherry, C. Fink, N. Kurinsky, R. Partridge, M. Pyle, B. Sadoulet, *et al.*, Modeling of Impact Ionization and Charge Trapping in SuperCDMS HVeV Detectors, *J. Low Temp. Phys.* **199**, 598 (2020).
- [13] K. Ramanathan and N. Kurinsky, Ionization yield in silicon for eV-scale electron-recoil processes, *Phys. Rev. D* **102**, 063026 (2020).
- [14] Y. Hochberg, T. Lin, and K. M. Zurek, Absorption of light dark matter in semiconductors, *Phys. Rev. D* **95**, 023013 (2017).
- [15] R. Essig, M. Fernández-Serra, J. Mardon, A. Soto, T. Volansky, and T.-T. Yu, Direct detection of sub-GeV dark matter with semiconductor targets, *JHEP* **2016** (5), 46.
- [16] Z. Hong, R. Ren, N. Kurinsky, E. Figueroa-Feliciano, L. Wills, S. Ganjam, R. Mahapatra, N. Mirabolfathi, B. Nebolsky, H. D. Pinckney, *et al.*, Single electron-hole pair sensitive silicon detector with surface event discrimination, *Nucl. Instrum. Methods A* **963**, 163757 (2020).
- [17] M. Kelsey, R. Agnese, Y. Alam, I. A. Langroudy, E. Azadbakht, D. Brandt, R. Bunker, B. Cabrera, Y.-Y. Chang, H. Coombes, *et al.*, G4CMP: Condensed matter physics simulation using the Geant4 toolkit, *Nucl. Instrum. Methods A* **1055**, 168473 (2023).
- [18] M. Kelsey, G4CMP code repository on GitHub (2022).
- [19] F. Ponce, C. Stanford, S. Yellin, W. Page, C. Fink, M. Pyle, B. Sadoulet, B. Serfass, S. L. Watkins, P. L. Brink, *et al.*, Measuring the impact ionization and charge trapping probabilities in SuperCDMS HVeV phonon sensing detectors, *Phys. Rev. D* **101**, 031101 (2020).
- [20] P. Adamson, I. Anghel, A. Aurisano, G. Barr, M. Bishai, A. Blake, G. J. Bock, D. Bogert, S. V. Cao, C. M. Castromonte, *et al.* (MINOS Collaboration), Observation of seasonal variation of atmospheric multiple-muon events in the MINOS Near and Far Detectors, *Phys. Rev. D* **91**, 112006 (2015).
- [21] (SuperCDMS Collaboration), HVeV Run 4 Dark Matter Search, in-preparation.
- [22] K. D. Irwin, S. W. Nam, B. Cabrera, B. Chugg, and B. A. Young, A quasiparticle-trap-assisted transition-edge sensor for phonon-mediated particle detection, *Rev. Sci. Instrum.* **66**, 5322 (1995).
- [23] K. M. Sundqvist, *Carrier Transport and Related Effects in Detectors of the Cryogenic Dark Matter Search*, Ph.D. thesis, University of California, Berkeley (2012).
- [24] A. T. J. Phipps, *Ionization Collection in Detectors of the Cryogenic Dark Matter Search*, Ph.D. thesis, University of California, Berkeley (2016).
- [25] P. Adari, I. M. Bloch, A. M. Botti, M. Cababie, G. Canelo, B. A. Cervantes-Vergara, M. Crisler, M. Daal, A. Desai, A. Drlica-Wagner, *et al.*, SENSEI: First Direct-Detection Results on sub-GeV Dark Matter from SENSEI at SNOLAB (2023), SENSEI Collaboration, arXiv:2312.13342 [astro-ph.CO].
- [26] I. Arnquist, N. Avalos, D. Baxter, X. Bertou, N. Castelló-Mor, A. E. Chavarria, J. Cuevas-Zepeda, J. C. Gutiérrez, J. Duarte-Campderros, A. Dastgheibi-Fard, *et al.* (DAMIC-M Collaboration), First Constraints from DAMIC-M on Sub-GeV Dark-Matter Particles Interacting with Electrons, *Phys. Rev. Lett.* **130**, 171003 (2023).
- [27] B. A. Cervantes-Vergara, S. Perez, J. Estrada, A. Botti, C. R. Chavez, F. Chierchie, N. Saffold, A. Aguilar-Arevalo, F. Alcalde-Bessia, N. Avalos, *et al.*, Skipper-CCD sensors for the Oscura experiment: requirements and preliminary tests, *Journal of Instrumentation* **18** (08), P08016.
- [28] M. F. Albakry *et al.* (SuperCDMS Collaboration), First Measurement of the Nuclear-Recoil Ionization Yield in Silicon at 100 eV, *Phys. Rev. Lett.* **131**, 091801 (2023).

Electron Spectroscopy using Transition-Edge Sensors

K. M. Patel,^{1,2} S. Withington,³ A. G. Shard,² D. J. Goldie,¹ and C. N. Thomas¹

¹*Cavendish Laboratory, University of Cambridge, JJ Thomson Avenue, Cambridge CB3 0HE, United Kingdom*

²*National Physical Laboratory, Hampton Road, Teddington TW11 0LW, United Kingdom*

³*Department of Physics, University of Oxford, Oxford OX1 3PU, United Kingdom*

(Dated: 5 March 2024)

Transition-edge sensors (TESs) have the potential to perform electron spectroscopic measurements with far greater measurement rates and efficiencies than can be achieved using existing electron spectrometers. Existing spectrometers filter electrons by energy before detecting a narrow energy band at a time, discarding the vast majority of electrons available for measurement. In contrast, transition-edge sensors (TES) have intrinsic energy sensitivity and so do not require prior filtering to perform energy-resolved measurements. Despite this fundamental advantage, TES electron spectroscopy has not, to our knowledge, previously been reported in the literature. We present the results of a set of proof-of-principle experiments demonstrating TES electron spectroscopy experiments using Mo/Au TESs repurposed for electron calorimetry. Using these detectors, we successfully measured the electron spectrum generated by an electron beam striking a graphite target with energies between 750 and 2000 eV, at a noise-limited energy resolution of 4 eV. Based on the findings of these experiments, we suggest improvements that could be made to TES design to enhance their electron detection capabilities through the use of a dedicated electron absorber in the device with integrated electron optics.

I. INTRODUCTION

Transition-edge sensors (TESs) are thin-film superconducting devices capable of high-sensitivity, energy-resolved photon measurement. Over the last thirty years, TESs have found applications across an increasing range of fields from astronomical observations to dark matter searches^{1–6}. However, one area of TES research that has received little attention is massive particle spectroscopy, encompassing molecular, ion-beam and electron measurement techniques. The lack of research into TES electron spectroscopy is of particular note due to the widespread usage of electron spectroscopic techniques and the potential benefits offered by TESs over conventional electron spectrometers.

All modern commercial electron spectrometers follow the same fundamental operating principle where electrons are collected, dispersed by energy and then counted using energy-insensitive detectors. For example, the concentric hemispherical analyser (CHA), the analyser of choice for X-ray photoelectron spectroscopy (XPS) measurements, uses the electric field between two concentric hemispheres of differing electric potentials to disperse electrons in space depending on their energy. This arrangement sets up an energy filter where only electrons within a narrow energy band, defined by the hemisphere potentials, can pass through the hemispheres to the particle-counting microchannel plate.

The inefficiency in this form of measurement lies in the fact that only a narrow electron energy band, approximately 1 to 10 eV in width, can be measured at a time. To perform a wide spectrum measurement, this narrow band must be swept across the entire spectral range and so, at every individual moment in time, the vast majority of electrons emitted from the sample and collected by the instrument cannot be measured. If an

energy range of 1 keV is to be measured, a CHA measuring a window of 1 eV would have at best a measurement efficiency of 0.1% across the measurement. The effect of this inefficiency can be mitigated by increasing the number of electrons collected, either by emitting more electrons from the sample or widening the solid angle of collection; however, these measures cannot address the underlying inefficiency within the operating principle of the spectrometer itself.

An alternate approach is time-of-flight electron spectrometry⁷. In this case, a pulsed X-ray source is required and this is only achievable with specialized and expensive equipment such as an X-ray Free Electron Laser (XFEL). The operation requires fast detection electronics and the electron time-of-flight can be converted into kinetic energy, which scales as the inverse square of the flight time. In principle, all emitted electrons entering the analyzer can be detected, but with variable energy resolution which depends upon the pulse width of the X-ray source, the detector electronics and the time of flight. Only low-energy electrons are detected with good energy resolution and thus the electrons are typically retarded using an electric field prior to entering the analyzer. For practical purposes, the efficiency, resulting from the duty cycle of X-rays and the necessity to collect multiple kinetic energy regions, is low.

The ideal solution is to use a detector that is intrinsically able to resolve the energy of an incident electron, removing the need for filtering in space or time. Such a detector would be capable of continuous measurement and the instantaneous fraction of electrons emitted from the sample that can be characterized will scale with the number of detectors used. TESs are near-ideal candidate, as they have high energy sensitivities and the technology exists to readout out arrays of several thousand devices concurrently^{8–10}.

TESs perform high-resolution particle calorimetry by

exploiting the extremely sharp resistance-temperature dependence of certain metals in their superconducting transition. Voltage-biasing a TES at a point within its superconducting transition creates an electrothermal feedback loop that maintains the device's temperature by balancing the thermal power received from particle absorption with a reduction in ohmic power dissipated. The TES current drop associated to the drop in ohmic power dissipation can be monitored to precisely determine the energy of the absorbed particle.

An additional advantage of TES measurement over existing electron analysers is the ability of every pixel to independently measure both electron arrival time and energy simultaneously. This ability allows for coincidence spectroscopy measurements, where coincident electron emission events are analysed to probe energy transfer mechanisms within the sample¹¹; these measurements could be performed alongside conventional electron spectroscopic techniques without requiring additional, specialised apparatus.

In a previous article, we simulated the capabilities of a TES array measuring an X-ray photoelectron spectrum¹², the results of which showed that small arrays of TESs, numbering tens of devices, could be capable of comparable energy resolutions and measurement rates to existing XPS analysers, with considerable scope of improving measurement rates by increasing array size. Based upon these simulations, TES electron spectroscopy is a realistic proposal but experimental validation of TES electron spectroscopy has not previously been provided. This paper reports the first experimental demonstration of TES electron spectroscopy.

II. EXPERIMENTAL

Proof-of-principle TES electron measurements were performed using Mo/Au TESs that were adapted for the purposes of electron calorimetry. The Mo/Au TES used consisted of a square superconducting bilayer, 70 μm in length, with film thicknesses of 120 nm gold atop 40 nm of molybdenum; this bilayer was suspended by four 1.41 μm long Si_xN_y legs, and displayed a transition temperature (T_c) of 200 mK. Further details on the device design and fabrication have been reported previously¹³.

A SPECS EQ22 electron source was mounted on a closed-cycle adiabatic demagnetisation refrigerator in the manner shown in Fig. 1. The electron source was used to generate electron beams with energies ranging from 250 to 2000 eV with the position of the beam controlled by X- and Y- electrostatic deflector plates within the source itself. The electron beam was directed into the cryogenic volume through two tubes mounted to the cryostat heat shields and capped with apertures.

The TES device chip was mounted to the 100 mK stage of the cryostat and read-out with an amplifier that uses superconducting quantum interference devices (SQUIDs). To prevent charge accumulation, the TES

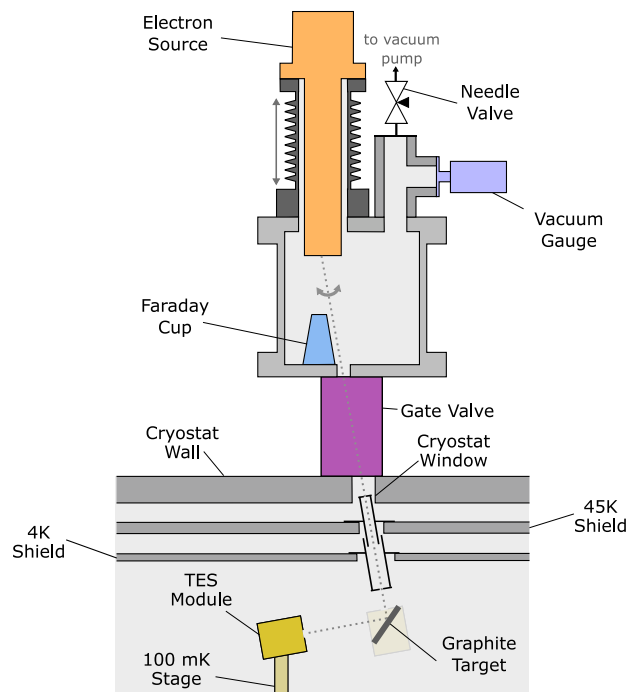


FIG. 1. TES electron measurement experiment in the scattered electron measurement beam configuration.

was connected to a shared cryostat ground through the TES bias circuit.

Two experimental configurations were tested which will be referred to as direct and scattered measurements. The direct measurements were performed by positioning the TES module, containing the TES and SQUID arrays, in front of the cryostat window, receiving the electron beam directly. The purpose of these direct measurements were to determine beam alignment through the cryostat windows, demonstrate TES electron detection and characterise the response of the TES to differing electron beam energies. For the scattered measurements, the electron beam was aimed at a target of 0.254 mm thick graphite foil (99.8% purity) at an incidence angle of 60°, with the TES measuring the scattered electron spectrum.

A key consideration in the experimental design was mitigating infrared black-body radiation emitted from room-temperature components onto the TES module. No suitable window material exists that allows unobstructed electron passage through it whilst filtering infrared radiation at the electron energies being tested, a free space path was used from the source to the TES. Infrared loading was reduced along this path using a combination of four approaches.

Firstly, the electron beam was deflected off-axis into the cryostat, as shown in Fig. 1; this deflection removed line-of-sight from the high-temperature electron source filament into the cryostat.

The electrons passed through two tubes mounted to the 45 K and 4 K stages respectively before entering

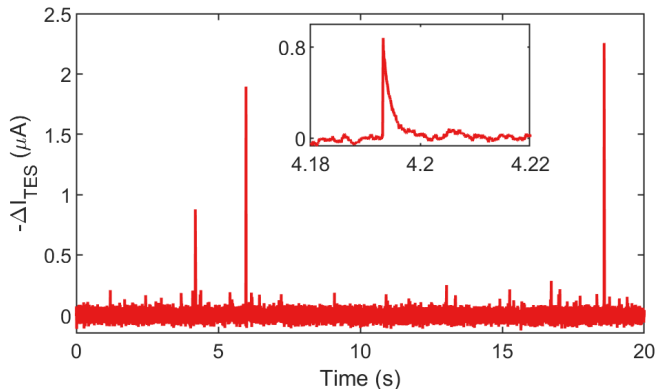


FIG. 2. Time series TES measurement of a 2 keV electron beam. The inset shows a measurement event with estimated 190 eV energy.

the cryostat chamber. These tubes were painted black with colloidal graphite paint to absorb infrared radiation whilst providing an electrically grounded surface to prevent charge accumulation.

The third modification was to place apertures on the TES module (200 μm diameter), 4 K tube (3 mm diameter for direct measurements, 1 mm diameter for scattered measurements) and 45 K tube (5 \times 3 mm slotted aperture), to block stray infrared photons reaching the detector.

The final infrared mitigation was the use of mesh grid across the 45 K aperture to diffract and screen incident radiation. A mesh grid was also used on the 4 K aperture for the direct measurements. The meshes consisted of 1500 lines per inch copper grids with 55% open area and approximately 10 μm hole width. The presence of the mesh grids was a compromise between greatly reducing infrared loading and blocking or scattering a portion of the electron beam entering the cryostat.

The experiment was designed to measure electrons with energies from 0 to 2000 eV; at these energies, electrons are highly susceptible to deflection by the Earth's magnetic field. To reduce the impact of this deflection on the measurements, the electron source was shielded with mu-metal and Metglas 2705M magnetic shielding foil was wrapped around the electron source vacuum chamber and infrared tubes. The aperture on the 45 K tube was not circular but horizontally slotted with dimensions of 5 \times 3 mm to compensate for magnetic beam deflection prior to entering the cryostat.

III. RESULTS

A. Direct Measurements

The response of a TES to an incident particle is an exponentially decaying pulse in current whose area directly relates to the energy absorbed by the device. Fig. 2 shows a time series TES measurement of a 2 keV electron beam

aimed at the TES module in which a series of such pulses were observed.

Measurements such as that shown in Fig. 2 were analysed to determine the energy spectrum of observed electron events. The analysis software used to identify, extract and calculate the energies of individual TES events was adapted from a previous work simulating TES electron spectroscopy¹². The energies of TES calorimetry peaks would typically be determined by comparison to a known energy standard, such as X-ray emission lines in the case of TES X-ray calorimetry. For these electron measurements, in the absence of such a calibration standard, the absorbed particle energies E_{TES} have been calculated by¹⁴

$$E_{\text{TES}} = \int_{t_1}^{t_2} -\Delta I_{\text{TES}}(t) V_{\text{TES}} dt, \quad (1)$$

where t_1 and t_2 are the start and end times of the electron absorption event, V_{TES} is the TES bias voltage and I_{TES} is the change in TES current from equilibrium. The calculated energy corresponds to the integrated change in the Joule heating within the TES due to an electron absorption event. This energy is equivalent to energy absorbed by the TES in the limit of strong electrothermal feedback where all of the received energy is compensated for electrically; in practice, a portion of the received thermal energy instead diffuses to the bath. The energy difference can be approximated by¹⁵

$$E_{\text{TES}} = \frac{\left(1 - \frac{T_b^n}{T_c^n}\right)}{\left(1 - \frac{T_b^n}{T_c^n}\right) + \frac{n}{\alpha}} E_{\text{abs}} \quad (2)$$

where T_b is the bath temperature, n is a device parameter with a value between 2 and 4 that is characteristic of the thermal link between the TES and surrounding thermal bath, and α is a measure of the sharpness of the TES superconducting transition at the device temperature. For example, a device with $\alpha = 30$, $n = 2$, $T_b = 130$ mK and $T_c = 200$ mK would lose 10% of the received energy by thermal diffusion. It should be noted that α is a function of temperature and will vary within a pulse as the TES temperature moves within the superconducting transition, which further complicates the calculation. The presence of this energy underestimate is not significant for the purposes of these proof-of-principle experiments because it is systematic to all electron observations and is caused by the analysis method used rather than the intrinsic behaviour of the device.

The measurement in Fig. 2 was repeated across multiple beam energies ranging from 250 eV to 2000 eV; the resulting measured electron energy distributions are shown in Fig. 3a. Several common features are seen across all energies: a high energy peak that tracks the beam energy, a fixed low energy peak at 20 eV and a flat background of events. The high energy peak very likely corresponds to primary electrons from the electron source, with the low energy events being secondary electrons emitted from

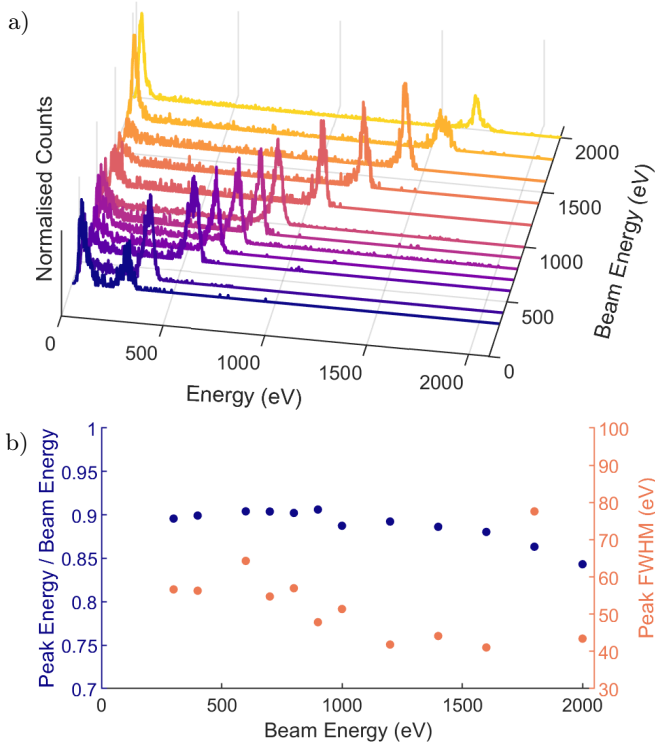


FIG. 3. a) Measured electron spectra taken at beam energies spanning 300 eV to 2000 eV. The spectra have been normalised by total area and energy bin widths of 2 eV have been used. b) Ratio between measured energy of the high energy peak and the applied beam energy plotted on the left axis. The measured peak energy was calculated by applying a Gaussian fit. Full-width at half maximum of the fitted high-energy peak plotted against beam energy on the right axis.

the meshes used to reduce thermal loading or other surfaces between the electron source and the TES itself. The low-level background of events is likely a result of inelastic scattering during flight, or upon striking the TES. In either case, this scattering would result in partial energy absorption by the TES. A small number of events with energies in excess of the beam energy were observed; these result when two or more electrons are detected near simultaneously and are resolved by the analysis software as a single event, with energy equal to the sum of their individual energies. This effect, termed pile-up, is common to other detectors.

The primary electron peaks were fitted with Gaussian distributions to identify the peak location relative to the beam energy, and the peak full-width at half maximum (FWHM) (Fig. 3b). The ratio of central peak energy to beam energy is approximately 0.9 up to 1000 eV and then falls at greater beam energies. This trend is consistent with the expected bias from the energy analysis method. The energy received by electron absorption briefly increases the TES temperature before being compensated for by the electrothermal feedback loop. For high energy particles, the TES temperature can rise through a significant portion of its superconducting transition or be

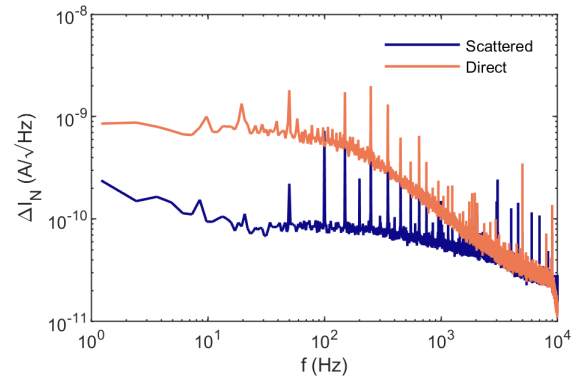


FIG. 4. TES current noise spectral densities for direct beam and scattered measurements.

driven into its normal state. As the TES reaches the upper region of its transition, α falls in value, reducing the effectiveness of the electrothermal feedback loop and increasing the energy underestimate.

The broad FWHM of the primary electron peak is primarily due to the energy resolution of the TES. A disadvantage of the direct beam configuration is infrared loading from the room-temperature apparatus onto the TESs with the corresponding photon noise significantly degrading energy sensitivity. This degradation is shown by the current-noise spectral density measurements in Fig. 4. The TES FWHM energy resolution can be approximated by¹⁶

$$\Delta E_{abs} = 2\sqrt{2\log(2)} \text{NEP}(0) \sqrt{\tau_{\text{eff}}}, \quad (3)$$

where $\text{NEP}(0)$ is the zero-frequency noise-equivalent power and τ_{eff} is the TES effective response time. $\text{NEP}(0)$ can be calculated using the zero-frequency TES responsivity $s_I(0)$, following¹⁴

$$\text{NEP}(0) = \frac{\Delta I_N(0)}{s_I(0)} \quad (4)$$

where ΔI_N is the current-noise spectral density. With $\tau_{\text{eff}} = 1.1$ ms and $s_I(0) = 17$ and $21 \mu\text{A/pW}$ for the direct and scattered measurements respectively, the predicted resolutions are calculated as 20 eV for the direct measurements compared to 4 eV for the scattered measurements using the same device; this change in resolution can be attributed to a reduction in thermal loading and corresponding photon noise in the scattered measurements.

B. Scattered Measurements

The scattered electron measurements show the use of a TES in a spectroscopic role measuring the scattered electron spectrum emitted from a graphite target. The form of this spectrum can be predicted using the measurements by Goto and Takeichi¹⁷ where such an electron spectrum was generated by a 1 keV beam and measured

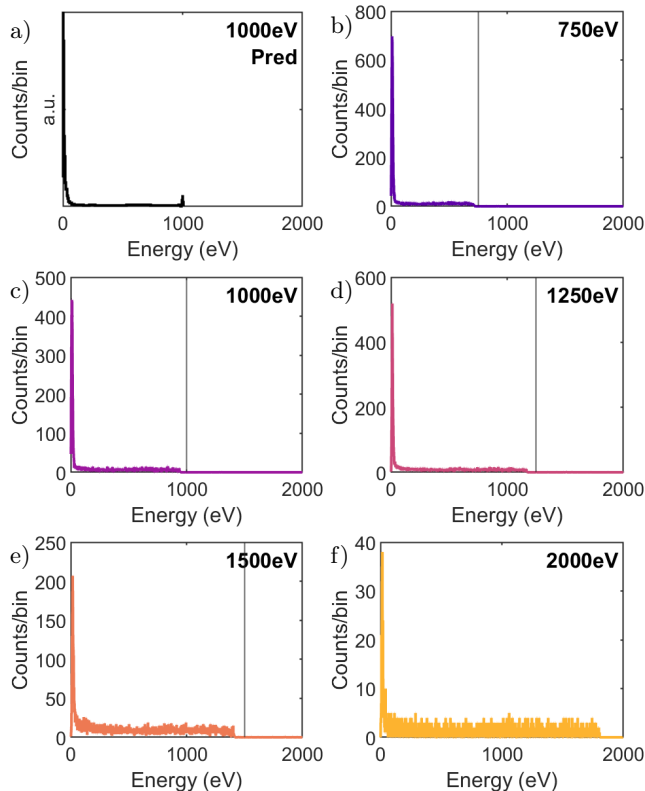


FIG. 5. Measured electron energy spectra generated by electron impact on a graphite target with a 1 eV bin width. The incident electron beam energy on the target is shown by the vertical line. The predicted spectrum in (a) has been reproduced from measurements by Goto and Takeichi¹⁷ for comparison to observed TES spectra.

using a cylindrical mirror analyser (Fig. 5a). The TES measured electron spectra are shown in Fig. 5b-f at beam energies from 750 eV to 2000 eV. These measurements agree well with the comparison spectrum in Fig. 5a, showing a sharp secondary electron peak below 50 eV and a background of inelastically backscattered electrons extending up to, but not exceeding the beam energy. It is important to highlight that the spectra in Fig. 3a and Fig. 5 were constructed by aggregating the energies of individual electron detection events. As such, the low-level fluctuations in the observed spectra reflect the number of electrons observed in the relevant energy bin and are not background noise.

The observed spectra do not show the elastic peak, likely due to the peak being broadened into the background as a result of electron absorption inefficiency of the TES, the energy resolution of the detector and analysis method used. In these devices, which were not designed for electron detection, the electrons were absorbed directly in the Mo/Au TES. The gold surface of the device will have emitted a significant number of secondary electrons. Based on previous measurements¹⁸, we estimate a secondary electron yield of 1.4 from the gold film per primary electron at 1 keV beam energy with the vast

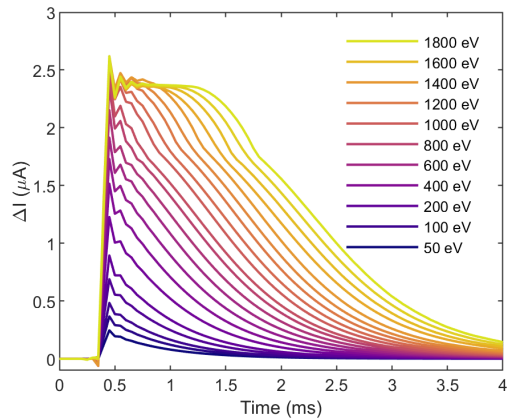


FIG. 6. Average TES responses based on calculated event energy. Each plotted response has been averaged from observed responses within 5 eV of the nominal event energies. Responses between 200 eV and 1800 eV event energies have been plotted at 100 eV intervals; the legend only shows events in this range at 200 eV intervals for concision.

majority of secondary electrons with energies between 0 and 20 eV. In a device designed specifically for electron detection, this effect can be greatly mitigated by using a separate absorber made from a more favorable material, such as carbon.

The TES response to electron events of different energies is shown in Fig. 6 where TES pulse shapes have been grouped and averaged by energy. The figure clearly demonstrates the progression of the TES response into saturation as electron energy increases. The TES is said to saturate when the absorbed energy drives the device into its normal state where the device loses sensitivity to additional energy input, and the TES response plateaus. This effect can be seen at electron energies at 1400 eV and above. While the TES loses sensitivity to additional energy input under these conditions, the electrothermal feedback loop continues to compensate for the thermal energy within the device leading to a lengthened TES response and the particle energy can still be estimated, as demonstrated in Fig. 5f.

IV. DISCUSSION

The measurements in Fig. 5 experimentally demonstrate the principle of TES electron spectroscopy and highlight the most important areas of development required to improve detector performance. The advantage of TES electron spectroscopy over existing methods is potential orders of magnitude improvement to electron measurement efficiency. However, to be of practical use, the TES must provide energy resolutions within the ranges achievable by existing electron spectrometers.

In the case of XPS measurements, the resolution of an XPS analyser typically lies in the range of 0.1-5 eV for electrons below 1500 eV. For comparison, phonon-noise-

limited TESs with a transition temperature of 200 mK are capable of energy resolutions better than 1 eV. The noise-limited TES resolution scales with temperature, with lower transition temperatures providing improved resolution. As such, within the bounds of current cryostat capabilities, a practical TES spectrometer for XPS would be operating near its phonon-noise-limited resolution and so should be optimised for energy resolution.

The resolution of a TES is determined by the efficiency of the device at capturing the energy of the absorbed particle, and the ability to extract the magnitude of absorbed energy from the measured detector response. The measurements in the previous section show no apparent differences in the behaviour of the TES after electron absorption compared to TES behaviour in photon calorimetry. Sub-eV resolutions have been demonstrated using TES X-ray calorimeters occupying a similar energy range to that investigated here¹⁹, indicating that such TES performance in electron calorimetry is entirely reasonable. However, achieving such resolutions would require near ideal electron energy absorption efficiencies.

The main energy loss pathways during electron absorption are backscattered electron emission and secondary electron emission, examples of which can be clearly seen in Fig. 5 where such electrons scattered from a graphite surface were measured. Backscattered electrons can carry a wide range of energies up to the primary incident electron energy whereas nearly all secondary electrons have energies below 50 eV^{20,21}. In a TES electron spectroscopy measurement, the effect of backscattered emission is to map received electron energies across a range of energies throughout the spectrum, distorting the background. Secondary electrons shift observed electron energies by relatively small amounts, distorting the characteristic spectral peaks. In both cases, the rate of emission from the TES absorber can be reduced by using absorbing material made of low atomic mass materials due to their lower inelastic scattering cross-sections²². In addition, using roughened or structured (e.g. pitted) absorber surfaces can reduce electron emission.

A promising method to greatly improve electron absorption efficiencies is through the use of electron optics. For example, placing a surface above a TES (with an aperture for electron transmission), biased at -20 V, would suppress the majority of secondary electron emitted from the TES surface. The use of electron optics to enhance TES electron absorption raises the question of possible electric field coupling to the TES and degradation in performance. Measurements of the behaviour of a TES in the presence of DC electric fields up to 90 kV/m showed no observable impact on TES behaviour, indicating that electrostatic optics can be practically implemented in a TES electron spectrometer²³.

An alternative approach could be to integrate electron micro-optics into the TES itself. A TES design based upon this approach is shown in Fig. 7 using a Ti/Au bilayer superconductor and a dedicated Au/Ti electron absorber, with the surface layer of the absorber being tita-

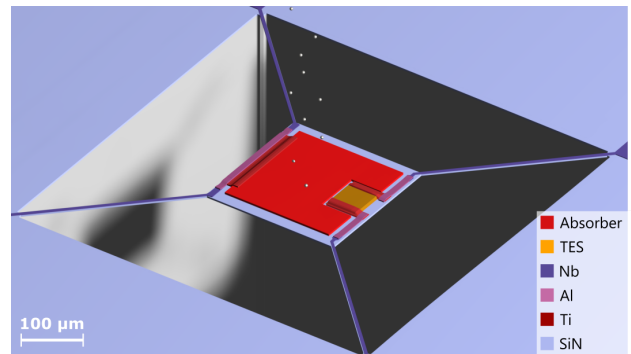


FIG. 7. Proposed design of a bespoke electron spectroscopy TES with an independently biased absorber.

ni-um. In this design, the absorber is electrically isolated from the TES allowing it to be biased independently; applying a +20 V DC bias to this absorber would have an equivalent effect as applying a -20 V bias to an external surface as described previously. In this way, it is possible to achieve highly-efficient electron absorption independent of absorber material choice.

There also exists a range of possibilities with regards to the manner in which a TES can be used in an electron spectrometer. The TESs could perform the entirety of the electron energy discrimination, as was the case in Fig. 5 but there may be advantages in a hybrid approach, combining TES calorimetry with electron energy dispersion used in existing electron spectrometers. TES energy resolution follows $\Delta E \propto \sqrt{E_{\text{sat}}}$ where E_{sat} is the TES saturation energy, and so TESs with lower saturation energy display improved resolution. If the electrons collected by a spectrometer are spatially dispersed by energy and separated into bins, the electrons can be uniformly decelerated by a known amount within each bin independently, before reaching the TES detector array. Controllable electron deceleration prior to detection would allow for TESs with saturation energies far below the maximum of the emitted electron spectrum, greatly improving the available energy resolution and the presence of multiple bins would allow for concurrent measurement of the entire spectral range. Larger number of bins can be used with reduced saturation energies and improved resolutions, with the possibility of exceeding the energy resolution, detection efficiency and count rate capabilities of existing electron spectrometers simultaneously.

V. CONCLUSION

Due to their fundamentally different method of performing energy-resolved measurements, TESs offer significant benefits in electron measurement over existing electron spectrometers. The inherent energy sensitivity of TESs allows for orders of magnitude improvement in electron detection efficiency, and therefore measure-

ment rate, over what is currently achievable. We believe the presented measurements experimentally demonstrate TES electron spectroscopic measurement, opening the door to further investigation in this field. The ability to perform spectroscopic measurements using TESs that have been adapted for electron calorimetry suggests far greater performance is achievable using devices designed specifically for electron measurement and that creating a TES array capable of exceeding the capabilities of traditional electron spectrometers is entirely possible.

The experimental work has been performed in the context of electron spectroscopy but applies more widely to TES massive particle spectroscopy in general, an area that has received little attention in comparison to TES photon measurement. The ability to use TESs for the measurement of charged particles is of particular interest as the use of electron optics allows for precise control of the acceleration and position of these particles. Integrating electron optical systems with TES spectrometers can allow for manipulating the interaction between the particle and the TES, enhancing or reducing absorption efficiency, modifying the energy of the incident particles or screening them entirely. The ability to screen charged particles is also of interest in applications beyond massive particle spectroscopy, such as in space-based astronomical observation where secondary electrons produced by cosmic ray strikes can result in unwanted measurement events in the detector. An elegant route control the interaction between TESs and charged particles is to integrate electron optics into the detector itself. The proposed TES electron calorimeter design uses an independently biased absorber to enhance electron energy absorption efficiency but such a structure can equally be used to screen low energy electrons or indicating the scope of possibility in this approach to particle detection.

ACKNOWLEDGMENTS

KMP acknowledges support from EPSRC Cambridge NanoDTC (EP/L015978/1). KMP and AGS acknowledge support from the National Measurement System of the UK Department for Science, Innovation and Technology. We would also like to thank Rebecca Harwin and Michael Crane for their work on the initial device designs and fabrication, as well as David Sawford and Dennis Molloy for their assistance in preparing the experiments.

AUTHOR DECLARATIONS

Conflict of Interest

The authors have no conflicts to disclose.

Author Contributions

K. M. Patel: Conceptualization, Methodology, Investigation (lead), Software, Formal analysis (lead), Writing - original draft, Visualization. **S. Withington:** Conceptualization, Methodology, Supervision, Project administration, Funding acquisition, Writing - review and editing. **A. G. Shard:** Conceptualisation, Methodology, Supervision, Funding acquisition, Writing - review and editing. **D. J. Goldie:** Conceptualization, Investigation (supporting), Formal analysis (supporting), Writing - review and editing. **C. N. Thomas:** Conceptualization, Formal analysis (supporting), Resources, Writing - review and editing.

DATA AVAILABILITY STATEMENT

The data that support the findings of this study are openly available in the Apollo repository at <http://doi.org/10.17863/CAM.106426>, reference number.

- ¹J. N. Ullom and D. A. Bennett, *Supercond. Sci. Technol.* **28**, 084003 (2015).
- ²S. J. Smith, J. S. Adams, S. R. Bandler, S. Beaumont, J. A. Chervenak, E. V. Denison, W. B. Doriese, M. Durkin, F. M. Finkbeiner, J. W. Fowler, G. C. Hilton, R. Hummatov, K. D. Irwin, R. L. Kelley, C. A. Kilbourne and others, *IEEE Transactions on Applied Superconductivity* **31**, 1 (2021).
- ³J. A. Sobrin, A. J. Anderson, A. N. Bender, B. A. Benson, D. Dutcher, A. Foster, N. Goekner-Wald, J. Montgomery, A. Nadolski, A. Rahlin, P. A. R. Ade, Z. Ahmed, E. Anderes, M. Archipley, J. E. Austermann and others, *ApJS* **258**, 42 (2022).
- ⁴M. Hazumi, P. A. R. Ade, Y. Akiba, D. Alonso, K. Arnold, J. Aumont, C. Baccigalupi, D. Barron, S. Basak, S. Beckman, J. Borrill, F. Boulanger, M. Bucher, E. Calabrese, Y. Chinone and others, *J Low Temp Phys* **194**, 443 (2019).
- ⁵R. Strauss, G. Angloher, P. Bauer, X. Defay, A. Erb, F. v. Feilitzsch, N. F. Iachellini, R. Hampf, D. Hauff, M. Kiefer, J. C. Lanfranchi, A. Langenkämper, E. Mondragon, A. Münster, C. Oppenheimer and others, *Nuclear Instruments and Methods in Physics Research Section A: Accelerators, Spectrometers, Detectors and Associated Equipment Proceedings of the Vienna Conference on Instrumentation 2016*, **845**, 414 (2017).
- ⁶W. Rau and f. S. Collaboration, *J. Phys.: Conf. Ser.* **1342**, 012077 (2020).
- ⁷A. De Fanis, M. Ilchen, A. Achner, T. M. Baumann, R. Boll, J. Buck, C. Danilevsky, S. Esenov, B. Erk, P. Grychtol, G. Hartmann, J. Liu, T. Mazza, J. Montañó, V. Music and others, *Journal of Synchrotron Radiation* **29**, 755 (2022).
- ⁸S. J. Smith, J. S. Adams, S. R. Bandler, S. Beaumont, J. A. Chervenak, A. M. Datesman, F. M. Finkbeiner, R. Hummatov, R. L. Kelly, C. A. Kilbourne, A. R. Miniussi, F. S. Porter, J. E. Sadleir, K. Sakai, N. A. Wakeham and others, *J Low Temp Phys* **199**, 330 (2020).
- ⁹J. R. Stevens, N. F. Cothard, E. M. Vavagiakis, A. Ali, K. Arnold, J. E. Austermann, S. K. Choi, B. J. Dober, C. Duell, S. M. Duff, G. C. Hilton, S.-P. P. Ho, T. D. Hoang, J. Hubmayr, A. T. Lee and others, *J Low Temp Phys* **199**, 672 (2020), 1912.00860.
- ¹⁰L. Gottardi and K. Nagayashi, *Applied Sciences* **11**, 3793 (2021).
- ¹¹T. Arion and U. Hergenbahn, *Journal of Electron Spectroscopy and Related Phenomena Special Anniversary Issue: Volume 200*, **200**, 222 (2015).
- ¹²K. M. Patel, S. Withington, C. N. Thomas, D. J. Goldie, and A. G. Shard, *Supercond. Sci. Technol.* **34**, 125007 (2021).

- ¹³R. Harwin, *Microscopic Physics of Transition Edge Sensors*, Thesis, University of Cambridge (2021).
- ¹⁴K. Irwin and G. Hilton, in *Cryogenic Particle Detection*, Topics in Applied Physics, edited by C. Enss (Springer, Berlin, Heidelberg, 2005) pp. 63–150.
- ¹⁵E. Figueroa-Feliciano, *Theory and Development of Position-Sensitive Quantum Calorimeters*, Ph.D. thesis, Stanford University (2001).
- ¹⁶S. H. Moseley, J. C. Mather, and D. McCammon, *Journal of Applied Physics* **56**, 1257 (1984).
- ¹⁷K. Goto and Y. Takeichi, *Journal of Vacuum Science & Technology A* **14**, 1408 (1996).
- ¹⁸K. M. Patel, *Transition-Edge Sensors for Electron Spectroscopy*, Ph.D. thesis, University of Cambridge (2023).
- ¹⁹S. J. Lee, J. S. Adams, S. R. Bandler, J. A. Chervenak, M. E. Eckart, F. M. Finkbeiner, R. L. Kelley, C. A. Kilbourne, F. S. Porter, J. E. Sadleir, S. J. Smith, and E. J. Wassell, *Applied Physics Letters* **107**, 223503 (2015).
- ²⁰Z. J. Ding, H. M. Li, K. Goto, Y. Z. Jiang, and R. Shimizu, *Journal of Applied Physics* **96**, 4598 (2004).
- ²¹C. Walker, M. El-Gomati, A. Assa'd, and M. Zdražil, *Scanning* **30**, 365 (2008).
- ²²Albert C. Thompson, Janos Kirz, David T. Atwood, Eric M. Gullikson, Malcom R. Howells, Jeffrey B. Kortright, Yanwei Liu, Arthur L. Robinson, James H. Underwood, Kwang-Je Kim, Ingolf Lindau, Piero Pianetta, Herman Winick, Gwyn P. Williams, and James H. Scofield, *X-Ray Data Booklet*, third edition ed. (Lawrence Berkeley National Laboratory, University of California, 2009).
- ²³K. M. Patel, D. J. Goldie, S. Withington, and C. N. Thomas, in *SPIE Future Sensing Technologies 2023*, Vol. 12327 (SPIE, 2023) pp. 36–41.

eeMC: Comments on Asymmetries in QED

Ian M. Nugent*
Victoria, B.C., Canada

Abstract

In the Quantum Electrodynamics process $e^+e^- \rightarrow l^+l^-(n\gamma)$, there are two well known angular asymmetries in the $\cos(\theta)$ and the $\cos(\theta^*)$ distributions. In this paper, the QED angular asymmetry related to the $\cos(\theta^*)$ distribution is investigated in terms of the Dirac propagator and the associated boundary conditions from which the Dirac propagator is constructed and the potential implications are examined.

Keywords: Electron-Positron Collider, Tau Lepton, Monte-Carlo Simulation

1 Introduction

In Quantum Electrodynamics (QED) processes, the higher order emission of hard photons directly influences the angular dependence in the differential cross-section. Consequently, for the $e^+e^- \rightarrow \mu^+\mu^-(\gamma)$ and $e^+e^- \rightarrow \tau^+\tau^-(\gamma)$ processes, this is related to the angular asymmetry between the outgoing charged leptons $\cos(\theta)$ [1, 2, 3, 4, 5, 6, 7] and $\cos(\theta^*)$ [8], asymmetry in the angle between the outgoing lepton and the radiated hard photon in the center-of-mass frame of the outgoing lepton pair. Higher order contributions, in particular, Feynman Diagrams with $k=2, \dots$ internal photon exchanges further modify the $\cos(\theta)$ asymmetry [9]¹, where the virtual and soft-photon contributions are most significant. This is in contrast to the $\cos(\theta^*)$ angular distributions, where the asymmetry originates from the inclusion of Feynman Diagrams that contain $n=1$ or more real hard photon emissions. In *eeMC* [10], each of the hard matrix elements, \mathcal{M}_n^k for n real hard photon emissions and k internal photon exchanges, are explicitly calculated without approximations from the Gamma-Matrices and Dirac spinors using an object-oriented structure. This allows for the investigation of the angular asymmetry $\cos(\theta^*)$ in terms of the treatment of the Dirac propagator and the associated boundary conditions.

2 Overview of eeMC Formalism

The *eeMC* [10] Monte-Carlo generator, is a stand-alone software program which contains the random-number generation [11, 12, 13, 14, 15], the phase-space generation [10, 16] based on the [17] algorithm modified to include embedded importance sampling [18, 19] and the theoretical models for the QED processes $e^-e^+ \rightarrow \mu^+\mu^-(n\gamma)$, $e^-e^+ \rightarrow \tau^+\tau^-(n\gamma)$, $e^-e^+ \rightarrow \text{hadrons}(n\gamma)$ and τ lepton decays. The cross-section for the QED processes $e^-e^+ \rightarrow \mu^+\mu^-(n\gamma)$, $e^-e^+ \rightarrow \tau^+\tau^-(n\gamma)$ and $e^-e^+ \rightarrow \text{hadrons}(n\gamma)$ is

constructed within the Yennie-Frautschi-Suura (YFS) Exponentiation Formalism [20] for the infra-red subtraction

$$d\sigma = \frac{\sum_{n=0}^{\infty} \prod_{i=0}^n \prod_{j=0}^i F(Y_{i,j}^{O(\alpha)}(P_i^\mu, P_j^\mu)) |\sum_{k=1}^{\infty} \bar{\mathcal{M}}_n^k|^2 dPS_n}{4(|\vec{P}_{e^-} - |\vec{E}_{e^+} + \vec{E}_{e^-} - |\vec{P}_{e^+}|)} \quad (1)$$

where $F(x)$ is some functional form representing the resummation of all permutations for soft or virtual photon exchanges. For the Initial and Final YFS multiplicative subtraction, the function form $F(x)$ is the standard exponential YSF Form-Factor for the Yennie-Frautschi-Suura calculation [20]; the KK2F approximation [21]; and the Sudakov Form-Factor [3]. For the Full LO calculation from [22] applying corrections from [3, 10, 23], the $F(x)$ is the product of the exponential Form-Factor determined from [22] with the Coulomb potential factored out into a separate multiplicative resummation series, the Sommerfeld-Sakharov resummation factor [23]. The hard matrix elements, $\bar{\mathcal{M}}_n^k$, is determined with the spin-average-sum for an arbitrary Initial-State spin configuration [24] and is explicitly determined from the Feynman calculus corresponding to each Feynman Diagrams using an object-orientated representation of the Gamma-Matrices and Dirac Spinors [10]. Ward's Identity [6] is applied to incorporate the renormalization through the running of electromagnetic coupling constant [10, 25, 26]. Details on the simulation of the τ decays can be found in [10, 27].

3 Dirac Propagator Formalism

It is well known that the Dirac propagator can be described in terms of the retarded Green's function for a free particle with retarded boundary conditions [3],

$$G = i < 0 | \{ \psi_a(x') \bar{\psi}_b(x) \} | 0 > \theta(x'_{(0)} - x_{(0)}). \quad (2)$$

From which it follows that:

$$\left(\gamma^\mu \frac{\partial}{\partial x_\mu} - m \right) G(x' - x) = \delta^4(x' - x). \quad (3)$$

*Corresponding Author

Email: inugent.physics@outlook.com

¹These are the most significant terms in the infinite perturbative series.

Using the Fourier Transform between the momentum and the coordinate space [2, 3, 4], this can trivially be represented as:

$$G(p) = \frac{1}{\not{p}-m} = \frac{\not{p}+m}{p^2-m^2} \quad (4)$$

[2, 3, 4]. It is the retarded Green's function, Equation 4, which is generally used to describe the propagator for each internal fermion line in perturbation theory [2, 3, 4, 5, 6, 7]. In contrast, the Dirac propagator defined with the Feynman Boundary conditions is written as:

$$\begin{aligned} G(x'-x) &= \int \frac{d^4p}{(2\pi)^4} e^{-ip \cdot (x'-x)} G(p) \\ &= -i \int \frac{d^4p e^{ip \cdot (x'-x)}}{(2\pi)^3 2E} \left((\gamma^0 E - \boldsymbol{\gamma} \cdot \mathbf{p} + m) e^{-iE(t'-t)} \theta(t'-t) \right. \\ &\quad \left. + (-\gamma^0 E - \boldsymbol{\gamma} \cdot \mathbf{p} + m) e^{-iE(t-t')} \theta(t-t') \right) \\ &= -i \int \frac{d^3p}{(2\pi)^3 2E} \left(\sum_s u_a^s(p) \bar{u}_b^s e^{-ip \cdot (x'-x)} \theta(t'-t) \right. \\ &\quad \left. - \sum_s v_a^s(p) \bar{v}_b^s e^{-ip \cdot (x-x')} \theta(t-t') \right) \\ &= -i \int \frac{d^3p}{(2\pi)^3} \left(\frac{m}{E} \Lambda_+ e^{-ip \cdot (x'-x)} \theta(t'-t) \right. \\ &\quad \left. + \frac{m}{E} \Lambda_- e^{-ip \cdot (x-x')} \theta(t-t') \right) \\ &= -i \langle 0 | T \{ \psi_a(x') \bar{\psi}_b(x) \} | 0 \rangle. \end{aligned} \quad (5)$$

[2, 3] Λ_+ and Λ_- are the standard positive and negative projection operators for the Dirac spinors,

$$\Lambda_+ = \frac{(\not{p}+m)}{2m}, \quad \Lambda_- = \frac{(-\not{p}+m)}{2m} \quad (6)$$

[2]. This is a time-ordered solution, where the integration contour for $t'-t > 0$ is in the lower half of the plane and corresponds to the positive energy solution while the integration contour for $t'-t < 0$ is in the upper half plane and corresponds to the negative energy solution. The $\not{p}-m$ and $\not{p}+m$ factors project out the positive and negative contribution to the propagator. Then, given that $(\sum_s u_a^s(p) \bar{u}_b^s = (\not{p}+m)$ and $\sum_s v_a^s(p) \bar{v}_b^s = (-\not{p}+m)$, and Equation 5 it follows that $G_+ = \frac{\not{p}+m}{p^2-m^2}$ and $G_- = \frac{-\not{p}+m}{p^2-m^2}$ for the positive and negative energy states going forward and backward in time respectively. From the derivation of the Feynman calculus, it can be seen that before applying Wick's Theorem to obtain the non-vanishing propagators and vertices, the expectation values in the s -matrix for the perturbative expansion must be time-ordered [2]. Naively, this implies that the Dirac propagators should also be time-ordered. Therefore, if one applies the Green's function with Feynman boundary conditions directly to the positive energy fermion states ($u^s(p)$) and negative energy fermion states ($v^s(p)$), taking into account the time-ordered direction of the particle/anti-particle states one obtains interesting results in terms of the angular asymmetries in QED²³. Fig-

²At this stage we would like to remind the reader of the Feynman rules for writing down the fermion line in the QED process $f^+ f^- \rightarrow f'^+ f'^-$. More specifically, going right to left for incoming particles, one starts with the positive energy state going forward in time to the electro-magnetic vertex and then proceeds backwards in time for the anti-fermion line. Similarly, for the outgoing particles one starts with the anti-fermion line going backwards in time to the QED vertex, and then proceeds forward in time for the outgoing fermion line.

³This formulation of the Dirac propagator also has implications for the box-diagram terms. We noted that in other processes, for example the $K_L K_S$ mass difference [2], that Feynman boundary conditions for the Dirac propagator are consistent with known results.

ure 1 presents radiative Born plus LO cross-section dependence on the angle between the emitted γ and the outgoing lepton (μ^- or τ^-) in the center-of-mass frame for the outgoing lepton-pair, $\cos(\theta^*)$. The reported asymmetry in the $\cos(\theta^*)$ distribution [8, 28], is reproduced by the Dirac propagator corresponding to the retarded Green's function solution. The asymmetry is most significant at $\cos(\theta^*) = \pm 1$. This region is removed in many other MC generators. The $\cos(\theta^*)$ angular asymmetry is more strongly peaked in the $e^+ e^- \rightarrow \mu^+ \mu^- (\gamma)$ process while the $e^+ e^- \rightarrow \tau^+ \tau^- (\gamma)$ process is more spread out, a consequence of the larger τ mass. When the time-ordered propagator is applied for the corresponding particle and anti-particle respectively, no asymmetry is observed in the $\cos(\theta^*)$ distribution. This suggests that the $\cos(\theta^*)$ asymmetry in QED is directly related to the choice of the Dirac propagator and the application in the perturbation theory.

4 Conclusion

The $\cos(\theta^*)$ asymmetries in the $e^+ e^- \rightarrow \mu^+ \mu^- (\gamma)$ and $e^+ e^- \rightarrow \tau^+ \tau^- (\gamma)$ QED interactions were investigated in terms of the choice of boundary conditions applied in the formulation of the Dirac propagators. The differential cross-section is symmetric in $\cos(\theta^*)$ for the Feynman boundary conditions which incorporate the time-ordering of the positive and negative energy Dirac states when applied to the Born and LO simulation, while the retarded Green's function for the Dirac propagator has a clear asymmetry. The asymmetry is most significant at $\cos(\theta^*) = \pm 1$, where due to the mass of the τ lepton is more visible away from the angular boundaries for the $e^+ e^- \rightarrow \tau^+ \tau^- (\gamma)$. We argue that applying the Feynman boundary conditions for the Dirac propagator is more consistent with the time-ordering from which the perturbative s -matrix is constructed.

Acknowledgement

GCC Version 4.8.5 was used for compilation and the plots are generated using the external program GNUPlot [29].

References

- [1] ALEPH Collaboration, DELPHI Collaboration, L3 Collaboration, OPAL Collaboration, SLD Collaboration, LEP Electroweak Working Group, SLD Electroweak, Heavy Flavour Groups. Precision Electroweak Measurements on the Z Resonance. *Physics Reports*, 427(5):257-454, 2006. doi: 10.1016/j.physrep.2005.12.006.
- [2] P. Renton. *Electroweak Interactions: An Introduction to the Physics of Quarks and Leptons*. Cambridge University Press, New York, USA, 5 1990. ISBN 978-0-521-36692-2.
- [3] Michael E. Peskin and Daniel V. Schroeder. *An Introduction to Quantum Field Theory*. Addison-Wesley, Reading, USA, 1995. ISBN 978-0-201-50397-5.
- [4] F. Halzen and Alan D. Martin. *Quarks And Leptons: An Introductory Course In Modern Particle Physics*. John Wiley & Sons, USA, 1 1984. ISBN 978-0-471-88741-6.
- [5] L.H. Ryder. *Quantum Field Theory*. Cambridge University Press, New York, USA, 6 1996. ISBN 978-0-521-47814-4, 978-1-139-63239-3, 978-0-521-23764-2.
- [6] Franz Mandl and Graham Shaw. *Quantum Field Theory: Revised Edition*. John Wiley & Sons, Great Britain, 1 1985.

- [7] David J. Griffiths. *Introduction to Elementary Particle*. John Wiley & Sons, USA, 1987.
- [8] J.P. Lees et al. Measurement of Initial-State/Final-State Radiation Interference in the Processes $e^+e^-\mu^+\mu^-\gamma$ and $e^+e^-\pi^+\pi^-\gamma$. *Phys. Rev. D*, 92:072015, 2015. doi: 10.1103/PhysRevD.92.072015.
- [9] F. Campanario, H. Czyż, J. Gluza, M. Gunia, T. Riemann, G. Rodrigo, and V. Yundin. Complete QED NLO Contributions to the Reaction $e^+e^-\rightarrow\mu^+\mu^-\gamma$ and Their Implementation in the Event Generator PHOKHARA. *JHEP*, 02:114, 2014. doi: 10.1007/JHEP02(2014)114.
- [10] I. M. Nugent. **eeMC**: Simulation of $e^+e^-\rightarrow\mu^+\mu^-(\gamma)$ and $e^+e^-\rightarrow\tau^+\tau^-(\gamma)$ Events. 2022. arXiv: 2202.02318 [hep-ph].
- [11] M. Matsumoto and T. Nishimura. Mersenne Twister: a 623-Dimensionally Equidistributed Uniform Pseudo-Random Number Generator. *ACM Trans. Model. Comput. Simul.*, 8:3–30, 1998. doi: 10.1145/272991.272995.
- [12] T. Nishimura. Tables of 64-bit Mersenne twisters. *ACM Trans. Model. Comput. Simul.*, 10:348–357, 2000. doi: 10.1145/369534.369540.
- [13] S. Harase and T. Kimoto. Implementing 64-bit Maximally Equidistributed F2-Linear Generators with Mersenne Prime Period. *ACM Trans. on Mathematical Software*, 44:1–11, 2018. doi: 10.1145/3159444.
- [14] S. Vigna. An Experimental Exploration of Marsaglia’s xorshift Generators, Scrambled. 2016. arXiv: 1402.6246.
- [15] D. E. Knuth. *The Art of Computer Programming Vol 2 (2nd Ed.)*. Addison-Wesley, Reading, USA, 1981.
- [16] I. M. Nugent. **eeMC**: Higher Order Radiative Emissions for $e^+e^-\rightarrow\mu^+\mu^-(n\gamma)$ and $e^+e^-\rightarrow\tau^+\tau^-(n\gamma)$ Events. 2022. arXiv: 2212.05388 [hep-ph].
- [17] E. Byckling and K. Kajantie. n-Particle Phase Space in Terms of Invariant Momentum Transfer. *Nucl. Phys. B*, 9:568–576, 1969. doi: 10.1016/0550-3213(69)90271-5.
- [18] Dani Gamerman and Hedibert F. Lopes. *Markov Chain Monte Carlo: Stochastic Simulation for Bayesian Inference 2nd ed.* Chapman & Hall/CRC Taylor & Francis Group, 2006.
- [19] Andrew Gelman, John B. Carlin, Hal S. Stern, David B. Dunson, Aki Vehtari, and Donald B. Rubin. *Bayesian Data Analysis 3rd Ed.* CRC Press Taylor & Francis Group, 2014.
- [20] D. R. Yennie, S. C. Frautschi, and H. Suura. The Infrared Divergence Phenomena and High-Energy Processes. *Annals of Physics*, 13:379–452, 1961. doi: 10.1016/0003-4916(61)90151-8.
- [21] S. Jadach, B.F.L. Ward, and Z. Wąs. The Precision Monte Carlo Event Generator KK For Two-Fermion Final States In e^+e^- Collisions. *Comput. Phys. Commun.*, 130:260–325, 2000. doi: 10.1016/S0010-4655(00)00048-5.
- [22] J. Schwinger. *Particle, Sources, and Fields Volumes I-III*. Perseus Books Publishing, L.L.C., Reading, Massachusetts, USA, 1998.
- [23] B. Smith and M.B. Voloshin. $e^+e^-\rightarrow\tau^+\tau^-$ at Threshold and Beyond. *Phys. Lett. B*, 324(1):117–120, 1994. doi: 10.1016/0370-2693(94)00095-6.
- [24] I. M. Nugent. **eeMC**: Arbitrary Initial Spin States for the Production of $e^+e^-\rightarrow\mu^+\mu^-(\gamma)$ and $e^+e^-\rightarrow\tau^+\tau^-(\gamma)$ Events. 2022. arXiv: 2202.02318 [hep-ph].
- [25] Friedrich Jegerlehner. *The Anomalous Magnetic Moment of the Muon*. Springer Tracts in Modern Physics 226, Heidelberg, Germany, 2007.
- [26] Christian Sturm. Leptonic Contributions to the Effective Electromagnetic Coupling at Four-Loop Order in QED. *Nuclear Physics B*, 874(3):698–719, Sep 2013. ISSN 0550-3213. doi: 10.1016/j.nuclphysb.2013.06.009.
- [27] I. M. Nugent. **eeMC**: Low energy Mesons and the residual QCD Potential. 2023. arXiv: 2312.01470 [hep-ph].
- [28] S. Actis et al. Quest for Precision in Hadronic Cross-Sections at Low Energy: Monte Carlo Tools vs. experimental Data. *The European Physical Journal C*, 66(3-4):585–686, 2010. doi: 10.1140/epjc/s10052-010-1251-4.
- [29] Thomas Williams, Colin Kelley, et al. Gnuplot 4.2: An Interactive Plotting Program. <http://gnuplot.sourceforge.net/>, 2007.

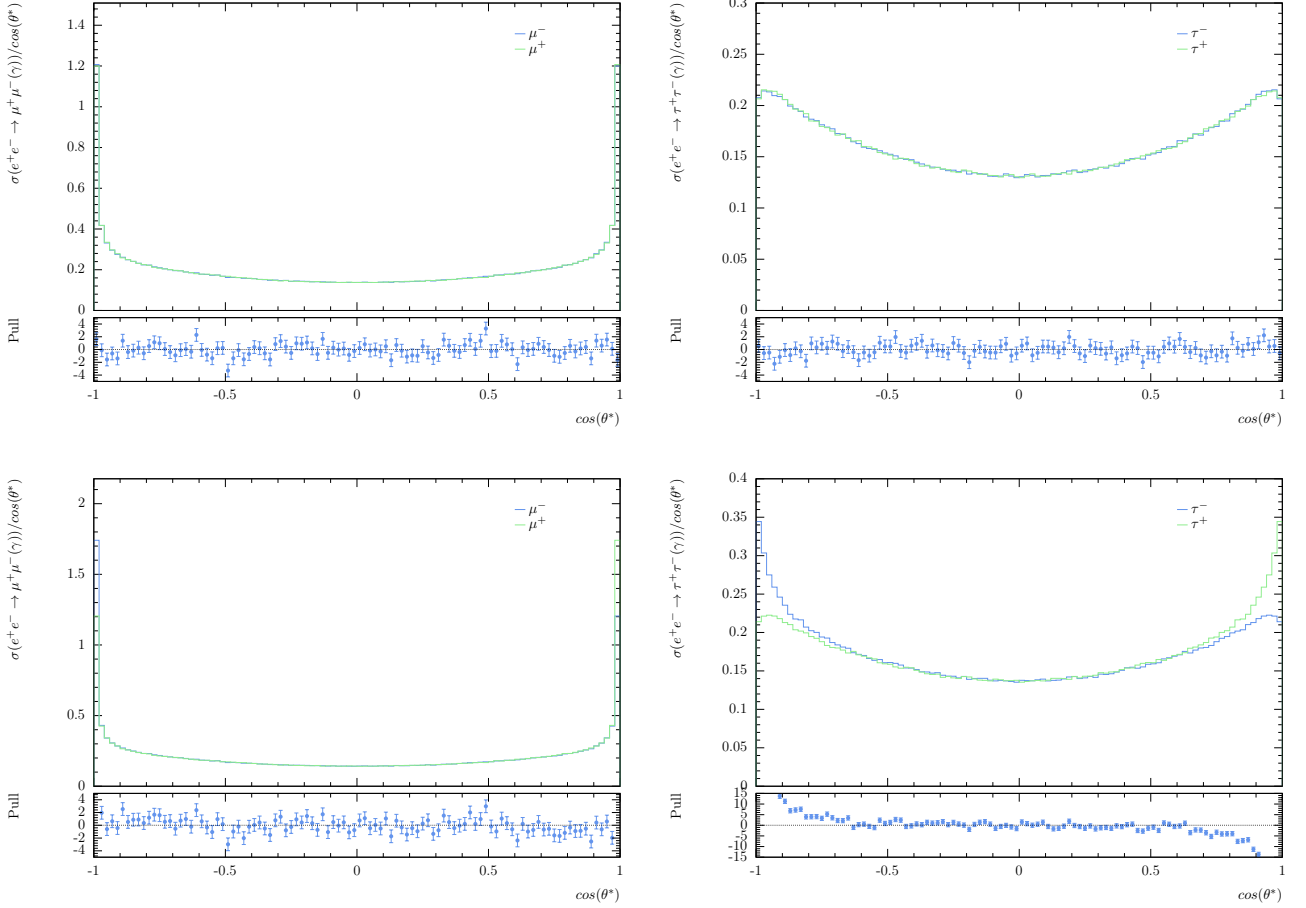


Figure 1: The $\cos(\theta^*)$ distribution for Born+LO determined with the Dirac propagator constructed from the Feynman boundary conditions (top) and the retarded Dirac propagator (bottom) for the $e^+e^- \rightarrow \mu^+\mu^-(\gamma)$ (left) and $e^+e^- \rightarrow \tau^+\tau^-(\gamma)$ (right) QED interactions for a center-of-mass energy of $10.58 GeV/c^2$ and a soft-photon cut-off of $E_l=1 MeV$. The blue line represents the $\cos(\theta^*)$ angle between the photon and l^- in the rest frame of the outgoing lepton pair, while the green line represents the $\cos(\theta^*)$ angle between the photon and l^+ in the rest frame of the outgoing lepton pair.

Quantum-enhanced sensing of axion dark matter with a transmon-based single microwave photon counter

C. Braggio^{1,2,*}, L. Balembois³, R. Di Vora⁴,
Z. Wang³, G. Carugno², A. Ortolan⁴, G. Ruoso⁴, U. Gambardella⁵, D. D'Agostino⁵,
P. Bertet³, E. Flurin^{3,*}

¹ Dipartimento di Fisica e Astronomia, Padova, Italy

² INFN, Sezione di Padova, Padova, Italy

³ Quantronics group, Université Paris-Saclay, CEA, CNRS, SPEC, 91191 Gif-sur-Yvette Cedex, France

⁴ Laboratori Nazionali di Legnaro, Legnaro, Padova, Italy

⁵ INFN, Sezione di Napoli, Napoli, Italy

*To whom correspondence should be addressed;
e-mail: caterina.braggio@unipd.it, emmanuel.flurin@cea.fr.

We report an axion dark matter search with a haloscope equipped with a microwave photon counter. The haloscope is a tunable high quality factor 3-dimensional microwave cavity placed in a magnetic field. The photon counter, operated cyclically, maps an incoming microwave photon onto the state of a superconducting transmon qubit. The measurement protocol continuously monitors the power emitted by the haloscope cavity as well as the dark count background, and enables tuning of the cavity frequency to probe different axion masses. With this apparatus we enhance by a factor 20 the search speed that can be reached with quantum-limited linear amplifiers, and set a new standard for probing the existence of axions with resonant detectors.

Introduction

The cosmological model that best complies with the astronomical observations collected over years (1) invokes the existence of dark matter (DM), having observable gravitational effects but interacting weakly with ordinary matter. For decades, experiments with increasing scale and cost have been deployed relying on the hypothetical interaction of DM with the particles of the standard model as devised in specific theoretical models. These tests have set stringent constraints to the concept of the weakly interacting massive particle (2) in the mass range 1 GeV - 10 TeV (3, 4). On the ultralight side of the open parameter space, the cold-dark-matter paradigm is pursued with a radically different approach (5, 6). At this frontier of fundamental physics, diverse small-scale experiments rely on quantum sensing (7) to improve their sensitivity to new particles and forces in specific mass ranges, with a large discovery potential.

A prominent example is the cavity axion haloscope, a detector consisting of a 3D microwave resonator permeated by an intense magnetic field and readout by an heterodyne receiver (8). The extremely weak interaction of the axion with electromagnetism is parametrized by $g_{a\gamma\gamma}$ in the Lagrangian $\mathcal{L} = g_{a\gamma\gamma} a \mathbf{E} \cdot \mathbf{B}$, where a is the axion field, and \mathbf{E} and \mathbf{B} are respectively the electric and magnetic fields. This coupling allows the axion to decay to a photon in a static magnetic field $\mathbf{B} = B_0$, with a conversion rate scaling with B_0^2 . The cavity frequency ν_c sets the particle mass $m_a = h\nu_c$ ($10 \mu\text{eV} \simeq 2.5 \text{ GHz}$) at which the signal is resonantly enhanced, therefore wide tunability is a main requirement beyond sensitivity. For axions, best sensitivity results are reported in exclusion plots around a sweet spot for state-of-the-art cavity and magnet technology, in the frequency range around 600 MHz to 1 GHz where signal and noise power compare favorably. Here, SQUID technology and quantum-limited linear amplifiers have enabled probing axion-photon couplings down to $3 \times 10^{-15} \text{ GeV}^{-1}$ (9, 10) predicted by quantum chromodynamics (QCD) axion models. However, a large part of the parameter space is yet unexplored at

higher frequencies as the scan rate decreases with the search frequency as ν_c^{-8} (see Methods). Even in the most favorable conditions, assuming haloscopes equipped with the best superconducting magnets delivering fields up to 14 T and state-of-the-art superconducting cavities (11) with linewidths $\Delta\nu_c$ matching that of the axion signal $\Delta\nu_a = \nu_c/10^6$ (12), the time needed to scan the 1-10 GHz decade with relevant sensitivity can be estimated around hundreds of years if a detection chain based on the measurement of the field quadratures with a linear amplifier is employed (See Methods). The limiting factor arises from the vacuum state not being an eigenstate of the quadrature operators, which causes the output standard deviation to reach at best an effective noise temperature of half a photon (effective mean occupation number $\bar{n}_{\text{SQL}} = 1$); this is called the Standard Quantum Limit (SQL).

Here, we target a significant scan rate reduction in axion DM search by circumventing SQL noise through quantum technologies. Injection of squeezed states of light has further expanded the probed volume of the gravitational-wave Universe (13, 14), while in DM search microwave squeezing has allowed for improving the search rate by a factor of 2 (15, 16). A larger scan rate improvement can in principle be obtained through single microwave photon detectors (SMPDs) (17), which escape SQL noise since the vacuum is an energy eigenstate. The scan rate enhancement \mathcal{R} obtained by using a SMPD compared to a quadrature detection at the SQL can be shown to be given by $\mathcal{R} = \eta^2 \Delta\nu_a / \Gamma_{\text{dc}}$, where η is the SMPD quantum efficiency and Γ_{dc} is the SMPD dark count rate (see Methods).

A lower bound for the SMPD dark count rate is given by $\Gamma_{\text{dc}} / (\eta \Delta\nu_c) = \bar{n}_{\text{th}} = 1 / (e^{h\nu/k_B T} - 1) = 2.4 \times 10^{-8}$, for an experiment at $T = 20$ mK and frequency $\nu = 7.3$ GHz. However, present-day devices do not reach this figure due to technical issues such as inefficient thermalization of the microwave field at millikelvin temperatures and the presence of out-of-equilibrium quasiparticles in superconductors (18–20). Nonetheless, even with realistically achievable dark count rates $\Gamma_{\text{dc}} = 10 \text{ s}^{-1}$ and $\eta = 0.8$, scan rate enhancements $\mathcal{R} \sim 500$ can be obtained for state-of-

the-art cavities with a quality factor $Q_0 \sim Q_a = \nu_a/\Delta\nu_a = 10^6$. Reducing the operational dark count rate Γ_{dc} is therefore essential to achieve a fast scan rate.

The potential of microwave photon counting has been recently demonstrated in the field of dark matter search with quantum non-demolition measurements of cavity photons, using a device based on a transmon qubit coupled to the signal 3D cavity and to another 3D cavity for signal readout (21). In this method, the noise has been reduced to the background photons $\bar{n}_{th} = 7.3 \times 10^{-4}$ compared to $\bar{n}_{SQL} = 1$ at SQL, corresponding to a projected scan speed enhancement by a factor ~ 1300 . For axion search however, a large magnetic field must be applied to the axion cavity, which makes it difficult to integrate the transmon. In this work, we take a different approach by spatially separating the axion cavity from the detector, using a transmon-based SMPD which can count photons propagating in a coaxial cable. This makes it possible to perform an axion search in magnetic fields up to 2T, while still obtaining state-of-the-art dark count rates of less than 100 s^{-1} .

Setup and protocol

The present haloscope is based on a hybrid surfaced cylindrical NbTi-copper cavity (22), mounted to the base stage of a dilution refrigerator at 14 mK. At the maximum applied field of 2 T we measured $Q_0 = 0.9 \times 10^6$ for its axion-sensitive TM_{010} mode. Its frequency can be varied within a few MHz around 7.37 GHz by a system of three 1 mm-diameter sapphire rods controlled by a cryogenic nanopositioner. The cavity TM_{010} mode is readout by a fixed antenna with coupling coefficient $\beta = 3$, thus the loaded quality factor is $Q_L = Q_0/(1 + \beta) = 2.25 \times 10^5$ in the overall frequency range investigated in the present work. The expected axion signal power is at the 10^{-24} W level (see Methods). A circulator routes pulses from input lines towards the cavity for calibration of the cavity parameters, and the photons leaking out of the cavity towards the input of the SMPD (see Fig. 1a).

The SMPD is a superconducting circuit with a transmon qubit coupled to two resonators: a ‘buffer’ resonator whose frequency ω_b can be tuned to the incoming photon frequency by applying a magnetic flux to an embedded superconducting quantum interference device (SQUID), and a ‘waste’ resonator with fixed frequency ω_w . In this circuit, an itinerant photon entering the buffer resonator is converted with close to unit efficiency into a qubit excitation ω_q and a waste photon via a four-wave-mixing (4WM) process (23) activated by a pump pulse at frequency ω_p such that $\omega_p + \omega_b = \omega_q + \omega_w$, corresponding to the energy conservation throughout the 4WM process. The waste resonator quickly damps its converted photon in the environment ensuring the irreversibility of the 4WM process and forcing the qubit to remain in its excited state. The qubit state is then measured using the dispersive readout method (24). If it is found in its excited state, then a click of the detector is recorded and the qubit is reset in its ground state. These operations are repeated in cycles of 17 μs on average yielding to measurement records of click arrival time as displayed in Fig.1d. This detector also finds applications in magnetic resonance (25) and in particular it recently enabled single-electron-spin detection (26).

Axion dark matter experiments search for a power excess above a background that must be reliably estimated at each cavity frequency. We estimate the background by recording off-resonance clicks when ω_b is detuned by 1 and 2 MHz, and the source plus background when $\omega_b = 2\pi\nu_c$. To explore different axion masses, the cavity frequency ν_c is tuned during the quantum sensing protocol, with parameters ν_c , loaded quality factor Q_L and coupling β to the transmission line being monitored periodically with the SMPD (see Fig. 2).

The detector efficiency η is measured by monitoring the count rate of the detector while applying a microwave tone at its input, whose power is calibrated by measuring the AC-stark shift and photon-induced dephasing of the transmon qubit (see methods). We measure an operational efficiency $\eta = 0.47 \pm 0.013$ on average including dead times and imperfections of the SMPD. We observe efficiency fluctuations on time scale of minutes of the order of $\pm 10\%$

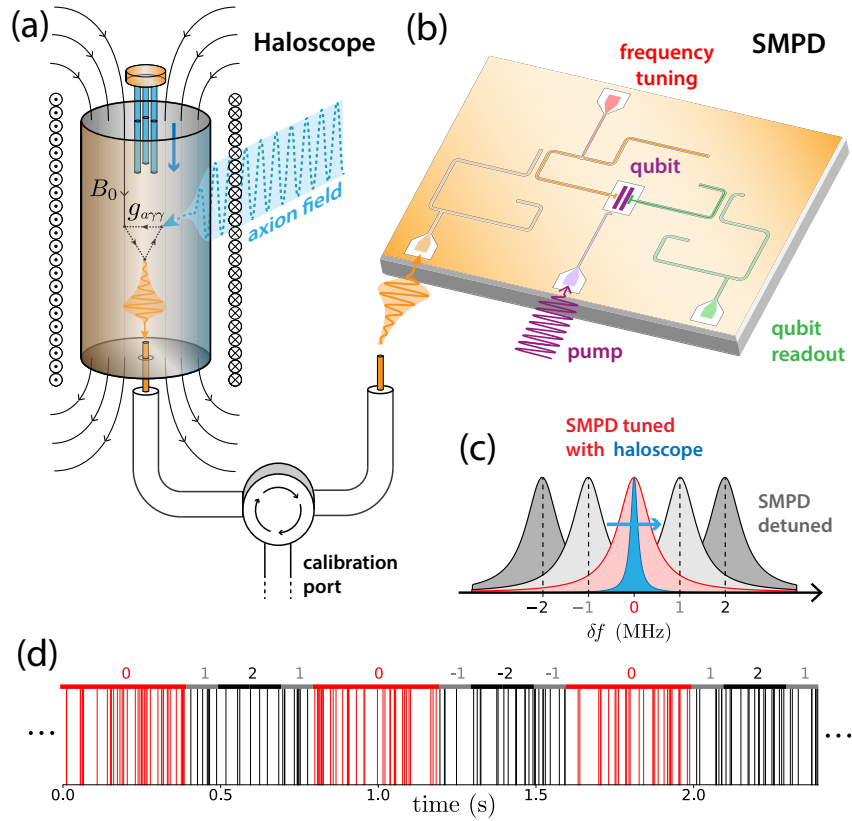


Figure 1: Schematic of the axion search setup: (a) The haloscope cavity, located in a 2T magnet, connects to the detector via a fixed antenna port and features cryogenic frequency tuning through three sapphire rods attached to a nano-positioner. (b) The SMPD, a superconducting circuit with $\lambda/2$ coplanar waveguide resonators linked to a transmon qubit, is positioned approximately 50 cm above the magnet and connects via standard coaxial cables. Its frequency is adjustable by threading the flux through a SQUID embedded in the buffer resonator. Upon activating the four-wave mixing process, the qubit cycles through photon detection phases. (c) The detector center frequency alternates between resonance (red) and off-resonance (grey) settings relative to the haloscope’s frequency (blue) in differential mode. (d) Measurement records from the photon counter display clicks over time, with color indicating the detector’s frequency setting.

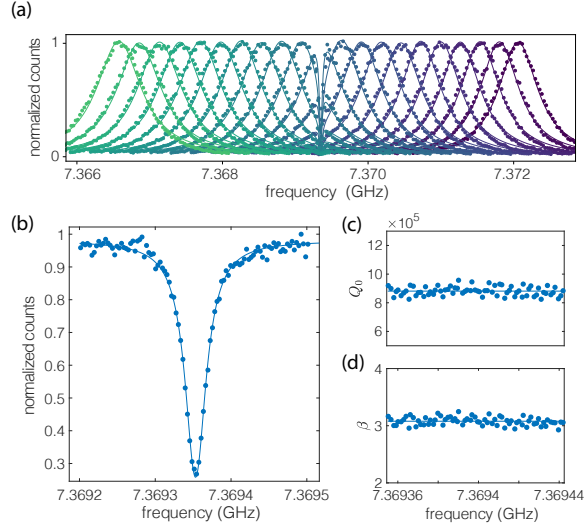


Figure 2: Microwave cavity spectroscopy by a photon counter. (a) SMPD response to a continuous calibration tone as function of its frequency. While the SMPD bandwidth is 0.7 MHz, its center frequency is tunable over a frequency range of over 100 MHz by threading magnetic flux in the SQUID loop. Here the SMPD is tuned over a 5 MHz-span around the haloscope frequency that appears as a dip in the measured counts. (b) The SMPD frequency is swept around haloscope resonance to estimate the cavity parameters Q_0 and β . (c-d) Measurements of the cavity parameters are repeated cyclically within the quantum protocol upon cavity frequency scanning. For the interval $[7.369355 - 7.369442]$ GHz, the quality factor is $Q_0 = (8.8135 \pm 0.31) \times 10^5$ and the coupling coefficient is $\beta = 3.08 \pm 0.07$, therefore independent of the cavity frequency to within a few percent. The average value of Q_0 and β for the $N = 72$ measurements are represented by the horizontal lines.

mainly due to slow drifts of the flux threading the detector SQUID loop as well as fluctuations of the relaxation time fluctuation of the transmon qubit (20).

Data analysis and SMPD diagnostics

The counts acquired as described in the previous section are then grouped into resonance and off-resonance counts. Due to the chosen quantum protocol structure, the acquisition duration at frequency step is 28.6 s at resonance, and $7.15 \text{ s} \times 4 = 28.6 \text{ s}$ at sidebands frequency. Over the long timescales required in cavity haloscope searches, the SMPD dark count rate is non

stationary with variations within 10 % as shown in Fig. 3 (b). We observe that about 600-700 clicks are recorded in 7.15 sec on each sideband frequency, while about 2700-2900 on resonance clicks are registered for 28.6 s-duration intervals. These clicks are originating from photons present at the SMPD input due to an effective temperature of the input line, and only to a minor extent from spurious excitation of the transmon qubit in absence of incoming photons (20). The sum of the counts associated with the four sidebands is an estimator of the background B , that can be compared with on resonance counts in the same 28.6 s-duration time window as shown in Fig. 3 (c), where a correlation between the two measured quantities is evident. Both the counts registered at cavity frequency (0) and on sidebands (-2,-1,1,2) vary beyond statistical uncertainty expected for poissonian counts, as indicated by the $\pm 1 \sigma$ belts. If $\{t_i\}$ is the set of click arrival times t_i , we indicate with N_c and N_b the number of the cavity and background clicks, respectively. The difference between the cavity N_c and background counts N_b (see Fig. 3 (d)) in the overall 0.4 MHz probed frequency range is unrelated to any dark matter signal inasmuch as it is independent of the cavity frequency, as detailed in the following. This excess at the cavity frequency is instead ascribed to a slightly higher temperature for the cavity resonator compared to the SMPD temperature. In the data analysis this difference is treated as a bias k_b (see below).

The SMPD long term stability can be assessed by calculating the Allan variance for N_c and N_b (see Fig. 3). The click number fluctuations is computed as function of the total integration time τ , at early times, the Allan variance decreases as $1/\tau$ but after only few minutes the Allan variance increases again, indicating that a random walk contribution to the click rate comes into play. However, the Allan variance of the difference $N_c - N_b$ follows the $1/\tau$ trend up to a much longer time interval $\tau \sim 30$ min, suggesting that there are common processes affecting the counter operation. Moreover, the plots in Fig. 3 show that there is no additional noise in the data recorded between successive step motion intervals compared to those acquired with the

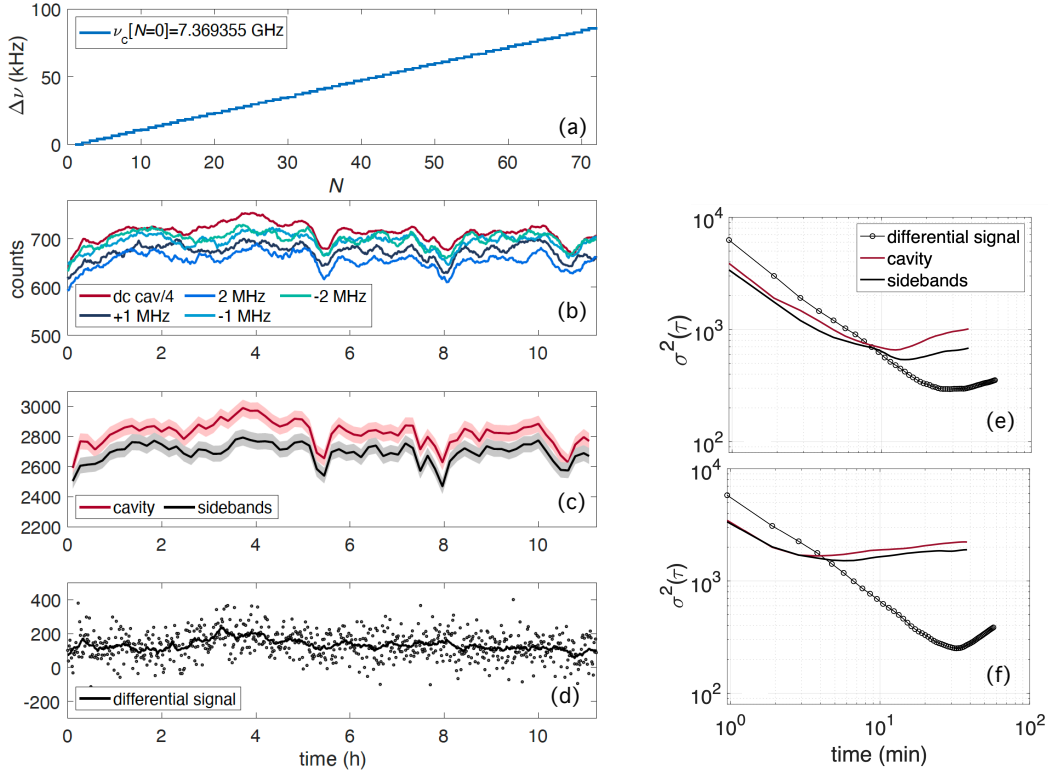


Figure 3: A selection of data taken at about 5 kHz/h frequency tuning speed, corresponding to the cavity frequency range $[7.369355 - 7.369442]$ GHz. (a) The cavity frequency changes linearly with cycle number ($N = 72$ in this run). (b) Counts recorded with SMPD buffer $\nu_c \pm 1$ MHz, $\nu_c \pm 2$ MHz and at resonance. Each data point represents counts recorded in 7.15 sec at sidebands frequency. For comparison, the counts recorded at resonance have been divided by a factor 4. (c) Sidebands counts are summed to obtain a single series of data, that is compared to counts recorded at resonance ($\nu_b = \nu_c$). The $\pm\sigma$ belts indicate the statistical uncertainty expected for poissonian counts. (d) Excess counts at cavity frequency obtained by the difference between cavity and sideband counts. The thick black curve is obtained by computing the mean over a sliding window of 20 minutes. (e) Allan variance calculated for data recorded at fixed cavity frequency, and (f) for the data displayed in (c)-(d).

cavity unperturbed for several hours.

Axion dark matter sensing

The clicks recorded with SMPD frequency tuned at the cavity frequency and those at sidebands frequency can be used not only to learn about the long-term stability of the SMPD, but also to obtain an upper limit on the axion-photon interaction $g_{a\gamma\gamma} = g_\gamma \alpha f_a^{-1} / \pi$, where α is the fine structure constant and f_a is the scale of the breaking of the Peccei-Quinn symmetry, with $f_a / 10^{12} \text{ GeV} = 5.691 \mu\text{eV} / m_a$ (27).

The system has been investigated for 12 h at fixed cavity frequency, and for an overall range of about 420 kHz centred at 7.3695 GHz by tuning the cavity frequency at about 4.5 – 5 kHz/h, as heating introduced at the 15 mK stage by the currents needed to drive the nanopositioner degraded the SMPD sensitivity for tuning speeds above approximately 12 kHz/h. The probed frequency range corresponds to 14 cavity linewidths, each providing independent values of N_b and N_c useful for the dark matter search. Clearly, the measurement time Δt spent probing $[\nu_c, \nu_c + \Delta\nu_c]$, with $\Delta\nu_c = 32 \text{ kHz}$, largely exceeds τ_m , thus we selected a subset of data to optimize the haloscope speed. Each Δt has been divided into sub-intervals of duration $\Delta t_m = 10 \text{ min}$ and the interval with the maximum SMPD sensitivity, i.e. having the lowest cavity counts N_c^* , was selected to devise the plot in Fig. 4.

In each sub-interval, the counts mean equals their variance as expected for Poissonian statistics, therefore to infer the upper limit we can apply the maximum likelihood ratio test to assess the significance of an excess at the cavity frequency (28). In the recorded data we observe that for the selected minimum cavity counts N_c^* in the 10 min duration sub-intervals, the corresponding background counts N_b^* is biased by $k_b = N_c / N_b - 1$, which amount to a few percent on average in the collected data set. Using the Wilks' theorem (28) for large sample size, as is the case for the present data ($O(10^4)$ counts in each sub-interval), the significance for N_c counts for each cavity linewidth is given by

$$\begin{aligned}
S &= \sqrt{2} \left\{ N_b^* \log \left[\frac{(k_b + 2)N_b^*}{N_b^* + N_c^*} \right] \right. \\
&\quad \left. + N_c^* \log \left[\frac{(k_b + 2)N_c^*}{(1 + k_b)(N_b^* + N_c^*)} \right] \right\}^{1/2}, \tag{1}
\end{aligned}$$

where we have taken the same detection efficiency for cavity and background counts.

The required significance to claim a detection is set at 5σ , corresponding to a false alarm probability of $\sim 10^{-7}$ for a Gaussian distribution. In the four acquisition runs, representing 14 cavity linewidths, no significant excess was found assuming a conservative bias value $k_b = 0.05$. Therefore we set the upper limits N_{95}^* on source counts at 95 % C. L. (i.e. 2σ significance), by interpreting excess counts $N_{95}^* - N_b^*$ as signal power P_{95} due to axion to photon conversion:

$$P_{95} = \eta h \nu_c \frac{N_{95}^* - N_b^*}{\Delta t_m}. \tag{2}$$

The upper limit on $g_{a\gamma\gamma}$ obtained from the calculated axion signal power (see Methods) and eq. 1 is reported in Fig. 4 for the probed frequency range.

Conclusions and outlook

At sensitivity given by the potential interaction of axions with photons, we devised an axion search protocol whereby clicks are recorded at both the cavity and the sidebands frequency while the cavity frequency is changed much more slowly than the execution time of the protocol. Allan variance plots indicate that for the present device the most convenient haloscope integration time is of about 10-15 min. As the inhomogeneity of the poisson process sets in for temporal intervals much larger than the chosen integration time of 10 minutes, we are able to give an upper limit $g_{a\gamma\gamma} < 7 \times 10^{-14} \text{ GeV}^{-1}$ in the mass range $(30.477 - 30.479) \mu\text{eV}$.

The exclusion plot we obtained corresponds to a search speed of 4.3 MHz/day. As $\Delta f / \Delta t_m$ is

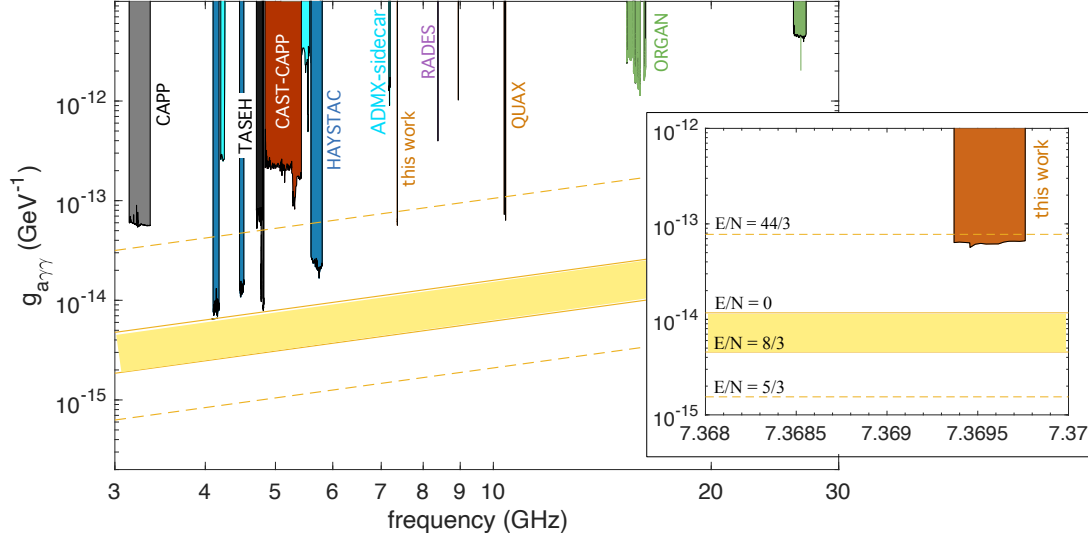


Figure 4: (a) Constraints on axion-photon coupling: haloscopes closeup in the range 2–50 GHz. Experimental data taken from Ref. (29). The bounds represented by the dotted lines enclose the region of parameter space of phenomenologically preferred axion models (30), extending beyond the commonly assumed QCD axion window (yellow band). E and N are respectively the electromagnetic and QCD anomaly coefficients, setting the axion-photon coupling constant $g_{a\gamma\gamma} = (\alpha/2\pi f_a)(E/N)$ (31). (b) Exclusion limit at 95% confidence level on the axion mass coupling parameter space. We obtain an upper limit on the axion induced power that translates to an upper limit on $g_{a\gamma\gamma}$ for $m_a \in [30.477, 30.479] \mu\text{eV}$, corresponding to a cavity frequency window of 0.4 MHz centred around 7.3696 GHz.

proportional to the $B^4 g_{a\gamma\gamma}^4 V_{eff}^2$, with $V_{eff} = C_{010}V$ the effective cavity volume, we can estimate a scan rate exceeding a hundred MHz/year at the sensitivity required to probe the full QCD axion band for an experiment equipped with a commercially available magnetic field of 12 T in place of the 2 T magnet used in these tests, and a state-of-the-art 3D resonator with 10 times as much the effective volume. Compared to a haloscope based on a SQL linear amplifier, photon counting allows for running the search at a speed larger by a factor of $\mathcal{R} = \eta^2 \Delta\nu_a / \Gamma_{dc} \sim 20$, with the signal linewidth $\Delta\nu_a = 7.3$ kHz, the dark count rate $\Gamma_{dc} = 85 \text{ s}^{-1}$ and the efficiency $\eta = 0.46$.

The gain in scan speed we have demonstrated is currently limited by the dark count rate, which can be further suppressed by improving the thermalization of the lines or by narrowing

the bandwidth of the input resonator. In addition, we have devised a detection method applicable to broad frequency ranges, as the SMPD input resonator frequency can very rapidly be adjusted to the cavity frequency while the latter is tuned across a few hundred MHz. Note that a Josephson mixer (32) allows to virtually expand the bandwidth of the present SMPD to include any cavity haloscope in the interesting, yet unprobed high frequency range where heavier axions can be detected. Our results demonstrate the potential of microwave photon counting in axion DM searches above 5 GHz frequency, accelerating by orders of magnitude the search and significantly simplifying the data acquisition and analysis without losing the required robustness thanks to the employed metrological methods.

References

1. J. R. Primack, *Annalen der Physik* **524**, 535 (2012).
2. G. Bertone, D. Hooper, *Rev. Mod. Phys.* **90**, 045002 (2018).
3. G. Bertone, *Nature* **468**, 389 (2010).
4. J. Liu, X. Chen, X. Ji, *Nature Physics* **13**, 212 (2017).
5. D. DeMille, J. M. Doyle, A. O. Sushkov, *Science* **357**, 990 (2017).
6. A. O. Sushkov, *PRX Quantum* **4**, 020101 (2023).
7. C. L. Degen, F. Reinhard, P. Cappellaro, *Rev. Mod. Phys.* **89**, 035002 (2017).
8. P. Sikivie, *Rev. Mod. Phys.* **93**, 015004 (2021).
9. C. Bartram, *et al.*, *Phys. Rev. Lett.* **127**, 261803 (2021).
10. A. K. Yi, *et al.*, *Phys. Rev. Lett.* **130**, 071002 (2023).

11. D. Ahn, *et al.*, *Phys. Rev. Appl.* **17**, L061005 (2022).
12. M. S. Turner, *Physical Review D* **33**, 889 (1986).
13. F. Acernese, *et al.*, *Phys. Rev. Lett.* **123**, 231108 (2019).
14. M. Tse, *et al.*, *Phys. Rev. Lett.* **123**, 231107 (2019).
15. K. M. Backes, *et al.*, *Nature* **590**, 238 (2021).
16. M. Malnou, *et al.*, *Phys. Rev. X* **9**, 021023 (2019).
17. S. K. Lamoreaux, K. A. van Bibber, K. W. Lehnert, G. Carosi, *Phys. Rev. D* **88**, 035020 (2013).
18. S. Diamond, *et al.*, *PRX Quantum* **3**, 040304 (2022).
19. T. Connolly, *et al.*, *arXiv.2302.12330* (2023).
20. L. Balembois, *et al.*, *Phys. Rev. Appl.* **21**, 014043 (2024).
21. A. V. Dixit, *et al.*, *Phys. Rev. Lett.* **126**, 141302 (2021).
22. D. Alesini, *et al.*, *Phys. Rev. D* **99**, 101101 (2019).
23. R. Lescanne, *et al.*, *Physical Review X* **10**, 021038 (2020).
24. J. Gambetta, *et al.*, *Phys. Rev. A* **74**, 042318 (2006).
25. E. Albertinale, *et al.*, *Nature* **600**, 434 (2021).
26. Z. Wang, *et al.*, *Nature* **619**, 276 (2023).
27. F. Chadha-Day, J. Ellis, D. J. E. Marsh, *Science Advances* **8**, eabj3618 (2022).

28. G. Vianello, *Astrop. J. Suppl. Ser.* **236**, 17 (2018).
29. <https://cajohare.github.io/axionlimits/docs/ap.html>.
30. L. Di Luzio, F. Mescia, E. Nardi, *Phys. Rev. Lett.* **118**, 031801 (2017).
31. L. Di Luzio, M. Giannotti, E. Nardi, L. Visinelli, *Phys. Rep.* **870**, 1 (2020).
32. N. Roch, *et al.*, *Phys. Rev. Lett.* **108**, 147701 (2012).
33. Y. K. Semertzidis, S. Youn, *Science Advances* **8**, eabm9928 (2022).
34. B. M. Brubaker, *et al.*, *Phys. Rev. Lett.* **118**, 061302 (2017).
35. J. E. Kim, *Phys. Rev. Lett.* **43**, 103 (1979).
36. M. Shifman, A. Vainshtein, V. Zakharov, *Nucl. Phys. B* **166**, 493 (1980).
37. M. Dine, W. Fischler, M. Srednicki, *Phys. Lett. B* **104**, 199 (1981).
38. A. R. Zhitnitsky, *Sov. J. Nucl. Phys.* **31**, 260 (1980).
39. D. Kim, J. Jeong, S. Youn, Y. Kim, Y. K. Semertzidis, *J. Cosm. Astrop. Phys.* **2020**, 066 (2020).
40. A. B. Pippard, W. L. Bragg, *Proc. Roy. Soc A.* **191**, 385 (1947).

Acknowledgments

We are grateful to E. Berto (University of Padova and INFN) who substantially contributed to the mechanical realization of the cavity and of its tuning system. We thank the sputtering laboratory of the INFN Legnaro Laboratory (C. Pira) for the preparation of the NbTi films on

the copper resonators. The contribution of M. Tessaro and F. Calaon (INFN Padova) to the experiment electronics and cryogenics respectively is gratefully acknowledged. We acknowledge technical support from P. Sénat, D. Duet, P.-F. Orfila and S. Delprat, from CEA/SPEC and are grateful for fruitful discussions within the Quantronics group. We acknowledge IARPA and Lincoln Labs for providing the Josephson Traveling-Wave Parametric Amplifier.

This research is supported by the U.S. Department of Energy, Office of Science, National Quantum Information Science Research Centers, Superconducting Quantum Materials and Systems Center (SQMS) under the Contract No. DE-AC02-07CH11359, by the MUR Departments of Excellence grant 2023-2027 “Quantum Frontiers”, and by INFN through the QUAX experiment. This project has received funding from the European Union Horizon 2020 research and innovation program under ERC-2021-STG grant agreement no. 101042315 (INGENIOUS)

Additional information

Competing interests The authors declare no competing interests.

Data and code availability Raw data, analysis codes are available from the corresponding author on reasonable request.

Supplementary materials

0.1 SMPD Circuit fabrication

First, a 2-inch sapphire substrate is cleaned by dipping it in a 2:1 mixture of H_2SO_4 and H_2O_2 during 20 min. The substrate is then loaded in a sputtering machine where a 60-nm thick tantalum thin film is deposited at 600°C to favor growth in the α -phase. The wafer is then diced into rectangular chips of $10 \cdot 11\text{mm}^2$. The patterning of the main elements of the circuit is achieved by wet etching tantalum with Transene 111 through an optically patterned AZ1518 resist mask. The chip is then cleaned by immersing it in successive baths: IPA, acetone and 2:1 mixture of H_2SO_4 and H_2O_2 . Aluminum junctions are made using the Dolan bridge technique. The mask consists of a double layer PMMA (110 nm) - MAA (1100 nm) resist and a discharging layer of 7 nm of aluminum, it is then patterned using electron beam lithography (at 30 kV). After the exposure, the discharging layer is first removed by immersing the chip in a KOH solution ($10\text{g} \cdot \text{L}^{-1}$). The resist is then developed in a 1:3 MIBK/IPA mixture. The chip is then loaded in an electron beam evaporator to make the junctions. The two aluminum layers are evaporated with 28° and -28° angles creating overlaps over well-defined area, controlled by the mask geometry. The first aluminum layer is 35 nm thick and the second 65 nm thick. Between the two deposition steps, the aluminum is oxidized during 5 min by injecting an argon-oxygen gas mixture into the deposition chamber at a pressure of 10 mbar. Finally, the resist mask is lifted-off by immersing the chip in an acetone bath. Then, the junctions are then recontacted to the tantalum circuit with aluminum patches. After coating the chip with an optical resist (Microposit S1805), windows overlapping the junctions and the ground plane areas to be recontacted are opened using optical lithography. The chip is then loaded in an electron-beam evaporator. We first perform an ion milling based on an argon ion beam accelerated at 500V. Finally, a 100 nm aluminium layer is then deposited on the chip covering the areas etched by the ion milling step.

The resist is then removed.

In Table Supplementary Table the measured SMPD parameters are reported.

Qubit	
$\omega_q/2\pi$	6.222 GHz
T_1	17 – 20 μ s
T_2^*	28 μ s
$\chi_{qq}/2\pi$	240 MHz
$\chi_{qb}/2\pi$	3.4 MHz
$\chi_{qw}/2\pi$	15 MHz
Waste mode	
$\omega_w/2\pi$	7.9925 GHz
$\kappa_{\text{ext}}/2\pi$	1.0 MHz
$\kappa_{\text{int}}/2\pi$	< 100 kHz
Buffer mode	
$\omega_b/2\pi$	7.3693 GHz
$\kappa_{\text{ext}}/2\pi$	0.48 MHz
$\kappa_{\text{int}}/2\pi$	40 kHz

Table Supplementary Table: Measured SMPD parameters.

Quantum Sensing Protocol

The quantum sensing sequence consists of nested cycles as follows (see Fig. fig:M1):

(i) The detection cycle begins with a 10.5 μ s pump pulse applied to the qubit port to activate the 4WM process, followed by a 0.8 μ s readout pulse directed to the waste port. The qubit is then reset utilizing the real-time feedback capabilities of the quantum machine OPX, resulting in a latency of 0.7 μ s that includes electrical delay, signal processing, and FPGA latency. If the qubit is in its ground state, an additional 0.3 μ s waiting time is imposed before the cycle restarts. If the qubit is in its excited state, a 0.2 μ s qubit π -pulse is applied, followed by a 0.8 μ s readout pulse. This reset procedure continues until successful. The detection cycle time varies, with an average duration of 12.4 μ s.

(ii) To change the SMPD frequency, a slow flux ramp is applied for 0.72 ms, followed by a 0.1 ms pause to mitigate potential heating. Subsequently, dark counts are logged over 8001 detection cycles (signal OFF), yielding an average time of 99.075 ms. The detector's efficiency (signal ON) is assessed over 801 detection cycles by evaluating the SMPD count rate with a calibrated microwave pulse in use. This efficiency assessment averages 9.91 ms per cycle.

(iii) Sequence (ii) is repeated for buffer frequencies ω_b matching the cavity frequency, identified as 0, $\omega_c/2\pi \pm 1$ MHz (labeled as 1,-1), and $\omega_c/2\pi \pm 2$ MHz (labeled as 2,-2). This arrangement facilitates the recording of dark counts for equal durations when at and away from cavity resonance (0 0 1 2 2 1 0 0 0 0 -1 -2 -2 -1 0 0), thus halving the haloscope detector's duty cycle to 50%. This sequence design ensures all flux ramps share identical amplitude to circumvent systematics related to spurious heating.

(iv) A minimal nano-positioner voltage pulse is applied, followed by a 5 s waiting period. Then, sequence (iii) is executed $N_r = 36$ times. This cycle (iv) spans an average of 78 s, covering sequence loading, data collection, and data saving phases.

(v) Cycle (iv) is reiterated 10 times, interspersed with a calibration sequence lasting 78 s, initiated by a subtle nano-positioner voltage pulse to evenly distribute nano-positioner voltage pulses over time and prevent slow thermal fluctuations. The calibration process is twofold. Initially, the haloscope frequency is determined by gauging the photon count reflected from the haloscope cavity across various illumination frequencies using the SMPD. A Lorentzian fit to the haloscope power absorption curve provides an accurate frequency estimate $\omega_c/2\pi$ of the haloscope, down to sub-kHz precision. Next, the SMPD's central frequency and bandwidth are gauged across different bias voltage levels close to the operational point to adjust for low-frequency magnetic flux drifts. Subsequently, the SMPD's central frequency is aligned with the newly measured haloscope frequency. Additionally, a list of bias voltage values is compiled for adjusting the buffer frequency to ω_c (0), $\omega_c/2\pi \pm 1$ MHz (1,-1), and $\omega_c/2\pi \pm 2$ MHz (2,-2).

(vi) Cycle (v) is executed continuously, ensuring a consistent operation flow. The active measurement time dedicated to haloscope observation within cycle (v) amounts to $99.075 \text{ ms} \times 36 \times 8 \times 10 = 285 \text{ s}$, equivalent to 4.76 minutes. This duration is intentionally mirrored for the SMPD background measurement to maintain the differential mode operation of the SMPD-based axion search. Consequently, the total span of cycle (v) averages to 920 seconds or approximately 15.3 minutes. Within this timeframe, approximately 350 seconds are identified as dead times per cycle, accounting for about 38% of the total cycle duration. This segment includes critical operations like efficiency verifications and frequency adjustments alongside other less crucial intervals for tasks such as extended waiting periods, data processing, and saving. Opportunities to refine and reduce these dead times will be explored in subsequent experimental setups, aiming for enhanced efficiency and throughput.

Efficiency Calibration. The calibration of the SMPD is conducted by measuring the dephasing and AC-Stark shift of the qubit, which is induced by the illumination of the input resonator of the SMPD with a weak coherent tone. This calibration is carried out without any pump tone, and thus the SMPD is treated merely as an elementary component of a circuit quantum electrodynamics system. In this setup, the qubit is dispersively coupled to the input resonator, following the Hamiltonian in the rotating frame of the coherent drive:

$$\hat{H}/\hbar = \Delta \hat{a}^\dagger \hat{a} + \frac{\omega_q}{2} \hat{\sigma}_z - \frac{\chi}{2} \hat{a}^\dagger \hat{a} \hat{\sigma}_z + \epsilon (\hat{a}^\dagger + \hat{a}) \quad (3)$$

where ω_q represents the qubit frequency, χ the qubit dispersive shift, Δ the detuning between the coherent drive and the resonator frequency, and ϵ the coherent drive rate of the resonator.

The qubit, influenced by the coherent drive, experiences a frequency shift corresponding to the average number of photons in the cavity, while photon number fluctuations lead to a qubit dephasing also dependent on the photon number.

Following the method detailed in (24), the frequency shift $\delta\omega$ and dephasing $\delta\gamma$ are directly

linked to the coherent complex amplitudes α_g and α_e of the photon field inside the resonator induced by the coherent drive, for the qubit in its ground and excited states respectively, as given by the expression:

$$\delta\omega + i\delta\gamma = -\chi\alpha_g\bar{\alpha}_e = \frac{-4\chi|\epsilon|^2}{(\kappa + i\chi)^2 + 4\Delta^2} \quad (4)$$

where κ is the dissipation rate of the resonator. The coherent complex amplitudes are defined as:

$$\alpha_{g/e} = \frac{\epsilon}{\kappa/2 + i(\Delta \mp \chi/2)} \quad (5)$$

The qubit frequency shift and dephasing are experimentally measured by performing a Ramsey experiment on the qubit, varying the frequency of the coherent drive applied to the cavity. The measured quantities, which include qubit decay rates and frequency shift, are plotted as a function of the frequency detuning of the coherent drive. The dispersive shift χ and the cavity decay rate κ are extracted from the overall shape of the curve, with ϵ serving as the frequency scaling parameter.

The power of the coherent drive at the input of the cavity is calculated using input-output relations:

$$P_{\text{in}} = \hbar\omega_0\kappa \frac{|\epsilon|^2}{(\kappa - \kappa_1)^2} \quad (6)$$

where κ_1 is the rate of the resonator loss channel, measured independently through reflectometry using a vector network analyzer. The power input, expressed in units of photon flux, is $P_{\text{in}}/\hbar\omega$. The error bars are computed from statistical uncertainty associated from the data shown in Fig.6.

As illustrated in Fig.6, this calibration process determines that the photon flux at the input of the resonator for the calibration coherent tone is $P_{\text{in}}/\hbar\omega = 20050 \pm 340$ photon.s⁻¹, or in

power units, $P_{\text{in}} = 0.979 \pm 0.016 \times 10^{-19}$ W.

With the input tone calibrated, the operational efficiency of the SMPD, based on the 4-wave-mixing process and including duty cycles and dead times, is assessed by measuring the click rate of the device over a minute while continuously illuminated with the calibrated coherent tone. This process reveals an excess click rate over the background dark count of 9233 ± 30 click.s⁻¹, leading to an efficiency of $\eta = 0.460 \pm 0.009$. Note that due to fluctuations in the relaxation time of the qubit typical of transmon circuits, a slow drift of the efficiency is expected on hour timescales, this is why the count rate is continuously monitored during the cycle (ii) of the haloscope measurement.

Basic Characterization of the SMPD. The readout of the SMPD utilizes the standard dispersive readout method. A $0.8 \mu\text{s}$ coherent pulse is directed onto the waste resonator at its resonant frequency when the qubit is in its excited state ($\omega_w - \chi_{\text{qw}}$). The reflected signal, encoding the qubit state's complex amplitude, is amplified by a Josephson Parametric Travelling Wave Amplifier (JTWPA) at base temperature, followed by a High Electron Mobility Transistor (HEMT) amplifier at 4K and a low noise amplifier at room temperature. This signal is then demodulated and integrated into a voltage reading, which is compared against a threshold to determine a click event in the SMPD. Fig.2 displays the integrated voltage as a function of the qubit state. From this data, we determine the readout fidelity of the qubit when it is in its excited state as $p(1|e) = 0.93$, and the thermal equilibrium population of the qubit in its resting state as $p_{\text{th}} = 2 \times 10^{-4}$. Additionally, the readout fidelity for the ground state is estimated through consecutive measurements, revealing that the probability of incorrectly identifying the qubit's ground state is less than 5×10^{-5} .

The four-wave mixing process is calibrated by measuring the probability of the qubit's excited state while simultaneously illuminating the detector with a pump tone at the matching frequency for four-wave mixing and a coherent tone at the input resonator frequency. As shown

in Fig.6a-b, by adjusting the frequencies of these two tones, we identify the optimal conditions where the excited state probability is maximized. We further confirm the accuracy of the mixing process by observing the disappearance of the excited state population when the coherent drive at the input resonator is deactivated. The input resonator's frequency is made adjustable by incorporating a Superconducting Quantum Interference Device (SQUID) at its voltage node. The resonator frequency is modulated by applying a magnetic flux through the SQUID. This adjustment ensures that the resonator's frequency aligns with the haloscope frequency for effective four-wave mixing. The presence of a dark line in Fig.6a, indicative of the absorption of photons resonant with the haloscope, validates that the SMPD is correctly tuned to the haloscope.

Frequency Calibration Routine. This section details the calibration routine executed in each cycle (v), performed every 920 seconds and typically lasting 78 seconds.

SMPD Frequency Routine. In the frequency calibration routine, we assess the excited state population of the qubit as it relates to the frequency of the coherent drive on the input resonator, spanning 3 MHz.

A 2 mV span voltage bias is applied to control the magnetic flux through the SQUID, thereby altering the input resonator frequency by approximately ± 3 MHz. The results, as depicted in Fig.7, are presented in a colorplot, detailing the relative detuning in comparison to the expected frequency of the input resonator. In Fig.7c, the data are shown based on the absolute driving frequency of the input resonator. Key detuned SMPD bias points, such as ± 1 MHz and ± 2 MHz (targeted for background measurements), are highlighted by vertical lines. The dataset demonstrates a consistent response of the SMPD across a broad frequency range. Through meticulous analysis, we adjust the pump and flux bias for each scanning frequency, countering slow magnetic drifts in the SQUID bias, which is recalibrated every 15 minutes.

Haloscope Frequency Routine. As established earlier, the SMPD's capability to scan frequencies beyond its linewidth, while maintaining steady efficiency, enables reflection spectroscopy

of the haloscope, independent of the SMPD's linewidth. In this process, shown in Fig.7b, the SMPD's click rate is recorded while the coherent drive frequency is scanned across a 0.3 MHz range centered on the haloscope's anticipated resonance frequency. This method ensures a uniform SMPD response as both the SQUID bias and pump frequency are concurrently adjusted. The resultant detailed absorption spectrum of the haloscope is fitted with a Lorentzian curve, from which we extract the haloscope's frequency and linewidth with remarkable sub-kHz precision.

Resolving the Beta Factor Ambiguity of the Haloscope. The SMPD's reflection spectrum exclusively reflects the magnitude of the reflection coefficient, leaving an inherent ambiguity: identical spectra can result from distinct beta factors, signifying either an overcoupled ($\beta > 1$) or undercoupled ($\beta < 1$) state. To resolve this uncertainty, one could analyze the pulsed response of the cavity over time and across frequencies. However, the SMPD's time resolution, limited by its $10 \mu\text{s}$ detection window, necessitates a reduction in the detection window duration to $1 \mu\text{s}$ to improve resolution, albeit at the cost of reduced duty cycle (28%). Fig.8 showcases the SMPD's click rate in response to a $80 \mu\text{s}$ pulse applied to the haloscope, with the excitation pulse frequency spanning a 200 kHz range centered around the haloscope's frequency, and the SMPD frequency adjusted accordingly. This measurement conclusively indicates that the haloscope's temporal response is consistent only with an overcoupled configuration ($\beta = 3.1 > 1$).

Microwave 3D resonator. The 3D resonator where axions might convert to photons is a clamshell cavity of cylindrical body 128 mm-long and with 31.64 mm diameter, closed with 10 mm-long conical end caps to reduce current dissipation at copper interfaces. The two halves are machined from oxygen-free high thermal conductivity copper, treated with electrochemical polishing before deposition of a superconducting NbTi film by magnetron sputtering. As a type-II superconductor, below its critical temperature NbTi is not in the Meissner state but rather in the vortex state, with partial penetration of the magnetic flux in the material. The dissipation

mechanism is vortex motion, thus to minimize the overall cavity surface resistance R_s only the cylindrical body, where the currents of the mode TM_{010} are parallel to the applied field, is covered by the NbTi film. The internal quality factor Q_0 , inversely proportional to R_s , deteriorates with increasing static B field amplitude as shown in Fig. 4, where measurements of Q_0 made with a twin cavity are reported. This cavity differs from the one used for the present axion search in its diameter, which was slightly larger (diameter $\phi = 33.2$ mm, with measured TM_{010} mode frequency $\nu_c = 6.991$ GHz at room temperature). In the measurements shown the cavity was mounted in a flow cryostat, in which the temperature of the He flow, kept at a pressure of about 600 mbar, is controlled with a thermostat down to 3.5 K. The cavity is inserted in the bore of a solenoid magnet capable of delivering fields exceeding 10 T. Values reported are obtained by doing temperature measurements up to the NbTi critical temperature at zero-field and then by cooling down the cavity to the minimum temperature before increasing the magnetic field.

Axion signal power. QCD axion models can be probed with cavity haloscope detectors (8, 33) in a range from a few hundred MHz up to about 50 GHz, corresponding to $m_a = h\nu_a = 200 \mu\text{eV}$ axion mass. In addition to assuming the existence of axions as exclusive constituent of the Galactic dark matter halo (12), detectors rely on their resonant conversion into excitations of a high-quality factor electromagnetic cavity mode, whose electric field is parallel to an applied intense magnetic field. As is the case for the experiment described in this work, the fundamental mode of an empty copper cylinder resonator is typically used, and the signal power P_{sig} is proportional to $(VC_{010}Q_L)$, with $C_{010} = |\int_V dV \mathbf{E}_{010}(\mathbf{x}, t) \cdot \mathbf{B}(\mathbf{x})|^2 / (\mathbf{B}^2 V \int_V dV \mathbf{E}_{010}^2)$, \mathbf{B} external field, \mathbf{E}_{010} is the microwave cavity electric field, V and $Q_L = Q_c / (1 + \beta)$ respectively volume and loaded quality factor of the cavity. β is the coupling strength of a coaxial antenna to the cavity mode. In natural units the axion power extracted with the antenna at

resonance is given by (34):

$$P_{\text{sig}} = g_\gamma^2 \frac{\alpha^2}{\pi^2} \frac{\rho_a}{\Lambda^4} \frac{\beta}{1 + \beta} \omega_c B_0^2 V C_{010} \frac{Q_a Q_L}{Q_a + Q_L} \quad (7)$$

where α is the fine-structure constant, $\rho_a \simeq 0.45 \text{ GeV/cm}^3$ is the dark matter density in the galactic halo, $\Lambda = 78 \text{ MeV}$ a parameter linking the axion mass to hadronic physics, and g_γ is the dimensionless axion-photon coupling. The coupling that appears in the axion-photon Lagrangian is $g_{a\gamma\gamma} = (g_\gamma \alpha / \pi \Lambda^2) m_a$. A useful benchmark for experiments is the QCD axion band, delimited by the KSVZ (Kim-Shifman-Vainshtein-Zakharov) (35, 36) and DFSZ (Dine-Fischler-Srednicki-Zhitnitsky) (37, 38) families of models, with couplings $g_\gamma = 0.97$ and 0.36 respectively. A practical expression for the signal power is:

$$P_{a\gamma\gamma} = 0.72 \text{ yW} \left(\frac{g_\gamma}{0.97} \right)^2 \frac{\rho_a}{0.45 \text{ GeV/cm}^3} \left(\frac{B}{2 \text{ T}} \right)^2 \cdot \frac{V}{0.11 \text{ l}} \cdot \frac{\nu_c}{7.37 \text{ GHz}} \cdot \frac{Q_L}{225000} \cdot \frac{C_{010}}{0.64}, \quad (8)$$

in which the parameters of the present experiment are made explicit. The smallness of the signal power, which at DFSZ models is at the yoctowatt (10^{-24} W) level even when state-of-the-art equipment is employed (see table Supplementary Table), is thus the key methodological challenge for haloscope detectors.

	B [T]	$P_{\text{sig}}^{\text{KSVZ}}$ [yW(ph/s)]	$P_{\text{sig}}^{\text{DFSZ}}$ [yW(ph/s)]
$\nu_c = 7.37 \text{ GHz}$	2	0.84(0.17)	0.11(0.026)
	12	30.4(6.2)	6.3(0.86)
$\nu_c = 10 \text{ GHz}$	12	22.39(3.38)	3.11(0.47)

Table Supplementary Table: Signal power for benchmark QCD axion models in yoctowatt (yW= 10^{-24} W) and photon rate calculated with eq.7. The right cylinder hybrid surfaced cavity employed in the present experimental apparatus has a fundamental frequency of resonance $\nu_c = 7.37 \text{ GHz}$ ($30.48 \mu\text{eV}$ axion mass), volume $V = 0.11$, form factor $C_{010} = 0.64$, and loaded quality factor $Q_L = 2.25 \times 10^5$). The signal power is also given in the second row for a magnetic field of 12 T, in place of the present superconducting magnet delivering up to a maximum field of 2 T. Coupling coefficient $\beta = 1$ has been assumed. For comparison, a haloscope probing heavier axions ($\nu_c = 10 \text{ GHz}$ corresponds to $41.36 \mu\text{eV}$) is also considered, having the same pill-box cavity length (0.135 m).

The signal power spectrum is a Maxwell-Boltzmann distribution, with $\Delta\nu_a = \nu_a/Q_a$ width, and $Q_a = 10^6$ set by axion velocities dispersion in the standard halo model (12). Note that, though the resonant enhancement is reduced at critical coupling to the receiver chain ($\beta = 1$) in a cavity haloscope the optimal coupling maximizes the search speed, and $\beta \sim 2$ or greater is typically chosen.

Scan rate. Given that the axion mass m_a is unknown, the merit of a cavity haloscope design is typically evaluated using the scan rate df/dt . This parameter quantifies the maximum speed at which a search can be run for a given sensitivity to $g_{a\gamma\gamma}$ and is given by (39):

$$\frac{df}{dt} \approx \frac{g_{a\gamma\gamma}^4 \rho_a^2 B_0^4 C_{010}^2 V^2}{\Sigma^2 m_a^2 N_{sys}^2} \left(\frac{\beta}{1 + \beta} \right)^2 \frac{Q_L Q_a^2}{Q_L + Q_a}, \quad (9)$$

where $N_{sys} = k_B T_s$ is the system noise (17) with known noise temperature T_n . For an amplifier at SQL, $k_B T_s = h\nu$, thus $df/dt \propto \nu^{-8}$ if we fix the cavity length to a value h comparable with the typical length of a commercially available SC solenoid (~ 25 cm). In fact, $V \propto \nu_c^{-2}$ because in a cylindrical cavity $r = 2.405 c/(2\pi\nu_c)$, $m_a \simeq h\nu_c$, and in addition we drop the quality factor frequency dependence $Q_L \propto \nu^{-2/3}$ related to the anomalous skin effect (40) because we consider superconducting cavities. Even though we allow for rather extreme values of cavity aspect ratio $h/r \simeq 10$, with r cavity radius, the intruder modes density is acceptable in the 5-10 GHz range, where a few different radius resonators could be envisaged to cover the whole range.

Photon counting versus linear detection

The comparison between linear detection and photon counting was thoroughly analyzed in the foundational study by Lamoureaux et al. in Ref. (17). This analysis is revised and contextualized here, articulated through the lens of experimental parameters, especially focusing on detector efficiency and dark counts. The case where the axion linewidth is smaller than the

haloscope linewidth $\Delta\nu_a < \Delta\nu_c$ is considered. In the opposite limit, the analysis holds by substituting the axion linewidth with the haloscope linewidth ($\Delta\nu_a \leftarrow \Delta\nu_c$).

Linear amplifiers are widely utilized for detecting incoherent signals. Consideration is given to an axion signal with power P_a , incoherently emitted across a bandwidth $\Delta\nu_a$ at a frequency ν_a , which is predicted by the axion model to typically have a quality factor $Q_a = \nu_a/\Delta\nu_a \sim 10^6$. The noise generated by the linear receiver over a measurement duration t is expressed as:

$$P_{\text{lin}} = h\nu_a(\bar{n} + 1)\sqrt{\frac{\Delta\nu_a}{t}} \quad (10)$$

where the mean photon number per mode is given by $\bar{n} = (\exp(h\nu_a/k_bT) - 1)^{-1}$.

On the one hand, when k_bT significantly exceeds $h\nu_a$, this noise limit simplifies to the Dicke radiometer formula: $P_{\text{RM}} = k_bT\sqrt{\Delta\nu_a/t}$. On the other hand, the optimal noise power is achievable at zero temperature and defined as the standard quantum limit (SQL):

$$P_{\text{SQL}} = h\nu_a\sqrt{\Delta\nu_a/t} \quad (11)$$

It is noteworthy that, given the incoherent nature of the expected signal, both I and Q quadratures contribute a vacuum noise of $h\nu_a/2$ leading to noise power of $h\nu_a$ as described in Ref. (17). The detection's signal-to-noise ratio (SNR) is therefore capped as follows:

$$\text{SNR}_{\text{SQL}} = \frac{P_a}{h\nu_a}\sqrt{\frac{t}{\Delta\nu_a}} \quad (12)$$

In the current setup, we examine a photon detector characterized by an efficiency η and a dark count rate Γ . The signal is obtained by accumulating counts over a period of t , yielding $S = \eta P_a/h\nu_a t + \Gamma t$. Given its Poisson distribution, the variance associated with this signal is $\delta S^2 = \eta P_a/h\nu_a t + \Gamma t$. The SNR therefore reads:

$$\text{SNR}_{\text{PC}} = \frac{\eta P_a t/h\nu_a}{\sqrt{\Gamma_{\text{dc}} t + \eta P_a t/h\nu_a}} = \frac{\eta P_a}{h\nu_a} \frac{\sqrt{t}}{\sqrt{\Gamma_{\text{dc}} + \eta P_a/h\nu_a}} \quad (13)$$

In situations where signal contribution $\eta P_a/h\nu_a$ is negligible compared to the darkcount Γ_{dc} , the noise due to signal shot can be disregarded, leading to the following SNR expression:

$$\text{SNR}_{\text{PC}} \approx \frac{\eta P_a}{h\nu_a} \sqrt{\frac{t}{\Gamma_{\text{dc}}}} \quad (14)$$

The darkcount rate can be breakdown in two main contributions $\Gamma_{\text{dc}} = \Gamma_{\text{th}} + \Gamma_{\text{int}}$, where $\Gamma_{\text{th}} = \eta\Delta\nu_{\text{det}}n_{\text{th}}$ is the background thermal fluctuation integrated over the detector bandwidth $\Delta\nu_{\text{det}}$ and where Γ_{int} is the intrinsic detector darkcount due to technical counts due to for instance errors in the qubit readout or out-of-equilibrium excitation of the qubit. In the limit where the darkcount is dominated by thermal background contribution ($\Gamma_{\text{int}} \ll \eta\Delta\nu_{\text{det}}n_{\text{th}}$) the SNR reads

$$\text{SNR}_{\text{PC}}^{\text{th}} \approx \frac{P_a}{h\nu_a} \sqrt{\frac{\eta t}{\Delta\nu_{\text{det}}n_{\text{th}}}} \quad (15)$$

Note that the SMPD used in this experiment operates in this regime (20) where the intrinsic darkcount is of the order of $\Gamma_{\text{int}} \sim 10 \text{ s}^{-1}$ while $\Gamma_{\text{th}} \sim 75 \text{ s}^{-1}$ corresponding to a microwave temperature of 44 mK where the effective bandwidth of the detector taking into account the Lorentzian linewidth is given by $\Delta\nu_{\text{det}} = \kappa/4 = 2\pi/4 \times 0.7 \text{ MHz}$.

Comparison

Our goal is to assess the improvement in measurement speed for achieving a specified SNR. For operations of a linear receiver at the quantum standard limit, the required measurement time is:

$$t_{\text{SQL}} = \Delta\nu_a \left(\frac{h\nu_a \text{SNR}}{P_a} \right)^2 \quad (16)$$

Conversely, for photon counting the required measurement time is:

$$t_{\text{PC}} = \frac{\Gamma_{\text{dc}}}{\eta^2} \left(\frac{h\nu_a \text{SNR}}{P_a} \right)^2 \quad (17)$$

Hence, the comparative gain in measurement speed or scanning rate in this experiment relative to the quantum standard limit is:

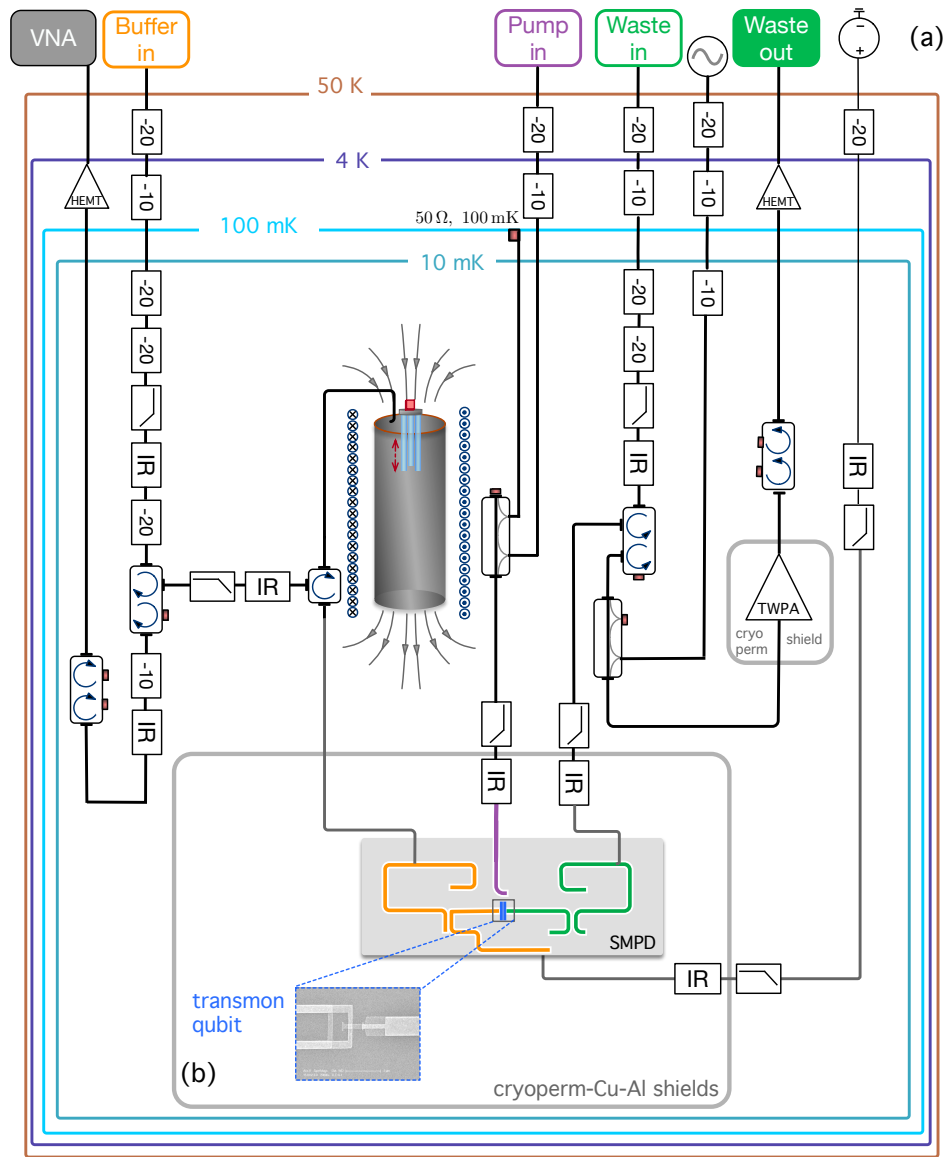
$$\mathcal{R} = \frac{t_{\text{SQL}}}{t_{\text{PC}}} = \eta^2 \frac{\Delta\nu_a}{\Gamma_{\text{dc}}} \sim 20. \quad (18)$$

Discussion

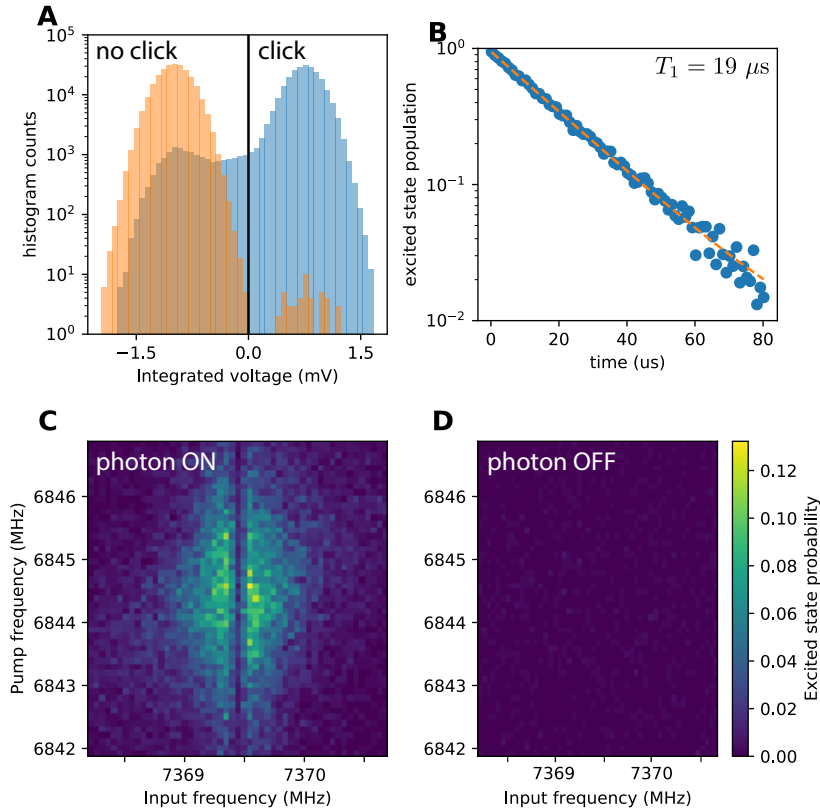
The gain in measurement time can be evaluated in the ideal limit where the darkcount is dominated by the background thermal noise and where the detector bandwidth is perfectly matched with the haloscope linewidth ($\Delta\nu_{\text{det}} \approx \Delta\nu_c$), then the gain is given by:

$$\mathcal{R}^{\text{th}} = \frac{t_{\text{SQL}}}{t_{\text{PC}}^{\text{th}}} = \eta \frac{\Delta\nu_a}{n_{\text{th}} \Delta\nu_c}. \quad (19)$$

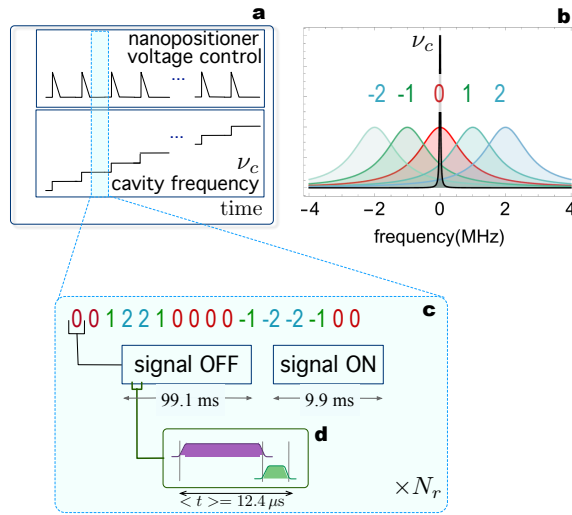
Crucially, the enhancement in scan rate achievable through photon counting, as compared to linear detection, is not subject to any fundamental limits. In particular, expected advancements in reducing the dark count rate, enhancing efficiency, and achieving stability (thereby negating the need for the differential method) promise to unlock substantially greater improvements in speed.



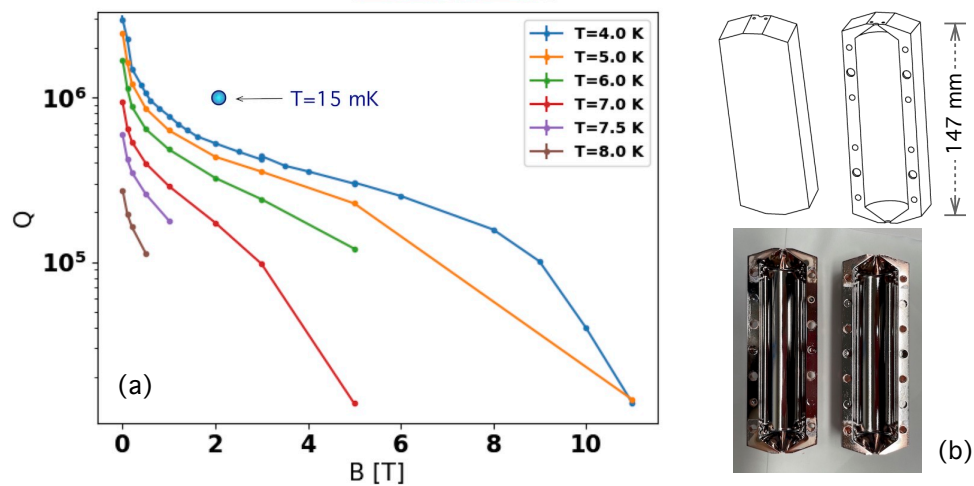
Supplementary Figure 1: (a) Schematic cabling of the dilution refrigerator. (b) The SMPD is enclosed in a box made with three screens (Al, Cu and cryoperm), while the Traveling Wave parametric Amplifier (TWPA) is within a separate cylindrical cryoperm shield.



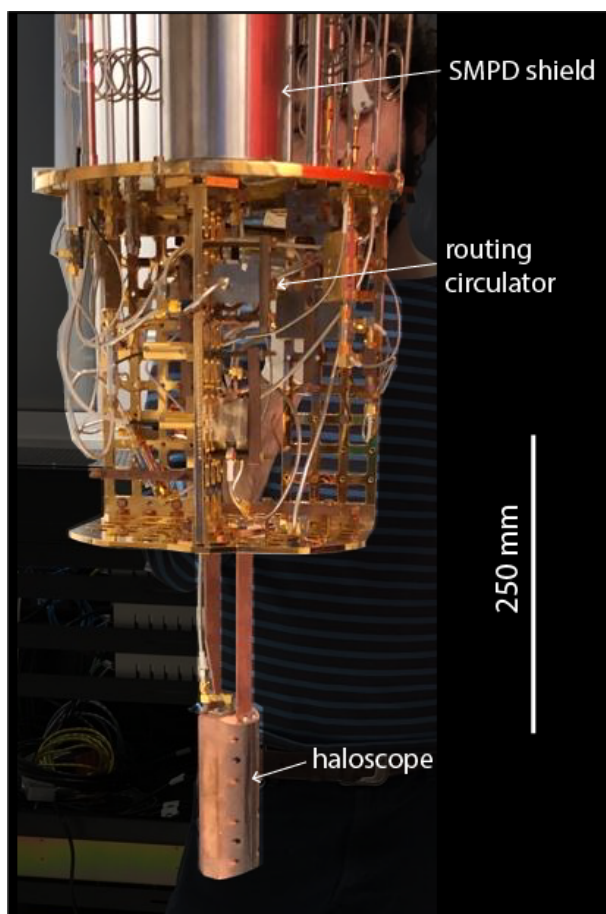
Supplementary Figure 2: **SMPD Characterization** - **A:** Readout histogram of the transmon qubit measurement. Readout fidelity for the excited state is 0.93, while the ground state readout infidelity is less than 5×10^{-5} . The thermal equilibrium population of the qubit is $p_{\text{th}} = 2 \times 10^{-4}$. **B:** Relaxation measurement of the transmon qubit indicates a T_1 value of $19 \mu\text{s}$. **C:** Pump frequency tuning involves measuring the qubit state population while driving the pump and a coherent tone on the input resonator. Optimal working points are identified by varying the frequencies of the two drives. **D:** With the coherent tone turned off, the qubit population remains close to zero, confirming that the correct 4-wave mixing process is at play.



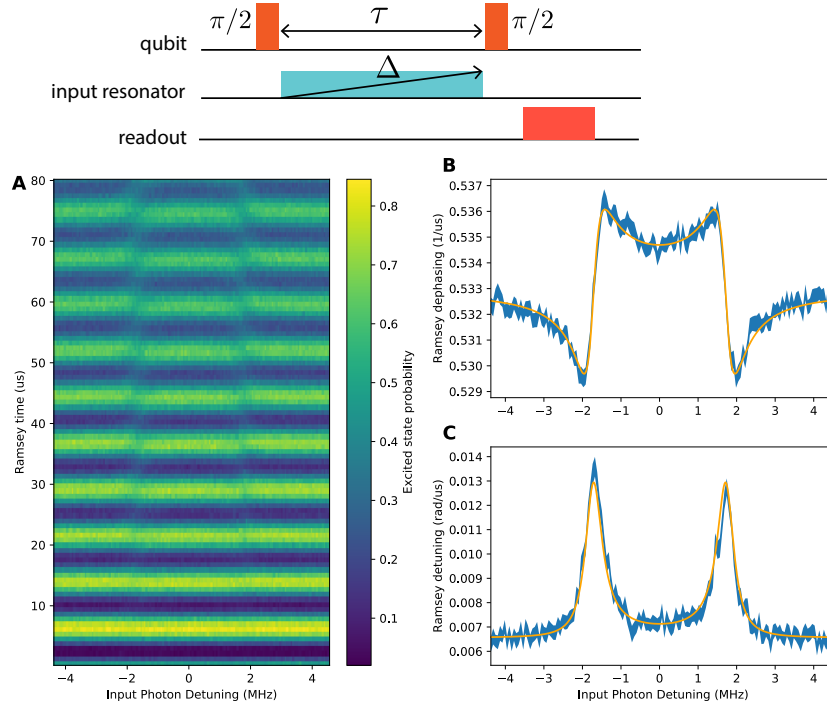
Supplementary Figure 3: (a) We tune the cavity by displacing dielectric rods inside the cavity's volume with a linear z-nanopositioner driven by a sawtooth voltage. (b) Values of ω_b set within the protocol. Labels $-2, -1, 1, 2$ indicate that clicks are recorded with $\omega_b/2\pi$ differing from the cavity frequency of resonance $\nu_c = \omega_c/2\pi$ by the label numerical value given in MHz. "0" corresponds to the resonance condition $\omega_b = \omega_c$. To monitor the counter detection efficiency, white noise is injected during the "signal ON" phase at the buffer input, while with the counts recorded in the "signal OFF" phase the operational dark count can be assessed under different experimental conditions. (c) The buffer frequency $\omega_b/2\pi$ is cycled through the sequence shown for $N_r = 36$ times. Before each cycle, a tuning step is devised, in which a weak voltage pulse is applied to the nanopositioner, followed by 5 s-duration waiting time. (d) The detection cycle includes a $10.5 \mu\text{s}$ -duration pump pulse (violet), followed by the readout time (green), which is not deterministic. The average duration of this block is $12.4 \mu\text{s}$.



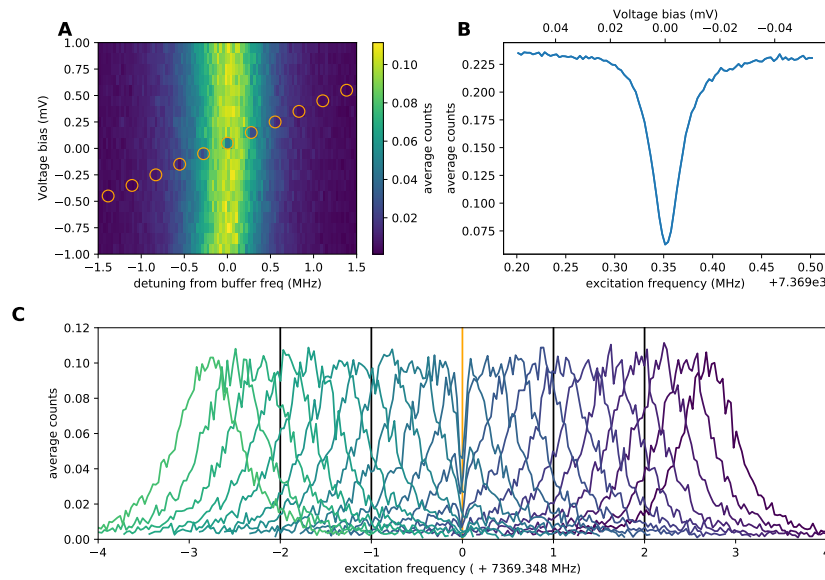
Supplementary Figure 4: (a) Microwave cavity quality factor Q_0 versus applied magnetic field for a few temperature values, as measured in a Helium flow cryostat. The blue dot is the quality factor measured at 2 T field in the delfridge at about 15 mK base temperature. (b) Cavity geometry, realized in two hollowed out copper bodies. Only the central cylindrical part is covered with a superconducting NbTi film. The cavity endcaps are shaped as cones.



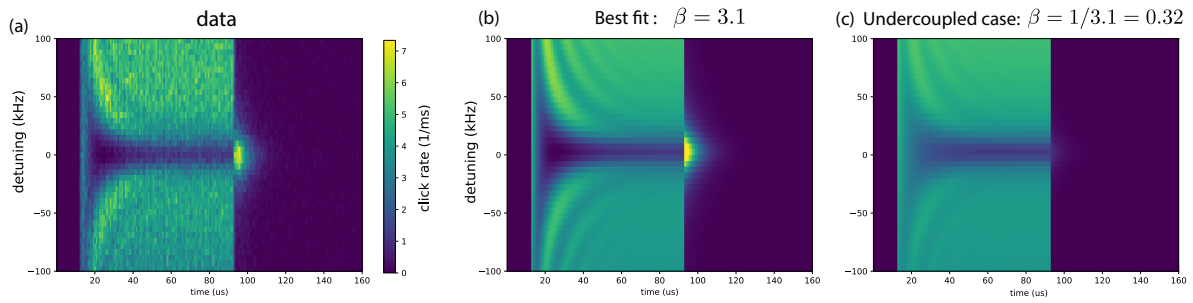
Supplementary Figure 5: Photo of the cryostat at room temperature. The haloscope is positioned at the bottom of the cryostat, which operates at millikelvin temperatures, with a superconducting magnet to be mounted around it at 4K. The magnetic shield for the SMPD is situated on the mixing chamber plate, approximately 50 cm from the magnet's center. A circulator directs the signal from the haloscope to the SMPD.



Supplementary Figure 6: **Coherent Tone Calibration by Ramsey Measurement Under Illumination.** The pulse sequence consists of two $\pi/2$ pulses separated by a Ramsey interval τ . A coherent drive populates the input resonator during the waiting time. Following the sequence, the qubit is read out. **A:** Qubit population as a function of the waiting time and the frequency of the coherent drive. Ramsey oscillations are observed in the qubit population. When the drive resonates with the input resonator, both a frequency shift and an accelerated decay of the Ramsey oscillations occur. **B and C:** Simultaneous determination of the frequency shift and decay rate as a function of drive detuning (blue line) by fitting individual Ramsey traces. The width of the line represents the uncertainty in the fit results. The orange line corresponds to the theoretical model described in the main text, enabling the determination of the resonator decay rate ($\kappa/2\pi = 0.523 \pm 0.014$ MHz), the dispersive shift ($\chi/2\pi = 3.461 \pm 0.015$ MHz), and the coherent drive rate ($\epsilon/2\pi = 40.9 \pm 0.5$ kHz).



Supplementary Figure 7: **Frequency Calibration Routine.** **A:** The click count is measured as a function of the SQUID bias voltage and the detuning between the coherent drive and the expected input resonator frequency at each SQUID bias voltage. Pump frequency adjustments accompany each SQUID bias voltage change. **B:** The same data presented as a function of the absolute frequency of the coherent drive. Note the sharp decrease in the count number (circled in orange in A), indicating the absorption by the haloscope cavity. **C:** Both the SMPD frequency and the coherent drive frequency are scanned across the haloscope resonance. The absorption dip observed in the reflection coefficient enables the determination of the haloscope's frequency and linewidth.



Supplementary Figure 8: **Time-Domain Response of the Haloscope Cavity Measured with the SMPD.** (a). The click rate of the SMPD is measured in response to a square pulse applied to the haloscope. This measurement is conducted as a function of time and pulse frequency. The SMPD’s time resolution is enhanced to $1 \mu\text{s}$ by reducing the duration of the detection windows. The detection times of the SMPD are sampled to cover the entire time window. (b). Theoretical prediction fitted with $\beta = 3.15$ for the haloscope. All transient features are quantitatively captured by the model lifting the ambiguity toward the overcoupled regime. (c) Theoretical prediction for to the same loaded quality factor Q_L but in the undercoupled regime with $\beta = 1/3.15 = 0.32 < 1$. The transient features at the loading and unloading of the haloscope are not reproduced despite that the steady-state absorption is identical to the overcoupled case as expected.

Towards a SM prediction for CP violation in charm

Alexander Lenz,^a Maria Laura Piscopo^{a,*} and Aleksey V. Rusov^a

^a*Theoretische Teilchenphysik, Center for Particle Physics Siegen, Physik Department, Universität Siegen, Walter-Flex-Str. 3, 57068 Siegen, Germany*

E-mail: alexander.lenz@uni-siegen.de, maria.piscopo@uni-siegen.de,
rusov@physik.uni-siegen.de

We provide an overview of the current experimental and theoretical status of charm CP violation and discuss recent progress in obtaining a Standard Model prediction for $\Delta a_{\text{CP}}^{\text{dir}}$ using the framework of light-cone sum rules. Furthermore, we present new results for the ratios of the direct CP asymmetries and of the branching fractions for the modes $D^0 \rightarrow \pi^+\pi^-$ and $D^0 \rightarrow K^+K^-$.

*20th International Conference on B-Physics at Frontier Machines (Beauty2023)
3-7 July, 2023
Clermont-Ferrand, France*

*Speaker

1. Introduction

The charm sector offers a unique system for testing the Standard Model of particle physics (SM), see Ref. [1] for a recent review. The peculiarities of charm are twofold. On the one hand, achieving precise theoretical predictions for charm observables is currently very challenging. This follows from the value of the charm quark mass which lies at the boundary between the heavy and the light quark regimes, such that the typical theoretical methods employed for the study of heavy hadrons might be less suitable or even inapplicable for the description of charmed systems. The behaviour of both the perturbative and power expansions becomes, in fact, a priori questionable as

$$\alpha_s(m_c) \sim 0.35, \quad \frac{\Lambda_{\text{QCD}}}{m_c} \sim 0.30. \quad (1)$$

On the other hand, charmed hadrons provide essential complementary information with respect to kaon- and b -physics, constituting, for instance, the only system to study meson-mixing in the up-quark sector. Additionally, the sensitivity to potential new physics (NP) contributions is high for charm observables, as pronounced cancellations often affect their SM predictions. The latter follow from the Glashow-Iliopoulos-Maiani (GIM) mechanism due to $m_b, m_s, m_d \ll m_W$, as well as from the size of the relevant elements of the Cabibbo-Kobayashi-Maskawa (CKM) matrix i.e. $\lambda_q \equiv V_{cq}^* V_{uq}$, namely

$$\lambda_d = -0.21874 + 2.51 \times 10^{-5}i, \quad \lambda_s = 0.21890 + 0.13 \times 10^{-5}i, \quad (2)$$

$$\lambda_b = 6.3 \times 10^{-5} - 1.4 \times 10^{-4}i. \quad (3)$$

In particular, having λ_b the biggest relative imaginary part but being much smaller in magnitude compared to $\lambda_{d,s}$, the amount of CP violation in the charm sector is expected to be small in the SM. Testing this result against the experimental data, although theoretically difficult, is clearly a task of primary importance in order to strengthen the current understanding of the SM and search for NP.

2. Experimental status of CP violation in charm

The observation of CP violation in the charm sector was made in 2019 by the LHCb Collaboration [2], by measuring the difference of the time-integrated CP asymmetries in the $D^0 \rightarrow K^+K^-$ and $D^0 \rightarrow \pi^+\pi^-$ modes, that is $\Delta A_{\text{CP}} \equiv A_{\text{CP}}(K^+K^-) - A_{\text{CP}}(\pi^+\pi^-)$. The corresponding difference of the direct CP asymmetries in the above channels turned out to be

$$\Delta a_{\text{CP}}^{\text{dir}}|_{\text{exp}} = (-15.7 \pm 2.9) \times 10^{-4}. \quad (4)$$

Recently, also a measurement of the CP asymmetry in $D^0 \rightarrow K^+K^-$ was published by the LHCb Collaboration [3], which yields, when combined with the result in Eq. (4), the following values for the direct CP asymmetries in the two individual modes, namely

$$a_{\text{CP}}^{\text{dir}}(K^+K^-)|_{\text{exp}} = (7.7 \pm 5.7) \times 10^{-4}, \quad a_{\text{CP}}^{\text{dir}}(\pi^+\pi^-)|_{\text{exp}} = (23.2 \pm 6.1) \times 10^{-4}. \quad (5)$$

While the result for $a_{\text{CP}}^{\text{dir}}(\pi^+\pi^-)$ provides the first evidence for CP violation in a specific D -meson decay, a clear theoretical interpretation of the measurements in Eqs. (4), (5) is currently still missing, particularly as the values of the individual CP asymmetries in Eq. (5) would imply a surprisingly large breaking of the U-spin symmetry [4].

3. Theoretical status of CP violation in charm

Exclusive hadronic decays of charmed hadrons pose significant challenges for robust theoretical predictions and although several studies have been carried out in the literature, no unanimous conclusion has yet been reached on the origin of the experimental value of $\Delta a_{\text{CP}}^{\text{dir}}$. Naive estimates, see e.g. Ref. [5], point towards a value of $\Delta a_{\text{CP}}^{\text{dir}}$ about an order of magnitude smaller than the one in Eq. (4). This result was confirmed in Refs. [6, 7] using the framework of light-cone sum rule (LCSR) [8], and analogous conclusions were also obtained in a recent study of final state interactions [9]. Consequently, following these findings, several investigations of possible NP scenarios have been triggered in the effort to accommodate the experimental data [10]. Furthermore, also SM interpretations of the experimental value of ΔA_{CP} have been advanced. These include analyses based on U-spin relations, see e.g. Ref. [11], as well as studies of rescattering contributions [12] and of final state interactions [13]. In particular, in Ref. [12], the possibility that nearby resonances, like the $f_0(1710)$ or $f_0(1790)$, could lead to a large enhancement of the SM value of ΔA_{CP} , was pointed out. No sign of this effect, however, has been observed in the analysis of Ref. [9], and the latter work also indicated some inconsistencies in Ref. [13]. Finally, approaches based on topological diagram analyses have also been employed [14], although these often rely on qualitative studies and do not provide a first principle determination.

4. Theory of the decays $D^0 \rightarrow \pi^+\pi^-$ and $D^0 \rightarrow K^+K^-$

Using the unitarity of the CKM matrix $\lambda_d + \lambda_s + \lambda_b = 0$, the amplitudes for the non-leptonic decays $D^0 \rightarrow \pi^+\pi^-$ and $D^0 \rightarrow K^+K^-$ can be recast in the form [6]

$$\mathcal{A}(D^0 \rightarrow \pi^+\pi^-) = \lambda_d \mathcal{A}_{\pi\pi} \left[1 - \frac{\lambda_b \mathcal{P}_{\pi\pi}}{\lambda_d \mathcal{A}_{\pi\pi}} \right], \quad (6)$$

$$\mathcal{A}(D^0 \rightarrow K^+K^-) = \lambda_s \mathcal{A}_{KK} \left[1 - \frac{\lambda_b \mathcal{P}_{KK}}{\lambda_s \mathcal{A}_{KK}} \right], \quad (7)$$

by singling out, respectively, the contribution due to the CKM dominant combination $\lambda_{d,s}$ from that of the strongly suppressed factor λ_b , with the definitions

$$\mathcal{A}_{\pi\pi} = \langle \pi^+\pi^- | \mathcal{O}^d | D^0 \rangle - \langle \pi^+\pi^- | \mathcal{O}^s | D^0 \rangle, \quad (8)$$

$$\mathcal{A}_{KK} = \langle K^+K^- | \mathcal{O}^s | D^0 \rangle - \langle K^+K^- | \mathcal{O}^d | D^0 \rangle, \quad (9)$$

and

$$\mathcal{P}_{\pi\pi} = \langle \pi^+\pi^- | \mathcal{O}^s | D^0 \rangle, \quad \mathcal{P}_{KK} = \langle K^+K^- | \mathcal{O}^d | D^0 \rangle. \quad (10)$$

In Eqs. (8) - (10), the notation $\mathcal{O}^q \equiv -(G_F/\sqrt{2}) \sum_{i=1,2} C_i \mathcal{O}_i^q$ is used, where $\mathcal{O}_1^q = (\bar{q}^i \Gamma_\mu c^i)(\bar{u}^j \Gamma^\mu q^j)$ and $\mathcal{O}_2^q = (\bar{q}^i \Gamma_\mu c^j)(\bar{u}^j \Gamma^\mu q^i)$, with $q = d, s$, denote the current-current operators in the weak effective Hamiltonian describing the charm-quark transitions $c \rightarrow q\bar{q}u$ [15], and $C_{1,2}$ are the corresponding Wilson coefficients. The leading CKM amplitudes $\mathcal{A}_{\pi\pi}$, \mathcal{A}_{KK} in Eqs. (6), (7) receive contributions from color-allowed tree-level, exchange and penguin topologies, whereas only the penguin topology can contribute to $\mathcal{P}_{\pi\pi}$, \mathcal{P}_{KK} , cf. Fig. 1.

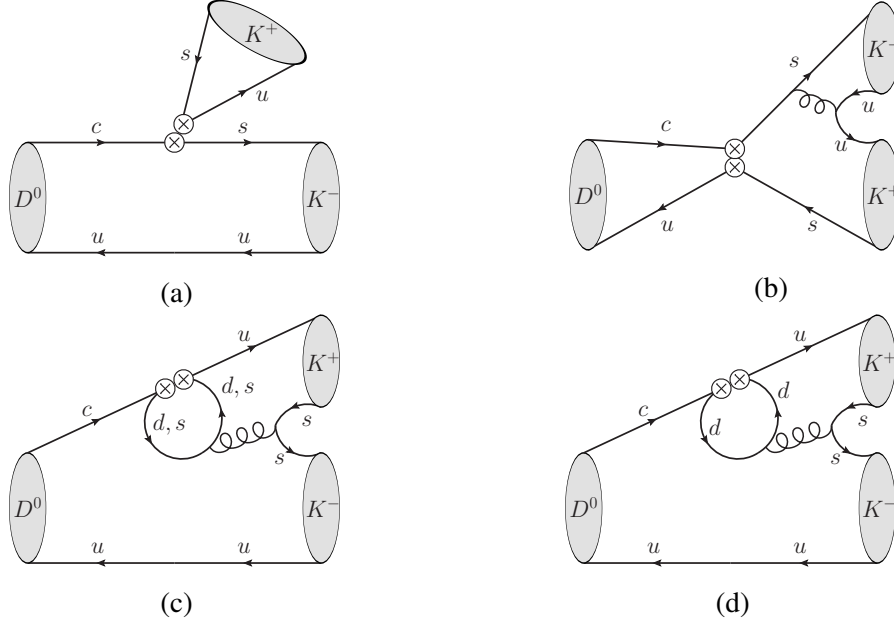


Figure 1: Examples of tree-level (a), exchange (b) and penguin (c) topologies contributing to \mathcal{A}_{KK} . Example of penguin topology contributing to \mathcal{P}_{KK} (d). The corresponding diagrams for $\mathcal{A}_{\pi\pi}$ and $\mathcal{P}_{\pi\pi}$ can be obtained replacing $K \rightarrow \pi$, $s \leftrightarrow d$.

Considering for simplicity only the decay $D^0 \rightarrow K^+K^-$, the corresponding branching fraction reads

$$\mathcal{B}(D^0 \rightarrow K^+K^-) \propto |\lambda_s|^2 |\mathcal{A}_{KK}|^2 \left| 1 - \frac{\lambda_b}{\lambda_s} \frac{\mathcal{P}_{KK}}{\mathcal{A}_{KK}} \right|^2, \quad (11)$$

up to phase-space and normalisation factors. Similarly, the direct CP asymmetry, defined as

$$a_{\text{CP}}^{\text{dir}}(f) \equiv \frac{\Gamma(D^0 \rightarrow f) - \Gamma(\bar{D}^0 \rightarrow \bar{f})}{\Gamma(D^0 \rightarrow f) + \Gamma(\bar{D}^0 \rightarrow \bar{f})}, \quad (12)$$

becomes

$$a_{\text{CP}}^{\text{dir}}(K^+K^-) = - \frac{2 \left| \frac{\lambda_b}{\lambda_s} \right| \sin \gamma \left| \frac{\mathcal{P}_{KK}}{\mathcal{A}_{KK}} \right| \sin \phi_{KK}}{1 - 2 \left| \frac{\lambda_b}{\lambda_s} \right| \cos \gamma \left| \frac{\mathcal{P}_{KK}}{\mathcal{A}_{KK}} \right| \cos \phi_{KK} + \left| \frac{\lambda_b}{\lambda_s} \right|^2 \left| \frac{\mathcal{P}_{KK}}{\mathcal{A}_{KK}} \right|^2}, \quad (13)$$

where we have defined the strong phase difference $\phi_{KK} \equiv \arg(\mathcal{P}_{KK}/\mathcal{A}_{KK})$, and introduced the angle $\gamma \equiv -\arg(\lambda_b/\lambda_s)$. Analogous expressions can be straightforwardly obtained for the mode $D^0 \rightarrow \pi^+\pi^-$ by replacing $KK \rightarrow \pi\pi$, $\lambda_s \rightarrow \lambda_d$ and $\sin \gamma \rightarrow -\sin \gamma$ in Eqs. (11), (13).

Taking into account the large hierarchy $\lambda_b/\lambda_{d,s} \ll 1$, it follows that the amplitudes $\mathcal{A}_{\pi\pi}$, \mathcal{A}_{KK} give the dominant contribution to the branching fractions, i.e.

$$\mathcal{B}(D^0 \rightarrow \pi^+\pi^-) \sim |\lambda_d|^2 |\mathcal{A}_{\pi\pi}|^2, \quad \mathcal{B}(D^0 \rightarrow K^+K^-) \sim |\lambda_s|^2 |\mathcal{A}_{KK}|^2, \quad (14)$$

whereas the direct CP asymmetries are driven only by the ratio of the penguin over the CKM leading amplitudes, that is

$$a_{\text{CP}}^{\text{dir}}(\pi^+\pi^-) \simeq 2 \left| \frac{\lambda_b}{\lambda_d} \right| \sin \gamma \left| \frac{\mathcal{P}_{\pi\pi}}{\mathcal{A}_{\pi\pi}} \right| \sin \phi_{\pi\pi}, \quad a_{\text{CP}}^{\text{dir}}(K^+K^-) \simeq -2 \left| \frac{\lambda_b}{\lambda_s} \right| \sin \gamma \left| \frac{\mathcal{P}_{KK}}{\mathcal{A}_{KK}} \right| \sin \phi_{KK}. \quad (15)$$

Finally, the above results, together with $|\lambda_d| \simeq |\lambda_s|$, yield the following expression for the difference of direct CP asymmetries $\Delta a_{\text{CP}}^{\text{dir}}$, namely

$$\Delta a_{\text{CP}}^{\text{dir}} \simeq -2 \left| \frac{\lambda_b}{\lambda_s} \right| \sin \gamma \left(\left| \frac{\mathcal{P}_{KK}}{\mathcal{A}_{KK}} \right| \sin \phi_{KK} + \left| \frac{\mathcal{P}_{\pi\pi}}{\mathcal{A}_{\pi\pi}} \right| \sin \phi_{\pi\pi} \right). \quad (16)$$

5. Determination of $\Delta a_{\text{CP}}^{\text{dir}}$ within LCSR

A first computation of the penguin amplitudes $\mathcal{P}_{\pi\pi}$, \mathcal{P}_{KK} was performed in Ref. [6] using the framework of LCSR with, respectively, pion and kaon light-cone distribution amplitudes (LCDAs), and following previous studies for the $B \rightarrow \pi\pi$ decay [16]. The values of $|\mathcal{A}_{\pi\pi}|$ and $|\mathcal{A}_{KK}|$ needed to determine the direct CP asymmetries were instead extracted, taking into account the relations in Eq. (14), from the precise experimental data on the branching ratios [17]

$$\mathcal{B}(D^0 \rightarrow \pi^+\pi^-)|_{\text{exp}} = (1.454 \pm 0.024) \times 10^{-3}, \quad (17)$$

$$\mathcal{B}(D^0 \rightarrow K^+K^-)|_{\text{exp}} = (4.08 \pm 0.06) \times 10^{-3}. \quad (18)$$

The authors of Ref. [6] obtained the following SM bound for the difference of CP asymmetries

$$|\Delta a_{\text{CP}}^{\text{dir}}|_{\text{SM}} \leq 2.3 \times 10^{-4}, \quad (19)$$

which is about a factor of 6 lower than the experimental value in Eq. (4). Recently, a study of the leading decay amplitudes $\mathcal{A}_{\pi\pi}$, \mathcal{A}_{KK} has been performed in Ref. [7], where the corresponding tree-level matrix elements have also been determined using LCSR with pion and kaon LCDAs, see also Ref. [18] for more details on the general framework. Specifically, from naive power counting, Eqs. (8), (9) can be expressed as

$$\mathcal{A}_{\pi\pi} = \langle \pi^+\pi^- | \mathcal{O}^d | D^0 \rangle \Big|_{\text{tree}} + \mathcal{O}(\alpha_s) + \mathcal{O}(1/m_c), \quad (20)$$

$$\mathcal{A}_{KK} = \langle K^+K^- | \mathcal{O}^s | D^0 \rangle \Big|_{\text{tree}} + \mathcal{O}(\alpha_s) + \mathcal{O}(1/m_c), \quad (21)$$

retaining the dominant contribution due to the tree-level amplitude and neglecting sub-leading diagrams due to both hard and soft QCD corrections. In this approximation it follows that

$$\mathcal{A}_{\pi\pi} \simeq -\frac{G_F}{\sqrt{2}} \left(C_1 + \frac{C_2}{3} \right) \langle \pi^+\pi^- | \mathcal{O}_1^d | D^0 \rangle \Big|_{\text{tree}}, \quad (22)$$

$$\mathcal{A}_{KK} \simeq -\frac{G_F}{\sqrt{2}} \left(C_1 + \frac{C_2}{3} \right) \langle K^+K^- | \mathcal{O}_1^s | D^0 \rangle \Big|_{\text{tree}}. \quad (23)$$

A first estimate of the matrix elements in Eqs. (22), (23) can be derived using the naive QCD factorisation approximation, which, surprisingly, already yields values for the branching fractions in very good agreement with the experimental data [7]. Furthermore, the computation of the tree-level matrix elements within the framework of LCSR gives [7]

$$\mathcal{B}(D^0 \rightarrow \pi^+ \pi^-)|_{\text{LCSR}} = \left(1.40^{+1.53}_{-1.06}\right) \times 10^{-3}, \quad (24)$$

$$\mathcal{B}(D^0 \rightarrow K^+ K^-)|_{\text{LCSR}} = \left(3.67^{+3.90}_{-2.69}\right) \times 10^{-3}, \quad (25)$$

where the central values again agree very well with the data, however, the uncertainties are large and mostly follow from a conservative treatment of missing contributions. Importantly, these results do not indicate any sign of potential large enhancement due to subleading topologies. On the other hand, in the ratio of branching fractions many theoretical uncertainties cancel, leading, after taking into account correlations due to common inputs, to the significantly more precise prediction

$$\left. \frac{\mathcal{B}(D^0 \rightarrow K^+ K^-)}{\mathcal{B}(D^0 \rightarrow \pi^+ \pi^-)} \right|_{\text{LCSR}} = 2.63 \pm 0.86, \quad (26)$$

which perfectly reproduces the observed size of $SU(3)_F$ breaking in the two modes, namely

$$\left. \frac{\mathcal{B}(D^0 \rightarrow K^+ K^-)}{\mathcal{B}(D^0 \rightarrow \pi^+ \pi^-)} \right|_{\text{exp}} = 2.81 \pm 0.06. \quad (27)$$

Combining the LCSR results for the penguin and tree-level amplitudes, as computed in Ref. [6] and Ref. [7], respectively, then yields the following value for the ratio of the two direct CP asymmetries defined in Eq. (15), i.e.

$$\left. \frac{a_{\text{CP}}^{\text{dir}}(K^+ K^-)}{a_{\text{CP}}^{\text{dir}}(\pi^+ \pi^-)} \right|_{\text{LCSR}} = -0.65^{+0.09}_{-0.08}, \quad (28)$$

where we have used the estimates of the strong phases as obtained in Ref. [6], since the sensitivity to potential missing contributions not yet accounted in the LCSR result is expected to be softened in the ratio $\sin \phi_{KK}/\sin \phi_{\pi\pi}$. The value in Eq. (28) is well consistent with -1, the result that would be obtained in the limit of exact U-spin symmetry, and must be compared with the corresponding experimental ratio

$$\left. \frac{a_{\text{CP}}^{\text{dir}}(K^+ K^-)}{a_{\text{CP}}^{\text{dir}}(\pi^+ \pi^-)} \right|_{\text{exp}} = 0.33^{+0.45}_{-0.26}. \quad (29)$$

Finally, allowing for arbitrary strong phase differences, that is varying both $\sin \phi_{\pi\pi}$ and $\sin \phi_{KK}$ from -1 to 1, the bound on $\Delta a_{\text{CP}}^{\text{dir}}$ obtained entirely using LCSR, reads [7]

$$|\Delta a_{\text{CP}}^{\text{dir}}|_{\text{LCSR}} \leq 2.4 \times 10^{-4}, \quad (30)$$

in perfect agreement with the result in Eq. (19), and again about a factor of 6 lower than the corresponding measurement.

6. Conclusion

We have briefly described the current experimental and theoretical status of charm CP violation and discussed recent progress obtained in the study of the hadronic decays $D^0 \rightarrow K^+K^-$ and $D^0 \rightarrow \pi^+\pi^-$ using the framework of LCSR. In particular, we have shown that first steps towards a description of the corresponding branching fractions using this method yields very promising results ¹, and that LCSR leads to a bound on the value of $\Delta a_{\text{CP}}^{\text{dir}}$ in the SM which is about a factor of 6 lower than the experimental data.

7. Acknowledgements

MLP is very grateful to the organisers of *Beauty2023* for the invitation and for creating a lively atmosphere rich of fruitful discussions. Moreover, AL and MLP would like to thank the participants of the recent LHCb school in Meinerzhagen for the interesting discussions and for proposing the computation of some of the observables presented in this manuscript. The work of MLP is funded by the Deutsche Forschungsgemeinschaft (DFG, German Research Foundation) - project number 500314741.

References

- [1] A. Lenz and G. Wilkinson, *Ann. Rev. Nucl. Part. Sci.* **71**, 59-85 (2021).
- [2] R. Aaij *et al.* [LHCb], *Phys. Rev. Lett.* **122** (2019) no.21, 211803.
- [3] R. Aaij *et al.* [LHCb], *Phys. Rev. Lett.* **131** (2023) no.9, 091802.
- [4] S. Schacht, *JHEP* **03** (2023), 205; R. Bause, H. Gisbert, G. Hiller, T. Höhne, D. F. Litim and T. Steudtner, *Phys. Rev. D* **108** (2023).
- [5] Y. Grossman, A. L. Kagan and Y. Nir, *Phys. Rev. D* **75** (2007), 036008.
- [6] A. Khodjamirian and A. A. Petrov, *Phys. Lett. B* **774** (2017), 235-242.
- [7] A. Lenz, M. L. Piscopo and A. V. Rusov, [arXiv:2312.13245 [hep-ph]].
- [8] I. I. Balitsky, V. M. Braun and A. V. Kolesnichenko, *Sov. J. Nucl. Phys.* **44** (1986), *Nucl. Phys. B* **312** (1989); V. L. Chernyak and I. R. Zhitnitsky, *Nucl. Phys. B* **345** (1990).
- [9] A. Pich, E. Solomonidi and L. Vale Silva, *Phys. Rev. D* **108** (2023).
- [10] M. Chala, A. Lenz, A. V. Rusov and J. Scholtz, *JHEP* **07** (2019), 161; A. Dery and Y. Nir, *JHEP* **12** (2019), 104; L. Calibbi, T. Li, Y. Li and B. Zhu, *JHEP* **10** (2020), 070; R. Bause, H. Gisbert, M. Golz and G. Hiller, *Phys. Rev. D* **101** (2020).
- [11] Y. Grossman and S. Schacht, *JHEP* **07** (2019), 020.

¹See Section 6 of Ref. [7] for a list of future improvements.

- [12] S. Schacht and A. Soni, *Phys. Lett. B* **825** (2022).
- [13] I. Bediaga, T. Frederico and P. C. Magalhães, *Phys. Rev. Lett.* **131** (2023).
- [14] H. N. Li, C. D. Lü and F. S. Yu, [arXiv:1903.10638 [hep-ph]]; H. Y. Cheng and C. W. Chiang, *Phys. Rev. D* **100** (2019); D. Wang, C. P. Jia and F. S. Yu, *JHEP* **21** (2020), 126.
- [15] G. Buchalla, A. J. Buras and M. E. Lautenbacher, *Rev. Mod. Phys.* **68** (1996).
- [16] A. Khodjamirian, *Nucl. Phys. B* **605** (2001); A. Khodjamirian, T. Mannel and B. Melic, *Phys. Lett. B* **571** (2003).
- [17] R. L. Workman *et al.* [Particle Data Group], *PTEP* **2022** (2022), 083C01.
- [18] M. L. Piscopo and A. V. Rusov, *JHEP* **10** (2023), 180.

The Z_b states as the mixture of the molecular and diquark-anti-diquark components within the effective field theory

Wei He^{1,2,*}, De-Shun Zhang^{1,2,†} and Zhi-Feng Sun^{1,2,3,4‡}

¹*School of Physical Science and Technology, Lanzhou University, Lanzhou 730000, China*

²*Research Center for Hadron and CSR Physics, Lanzhou University and Institute of Modern Physics of CAS, Lanzhou 730000, China*

³*Lanzhou Center for Theoretical Physics, Key Laboratory of Theoretical Physics of Gansu Province, and Key Laboratory of Quantum Theory and Applications of the Ministry of Education, Lanzhou University, Lanzhou, 730000, China*

⁴*Frontiers Science Center for Rare Isotopes, Lanzhou University, Lanzhou, Gansu 730000, China*
(Dated: March 5, 2024)

In this study, we reconsider the states $Z_b(10610)$ and $Z_b(10650)$ by investigating the presence of diquark-anti-diquark components as well as the hadronic molecule components in the framework of effective field theory. The different masses of pseudoscalar mesons such as π^0 , η_8 , and η_0 , as well as vector mesons like ρ^0 and ω violate the OZI rule that is well depicted under the $[U(3)_L \otimes U(3)_R]_{global} \otimes [U(3)_V]_{local}$ symmetry. To account for the contribution of intermediate bosons of heavy masses within the OBE model, we introduce an exponential form factor instead of the commonly used monopole form factor in the past. By solving the coupled-channel Schrödinger equation with the Gaussian expansion method, our numerical results indicate that the $Z_b(10610)$ and $Z_b(10650)$ states can be explained as hadronic molecules slightly mixing with diquark-anti-diquark states.

PACS numbers:

I. INTRODUCTION

In the past decades, a series of quarkonium-like states were discovered. In the $b\bar{b}$ sector, Belle Collaboration reported two charged bottomonium-like states which are known as $Z_b(10610)$ and $Z_b(10650)$ [1] in 2011. Both of them were observed in $\Upsilon(5S) \rightarrow \pi^\pm h_b(mP)$ ($m = 1, 2$) and $\Upsilon(5S) \rightarrow \pi^\pm \Upsilon(nS)$ ($n = 1, 2, 3$), respectively. Later, Belle confirmed their observations [2, 3]. The next year of the first discovery, the neutral state $Z_b^0(10610)$ was found in the $\Upsilon(5S) \rightarrow \Upsilon(2S, 3S)\pi^0\pi^0$ decay [4]. The masses and widths of these states listed in PDG (Particle Data Group) are shown below

$$M_{Z_b^\pm} = 10607.2 \pm 2.0 \text{ MeV}, \quad \Gamma_{Z_b^\pm} = 18.4 \pm 2.4 \text{ MeV},$$

$$M_{Z_b^0} = 10609 \pm 4.0 \pm 4 \text{ MeV},$$

$$M_{Z_b'^\pm} = 10652.2 \pm 1.5 \text{ MeV}, \quad \Gamma_{Z_b'^\pm} = 11.5 \pm 2.2 \text{ MeV}$$

with the quantum numbers $I^G(J^P) = 1^+(1^+)$. For simplicity, here we label the two states $Z_b(10610)$ and $Z_b(10650)$ by Z_b and Z_b' , respectively.

Theoretical research had already been performed before the observations of the Z_b states. The authors in Ref. [5, 6] indicated that there may exist a loosely bound S-wave $B\bar{B}^*/B^*\bar{B}$ molecular state.

After the observation, the explanations of the nature of the Z_b states were proposed through different assump-

tions and theoretical methods. Since the masses of the $Z_b(10610)$ and the $Z_b(10650)$ are close to the $B\bar{B}^*$ and $B^*\bar{B}^*$ thresholds, they are good candidates of $B\bar{B}^*$ and $B^*\bar{B}^*$ molecular states [7–40]. However, tetraquark interpretations including diquark-anti-diquark explanation can not be ruled out [17, 37, 41–47]. As a consequence, in this work we study these two states in the picture of the mixture of molecular and diquark-anti-diquark components, which is used to investigate the nature of the Z_{cs} states observed by LHCb in our previous work [48].

The hadronic molecule has been proposed based on the study of deuteron composed of a proton and a neutron. And this kind of topic has been widely discussed [49–52] within different methods, especially after the observation of $X(3872)$ in 2003 [53]. On the other hand, the concept of the diquark-anti-diquark state was proposed for the first time by Maiani *et al.* [54, 55] following the revitalization of interest on the σ meson. In this work, we use both the molecular state and the diquark-anti-diquark state, and make the calculation in the framework of the effective field theory. In this way, the mesons and the diquarks are viewed as point-like particles, which finally form the color singlet system. The forces between these clusters are provided by exchanging pseudoscalar and vector mesons as well as scalar and axial-vector diquarks.

In order to calculate the effective potentials in the coordinate space, form factors for each vertex are needed, such that the high-momentum contributions are suppressed. In the works related to the One-Boson-Exchange model in the past, the monopole form factor is intro-

*hewei1999@outlook.com

†220220940071@lzu.edu.cn

‡Corresponding Author: sunzf@lzu.edu.cn

duced (see the review [49]). However, in some of our cases, since the exchanged particles' masses are not so small, the monopole form factor does not work very well for it suppressing the corresponding potentials by its numerator. So we introduce the exponentially parameterized form factor and obtain the analytical expressions of the potential in the coordinate space. Considering both the S- and D-wave contributions, we solve the coupled channel Schrödinger equation to see the existence of the composite particles.

The structure of this paper is organized as follows. After the introduction, the theoretical framework is presented in Sec. II. The results and discussion are shown in Sec. III. Finally, a brief summary is given in Sec. IV.

II. FORMALISM

A. Wave functions

We give here the flavour wave functions of the negative and neutral $B\bar{B}^*/B^*\bar{B}$ and $B^*\bar{B}^*$ systems constructed in Ref. [12]

$$\begin{aligned} |Z_{B\bar{B}^*/B^*\bar{B}}^- \rangle &= \frac{1}{\sqrt{2}}(|B^{*-}B^0\rangle + c|B^-B^{*0}\rangle), \\ |Z_{B\bar{B}^*/B^*\bar{B}}^0 \rangle &= \frac{1}{2}[|B^{*+}B^-\rangle - |B^{*0}\bar{B}^0\rangle + c(|B^+B^{*-}\rangle \\ &\quad - |B^0\bar{B}^{*0}\rangle)], \\ |Z_{B^*\bar{B}^*}^- \rangle &= |B^{*-}B^{*0}\rangle, \\ |Z_{B^*\bar{B}^*}^0 \rangle &= \frac{1}{\sqrt{2}}(|B^{*+}B^{*-}\rangle - |B^{*0}\bar{B}^{*0}\rangle). \end{aligned} \quad (1)$$

The flavour wave functions of diquark and anti-diquark systems are constructed in analogy to the meson-meson systems by swapping b quark and \bar{b} quark,

$$\begin{aligned} |Z_{S\bar{A}/A\bar{S}}^- \rangle &= \frac{1}{\sqrt{2}}(|\bar{A}_{bu}S_{bd}\rangle + c|\bar{S}_{bu}A_{bd}\rangle), \\ |Z_{S\bar{A}/A\bar{S}}^0 \rangle &= \frac{1}{2}[|A_{bu}\bar{S}_{bu}\rangle - |A_{bd}\bar{S}_{bd}\rangle + c(|S_{bu}\bar{A}_{bu}\rangle - |S_{bd}\bar{A}_{bd}\rangle)], \\ |Z_{A\bar{A}}^- \rangle &= |A_{bd}\bar{A}_{bu}\rangle, \\ |Z_{A\bar{A}}^0 \rangle &= \frac{1}{\sqrt{2}}(|A_{bu}\bar{A}_{bu}\rangle - |A_{bd}\bar{A}_{bd}\rangle). \end{aligned} \quad (2)$$

The value of c depends on the G-parity, i.e., $c = \pm 1$ corresponds to $G = \pm 1$. Here we only pay attention to the situation of $c = +1$, since the G-parity of the considered systems are all +1.

In this work, both S- and D-wave interactions between the composed particles are considered. In general, the Z_b

and Z'_b states can be expressed as

$$|Z_b\rangle = \begin{pmatrix} Z_{B\bar{B}^*/B^*\bar{B}}^-(^3S_1) \\ Z_{B\bar{B}^*/B^*\bar{B}}^-(^3D_1) \\ Z_{B^*\bar{B}^*}^-(^3S_1) \\ Z_{B^*\bar{B}^*}^-(^3D_1) \\ Z_{S\bar{A}/A\bar{S}}^-(^3S_1) \\ Z_{S\bar{A}/A\bar{S}}^-(^3D_1) \\ Z_{A\bar{A}}^-(^3S_1) \\ Z_{A\bar{A}}^-(^3D_1) \end{pmatrix}, \quad |Z'_b\rangle = \begin{pmatrix} Z_{B^*\bar{B}^*}^-(^3S_1) \\ Z_{B^*\bar{B}^*}^-(^3D_1) \\ Z_{S\bar{A}/A\bar{S}}^-(^3S_1) \\ Z_{S\bar{A}/A\bar{S}}^-(^3D_1) \\ Z_{A\bar{A}}^-(^3S_1) \\ Z_{A\bar{A}}^-(^3D_1) \end{pmatrix}. \quad (3)$$

Note that for Z'_b , $|^5D_1\rangle$ state is forbidden due to its G-even parity.

B. The Effective Lagrangians and Coupling Constants

Next we introduce the interactions of meson-meson and diquark-anti-diquark by constructing the corresponding Lagrangians.

As we all know, each quark is a color triplet resulting in a diquark being a color antitriplet or sextet. The interaction between the two quarks of an antitriplet is attractive, while that of a sextet is repulsive. Consequently, we only consider the effective Lagrangian containing antitriplet. The diquark fields are depicted as

$$S^a = \begin{pmatrix} 0 & S_{ud} & S_{us} \\ -S_{ud} & 0 & S_{ds} \\ -S_{us} & -S_{ds} & 0 \end{pmatrix}^a, \quad (4)$$

$$A_\mu^a = \begin{pmatrix} A_{uu} & \frac{1}{\sqrt{2}}A_{ud} & \frac{1}{\sqrt{2}}A_{us} \\ \frac{1}{\sqrt{2}}A_{ud} & A_{dd} & \frac{1}{\sqrt{2}}A_{ds} \\ \frac{1}{\sqrt{2}}A_{us} & \frac{1}{\sqrt{2}}A_{ds} & A_{ss} \end{pmatrix}_\mu^a, \quad (5)$$

$$S_b^a = (S_{bu} \ S_{bd} \ S_{bs})^a, \quad (6)$$

$$A_{b\mu}^a = (A_{bu} \ A_{bd} \ A_{bs})_\mu^a, \quad (7)$$

where S^a is the light scalar diquark, A_μ^a the light axial vector diquark, S_b the bottomed scalar diquark, and $A_{b\mu}^a$ the bottomed axial vector diquark. The superscript $a = 1, 2, 3$ is the color index. The meson fields read

$$\Phi = \begin{pmatrix} \frac{\sqrt{3}\pi^0 + \eta_8 + \sqrt{2}\eta_0}{\sqrt{3}} & \sqrt{2}\pi^+ & \sqrt{2}K^+ \\ \sqrt{2}\pi^- & \frac{-\sqrt{3}\pi^0 + \eta_8 + \sqrt{2}\eta_0}{\sqrt{3}} & \sqrt{2}K^0 \\ \sqrt{2}K^- & \sqrt{2}K^0 & \frac{-2\eta_8 + \sqrt{2}\eta_0}{\sqrt{3}} \end{pmatrix}, \quad (8)$$

$$V_\mu = \frac{g_V}{\sqrt{2}} \begin{pmatrix} \frac{1}{\sqrt{2}}(\rho^0 + \omega) & \rho^+ & K^{*+} \\ \rho^- & -\frac{1}{\sqrt{2}}(\rho^0 - \omega) & K^{*0} \\ K^{*-} & \bar{K}^{*0} & \phi \end{pmatrix}_\mu, \quad (9)$$

$$P = (B^-, \bar{B}^0, \bar{B}_s^0), \quad (10)$$

$$P_\tau^* = (B^{*-}, \bar{B}^{*0}, \bar{B}_s^{*0})_\tau, \quad (11)$$

with Φ and V_μ the light pseudoscalar and vector, P and P_τ^* the bottomed pseudoscalar and vector.

Considering the $[U(3)_L \otimes U(3)_R]_{global} \otimes [U(3)]_{local}$ symmetry, parity and charge conjugation, the Lagrangians containing mesons and diquarks are shown as follows

$$\begin{aligned} \mathcal{L}_1 = & -\frac{\beta}{m_P}(iP\hat{\alpha}_{\parallel\mu}D^\mu P^\dagger + h.c.) \\ & -2g(iP\hat{\alpha}_{\perp\mu}P^{*\mu\dagger} + h.c.) \\ & -\frac{g}{m_{P^*}}(\xi^{\mu\nu\alpha\beta}P_\nu^*\hat{\alpha}_{\perp\alpha}D_\mu P_\beta^{*\dagger} + h.c.) \\ & +\frac{\beta}{m_{P^*}}(iP_\nu^*\hat{\alpha}_{\parallel}^\mu D_\mu P^{*\nu\dagger} + h.c.), \end{aligned} \quad (12)$$

$$\begin{aligned} \mathcal{L}_2 = & e_1(iPD_\mu S^a A_b^{a\mu\dagger} - iA_b^{a\mu}D_\mu S^{a\dagger}P^\dagger) \\ & +e_2(iPA_\mu^a D^\mu S_b^{a\dagger} - iD_\mu^a S_b^a A_\mu^{a\dagger}P^\dagger) \\ & +e_3(\epsilon^{\mu\nu\alpha\beta}PA_{\mu\nu}^a A_{b\alpha\beta}^{a\dagger} + \epsilon^{\mu\nu\alpha\beta}A_{b\alpha\beta}^a A_{\mu\nu}^{a\dagger}P^\dagger) \\ & +e_4(iP_\mu^* D^\mu S^a S_b^{a\dagger} - iS_b^a D^\mu S^{a\dagger}P_\mu^{*\dagger}) \\ & +e_5(\epsilon^{\mu\nu\alpha\beta}P_\mu^* D_\nu S^a A_{b\alpha\beta}^{a\dagger} + \epsilon^{\mu\nu\alpha\beta}A_{b\alpha\beta}^a D_\nu S^{a\dagger}P_\mu^{*\dagger}) \\ & +e_6(\epsilon^{\mu\nu\alpha\beta}P_\mu^* A_{\nu\alpha}^a D_\beta S_b^{a\dagger} + \epsilon^{\mu\nu\alpha\beta}D_\beta S_b^a A_{\nu\alpha}^{a\dagger}P_\mu^{*\dagger}) \\ & +e_7(iP_\mu^* A^{a\mu\nu} A_{b\nu}^{a\dagger} - iA_{b\nu}^a A^{a\mu\nu\dagger}P_\mu^{*\dagger}) \\ & +e_8(iP_\mu^* A_\nu^a A_b^{a\mu\nu\dagger} - iA_b^{a\mu\nu} A_\nu^{a\dagger}P_\mu^{*\dagger}) \\ & +e_9(iP_{\mu\nu}^* A^{a\mu} A_b^{a\nu\dagger} - iA_b^{a\nu} A^{a\mu\dagger}P_{\mu\nu}^{*\dagger}), \end{aligned} \quad (13)$$

$$\begin{aligned} \mathcal{L}_3 = & h_1(iS_b^a \hat{\alpha}_{\parallel}^{\mu T} D_\mu S_b^{a\dagger} - iD_\mu S_b^a \hat{\alpha}_{\parallel}^{\mu T} S_b^{a\dagger}) \\ & +h_2(\xi^{\mu\nu\alpha\beta}A_{b\mu\nu}^a \hat{\alpha}_{\parallel\alpha}^{\mu T} D_\beta S_b^{a\dagger} + \xi^{\mu\nu\alpha\beta}D_\beta S_b^a \hat{\alpha}_{\parallel\alpha}^{\mu T} A_{b\mu\nu}^{a\dagger}) \\ & +h_3(iA_{b\mu}^a \hat{\alpha}_{\perp}^{\mu T} S_b^{a\dagger} - iS_b^a \hat{\alpha}_{\perp}^{\mu T} A_{b\mu}^{a\dagger}) \\ & +h_4(iA_{b\mu}^a \hat{\alpha}_{\parallel\nu}^T A_b^{a\mu\nu\dagger} - iA_b^{a\mu\nu} \hat{\alpha}_{\parallel\nu}^T A_{b\mu}^{a\dagger}) \\ & +h_5(\xi^{\mu\nu\alpha\beta}A_{b\mu}^a \hat{\alpha}_{\perp\nu}^T A_{b\alpha\beta}^{a\dagger} \\ & +\xi^{\mu\nu\alpha\beta}A_{b\alpha\beta}^a \hat{\alpha}_{\perp\nu}^T A_{b\mu}^{a\dagger}), \end{aligned} \quad (14)$$

where

$$D_\mu P = \partial_\mu P + iP\alpha_{\parallel\mu}^\dagger = \partial_\mu P + iP\alpha_{\parallel\mu}, \quad (15)$$

$$D_\mu P_\tau^* = \partial_\mu P_\tau^* + iP_\tau^* \alpha_{\parallel\mu}^\dagger = \partial_\mu P_\tau^* + iP_\tau^* \alpha_{\parallel\mu}, \quad (16)$$

$$\alpha_{\perp\mu} = (\partial_\mu \xi_R \xi_R^\dagger - \partial_\mu \xi_L \xi_L^\dagger)/(2i), \quad (17)$$

$$\alpha_{\parallel\mu} = (\partial_\mu \xi_R \xi_R^\dagger + \partial_\mu \xi_L \xi_L^\dagger)/(2i), \quad (18)$$

$$\hat{\alpha}_{\perp\mu} = (D_\mu \xi_R \xi_R^\dagger - D_\mu \xi_L \xi_L^\dagger)/(2i), \quad (19)$$

$$\hat{\alpha}_{\parallel\mu} = (D_\mu \xi_R \xi_R^\dagger + D_\mu \xi_L \xi_L^\dagger)/(2i), \quad (20)$$

$$\xi_L = e^{i\sigma/F_\sigma} e^{-i\Phi/(2F_\pi)}, \quad (21)$$

$$\xi_R = e^{i\sigma/F_\sigma} e^{i\Phi/(2F_\pi)}, \quad (22)$$

$$A_{\mu\nu}^a = D_\mu A_\nu^a - D_\nu A_\mu^a, \quad (23)$$

$$A_{b\mu\nu}^a = D_\mu A_{b\nu}^a - D_\nu A_{b\mu}^a, \quad (24)$$

$$D_\mu A_\nu^a = \partial_\mu A_\nu^a - iV_\mu A_\nu^a - iA_\nu^a V_\mu^T, \quad (25)$$

$$D_\mu S^a = \partial_\mu S^a - iV_\mu S^a - iS^a V_\mu^T, \quad (26)$$

$$D_\mu A_{b\nu}^a = \partial_\mu A_{b\nu}^a - iA_{b\nu}^a \alpha_{\parallel\mu}^T, \quad (27)$$

$$D_\mu S_b^a = \partial_\mu S_b^a - iS_b^a \alpha_{\parallel\mu}^T. \quad (28)$$

In Eqs. (13) and (14), the Einstein summation conven-

TABLE I: The values of the low energy constants in the Lagrangians containing diquarks.

e_1 (GeV ⁻¹)	e_2 (GeV ⁻¹)	e_3 (GeV ⁻²)	e_4 (GeV ⁻¹)	e_5 (GeV ⁻²)
-6.353	1.657	±0.555	4.885	±0.566
e_6 (GeV ⁻²)	e_7 (GeV ⁻¹)	e_8 (GeV ⁻¹)	e_9 (GeV ⁻¹)	
±1.005	-0.909	-13.348	11.530	
h_1 (GeV ⁻¹)	h_2 (GeV ⁻¹)	h_3 (GeV ⁻¹)	h_4 (GeV ⁻¹)	h_5 (GeV ⁻¹)
0.084	-0.130	0.266	1.457	0.011

tion is used, i.e., the repeated superscripts “ a ” mean the summation over them. For \mathcal{L}_1 , the constants $\beta = 0.9$ and $g = 0.59$. For \mathcal{L}_2 and \mathcal{L}_3 , there are two set of coupling constants e_i ($i = 1, 2, \dots, 9$) and h_j ($j = 1, 2, \dots, 5$) whose values are still unknown. In this work, we naively use the 3P_0 model to determine them. Their values are listed in Table I. Note that we can not fix the sign of e_3 , e_5 and e_6 because the relative phase between the amplitudes obtained from the Lagrangian and 3P_0 model can not be determined. For e_7 , e_8 and e_9 , we use the phase in Ref. [48] which explains the Z_{cs} well and get the values of them. In Eqs. (21) and (22), we choose $\sigma = 0$ according to the unitary gauge [56].

C. Effective Potentials With The Exponential Form Factor

Making use of the Breit approximation, we obtain the effective potentials in the momentum space

$$\mathcal{V}^{H_1 H_2 \rightarrow H_3 H_4}(\mathbf{q}) = \frac{\mathcal{M}^{H_1 H_2 \rightarrow H_3 H_4}(\mathbf{q})}{\sqrt{\prod_i 2m_i \prod_f 2m_f}} \quad (29)$$

where m_i ($i = 1, 2, 3, 4$) denotes the mass of the particle labeled by i . By performing the Fourier transformation, we get the effective potential in the coordinate space

$$\mathcal{V}^{H_1 H_2 \rightarrow H_3 H_4}(\mathbf{r}) = \int \frac{d^3 \mathbf{q}}{(2\pi)^3} e^{i\mathbf{q} \cdot \mathbf{r}} \mathcal{V}^{H_1 H_2 \rightarrow H_3 H_4}(\mathbf{q}) F^2(q^2). \quad (30)$$

Here, $F(\vec{q}^2)$ is the form factor which suppresses the contribution of high momenta, i.e., small distance. And the presence of such a form factor is dictated by the extended (quark) structure of the hadrons. In this work, we adopt the exponentially parameterized form factor

$$F(q^2) = e^{q^2/\Lambda^2} = e^{(q_0^2 - \vec{q}^2)/\Lambda^2} \quad (31)$$

with Λ the cut-off.

Another option of the form factor is monopole expression, i.e.,

$$F_M(q^2) = \frac{\Lambda^2 - m_E^2}{\Lambda^2 - q^2} \quad (32)$$

with m_E the mass of the exchanged particle. If the exchanged meson's mass is large, for instance in the case of ϕ - or diquark-exchange, $F_M(q^2)$ is highly suppressed by the numerator $\Lambda^2 - m_E^2$, which would lead to unreasonable results. Consequently, we choose the exponentially parameterized form factor in this work.

In Eqs. (33-51), we list the specific expressions of the non-zero effective subpotentials which are isospin-independent:

$$V_v^{\bar{B}^*B \rightarrow \bar{B}^*B/\bar{B}B^* \rightarrow \bar{B}B^*} = C_v \frac{(\beta g_V)^2 m_{B^*} m_B}{4M_P M_{P^*}} (\epsilon_{1/2} \cdot \epsilon_{3/4}^\dagger) \times Y(\Lambda, m_v, r), \quad (33)$$

$$V_p^{\bar{B}B^* \rightarrow \bar{B}^*B} = C_p \left(\frac{g}{2F_\pi} \right)^2 \left[(\epsilon_2 \cdot \epsilon_3^\dagger) Z(\Lambda, \tilde{m}_p, r) + S(\hat{r}, \epsilon_2, \epsilon_3^\dagger) T(\Lambda, \tilde{m}_p, r) \right], \quad (34)$$

$$V_p^{\bar{B}^*B/\bar{B}B^* \rightarrow \bar{B}^*B^*} = \delta_{B\bar{B}^*/B^*\bar{B}} C_p \frac{g^2 m_{B^*}}{4M_{P^*} F_\pi^2} \times \left[\epsilon_{4/3}^\dagger \cdot (\epsilon_{1/2} \times \epsilon_{3/4}^\dagger) Z(\Lambda, \tilde{m}_p, r) + S(\hat{r}, \epsilon_{4/3}^\dagger, \epsilon_{1/2} \times \epsilon_{3/4}^\dagger) \times T(\Lambda, \tilde{m}_p, r) \right], \quad (35)$$

$$V_{S_{ud}}^{\bar{B}^*B \rightarrow S\bar{A}/\bar{B}B^* \rightarrow A\bar{S}} = -\frac{\sqrt{3}}{12} e_1 e_4 \left[(\epsilon_{1/2} \cdot \epsilon_{4/3}^\dagger) Z(\Lambda, \tilde{m}_{S_{ud}}, r) + S(\hat{r}, \epsilon_{1/2}, \epsilon_{4/3}^\dagger) T(\Lambda, \tilde{m}_{S_{ud}}, r) \right], \quad (36)$$

$$V_{A_{ud}}^{\bar{B}^*B \rightarrow S\bar{A}/\bar{B}B^* \rightarrow A\bar{S}} = \sqrt{3} e_3 e_6 m_{S_{bq}} m_{A_{bq}} \left[\frac{2}{3} (\epsilon_{1/2} \cdot \epsilon_{4/3}^\dagger) \times Z(\Lambda, \tilde{m}_{A_{ud}}, r) - \frac{1}{3} S(\hat{r}, \epsilon_{1/2}, \epsilon_{4/3}^\dagger) \times T(\Lambda, \tilde{m}_{A_{ud}}, r) \right], \quad (37)$$

$$V_{A_{ud}}^{\bar{B}^*B \rightarrow A\bar{S}/\bar{B}B^* \rightarrow S\bar{A}} = -\frac{\sqrt{3}}{8} e_2 (e_8 m_{A_{bq}} + e_9 m_{B^*}) m_{S_{bq}} \times \left(\frac{\tilde{m}_{A_{ud}}}{m_{A_{ud}}} \right)^2 (\epsilon_{1/2} \cdot \epsilon_{3/4}^\dagger) \times Y(\Lambda, \tilde{m}_{A_{ud}}, r), \quad (38)$$

$$V_{S_{ud}}^{\bar{B}^*B/\bar{B}B^* \rightarrow A\bar{A}} = \delta_{B\bar{B}^*/B^*\bar{B}} \frac{1}{2\sqrt{3}} e_1 e_5 m_{A_{bq}} \times \left[\epsilon_{4/3}^\dagger \cdot (\epsilon_{1/2} \times \epsilon_{3/4}^\dagger) Z(\Lambda, \tilde{m}_{S_{ud}}, r) + S(\hat{r}, \epsilon_{4/3}^\dagger, \epsilon_{1/2} \times \epsilon_{3/4}^\dagger) \times T(\Lambda, \tilde{m}_{S_{ud}}, r) \right], \quad (39)$$

$$V_{A_{ud}}^{\bar{B}^*B/\bar{B}B^* \rightarrow A\bar{A}} = \delta_{B\bar{B}^*/B^*\bar{B}} \sqrt{\frac{1}{3}} e_3 e_7 m_{A_{bq}} \times \left[\epsilon_{1/2} \cdot (\epsilon_{3/4}^\dagger \times \epsilon_{4/3}^\dagger) Z(\Lambda, \tilde{m}_{A_{ud}}, r) - \frac{1}{2} S(\hat{r}, \epsilon_{3/4}^\dagger, \epsilon_{1/2} \times \epsilon_{4/3}^\dagger) \times T(\Lambda, \tilde{m}_{A_{ud}}, r) + \frac{1}{2} S(\hat{r}, \epsilon_{1/2}, \epsilon_{3/4}^\dagger \times \epsilon_{4/3}^\dagger) \right]$$

$$\times T(\Lambda, \tilde{m}_{A_{ud}}, r)], \quad (40)$$

$$V_v^{\bar{B}^*B^* \rightarrow \bar{B}^*B^*} = C_v \left(\frac{\beta g_V m_{B^*}}{2M_{P^*}} \right)^2 (\epsilon_1 \cdot \epsilon_3^\dagger) (\epsilon_2 \cdot \epsilon_4^\dagger) \times Y(\Lambda, m_v, r), \quad (41)$$

$$V_p^{\bar{B}^*B^* \rightarrow \bar{B}^*B^*} = C_p \left(\frac{g m_{B^*}}{2m_{P^*} F_\pi} \right)^2 \left[(\epsilon_1 \times \epsilon_3^\dagger) \cdot (\epsilon_2 \times \epsilon_4^\dagger) \times Z(\Lambda, m_p, r) + S(\hat{r}, \epsilon_1 \times \epsilon_3^\dagger, \epsilon_2 \times \epsilon_4^\dagger) \times T(\Lambda, m_p, r) \right], \quad (42)$$

$$V_{S_{ud}}^{\bar{B}^*B^* \rightarrow S\bar{A}/\bar{S}A} = -\frac{\delta_{S\bar{A}/A\bar{S}}}{2\sqrt{3}} e_4 e_5 m_{A_{bq}} \left[\epsilon_{1/2} \cdot (\epsilon_{2/1} \times \epsilon_{4/3}^\dagger) \times Z(\Lambda, \tilde{m}_{S_{ud}}, r) + S(\hat{r}, \epsilon_{1/2}, \epsilon_{2/1} \times \epsilon_{4/3}^\dagger) \times T(\Lambda, \tilde{m}_{S_{ud}}, r) \right], \quad (43)$$

$$V_{A_{ud}}^{\bar{B}^*B^* \rightarrow S\bar{A}/A\bar{S}} = -\delta_{S\bar{A}/A\bar{S}} \frac{1}{2\sqrt{3}} e_6 e_7 m_{S_{bq}} \times \left[\epsilon_{2/1} \cdot (\epsilon_{1/2} \times \epsilon_{4/3}^\dagger) Z(\Lambda, \tilde{m}_{A_{ud}}, r) + \frac{1}{2} S(\hat{r}, \epsilon_{2/1}, \epsilon_{1/2} \times \epsilon_{4/3}^\dagger) T(\Lambda, \tilde{m}_{A_{ud}}, r) - \frac{1}{2} S(\hat{r}, \epsilon_{4/3}^\dagger, \epsilon_{1/2} \times \epsilon_{2/1}) T(\Lambda, \tilde{m}_{A_{ud}}, r) \right], \quad (44)$$

$$V_{S_{ud}}^{\bar{B}^*B^* \rightarrow A\bar{A}} = \frac{e_5^2 m_{A_{bq}}^2}{\sqrt{3}} \left[(\epsilon_1 \times \epsilon_3^\dagger) \cdot (\epsilon_2 \times \epsilon_4^\dagger) Z(\Lambda, \tilde{m}_{S_{ud}}, r) + S(\hat{r}, \epsilon_1 \times \epsilon_3^\dagger, \epsilon_2 \times \epsilon_4^\dagger) T(\Lambda, \tilde{m}_{S_{ud}}, r) \right], \quad (45)$$

$$V_{A_{ud}}^{\bar{B}^*B^* \rightarrow A\bar{A}} = -\frac{\sqrt{3} e_7^2}{24} \left[2(\epsilon_2 \cdot \epsilon_3^\dagger) (\epsilon_1 \cdot \epsilon_4^\dagger) Z(\Lambda, \tilde{m}_{A_{ud}}, r) - 2(\epsilon_1 \cdot \epsilon_2) (\epsilon_3^\dagger \cdot \epsilon_4^\dagger) Z(\Lambda, \tilde{m}_{A_{ud}}, r) + (\epsilon_2 \cdot \epsilon_3^\dagger) S(\hat{r}, \epsilon_1, \epsilon_4^\dagger) T(\Lambda, \tilde{m}_{A_{ud}}, r) - (\epsilon_3^\dagger \cdot \epsilon_4^\dagger) S(\hat{r}, \epsilon_1, \epsilon_2) T(\Lambda, \tilde{m}_{A_{ud}}, r) + (\epsilon_1 \cdot \epsilon_4^\dagger) S(\hat{r}, \epsilon_2, \epsilon_3^\dagger) T(\Lambda, \tilde{m}_{A_{ud}}, r) - (\epsilon_1 \cdot \epsilon_2) S(\hat{r}, \epsilon_3^\dagger, \epsilon_4^\dagger) T(\Lambda, \tilde{m}_{A_{ud}}, r) \right] - \frac{\sqrt{3}}{8} (e_8 m_{A_{bq}} + e_9 m_{B^*})^2 \left(\frac{\tilde{m}_{A_{ud}}}{m_{A_{ud}}} \right)^2 \times (\epsilon_1 \cdot \epsilon_3^\dagger) (\epsilon_2 \cdot \epsilon_4^\dagger) Y(\Lambda, \tilde{m}_{A_{ud}}, r), \quad (46)$$

$$V_v^{S\bar{A} \rightarrow S\bar{A}/A\bar{S} \rightarrow A\bar{S}} = C_v \left(\frac{g_V}{2} \right)^2 h_1 h_4 m_{A_{bq}} m_{S_{bq}} (\epsilon_{2/1} \cdot \epsilon_{4/3}^\dagger) \times Y(\Lambda, m_v, r), \quad (47)$$

$$V_p^{S\bar{A} \rightarrow A\bar{S}/A\bar{S} \rightarrow S\bar{A}} = C_p \left(\frac{h_3}{4F_\pi} \right)^2 \left[(\epsilon_{1/2} \cdot \epsilon_{4/3}^\dagger) Z(\Lambda, \tilde{m}_p, r) + S(\hat{r}, \epsilon_{1/2}, \epsilon_{4/3}^\dagger) T(\Lambda, \tilde{m}_p, r) \right], \quad (48)$$

$$V_p^{S\bar{A}/A\bar{S} \rightarrow A\bar{A}} = \delta_{S\bar{A}/A\bar{S}} C_p \frac{h_3 h_5}{4F_\pi^2} m_{A_{bq}} \times \left[\epsilon_{3/4}^\dagger \cdot (\epsilon_{2/1} \times \epsilon_{4/3}^\dagger) Z(\Lambda, \tilde{m}_p, r) + S(\hat{r}, \epsilon_{3/4}^\dagger, \epsilon_{2/1} \times \epsilon_{4/3}^\dagger) T(\Lambda, \tilde{m}_p, r) \right], \quad (49)$$

$$V_v^{A\bar{A} \rightarrow A\bar{A}} = C_v \frac{g_V^2 h_4^2 m_{A_{bq}}^2}{4} (\epsilon_1 \cdot \epsilon_3^\dagger) (\epsilon_2 \cdot \epsilon_4^\dagger) Y(\Lambda, m_v, r), \quad (50)$$

$$V_p^{A\bar{A} \rightarrow A\bar{A}} = C_p \left(\frac{h_5 m_{A_{bq}}}{F_\pi} \right)^2 \left[(\epsilon_1 \times \epsilon_3^\dagger) \cdot (\epsilon_2 \times \epsilon_4^\dagger) \times Z(\Lambda, m_p, r) + S(\hat{r}, \epsilon_1 \times \epsilon_3^\dagger, \epsilon_2 \times \epsilon_4^\dagger) \times T(\Lambda, m_p, r) \right]. \quad (51)$$

In the above equations, the subscript p denotes the light pseudoscalar mesons π , η_8 and η_0 , and v denotes the light vectors ρ and ω . The coefficients $C_{\pi^0} = \frac{1}{3}$, $C_{\eta_8} = -\frac{1}{9}$, $C_{\eta_0} = -\frac{2}{9}$, $C_\rho = 1$, $C_\omega = -1$, $\delta_{B\bar{B}^*} = 1$, $\delta_{B^*\bar{B}} = -1$, $\delta_{S\bar{A}} = 1$, $\delta_{A\bar{S}} = -1$. And $S(\hat{r}, \mathbf{a}, \mathbf{b}) = 3(\hat{r} \cdot \mathbf{a})(\hat{r} \cdot \mathbf{b}) - \mathbf{a} \cdot \mathbf{b}$, $q_0 = \frac{m_2^2 - m_1^2 + m_3^2 - m_4^2}{2(m_3 + m_4)}$, $\tilde{m}_E^2 = m_E^2 - q_0^2$ with E the exchanged particle. The functions $Y(\Lambda, m, r)$, $Z(\Lambda, m, r)$ and $T(\Lambda, m, r)$ are defined as

$$Y(\Lambda, m, r) = -\frac{e^{2q_0^2/\Lambda^2}}{(2\pi)^2 r} \frac{\partial}{\partial r} \left\{ e^{2m^2/\Lambda^2} \frac{\pi}{2m} \left[e^{mr} + e^{-mr} - e^{mr} \operatorname{erf} \left(\frac{\Lambda r}{2\sqrt{2}} + \frac{\sqrt{2}m}{\Lambda} \right) + e^{-mr} \operatorname{erf} \left(\frac{\Lambda r}{2\sqrt{2}} - \frac{\sqrt{2}m}{\Lambda} \right) \right] \right\},$$

$$Z(\Lambda, m, r) = \frac{1}{r^2} \frac{\partial}{\partial r} r^2 \frac{\partial}{\partial r} Y(\Lambda, m, r),$$

$$T(\Lambda, m, r) = r \frac{\partial}{\partial r} \frac{1}{r} \frac{\partial}{\partial r} Y(\Lambda, m, r).$$

Taking into account S- and D-wave functions, the products of the polarization vectors in the subpotentials are presented below

$$\left. \begin{array}{l} \epsilon_1 \cdot \epsilon_{3/4}^\dagger \\ \epsilon_2 \cdot \epsilon_{3/4}^\dagger \\ (\epsilon_1 \cdot \epsilon_3^\dagger)(\epsilon_2 \cdot \epsilon_4^\dagger) \\ -(\epsilon_1 \cdot \epsilon_4^\dagger)(\epsilon_2 \cdot \epsilon_3^\dagger) \\ (\epsilon_1 \times \epsilon_3^\dagger) \cdot (\epsilon_2 \times \epsilon_4^\dagger) \end{array} \right\} \rightarrow \begin{pmatrix} 1 & 0 \\ 0 & 1 \end{pmatrix},$$

$$\left. \begin{array}{l} S(\hat{r}, \epsilon_1, \epsilon_4^\dagger) \\ S(\hat{r}, \epsilon_2, \epsilon_3^\dagger) \\ S(\hat{r}, \epsilon_1 \times \epsilon_3^\dagger, \epsilon_2 \times \epsilon_4^\dagger) \\ 2(\epsilon_2 \cdot \epsilon_3^\dagger)S(\hat{r}, \epsilon_1, \epsilon_4^\dagger) \\ 2(\epsilon_1 \cdot \epsilon_4^\dagger)S(\hat{r}, \epsilon_2, \epsilon_3^\dagger) \end{array} \right\} \rightarrow \begin{pmatrix} 0 & -\sqrt{2} \\ -\sqrt{2} & 1 \end{pmatrix},$$

$$\left. \begin{array}{l} \epsilon_{1/2} \cdot (\epsilon_4^\dagger \times \epsilon_3^\dagger) \\ \epsilon_1 \cdot (\epsilon_2 \times \epsilon_{3/4}^\dagger) \end{array} \right\} \rightarrow \begin{pmatrix} i\sqrt{2} & 0 \\ 0 & i\sqrt{2} \end{pmatrix},$$

$$\left. \begin{array}{l} 2S(\hat{r}, \epsilon_4^\dagger, \epsilon_3^\dagger \times \epsilon_{1/2}) \\ 2S(\hat{r}, \epsilon_3^\dagger, \epsilon_{1/2} \times \epsilon_4^\dagger) \\ 2S(\hat{r}, \epsilon_1, \epsilon_2 \times \epsilon_{3/4}^\dagger) \\ 2S(\hat{r}, \epsilon_2, \epsilon_{3/4}^\dagger \times \epsilon_1) \\ S(\hat{r}, \epsilon_{1/2}, \epsilon_3^\dagger \times \epsilon_4^\dagger) \\ S(\hat{r}, \epsilon_{3/4}^\dagger, \epsilon_2 \times \epsilon_1) \end{array} \right\} \rightarrow \begin{pmatrix} 0 & 2i \\ 2i & -i\sqrt{2} \end{pmatrix},$$

$$\left. \begin{array}{l} \epsilon_1 \cdot \epsilon_2, \epsilon_3^\dagger \cdot \epsilon_4^\dagger \\ (\epsilon_3^\dagger \cdot \epsilon_4^\dagger)S(\hat{r}, \epsilon_1, \epsilon_2) \\ (\epsilon_1 \cdot \epsilon_2)S(\hat{r}, \epsilon_3^\dagger, \epsilon_4^\dagger) \end{array} \right\} \rightarrow \begin{pmatrix} 0 & 0 \\ 0 & 0 \end{pmatrix}.$$

Hereafter, we label the channels $B\bar{B}^*/B^*\bar{B}$, $B^*\bar{B}^*$, $S\bar{A}/A\bar{S}$ and $A\bar{A}$ by CH_1 , CH_2 , CH_3 and CH_4 , respec-

tively. The elements of the total potential matrix \hat{V} is

$$V^{CH_1 \rightarrow CH_1} = \frac{1}{2} \left(V_{\rho, \omega}^{\bar{B}B^* \rightarrow \bar{B}B^*} + 2V_{\pi, \eta_8, \eta_0}^{\bar{B}B^* \rightarrow \bar{B}^*B} + V_{\rho, \omega}^{\bar{B}^*B \rightarrow \bar{B}^*B} \right), \quad (52)$$

$$V^{CH_1 \rightarrow CH_2} = \frac{1}{\sqrt{2}} \left(V_{\pi, \eta_8, \eta_0}^{\bar{B}^*B \rightarrow \bar{B}^*B^*} + V_{\pi, \eta_8, \eta_0}^{\bar{B}B^* \rightarrow \bar{B}^*B^*} \right), \quad (53)$$

$$V^{CH_1 \rightarrow CH_3} = \frac{1}{2} \left(V_{A_{ud}}^{\bar{B}^*B \rightarrow A\bar{S}} + V_{S_{ud}, A_{ud}}^{\bar{B}B^* \rightarrow A\bar{S}} + V_{S_{ud}, A_{ud}}^{\bar{B}^*B \rightarrow S\bar{A}} + V_{A_{ud}}^{\bar{B}^*B \rightarrow A\bar{S}} \right), \quad (54)$$

$$V^{CH_1 \rightarrow CH_4} = \frac{1}{\sqrt{2}} \left(V_{S_{ud}, A_{ud}}^{\bar{B}^*B \rightarrow A\bar{A}} + V_{S_{ud}, A_{ud}}^{\bar{B}B^* \rightarrow A\bar{A}} \right), \quad (55)$$

$$V^{CH_2 \rightarrow CH_2} = V_{\rho, \omega}^{\bar{B}^*B^* \rightarrow \bar{B}^*B^*} + V_{\pi, \eta_8, \eta_0}^{\bar{B}^*B^* \rightarrow \bar{B}^*B^*}, \quad (56)$$

$$V^{CH_2 \rightarrow CH_3} = \frac{1}{\sqrt{2}} \left(V_{S_{ud}, A_{ud}}^{\bar{B}^*B^* \rightarrow A\bar{S}} + V_{S_{ud}, A_{ud}}^{\bar{B}^*B^* \rightarrow S\bar{A}} \right), \quad (57)$$

$$V^{CH_2 \rightarrow CH_4} = V_{S_{ud}, A_{ud}}^{\bar{B}^*B^* \rightarrow A\bar{A}}, \quad (58)$$

$$V^{CH_3 \rightarrow CH_3} = \frac{1}{2} \left(V_{\rho, \omega}^{S\bar{A} \rightarrow S\bar{A}} + 2V_{\pi, \eta_8, \eta_0}^{S\bar{A} \rightarrow A\bar{S}} + V_{\rho, \omega}^{A\bar{S} \rightarrow A\bar{S}} \right), \quad (59)$$

$$V^{CH_3 \rightarrow CH_4} = \frac{1}{\sqrt{2}} \left(V_{\pi, \eta_8, \eta_0}^{S\bar{A} \rightarrow A\bar{A}} + V_{\pi, \eta_8, \eta_0}^{A\bar{S} \rightarrow A\bar{A}} \right), \quad (60)$$

$$V^{CH_4 \rightarrow CH_4} = V_{\rho, \omega}^{A\bar{A} \rightarrow A\bar{A}} + V_{\pi, \eta_8, \eta_0}^{A\bar{A} \rightarrow A\bar{A}}. \quad (61)$$

The subscripts mean the following summation

$$V_{E_1, E_2, \dots}^{CH_i \rightarrow CH_j} = \sum_{a=E_1, E_2, \dots} V_a^{CH_i \rightarrow CH_j}. \quad (62)$$

III. RESULTS AND DISCUSSION

With the preparation above, adopting the Gaussian expansion method (GEM) [57], we solve the coupled channel Schrödinger equation to find the bound state solutions,

$$\left(\hat{K} + \hat{M} + \hat{V} \right) \Psi = E\Psi. \quad (63)$$

Here, $\hat{K} = \operatorname{diag}(-\frac{\Delta}{2\mu_1}, -\frac{\Delta}{2\mu_2}, \dots)$, $\hat{M} = \operatorname{diag}(0, M_2 - M_1, M_3 - M_1, \dots)$. In the central force field problem, the system does not depend on the azimuth and polar angle, so the operator $\Delta = \frac{1}{r^2} \frac{\partial}{\partial r} \left(r^2 \frac{\partial}{\partial r} \right)$. The coupled channel Schrödinger equation Eq. (63) is symmetric under the following transformation

$$U \left(\hat{K} + \hat{M} + \hat{V} \right) \Psi = UE\Psi, \quad (64)$$

$$\Rightarrow U \left(\hat{K} + \hat{M} + \hat{V} \right) U^{-1} U\Psi = EU\Psi, \quad (65)$$

$$\Rightarrow \left(\hat{K} + \hat{M} + U\hat{V}U^{-1} \right) \tilde{\Psi} = E\tilde{\Psi}, \quad (66)$$

where $U = \operatorname{diag}(e^{i\theta_1}, e^{i\theta_2}, \dots)$, $\tilde{\Psi} = U\Psi$. Here the word "symmetric" means the energy E does not change under the transformation of the Schrödinger equation. All the U form a reducible Lie group $U(1) \otimes U(1) \otimes \dots \otimes U(1)$.

TABLE II: The diquark masses we use in effective potentials from Ref. [58]. q indicates u or d quark.

$m_{S_{bq}}$ (GeV)	$m_{A_{bq}}$ (GeV)	$m_{S_{qq}}$ (GeV)	$m_{A_{qq}}$ (GeV)
5.451	5.465	0.691	0.840

In this work, some of the off-diagonal elements of the potential matrix are imaginary, which is not convenient for solving the Schrödinger equation. If we perform the transformation mentioned above, the problem is solved which means that the potential matrix becomes real. The corresponding parameters are chosen as $\theta_1 = \frac{\pi}{2}$, $\theta_2 = 0$, $\theta_3 = \frac{\pi}{2}$, $\theta_4 = 0, \dots$.

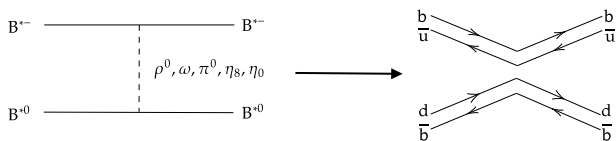


FIG. 1: The diagram of $B^{*-} B^{*0} \rightarrow B^{*-} B^{*0}$ on quark and hadron levels.

It is also interesting to discuss the OZI suppressed processes on both the quark and hadron levels. We take the $B^{*-} \bar{B}^{*0} \rightarrow B^{*-} \bar{B}^{*0}$ process as an example. On the quark level, we can see from Fig. 1 that the diagram is non-connected, which means it is OZI suppressed. On the hadron level, the exchanged particle could be the pseudoscalar mesons π, η_8, η_0 and the vector mesons ρ, ω . Since the masses of ρ and ω are almost close to each other, their contributions to the total potential cancel out, which can be seen from Eqs. (41) and (56). Under the $[U(3)_L \otimes U(3)_R]_{global} \otimes [U(3)]_{local}$ symmetry, the pseudoscalar mesons appearing in Φ (see Eq. (8)) have the same mass. In this case, The contributions of π, η_8 and η_0 to the total potential also cancel out. This conclusion coincides with the OZI rule. However, the real masses of π, η_8 and η_0 are different, so the total potential is non-zero which depicts the phenomenon of the violation of the OZI rule.

As we mentioned above, in this work, we use the exponentially parameterized form factor in our calculation. For comparison, we take the $B^* \bar{B}^* \rightarrow B^* \bar{B}^*$ process as an example, and plot in Fig. 2 the potentials with both the exponential form factor and the monopole one. We notice that

- $V_{\rho^0}^{B^* \bar{B}^* \rightarrow B^* \bar{B}^*}$ and $V_{\omega}^{B^* \bar{B}^* \rightarrow B^* \bar{B}^*}$ have almost the same absolute value, but different signs, i.e., the contribution of ρ - and ω -exchange is approximately zero. So $V^{B^* \bar{B}^* \rightarrow B^* \bar{B}^*}$ is mainly con-

tributed by π -, η_8 - and η_0 -exchange;

- the monopole form factor suppresses the contribution from the exchanged particle with heavier mass, which can be clearly seen from the situation of η_0 -exchange, since $m_{\eta_0} \simeq 0.96$ GeV;
- in the long interaction range, the pion-exchange subpotential is dominant with both monopole and exponential form factors;
- in the short and medium range, the vector-exchange subpotentials are compatibly larger than that of the pion-exchange with exponential form factor. However, for the monopole form factor, the pion-exchange contribution is still dominant.

The values of the masses of diquarks taken from Ref. [58] are listed in Table II, and the meson-masses are taken from PDG. Then we solve the Schrödinger equation, and the numerical results are presented in Table III. For $B \bar{B}^* / B^* \bar{B}^* / S \bar{A} / A \bar{A}$ and $B^* \bar{B}^* / S \bar{A} / A \bar{A}$ systems, loosely bound states exist when the cut-off is reasonably chosen as $\Lambda \sim 1$ GeV. If the value of Λ increases, the binding energies increase as well while the root-mean-square radii decrease. For both of these two systems, the D-wave contribution is much smaller than that of the S-wave. Besides, the meson-meson component is much larger than the diquark-antidiquark component. That is to say, both $Z_b(10610)$ and $Z_b(10650)$ can be explained as hadronic molecules mixing with a little diquark-antidiquark components.

IV. SUMMARY

In this work, we extend the $[U(3)_L \otimes U(3)_R]_{global} \otimes [U(3)]_{local}$ symmetry to the diquark sector and construct the Lagrangians containing diquarks. In this way, we can introduce the diquark-exchange interactions and study the nature of the Z_b states as the mixture of hadronic molecule and diquark-antidiquark state. In order to make the small distance interaction suppressed, we introduce the exponential form factor instead of the monopole form factor for each vertex, and calculate the effective potentials in the coordinate space analytically. We see that in the short and medium range, ρ - or ω -exchange contribution is larger than that of pion-exchange, while the pion-exchange is dominant in the long range. Besides, $B^{(*)-} \bar{B}^{(*)0} \rightarrow B^{(*)-} \bar{B}^{(*)0}$ processes are OZI suppressed which can be easily seen on the quark level. This is well depicted under the $[U(3)_L \otimes U(3)_R]_{global} \otimes [U(3)]_{local}$ symmetry, since the π -, η_8 -, η_0 -, ρ - and ω -exchange contributions cancel out. If taking the real masses of the

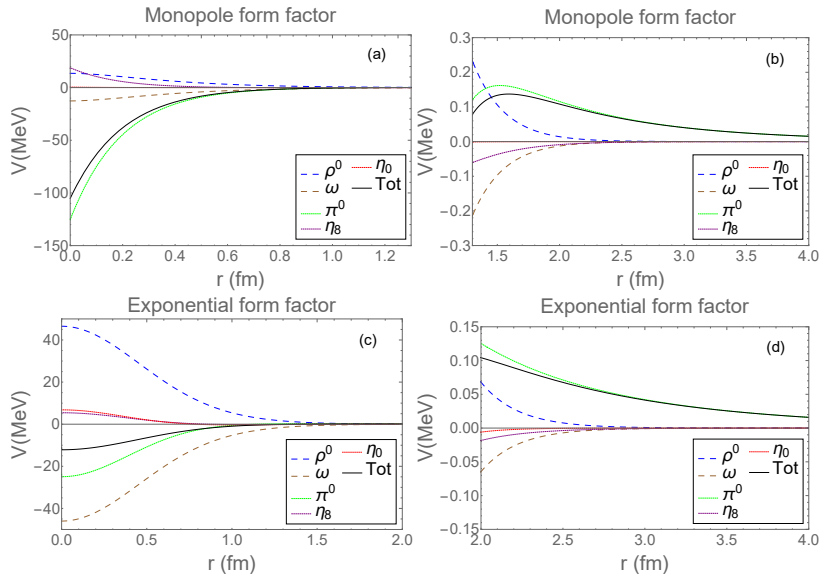


FIG. 2: (Color online) The effective potential for S-wave $B^*\bar{B}^*$ to S-wave $B^*\bar{B}^*$ with different form factor.

TABLE III: The obtained bound state solutions (binding energy E and root-mean-square radius r_{RMS}) for the charged Z_b system.

State	$\Lambda(\text{GeV})$	$E(\text{MeV})$	$r_{\text{RMS}}(\text{fm})$	$P(M/D)(\%)$	$P(^3S_1/^3D_1)(\%)$
$Z_b(10610)$	1.0	-1.83	1.64	97.20/2.80	99.84/0.16
	1.1	-9.96	0.82	92.60/7.40	99.82/0.18
	1.2	-26.14	0.57	87.48/12.52	99.68/0.32
$Z_b(10650)$	1.0	-2.60	1.45	96.37/3.63	99.66/0.34
	1.1	-9.01	0.88	92.62/7.38	99.66/0.34
	1.2	-19.82	0.66	88.55/11.45	99.64/0.36

exchanged particles which are different, the potential is non-zero corresponding to OZI violation.

Taking into account S- and D-wave contributions, we solve the coupled channel Schrödinger equation which obeys the $U(1) \otimes U(1) \otimes \dots \otimes U(1)$ symmetry. The numerical results show that both $Z_b(10610)$ and $Z_b(10650)$ can be explained as hadronic molecules slightly mixing with diquark-antidiquark states. If the cut-off is typically taken as $\Lambda = 1$ GeV for both the $Z_b(10610)$ and the $Z_b(10650)$ states, the molecular components are about 97% compared to around 3% diquark-antidiquark state components. Besides, the S-wave contribution is much larger than that of the D-wave. Our work can help to

understand the nature of the Z_b states.

Acknowledgments

We would like to thank Zhi-Peng Wang for very useful discussion. This project is supported by the Fundamental Research Funds for the Central Universities under Grant No. lzujbky-2022-sp02, the National Natural Science Foundation of China (NSFC) under Grants No. 11965016, 11705069 and 12247101, and the National Key Research and Development Program of China under Contract No. 2020YFA0406400.

- [1] A. Bondar et al. Observation of two charged bottomonium-like resonances in $Y(5S)$ decays. *Phys. Rev. Lett.*, 108:122001, 2012.
- [2] A. Garmash et al. Amplitude analysis of $e^+e^- \rightarrow \Upsilon(nS)\pi^+\pi^-$ at $\sqrt{s} = 10.865$ GeV. *Phys. Rev. D*,

91(7):072003, 2015.

- [3] A. Garmash et al. Observation of $Z_b(10610)$ and $Z_b(10650)$ Decaying to B Mesons. *Phys. Rev. Lett.*, 116(21):212001, 2016.
- [4] I. Adachi et al. Evidence for a $Z_b(10610)$ in Dalitz anal-

- ysis of $Y(5S) \rightarrow Y(nS) \pi^0 \pi^0$. 7 2012.
- [5] Yan-Rui Liu, Xiang Liu, Wei-Zhen Deng, and Shi-Lin Zhu. Is $X(3872)$ Really a Molecular State? *Eur. Phys. J. C*, 56:63–73, 2008.
- [6] Xiang Liu, Zhi-Gang Luo, Yan-Rui Liu, and Shi-Lin Zhu. $X(3872)$ and Other Possible Heavy Molecular States. *Eur. Phys. J. C*, 61:411–428, 2009.
- [7] A. E. Bondar, A. Garmash, A. I. Milstein, R. Mizuk, and M. B. Voloshin. Heavy quark spin structure in Z_b resonances. *Phys. Rev. D*, 84:054010, 2011.
- [8] Martin Clevelen, Feng-Kun Guo, Christoph Hanhart, and Ulf-G. Meissner. Bound state nature of the exotic Z_b states. *Eur. Phys. J. A*, 47:120, 2011.
- [9] J. Nieves and M. Pavon Valderrama. Deriving the existence of $B\bar{B}^*$ bound states from the $X(3872)$ and Heavy Quark Symmetry. *Phys. Rev. D*, 84:056015, 2011.
- [10] Jian-Rong Zhang, Ming Zhong, and Ming-Qiu Huang. Could $Z_b(10610)$ be a $B^*\bar{B}$ molecular state? *Phys. Lett. B*, 704:312–315, 2011.
- [11] Youchang Yang, Jialun Ping, Chengrong Deng, and Hong-Shi Zong. Possible interpretation of the $Z_b(10610)$ and $Z_b(10650)$ in a chiral quark model. *J. Phys. G*, 39:105001, 2012.
- [12] Zhi-Feng Sun, Jun He, Xiang Liu, Zhi-Gang Luo, and Shi-Lin Zhu. $Z_b(10610)^\pm$ and $Z_b(10650)^\pm$ as the $B^*\bar{B}$ and $B^*\bar{B}^*$ molecular states. *Phys. Rev. D*, 84:054002, 2011.
- [13] Shunsuke Ohkoda, Yasuhiro Yamaguchi, Shigehiro Yasui, Kazutaka Sudoh, and Atsushi Hosaka. Exotic Mesons with Hidden Bottom near Thresholds. *Phys. Rev. D*, 86:014004, 2012.
- [14] M. T. Li, W. L. Wang, Y. B. Dong, and Z. Y. Zhang. $Z_b(10650)$ and $Z_b(10610)$ States in A Chiral Quark Model. *J. Phys. G*, 40:015003, 2013.
- [15] J. M. Dias, F. Aceti, and E. Oset. Study of $B\bar{B}^*$ and $B^*\bar{B}^*$ interactions in $I = 1$ and relationship to the $Z_b(10610)$, $Z_b(10650)$ states. *Phys. Rev. D*, 91(7):076001, 2015.
- [16] Q. Wang, V. Baru, A. A. Filin, C. Hanhart, A. V. Nefediev, and J. L Wynen. Line shapes of the $Z_b(10610)$ and $Z_b(10650)$ in the elastic and inelastic channels revisited. *Phys. Rev. D*, 98(7):074023, 2018.
- [17] Chun-Yu Cui, Yong-Lu Liu, and Ming-Qiu Huang. Investigating different structures of the $Z_b(10610)$ and $Z_b(10650)$. *Phys. Rev. D*, 85:074014, 2012.
- [18] M. B. Voloshin. Radiative transitions from Upsilon(5S) to molecular bottomonium. *Phys. Rev. D*, 84:031502, 2011.
- [19] Martin Clevelen, Qian Wang, Feng-Kun Guo, Christoph Hanhart, Ulf-G. Meissner, and Qiang Zhao. Confirming the molecular nature of the $Z_b(10610)$ and the $Z_b(10650)$. *Phys. Rev. D*, 87(7):074006, 2013.
- [20] Thomas Mehen and Joshua W. Powell. Heavy Quark Symmetry Predictions for Weakly Bound B-Meson Molecules. *Phys. Rev. D*, 84:114013, 2011.
- [21] Thomas Mehen and Josh Powell. Line shapes in $Y(5S) \rightarrow B^{(*)}\bar{B}^*\pi$ with $Z(10610)$ and $Z(10650)$ using effective field theory. *Phys. Rev. D*, 88(3):034017, 2013.
- [22] Zhi-Gang Wang and Tao Huang. Possible assignments of the $X(3872)$, $Z_c(3900)$ and $Z_b(10610)$ as axial-vector molecular states. *Eur. Phys. J. C*, 74(5):2891, 2014.
- [23] Zhi-Gang Wang. Reanalysis of the $Y(3940)$, $Y(4140)$, $Z_c(4020)$, $Z_c(4025)$ and $Z_b(10650)$ as molecular states with QCD sum rules. *Eur. Phys. J. C*, 74(7):2963, 2014.
- [24] Yubing Dong, Amand Faessler, Thomas Gutsche, and Valery E. Lyubovitskij. Decays of $Z_b(+)$ and $Z_b'(+)$ as Hadronic Molecules. *J. Phys. G*, 40:015002, 2013.
- [25] Wei Chen, T. G. Steele, Hua-Xing Chen, and Shi-Lin Zhu. Mass spectra of Z_c and Z_b exotic states as hadron molecules. *Phys. Rev. D*, 92(5):054002, 2015.
- [26] Fabian Goerke, Thomas Gutsche, Mikhail A. Ivanov, Jürgen G. Körner, and Valery E. Lyubovitskij. $Z_b(10610)$ and $Z_b'(10650)$ decays in a covariant quark model. *Phys. Rev. D*, 96(5):054028, 2017.
- [27] Martin Clevelen. *Systematic Study of Hadronic Molecules in the Heavy-Quark Sector*. PhD thesis, Bonn U., 2013.
- [28] Shunsuke Ohkoda, Shigehiro Yasui, and Atsushi Hosaka. Decays of $Z_b \rightarrow \Upsilon\pi$ via triangle diagrams in heavy meson molecules. *Phys. Rev. D*, 89(7):074029, 2014.
- [29] Xin Li and M. B. Voloshin. $Z_b(10610)$ and $Z_b(10650)$ decays to bottomonium plus pion. *Phys. Rev. D*, 86:077502, 2012.
- [30] Thomas Gutsche, Valery E. Lyubovitskij, and Ivan Schmidt. Tetraquarks in holographic QCD. *Phys. Rev. D*, 96(3):034030, 2017.
- [31] You-Chang Yang, Zhi-Yun Tan, Hong-Shi Zong, and Jialun Ping. Dynamical study of S -wave $\bar{Q}Q\bar{q}q$ system. *Few Body Syst.*, 60(1):9, 2019.
- [32] Lu Zhang, Xian-Wei Kang, and Xin-Heng Guo. Composite nature of Z_b states from data analysis. *Eur. Phys. J. C*, 82(4):375, 2022.
- [33] Guang-Juan Wang, Xiao-Hai Liu, Li Ma, Xiang Liu, Xiao-Lin Chen, Wei-Zhen Deng, and Shi-Lin Zhu. The strong decay patterns of Z_c and Z_b states in the relativized quark model. *Eur. Phys. J. C*, 79(7):567, 2019.
- [34] Shunsuke Ohkoda, Yasuhiro Yamaguchi, Shigehiro Yasui, and Atsushi Hosaka. Decays and productions via bottomonium for Z_b resonances and other $B\bar{B}$ molecules. *Phys. Rev. D*, 86:117502, 2012.
- [35] Feng-Kun Guo, Carlos Hidalgo-Duque, Juan Nieves, and Manuel Pavon Valderrama. Consequences of Heavy Quark Symmetries for Hadronic Molecules. *Phys. Rev. D*, 88:054007, 2013.
- [36] V. Baru, E. Epelbaum, A. A. Filin, C. Hanhart, R. V. Mizuk, A. V. Nefediev, and S. Ropertz. Insights into $Z_b(10610)$ and $Z_b(10650)$ from dipion transitions from $\Upsilon(10860)$. *Phys. Rev. D*, 103(3):034016, 2021.
- [37] U. Ozdem and K. Azizi. Magnetic dipole moment of $Z_b(10610)$ in light-cone QCD. *Phys. Rev. D*, 97(1):014010, 2018.
- [38] Qi Wu, Yuanxin Zheng, Shidong Liu, and Gang Li. Investigations on the light hadron decays of $Z_b(10610)$ and $Z_b(10650)$. *Phys. Rev. D*, 107(3):034028, 2023.
- [39] Jian-Bo Cheng, Bo-Lin Huang, Zi-Yang Lin, and Shi-Lin Zhu. Z_{cs} , Z_c and Z_b states under the complex scaling method. *Eur. Phys. J. C*, 83(11):1071, 2023.

- [40] M. B. Voloshin. Mixing model for bottomoniumlike Z_b resonances. *Phys. Rev. D*, 96(9):094024, 2017.
- [41] Ahmed Ali, Christian Hambroek, and Wei Wang. Tetraquark Interpretation of the Charged Bottomonium-like states $Z_b^{+-}(10610)$ and $Z_b^{+-}(10650)$ and Implications. *Phys. Rev. D*, 85:054011, 2012.
- [42] Angelo Esposito, Andrea L. Guerrieri, Fulvio Piccinini, Alessandro Pilloni, and Antonio D. Polosa. Four-Quark Hadrons: an Updated Review. *Int. J. Mod. Phys. A*, 30:1530002, 2015.
- [43] L. Maiani, A. D. Polosa, and V. Riquer. A Theory of X and Z Multiquark Resonances. *Phys. Lett. B*, 778:247–251, 2018.
- [44] S. S. Agaev, K. Azizi, and H. Sundu. Spectroscopic parameters and decays of the resonance $Z_b(10610)$. *Eur. Phys. J. C*, 77(12):836, 2017.
- [45] Zhi-Gang Wang and Tao Huang. The $Z_b(10610)$ and $Z_b(10650)$ as axial-vector tetraquark states in the QCD sum rules. *Nucl. Phys. A*, 930:63–85, 2014.
- [46] A. Ali, L. Maiani, A. D. Polosa, and V. Riquer. Hidden-Beauty Charged Tetraquarks and Heavy Quark Spin Conservation. *Phys. Rev. D*, 91(1):017502, 2015.
- [47] Hong-Wei Ke, Xue-Qian Li, Yan-Liang Shi, Guo-Li Wang, and Xu-Hao Yuan. Is $Z_b(10610)$ a Molecular State? *JHEP*, 04:056, 2012.
- [48] Ze-Hua Cao, Wei He, and Zhi-Feng Sun. Zcs states and the mixture of hadronic molecule and diquark-antidiquark components within effective field theory. *Phys. Rev. D*, 107(1):014017, 2023.
- [49] Hua-Xing Chen, Wei Chen, Xiang Liu, and Shi-Lin Zhu. The hidden-charm pentaquark and tetraquark states. *Phys. Rept.*, 639:1–121, 2016.
- [50] Hua-Xing Chen, Wei Chen, Xiang Liu, Yan-Rui Liu, and Shi-Lin Zhu. An updated review of the new hadron states. *Rept. Prog. Phys.*, 86(2):026201, 2023.
- [51] Xiang-Kun Dong, Feng-Kun Guo, and Bing-Song Zou. A survey of heavy-heavy hadronic molecules. *Commun. Theor. Phys.*, 73(12):125201, 2021.
- [52] Lu Meng, Bo Wang, Guang-Juan Wang, and Shi-Lin Zhu. Chiral perturbation theory for heavy hadrons and chiral effective field theory for heavy hadronic molecules. *Phys. Rept.*, 1019:1–149, 2023.
- [53] S. K. Choi et al. Observation of a narrow charmonium-like state in exclusive $B^\pm \rightarrow K^\pm \pi^+ \pi^- J/\psi$ decays. *Phys. Rev. Lett.*, 91:262001, 2003.
- [54] L. Maiani, F. Piccinini, A. D. Polosa, and V. Riquer. A New look at scalar mesons. *Phys. Rev. Lett.*, 93:212002, 2004.
- [55] G. 't Hooft, G. Isidori, L. Maiani, A. D. Polosa, and V. Riquer. A Theory of Scalar Mesons. *Phys. Lett. B*, 662:424–430, 2008.
- [56] Masayasu Harada and Koichi Yamawaki. Hidden local symmetry at loop: A New perspective of composite gauge boson and chiral phase transition. *Phys. Rept.*, 381:1–233, 2003.
- [57] E. Hiyama, Y. Kino, and M. Kamimura. Gaussian expansion method for few-body systems. *Prog. Part. Nucl. Phys.*, 51:223–307, 2003.
- [58] J. Ferretti. Effective Degrees of Freedom in Baryon and Meson Spectroscopy. *Few Body Syst.*, 60(1):17, 2019.

Azimuthal Angular Correlation of J/ψ Plus Jet Production at the EIC

Luca Maxia^{1,*} and Feng Yuan^{2,†}

¹*Van Swinderen Institute for Particle Physics and Gravity,
University of Groningen, Nijenborgh 4, 9747 AG Groningen, The Netherlands*

²*Nuclear Science Division, Lawrence Berkeley National Laboratory, Berkeley, CA 94720, USA*

By investigating the soft gluon radiation in the J/ψ plus jet photoproduction at the electron-ion collider (EIC), we demonstrate that the azimuthal angular correlations between the leading jet and heavy quarkonium provide a unique probe to the production mechanism of the latter. In particular, a significant $\cos(\phi)$ asymmetry is found for the color-singlet channel, whereas it vanishes or has an opposite sign for color-octet production, depending on the jet transverse momentum. Numerical results of $\cos(\phi)$ and $\cos(2\phi)$ asymmetries employing both the color-singlet model and the nonrelativistic QCD approach are presented for typical kinematics at the future EIC.

Introduction. In recent years, heavy quarkonium production in various inclusive processes has attracted great interest as a way to probe gluon distributions both in initial (nucleon tomography) and final (fragmentation functions) states [1–17]. Among them, Refs. [10, 12] have studied the azimuthal angular correlation in semi-inclusive DIS between J/ψ and leading jet to probe the so-called linearly polarized gluon distribution. In this paper, we will investigate the dominant contributions from the soft gluon radiations and demonstrate that azimuthal correlations can also provide a unique opportunity to disentangle between the color-singlet (CS) and color-octet (CO) mechanisms.

In the nonrelativistic QCD (NRQCD) [18] approach, the heavy-quark pair forms a Fock state specified by $n = 2S+1 L_J^{[c]}$, with S denoting its spin, L the orbital angular momentum, J the total angular momentum and c its color. Note that, within this framework, the pair can couple either as a CS or CO state. Therefore, comprehending the significance of the CS and CO contributions is crucial. Although great progress has been made in understanding heavy quarkonium production in hadronic collisions (for recent reviews see [19, 20]), challenges remain to phenomenologically describe quarkonium formation and, in particular, to distinguish between these two mechanisms.

In this regard, we will demonstrate how azimuthal angular correlations in J/ψ plus jet photoproduction at the electron-ion collider (EIC) offer a unique probe of the underlying production mechanism. In particular, we will show that these correlations significantly differ between the CS and CO channels. We will focus on the correlation kinematics, i.e., the transverse momentum of individual particles is much larger than the total transverse momentum. Therefore, by combining the transverse momenta of the J/ψ and the jet, $k_{\psi\perp}$ and $k_{j\perp}$ respectively, we can identify two scales. The first one is given by $\vec{P}_\perp = \frac{\vec{k}_{\psi\perp} - \vec{k}_{j\perp}}{2}$, while the second by $\vec{q}_\perp = \vec{k}_{\psi\perp} + \vec{k}_{j\perp}$, with $|\vec{q}_\perp| \ll |\vec{P}_\perp|$. Hence, according to this limit, the

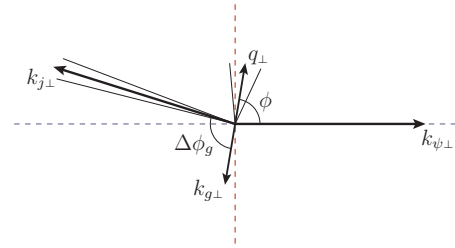


FIG. 1. Kinematic correlation between the leading jet and heavy quarkonium as viewed in the transverse plane. Here q_\perp (the total outgoing transverse momentum) is small compared to individual transverse momenta.

heavy quarkonium and jet are mainly produced back-to-back in the transverse plane (see Fig. 1). An imbalance between the two final-state particles with nonzero $|\vec{q}_\perp|$ can be generated by high-order perturbative corrections and from the intrinsic transverse momentum of the incoming parton. We identify this imbalance with the angle ϕ , namely the difference between the azimuthal angles of \vec{q}_\perp and $\vec{k}_{\psi\perp}$, where we can approximate the latter as $\vec{k}_{\psi\perp} \approx \vec{P}_\perp$ within the correlation limit.

Moreover, we remark that in this limit such azimuthal imbalance is mostly generated from the soft/collinear gluon radiation from perturbative diagrams (see for instance Ref. [21, 22]). This contribution, denoted by $k_{g\perp}$ in Fig. 1, tends to align with the jet direction at low q_\perp , which leads to significant $\cos(n\phi)$ asymmetries. Detailed examples have been shown for vector boson (photon/Z/Higgs) plus jet production in pp collisions [23, 24] and for lepton plus jet [21] and dijet [22] productions in ep collisions. Nonetheless, this feature is also particularly interesting to investigate the production mechanism of quarkonia.

With this paper, we suggest exploiting azimuthal angular distributions, especially the $\cos(\phi)$ and $\cos(2\phi)$, to unravel the production mechanism. Such findings can

* l.maxia@rug.nl

† fyuan@lbl.gov

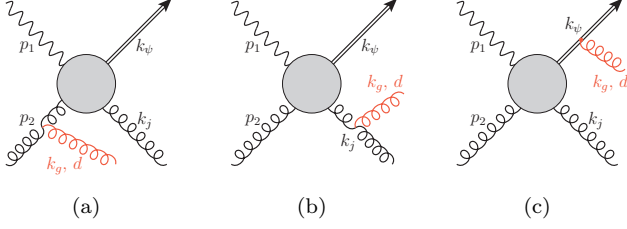


FIG. 2. *Soft gluon radiation in the J/ψ plus jet photoproduction process. All three diagrams contribute to the color-octet channel, whilst only the first two on the left are relevant for the color-singlet one.*

then be applied to electroproduction to investigate gluon distributions (e.g. linearly polarized gluons) in nucleons and nuclei.

Soft gluon radiation at one loop. In this section we discuss the implication of azimuthal correlation between the J/ψ and jet for photoproduction at the future EIC, $\gamma p \rightarrow J/\psi + jet + X$. The leading-order (LO) NRQCD contribution comes from the photon-gluon fusion partonic process, namely

$$\gamma(p_1) + g(p_2) \rightarrow [Q\bar{Q}]^{(1,8)}(k_\psi) + g(k_j), \quad (1)$$

where the momentum of each particle is given in the parenthesis. Moreover, the heavy-quark pair $Q\bar{Q}$ can be either in a CS (labeled with (1)) or CO (labeled with (8)) configuration. At this order, the J/ψ and jet are back-to-back in the transverse plane, so that $q_\perp = 0$. However, at higher orders, small nonzero q_\perp originates from parton intrinsic transverse momenta and soft gluon radiation. In the following, we will derive the LO soft gluon radiation contribution and the associated azimuthal angular asymmetries (Fig. 2), whereas the collinear gluon radiation can be factorized into the TMD gluon distributions.

The major difference between CS and CO channels is that the soft gluon radiation associated with the heavy quark pair only contributes to the latter. This occurs due to cancellations between the emissions from the heavy quark and antiquark when the pair is in a CS state. This difference has significant implications for the azimuthal asymmetries, as we will discuss in the following.

By adding Fig. 2a and Fig. 2b we obtain the amplitude squared (averaged over the color and spin of incoming particles) for the soft gluon radiation in the CS channel:

$$|\overline{\mathcal{A}}_1^{(1)}|^2 = g_s^2 C_A S_g(p_2, k_j) |\overline{\mathcal{A}}_0^{(1)}|^2, \quad (2)$$

where $A_0^{(1)}$ is the LO amplitude and $S_g(v_a, v_b)$ is a shorthand notation for

$$S_g(v_a, v_b) = \frac{2(v_a \cdot v_b)}{(v_a \cdot k_g)(v_b \cdot k_g)}. \quad (3)$$

Integration over the phase space of the emitted soft

gluon follows that in Ref. [21, 22, 25–28], leading to

$$\int \frac{d^3 k_g}{(2\pi)^3 2E_{k_g}} |\overline{\mathcal{A}}_1^{(1)}|^2 \delta^{(2)}(q_\perp + k_{g\perp}) = \frac{\alpha_s C_A}{2\pi^2 |\vec{q}_\perp|^2} |\overline{\mathcal{A}}_0^{(1)}|^2 \left[\ln \frac{\hat{s}}{|\vec{q}_\perp|^2} + \ln \frac{\hat{t}}{\hat{u}} + I_j(R, \phi) \right], \quad (4)$$

where $\hat{s} = (p_1 + p_2)^2$, $\hat{t} = (p_2 - k_j)^2$ and $\hat{u} = (p_1 - k_j)^2$. The first term in the bracket is the double logarithm (in b_T -space) that provides the dominant behavior at low q_\perp . The second logarithm, $\ln(\hat{t}/\hat{u})$, depends on the jet rapidity. The third term, I_j , is one of the subjects of this work, being the azimuthal distribution that arises from the soft gluon radiation. As a result of the removal of collinear divergences already included within the jet function, I_j depends on the jet size R . To further investigate this distribution, we expand it in a Fourier series according to

$$I_j(R, \phi) = C_0^{(j)}(R) + 2 \sum_{n=1}^{\infty} C_n^{(j)}(R) \cos(n\phi). \quad (5)$$

In line with previous works, we find that the soft gluon radiation associated with the jet leads to a dominant $\cos(\phi)$ asymmetry, with the $\cos(2\phi)$ one being much smaller.

At variance with the CS case, when the pair forms a CO state all diagrams in Fig. 2 are relevant. Independently from the color structures of the LO partonic process, one gluon radiation leads to the same contribution. While it is straightforward to prove that the first two diagrams do not depend on the Fock state, it is worthwhile to provide further elaboration on the last one (Fig. 2c), which corresponds to soft gluon radiation from the heavy-quark pair itself. Within NRQCD, the total soft gluon radiation from the quark and antiquark lines is given by $g_s \frac{k_\psi^\mu}{k_g \cdot k_\psi + i\epsilon} (\Phi_{ij} T^d - T^d \Phi_{ij}) \Gamma$ [13, 29], where Φ represents the wave function of the pair, i (j) and d are respectively the color indices for the quark (antiquark) and the radiated soft gluon, μ is connected to the soft gluon polarization vector, and Γ stands for other hard parts coming from the scattering amplitude. The minus sign in the second term comes from the interaction with the antiquark which is opposite to that with the quark. When the pair forms a CO state, the color matrix of the wave function can be parameterized as $\Phi_{ij}^{(8,c)} \propto T_{ij}^c$, where $c = 1, \dots, 8$ represents the color index of the pair. The sum of the two diagrams will then be proportional to $g_s \frac{k_\psi^\mu}{k_g \cdot k_\psi + i\epsilon} (-if_{c'd}) \Phi^{(8,c)} \Gamma^{c'}$, where we emphasized that the pair coupled with the rest of the diagram with a different color index c' before the soft gluon emission. Note that we have not taken any assumption on the spin and angular configuration entering in Φ , which implies that the result is independent of those quantum numbers. Moreover, the found result is similar to that for soft gluon radiation from a gluon jet in the final state [26]. The only difference originates from the gluon on-shell condition, $k^2 = 0$ for jets and $k^2 = M_V^2 \approx 4M_Q^2$ for quarkonia.

By including the soft gluon radiations from the initial and final state gluons (Figs. 2a and 2b), the averaged CO amplitude squared is summarized as follows

$$|\overline{\mathcal{A}}_1^{(8)}|^2 = g_s^2 C_A \left[S_g(p_2, k_j) + \frac{1}{2} \left(S_g(p_2, k_\psi) - S_g(k_\psi, k_\psi) + S_g(k_j, k_\psi) - S_g(p_2, k_j) \right) \right] |\overline{\mathcal{A}}_0^{g,(8)}|^2, \quad (6)$$

where $\overline{\mathcal{A}}_0^{g,(8)}$ represents the LO (gluon) amplitude. In principle, $|\overline{\mathcal{A}}_1^{(8)}|^2$ depends on quarks too. However, we will neglect the quark contribution in the following, since it is reasonable to expect that it will be suppressed compared to the gluon one. Note that the first term of Eq. (6) is equivalent to that in Eq. (2) for the CS case and, therefore, is a contribution purely driven by the gluon jet. Consequently, all the terms in the round brackets can be associated with the J/ψ .

From Eq. (6), the integration over the phase space of the emitted soft gluon gives

$$\begin{aligned} & \int \frac{d^3 k_g}{(2\pi)^3 2E_{k_g}} |\overline{\mathcal{A}}_1^{(8)}|^2 \delta^{(2)}(q_\perp + k_{g\perp}) \\ &= \frac{\alpha_s C_A}{2\pi^2 |\vec{q}_\perp|^2} |\overline{\mathcal{A}}_0^{g,(8)}|^2 \left[\ln \frac{\hat{s}}{|\vec{q}_\perp|^2} + \frac{1}{2} \ln \frac{1 - M_\psi^2/\hat{u}}{1 - M_\psi^2/\hat{t}} \right. \\ &+ I_j(R, \phi) + I_\psi(m_{\psi\perp}, \phi) + \frac{1}{2} I_{\psi-j}(m_{\psi\perp}, \Delta y, 2\phi) \\ &\left. - \frac{1}{2} I_\psi^{\text{jet}}(R, m_{\psi\perp}, \Delta y, \phi) \right], \quad (7) \end{aligned}$$

where we have introduced $m_{\psi\perp} = M_\psi/k_{\psi\perp}$, while $\Delta y = y_\psi - y_j$ is the rapidity difference between the J/ψ (y_ψ) and the leading jet (y_j). The first term of Eq. (7) corresponds to the leading, double logarithmic behavior at low q_\perp , which is the same as the CS case. This implies that the soft gluon emission from the (massive) quarkonium does not provide double logarithms, a conclusion in line with other works [13, 30–34]. The second term comes from the sum of rapidities $y_j + y_\psi$, which differs from zero due to the presence of the J/ψ mass. The third term, I_j , is the same azimuthal dependence associated with the jet in Eq. (4), and its Fourier expansion follows Eq. (5). The last three azimuthal distributions, I_ψ , $I_{\psi-j}$ and I_ψ^{jet} , are the novel terms due to the production of a CO state. Their definitions and derivations are in the supplemental material. Again, we expand them in terms of $\cos(n\phi)$ harmonics according to

$$I_{[\psi]}(K, \phi) = C_0^{([\psi])}(K) + 2 \sum_{n=1}^{\infty} C_n^{([\psi])}(K) \cos(n\phi), \quad (8)$$

where $I_{[\psi]}$ is either I_ψ , $I_{\psi-j}$ or I_ψ^{jet} , and K is a short-hand notation for the dependence on the kinematical variables of each distribution.

Mechanism	$C_0^{(c)}$	$C_1^{(c)}$	$C_2^{(c)}$
CS	0.89	2.61	0.95
CO ($m_{\psi\perp} = 0.26$)	2.46	-0.02	1.72
CO ($m_{\psi\perp} = 0.1$)	3.40	-1.80	3.28

TABLE I. First coefficients of the azimuthal correlation Fourier expansions for the CS and CO mechanisms with $R = 0.4$. Note that the coefficients within the CS channel are independent of $k_{j\perp}$.

Summarizing the above results, the differential cross section including the soft gluon radiation in the correlation limit is given by

$$\begin{aligned} \frac{d^4 \sigma^{(1,8)}}{d\Omega} &= \sigma_0^{(1,8)} x_g f_g(x_g) \frac{\alpha_s C_A}{2\pi^2 |\vec{q}_\perp|^2} \left[\ln \frac{\hat{s}}{|\vec{q}_\perp|^2} \right. \\ &\left. + 2 \sum_{n=0}^{\infty} C_n^{(1,8)}(R, m_{\psi\perp}, \Delta y = 0) \cos(n\phi) \right], \quad (9) \end{aligned}$$

where $\sigma_0^{(1,8)}$ represents the LO cross section [35], $d\Omega \equiv dy_j dy_\psi d^2 \vec{P}_\perp d^2 \vec{q}_\perp$ the phase space, and $f_g(x_g)$ is the gluon distribution. Moreover, we are considering the case where $y_j = y_\psi = 0$ for simplicity, since this scenario does not present additional, non-divergent logarithms. Hence, in Eq. (9) we have that the first term corresponds to the leading double logarithm, while the second line stands for the single logarithms. Since the latter carries the azimuthal dependence, we have already expanded it into harmonics, with the coefficients $C_n^{(1,8)}$ connected to those in the Fourier series of each distribution. Therefore they depend on the jet size R , the heavy quarkonium mass via $m_{\psi\perp} = M_\psi/P_\perp$ and the rapidity difference $\Delta y = y_\psi - y_j$. Most importantly, these coefficients depend crucially on the production channel considered. To illustrate these differences, we consider typical kinematics for future EIC measurements. We take $R = 0.4$ and $m_{\psi\perp} = 0.26, 0.1$, that correspond to $k_{j\perp} \approx 12, 30$ GeV. Within these choices, the first three coefficients of the Fourier expansion in Eq. (9) are given in Table I, displaying a clear difference between CS and CO channels. In particular, the coefficient $C_1^{(1)}$ is significantly positive due to the soft gluon radiation associated with the jet in the final state. However, the soft gluon radiation associated with heavy quark pair has an opposite sign. Thus, a proper choice of $m_{\psi\perp}$ can reduce the magnitude, or even change the sign, of $C_1^{(8)}$ when compared to $C_1^{(1)}$, while on the other hand $C_2^{(8)}$ and $C_2^{(1)}$ stay of more or less the same order. For more details on the comparison between the CS and CO channels we refer the reader to the supplemental materials.

All order resummation and predictions for the EIC. All order resummation is needed to make reliable

predictions for the soft gluon radiation contributions. Following the standard TMD framework, we have

$$\frac{d^4\sigma^{(1,8)}}{d\Omega} = \sigma_0^{(1,8)} \int \frac{|\vec{b}_\perp| d|\vec{b}_\perp|}{(2\pi)} \left[J_0(|\vec{b}_\perp||\vec{q}_\perp|) \widetilde{W}_0^{(1,8)}(|\vec{b}_\perp|) + 2 J_n(|\vec{b}_\perp||\vec{q}_\perp|) \widetilde{W}_n^{(1,8)}(|\vec{b}_\perp|) \cos(n\phi) \right], \quad (10)$$

where

$$\widetilde{W}_0^{(1,8)}(|\vec{b}_\perp|) = x_g f_g(x_g, \mu_b) e^{-S^{(1,8)}(P_\perp, b_\perp)}, \quad (11)$$

and

$$\widetilde{W}_n^{(1,8)}(|\vec{b}_\perp|) = \frac{C_A \alpha_s}{n\pi} C_n^{(1,8)} \widetilde{W}_0^{(1,8)}(|\vec{b}_\perp|). \quad (12)$$

Note that in Eq. (10) we have already included higher-order double logarithmic corrections present also for the angular dependent term [23, 24]. The Sudakov form factor $S(P_\perp, b_\perp)$ is separated into perturbative and non-perturbative parts: $S(P_\perp, b_\perp) = S_{\text{pert.}}(P_\perp, b_\perp) + S_{\text{NP}}(P_\perp, b_\perp)$. The perturbative part at one loop is defined as

$$S_{\text{pert.}}^{(1,8)} = \int_{\mu_0^2}^{\hat{s}} \frac{d\mu^2}{\mu^2} \frac{\alpha_s C_A}{2\pi} \left[\ln \frac{\hat{s}}{\mu^2} - 2\beta_0 + 2C_0^{(1,8)} \right], \quad (13)$$

where $\beta_0 = 11/12 - N_f/18$ and $\mu_b = b_0/b_\perp$ with $b_0 = 2e^{\Gamma_E}$ and Γ_E being the Euler's constant. Moreover, in Eq. (13) we have already introduced the b_* -prescription [36], where $b_* = b_\perp / \sqrt{1 + (b_\perp/b_{\text{max}})^2}$ with $b_{\text{max}} = 1.5$ GeV. For the non-perturbative part, we have contributions driven by the incoming gluon and the outgoing jet and quarkonium. For the first one, we employ the non-perturbative Sudakov found for TMD quark distributions in Refs. [37, 38] with the appropriate Casimir scaling

$$S_{\text{NP}}^g = \frac{C_A}{C_F} \left[0.106 b_\perp^2 + 0.42 \ln \frac{P_\perp}{Q_0} \ln \frac{b_\perp}{b_*} \right], \quad (14)$$

where $Q_0^2 = 2.4$ GeV². For the others, we assume that the non-perturbative contribution associated with the jet is given by $S_{\text{NP}}^{\text{jet}} = g_\Lambda^{\text{jet}} b_\perp^2$, and the J/ψ one by $S_{\text{NP}}^\psi = g_\Lambda^\psi b_\perp^2$. Overall, we employ $S_{\text{NP}}^{(1)} = S_{\text{NP}}^g + S_{\text{NP}}^{\text{jet}}$ for the CS mechanism and $S_{\text{NP}}^{(8)} = S_{\text{NP}}^g + S_{\text{NP}}^{\text{jet}} + S_{\text{NP}}^\psi$ for the CO channel, with $g_\Lambda^{\text{jet}} = g_\Lambda^\psi = 0.225$ GeV², a choice in line with [21, 22]. We also checked that the final azimuthal asymmetries do not depend significantly on these parameters, as expected.

From the above expressions, we find that the azimuthal asymmetries of $\cos(\phi)$ and $\cos(2\phi)$ are linearly proportional to the respective $C_{1,2}$ coefficients which are different between the CS and CO channels. Therefore, they can be used to probe these two production mechanisms.

As an example, in Fig. 3, we show the numerical results for $\langle \cos(\phi) \rangle$ and $\langle \cos(2\phi) \rangle$ as functions of q_\perp for kinematics accessible at the EIC, with $\sqrt{s_{\gamma p}} = 100$ GeV, $R = 0.4$

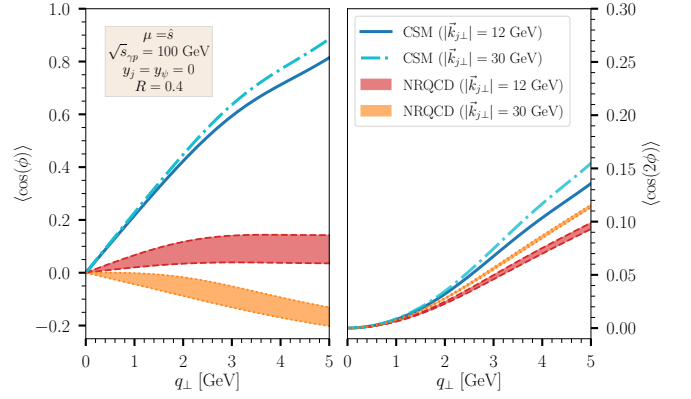


FIG. 3. Averaged resummed azimuthal asymmetries for J/ψ plus jet photoproduction at $\sqrt{s_{\gamma p}} = 100$ GeV. Solid blue and dash-dotted cyan lines are the CSM predictions at $|\vec{k}_{j\perp}| = 12$ GeV and $|\vec{k}_{j\perp}| = 30$ GeV, whereas for the NRQCD approach we have the dashed red and dotted orange lines, respectively. Bands are obtained by combining the results from different LDMEs central values. Jet size is $R = 0.4$ in all cases.

and $|\vec{k}_{j\perp}| = 12, 30$ GeV. For the parton distribution function we have employed the MSHT20 LO set [39]. Predictions are shown for both the color-singlet model (CSM) and NRQCD approach, with the latter mainly depending on the relative fraction of the CS and total CO contributions. Indeed, note that NRQCD predictions are not strongly dependent on the individual CO long-distance matrix elements (LDMEs), as can be understood from the bands in Fig. 3 which are constructed by combining several central values of the associated LDMEs from different global analyses [40–44].

As expected, the resummed form of $\langle \cos(n\phi) \rangle$ is exactly 0 at $q_\perp = 0$, and at small q_\perp they scale as $\langle \cos(n\phi) \rangle \propto q_\perp^n$ [24]. At large q_\perp , we expect they will decrease as functions of q_\perp , where the hard gluon radiation dominates and there is no preferred direction. This will modify the behavior of both $\langle \cos(\phi) \rangle$ and $\langle \cos(2\phi) \rangle$ asymmetries at large q_\perp in Fig. 3. Meanwhile, this figure shows a distinct behavior between $\langle \cos(\phi) \rangle$ and $\langle \cos(2\phi) \rangle$ predictions. Indeed, the former highly depends on the model considered, whereas the CSM and NRQCD outcomes are comparable, and in general non-negligible, for $\langle \cos(2\phi) \rangle$. As demonstrated, such differences offer a unique opportunity to determine the underlying quarkonium production mechanism.

Conclusions. In summary, we have demonstrated that the soft gluon radiation leads to significantly different azimuthal angular correlations between the CS and CO mechanisms in the J/ψ plus jet photoproduction process at the future EIC. This directly affects azimuthal asymmetry predictions within the CSM and the NRQCD approach, where the latter presents a soft dependence on the LDME. Thus, we consider these observables as the stems to disentangle these two production mechanisms. We also expect that similar conclusions can be drawn for

other experiments as well, like in hadronic processes at the LHC. Moreover, $\cos(2\phi)$ has been proposed to study the linearly polarized gluon distribution in the electroproduction of J/ψ plus jet at the EIC. We expect that the soft gluon radiation will lead to sizable contributions to $\cos(2\phi)$ asymmetry in this process as well, with a behavior similar to that shown in Fig. 3 for photoproduction. Understanding the soft gluon radiation will be a crucial step to unambiguously determine the gluon tomography of linearly polarized distribution from this measurement.

We will explore all these physics, including higher-order perturbative and power corrections, in the future.

ACKNOWLEDGMENTS

We thank Prof. D. Boer for the valuable discussions. This material is based upon work supported by the U.S. Department of Energy, Office of Science, Office of Nuclear Physics, under contract numbers DE-AC02-05CH11231.

-
- [1] R. M. Godbole, A. Misra, A. Mukherjee, and V. S. Rao, *Phys. Rev. D* **85**, 094013 (2012), arXiv:1201.1066 [hep-ph].
- [2] D. Boer and C. Pisano, *Phys. Rev. D* **86**, 094007 (2012), arXiv:1208.3642 [hep-ph].
- [3] R. M. Godbole, A. Misra, A. Mukherjee, and V. S. Rao, *Phys. Rev. D* **88**, 014029 (2013), arXiv:1304.2584 [hep-ph].
- [4] W. J. den Dunnen, J. P. Lansberg, C. Pisano, and M. Schlegel, *Phys. Rev. Lett.* **112**, 212001 (2014), arXiv:1401.7611 [hep-ph].
- [5] A. Mukherjee and S. Rajesh, *Phys. Rev. D* **93**, 054018 (2016), arXiv:1511.04319 [hep-ph].
- [6] A. Mukherjee and S. Rajesh, *Phys. Rev. D* **95**, 034039 (2017), arXiv:1611.05974 [hep-ph].
- [7] A. Mukherjee and S. Rajesh, *Eur. Phys. J. C* **77**, 854 (2017), arXiv:1609.05596 [hep-ph].
- [8] S. Rajesh, R. Kishore, and A. Mukherjee, *Phys. Rev. D* **98**, 014007 (2018), arXiv:1802.10359 [hep-ph].
- [9] F. Scarpa, D. Boer, M. G. Echevarria, J.-P. Lansberg, C. Pisano, and M. Schlegel, *Eur. Phys. J. C* **80**, 87 (2020), arXiv:1909.05769 [hep-ph].
- [10] U. D'Alesio, F. Murgia, C. Pisano, and P. Tael, *Phys. Rev. D* **100**, 094016 (2019), arXiv:1908.00446 [hep-ph].
- [11] R. Kishore, A. Mukherjee, and M. Siddiqah, *Phys. Rev. D* **104**, 094015 (2021), arXiv:2103.09070 [hep-ph].
- [12] R. Kishore, A. Mukherjee, A. Pawar, and M. Siddiqah, *Phys. Rev. D* **106**, 034009 (2022), arXiv:2203.13516 [hep-ph].
- [13] D. Boer, J. Bor, L. Maxia, C. Pisano, and F. Yuan, *JHEP* **08**, 105 (2023), arXiv:2304.09473 [hep-ph].
- [14] M. Copeland, S. Fleming, R. Gupta, R. Hodges, and T. Mehen, (2023), arXiv:2308.08605 [hep-ph].
- [15] M. G. Echevarria, S. F. Romera, and I. Scimemi, (2023), arXiv:2308.12356 [hep-ph].
- [16] M. Copeland, S. Fleming, R. Gupta, R. Hodges, and T. Mehen, (2023), arXiv:2310.13737 [hep-ph].
- [17] Z.-B. Kang, E. Li, and F. Salazar, (2023), arXiv:2310.12102 [hep-ph].
- [18] G. T. Bodwin, E. Braaten, and G. P. Lepage, *Phys. Rev. D* **51**, 1125 (1995), [Erratum: *Phys.Rev.D* 55, 5853 (1997)], arXiv:hep-ph/9407339.
- [19] N. Brambilla *et al.*, *Eur. Phys. J. C* **71**, 1534 (2011), arXiv:1010.5827 [hep-ph].
- [20] J.-P. Lansberg, *Phys. Rept.* **889**, 1 (2020), arXiv:1903.09185 [hep-ph].
- [21] Y. Hatta, B.-W. Xiao, F. Yuan, and J. Zhou, *Phys. Rev. Lett.* **126**, 142001 (2021), arXiv:2010.10774 [hep-ph].
- [22] Y. Hatta, B.-W. Xiao, F. Yuan, and J. Zhou, *Phys. Rev. D* **104**, 054037 (2021), arXiv:2106.05307 [hep-ph].
- [23] S. Catani, M. Grazzini, and A. Torre, *Nucl. Phys. B* **890**, 518 (2014), arXiv:1408.4564 [hep-ph].
- [24] S. Catani, M. Grazzini, and H. Sargsyan, *JHEP* **06**, 017 (2017), arXiv:1703.08468 [hep-ph].
- [25] P. Sun, C. P. Yuan, and F. Yuan, *Phys. Rev. Lett.* **113**, 232001 (2014), arXiv:1405.1105 [hep-ph].
- [26] P. Sun, C. P. Yuan, and F. Yuan, *Phys. Rev. D* **92**, 094007 (2015), arXiv:1506.06170 [hep-ph].
- [27] X. Liu, F. Ringer, W. Vogelsang, and F. Yuan, *Phys. Rev. Lett.* **122**, 192003 (2019), arXiv:1812.08077 [hep-ph].
- [28] X. Liu, F. Ringer, W. Vogelsang, and F. Yuan, *Phys. Rev. D* **102**, 094022 (2020), arXiv:2007.12866 [hep-ph].
- [29] F. Yuan, *Phys. Rev. D* **78**, 014024 (2008), arXiv:0801.4357 [hep-ph].
- [30] P. Sun, C. P. Yuan, and F. Yuan, *Phys. Rev. D* **88**, 054008 (2013), arXiv:1210.3432 [hep-ph].
- [31] H. X. Zhu, C. S. Li, H. T. Li, D. Y. Shao, and L. L. Yang, *Phys. Rev. Lett.* **110**, 082001 (2013), arXiv:1208.5774 [hep-ph].
- [32] R. Zhu, P. Sun, and F. Yuan, *Phys. Lett. B* **727**, 474 (2013), arXiv:1309.0780 [hep-ph].
- [33] M. G. Echevarria, *JHEP* **10**, 144 (2019), arXiv:1907.06494 [hep-ph].
- [34] S. Fleming, Y. Makris, and T. Mehen, *JHEP* **04**, 122 (2020), arXiv:1910.03586 [hep-ph].
- [35] P. Ko, J. Lee, and H. S. Song, *Phys. Rev. D* **54**, 4312 (1996), [Erratum: *Phys.Rev.D* 60, 119902 (1999)], arXiv:hep-ph/9602223.
- [36] J. C. Collins, D. E. Soper, and G. F. Sterman, *Nucl. Phys. B* **250**, 199 (1985).
- [37] P. Sun, J. Isaacson, C. P. Yuan, and F. Yuan, *Int. J. Mod. Phys. A* **33**, 1841006 (2018), arXiv:1406.3073 [hep-ph].
- [38] A. Prokudin, P. Sun, and F. Yuan, *Phys. Lett. B* **750**, 533 (2015), arXiv:1505.05588 [hep-ph].
- [39] S. Bailey, T. Cridge, L. A. Harland-Lang, A. D. Martin, and R. S. Thorne, *Eur. Phys. J. C* **81**, 341 (2021), arXiv:2012.04684 [hep-ph].
- [40] M. Butenschoen and B. A. Kniehl, *Phys. Rev. D* **84**, 051501 (2011), arXiv:1105.0820 [hep-ph].
- [41] K.-T. Chao, Y.-Q. Ma, H.-S. Shao, K. Wang, and Y.-J. Zhang, *Phys. Rev. Lett.* **108**, 242004 (2012), arXiv:1201.2675 [hep-ph].
- [42] B. Gong, L.-P. Wan, J.-X. Wang, and H.-F. Zhang, *Phys. Rev. Lett.* **110**, 042002 (2013), arXiv:1205.6682 [hep-ph].

- [43] R. Sharma and I. Vitev, *Phys. Rev. C* **87**, 044905 (2013), [arXiv:1203.0329 \[hep-ph\]](#).
- [44] N. Brambilla, H. S. Chung, A. Vairo, and X.-P. Wang, *Phys. Rev. D* **105**, L111503 (2022), [arXiv:2203.07778 \[hep-ph\]](#).

SUPPLEMENTAL MATERIAL

As the supplemental material of the paper, we provide all the technical details below.

I. EVALUATION OF SOFT GLUON RADIATIONS

In this section, we provide detailed derivations of the soft gluon radiation contributions obtained by integrating the relevant rapidity phase space. This requires discussing four functions of the kind presented in Eq. (3): $S_g(p_2, k_j)$, $S_g(p_2, k_\psi)$, $S_g(k_j, k_\psi)$, and $S_g(k_\psi, k_\psi)$.

Integral of $S_g(p_2, k_j)$. We start with the first one on the list, which is the only one contributing to the CS channel. Although its integral was relevant, and therefore computed, in other works [21, 22, 25–28], for completeness we report the calculation in the following. To better analyze the physical content of this derivation, we can divide $S_g(p_2, k_2)$ into three contributions as follows

$$\begin{aligned} S_g(p_2, k_j) &= \frac{2(p_2 \cdot k_j)}{(p_2 \cdot k_g)(k_j \cdot k_g)} \\ &= \frac{2}{|\vec{k}_{g\perp}|^2} \frac{e^{\Delta y_g}}{\cosh(\Delta y_g) - \cos(\Delta\phi_g)} \\ &\approx \frac{2}{|\vec{k}_{g\perp}|^2} \left(1 + \frac{\sinh(\Delta y_g)}{\cosh(\Delta y_g) - \cos(\phi)} \right. \\ &\quad \left. + \frac{\cos(\phi)}{\cosh(\Delta y_g) - \cos(\phi)} \right), \end{aligned} \quad (15)$$

where we have defined $\Delta y_g = y_g - y_j$, namely the difference between the emitted soft gluon and jet rapidities. The first term in the bracket of Eq. (15) leads to the double-logarithm. The second one, being an odd function of Δy_g , receives contributions only from the boundaries of the integration region, which causes the presence of the additional logarithmic term, $\ln(\hat{t}/\hat{u})$, in Eq. (4). The last term in Eq. (15) contains the jet contribution to azimuthal angular asymmetries.

In particular, this distribution is described by the function

$$\begin{aligned} I_j(R, \phi) &= \int d\Delta y_g \frac{\cos(\phi)}{\cosh(\Delta y_g) - \cos(\phi)} \\ &\quad - \frac{|\vec{k}_{g\perp}|^2}{2} \int d\Delta y_g S_g(p_2, k_j) \Theta(\Delta_{k_g k_j} < R^2) \\ &= \int d\Delta y_g \frac{\cos(\phi)}{\cosh(\Delta y_g) - \cos(\phi)} \Theta(\Delta_{k_j k_g} > R^2) \\ &\quad - 2\sqrt{R^2 + \phi^2}, \end{aligned} \quad (16)$$

where $\Theta(\Delta_{k_j k_g} \lesseqgtr R^2)$ implies that the integration is restricted inside ($<$) or outside ($>$) the rapidity region occupied by the jet cone with size R , namely

$$|\Delta y_g| > \sqrt{R^2 + \phi^2}. \quad (17)$$

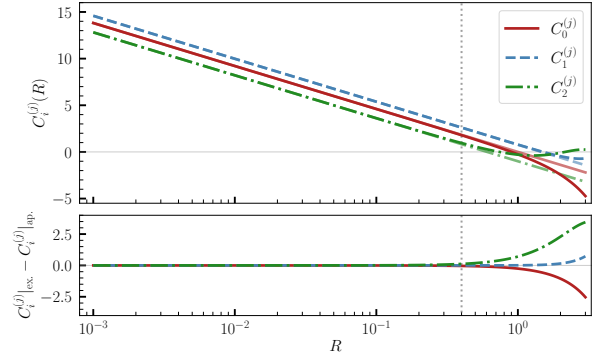


FIG. 4. Dependence of the first coefficients of Eq. (5) with respect to R . In the upper panel we show both the exact result obtained from a numerical computation (full color) and the approximated one given in Eq. (18) (softer color). In the lower panel, we present the difference between the two. The vertical dotted line corresponds to $R = 0.4$, beyond which the approximation fails.

For a general R , the Fourier expansion of $I_j(R, \phi)$ (Eq. (5)) is manageable only via computational methods. However, the analytical evaluation of this expansion within the small- R limit is possible. Hence we find

$$\begin{aligned} I_j(R, \phi) &= \ln \frac{1}{R^2} + 2 \cos(\phi) \left(\ln \frac{1}{R^2} + 2 \ln(4) - 2 \right) \\ &\quad + 2 \cos(2\phi) \left(\ln \frac{1}{R^2} - 1 \right) + \dots, \end{aligned} \quad (18)$$

from which it is evident that there is a non-negligible $\cos(\phi)$ azimuthal angular dependence in $I_j(R, \phi)$.

In Fig. 4, we show how the first three coefficients of the Fourier expansion behave with respect to R . From this figure, we conclude that the approximation used in Eq. (18) is reasonably adequate for $R < 0.4$.

Integral of $S_g(p_2, k_\psi)$. Similarly to $S_g(p_2, k_j)$, we divide $S_g(p_2, k_\psi)$ in the following three terms

$$\begin{aligned} S_g(p_2, k_\psi) &= \frac{2(p_2 \cdot k_\psi)}{(p_2 \cdot k_g)(k_\psi \cdot k_g)} \\ &= \frac{2}{|\vec{k}_{g\perp}|^2} \frac{e^{\Delta y_{g\psi}}}{\sqrt{1 + m_{\psi\perp}^2} \cosh(\Delta y_{g\psi}) - \cos(\Delta\phi_{g\psi})} \\ &\approx \frac{2}{|\vec{k}_{g\perp}|^2} \left(1 + \frac{\sqrt{1 + m_{\psi\perp}^2} \sinh(\Delta y_{g\psi})}{\sqrt{1 + m_{\psi\perp}^2} \cosh(\Delta y_{g\psi}) + \cos(\phi)} \right. \\ &\quad \left. - \frac{\cos(\phi)}{\sqrt{1 + m_{\psi\perp}^2} \cosh(\Delta y_{g\psi}) + \cos(\phi)} \right), \end{aligned} \quad (19)$$

where we have defined $\Delta y_{g\psi} = y_g - y_\psi$, namely the difference between the emitted soft gluon and J/ψ rapidities, and $\Delta\phi_{g\psi} = \phi_g - \phi_\psi = \phi_g$ in a frame where $\phi_\psi = 0$. As for Eq. (15), the first term in the bracket of Eq. (19) leads to the double-logarithm while the second one receives

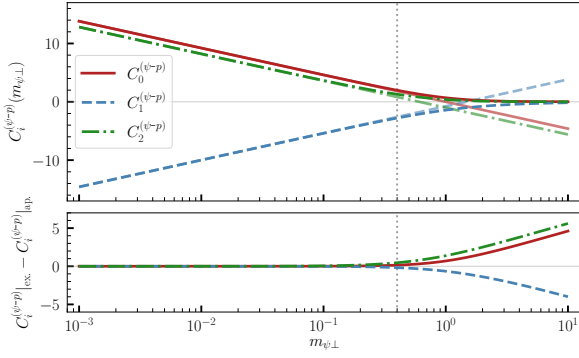


FIG. 5. Dependence of the first coefficients of Eq. (22) with respect to $m_{\psi\perp}$. Vertical dotted line corresponds to $m_{\psi\perp} = 0.4$. Panels follow the same logic as Fig. 4.

contributions only from the boundaries of the integration region, providing the logarithms: $\ln \frac{\hat{u}}{\hat{t}} + \ln \frac{1-M_\psi^2/\hat{u}}{1-M_\psi^2/\hat{t}}$. These, once combined with the other analogous logarithms arising from $S_g(p_2, k_j)$, cause the presence of the second term in Eq. (7). The last term in Eq. (19) contains part of the J/ψ contribution to azimuthal angular asymmetries.

We identify this angular distribution as

$$I_{\psi-p}(m_{\psi\perp}, \phi) = \int d\Delta y_{g\psi} \left[-\frac{\cos(\phi)}{\sqrt{1+m_{\psi\perp}^2} \cosh(\Delta y_{g\psi}) + \cos(\phi)} \right] \quad (20)$$

Note that the presence of the mass in the denominator

acts as a regulator, and therefore $I_{\psi-p}$ is continuous for all values of ϕ . Moreover, when evaluated within the jet rapidity region, Eq. (19) leads to

$$I_{\psi-p}^{\text{jet}}(R, m_{\psi\perp}, \Delta y, \phi) = \frac{|\vec{k}_{g\perp}|^2}{2} \int d\Delta y_g S_g(p_2, k_\psi) \Theta(\Delta_{k_g k_j} < R^2), \quad (21)$$

which not only depends on both parameters R and $m_{\psi\perp}$, but on the rapidity difference $\Delta y = y_\psi - y_j$ too. The distribution in Eq. (20) can be expanded according to Eq. (8), which leads to

$$I_{\psi-p}(m_{\psi\perp}, \phi) = C_0^{(\psi-p)}(m_{\psi\perp}) + 2 \sum_{n=1}^{\infty} C_n^{(\psi-p)}(m_{\psi\perp}) \cos(n\phi). \quad (22)$$

These coefficients can be analytically evaluated only in the small- $m_{\psi\perp}$ limit, for which

$$I_{\psi-p}(m_{\psi\perp}, \phi) = \ln \frac{1}{m_{\psi\perp}^2} - 2 \cos(\phi) \left(\ln \frac{1}{m_{\psi\perp}^2} + 2 \ln(4) - 2 \right) + 2 \cos(2\phi) \left(\ln \frac{1}{m_{\psi\perp}^2} - 1 \right) + \dots \quad (23)$$

Fig. 5 shows the dependence of the first three coefficients with respect to $m_{\psi\perp}$, together with the reliability of the approximation introduced in Eq. (23).

Integral of $S_g(k_j, k_\psi)$. Compared to the previous functions, deriving the azimuthal distribution arising from $S_g(k_j, k_\psi)$ requires some extra care. Firstly, we recast the function as follows

$$S_g(k_j, k_\psi) = \frac{2(k_j \cdot k_\psi)}{(k_j \cdot k_g)(k_\psi \cdot k_g)} \approx \frac{2}{|\vec{k}_{g\perp}|^2} \frac{\sqrt{1+m_{\psi\perp}^2} \cosh(\Delta y) + 1}{\left[\cosh(\Delta y_g) - \cos(\phi) \right] \left[\sqrt{1+m_{\psi\perp}^2} \cosh(\Delta y_{g\psi}) + \cos(\phi) \right]} = \frac{2}{|\vec{k}_{g\perp}|^2} \left(\frac{\cos(\phi)}{\cosh(\Delta y_g) - \cos(\phi)} - \frac{\cos(\phi)}{\sqrt{1+m_{\psi\perp}^2} \cosh(\Delta y_{g\psi}) + \cos(\phi)} + \widehat{S}_g(k_j, k_\psi) \right), \quad (24)$$

where we remark that $\Delta y = y_\psi - y_j$, $\Delta y_g = y_g - y_j$ and $\Delta y_{g\psi} = y_j - y_\psi$, with y_j , y_ψ and y_g being respectively the jet, J/ψ and emitted soft gluon rapidities. The first two terms in the last line of Eq. (24) coincide with the last

terms of Eqs. (15) and (19), respectively, and thus remove the double counting in the azimuthal dependences. The last term, which is explicitly given by

$$\widehat{S}_g(k_j, k_\psi) = \frac{1 + \sqrt{1 + m_{\psi\perp}^2} \cosh(\Delta y)}{\cosh(\Delta y_g) + \sqrt{1 + m_{\psi\perp}^2} \cosh(\Delta y_{g\psi})} \left(\frac{1}{\cosh(\Delta y_g) - \cos(\phi)} + \frac{1}{\sqrt{1 + m_{\psi\perp}^2} \cosh(\Delta y_{g\psi}) + \cos(\phi)} \right) - \frac{\left(\cosh(\Delta y_g) + \sqrt{1 + m_{\psi\perp}^2} \cosh(\Delta y_{g\psi}) \right) \cos(\phi)}{\cosh(\Delta y_g) + \sqrt{1 + m_{\psi\perp}^2} \cosh(\Delta y_{g\psi})} \left(\frac{1}{\cosh(\Delta y_g) - \cos(\phi)} - \frac{1}{\sqrt{1 + m_{\psi\perp}^2} \cosh(\Delta y_{g\psi}) + \cos(\phi)} \right), \quad (25)$$

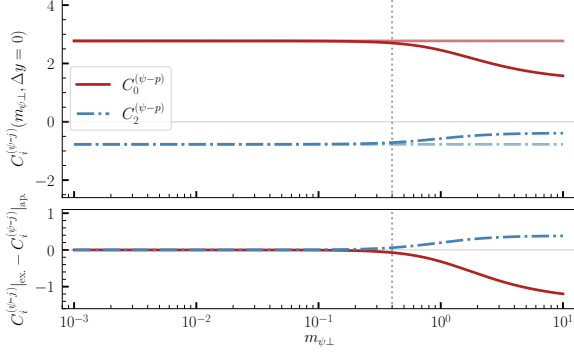


FIG. 6. Dependence of the first coefficients of Eq. (29) with respect to $m_{\psi\perp}$ and for $\Delta y = 0$. The coefficient C_1 , being zero, is not shown here. Vertical dotted line corresponds to $m_{\psi\perp} = 0.4$. Panels follow the same logic as Fig. 4.

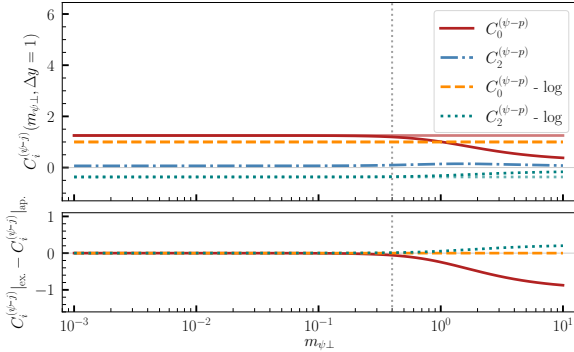


FIG. 7. Same as Fig. 6 but for $\Delta y = 1$. At variance with the previous figure, we have that the coefficients include extra logarithms (see Eq. (30)), which are shown separately.

produces the unique azimuthal distribution of $S_g(k_j, k_\psi)$.

Therefore, we identify the azimuthal distribution driven by the first two terms as

$$I_{\psi-j}(R, m_{\psi\perp}, \phi) = \int dy_g \left(\frac{\cos(\phi)}{\cosh(\Delta y_g) - \cos(\phi)} - \frac{\cos(\phi)}{\sqrt{1 + m_{\psi\perp}^2} \cosh(\Delta y_{g\psi}) + \cos(\phi)} \right), \quad (26)$$

which is independent of Δy and part of I_ψ in Eq. (7) (see also the end of this section), while the last term gives

$$I_{\psi-j}(m_{\psi\perp}, \Delta y, 2\phi) = \int dy_g \widehat{S}_g(k_j, k_\psi), \quad (27)$$

which is exactly the same of Eq. (7). Moreover, $S_g(k_j, k_\psi)$ provides another azimuthal distribution when evaluated within the jet region

$$I_{\psi-j}^{\text{jet}}(R, m_{\psi\perp}, \Delta y, \phi) = \frac{|\vec{k}_{g\perp}|^2}{2} \int d\Delta y_g S_g(k_j, k_\psi) \Theta(\Delta_{k_j k_\psi} < R^2). \quad (28)$$

Among these three distribution, Eq. (27) is the most interesting. Note that this distribution only contributes to the even modes of the Fourier expansion and does not depend on the jet variable R , since the integration of $\widehat{S}_g(k_j, k_\psi)$ is continuous at $\phi = 0$. However, it presents an additional dependence on the rapidity difference Δy , which affects its harmonic expansion, given by

$$I_{\psi-j}(m_{\psi\perp}, \Delta y, 2\phi) = C_0^{(\psi-j)}(m_{\psi\perp}, \Delta y) + 2 \sum_{n=1}^{\infty} C_{2n}^{(\psi-p)}(m_{\psi\perp}, \Delta y) \cos(2n\phi). \quad (29)$$

In particular, depending on the value of Δy we can have additional logarithms of \hat{u}/\hat{t} within the coefficients. Moreover, the closer the two outgoing particles are to the production axis (namely $|\Delta y| \rightarrow \infty$), the less relevant the angular distribution in $I_{\psi-j}(m_{\psi\perp}, \Delta y, 2\phi)$ becomes, with its sole contribution being restricted to the logarithm of \hat{u}/\hat{t} in the constant term. To see this effect, we consider the analytical expansion in the small- $m_{\psi\perp}$ limit for two values of Δy , namely $\Delta y = 0$ and $\Delta y = 1$:

$$\begin{aligned}
I_{\psi-j}(m_{\psi\perp}, \Delta y = 0, 2\phi) &= 2 \ln(4) - 4 \cos(2\phi) (\ln(4) - 1) + \dots, \\
I_{\psi-j}(m_{\psi\perp}, \Delta y = 1, 2\phi) &= 2 \left[2 \left(\ln(1+e) - 1 \right) - \ln \frac{\hat{u}}{\hat{t}} - \frac{1}{2} \ln \frac{1 - M_\psi^2/\hat{u}}{1 - M_\psi^2/\hat{t}} \right] \\
&\quad - \frac{4}{e} \cos(2\phi) \left[(1+e^2) \left(\ln(1+e) - 1 \right) + e - \ln \frac{\hat{u}}{\hat{t}} - \frac{1}{2} \ln \frac{1 - M_\psi^2/\hat{u}}{1 - M_\psi^2/\hat{t}} \right] + \dots
\end{aligned} \tag{30}$$

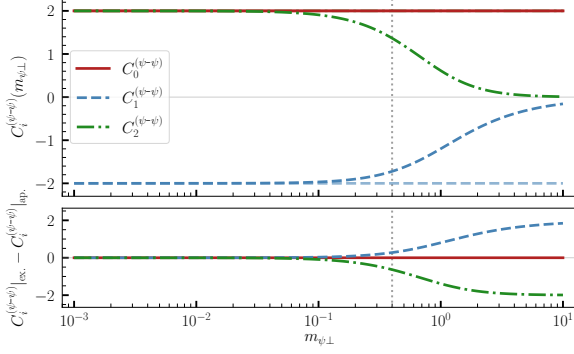


FIG. 8. Dependence of the first coefficients of Eq. (34) with respect to $m_{\psi\perp}$. Note that the coefficient C_0 does not vary with $m_{\psi\perp}$. Vertical dotted line corresponds to $m_{\psi\perp} = 0.4$. Panels follow the same logic as Fig. 4.

The complete dependence of the first coefficients of Eq. (29) for the same values of Δy is shown in Figs. 6 and 7.

Integral of $S_g(k_\psi, k_\psi)$. The function $S_g(k_\psi, k_\psi)$, non-zero only for massive particles, is given by

$$\begin{aligned}
S_g(k_\psi, k_\psi) &\approx \frac{2}{|\vec{k}_{g\perp}|^2 \left(\sqrt{1 + m_{\psi\perp}^2} \cosh(\Delta y_{g\psi}) + \cos(\phi) \right)^2}, \tag{31}
\end{aligned}$$

where we recall that $m_{\psi\perp} = M_\psi/|\vec{P}_\perp|$ with M_ψ being the J/ψ mass, and $\Delta y_{g\psi}$ is the rapidity difference between the soft gluon and the quarkonium.

The azimuthal distribution arising from $S_g(k_\psi, k_\psi)$ is identify by

$$\begin{aligned}
I_{\psi-\psi}(m_{\psi\perp}, \phi) &= \int d\Delta y_{g\psi} \frac{m_{\psi\perp}^2}{\left(\sqrt{1 + m_{\psi\perp}^2} \cosh(\Delta y_{g\psi}) + \cos(\phi) \right)^2}, \tag{32}
\end{aligned}$$

Moreover, when evaluated within the jet region, $S_g(k_\psi, k_\psi)$ generates

$$\begin{aligned}
I_{\psi-\psi}^{\text{jet}}(R, m_{\psi\perp}, \Delta y, \phi) &= \frac{|\vec{k}_{g\perp}|^2}{2} \int d\Delta y_g S_g(k_\psi, k_\psi) \Theta(\Delta_{k_g k_j} < R^2). \tag{33}
\end{aligned}$$

The harmonic expansion of Eq. (32), following that of Eq. (8), is given by

$$\begin{aligned}
I_{\psi-\psi}(m_{\psi\perp}, \phi) &= C_0^{(\psi-\psi)}(m_{\psi\perp}) + 2 \sum_{n=1}^{\infty} C_n^{(\psi-\psi)}(m_{\psi\perp}) \cos(n\phi). \tag{34}
\end{aligned}$$

It is interesting to notice that these coefficients are non-zero for all $m_{\psi\perp}$. In particular, we have residual contributions in the small- $m_{\psi\perp}$ limit, with $C_0^{(\psi-\psi)}, C_2^{(\psi-\psi)} \rightarrow 2$ and $C_1^{(\psi-\psi)} \rightarrow -2$, which is expected due to the singular behaviour of $I_{\psi-\psi}$ at $\phi = \pi$.

For completeness, Fig. 8 shows the exact dependence of the coefficients on $m_{\psi\perp}$. From this figure we understand that $C_0^{(\psi-\psi)}$ is independent of $m_{\psi\perp}$, whereas $C_1^{(\psi-\psi)}$ and $C_2^{(\psi-\psi)}$ are negligible when $m_{\psi\perp} \approx 1$.

Overall azimuthal distribution. By combining all the soft gluon emission evaluated above, one gets the differential cross section as a function of q_\perp given in Eq. (9), where the expansion in terms of $\cos(n\phi)$ harmonics has already being performed. The coefficients of this expansion depend on the production mechanism considered. For the CS channel, we have that $C_n^{(1)}$ are directly related to the Fourier expansion of I_j in Eq. (5). On the other hand, in the CO channel the coefficients $C_n^{(8)}$ are driven by all distributions in Eq. (7). More specifically, we have:

- $I_\psi(m_{\psi\perp}, \phi) = I_{\psi-p}(m_{\psi\perp}, \phi) - \frac{1}{2} I_{\psi-\psi}(m_{\psi\perp}, \phi)$;
- $I_{\psi-j}(R, m_{\psi\perp}, \Delta y, 2\phi)$ is given in Eq. (27);
- $I_\psi^{\text{jet}} = I_{\psi-p}^{\text{jet}} + I_{\psi-j}^{\text{jet}} - I_{\psi-\psi}^{\text{jet}} - I_j^{\text{jet}}(R, \phi)$, where I_j^{jet} is the contribution of I_j inside the jet region (namely the term in the second line of Eq. (16)).

In Fig. 9 we present the dependence of the coefficients with respect to R and $m_{\psi\perp}$ for $\Delta y = 0$. From a direct comparison between the CS and CO channels, it is evident that predictions that include the CO mechanism are significantly different from those exclusively driven by the CS one.

II. AZIMUTHAL ASYMMETRIES IN THE CS AND CO CHANNELS SEPARATELY

In this section we present direct comparisons between the CS and CO mechanisms, providing more insights on

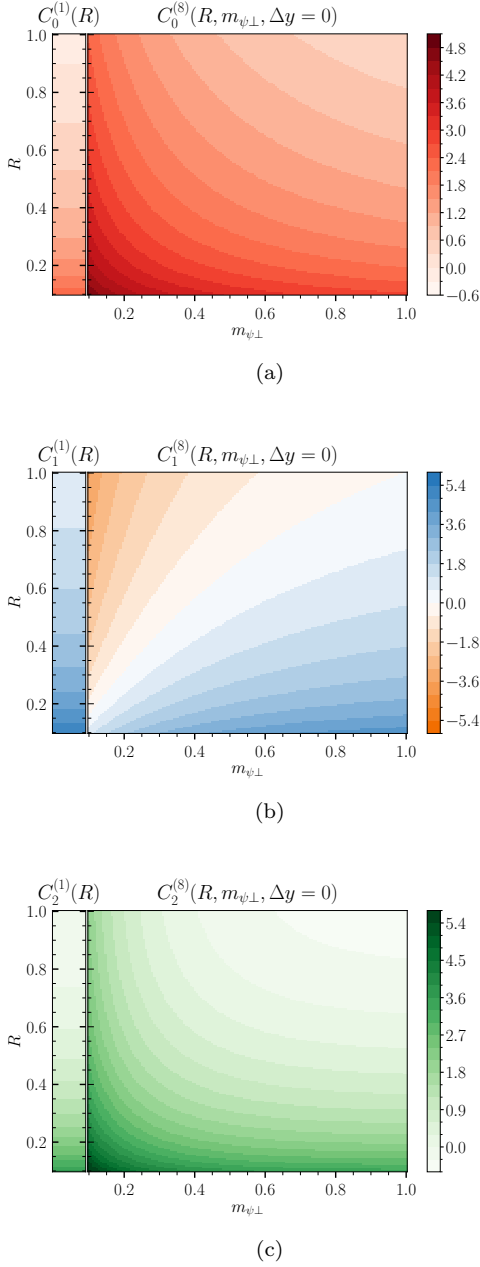


FIG. 9. Dependence of the first coefficients on the jet size R and the variable $m_{\psi\perp}$ in the CO channel for transverse production ($\Delta y = 0$). A comparison with the CS channel, for which coefficients solely depend on R , is given by the column on the left.

the results shown in Fig. 3.

In Fig. 10 we present the normalized differential cross section within both the CS and CO channels and for the same kinematics considered for Fig. 3. The CO channel has a much wider distribution as compared to the CS one as a result of the final state gluon radiation associated with the heavy quark pair, which leads to a significant difference in the associated $C_0^{(c)}$ coefficients (see Table I). Note that, although the normalized distribu-

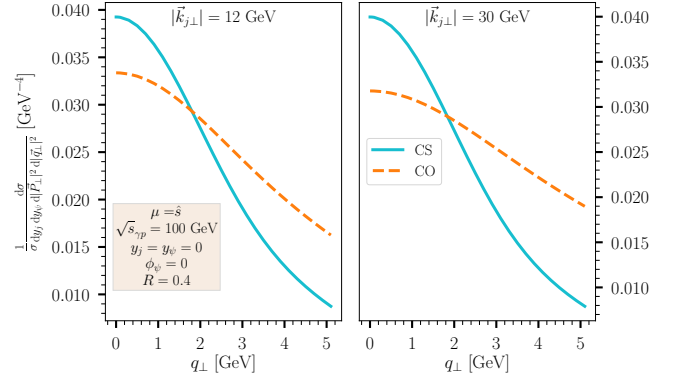


FIG. 10. Normalized differential cross section of isotropic J/ψ plus jet photoproduction at $\sqrt{s}_{\gamma p} = 100 \text{ GeV}$ in a frame where the azimuthal angle of \vec{P}_{\perp} is zero and $y_j = y_{\psi} = 0$. We considered two values of $|\vec{k}_{j\perp}|$, while $R = 0.4$. Solid cyan lines are obtained employing the CS channel, whereas the dashed orange lines the CO one.

tions are similar for the two values of $|\vec{k}_{j\perp}|$ taken, the differential cross sections decrease significantly (approximately by an order of magnitude). It is worth mentioning that Fig. 10 is obtained for $y_j = y_{\psi} = 0$ and different rapidities values can slightly modify the picture, e.g. less broadened distributions for $y_j = 1$. Nonetheless, other choices of y_j and y_{ψ} do not spoil the main conclusion of Fig. 10, namely that we identify different shapes of the normalized differential cross sections within the CS and CO mechanisms.

Moving to the asymmetries, in Fig. 11 we present, as functions of q_{\perp} and for the same kinematic choices of Fig. 3, $\langle \cos(\phi) \rangle$ and $\langle \cos(2\phi) \rangle$ predictions in the CS and CO channels. For comparison, we also show the fixed-order results. In this figure, the behaviors of the resummed asymmetries within the CS and CO mechanisms are analogous to those of the CSM and NRQCD in Fig. 3. Thus, we may conclude that the NRQCD outcomes are mostly driven by the CO channel, at least for the kinematics considered.

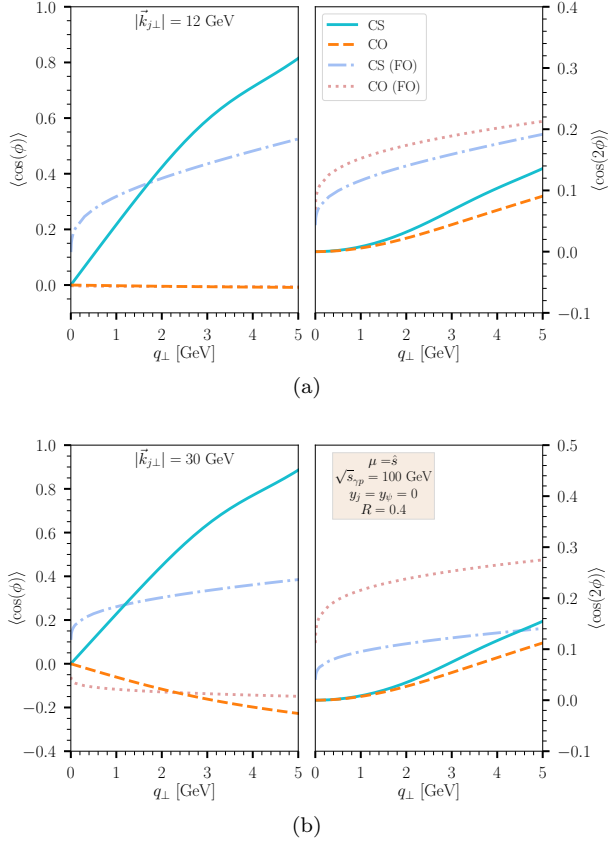


FIG. 11. Averaged azimuthal asymmetries for J/ψ plus jet photoproduction at $\sqrt{s_{\gamma p}} = 100$ GeV obtained within the CS (solid cyan line) and CO (dashed orange line) mechanisms. The dash-dotted blue and dotted red lines are the fixed-order results for the CS and CO channels, respectively. The curves in the top panel (11a) are evaluated at $|\vec{k}_{j\perp}| = 12$ GeV, whereas those in the bottom panel (11b) at $|\vec{k}_{j\perp}| = 30$ GeV. Jet size is $R = 0.4$ in both panels.

Constraints from the Neutron EDM on Subleading Effective Operators for Direct Dark Matter Searches

Manuel Drees,^a Rahul Mehra^{a,1}

^a*Bethe Center for Theoretical Physics and Physikalisches Institut, Universität Bonn, Nussallee 12, D-53115 Bonn, Germany*

E-mail: drees@th.physik.uni-bonn.de, rmehra@physik.uni-bonn.de

ABSTRACT: Interactions between Dark Matter (DM) and nucleons relevant for direct search experiments can be organised in a model independent manner using a Galilean invariant, non-relativistic effective field theory (NREFT). Here one expands the interactions in powers of the momentum transfer \vec{q} and DM velocity \vec{v} . This approach generates many operators. The potentially most important subleading operators are odd under T , and can thus only be present in a theory with CP violating interactions. We consider two such operators, called \mathcal{O}_{10} and \mathcal{O}_{11} in the literature, in simplified models with neutral spin-0 mediators; the couplings are chosen such that the coefficient of the leading spin-independent (SI) operator, which survives for $\vec{v} \rightarrow 0$, vanishes at tree level. However, it is generically induced at the next order in perturbation theory. We perform a numerical comparison of the number of scattering events between interactions involving the T -odd operators and the corresponding loop induced SI contributions. We find that for “maximal” CP violation the former can dominate over the latter. However, in two of the three models we consider, an electric dipole moment of the neutron (nEDM) is induced at two-loop order. We find that the experimental bound on the nEDM typically leads to undetectably small rates induced by \mathcal{O}_{10} . On the other hand, the model leading to a nonvanishing coefficient of \mathcal{O}_{11} does not induce an nEDM.

¹Corresponding author.

Contents

1	Introduction	1
2	NREFT and Simplified Models	4
2.1	Model I	6
2.2	Model II	10
2.2.1	Model IIa	11
2.2.2	Model IIb	14
2.3	The Neutron EDM	16
3	Results and Discussions	18
4	Summary and Conclusions	29
A	1-loop calculations	32
A.1	Model I Matrix Element	32
A.1.1	Model I Loop Functions	34
A.2	Model IIa and IIb Matrix Elements	35
A.2.1	Model IIa and IIb Loop Functions	39
B	2-Loop Calculations	42

1 Introduction

The search for non-gravitational interactions of Dark Matter (DM) has not yielded a convincing signal so far. This is in stark contrast with the accumulated evidence for its gravitational interactions across a broad range of astrophysical length scales. Direct searches aim to detect non-gravitational interactions by observing the recoil of a target nucleus after an incoming DM particle has scattered off it. Terrestrial experiments using this search principle have led to tight constraints on the DM mass and cross-section parameter space [1–14]. For the past few decades such experimental efforts have focused on particle DM with weak scale interactions termed as Weakly Interacting Massive Particles (WIMPs). WIMPs can be produced in the early universe through freeze-out from the thermal plasma, which yields the observed DM relic abundance [15] for very roughly electroweak strength effective couplings. This has made WIMPs a particularly compelling category of DM candidates.

In order to interpret the results of direct search experiments one has to make assumptions regarding the nature of the interaction between DM and nucleons. Traditionally it was assumed that DM-nucleon interactions are dominated by just two operators describing spin independent (SI) and spin dependent (SD) interactions in the limit of zero WIMP velocity

[16]. These SI and SD operators are the leading terms of an EFT description, which is an expansion in powers of small parameters such as the DM velocity v and three momentum transfer scaled by the nucleon mass \vec{q}/m_N . Since $v/c \lesssim \mathcal{O}(10^{-3})$ in the solar neighborhood, the momentum transfer is restricted to $|\vec{q}| \lesssim \mathcal{O}(100 \text{ MeV})$. Although the momentum exchange can be substantial on nuclear physics scales, it is far below the electroweak scale, and also below the range of WIMP masses most direct search experiments can probe. Hence, it is reasonable to expect that the canonical SI and SD interactions (zeroth order terms) dominate the EFT expansion.

A detailed non-relativistic effective field theory (NREFT) description of elastic DM–nucleus scattering retains NLO and NNLO terms by modeling the nucleus as a spatially extended composite particle with spin and charge densities [17–20]. For WIMPs of spins 0 or 1/2, truncating the EFT expansion at second order generates a total of 14 operators.¹ Since these higher order terms vanish for $v \rightarrow 0$, they lead to a spectrum of recoil energies quite different from the usual quasi-exponential fall-off, often preferring energies larger than the typical range of values implemented for SI and SD searches in experiments [23]. Multiple experiments have now extended their recoil energy search window in order to optimize the search strategy in the NREFT framework [24–33].

The NREFT contains, at least, 28 free parameters when the operators for neutrons and protons are counted separately. Probing this large parameter space is an arduous task. A number of global analyses using data from current and planned direct detection experiments have placed upper limits on the coupling strengths in this multi-dimensional parameter space [34–40]. A common conclusion drawn from these global analyses is that experiments are nearly as sensitive to some momentum- or velocity-dependent operators that are odd under P (parity) and T (time reversal) transformations as they are to the leading SD operator. These subleading operators have been scrutinized less in the literature. It is therefore interesting to study the phenomenology of models where they are generated in the non-relativistic (NR) limit, and to understand when these operators can dominate over the traditional SI and SD interactions.

The CPT theorem [41, 42] implies that every T -odd NREFT operator must arise from a CP -violating (CPV) quantum field theory, where C refers to charge conjugation. However, there are extremely stringent experimental constraints on CP violation [43], which can be used to place constraints on such NREFT operators. The electric dipole moment of the neutron (nEDM) is one such observable. The sensitivity of current experiments [44–46] is several orders of magnitude above the prediction of the standard model of particle physics (SM), but they provide tight constraints on flavor diagonal CP violation in extensions of the SM. The experimental upper limit on the nEDM is

$$|d_n| < 1.8 \times 10^{-26} \text{ e} \cdot \text{cm} \quad (90 \% \text{ C.L.}) . \quad (1.1)$$

There have been a number of articles linking extensions of the SM to low energy NREFT operators [47–49]. In particular, Ref. [47] lists a set of simplified models for scalar, spinorial and vector DM candidates and derives the full set of NREFT operators in terms of the

¹The set of NREFT operators is substantially enlarged for WIMPs of higher spin [21, 22].

parameters for each simplified model. However, it is worth noting that most extensions of the SM only generate a small subset of the NREFT operators. Moreover, in most cases the leading order operators describing the SI and SD interactions are generated as well, and will then typically dominate. However, it is conceivable that the standard operators are strongly suppressed, in which case formally subleading operators actually provide the dominant contribution to scattering.

In Ref. [50], we considered simplified models with charged mediators, which are exchanged in the s -channel in DM-nucleon scattering. We found that suppressing the leading SI operator required finetuning of couplings; moreover, the bound on the nEDM, which is generated at one-loop in these models, implies that the subleading operators lead to undetectably small DM scattering rates. The P -odd, T -odd operators can thus be neglected in such scenarios.

In this article, we consider models that augment the SM by a WIMP candidate and a mediator particle which does not carry electric or color charge; DM-nucleon scattering then proceeds via t -channel diagrams. If one allows all couplings that respect the $SU(3)_C \times U(1)_{\text{em}}$ gauge symmetry of the simplified Lagrangian, the leading SI term will be generated at tree level. However, the coefficient of this operator can be “switched off” by setting relevant coupling(s) to zero. This is an ad hoc choice, which cannot be justified by any symmetry. In this case, at the lowest order in perturbation theory, these models generate the P -odd, T -odd operators \mathcal{O}_{10} or \mathcal{O}_{11} without giving rise to the leading order operators. However, since the vanishing of the coefficient of the leading SI operator is not enforced by a symmetry, it will usually be generated at the next order in perturbation theory. Since now the contribution from the leading operator to DM-nucleon scattering is loop suppressed² while the contributions from \mathcal{O}_{10} and \mathcal{O}_{11} are suppressed by powers of v or $|\vec{q}|/m_N$, it is not a priori obvious which contribution is more important. We therefore numerically compare these contributions to the total number of events for a Xenon target. We find that for large regions in the parameter space of these models, the subleading P -odd, T -odd operators actually dominate over the SI term if the latter is purely loop-induced.

However, in models where tree level interactions generate only \mathcal{O}_{10} , we find that an nEDM is generically induced at two-loop order. The resulting upper bound on the couplings then again leads to unobservably small scattering rates, so that contributions from \mathcal{O}_{10} to DM-nucleon scattering can be neglected. On the other hand, in the model where \mathcal{O}_{11} is generated at tree level, the CP violation is restricted to the dark sector, and no nEDM is generated (apart from the tiny SM contribution). This case then provides an example of an NLO operator dominating over the traditional SI operator in DM-nucleon scattering, at least at the level of a simplified model.

The remainder of this article is organized as follows. In Section 2, we provide a brief introduction to the NREFT formalism, and introduce three CP violating simplified models

²For a purely pseudoscalar mediator, loop-induced contributions to \mathcal{O}_1 typically dominate the DM scattering rate [51–54]. However, the mediator has to have both scalar and pseudoscalar couplings in order to generate \mathcal{O}_{10} or \mathcal{O}_{11} . A light mediator with general CP phases was considered in ref.[55], but constraints on these phases from EDMs were not considered, minimal flavor violation was assumed, and a trilinear coupling of the mediator to the SM Higgs boson was introduced.

yielding the P - and T -odd NREFT operators. We also compute the loop diagrams for WIMP–nucleon scattering that give rise to the leading SI operator in the non-relativistic limit. We then match the different scattering contributions to the corresponding four-field effective operators and finally match these to the set of NREFT operators. We also compute the two-loop Feynman diagrams that induce a nEDM and discuss the implications for the corresponding P -, T -odd operator in the NREFT. In Section 3 we compute the number of events for a Xenon target for the three simplified models. We discuss our main numerical results, comparing the contributions of the NREFT operators to elastic WIMP–nucleon scattering. We conclude in Section 4. Details of our loop computations are given in Appendices A and B.

2 NREFT and Simplified Models

A non-relativistic effective field theory (NREFT) of elastic scattering between DM and nuclei exhaustively categorizes the possible interactions involved in direct searches. An incoming DM particle striking a target nucleus on Earth is quite slow in the detector rest frame, $v/c \sim \mathcal{O}(10^{-3})$, and therefore a non-relativistic EFT can be used to describe the scattering. This simplifies the nuclear physics required to compute the scattering rate, which is nevertheless rather nontrivial [18]. Traditionally only the leading terms were kept, which remain finite as $v \rightarrow 0$ [16]. The first and second order terms in DM velocity v and momentum transfer \vec{q}/m_N (in units of the nucleon mass) were considered only relatively recently [18–20, 49, 56]. In the following we briefly summarize the salient points.

In this NREFT elastic DM–nucleon scattering is described using a basis of operators constructed from the following Hermitian quantities invariant under Galilean transformations:

$$i\vec{q}, \quad \vec{v}^\perp \equiv \vec{v} + \frac{\vec{q}}{2\mu_N}, \quad \vec{S}_N, \quad \vec{S}_\chi. \quad (2.1)$$

Here $\mu_N = m_N m_{\text{DM}} / (m_N + m_{\text{DM}})$ is the reduced mass of the DM–nucleon system. Energy conservation implies that the transverse velocity \vec{v}^\perp is orthogonal to the momentum transfer \vec{q} . \vec{S}_N and \vec{S}_χ are the spin of the nucleon and the WIMP χ ; of course, the latter may be zero. Using these four building blocks, and only imposing Galilean invariance, one obtains a set of linearly independent operators \mathcal{O}_i when the EFT is truncated at second order in the expansion parameter \vec{q}/m_N . Table 1 lists this set of 14 operators; the operators \mathcal{O}_1 and \mathcal{O}_4 describe the traditional leading SI and SD interaction, respectively. Note that the coefficients of these operators are in general different for neutrons and protons.

No invariance under any discrete symmetry was imposed in the construction of the NREFT operators. Their behavior under discrete transformations, in particular parity (P) and time reversal (T), can thus be used to classify the operators. A parity transformation corresponds to $\vec{q} \rightarrow -\vec{q}$, $\vec{v}^\perp \rightarrow -\vec{v}^\perp$, while \vec{S}_N and \vec{S}_χ , being pseudovectors, remain unchanged. On the other hand, under time reversal, all four vectors listed in (2.1) change sign, and in addition $i \rightarrow -i$ (i.e. the Hermitian operator $i\vec{q}$ remains unchanged). This leads to the following

$$\begin{aligned}
\mathcal{O}_1 &= 1_{\chi} 1_N; & \mathcal{O}_6 &= \left(\frac{\vec{q}}{m_N} \cdot \vec{S}_N \right) \left(\frac{\vec{q}}{m_N} \cdot \vec{S}_\chi \right); & \mathcal{O}_{10} &= i \frac{\vec{q}}{m_N} \cdot \vec{S}_N; \\
\mathcal{O}_3 &= i \vec{S}_N \cdot \left(\frac{\vec{q}}{m_N} \times \vec{v}^\perp \right); & \mathcal{O}_7 &= \vec{S}_N \cdot \vec{v}^\perp; & \mathcal{O}_{11} &= i \frac{\vec{q}}{m_N} \cdot \vec{S}_\chi; \\
\mathcal{O}_4 &= \vec{S}_\chi \cdot \vec{S}_N; & \mathcal{O}_8 &= \vec{S}_\chi \cdot \vec{v}^\perp; & \mathcal{O}_{12} &= \vec{S}_\chi \cdot (\vec{S}_N \times \vec{v}^\perp); \\
\mathcal{O}_5 &= i \vec{S}_\chi \cdot \left(\frac{\vec{q}}{m_N} \times \vec{v}^\perp \right); & \mathcal{O}_9 &= i \vec{S}_\chi \cdot \left(\vec{S}_N \times \frac{\vec{q}}{m_N} \right); & \mathcal{O}_{13} &= i (\vec{S}_\chi \cdot \vec{v}^\perp) \left(\frac{\vec{q}}{m_N} \cdot \vec{S}_N \right); \\
& & \mathcal{O}_{14} &= i (\vec{S}_N \cdot \vec{v}^\perp) \left(\frac{\vec{q}}{m_N} \cdot \vec{S}_\chi \right)
\end{aligned}$$

Table 1: List of operators in the NREFT for elastic WIMP–nucleon scattering. We adopt the conventions of [20] by defining the operators normalized by the nucleon mass m_N in order to have a dimensionless basis. We omit the invariant $\mathcal{O}_2 = v_\perp^2$ because it is a second order correction to the SI operator \mathcal{O}_1 , as well as $\mathcal{O}_{15} = -\left(\vec{S}_\chi \cdot \frac{\vec{q}}{m_N}\right) \left((\vec{S}_N \times \vec{v}^\perp) \cdot \frac{\vec{q}}{m_N}\right)$ since it generates a cross section of order v_T^6 , which is N³LO.

classification:

$$\begin{aligned}
\mathcal{O}_1, \mathcal{O}_3, \mathcal{O}_4, \mathcal{O}_5, \mathcal{O}_6 &: P\text{-even and } T\text{-even,} \\
\mathcal{O}_7, \mathcal{O}_8, \mathcal{O}_9 &: P\text{-odd and } T\text{-even,} \\
\mathcal{O}_{13}, \mathcal{O}_{14} &: P\text{-even and } T\text{-odd,} \\
\mathcal{O}_{10}, \mathcal{O}_{11}, \mathcal{O}_{12} &: P\text{-odd and } T\text{-odd.}
\end{aligned}$$

The P and T quantum numbers of the NREFT operators must match those of the relativistic operators generating them. In particular, the CPT theorem stipulates that only a CP violating quantum field theory with a DM candidate can yield any of the T -odd operators. Out of those, the operators \mathcal{O}_{12} , \mathcal{O}_{13} and \mathcal{O}_{14} are not generated in scenarios with t -channel mediator with spin ≤ 1 ;³ the latter two operators anyway contribute little to the scattering cross section if all operators have coefficients of similar size [39]. Therefore, we focus on \mathcal{O}_{10} and \mathcal{O}_{11} in the following.

Connecting a relativistic model for DM leading to specific DM–quark and/or DM–gluon interactions with the NREFT in general involves two steps. First, one integrates out the heavy mediator(s), where “heavy” here refers to all mediators ϕ with mass m_ϕ well above 100 MeV, which is the maximal three-momentum exchange in DM–nucleus scattering.⁴ This results in relativistic but non-renormalizable four-field DM–quark and/or DM–gluon operators. In the second step one takes the non-relativistic limit of these four-field operators and matches them onto the NREFT operators listed in Table 1. This leads to an effective Lagrangian containing some (or all) of these operators, with coefficients determined by the couplings and masses of the original relativistic theory. The computation of DM–nucleus

³ \mathcal{O}_{12} can be generated in a model with a spin-1/2 WIMP and spin-0 s -channel mediator, but the constraint from the nEDM forces this contribution to be negligible [50].

⁴In order to include light mediators in the NREFT the differential cross section should be multiplied with $[m_\phi^2/(m_\phi^2 + \vec{q}^2)]^2$; this will lead to a softening of the recoil spectrum for $\vec{q}^2 \gtrsim m_\phi^2$.

scattering rates from these coefficients involves numerous nuclear “response functions”; we refer to ref.[20], whose expressions we used in our own numerical code.

As already mentioned, the NREFT is an expansion in powers of v or \vec{q} . If all coefficients in the NREFT are of comparable magnitude, the total scattering rate typically receives the largest contribution from the SI operator \mathcal{O}_1 , which is of zeroth order in the expansion. Moreover, this contribution is enhanced by A^2 , where A is the nucleon number. For large momentum exchange, $|\vec{q}| \gtrsim 1/r_N$ where r_N is the radius of the target nucleus, the rate is somewhat suppressed by a form factor, but even without form factor this contribution to the scattering rate peaks at $|\vec{q}| \rightarrow 0$.

\mathcal{O}_4 is also of zeroth order in the expansion. However, since the spins of the nucleons largely cancel in any given nucleus, there is no A^2 enhancement; in fact, \mathcal{O}_4 does not contribute at all if the target nucleus has no spin.

As already noted, for sufficiently heavy DM particle (and target nucleus) the three-momentum exchange can reach $|\vec{q}| \sim 100$ MeV. In this high momentum exchange region of phase space the operators that are linear in \vec{q} and independent of \vec{v}^\perp are therefore only suppressed by a factor ~ 0.1 ; these are the operators \mathcal{O}_{10} and \mathcal{O}_{11} which are the focus of our study.⁵ The contribution from \mathcal{O}_{11} is A^2 enhanced, up to a form factor, but requires the DM particle to carry spin. The contribution from \mathcal{O}_{10} suffers similar cancellations as that from \mathcal{O}_4 , but can survive even for scalar DM particle.

Naively the contributions of operators involving \vec{v}^\perp should be suppressed by a factor $v^2 \sim 10^{-6}$; indeed, compared to the contribution from \mathcal{O}_1 this is almost true. However, the richer structures can lead to nuclear response $\propto \vec{S}_N \cdot \vec{L}_N$ [20], \vec{L}_N being the orbital angular momentum of a given nucleon; in this product the contributions of paired nucleons do *not* cancel. As a result, for heavy target nuclei and similar coefficients the contribution from \mathcal{O}_{12} often exceeds that from \mathcal{O}_4 [39]; however, as already noted \mathcal{O}_{12} is not generated in the models with neutral mediator that we consider in this article. Similarly, for equal coefficients \mathcal{O}_3 typically contributes almost as much as \mathcal{O}_{10} does [39], but \mathcal{O}_3 is not generated in leading order when starting from a relativistic theory [47]. \mathcal{O}_{10} and \mathcal{O}_{11} are therefore the potentially most important higher order NREFT operators that can be generated from a relativistic QFT.

After these preliminaries, we are ready to introduce the simplified models we consider in this analysis. Recall that, in the spirit of ref.[47], we only impose invariance under $SU(3)_C \times U(1)_{\text{em}}$, not under the complete gauge group of the SM.

2.1 Model I

Model I contains a complex spin-zero WIMP S and a real spin-zero mediator ϕ ; both are gauge singlets. We assume that the WIMP is odd and the mediator and all the SM particles are even under a new discrete symmetry \mathbb{Z}_2 . This forbids dark matter decay, but allows ϕ to couple to both S and to SM quarks q . The most general gauge invariant Lagrangian

⁵However, simplified models yielding \mathcal{O}_{11} in the non-relativistic limit always seem to result in the coefficient c_{11} containing an extra factor m_N/m_{DM} [47–50]; see also eq.(2.21) below. A discussion assuming m_{DM} independent Wilson coefficients therefore overestimates the importance of \mathcal{O}_{11} . Even with this caveat, \mathcal{O}_{11} remains the potentially most important non-leading NREFT operator for $m_{\text{DM}} \lesssim 100$ GeV.

respecting the new \mathbb{Z}_2 symmetry and keeping the real and imaginary parts of S degenerate thus is:⁶

$$\begin{aligned} \mathcal{L}^I = & (\partial_\mu S)^\dagger (\partial^\mu S) - m_S^2 S^\dagger S - \frac{\lambda_S}{2} (S^\dagger S)^2 + \frac{1}{2} \partial_\mu \phi \partial^\mu \phi - \frac{1}{2} m_\phi^2 \phi^2 - \frac{m_\phi \mu_1}{3} \phi^3 - \frac{\mu_2}{4} \phi^4 \\ & - g_1 m_S S^\dagger S \phi - \frac{g_2}{2} S^\dagger S \phi^2 - h_1^{ij} \phi \bar{q}_i q_j - i h_2^{ij} \phi \bar{q}_i \gamma^5 q_j . \end{aligned} \quad (2.2)$$

$U(1)_{\text{em}}$ invariance implies that the mediator ϕ can only couple to quarks with identical electric charge. Hence the quark flavor indices i and j in the Yukawa coupling matrices are restricted to the same quark type. However, non-vanishing couplings of the mediator to quarks of different generations generate flavor changing neutral currents (FCNC) processes at tree level. Experimental constraints arising from meson mixing along with rare flavor changing decays severely limit these flavor non-diagonal couplings. Therefore we assume that the Yukawa coupling matrices in eq.(2.2) are diagonal in flavor space, in particular $h_{1,2}^q \equiv h_{1,2}^{ii}$ where q denotes the quark flavor the mediator couples to.

In eq.(2.2) we have allowed both scalar and pseudoscalar couplings of ϕ to the SM quarks. However, if $g_1 h_1^q \neq 0$ there will be tree level contributions to \mathcal{O}_1 , which will then completely dominate WIMP–nucleus scattering, in which case the nonleading operators in the NREFT would not need to be considered. Moreover, $h_1^q h_2^q \neq 0$ for any quark q would yield an electric dipole moment of that quark at one-loop order, leading to very strong constraints on the parameters of the model. We therefore impose

$$h_1^q = 0 \quad \forall q . \quad (2.3)$$

We emphasize that this is completely ad hoc but necessary for considering the non-leading operators in the NREFT. In particular, it cannot be justified by any symmetry. In contrast, the requirement $h_2^q = 0$, which would also remove the EDMs but allow \mathcal{O}_1 , could be justified by demanding CP conservation. Nevertheless “switching off” \mathcal{O}_1 via eq.(2.3) is still less inelegant than requiring specific relations between non-zero couplings, as we had to do in our earlier analysis of models with charged s –channel mediators [50]. On the other hand, since eq.(2.3) cannot be enforced by a symmetry, we can already anticipate that higher order contributions will generate an effective h_1^q or, more generally, lead to nonvanishing \mathcal{O}_1 .

The matrix element for tree level t –channel scattering $S(p_S) + q(p_q) \rightarrow S(p'_S) + q(p'_q)$ is given by

$$\mathcal{M}_{Sq \rightarrow Sq}^I = - \frac{h_2^q g_1 m_S}{q^2 - m_\phi^2} \bar{u}(p'_q) i \gamma^5 u(p_q) . \quad (2.4)$$

For $|q^2| \ll m_\phi^2$ we can ignore the q^2 term in the ϕ propagator. The matrix element can then be matched on to a relativistic effective operator $S^\dagger S \bar{q} i \gamma^5 q$, which reduces to the operator \mathcal{O}_{10} in the non-relativistic limit.

For Model I, at the lowest order in perturbation theory, thus only the operator \mathcal{O}_{10} contributes to DM–nucleus scattering. However, at the next-to-leading order the one-loop

⁶Essentially identical results can be derived for a real spin-zero WIMP.

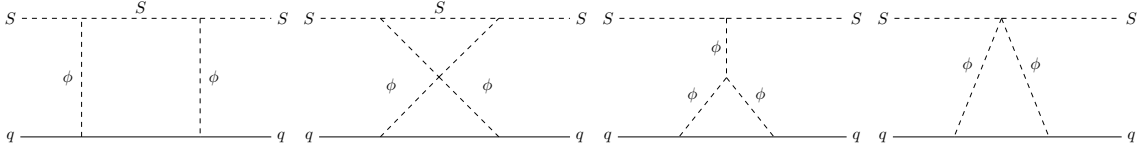


Figure 1: One-loop box and triangle Feynman diagrams in Model I which give contributions to \mathcal{O}_1 .

Feynman diagrams shown in Fig. 1 can induce contributions from the operator \mathcal{O}_1 . We use the Dirac equation and four-momentum conservation to write the resulting matrix elements in a form that is symmetric in DM momenta; see Appendix A.1 for details. The relativistic effective Lagrangian for Model I derived in this manner can be written as

$$\mathcal{L}_{\text{eff}}^{\text{I}} \supset c_{1,S}^{q,d5} S^\dagger S \bar{q}q + c_{10}^{q,d5} S^\dagger S \bar{q} i\gamma^5 q + c_{1,V}^{q,d6} i \left(S^\dagger \overleftrightarrow{\partial}_\mu S \right) \bar{q}\gamma^\mu q. \quad (2.5)$$

The Hermitean derivative on the complex scalars is defined as $iS^\dagger \overleftrightarrow{\partial}_\mu S \equiv \frac{i}{2}(S^\dagger \partial_\mu S - S \partial_\mu S^\dagger)$. The subscripts i on the quark-level Wilson coefficients $c_i^{q,dj}$ ($j = 5, 6$) denote the NREFT operator that the corresponding relativistic effective operator reduces; in case of \mathcal{O}_1 we have distinguished the coefficient $c_{1,S}$ of the product of two scalar currents from $c_{1,V}$ which multiplies the product of two vector currents. Finally, the superscripts $d5$ and $d6$ refer to field operators with mass dimension 5 and 6, respectively.

Table 2 describes the matching of the relativistic effective operators onto the NREFT operators in terms of the parameters of Model I. The Wilson coefficients for the dimension-5 operators $(S^\dagger S)(\bar{q}q)$ and $(S^\dagger S)(\bar{q}i\gamma^5 q)$ have been divided by a factor of m_S , i.e. these are coefficients of the dimension-6 operators $m_S(S^\dagger S)(\bar{q}q)$ and $m_S(S^\dagger S)(\bar{q}i\gamma^5 q)$; this ensures that the expressions for all DM-nucleon cross sections contain the same factor $\frac{\mu_{\chi N}^2}{\pi} (c_i^N)^2$ irrespective of the mass dimension of the relativistic operator involved. The loop functions $M_i(r, s)$ and $L_i(r)$ appearing in the box and triangle diagrams have been expressed as functions of dimensionless parameters $r \equiv m_q/m_\phi$ and $s \equiv m_S/m_\phi$. Analytical expressions for these loop functions for Model I, and their $m_q \rightarrow 0$ limits, can be found in Appendix A.1.1. The dimension-5 scalar-scalar operator $(S^\dagger S)(\bar{q}q)$ as well as the dimension-6 vector-vector operator $i \left(S^\dagger \overleftrightarrow{\partial}_\mu S \right) \bar{q}\gamma^\mu q$ both reduce to the leading order SI operator \mathcal{O}_1 in the non-relativistic limit. Only the box diagrams give rise to both vector-vector and scalar-scalar relativistic operators, whereas the two triangle diagrams yield only the scalar-scalar operator. The first triangle diagram could be described in terms of an effective, loop-generated coupling h_1^q , thereby confirming our expectation that the choice $h_1^q = 0$ is not technically natural; however, all four diagrams shown in Fig. 1 contribute at the same order in perturbation theory, and should therefore be included in a full NLO treatment. The loop-generated Wilson coefficients are all suppressed by the loop factor $1/16\pi^2$ compared to the tree level diagram. The loop functions M_i have mass dimension -4 while L_1 has mass dimension -2 , hence the quark-level Wilson coefficients c_i^q all have the same mass dimension -2 . Since the scalar-scalar operator violates chirality, the contributions to $c_{1,S}^{q,d5}$ are all $\propto m_q$.

	$S^\dagger \Gamma_S S \bar{q} \Gamma_q q$	c_i^q
Tree	$c_{10}^{q,d5} S^\dagger S \bar{q} i \gamma^5 q$	$\frac{h_2^q g_1}{m_\phi^2}$
Box	$c_{1,V,B}^{q,d6} i \left(S^\dagger \overleftrightarrow{\partial}_\mu S \right) \bar{q} \gamma^\mu q$	$\frac{(h_2^q)^2 g_1^2 m_S^2}{16\pi^2} M_1$
	$c_{1,S,B}^{q,d5} S^\dagger S \bar{q} q$	$\frac{(h_2^q)^2 g_1^2 m_S m_q}{16\pi^2} M_2$
Crossed	$c_{1,V,C}^{q,d6} i \left(S^\dagger \overleftrightarrow{\partial}_\mu S \right) \bar{q} \gamma^\mu q$	$-\frac{(h_2^q)^2 g_1^2 m_S^2}{16\pi^2} M_3$
Box	$c_{1,S,C}^{q,d5} S^\dagger S \bar{q} q$	$\frac{(h_2^q)^2 g_1^2 m_S m_q}{16\pi^2} M_4$
Triangle 1	$c_{1,S,T1}^{q,d5} S^\dagger S \bar{q} q$	$\frac{(h_2^q)^2 g_1 \mu_1 m_q}{16\pi^2 m_\phi} L_1$
Triangle 2	$c_{1,S,T2}^{q,d5} S^\dagger S \bar{q} q$	$-\frac{(h_2^q)^2 g_2 m_q}{16\pi^2 2m_S} L_1$

Table 2: Non-relativistic reduction of relativistic effective operators in Model I. The middle column gives the relativistic four-field operators that appear in the matrix element for WIMP–nucleon scattering. The right column gives the corresponding quark-level Wilson coefficient c_i^q of the relevant NREFT operators, where we have suppressed the dependence of the loop functions on dimensionless parameters, i.e. $M_i \equiv M_i(r, s)$ and $L_1 \equiv L_1(r)$ with $r \equiv m_q/m_\phi$ and $s \equiv m_S/m_\phi$. The first line contributes to the coefficient of \mathcal{O}_{10} , all other lines describe contributions $\propto \mathcal{O}_1$.

The quark bilinears in eq.(2.5) and Table 2 must be promoted to nucleon bilinears in order to describe DM–nucleon scattering. The quark-level Wilson coefficients therefore have to be combined with corresponding nucleon embedding factors in order to derive the Wilson coefficients at the nucleonic level [18, 57]. Including contributions from the box and the triangle diagrams, the nucleonic Wilson coefficient c_1^N of the NREFT operator \mathcal{O}_1 becomes:

$$\begin{aligned}
c_1^N|^{\text{I}} &= \frac{1}{16\pi^2} \left[g_1^2 m_S^2 \left\{ \sum_{u,d} (h_2^q)^2 \mathcal{N}_q^N (M_1(r_q, s) - M_3(r_q, s)) \right\} \right. \\
&\quad + m_N \left(\sum_{u,d,s} (h_2^q)^2 f_{Tq}^N + \frac{2}{27} f_{TG}^N \sum_{c,b,t} (h_2^q)^2 \right) \\
&\quad \left. \times \left\{ g_1^2 m_S \left(M_2(r_q, s) + M_4(r_q, s) \right) + \left(\frac{g_1 \mu_1}{m_\phi} - \frac{g_2}{2m_S} \right) L_1(r_q) \right\} \right]. \quad (2.6)
\end{aligned}$$

Promoting the vector quark bilinear $\mathcal{N}_q^N \equiv \langle \bar{N} | \bar{q} \gamma^\mu q | N \rangle$ to the vector nucleon bilinear yields the number of valence quarks of flavor q in the nucleon N , i.e. $\mathcal{N}_u^p = \mathcal{N}_d^n = 2$, $\mathcal{N}_d^p = \mathcal{N}_u^n = 1$. The contribution of light quarks to the nucleon mass (scalar nucleon bilinear) is

given by

$$q = u, d, s : \langle \bar{N} | m_q \bar{q} q | N \rangle = m_N f_{Tq}^N. \quad (2.7)$$

The heavy quarks contribute to the nucleon mass via the trace anomaly of the energy–momentum tensor [58]:

$$q = c, b, t : \langle \bar{N} | m_q \bar{q} q | N \rangle = \frac{2}{27} m_N f_{TG}^N = \frac{2}{27} m_N \left(1 - \sum_{q'=u,d,s} f_{Tq'}^N \right). \quad (2.8)$$

At first sight one might think that the contribution from the product of two vector currents dominates, since the corresponding nucleonic matrix elements \mathcal{N}_q^N are large. However, in the limit $r_q \rightarrow 0$ the difference $M_1(r_q, s) - M_3(r_q, s)$ vanishes $\propto r_q^2$. In contrast, the sum $M_2(r_q, s) + M_4(r_q, s) \rightarrow 2M_2(0, s)$ remains finite for massless quarks. As a result, the first term in eq.(2.6) typically contributes much less than the remaining terms, which originate from the product of scalar currents.

For the tree–level scattering contribution reducing to \mathcal{O}_{10} , the nucleonic Wilson coefficient in the limit of vanishing momentum transfer is [18]

$$c_{10}^{N|I} = \frac{g_1}{m_\phi^2} \left(\sum_{u,d,s} h_2^q \Delta \tilde{q}^N - \Delta \tilde{G}^N \sum_{c,b,t} \frac{h_2^q}{m_q} \right) \quad (2.9)$$

where $\Delta \tilde{q}^N$ and $\Delta \tilde{G}^N$ are the light and heavy quark contributions to the nucleon level pseudoscalar bilinear, respectively. The latter hadronic matrix element is due to the QCD chiral anomaly:

$$q = c, b, t : \langle \bar{N} | \partial_\mu (\bar{q} \gamma^\mu \gamma^5 q) | N \rangle = 2m_q \langle \bar{N} | \bar{q} i \gamma^5 q | N \rangle + \frac{\alpha_s}{4\pi} \langle \bar{N} | G^{a\mu\nu} \tilde{G}_{\mu\nu}^a | N \rangle, \quad (2.10)$$

where G and \tilde{G} are the gluonic field strength tensor and its dual, respectively. The left–hand side can be set to zero since heavy quarks have no significant dynamics in the nucleon. Throughout our calculations, we take the numerical values of the coefficients that appear when quark bilinears are promoted to nucleon bilinears as given in the Appendix of Ref. [47].

2.2 Model II

In Model II we replace the complex scalar WIMP by a spin–1/2 gauge singlet Dirac fermion χ , again using a real spin–zero mediator ϕ . The couplings of the SM quarks q to the mediator are as in Model I. The WIMP χ can also couple to the mediator ϕ via a scalar (λ_1) and a pseudoscalar coupling (λ_2). The renormalizable $SU(3)_C \times U(1)_{\text{em}}$ invariant Lagrangian is thus given by

$$\begin{aligned} \mathcal{L}^{\text{IIa}} = & i \bar{\chi} \not{D} \chi - m_\chi \bar{\chi} \chi + \frac{1}{2} \partial_\mu \phi \partial^\mu \phi - \frac{1}{2} m_\phi^2 \phi^2 + \frac{m_\phi \mu_1}{3} \phi^3 - \frac{\mu_2}{4} \phi^4 \\ & - \lambda_1 \phi \bar{\chi} \chi - i \lambda_2 \phi \bar{\chi} \gamma^5 \chi - h_1^{ij} \phi \bar{q}_i q_j - i h_2^{ij} \phi \bar{q}_i \gamma^5 q_j. \end{aligned} \quad (2.11)$$

We assume that the DM particle is odd and the SM particles along with the mediator are even under a new discrete \mathbb{Z}_2 symmetry in order to prevent DM decay. In order to avoid

potentially very large new contributions to FCNC processes we again take flavor diagonal quark couplings, i.e. $h_1^q \equiv h_1^{ij} \delta_{ij}$ and $h_2^q \equiv h_2^{ij} \delta_{ij}$.

If all Yukawa couplings (of a given flavor) appearing in the Lagrangian (2.11) are of similar magnitude, WIMP–nucleus scattering on heavy target nuclei will be completely dominated by a tree level contribution from \mathcal{O}_1 , with coefficient $\propto \lambda_1 h_1^q$. We thus have to set at least one of these couplings to zero. On the other hand, setting both of them to zero would also “switch off” the operators \mathcal{O}_{10} and \mathcal{O}_{11} which we seek to generate. We thus consider two variants of Model II:

$$\begin{aligned} \text{Model IIa : } & h_1^q = 0 \quad \forall q; \\ \text{Model IIb : } & \lambda_1 = h_2^q = 0 \quad \forall q. \end{aligned} \quad (2.12)$$

Setting $h_1^q \cdot h_2^q = 0$ again ensures that no electric dipole moments are generated at one–loop level. As before, neither of these choices is protected by a symmetry, i.e. they are not technically natural. We therefore again expect that \mathcal{O}_1 will be generated by radiative corrections. On the other hand, CP is violated if for some flavor q ,

$$\lambda_1 h_2^q \neq 0 \quad \text{or} \quad \lambda_2 h_1^q \neq 0. \quad (2.13)$$

We will discuss both variants of Model II in turn.

2.2.1 Model IIa

The matrix element for tree–level DM–quark scattering, $\chi(p_\chi) + q(p_q) \rightarrow \chi(p'_\chi) + q(p'_q)$, via ϕ exchange in the t –channel is given by

$$\mathcal{M}_{\chi q \rightarrow \chi q}^{\text{IIa}} = -\frac{h_2^q}{q^2 - m_\phi^2} \bar{u}(p'_\chi)(\lambda_1 + i\gamma^5 \lambda_2)u(p_\chi) \bar{u}(p'_q)i\gamma^5 u(p_q). \quad (2.14)$$

Taking the vanishing momentum transfer limit, $q^2 \rightarrow 0$, in the ϕ propagator, the matrix element can be matched onto the relativistic effective operators $(\bar{\chi}\chi)(\bar{q}i\gamma^5 q)$ and $(\bar{\chi}i\gamma^5\chi)(\bar{q}i\gamma^5 q)$, which reduce to the operators \mathcal{O}_{10} and \mathcal{O}_6 , respectively, in the non–relativistic limit. Recall, however, from Table 1 that \mathcal{O}_6 is doubly suppressed by momentum transfer \vec{q} , therefore generating a cross section suppressed by $\mathcal{O}(\vec{q}^2/m_N^2) \sim 10^{-2} - 10^{-3}$ relative to the contribution from \mathcal{O}_{10} . Hence, at the leading order in perturbation theory, \mathcal{O}_{10} dominates the scattering matrix element in Model IIa.

Although the operator \mathcal{O}_1 is not generated from leading order Feynman diagrams, one–loop corrections to DM–nucleus scattering again include contributions that reduce to \mathcal{O}_1 in the low energy limit; the corresponding Feynman diagrams are shown in Fig. 2.

In this model, there are two different box (and crossed box) diagrams: one involves the scalar coupling λ_1 and the other involves the pseudoscalar coupling λ_2 . The triangle diagram involves the scalar coupling λ_1 between the DM and the mediator,⁷ as well as the cubic self–interaction of the mediator μ_1 . All diagrams contain two vertices with the pseudoscalar coupling h_2^q on the quark line.

⁷There is also a triangle diagram involving λ_2 , as well as (crossed) box diagrams with one λ_1 vertex and one λ_2 vertex; however, these diagrams do not contribute to \mathcal{O}_1 . Moreover, the diagrams shown in Fig. 2 also generate other operators in the non–relativistic limit. We ignore these contributions, since they are of higher order in both the loop and NREFT expansions.

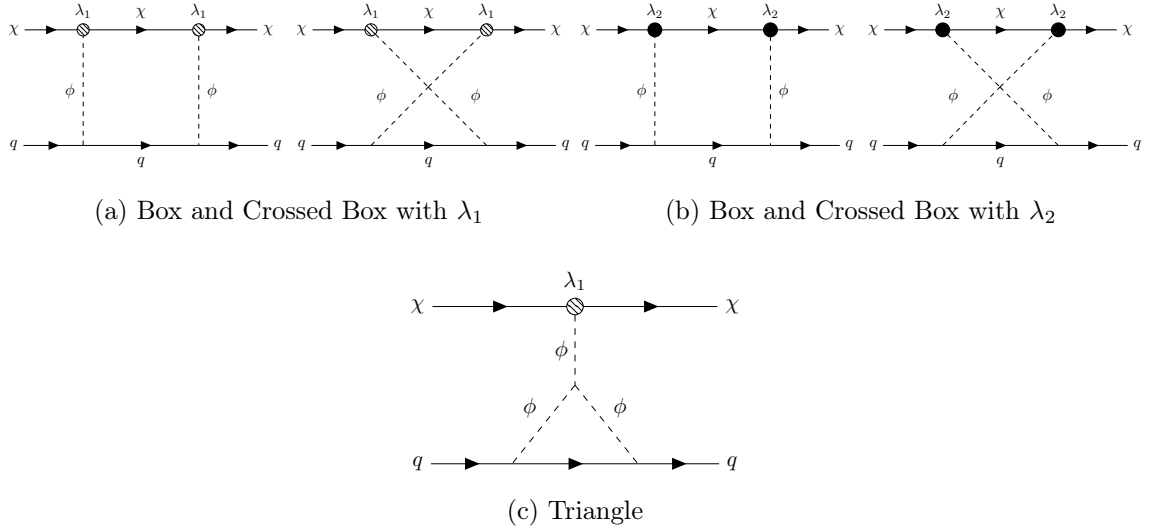


Figure 2: One-loop box and triangle Feynman diagrams in Model IIa which contribute to \mathcal{O}_1 . The shaded blob denotes the scalar DM–mediator coupling λ_1 while the dark blob denotes the pseudoscalar DM–mediator coupling λ_2 .

In order to simplify the loop calculation, we have used the Dirac equation as well as 4–momentum conservation, and took the limit of vanishing momentum transfer. Further details can be found in Appendix A.2. Finally, we find the following effective Lagrangian for Model IIa:

$$\mathcal{L}_{\text{eff}}^{\text{IIa}} \supset c_{10}^{q,d6} (\bar{\chi}\chi) (\bar{q}i\gamma^5 q) + c_6^{q,d6} (\bar{\chi}i\gamma^5\chi) (\bar{q}i\gamma^5 q) + c_{1,S}^{q,d6} (\bar{\chi}\chi) (\bar{q}q) + c_{1,V}^{q,d6} (\bar{\chi}\gamma_\mu\chi) (\bar{q}\gamma^\mu q) ; \quad (2.15)$$

the notation is as in (2.5). For completeness we have retained $(\bar{\chi}i\gamma^5\chi) (\bar{q}i\gamma^5 q)$ in the set of effective operators, although it can safely be neglected as reasoned earlier. Table 3 displays the list of relativistic effective operators and their matching to the NREFT operators in terms of the parameters of Model IIa. The quark–level Wilson coefficients contain loop-level Wilson coefficients $N_k(r, s)$, $k = 1, \dots, 8$, $P_l(r, s)$, $l = 1, \dots, 4$ and $R_1(r)$, which have been expressed as functions of dimensionless parameters $r \equiv m_q/m_\phi$ and $s \equiv m_\chi/m_\phi$. Analytic expressions for these loop functions can be found in Appendix A.2.1.

Collecting the results of Table 3, and embedding the quark bilinears in nucleonic matrix

	$\bar{\chi}\Gamma_\chi\chi\bar{q}\Gamma_qq$	c_i^q
Tree	$c_{10}^{q,d6}\bar{\chi}\chi\bar{q}i\gamma^5q \longrightarrow$	$\frac{h_2^q\lambda_1}{m_\phi^2}$
Box $ \lambda_1$	$c_{1,V,B1}^{q,d6}\bar{\chi}\gamma_\mu\chi\bar{q}\gamma^\mu q \longrightarrow$	$-\frac{\lambda_1^2(h_2^q)^2}{16\pi^2}N_1$
	$c_{1,S,B1}^{q,d6}\bar{\chi}\chi\bar{q}q \longrightarrow$	$-\frac{\lambda_1^2(h_2^q)^2}{16\pi^2}(2m_\chi m_q(N_2 - P_2) + m_\chi^2(N_3 - 2P_1) + m_q^2 N_4)$
Crossed	$c_{1,V,C1}^{q,d6}\bar{\chi}\gamma_\mu\chi\bar{q}\gamma^\mu q \longrightarrow$	$\frac{\lambda_1^2(h_2^q)^2}{16\pi^2}N_5$
Box $ \lambda_1$	$c_{1,S,C1}^{q,d6}\bar{\chi}\chi\bar{q}q \longrightarrow$	$\frac{\lambda_1^2(h_2^q)^2}{16\pi^2}(2m_\chi m_q(N_6 - P_4) + m_\chi^2(N_7 - 2P_3) + m_q^2 N_8)$
Box $ \lambda_2$	$c_{1,V,B2}^{q,d6}\bar{\chi}\gamma_\mu\chi\bar{q}\gamma^\mu q \longrightarrow$	$-\frac{\lambda_2^2(h_2^q)^2}{16\pi^2}N_1$
	$c_{1,S,B2}^{q,d6}\bar{\chi}\chi\bar{q}q \longrightarrow$	$-\frac{\lambda_2^2(h_2^q)^2}{16\pi^2}(2m_\chi m_q N_2 + m_\chi^2 N_3 + m_q^2 N_4)$
Crossed	$c_{1,V,C2}^{q,d6}\bar{\chi}\gamma_\mu\chi\bar{q}\gamma^\mu q \longrightarrow$	$\frac{\lambda_2^2(h_2^q)^2}{16\pi^2}N_5$
Box $ \lambda_2$	$c_{1,S,C2}^{q,d6}\bar{\chi}\chi\bar{q}q \longrightarrow$	$\frac{\lambda_2^2(h_2^q)^2}{16\pi^2}(2m_\chi m_q N_6 + m_\chi^2 N_7 + m_q^2 N_8)$
Triangle	$c_{1,S,T}^{q,d6}\bar{\chi}\chi\bar{q}q \longrightarrow$	$-\frac{\lambda_1\mu_1(h_2^q)^2}{16\pi^2}\frac{m_q}{m_\phi}R_1$

Table 3: Non-relativistic reduction of effective operators in Model IIa. In the expression for the quark-level Wilson coefficients, we have again suppressed the dependence of the loop functions on dimensionless parameters, i.e. $N_k \equiv N_k(r, s)$, $P_l \equiv P_l(r, s)$ and $R_1 \equiv R_1(r)$, where $r \equiv m_q/m_\phi$ and $s \equiv m_\chi/m_\phi$. The first line contributes to the coefficient of \mathcal{O}_{10} , all other lines describe contributions $\propto \mathcal{O}_1$.

elements, the Wilson coefficient c_1^N of the NREFT operator \mathcal{O}_1 is given by

$$\begin{aligned}
c_1^N|_{\text{IIa}} = & -\frac{1}{16\pi^2} \left[(\lambda_1^2 + \lambda_2^2) \left(\sum_{q=u,d} (h_2^q)^2 \mathcal{N}_q^N (N_1(r, s) - N_5(r, s)) \right) \right. \\
& + m_N \left(\sum_{q=u,d,s} (h_2^q)^2 f_{Tq}^N + \frac{2}{27} f_{TG}^N \sum_{q=c,b,t} (h_2^q)^2 \right) \\
& \times \left\{ (\lambda_1^2 + \lambda_2^2) \left(2m_\chi (N_2(r_q, s) - N_6(r_q, s)) + \frac{m_\chi^2}{m_q} (N_3(r_q, s) - N_7(r_q, s)) \right) \right. \\
& + m_q (N_4(r_q, s) - N_8(r_q, s)) \\
& - 2m_\chi \lambda_1^2 \left(P_2(r_q, s) - P_4(r_q, s) + \frac{m_\chi}{m_q} (P_1(r_q, s) - P_3(r_q, s)) \right) \\
& \left. \left. + \frac{\lambda_1\mu_1}{m_\phi} R_1(r_q) \right\} \right]. \tag{2.16}
\end{aligned}$$

The nuclear bilinear coefficients \mathcal{N}_q^N , f_{Nq}^T and f_{NG}^T are the same as in eq.(2.6). At first sight $c_1^N|^{IIa}$ appears to be singular in the limit $m_q \rightarrow 0$. Note that f_{Nq}^T contains a factor of m_q , see eq.(2.7); hence contributions to $c_{1,S}^{q,d6}$ in Table 3 without an explicit factor m_q appear $\propto 1/m_q$ in eq.(2.16). However, they get multiplied with the differences of loop functions $N_3(r_q, s) - N_7(r_q, s)$ or $P_1(r_q, s) - P_3(r_q, s)$, which scale like r_q for $r_q \rightarrow 0$; these contributions therefore approach a finite value as $m_q \rightarrow 0$. In contrast, the difference $N_1(r_q, s) - N_5(r_q, s)$, which appears in the contribution from the product of two vector currents, vanishes for $r_q \rightarrow 0$. As a result, the dominant contributions to $c_1^N|^{IIa}$ also originate from the product of two scalar currents, as for Model I. Within this category, the contribution $\propto N_4 - N_8$ vanishes as $r_q \rightarrow 0$ and is therefore negligible for generation-independent couplings h_2^q , but all other terms are very roughly comparable and must be taken into account.

The Wilson coefficient of the operator \mathcal{O}_{10} arising from the t -channel tree-level scattering diagram is

$$c_{10}^N|^{IIa} = \frac{\lambda_1}{m_\phi^2} \left(\sum_{q=u,d,s} h_2^q \Delta \tilde{q}^N - \Delta \tilde{G}^N \sum_{q=c,b,t} \frac{h_2^q}{m_q} \right). \quad (2.17)$$

2.2.2 Model IIb

We next turn to Model IIb. It is also described by the Lagrangian of eq.(2.11), but we now postulate purely scalar Yukawa couplings h_1^q on the quark side and a purely pseudoscalar coupling λ_2 on the dark matter side, see eq.(2.12). The tree-level matrix element for DM-quark scattering, $\chi(p_\chi) + q(p_q) \rightarrow \chi(p'_\chi) + q(p'_q)$, proceeding via t -channel ϕ exchange is then:

$$\mathcal{M}_{\chi q \rightarrow \chi q}^{IIb} = -\frac{h_1^q \lambda_2}{q^2 - m_\phi^2} \bar{u}(p'_\chi) i\gamma^5 u(p_\chi) \bar{u}(p'_q) u(p_q). \quad (2.18)$$

This matrix element matches onto the dimension-6 effective operator $(\bar{\chi} i\gamma^5 \chi)(\bar{q}q)$, which reduces to the momentum-suppressed SI NREFT operator \mathcal{O}_{11} in the non-relativistic limit. Once again, the choice $\lambda_1 = 0$, which ensures the absence of \mathcal{O}_1 at tree-level, is not protected by any symmetry. We therefore again expect contributions $\propto \mathcal{O}_1$ to be generated at the next order in perturbation theory. The relevant Feynman diagrams are shown in Fig. 3. Each diagram involves two factors of the pseudoscalar DM-mediator coupling λ_2 ; the two γ_5 factors multiply to unity. The triangle and (crossed) box diagrams in addition involve one or two factors of the scalar DM-quark coupling h_1^q , respectively; the former also involves the cubic self-coupling μ_1 of the mediator. The triangle diagram can be interpreted as generating a scalar DM-mediator coupling. Explicit expressions for the resulting amplitudes are provided in Appendix A.2.

When the mediator ϕ is integrated out, the following relativistic effective Lagrangian describes DM-quark scattering:

$$\mathcal{L}_{\text{eff}}^{IIb} \supset c_{11}^{q,d6} (\bar{\chi} i\gamma^5 \chi)(\bar{q}q) + c_{1,S}^{q,d6} (\bar{\chi}\chi)(\bar{q}q) + c_{1,V}^{q,d6} (\bar{\chi}\gamma_\mu \chi)(\bar{q}\gamma^\mu q). \quad (2.19)$$

Table 4 displays the quark-level Wilson coefficients in terms of the parameters of Model IIb. The loop functions N_k and P_l are identical to the ones appearing in Model IIa. S_1 is

	$\bar{\chi}\Gamma\chi\bar{N}\Gamma_N N$	c_i^q
Tree	$c_{11}^{q,d6} \bar{\chi} i \gamma^5 \chi \bar{q} \gamma^\mu q \longrightarrow$	$\frac{h_1^q \lambda_2 m_N}{m_\phi^2 m_\chi}$
Box	$c_{1,V,B}^{q,d6} \bar{\chi} \gamma_\mu \chi \bar{q} \gamma^\mu q \longrightarrow$	$-\frac{\lambda_2^2 h_1^{q2}}{16\pi^2} N_1$
	$c_{1,S,B}^{q,d6} \bar{\chi} \chi \bar{q} q \longrightarrow$	$-\frac{\lambda_2^2 h_1^{q2}}{16\pi^2} (2m_\chi m_q (N_2 + P_1) + m_\chi^2 N_3 + m_q^2 (N_4 + 2P_2))$
Crossed	$c_{1,V,C}^{q,d6} \bar{\chi} \gamma_\mu \chi \bar{q} \gamma^\mu q \longrightarrow$	$\frac{\lambda_2^2 h_1^{q2}}{16\pi^2} N_5$
Box	$c_{1,S,C}^{q,d6} \bar{\chi} \chi \bar{q} q \longrightarrow$	$\frac{\lambda_2^2 h_1^{q2}}{16\pi^2} (2m_\chi m_q (N_6 - P_3) + m_\chi^2 N_7 + m_q^2 (N_8 - 2P_4))$
Triangle	$c_{1,S,T}^{q,d6} \bar{\chi} \chi \bar{q} q \longrightarrow$	$-\frac{h_1^q \mu_1 \lambda_2^2}{16\pi^2} \frac{m_\chi}{m_\phi} S_1$

Table 4: Non-relativistic reduction of effective operators in Model IIb. The arguments of the loop functions N_k , P_l and S_1 have again been suppressed; explicit expressions for these functions can be found in Appendix A.2.1.

the only loop function not defined previously, and its analytic expression along with that of the others can be found in Appendix A.2.1.

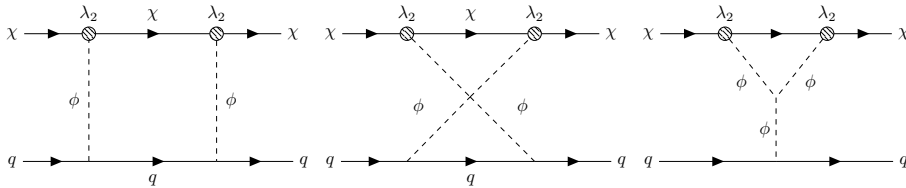


Figure 3: One-loop (crossed) box and triangle Feynman diagrams in Model IIb which contribute to \mathcal{O}_1 in the non-relativistic limit.

Collecting the results of Table 4, and inserting the appropriate hadronic coefficients for the nucleonic matrix elements of the quark bilinears, the Wilson coefficient of the operator \mathcal{O}_1

is:

$$\begin{aligned}
c_{11}^N|_{\text{IIb}} = & -\frac{\lambda_2^2}{16\pi^2} \left\{ \sum_{q=u,d} \mathcal{N}_q^N (h_1^q)^2 \left(N_1(r_q, s) - N_5(r_q, s) \right) \right. \\
& + m_N \left(\sum_{q=u,d,s} f_{Tq}^N + \frac{2}{27} f_{TG}^N \sum_{q=c,b,t} \right) \\
& \times \left[(h_1^q)^2 \left(2m_\chi \left(N_2(r_q, s) - N_6(r_q, s) + P_1(r_q, s) + P_3(r_q, s) \right) \right. \right. \\
& \quad + m_q \left(N_4(r_q, s) - N_8(r_q, s) + 2 \left(P_2(r_q, s) + P_4(r_q, s) \right) \right) \\
& \quad \left. \left. + \frac{m_\chi^2}{m_q} \left(N_3(r_q, s) - N_7(r_q, s) \right) \right) \right] \\
& \left. + \mu_1 h_1^q \frac{m_\chi}{m_\phi} \frac{S_1(s)}{m_q} \right\}; \tag{2.20}
\end{aligned}$$

recall that $r_q = m_q/m_\phi$ and $s = m_\chi/m_\phi$. As in case of Model IIa, the combinations of loop functions multiplying \mathcal{N}_q^N and m_χ^2/m_q vanish for $m_q \rightarrow 0$; the term $\propto m_\chi^2/m_q$ thus yields a finite result in this limit. However, the very last term in eq.(2.20) also contains an explicit $1/m_q$ factor; the loop function appearing in this term does not depend on m_q at all. Here the required chirality breaking on the quark line is due to the *single* factor of h_1^q . We therefore expect this term to dominate, unless the trilinear scalar coupling μ_1 is for some reason very small.

From eq.(2.18) the tree-level contribution to the Wilson coefficient of \mathcal{O}_{11} is:

$$c_{11}^N|_{\text{IIb}} = \frac{\lambda_2}{m_\phi^2} \frac{m_N^2}{m_\chi} \left(\sum_{q=u,d,s} \frac{h_1^q f_{Tq}^N}{m_q} + \frac{2}{27} f_{TG}^N \sum_{q=c,b,t} \frac{h_1^q}{m_q} \right) = \frac{\lambda_2}{m_\phi^2} \frac{m_N^2}{m_\chi} \tilde{f}^N. \tag{2.21}$$

Here we have defined $\tilde{f}^N \equiv \left(\sum_{q=u,d,s} \frac{h_1^q f_{Tq}^N}{m_q} + \frac{2}{27} f_{TG}^N \sum_{q=c,b,t} \frac{h_1^q}{m_q} \right)$, and as usual neglected the q^2 term in the ϕ propagator. As in the last term in eq.(2.20) the required chirality breaking on the quark line is provided by h_1^q . Since the hadronic matrix elements f_{Tq}^N have been defined including an explicit factor of m_q , the contributions in \tilde{f}^N scale $\propto 1/m_q$, leading to a large enhancement of the contribution of light quarks. On the other hand, an extra factor m_N/m_χ appears since the pseudoscalar DM current is $\propto |\vec{q}|/m_\chi = (|\vec{q}|/m_N) \times (m_N/m_\chi)$. As already noted in the discussion of Table 1, this appears to be quite generic [47–50].

2.3 The Neutron EDM

In all three cases we considered, the tree-level contribution to the Wilson coefficient of \mathcal{O}_{10} or \mathcal{O}_{11} is nonzero only if CP is violated: in Model I one needs $g_1 h_2^q \neq 0$, where g_1 is a scalar coupling while h_2^q is a pseudoscalar coupling; in Model IIa, $\lambda_1 h_2^q \neq 0$ is required, where λ_1 is a scalar coupling; and in Model IIb, $c_{11}^{d6} \propto \lambda_2 h_1^q$, where λ_2 is pseudoscalar but h_1^q is scalar. Since we assume the quark Yukawa couplings to be flavor diagonal, the most sensitive probe

of CP violation is the EDM of the neutron (or of heavier nuclei). However, CP violation is a necessary condition for the generation of an EDM; it is not by itself sufficient. In the case at hand, since we set $h_1^q = 0$ in Models I and IIa and $h_2^q = 0$ in Model IIb, there is no one-loop contribution to the neutron EDM, in contrast to the models with charged mediator we considered in ref.[50]. In case of Model IIb, as far as the one-loop diagram with a quark and a mediator ϕ in the loop is concerned, the mediator can consistently be defined as being CP -even, since only the coupling h_1^q appears in the diagram. Similarly, in Model I and Model IIa, in the one-loop diagram with a quark-mediator loop the mediator can consistently be defined as being CP -odd, since only the coupling h_2^q appears.

Turning to higher loops, a CP -even mediator can have any self coupling. Hence in Model IIb embellishing the one-loop diagram with additional scalar vertices does not lead to CP violation. In fact, in this model the only coupling that is not consistent with interpreting ϕ to be CP -even is λ_2 , which couples ϕ to the DM particle. However, this coupling cannot contribute to electric dipole moments. It could appear in any diagram where the only external particles are a through-going quark and a photon (or gluon) only via a closed χ loop, which will either vanish (if an odd number of ϕ legs is attached to it), or simply renormalize a CP -even quantity like the ϕ 2-point function. We thus conclude that in Model IIb, *no* new contributions to the electric dipole moments of SM particles are generated. The conceptually easiest way to prove the existence of CP violation in this model is via χq scattering; in case of $2 \rightarrow 2$ scattering, spin observables would have to be included in the construction of a CP -odd quantity. While conceptually straightforward, experimentally this seems prohibitively difficult; certainly there are no current experimental constraints from such experiments.

The situation is very different in Models I and IIa, where in the relevant one-loop diagram the mediator behaves like a pseudoscalar. The reason is that a pseudoscalar cannot have a ϕ^3 coupling. Hence, two-loop diagrams containing both the (pseudoscalar) Yukawa coupling h_2^q and the (scalar) trilinear coupling μ_1 , see Fig. 4, can be expected to generate a nonvanishing (chromo-)EDM for quark q . It should be noted that here μ_1 is relevant, not the couplings λ_1 or g_1 appearing in the coefficient of \mathcal{O}_{10} . However, a theory with $\mu_1 = 0$ but $\lambda_1 \neq 0$ is, strictly speaking, not renormalizable, since a triangle diagram with χ in the loop will generate a *divergent* contribution to $\mu_1 m_\phi \propto m_\chi \lambda_1^3$; similarly, in Model I there are divergent one-loop contributions $\propto g_1 g_2 m_S$ to the ϕ^3 vertex. We will come back to this point later. Because only the trilinear self-coupling of the mediator and its pseudoscalar Yukawa coupling to quarks are relevant here, the calculation of the quark (chromo) EDM is exactly the same in these two models.

The quark EDM d_q is calculated as the coefficient of a dimension-5 P - and T -odd interaction term $(-i/2) \bar{q} \sigma_{\mu\nu} \gamma_5 q F^{\mu\nu}$ at zero momentum transfer. The same quark radiating a gluon instead a photon leads to non-vanishing chromo EDM. These are calculated similar to quark EDMs, by finding the coefficient of $(-i/2) \bar{q} \sigma_{\mu\nu} t_a \gamma_5 q G_a^{\mu\nu}$ at zero momentum transfer.

The EDM operator breaks chirality, hence d_q is proportional to an odd number of chirality flips. These can come either from fermion masses or from Yukawa couplings in the relevant Feynman diagrams. The diagrams shown in Fig. 4 contain three Yukawa couplings, hence

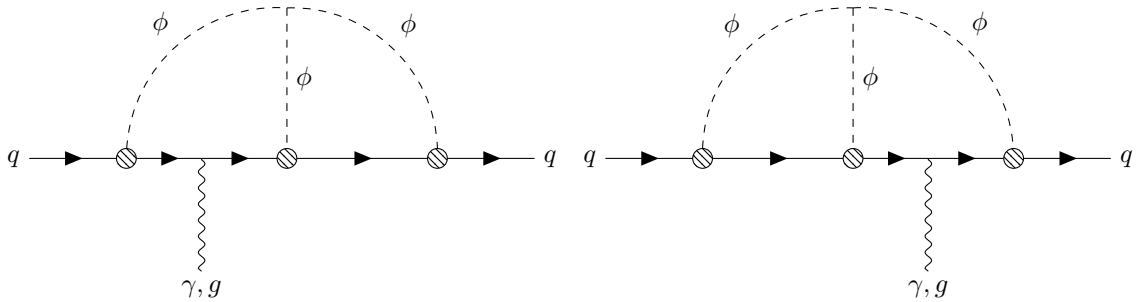


Figure 4: Two-loop Feynman diagrams for quark EDMs and color-EDMs in Model I and IIa. The blobs here indicate the insertion of the mediator pseudoscalar Yukawa coupling.

they can contribute even for $m_q \rightarrow 0$. We provide the details of the computation of these two-loop diagrams in Appendix B. We calculate the quark EDM to be

$$d_q = \frac{2e Q_q (h_2^q)^3}{(16\pi^2)^2} \mu_1 m_\phi \lim_{q^2 \rightarrow 0} \left([\mathcal{X}] + [\mathcal{Y}] \right), \quad (2.22)$$

where Q_q is the electric charge of quark q ; $[\mathcal{X}]$ and $[\mathcal{Y}]$ are loop functions expressed as five dimensional integrals over five Feynman parameters given in eqs.(B.19) and (B.20). The color-EDM \tilde{d}_q can be obtained by replacing the external photon with a gluon. Hence \tilde{d}_q can be obtained from eq.(2.22) by replacing eQ_q with the strong coupling g_s .

In order to calculate the value of the nEDM from d_q and \tilde{d}_q , we use

$$d_n = g_T^u d_u + g_T^d d_d + g_T^s d_s + 1.1 e (0.5 \tilde{d}_u + \tilde{d}_d). \quad (2.23)$$

Here the tensor charges $g_T^u = -0.233(28)$, $g_T^d = 0.774(66)$ and $g_T^s = 0.009(8)$ have been calculated using lattice QCD [59, 60] (see also Refs.[61–63]) at a renormalization scale of 2 GeV. We are not aware of a reliable lattice computation of the contribution of the chromo-EDMs to d_n ; we therefore employ a computation using QCD sum rules, again evaluated at a renormalization scale of 2 GeV [64], although there is an $\mathcal{O}(50\%)$ uncertainty in these results [65, 66]. In this case the uncertainty in the coefficients in Eq.(2.23) might shift the boundary of the excluded region slightly, without affecting our results qualitatively. Since in our numerical analyses we will assume flavor universal quark Yukawa couplings, the contributions from the (chromo-)EDMs of heavy quarks to the EDM of the neutron can safely be neglected; in fact, since $g_T^s \ll g_T^d$ already the contribution from the strange quark is essentially negligible for equal couplings.

3 Results and Discussions

In the previous section, we described the different contributions to DM–nucleus scattering in Models I, IIa and IIb. These simplified models were designed such there are no tree-level contributions to the NREFT operator \mathcal{O}_1 ; instead, at tree-level only the P - and T -odd operators \mathcal{O}_{10} (in Model I and IIa) or \mathcal{O}_{11} (in Model IIb) were generated. Recall that \mathcal{O}_1 often gives the dominant contribution to DM–nucleus scattering: it appears in

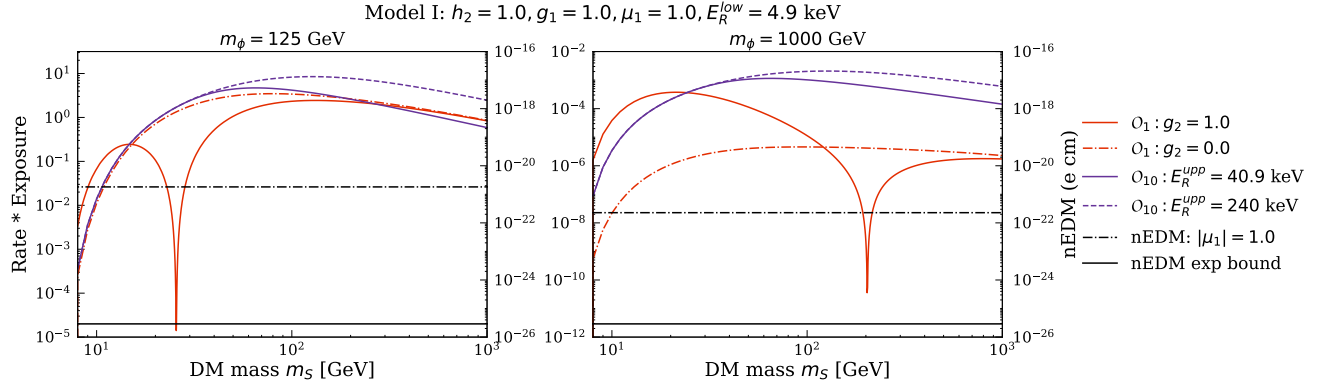


Figure 5: The left y -axis shows the total number of scattering events in Model I with $\mu_1 = 1.0$ at XENON1T with a run time exposure of 1 tonne-year as a function of the DM mass m_S for two values of the mediator mass, $m_\phi = 125 \text{ GeV}$ (left frame) and $m_\phi = 1000 \text{ GeV}$ (right frame). The **violet** and **red** curves show the number of events due to \mathcal{O}_{10} and \mathcal{O}_1 , respectively. The **black** lines refer to the right y -axis; the **solid black** line is the experimental upper limit on nEDM at 90% C.L., while the **dashed black** line is the predicted nEDM for the given choice of parameters.

leading order in the NREFT expansion, and its contribution is coherently enhanced by A^2 if $c_1^n \simeq c_1^p$, where c_1^n and c_1^p are the Wilson coefficients accompanying \mathcal{O}_1 for neutron and proton respectively. However, in the models considered here, \mathcal{O}_1 arises from box and triangle diagrams appearing at next-to-leading order in perturbation theory. Therefore, it is not obvious *a priori* which operator provides the dominant contribution to DM-nucleus scattering.

In this section we compare the contributions from \mathcal{O}_1 quantitatively to the contributions from \mathcal{O}_{10} or \mathcal{O}_{11} . To that end, we compute the number of events due to these operators for a recent XENON1T run [2] for a variety of benchmark model parameters. Here we use the explicit expressions for the loop functions contributing to the Wilson coefficient of \mathcal{O}_1 given in Appendix A. It should be noted that the contribution from \mathcal{O}_1 does not interfere with those from \mathcal{O}_{10} and \mathcal{O}_{11} , due to the different CP properties of these operators. Hence the total scattering rate is simply given by the sum of these contributions.⁸

Moreover, for Models I and IIa we check numerically if the nEDM surpasses its experimental upper bound [44–46]. We perform the integration of the loop functions in eq.(2.22) using the Monte Carlo integration routine **SUAVE** of the **CUBA** numerical library [67]. The absolute numerical error reported by the routine is around $\mathcal{O}(10^{-8})$ for the two values of the mediator mass m_ϕ we consider.

In order to compute the number of events for the 2018 run of XENON1T [2], we integrate the differential event rate, computed using the the Mathematica code **dmformfactor**, which is based on the formalism of ref.[20], over the recoil energy E_R from 4.9 keV to 40.9 keV,

⁸Recall that we only extract the contribution to \mathcal{O}_1 from our loop diagrams. These diagrams will also contribute to additional NREFT operators; however, those contributions will be of higher order both in the loop and NREFT expansions, and can thus safely be neglected.

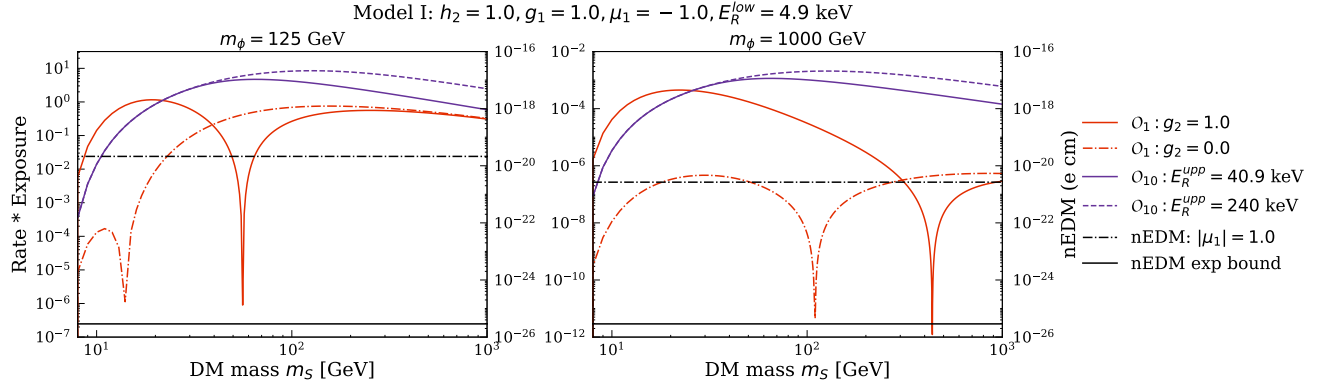


Figure 6: As in Fig. 5, except for $\mu_1 = -1.0$.

in accordance with the recoil energy region of interest (ROI) used in that run. In addition, we include results (shown as dashed curves) where the upper end of integration is set at $E_R^{upp} = 240 \text{ keV}$, as considered in a dedicated effective field theory search by the XENON experiment. We multiply the integrated rate with the 2018 XENON1T runtime exposure of $278.8 \text{ days} \times 1.3 \text{ tonne} = 1.0 \text{ tonne}\cdot\text{yr}$. We have further assumed a standard isothermal DM halo with $\rho_\chi = 0.3 \text{ GeVcm}^{-3}$, $v_0 = 220 \text{ km/s}$, $v_e = 232 \text{ km/s}$ and $v_{esc} = 544 \text{ km/s}$. We calculate our event rates using a weighted sum over the different isotopes occurring in naturally abundant Xenon.

We choose the following sets of parameter values for Model I: $h_2^q \equiv h_2 = g_1 = 1.0$ with $m_\phi = 125 \text{ GeV}$ or $m_\phi = 1000 \text{ GeV}$. Note that we choose a rather large and flavor universal Yukawa coupling of the quarks. For the given couplings, the former (smaller) mediator mass value leads to a DM–nucleon cross section from the operator \mathcal{O}_{10} that lies just below the sensitivity of the 2018 XENON1T run in the $\sigma_{\chi p} - m_S$ exclusion plane. The latter (larger) mediator mass corresponds to a DM–nucleon cross section from the operator \mathcal{O}_{10} that lies just above the irreducible background from coherent neutrino–nucleus scattering (the so–called “neutrino floor”); it will be very difficult to probe even smaller cross sections in direct search experiments.

Figures 5 and 6 depict the resulting number of events from the operators \mathcal{O}_{10} and \mathcal{O}_1 as a function of the DM mass m_S in Model I, for different values of the trilinear mediator coupling μ_1 . Each figure contains two frames, corresponding to the two values of m_ϕ we consider.

Since the tree–level contribution from \mathcal{O}_{10} does not depend on μ_1 , it remains the same in both figures. We note that this contribution is enhanced by up to an order of magnitude once the DM mass m_S exceeds the mass of the target nuclei ($\simeq 125 \text{ GeV}$ for Xenon) if the upper end of the ROI is increased from 40.9 keV to 240 keV . This is not surprising, since \mathcal{O}_{10} predicts a recoil energy spectrum that peaks at sizable energy, due to the explicit factor of \vec{q} that appears in the definition of this operator. Note that at $m_S < m_{Xe}$, the maximal recoil energy is $\mathcal{O}(v^2 m_S^2 / m_{Xe})$ rather than $\mathcal{O}(v^2 m_{Xe})$ for $m_S > m_{Xe}$; hence this enhancement only occurs at larger DM masses.

Figure 5 is for $\mu_1 = 1.0$. We see that the contribution from \mathcal{O}_{10} generally exceeds that

from \mathcal{O}_1 , except at low DM mass where the low maximal recoil energy leads to low values of $|\vec{q}|$. We also note that for $g_2 = 0$, i.e. in the absence of the last diagram in Fig. 1, the \mathcal{O}_1 contribution, shown by the dashed red lines, drops faster with increasing m_ϕ than the (tree-level) contribution from \mathcal{O}_{10} does. For a positive coupling $g_2 = 1.0$ the contributions from the (crossed) box and g_2 triangle diagrams have opposite signs, leading to a vanishing \mathcal{O}_1 contribution for $m_S \simeq 0.2m_\phi$.

In order to understand the comparison of the tree-level \mathcal{O}_{10} contributions with the loop suppressed \mathcal{O}_1 contributions semi-quantitatively, we estimate the ratio of the number of events from the two contributions $N_{\mathcal{O}_1}/N_{\mathcal{O}_{10}}$ as:

$$\frac{N_{\mathcal{O}_1}}{N_{\mathcal{O}_{10}}}\Big|_{\text{I}} = \frac{R_{\mathcal{O}_1}}{R_{\mathcal{O}_{10}}}\Big|_{\text{I}} \sim \frac{(c_1^N|_{\text{I}})^2}{(c_{10}^N|_{\text{I}})^2} \frac{A^2}{\langle S_{\text{Xe}} \rangle^2} \frac{m_N^2}{\vec{q}^2}. \quad (3.1)$$

Here $R_{\mathcal{O}_i}$ denotes the scattering rate due to operator \mathcal{O}_i integrated over the recoil energy window. The factor $(\vec{q}^2/m_N^2)^{-1}$ is due to the momentum suppression of \mathcal{O}_{10} . In this estimate, we have assumed the nuclear response functions to be independent of the recoil energy, and approximated the ratio of the nuclear response functions as $A^2/\langle S_N \rangle^2$ since the SI response (from \mathcal{O}_1) is coherently enhanced by A^2 while the SD response (from \mathcal{O}_{10}) is suppressed by the spin expectation value squared $\langle S_{\text{Xe}} \rangle^2$. We estimate $c_1^N|_{\text{I}}$ using the vanishing quark mass limit of eq.(2.6):

$$c_1^N|_{m_q \rightarrow 0}^{\text{I}} = \frac{h_2^2}{16\pi^2} m_N f_T^N \left\{ g_1^2 m_S (M_2 + M_4)|_{r \rightarrow 0} + \left(\frac{g_1 \mu_1}{m_\phi} - \frac{g_2}{2m_S} \right) L_1(r)|_{r \rightarrow 0} \right\}. \quad (3.2)$$

For small $s = m_S/m_\phi$ and $g_2 = 1.0$, the last (triangle) term in eq.(3.2) dominates:

$$c_1^N|_{\text{I}} \approx \frac{h_2^2}{16\pi^2} \frac{g_2}{4} m_N f_T^N \frac{1}{m_S} \frac{1}{m_\phi^2}, \quad (3.3)$$

where we used $L_1(0) = -1/2m_\phi^2$ and defined $f^N \equiv \left(\sum_{u,d,s} f_{Tq}^N + \frac{2}{27} f_{TG}^N \sum_{c,b,t} \right)$. Inserting eq.(3.3) and eq.(2.9) for $c_{10}^N|_{\text{I}}$ in eq. (3.1), we obtain for $m_S < m_\phi = 1000$ GeV:

$$\frac{N_{\mathcal{O}_1}}{N_{\mathcal{O}_{10}}}\Big|_{\text{I}} \approx \left(\frac{h_2}{16\pi^2} \frac{g_2}{4g_1} \frac{f_T^N}{\tilde{\Delta}^N} \frac{m_N}{m_S} \right)^2 \frac{A}{\langle S_N \rangle^2} \frac{m_N}{2E_R}, \quad (3.4)$$

where we defined $\tilde{\Delta}^N = \left(\sum_{q=u,d,s} \Delta \tilde{q}^N - \Delta \tilde{G}^N \sum_{q=c,b,t} \frac{1}{m_q} \right)$ and used $m_{\text{Xe}} = Am_N$. Plugging in $h_2 = g_1 = g_2 = 1.0$, $E_R = 30$ keV for Xenon ($A = 131$) at $m_S = 30$ GeV results in a ratio of 0.8, which agrees well with the solid red curve for \mathcal{O}_1 being marginally below the purple curve for \mathcal{O}_{10} in the right frame of Figure 5.

For $m_\phi = 125$ GeV and not too large m_S $c_1^N|_{\text{I}}$ is instead dominated by the scattering contribution from the g_1 triangle diagram since $g_1 \mu_1/m_\phi$ is less suppressed than $g_2/2m_S$. In that case we should replace $g_2/(2m_S)$ by $g_1 \mu_1/m_\phi$ in eq.(3.4). Again using $E_R = 30$ keV and $h_2 = g_1 = \mu_1 = 1.0$, the estimated contribution from \mathcal{O}_1 is then 0.2 times that from \mathcal{O}_{10} . This is in good agreement with the left panel of Figure 5 for $m_S \geq 100$ GeV, above the accidental cancellation around $m_S \simeq 30$ GeV.

For $m_S > m_\phi$ and unit couplings, the box diagrams instead dominate, in which case

$$c_1^N|_I \approx \frac{h_2^2 g_1^2}{16\pi^2} f_T^N m_N m_S (M_2 + M_4)|_{r \rightarrow 0} . \quad (3.5)$$

The ratio of the number of scattering events then becomes

$$\frac{N_{\mathcal{O}_1}}{N_{\mathcal{O}_{10}}}|_I \approx \left(\frac{h_2 g_1}{16\pi^2} \frac{f_T^N}{\Delta^N} m_N m_S m_\phi^2 (M_2 + M_4)|_{r \rightarrow 0} \right)^2 \frac{A}{\langle S_N \rangle^2} \frac{m_N}{2E_R} . \quad (3.6)$$

Using $E_R = 30$ keV and $h_2 = g_1 = \mu_1 = 1.0$, for $m_S = 1000$ GeV and $m_\phi = 125$ GeV the estimated number of events for \mathcal{O}_1 is 2.8 times that for \mathcal{O}_{10} . The left panel of Fig. 5 shows that this is a slight overestimate even if the smaller ROI is used. For the larger maximal recoil energy, $E_R^{\text{upp}} = 240$ keV, \mathcal{O}_{10} still contributes roughly three times more scattering events than \mathcal{O}_1 . Using the same couplings, for $m_S = m_\phi = 1000$ GeV, the estimated contribution from \mathcal{O}_1 is smaller by a factor 2.5×10^{-2} relative to that from \mathcal{O}_{10} . This rough estimate matches the ratio between the \mathcal{O}_1 and \mathcal{O}_{10} contributions in the right frame of Figure 5.

In Fig. 6 we have changed the sign of μ_1 while keeping g_1 and g_2 positive (or zero). Both triangle diagrams therefore now contribute with opposite signs than the (crossed) box diagrams. As a result, the coefficient of \mathcal{O}_1 now vanishes at $m_S \simeq 0.5m_\phi$ for $g_2 = 1.0$, and at $m_S \simeq 0.1m_\phi$ for $g_2 = 0$.

As before, for $g_2 = 1.0$ and small DM masses the Wilson coefficient of \mathcal{O}_1 can be approximated by the triangle diagram involving the g_2 coupling. From eq.(3.4) for $m_S = 100$ GeV, $m_\phi = 1000$ GeV and $h_2 = g_1 = 1.0$ we estimate 7.2×10^{-2} as ratio of the \mathcal{O}_1 and \mathcal{O}_{10} contributions, in rough agreement with the right panel of Fig. 6. For $m_S > m_\phi$, the box diagrams again dominate. Since they do not depend on μ_1 our earlier estimates still apply. However, since the triangle diagrams aren't quite negligible even at $m_S = 8m_\phi$, the largest ratio covered in Fig. 6, this somewhat overestimates the importance of \mathcal{O}_1 .

Before turning to the neutron EDM, we discuss results for DM–Xenon scattering for Model IIa. We again chose a flavor–universal Yukawa coupling $h_2^q \equiv h_2 = 1$, and the same two values of mediator mass as for Model I. The coupling λ_1 appearing in c_{10} is set to 1, and we show results for the pseudoscalar mediator–WIMP coupling $\lambda_2 = 1$ or 0.

Figure 7 shows the number of scattering events from \mathcal{O}_{10} and \mathcal{O}_1 for $\mu_1 = 1.0$. We again find that for the large mediator mass ($m_\phi = 1000$ GeV, right frame) the tree–level contribution from \mathcal{O}_{10} dominates by approximately two orders of magnitude for the entire range of m_χ shown.⁹ On the other hand, for $m_\phi = 125$ GeV the two contributions are roughly comparable, with \mathcal{O}_1 dominating at small WIMP masses and \mathcal{O}_{10} dominating for larger masses, in particular if the upper cut on the recoil energy is relaxed to 240 keV.

The main qualitative difference to the results of Model I is that c_1 remains nonzero over the entire range of DM mass shown. The terms from the scalar–scalar current $\propto \lambda_1^2 + \lambda_2^2$ in eq.(2.16), third line, contribute with opposite sign from those $\propto \lambda_1^2$ (in the fifth line), which have the same sign as the contribution from the triangle diagram (the last term).

⁹Due to the lower cut on the recoil energy and the upper limit on the WIMP velocity related to the galactic escape velocity, the entire scattering rate vanishes for WIMP masses below 5 GeV.

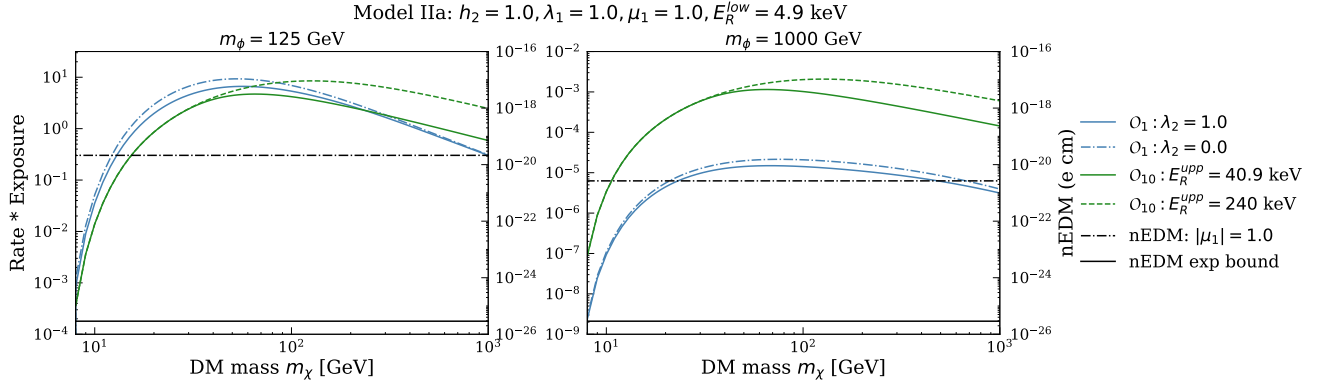


Figure 7: The left y -axes show the total number of scattering events in Model IIa with $\mu_1 = 1.0$ at XENON1T with a runtime exposure of 1 tonne-year as a function of the DM mass m_χ for two values of the mediator mass, $m_\phi = 125$ GeV (left frame) and $m_\phi = 1000$ GeV (right frame). The **green** and **blue** curves show the number of events due to \mathcal{O}_{10} and \mathcal{O}_1 respectively. The **black** lines refer to the right y -axes; **solid black** line is the experimental upper limit on the nEDM, and the **dashed black** line is value of nEDM predicted by Model IIa.

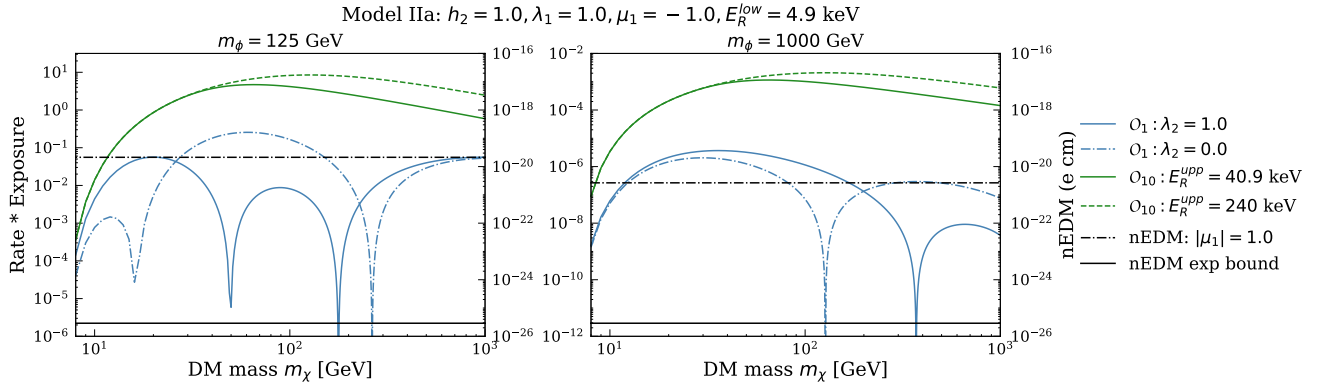


Figure 8: As in Fig. 7, but for $\mu_1 = -1.0$.

This last (triangle) term dominates both for $m_\chi \ll m_\phi$ and for $m_\chi \gg m_\phi$, but is slightly smaller than the total contribution from box diagrams for $m_\chi \sim m_\phi$. As a result, when the (relative) sign between these contributions is flipped by choosing $\mu_1 = -1$, as in Fig. 8, c_1 vanishes at the two values of $s = m_\chi/m_\phi$ where the total box contribution has the same magnitude as the contribution from the triangle diagram. Since this cancellation happens at fixed values of s , it occurs at larger m_χ when m_ϕ is increased (right frame).

The upshot of this discussion is that both in Model I and in Model IIa the contribution from the non-leading NREFT operator \mathcal{O}_{10} can indeed dominate the loop suppressed contribution from the leading operator \mathcal{O}_1 , especially for large mediator masses. However, we saw at the end of the previous Chapter that in these models an nEDM is produced by two-loop diagrams involving a quark and the mediator ϕ , see Fig. 4. Its 90% C.L. experimental upper

bound is depicted by the solid black curves in Figs 5 to 8 which refer to the right y -axes, while the nEDM predicted by the models for the given choice of parameters is shown by the dashed black curves. We estimate the numerical value of the nEDM from the dominant contribution from the down quark cEDM \tilde{d}_d . Using eqs.(2.22) and (2.23), we obtain for $h_2 = \mu_1 = 1.0$:

$$|d_n| \approx \frac{2g_S}{(16\pi^2)^2} \left(\frac{m_\phi}{\text{GeV}} \right) \frac{5.28 \times 10^{-2}}{(m_\phi/\text{GeV})^2} e \cdot \text{GeV}^{-1} \approx \frac{1.58 \times 10^{-19}}{(m_\phi/\text{GeV})} e \cdot \text{cm}, \quad (3.7)$$

where we used $g_S = 1.9$ for the strong coupling at scale of a few GeV. The loop integrals in eq.(2.22) only depend on the quark mass m_q and the mediator mass m_ϕ . On dimensional grounds, they can be written as $1/m_\phi^2$ times a function of the dimensionless ratio m_q/m_ϕ . For the down quark we can safely set $m_q \rightarrow 0$ for the values of m_ϕ we consider; the loop integral then evaluates to $5.28 \times 10^{-2}/m_\phi^2$. Eq.(3.7) therefore predicts $|d_n| \sim \mathcal{O}(10^{-21}) e \cdot \text{cm}$ for $m_\phi = 125$ GeV. Increasing m_ϕ to 1 TeV reduces the nEDM value by a factor of 8; recall that we parameterize the trilinear scalar coupling as $\mu_1 m_\phi$, so for fixed $|\mu_1|$, $d_n \propto 1/m_\phi$. This agrees with the dashed black lines in the panels of Figs. 5 to 8.

Evidently for this set of couplings and $m_\phi = 125$ GeV, the predicted nEDM exceeds the upper bound by about 5 orders of magnitude; increasing m_ϕ to 1 TeV still leads to a discrepancy by about 4 orders of magnitude. Clearly these sets of parameters, which led to in principle observable effects from \mathcal{O}_{10} , are not realistic.

We saw in eq.(2.22) that the predicted nEDM scales like $h_2^3 \mu_1$. In order to suppress the produced nEDM below the upper limit, one thus has to reduce this product of couplings by $\mathcal{O}(10^{-4} - 10^{-5})$. This could be achieved by reducing the Yukawa coupling h_2 by a factor of at least 30 while keeping $|\mu_1| = 1.0$ the same. However, this would reduce the contribution from \mathcal{O}_{10} to the scattering rate by a factor of 10^3 ; the contribution from \mathcal{O}_1 would even be reduced by a factor of 10^6 . The resulting cross sections lie below their corresponding neutrino floor(s); this part of parameter space of Models I and IIa is thus beyond the sensitivity of direct search experiments.

Alternatively one can reduce μ_1 by a factor $\geq 10^4$. This effectively removes one of the triangle diagrams contributing to \mathcal{O}_1 , but the contribution from \mathcal{O}_{10} as well as the box and – for Model I – the second triangle diagram for \mathcal{O}_1 remain unchanged. The contribution from \mathcal{O}_{10} would then still dominate over that \mathcal{O}_1 , except for small m_S as discussed above. However, setting $\mu_1 = 0$ does not increase the symmetry of the theory. Therefore setting μ_1 to zero only suppresses it at the lowest order in perturbation theory. Radiative corrections will in general induce a non-zero value of this cubic self-coupling.

As shown in Fig. 9, this happens at one-loop level in both Model I and Model IIa, via triangle diagrams with the DM particle running in the loop. Crucially, in both cases the DM-mediator coupling used here is the same coupling that appears in c_{10} , i.e. one cannot “switch off” these triangle diagrams without simultaneously setting the contribution from \mathcal{O}_{10} to zero. In case of Model IIa, the diagram shown in Fig. 9 is (logarithmically) divergent, i.e. setting $\mu_1 = 0$ leads, strictly speaking, to a non-renormalizable theory. The triangle diagram shown for Model I is convergent. If the quartic coupling g_2 is nonzero, there is also

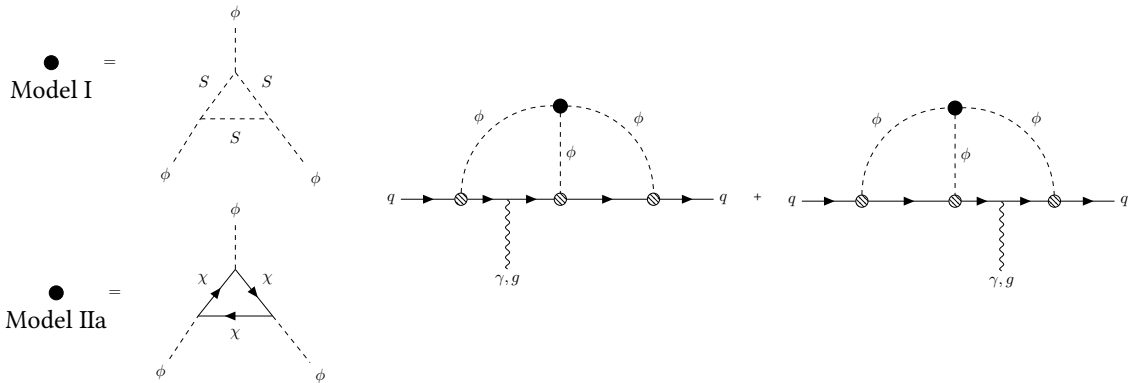


Figure 9: One-loop radiative corrections to the three-point function of the mediator $\langle\phi^3\rangle$ given by triangle diagrams in Model I and Model IIa; such diagrams induce a non-vanishing effective μ_1 even if this trilinear coupling is initially set to zero. The quark EDM and cEDMs are then induced at the three-loop level.

a divergent “bubble” diagram involving one g_2 vertex and one g_1 vertex, but g_2 does not contribute to c_{10} at tree-level, so in the following discussion we will set $g_2 = 0$.

Inserting these one-loop triangle diagrams into the upper vertex of the EDM diagrams results in three-loop diagrams. Rather than performing the challenging full three-loop calculation, we use our earlier two-loop result for d_q and insert a lower bound on μ_1 due to the triangle diagrams:

$$\text{Model I: } \mu_1 \gtrsim \frac{g_1^3}{16\pi^2} \frac{m_S}{2m_\phi}, \quad (3.8)$$

$$\text{Model IIa: } \mu_1 \gtrsim \frac{\lambda_1^3}{16\pi^2} \frac{2m_\chi}{m_\phi}. \quad (3.9)$$

The relative factor of 4 accounts for the four degrees of freedom running in the loop in Model IIa; computationally it results from the Dirac trace appearing in the evaluation of the fermionic triangle diagram. In the next step, we convert this lower bound on μ_1 into a lower bound on the quark EDM (and cEDM) using eq.(2.22):

$$\text{Model I: } d_q \gtrsim \frac{e Q_q}{(16\pi^2)^3} (h_2 g_1)^3 m_S \lim_{q^2 \rightarrow 0} \left([\mathcal{X}] + [\mathcal{Y}] \right); \quad (3.10)$$

$$\text{Model IIa: } d_q \gtrsim 4 \frac{e Q_q}{(16\pi^2)^3} (h_2 \lambda_1)^3 m_\chi \lim_{q^2 \rightarrow 0} \left([\mathcal{X}] + [\mathcal{Y}] \right). \quad (3.11)$$

This leads directly to a lower bound on the nEDM, which can be translated into upper bounds on $|h_2^3 g_1^3|$ and $|h_2^3 \lambda_1^3|$ in Model I and Model IIa, respectively, by requiring our theoretical lower bound on d_n not exceed the stringent experimental upper bound.

Note that the products of couplings which are bounded by the nEDM also appear in the coefficient c_{10} , see eqs.(2.9) and (2.17), although with different powers: the bound on the nEDM scales cubically with the product of couplings whereas c_{10} scales linearly, i.e. the contribution from \mathcal{O}_{10} to the DM scattering rate scales quadratically. The same is true for

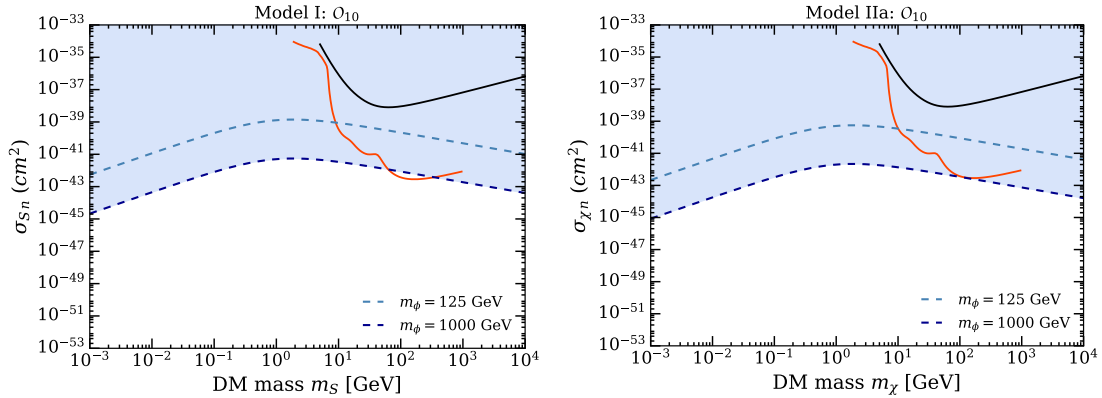


Figure 10: The **black** curves show the XENON1T upper bound on the DM–nucleon cross section from \mathcal{O}_{10} in Model I (left frame) and Model IIa (right frame) as a function of DM mass. The indirect constraint from the nEDM is shown by the **dashed light blue** curve for $m_\phi = 125$ GeV and the **dashed dark blue** curve for $m_\phi = 1000$ GeV; the shaded region is thus excluded by the nEDM bound for $m_\phi = 1000$ GeV. The **red** curve denotes the neutrino floor for \mathcal{O}_{10} and has been taken from Ref. [68].

the “DM–nucleon scattering cross section” due to \mathcal{O}_{10} , defined by:

$$\sigma_{\mathcal{O}_{10}|^I} = \frac{3\mu_{SN}^2}{\pi} (c_{10|}^N|^I)^2 \quad \text{and} \quad \sigma_{\mathcal{O}_{10}|^{IIa}} = \frac{3\mu_{\chi N}^2}{\pi} (c_{10|}^N|^{IIa})^2. \quad (3.12)$$

The upper bounds on $|h_2 g_1|$ and $|h_2 \lambda_1|$ from the nEDM will thus lead to upper bounds on this cross section.

This is illustrated in Figs. 10, which show excluded regions in the plane spanned by $\sigma_{\mathcal{O}_{10}}$ and the DM mass, for Model I (left) and Model IIa (right). The dashed blue curves depict the nEDM–derived 90% c.l. upper limit on the cross section for our two standard choices of the mediator mass m_ϕ . This bound becomes weakest at DM mass $m_{\text{DM}} \simeq 1$ GeV, i.e. close to the nucleon mass; here $m_{\text{DM}} = m_S$ (m_χ) for Model I (Model IIa). For fixed couplings our estimated d_n of eq.(3.10) increases linearly with m_{DM} , while $\sigma_{\mathcal{O}_{10}} \propto m_{\text{DM}}^2$ for $m_{\text{DM}} \ll 1$ GeV but becomes independent of it for large DM mass. As a result, taking into account the different powers of couplings involved in the two quantities, the d_n –derived upper bound on $\sigma_{\mathcal{O}_{10}}$ grows like $m_{\text{DM}}^{4/3}$ for $m_{\text{DM}} \ll 1$ GeV, but declines like $m_{\text{DM}}^{-2/3}$ for $m_{\text{DM}} \gg 1$ GeV. Moreover, $\sigma_{\mathcal{O}_{10}} \propto m_\phi^{-4}$ while our estimated bound on $d_n \propto m_\phi^{-2}$; the d_n –derived upper bound on $\sigma_{\mathcal{O}_{10}}$ therefore scales $\propto m_\phi^{-8/3}$ for all DM masses, i.e. the bound becomes more stringent for larger mediator mass. Finally, the bound is stronger in Model IIa by a factor of $4^{2/3} \simeq 2.5$ due to the relative factor of 4 between the radiatively generated value of μ_1 given in eqs.(3.8).

The red curves in Fig. 10 show the irreducible background level from coherent neutrino–nucleus scattering (“neutrino floor”) as estimated in Ref. [68]. We see that the indirect constraint is around five orders of magnitude below the present XENON1T sensitivity, and for most DM masses well below the neutrino floor for $m_\phi = 1000$ GeV. For this value of the mediator mass the current constraints on d_n therefore imply that the interactions due

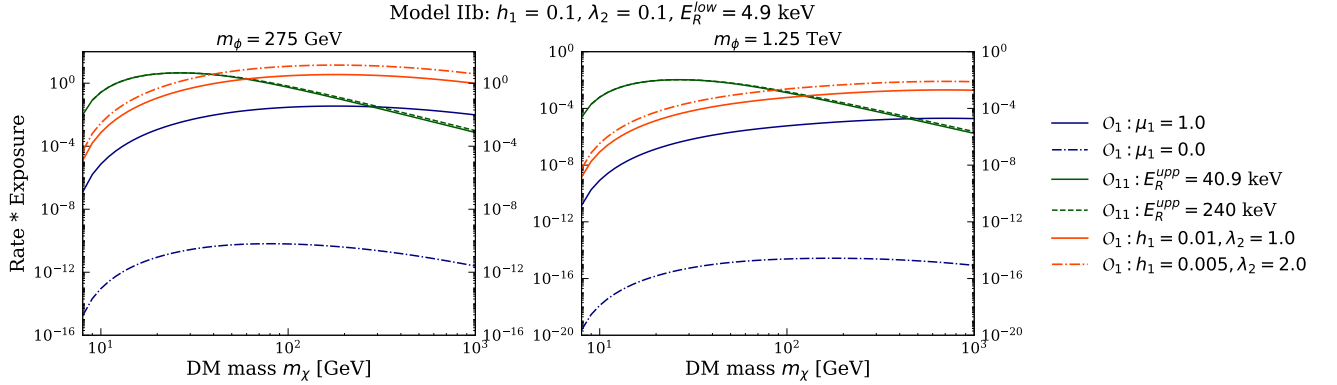


Figure 11: Total number of scattering events in Model IIb at XENON1T with a runtime exposure of 1 tonne–year as a function of the DM mass m_χ for $h_1 = \lambda_2 = 0.1$, with $m_\phi = 275 \text{ GeV}$ (left) and $m_\phi = 1.25 \text{ TeV}$ (right). The **green** curves show the number of events due to \mathcal{O}_{11} and the **blue** curves show the number of events due to \mathcal{O}_1 . The **red** curves also show contributions from \mathcal{O}_1 with the same product $h_1\lambda_2$, and hence the same contribution from \mathcal{O}_{11} , but larger λ_2 .

to \mathcal{O}_{10} are essentially unobservable; recall that for this large mediator mass, \mathcal{O}_1 contributes even less to the scattering rate.

For $m_\phi = 125 \text{ GeV}$, the nEDM constraint still lies well below the current sensitivity. On the other hand, for $m_{\text{DM}} \gtrsim 7 \text{ GeV}$ it is up to two orders of magnitude above the neutrino floor. Our analysis can therefore not completely exclude the possibility that future Xenon experiments might become sensitive to contributions from \mathcal{O}_{10} , if the upper bound on d_n remains unchanged. It should be noted, however, that saturating the bound on d_n requires relatively large couplings. Setting $g_1 = \lambda_1 = 1$ and $m_\phi = 125 \text{ GeV}$, the estimate (3.10) is saturated for Yukawa coupling $h_2 \simeq 0.13[m_\phi/(\kappa m_{\text{DM}})]^{1/3}$, where $\kappa = 1/2$ (2) in Model I (Model IIa); reducing the size of the DM–mediator coupling would require even larger h_2 . Given our assumption of flavor–universal Yukawa couplings, experiments at LEP, the Tevatron and the LHC should be able to set quite stringent bounds on h_2 for $m_\phi \lesssim 125 \text{ GeV}$. We finally discuss numerical results for Model IIb. We recall that this model had been constructed to generate the operator \mathcal{O}_{11} at tree–level, which is independent of the spin of the target nucleus. This required a scalar Yukawa coupling of the mediator to quarks, and a pseudoscalar coupling to the DM fermion. While this assignment quite manifestly again violates CP , it does not generate new contributions to the neutron EDM. However, at one–loop contributions to the leading spin–independent operator \mathcal{O}_1 are generated also in this model.

In Figs. 11 and 12, we display the number of scattering events due to \mathcal{O}_1 and \mathcal{O}_{11} for 1.0 tonne–year exposure of the XENON1T experiment as a function of the DM mass m_χ . In each figure the mediator mass in the left frame is chosen such that the contribution from \mathcal{O}_{11} saturates the XENON1T constraint for $m_\chi \simeq 30 \text{ GeV}$, while in the right frame this contribution is barely above the neutrino floor for $10 \text{ GeV} \lesssim m_\chi \lesssim 50 \text{ GeV}$ (and slightly below it for larger m_χ). We again assume flavor–universal Yukawa couplings $h_1^q \equiv h_1$. The

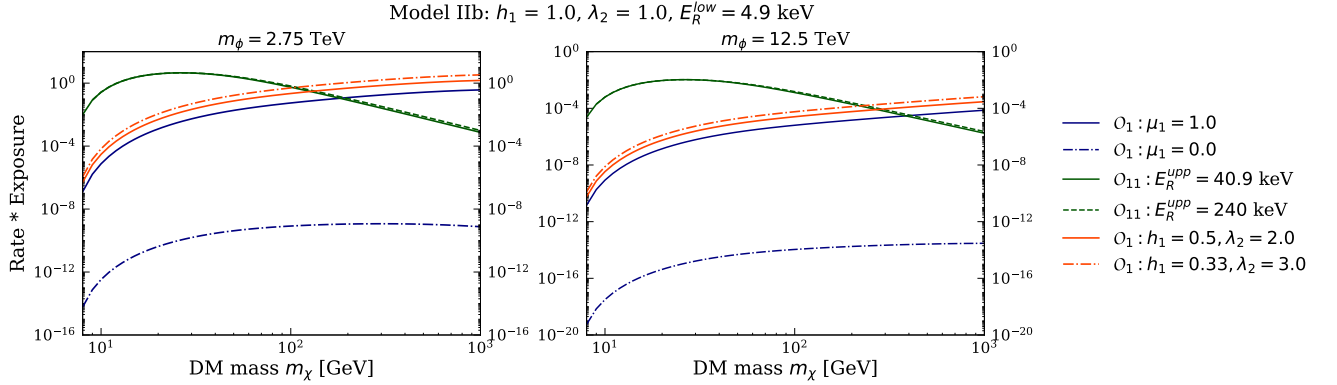


Figure 12: As in Fig. 11, but with $\lambda_2 = h_1 = 1$ and correspondingly larger mediator masses: $m_\phi = 2.75$ TeV (left) and $m_\phi = 12.5$ TeV (right).

event rates due to \mathcal{O}_{11} are shown by the green lines, while the blue curves show the event rate due to \mathcal{O}_1 for $h_1 = \lambda_2 = 0.1$, with ($\mu_1 = 1$, solid) or without ($\mu_1 = 0$, dashed) the triangle diagram. The red curves also show contribution due to \mathcal{O}_1 with $\mu_1 = 1$, but for $\lambda_2 > h_1$, keeping the product $\lambda_2 \cdot h_1$, and hence the contribution from \mathcal{O}_{11} , constant.

Evidently the loop-induced contribution from \mathcal{O}_1 can only be competitive if the triangle diagram is not suppressed. This is in accord with our discussion of eq.(2.20), which showed that this contribution is expected to dominate if μ_1 is sizable. We reiterate that there are logarithmically divergent one-loop contributions of order $h_1^3 m_q / (16\pi^2 m_\phi)$ to this coupling from quark triangle diagrams, hence there is no reason to assume that μ_1 is very small.

We also see that in all cases the tree-level contribution from \mathcal{O}_{11} drops quickly for $m_\chi \gtrsim 50$ GeV. This is partly due to the reduced flux of DM particles, which scales $\propto 1/m_\chi$, but mostly because $c_{11} \propto 1/m_\chi$, as shown in eq.(2.21). In contrast, the loop-induced contribution from \mathcal{O}_1 in many cases keeps increasing with increasing m_χ over the entire range shown. This is because for $m_\chi \ll m_\phi$, the triangle loop function satisfies $sS_1(s) \simeq m_\chi / (2m_\phi^2)$, hence this contribution to the scattering cross section scales $\propto m_\chi^2$ for $m_\chi \ll m_\phi$. As a result, for $\mu_1 = 1$ we always find that the contribution from \mathcal{O}_{11} dominates for small m_χ , while that from \mathcal{O}_1 is dominant at large m_χ ; the DM mass where the two contributions are equal depends on the values of the other parameters. The behavior of the loop function S_1 also explains why the contribution due to \mathcal{O}_1 drops faster with increasing m_ϕ than that due to \mathcal{O}_{11} , as long as $m_\phi > m_\chi$.

We note that the number of events from \mathcal{O}_{11} remains essentially unchanged when the maximal recoil energy is increased from 40.9 keV to 240 keV. As in case of \mathcal{O}_{10} , the scattering rate due to \mathcal{O}_{11} is peaked at non-zero recoil energies, due to the \vec{q} factor in the definition of this operator. However, unlike \mathcal{O}_{10} , \mathcal{O}_{11} leads to coherent scattering on the entire nucleus. The rate is thus proportional to the square of the spin-independent elastic form factor of Xenon, which is quite soft. It is this coherent enhancement which leads to a much larger scattering rate from \mathcal{O}_{11} than from \mathcal{O}_{10} , for similar Wilson coefficients. However, the product of recoil energy E_R (which is $\propto \vec{q}^2$) and squared form factor already peaks at $E_R \simeq 20$ keV; the convolution with the DM velocity distribution further suppresses

the rate at large E_R .

Semi-quantitatively, the ratio of the two contributions can be estimated as follows:

$$\frac{N_{\mathcal{O}_1}}{N_{\mathcal{O}_{11}}}\Big|_{\text{IIb}} = \frac{R_{\mathcal{O}_1}}{R_{\mathcal{O}_{11}}}\Big|_{\text{IIb}} \sim \frac{(c_1^N|^{\text{IIb}})^2}{(c_{11}^N|^{\text{IIb}})^2} \frac{m_N^2}{\vec{q}^2}. \quad (3.13)$$

The nuclear response is the same for both contributions and therefore does not appear in the ratio. The factor $(q^2/m_N^2)^{-1}$ is due to the momentum transfer dependence of \mathcal{O}_{11} . We only retain the leading triangle contribution to $c_1^N|^{\text{IIb}}$, see eq.(2.20),

$$c_1^N|^{\text{IIb}} \approx -\frac{\lambda_2^2}{16\pi^2} \mu_1 m_N \tilde{f}^N \frac{m_\chi}{m_\phi} S_1. \quad (3.14)$$

Using $c_{11}^N|^{\text{IIb}}$ from eq.(2.21), the ratio of events is thus given by

$$\frac{N_{\mathcal{O}_1}}{N_{\mathcal{O}_{11}}}\Big|_{\text{IIb}} \approx \left(\frac{\lambda_2 \mu_1}{16\pi^2} \frac{m_\chi^2 m_\phi}{m_N} S_1(s) \right)^2 \frac{m_N}{2AE_R}. \quad (3.15)$$

For example, for $\lambda_2 = \mu_1 = 1.0$, $m_\phi = 2.75$ TeV and $m_\chi = 200$ GeV, and taking $E_R = 20$ keV as typical recoil energy in order to account for the soft form factor for coherent scattering, gives 0.45 for the ratio of event numbers, in rough agreement with the results shown in the left frame of Fig. 12. For the same couplings but increasing m_ϕ to 12.5 TeV, eq.(3.15) predicts equal event rates for $m_\chi = 520$ GeV, quite close to the intersection point between the green and blue lines in the right frame of Fig. 12. Moreover, eq.(3.15) also explains why increasing λ_2 while keeping $\lambda_2 \cdot h_1$ fixed (red curves) increases the contribution from \mathcal{O}_1 . In fact, for $m_\phi \lesssim 1$ TeV reducing h_1 should help to avoid possible constraints on the model from searches at the LHC.

4 Summary and Conclusions

In this paper we explored the detection prospects involving P - and T -odd operators arising in the NREFT formalism of WIMP-nucleon scattering. These operators appear at next-to-leading order in an expansion in WIMP velocity v and momentum transfer \vec{q} . Since these quantities accompanying the P - and T -odd operators are quite small, these operators are expected to be insignificant relative to the leading order operators *if* the corresponding Wilson coefficients are of similar magnitude. Hence the additional operators can make significant contributions only when the coefficient of the leading spin-independent operator \mathcal{O}_1 is strongly suppressed or vanishes entirely. This typically requires ad hoc choices of couplings in a relativistic QFT, i.e. one can generally not find a symmetry that suppresses the contribution from \mathcal{O}_1 without also suppressing the Wilson coefficients of the additional operators.

Crucially, the P - and T -odd NREFT operators can only occur in the low energy limit of a QFT that violates the CP symmetry. This can lead to stringent constraints on the theory, in particular from electric dipole moments.

We addressed these concerns in the framework of three simplified models with uncharged t -channel mediators, taken from ref. [47]. These models extend the SM by a real scalar

mediator particle ϕ which does not carry electric or color charge, and a DM particle which has spin 0 (Model I) or spin 1/2 (Model IIa and IIb). These models can generate flavor changing neutral currents already at tree-level unless the Yukawa couplings of the mediator are diagonal in the quark mass basis. This can easily be ensured if these new couplings are flavor-universal, which we therefore assumed in our numerical examples.

The couplings in these models are chosen such that at the lowest order in perturbation theory, only the P - and T -odd operators \mathcal{O}_{10} and \mathcal{O}_{11} arise in the non-relativistic limit. In particular, ϕ must not have scalar couplings to both quarks and the DM particle. In Models I and IIa, the quark couplings are pseudoscalar while the DM couplings are scalar, while in Model IIb the quark couplings are scalar but the DM couplings are pseudoscalar. Note that there is no symmetry that forbids scalar quark couplings in Models I and IIa, or scalar DM couplings in Model IIb. It is therefore not surprising that at the next order in perturbation theory, one-loop box and triangle diagrams do induce the canonical SI interactions described by the operator \mathcal{O}_1 in these models. We compared the tree-level interactions giving rise to \mathcal{O}_{10} or \mathcal{O}_{11} with the one-loop suppressed interactions yielding \mathcal{O}_1 . To that end we computed the total number of events due to the two types of interactions for a Xenon target.

In the case of Model I and Model IIa and assuming large couplings in order to generate detectable event rates, we found that the contributions from \mathcal{O}_{10} can be roughly comparable to those from \mathcal{O}_1 for mediator mass $m_\phi = 125$ GeV, but for heavier mediator the contributions from \mathcal{O}_{10} clearly dominates. It thus appears as if \mathcal{O}_{10} could indeed be the most relevant NREFT operator in these models.

However, we pointed out that the quark-mediator interactions in both models produce two-loop contributions to d_n , the electric dipole moment of the neutron (nEDM). These contributions scale linearly with the cubic self-interaction of the mediator μ_1 . For parameter choices that lead to detectable event rates from \mathcal{O}_{10} and μ_1 of order unity (in units of m_ϕ), the predicted d_n is several orders of magnitude larger than the upper limit reported by experiments. Even if we set $\mu_1 = 0$, non-vanishing trilinear self-interactions are generated at one-loop level by couplings that also appear in the Wilson coefficient of \mathcal{O}_{10} . Estimating a lower bound on μ_1 from these loop diagrams, we find that the resulting upper bound on the WIMP-nucleus scattering rate is still well below current sensitivity, and often even below the irreducible background (“neutrino floor”), especially for large m_ϕ where \mathcal{O}_{10} potentially dominates the scattering rate. As in case of models with charged, s -channel mediator, where d_n is generated already at one-loop level [50], it is thus essential to consider the d_n constraint when considering prospects for detecting WIMP-nucleus scattering due to \mathcal{O}_{10} . In Model IIb, which generates the spin-independent NREFT operator \mathcal{O}_{11} , we again found that the loop-induced contributions from \mathcal{O}_1 can be larger than the tree-level contribution due to \mathcal{O}_{11} , if the trilinear scalar coupling μ_1 is not suppressed. We emphasized that in this model quark loops generate a logarithmically divergent one-loop contribution to μ_1 . For $\mu_1 = 1$, \mathcal{O}_1 typically dominates for large DM masses, while \mathcal{O}_{11} is dominant for small masses, the cross-over point depending on the values of the other parameters. In this model no new contributions to d_n are generated, and therefore this operator is not subject to the stringent constraints of the neutron EDM, even though it is also P - and T -odd.

At least at the level of a simplified model one can therefore engineer a scenario where the non-leading operator \mathcal{O}_{11} dominates the WIMP–nucleon scattering rate.

However, it is by no means clear whether this remains true in the framework of UV-complete theories. Recall that we only require our Lagrangians to be invariant under $SU(3)_C \times U(1)_{em}$; we did not enforce invariance under the electroweak gauge symmetry. In particular, the $\phi\bar{q}q$ couplings are not $SU(2) \times U(1)_Y$ invariant if ϕ is a singlet. The simplest choice would be to identify ϕ with the Higgs boson of the SM, which resides in a doublet of $SU(2)$. However, the $\phi\bar{q}q$ couplings are then known to be very small. Moreover, the WIMP can then also not be a gauge singlet, and would thus have additional (gauge) interactions leading to additional constraints as well as new contributions to WIMP–nucleon scattering. Alternatively one can couple a singlet WIMP to a singlet scalar which mixes with the SM Higgs boson; however, in such a scenario the WIMP–nucleon scattering rate would be suppressed even further by the mediator–Higgs mixing angle, which has to be rather small in order not to distort the properties of the physical 125 GeV particle too much.

We remind the reader that we assumed universal flavor–diagonal couplings of the mediator to the quarks. This simplifies the model building, since these couplings are then flavor–diagonal in any basis. On the other hand, it might appear more natural to assume that the new couplings increase with increasing quark mass, just as the Yukawa couplings of the SM do. In this case tree–level FCNC are avoided if the matrices of new Yukawa couplings commute with the Yukawa coupling matrices of the SM; from the model building point of view it is not clear why this should be the case. Moreover, keeping the couplings to the top quark $\lesssim 1$ would then require very small couplings to the first generation. In such a scenario the contributions from heavy quarks might well dominate the DM scattering cross section, as well as – in Models I and IIa – the electric dipole moment of the neutron. In order to yield detectable event rates, the couplings to third generation quarks would have to be larger, and/or the mediator lighter, than in our numerical examples. It seems rather unlikely to us that this would lead to qualitatively different conclusions in Models I and IIa with unsuppressed trilinear self–coupling of the mediator, given the very large discrepancy between the predicted nEDM and its experimental upper bound that we found in our numerical examples; however, we have not performed an explicit computation to check this.¹⁰

In summary, the results presented in this paper as well as ref.[50] strongly indicate that the current experimental upper bound on the electric dipole moment of the neutron excludes the possibility that the operator \mathcal{O}_{10} can make contributions to WIMP–nucleus scattering to which current or near–future experiments are sensitive. While no such strong statement can be made for the operator \mathcal{O}_{11} generated by the exchange of a neutral mediator in the t –channel, it is currently unclear whether such a model can be constructed that respects the full gauge symmetry of the SM and leads to detectable WIMP–nucleon scattering being dominated by \mathcal{O}_{11} .

¹⁰The cEDMs of heavy quarks generate light quark cEDMs, as well as an electron EDM, at the three–loop level [69]. Moreover, the contribution of the gluonic Weinberg operator, which will generically be generated at three–loop level in Models I and IIa, would probably also have to be taken into account [70].

Acknowledgments

We acknowledge the use of TikZ–Feynman [71] for creating Feynman diagrams and Package–X [72] for verifying parts of our loop computations. We thank Claude Duhr for discussions about the two loop diagram. RM was partially supported by the Bonn Cologne Graduate School of Physics and Astronomy.

A 1-loop calculations

In this appendix we provide details of the calculations of the one–loop box and triangle diagrams appearing in Model I, IIa and IIb.

A.1 Model I Matrix Element

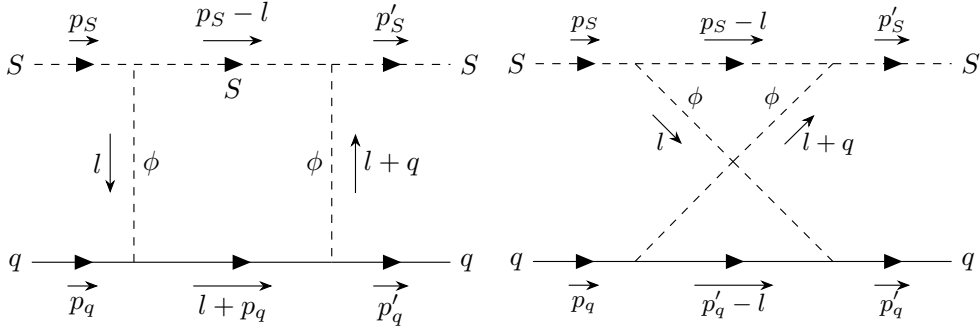


Figure 13: One–loop box and crossed box diagrams contributing to \mathcal{O}_1 in Model I.

The box diagram shown in the left Fig. 13 gives the following contribution to the matrix element for DM–quark scattering:

$$i\mathcal{M}_1^I = (-ig_1 m_S)^2 \int \frac{d^4 l}{(2\pi)^4} \frac{i}{(p_S - l)^2 - m_S^2} \frac{i}{l^2 - m_\phi^2} \frac{i}{(l + q)^2 - m_\phi^2} \frac{i}{(p_q + l)^2 - m_q^2} \\ \times \bar{u}(p'_q) h_2^q \gamma^5 (\not{p}_q + \not{l} + m_q) h_2^q \gamma^5 u(p_q); \quad (\text{A.1})$$

the crossed box diagram shown in the right Fig. 13 contributes:

$$i\mathcal{M}_2^I = (-ig_1 m_S)^2 \int \frac{d^4 l}{(2\pi)^4} \frac{i}{(p_S - l)^2 - m_S^2} \frac{i}{l^2 - m_\phi^2} \frac{i}{(l + q)^2 - m_\phi^2} \frac{i}{(p'_q - l)^2 - m_q^2} \\ \times \bar{u}(p'_q) h_2^q \gamma^5 (\not{p}'_q - \not{l} + m_q) h_2^q \gamma^5 u(p_q). \quad (\text{A.2})$$

After simplifying the numerator by commuting the two γ^5 matrices and using the Dirac equation, we obtain for the two diagrams:

$$i\mathcal{M}_1^I = g_1^2 (h_2^q)^2 m_S^2 M_{1,\mu}^I \bar{u}(p'_q) \gamma^\mu u(p_q) \quad \text{and} \quad (\text{A.3})$$

$$i\mathcal{M}_2^I = -g_1^2 (h_2^q)^2 m_S^2 M_{2,\mu}^I \bar{u}(p'_q) \gamma^\mu u(p_q). \quad (\text{A.4})$$

Here $M_{1,\mu}^I$ and $M_{2,\mu}^I$ are loop integrals:

$$M_{1,\mu}^I = \int \frac{d^4l}{(2\pi)^4} \frac{l_\mu}{[(p_S - l)^2 - m_S^2] [l^2 - m_\phi^2] [(l + q)^2 - m_\phi^2] [(p_q + l)^2 - m_q^2]}, \quad (\text{A.5})$$

$$M_{2,\mu}^I = \int \frac{d^4l}{(2\pi)^4} \frac{l_\mu}{[(p_S - l)^2 - m_S^2] [l^2 - m_\phi^2] [(l + q)^2 - m_\phi^2] [(p'_q - l)^2 - m_q^2]}. \quad (\text{A.6})$$

After Feynman parametrization, these loop integrals can be expressed in the vanishing momentum transfer limit ($q \rightarrow 0$, i.e. $p_S \rightarrow p'_S$ and $p_q \rightarrow p'_q$) in terms of loop functions $M_i(r = m_q/m_\phi, s = m_S/m_\phi)$, $i = 1, \dots, 4$, which are given in Appendix A.1.1. The contributions from the box diagram and crossed box diagrams can then finally be written as:

$$\mathcal{M}_1^I = \frac{(h_2^q)^2 g_1^2 m_S^2}{16\pi^2} \left[\left(\frac{p_{S,\mu} + p'_{S,\mu}}{2} \right) M_1 \bar{u}(p'_q) \gamma^\mu u(p_q) + m_q M_2 \bar{u}(p'_q) u(p_q) \right], \quad (\text{A.7})$$

$$\mathcal{M}_2^I = -\frac{(h_2^q)^2 g_1^2 m_S^2}{16\pi^2} \left[\left(\frac{p_{S,\mu} + p'_{S,\mu}}{2} \right) M_3 \bar{u}(p'_q) \gamma^\mu u(p_q) - m_q M_4 \bar{u}(p'_q) u(p_q) \right]. \quad (\text{A.8})$$

Even though $p_S = p'_S$ for $q = 0$ we've written these contributions in terms of the symmetric sum $p_S + p'_S$, which facilitates matching onto the effective Lagrangian of eq.(2.5) after integrating out the mediator.

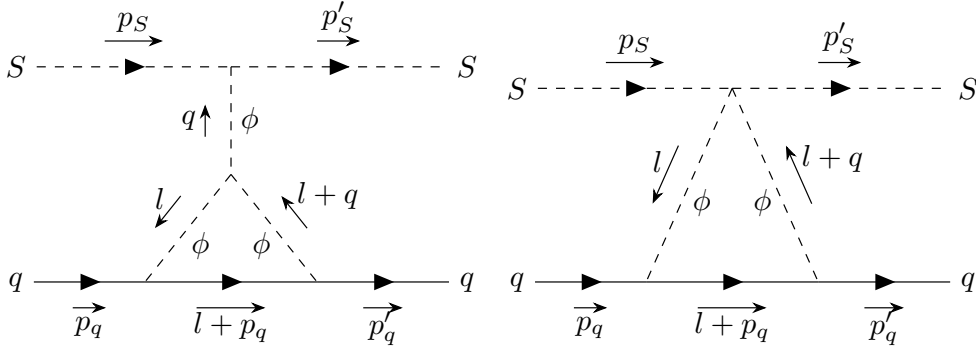


Figure 14: One-loop triangle diagrams contributing to \mathcal{O}_1 in Model I.

Fig. 14 shows contributions to WIMP–quark scattering in Model I from triangle diagrams. The matrix element for the left diagram reads:

$$i\mathcal{M}_{\Delta_1}^I = (-im_\phi \mu_1) (-ig_1 m_S) \frac{i}{q^2 - m_\phi^2} \int \frac{d^4l}{(2\pi)^4} \frac{i}{l^2 - m_\phi^2} \frac{i}{(l + q)^2 - m_\phi^2} \frac{i}{(p_q + l)^2 - m_q^2} \\ \times \bar{u}(p'_q) h_2^q \gamma^5 (\not{p}_q + \not{l} + m_q) h_2^q \gamma^5 u(p_q); \quad (\text{A.9})$$

the right triangle diagram contributes:

$$i\mathcal{M}_{\Delta_2}^I = \left(\frac{-ig_2}{2} \right) \int \frac{d^4l}{(2\pi)^4} \frac{i}{l^2 - m_\phi^2} \frac{i}{(l + q)^2 - m_\phi^2} \frac{i}{(p_q + l)^2 - m_q^2} \\ \times \bar{u}(p'_q) h_2^q \gamma^5 (\not{p}_q + \not{l} + m_q) h_2^q \gamma^5 u(p_q). \quad (\text{A.10})$$

Again commuting the two γ^5 matrices and using the Dirac equation, we obtain for these two diagrams:

$$i\mathcal{M}_{\Delta_1}^I = g_1\mu_1(h_2^q)^2 \frac{m_S m_\phi}{q^2 - m_\phi^2} M_{3,\mu}^I \bar{u}(p'_q)\gamma^\mu u(p_q) \quad \text{and} \quad (\text{A.11})$$

$$i\mathcal{M}_{\Delta_2}^I = \frac{g_2}{2}(h_2^q)^2 M_{3,\mu}^I \bar{u}(p'_q)\gamma^\mu u(p_q) . \quad (\text{A.12})$$

The loop integral $M_{3,\mu}^I$ is:

$$M_{3,\mu}^I = \int \frac{d^4l}{(2\pi)^4} \frac{l_\mu}{[l^2 - m_\phi^2] [(l+q)^2 - m_\phi^2] [(p_q+l)^2 - m_q^2]} . \quad (\text{A.13})$$

In the limit $q \rightarrow 0$ it can be expressed in terms of the loop function L_1 , whose analytic expression is given in Appendix A.1.1. The contribution of the two triangle diagrams to the matrix element can then finally be written as

$$\mathcal{M}_{\Delta_1}^I = \frac{g_1\mu_1(h_2^q)^2}{16\pi^2} \frac{m_q m_S}{m_\phi} L_1(m_q^2, m_\phi^2) \bar{u}(p'_q) u(p_q) , \quad (\text{A.14})$$

$$\mathcal{M}_{\Delta_2}^I = -\frac{g_2(h_2^q)^2}{16\pi^2} \frac{m_q}{2} L_1(m_q^2, m_\phi^2) \bar{u}(p'_q) u(p_q) . \quad (\text{A.15})$$

A.1.1 Model I Loop Functions

We first define the function $L(x)$ of the real variable x as:

$$L(x) = \begin{cases} \sqrt{1-4x^2} \cdot \ln\left(\frac{1+\sqrt{1-4x^2}}{2|x|}\right) & \text{for } |x| \leq 0.5 \\ -\sqrt{4x^2-1} \cdot \arctan\left(\sqrt{4x^2-1}\right) & \text{for } |x| \geq 0.5 \end{cases} . \quad (\text{A.16})$$

In terms of this function, the loop functions M_i , $i = 1, \dots, 4$ and L_1 can be written as:

$$M_1 = \frac{1}{3m_\phi^4} \left[\frac{1}{s(r+s)} - \frac{(1+2r^2)}{2r^2(r+s)^2} L(r) + \frac{s-2r}{4r^2s^3} \ln(1/s^2) - \frac{\ln(r^2/s^2)}{4r^2(r+s)^2} + \frac{2r+3s-4rs^2-6s^3+8rs^4}{2s^3(r+s)^2(1-4s^2)} L(s) \right]; \quad (\text{A.17})$$

$$M_2 = \frac{1}{3m_\phi^4} \left[-\frac{1}{r(r+s)} + \frac{1+2s^2}{2s^2(r+s)^2} L(s) - \frac{r-2s}{4r^3s^2} \ln(1/s^2) - \frac{(3r+2s)\ln(r^2/s^2)}{4r^3(r+s)^2} + \frac{2s+3r-4r^2s-6r^3+8r^4s}{2r^3(4r^2-1)(r+s)^2} L(r) \right]; \quad (\text{A.18})$$

$$M_3 = \frac{1}{3m_\phi^4} \left[\frac{1}{s(s-r)} - \frac{1+2r^2}{2r^2(r-s)^2} L(r) + \frac{s+2r}{4r^2s^3} \ln(1/s^2) - \frac{\ln(r^2/s^2)}{4r^2(r-s)^2} - \frac{2r-3s-4rs^2+6s^3+8rs^4}{2s^3(r-s)^2(1-4s^2)} L(s) \right]; \quad (\text{A.19})$$

$$M_4 = \frac{1}{3m_\phi^4} \left[-\frac{1}{r(r-s)} + \frac{1+2s^2}{2s^2(r-s)^2} L(s) - \frac{r+2s}{4r^3s^2} \ln(1/s^2) - \frac{(3r-2s)\ln(r^2/s^2)}{4r^3(r-s)^2} + \frac{2s-3r-4r^2s+6r^3+8r^4s}{2r^3(1-4r^2)(r-s)^2} L(r) \right]; \quad (\text{A.20})$$

$$L_1 = \frac{1}{m_\phi^2} \left[\frac{1}{r^2} + \frac{r^2-1}{2r^4} \ln(1/r^2) + \frac{1-3r^2}{r^4(1-4r^2)} L(r) \right]. \quad (\text{A.21})$$

We note that $M_3(r, s) = M_1(-r, s) = M_1(r, -s)$ and $M_4(r, s) = M_2(-r, s) = M_2(r, -s)$, i.e. the functions M_i remain invariant when both arguments change their sign. Of course, in our application only positive arguments are physical, since $r = m_q/m_\phi$ and $s = m_S/m_\phi$. In our examples we assume flavor-universal Yukawa couplings. In this case the contribution from the light quarks will dominate the WIMP-nucleon scattering matrix elements. We therefore also give the **massless quark limits of the loop functions**:

$$M_1, M_3 \xrightarrow{r \rightarrow 0} \frac{1}{2m_\phi^4} \frac{1}{s^2} \left[1 - \frac{1}{2s^2} \ln\left(\frac{1}{s^2}\right) + \frac{1-2s^2}{s^2(1-4s^2)} L(s) \right]; \quad (\text{A.22})$$

$$M_2, M_4 \xrightarrow{r \rightarrow 0} \frac{1}{6m_\phi^4} \frac{1}{s^2} \left[1 - \frac{1}{2s^2} \ln\left(\frac{1}{s^2}\right) + \frac{1+2s^2}{s^2} L(s) \right]; \quad (\text{A.23})$$

$$L_1 \xrightarrow{r \rightarrow 0} -\frac{1}{2m_\phi^2}. \quad (\text{A.24})$$

A.2 Model IIa and IIb Matrix Elements

We now turn to the models with fermionic WIMP χ . We again begin with the box and crossed box diagrams shown in Fig. 15. The contribution to the matrix element for DM-quark scattering from the box diagram in Model IIa, involving the scalar DM-mediator

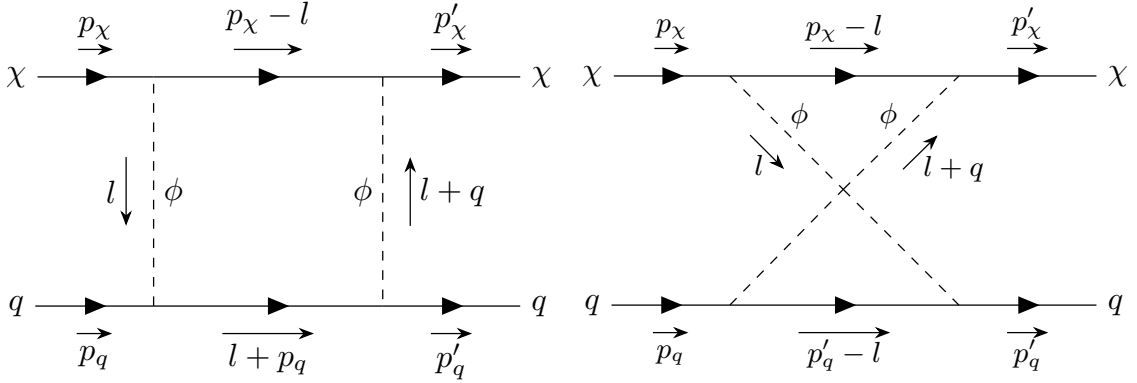


Figure 15: One-loop box diagrams contributing to \mathcal{O}_1 in Model IIa or Model IIb.

coupling λ_1 , is

$$i\mathcal{M}_1^{\text{IIa}} = (-i\lambda_1)^2 \int \frac{d^4l}{(2\pi)^4} \frac{i}{(p_\chi - l)^2 - m_\chi^2} \frac{i}{l^2 - m_\phi^2} \frac{i}{(l + q)^2 - m_\phi^2} \frac{i}{(p_q + l)^2 - m_\phi^2} \\ \times \bar{u}(p'_\chi)(\not{p}_\chi - \not{l} + m_\chi)u(p_\chi)\bar{u}(p'_q)h_2^q\gamma^5(\not{p}_q + \not{l} + m_q)h_2^q\gamma^5u(p_q); \quad (\text{A.25})$$

the crossed box diagram contributes:

$$i\mathcal{M}_2^{\text{IIa}} = (-i\lambda_1)^2 \int \frac{d^4l}{(2\pi)^4} \frac{i}{(p_\chi - l)^2 - m_\chi^2} \frac{i}{l^2 - m_\phi^2} \frac{i}{(l + q)^2 - m_\phi^2} \frac{i}{(p'_q - l)^2 - m_\phi^2} \\ \times \bar{u}(p'_\chi)(\not{p}_\chi - \not{l} + m_\chi)u(p_\chi)\bar{u}(p'_q)h_2^q\gamma^5(\not{p}'_q - \not{l} + m_q)h_2^q\gamma^5u(p_q). \quad (\text{A.26})$$

After simplifying the numerator by commuting the two γ^5 matrices and using the Dirac equation for the external quarks and WIMPs, we obtain for the two diagrams:

$$i\mathcal{M}_1^{\text{IIa}} = -\lambda_1^2 (h_2^q)^2 \left(N_{1,\mu\nu}^{\text{IIa}} [\bar{u}(p'_q)\gamma^\mu u(p_q)] [\bar{u}(p'_\chi)\gamma^\nu u(p_\chi)] \right. \\ \left. - 2m_\chi N_{2,\mu}^{\text{IIa}} [\bar{u}(p'_q)\gamma^\mu u(p_q)] [\bar{u}(p'_\chi)u(p_\chi)] \right); \quad (\text{A.27})$$

$$i\mathcal{M}_2^{\text{IIa}} = \lambda_1^2 (h_2^q)^2 \left(N_{3,\mu\nu}^{\text{IIa}} [\bar{u}(p'_q)\gamma^\mu u(p_q)] [\bar{u}(p'_\chi)\gamma^\nu u(p_\chi)] \right. \\ \left. - 2m_\chi N_{4,\mu}^{\text{IIa}} [\bar{u}(p'_q)\gamma^\mu u(p_q)] [\bar{u}(p'_\chi)u(p_\chi)] \right). \quad (\text{A.28})$$

Here $N_{1,\mu\nu}^{\text{IIa}}$, $N_{3,\mu\nu}^{\text{IIa}}$, $N_{3,\mu}^{\text{IIa}}$ and $N_{4,\mu}^{\text{IIa}}$ are loop integrals:

$$N_{1,\mu\nu}^{\text{IIa}} = \int \frac{d^4l}{(2\pi)^4} \frac{l_\mu l_\nu}{[(p_\chi - l)^2 - m_\chi^2] [l^2 - m_\phi^2] [(l + q)^2 - m_\phi^2] [(p_q + l)^2 - m_\phi^2]}; \quad (\text{A.29})$$

$$N_{2,\mu}^{\text{IIa}} = \int \frac{d^4l}{(2\pi)^4} \frac{l_\mu}{[(p_\chi - l)^2 - m_\chi^2] [l^2 - m_\phi^2] [(l + q)^2 - m_\phi^2] [(p_q + l)^2 - m_\phi^2]}; \quad (\text{A.30})$$

$$N_{3,\mu\nu}^{\text{IIa}} = \int \frac{d^4l}{(2\pi)^4} \frac{l_\mu l_\nu}{[(p_\chi - l)^2 - m_\chi^2] [l^2 - m_\phi^2] [(l + q)^2 - m_\phi^2] [(p'_q - l)^2 - m_\phi^2]}; \quad (\text{A.31})$$

$$N_{4,\mu}^{\text{IIa}} = \int \frac{d^4l}{(2\pi)^4} \frac{l_\mu}{[(p_\chi - l)^2 - m_\chi^2] [l^2 - m_\phi^2] [(l + q)^2 - m_\phi^2] [(p'_q - l)^2 - m_\phi^2]}. \quad (\text{A.32})$$

After Feynman parametrization and taking the limit $q \rightarrow 0$, the loop integrals in eqs.(A.29) to (A.32) can be expressed in terms of loop functions N_i , $i = 1, \dots, 8$ and P_j , $j = 1, \dots, 4$ whose analytic expressions can be found in Appendix A.2.1. Both sets of functions depend on $r = m_q/m_\phi$ and $s = m_\chi/m_\phi$. The contributions from the box and crossed box diagrams can then be written as:

$$\begin{aligned} \mathcal{M}_1^{\text{IIa}} = & -\frac{\lambda_1^2 (h_2^q)^2}{16 \pi^2} \left\{ N_1 [\bar{u}(p'_\chi) \gamma^\mu \bar{u}(p_\chi)] [\bar{u}(p'_q) \gamma_\mu u(p_q)] \right. \\ & + \left(2m_\chi m_q (N_2 - P_2) + m_\chi^2 (N_3 - 2P_1) + m_q^2 N_4 \right) \\ & \left. \times [\bar{u}(p'_\chi) \bar{u}(p_\chi)] [\bar{u}(p'_q) u(p_q)] \right\}; \end{aligned} \quad (\text{A.33})$$

$$\begin{aligned} \mathcal{M}_2^{\text{IIa}} = & \frac{\lambda_1^2 (h_2^q)^2}{16 \pi^2} \left\{ N_5 [\bar{u}(p'_\chi) \gamma^\mu \bar{u}(p_\chi)] [\bar{u}(p'_q) \gamma_\mu u(p_q)] \right. \\ & + \left(2m_\chi m_q (N_6 - P_4) + m_\chi^2 (N_7 - 2P_3) + m_q^2 N_8 \right) \\ & \left. \times [\bar{u}(p'_\chi) \bar{u}(p_\chi)] [\bar{u}(p'_q) u(p_q)] \right\}. \end{aligned} \quad (\text{A.34})$$

The diagrams of Fig. 15 also contribute when both DM–mediator couplings are λ_2 . The contribution from the box diagram reads:

$$\begin{aligned} i\mathcal{M}_3^{\text{IIa}} = & \lambda_2^2 (h_2^q)^2 \int \frac{d^4 l}{(2\pi)^4} \frac{i}{(p_\chi - l)^2 - m_\chi^2} \frac{i}{l^2 - m_\phi^2} \frac{i}{(l + q)^2 - m_\phi^2} \frac{i}{(p_q + l)^2 - m_q^2} \\ & \times \bar{u}(p'_\chi) \gamma^5 (\not{p}_\chi - \not{l} + m_\chi) \gamma^5 u(p_\chi) \bar{u}(p'_q) \gamma^5 (\not{p}_q + \not{l} + m_q) \gamma^5 u(p_q). \end{aligned} \quad (\text{A.35})$$

The crossed box contributes:

$$\begin{aligned} i\mathcal{M}_4^{\text{IIa}} = & \lambda_2^2 (h_2^q)^2 \int \frac{d^4 l}{(2\pi)^4} \frac{i}{(p_\chi - l)^2 - m_\chi^2} \frac{i}{l^2 - m_\phi^2} \frac{i}{(l + q)^2 - m_\phi^2} \frac{i}{(p'_q - l)^2 - m_q^2} \\ & \times \bar{u}(p'_\chi) \gamma^5 (\not{p}_\chi - \not{l} + m_\chi) \gamma^5 u(p_\chi) \bar{u}(p'_q) \gamma^5 (\not{p}'_q - \not{l} + m_q) \gamma^5 u(p_q). \end{aligned} \quad (\text{A.36})$$

After commuting the two γ^5 matrices and using the Dirac equation, these simplify to

$$i\mathcal{M}_3^{\text{IIa}} = -\lambda_2^2 (h_2^q)^2 N_{1,\mu\nu}^{\text{IIa}} [\bar{u}(p'_q) \gamma^\mu u(p_q)] [\bar{u}(p'_\chi) \gamma^\nu u(p_\chi)]; \quad (\text{A.37})$$

$$i\mathcal{M}_4^{\text{IIa}} = \lambda_2^2 (h_2^q)^2 N_{3,\mu\nu}^{\text{IIa}} [\bar{u}(p'_q) \gamma^\mu u(p_q)] [\bar{u}(p'_\chi) \gamma^\nu u(p_\chi)], \quad (\text{A.38})$$

where $N_{1,\mu\nu}^{\text{IIa}}$ and $N_{3,\mu\nu}^{\text{IIa}}$ are loop integrals defined in eqs.(A.29) and (A.31). In the $q \rightarrow 0$ limit we finally obtain:

$$\begin{aligned} \mathcal{M}_3^{\text{IIa}} = & -\frac{\lambda_2^2 (h_2^q)^2}{16 \pi^2} \left\{ N_1 [\bar{u}(p'_\chi) \gamma^\mu \bar{u}(p_\chi)] [\bar{u}(p'_q) \gamma_\mu u(p_q)] \right. \\ & \left. + (2m_\chi m_q N_2 + m_\chi^2 N_3 + m_q^2 N_4) [\bar{u}(p'_\chi) \bar{u}(p_\chi)] [\bar{u}(p'_q) u(p_q)] \right\}; \end{aligned} \quad (\text{A.39})$$

$$\begin{aligned} \mathcal{M}_4^{\text{IIa}} = & \frac{\lambda_2^2 (h_2^q)^2}{16 \pi^2} \left\{ N_5 [\bar{u}(p'_\chi) \gamma^\mu \bar{u}(p_\chi)] [\bar{u}(p'_q) \gamma_\mu u(p_q)] \right. \\ & \left. + (2m_\chi m_q N_6 + m_\chi^2 N_7 + m_q^2 N_8) [\bar{u}(p'_\chi) \bar{u}(p_\chi)] [\bar{u}(p'_q) u(p_q)] \right\}. \end{aligned} \quad (\text{A.40})$$

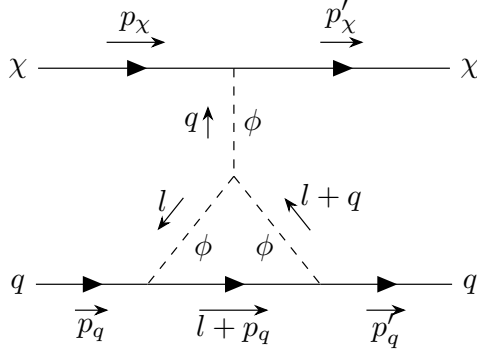


Figure 16: One-loop triangle diagram contributing to \mathcal{O}_1 in Model IIa involving the couplings λ_1 , μ_1 and h_2^q .

The functions N_i already appeared in the contributions $\propto \lambda_1^2$; they are defined in Appendix A.2.1. This completes the contribution from the diagrams of Fig 15, since diagrams involving one scalar and one pseudoscalar coupling on the WIMP line do not contribute to \mathcal{O}_1 .

There is only one triangle diagram contributing to \mathcal{O}_1 at one-loop order in Model IIa, as shown in Fig. 16; note that only the diagram involving the scalar DM-mediator coupling λ_1 contributes to \mathcal{O}_1 . Its contribution to the DM-quark scattering matrix element is given by:

$$i\mathcal{M}_{\Delta}^{\text{IIa}} = \frac{i(-i\lambda_1)(-im_\phi\mu_1)}{q^2 - m_\phi^2} \int \frac{d^4l}{(2\pi)^4} \frac{i}{l^2 - m_\phi^2} \frac{i}{(l+q)^2 - m_\phi^2} \frac{i}{(l+q)^2 - m_\phi^2} \quad (\text{A.41})$$

$$\times [\bar{u}(p'_\chi) u(p_\chi)] \bar{u}(p'_q) h_2^q \gamma^5 (\not{p}_q + \not{l} + m_q) h_2^q \gamma^5 u(p_q). \quad (\text{A.42})$$

After simplifying the numerator as before, we get:

$$\mathcal{M}_{\Delta}^{\text{IIa}} = -\frac{\lambda_1 (h_2^q)^2 \mu_1}{16 \pi^2} \left(\frac{m_q}{m_\phi} \right) R_1 [\bar{u}(p'_\chi) u(p_\chi)] [\bar{u}(p'_q) u(p_q)]. \quad (\text{A.43})$$

Here a new loop function R_1 appears, which is also defined in Appendix A.2.1.

The calculations for Model IIb are very similar. The (crossed) box diagrams look exactly the same as in Model IIa, but now we have scalar Yukawa couplings on the quark line and pseudoscalar couplings on the WIMP line. We only list the final results. For the box and crossed box we obtain:

$$\begin{aligned} \mathcal{M}_1^{\text{IIb}} = & -\frac{\lambda_2^2 (h_1^q)^2}{16 \pi^2} \left[N_1 [\bar{u}(p'_\chi) \gamma^\mu \bar{u}(p_\chi)] [\bar{u}(p'_q) \gamma_\mu u(p_q)] \right. \\ & + (2m_\chi m_q (N_2 + P_1) + m_\chi^2 N_3 + m_q^2 (N_4 + 2P_2)) \\ & \left. \times [\bar{u}(p'_\chi) \bar{u}(p_\chi)] [\bar{u}(p'_q) u(p_q)] \right] \quad (\text{A.44}) \end{aligned}$$

$$\begin{aligned} \mathcal{M}_2^{\text{IIb}} = & \frac{\lambda_2^2 (h_1^q)^2}{16 \pi^2} \left[N_5 [\bar{u}(p'_\chi) \gamma^\mu \bar{u}(p_\chi)] [\bar{u}(p'_q) \gamma_\mu u(p_q)] \right. \\ & + (2m_\chi m_q (N_6 - P_3) + m_\chi^2 N_7 + m_q^2 (N_8 - 2P_4)) \\ & \left. \times [\bar{u}(p'_\chi) \bar{u}(p_\chi)] [\bar{u}(p'_q) u(p_q)] \right]. \quad (\text{A.45}) \end{aligned}$$

The functions N_i and P_k are the same as in Model IIa, and are defined in Appendix A.2.1. The Model IIb triangle diagram shown in Fig. 3 yields:

$$\mathcal{M}_{\Delta}^{\text{IIb}} = -\frac{h_1^q \lambda_2^2 \mu_1}{16 \pi^2} \left(\frac{m_\chi}{m_\phi} \right) S_1 [\bar{u}(p'_\chi) u(p_\chi)] [\bar{u}(p'_q) u(p_q)] . \quad (\text{A.46})$$

Here a new loop function S_1 appears; it is also defined in Appendix A.2.1.

A.2.1 Model IIa and IIb Loop Functions

These functions are again expressed in terms of the function $L(x)$ defined in eq.(A.16).

$$N_1 = -\frac{1}{6 m_\phi^2} \left[\frac{1}{rs} - \frac{r^2 - 1}{r^3(r+s)} L(r) + \frac{rs - s^2 + r^2(3s^2 - 1)}{2r^3 s^3} \ln\left(\frac{1}{s^2}\right) + \frac{1 - 3r^2}{2r^3(r+s)} \ln\left(\frac{r^2}{s^2}\right) - \frac{s^2 - 1}{s^3(r+s)} L(s) \right] ; \quad (\text{A.47})$$

$$N_2 = \frac{1}{30 m_\phi^4} \left[\frac{3r^2 + 2rs + 3s^2 - 8r^2 s^2}{r^2 s^2 (r+s)^2} + \frac{5r - 5r^3 + 3s + r^2 s + 8r^4 s}{r^4 (r+s)^3} L(r) + \frac{-3r^2 + 4rs - 3s^2 + 5r^2 s^2}{2r^4 s^4} \ln\left(\frac{1}{s^2}\right) + \frac{5r - 15r^3 + 3s - 5r^2 s}{2r^4 (r+s)^3} \ln\left(\frac{r^2}{s^2}\right) + \frac{3r + 5s + rs^2 - 5s^3 + 8rs^4}{s^4 (r+s)^3} L(s) \right] ; \quad (\text{A.48})$$

$$N_3 = \frac{1}{15 m_\phi^4} \left[\frac{6r^2 + 9rs + s^2 + 4r^2 s^2}{rs^3 (r+s)^2} + \frac{1 - 3r^2 - 4r^4}{r^3 (r+s)^3} L(r) + \frac{-6r^2 + 3rs - s^2 + 5r^2 s^2}{2r^3 s^5} \ln\left(\frac{1}{s^2}\right) + \frac{1 - 5r^2}{2r^3 (r+s)^3} \ln\left(\frac{r^2}{s^2}\right) + \frac{6r^2 + 15rs + 10s^2 - 17r^2 s^2 - 45rs^3 - 35s^4 - 2r^2 s^4 + 10s^6 + 16r^2 s^6}{s^5 (r+s)^3 (1 - 4s^2)} L(s) \right] ; \quad (\text{A.49})$$

$$N_4 = \frac{1}{15 m_\phi^4} \left[\frac{r^2 + 9rs + 6s^2 + 4r^2 s^2}{r^3 s (r+s)^2} + \frac{-r^2 + 3rs - 6s^2 + 5r^2 s^2}{2r^5 s^3} \ln\left(\frac{1}{r^2}\right) + \frac{10r^2 - 35r^4 + 10r^6 + 15rs - 45r^3 s + 6s^2 - 17r^2 s^2 - 2r^4 s^2 + 16r^6 s^2}{r^5 (1 - 4r^2) (r+s)^3} L(r) + \frac{-1 + 5s^2}{2s^3 (r+s)^3} \ln\left(\frac{r^2}{s^2}\right) + \frac{1 - 3s^2 - 4s^4}{s^3 (r+s)^3} L(s) \right] ; \quad (\text{A.50})$$

$$N_5 = \frac{1}{6 m_\phi^2} \left[\frac{1}{rs} - \frac{1 - r^2}{r^3 (r-s)} L(r) + \frac{-r^2 - rs - s^2 + 3r^2 s^2}{2r^3 s^3} \ln\left(\frac{1}{s^2}\right) + \frac{-1 + 3r^2}{2r^3 (r-s)} \ln\left(\frac{r^2}{s^2}\right) - \frac{1 - s^2}{s^3 (-r+s)} L(s) \right] ; \quad (\text{A.51})$$

$$\begin{aligned}
N_6 = \frac{1}{30 m_\phi^4} & \left[-\frac{3r^2 - 2rs + 3s^2 - 8r^2s^2}{r^2s^2(r-s)^2} - \frac{5r - 5r^3 - 3s - r^2s - 8r^4s}{r^4(r-s)^3} \text{L}(r) \right. \\
& + \frac{3r^2 + 4rs + 3s^2 - 5r^2s^2}{2r^4s^4} \ln\left(\frac{1}{s^2}\right) + \frac{-5r + 15r^3 + 3s - 5r^2s}{2r^4(r-s)^3} \ln\left(\frac{r^2}{s^2}\right) \\
& \left. - \frac{3r - 5s + rs^2 + 5s^3 + 8rs^4}{s^4(r-s)^3} \text{L}(s) \right]; \tag{A.52}
\end{aligned}$$

$$\begin{aligned}
N_7 = \frac{1}{15 m_\phi^4} & \left[-\frac{6r^2 - 9rs + s^2 + 4r^2s^2}{rs^3(r-s)^2} + \frac{1 - 3r^2 - 4r^4}{r^3(r-s)^3} \text{L}(r) \right. \\
& + \frac{6r^2 + 3rs + s^2 - 5r^2s^2}{2r^3s^5} \ln\left(\frac{1}{s^2}\right) + \frac{1 - 5r^2}{2r^3(r-s)^3} \ln\left(\frac{r^2}{s^2}\right) \\
& \left. - \frac{6r^2 - 15rs + 10s^2 - 17r^2s^2 + 45rs^3 - 35s^4 - 2r^2s^4 + 10s^6 + 16r^2s^6}{s^5(r-s)^3(1-4s^2)} \text{L}(s) \right]; \tag{A.53}
\end{aligned}$$

$$\begin{aligned}
N_8 = \frac{1}{15 m_\phi^4} & \left[-\frac{r^2 - 9rs + 6s^2 + 4r^2s^2}{r^3s(r-s)^2} + \frac{r^2 + 3rs + 6s^2 - 5r^2s^2}{2r^5s^3} \ln\left(\frac{1}{r^2}\right) \right. \\
& + \frac{10r^2 - 35r^4 + 10r^6 + 15rs + 45r^3s + 6s^2 - 17r^2s^2 - 2r^4s^2 + 16r^6s^2}{r^5(1-4r^2)(r-s)^3} \text{L}(r) \\
& \left. + \frac{-1 + 5s^2}{2s^3(-r+s)^3} \ln\left(\frac{r^2}{s^2}\right) + \frac{1 - 3s^2 - 4s^4}{s^3(-r+s)^3} \text{L}(s) \right]; \tag{A.54}
\end{aligned}$$

$$\begin{aligned}
P_1 = \frac{1}{3 m_\phi^4} & \left[\frac{1}{s(r+s)} - \frac{1 + 2r^2}{2r^2(r+s)^2} \text{L}(r) + \frac{-2r + s}{4r^2s^3} \ln\left(\frac{1}{s^2}\right) \right. \\
& \left. - \frac{1}{4r^2(r+s)^2} \ln\left(\frac{r^2}{s^2}\right) + \frac{2r + 3s - 4rs^2 - 6s^3 + 8rs^4}{2s^3(r+s)^2(1-4s^2)} \text{L}(s) \right]; \tag{A.55}
\end{aligned}$$

$$\begin{aligned}
P_2 = \frac{1}{3 m_\phi^4} & \left[-\frac{1}{r(r+s)} + \frac{-r + 2s}{4r^3s^2} \ln\left(\frac{1}{r^2}\right) + \frac{1 + 2s^2}{2s^2(r+s)^2} \text{L}(s) \right. \\
& \left. - \frac{1}{4s^2(r+s)^2} \ln\left(\frac{r^2}{s^2}\right) - \frac{3r - 6r^3 + 2s - 4r^2s + 8r^4s}{2r^3(r+s)^2(1-4r^2)} \text{L}(r) \right]; \tag{A.56}
\end{aligned}$$

$$\begin{aligned}
P_3 = \frac{1}{3 m_\phi^4} & \left[-\frac{1}{s(r-s)} - \frac{1 + 2r^2}{2r^2(r-s)^2} \text{L}(r) + \frac{2r + s}{4r^2s^3} \ln\left(\frac{1}{s^2}\right) \right. \\
& \left. - \frac{1}{4r^2(r-s)^2} \ln\left(\frac{r^2}{s^2}\right) - \frac{2r - 3s - 4rs^2 + 6s^3 + 8rs^4}{2s^3(r-s)^2(1-4s^2)} \text{L}(s) \right]; \tag{A.57}
\end{aligned}$$

$$P_4 = \frac{1}{3m_\phi^4} \left[\frac{1}{r(r-s)} + \frac{r+2s}{4r^3s^2} \ln\left(\frac{1}{r^2}\right) - \frac{1+2s^2}{2s^2(-r+s)^2} L(s) \right. \\ \left. + \frac{1}{4s^2(r-s)^2} \ln\left(\frac{r^2}{s^2}\right) + \frac{3r-6r^3-2s+4r^2s-8r^4s}{2r^3(r-s)^2(1-4r^2)} L(r) \right]; \quad (\text{A.58})$$

$$R_1 = \frac{1}{m_\phi^2} \left[-\frac{1}{r^2} - \frac{-1+r^2}{2r^4} \ln\left(\frac{1}{r^2}\right) - \frac{1-3r^2}{r^4(1-4r^2)} L(r) \right]; \quad (\text{A.59})$$

$$S_1 = \frac{1}{m_\phi^2} \left[-\frac{1}{s^2} - \frac{-1+s^2}{2s^4} \ln\left(\frac{1}{s^2}\right) - \frac{1-3s^2}{s^4(1-4s^2)} L(s) \right]. \quad (\text{A.60})$$

The functions appearing in the evaluation of the (crossed) box diagrams are again invariant under a simultaneous sign change of both arguments. In addition, they are pairwise related: $N_5(r, s) = N_1(-r, s)$, $N_6(r, s) = -N_2(-r, s)$, $N_7(r, s) = N_3(-r, s)$, $N_8(r, s) = N_4(-r, s)$, $P_3(r, s) = P_1(-r, s)$ and $P_4(r, s) = -P_2(-r, s)$.

We also again provide the **massless quark limits of the loop functions**. Since N_3 , N_7 , P_1 and P_3 get multiplied with $1/m_q$, we keep terms up to linear in r in these functions:

$$P_1, P_3 \xrightarrow{r \rightarrow 0} \frac{1}{2m_\phi^4} \left[\frac{1}{s^2} - \frac{1}{2s^4} \ln\left(\frac{1}{s^2}\right) + \frac{1-2s^2}{s^4} L(s) \right] \\ \pm \frac{r}{3sm_\phi^4} \left[-\frac{2}{s^2} + \frac{1}{s^4} \ln\left(\frac{1}{s^2}\right) + \frac{4s^4+4s^2-2}{s^4(1-4s^2)} L(s) \right]; \quad (\text{A.61})$$

$$P_2, -P_4 \xrightarrow{r \rightarrow 0} \frac{1}{6m_\phi^4} \left[\frac{1}{s^2} - \frac{1}{2s^4} \ln\left(\frac{1}{s^2}\right) + \frac{1+2s^2}{s^4} L(s) \right]; \quad (\text{A.62})$$

$$N_1, N_5 \xrightarrow{r \rightarrow 0} -\frac{1}{6m_\phi^4} \left[\frac{1}{s^2} - \frac{1-3s^2}{2s^4} \ln\left(\frac{1}{s^2}\right) + \frac{1-s^2}{s^4} L(s) \right]; \quad (\text{A.63})$$

$$N_2, -N_6 \xrightarrow{r \rightarrow 0} \frac{1}{6m_\phi^4} \left[\frac{1}{s^4} - \frac{3}{2s^2} + \frac{-1+3s^2}{2s^6} \ln\left(\frac{1}{s^2}\right) + \frac{1-s^2}{s^6} L(s) \right]; \quad (\text{A.64})$$

$$N_3, N_7 \xrightarrow{r \rightarrow 0} \frac{1}{3m_\phi^4} \left[\frac{2}{s^4} + \frac{3s^2-2}{2s^6} \ln\left(\frac{1}{s^2}\right) + \frac{2-7s^2+2s^4}{s^6(1-4s^2)} L(s) \right] \\ \mp \frac{r}{2s^3m_\phi^4} \left[1 - \frac{2}{s^2} - \frac{2s^2-1}{s^4} \ln\left(\frac{1}{s^2}\right) - \frac{2}{s^4} \left(\frac{1-4s^2+2s^4}{1-4s^2} \right) L(s) \right]; \quad (\text{A.65})$$

$$N_4, N_8 \xrightarrow{r \rightarrow 0} \frac{1}{15m_\phi^4} \left[\frac{1}{s^4} - \frac{7}{2s^2} - \frac{1-5s^2}{2s^6} \ln\left(\frac{1}{s^2}\right) + \frac{1-3s^2-4s^4}{s^6} L(s) \right]; \quad (\text{A.66})$$

$$R_1 \xrightarrow{r \rightarrow 0} \frac{1}{2m_\phi^2}. \quad (\text{A.67})$$

In eq.(A.61) the + sign in the second line refers to P_1 and the - sign to P_3 ; similarly, in the second line of eq.(A.65) the + sign refers to N_3 and the - sign to N_7 .

B 2-Loop Calculations

In this appendix we provide details of the calculation of the two-loop diagrams contributing to the neutron EDM.

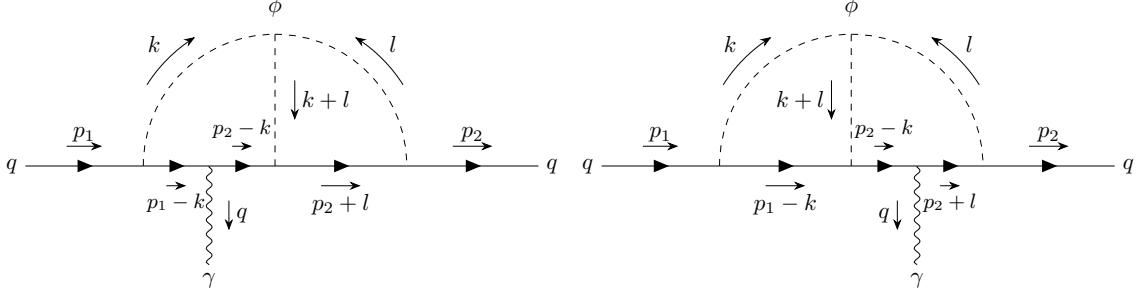


Figure 17: Two-loop Feynman diagrams generating quark EDMs and color-EDMs in Model I and IIa.

The matrix elements for diagram 1 (left) and diagram 2 (right) of Fig.17 generating EDMs in Model I and IIa can be written as:

$$i\mathcal{M}_1 = -\frac{i}{(16\pi^2)^2} 2eQ_q (h_2^q)^3 \mu_1 m_\phi \epsilon_\mu^*(q) [u(p_2) \mathcal{X}^\mu \gamma^5 u(p_1)] ; \quad (\text{B.1})$$

$$i\mathcal{M}_2 = -\frac{i}{(16\pi^2)^2} 2eQ_q (h_2^q)^3 \mu_1 m_\phi \epsilon_\mu^*(q) [u(p_2) \mathcal{Y}^\mu \gamma^5 u(p_1)] . \quad (\text{B.2})$$

Here Q_q is the electric charge of the quark and the loop functions $\mathcal{X}^\mu = \sum_i^4 \mathcal{X}_i^\mu$ and $\mathcal{Y}^\mu = \sum_i^4 \mathcal{Y}_i^\mu$ are described below.

$$\mathcal{X}_1^\mu = \int_X \frac{-2x_1}{\xi^4} p_2^\mu (t_3 + x_1 z_1 t_1) \left[\frac{-3}{\Delta'} + \frac{1}{\xi^2} \frac{2(p_1 \cdot p_2) t_2 (t_3 + x_1 z_1 t_1) + m_q^2 (t_2^2 + (t_3 + x_1 z_1 t_1)^2)}{\Delta'^2} \right] ; \quad (\text{B.3})$$

$$\mathcal{X}_2^\mu = \int_X \frac{2x_1}{\xi^2} p_2^\mu \left[\frac{-1}{\Delta'} + \frac{2}{\xi^2} \frac{(t_2 (p_1 \cdot p_2) + m_q^2 (t_3 + x_1 z_1 t_1)) (t_3 + x_1 z_1 t_1)}{\Delta'^2} \right] ; \quad (\text{B.4})$$

$$\mathcal{X}_3^\mu = \int_X \frac{-2z_1 m_q^2}{\xi^4} \frac{(t_3 + x_1 z_1 t_1 - t_2)}{\Delta'^2} (t_2 p_1^\mu + (t_3 + x_1 z_1 t_1) p_2^\mu) ; \quad (\text{B.5})$$

$$\mathcal{X}_4^\mu = \int_X \frac{4z_1 m_q^2}{\xi^2} \frac{(t_3 + x_1 z_1 t_1)}{\Delta'^2} p_2^\mu . \quad (\text{B.6})$$

Here $t_{1,2,3}$, x_1 and z_1 are the five Feynman parameters required to describe diagram 1. The five dimensional measure \int_X is

$$\int_X \equiv \int_0^1 dt_1 \int_0^{1-t_1} dt_2 \int_0^{1-t_1-t_2} dt_3 \int_0^1 dx_1 \int_0^{1-x_1} dz_1, \quad \xi = [1 - t_1(1 - x_1(1 - x_1))]^{1/2} . \quad (\text{B.7})$$

Finally, the denominator Δ' is given by:

$$\Delta' = -m_\phi^2 (z_1 t_1 + t_2 + t_3 - 1) + z_1^2 m_q^2 t_1 + \left(\frac{x_1 z_1 p_2 t_1 + p_1 t_2 + p_2 t_3}{\xi} \right)^2 . \quad (\text{B.8})$$

The loop functions \mathcal{Y}_i^μ for the second diagram are obtained by the following replacements of Feynman parameters in the \mathcal{X}_i^μ in eqs.(B.3) to (B.6): $t_1 \rightarrow u_1$, $t_2 \rightarrow u_3$, $t_3 \rightarrow u_2$, $x_1 \rightarrow x_2$ and $z_1 \rightarrow z_2$, as well as the replacement $p_2^\mu \leftrightarrow p_1^\mu$. This yields:

$$\mathcal{Y}_1^\mu = \int_Y \frac{-2x_2}{\chi^4} p_1^\mu (u_2 + x_2 z_2 u_1) \left[\frac{-3}{\Delta''} + \frac{1}{\chi^2} \frac{2(p_1 \cdot p_2) u_3 (u_2 + x_2 z_2 u_1) + m_q^2 (u_3^2 + (u_2 + x_2 z_2 u_1)^2)}{\Delta''^2} \right]; \quad (\text{B.9})$$

$$\mathcal{Y}_2^\mu = \int_Y \frac{2x_2}{\chi^2} p_1^\mu \left[\frac{-1}{\Delta''} + \frac{2}{\chi^2} \frac{(u_3 (p_1 \cdot p_2) + m_q^2 (u_2 + x_2 z_2 u_1)) (u_2 + x_2 z_2 u_1)}{\Delta''^2} \right]; \quad (\text{B.10})$$

$$\mathcal{Y}_3^\mu = \int_Y \frac{2z_2 m_q^2}{\chi^4} \frac{(u_3 - x_2 z_2 u_1 - u_2)}{\Delta''^2} (u_3 p_2^\mu + (u_2 + x_2 z_2 u_1) p_1^\mu); \quad (\text{B.11})$$

$$\mathcal{Y}_4^\mu = \int_Y \frac{4z_2 m_q^2}{\chi^2} \frac{(u_2 + x_2 z_2 u_1)}{\Delta''^2} p_1^\mu. \quad (\text{B.12})$$

The integration measure \int_Y is

$$\int_Y \equiv \int_0^1 du_1 \int_0^{1-u_1} du_2 \int_0^{1-u_1-u_2} du_3 \int_0^1 dx_2 \int_0^{1-x_2} dz_2, \quad \chi = [1 - u_1(1 - x_2(1 - x_2))]^{1/2}, \quad (\text{B.13})$$

and the denominator Δ'' is given by

$$\Delta'' = -m_\phi^2 (z_2 u_1 + u_2 + u_3 - 1) + z_2^2 m_q^2 u_1 + \left(\frac{x_2 z_2 p_1 u_1 + p_1 u_2 + p_2 u_3}{\chi} \right)^2. \quad (\text{B.14})$$

The qEDM is given by the coefficient of the dimension -5 CP -odd term $\bar{u}(p_2) i \sigma_{\mu\nu} q^\nu \gamma^5 u(p_1)$ in the limit of vanishing momentum transfer $q^2 \rightarrow 0$. The γ^5 -version of the Gordon identity

$$\bar{u}(p_2) (p_1 + p_2)^\mu \gamma^5 u(p_1) = \bar{u}(p_2) i \sigma^{\mu\nu} q_\nu \gamma^5 u(p_1) \quad (\text{B.15})$$

converts the matrix elements (B.1) into a suitable form to extract the qEDM. To that end the loop functions X_i^μ and Y_i^μ need to be transformed such that they are symmetric in the external quark momenta p_1 and p_2 :

$$\mathcal{X}^\mu = [\mathcal{X}] (p_1 + p_2)^\mu + \{\mathcal{X}\} q^\mu, \quad (\text{B.16})$$

$$\mathcal{Y}^\mu = [\mathcal{Y}] (p_1 + p_2)^\mu + \{\mathcal{Y}\} q^\mu. \quad (\text{B.17})$$

The parts of the loop functions proportional to q^μ , denoted by $\{\mathcal{X}\}$ and $\{\mathcal{Y}\}$ respectively, can be ignored once the external spinors are taken into account by virtue of the Ward identity. The qEDM generated by the two diagrams is finally given by

$$d_q = \frac{2 e Q_q (h_2^q)^3 \mu_1 m_\phi}{(16 \pi^2)^2} \lim_{q^2 \rightarrow 0} \left([\mathcal{X}] + [\mathcal{Y}] \right), \quad (\text{B.18})$$

where

$$\begin{aligned} \lim_{q^2 \rightarrow 0} [\mathcal{X}] &= \frac{1}{2} \int_X -\frac{2z_1 m_q^2 (t_3 + x_1 z_1 t_1)^2 - t_2^2}{\xi^4 (\Delta'|_{q^2 \rightarrow 0})^2} + \frac{4z_1 m_q^2 t_3 + x_1 z_1 t_1}{\xi^2 (\Delta'|_{q^2 \rightarrow 0})^2} \\ &\quad - \frac{2x_1}{\xi^4} (t_3 + x_1 z_1 t_1) \left[\frac{-3}{\Delta'|_{q^2 \rightarrow 0}} + \frac{m_q^2 (t_3 + t_2 + x_1 z_1 t_1)^2}{\xi^2 (\Delta'|_{q^2 \rightarrow 0})^2} \right] \\ &\quad + \frac{2x_1}{\xi^2} \left[\frac{-1}{\Delta'|_{q^2 \rightarrow 0}} + \frac{2m_q^2 (t_3 + t_2 + x_1 z_1 t_1)(t_3 + x_1 z_1 t_1)}{\xi^2 (\Delta'|_{q^2 \rightarrow 0})^2} \right]; \end{aligned} \quad (\text{B.19})$$

$$\begin{aligned} \lim_{q^2 \rightarrow 0} [\mathcal{Y}] &= \frac{1}{2} \int_Y -\frac{2z_2 m_q^2 (u_2 + x_2 z_2 u_1)^2 - u_3^2}{\chi^4 (\Delta''|_{q^2 \rightarrow 0})^2} + \frac{4z_2 m_q^2 u_2 + x_2 z_2 u_1}{\chi^2 (\Delta''|_{q^2 \rightarrow 0})^2} \\ &\quad - \frac{2x_2}{\chi^4} (u_2 + x_2 z_2 u_1) \left[\frac{-3}{\Delta''|_{q^2 \rightarrow 0}} + \frac{m_q^2 (u_3 + u_2 + x_2 z_2 u_1)^2}{\chi^2 (\Delta''|_{q^2 \rightarrow 0})^2} \right] \\ &\quad + \frac{2x_2}{\chi^2} \left[\frac{-1}{\Delta''|_{q^2 \rightarrow 0}} + \frac{2m_q^2 (u_3 + u_2 + x_2 z_2 u_1)(u_2 + x_2 z_2 u_1)}{\chi^2 (\Delta''|_{q^2 \rightarrow 0})^2} \right]. \end{aligned} \quad (\text{B.20})$$

The limit $q^2 \rightarrow 0$ implies $p_1 \cdot p_2 \rightarrow m_q^2$, hence the denominators simplify to

$$\Delta'|_{q^2 \rightarrow 0} \equiv \lim_{q^2 \rightarrow 0} \Delta' = -m_\phi^2 (z_1 t_1 + t_2 + t_3 - 1) + m_q^2 \left(z_1^2 t_1 + \frac{(t_2 + t_3 + x_1 z_1 t_1)^2}{\xi^2} \right); \quad (\text{B.21})$$

$$\Delta''|_{q^2 \rightarrow 0} \equiv \lim_{q^2 \rightarrow 0} \Delta'' = -m_\phi^2 (z_2 u_1 + u_2 + u_3 - 1) + m_q^2 \left(z_2^2 u_1 + \frac{(u_3 + u_2 + x_2 z_2 u_1)^2}{\chi^2} \right). \quad (\text{B.22})$$

References

- [1] XENON collaboration, *Excess electronic recoil events in XENON1T*, *Phys. Rev. D* **102** (2020) 072004 [2006.09721].
- [2] XENON collaboration, *Dark Matter Search Results from a One Ton-Year Exposure of XENON1T*, *Phys. Rev. Lett.* **121** (2018) 111302 [1805.12562].
- [3] PANDAX-4T collaboration, *Dark Matter Search Results from the PandaX-4T Commissioning Run*, *Phys. Rev. Lett.* **127** (2021) 261802 [2107.13438].
- [4] LUX collaboration, *Results from a search for dark matter in the complete LUX exposure*, *Phys. Rev. Lett.* **118** (2017) 021303 [1608.07648].
- [5] LUX collaboration, *Limits on spin-dependent WIMP-nucleon cross section obtained from the complete LUX exposure*, *Phys. Rev. Lett.* **118** (2017) 251302 [1705.03380].
- [6] LZ collaboration, *First Dark Matter Search Results from the LUX-ZEPLIN (LZ) Experiment*, *Phys. Rev. Lett.* **131** (2023) 041002 [2207.03764].
- [7] DEAP collaboration, *Search for dark matter with a 231-day exposure of liquid argon using DEAP-3600 at SNOLAB*, *Phys. Rev. D* **100** (2019) 022004 [1902.04048].

- [8] SUPERCDMS collaboration, *Results from the Super Cryogenic Dark Matter Search Experiment at Soudan*, *Phys. Rev. Lett.* **120** (2018) 061802 [[1708.08869](#)].
- [9] DARKSIDE collaboration, *DarkSide-50 532-day Dark Matter Search with Low-Radioactivity Argon*, *Phys. Rev. D* **98** (2018) 102006 [[1802.07198](#)].
- [10] CRESST collaboration, *First results from the CRESST-III low-mass dark matter program*, *Phys. Rev. D* **100** (2019) 102002 [[1904.00498](#)].
- [11] NEWS-G collaboration, *First results from the NEWS-G direct dark matter search experiment at the LSM*, *Astropart. Phys.* **97** (2018) 54 [[1706.04934](#)].
- [12] DAMIC collaboration, *Results on low-mass weakly interacting massive particles from a 11 kg-day target exposure of DAMIC at SNOLAB*, *Phys. Rev. Lett.* **125** (2020) 241803 [[2007.15622](#)].
- [13] PICO collaboration, *Dark Matter Search Results from the Complete Exposure of the PICO-60 C₃F₈ Bubble Chamber*, *Phys. Rev. D* **100** (2019) 022001 [[1902.04031](#)].
- [14] LZ collaboration, *First Constraints on WIMP-Nucleon Effective Field Theory Couplings in an Extended Energy Region From LUX-ZEPLIN*, [2312.02030](#).
- [15] PLANCK collaboration, *Planck 2018 results. VI. Cosmological parameters*, *Astron. Astrophys.* **641** (2020) A6 [[1807.06209](#)].
- [16] G. Bertone, D. Hooper and J. Silk, *Particle dark matter: Evidence, candidates and constraints*, *Phys. Rept.* **405** (2005) 279 [[hep-ph/0404175](#)].
- [17] J. Fan, M. Reece and L.-T. Wang, *Non-relativistic effective theory of dark matter direct detection*, *JCAP* **11** (2010) 042 [[1008.1591](#)].
- [18] A.L. Fitzpatrick, W. Haxton, E. Katz, N. Lubbers and Y. Xu, *The Effective Field Theory of Dark Matter Direct Detection*, *JCAP* **02** (2013) 004 [[1203.3542](#)].
- [19] A.L. Fitzpatrick, W. Haxton, E. Katz, N. Lubbers and Y. Xu, *Model Independent Direct Detection Analyses*, [1211.2818](#).
- [20] N. Anand, A.L. Fitzpatrick and W.C. Haxton, *Weakly interacting massive particle-nucleus elastic scattering response*, *Phys. Rev. C* **89** (2014) 065501 [[1308.6288](#)].
- [21] R. Catena, K. Fridell and M.B. Krauss, *Non-relativistic Effective Interactions of Spin 1 Dark Matter*, *JHEP* **08** (2019) 030 [[1907.02910](#)].
- [22] P. Gondolo, S. Kang, S. Scopel and G. Tomar, *Effective theory of nuclear scattering for a WIMP of arbitrary spin*, *Phys. Rev. D* **104** (2021) 063017 [[2008.05120](#)].
- [23] N. Bozorgnia, D.G. Cerdeño, A. Cheek and B. Penning, *Opening the energy window on direct dark matter detection*, *JCAP* **12** (2018) 013 [[1810.05576](#)].
- [24] XENON collaboration, *Effective field theory search for high-energy nuclear recoils using the XENON100 dark matter detector*, *Phys. Rev. D* **96** (2017) 042004 [[1705.02614](#)].
- [25] PANDAX-II collaboration, *PandaX-II Constraints on Spin-Dependent WIMP-Nucleon Effective Interactions*, *Phys. Lett. B* **792** (2019) 193 [[1807.01936](#)].
- [26] SUPERCDMS collaboration, *Dark matter effective field theory scattering in direct detection experiments*, *Phys. Rev. D* **91** (2015) 092004 [[1503.03379](#)].
- [27] CRESST collaboration, *Limits on Dark Matter Effective Field Theory Parameters with CRESST-II*, *Eur. Phys. J. C* **79** (2019) 43 [[1809.03753](#)].

- [28] DARKSIDE-50 collaboration, *Effective field theory interactions for liquid argon target in DarkSide-50 experiment*, *Phys. Rev. D* **101** (2020) 062002 [2002.07794].
- [29] LUX collaboration, *Effective field theory analysis of the first LUX dark matter search*, *Phys. Rev. D* **103** (2021) 122005 [2003.11141].
- [30] DEAP collaboration, *Constraints on dark matter-nucleon effective couplings in the presence of kinematically distinct halo substructures using the DEAP-3600 detector*, *Phys. Rev. D* **102** (2020) 082001 [2005.14667].
- [31] CDEX collaboration, *First experimental constraints on WIMP couplings in the effective field theory framework from CDEX*, *Sci. China Phys. Mech. Astron.* **64** (2021) 281011 [2007.15555].
- [32] LUX collaboration, *Constraints on effective field theory couplings using 311.2 days of LUX data*, *Phys. Rev. D* **104** (2021) 062005 [2102.06998].
- [33] SUPERCDMS collaboration, *Effective Field Theory Analysis of CDMSlite Run 2 Data*, 2205.11683.
- [34] R. Catena and P. Gondolo, *Global fits of the dark matter-nucleon effective interactions*, *JCAP* **09** (2014) 045 [1405.2637].
- [35] R. Catena, *Prospects for direct detection of dark matter in an effective theory approach*, *JCAP* **07** (2014) 055 [1406.0524].
- [36] R. Catena and P. Gondolo, *Global limits and interference patterns in dark matter direct detection*, *JCAP* **08** (2015) 022 [1504.06554].
- [37] H. Rogers, D.G. Cerdeno, P. Cushman, F. Livet and V. Mandic, *Multidimensional effective field theory analysis for direct detection of dark matter*, *Phys. Rev. D* **95** (2017) 082003 [1612.09038].
- [38] Z. Liu, Y. Su, Y.-L. Sming Tsai, B. Yu and Q. Yuan, *A combined analysis of PandaX, LUX, and XENON1T experiments within the framework of dark matter effective theory*, *JHEP* **11** (2017) 024 [1708.04630].
- [39] S. Kang, S. Scopel, G. Tomar and J.-H. Yoon, *Present and projected sensitivities of Dark Matter direct detection experiments to effective WIMP-nucleus couplings*, *Astropart. Phys.* **109** (2019) 50 [1805.06113].
- [40] N.P. Avis Kozar, P. Scott and A.C. Vincent, *A Global Fit of Non-Relativistic Effective Dark Matter Operators Including Solar Neutrinos*, 2310.15392.
- [41] G. Lüders, *On the equivalence of invariance under time reversal and under particle-antiparticle conjugation for relativistic field theories*, *Dan. Mat. Fys. Medd.* **28** (1954) 1.
- [42] W. Pauli, *Exclusion Principle, Lorentz Group, and reversal of space-time and charge*, *Niels Bohr and the Development of Physics*, W. Pauli (ed.) New York: Pergamon (1955) .
- [43] PARTICLE DATA GROUP collaboration, *Review of Particle Physics*, *PTEP* **2022** (2022) 083C01.
- [44] C. Abel et al., *Measurement of the Permanent Electric Dipole Moment of the Neutron*, *Phys. Rev. Lett.* **124** (2020) 081803 [2001.11966].
- [45] J.M. Pendlebury et al., *Revised experimental upper limit on the electric dipole moment of the neutron*, *Phys. Rev. D* **92** (2015) 092003 [1509.04411].

- [46] M. Burghoff et al., *An Improved Search for the Neutron Electric Dipole Moment*, in *Meeting of the APS Division of Particles and Fields*, 10, 2011 [[1110.1505](#)].
- [47] J.B. Dent, L.M. Krauss, J.L. Newstead and S. Sabharwal, *General analysis of direct dark matter detection: From microphysics to observational signatures*, *Phys. Rev. D* **92** (2015) 063515 [[1505.03117](#)].
- [48] F. Bishara, J. Brod, B. Grinstein and J. Zupan, *From quarks to nucleons in dark matter direct detection*, *JHEP* **11** (2017) 059 [[1707.06998](#)].
- [49] E. Del Nobile, *Complete Lorentz-to-Galileo dictionary for direct dark matter detection*, *Phys. Rev. D* **98** (2018) 123003 [[1806.01291](#)].
- [50] M. Drees and R. Mehra, *Neutron EDM constrains direct dark matter detection prospects*, *Phys. Lett. B* **799** (2019) 135039 [[1907.10075](#)].
- [51] G. Arcadi, M. Lindner, F.S. Queiroz, W. Rodejohann and S. Vogl, *Pseudoscalar Mediators: A WIMP model at the Neutrino Floor*, *JCAP* **03** (2018) 042 [[1711.02110](#)].
- [52] N.F. Bell, G. Busoni and I.W. Sanderson, *Loop Effects in Direct Detection*, *JCAP* **08** (2018) 017 [[1803.01574](#)].
- [53] T. Li, *Revisiting the direct detection of dark matter in simplified models*, *Phys. Lett. B* **782** (2018) 497 [[1804.02120](#)].
- [54] T. Abe, M. Fujiwara and J. Hisano, *Loop corrections to dark matter direct detection in a pseudoscalar mediator dark matter model*, *JHEP* **02** (2019) 028 [[1810.01039](#)].
- [55] F. Ertas and F. Kahlhoefer, *Loop-induced direct detection signatures from CP-violating scalar mediators*, *JHEP* **06** (2019) 052 [[1902.11070](#)].
- [56] E. Del Nobile, *The Theory of Direct Dark Matter Detection: A Guide to Computations*, [2104.12785](#).
- [57] G. Jungman, M. Kamionkowski and K. Griest, *Supersymmetric dark matter*, *Phys. Rept.* **267** (1996) 195 [[hep-ph/9506380](#)].
- [58] M.A. Shifman, A.I. Vainshtein and V.I. Zakharov, *Remarks on Higgs Boson Interactions with Nucleons*, *Phys. Lett. B* **78** (1978) 443.
- [59] T. Bhattacharya, V. Cirigliano, R. Gupta, H.-W. Lin and B. Yoon, *Neutron Electric Dipole Moment and Tensor Charges from Lattice QCD*, *Phys. Rev. Lett.* **115** (2015) 212002 [[1506.04196](#)].
- [60] PNDME collaboration, *Iso-vector and Iso-scalar Tensor Charges of the Nucleon from Lattice QCD*, *Phys. Rev. D* **92** (2015) 094511 [[1506.06411](#)].
- [61] R. Gupta, B. Yoon, T. Bhattacharya, V. Cirigliano, Y.-C. Jang and H.-W. Lin, *Flavor diagonal tensor charges of the nucleon from (2+1+1)-flavor lattice QCD*, *Phys. Rev. D* **98** (2018) 091501 [[1808.07597](#)].
- [62] JLQCD collaboration, *Nucleon charges with dynamical overlap fermions*, *Phys. Rev. D* **98** (2018) 054516 [[1805.10507](#)].
- [63] C. Alexandrou et al., *Nucleon scalar and tensor charges using lattice QCD simulations at the physical value of the pion mass*, *Phys. Rev. D* **95** (2017) 114514 [[1703.08788](#)].
- [64] M. Pospelov and A. Ritz, *Neutron EDM from electric and chromoelectric dipole moments of quarks*, *Phys. Rev. D* **63** (2001) 073015 [[hep-ph/0010037](#)].

- [65] J. Hisano, J.Y. Lee, N. Nagata and Y. Shimizu, *Reevaluation of Neutron Electric Dipole Moment with QCD Sum Rules*, *Phys. Rev. D* **85** (2012) 114044 [[1204.2653](#)].
- [66] K. Fuyuto, J. Hisano and N. Nagata, *Neutron electric dipole moment induced by strangeness revisited*, *Phys. Rev. D* **87** (2013) 054018 [[1211.5228](#)].
- [67] T. Hahn, *CUBA: A Library for multidimensional numerical integration*, *Comput. Phys. Commun.* **168** (2005) 78 [[hep-ph/0404043](#)].
- [68] J.B. Dent, B. Dutta, J.L. Newstead and L.E. Strigari, *Effective field theory treatment of the neutrino background in direct dark matter detection experiments*, *Phys. Rev. D* **93** (2016) 075018 [[1602.05300](#)].
- [69] Y. Ema, T. Gao and M. Pospelov, *Reevaluation of heavy-fermion-induced electron EDM at three loops*, *Phys. Lett. B* **835** (2022) 137496 [[2207.01679](#)].
- [70] N. Yamanaka and E. Hiyama, *Weinberg operator contribution to the nucleon electric dipole moment in the quark model*, *Phys. Rev. D* **103** (2021) 035023 [[2011.02531](#)].
- [71] J. Ellis, *TikZ-Feynman: Feynman diagrams with TikZ*, *Comput. Phys. Commun.* **210** (2017) 103 [[1601.05437](#)].
- [72] H.H. Patel, *Package-X 2.0: A Mathematica package for the analytic calculation of one-loop integrals*, *Comput. Phys. Commun.* **218** (2017) 66 [[1612.00009](#)].

Single charged Higgs pair production in exclusive processes at the LHC

Laura DUARTE,^{1,*} Victor P. GONÇALVES,^{1,†} Daniel E. MARTINS,^{2,‡} and Têssio B. de MELO^{3,4,§}

¹*Institute of Physics and Mathematics, Federal University of Pelotas,
Postal Code 354, 96010-900, Pelotas, RS, Brazil*

²*The Henryk Niewodniczanski Institute of Nuclear Physics (IFJ)
Polish Academy of Sciences (PAN), 31-342, Krakow, Poland*

³*Universidad Andrés Bello, Facultad de Ciencias Exactas,
Departamento de Ciencias Físicas-Center for Theoretical and Experimental Particle Physics,
Fernández Concha 700, Santiago, Chile*

⁴*Millennium Institute for Subatomic Physics at the High-Energy Frontier, SAPHIR, Chile*

Abstract

The production of a single charged Higgs boson pair by photon - photon interactions in pp collisions at the LHC is investigated in this exploratory study. We focus on the exclusive production, which is characterized by intact protons and two - rapidity gaps in the final state, and assume the type - I two - Higgs - doublet model, which still allows a light charged Higgs. Assuming the leptonic $H^\pm \rightarrow [\tau\nu_\tau]$ decay mode, we derive predictions for the transverse momentum, rapidity and invariant mass distributions of the $\tau^+\tau^-$ pair for different values of the charged Higgs mass. The contribution of different background processes are also estimated. Our results indicate that the contribution of the exclusive H^+H^- production for the $[\tau^+\nu_\tau][\tau^-\nu_\tau]$ final state is non - negligible and can, in principle, be used to searching for a light charged Higgs.

PACS numbers:

Keywords:

*Electronic address: l.duarte@unesp.br

†Electronic address: Barros@ufpel.edu.br

‡Electronic address: daniel.ernani@ifj.edu.pl

§Electronic address: tessiomelo@institutosaphir.cl

I. INTRODUCTION

The discovery of the Higgs boson at the LHC in 2012 is one of the great triumphs of the Particle Physics, and represents the completion of the Standard Model (SM) [1, 2]. However, there are still many unanswered questions that suggest that the SM is an effective low - energy realization of a more complete and fundamental theory. Several scenarios for the beyond the Standard Model (BSM) physics predict the presence of extra physical Higgs boson states, which has motivated the searching for these additional states in various production and decay channels over a wide range of kinematical regimes at LEP, Tevatron and now at the LHC [3–15]. As these studies have yield negative, constraints have been placed on the associated masses and branching ratios of different decay channels. In particular, the existence of a light charged Higgs boson, with mass below the top quark mass, is still allowed only in a restrict number of BSM models [16–21].

The two-Higgs-Doublet model (2HDM) is one of the simplest BSM frameworks that predict charged Higgs bosons [22, 23]. In this model, an additional complex doublet is added and its Higgs sector involves five scalars: CP-even neutral h and H , CP - odd neutral A , and a pair of charged Higgs H^\pm . Four distinct interaction modes arise when a Z_2 symmetry is introduced to prevent the Flavor Changing Neutral Currents (FCNC) at the tree level. Current experimental measurements imply that a light H^\pm can only be accommodated in type-I 2HDM and type-X 2HDM [18, 24, 25]. In this paper, we will concentrate our analysis in the type - I 2HDM, where one of doublets couples to all fermions, and a light charged Higgs with mass below 100 GeV is still allowed.

Over the last decades, extensive phenomenological studies on the H^\pm production in e^+e^- , $\gamma\gamma$, ep and pp collisions have been performed assuming the type - I 2HDM. In particular, a comprehensive analysis of the single charged Higgs pair production at the LHC has been recently performed in Ref.[24]. Such a study considers the charged Higgs pair production in inelastic processes, where both the incident protons breakup, and the dominant subprocesses are initiated by the quarks and gluons present in the proton wave function. Moreover, they have explored the entire parameter of type - I 2HDM and obtained the phenomenologically viable parameters. The authors also have demonstrated that the significance for the $pp \rightarrow H^+H^- \rightarrow [\tau\nu][\tau\nu]$ channel is large and that a future experimental analysis of this final state is a promising way for searching and discover the single charged Higgs boson.

The main goal in this paper is to extend the analysis performed in Ref. [24] for elastic processes, where the two incident protons remain intact in the final state. In order to protons remain intact, the H^+H^- pair should be produced by the interaction of color singlet objects, which can be a photon γ , a Z boson or a Pomeron \mathbb{P} , which is a color singlet particle with partonic structure. As the dominant channel is the $\gamma\gamma \rightarrow H^+H^-$ subprocess [26], we will focus on the process represented in Fig. 1, which is usually denoted the exclusive H^+H^- production, since only the H^+H^- pair is present in the final

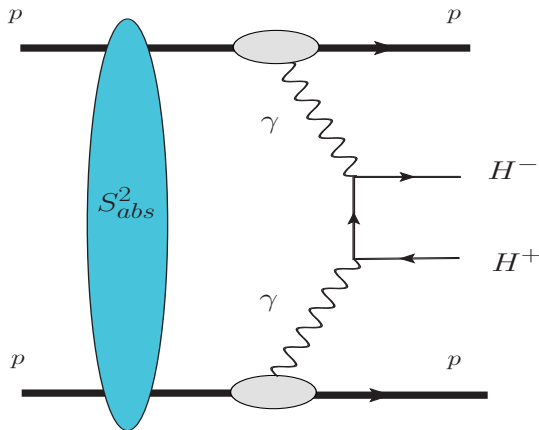


FIG. 1: Single charged Higgs pair production by $\gamma\gamma$ interactions in pp collisions at the LHC.

state. Our analysis is strongly motivated by the recent study performed in Ref. [27], where we have considered the exclusive production of a pair of doubly charged Higgs and demonstrated that such a process can be used to search for signatures of the type II seesaw mechanism and to obtain lower mass bounds on $H^{\pm\pm}$. We will focus on the $pp \rightarrow p \otimes H^+H^- \otimes p \rightarrow p \otimes [\tau\nu][\tau\nu] \otimes p$ channel, where \otimes represents the presence of rapidity gaps in the final state, and will estimate the total cross-section and associated differential distributions on the transverse momentum, rapidity and invariant mass of the $\tau\tau$ pair, considering pp collisions at $\sqrt{s} = 14$ TeV and different values of the H^\pm mass. A comparison with the predictions associated to the potential SM backgrounds will also be performed.

This paper is organized as follows. In the next section, we present a brief review of the type - I 2HDM and of the formalism used for the treatment of the H^+H^- pair production by photon-induced interactions in pp collisions. In Section III we discuss the backgrounds considered in our analysis and present our predictions for the invariant mass, transverse momentum and rapidity distributions, as well as for the total cross-section for the H^+H^- pair production in $\gamma\gamma$ interactions. Finally, in Section IV we summarize our main conclusions.

II. FORMALISM

A. The type-I 2HDM

The charged scalar bosons appear in several extensions of the SM [23, 24, 28–30]. A two-Higgs-doublet model (2HDM) is a simple extension of the SM by introducing an additional $SU(2)_L$ Higgs doublet, which predicts three neutral Higgs bosons and a pair of charged Higgs bosons H^\pm . To realize this model, the fermion content are the same as in the SM, while the scalar sector is extended with

two $SU(2)_L$ scalar doublets Φ_1 and Φ_2 , which have weak hypercharge $Y = 1$:

$$\Phi_i = \begin{pmatrix} \phi_i^+ \\ \frac{v_i + \rho_i + i\eta_i}{\sqrt{2}} \end{pmatrix}, \quad i = 1, 2, \quad (1)$$

with v_1 and v_2 the vacuum expectation values (VEVs) of Φ_1 and Φ_2 , respectively. v_1 and v_2 satisfy the relation $v = \sqrt{v_1^2 + v_2^2} = 246$ GeV, in order to successfully generate the electroweak symmetry breaking, and the ratio of v_2 and v_1 defines the mixing angle β as $\tan \beta = \frac{v_2}{v_1}$. In what follows, we use the simplified notation of $s_x = \sin x$, $c_x = \cos x$ and $t_x = \tan x$.

The physical mass eigenstates are given by

$$\begin{pmatrix} G^\pm \\ H^\pm \end{pmatrix} = R(\beta) \begin{pmatrix} \phi_1^\pm \\ \phi_2^\pm \end{pmatrix}, \quad \begin{pmatrix} G \\ A \end{pmatrix} = R(\beta) \begin{pmatrix} \eta_1 \\ \eta_2 \end{pmatrix}, \quad \begin{pmatrix} H \\ h \end{pmatrix} = R(\beta) \begin{pmatrix} \rho_1 \\ \rho_2 \end{pmatrix}. \quad (2)$$

Here G^\pm and G are the Nambu-Goldstone bosons that are eaten as the longitudinal components of the massive gauge bosons. The rotation matrix is

$$R(\theta) = \begin{pmatrix} \cos \theta & \sin \theta \\ -\sin \theta & \cos \theta \end{pmatrix}. \quad (3)$$

General 2HDMs are troubled by the presence of flavor changing neutral currents (FCNC) at tree level, as the gauge symmetries allow both doublets to couple to all fermions. In order to prevent large FCNC, additional symmetries may be employed, in order to forbid some of the offending couplings. A popular choice is to impose a discrete Z_2 symmetry¹, under which $\Phi_1 \rightarrow -\Phi_1$. The fermion Z_2 parities are such that each type of fermion couples to only one of the doublets. The different possibilities to fulfill this condition give rise to the well known four types of 2HDMs [23]: In the type-I model, only the doublet Φ_2 couples to all the fermions so all the quarks and charged leptons get their masses from the VEV of Φ_2 (ie. v_2); in the type-II, Φ_1 couples to charged leptons and down-type quarks and Φ_2 to up-type quarks; in the type-X, the charged leptons couple to Φ_1 and all the quarks couple to Φ_2 , while in the type-Y model, Φ_1 couples to down-type quarks and Φ_2 to up-type quarks and charged leptons.

The most general scalar potential which is CP-conserving and invariant under the Z_2 symmetry (up to the soft-breaking term proportional to m_{12}^2) is given by:

$$\begin{aligned} V = & m_{11}^2 \Phi_1^\dagger \Phi_1 + m_{22}^2 \Phi_2^\dagger \Phi_2 - m_{12}^2 \left(\Phi_1^\dagger \Phi_2 + \Phi_2^\dagger \Phi_1 \right) + \frac{\lambda_1}{2} \left(\Phi_1^\dagger \Phi_1 \right)^2 + \frac{\lambda_2}{2} \left(\Phi_2^\dagger \Phi_2 \right)^2 \\ & + \lambda_3 \Phi_1^\dagger \Phi_1 \Phi_2^\dagger \Phi_2 + \lambda_4 \Phi_1^\dagger \Phi_2 \Phi_2^\dagger \Phi_1 + \frac{\lambda_5}{2} \left[\left(\Phi_1^\dagger \Phi_2 \right)^2 + \left(\Phi_2^\dagger \Phi_1 \right)^2 \right]. \end{aligned} \quad (4)$$

After spontaneous symmetry breaking, five physical scalars arise, three neutral h , H , A and a pair of charged scalars H^\pm . The remaining three scalars become the longitudinal components of the massive

¹ Continuous Abelian symmetries, either global or gauged, have also been considered in this context. See, e.g., [31–35].

W^\pm and Z gauge bosons. As the CP symmetry is conserved, the neutral CP-even and CP-odd states do not mix, which means they can be diagonalized separately. The mixing angle for the CP-even sector is denoted by α , while β is the mixing angle for the CP-odd sector, as well as for the charged sector.

The eight parameters m_{ij}^2 and $\lambda_1 - \lambda_5$ in the potential (4) are replaced by the VEV v , the mixing angles α and β the scalar masses M_h , M_H , M_A and M_{H^\pm} , and the soft Z_2 breaking parameter $M^2 = m_{12}^2/s_\beta c_\beta$. In particular, the quartic coupling constants are given as [24]

$$\begin{aligned}
\lambda_1 &= \frac{1}{v^2} [(s_{\beta-\alpha} - c_{\beta-\alpha} t_\beta)^2 + M_H^2 (s_{\beta-\alpha} t_\beta + c_{\beta-\alpha})^2 + M^2 t_\beta^2] \\
\lambda_2 &= \frac{1}{v^2} \left[M_h^2 \left(s_{\beta-\alpha} + \frac{c_{\beta-\alpha}}{t_\beta} \right)^2 - \frac{M^2}{t_\beta^2} + M_H^2 \left(\frac{s_{\beta-\alpha}}{t_\beta} - c_\beta \right)^2 \right] \\
\lambda_3 &= \frac{1}{v^2} \left[(M_h^2 - M_H^2) \left\{ s_{\beta-\alpha}^2 - s_{\beta-\alpha} c_{\beta-\alpha} \left(t_\beta - \frac{1}{t_\beta} \right) - c_{\beta-\alpha}^2 \right\} + 2M_{H^\pm}^2 - M^2 \right] \\
\lambda_4 &= \frac{1}{v^2} [M^2 + M_A^2 - 2M_{H^\pm}^2] \\
\lambda_5 &= \frac{1}{v^2} [M^2 - M_A^2].
\end{aligned} \tag{5}$$

The general Yukawa Lagrangian with two scalar doublets is

$$\begin{aligned}
-\mathcal{L}_Y &= y^{1d} \bar{Q}_L \Phi_1 d_R + y^{1u} \bar{Q}_L \tilde{\Phi}_1 u_R + y^{1e} \bar{L}_L \Phi_1 e_R \\
&+ y^{2d} \bar{Q}_L \Phi_2 d_R + y^{2u} \bar{Q}_L \tilde{\Phi}_2 u_R + y^{2e} \bar{L}_L \Phi_2 e_R,
\end{aligned} \tag{6}$$

where $Q_L^T = (u_L, d_L)$, $L_L^T = (\nu_l, l_l)$ and $y^{(1,2)(d,u,e)}$ are 3×3 matrices in family space. After imposing the Z_2 symmetry, some of these terms are forbidden. The production of a charged Higgs particle, depending on its mass with respect to the top quark, can be divided into light ($M_{H^\pm} \ll M_t$), intermediate ($M_{H^\pm} \sim M_t$) and heavy ($M_{H^\pm} \gg M_t$) scenarios [24, 36, 37]. Current searches impose stringent constraints on the mass of H^\pm depending on the 2HDM type. For instance, the charged Higgs boson in type-II and type-Y is tightly constrained to be as heavy as $M_{H^\pm} \gtrsim 800$ GeV due to the measurements of the inclusive weak radiative B meson decay into $s\gamma$ [38, 39]. Only type-I and type-X can accommodate a light H^\pm . As we are interested in studying relatively light charged scalars, with a mass ~ 100 GeV, we will focus here in the type-I 2HDM, in which such small masses are allowed provided that $\tan\beta$ is not too small. In this case, all the Yukawa couplings of H^\pm are inversely proportional to $\tan\beta$ and the decay branching ratios into a fermion pair are proportional to the fermion mass. Restricting to the type-I model, the Yukawa Lagrangian (6) in the physical basis takes the form:

$$\begin{aligned}
-\mathcal{L}_Y^{\text{Type-I}} &= \frac{1}{t_\beta} \left\{ \sum_f \frac{m_f}{v} \left(\frac{c_\alpha}{c_\beta} h \bar{f} f + \frac{s_\alpha}{c_\beta} H \bar{f} f \right) - iA (\bar{u} \gamma_5 u - \bar{d} \gamma_5 d - \bar{l} \gamma_5 l) \right. \\
&\left. + \left[\frac{\sqrt{2} V_{ud}}{v} H^+ \bar{u} (m_u P_L - m_d P_R) d - \frac{\sqrt{2} m_l}{v} H^+ \bar{\nu}_L l_R + h.c. \right] \right\}
\end{aligned} \tag{7}$$

with $f = u, d, l$. Notice that the coupling of the Higgs bosons to the fermions become suppressed when $t_\beta > 1$. The interaction of the scalars with the gauge bosons is given by,

$$\begin{aligned} \mathcal{L}_{\text{gauge}} = & \left(gm_W W_\mu^\dagger W^\mu + \frac{1}{2} g_Z m_Z Z_\mu Z^\mu \right) [s_{\beta-\alpha} h + c_{\beta-\alpha} H] \\ & + \frac{g}{2} i [W_\mu^+ [c_{\beta-\alpha} h - s_{\beta-\alpha} H] \overleftrightarrow{\partial}^\mu H^- - h.c.] - \frac{g}{2} [W_\mu^+ H^- \overleftrightarrow{\partial}^\mu A + h.c.] \\ & + i \left[e A_\mu + \frac{g_Z}{2} (\sin^2 \theta_W - \cos^2 \theta_W) Z_\mu \right] H^+ \overleftrightarrow{\partial}^\mu H^- + \frac{g_Z}{2} Z_\mu [\cos(\beta - \alpha) A \overleftrightarrow{\partial}^\mu h - \sin(\beta - \alpha) A \overleftrightarrow{\partial}^\mu H], \end{aligned} \quad (8)$$

where $g_Z = g/\cos\theta_W$ and $f \overleftrightarrow{\partial}^\mu g \equiv (f \partial^\mu g - g \partial^\mu f)$.

We concentrate on the usual scenario where h is the SM-like 125 GeV Higgs boson, with being H the heavier neutral scalar. The pseudoscalar A can be either heavier or lighter than h . The parameter ranges are determined by the small H^\pm mass scenario we are interested in, and also by the several experimental constraints: LEP experiments [3] have given limits on the mass of the charged Higgs boson in 2HDM from the charged Higgs searches in Drell-Yan events, $e^+e^- \rightarrow Z\gamma \rightarrow H^+H^-$, excluding $m_{H^\pm} \lesssim 80$ GeV (Type II) and $m_{H^\pm} \lesssim 72.5$ GeV (Type I) at 95% confidence level. Among the constraints from B meson decays (flavor physics constraints), the $B \rightarrow X_s \gamma$ decay [40] puts a very strong constraint on Type II and Type Y 2HDM, excluding $m_H^\pm \lesssim 580$ GeV and almost independently of t_β . For Type I and Type X, the $B \rightarrow X_s \gamma$ constraint is sensitive only for low t_β .

In Ref. [24], the authors have performed a comprehensive study and explored the entire parameter space for type - I 2DHM, deriving the current viable parameters for these models, taking into account the current theoretical and experimental constraints. In our analysis, we will make use of the results obtained in Ref. [24] and, in particular, we will estimate the exclusive cross-section for the parameters associated to the benchmark point 1 defined in Table III of that reference, in which $M_H = 138.6$ GeV, $M_A = 120.7$ GeV, $\tan\beta = 16.8$, $\sin(\beta - \alpha) = 0.975$, $m_{12}^2 = 1089.7$ GeV² and m_h being the mass of the observed Higgs boson. For M_{H^\pm} , three distinct values will be considered: $M_{H^\pm} = 80, 100$ and 140 GeV.

B. Single charged Higgs pair production by $\gamma\gamma$ interactions

Assuming the validity of the equivalent photon approximation (EPA) [41], the total cross section for the H^+H^- production by $\gamma\gamma$ interactions in pp collisions can be factorized in terms of the equivalent flux of photons into the proton projectiles and the $\gamma\gamma \rightarrow H^+H^-$ cross section, as follows

$$\sigma(pp \rightarrow p \otimes H^+H^- \otimes p) = S_{abs}^2 \int dx_1 \int dx_2 \gamma_1^{el}(x_1) \cdot \gamma_2^{el}(x_2) \cdot \hat{\sigma}(\gamma\gamma \rightarrow H^+H^-), \quad (9)$$

where x is the fraction of the proton energy carried by the photon and $\gamma^{el}(x)$ is the elastic equivalent photon distribution of the proton. The general expression for the elastic photon flux of the proton has

been derived in Ref. [42] and is given by

$$\gamma^{el}(x) = -\frac{\alpha}{2\pi} \int_{-\infty}^{-\frac{m^2 x^2}{1-x}} \frac{dt}{t} \left\{ \left[2 \left(\frac{1}{x} - 1 \right) + \frac{2m^2 x}{t} \right] H_1(t) + x G_M^2(t) \right\}, \quad (10)$$

where $t = q^2$ is the momentum transfer squared of the photon,

$$H_1(t) \equiv \frac{G_E^2(t) + \tau G_M^2(t)}{1 + \tau} \quad (11)$$

with $\tau \equiv -t/m^2$, m being the proton mass, and where G_E and G_M are the Sachs elastic form factors. In our analysis, we will use the photon flux derived in Ref. [41], where an analytical expression is presented. Moreover, S_{abs}^2 is the absorptive factor, which takes into account of additional soft interactions between incident protons which leads to an extra production of particles that destroy the rapidity gaps in the final state [43]. In our study, we will assume that $S_{abs}^2 = 1$, which is a reasonable approximation since the contribution of the soft interactions is expected to be small in $\gamma\gamma$ interactions due to the long range of the electromagnetic interaction (For a more detailed discussion see, e.g., Ref. [26]). The cross section for the $\gamma\gamma \rightarrow H^+H^-$ subprocess, $\hat{\sigma}(\gamma\gamma \rightarrow H^+H^-)$, will be estimated using the type - I 2DHM and the events associated with the signal will be generated by MadGraph 5 [44].

A comment is in order here. The cross sections for the exclusive production of a given final state system, in general, two orders of magnitude smaller than for the production in inelastic proton - proton collisions, where both incident protons break up and a large number of particles is produced in addition to the final state. It turned out that the analysis of e.g. the H^+H^- production in inelastic collisions, generally involve serious backgrounds, thus making the search for new physics a hard task. In contrast, exclusive processes have smaller backgrounds and are characterized by a very clean final state, identified by the presence of two rapidity gaps, i.e. two regions devoid of hadronic activity separating the intact very forward protons from the central system. Such exclusive events can be clearly distinguished from the inelastic one by detecting the scattered protons in spectrometers placed in the very forward region close to the beam pipe, such as the ATLAS Forward Proton detector (AFP) [45, 46] and the CMS-Totem Precision Proton Spectrometer (CT-PPS) [47], and selecting events with two rapidity gaps in the central detector. For a more detailed discussion about the separation of exclusive processes we refer the interested reader to the recent studies performed in Refs. [48, 49].

III. RESULTS

In what follows we will present our results for the single charged Higgs pair production in exclusive processes considering pp collisions at $\sqrt{s} = 14$ TeV. In our analysis, we assume that the H^+H^- system decays leptonically, $H^+H^- \rightarrow [\tau^+\nu_\tau][\tau^-\bar{\nu}_\tau]$ and analyze two distinct experimental scenarios:

pp @ 14 TeV	Signal			Backgrounds	
	$pp \rightarrow p H^+ H^- p \rightarrow p[\tau^+ \nu_\tau][\tau^- \bar{\nu}_\tau] p$			$pp \rightarrow p W^+ W^- p \rightarrow p[\tau^+ \nu_\tau][\tau^- \nu_\tau] p$	$pp \rightarrow p \tau^- \tau^+ p$
M_{H^\pm} [GeV]	80	110	140	-	-
σ (fb)	0.20	0.14	0.10	1.21	235500

TABLE I: Predictions at the generation level for the total cross-sections for the single charged Higgs pair production via photon-photon interactions in pp collisions at $\sqrt{s} = 14$ TeV, derived assuming the Type - I 2HDM and different values for the mass M_{H^\pm} . Results for the main backgrounds are also presented.

- **Scenario I:** the $\tau^+ \tau^-$ pair is produced at central rapidities ($-2.0 \leq y(\tau\tau) \leq +2.0$) and both forward protons are tagged, which is the configuration that can be studied by the ATLAS and CMS Collaborations. We require both forward protons to be detected by Forward Proton Detectors (FPDs) and we will assume an efficient reconstruction in the range $0.012 < \xi_{1,2} < 0.15$, where $\xi_{1,2} = 1 - p_{z1,2}/E_{\text{beam}}$ is the fractional proton momentum loss on either side of the interaction point (side 1 or 2) and p_{z1} is the longitudinal momentum of the scattered proton on the side 1. This, in principle, allows one to measure masses of the central system by the missing mass method, $m_X = \sqrt{\xi_1 \xi_2 s}$, starting from about 160 GeV.
- **Scenario II:** the $\tau^+ \tau^-$ pair is produced at forward rapidities ($+2.0 \leq y(\tau\tau) \leq +4.5$), but the protons in the final state are not tagged, which is the case that can be analyzed by the LHCb Collaboration.

The signal is assumed to be the $pp \rightarrow p H^+ H^- p \rightarrow p[\tau^+ \nu_\tau][\tau^- \bar{\nu}_\tau] p$ process, which will be generated using the MadGraph 5 [44, 50]. For the background we will consider the photon - induced processes $pp \rightarrow p \otimes W^+ W^- \otimes p \rightarrow p \otimes [\tau^+ \nu_\tau][\tau^- \bar{\nu}_\tau] \otimes p$ and $pp \rightarrow p \otimes \tau^+ \tau^- \otimes p$. All these backgrounds are also generated by MadGraph 5 [44].

In Table I we present our predictions for the total cross-sections associated with the signal and backgrounds considered in our analysis. The results for the signal have been derived assuming the type - I 2HDM for the benchmark point 1 [24], discussed in the previous Section, and different values for the mass M_{H^\pm} . The predictions for the signal at the generation level are similar to that derived in Ref. [26]. One has that the $pp \rightarrow p \otimes \tau^+ \tau^- \otimes p$ process dominates the production of a $\tau^+ \tau^-$ pair. However, such a process is characterized by a distinct topology in comparison to the other channels, where neutrinos (not seen by the detector) are also produced. In particular, this process is characterized by a pair with small acoplanarity [$\equiv 1 - (\Delta\phi/\pi)$], where $\Delta\phi$ is the angle between the τ particles, since the pair is dominantly produced back - to - back. Moreover, it is also characterized by an invariant mass $m_{\tau\tau}$ almost identical to the measured mass of the central system m_X , since other particles are not produced in addition to the $\tau^+ \tau^-$ pair. Such expectations are confirmed by the results presented

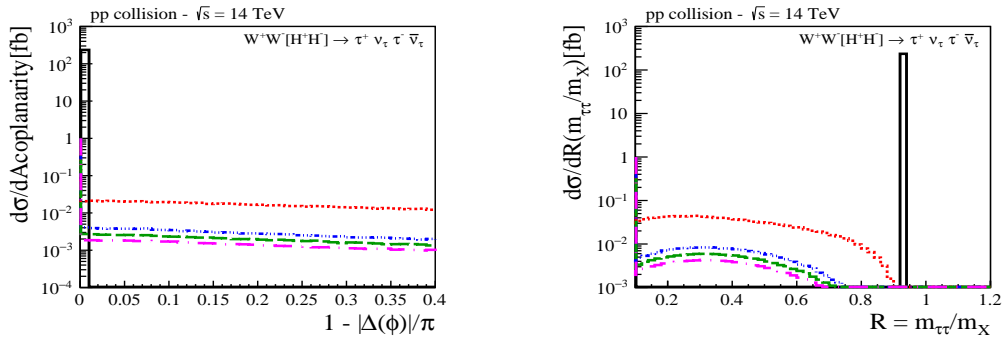


FIG. 2: Predictions for the acoplanarity distribution (left panel) and for the dependence on the ratio $R = m_{\tau\tau}/m_X$ (right panel) for the cross sections associated with the signal and backgrounds. The results for the signal have been derived assuming different values for the mass M_{H^\pm} .

in Fig. 2, where we show the acoplanarity distribution associated to the different channels (left panel) and the cross-sections as a function of the ratio $R = m_{\tau\tau}/m_X$ (right panel). These results suggest that the contribution of the $pp \rightarrow p \otimes \tau^+ \tau^- \otimes p$ process can be strongly suppressed by assuming cuts on the acoplanarity and on the ratio R . In what follows, we will explore such expectations.

In Fig. 3 we present our predictions for the transverse momentum [$p_T(\tau\tau)$], invariant mass [$m_{\tau\tau}$] and rapidity [$y(\tau\tau)$] distributions of the $\tau\tau$ pair associated with the $pp \rightarrow p H^+ H^- p \rightarrow p[\tau^+ \nu_\tau][\tau^- \bar{\nu}_\tau]p$ and $pp \rightarrow p \otimes W^+ W^- \otimes p \rightarrow p \otimes [\tau^+ \nu_\tau][\tau^- \bar{\nu}_\tau] \otimes p$ processes. The shape of the distributions for the signal assuming different values for the single charged Higgs mass are similar, decreasing in magnitude for larger values of M_{H^\pm} . Moreover, the position of the maximum in the $p_T(\tau\tau)$ and $m_{\tau\tau}$ distributions is dependent on the mass of the charged Higgs. Our results also indicate that the background predicts distributions that are similar to those from the signal, but with a larger normalization. In order to quantify the difference between the signal and background results for different values of $p_T(\tau\tau)$, $m_{\tau\tau}$ and $y(\tau\tau)$, we present in the lower panels of the plots shown in Fig. 3, the predictions for the ratio between the distributions associated with the $W^+ W^-$ and $H^+ H^-$ production, derived assuming distinct values of M_{H^\pm} . One has that the background dominates and is, in general, a factor ≥ 4 than the signal.

In what follows, we will investigate the impact of distinct kinematical cuts on the predictions for the total cross-sections considering the two scenarios discussed above. In particular, a cut on the ratio $R = m_{\tau\tau}/m_X$ will be considered in the case of the scenario I, since the protons in the final state are assumed to be tagged, and the central mass m_X can be estimated. In contrast, such a cut cannot be applied for the scenario II. Our results for the scenario I are presented in Table II. As expected from the results presented in Fig. 2, the cut on R is able to suppress the contribution associated with the $pp \rightarrow p \tau^- \tau^+ p$ process, without impact on the other channels. The cut on the acoplanarity implies a small reduction of the $W^+ W^-$ background. On the other hand, if we impose that the $\tau^+ \tau^-$

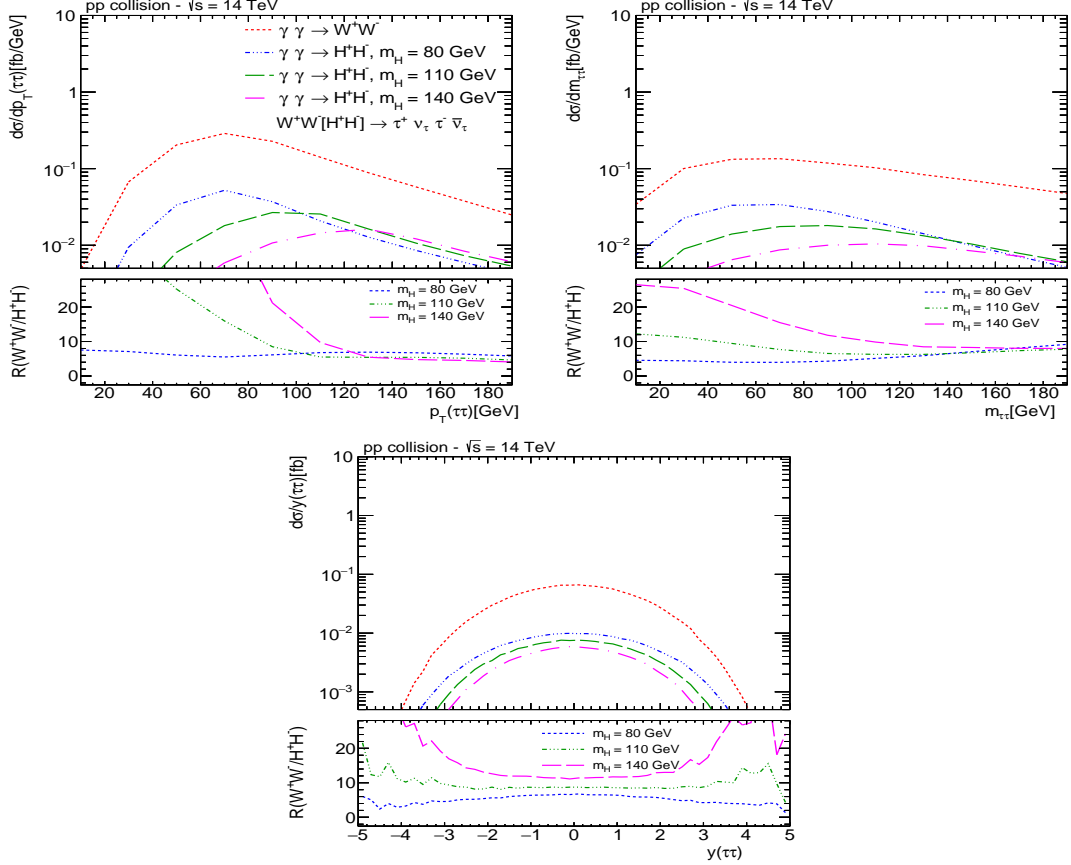


FIG. 3: Predictions for the transverse momentum $[p_T(\tau\tau)]$, invariant mass $[m_{\tau\tau}]$ and rapidity $[y(\tau\tau)]$ distributions of the $\tau\tau$ pair associated with the signal $[pp \rightarrow p H^+ H^- p \rightarrow p[\tau^+ \nu_\tau][\tau^- \bar{\nu}_\tau]p]$, derived assuming distinct values of M_{H^\pm} and considering pp collisions at $\sqrt{s} = 14$ TeV. The predictions for the background $pp \rightarrow p \otimes W^+ W^- \otimes p \rightarrow p \otimes [\tau^+ \nu_\tau][\tau^- \bar{\nu}_\tau] \otimes p$ are also presented. The lower panels in the distinct plots present the ratio between the background and signal predictions.

pair must be produced at central rapidities, the predictions associated with the signal and background are reduced by $\approx 17\%$. One has that the signal predictions are of the order of ≈ 0.1 fb, while the background one is 1 fb. In addition, one has analyzed the impact of a cut on the invariant mass of the $\tau^+ \tau^-$ pair. In particular, motivated by the results presented in Fig. 3 for the ratio between background and signal predictions for the invariant mass distributions, we have considered the selection of events in different ranges of $m_{\tau\tau}$, where this ratio assumes its smaller values. One has that such a cut implies the reduction of the total cross-sections, especially if events with smaller $m_{\tau\tau}$ are selected. However, in these cases we have the larger signal/background ratio, being $\approx 1/4$, in agreement with the results presented in Fig. 3. Such a result indicates that, for a single charged Higgs with a small mass, the exclusive $H^+ H^-$ production gives a non-negligible contribution for the $[\tau^+ \nu_\tau][\tau^- \bar{\nu}_\tau]$ final state.

In Table III we present the results associated with the scenario II, which can be investigated by the LHCb Collaboration. As explained before, for this scenario, the cut on R cannot be applied, since

pp @ 14 TeV	Signal			Backgrounds	
	$pp \rightarrow pH^+H^-p \rightarrow p[\tau^+\nu_\tau][\tau^-\bar{\nu}_\tau]p$			$pp \rightarrow pW^+W^-p \rightarrow p[\tau^+\nu_\tau][\tau^-\nu_\tau]p$	$pp \rightarrow p\tau^-\tau^+p$
M_{H^\pm} [GeV]	80	110	140	-	-
$\sigma(\text{fb})$ - w/o cuts	0.20	0.14	0.10	1.21	235500
$R \leq 0.9$	0.2	0.14	0.1	1.21	0.0
$[1 - (\Delta\phi/\pi)] \geq 0.01$	0.2	0.14	0.1	1.19	0.0
$-2.0 \leq y(\tau\tau) \leq +2.0$	0.16	0.12	0.086	1.00	0.0
$70.0 \leq m_{\tau\tau} \leq 90.0$ GeV	0.024	0.015	0.008	0.101	0.0
$100.0 \leq m_{\tau\tau} \leq 120.0$ GeV	0.097	0.049	0.025	0.410	0.0
$130.0 \leq m_{\tau\tau} \leq 150.0$ GeV	0.149	0.106	0.077	0.94	0.0

TABLE II: Predictions associated with the scenario I for the total cross-sections of single charged Higgs pair production via photon-photon interactions in pp collisions at $\sqrt{s} = 14$ TeV, derived assuming the Type - I 2HDM, different values for the mass M_{H^\pm} . The results were estimated considering a central detector and kinematical cuts on the acoplanarity, ratio R , rapidity and invariant mass of the $\tau\tau$ pair system. Results for the main backgrounds are also presented.

pp @ 14 TeV	Signal			Backgrounds	
	$pp \rightarrow pH^+H^-p \rightarrow p[\tau^+\nu_\tau][\tau^-\bar{\nu}_\tau]p$			$pp \rightarrow pW^+W^-p \rightarrow p[\tau^+\nu_\tau][\tau^-\nu_\tau]p$	$pp \rightarrow p\tau^-\tau^+p$
M_{H^\pm} [GeV]	80	110	140	-	-
$\sigma(\text{fb})$ - w/o cuts	0.20	0.14	0.10	1.21	235500
$[1 - (\Delta\phi/\pi)] \geq 0.01$	0.19	0.14	0.098	1.19	0.0
$2.0 \leq y(\tau\tau) \leq 4.5$	0.019	0.011	0.006	0.093	0.0
$70.0 \leq m_{\tau\tau} \leq 90.0$ GeV	0.003	0.0015	0.0007	0.012	0.0
$100.0 \leq m_{\tau\tau} \leq 120.0$ GeV	0.002	0.0008	0.0006	0.009	0.0
$130.0 \leq m_{\tau\tau} \leq 150.0$ GeV	0.001	0.0009	0.0006	0.006	0.0

TABLE III: Predictions associated with the scenario II for the total cross-sections of single charged Higgs pair production via photon-photon interactions in pp collisions at $\sqrt{s} = 14$ TeV, derived assuming the Type - I 2HDM, different values for the mass M_{H^\pm} . The results were estimated considering a forward detector and kinematical cuts on the acoplanarity, rapidity and invariant mass of the $\tau\tau$ pair system. Results for the main backgrounds are also presented.

the central mass m_X cannot be reconstructed without the tagging of the protons in the final state. However, the results presented in Table III indicate that the cut on the acoplanarity is able to fully suppress the contribution associated with the $pp \rightarrow p\tau^-\tau^+p$ process. The selection of forward events implies the reduction of the cross - sections by almost one order of magnitude. Moreover, the cut on the invariant mass suppress the predictions by a factor ≥ 8 , implying that the cross - sections become of the order of 10^{-3} fb, making a future experimental analysis of the exclusive H^+H^- production at forward rapidities a hard task.

IV. SUMMARY AND CONCLUDING REMARKS

Over the last decades, the study of photon - induced interactions in hadronic colliders became a reality, such that currently the Large Hadron Collider (LHC) is also considered a powerful photon - photon collider, which can be used to improve our understanding of the Standard Model as well as to searching for New Physics. The current data have already constrained several BSM scenarios, and more precise measurements are expected in the forthcoming years. Such an expectation has motivated the exploratory study performed in this paper, where we have considered the exclusive single charged Higgs pair production in pp collisions at $\sqrt{s} = 14$ TeV. One has assumed the type - I two - Higgs-Doublet model, which is one of the simplest BSM frameworks that predict charged Higgs bosons and that allows light charged Higgs with mass below 100 GeV. Our study complements the analysis performed in Ref. [24], where the single charged Higgs pair production in inelastic pp collisions was estimated and the current viable parameters for the type - I 2HDM were derived. The exclusive H^+H^- production cross - section was estimated considering different values for the charged Higgs and two distinct experimental configurations, whose are similar to those present in central (ATLAS/CMS) and forward (LHCb) detectors. We focused on the leptonic $H^\pm \rightarrow [\tau\nu_\tau]$ decay mode, which one has verified to be the final state with larger signal/background ratio. We have demonstrated that the background associated to the $pp \rightarrow p\tau^-\tau^+p$ can be fully removed by assuming a cut on the ratio $R = m_{\tau\tau}/m_X$ and/or in the acoplanarity. In contrast, the contribution of the $pp \rightarrow pW^+W^-p \rightarrow p[\tau^+\nu_\tau][\tau^-\nu_\tau]p$ background process dominates and generates distributions that are similar those predicted by the signal. However, the signal/background ratio is of the order of 1/4 for a light charged Higgs, which implies a non - negligible contribution for the $[\tau^+\nu_\tau][\tau^-\nu_\tau]$ final state. Such a promising result motivates the extension of this exploratory study by considering more sophisticated separation methods, as e.g. those used by the experimental collaborations in Refs. [11, 13], where kinematic variables that differentiate between the signal and backgrounds are identified and combined into a multivariate discriminant, with the output score of the boosted decision tree (BDT) used in order to separate the single charged signal from the SM background processes. We plan to perform such an extension in a forthcoming study.






Acknowledgments

D.E.M. thanks dearly, in the person of Janusz Chwastowski, the total support of the Henryk Niewodniczanski Institute of Nuclear Physics Polish Academy of Sciences (grant no. UMO2021/43/P/ST2/02279). T.B.M. acknowledges ANID-Chile grant FONDECYT No. 3220454 for financial support. This work was partially financed by the Brazilian funding agencies CNPq,

- [1] G. Aad *et al.* [ATLAS], Phys. Lett. B **716**, 1-29 (2012)
- [2] S. Chatrchyan *et al.* [CMS], Phys. Lett. B **716**, 30-61 (2012)
- [3] [LEP Higgs Working Group for Higgs boson searches, ALEPH, DELPHI, L3 and OPAL], [arXiv:hep-ex/0107031 [hep-ex]].
- [4] A. G. Akeroyd, S. Moretti and M. Song, Phys. Rev. D **101**, no.3, 035021 (2020)
- [5] H. Bahl, T. Stefaniak and J. Wittbrodt, JHEP **06**, 183 (2021)
- [6] S. Moretti, R. Santos and P. Sharma, Phys. Lett. B **760**, 697-705 (2016)
- [7] M. Guchait and S. Moretti, JHEP **01**, 001 (2002)
- [8] A. Arhrib, A. Jueid and S. Moretti, Phys. Rev. D **98**, no.11, 115006 (2018)
- [9] A. M. Sirunyan *et al.* [CMS], JHEP **09** (2018), 007
- [10] G. Aad *et al.* [ATLAS], Phys. Rev. Lett. **125** (2020) no.5, 051801
- [11] M. Aaboud *et al.* [ATLAS], JHEP **09** (2018), 139
- [12] G. Aad *et al.* [ATLAS], JHEP **06** (2021), 145
- [13] A. M. Sirunyan *et al.* [CMS], JHEP **07** (2019), 142
- [14] A. M. Sirunyan *et al.* [CMS], JHEP **01** (2020), 096
- [15] A. Arhrib, R. Benbrik, H. Harouiz, S. Moretti and A. Rouchad, Front. in Phys. **8** (2020), 39
- [16] A. G. Akeroyd, S. Moretti, K. Yagyu and E. Yildirim, Int. J. Mod. Phys. A **32**, no.23n24, 1750145 (2017)
- [17] M. Drees, E. Ma, P. N. Pandita, D. P. Roy and S. K. Vempati, Phys. Lett. B **433**, 346-354 (1998)
- [18] A. Arhrib, R. Benbrik, R. Enberg, W. Klemm, S. Moretti and S. Munir, Phys. Lett. B **774**, 591-598 (2017)
- [19] M. Chakraborti, D. Das, M. Levy, S. Mukherjee and I. Saha, Phys. Rev. D **104** (2021) no.7, 075033
- [20] M. Aoki, R. Guedes, S. Kanemura, S. Moretti, R. Santos and K. Yagyu, Phys. Rev. D **84** (2011), 055028
- [21] H. Davoudiasl, W. J. Marciano, R. Ramos and M. Sher, Phys. Rev. D **89** (2014) no.11, 115008
- [22] M. Aoki, S. Kanemura, K. Tsumura and K. Yagyu, Phys. Rev. D **80**, 015017 (2009)
- [23] G. C. Branco, P. M. Ferreira, L. Lavoura, M. N. Rebelo, M. Sher and J. P. Silva, Phys. Rept. **516**, 1-102 (2012)
- [24] K. Cheung, A. Jueid, J. Kim, S. Lee, C. T. Lu and J. Song, Phys. Rev. D **105**, no.9, 095044 (2022)
- [25] A. Arhrib, R. Benbrik, M. Krab, B. Manaut, S. Moretti, Y. Wang and Q. S. Yan, JHEP **10**, 073 (2021)
- [26] P. Lebiedowicz and A. Szczurek, Phys. Rev. D **91**, 095008 (2015)
- [27] L. Duarte, V. P. Goncalves, D. E. Martins, T. B. de Melo and F. S. Queiroz, Phys. Rev. D **107**, no.3, 035010 (2023)
- [28] D. Erikliison, F. Mahmoudi and O. Stal, JHEP **11**, 035 (2008)
- [29] N. Craig and S. Thomas, JHEP **11**, 083 (2012)
- [30] O. Eberhardt, U. Nierste and M. Wiebusch, JHEP **07**, 118 (2013)
- [31] M. D. Campos, D. Cogollo, M. Lindner, T. Melo, F. S. Queiroz and W. Rodejohann, JHEP **08**, 092 (2017)
- [32] S. M. Davidson and H. E. Logan, Phys. Rev. D **80**, 095008 (2009)

- [33] D. A. Camargo, A. G. Dias, T. B. de Melo and F. S. Queiroz, *JHEP* **04** (2019), 129
- [34] P. Ko, Y. Omura and C. Yu, *Phys. Lett. B* **717** (2012), 202-206
- [35] P. Ko, Y. Omura and C. Yu, *JHEP* **01** (2014), 016
- [36] M. Flechl, R. Klees, M. Kramer, M. Spira and M. Ubiali, *Phys. Rev. D* **91**, no.7, 075015 (2015)
- [37] C. Degrande, R. Frederix, V. Hirschi, M. Ubiali, M. Wiesemann and M. Zaro, *Phys. Lett. B* **772**, 87-92 (2017)
- [38] J. Haller, A. Hoecker, R. Kogler, K. Mönig, T. Peiffer and J. Stelzer, *Eur. Phys. J. C* **78**, no.8, 675 (2018)
- [39] M. Misiak, H. M. Asatrian, R. Boughezal, M. Czakon, T. Ewerth, A. Ferroglia, P. Fiedler, P. Gambino, C. Greub and U. Haisch, *et al.* *Phys. Rev. Lett.* **114**, no.22, 221801 (2015)
- [40] Y. Amhis *et al.* [HFLAV], [arXiv:1412.7515 [hep-ex]].
- [41] V. M. Budnev, I. F. Ginzburg, G. V. Meledin and V. G. Serbo, *Phys. Rept.* **15**, 181 (1975).
- [42] B. A. Kniehl, *Phys. Lett. B* **254**, 267 (1991).
- [43] J. D. Bjorken, *Phys. Rev. D* **47**, 101 (1993).
- [44] J. Alwall, M. Herquet, F. Maltoni *et al.*, *JHEP* **06**, 128 (2011).
- [45] L. Adamczyk *et al.*, CERN-LHCC-2015-009, ATLAS-TDR-024.
- [46] M. Tasevsky [ATLAS Collaboration], *AIP Conf. Proc.* **1654**, 090001 (2015).
- [47] M. Albrow *et al.* [CMS and TOTEM Collaborations], CERN-LHCC-2014-021, TOTEM-TDR-003, CMS-TDR-13.
- [48] V. P. Gonçalves, D. E. Martins, M. S. Rangel and M. Tasevsky, *Phys. Rev. D* **102**, no.7, 074014 (2020).
- [49] D. E. Martins, M. Tasevsky and V. P. Goncalves, *Phys. Rev. D* **105**, no.11, 114002 (2022).
- [50] N. D. Christensen and C. Duhr, *Comput. Phys. Commun.* **180**, 1614-1641 (2009)

Identify the new state $Y(3872)$ as the P-wave $D\bar{D}^*/\bar{D}D^*$ resonance

Zi-Yang Lin ^{1,*} Jun-Zhang Wang ^{2,†} Jian-Bo Cheng ^{3,‡} Lu Meng ^{4,§} and Shi-Lin Zhu ^{2,¶}

¹*School of Physics, Peking University, Beijing 100871, China*

²*School of Physics and Center of High Energy Physics, Peking University, Beijing 100871, China*

³*College of Science, China University of Petroleum, Qingdao, Shandong 266580, China*

⁴*Institut für Theoretische Physik II, Ruhr-Universität Bochum, D-44780 Bochum, Germany*

The BESIII Collaboration recently observed a new charmonium-like vector state $Y(3872)$ in $e^+e^- \rightarrow D\bar{D}$, which should be the first P-wave $D\bar{D}^*/\bar{D}D^*$ molecular resonance. The experimental and theoretical identification of the P-wave dimeson state holds paramount importance in enhancing our comprehension of the non-perturbative QCD and few-body physics. Its existence is firmly established in a unified meson-exchange model which simultaneously depicts the features of the $\chi_{c1}(3872)$, $Z_c(3900)$ and $T_{cc}(3875)$. This scenario can be directly examined in the $e^+e^- \rightarrow D\bar{D}^*/\bar{D}D^*$ cross section to see whether a resonance exists at the threshold. The credibility of the investigations is also ensured by the fact that the P-wave interaction dominantly arises from the well-known long-range pion exchange. Additionally, the existence of the P-wave resonance only depends on the interaction strength and is less sensitive to the potential shapes. We extensively calculate all systems up to P-wave with various quantum numbers and predict a dense population of the $D\bar{D}^*/\bar{D}D^*$ and DD^* states, where the S-wave $D\bar{D}^*/\bar{D}D^*$ state with $I^G(J^{PC}) = 0^-(1^{+-})$, P-wave $D\bar{D}^*/\bar{D}D^*$ state with $I^G(J^{PC}) = 0^+(0^{-+})$, and P-wave DD^* state with $I(J^P) = 0(0^-)$ are more likely to be observed in experiments.

Introduction.— Over the past two decades, a significant number of hadrons defying the spectra predicted by quark models have been observed in the heavy flavor sector, which are typically regarded as the exotica within the realm of Quantum Chromodynamics (QCD), see Refs. [1–7] for reviews. Delving into the structure and dynamics associated with these exotic states holds paramount importance in enhancing our comprehension of the non-perturbative features of low-energy QCD. These states also serve as promising examples for studying the general few-body physics.

Among these exotic states, the $\chi_{c1}(3872)$, $Z_c(3900)$, and $T_{cc}(3875)$ stand out as undeniable “star” examples, believed to be the first charmonium-like state [8], the first manifestly exotic charmonium-like state [9, 10], and the first doubly charmed tetraquark state [11, 12] observed in experiments, respectively. It is particularly intriguing that these three states are closely interconnected. The proximity of the former two states to the $D\bar{D}^*/\bar{D}D^*$ threshold and the latter one to the DD^* threshold positions them as strong candidates for corresponding hadronic molecules. Indeed, prior to the observation of $T_{cc}(3875)$, Li *et al.* had predicted a very loosely bound state of DD^* utilizing the one-boson-exchange model (OBE), with parameters established beforehand while investigating the $\chi_{c1}(3872)$ [13, 14].

In the realm of doubly heavy exotic states, such as the $\chi_{c1}(3872)$, $Z_c(3900)$, and $T_{cc}(3875)$, previous studies have predominantly focused on S-wave dimeson states,

encompassing bound states, virtual states, or resonances. However, P-wave states near the threshold are of particular interest and arouse the attention in many fields of physics, see the halo nuclei as P-wave resonances in nuclear physics [15] and the P-wave Feshbach resonances in cold atomic physics [16]. Recently, the BESIII Collaboration discovered a new resonance in $e^+e^- \rightarrow D\bar{D}$ [17]. Apart from the established 1^{--} states $\psi(3770)$, $\psi(4040)$, $\psi(4160)$, $\psi(4230)$, $\psi(4360)$, $\psi(4415)$, $\psi(4660)$, they observed a new resonance with a significance of over 20σ . Its mass and width are fitted to be $3872.5 \pm 14.2 \pm 3.0$ MeV and $179.7 \pm 14.1 \pm 7.0$ MeV, respectively. Hereafter we use $Y(3872)$ to denote this state. It is worth noting that the coupled-channel analysis of data from Belle and BESIII has the potential to generate a bump at this position without introducing new states. However, it appears to be very challenging in accurately depicting the nearby points [18, 19]. The newly observed state, locating exactly at the $D\bar{D}^*$ threshold, turns out a good candidate of the P-wave $D\bar{D}^*$ resonance.

In this work, we aim to identify it as the first P-wave dimeson state in the doubly heavy sector in the meson-exchange model. By relating the $Y(3872)$ to the S-wave states $\chi_{c1}(3872)$, $Z_c(3900)$ and $T_{cc}^+(3985)$, we make a unified description of these states in the one-boson-exchange (OBE) interaction. The resonance poles are obtained by solving the complex scaled Schrödinger equation in momentum space (The details can be found in Ref. [20]).

For the following three reasons, the predictions regarding the existence of the P-wave resonance are highly reliable. Just as the OBE model has provided a high-precision description of nuclear forces [21], meson-exchange models have also achieved notable success in elucidating heavy flavor hadronic molecules [22–30]. In the 1990s, Törnqvist predicted a deuteron-like $D\bar{D}^*$ bound state, which has been confirmed by the observa-

* lzy_15@pku.edu.cn

† wangjzh2022@pku.edu.cn

‡ jcheng@upc.edu.cn

§ lu.meng@rub.de

¶ zhushl@pku.edu.cn

tion of the $\chi_{c1}(3872)$ [22, 23]. The interactions stemming from the exchange of π , η , ρ , ω , and σ particles naturally predict T_{cc} as a DD^* bound state once their parameters are determined in the $DD^*/\bar{D}D^*$ systems, specifically the $\chi_{c1}(3872)$ [13, 14]. The interactions governing T_{cc} and $\chi_{c1}(3872)$ adhere to the G-parity rules. Given that both P-wave and S-wave states arise from the partial wave expansion of the same potential, the existence of these P-wave resonances could be firmly established once the S-wave interaction is fixed in depicting the $\chi_{c1}(3872)$, $Z_c(3900)$ and $T_{cc}^+(3985)$ states. Recently, similar ideas have been used to investigate the P-wave DD_1 , D^*D_1 and $D^*D_2^*$ states [31], inspired by the corresponding deeply bound S-wave states in Ref. [32]. The states of D^*N in the P-wave were also considered during the investigation of $\Lambda_c(2940)^+$ and its counterparts [33].

In principle, the generation of S-wave resonance poles typically hinges on the specifics of the potential, including its shape, coupled-channel effects, or the regularization method employed (see, for instance, Ref. [34]). Conversely, P-wave resonances can be generated by simply adjusting the strength of the interaction in a single-channel scenario. As the parameters in the potential are adjusted to make it less attractive (see Fig. 1), the bound state poles in the physical Riemann sheet tend to migrate into the unphysical sheet, manifesting as virtual states (S-wave) or resonances (higher partial waves)[35]. Consequently, the presence of S-wave virtual states and P- or higher-wave resonances relies primarily on the strength of the interaction rather than the shape of the potential. Thus the existence and the pole position of the P-wave resonance as well as the S-wave virtual state tend to be robust across different regularization methods and cutoff parameters.

Given the repulsion effect of the centrifugal barrier at the short range, the long-range interactions, specifically the one-pion-exchange (OPE) potential, will play a vital role in higher partial wave systems as the most peripheral part among the meson-exchange interactions. Indeed, taking the chiral effective field theory as an example, the leading-order chiral interaction of the P-wave system solely stems from the OPE interaction, while for the S-wave systems, the OPE interaction is accompanied with contact interactions to ensure the renormalization [7, 36–41]. Similar conclusions were also supported by analysing the lattice data [42]. Given that the coupling constants of OPE have been well determined by the partial decay width of D^* , P-wave resonances are typically predicted with high credibility.

Framework.— We adopt a framework established in Refs. [13, 14, 24, 25]. Under the heavy quark spin symmetry, the pseudoscalar D , the vector meson D^* and their antiparticles are combined into the superfield \mathcal{H} and $\tilde{\mathcal{H}}$,

$$\mathcal{H} = \frac{1+\not{v}}{2}(P_\mu^*\gamma^\mu - P\gamma_5), \quad \tilde{\mathcal{H}} = (\tilde{P}_\mu^*\gamma^\mu - \tilde{P}\gamma_5)\frac{1-\not{v}}{2}, \quad (1)$$

where $P = (D^0, D^+)$, $P_\mu^* = (D^{*0}, D^{*+})_\mu$, $\tilde{P} =$

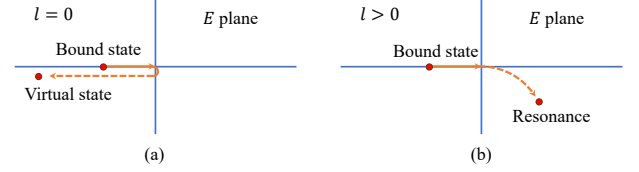


FIG. 1. Transition of the bound state pole to the virtual state (a) and resonance (b) for S-wave and higher partial waves, respectively by adjusting the strength of the potential to be less attractive [35]. The solid (dashed) lines represent the pole trajectories in the physical (unphysical) Riemann sheets.

$(\bar{D}^0, D^-)^T$, $\tilde{P}_\mu^* = (\bar{D}^{*0}, D^{*-})_\mu^T$. $v = (1, 0, 0, 0)$ is the velocity of the heavy meson. The conjugation of \mathcal{H} and $\tilde{\mathcal{H}}$ is defined as $\tilde{\mathcal{H}} = \gamma_0 \mathcal{H}^\dagger \gamma_0$ and $\tilde{\tilde{\mathcal{H}}} = \gamma_0 \tilde{\mathcal{H}}^\dagger \gamma_0$. For the charge conjugation transformation, we adopt the convention $D \xrightarrow{C} \bar{D}$ and $D^* \xrightarrow{C} -\bar{D}^*$, namely $\mathcal{H} \xrightarrow{C} C^{-1} \tilde{\mathcal{H}}^T C$, where $C = i\gamma^2 \gamma^0$. We include the π , η , σ , ρ , ω exchanges in the OBE model via the following Lagrangians,

$$\begin{aligned} \mathcal{L} = & g_s \text{Tr} [\mathcal{H} \sigma \tilde{\mathcal{H}}] + i g_a \text{Tr} [\mathcal{H} \gamma_\mu \gamma_5 \mathcal{A}^\mu \tilde{\mathcal{H}}] \\ & + i \beta \text{Tr} [\tilde{\mathcal{H}} v_\mu (\mathcal{V}^\mu - \rho^\mu) \tilde{\mathcal{H}}] + i \lambda \text{Tr} [\mathcal{H} \sigma_{\mu\nu} F^{\mu\nu} \tilde{\mathcal{H}}] \\ & + g_s \text{Tr} [\tilde{\tilde{\mathcal{H}}} \sigma \tilde{\tilde{\mathcal{H}}}] + i g_a \text{Tr} [\tilde{\tilde{\mathcal{H}}} \gamma_\mu \gamma_5 \mathcal{A}^\mu \tilde{\tilde{\mathcal{H}}}] \\ & - i \beta \text{Tr} [\tilde{\tilde{\mathcal{H}}} v_\mu (\mathcal{V}^\mu - \rho^\mu) \tilde{\tilde{\mathcal{H}}}] + i \lambda \text{Tr} [\tilde{\tilde{\mathcal{H}}} \sigma_{\mu\nu} F^{\mu\nu} \tilde{\tilde{\mathcal{H}}}] \quad (2) \end{aligned}$$

The vector meson fields ρ^μ and the pseudoscalar meson fields \mathcal{M} are defined as

$$\rho^\mu = \frac{i g_V}{\sqrt{2}} \begin{pmatrix} \frac{\rho_0}{\sqrt{2}} + \frac{\omega}{\sqrt{2}} & \rho^+ \\ \rho^- & -\frac{\rho_0}{\sqrt{2}} + \frac{\omega}{\sqrt{2}} \end{pmatrix}^\mu, \quad (3)$$

$$\mathbb{P} = \begin{pmatrix} \frac{\pi_0}{\sqrt{2}} + \frac{\eta}{\sqrt{6}} & \pi^+ \\ \pi^- & -\frac{\pi_0}{\sqrt{2}} + \frac{\eta}{\sqrt{6}} \end{pmatrix}. \quad (4)$$

$F^{\mu\nu} = \partial^\mu \rho^\nu - \partial^\nu \rho^\mu - [\rho^\mu, \rho^\nu]$ represents the field strength tensor of vector mesons. \mathcal{V}^μ and \mathcal{A}^μ represent the vector and axial currents of pseudoscalar mesons, respectively

$$\begin{aligned} \mathcal{V}^\mu &= \frac{1}{2} [\xi^\dagger, \partial_\mu \xi], \quad \mathcal{A}^\mu = \frac{1}{2} \{\xi^\dagger, \partial_\mu \xi\}, \\ \xi &= \exp(i\mathbb{P}/f_\pi). \quad (5) \end{aligned}$$

$f_\pi = 132$ MeV is the pion decay constant. The coupling constants are fixed to be consistent with Refs. [13, 14], resulting in a good depiction of $\chi_{c1}(3872)$ and a remarkable prediction of the T_{cc} state. The axial coupling constant $g_a = 0.59$ is extracted from the D^* width. The other coupling constants are $g_V = 5.8$, $\beta = 0.9$, $\lambda = 0.56$ GeV $^{-1}$, and $g_s = 0.76$. The isospin average masses of particles are taken from the Review of Particle Physics [43]: $m_\pi = 137$ MeV, $m_\eta = 548$ MeV, $m_\rho = 775$ MeV, $m_\omega = 783$ MeV, $m_D = 1867$ MeV, $m_{D^*} = 2009$ MeV. For the scalar meson exchange, we choose $m_\sigma = 600$ MeV.

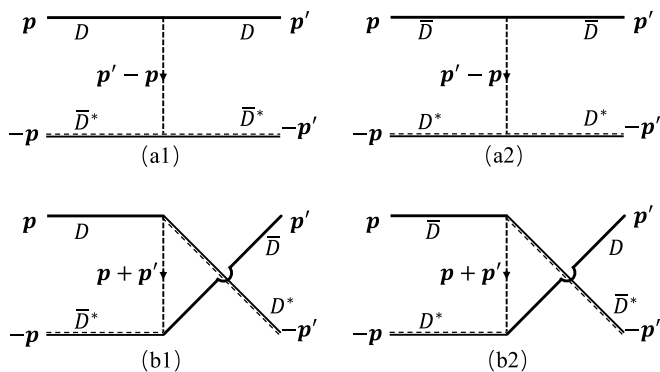


FIG. 2. The direct diagrams (upper row) and cross diagrams (lower row) in the OBE, where the transferred momenta are $\mathbf{p}' - \mathbf{p}$ and $\mathbf{p}' + \mathbf{p}$, respectively.

We construct the $D\bar{D}^*$ wave functions as the C-parity eigenstates for neutral channels,

$$|C = \pm\rangle = \frac{1}{\sqrt{2}}(|D(\mathbf{p})\bar{D}^*(-\mathbf{p})\rangle \mp |\bar{D}(\mathbf{p})D^*(-\mathbf{p})\rangle). \quad (6)$$

Here the momenta of the particles are shown explicitly. For the charged channels, we can similarly construct the wave functions as the eigenstates of G-parity. As depicted in Fig. 2, the transfer momentum in the cross diagrams corresponding to the u -channel turns out $\mathbf{k} = \mathbf{p} + \mathbf{p}'$, while it is $\mathbf{q} = \mathbf{p} - \mathbf{p}'$ in the direct diagrams or t -channel exchanges. It is explained in Supplemental Material [44] that the momentum labeling is crucial to get the correct P-wave interactions. To show the key mechanism of the P-wave resonance, we ignore the isospin breaking effect and adopt the time-component of $q^0, k^0 = 0$.

The effective potential for the $D\bar{D}^*/\bar{D}D^*$ system can be related to the DD^* potential up to a factor G_m ($-G_m G_{MM}$) for the direct (cross) diagrams, with G_m and G_{MM} as the G-parities of the exchanged meson and the $D\bar{D}^*/\bar{D}D^*$ system, respectively. It is noticeable that the G-parity rule for cross diagrams is different from that for direct diagrams. The specific effective potentials and the derivation of the G-parity rule are presented in Supplemental Material [44]. With the complex scaling method $p \rightarrow pe^{-i\theta}$, the resonance and bound state poles can be derived as the eigenenergy in the Schrödinger equation

$$E\phi(\mathbf{p}) = \frac{\mathbf{p}^2}{2\mu}\phi(\mathbf{p}) + \int V(\mathbf{p}, \mathbf{k})\phi(\mathbf{k})\frac{d^3\mathbf{k}}{(2\pi)^3}. \quad (7)$$

To search for virtual states, we adopt the method in Ref. [45].

To regularize the ultraviolet divergence in the integral, we introduce a monopole regulator to suppress the potential at the large momentum

$$V(\mathbf{p}', \mathbf{p}) \rightarrow V(\mathbf{p}', \mathbf{p})\frac{\Lambda^2}{p'^2 + \Lambda^2}\frac{\Lambda^2}{p^2 + \Lambda^2}. \quad (8)$$

Our final results are nearly irrelevant to the specific choice of regulator. The cutoff Λ is the only parameter to be determined. We adjust Λ to generate a pole at the threshold (a loosely bound state or a near-threshold virtual state) in the 3S_0 isosinglet $D\bar{D}^*/\bar{D}D^*$ system with the positive C-parity for neutral components, namely the 1^{++} channel corresponding to χ_{c1} (3872). Then we search for poles with different isospins, C-parities, orbital angular momenta (S-wave and P-wave) in $D\bar{D}^*/\bar{D}D^*$ and DD^* systems.

Results and discussion.— The partial-wave potentials of $J = 1$ isosinglet $D\bar{D}^*/\bar{D}D^*$ systems are depicted in Fig. 3. In P-wave interactions, the significance of the pion exchange increases, whereas the S-wave interaction is predominantly governed by the ρ exchange. The χ_{c1} (3872) corresponds to the 1^{++} S-wave channel, exhibiting the most pronounced attraction. Its negative C-parity counterpart, the 1^{+-} S-wave channel, also displays an attractive potential. Consequently, these two S-wave channels may give rise to near-threshold bound states or virtual states. The 1^{-+} channel, serving as the P-wave counterpart of 1^{++} , demonstrates substantial repulsion, thus making it unlikely to produce poles near the threshold. However, the potential of the 1^{--} channel, which is the P-wave partner of the 1^{+-} channel, is attractive, suggesting a possible resonance pole corresponding to the Y (3872).

In Fig. 4, we illustrate the pole trajectories of four particularly intriguing states: the χ_{c1} (3872), T_{cc} (3875), Z_c (3900), and the recently observed Y (3872), as the cutoff parameter Λ varies from 0.4 GeV to 1.3 GeV. With a cutoff of around 0.5 GeV, the χ_{c1} (3872) manifests as a loosely bound state. The T_{cc} is also a near-threshold bound state, which agrees with the results in Ref. [14]. Simultaneously, the Z_c (3900) emerges as a virtual state, aligning with the pole position deduced through a data-driven coupled-channel analysis in Ref. [19]. Remarkably, within this same cutoff range, a P-wave resonance materializes in the 1^{--} channel, corresponding to the Y (3872) state. If the cutoff is increased to strengthen the attraction, the Y (3872) resonance will move to the physical Riemann sheet and turns into a bound state, thereby confirming the Y (3872) as indeed a P-wave resonance engendered by adjusting the interaction strength. The value of the cutoff differs from the results in Refs. [14, 46], since the regulator is different. However, our conclusion holds under different regulators. We test the results using the regulator and cutoff fixed in Ref. [46]. We validate these findings using the regulator and cutoff parameters established in Ref. [46]. The results indicate that as long as the cutoff is set to generate a loosely bound χ_{c1} (3872) state, a corresponding P-wave resonance emerges in the 1^{--} channel as the Y (3872), while the poles of T_{cc} and Z_c (3900) remain qualitatively unchanged, see the Supplemental Material [44].

We delve into the resonances with alternative quantum numbers, as summarized in Table I. We neglect the tiny imaginary part of virtual state pole arising from the left-

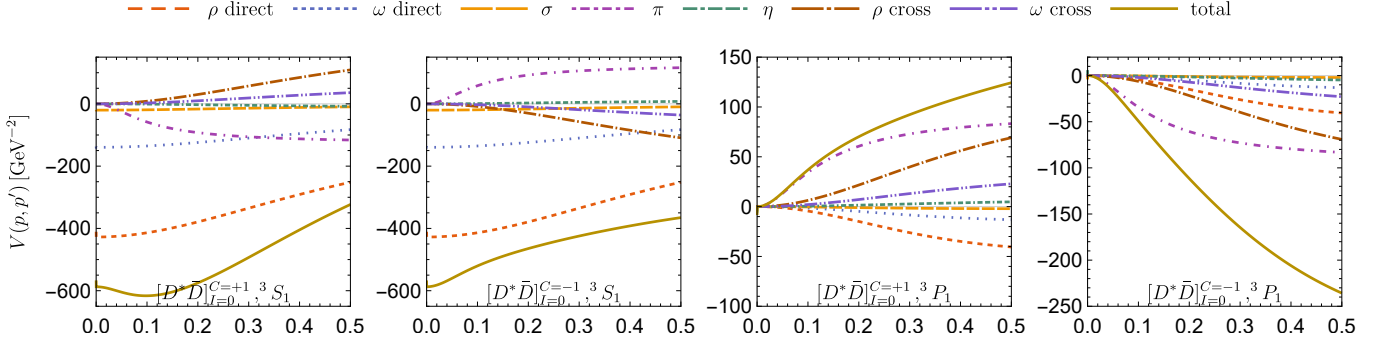


FIG. 3. The OBE potentials in the 1^{++} , 1^{+-} , 1^{-+} and 1^{--} isoscalar $DD^*/\bar{D}\bar{D}^*$ channels. The 1^{++} and 1^{-+} channel correspond to the $\chi_{c1}(3872)$ and its P-wave counterpart, respectively. The 1^{--} and 1^{+-} channel corresponds to the $Y(3872)$ and its S-wave counterpart, respectively. Only $p = p'$ cases are shown.

TABLE I. The poles in all channels of DD^* and DD^* , up to the orbital angular momentum $L = 1$. The B and V superscripts denote the bound state and the virtual state, respectively. Otherwise the pole refers to a resonance.

	$D\bar{D}^*, C = +$		$D\bar{D}^*, C = -$		DD^*		
	$I = 0$	$I = 1$	$I = 0$	$I = 1$	$I = 0$	$I = 1$	
$\Lambda = 0.5\text{GeV}$	$1^+(^3S_1)$	$-3.1^B, \chi_{c1}(3872)$	-	-1.60^B	$-35.6^V, Z_c(3900)$	$-0.41^B, T_{cc}(3875)$	-
	$0^-(^3P_0)$	$-1.5 - 14.5i$	-	-	-	$-9.6 - 9.7i$	-
	$1^-(^3P_1)$	-	-	$-4.0 - 27.3i, Y(3872)$	-	$-31.7 - 70.6i$	-
	$2^-(^3P_2)$	$-42.6 - 39.4i$	-	$-21.3 - 50.7i$	-	$-37.8 - 40.9i$	-
$\Lambda = 0.6\text{GeV}$	$1^+(^3S_1)$	$-6.5^B, \chi_{c1}(3872)$	-	-5.8^B	$-34.6^V, Z_c(3900)$	$-4.3^B, T_{cc}(3875)$	-
	$0^-(^3P_0)$	$3.2 - 13.7i$	-	-	-	$-10.2 - 12.1i$	-
	$1^-(^3P_1)$	-	-	$2.0 - 27.3i, Y(3872)$	-	$-33.7 - 84.8i$	-
	$2^-(^3P_2)$	$-44.2 - 49.0i$	-	$-19.3 - 58.8i$	-	$-37.8 - 49.3i$	-

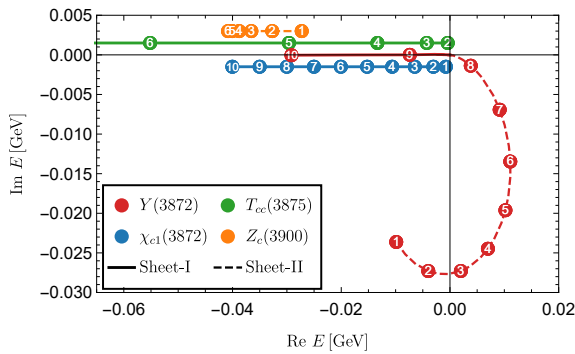


FIG. 4. The pole trajectories with the cutoff parameters correspond to $\chi_{c1}(3872)$, $T_{cc}(3875)$, $Z_c(3900)$ and the newly observed $Y(3872)$ states. The circled number 1-10 represent the increasing cutoff 0.4-1.3 GeV in order. The solid (dashed) lines represent the pole trajectories in the physical (unphysical) Riemann sheets. The poles on the negative real axis are slightly shifted for transparency.

hand cut of the pion exchange. For $DD^*/\bar{D}\bar{D}^*$ isospin singlets, aside from the $\chi_{c1}(3872)$ and $Y(3872)$, a loosely bound state exists in the S-wave partner channel of the $Y(3872)$. In channels with $J = 0$ and $J = 2$, resonances emerge in 0^{-+} , 2^{-} , and 2^{-+} channels. For the DD^* systems, in addition to the T_{cc} state as the S-wave isospin singlet, its P-wave partner with $J^P = 0^-$ also emerges as a near-threshold resonance. P-wave resonance poles are obtained in the 1^- and 2^- channels but are distant from the thresholds.

Concerning $I = 1$ channels, besides a virtual state pole in the S-wave 1^{+-} channel, corresponding to the $Z_c(3900)$, no additional states are obtained. This is because the isospin factor $\tau \cdot \tau$ is only $\frac{1}{3}$ of the $I = 0$ channels, rendering the potentials generally insufficient to generate bound states or P-wave resonances. For clarification, we do find resonance poles in 0^{-+} , 1^{-} isovector $DD^*/\bar{D}\bar{D}^*$ channels and 1^- , 2^- isovector DD^* channels, but they are very sensitive to the cutoff. They transform into virtual states rather than bound states when adjust-

ing the interaction strength, thereby are not the kind of P-wave resonances we refer to in Fig. 1 (b). Their existence depends on the particular regularization, making them less credible. So we omit them in the final results.

To sum up, aside from the $\chi_{c1}(3872)$, $Z_c(3900)$, $Y(3872)$, and T_{cc} states, the S-wave $D\bar{D}^*/\bar{D}D^*$ state with $I^G(J^{PC}) = 0^-(1^{+-})$, P-wave $D\bar{D}^*/\bar{D}D^*$ state with $I^G(J^{PC}) = 0^+(0^{-+})$, and P-wave DD^* state with $I(J^P) = 0(0^-)$ are more likely to be observed due to their proximity to the thresholds.

Conclusion and outlook.— The newly observed $Y(3872)$ is interpreted as the P-wave $D\bar{D}^*/\bar{D}D^*$ resonance in a novel scenario. The existence of the P-wave resonance is firmly established on a unified meson-exchange model which well depicts the features of $\chi_{c1}(3872)$, $Z_c(3900)$ and $T_{cc}(3875)$ simultaneously. Compared with the S-wave state, the P-wave interaction dominantly arises from the well-known long-range pion exchange, ensuring robust conclusions when shifting between different models. The appearance of the P-wave resonance is also quite natural, particularly when the P-wave channels lack sufficient attraction, thus rendering them less sensitive to the potential shape compared with the S-wave resonance. This mechanism contributes to the dense population of P-wave resonances in both the $D\bar{D}^*/\bar{D}D^*$ and DD^* systems, which is validated by our extensive calculations spanning all systems up to P-wave with various quantum numbers.

Furthermore, there is promise in identifying P-wave resonances in other systems. For instance, the odd-parity $X_1(2900)$ observed in LHCb alongside $X_0(2900)$ [47, 48] may be plausibly interpreted as the P-wave \bar{D}^*K^* resonance. The $\psi(4220)$ state may potentially be interpreted as the P-wave $D_s^*\bar{D}_s^*$ resonance $Y(4220)$. Similarly, there may exist the P-wave $D_s^*\bar{D}_s/D_s\bar{D}_s^*$, $D_s\bar{D}_s$, $D^*\bar{D}^*$ and DD near-threshold resonances. One may also expect similar P-wave structures in the two bottom meson systems.

The scenario of identifying $Y(3872)$ as the P-wave resonance can be directly examined in the $e^+e^- \rightarrow D\bar{D}^*$ cross section to see whether a resonance exists at the threshold. In the case of the $Y(3872)$ being a resonance with the real part of the pole position below the threshold, its width comes from the decay to the $D\bar{D}^*$ final state, where the large width renders the decay allowable. Remarkably, for the pole below the threshold, the line shape deviates severely from the Breit-Wigner form and needs other parameterization methods like the Flatté form.

Among the abundant predictions, the S-wave $D\bar{D}^*/\bar{D}D^*$ state with $I^G(J^{PC}) = 0^-(1^{+-})$, P-wave $D\bar{D}^*/\bar{D}D^*$ state with $I^G(J^{PC}) = 0^+(0^{-+})$, and P-wave DD^* state with $I(J^P) = 0(0^-)$ are more likely to be observed due to their proximity to the thresholds. Unlike the 1^{--} $Y(3872)$ state, their decay mode to $D\bar{D}$ system is forbidden. Thus, these predictions could be searched in the hidden charmed channels, for example, the 1^{+-} state in $\eta_c\omega$, $J/\psi\eta$, $J/\psi\pi\pi$, the 0^{-+} state in $J/\psi\omega$, $\eta_c\pi\pi$ and $\chi_{c1}\pi\pi$, the 2^{-+} state in $J/\psi\omega$, $\chi_{c1}\pi\pi$,

the 2^{--} state in $J/\psi\eta$, $\eta_c\omega$ etc.

ACKNOWLEDGMENTS

This project was supported by the National Natural Science Foundation of China (11975033, 12147168 and 12070131001). This project was also funded by the Deutsche Forschungsgemeinschaft (DFG, German Research Foundation, Project ID 196253076-TRR 110). J.Z.W. is also supported by the National Postdoctoral Program for Innovative Talent.

Appendix A: Sign problem of the u -channel potentials

In Fig. 2 of the main text, the u -channel diagrams of the OBE are involved. However, a prevailing misconception exists in much of the literature regarding these u -channel OBE diagrams. We aim to address this misconception and illustrate its impact, revealing that while it does not introduce errors for the systems with even orbital angular momentum, it does induce a sign alteration in the partial wave potential for odd orbital angular momentum.

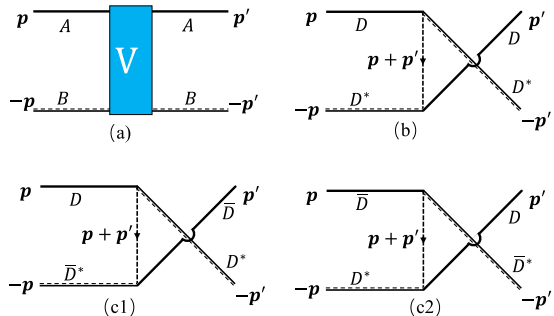


FIG. 5. The momentum labeling for the u -channel diagrams.

In the general elastic scattering depicted for two distinguishable particles, denoted as A and B , as illustrated in Fig. 5 (a), the nonlocal potential in the center-of-mass frame can be expressed as:

$$V(\mathbf{p}', \mathbf{p}) \equiv \langle \mathbf{p}' | \hat{V} | \mathbf{p} \rangle \equiv \langle A(\mathbf{p}')B(-\mathbf{p}') | \hat{V} | A(\mathbf{p})B(-\mathbf{p}) \rangle, \quad (\text{A1})$$

Here, we adopt the momentum of the particle A to label the two-particle states, denoted as $|\mathbf{p}\rangle$, which signifies $|A(\mathbf{p})B(-\mathbf{p})\rangle$. One can get the Lippmann-Schwinger equation in momentum space by sandwiching the operator equation $\hat{T} = \hat{V} + \hat{V}\hat{G}\hat{T}$ between initial and final two-body states and inserting complete basis between operators,

$$T(\mathbf{p}', \mathbf{p}; E) = V(\mathbf{p}', \mathbf{p}) + \int \frac{d\mathbf{p}''}{(2\pi)^3} V(\mathbf{p}', \mathbf{p}'')G(E, \mathbf{p})T(\mathbf{p}'', \mathbf{p}; E), \quad (\text{A2})$$

with

$$G(E, \mathbf{p}) = \frac{1}{E - m_A - m_B - \frac{p^2}{2m_A} - \frac{p^2}{2m_B} + i\epsilon}. \quad (\text{A3})$$

It is worth noting that in Eq. (A2), all the three-momenta refer specifically to those of particle A .

Now we can specify A and B as D and D^* , respectively taking OPE interaction as an example as shown in Fig 5 (b). Apparently, the momentum of the exchanged pion should be $\mathbf{k} = \mathbf{p} + \mathbf{p}'$ rather than the conventional $\mathbf{q} = \mathbf{p}' - \mathbf{q}$ used for the t-channel diagram.

For the $D^*\bar{D}/\bar{D}^*D$ system, one can construct the state with C-parity for the neutron channel,

$$|D\bar{D}^*/\bar{D}D^*, \{\beta, \mathbf{p}\}\rangle \equiv |D(\mathbf{p})\bar{D}^*(-\mathbf{p}) + \beta\bar{D}(\mathbf{p})D^*(-\mathbf{p})\rangle. \quad (\text{A4})$$

To ensure the fixed C-parity, the $\bar{D}(D^*)$ in the second component should has the same momentum as the $D(\bar{D}^*)$ in the first component. One can get

$$\hat{C}|D\bar{D}^*/\bar{D}D^*, \{\beta, \mathbf{p}\}\rangle = -\beta|D\bar{D}^*/\bar{D}D^*, \{\beta, \mathbf{p}\}\rangle. \quad (\text{A5})$$

with the convention

$$\hat{C}|D(\mathbf{p})\rangle = |\bar{D}(\mathbf{p})\rangle; \hat{C}|D^*(\mathbf{p})\rangle = -|\bar{D}^*(\mathbf{p})\rangle \quad (\text{A6})$$

Taking OPE as an example, the Feynman diagrams involved are shown in Fig. 5 (c1) and (c2). Once again, the momentum of the exchanged pion should be $\mathbf{k} = \mathbf{p} + \mathbf{p}'$.

As far as we know, in much of the literature discussing u -channel OBE diagrams, there is a common mistake regarding the momentum of the exchanged meson, where it is erroneously taken as $\mathbf{q} = \mathbf{p}' - \mathbf{p}$. Using \mathbf{q} as \mathbf{k} is equivalent to substituting $V(\mathbf{p}', \mathbf{p})$ with $V(\mathbf{p}', -\mathbf{p})$. Consequently, the potential term in the Schrödinger equation becomes:

$$\begin{aligned} & \int d^3\mathbf{p} V(\mathbf{p}', -\mathbf{p}) \phi_L(\mathbf{p}) \\ &= \int d^3\mathbf{p} V(\mathbf{p}', \mathbf{p}) \phi_L(-\mathbf{p}) \\ &= (-1)^L \int d^3\mathbf{p} V(\mathbf{p}', \mathbf{p}) \phi_L(\mathbf{p}) \end{aligned} \quad (\text{A7})$$

where $\phi_L(\mathbf{p})$ represents wave function with orbital angular momentum L . One can see the mistake only affects states with odd L . Fortunately, the majority of past literature has focused on S-wave and D-wave systems, rendering this mistake inconsequential for them. Recent studies concerning P-wave systems have acknowledged this issue and adopted the correct notations [31, 42].

Appendix B: The OBE potentials and the G-parity rule

The effective potentials for the DD^* system in momentum space are listed as follows,

$$V_\sigma^D(\mathbf{p}', \mathbf{p}) = -\frac{g_s^2}{q^2 + m_\sigma^2},$$

$$\begin{aligned} V_\pi^C(\mathbf{p}', \mathbf{p}) &= -\frac{g^2}{2f_\pi^2} \frac{(\boldsymbol{\epsilon} \cdot \mathbf{k})(\boldsymbol{\epsilon}' \cdot \mathbf{k})}{\mathbf{k}^2 - k_0^2 + m_\pi^2} \boldsymbol{\tau} \cdot \boldsymbol{\tau}, \\ V_\eta^C(\mathbf{p}', \mathbf{p}) &= -\frac{g^2}{6f_\pi^2} \frac{(\boldsymbol{\epsilon} \cdot \mathbf{k})(\boldsymbol{\epsilon}' \cdot \mathbf{k})}{\mathbf{k}^2 - k_0^2 + m_\eta^2} \mathbb{1} \cdot \mathbb{1}, \\ V_{\rho/\omega}^D(\mathbf{p}', \mathbf{p}) &= \frac{\frac{1}{4}\beta^2 g_V^2 (\boldsymbol{\epsilon} \cdot \boldsymbol{\epsilon}')}{q^2 + m_{\rho/\omega}^2} \times \begin{cases} \boldsymbol{\tau} \cdot \boldsymbol{\tau}, & \text{for } \rho, \\ \mathbb{1} \cdot \mathbb{1}, & \text{for } \omega, \end{cases} \\ V_{\rho/\omega}^C(\mathbf{p}', \mathbf{p}) &= \frac{\lambda^2 g_V^2}{\mathbf{k}^2 - k_0^2 + m_{\rho/\omega}^2} \{(\mathbf{k} \cdot \boldsymbol{\epsilon})(\mathbf{k} \cdot \boldsymbol{\epsilon}') \\ & \quad - \mathbf{k}^2(\boldsymbol{\epsilon} \cdot \boldsymbol{\epsilon}')\} \times \begin{cases} \boldsymbol{\tau} \cdot \boldsymbol{\tau}, & \text{for } \rho, \\ \mathbb{1} \cdot \mathbb{1}, & \text{for } \omega, \end{cases} \end{aligned} \quad (\text{B1})$$

where D and C denotes the direct and cross diagrams, respectively. The isospin factors are

$$\boldsymbol{\tau} \cdot \boldsymbol{\tau} = \begin{cases} 1, & I = 1, D, \\ -3, & I = 0, D, \\ 1, & I = 1, C, \\ 3, & I = 0, C, \end{cases} \quad \mathbb{1} \cdot \mathbb{1} = \begin{cases} 1, & I = 1, D, \\ 1, & I = 0, D, \\ 1, & I = 1, C, \\ -1, & I = 0, C. \end{cases} \quad (\text{B2})$$

The results of the partial-wave expansion potential $V = (\boldsymbol{\epsilon} \cdot \mathbf{k})(\boldsymbol{\epsilon}' \cdot \mathbf{k})D(p', p, z)$ with $z = \mathbf{p}' \cdot \mathbf{p}/pp'$, are listed as follows,

$$\begin{aligned} V_S^{J=0} &= \frac{2\pi}{3} \int_{-1}^1 D(p', p, z)(p^2 + p'^2 + 2pp'z)dz, \\ V_P^{J=0} &= 2\pi \int_{-1}^1 D(p', p, z)\{(p^2 + p'^2)z + pp'(1 + z^2)\}dz, \\ V_P^{J=1} &= 2\pi \int_{-1}^1 D(p', p, z)\frac{1}{2}(z^2 - 1)pp'zdz, \\ V_P^{J=2} &= \frac{2\pi}{5} \int_{-1}^1 D(p', p, z)\{2(p^2 + p'^2)z \\ & \quad + \frac{1}{2}pp'(1 + 7z^2)\}dz. \end{aligned} \quad (\text{B3})$$

In Fig. 6, we list the the OBE potentials of DD^* channels with various meson exchanges.

The effective potential for the $D\bar{D}^*/\bar{D}D^*$ system can be related to the DD^* potential up to a factor G_m ($-G_m G_{MM}$) for the direct (cross) diagrams, with G_m and G_{MM} as the G-parities of the exchanged meson and the $D\bar{D}^*/\bar{D}D^*$ system, respectively. In Fig. 7, the total potentials for all DD^* and $D\bar{D}^*/\bar{D}D^*$ up to P-wave with various quantum numbers are illustrated. One can read out the $D\bar{D}^*/\bar{D}D^*$ potential of the specific meson exchange from Fig. 6 via G-parity rule. It is noteworthy that the G-parity rule for cross diagrams is different from that in direct diagrams. We will present the derivation of the G-parity rule as follows.

With the C-parity convention in Eq. (A6) (the final result is irrelevant to the convention), the G-parity transformation reads

$$D = (-D^+, D^0) \xrightarrow{G} \bar{D} = (\bar{D}^0, D^-) \xrightarrow{G} -D,$$

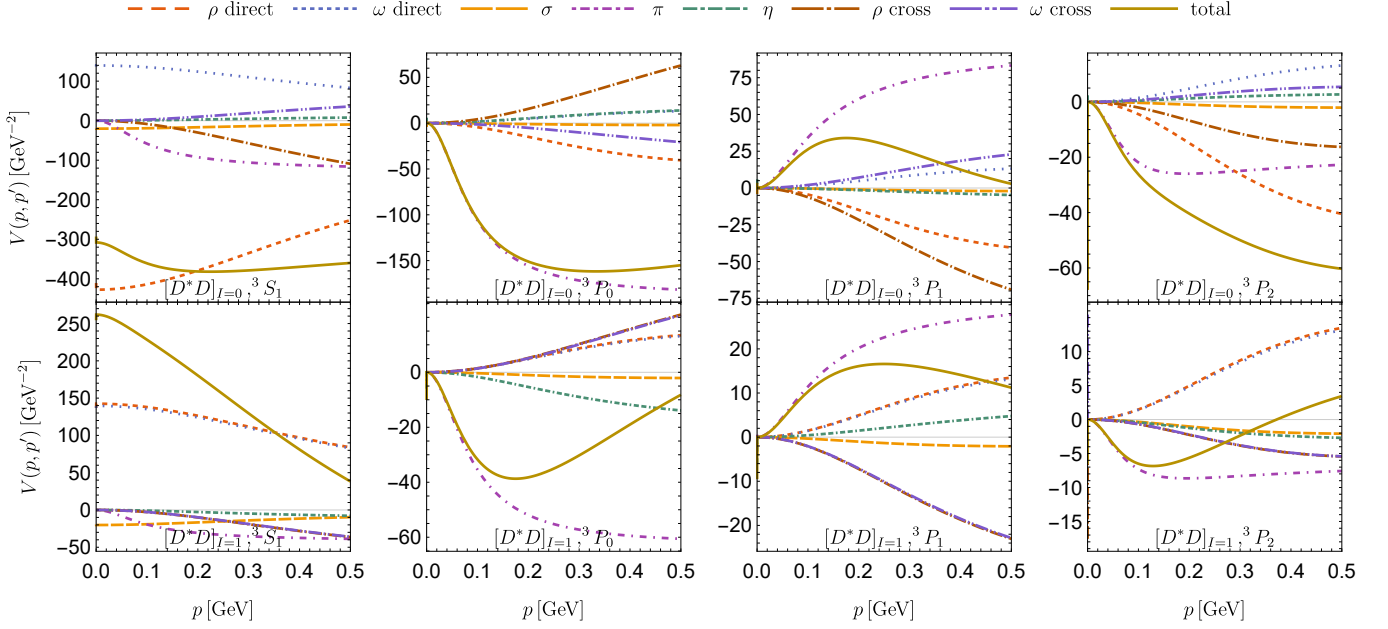


FIG. 6. The OBE potentials of DD^* channels are illustrated with various meson exchanges. Only $p = p'$ cases are depicted.

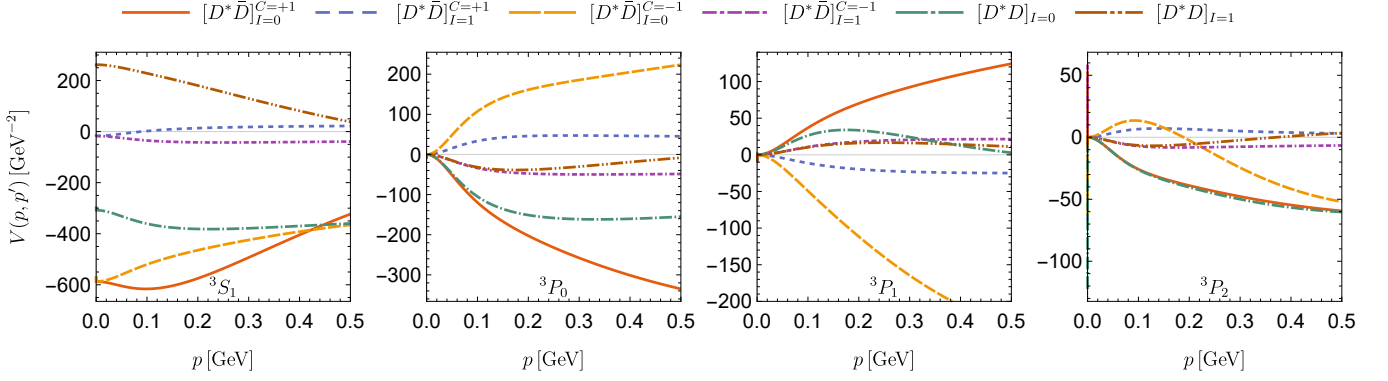


FIG. 7. The OBE potentials for all DD^* and $DD^*\bar{D}/\bar{D}D^*$ systems up to P-wave with various quantum numbers. Only $p = p'$ cases are shown.

$$D^* = (-D^{*+}, D^{*0}) \xrightarrow{G} -\bar{D}^* = -(\bar{D}^{*0}, D^{*-}) \xrightarrow{G} -D^*, \quad (\text{B4})$$

where the charmed mesons are written in the form of isospin doublets. The G-parity eigenstates can be constructed,

$$|D\bar{D}^*/\bar{D}D^*, G = \pm\rangle = \frac{1}{\sqrt{2}}(|D\bar{D}^*\rangle \pm |\bar{D}D^*\rangle). \quad (\text{B5})$$

Since the exchanged mesons are eigenstates of the G-parity, we can apply the G-parity transformation to one of the vertex in $DD^* \rightarrow DD^*$, as shown in Fig. 8. The overall factor G_m arises from the G-parity of the exchanged meson. Then we derive

$$\begin{aligned} V_{\bar{D}D^* \rightarrow D\bar{D}^*}^C &= (-G_m)V_{DD^* \rightarrow DD^*}^C, \\ V_{\bar{D}D^* \rightarrow \bar{D}D^*}^D &= V_{DD^* \rightarrow DD^*}^D. \end{aligned} \quad (\text{B6})$$

Combining Eq. (B5) and Eq. (B6), we derive

$$V_{D\bar{D}^*/\bar{D}D^*, G_{MM}} = G_m V_{DD^* \rightarrow DD^*}^D - G_m G_{MM} V_{DD^* \rightarrow DD^*}^C. \quad (\text{B7})$$

Appendix C: Regulator dependence

We also estimate the uncertainty of our results arising from the different regulators. For example, we choose the following regulators for the direct and cross diagrams, respectively,

$$V^D(\mathbf{q}) \rightarrow V^D(\mathbf{q}) \left(\frac{\Lambda^2 - m^2}{\Lambda^2 + \mathbf{q}^2} \right)^2, \quad (\text{C1})$$

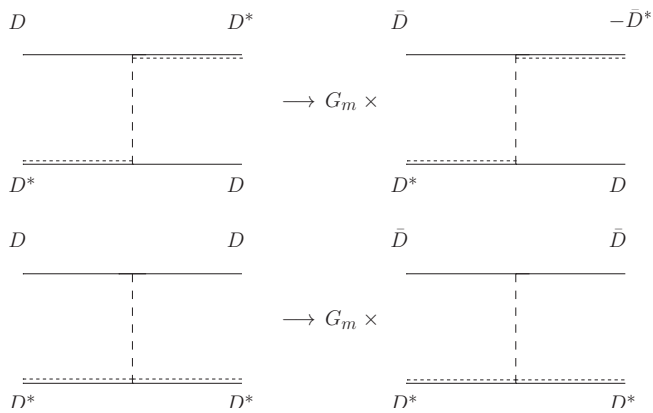


FIG. 8. The G-parity transformation for cross and direct diagrams, respectively. The signs are determined by the G-parity of the exchanged meson and Eq. (B4).

$$V^C(\mathbf{k}) \rightarrow V^C(\mathbf{k}) \left(\frac{\Lambda^2 - m^2}{\Lambda^2 + \mathbf{k}^2} \right)^2,$$

where the potentials from the direct and cross diagrams are the functions of \mathbf{q} and \mathbf{k} , respectively. m is the mass of the transferred meson. The cutoff $\Lambda = 1.25$ and 1.35 GeV is adjusted to get the loosely bound state $\chi_{c1}(3872)$. The pole positions for all other channels are presented in Table II. One can see as long as the cutoff is set to generate a loosely bound $\chi_{c1}(3872)$ state, a corresponding P-wave resonance emerges in the 1^{--} channel as the $Y(3872)$, while the poles of T_{cc} and $Z_c(3900)$ remain qualitatively unchanged. Our predictions are robust under various regularization schemes.

-
- [1] H.-X. Chen, W. Chen, X. Liu, and S.-L. Zhu, The hidden-charm pentaquark and tetraquark states, *Phys. Rept.* **639**, 1 (2016), arXiv:1601.02092 [hep-ph].
- [2] A. Esposito, A. Pilloni, and A. D. Polosa, Multiquark Resonances, *Phys. Rept.* **668**, 1 (2017), arXiv:1611.07920 [hep-ph].
- [3] F.-K. Guo, C. Hanhart, U.-G. Meißner, Q. Wang, Q. Zhao, and B.-S. Zou, Hadronic molecules, *Rev. Mod. Phys.* **90**, 015004 (2018), arXiv:1705.00141 [hep-ph].
- [4] Y.-R. Liu, H.-X. Chen, W. Chen, X. Liu, and S.-L. Zhu, Pentaquark and Tetraquark states, *Prog. Part. Nucl. Phys.* **107**, 237 (2019), arXiv:1903.11976 [hep-ph].
- [5] N. Brambilla, S. Eidelman, C. Hanhart, A. Nefediev, C.-P. Shen, C. E. Thomas, A. Vairo, and C.-Z. Yuan, The XYZ states: experimental and theoretical status and perspectives, *Phys. Rept.* **873**, 1 (2020), arXiv:1907.07583 [hep-ex].
- [6] H.-X. Chen, W. Chen, X. Liu, Y.-R. Liu, and S.-L. Zhu, An updated review of the new hadron states, *Rept. Prog. Phys.* **86**, 026201 (2023), arXiv:2204.02649 [hep-ph].
- [7] L. Meng, B. Wang, G.-J. Wang, and S.-L. Zhu, Chiral perturbation theory for heavy hadrons and chiral effective field theory for heavy hadronic molecules, *Phys. Rept.* **1019**, 1 (2023), arXiv:2204.08716 [hep-ph].
- [8] S. K. Choi *et al.* (Belle), Observation of a narrow charmonium-like state in exclusive $B^\pm \rightarrow K^\pm \pi^+ \pi^- J/\psi$ decays, *Phys. Rev. Lett.* **91**, 262001 (2003), arXiv:hep-ex/0309032.
- [9] M. Ablikim *et al.* (BESIII), Observation of a Charged Charmoniumlike Structure in $e^+e^- \rightarrow \pi^+\pi^-J/\psi$ at $\sqrt{s} = 4.26$ GeV, *Phys. Rev. Lett.* **110**, 252001 (2013), arXiv:1303.5949 [hep-ex].
- [10] Z. Q. Liu *et al.* (Belle), Study of $e^+e^- \rightarrow \pi^+\pi^-J/\psi$ and Observation of a Charged Charmoniumlike State at Belle, *Phys. Rev. Lett.* **110**, 252002 (2013), [Erratum: *Phys.Rev.Lett.* 111, 019901 (2013)], arXiv:1304.0121 [hep-ex].
- [11] R. Aaij *et al.* (LHCb), Observation of an exotic narrow doubly charmed tetraquark, *Nature Phys.* **18**, 751 (2022), arXiv:2109.01038 [hep-ex].
- [12] R. Aaij *et al.* (LHCb), Study of the doubly charmed tetraquark T_{cc}^+ , *Nature Commun.* **13**, 3351 (2022), arXiv:2109.01056 [hep-ex].
- [13] N. Li and S.-L. Zhu, Isospin breaking, Coupled-channel effects and Diagnosis of X(3872), *Phys. Rev. D* **86**, 074022 (2012), arXiv:1207.3954 [hep-ph].
- [14] N. Li, Z.-F. Sun, X. Liu, and S.-L. Zhu, Coupled-channel analysis of the possible $D^{(*)}D^{(*)}$, $\bar{B}^{(*)}\bar{B}^{(*)}$ and $D^{(*)}\bar{B}^{(*)}$ molecular states, *Phys. Rev. D* **88**, 114008 (2013), arXiv:1211.5007 [hep-ph].
- [15] C. A. Bertulani, H. W. Hammer, and U. Van Kolck, Effective field theory for halo nuclei, *Nucl. Phys. A* **712**, 37 (2002), arXiv:nucl-th/0205063.
- [16] C. Chin, R. Grimm, P. Julienne, and E. Tiesinga, Feshbach resonances in ultracold gases, *Reviews of Modern Physics* **82**, 1225 (2010).
- [17] M. Ablikim *et al.* (BESIII), Precise Measurement of Born Cross Sections for $e^+e^- \rightarrow D\bar{D}$ and Observation of One Structure between $\sqrt{s} = 3.80 - 4.95$ GeV, (2024), arXiv:2402.03829 [hep-ex].
- [18] T. V. Uglov, Y. S. Kalashnikova, A. V. Nefediev, G. V. Pakhlova, and P. N. Pakhlov, Exclusive open-charm near-threshold cross sections in a coupled-channel approach, *JETP Lett.* **105**, 1 (2017), arXiv:1611.07582 [hep-ph].
- [19] S. X. Nakamura, X. H. Li, H. P. Peng, Z. T. Sun, and X. R. Zhou, Global coupled-channel analysis of $e^+e^- \rightarrow c\bar{c}$ processes in $\sqrt{s} = 3.75 - 4.7$ GeV, (2023), arXiv:2312.17658 [hep-ph].
- [20] Z.-Y. Lin, J.-B. Cheng, B.-L. Huang, and S.-L. Zhu, Partial widths from analytical extension of the wave function: Pc states, *Phys. Rev. D* **108**, 114014 (2023), arXiv:2305.19073 [hep-ph].
- [21] R. Machleidt, K. Holinde, and C. Elster, The Bonn Meson Exchange Model for the Nucleon Nucleon Interaction, *Phys. Rept.* **149**, 1 (1987).
- [22] N. A. Tornqvist, Possible large deuteron - like meson meson states bound by pions, *Phys. Rev. Lett.* **67**, 556 (1991).
- [23] N. A. Tornqvist, From the deuteron to deusons, an analysis of deuteron - like meson meson bound states, *Z. Phys. C* **61**, 525 (1994), arXiv:hep-ph/9310247.

TABLE II. The poles in all channels of $D\bar{D}^*$ and DD^* , up to the orbital angular momentum $L = 1$ with the regularization in Eq. (C2). The B and V superscripts denote the bound state and the virtual state, respectively. Otherwise the pole refers to a resonance.

		$D\bar{D}^*, C = +$		$D\bar{D}^*, C = -$		DD^*	
		$I = 0$	$I = 1$	$I = 0$	$I = 1$	$I = 0$	$I = 1$
$\Lambda = 1.25$ GeV	$1^+(^3S_1)$	$-0.40^B, \chi_{c1}(3872)$	-	-25.0^V	$-39.6^V, Z_c(3900)$	$-0.79^B, T_{cc}(3875)$	-
	$0^-(^3P_0)$	$3.3 - 17.2i$	-	-	-	$-11.2 - 16.7i$	-
	$1^-(^3P_1)$	-	-	$4.4 - 39.9i, Y(3872)$	-	$-96.6 - 87.3i$	-
	$2^-(^3P_2)$	$-71.2 - 63.5i$	-	$-31.0 - 96.5i$	-	$-61.3 - 53.6i$	-
$\Lambda = 1.35$ GeV	$1^+(^3S_1)$	$-2.8^B, \chi_{c1}(3872)$	-	-2.2^V	$-38.5^V, Z_c(3900)$	$-8.8^B, T_{cc}(3875)$	-
	$0^-(^3P_0)$	$6.6 - 11.6i$	-	-	-	$-10.2 - 18.0i$	-
	$1^-(^3P_1)$	-	-	$10.2 - 33.7i, Y(3872)$	-	$-92.9 - 97.7i$	-
	$2^-(^3P_2)$	$-68.0 - 75.4i$	-	$-23.3 - 97.2i$	-	$-58.4 - 59.6i$	-

- [24] X. Liu, Z.-G. Luo, Y.-R. Liu, and S.-L. Zhu, X(3872) and Other Possible Heavy Molecular States, *Eur. Phys. J. C* **61**, 411 (2009), [arXiv:0808.0073 \[hep-ph\]](#).
- [25] Y.-R. Liu, X. Liu, W.-Z. Deng, and S.-L. Zhu, Is X(3872) Really a Molecular State?, *Eur. Phys. J. C* **56**, 63 (2008), [arXiv:0801.3540 \[hep-ph\]](#).
- [26] X. Liu, Y.-R. Liu, W.-Z. Deng, and S.-L. Zhu, Z+(4430) as a D(1)-prime D* (D(1) D*) molecular state, *Phys. Rev. D* **77**, 094015 (2008), [arXiv:0803.1295 \[hep-ph\]](#).
- [27] G.-J. Ding, J.-F. Liu, and M.-L. Yan, Dynamics of Hadronic Molecule in One-Boson Exchange Approach and Possible Heavy Flavor Molecules, *Phys. Rev. D* **79**, 054005 (2009), [arXiv:0901.0426 \[hep-ph\]](#).
- [28] Z.-F. Sun, J. He, X. Liu, Z.-G. Luo, and S.-L. Zhu, $Z_b(10610)^\pm$ and $Z_b(10650)^\pm$ as the $B^*\bar{B}$ and $B^*\bar{B}^*$ molecular states, *Phys. Rev. D* **84**, 054002 (2011), [arXiv:1106.2968 \[hep-ph\]](#).
- [29] C. E. Thomas and F. E. Close, Is X(3872) a molecule?, *Phys. Rev. D* **78**, 034007 (2008), [arXiv:0805.3653 \[hep-ph\]](#).
- [30] I. W. Lee, A. Faessler, T. Gutsche, and V. E. Lyubovitskij, X(3872) as a molecular DD^* state in a potential model, *Phys. Rev. D* **80**, 094005 (2009), [arXiv:0910.1009 \[hep-ph\]](#).
- [31] Z.-P. Wang, F.-L. Wang, G.-J. Wang, and X. Liu, Exploring Charmonium-like Molecular Resonances from Deeply Bound DD_1 , $D^*\bar{D}_1$, and $D^*\bar{D}_2^*$ Molecules, (2023), [arXiv:2312.03512 \[hep-ph\]](#).
- [32] T. Ji, X.-K. Dong, F.-K. Guo, and B.-S. Zou, Prediction of a Narrow Exotic Hadronic State with Quantum Numbers $J^{PC}=0^-$, *Phys. Rev. Lett.* **129**, 102002 (2022), [arXiv:2205.10994 \[hep-ph\]](#).
- [33] J. He, Y.-T. Ye, Z.-F. Sun, and X. Liu, The observed charmed hadron $\Lambda_c(2940)^+$ and the D^*N interaction, *Phys. Rev. D* **82**, 114029 (2010), [arXiv:1008.1500 \[hep-ph\]](#).
- [34] J.-B. Cheng, B.-L. Huang, Z.-Y. Lin, and S.-L. Zhu, Z_{cs} , Z_c and Z_b states under the complex scaling method, *Eur. Phys. J. C* **83**, 1071 (2023), [arXiv:2305.15787 \[hep-ph\]](#).
- [35] J. R. Taylor, *Scattering Theory: The Quantum Theory of Nonrelativistic Collisions* (John Wiley & Sons, Inc., New York, 1972).
- [36] E. Epelbaum, H.-W. Hammer, and U.-G. Meissner, Modern Theory of Nuclear Forces, *Rev. Mod. Phys.* **81**, 1773 (2009), [arXiv:0811.1338 \[nucl-th\]](#).
- [37] V. Baru, E. Epelbaum, A. A. Filin, F. K. Guo, H. W. Hammer, C. Hanhart, U. G. Meißner, and A. V. Nefediev, Remarks on study of X(3872) from effective field theory with pion-exchange interaction, *Phys. Rev. D* **91**, 034002 (2015), [arXiv:1501.02924 \[hep-ph\]](#).
- [38] M.-L. Du, V. Baru, X.-K. Dong, A. Filin, F.-K. Guo, C. Hanhart, A. Nefediev, J. Nieves, and Q. Wang, Coupled-channel approach to $T_{cc}+$ including three-body effects, *Phys. Rev. D* **105**, 014024 (2022), [arXiv:2110.13765 \[hep-ph\]](#).
- [39] B. Wang and L. Meng, Revisiting the DD^* chiral interactions with the local momentum-space regularization up to the third order and the nature of $T_{cc}+$, *Phys. Rev. D* **107**, 094002 (2023), [arXiv:2212.08447 \[hep-ph\]](#).
- [40] L. Meng, B. Wang, G.-J. Wang, and S.-L. Zhu, The hidden charm pentaquark states and $\Sigma_c\bar{D}^{(*)}$ interaction in chiral perturbation theory, *Phys. Rev. D* **100**, 014031 (2019), [arXiv:1905.04113 \[hep-ph\]](#).
- [41] Z.-Y. Lin, J.-B. Cheng, and S.-L. Zhu, T_{cc}^+ and X(3872) with the complex scaling method and $DD(\bar{D})\pi$ three-body effect, (2022), [arXiv:2205.14628 \[hep-ph\]](#).
- [42] L. Meng, V. Baru, E. Epelbaum, A. A. Filin, and A. M. Gasparyan, Solving the left-hand cut problem in lattice QCD: $T_{cc}(3875)^+$ from finite volume energy levels, (2023), [arXiv:2312.01930 \[hep-lat\]](#).
- [43] R. L. Workman *et al.* (Particle Data Group), Review of Particle Physics, *PTEP* **2022**, 083C01 (2022).
- [44] Z.-Y. Lin, J.-Z. Wang, J.-B. Cheng, L. Meng, and S.-L. Zhu, See Supplemental Material for additional details on sign problem of the potential in cross diagrams, the OBE potentials, the G-parity rule and the uncertainties from various regulators, (2024).
- [45] Y.-K. Chen, L. Meng, Z.-Y. Lin, and S.-L. Zhu, Vir-

- tual states in the coupled-channel problems with an improved complex scaling method, *Phys. Rev. D* **109**, 034006 (2024), arXiv:2308.12424 [hep-ph].
- [46] J.-B. Cheng, Z.-Y. Lin, and S.-L. Zhu, Double-charm tetraquark under the complex scaling method, *Phys. Rev. D* **106**, 016012 (2022), arXiv:2205.13354 [hep-ph].
- [47] R. Aaij *et al.* (LHCb), A model-independent study of resonant structure in $B^+ \rightarrow D^+ D^- K^+$ decays, *Phys. Rev. Lett.* **125**, 242001 (2020), arXiv:2009.00025 [hep-ex].
- [48] R. Aaij *et al.* (LHCb), Amplitude analysis of the $B^+ \rightarrow D^+ D^- K^+$ decay, *Phys. Rev. D* **102**, 112003 (2020), arXiv:2009.00026 [hep-ex].

Heavy neutral lepton search and $\mu \rightarrow e\gamma$ constraints in case of type-I seesaw

Stefano Morisi^{1,2}

¹*Dipartimento di Fisica “Ettore Pancini”, Università degli studi di Napoli “Federico II”,
Complesso Univ. Monte S. Angelo, I-80126 Napoli, Italy*

²*INFN - Sezione di Napoli, Complesso Univ. Monte S. Angelo, I-80126 Napoli, Italy*

Abstract

Within type-I seesaw mechanism it is possible to have large (order one) light-heavy neutrino mixing even in case of low right-handed neutrino mass scale (of the order of GeV). This implies large lepton flavor violation. As example we consider the process $\mu \rightarrow e\gamma$ that can have a branching up to 10^{-8} within type-I seesaw (in contrast with the tiny value 10^{-54} expected). Such an enhancing of lepton flavor violation can be used to constraint the parameter space of long lived particle experiments.

Observation of neutrino oscillation is an evidence that neutrino are massive and that flavor neutrino states do not coincide with the massive one. The unitary lepton mixing matrix U_ν connecting the two basis introduced by Pontecorvo-Maki-Nakagawa-Sakata (PMNS) has been observed experimentally to be very different from the identity. Indeed one of the three angles parametrizing U is close to be maximal $\sin^2 \theta_{23} \sim 0.5$ and one is large $\sin^2 \theta_{12} \sim 0.3$ while the third is small but not zero $\sin^2 \theta_{13} \sim 0.02$. Lepton mixing suggests that in the Standard Model can be present Lepton Flavor Violation (LFV) phenomena like $\mu \rightarrow e\gamma$. Early computation of this process mediated by the three active light neutrinos gives [1, 2] (see [3, 4] for a recent overview)

$$Br(\mu \rightarrow e\gamma) \approx \frac{3\alpha_e}{32\pi} \left| U_{\nu_{13}}^* U_{\nu_{23}} \frac{\Delta m_{31}^2}{M_W^2} \right|^2 \sim 10^{-54}, \quad (1)$$

that is very far from actual experimental sensitivity that is $7.5 \cdot 10^{-13}$ [5].

If the standard model is extended by means of n right-handed neutrino N_k (where $k = 1, \dots, n$) having Majorana mass given by $n \times n$ mass matrix M_N , the neutrino mass matrix is a $(3 + n) \times (3 + n)$ matrix

$$M_\nu = \begin{pmatrix} 0 & m_D \\ m_D^T & M_N \end{pmatrix}, \quad (2)$$

where $m_D = Y_D v$ is the $3 \times n$ Dirac mass matrix (v is the standard model vev) and Y_D is the corresponding Yukawa coupling and we assume $m_D \ll M_N$. Without loss of generality we can go in the basis where M_N is diagonal. The neutrino mass matrix M_ν is diagonalized by a $(3 + n) \times (3 + n)$ unitary matrix V given in block form by

$$V = \begin{pmatrix} U_\nu & U_{\nu N} \\ U_{\nu N}^\dagger U_\nu & \mathbb{I} \end{pmatrix} + \mathcal{O}(\theta^2), \quad (3)$$

where $U_{\nu N} = m_D \cdot M_N^{-1}$ is a $3 \times n$ matrix that mixes light and heavy neutrino. It follows that the 3×3 lepton mixing matrix U_ν is a sub-block of the unitary matrix V and therefore there is violation of unitarity in PMNS that is typically parametrized by $\theta^2 \equiv U_{\nu N} U_{\nu N}^\dagger$, see for instance [6]. Block diagonalizing M_ν one obtain the well know (type-I) seesaw relation for the three light active neutrinos

$$m_\nu = -m_D \frac{1}{M_N} m_D^T. \quad (4)$$

Using this expression naively, namely assuming only one active neutrino with mass m_ν and one right-handed neutrino with mass m_N , it follows that

$$\theta^2 \sim m_\nu / m_N, \quad (5)$$

that is suppressed even for light m_N , indeed $\theta^2 \sim [10^{-10} - 10^{-25}]$ for $m_N \sim [10^{-1} - 10^{14}]$ GeV. This estimation does not really change in the $3 + n$ realistic case.

In the case of type-I seesaw the branching ratio of the process $\mu \rightarrow e\gamma$ is given by

$$Br(\mu \rightarrow e\gamma) \approx \frac{3\alpha_e}{32\pi} \left| \sum_{k=4}^n (U_{\nu N}^*)_{1k} (U_{\nu N})_{2k} F(x_k) \right|^2, \quad (6)$$

where $x_k = m_{N_k}^2 / m_W^2$ and $F(x) = (10 - 43x + 78x^2 - 49x^3 + 18x^3 \log x + 4x^4) / (6(1 - x)^4)$ [7]. Because of eq. (1), the contribution from light active neutrino is negligible, so here we

consider only heavy right-handed neutrino in the sum of (6). Therefore in case of type-I seesaw naively it is expected that $Br(\mu \rightarrow e\gamma) \sim \theta^2$ is suppressed.

Even if this suppression is true in some limit, this is not the most general result, in fact θ^2 can be (theoretically) up to $10^{-1} - 10^{-2}$ (as long as $m_D \ll M_N$ is guaranteed). For large θ^2 the branching (6) is enhanced and can be up to 10^{-8} [8] (see also [9] for an effective approach). The aim of the present paper is to update the main idea of [8] in a different language that can be useful for experiments searching for long lived particles like heavy neutral leptons, see for instance ANUBIS [10, 11], MATHUSLA [12], SHADOWS [13], NA62 [14, 15], FASER [16], CODEX-b [17].

Heavy neutral leptons (here right-handed neutrino N s) can be produced from D , B meson decay, gauge boson W , Z , standard model Higgs H and top quark. Indeed in the minimal type-I scenario with n right handed neutrino, N_k enter in the charged and neutral current that leads to a coupling of N_k with Z and W bosons,

$$\mathcal{L} \supset -\frac{g}{\sqrt{2}} Z_\mu \bar{\nu}_{L\alpha k} \gamma^\mu N_k (U_{\nu N})_{\alpha k} - \frac{g}{\sqrt{2}} Z_\mu \bar{\ell}_{\alpha k} \gamma^\mu N_k (U_{\nu N})_{\alpha k}. \quad (7)$$

Such a couplings are at the origin of both N production and decay. Then heavy neutral leptons decay quite far from the production point depending on the $U_{\nu N} \sim \theta$ mixing. Being such a mixing quite small in case of heavy neutral leptons, the lifetime can be up to $\tau_N < 0.1s$ (this upper limit come from Big-Bang Nucleosynthesis constraints). As a consequence the decay length can be much bigger then $100m$ and so any detector can catch a small fraction of long-lived particle decay. For this reason all this experiment try to maximize the distance from the interaction point and the detector. Just to give an idea the distance is about $20m$ for ANUBIS and CODEX-b, $200m$ for MATHUSLA and $480m$ for FASER. In [18] has been shown that the dominant branching of heavy neutral lepton N is into hadrons, but decays into leptons are also possible.

The rate for production and decay of N are both proportional to $U_{\nu N}$. The mixing parameters that are typically considered in long lived experiments are

$$U_\alpha^2 = \sum_{i=1}^3 |(U_{\nu N})_{\alpha i}|^2, \quad U^2 = \sum_{\alpha} |U_\alpha|^2, \quad (8)$$

where $\alpha = e, \mu, \tau$. The sensitivity of heavy neutral lepton experiments is typically reported in the $(U_\alpha^2 - m_N)$ or $(U^2 - m_N)$ plane.

To understand the origin of the enhancing of θ^2 we need to go deeply into the detail of type-I seesaw mechanism. The Dirac Yukawa coupling Y_D can be parametrized in terms of the physical observable, namely the masses of the light active neutrino and the

parameters of the PMNS mixing matrix and the right handed masses by means of the Casas-Ibarra parametrization [8]

$$Y_D = v^{-1} U_{PMNS} \sqrt{m_\nu^{diag}} R \sqrt{M_N^{diag}}, \quad (9)$$

where R is an arbitrary complex $3 \times n$ orthogonal matrix. From relation (4) it is possible to fit the two square mass differences if $n \geq 2$. The minimal case with $n = 2$ predicts one massless light active neutrino. In the following for simplicity we will consider the case $n = 2$ and degenerate heavy right-handed neutrino

$$m_N \equiv (M_N)_{11} = (M_N)_{22}.$$

When $n = 2$, the matrix R is given by (for normal neutrino mass ordering considered here)

$$R = \begin{pmatrix} 0 & 0 \\ \cos \beta & \sin \beta \\ -\sin \beta & \cos \beta \end{pmatrix}, \quad (10)$$

where $\beta = x + iy$ is an arbitrary complex number. The value of θ^2 strongly depends on the parameter y while only mildly on the parameter x that for simplicity we assume to be $x = 0$. The parameter y can be in principle very large as soon as the seesaw regime is preserved, namely $m_D \ll M_N$. In the present analysis we take $0 < y < 30$. The fact that θ^2 is not suppressed by the neutrino mass m_ν as in eq. (5) is possible only for large values of y . If y is large enough the magnitude of the neutrino Yukawa couplings could be of order one even for $m_N \sim \text{GeV}$. This seems to be in contradiction with common sense (5) but is a possibility. Using large value of y is therefore possible to obtain an enhancing of $Br(\mu \rightarrow e\gamma)$. Barring large y is possible in case of low-scale seesaw mechanism, for a review see [19]. A study of large lepton flavor violation coming from unitarity violation in case of low-scale seesaw is given for instance in [20].

Here we assume for simplicity as benchmark case the following choice of the parameters appearing in (9): $\sin^2 \theta_{23} \sim 0.5$, $\sin^2 \theta_{12} \sim 0.3$, $\sin^2 \theta_{13} \sim 0.02$, $m_{\nu 1} = 0$, $m_{\nu 2} = \sqrt{\Delta m_{12}^2}$, $m_{\nu 3} = \sqrt{\Delta m_{13}^2}$ where $\Delta m_{12}^2 \simeq 7 \cdot 10^{-5} eV$, $\Delta m_{13}^2 \simeq 2 \cdot 10^{-3} eV$. Moreover the Dirac and Majorana phases as well as the parameter x are taken to be zero. With all these assumptions it follows that $Br(\mu \rightarrow e\gamma) \sim \theta^2$ depends only by the two free parameters y and m_N . For each set of y and m_N value chosen, the neutrino mass matrix M_ν is fixed and we obtain numerically the $\mu \rightarrow e\gamma$ branching from (6), m_D from (9) and the mixing matrix $U_{\nu N}$ and therefore also the corresponding parameter U_α^2 and U^2 from (8).

We graph U_e^2 as function of m_N marginalizing with respect to $Br(\mu \rightarrow e\gamma) < 7.5 \cdot 10^{-13}$ (similar graphs can be obtained for U_μ^2 , U_τ^2 , U^2). The result is shown in figure (1) where

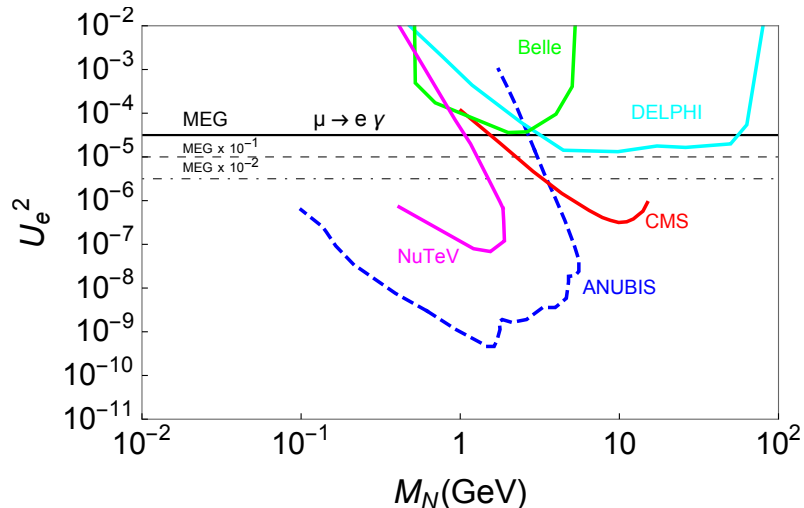


Figure 1: Light-heavy neutrino mixing parameter U_e^2 as a function of the right-handed neutrino mass m_N , the horizontal line represents MEG constraint, for details see the text.

we report with continues lines existing experimental limits (see for instance [15]). In figure we report with the dashed line in the graph the expected sensitivity of ANUBIS [21] taken as representative of long lived particle experiments. The horizontal continuous line is the limit coming from MEG. In order to better understand the role of $Br(\mu \rightarrow e\gamma)$ in the (U_e^2, m_N) plane, we show with dashed horizontal lines the constraints coming assuming a sensitivity of MEG improved by a factor 10 and 100.

The main result of this analysis is that constraints coming from $\mu \rightarrow e\gamma$ lepton flavor violation process is in agreement with the actual constraints coming from other experiments. In particular such a limit are of the same order for masses $1 \text{ GeV} \lesssim m_N \lesssim 80 \text{ GeV}$. However above 80 GeV MEG provide new limits. In principle MEG limits can be extended up to grand unified scale, but above 100 GeV the future heavy neutral leptons experiments are not sensitive. If MEG sensitivity will be improved by a factor 100, then $\mu \rightarrow e\gamma$ constraints could dominate for $m_N \gtrsim 10 \text{ GeV}$.

In summary in this analysis we provide a prove of the potentiality of lepton flavor violation in discriminating standard type-I seesaw with the interplay of long lived particle experiments.

References

- [1] S. T. Petcov, Sov. J. Nucl. Phys. **25** (1977), 340 [erratum: Sov. J. Nucl. Phys. **25** (1977), 698; erratum: Yad. Fiz. **25** (1977), 1336] JINR-E2-10176.
- [2] S. M. Bilenky, S. T. Petcov and B. Pontecorvo, Phys. Lett. B **67** (1977), 309 doi:10.1016/0370-2693(77)90379-3
- [3] M. Lindner, M. Platscher and F. S. Queiroz, Phys. Rept. **731** (2018), 1-82 doi:10.1016/j.physrep.2017.12.001 [arXiv:1610.06587 [hep-ph]].
- [4] M. Ardu and G. Pezzullo, Universe **8** (2022) no.6, 299 doi:10.3390/universe8060299 [arXiv:2204.08220 [hep-ph]].
- [5] K. Afanaciev *et al.* [MEG II], [arXiv:2310.12614 [hep-ex]].
- [6] S. Antusch, E. Cazzato, M. Drewes, O. Fischer, B. Garbrecht, D. Gueter and J. Klaric, JHEP **09** (2018), 124 doi:10.1007/JHEP09(2018)124 [arXiv:1710.03744 [hep-ph]].
- [7] B. He, T. P. Cheng and L. F. Li, Phys. Lett. B **553** (2003), 277-283 doi:10.1016/S0370-2693(02)03258-6 [arXiv:hep-ph/0209175 [hep-ph]].
- [8] J. A. Casas and A. Ibarra, Nucl. Phys. B **618** (2001), 171-204 doi:10.1016/S0550-3213(01)00475-8 [arXiv:hep-ph/0103065 [hep-ph]].
- [9] S. Antusch, C. Biggio, E. Fernandez-Martinez, M. B. Gavela and J. Lopez-Pavon, JHEP **10** (2006), 084 doi:10.1088/1126-6708/2006/10/084 [arXiv:hep-ph/0607020 [hep-ph]].
- [10] M. Bauer, O. Brandt, L. Lee and C. Ohm, [arXiv:1909.13022 [physics.ins-det]].
- [11] A. Shah *et al.* [ANUBIS], PoS **EPS-HEP2023** (2024), 051 doi:10.22323/1.449.0051 [arXiv:2401.11604 [hep-ex]].
- [12] D. Curtin, M. Drewes, M. McCullough, P. Meade, R. N. Mohapatra, J. Shelton, B. Shuve, E. Accomando, C. Alpigiani and S. Antusch, *et al.* Rept. Prog. Phys. **82** (2019) no.11, 116201 doi:10.1088/1361-6633/ab28d6 [arXiv:1806.07396 [hep-ph]].
- [13] W. Baldini, A. Balla, J. Bernhard, A. Calcaterra, V. Cafaro, A. Ceccucci, V. Cicero, P. Ciambriano, H. Danielsson and G. D'Alessandro, *et al.* [arXiv:2110.08025 [hep-ex]].
- [14] E. Cortina Gil *et al.* [NA62], JINST **12** (2017) no.05, P05025 doi:10.1088/1748-0221/12/05/P05025 [arXiv:1703.08501 [physics.ins-det]].

- [15] M. Drewes, J. Hajer, J. Klaric and G. Lanfranchi, *JHEP* **07** (2018), 105
doi:10.1007/JHEP07(2018)105 [arXiv:1801.04207 [hep-ph]].
- [16] A. Ariga *et al.* [FASER], *Phys. Rev. D* **99** (2019) no.9, 095011
doi:10.1103/PhysRevD.99.095011 [arXiv:1811.12522 [hep-ph]].
- [17] V. V. Gligorov, S. Knapen, M. Papucci and D. J. Robinson, *Phys. Rev. D* **97** (2018)
no.1, 015023 doi:10.1103/PhysRevD.97.015023 [arXiv:1708.09395 [hep-ph]].
- [18] F. Kling and S. Trojanowski, *Phys. Rev. D* **97** (2018) no.9, 095016
doi:10.1103/PhysRevD.97.095016 [arXiv:1801.08947 [hep-ph]].
- [19] S. M. Boucenna, S. Morisi and J. W. F. Valle, *Adv. High Energy Phys.* **2014** (2014),
831598 doi:10.1155/2014/831598 [arXiv:1404.3751 [hep-ph]].
- [20] D. V. Forero, S. Morisi, M. Tortola and J. W. F. Valle, *JHEP* **09** (2011), 142
doi:10.1007/JHEP09(2011)142 [arXiv:1107.6009 [hep-ph]].
- [21] M. Hirsch and Z. S. Wang, *Phys. Rev. D* **101** (2020) no.5, 055034
doi:10.1103/PhysRevD.101.055034 [arXiv:2001.04750 [hep-ph]].

Improving the performance of weak supervision searches using transfer and meta-learning

Hugues Beauchesne,^a Zong-En Chen^b and Cheng-Wei Chiang^{b,a}

^a*Physics Division, National Center for Theoretical Sciences,
Taipei 10617, Taiwan*

^b*Department of Physics and Center for Theoretical Physics, National Taiwan University,
Taipei 10617, Taiwan*

E-mail: beauchesneh@phys.ncts.ntu.edu.tw, r10222045@ntu.edu.tw,
chengwei@phys.ntu.edu.tw

ABSTRACT: Weak supervision searches have in principle the advantages of both being able to train on experimental data and being able to learn distinctive signal properties. However, the practical applicability of such searches is limited by the fact that successfully training a neural network via weak supervision can require a large amount of signal. In this work, we seek to create neural networks that can learn from less experimental signal by using transfer and meta-learning. The general idea is to first train a neural network on simulations, thereby learning concepts that can be reused or becoming a more efficient learner. The neural network would then be trained on experimental data and should require less signal because of its previous training. We find that transfer and meta-learning can substantially improve the performance of weak supervision searches.

Contents

1	Introduction	1
2	Events generation	3
3	CWoLa	6
4	Transfer learning	8
5	Meta-learning	10
6	Conclusion	13
A	Impact of systematic uncertainties	15

1 Introduction

The recent advances in deep learning have created many opportunities for collider physics. A potential albeit obvious application of deep learning is to help discriminate a signal from background and thus possibly discover new particles. To be able to do so, a neural network (NN) needs to be trained. How this training is performed and which kind of training data to use are non-trivial questions and many strategies have been proposed.

Fully supervised learning, where all training data are labelled, is one such potential strategy and was considered in, e.g., Refs. [1–4]. However, since the goal would be to find a signal that has not been observed yet, training must be performed based upon simulations. There are two potential risks that arise from this. First, simulations unavoidably contain artefacts. This can result in the neural network learning from these artefacts and behaving in a suboptimal and difficult-to-predict way on real data [5]. Second, how the neural network would react to a signal that differs from the expected one is unclear. This can potentially result in a search that is only sensitive to a very narrow range of models and thus possibly missing a discoverable signal.

Unsupervised learning, where the training data are not labelled, is another potential training strategy. Up to now, the most common approach has been to train an autoencoder on what is presumably mostly background events and use the reconstruction error as a test statistic [6]. There are again two potential drawbacks to this. First, the reconstruction error has been shown to sometimes be a very poor discriminating factor [7]. Second, being trained on background only, autoencoders cannot learn any special properties the signal may possess and thus lose some of their potential discriminative power. Alternative unsupervised learning approaches exist [8–13], but by their nature will be subject to at least the second drawback.

Weakly supervised learning, where the training data only contain imperfect labels, is a training strategy that potentially circumvents the problems of both fully supervised and unsupervised learning. In the Classification Without Label (CWoLa) method [5], two samples of experimental data with presumably different fractions of signal and background are considered. Assuming the properties of the signal and background to be the same between the two samples, it is a theorem that the most powerful test statistic to distinguish the two samples is also the most powerful test statistic to distinguish the signal from the background. As such, a neural network that has been optimally trained to tell the two samples apart would also be optimally trained to tell the signal apart from the background. This neural network could then be used to suppress the background. It would also be a neural network trained specifically for the signal present in the data. As such, it would not suffer from the problem of the training and actual signal being different, unlike full supervision. This approach would combine the advantages of both unsupervised learning, i.e., being trained on data, and supervised learning, i.e., learning to exploit the special properties of the signal. An experimental search using CWoLa was performed in Ref. [14].

However, there are some practical limitations associated with weak supervision that come from the fact that the amount of signal is limited [15]. In practice, there is a threshold in the amount of signal below which the neural network fails to learn properly. If not careful, this threshold can be close or above what would be sufficient for discovery even without the network. This greatly reduces the usefulness of such neural networks. This can happen for example when the input of the neural network is too large [16] and has been circumvented in Ref. [17] by providing a very simple but limiting input to the network. Recent attempts at overcoming this problem include Refs. [18, 19].

What seems to be fundamentally the problem and which we will illustrate abundantly throughout this work is that a neural network can require a very large amount of training data to properly learn a task. In the context of a search, the small amount of signal limits the ability of the neural network to learn and decreases the effectiveness of the CWoLa method. What is ultimately the goal is then to create a neural network that requires less data to learn a task. This way, the learning threshold would be lowered and the overall performance of the CWoLa method would improve.

The strategy that we propose in this work is to use simulations to create neural networks that can learn faster from the actual data. In broad terms, the amount of signal is limited, but it is generally easy to produce simulations of it. A neural network would then first be trained on simulations to either learn certain concepts or become a more efficient learner. After this, the neural network would be trained on the data itself. It should then require less signal to learn because of what it has already learned from the simulations. In more precise terms, we will consider the use of transfer and meta-learning.

The general idea of transfer learning is for a neural network to acquire knowledge from a previous task and apply it to learning a new task [20, 21]. While training on the new task, the neural network will be able to reuse previous knowledge without having to reacquire it and should therefore learn faster. In the context of a search, the neural network might learn from simulations concepts like multiplicity or thrust and then reuse these concepts once it starts learning from the actual data. Before being exposed to the data, the neural

network would not know the expected distributions of multiplicity or thrust, but it would at least know what they are and that they are potentially useful observables. In practice, we will use pretraining, which will be more carefully explained in Sec. 4.

The general idea of meta-learning is not so much to learn a given task, but more to create a better learner. This is why it is sometimes referred to as learning-to-learn (see Ref. [22] for a useful review). The general approach is to first submit the neural network to a phase of meta-training. During this process, the neural network learns multiple tasks and some adjustments are performed to make the neural network learn new tasks increasingly faster. Hopefully, the neural network should learn faster once trained on the actual data. The different meta-learning techniques fall into three categories: Optimization-based, model-based and metric-based. In practice, the technique we will explore is meta-transfer learning (MTL) [23], which will be more carefully explained in Sec. 5.¹

As a benchmark, we will use so-called dark showers. These are jets that originate from new confining dark sectors (see Ref. [25] for a review). They are common in various solutions to the hierarchy problem (see, e.g., Refs. [26, 27]), can provide many potential dark matter candidates (see, e.g., Refs. [28–30]), and have been the subject of several experimental searches [31–34]. They are also a prime target for weak supervision, as they could take many forms and our ability to simulate them accurately is still not firmly established [35]. Most importantly, the `Pythia` [36] Hidden Valley (HV) module [37, 38] offers great flexibility in the choice of parameters, which will enable learning from a wide scope of signals.

We find the following results. Transfer learning can substantially improve the performance of CWoLa searches. The improvement is most drastic at low significance and the amount of signal necessary for discovery can sometimes be several times smaller. Meta-transfer learning can further enhance the performance of CWoLa searches, but the improvement is less than between regular CWoLa and transfer learning.

The paper is organized as follows. The event generation is presented in Sec. 2. Sec. 3 reviews the CWoLa method. Transfer learning is discussed in Sec. 4 and meta-learning in Sec. 5. Some concluding remarks are presented in Sec. 6. The potential impact of systematic uncertainties is discussed in Appendix A.

2 Events generation

The `Pythia` Hidden Valley module is used to simulate dark showers. The presence of many adjustable parameters allows for the generation of a wide range of signals, which makes this module especially convenient for transfer and meta-learning. More precisely, the signal considered is $pp \rightarrow Z' \rightarrow \bar{q}_D q_D$. The dark quarks q_D are a set of new fermions charged under a new confining gauge group but neutral under the Standard Model (SM) gauge groups and assumed to be degenerate in mass. The particle Z' is a massive Abelian gauge boson that interacts with both quarks and dark quarks. The resulting signature is a pair of dark jets with an invariant mass consistent with Z' .

¹See Ref. [24] for another application of meta-learning to collider physics.

Once produced, the dark quarks are showered and hadronized by `Pythia` 8.307. The resulting dark hadrons are either vector mesons ρ_D or pseudo-scalar mesons π_D . The ratio of their masses is set following the recommendations of Ref. [25]:

$$\frac{m_{\pi_D}}{\Lambda_D} = 5.5 \sqrt{\frac{m_{q_D}}{\Lambda_D}}, \quad \frac{m_{\rho_D}}{\Lambda_D} = \sqrt{5.76 + 1.5 \frac{m_{\pi_D}^2}{\Lambda_D^2}}, \quad m_{q_{\text{const}}} = m_{q_D} + \Lambda_D, \quad (2.1)$$

where m_{q_D} and $m_{q_{\text{const}}}$ are the current and constituent mass of the dark quarks respectively and Λ_D is the dark confining scale. Note that the dark quark mass in the HV settings of `Pythia` is the constituent mass. The decay of $\rho_D \rightarrow \pi_D \pi_D$ is allowed if $m_{\pi_D}/\Lambda_D < 1.52$.

Two scenarios are considered for the decay of ρ_D . In the first scenario, $m_{\rho_D} > 2m_{\pi_D}$ and the decay $\rho_D \rightarrow \pi_D \pi_D$ is allowed. Since this decay is expected to dominate, the corresponding branching ratio is set to 1. We choose seven benchmarks for this scenario, each corresponding to a different Λ_D but a constant mass ratio $m_{\pi_D}/\Lambda_D = 1$. The choices of Λ_D are 1, 5, 10, 20, 30, 40, and 50 GeV, and the corresponding m_{π_D} , m_{ρ_D} , m_{q_D} and $m_{q_{\text{const}}}$ are set by Eq. (2.1) or the ratio m_{π_D}/Λ_D . We simply impose the dark pions to decay to the SM $d\bar{d}$. This scenario is referred to as Indirect Decay (ID).

In the second scenario, $m_{\rho_D} < 2m_{\pi_D}$ and the $\rho_D \rightarrow \pi_D \pi_D$ decay is forbidden. We also choose seven benchmarks for this scenario, each corresponding to a different Λ_D but a constant ratio $m_{\pi_D}/\Lambda_D = 1.8$. The choices of Λ_D are the same as in the ID scenario, and the corresponding m_{π_D} , m_{ρ_D} , m_{q_D} and $m_{q_{\text{const}}}$ are set by Eq. (2.1) or the ratio m_{π_D}/Λ_D . We also simply impose both dark pions and dark vector mesons to decay to the SM $d\bar{d}$. This scenario is referred to as Direct Decay (DD).

The other relevant signal parameters are as follows. The mass of Z' is set to 5.5 TeV, which leads to an invariant mass of the leading two jets of around 5.2 TeV. The slight difference is due to some constituents falling outside the reconstructed jets. Fig. 1 shows the distribution of the invariant mass of the two leading jets M_{jj} . The width of Z' is taken as 10 GeV, which does not lead to any sizeable peak widening that could adversely affect the search. The values of the other HV parameters are shown in Table 1a.

The dominant background is expected to be pair production of QCD jets. Background events are generated at parton level using `Madgraph` 2.7.3 [39] and hadronized using `Pythia` 8.307. To speed up event generations, the preliminary cuts of Table 1b are imposed in `Madgraph`. It has been verified that these cuts are sufficiently weaker than the final cuts not to have any significant impact on the distributions. The parton distribution function used for both event generations is NN23LO1 [40]. For the background, the default `Pythia` settings are used. For both signal and background, detector simulation is handled with `Delphes` 3.4.2 [41]. The default CMS card is used, except for the jet radius which is set to $R = 0.8$. After detector simulations, we impose the selection criteria described in Table 1b. A Signal Region (SR) and Sidebands (SB) are defined and will come into play in the CWoLa procedure.

Finally, the two leading jets in P_T are converted into jet images according to the following procedure [42–44]. First, the jet constituents are translated so that the center of the image is along the jet axis. Second, the image is rotated such that the principal axis of the P_T -weighted constituents is along the horizontal direction. Third, the image is

HV parameters in Pythia	
HiddenValley: alphaOrder	1
HiddenValley: nFlav	3
HiddenValley: Ngauge	3
HiddenValley: pTminFSR	$1.1\Lambda_D$
HiddenValley: separateFlav	on
HiddenValley: aLund	0.1
HiddenValley: bmqv2	1.9
HiddenValley: rFactqv	1.0
HiddenValley: probVector	0.75
HiddenValley: fragment	on
HiddenValley: FSR	on

(a)

Preliminary cuts in Madgraph
$\sqrt{s} = 13$ TeV
Both P_T of the leading two jets > 700 GeV
Both η of leading two jets $ \eta_j < 2.2$
$M_{jj} > 3000$ GeV
Selection criteria after Delphes
Number of jets $n_j \geq 2$
Both P_T of the leading two jets > 750 GeV
Both η of leading two jets $ \eta_j < 2$
SR = $\{M_{jj} \in [4700, 5500]\}$
SB = $\{M_{jj} \in [4400, 4700] \cup [5500, 5800]\}$

(b)

Table 1: (a) Parameters for dark showering in Pythia. (b) Parameters in Madgraph and the selection criteria after Delphes.

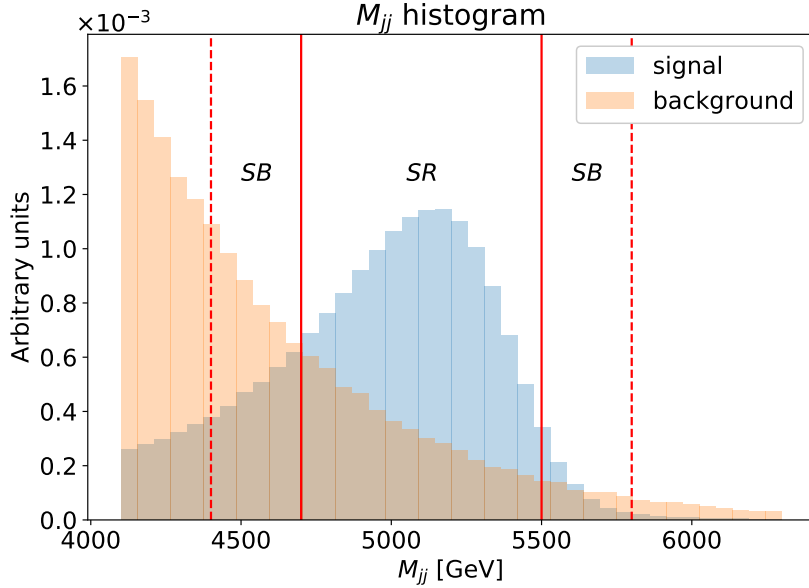


Figure 1: Dijet invariant mass distributions for the indirect decaying scenario with $\Lambda_D = 10$ GeV and for the SM background. Distributions are normalized to unity. Both signal and background satisfy the selection criteria of Table 1b except for the SR or SB conditions.

flipped such that the highest P_T constituent is in the upper right plane. After the above preprocessing, the image is pixelated using resolutions of either 25×25 , 50×50 or 75×75 . The ranges of η and ϕ are both from -1 to 1 . Fig. 2 shows the jets before and after preprocessing, as well as the average histogram plots. Jet images are chosen as the input

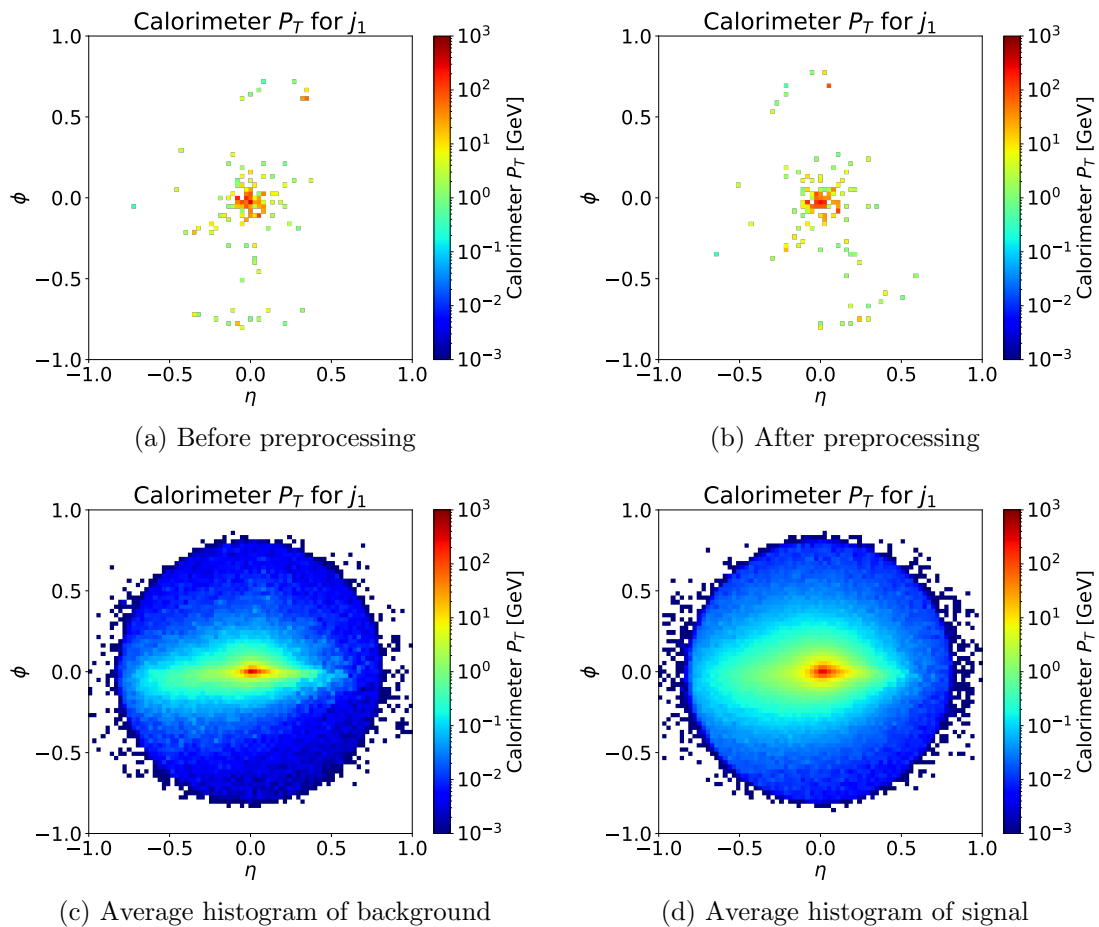


Figure 2: (a) A 2D P_T histogram for one signal event in the SR before rotation and flipping. (b) A 2D P_T histogram of the same event after complete preprocessing. (c) The average histogram for 10k background events in the SR after preprocessing. (d) The average histogram for 10k signal events in the SR after preprocessing. These plots are for the leading jet with 75×75 resolution and the ID scenario with $\Lambda_D = 10$ GeV.

of the neural networks as learning from them can be challenging. This will display more clearly the improvements provided by transfer and meta-learning. The ability to adjust the resolution will also prove useful to illustrate certain features.

3 CWoLa

As explained in the Introduction, the CWoLa method requires the existence of two mixed samples of signal and background in different proportions. A neural network is then trained to distinguish the two samples, which should hopefully result in the network learning the difference between the signal and background. In our case, a neural network is trained to distinguish the signal and sideband regions of Fig. 1. In this section, we explain the details of our implementation of this procedure, which is partially inspired by Ref. [17].

Layers of CNN subnetwork	$\left(\begin{array}{l} \text{convolutional 2D layer: 64 filters with } 5 \times 5 \text{ kernel size} \\ \text{maxpooling layer: } 2 \times 2 \text{ pool size} \end{array} \right) \times 2$ convolutional 2D layer: 128 filters with 3×3 kernel size maxpooling layer: 2×2 pool size convolutional 2D layer: 128 filters with 3×3 kernel size flatten layer (dense layer: 128 units) $\times 3$ dense layer (output): 1 unit
Layer setting	convolutional layer padding: same hidden layer activation function: ReLU output layer activation function: Sigmoid
Other	loss function: binary cross-entropy optimizer: Adam metric: accuracy batch size: 500 learning rate: 1e-3 (base learning, pretraining) learning rate: 1e-4 (CWoLa, fine-tuning, meta-learner updating) patience number: 20 (pretraining, meta-learning) patience number: 30 (CWoLa, fine-tuning)

Table 2: The CNN model subarchitecture and the hyperparameters

The background in the SR consists of 25k events passing the SR selection cuts of Table 1b. A fifth of these are used for validation, leaving an integrated luminosity roughly corresponding to the expected number of events from Run 2 of the LHC. Considering the conceptual nature of this work, we did not implement k -fold cross-validation, but nothing would prevent its implementation in an actual search. The number of background events in the SBs is determined by using the same integrated luminosity as the SR. The amount of signal in the SR is varied throughout the analysis and the amount of signal in the SBs is set again by using the same integrated luminosity as the SR. The callbacks function is used to save the best model during training by monitoring the validation loss. To test the performance of the CWoLa method, we use 20k additional signal passing the SR requirements and 20k similar background.

We use as training data the jet images of the two leading jets. The distributions of each of them are independently batched normalized. Each jet image is then passed through a common Convolutional Neural Network (CNN) subnetwork and each returns a single number. The output of the full neural network is then the product of these two numbers. The subarchitecture and training procedure are described in Table 2. All NNs are implemented using Keras [45] with TensorFlow [46] backend. We did investigate the possibility of using two distinct networks, but found this alternative to give typically inferior results. This seems to be caused by the lack of signal. The convolutional part of the neural network is referred to as the feature extractor and its weights and biases are collectively

labelled as Θ . The weights and biases of the dense layers are collectively labelled as θ .

In order to evaluate the performance of the NN, we use the significance formula [47]

$$\sigma = \sqrt{2 \left((N_s + N_b) \log \left(\frac{N_s}{N_b} + 1 \right) - N_s \right)}, \quad (3.1)$$

where N_s and N_b are respectively the numbers of signal and background after the NN classification. We choose certain background efficiencies ϵ_b and calculate the corresponding signal efficiencies ϵ_s from the receiver operating characteristic (ROC) curve with testing data after training. It has also been verified that no significant excesses are produced via sculpting [17]. The training is performed 10 times for each significance value, including sampling new events in each pseudo-experiment, and averaged. The standard deviations are computed and correspond to fluctuations from both the training and the sampling.

Fig. 3 shows two benchmarks with three different resolutions each. Several comments are in order. First, the different curves display a threshold below which the neural network fails to learn from the data. This is the threshold alluded to in the Introduction and corresponds to the upward turn of the curves around 2 to 4σ . Below this threshold, the NN cuts background and signal indiscriminately and the significance is even worse than without employing the NN. Second, increasing the resolution tends to move the position of the threshold to higher significance. This is due to the fact that classifying a higher-resolution image is a more difficult task and more parameters must be learned inside the NN.

4 Transfer learning

As illustrated in the last section, the existence of a learning threshold renders the use of CWoLa problematic for small amounts of signal. A potential solution to this problem is transfer learning, which we introduce in this section.

The general idea of transfer learning is to have an NN first learn from a related problem with a large amount of data and then transfer some of this knowledge to the problem of interest. In practice, the technique that we use for transfer learning is pretraining, in which information is transferred via pretraining NN parameters on the larger dataset. From a terminology point of view, training an NN on a larger dataset is known as pretraining, while fine-tuning refers to the subsequent training on a smaller dataset. Furthermore, these larger and smaller datasets are respectively referred to as the source and target data.

We implement the pretraining strategy as follows. First, the NN is pretrained to distinguish a sample of pure background from a pure combination of different signals. This combination includes all the models mentioned in Sec. 2, except the benchmark on which the model will be tested on. In a real experiment, this would represent training on simulations. A total of 250k signal and 250k background from the SR are used as the source data. A fifth of the sample is used for validation, which is also performed on pure samples. Second, the neural network is trained to distinguish the mixed samples, i.e., the SR and SB regions with the benchmark signal mixed within the background. In a real experiment, this would represent fine-tuning on the actual data as target data. The NN

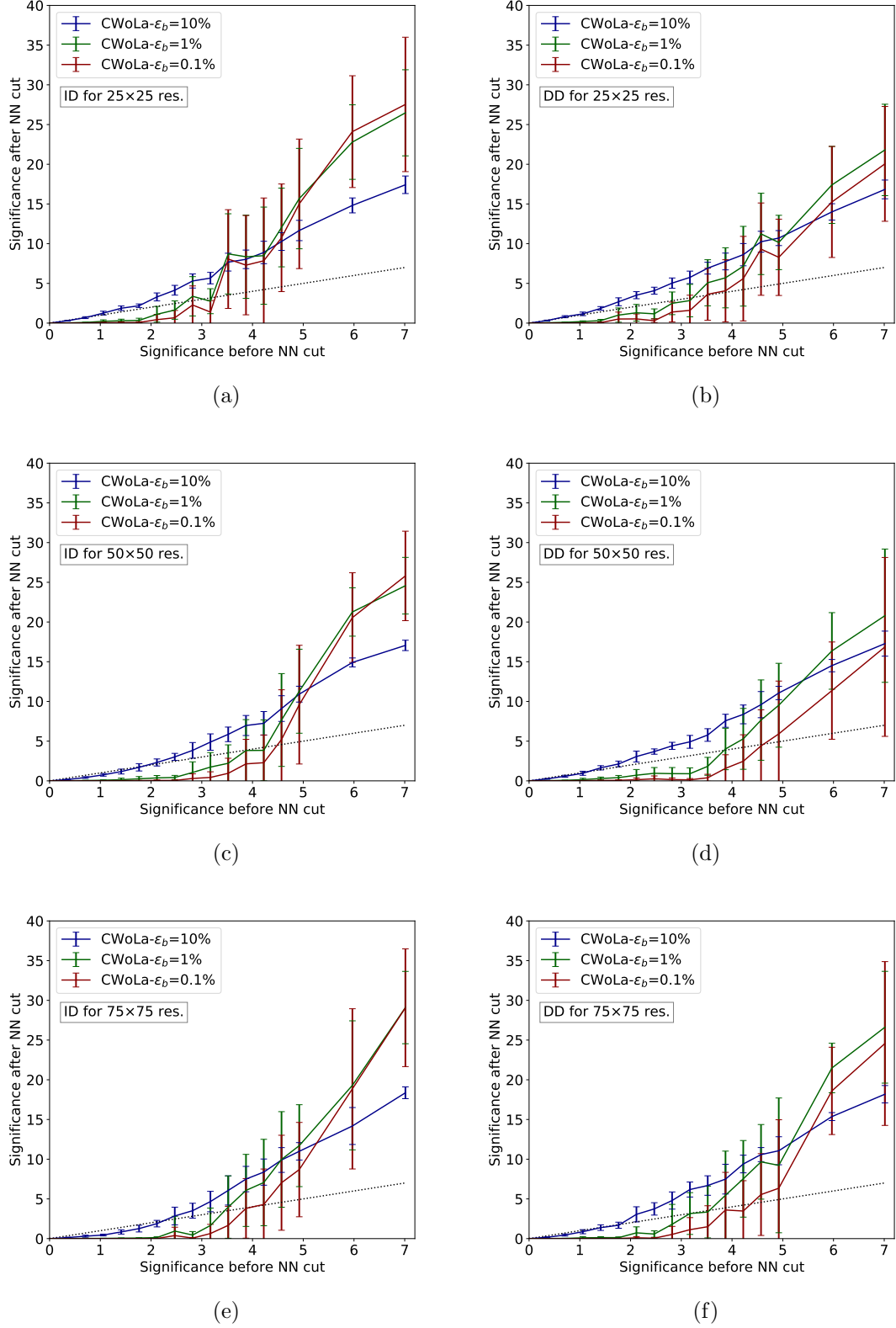


Figure 3: The results of CNN CWoLa for the ID (left column) and DD (right column) scenarios with $\Lambda_D = 10$ GeV for 25×25 , 50×50 and 75×75 resolutions. The dotted line in each plot has a slope of 1.

model parameters of the feature extractor Θ are initialized at their values learned during pretraining and the NN parameters of the dense layers θ are reinitialized randomly. During the fine-tuning step, Θ are frozen and only θ are trained.

Fig. 4 shows the comparison between pure CWoLa and transfer learning. First, transfer learning not only improves the general NN performance but also considerably reduces the learning threshold for all three different resolutions. In practice, the amount of signal necessary to claim a 5σ discovery can be reduced by a factor of a few, which is due to the fact that the NN can better identify and reduce the background. Second, the relative fluctuations in the significance are reduced. This is due to a smaller amount of trainable parameters and more successful learning. Overall, the use of transfer learning displays a massive improvement over the standard CWoLa.

5 Meta-learning

Meta-learning is an alternative approach for creating neural networks that can learn from less data. The general idea is not so much to reuse concepts from related tasks, but more to teach the neural network how to learn tasks more efficiently. More specifically, we will study the use of meta-transfer learning (MTL) [23]. Although many other techniques exist, we choose MTL because it is closely related to transfer learning, which has already been shown in the previous section to be very successful. We will present in this section our implementation of MTL, which we simplify and modify somewhat, and refer to Ref. [23] for more details.

MTL uses so-called scaling and shifting parameters. Consider a rectangular image A of arbitrary dimensions and M channels. Assume a set of N convolutional filters have previously been created. Label the filters and their indices as

$$F_{ij}^{cf}, \quad (5.1)$$

where the index f refers to the label of the filter and runs from 1 to N , the i and j indices correspond to the positional arguments of the filter (η and ϕ in our case), and the index c corresponds to the channel and runs from 1 to M . Scaling is then applied as

$$\bar{F}_{ij}^{cf} = S^{cf} F_{ij}^{cf}, \quad (5.2)$$

where S^{cf} are the scaling parameters and \bar{F}^f are the scaled filters. The scaled filter \bar{F}^f is then applied to image A at point (i, j) as

$$B_{i'j'}^f = g\left(\left(\bar{F}^f \star A\right)_{ij} + b^f + \bar{S}^f\right), \quad (5.3)$$

where B is the resulting image, g is the activation function, \star is the cross-correlation operation, b^f are the previously determined bias and \bar{S}^f are the shifting parameters. The indices i' and j' are related to the positions i and j , though the exact relation depends on other parameters (stride, padding, etc). The scaling and shifting parameters are what will be optimized to make the neural network learn faster and are meant to emphasize more on important features. They are how the neural network ‘learns-to-learn’.

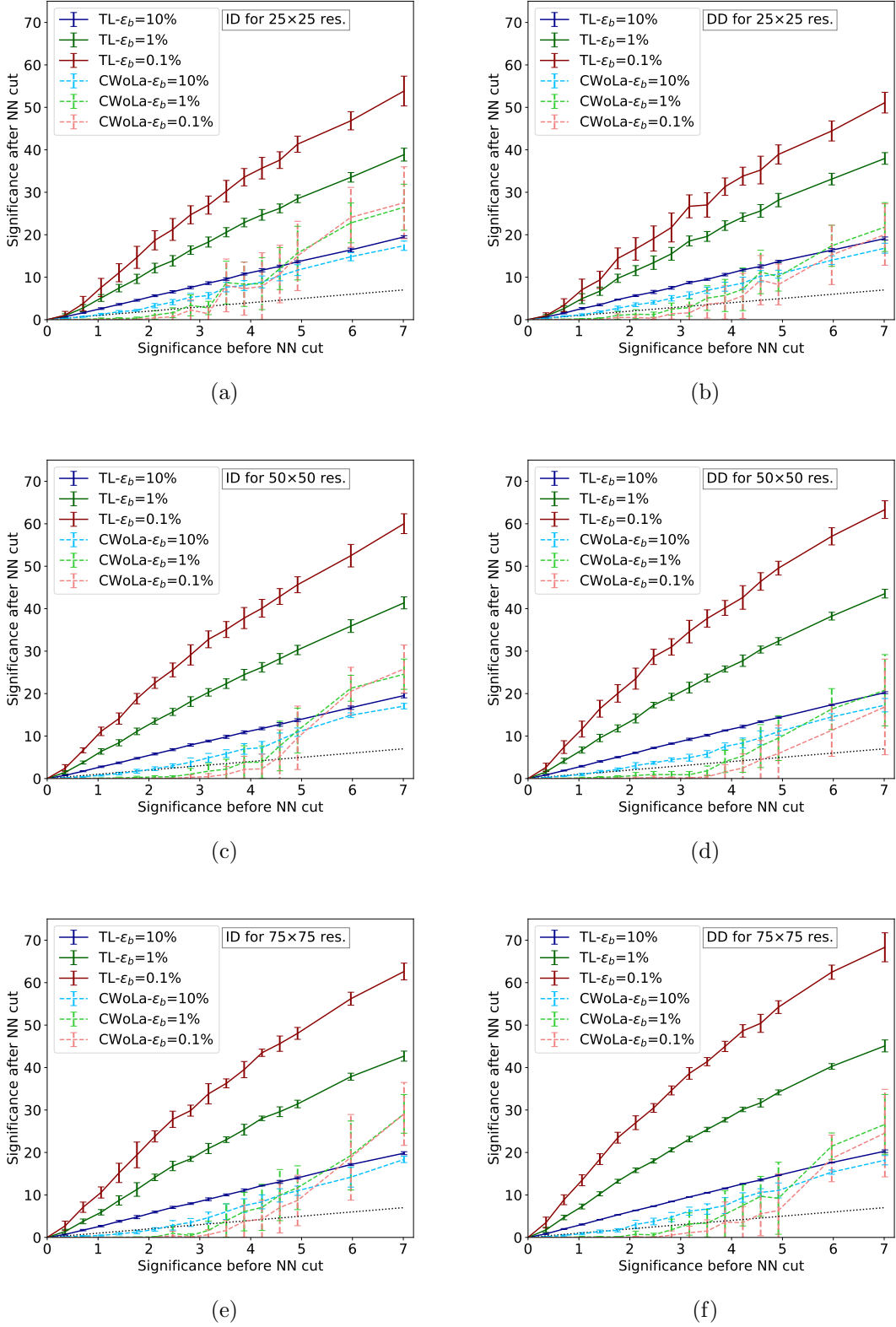


Figure 4: The results of transfer learning (solid curves) and of CWoLa (dashed curves, same as those in Fig. 3) for the ID (left column) and DD (right column) scenarios with $\Lambda_D = 10$ GeV for 25×25 , 50×50 and 75×75 resolutions. The dotted line in each plot has a slope of 1.

The architecture of our neural network is mostly the same as in Table 2. The only difference is the inclusion of scaling and shifting parameters in all the convolutional layers. Once again, the NN parameters of the feature extractor are referred to as Θ and those of the dense layers as θ . Training proceeds in the following three phases.

First, pretraining is performed as in Sec. 4, i.e., the neural network is trained to distinguish a sample of background from a mixture of different signals. The scaling parameters and the shifting parameters are kept at 1 and 0, respectively, throughout this phase. Once the pretraining is complete, the NN model parameters Θ will be fixed forever. The θ parameters are however not reinitialized randomly, which differs from the approach of Ref. [23] but gives better results in our case.

Second, a new phase of so-called meta-training is performed. Assume a series of tasks \mathcal{T} forming a task-space $p(\mathcal{T})$. For us, the tasks correspond to the different models of Sec. 2 except the benchmark under study. The training goes schematically as follows:

```

for episode do
  for  $\mathcal{T}$  in  $p(\mathcal{T})$  do
    base learning
    meta-learner update
    evaluation of  $\mathcal{L}_{\mathcal{T}}$ 
  end for
  average  $\mathcal{L}_{\mathcal{T}}$  over  $p(\mathcal{T})$ 
  test for early stopping
end for

```

In more details, an episode is the meta-learning equivalent of an epoch. In other words, each possible task in the task-space is considered during an episode and only once. The first step of every episode is an inner-loop. For each task in the task-space, the following steps are performed:

- **base learning:** A series of temporary θ parameters labelled as θ' are obtained via gradient descent as

$$\theta' \leftarrow \theta - \beta \nabla_{\theta} \mathcal{L}_{\mathcal{T}}(\Theta, \theta, S, \bar{S}), \quad (5.4)$$

where β is the learning rate in the base learning step and $\mathcal{L}_{\mathcal{T}}$ the loss function. The training is performed over only 3 epochs to prevent overfitting.

- **meta-learner update:** The θ , scaling and shifting parameters are updated by one step of gradient descent as

$$\begin{aligned} \theta &=: \theta - \gamma \nabla_{\theta} \mathcal{L}_{\mathcal{T}}(\Theta, \theta', S, \bar{S}), \\ S &=: S - \gamma \nabla_S \mathcal{L}_{\mathcal{T}}(\Theta, \theta', S, \bar{S}), \\ \bar{S} &=: \bar{S} - \gamma \nabla_{\bar{S}} \mathcal{L}_{\mathcal{T}}(\Theta, \theta', S, \bar{S}), \end{aligned} \quad (5.5)$$

where γ is the learning rate in the meta-learner updating step. After completing this step, the temporary parameters θ' will not be used anymore and can be discarded.

- **evaluation of $\mathcal{L}_{\mathcal{T}}$:** The loss function is evaluated using the updated parameters: $\mathcal{L}_{\mathcal{T}}(\Theta, \theta, S, \bar{S})$. This will be used to determine when to stop meta-training.

During the base learning and meta-learner update, the NN is trained to distinguish pure samples of 2.5k signal and 2.5k background from the SR region. A fifth of the sample is used for validation, which is also performed on pure samples. Different events are used for each of the three steps in the inner-loop of every episode. Once the inner-loop is complete, the $\mathcal{L}_{\mathcal{T}}$ are averaged and used to test for early stopping. Once the meta-training phase has been completed, the θ are reinitialized randomly.

Third, fine-tuning is performed in an almost identical manner to Sec. 4. The only difference is now the presence of the scaling and shifting parameters that are learned during meta-training but kept fixed in this phase.

We mention that our method is simplified with respect to the original method of Ref. [23]. The main difference was that we dropped the use of the hard tasks algorithm, as we considered this beyond the scope of a first study on the applicability of meta-learning to CWoLa. We also did not implement meta-batches, the meta-learning equivalent of a batch, as this was mostly irrelevant without the hard tasks algorithm.

Fig. 5 shows the comparison between transfer learning and meta-transfer learning. First, meta-transfer learning displays mostly a slight improvement in performance for the 25×25 and 50×50 resolutions compared with transfer learning due to the additional adjustment provided by the scaling and shifting. Note that the results from transfer learning are already good enough that mathematically there is not much room for improvement at large significance. The relative improvement at low significance can however be sizable. The difference between transfer and meta-transfer learning is negligible for the 75×75 resolution. However, we find that meta-transfer learning can display superior results to transfer learning even for the 75×75 resolution if a larger kernel size is used, and Fig. 6 shows the comparison. A full study of this is beyond the scope of this work though.

6 Conclusion

Weak supervision searches have the advantages of both being able to train on data and being able to exploit distinctive signal properties. However, training a neural network via weak supervision can require a prohibitive amount of signal, often close to the point that the signal would already have been discovered without employing the neural network. In our work, we seek to address this problem by creating neural networks that can learn from less signal by using transfer and meta-learning. The general idea is to first train a neural network on simulations. During this stage, the neural network should learn relevant concepts or become a more efficient learner. The neural network is then trained on the experimental data and should require less signal because of its previous training. Our actual implementation of this procedure was via pretraining and meta-transfer learning.

We find that transfer learning can drastically improve the performance of CWoLa searches. The improvement is most important at low significance and the amount of signal necessary for discovery can be reduced by a factor of a few. Meta-transfer learning can further improve the performance of CWoLa searches, but not drastically so.

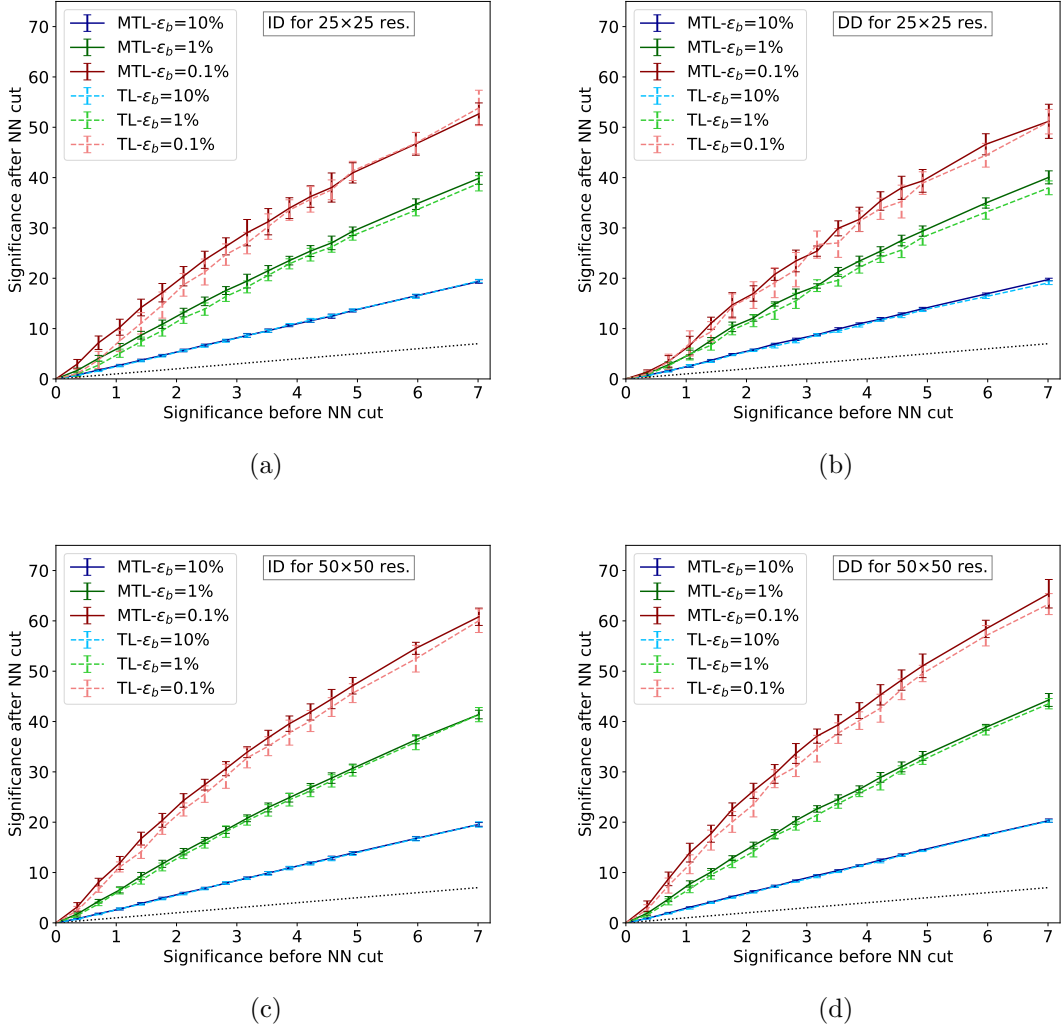


Figure 5: The results of meta-transfer learning (solid curves) and transfer learning (dashed curves, same as those in Fig. 4) for the ID (left column) and DD (right column) scenarios with $\Lambda_D = 10$ GeV for 25×25 and 50×50 resolutions. The dotted line in each plot has a slope of 1.

We mention that this work was intended more as a proof of principle and that there are still questions that are left unanswered. Namely, the choice of models on which to train could potentially have an effect on the ability to discover signals that differ considerably from them. The exact extent of this effect is left for future work. However, a small reduction to the scope of model sensitivity seems a fair prize to pay for the magnitude of our improvement over the regular CWoLa method.

Finally, we emphasize that transfer and meta-learning are vast and fast-evolving fields. Though we did demonstrate their potential, we only considered two specific techniques. It is plausible that more powerful techniques already exist or, even more likely, could be

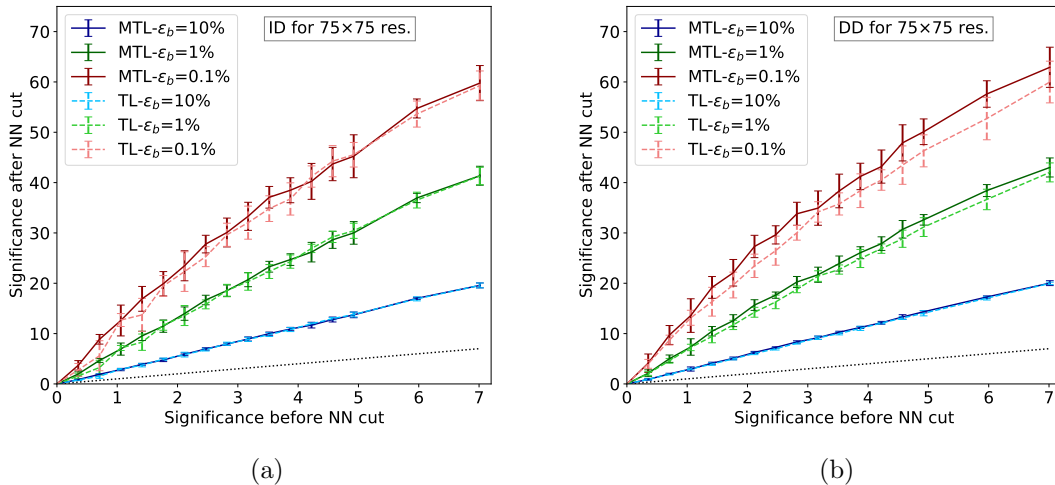


Figure 6: The results of meta-transfer learning (solid curves) and transfer learning (dashed curves) for the ID (left) and DD (right) scenarios with $\Lambda_D = 10$ GeV for 75×75 resolution with a larger size of kernels. The kernel sizes are 10×10 and 5×5 respectively instead of 5×5 and 3×3 mentioned in Table 2. The dotted line in each plot has a slope of 1.

created in the future. Likewise, we have not sought to fully optimize our analysis and it is clear that some smaller details could be improved. As such and considering our very promising results, we believe that further studies of transfer and meta-learning for weak supervision are warranted.

Acknowledgments

We thank Chun-Hung Lin for collaboration in the early stage of this work. This work was supported by the National Science and Technology Council under Grant No. NSTC-111-2112-M-002-018-MY3, the Ministry of Education (Higher Education Sprout Project NTU-112L104022), and the National Center for Theoretical Sciences of Taiwan.

A Impact of systematic uncertainties

A legitimate question is whether systematic uncertainties, which were not included up to now, can affect whether transfer and meta-learning provide an improvement over regular CWoLa. Although a full study is beyond the scope of this work, we try to answer this question in this appendix.

The only practical difference is that the significance should now be computed using the formula [47]

$$\sigma = \sqrt{2 \left(N \log \left(\frac{N(N_b + \sigma^2)}{N_b^2 + N\sigma^2} \right) - \frac{N_b^2}{\sigma^2} \log \left(1 + \frac{\sigma^2 N_s}{N_b(N_b + \sigma^2)} \right) \right)}, \quad (\text{A.1})$$

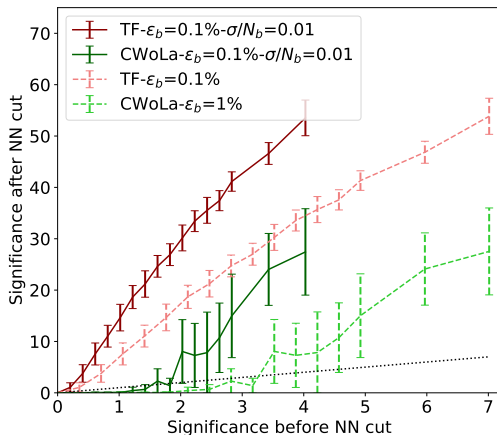


Figure 7: The results of transfer learning and pure CWoLa for the ID scenarios with $\Lambda_D = 10$ GeV for 25×25 resolutions with a systematic uncertainty of 1%. The solid curves are the results with systematic uncertainty and the dashed curves are the same as in Fig. 4a. The dotted line has a slope of 1.

where N_s and N_b are respectively the numbers of signal and background, $N = N_s + N_b$ is the total number of events and σ is the background systematic uncertainty.

Fig. 7 illustrates the impact of systematic uncertainties. Results for regular CWoLa and transfer learning are included. A relative systematic uncertainty of 1% is assumed for the number of background events both before and after the NN cuts. This choice is made for illustration purposes, as it is somewhat smaller than the typical current precision of about 5% for these masses, see e.g., Ref. [48]. Essentially, the inclusion of systematic uncertainties simply compresses the curves along the horizontal direction. This effect is accentuated as the systematic uncertainties increase. The reason is that systematic uncertainties reduce far more the significance before the NN cut than after. Unless the systematic uncertainties associated with transfer or meta-learning are far larger than those associated with CWoLa, transfer and meta-learning will therefore still outperform regular CWoLa.

References

- [1] Y.-C. J. Chen, C.-W. Chiang, G. Cottin, and D. Shih, “Boosted W and Z tagging with jet charge and deep learning,” *Phys. Rev. D* **101** no. 5, (2020) 053001, [arXiv:1908.08256 \[hep-ph\]](#).
- [2] E. Bernreuther, T. Finke, F. Kahlhoefer, M. Krämer, and A. Mück, “Casting a graph net to catch dark showers,” *SciPost Phys.* **10** no. 2, (2021) 046, [arXiv:2006.08639 \[hep-ph\]](#).
- [3] S. Chang, T.-K. Chen, and C.-W. Chiang, “Distinguishing W' signals at hadron colliders using neural networks,” *Phys. Rev. D* **103** no. 3, (2021) 036016, [arXiv:2007.14586 \[hep-ph\]](#).
- [4] C.-W. Chiang, D. Shih, and S.-F. Wei, “VBF vs. GGF Higgs with Full-Event Deep Learning:

- Towards a Decay-Agnostic Tagger,” *Phys. Rev. D* **107** no. 1, (2023) 016014, [arXiv:2209.05518 \[hep-ph\]](#).
- [5] E. M. Metodiev, B. Nachman, and J. Thaler, “Classification without labels: Learning from mixed samples in high energy physics,” *JHEP* **10** (2017) 174, [arXiv:1708.02949 \[hep-ph\]](#).
- [6] M. Farina, Y. Nakai, and D. Shih, “Searching for New Physics with Deep Autoencoders,” *Phys. Rev. D* **101** no. 7, (2020) 075021, [arXiv:1808.08992 \[hep-ph\]](#).
- [7] J. Batson, C. G. Haaf, Y. Kahn, and D. A. Roberts, “Topological Obstructions to Autoencoding,” *JHEP* **04** (2021) 280, [arXiv:2102.08380 \[hep-ph\]](#).
- [8] R. T. D’Agnolo and A. Wulzer, “Learning New Physics from a Machine,” *Phys. Rev. D* **99** no. 1, (2019) 015014, [arXiv:1806.02350 \[hep-ph\]](#).
- [9] B. Nachman and D. Shih, “Anomaly Detection with Density Estimation,” *Phys. Rev. D* **101** (2020) 075042, [arXiv:2001.04990 \[hep-ph\]](#).
- [10] A. Andreassen, B. Nachman, and D. Shih, “Simulation Assisted Likelihood-free Anomaly Detection,” *Phys. Rev. D* **101** no. 9, (2020) 095004, [arXiv:2001.05001 \[hep-ph\]](#).
- [11] A. Hallin, J. Isaacson, G. Kasieczka, C. Krause, B. Nachman, T. Quadfasel, M. Schlaffer, D. Shih, and M. Sommerhalder, “Classifying anomalies through outer density estimation,” *Phys. Rev. D* **106** no. 5, (2022) 055006, [arXiv:2109.00546 \[hep-ph\]](#).
- [12] G. Kasieczka, R. Mastandrea, V. Mikuni, B. Nachman, M. Pettee, and D. Shih, “Anomaly detection under coordinate transformations,” *Phys. Rev. D* **107** no. 1, (2023) 015009, [arXiv:2209.06225 \[hep-ph\]](#).
- [13] A. Hallin, G. Kasieczka, T. Quadfasel, D. Shih, and M. Sommerhalder, “Resonant anomaly detection without background sculpting,” [arXiv:2210.14924 \[hep-ph\]](#).
- [14] ATLAS Collaboration, G. Aad *et al.*, “Dijet resonance search with weak supervision using $\sqrt{s} = 13$ TeV pp collisions in the ATLAS detector,” *Phys. Rev. Lett.* **125** no. 13, (2020) 131801, [arXiv:2005.02983 \[hep-ex\]](#).
- [15] J. H. Collins, P. Martín-Ramiro, B. Nachman, and D. Shih, “Comparing weak- and unsupervised methods for resonant anomaly detection,” *Eur. Phys. J. C* **81** no. 7, (2021) 617, [arXiv:2104.02092 \[hep-ph\]](#).
- [16] B. M. Dillon, L. Favaro, F. Feiden, T. Modak, and T. Plehn, “Anomalies, Representations, and Self-Supervision,” [arXiv:2301.04660 \[hep-ph\]](#).
- [17] J. H. Collins, K. Howe, and B. Nachman, “Anomaly Detection for Resonant New Physics with Machine Learning,” *Phys. Rev. Lett.* **121** no. 24, (2018) 241803, [arXiv:1805.02664 \[hep-ph\]](#).
- [18] T. Finke, M. Hein, G. Kasieczka, M. Krämer, A. Mück, P. Prangchaikul, T. Quadfasel, D. Shih, and M. Sommerhalder, “Back To The Roots: Tree-Based Algorithms for Weakly Supervised Anomaly Detection,” [arXiv:2309.13111 \[hep-ph\]](#).
- [19] M. Freytsis, M. Perelstein, and Y. C. San, “Anomaly Detection in Presence of Irrelevant Features,” [arXiv:2310.13057 \[hep-ph\]](#).
- [20] S. J. Pan and Q. Yang, “A survey on transfer learning,” *IEEE Transactions on Knowledge and Data Engineering* **22** no. 10, (2010) 1345–1359.
- [21] L. Y. Pratt, J. Mostow, and C. A. Kamm, “Direct transfer of learned information among neural networks,” in *AAAI Conference on Artificial Intelligence*. 1991.

- [22] T. Hospedales, A. Antoniou, P. Micaelli, and A. Storkey, “Meta-learning in neural networks: A survey,” *IEEE Transactions on Pattern Analysis; Machine Intelligence* **44** no. 09, (Sep, 2022) 5149–5169.
- [23] Q. Sun, Y. Liu, T.-S. Chua, and B. Schiele, “Meta-transfer learning for few-shot learning,” [arXiv:1812.02391 \[cs.CV\]](#).
- [24] M. J. Dolan and A. Ore, “Metalearning and data augmentation for mass-generalized jet taggers,” *Phys. Rev. D* **105** no. 9, (2022) 094030, [arXiv:2111.06047 \[hep-ph\]](#).
- [25] G. Albouy *et al.*, “Theory, phenomenology, and experimental avenues for dark showers: a Snowmass 2021 report,” *Eur. Phys. J. C* **82** no. 12, (2022) 1132, [arXiv:2203.09503 \[hep-ph\]](#).
- [26] Z. Chacko, H.-S. Goh, and R. Harnik, “The Twin Higgs: Natural electroweak breaking from mirror symmetry,” *Phys. Rev. Lett.* **96** (2006) 231802, [arXiv:hep-ph/0506256](#).
- [27] P. W. Graham, D. E. Kaplan, and S. Rajendran, “Cosmological Relaxation of the Electroweak Scale,” *Phys. Rev. Lett.* **115** no. 22, (2015) 221801, [arXiv:1504.07551 \[hep-ph\]](#).
- [28] H. Beauchesne, E. Bertuzzo, and G. Grilli Di Cortona, “Dark matter in Hidden Valley models with stable and unstable light dark mesons,” *JHEP* **04** (2019) 118, [arXiv:1809.10152 \[hep-ph\]](#).
- [29] E. Bernreuther, F. Kahlhoefer, M. Krämer, and P. Tunney, “Strongly interacting dark sectors in the early Universe and at the LHC through a simplified portal,” *JHEP* **01** (2020) 162, [arXiv:1907.04346 \[hep-ph\]](#).
- [30] H. Beauchesne and G. Grilli di Cortona, “Classification of dark pion multiplets as dark matter candidates and collider phenomenology,” *JHEP* **02** (2020) 196, [arXiv:1910.10724 \[hep-ph\]](#).
- [31] CMS Collaboration, A. M. Sirunyan *et al.*, “Search for new particles decaying to a jet and an emerging jet,” *JHEP* **02** (2019) 179, [arXiv:1810.10069 \[hep-ex\]](#).
- [32] CMS Collaboration, A. Tumasyan *et al.*, “Search for resonant production of strongly coupled dark matter in proton-proton collisions at 13 TeV,” *JHEP* **06** (2022) 156, [arXiv:2112.11125 \[hep-ex\]](#).
- [33] ATLAS Collaboration, G. Aad *et al.*, “Search for non-resonant production of semi-visible jets using Run 2 data in ATLAS,” *Phys. Lett. B* **848** (2024) 138324, [arXiv:2305.18037 \[hep-ex\]](#).
- [34] ATLAS Collaboration, G. Aad *et al.*, “Search for Resonant Production of Dark Quarks in the Dijet Final State with the ATLAS Detector,” [arXiv:2311.03944 \[hep-ex\]](#).
- [35] D. Bardhan, Y. Kats, and N. Wunch, “Searching for dark jets with displaced vertices using weakly supervised machine learning,” [arXiv:2305.04372 \[hep-ph\]](#).
- [36] C. Bierlich *et al.*, “A comprehensive guide to the physics and usage of PYTHIA 8.3,” [arXiv:2203.11601 \[hep-ph\]](#).
- [37] L. Carloni, J. Rathsman, and T. Sjostrand, “Discerning Secluded Sector gauge structures,” *JHEP* **04** (2011) 091, [arXiv:1102.3795 \[hep-ph\]](#).
- [38] L. Carloni and T. Sjostrand, “Visible Effects of Invisible Hidden Valley Radiation,” *JHEP* **09** (2010) 105, [arXiv:1006.2911 \[hep-ph\]](#).

- [39] J. Alwall, R. Frederix, S. Frixione, V. Hirschi, F. Maltoni, O. Mattelaer, H. S. Shao, T. Stelzer, P. Torrielli, and M. Zaro, “The automated computation of tree-level and next-to-leading order differential cross sections, and their matching to parton shower simulations,” *JHEP* **07** (2014) 079, [arXiv:1405.0301 \[hep-ph\]](#).
- [40] R. D. Ball *et al.*, “Parton distributions with LHC data,” *Nucl. Phys. B* **867** (2013) 244–289, [arXiv:1207.1303 \[hep-ph\]](#).
- [41] DELPHES 3 Collaboration, J. de Favereau, C. Delaere, P. Demin, A. Giammanco, V. Lemaitre, A. Mertens, and M. Selvaggi, “DELPHES 3, A modular framework for fast simulation of a generic collider experiment,” *JHEP* **02** (2014) 057, [arXiv:1307.6346 \[hep-ex\]](#).
- [42] A. Butter *et al.*, “The Machine Learning landscape of top taggers,” *SciPost Phys.* **7** (2019) 014, [arXiv:1902.09914 \[hep-ph\]](#).
- [43] L. de Oliveira, M. Kagan, L. Mackey, B. Nachman, and A. Schwartzman, “Jet-images — deep learning edition,” *JHEP* **07** (2016) 069, [arXiv:1511.05190 \[hep-ph\]](#).
- [44] G. Kasieczka, T. Plehn, M. Russell, and T. Schell, “Deep-learning Top Taggers or The End of QCD?,” *JHEP* **05** (2017) 006, [arXiv:1701.08784 \[hep-ph\]](#).
- [45] F. Chollet *et al.*, “Keras.” <https://keras.io>, 2015.
- [46] M. Abadi *et al.*, “TensorFlow: Large-Scale Machine Learning on Heterogeneous Distributed Systems,” [arXiv:1603.04467 \[cs.DC\]](#).
- [47] ATLAS Collaboration, “Formulae for Estimating Significance,” 2020.
- [48] CMS Collaboration, A. M. Sirunyan *et al.*, “Search for high mass dijet resonances with a new background prediction method in proton-proton collisions at $\sqrt{s} = 13$ TeV,” *JHEP* **05** (2020) 033, [arXiv:1911.03947 \[hep-ex\]](#).



Precise test of lepton flavour universality in W -boson decays into muons and electrons in pp collisions at $\sqrt{s} = 13$ TeV with the ATLAS detector

The ATLAS Collaboration

The ratio of branching ratios of the W boson to muons and electrons, $R_W^{\mu/e} = \mathcal{B}(W \rightarrow \mu\nu) / \mathcal{B}(W \rightarrow e\nu)$, has been measured using 140 fb^{-1} of pp collision data at $\sqrt{s} = 13$ TeV collected with the ATLAS detector at the LHC, probing the universality of lepton couplings. The ratio is obtained from measurements of the $t\bar{t}$ production cross-section in the ee , $e\mu$ and $\mu\mu$ dilepton final states. To reduce systematic uncertainties, it is normalised by the square root of the corresponding ratio $R_Z^{\mu\mu/ee}$ for the Z boson measured in inclusive $Z \rightarrow ee$ and $Z \rightarrow \mu\mu$ events. By using the precise value of $R_Z^{\mu\mu/ee}$ determined from e^+e^- colliders, the ratio $R_W^{\mu/e}$ is determined to be

$$R_W^{\mu/e} = 0.9995 \pm 0.0022 \text{ (stat)} \pm 0.0036 \text{ (syst)} \pm 0.0014 \text{ (ext)} .$$

The three uncertainties correspond to data statistics, experimental systematics and the external measurement of $R_Z^{\mu\mu/ee}$, giving a total uncertainty of 0.0045, and confirming the Standard Model assumption of lepton flavour universality in W -boson decays at the 0.5% level.

Contents

1	Introduction	2
2	Data and simulated event samples	3
3	Event reconstruction and selection	5
4	Analysis method	7
5	Lepton isolation efficiency measurements	12
6	Systematic uncertainties	13
7	Fit results	16
8	Conclusion	21

1 Introduction

The assumption of lepton flavour universality, i.e. that the couplings of the charged leptons e , μ and τ to the electroweak gauge bosons are independent of the lepton masses, is a key axiom of the Standard Model of particle physics. This assumption has been tested over a wide range of momentum transfers by studying ratios of partial decay widths (or equivalently, ratios of branching ratios) of various particles to electrons, muons and taus. After correction for mass, phase space and radiative effects, these ratios of decays into leptons of generations i and j are proportional to g_i^2/g_j^2 , where g_i is the coupling of lepton i ($= e, \mu, \tau$). The equality of these couplings has been tested to the 0.1–0.2% level in decays of τ leptons, π and K mesons (see for example Ref. [1]). More recently, hints of departures from lepton flavour universality at the level of a few standard deviations were seen in the so-called flavour anomalies in b -hadron decays, e.g. in the processes $B \rightarrow D^{(*)}\tau\nu$ vs. $B \rightarrow D^{(*)}\ell\nu$ (with $\ell = e$ or μ) [2–7], and in the loop-induced process $b \rightarrow s\ell\ell$. However, the latest measurement of $b \rightarrow s\ell\ell$ in $B \rightarrow K^{(*)}\mu^+\mu^-$ vs. $B \rightarrow K^{(*)}e^+e^-$ decays from the LHCb collaboration is in agreement with lepton flavour universality [8], and definitive conclusions have yet to be established.

At high momentum transfer, the branching ratios for the leptonic decays of the W boson to e , μ and τ are expected to be equal to very high precision, given the small sizes of the lepton masses compared to the W boson mass. This assumption has been tested in the production of W -boson pairs in e^+e^- collisions at LEP2, in the production of single W bosons at the Tevatron and Large Hadron Collider (LHC), and by exploiting the two W bosons produced in $t\bar{t}$ events at the LHC. The most precise measurement of $R_W^{\mu/e}$, the ratio of branching ratios for $W \rightarrow \mu\nu$ and $W \rightarrow e\nu$, was performed by the CMS collaboration with $pp \rightarrow t\bar{t}$ events at $\sqrt{s} = 13$ TeV, using a global fit to lepton and jet multiplicities, as well as b -tagging and kinematic information, and has a precision of 0.9% [9]. Measurements of $pp \rightarrow W$ cross-sections in the $W \rightarrow e\nu$ and $W \rightarrow \mu\nu$ decay channels from the ATLAS and LHCb experiments [10, 11], and measurements in $e^+e^- \rightarrow W^+W^-$ events from the ALEPH, DELPHI, L3 and OPAL experiments at LEP2 [12] also contribute significantly to the combined value of $R_W^{\mu/e} = 1.002 \pm 0.006$ determined by the Particle Data Group [13].

This paper describes a measurement of $R_W^{\mu/e}$ using W bosons produced from the decay of top quarks in $pp \rightarrow t\bar{t}$ events selected from the full Run 2 ATLAS pp collision data sample at $\sqrt{s} = 13$ TeV. Final states with two opposite-charge leptons (electrons or muons, $\ell = e$ or μ) and one or two jets tagged as likely to contain b -hadrons are selected, allowing $R_W^{\mu/e}$ to be derived from a comparison of the $t\bar{t}$ production cross-section measured in the ee , $e\mu$ and $\mu\mu$ channels. Many systematic uncertainties related to $t\bar{t}$ and background physics modelling cancel in this direct measurement of $R_W^{\mu/e}$, but it is still limited by uncertainties related to the identification of electrons and muons. The latter can be reduced by making a simultaneous measurement of the analogous ratio $R_Z^{\mu\mu/ee}$ for Z bosons, i.e. the ratio of branching ratios for $Z \rightarrow \mu\mu$ and $Z \rightarrow ee$, using inclusive $Z \rightarrow \ell\ell$ events in the same data sample. The main measured parameter of interest becomes $R_{WZ}^{\mu/e} = R_W^{\mu/e} / \sqrt{R_Z^{\mu\mu/ee}}$, and the final result is then obtained from $R_{WZ}^{\mu/e}$ and the precise measurement of $R_Z^{\mu\mu/ee} = 1.0009 \pm 0.0028$ from the LEP and SLD experiments [13, 14], taken as an external input parameter. The $t\bar{t}$ and $Z \rightarrow \ell\ell$ cross-sections, $\sigma_{t\bar{t}}$ and $\sigma_{Z \rightarrow \ell\ell}$, are also measured as by-products of this procedure. The value of $\sigma_{t\bar{t}}$ is defined inclusively with respect to all $t\bar{t}$ final states, whereas $\sigma_{Z \rightarrow \ell\ell}$ is defined for decays into a single dilepton flavour $\ell\ell$.

The data and samples of Monte Carlo simulated events used in this analysis are described in Section 2, followed by the event reconstruction and selection in Section 3. The analysis method is described in Section 4, and supporting measurements of lepton isolation efficiencies are outlined in Section 5. Systematic uncertainties are detailed in Section 6 and the results in Section 7. Finally, the conclusion is given in Section 8.

2 Data and simulated event samples

The ATLAS detector [15–17] at the LHC covers nearly the entire solid angle around the collision point. It consists of an inner tracking detector surrounded by a thin superconducting solenoid producing a 2T axial magnetic field, electromagnetic and hadronic calorimeters, and an external muon spectrometer incorporating three large toroidal magnet assemblies. The analysis was performed on samples of proton–proton collision data collected at $\sqrt{s} = 13$ TeV in 2015–18, corresponding to an integrated luminosity of $140.1 \pm 1.2 \text{ fb}^{-1}$ after data quality requirements [18, 19]. Events were required to pass a single-electron or single-muon trigger [20, 21], with transverse momentum (p_T) thresholds that were progressively raised during the data-taking period.¹ The electron trigger reached the efficiency plateau region for electrons with reconstructed $p_T > 25$ GeV in 2015 and for $p_T > 27$ GeV for 2016–18, the corresponding thresholds for the muon trigger being 21 GeV for 2015 and 27.3 GeV thereafter. Each triggered event also includes the signals from on average 33 superimposed inelastic pp collisions, referred to as pileup.

Monte Carlo simulated event samples were used to develop the analysis procedures, to evaluate signal and background contributions, and to compare with data. Samples were processed using either the full ATLAS detector simulation [22] based on GEANT4 [23], or with a faster simulation making use of parameterised showers in the calorimeters [24]. The effects of pileup were simulated by generating additional inelastic pp collisions with PYTHIA8 (v8.186) [25] using the A3 set of parameter values (tune) [26] and overlaying them on the primary simulated events, so as to match the distribution of the number of inelastic events per bunch

¹ ATLAS uses a right-handed coordinate system with its origin at the nominal interaction point in the centre of the detector, and the z -axis along the beam line. Pseudorapidity is defined in terms of the polar angle θ as $\eta = -\ln \tan \theta/2$, and transverse momentum is defined relative to the beam line as $p_T = p \sin \theta$. The azimuthal angle around the beam line is denoted by ϕ , and distances in (η, ϕ) space by $\Delta R = \sqrt{(\Delta\eta)^2 + (\Delta\phi)^2}$.

crossing observed in the data. These combined events were then processed using the same reconstruction and analysis chain as the data [27]. Small corrections were applied to lepton and jet energy scales [28–30], and to lepton and b -tagging efficiencies [31–33], in order to improve agreement with the response observed in data. Further topology-specific lepton isolation corrections were applied as discussed in Section 5.

The baseline simulated $t\bar{t}$ sample was produced with the POWHEG-BOX v2 event generator [34–37] (referred to hereafter as POWHEG), which implements matrix-elements at next-to-leading-order (NLO) in the strong coupling constant α_s , using the NNPDF3.0 NLO parton distribution function (PDF) set [38]. The parton shower, hadronisation and underlying event modelling was performed using PYTHIA8 (v8.210) with the NNPDF2.3 LO PDF set [39], the A14 tune [40], and additional parameters configured as described in Ref. [41]. Modelling uncertainties were assessed by using alternative samples generated using MADGRAPH5_AMC@NLO (referred to hereafter as AMC@NLO) [42] interfaced to PYTHIA8, and POWHEG interfaced to HERWIG7.1 [43, 44], as discussed in Ref. [45]. Further variations were obtained from the baseline POWHEG + PYTHIA8 sample, by using event weights to change the quantum chromodynamics (QCD) factorisation and renormalisation scales, and the amounts of initial and final state radiation. The top quark mass was set to $m_t = 172.5$ GeV, the $W \rightarrow \ell\nu$ branching ratio to the Standard Model prediction of 0.1082 for each lepton flavour (e , μ and τ) [46], and EVTGEN [47] was used to handle the decays of b - and c -flavoured hadrons. The $t\bar{t}$ samples were normalised to a reference cross-section of $832 \pm 35^{+20}_{-29}$ pb, where the first uncertainty corresponds to PDF uncertainties and the second to QCD scale uncertainties. This value was calculated at next-to-next-to-leading-order (NNLO) accuracy in α_s , including the resummation of next-to-next-to-leading-logarithmic (NNLL) soft gluon terms [48], using TOP++ 2.0 [49] as described in Ref. [50]. The associated production of a W boson and a top quark (Wt) is a background in the $t\bar{t}$ cross-section measurement but contributes sensitivity to $R_W^{\mu/e}$, as it gives rise to final states with two real W bosons. It was simulated with POWHEG + PYTHIA8 with the same setup as for the $t\bar{t}$ sample. The interference between the $t\bar{t}$ and Wt amplitudes was modelled using the diagram removal scheme [51, 52]. The Wt cross-section was taken to be 79.3 ± 2.2 (PDF) $^{+1.9}_{-1.8}$ (QCD scale) pb, based on an NLO calculation with the addition of third-order corrections resumming NNLL soft gluon contributions [53].

The dilepton plus b -tagged jet signature can also arise from Z -boson production with additional jets. In the $t\bar{t}$ measurement, this background was modelled using SHERPA 2.2.11 [54] for $Z \rightarrow ee/\mu\mu$ and SHERPA 2.2.14 for $Z \rightarrow \tau\tau$, with NLO matrix elements for up to two partons, and leading-order matrix elements for up to five partons, calculated with the COMIX [55] and OPENLOOPS [56] libraries and matched with the SHERPA parton shower [57] using the MEPS@NLO prescription [58–61]. The samples include the off-shell Z/γ^* and interference contribution and have dilepton invariant mass $m_{\ell\ell} > 10$ GeV. They were generated using the NNPDF3.0 PDF set and normalised to an NNLO cross-section prediction [62]. For the inclusive $Z \rightarrow \ell\ell$ selections used in the normalisation measurement of $R_Z^{\mu\mu/ee}$, where jets are less important, $Z \rightarrow \ell\ell$ events were modelled using POWHEG v1 [63] interfaced to PYTHIA8 (v8.186) with the AZNLO tune [64] and the CT10 PDF set [65], including Z/γ^* and interference contributions, and generating events with dilepton invariant mass $m_{\ell\ell} > 60$ GeV. These events were reweighted to data as a function of $p_T^{\ell\ell}$ in order to improve the modelling of the reconstructed Z -boson transverse momentum spectrum, and the samples were normalised to a reference cross-section of $\sigma_{Z \rightarrow \ell\ell} = 1951$ pb, based on predictions from FEWZ [66].

Smaller contributions to both selections arise from diboson production (WW , WZ and ZZ), which was modelled using SHERPA 2.2.2, analogously to Z +jets production. Production of $t\bar{t}$ in association with a leptonically decaying W , Z or Higgs boson, or an additional $t\bar{t}$ pair, gives a negligible contribution to the opposite-charge dilepton samples, but is significant in the same-charge control samples used to assess the background from misidentified leptons in the $t\bar{t}$ selection. These processes were modelled at NLO

using POWHEG + PYTHIA8 or AMC@NLO + PYTHIA8. Additional background arises from events where at least one lepton is not a prompt lepton from a W or Z decay (including via leptonic τ decays), but is a misidentified lepton, i.e. a non-prompt lepton from the decay of a bottom or charm hadron, an electron from a photon conversion, a hadronic jet misidentified as an electron, or a muon produced from the decay in flight of a pion or kaon. Events with one prompt and one misidentified lepton can arise from $t\bar{t}$ or Wt events with one hadronically decaying W boson (modelled as described above), W +jets production (modelled with SHERPA 2.2.1) or t -channel single top quark production (modelled with POWHEG + PYTHIA8). Processes with two misidentified leptons (e.g. from inclusive $b\bar{b}$ or $c\bar{c}$ production) are negligible for the $t\bar{t}$ selection, and the corresponding background in the inclusive $Z \rightarrow \ell\ell$ selection was modelled from data without relying on the simulation of such processes (see Section 4).

3 Event reconstruction and selection

This analysis makes use of reconstructed electrons, muons and b -tagged jets. Electron candidates were reconstructed from a localised cluster of energy deposits in the electromagnetic calorimeter matched to a track in the inner detector, passing the ‘Medium’ likelihood-based requirement of Ref. [28]. They were required to have transverse momentum $p_T > 20$ GeV and pseudorapidity $|\eta| < 2.47$, excluding the transition region between the barrel and endcap electromagnetic calorimeters, $1.37 < |\eta| < 1.52$, and to be consistent with originating from the signal primary vertex. The latter was defined as the reconstructed vertex with the highest sum of p_T^2 of associated tracks. To reduce background from non-prompt electrons, electron candidates were further required to pass the ‘Tight’ isolation requirements of Ref. [28], based on the amount of summed calorimeter energy and track transverse momentum close to the electron. Muon candidates were reconstructed by combining tracks from the inner detector with matching tracks reconstructed in the muon spectrometer, and were required to have $p_T > 20$ GeV, $|\eta| < 2.5$ and to satisfy the ‘Medium’ requirements of Ref. [32]. Muons were also required to be consistent with the signal primary vertex and to satisfy the ‘Tight’ isolation requirements of Ref. [32].

Jets were reconstructed using the anti- k_r algorithm [67, 68] with radius parameter $R = 0.4$, starting from particle-flow objects that combine information from topological clusters of calorimeter energy deposits and inner-detector tracks [69]. After calibration using information from both simulation and data [30], jets were required to have $p_T > 25$ GeV and $|\eta| < 2.5$, and jets with $p_T < 60$ GeV and $|\eta| < 2.4$ were subject to additional pileup rejection criteria using the multivariate jet-vertex tagger (JVT) [70]. To prevent double counting of electron energy deposits as jets, the closest jet to an electron candidate was removed if it was within $\Delta R = 0.2$ of the electron. Furthermore, to reduce the contribution of leptons from heavy-flavour hadron decays inside jets, leptons within $\Delta R = 0.4$ of selected jets were discarded, unless the lepton was a muon and the jet had fewer than three associated tracks, in which case the jet was discarded. Jets likely to contain b -hadrons were tagged using the DL1r algorithm [33, 71], a multivariate discriminant based on deep-learning techniques making use of track impact parameters and reconstructed secondary vertices. A tagger working point with an efficiency of 70% for tagging b -quark jets from top-quark decays in simulated $t\bar{t}$ events was used, corresponding to rejection factors of about 380 against light quark and gluon jets, and 10 against jets originating from charm quarks.

Selected events were required to have exactly two leptons (electrons or muons) passing the requirements above, of opposite charges, with at least one of the leptons being matched to a corresponding electron or muon trigger signature. The leptons were additionally required to have $p_T > 27.3$ GeV, to further reduce the contribution of events with misidentified leptons, and to ensure all leptons were above the

Table 1: Summary of the common object selection, and event selections for $t\bar{t}$ and Z final states.

Object selection		
Electrons	$p_T > 27.3 \text{ GeV}, \eta < 1.37 \text{ or } 1.52 < \eta < 2.47$	
Muons	$p_T > 27.3 \text{ GeV}, \eta < 2.5$	
b -tagged jets	$p_T > 30.0 \text{ GeV}, \eta < 2.5, b$ -tagging DL1r 70%	
Event selection	$t\bar{t} \rightarrow \ell\ell b\bar{b}v\bar{v}$	$Z \rightarrow \ell\ell$
Dilepton flavour ($\ell^+\ell^-$)	$ee, e\mu, \mu\mu$	$ee, \mu\mu$
Dilepton invariant mass	$m_{\ell\ell} > 30 \text{ GeV}$	$66 \text{ GeV} < m_{\ell\ell} < 116 \text{ GeV}$
b -tagged jet multiplicity	1 or 2	–

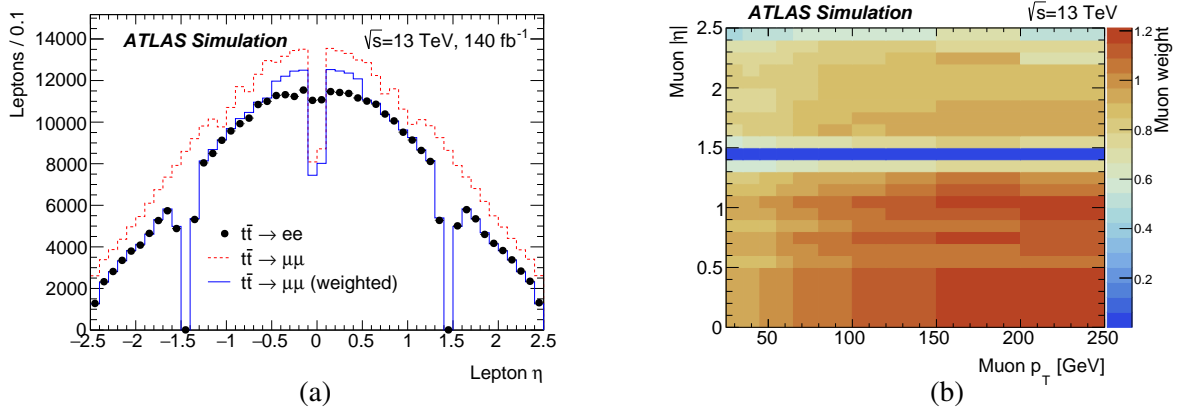


Figure 1: (a) Number of selected leptons as a function of η in simulated $t\bar{t}$ events with at least one b -tagged jet in the ee (points) and $\mu\mu$ (red dashed line) channels, and number of selected leptons in the $\mu\mu$ channel after muon weighting (blue solid line); (b) muon efficiency weights as a function of $|\eta|$ and p_T .

muon trigger p_T threshold. For the $t\bar{t}$ selection (ee , $e\mu$ and $\mu\mu$), events were additionally required to satisfy $m_{\ell\ell} > 30 \text{ GeV}$ and to have exactly one or exactly two b -tagged jets with $p_T > 30 \text{ GeV}$. For the inclusive $Z \rightarrow \ell\ell$ selection, only ee and $\mu\mu$ events were retained, with $66 \text{ GeV} < m_{\ell\ell} < 116 \text{ GeV}$, and no requirements were made on jet or b -tagged jet multiplicity. Table 1 summarises the event selection.

The numbers of leptons in simulated $t\bar{t}$ events passing the ee and $\mu\mu$ $t\bar{t}$ selections are shown as the points and dashed red lines in Figure 1(a). The distributions are different, due mainly to the smaller electron efficiency in the forward region at high $|\eta|$, the gap in electron acceptance at $1.37 < |\eta| < 1.52$, and the reduction in muon acceptance at $\eta \approx 0$ due to detector services. The electron and muon efficiencies also evolve differently with p_T . To minimise physics modelling uncertainties in the measurement of $R_W^{\mu/e}$, it is important that the kinematic dependencies of the electron and muon identification efficiencies are as similar as possible. This was achieved by applying an η - and p_T -dependent weight to each muon, as shown in Figure 1(b). The weights were derived so as to equalise the two-dimensional distributions of lepton p_T and η in simulated ee and $\mu\mu$ $t\bar{t}$ events, and normalised so that the total number of selected events is similar in the two channels. The effect on the muon η distribution is shown by the blue solid line in Figure 1(a). The muon efficiency loss at $\eta \approx 0$ was compensated over a wide region corresponding to a single bin with $|\eta| < 0.5$ to avoid giving muons at $\eta \approx 0$ large weights, but the physics modelling effects in this region are small. The muon efficiency weighting affects the event counts in the $t\bar{t} \rightarrow \mu\mu$ and $e\mu$ selections, and the inclusive $Z \rightarrow \mu\mu$ selection. It was applied to both data and simulation, and is included in all distributions, event counts and efficiencies shown in this paper.

Figure 2 shows comparisons of data and simulation for selected events in the ee (left column) and $\mu\mu$ (right column) channels, additionally requiring $|m_{\ell\ell} - m_Z| > 10$ GeV to reduce the Z +jets contribution. The simulation prediction uses the reference values for the $t\bar{t}$ and Z cross-sections given in Section 2 and assumes $R_W^{\mu/e} = R_Z^{\mu\mu/ee} = 1$. The baseline prediction shown by the black histogram uses POWHEG + PYTHIA8 $t\bar{t}$ events, which are known not to reproduce the top quark p_T spectrum measured in data [72] or predicted by NNLO calculations [73]. The red dotted line shows the prediction from POWHEG + PYTHIA8 reweighted using a linear function of top quark p_T as discussed in Ref. [50] in order to better describe the measurement of Ref. [72]. The green dashed line shows the prediction using $t\bar{t}$ events generated with POWHEG + HERWIG7. Figure 2(a–b) shows the multiplicity of b -tagged jets, $N_{b\text{-tag}}$, with the simulation normalised to the same integrated luminosity as the data; the simulation describes the data well for $N_{b\text{-tag}} \leq 2$, but shows a deficit for $N_{b\text{-tag}} \geq 3$. Figure 2(c–f) shows the lepton p_T and $|\eta|$ distributions for the $t\bar{t}$ -dominated samples with at least one b -tagged jet, normalising the simulation to the same number of selected events as the data to focus on shape comparisons. The samples with POWHEG + PYTHIA8 and POWHEG + HERWIG7 $t\bar{t}$ events both predict a harder p_T spectrum than the data, but the top-quark p_T -reweighted sample agrees well, as also seen in Ref. [50]. Similar features are seen in the $e\mu$ selection. The lepton p_T and $|\eta|$ distributions in the ee and $\mu\mu$ samples are similar (apart from at $\eta \approx 0$), demonstrating the effect of the muon efficiency weighting described above.

4 Analysis method

The $t\bar{t}$ cross-section was measured in each dilepton channel by fitting the numbers of selected events with one or two b -tagged jets to predictions based on the assumed $t\bar{t}$ cross-section, leptonic selection efficiencies $\epsilon_{\ell\ell}$ and estimated non- $t\bar{t}$ background. In the same-flavour channels, the dilepton invariant mass $m_{\ell\ell}$ was also exploited to separate signal events from the dominant Z +jets background. This method allows the efficiency $\epsilon_b^{\ell\ell'}$ for reconstructing and b -tagging a b -jet from the top quark decay to be determined from the data (separately for $\ell\ell' = ee, e\mu$ and $\mu\mu$), and minimises uncertainties due to the modelling of additional jets from QCD radiation in the $t\bar{t}$ events.

Following Ref. [50], the inclusive $t\bar{t}$ cross-section was determined in the $e\mu$ channel from the number of opposite-charge events with one ($N_1^{e\mu}$) or two ($N_2^{e\mu}$) b -tagged jets. The two event counts satisfy the tagging equations

$$\begin{aligned} N_1^{e\mu} &= L\sigma_{t\bar{t}} \epsilon_{e\mu} g_{e\mu}^{t\bar{t}} 2\epsilon_b^{e\mu} (1 - C_b^{e\mu} \epsilon_b^{e\mu}) + \sum_{k=\text{bkg}} s_1^k g_{e\mu}^k N_1^{e\mu,k} \text{ and} \\ N_2^{e\mu} &= L\sigma_{t\bar{t}} \epsilon_{e\mu} g_{e\mu}^{t\bar{t}} C_b^{e\mu} (\epsilon_b^{e\mu})^2 + \sum_{k=\text{bkg}} s_2^k g_{e\mu}^k N_2^{e\mu,k}, \end{aligned} \quad (1)$$

where L is the integrated luminosity of the sample, $\epsilon_{e\mu}$ is the efficiency for a $t\bar{t}$ event to pass the opposite-charge $e\mu$ selection (including the simulated values of the $W \rightarrow \ell\nu$ branching ratios), and $g_{e\mu}^{t\bar{t}}$ expresses possible deviations of these branching ratios from their simulated values. The parameter $C_b^{e\mu} \approx 1$ is a correlation coefficient that accounts for the fact that the tagging probabilities of the two b -quark jets from the top decays are not completely independent. It was evaluated from simulation as $C_b^{e\mu} = 4N_{e\mu}^{t\bar{t}} N_2^{t\bar{t}} / (N_1^{t\bar{t}} + 2N_2^{t\bar{t}})^2$, where $N_{e\mu}^{t\bar{t}}$ is the number of selected $e\mu$ $t\bar{t}$ events and $N_1^{t\bar{t}}$ and $N_2^{t\bar{t}}$ are the numbers of such events with one and two b -tagged jets [50]. Background contributions to N_1 and N_2 were divided into four sources indexed by k : Wt , Z +jets, dibosons and events with at least one misidentified lepton. The estimate of each background k was scaled by a factor s_n^k for events with $n = 1$ or 2 b -tagged jets, and additionally scaled by $g_{e\mu}^k$ to allow for changes in the W or Z leptonic branching ratios.

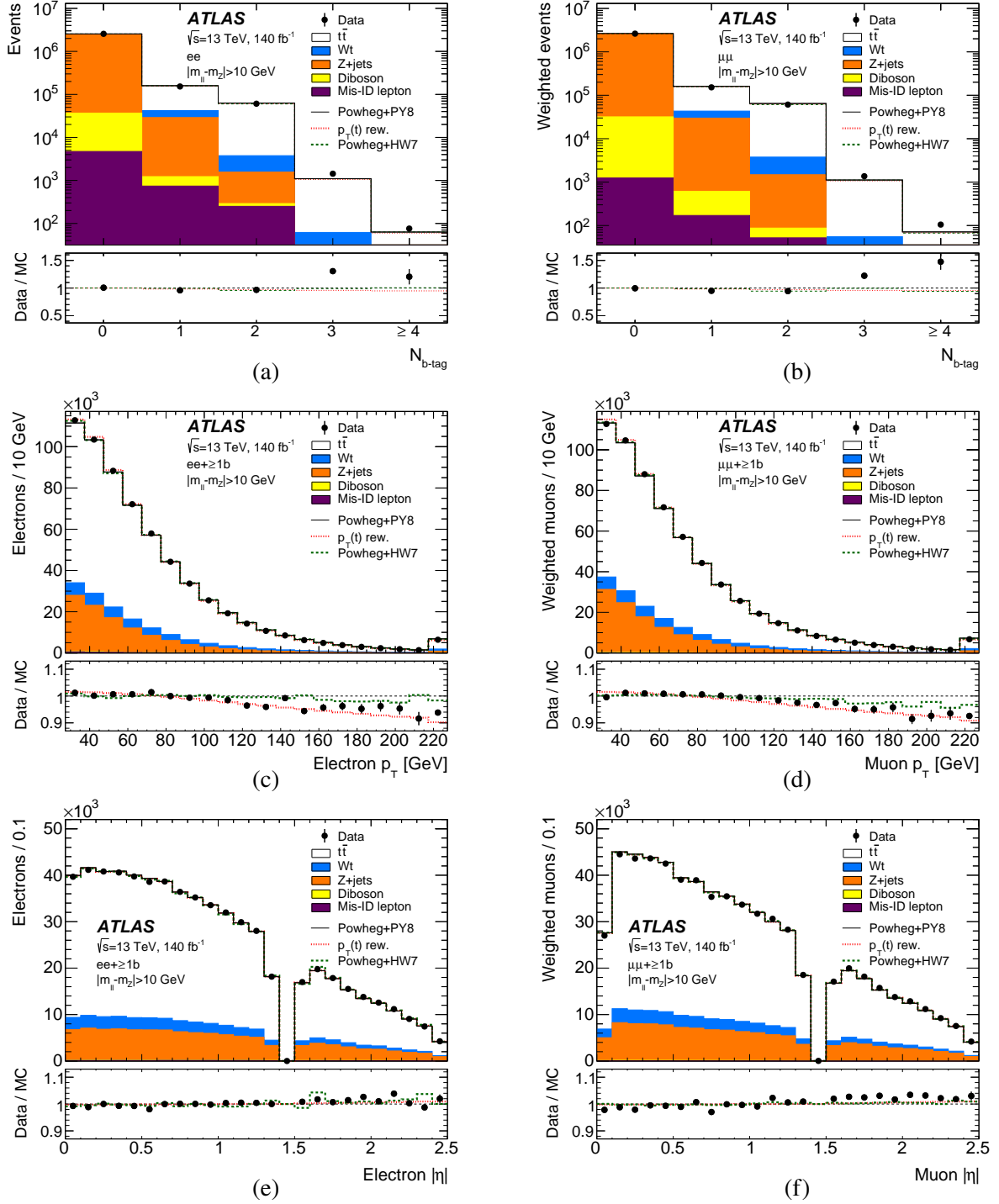


Figure 2: Distributions of (a, b) the number of b -tagged jets in selected opposite-sign dilepton events with $|m_{\ell\ell} - m_Z| > 10 \text{ GeV}$ (without applying the b -tagged jet multiplicity requirement), together with (c, d) the lepton transverse momentum and (e, f) the lepton pseudorapidity in such events with at least one b -tagged jet, showing ee (left column) and weighted $\mu\mu$ (right column) events separately. The data is shown by the points with statistical error bars, compared to the prediction from simulation normalised to the data integrated luminosity in (a, b) and to the same number of selected events in (c-f). The predicted contributions from $t\bar{t}$, Wt , Z +jets, dibosons and events with misidentified leptons are shown separately. The red dotted line shows the prediction with the reweighted top quark p_T distribution, and the green dashed line that with POWHEG + HERWIG7 $t\bar{t}$ events instead of POWHEG + PYTHIA8. The lower plots show the ratio of data to the baseline simulation, and the ratios of the alternative simulation predictions to the baseline. The last bins include the overflows in plots (a-d).

In the same-flavour channels, the events were divided into six bins of $m_{\ell\ell}$ to separate the $t\bar{t}$ signal from the large Z +jets background. The bins were indexed by subscript m , with lower bin boundaries at 30, 71, 81, 101, 111 and 151 GeV, the last bin including all events with $m_{\ell\ell} > 151$ GeV. Using the extension of the tagging formalism introduced in Ref. [74], the numbers of opposite-charge $\ell\ell$ events in each bin m with one and two b -tagged jets, $N_{1,m}^{\ell\ell}$ and $N_{2,m}^{\ell\ell}$ can then be expressed as

$$\begin{aligned} N_{1,m}^{\ell\ell} &= L\sigma_{t\bar{t}}\epsilon_{\ell\ell}g_{\ell\ell}^{t\bar{t}}2\epsilon_b^{\ell\ell}(1-C_b^{\ell\ell}\epsilon_b^{\ell\ell})f_{1,m}^{\ell\ell,t\bar{t}} + \sum_{k=\text{bkg}} s_1^k g_{\ell\ell}^k f_{1,m}^{\ell\ell,k} N_1^{\ell\ell,k} \text{ and} \\ N_{2,m}^{\ell\ell} &= L\sigma_{t\bar{t}}\epsilon_{\ell\ell}g_{\ell\ell}^{t\bar{t}}C_b^{\ell\ell}(\epsilon_b^{\ell\ell})^2 f_{2,m}^{\ell\ell,t\bar{t}} + \sum_{k=\text{bkg}} s_2^k g_{\ell\ell}^k f_{2,m}^{\ell\ell,k} N_2^{\ell\ell,k}, \end{aligned} \quad (2)$$

with separate selection efficiencies $\epsilon_{\ell\ell}$ and correlation coefficients $C_b^{\ell\ell}$ for each same-flavour channel ($\ell\ell = ee$ or $\mu\mu$). The coefficients $f_{1,m}^{\ell\ell,k}$ and $f_{2,m}^{\ell\ell,k}$ describe the $m_{\ell\ell}$ distributions, giving the fractions of events that appear in each mass bin, separately for each dilepton flavour $\ell\ell$, event source k and b -tagged jet multiplicity (1 or 2).

This analysis allows the branching ratios $\mathcal{B}(W \rightarrow e\nu)$ and $\mathcal{B}(W \rightarrow \mu\nu)$ to differ via a parameter Δ_W , whilst keeping their average fixed to $\bar{W} = 0.1082$, the Standard Model prediction used in the simulation. In this model

$$R_W^{\mu/e} = \frac{\mathcal{B}(W \rightarrow \mu\nu)}{\mathcal{B}(W \rightarrow e\nu)} = \frac{\bar{W}(1 + \Delta_W)}{\bar{W}(1 - \Delta_W)}, \quad (3)$$

so that $\Delta_W = (R_W^{\mu/e} - 1)/(R_W^{\mu/e} + 1)$. The selected $t\bar{t}$ dilepton samples also include events where one or both leptons arise from a $W \rightarrow \tau \rightarrow e/\mu$ decay, and the branching ratios for $W \rightarrow \tau\nu$, $\tau \rightarrow e\nu\bar{\nu}$ and $\tau \rightarrow \mu\nu\bar{\nu}$ were kept fixed at the values in the simulation. With these assumptions, the factors $g_{\ell\ell'}^{t\bar{t}}$ in Eqs. (1) and (2) are given by

$$\begin{aligned} g_{ee}^{t\bar{t}} &= f_{0\tau}^{ee}(1 - \Delta_W)^2 & + f_{1\tau}^{ee}(1 - \Delta_W) & + f_{2\tau}^{ee} \\ g_{e\mu}^{t\bar{t}} &= f_{0\tau}^{e\mu}(1 - \Delta_W)(1 + \Delta_W) & + f_{1\tau}^{e\mu} & + f_{2\tau}^{e\mu}, \\ g_{\mu\mu}^{t\bar{t}} &= f_{0\tau}^{\mu\mu}(1 + \Delta_W)^2 & + f_{1\tau}^{\mu\mu}(1 + \Delta_W) & + f_{2\tau}^{\mu\mu} \end{aligned} \quad (4)$$

where the parameters $f_{n\tau}^{\ell\ell'}$ give the fractions in each selected dilepton sample where n leptons resulted from $W \rightarrow \tau \rightarrow e/\mu$ rather than direct $W \rightarrow e/\mu$ decays. These fractions were taken from simulation, and are around $f_{0\tau}^{\ell\ell'} = 0.88$, $f_{1\tau}^{\ell\ell'} = 0.11$ and $f_{2\tau}^{\ell\ell'} = 0.004$ for all three dilepton flavour combinations. Increasing $f_{1\tau}^{\ell\ell'}$ by 1.3% and $f_{2\tau}^{\ell\ell'}$ by 2.6%, corresponding to the uncertainty of 1.3% in $\mathcal{B}(W \rightarrow \tau\nu)/\mathcal{B}(W \rightarrow \mu\nu)$ measured in Ref. [75], has a negligible effect on the fitted value of $R_W^{\mu/e}$ from this analysis.

The estimates of the Wt and diboson backgrounds $N_n^{\ell\ell',k}$ in Eqs. (1) and (2) (with $k = Wt$ or diboson) were taken directly from simulation, with s_n^k fixed to unity. However, since Wt events have two real W bosons and the diboson background is dominated by WW production, the corresponding values of $g_{\ell\ell'}^k$ were set equal to $g_{\ell\ell'}^{t\bar{t}}$ given by Eq. (4), effectively treating these backgrounds as signal for the determination of $R_W^{\mu/e}$. The normalisation factors $s_1^{Z+\text{jets}}$ and $s_2^{Z+\text{jets}}$ for the Z +jets background were determined from data, exploiting the binning of the same-flavour dilepton events in $m_{\ell\ell}$, and applying the same factors to all three dilepton channels. However, the introduction of the normalisation measurement of $R_Z^{\mu\mu/ee}$ also affects the Z +jets background estimate. Potential deviations of $R_Z^{\mu\mu/ee}$ from unity were described by a parameter Δ_Z , related to $R_Z^{\mu\mu/ee}$ by

$$R_Z^{\mu\mu/ee} = \frac{\mathcal{B}(Z \rightarrow \mu\mu)}{\mathcal{B}(Z \rightarrow ee)} = \frac{\bar{Z}(1 + \Delta_Z)}{\bar{Z}(1 - \Delta_Z)}, \quad (5)$$

where \bar{Z} is the average $Z \rightarrow \ell\ell$ branching ratio and $\Delta_Z = (R_Z^{\mu\mu/ee} - 1)/(R_Z^{\mu\mu/ee} + 1)$, in analogy to Eq. (3). Potential biases in the modelling of the lepton isolation efficiency in the busy hadronic environment of $Z+b$ -jet events (in particular differences between electrons and muons as discussed in Section 5) were taken into account by an additional ratio $R_{Z+b}^{\mu\mu/ee}$ and associated parameter $\Delta_{Z+b} = (R_{Z+b}^{\mu\mu/ee} - 1)/(R_{Z+b}^{\mu\mu/ee} + 1)$. With these ingredients, the values of $g_{\ell\ell'}^k$ for Z +jets events are given by

$$\begin{aligned} g_{ee}^{Z+jets} &= (1 - \Delta_Z)(1 - \Delta_{Z+b}) \\ g_{e\mu}^{Z+jets} &= 1 \\ g_{\mu\mu}^{Z+jets} &= (1 + \Delta_Z)(1 + \Delta_{Z+b}) \end{aligned} \quad . \quad (6)$$

The contributions to the backgrounds in Eqs. (1) and (2) from events with misidentified leptons were evaluated using a partially data-driven method, as discussed below.

The factors $g_{\ell\ell'}^{t\bar{t}}$, giving sensitivity to the W -boson branching ratios are related to Δ_W and hence $R_W^{\mu/e}$ by Eqs. (3) and (4). However, to reduce sensitivity to uncertainties in the electron and muon identification efficiencies, the fit was not performed with $R_W^{\mu/e}$ directly, but instead using $R_{WZ}^{\mu/e}$ and $R_Z^{\mu\mu/ee}$, where

$$R_{WZ}^{\mu/e} = \frac{R_W^{\mu/e}}{\sqrt{R_Z^{\mu\mu/ee}}} = \frac{\mathcal{B}(W \rightarrow \mu\nu)}{\mathcal{B}(W \rightarrow e\nu)} \cdot \sqrt{\frac{\mathcal{B}(Z \rightarrow ee)}{\mathcal{B}(Z \rightarrow \mu\mu)}} \quad (7)$$

The normalisation to $\sqrt{R_Z^{\mu\mu/ee}}$ ensures that the numerator and denominator of $R_{WZ}^{\mu/e}$ each contain one power of the electron and muon efficiencies, reducing the sensitivity of $R_{WZ}^{\mu/e}$ to uncertainties on these efficiencies. The value of $R_Z^{\mu\mu/ee}$ needed in Eq. (7) was determined from the event counts in the inclusive $Z \rightarrow \ell\ell$ selection, N_Z^{ee} and $N_Z^{\mu\mu}$, given by

$$\begin{aligned} N_Z^{ee} &= L \sigma_{Z \rightarrow \ell\ell} \epsilon_{Z \rightarrow ee} (1 - \Delta_Z) + \sum_{k=\text{bkg}} s_Z^k N_Z^{ee,k} \text{ and} \\ N_Z^{\mu\mu} &= L \sigma_{Z \rightarrow \ell\ell} \epsilon_{Z \rightarrow \mu\mu} (1 + \Delta_Z) + \sum_{k=\text{bkg}} s_Z^k N_Z^{\mu\mu,k}, \end{aligned} \quad (8)$$

where $\epsilon_{Z \rightarrow ee}$ and $\epsilon_{Z \rightarrow \mu\mu}$ are the selection efficiencies in simulation assuming equal branching ratios for $Z \rightarrow ee$ and $Z \rightarrow \mu\mu$, and the factors involving Δ_Z express the effects of deviations of $R_Z^{\mu\mu/ee}$ from unity. Five sources of backgrounds were considered, indexed by k : dibosons, $Z \rightarrow \tau\tau \rightarrow ee/\mu\mu$, $t\bar{t}$, Wt and events with misidentified leptons. The first four were estimated from simulation, with the $t\bar{t}$ background being scaled according to the fitted value of $\sigma_{t\bar{t}}$ via its normalisation $s_Z^{t\bar{t}}$, and all other s_Z^k values were fixed to unity. The misidentified-lepton background was estimated from data as discussed below.

All fit parameters were determined simultaneously using a single maximum likelihood fit to the observed event counts $N_1^{e\mu}$ and $N_2^{e\mu}$ in the $e\mu$ channel, the observed counts in each dilepton invariant mass bin $N_{1,m}^{\ell\ell}$ and $N_{2,m}^{\ell\ell}$ for each same-flavour channel, and the observed counts N_Z^{ee} and $N_Z^{\mu\mu}$ in the inclusive $Z \rightarrow \ell\ell$ selections. A Gaussian likelihood formulation was used, taking into account the probability distributions of the weighted event counts in the $\mu\mu$ and $e\mu$ channels. The fit has ten free parameters: the four parameters of interest $\sigma_{t\bar{t}}$, $\sigma_{Z \rightarrow \ell\ell}$, $R_{WZ}^{\mu/e}$ and $R_Z^{\mu\mu/ee}$, the three b -tagged jet efficiencies $\epsilon_b^{\ell\ell'}$, the scale factors s_1^{Z+jets} and s_2^{Z+jets} for the Z +jets background, and the Z +jets isolation efficiency parameter $R_{Z+b}^{\mu\mu/ee}$. Apart from the integrated luminosity L and the misidentified lepton backgrounds, all other quantities were determined from simulation, namely the efficiencies $\epsilon_{\ell\ell'}$, $\epsilon_{Z \rightarrow ee}$ and $\epsilon_{Z \rightarrow \mu\mu}$, b -tagging correlations $C_b^{\ell\ell'}$, τ fractions

$f_{n\tau}^{\ell\ell'}$, background counts $N_1^{\ell\ell',k}$, $N_2^{\ell\ell',k}$ and $N_Z^{\ell\ell,k}$, and mass distributions $f_{1,m}^{\ell\ell,k}$ and $f_{2,m}^{\ell\ell,k}$. In the baseline simulation, the $t\bar{t}$ dilepton selection efficiencies are $\epsilon_{ee} = 0.316\%$, $\epsilon_{e\mu} = 0.639\%$ and $\epsilon_{\mu\mu} = 0.314\%$, the correlation coefficients $C_b^{\ell\ell'}$ are about 1.003 for all dilepton flavours, and the Z selection efficiencies are $\epsilon_{Z\rightarrow ee} = 16.8\%$ and $\epsilon_{Z\rightarrow\mu\mu} = 17.3\%$. The fitted Z cross-section and $R_Z^{\mu\mu/ee}$ are constrained by the inclusive $Z \rightarrow \ell\ell$ selection, $\sigma_{t\bar{t}}$ is mainly determined from the $e\mu$ channel, and $R_{WZ}^{\mu/e}$, $s_1^{Z+\text{jets}}$, $s_2^{Z+\text{jets}}$ and $R_{Z+b}^{\mu\mu/ee}$ are mainly determined from the same-flavour $t\bar{t}$ selections. Around 1% of the events in the inclusive $Z \rightarrow \ell\ell$ selections are also included in the same-flavour $t\bar{t}$ selections, but this overlap has a negligible effect on the analysis. The analysis procedure was validated using simulation-based pseudo-experiments with various input values of $\sigma_{t\bar{t}}$, $\sigma_{Z\rightarrow\ell\ell}$, $R_W^{\mu/e}$ and $R_Z^{\mu\mu/ee}$. These tests verified that the fit gives correct uncertainty estimates and that any residual biases are much smaller than the data statistical uncertainty.

The background from events with misidentified leptons in the $t\bar{t}$ selection was estimated using same-sign (SS) control samples, selected as described in Section 3 but requiring two leptons of the same rather than opposite electric charges. In an extension of the method described in Ref. [50], the misidentified lepton background $N_j^{i,\text{mis-id}}$ in invariant mass bin i (using a single bin for the $e\mu$ channel) with j b -tagged jets, was estimated from the number of SS events in data, $N_j^{i,\text{d,SS}}$, after subtracting the number of prompt SS events $N_j^{i,\text{prompt,SS}}$ estimated using simulation, and then scaling by the ratio R_j^i of misidentified-lepton events in the opposite-sign (OS) and SS samples in simulation:

$$\begin{aligned} N_j^{i,\text{mis-id}} &= R_j^i (N_j^{i,\text{d,SS}} - N_j^{i,\text{prompt,SS}}), \\ R_j^i &= \frac{N_j^{i,\text{mis-id,OS}}}{N_j^{i,\text{mis-id,SS}}}. \end{aligned} \quad (9)$$

To reduce the pollution of the SS ee and $e\mu$ samples from true OS events where an electron charge sign was misreconstructed (particularly for $m_{\ell\ell}$ close to the $Z \rightarrow ee$ resonance), electrons in the SS sample were required to be accepted by a charge misidentification boosted decision tree (BDT) [28] that reduces the rate of electron charge misidentification by up to an order of magnitude. The values of R_j^i are sensitive to the composition of the misidentified lepton background in simulation, and the corresponding uncertainty was assessed by removing the photon conversion, misidentified hadron and muon decay in flight contributions in turn, and recalculating R_j^i . The modelling of the charge misidentification BDT was studied using $Z \rightarrow ee$ events. An uncertainty of 25% on the prompt SS contribution was assumed, covering the uncertainties in the dominant contributing processes ($t\bar{t} + W$, Z and H , and WZ) and in the rate of electron charge misidentification. The misidentified lepton background was evaluated to contribute 0.4–1.2% of the ee opposite-sign sample (depending on $m_{\ell\ell}$ and the b -tagged jet multiplicity), 0.2–0.8% of the $e\mu$ sample and less than 0.4% of the $\mu\mu$ sample. The estimates from data are compatible with the predictions from simulation within the evaluated uncertainties of 30–70%. The simulation was also found to provide a good description of data SS control samples where the isolation requirements were inverted to increase the misidentified lepton contributions.

The misidentified lepton background in the $Z \rightarrow \ell\ell$ selection was estimated from data in the region $66 \text{ GeV} < m_{\ell\ell} < 81 \text{ GeV}$ and $101 \text{ GeV} < m_{\ell\ell} < 116 \text{ GeV}$ by defining two orthogonal control samples (B and C) enriched in misidentified leptons. The B samples were defined by requiring the lower- p_T lepton to fail the isolation requirement, and in the case of electrons also requiring it to fail the Medium identification requirement but pass a looser requirement. The C samples were defined by requiring the two leptons to have the same rather than opposite electric charges. To reduce the background from genuine $Z \rightarrow ee$ events where one electron charge sign was mismeasured, both electrons were required to be accepted by the charge

misidentification BDT. A third control sample (D) was defined by applying both B and C requirements. Assuming the B and C requirements to be uncorrelated, the number $N_A^{\text{mis-id}}$ of misidentified lepton events in the A (signal) sample was then estimated from $N_A^{\text{mis-id}} = f N_B^{\text{mis-id}} N_C^{\text{mis-id}} / N_D^{\text{mis-id}}$ where $N_X^{\text{mis-id}}$ is the number of observed events in region X ($X = B, C$ or D) after subtracting the prompt lepton contribution using simulation, and the factor $f = (50 \text{ GeV}) / (15 \text{ GeV} + 15 \text{ GeV}) = 5/3$ linearly interpolates the estimate over the complete mass range $66 \text{ GeV} < m_{\ell\ell} < 116 \text{ GeV}$. The misidentified lepton contributions were found to be $0.39 \pm 0.37\%$ of the $Z \rightarrow ee$ sample and $0.06 \pm 0.27\%$ of the $Z \rightarrow \mu\mu$ sample, estimating the systematic uncertainties by using a tighter anti-isolation requirement in the B and D samples.

5 Lepton isolation efficiency measurements

The efficiency of the isolation requirements applied to the leptons was measured directly in data using a tag-and-probe methodology, separately for the $Z \rightarrow \ell\ell$ and busier $t\bar{t} \rightarrow \ell\ell$ environments, and for all leptons with $p_T > 20 \text{ GeV}$. In the $Z \rightarrow \ell\ell$ measurements, opposite-sign ee and $\mu\mu$ pairs were selected, requiring the tag lepton to satisfy the identification and isolation cuts described in Section 3 and to be matched to a corresponding trigger signature. The probe lepton was only required to satisfy the identification cuts, and the isolation efficiency was measured from the fraction of probe leptons with dilepton invariant mass in the range $80 \text{ GeV} < m_{\ell\ell} < 102 \text{ GeV}$ that pass the isolation requirement, after correcting for the background from non-prompt leptons, which reaches up to 1% in the samples failing the isolation requirement at low lepton p_T . This background was estimated using a template fit to the $m_{\ell\ell}$ distribution, with the templates for prompt leptons obtained from simulation, and those from misidentified lepton events obtained from control samples with modified selection cuts. The isolation efficiencies were measured as a function of lepton p_T for four bins in $|\eta|$. The data results are compared to the corresponding isolation efficiencies predicted by the POWHEG + PYTHIA8 and SHERPA $Z \rightarrow \ell\ell$ simulation samples in Figure 3(a, b). The data efficiencies in the lowest bin used in the analysis ($25 \text{ GeV} < p_T < 30 \text{ GeV}$) are around 80–85%, increasing to 99% at high lepton p_T . The POWHEG + PYTHIA8 simulation underestimates the electron efficiency by around 2% at low p_T , whereas the muon efficiency is overestimated by 1%. The SHERPA simulation also underestimates the electron efficiency by about 2% at low p_T , but overestimates the muon efficiency by about 3%.

The corresponding efficiencies in the $t\bar{t}$ environment were measured using $e\mu$ events with at least one b -tagged jet. Here, an invariant mass cut cannot be applied to suppress misidentified lepton background and the fraction of background in the probe lepton samples failing isolation reaches 25–30% in the samples with one b -tagged jet, but remains below 10% when two b -tagged jets are present. This background was estimated using same-charge events in a similar way as for the main analysis selection discussed in Section 4. The efficiencies were measured as a function of lepton p_T for $|\eta| < 1.5$ and $|\eta| > 1.5$, combining the results from the one b -tagged and two b -tagged jet samples, which were found to be consistent. The results from data are compared with the baseline POWHEG + PYTHIA8 $t\bar{t}$ simulation in Figure 3(c, d). In data, the efficiencies vary from around 80% at $p_T = 25 \text{ GeV}$ to 97–98% at high p_T , and the simulation underestimates the efficiency at low p_T for electrons, and overestimates it for muons, similar to the $Z \rightarrow \ell\ell$ case.

The ratios of data to simulation efficiencies shown in Figure 3 were used to define multiplicative efficiency corrections (scale factors) that were applied to simulation on a per-lepton basis. The systematic uncertainties on the $Z \rightarrow \ell\ell$ scale factors were assessed by varying selection cuts for the fit and control regions, leading to uncertainties of less than 0.05% on the values of $\epsilon_{Z \rightarrow ee}$ and $\epsilon_{Z \rightarrow \mu\mu}$. The systematic uncertainties on

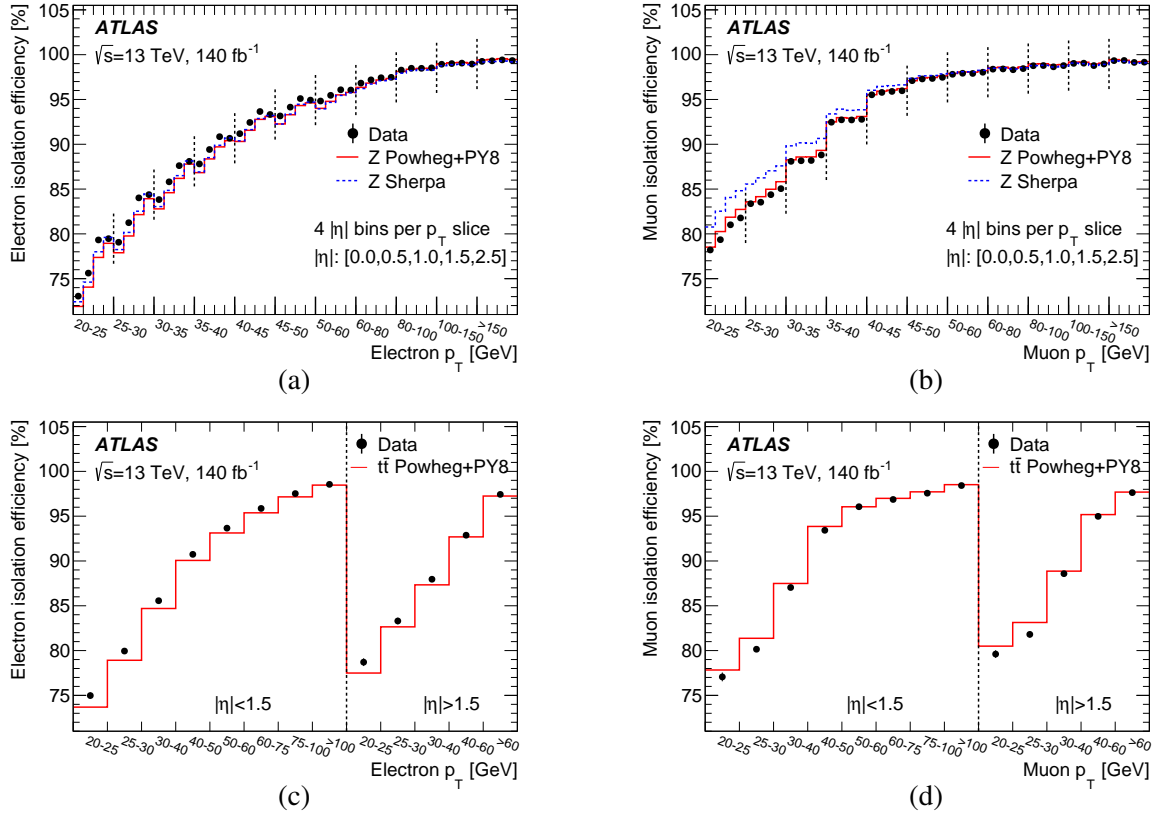


Figure 3: Lepton isolation efficiencies measured for (a, c) electrons and (b, d) muons as functions of lepton p_T and $|\eta|$. The data is shown by the points with error bars and the simulation by the histograms. The upper plots show measurements in $Z \rightarrow \ell\ell$ events, with four η bins (with boundaries at $|\eta| = 0, 0.5, 1.0, 1.5$ and 2.5) shown sequentially for each p_T slice. The lower plots show measurements in $t\bar{t} \rightarrow e\mu$ events, separately for leptons with $|\eta| < 1.5$ in the leftmost bins and $|\eta| > 1.5$ in the rightmost bins. The data is compared to POWHEG + PYTHIA8 simulation (without isolation efficiency scale factors) for both Z and $t\bar{t}$ events, and additionally to SHERPA Z events.

the $t\bar{t}$ scale factors include the modelling of prompt-lepton contributions to the same-charge samples, the extrapolation of misidentified leptons from same- to opposite-charge and the modelling of the electron charge misassignment, giving uncertainties of around 0.1% per lepton. The isolation efficiency scale factors calculated for POWHEG + PYTHIA 8 $t\bar{t}$ events were applied to all simulated events passing the $t\bar{t}$ selections, including the Z +jets events simulated with SHERPA. However, the results from inclusive $Z \rightarrow \mu\mu$ events shown in Figure 3(b) suggest that the modelling of the muon isolation efficiency in SHERPA Z +jets events may require different corrections to those measured for POWHEG + PYTHIA 8 $t\bar{t}$ events. A potential extra difference in lepton isolation efficiencies between $Z(\rightarrow ee)$ +jets and $Z(\rightarrow \mu\mu)$ +jets was therefore included in the likelihood fit, represented by the floating parameter $R_{Z+b}^{\mu\mu/ee}$ appearing via Δ_{Z+b} in Eq. (6).

6 Systematic uncertainties

Systematic uncertainties arise from uncertainties in the quantities appearing in Eqs. (1), (2) and (8). Each systematic uncertainty was evaluated by calculating the effect on all input parameters ($\epsilon_{\ell\ell'}$, $C_b^{\ell\ell'}$, $\epsilon_{Z \rightarrow \ell\ell}$, background estimates etc.) simultaneously and repeating the fit. For some sources of uncertainty,

e.g. lepton efficiencies and PDF variations, the effects on the different input quantities are only partially correlated, and this was taken into account by using the full covariance matrix expressing the dependence of the fit result on each parameter and their correlations. The resulting systematic uncertainties on $\sigma_{t\bar{t}}$, $\sigma_{Z\rightarrow\ell\ell}$, $R_{WZ}^{\mu/e}$ and $R_Z^{\mu\mu/ee}$ are discussed below, and summarised in Table 4 in Section 7. The methodologies generally follow those described in Ref. [50].

$t\bar{t}$ modelling: The values of $\epsilon_{\ell\ell'}$, $C_b^{\ell\ell'}$, $f_{n\tau}^{\ell\ell'}$ and $f_{j,m}^{\ell\ell',t\bar{t}}$ depend on the choice of $t\bar{t}$ simulation model. The uncertainty due to the choice of generator (in particular the matrix-element matching algorithm) was assessed by using the sample generated with AMC@NLO + PYTHIA8 instead of POWHEG + PYTHIA8, and the parton shower, hadronisation and underlying event modelling uncertainty was assessed by using the POWHEG + HERWIG7.1 sample. Uncertainties due to initial- and final-state radiation were assessed by using event weights to vary the QCD renormalisation and factorisation scales in the matrix element independently by factors of two up and down from their default values, by changing the h_{damp} parameter [41] from $1.5m_t$ to $3m_t$, using the VAR3C A14 tune variations [40], and by changing the renormalisation and factorisation scales used in the parton shower, again by factors of two up and down. Since some of these variations also induce changes in the amount of activity close to the leptons, they affect the simulated lepton isolation efficiencies. These variations were therefore evaluated without applying lepton isolation cuts, to avoid double-counting differences absorbed in the lepton isolation efficiency scale factors described in Section 5. The fraction of $t\bar{t}$ events with at least three b -jets at generator level was also varied by $\pm 50\%$, motivated by the discrepancies seen for $N_{b\text{-tag}} \geq 3$ in Figure 2(a, b), and the top quark mass was varied by ± 1 GeV.

Top quark p_T modelling: As none of the considered $t\bar{t}$ modelling variations reproduce the data lepton p_T distribution, the full effect of the top quark p_T reweighting shown as the red dotted line in Figure 2(c, d) was included as a systematic uncertainty.

Parton distribution functions: The PDF uncertainties were evaluated using the 30 eigenvectors of the PDF4LHC15 meta-PDF set [76], taking into account the differing effects on the $t\bar{t}$, Wt , Z +jets and inclusive Z processes and their correlations.

Single top modelling: The uncertainties on modelling the Wt background were assessed using alternative samples generated with AMC@NLO + PYTHIA8 and POWHEG + HERWIG7.0 [77], by varying the renormalisation and factorisation scales and by using the VAR3C tune variations, in the same way as for $t\bar{t}$ events. The Wt cross-section was varied by the QCD scale uncertainty of 2.4%, the PDF-related cross-section uncertainty being already accounted for coherently with the $t\bar{t}$ and Z PDF variations.

Single-top/ $t\bar{t}$ interference: The uncertainty in modelling the interference between the Wt and $t\bar{t}$ final states was assessed by using the diagram subtraction scheme [51, 52] instead of the baseline diagram removal scheme.

Z (+jets) modelling: Uncertainties in the Z +jets background in the $t\bar{t}$ selection were evaluated by changing the QCD factorisation and renormalisation scales in the SHERPA samples by factors of two up and down from their default values, separately or together and excluding variations in opposite directions. The SHERPA samples were also used to evaluate corresponding variations in $\epsilon_{Z\rightarrow ee}$ and $\epsilon_{Z\rightarrow\mu\mu}$ for the inclusive $Z \rightarrow \ell\ell$ selection. Simultaneous changes of both scales were found to have the largest effects on both $R_{WZ}^{\mu/e}$ and $R_Z^{\mu\mu/ee}$, and were used to define the corresponding uncertainty. Half the effect of the $p_T^{\ell\ell}$ weighting applied to the POWHEG + PYTHIA8 inclusive $Z \rightarrow \ell\ell$ samples was included as an additional Z modelling uncertainty.

Diboson modelling: The normalisation of the diboson contribution was varied by 20%, covering uncertainties in the cross-sections and acceptances. Alternative samples generated using POWHEG + PYTHIA8 instead of SHERPA were also considered.

Lepton energy/momentum scale and resolution: The electron energy scale and muon momentum scale and corresponding resolution were determined using $Z \rightarrow ee$ and $Z \rightarrow \mu\mu$ decays as discussed in Refs. [28, 29], and were varied within the corresponding uncertainties.

Lepton identification: The lepton identification efficiencies were measured using tag-and-probe techniques applied to $Z \rightarrow ee$ and $Z \rightarrow \mu\mu$ events [31, 32], as functions of lepton p_T and η for electrons, and η and ϕ for muons. The corresponding uncertainties are only partially correlated across p_T , η and ϕ , and the information was propagated to $\epsilon_{\ell\ell'}$ and $\epsilon_{Z \rightarrow \ell\ell}$ (and their correlations) by generating multiple sets of scale factor replicas whose variations represent the full uncertainty model. The uncertainties due to electron charge misidentification were studied using $Z \rightarrow ee$ events and taken into account using the same technique.

Lepton isolation: The lepton isolation efficiency uncertainties discussed in Section 5 were also propagated using scale factor replicas, and taken to be uncorrelated between electrons and muons, and between the $t\bar{t}$ and $Z \rightarrow \ell\ell$ selections.

Lepton trigger: The lepton trigger efficiencies were also measured in $Z \rightarrow ee$ and $Z \rightarrow \mu\mu$ events using tag-and-probe techniques [20, 21], and were varied within the corresponding uncertainties.

Jet energy scale and resolution: The jet energy scale was determined using a combination of simulation, test beam and in-situ measurements, and the jet energy resolution was studied using di-jet balance techniques [30]. The modelling of the pileup jet veto using the JVT requirement was studied using jets in $Z \rightarrow \mu\mu$ events [70].

b -tagging efficiency/mistag: The efficiency for reconstructing and tagging b -jets in $t\bar{t}$ events was measured in situ via the fit parameters $\epsilon_b^{\ell\ell'}$. However, the background yields and tagging correlations depend on the b -tagging efficiencies and mistag rates predicted by simulation, with the corresponding scale factors and uncertainties determined using $t\bar{t}$ and Z +jets events as described in Refs. [33, 78, 79].

Misidentified leptons: The uncertainties on the misidentified lepton backgrounds were evaluated as discussed in Section 4, and were taken to be uncorrelated between electrons and muons, and between the $t\bar{t}$ and $Z \rightarrow \ell\ell$ selections.

Simulation statistics: The limited size of the Monte Carlo simulation samples primarily affects the predictions of $\epsilon_{\ell\ell'}$ and $C_b^{\ell\ell'}$, and the fractions $f_{j,m}^{\ell\ell',t\bar{t}}$ of the Z +jets background entering each invariant mass bin.

Integrated luminosity: The integrated luminosity of the dataset was evaluated using the LUCID2 detector [80], complemented by measurements from the inner detector and calorimeters, and has an uncertainty of 0.83% [18].

Beam energy: The LHC beam energy is known to a precision of 0.1%, which translates into small uncertainties on $\sigma_{t\bar{t}}$ and $\sigma_{Z \rightarrow \ell\ell}$ as discussed in Ref. [50].

Table 2: Observed numbers of opposite-charge dilepton events (weighted events for the $e\mu$ and $\mu\mu$ channels) with one (upper block) and two (lower block) b -tagged jets in the $t\bar{t}$ selection in data, together with the estimated event counts from the fit prediction, including the associated statistical and systematic uncertainties. The five columns show the ee channel with $|m_{\ell\ell} - m_Z| > 10$ GeV (off- Z) and $|m_{\ell\ell} - m_Z| < 10$ GeV (on- Z), the $e\mu$ channel, and the $\mu\mu$ channel including off- Z and on- Z selections. The uncertainties in the total predictions are smaller than the individual component uncertainties due to correlations induced by the fit.

Event counts	$N_{1,\text{off-Z}}^{ee}$	$N_{1,\text{on-Z}}^{ee}$	$N_1^{e\mu}$	$N_{1,\text{off-Z}}^{\mu\mu}$	$N_{1,\text{on-Z}}^{\mu\mu}$
Data	222304	442108	405437	223085	448105
$t\bar{t}$	154800 ± 1700	24830 ± 850	361000 ± 4200	152500 ± 1800	24070 ± 860
Wt	17500 ± 1600	2770 ± 240	41500 ± 3800	17800 ± 1700	2730 ± 250
Z+jets	46880 ± 400	410700 ± 2000	859 ± 21	51010 ± 780	418000 ± 2000
Diboson	770 ± 160	3940 ± 840	790 ± 280	770 ± 160	3880 ± 830
Mis-ID leptons	1300 ± 500	360 ± 260	1740 ± 610	390 ± 150	172 ± 87
Total prediction	221280 ± 550	442600 ± 1100	405900 ± 1800	222390 ± 670	448900 ± 1100
Event counts	$N_{2,\text{off-Z}}^{ee}$	$N_{2,\text{on-Z}}^{ee}$	$N_2^{e\mu}$	$N_{2,\text{off-Z}}^{\mu\mu}$	$N_{2,\text{on-Z}}^{\mu\mu}$
Data	85936	37704	198502	86169	38512
$t\bar{t}$	79750 ± 920	13340 ± 480	191000 ± 1800	79770 ± 830	13180 ± 450
Wt	2860 ± 760	400 ± 110	6700 ± 1600	2940 ± 740	423 ± 90
Z+jets	2675 ± 68	23610 ± 590	78 ± 2	3095 ± 87	24110 ± 600
Diboson	67 ± 23	550 ± 110	29 ± 8	71 ± 30	570 ± 110
Mis-ID leptons	400 ± 290	96 ± 59	720 ± 520	350 ± 160	104 ± 56
Total prediction	85760 ± 360	38000 ± 190	198510 ± 440	86230 ± 300	38380 ± 210

7 Fit results

Table 2 shows the number of observed events in each of the dilepton channels of the $t\bar{t}$ selection together with the results of the fit, broken down into the estimated contributions from $t\bar{t}$, Wt , Z+jets, diboson and misidentified leptons. The counts are shown separately for events with one and two b -tagged jets, and separately for events off (with $|m_{\ell\ell} - m_Z| > 10$ GeV) and on (with $|m_{\ell\ell} - m_Z| < 10$ GeV) the Z resonance in the same-flavour channels. The full $m_{\ell\ell}$ distributions are shown in Figure 4. In the same-flavour samples with one b -tagged jet, the $t\bar{t}$ purity is about 70% and the background is dominated by Z+jets events. In the two b -tagged jets samples, the $t\bar{t}$ purity rises to 93%, with equal background contributions from Z+jets and Wt events. In the $e\mu$ channel, the Z+jets background is almost negligible, and the $t\bar{t}$ purity is 89% in the one b -tagged sample and 96% in the two b -tagged sample. Table 3 shows the corresponding event counts and predictions for the $Z \rightarrow \ell\ell$ selection; here the backgrounds are only around 0.5%.

Figure 4 shows that the fit generally models the data well, except for a data excess in the lowest $m_{\ell\ell}$ bin in all four same-flavour distributions, whose significance is however always less than two standard deviations. Part of this discrepancy can be attributed to the top-quark p_T mismodelling—the reweighted sample shown by the red dotted line in Figure 2 also predicts a softer $m_{\ell\ell}$ distribution for $t\bar{t}$ events, as also observed for the $m_{\ell\ell}$ distribution in the $t\bar{t}$ -dominated $e\mu$ channel. The effect of this reweighting defines the ‘Top quark p_T modelling’ uncertainty in Table 4 and is included in the cyan bands shown in Figure 4.

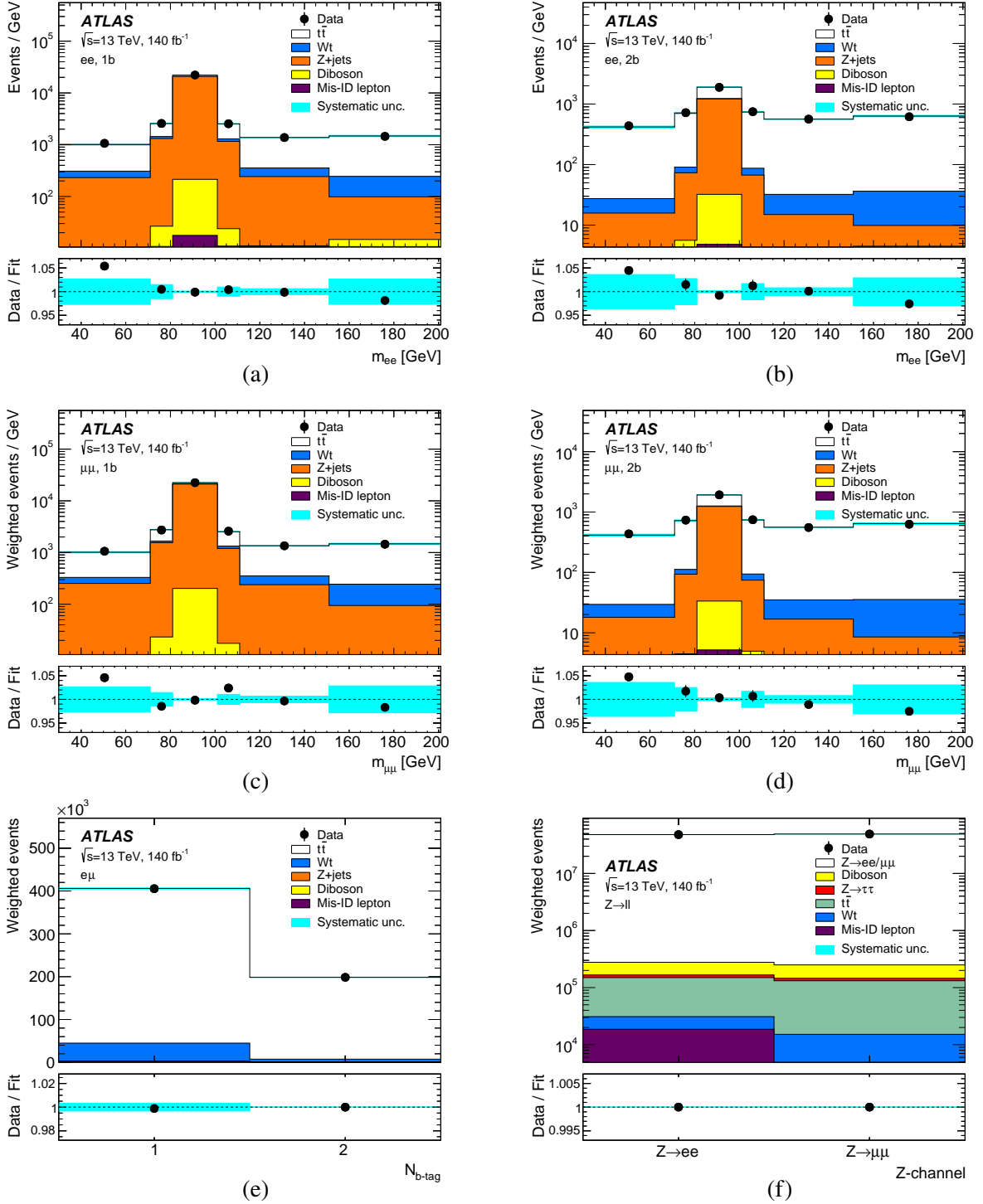


Figure 4: Results of the fit to data, showing the invariant mass distributions for the one and two b -tagged jet samples in the (a, b) ee and (c, d) $\mu\mu$ channels, (e) the b -tagged jet multiplicity in the $e\mu$ channel, and (f) the number of events in the inclusive $Z \rightarrow \ell\ell$ selection. The data are shown by the points with statistical error bars, and are compared with the results of the fit, showing the scaled contributions from $t\bar{t}$, Wt , Z +jets, dibosons, $Z \rightarrow \tau\tau$ and events with misidentified leptons. The total systematic uncertainty of the fit prediction in each bin is shown by the cyan band. The lower panels show the ratios of data to the fit predictions. In the invariant mass distributions, the last bin includes the overflow with $m_{\ell\ell} > 200$ GeV but is normalised to the displayed bin width.

Table 3: Observed numbers of opposite-charge dilepton events (weighted events for the $\mu\mu$ channel) in the inclusive $Z \rightarrow ee$ and $Z \rightarrow \mu\mu$ selections in data, together with the estimated event counts from the fit prediction, including the associated statistical and systematic uncertainties. The uncertainties in the total predictions are much smaller than the individual uncertainties due to correlations induced by the fit.

Event counts	$Z \rightarrow ee$	$Z \rightarrow \mu\mu$
Data	47898836	49016812
$Z \rightarrow \ell\ell$	47621000 ± 33000	48767000 ± 29000
Diboson	111000 ± 22000	104000 ± 21000
$Z \rightarrow \tau\tau$	16850 ± 140	13780 ± 110
$t\bar{t}$	119000 ± 14000	117000 ± 14000
Wt	12380 ± 890	12390 ± 880
Mis-ID leptons	19000 ± 18000	3000 ± 13000
Total prediction	47898800 ± 6900	49016800 ± 6200

The fit results for the cross-sections are

$$\begin{aligned}\sigma_{t\bar{t}} &= 809.5 \pm 1.1 \pm 20.1 \pm 7.5 \pm 1.9 \text{ pb} , \\ \sigma_{Z \rightarrow \ell\ell} &= 2019.4 \pm 0.2 \pm 20.7 \pm 16.8 \pm 1.8 \text{ pb} ,\end{aligned}$$

where the four uncertainties are due to data statistics, systematic effects, and the knowledge of the integrated luminosity and the LHC beam energy. As shown in Table 4, the $t\bar{t}$ cross-section result has a precision of 2.7%, dominated by the uncertainties from $t\bar{t}$ modelling, the top-quark p_T modelling and the integrated luminosity. It is compatible with the theoretical prediction discussed in Section 2 and with the result from the $e\mu$ channel alone reported in Ref. [81], taking into account the larger systematic uncertainty in this analysis due to the use of the same-flavour channels and the tighter lepton p_T requirement. The result for $\sigma_{Z \rightarrow \ell\ell}$ represents the inclusive cross-section for $Z/\gamma^* \rightarrow \ell\ell$ production for a single dilepton flavour with $m_{\ell\ell} > 60$ GeV. In order to compare with previous measurements, it was translated into a fiducial cross-section $\sigma_{Z \rightarrow \ell\ell}^{\text{fid}}$ requiring two Born-level leptons with $p_T > 25$ GeV and $\eta < 2.5$, and $66 < m_{\ell\ell} < 116$ GeV. The relationship between the total and fiducial cross-sections is given by $\sigma_{Z \rightarrow \ell\ell}^{\text{fid}} = A_Z \sigma_{Z \rightarrow \ell\ell}$, and the factor $A_Z = 0.3836 \pm 0.0005$ was evaluated from the POWHEG + PYTHIA8 $Z \rightarrow \ell\ell$ sample, including the extrapolation to the lower lepton p_T requirement of $p_T > 25$ GeV. The resulting fiducial cross-section is

$$\sigma_{Z \rightarrow \ell\ell}^{\text{fid}} = 774.7 \pm 0.1 \pm 1.8 \pm 6.4 \pm 0.7 \text{ pb} .$$

The systematic uncertainty is much smaller than that for $\sigma_{Z \rightarrow \ell\ell}$ because of strong reductions in the PDF and Z modelling uncertainties in the fiducial cross-section measurement. The result is compatible with that measured in Ref. [82].

The values of $\epsilon_b^{\ell\ell'}$ for the three dilepton channels were found to be compatible with the values expected from simulation, and are all close to 0.51. The Z +jets scaling parameters were measured to be $s_1^{Z+\text{jets}} = 0.89 \pm 0.09$ and $s_2^{Z+\text{jets}} = 1.12 \pm 0.32$, the uncertainties being dominated by the QCD scale variations in the Z +jets samples, which significantly change the predicted cross-sections. The Z +jets lepton isolation efficiency difference was fitted as $R_{Z+b}^{\mu\mu/ee} = 0.990 \pm 0.003$, compatible with the differences between SHERPA and POWHEG + PYTHIA8 lepton isolation efficiencies shown for inclusive $Z \rightarrow \ell\ell$ events in Figure 3.

The two ratios of branching ratios were fitted to be

$$\begin{aligned}R_{WZ}^{\mu/e} &= 0.9990 \pm 0.0022 \pm 0.0036 , \\ R_Z^{\mu\mu/ee} &= 0.9913 \pm 0.0002 \pm 0.0045 ,\end{aligned}$$

Table 4: Breakdown of the statistical and systematic uncertainties on the measured cross-sections $\sigma_{t\bar{t}}$ and $\sigma_{Z\rightarrow\ell\ell}$, and on the ratios of branching ratios $R_{WZ}^{\mu/e}$ and $R_Z^{\mu\mu/ee}$.

Uncertainty [%]	$\sigma_{t\bar{t}}$	$\sigma_{Z\rightarrow\ell\ell}$	$R_{WZ}^{\mu/e}$	$R_Z^{\mu\mu/ee}$
Data statistics	0.13	0.01	0.22	0.02
$t\bar{t}$ modelling	1.68	0.03	0.10	0.00
Top-quark p_T modelling	1.42	0.00	0.06	0.00
Parton distribution functions	0.67	0.68	0.15	0.03
Single-top modelling	0.65	0.00	0.05	0.00
Single-top/ $t\bar{t}$ interference	0.54	0.00	0.09	0.00
Z(+jets) modelling	0.06	0.73	0.13	0.20
Diboson modelling	0.05	0.04	0.01	0.00
Electron energy scale/resolution	0.05	0.06	0.10	0.11
Electron identification	0.10	0.07	0.04	0.13
Electron charge misidentification	0.06	0.06	0.01	0.13
Electron isolation	0.09	0.02	0.08	0.04
Muon momentum scale/resolution	0.04	0.02	0.06	0.04
Muon identification	0.18	0.12	0.11	0.23
Muon isolation	0.09	0.01	0.07	0.01
Lepton trigger	0.09	0.12	0.01	0.23
Jet energy scale/resolution	0.08	0.00	0.03	0.00
b -tagging efficiency/mistag	0.14	0.00	0.00	0.00
Misidentified leptons	0.17	0.02	0.15	0.05
Simulation statistics	0.04	0.00	0.06	0.00
Integrated luminosity	0.93	0.83	0.00	0.00
Beam energy	0.23	0.09	0.00	0.00
Total uncertainty	2.66	1.32	0.42	0.45

where the first uncertainties are statistical and the second systematic. A detailed breakdown of the uncertainties is shown in Table 4. The value of $R_Z^{\mu\mu/ee}$ is 1.9 standard deviations below unity, hinting at a potential bias in the electron or muon identification efficiencies. The normalisation of $R_{WZ}^{\mu/e}$ by $R_Z^{\mu\mu/ee}$ via Eq. (7) protects $R_{WZ}^{\mu/e}$ against such a bias, modulo differences in the lepton p_T and η distributions in dilepton $t\bar{t}$ and $Z \rightarrow \ell\ell$ events.

Consistent results were found when analysing the 2015–16, 2017 and 2018 datasets separately. The result for $R_{WZ}^{\mu/e}$ was found to be stable when tightening the lepton p_T requirement progressively up to $p_T > 40$ GeV, and when tightening the η requirement to $|\eta| < 1.5$, in each case removing around 40% of the $t\bar{t}$ sample. It also changed by less than 0.01% when removing the lowest $m_{\ell\ell}$ bin from the fit, demonstrating insensitivity to the mismodelling shown in Figure 4. This mismodelling is consistent between ee and $\mu\mu$ channels, as can be seen from Figure 5, which shows the ratio of $\mu\mu$ to ee events in each invariant mass bin, cancelling any common mismodelling. The data and fit predictions for this ratio agree well in all $m_{\ell\ell}$ bins.

The measured value of $R_{WZ}^{\mu/e}$ was converted to $R_W^{\mu/e}$ by using the external measurement of $R_{Z\text{-ext}}^{\mu\mu/ee} = 1.0009 \pm 0.0028$ from LEP and SLD [13, 14], giving a result of

$$R_W^{\mu/e} = R_{WZ}^{\mu/e} \sqrt{R_{Z\text{-ext}}^{\mu\mu/ee}} = 0.9995 \pm 0.0022 \text{ (stat)} \pm 0.0036 \text{ (syst)} \pm 0.0014 \text{ (ext)},$$

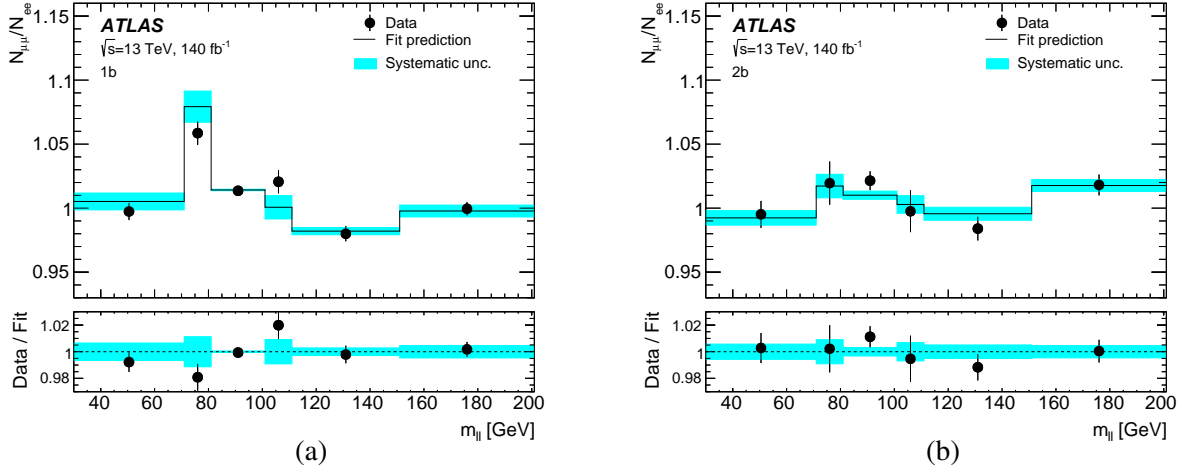


Figure 5: Ratio of the number of events in the $\mu\mu$ channel divided by that in the ee channel as a function of dilepton invariant mass for events with (a) one and (b) two b -tagged jets. The ratio in data is shown by the points with statistical error bars, and the results of the fit prediction by the solid lines, with the cyan band indicating the systematic uncertainty.

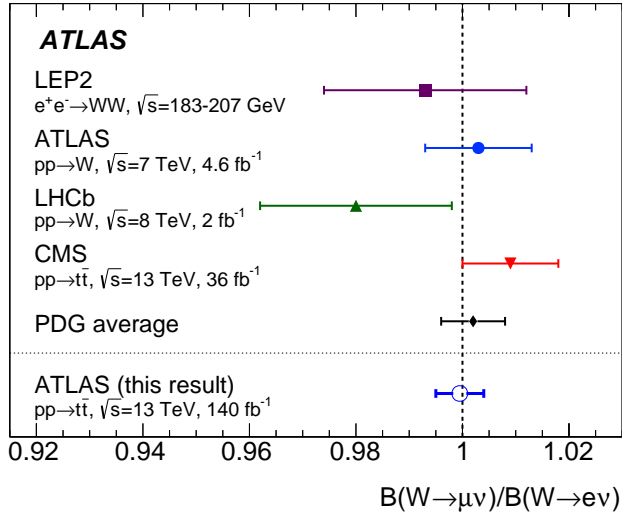


Figure 6: Measurement of $R_W^{\mu/e} = \mathcal{B}(W \rightarrow \mu\nu)/\mathcal{B}(W \rightarrow e\nu)$ from this analysis compared to previous results from LEP2 and LHC experiments [9–12] and the Particle Data Group average [13].

where the three uncertainties correspond to data statistics, systematic uncertainties from this analysis, and the uncertainty on the value of $R_{Z\text{-ext}}^{\mu\mu/ee}$ (considered uncorrelated), giving a total uncertainty of 0.0045. The result is consistent with the assumption of lepton flavour universality and with previous measurements, and has higher precision than the previous world average [13]. The result is compared with previous measurements of $R_W^{\mu/e}$ in Figure 6.

8 Conclusion

The ratio of branching ratios $R_W^{\mu/e} = \mathcal{B}(W \rightarrow \mu\nu)/\mathcal{B}(W \rightarrow e\nu)$ has been determined using the complete ATLAS Run 2 $\sqrt{s} = 13$ TeV pp collision data sample recorded at the LHC, by measuring the $t\bar{t}$ cross-section in the ee , $e\mu$ and $\mu\mu$ dilepton channels. Systematic uncertainties due to lepton identification and trigger efficiencies were minimised by normalising the result to a simultaneous measurement of $R_Z^{\mu\mu/ee} = \mathcal{B}(Z \rightarrow \mu\mu)/\mathcal{B}(Z \rightarrow ee)$, and utilising the high-precision measurement of $R_Z^{\mu\mu/ee}$ by the LEP and SLD collaborations. The resulting value of $R_W^{\mu/e} = 0.9995 \pm 0.0045$ is consistent with the assumption of lepton flavour universality. This is the most precise measurement of $R_W^{\mu/e}$ to date, with a smaller uncertainty than the previous world average.

Acknowledgements

We thank CERN for the very successful operation of the LHC and its injectors, as well as the support staff at CERN and at our institutions worldwide without whom ATLAS could not be operated efficiently.

The crucial computing support from all WLCG partners is acknowledged gratefully, in particular from CERN, the ATLAS Tier-1 facilities at TRIUMF/SFU (Canada), NDGF (Denmark, Norway, Sweden), CC-IN2P3 (France), KIT/GridKA (Germany), INFN-CNAF (Italy), NL-T1 (Netherlands), PIC (Spain), RAL (UK) and BNL (USA), the Tier-2 facilities worldwide and large non-WLCG resource providers. Major contributors of computing resources are listed in Ref. [83].

We gratefully acknowledge the support of ANPCyT, Argentina; YerPhI, Armenia; ARC, Australia; BMWFW and FWF, Austria; ANAS, Azerbaijan; CNPq and FAPESP, Brazil; NSERC, NRC and CFI, Canada; CERN; ANID, Chile; CAS, MOST and NSFC, China; Minciencias, Colombia; MEYS CR, Czech Republic; DNRf and DNSRC, Denmark; IN2P3-CNRS and CEA-DRF/IRFU, France; SRNSFG, Georgia; BMBF, HGF and MPG, Germany; GSRI, Greece; RGC and Hong Kong SAR, China; ISF and Benoziyo Center, Israel; INFN, Italy; MEXT and JSPS, Japan; CNRST, Morocco; NWO, Netherlands; RCN, Norway; MEiN, Poland; FCT, Portugal; MNE/IFA, Romania; MESTD, Serbia; MSSR, Slovakia; ARRS and MIZŠ, Slovenia; DSI/NRF, South Africa; MICINN, Spain; SRC and Wallenberg Foundation, Sweden; SERI, SNSF and Cantons of Bern and Geneva, Switzerland; MOST, Taipei; TENMAK, Türkiye; STFC, United Kingdom; DOE and NSF, United States of America.

Individual groups and members have received support from BCKDF, CANARIE, CRC and DRAC, Canada; PRIMUS 21/SCI/017, Czech Republic; COST, ERC, ERDF, Horizon 2020, ICSC-NextGenerationEU and Marie Skłodowska-Curie Actions, European Union; Investissements d’Avenir Labex, Investissements d’Avenir IDEX and ANR, France; DFG and AvH Foundation, Germany; Herakleitos, Thales and Aristeia programmes co-financed by EU-ESF and the Greek NSRF, Greece; BSF-NSF and MINERVA, Israel; Norwegian Financial Mechanism 2014-2021, Norway; NCN and NAWA, Poland; La Caixa Banking Foundation, CERCA Programme Generalitat de Catalunya and PROMETEO and GenT Programmes Generalitat Valenciana, Spain; Göran Gustafssons Stiftelse, Sweden; The Royal Society and Leverhulme Trust, United Kingdom.

In addition, individual members wish to acknowledge support from CERN: European Organization for Nuclear Research (CERN P.J.A.S.); Chile: Agencia Nacional de Investigación y Desarrollo (FONDECYT 1190886, FONDECYT 1210400, FONDECYT 1230987); China: National Natural Science Foundation of

China (NSFC - 12175119, NSFC 12275265); European Union: European Research Council (ERC - 948254, ERC 101089007), Horizon 2020 Framework Programme (MUCCA - CHIST-ERA-19-XAI-00), Italian Center for High Performance Computing, Big Data and Quantum Computing (ICSC, NextGenerationEU); France: Agence Nationale de la Recherche (ANR-20-CE31-0013, ANR-21-CE31-0022), Investissements d'Avenir Labex (ANR-11-LABX-0012); Germany: Baden-Württemberg Stiftung (BW Stiftung-Postdoc Eliteprogramme), Deutsche Forschungsgemeinschaft (DFG - 469666862, DFG - CR 312/5-2); Italy: Istituto Nazionale di Fisica Nucleare (ICSC, NextGenerationEU); Japan: Japan Society for the Promotion of Science (JSPS KAKENHI 22H01227, JSPS KAKENHI 22KK0227, JSPS KAKENHI JP21H05085, JSPS KAKENHI JP22H04944); Netherlands: Netherlands Organisation for Scientific Research (NWO Veni 2020 - VI.Veni.202.179); Norway: Research Council of Norway (RCN-314472); Poland: Polish National Agency for Academic Exchange (PPN/PPO/2020/1/00002/U/00001), Polish National Science Centre (NCN 2021/42/E/ST2/00350, NCN OPUS nr 2022/47/B/ST2/03059, NCN UMO-2019/34/E/ST2/00393, UMO-2022/47/O/ST2/00148); Slovenia: Slovenian Research Agency (ARIS grant J1-3010); Spain: Generalitat Valenciana (Artemisa, FEDER, IDIFEDER/2018/048), Ministry of Science and Innovation (RYC2019-028510-I, RYC2020-030254-I), PROMETEO and GenT Programmes Generalitat Valenciana (CIDEGENT/2019/023, CIDEGENT/2019/027); Sweden: Swedish Research Council (VR 2022-03845, VR 2023-03403), Knut and Alice Wallenberg Foundation (KAW 2022.0358); Switzerland: Swiss National Science Foundation (SNSF - PCEFP2_194658); United Kingdom: Leverhulme Trust (Leverhulme Trust RPG-2020-004); United States of America: Neubauer Family Foundation.

References

- [1] A. Pich, *Precision Tau Physics*, *Prog. Part. Nucl. Phys.* **75** (2014) 41, arXiv: [1310.7922 \[hep-ph\]](#).
- [2] BaBar Collaboration, *Evidence for an excess of $\bar{B} \rightarrow D^{(*)}\tau^-\bar{\nu}_\tau$ decays*, *Phys. Rev. Lett.* **109** (2012) 101802, arXiv: [1205.5442 \[hep-ex\]](#).
- [3] Belle Collaboration, *Measurement of the branching ratio of $\bar{B} \rightarrow D^{(*)}\tau^-\bar{\nu}_\tau$ relative to $\bar{B} \rightarrow D^{(*)}\ell^-\bar{\nu}_\ell$ decays with hadronic tagging at Belle*, *Phys. Rev. D* **92** (2015) 072014, arXiv: [1507.03233 \[hep-ex\]](#).
- [4] Belle Collaboration, *Measurement of the τ lepton polarization and $R(D^*)$ in the decay $\bar{B} \rightarrow D^*\tau^-\bar{\nu}_\tau$ with one-prong hadronic τ decays at Belle*, *Phys. Rev. D* **97** (2018) 012004, arXiv: [1709.00129 \[hep-ex\]](#).
- [5] Belle II Collaboration, *A test of lepton flavor universality with a measurement of $R(D^*)$ using hadronic B tagging at the Belle II experiment*, (2024), arXiv: [2401.02840 \[hep-ex\]](#).
- [6] LHCb Collaboration, *Measurement of the ratios of branching fractions $\mathcal{R}(D^*)$ and $\mathcal{R}(D^0)$* , *Phys. Rev. Lett.* **131** (2023) 111802, arXiv: [2302.02886 \[hep-ex\]](#).
- [7] LHCb Collaboration, *Test of lepton flavor universality using $B^0 \rightarrow D^{*-}\tau^+\nu_\tau$ decays with hadronic τ channels*, *Phys. Rev. D* **108** (2023) 012018, arXiv: [2305.01463 \[hep-ex\]](#).
- [8] LHCb Collaboration, *Test of lepton universality in $b \rightarrow s\ell^+\ell^-$ decays*, *Phys. Rev. Lett.* **131** (2023) 051803, arXiv: [2212.09152 \[hep-ex\]](#).
- [9] CMS Collaboration, *Precision measurement of the W boson decay branching fractions in proton–proton collisions at $\sqrt{s} = 13$ TeV*, *Phys. Rev. D* **105** (2022) 072008, arXiv: [2201.07861 \[hep-ex\]](#).
- [10] ATLAS Collaboration, *Precision measurement and interpretation of inclusive W^+ , W^- and Z/γ^* production cross sections with the ATLAS detector*, *Eur. Phys. J. C* **77** (2017) 367, arXiv: [1612.03016 \[hep-ex\]](#).
- [11] LHCb Collaboration, *Measurement of forward $W \rightarrow e\nu$ production in pp collisions at $\sqrt{s} = 8$ TeV*, *JHEP* **10** (2016) 030, arXiv: [1608.01484 \[hep-ex\]](#).
- [12] S. Schael et al., *Electroweak measurements in electron-positron collisions at W -boson-pair energies at LEP*, *Phys. Rept.* **532** (2013) 119, arXiv: [1302.3415](#).
- [13] Particle Data Group, *Review of Particle Physics*, *PTEP* **2022** (2022) 083C01.
- [14] S. Schael et al., *Precision electroweak measurements on the Z resonance*, *Phys. Rept.* **427** (2006) 257, arXiv: [hep-ex/0509008](#).
- [15] ATLAS Collaboration, *The ATLAS Experiment at the CERN Large Hadron Collider*, *JINST* **3** (2008) S08003.
- [16] B. Abbott et al., *Production and integration of the ATLAS Insertable B-Layer*, *JINST* **13** (2018) T05008, arXiv: [1803.00844 \[physics.ins-det\]](#).
- [17] ATLAS Collaboration, *ATLAS Insertable B-Layer: Technical Design Report*, ATLAS-TDR-19; CERN-LHCC-2010-013, 2010, URL: <https://cds.cern.ch/record/1291633>, Addendum: ATLAS-TDR-19-ADD-1; CERN-LHCC-2012-009, 2012, URL: <https://cds.cern.ch/record/1451888>.

- [18] ATLAS Collaboration, *Luminosity determination in pp collisions at $\sqrt{s} = 13$ TeV using the ATLAS detector at the LHC*, *Eur. Phys. J. C* **83** (2023) 982, arXiv: 2212.09379 [hep-ex].
- [19] ATLAS Collaboration, *ATLAS data quality operations and performance for 2015–2018 data-taking*, *JINST* **15** (2020) P04003, arXiv: 1911.04632 [physics.ins-det].
- [20] ATLAS Collaboration, *Performance of electron and photon triggers in ATLAS during LHC Run 2*, *Eur. Phys. J. C* **80** (2020) 47, arXiv: 1909.00761 [hep-ex].
- [21] ATLAS Collaboration, *Performance of the ATLAS muon triggers in Run 2*, *JINST* **15** (2020) P09015, arXiv: 2004.13447 [physics.ins-det].
- [22] ATLAS Collaboration, *The ATLAS Simulation Infrastructure*, *Eur. Phys. J. C* **70** (2010) 823, arXiv: 1005.4568 [physics.ins-det].
- [23] S. Agostinelli et al., *GEANT4—A simulation toolkit*, *Nucl. Instrum. Meth. A* **506** (2003) 250.
- [24] ATLAS Collaboration, *The simulation principle and performance of the ATLAS fast calorimeter simulation FastCaloSim*, ATL-PHYS-PUB-2010-013, 2010, URL: <https://cds.cern.ch/record/1300517>.
- [25] T. Sjöstrand, S. Mrenna and P. Skands, *A brief introduction to PYTHIA 8.1*, *Comput. Phys. Commun.* **178** (2008) 852, arXiv: 0710.3820 [hep-ph].
- [26] ATLAS Collaboration, *The Pythia 8 A3 tune description of ATLAS minimum bias and inelastic measurements incorporating the Donnachie–Landshoff diffractive model*, ATL-PHYS-PUB-2016-017, 2016, URL: <https://cds.cern.ch/record/2206965>.
- [27] ATLAS Collaboration, *The ATLAS Collaboration Software and Firmware*, ATL-SOFT-PUB-2021-001, 2021, URL: <https://cds.cern.ch/record/2767187>.
- [28] ATLAS Collaboration, *Electron and photon performance measurements with the ATLAS detector using the 2015–2017 LHC proton–proton collision data*, *JINST* **14** (2019) P12006, arXiv: 1908.00005 [hep-ex].
- [29] ATLAS Collaboration, *Studies of the muon momentum calibration and performance of the ATLAS detector with pp collisions at $\sqrt{s} = 13$ TeV*, *Eur. Phys. J. C* **83** (2023) 686, arXiv: 2212.07338 [hep-ex].
- [30] ATLAS Collaboration, *Jet energy scale and resolution measured in proton–proton collisions at $\sqrt{s} = 13$ TeV with the ATLAS detector*, *Eur. Phys. J. C* **81** (2021) 689, arXiv: 2007.02645 [hep-ex].
- [31] ATLAS Collaboration, *Electron and photon efficiencies in LHC Run 2 with the ATLAS experiment*, (2023), arXiv: 2308.13362 [hep-ex].
- [32] ATLAS Collaboration, *Muon reconstruction and identification efficiency in ATLAS using the full Run 2 pp collision data set at $\sqrt{s} = 13$ TeV*, *Eur. Phys. J. C* **81** (2021) 578, arXiv: 2012.00578 [hep-ex].
- [33] ATLAS Collaboration, *ATLAS b-jet identification performance and efficiency measurement with $t\bar{t}$ events in pp collisions at $\sqrt{s} = 13$ TeV*, *Eur. Phys. J. C* **79** (2019) 970, arXiv: 1907.05120 [hep-ex].
- [34] P. Nason, *A new method for combining NLO QCD with shower Monte Carlo algorithms*, *JHEP* **11** (2004) 040, arXiv: hep-ph/0409146.

- [35] S. Frixione, P. Nason and C. Oleari, *Matching NLO QCD computations with parton shower simulations: the POWHEG method*, *JHEP* **11** (2007) 070, arXiv: [0709.2092 \[hep-ph\]](#).
- [36] S. Alioli, P. Nason, C. Oleari and E. Re, *A general framework for implementing NLO calculations in shower Monte Carlo programs: the POWHEG BOX*, *JHEP* **06** (2010) 043, arXiv: [1002.2581 \[hep-ph\]](#).
- [37] S. Frixione, G. Ridolfi and P. Nason, *A positive-weight next-to-leading-order Monte Carlo for heavy flavour hadroproduction*, *JHEP* **09** (2007) 126, arXiv: [0707.3088 \[hep-ph\]](#).
- [38] NNPDF Collaboration, *Parton distributions for the LHC run II*, *JHEP* **04** (2015) 040, arXiv: [1410.8849 \[hep-ph\]](#).
- [39] NNPDF Collaboration, *Parton distributions with LHC data*, *Nucl. Phys. B* **867** (2013) 244, arXiv: [1207.1303 \[hep-ph\]](#).
- [40] ATLAS Collaboration, *ATLAS Pythia 8 tunes to 7 TeV data*, ATL-PHYS-PUB-2014-021, 2014, URL: <https://cds.cern.ch/record/1966419>.
- [41] ATLAS Collaboration, *Studies on top-quark Monte Carlo modelling for Top2016*, ATL-PHYS-PUB-2016-020, 2016, URL: <https://cds.cern.ch/record/2216168>.
- [42] J. Alwall et al., *The automated computation of tree-level and next-to-leading order differential cross sections, and their matching to parton shower simulations*, *JHEP* **07** (2014) 079, arXiv: [1405.0301 \[hep-ph\]](#).
- [43] M. Bähr et al., *Herwig++ physics and manual*, *Eur. Phys. J. C* **58** (2008) 639, arXiv: [0803.0883 \[hep-ph\]](#).
- [44] J. Bellm et al., *Herwig 7.1 Release Note*, (2017), arXiv: [1705.06919 \[hep-ph\]](#).
- [45] ATLAS Collaboration, *Study of top-quark pair modelling and uncertainties using ATLAS measurements at $\sqrt{s} = 13$ TeV*, ATL-PHYS-PUB-2020-023, 2020, URL: <https://cds.cern.ch/record/2730443>.
- [46] J. Erler and A. Freitas, *Electroweak model and constraints on new physics, in Review of Particle Physics*, *PTEP* **2022** (2022) 083C01.
- [47] D. J. Lange, *The EvtGen particle decay simulation package*, *Nucl. Instrum. Meth. A* **462** (2001) 152.
- [48] M. Czakon, P. Fiedler and A. Mitov, *Total Top-Quark Pair-Production Cross Section at Hadron Colliders Through $O(\alpha_S^4)$* , *Phys. Rev. Lett.* **110** (2013) 252004, arXiv: [1303.6254 \[hep-ph\]](#).
- [49] M. Czakon and A. Mitov, *Top++: A program for the calculation of the top-pair cross-section at hadron colliders*, *Comput. Phys. Commun.* **185** (2014) 2930, arXiv: [1112.5675 \[hep-ph\]](#).
- [50] ATLAS Collaboration, *Measurement of the $t\bar{t}$ production cross-section and lepton differential distributions in $e\mu$ dilepton events from pp collisions at $\sqrt{s} = 13$ TeV with the ATLAS detector*, *Eur. Phys. J. C* **80** (2020) 528, arXiv: [1910.08819 \[hep-ex\]](#).
- [51] E. Re, *Single-top Wt -channel production matched with parton showers using the POWHEG method*, *Eur. Phys. J. C* **71** (2011) 1547, arXiv: [1009.2450 \[hep-ph\]](#).

- [52] C. D. White, S. Frixione, E. Laenen and F. Maltoni, *Isolating Wt production at the LHC*, [JHEP **11** \(2009\) 074](#), arXiv: [0908.0631 \[hep-ph\]](#).
- [53] N. Kidonakis and N. Yamanaka, *Higher-order corrections for tW production at high-energy hadron colliders*, [JHEP **05** \(2021\) 278](#), arXiv: [2102.11300 \[hep-ph\]](#).
- [54] E. Bothmann et al., *Event generation with Sherpa 2.2*, [SciPost Phys. **7** \(2019\) 034](#), arXiv: [1905.09127 \[hep-ph\]](#).
- [55] T. Gleisberg and S. Höche, *Comix, a new matrix element generator*, [JHEP **12** \(2008\) 039](#), arXiv: [0808.3674 \[hep-ph\]](#).
- [56] F. Buccioni et al., *OpenLoops 2*, [Eur. Phys. J. C **79** \(2019\) 866](#), arXiv: [1907.13071 \[hep-ph\]](#).
- [57] S. Schumann and F. Krauss, *A parton shower algorithm based on Catani–Seymour dipole factorisation*, [JHEP **03** \(2008\) 038](#), arXiv: [0709.1027 \[hep-ph\]](#).
- [58] S. Höche, F. Krauss, M. Schönherr and F. Siegert, *A critical appraisal of NLO+PS matching methods*, [JHEP **09** \(2012\) 049](#), arXiv: [1111.1220 \[hep-ph\]](#).
- [59] S. Catani, F. Krauss, B. R. Webber and R. Kuhn, *QCD Matrix Elements + Parton Showers*, [JHEP **11** \(2001\) 063](#), arXiv: [hep-ph/0109231](#).
- [60] S. Höche, F. Krauss, M. Schönherr and F. Siegert, *QCD matrix elements + parton showers. The NLO case*, [JHEP **04** \(2013\) 027](#), arXiv: [1207.5030 \[hep-ph\]](#).
- [61] S. Höche, F. Krauss, S. Schumann and F. Siegert, *QCD matrix elements and truncated showers*, [JHEP **05** \(2009\) 053](#), arXiv: [0903.1219 \[hep-ph\]](#).
- [62] C. Anastasiou, L. Dixon, K. Melnikov and F. Petriello, *High-precision QCD at hadron colliders: Electroweak gauge boson rapidity distributions at next-to-next-to leading order*, [Phys. Rev. D **69** \(2004\) 094008](#), arXiv: [hep-ph/0312266](#).
- [63] S. Alioli, P. Nason, C. Oleari and E. Re, *NLO vector-boson production matched with shower in POWHEG*, [JHEP **07** \(2008\) 060](#), arXiv: [0805.4802 \[hep-ph\]](#).
- [64] ATLAS Collaboration, *Measurement of the Z/γ^* boson transverse momentum distribution in pp collisions at $\sqrt{s} = 7$ TeV with the ATLAS detector*, [JHEP **09** \(2014\) 145](#), arXiv: [1406.3660 \[hep-ex\]](#).
- [65] H.-L. Lai et al., *New parton distributions for collider physics*, [Phys. Rev. D **82** \(2010\) 074024](#), arXiv: [1007.2241 \[hep-ph\]](#).
- [66] R. Gavin, Y. Li, F. Petriello and S. Quackenbush, *FEWZ 2.0: A code for hadronic Z production at next-to-next-to-leading order*, [Comput. Phys. Commun. **182** \(2011\) 2388](#), arXiv: [1011.3540 \[hep-ph\]](#).
- [67] M. Cacciari, G. P. Salam and G. Soyez, *The anti- k_t jet clustering algorithm*, [JHEP **04** \(2008\) 063](#), arXiv: [0802.1189 \[hep-ph\]](#).
- [68] M. Cacciari, G. P. Salam and G. Soyez, *FastJet user manual*, [Eur. Phys. J. C **72** \(2012\) 1896](#), arXiv: [1111.6097 \[hep-ph\]](#).

- [69] ATLAS Collaboration, *Jet reconstruction and performance using particle flow with the ATLAS Detector*, *Eur. Phys. J. C* **77** (2017) 466, arXiv: [1703.10485 \[hep-ex\]](#).
- [70] ATLAS Collaboration, *Performance of pile-up mitigation techniques for jets in pp collisions at $\sqrt{s} = 8$ TeV using the ATLAS detector*, *Eur. Phys. J. C* **76** (2016) 581, arXiv: [1510.03823 \[hep-ex\]](#).
- [71] ATLAS Collaboration, *ATLAS flavour-tagging algorithms for the LHC Run 2 pp collision dataset*, *Eur. Phys. J. C* **83** (2023) 681, arXiv: [2211.16345 \[physics.data-an\]](#).
- [72] ATLAS Collaboration, *Measurements of top-quark pair differential cross-sections in the lepton+jets channel in pp collisions at $\sqrt{s} = 13$ TeV using the ATLAS detector*, *JHEP* **11** (2017) 191, arXiv: [1708.00727 \[hep-ex\]](#).
- [73] M. Czakon, D. Heymes and A. Mitov, *High-Precision Differential Predictions for Top-Quark Pairs at the LHC*, *Phys. Rev. Lett.* **116** (2016) 082003, arXiv: [1511.00549 \[hep-ph\]](#).
- [74] ATLAS Collaboration, *Measurement of the $t\bar{t}$ production cross-section in pp collisions at $\sqrt{s} = 5.02$ TeV with the ATLAS detector*, *JHEP* **06** (2023) 138, arXiv: [2207.01354 \[hep-ex\]](#).
- [75] ATLAS Collaboration, *Test of the universality of τ and μ lepton couplings in W-boson decays with the ATLAS detector*, *Nature Phys.* **17** (2021) 813, arXiv: [2007.14040 \[hep-ex\]](#).
- [76] J. Butterworth et al., *PDF4LHC recommendations for LHC Run II*, *J. Phys. G* **43** (2016) 023001, arXiv: [1510.03865 \[hep-ph\]](#).
- [77] J. Bellm et al., *Herwig 7.0/Herwig++ 3.0 release note*, *Eur. Phys. J. C* **76** (2016) 196, arXiv: [1512.01178 \[hep-ph\]](#).
- [78] ATLAS Collaboration, *Measurement of the c-jet mistagging efficiency in $t\bar{t}$ events using pp collision data at $\sqrt{s} = 13$ TeV collected with the ATLAS detector*, *Eur. Phys. J. C* **82** (2022) 95, arXiv: [2109.10627 \[hep-ex\]](#).
- [79] ATLAS Collaboration, *Calibration of the light-flavour jet mistagging efficiency of the b-tagging algorithms with Z+jets events using 139fb^{-1} of ATLAS proton–proton collision data at $\sqrt{s} = 13$ TeV*, *Eur. Phys. J. C* **83** (2023) 728, arXiv: [2301.06319 \[hep-ex\]](#).
- [80] G. Avoni et al., *The new LUCID-2 detector for luminosity measurement and monitoring in ATLAS*, *JINST* **13** (2018) P07017.
- [81] ATLAS Collaboration, *Inclusive and differential cross-sections for dilepton $t\bar{t}$ production measured in $\sqrt{s} = 13$ TeV pp collisions with the ATLAS detector*, *JHEP* **07** (2023) 141, arXiv: [2303.15340 \[hep-ex\]](#).
- [82] ATLAS Collaboration, *Measurements of top-quark pair to Z-boson cross-section ratios at $\sqrt{s} = 13, 8, 7$ TeV with the ATLAS detector*, *JHEP* **02** (2017) 117, arXiv: [1612.03636 \[hep-ex\]](#).
- [83] ATLAS Collaboration, *ATLAS Computing Acknowledgements*, ATL-SOFT-PUB-2023-001, 2023, URL: <https://cds.cern.ch/record/2869272>.

The ATLAS Collaboration

G. Aad ¹⁰³, E. Aakvaag ¹⁶, B. Abbott ¹²¹, S. Abdelhameed ^{117a}, K. Abeling ⁵⁵, N.J. Abicht ⁴⁹, S.H. Abidi ²⁹, M. Aboeela ⁴⁴, A. Aboulhorma ^{35e}, H. Abramowicz ¹⁵², H. Abreu ¹⁵¹, Y. Abulaiti ¹¹⁸, B.S. Acharya ^{69a,69b,k}, A. Ackermann ^{63a}, C. Adam Bourdarios ⁴, L. Adamczyk ^{86a}, S.V. Addepalli ²⁶, M.J. Addison ¹⁰², J. Adelman ¹¹⁶, A. Adiguzel ^{21c}, T. Adye ¹³⁵, A.A. Affolder ¹³⁷, Y. Afik ³⁹, M.N. Agaras ¹³, J. Agarwala ^{73a,73b}, A. Aggarwal ¹⁰¹, C. Agheorghiesei ^{27c}, A. Ahmad ³⁶, F. Ahmadov ^{38,x}, W.S. Ahmed ¹⁰⁵, S. Ahuja ⁹⁶, X. Ai ^{62e}, G. Aielli ^{76a,76b}, A. Aikot ¹⁶⁴, M. Ait Tamliah ^{35e}, B. Aitbenchikh ^{35a}, M. Akbiyik ¹⁰¹, T.P.A. Åkesson ⁹⁹, A.V. Akimov ³⁷, D. Akiyama ¹⁶⁹, N.N. Akolkar ²⁴, S. Aktas ^{21a}, K. Al Houry ⁴¹, G.L. Alberghi ^{23b}, J. Albert ¹⁶⁶, P. Albicocco ⁵³, G.L. Albouy ⁶⁰, S. Alderweireldt ⁵², Z.L. Alegria ¹²², M. Aleksa ³⁶, I.N. Aleksandrov ³⁸, C. Alexa ^{27b}, T. Alexopoulos ¹⁰, F. Alfonsi ^{23b}, M. Algren ⁵⁶, M. Alhroob ¹⁶⁸, B. Ali ¹³³, H.M.J. Ali ⁹², S. Ali ³¹, S.W. Alibocus ⁹³, M. Aliev ^{33c}, G. Alimonti ^{71a}, W. Alkahi ⁵⁵, C. Allaire ⁶⁶, B.M.M. Allbrooke ¹⁴⁷, J.F. Allen ⁵², C.A. Allendes Flores ^{138f}, P.P. Allport ²⁰, A. Aloisio ^{72a,72b}, F. Alonso ⁹¹, C. Alpigiani ¹³⁹, Z.M.K. Alsolami ⁹², M. Alvarez Estevez ¹⁰⁰, A. Alvarez Fernandez ¹⁰¹, M. Alves Cardoso ⁵⁶, M.G. Alvigi ^{72a,72b}, M. Aly ¹⁰², Y. Amaral Coutinho ^{83b}, A. Ambler ¹⁰⁵, C. Amelung ³⁶, M. Amerl ¹⁰², C.G. Ames ¹¹⁰, D. Amidei ¹⁰⁷, K.J. Amirie ¹⁵⁶, S.P. Amor Dos Santos ^{131a}, K.R. Amos ¹⁶⁴, S. An ⁸⁴, V. Ananiev ¹²⁶, C. Anastopoulos ¹⁴⁰, T. Andeen ¹¹, J.K. Anders ³⁶, S.Y. Andrean ^{47a,47b}, A. Andreazza ^{71a,71b}, S. Angelidakis ⁹, A. Angerami ^{41,z}, A.V. Anisenkov ³⁷, A. Annovi ^{74a}, C. Antel ⁵⁶, E. Antipov ¹⁴⁶, M. Antonelli ⁵³, F. Anulli ^{75a}, M. Aoki ⁸⁴, T. Aoki ¹⁵⁴, M.A. Aparo ¹⁴⁷, L. Aperio Bella ⁴⁸, C. Appelt ¹⁸, A. Apyan ²⁶, S.J. Arbiol Val ⁸⁷, C. Arcangeletti ⁵³, A.T.H. Arce ⁵¹, E. Arena ⁹³, J-F. Arguin ¹⁰⁹, S. Argyropoulos ⁵⁴, J.-H. Arling ⁴⁸, O. Arnaez ⁴, H. Arnold ¹⁴⁶, G. Artoni ^{75a,75b}, H. Asada ¹¹², K. Asai ¹¹⁹, S. Asai ¹⁵⁴, N.A. Asbah ³⁶, K. Assamagan ²⁹, R. Astalos ^{28a}, K.S.V. Astrand ⁹⁹, S. Atashi ¹⁶⁰, R.J. Atkin ^{33a}, M. Atkinson ¹⁶³, H. Atmani ^{35f}, P.A. Atmasiddha ¹²⁹, K. Augsten ¹³³, S. Auricchio ^{72a,72b}, A.D. Auriol ²⁰, V.A. Austrup ¹⁰², G. Avolio ³⁶, K. Axiotis ⁵⁶, G. Azuelos ^{109,ad}, D. Babal ^{28b}, H. Bachacou ¹³⁶, K. Bachas ^{153,o}, A. Bachi ³⁴, F. Backman ^{47a,47b}, A. Badea ³⁹, T.M. Baer ¹⁰⁷, P. Bagnaia ^{75a,75b}, M. Bahmani ¹⁸, D. Bahner ⁵⁴, K. Bai ¹²⁴, J.T. Baines ¹³⁵, L. Baines ⁹⁵, O.K. Baker ¹⁷³, E. Bakos ¹⁵, D. Bakshi Gupta ⁸, V. Balakrishnan ¹²¹, R. Balasubramanian ¹¹⁵, E.M. Baldin ³⁷, P. Balek ^{86a}, E. Ballabene ^{23b,23a}, F. Balli ¹³⁶, L.M. Baltos ^{63a}, W.K. Balunas ³², J. Balz ¹⁰¹, I. Bamwidhi ^{117b}, E. Banas ⁸⁷, M. Bandieramonte ¹³⁰, A. Bandyopadhyay ²⁴, S. Bansal ²⁴, L. Barak ¹⁵², M. Barakat ⁴⁸, E.L. Barberio ¹⁰⁶, D. Barberis ^{57b,57a}, M. Barbero ¹⁰³, M.Z. Barel ¹¹⁵, K.N. Barends ^{33a}, T. Barillari ¹¹¹, M-S. Barisits ³⁶, T. Barklow ¹⁴⁴, P. Baron ¹²³, D.A. Baron Moreno ¹⁰², A. Baroncelli ^{62a}, G. Barone ²⁹, A.J. Barr ¹²⁷, J.D. Barr ⁹⁷, F. Barreiro ¹⁰⁰, J. Barreiro Guimarães da Costa ^{14a}, U. Barron ¹⁵², M.G. Barros Teixeira ^{131a}, S. Barsov ³⁷, F. Bartels ^{63a}, R. Bartoldus ¹⁴⁴, A.E. Barton ⁹², P. Bartos ^{28a}, A. Basan ¹⁰¹, M. Baselga ⁴⁹, A. Bassalat ^{66,b}, M.J. Basso ^{157a}, R. Bate ¹⁶⁵, R.L. Bates ⁵⁹, S. Batlamous ¹⁰⁰, B. Batool ¹⁴², M. Battaglia ¹³⁷, D. Battulga ¹⁸, M. Baucé ^{75a,75b}, M. Bauer ³⁶, P. Bauer ²⁴, L.T. Bazzano Hurrell ³⁰, J.B. Beacham ⁵¹, T. Beau ¹²⁸, J.Y. Beaucamp ⁹¹, P.H. Beauchemin ¹⁵⁹, P. Bechtel ²⁴, H.P. Beck ^{19,n}, K. Becker ¹⁶⁸, A.J. Beddall ⁸², V.A. Bednyakov ³⁸, C.P. Bee ¹⁴⁶, L.J. Beemster ¹⁵, T.A. Beermann ³⁶, M. Begalli ^{83d}, M. Begel ²⁹, A. Behera ¹⁴⁶, J.K. Behr ⁴⁸, J.F. Beirer ³⁶, F. Beisiegel ²⁴, M. Belfkir ^{117b}, G. Bella ¹⁵², L. Bellagamba ^{23b}, A. Bellerive ³⁴, P. Bellos ²⁰, K. Beloborodov ³⁷, D. Benckekroun ^{35a}, F. Bendebba ^{35a}, Y. Benhammou ¹⁵²,

K.C. Benkendorfer ⁶¹, L. Beresford ⁴⁸, M. Beretta ⁵³, E. Bergeaas Kuutmann ¹⁶², N. Berger ⁴,
 B. Bergmann ¹³³, J. Beringer ^{17a}, G. Bernardi ⁵, C. Bernius ¹⁴⁴, F.U. Bernlochner ²⁴,
 F. Bernon ^{36,103}, A. Berrocal Guardia ¹³, T. Berry ⁹⁶, P. Berta ¹³⁴, A. Berthold ⁵⁰, S. Bethke ¹¹¹,
 A. Betti ^{75a,75b}, A.J. Bevan ⁹⁵, N.K. Bhalla ⁵⁴, S. Bhatta ¹⁴⁶, D.S. Bhattacharya ¹⁶⁷,
 P. Bhattarai ¹⁴⁴, K.D. Bhide ⁵⁴, V.S. Bhopatkar ¹²², R.M. Bianchi ¹³⁰, G. Bianco ^{23b,23a},
 O. Biebel ¹¹⁰, R. Bielski ¹²⁴, M. Biglietti ^{77a}, C.S. Billingsley ⁴⁴, M. Bindi ⁵⁵, A. Bingul ^{21b},
 C. Bini ^{75a,75b}, A. Biondini ⁹³, G.A. Bird ³², M. Birman ¹⁷⁰, M. Biros ¹³⁴, S. Biryukov ¹⁴⁷,
 T. Bisanz ⁴⁹, E. Bisceglie ^{43b,43a}, J.P. Biswal ¹³⁵, D. Biswas ¹⁴², I. Bloch ⁴⁸, A. Blue ⁵⁹,
 U. Blumenschein ⁹⁵, J. Blumenthal ¹⁰¹, V.S. Bobrovnikov ³⁷, M. Boehler ⁵⁴, B. Boehm ¹⁶⁷,
 D. Bogavac ³⁶, A.G. Bogdanchikov ³⁷, C. Bohm ^{47a}, V. Boisvert ⁹⁶, P. Bokan ³⁶, T. Bold ^{86a},
 M. Bomben ⁵, M. Bona ⁹⁵, M. Boonekamp ¹³⁶, C.D. Booth ⁹⁶, A.G. Borbély ⁵⁹,
 I.S. Bordulev ³⁷, H.M. Borecka-Bielska ¹⁰⁹, G. Borissov ⁹², D. Bortoletto ¹²⁷, D. Boscherini ^{23b},
 M. Bosman ¹³, J.D. Bossio Sola ³⁶, K. Bouaouda ^{35a}, N. Bouchhar ¹⁶⁴, L. Boudet ⁴,
 J. Boudreau ¹³⁰, E.V. Bouhova-Thacker ⁹², D. Boumediene ⁴⁰, R. Bouquet ^{57b,57a}, A. Boveia ¹²⁰,
 J. Boyd ³⁶, D. Boye ²⁹, I.R. Boyko ³⁸, L. Bozianu ⁵⁶, J. Bracinek ²⁰, N. Brahimi ⁴,
 G. Brandt ¹⁷², O. Brandt ³², F. Braren ⁴⁸, B. Brau ¹⁰⁴, J.E. Brau ¹²⁴, R. Brenner ¹⁷⁰,
 L. Brenner ¹¹⁵, R. Brenner ¹⁶², S. Bressler ¹⁷⁰, D. Britton ⁵⁹, D. Britzger ¹¹¹, I. Brock ²⁴,
 G. Brooijmans ⁴¹, E. Brost ²⁹, L.M. Brown ¹⁶⁶, L.E. Bruce ⁶¹, T.L. Bruckler ¹²⁷,
 P.A. Bruckman de Renstrom ⁸⁷, B. Brüers ⁴⁸, A. Bruni ^{23b}, G. Bruni ^{23b}, M. Bruschi ^{23b},
 N. Brusino ^{75a,75b}, T. Buanes ¹⁶, Q. Buat ¹³⁹, D. Buchin ¹¹¹, A.G. Buckley ⁵⁹, O. Bulekov ³⁷,
 B.A. Bullard ¹⁴⁴, S. Burdin ⁹³, C.D. Burgard ⁴⁹, A.M. Burger ³⁶, B. Burghgrave ⁸,
 O. Burlayenko ⁵⁴, J.T.P. Burr ³², J.C. Burzynski ¹⁴³, E.L. Busch ⁴¹, V. Büscher ¹⁰¹,
 P.J. Bussey ⁵⁹, J.M. Butler ²⁵, C.M. Buttar ⁵⁹, J.M. Butterworth ⁹⁷, W. Buttinger ¹³⁵,
 C.J. Buxo Vázquez ¹⁰⁸, A.R. Buzykaev ³⁷, S. Cabrera Urbán ¹⁶⁴, L. Cadamuro ⁶⁶, D. Caforio ⁵⁸,
 H. Cai ¹³⁰, Y. Cai ^{14a,14e}, Y. Cai ^{14c}, V.M.M. Cairo ³⁶, O. Cakir ^{3a}, N. Calace ³⁶,
 P. Calafiura ^{17a}, G. Calderini ¹²⁸, P. Calfayan ⁶⁸, G. Callea ⁵⁹, L.P. Caloba ^{83b}, D. Calvet ⁴⁰,
 S. Calvet ⁴⁰, M. Calvetti ^{74a,74b}, R. Camacho Toro ¹²⁸, S. Camarda ³⁶, D. Camarero Munoz ²⁶,
 P. Camarri ^{76a,76b}, M.T. Camerlingo ^{72a,72b}, D. Cameron ³⁶, C. Camincher ¹⁶⁶, M. Campanelli ⁹⁷,
 A. Camplani ⁴², V. Canale ^{72a,72b}, A.C. Canbay ^{3a}, E. Canonero ⁹⁶, J. Cantero ¹⁶⁴, Y. Cao ¹⁶³,
 F. Capocasa ²⁶, M. Capua ^{43b,43a}, A. Carbone ^{71a,71b}, R. Cardarelli ^{76a}, J.C.J. Cardenas ⁸,
 G. Carducci ^{43b,43a}, T. Carli ³⁶, G. Carlino ^{72a}, J.I. Carlotto ¹³, B.T. Carlson ^{130,p},
 E.M. Carlson ^{166,157a}, J. Carmignani ⁹³, L. Carminati ^{71a,71b}, A. Carnelli ¹³⁶, M. Carnesale ^{75a,75b},
 S. Caron ¹¹⁴, E. Carquin ^{138f}, S. Carrá ^{71a}, G. Carratta ^{23b,23a}, A.M. Carroll ¹²⁴, T.M. Carter ⁵²,
 M.P. Casado ^{13,h}, M. Caspar ⁴⁸, F.L. Castillo ⁴, L. Castillo Garcia ¹³, V. Castillo Gimenez ¹⁶⁴,
 N.F. Castro ^{131a,131e}, A. Catinaccio ³⁶, J.R. Catmore ¹²⁶, T. Cavaliere ⁴, V. Cavaliere ²⁹,
 N. Cavalli ^{23b,23a}, Y.C. Cekmecelioglu ⁴⁸, E. Celebi ^{21a}, S. Cella ³⁶, F. Celli ¹²⁷,
 M.S. Centonze ^{70a,70b}, V. Cepaitis ⁵⁶, K. Cerny ¹²³, A.S. Cerqueira ^{83a}, A. Cerri ¹⁴⁷,
 L. Cerrito ^{76a,76b}, F. Cerutti ^{17a}, B. Cervato ¹⁴², A. Cervelli ^{23b}, G. Cesarini ⁵³, S.A. Cetin ⁸²,
 D. Chakraborty ¹¹⁶, J. Chan ¹⁷¹, W.Y. Chan ¹⁵⁴, J.D. Chapman ³², E. Chapon ¹³⁶,
 B. Chargeishvili ^{150b}, D.G. Charlton ²⁰, M. Chatterjee ¹⁹, C. Chauhan ¹³⁴, Y. Che ^{14c},
 S. Chekanov ⁶, S.V. Chekulaev ^{157a}, G.A. Chelkov ^{38,a}, A. Chen ¹⁰⁷, B. Chen ¹⁵², B. Chen ¹⁶⁶,
 H. Chen ^{14c}, H. Chen ²⁹, J. Chen ^{62c}, J. Chen ¹⁴³, M. Chen ¹²⁷, S. Chen ¹⁵⁴, S.J. Chen ^{14c},
 X. Chen ^{62c,136}, X. Chen ^{14b,ac}, Y. Chen ^{62a}, C.L. Cheng ¹⁷¹, H.C. Cheng ^{64a}, S. Cheong ¹⁴⁴,
 A. Cheplakov ³⁸, E. Cheremushkina ⁴⁸, E. Cherepanova ¹¹⁵, R. Cherkaoui El Moursli ^{35e},
 E. Cheu ⁷, K. Cheung ⁶⁵, L. Chevalier ¹³⁶, V. Chiarella ⁵³, G. Chiarelli ^{74a}, N. Chiedde ¹⁰³,
 G. Chiodini ^{70a}, A.S. Chisholm ²⁰, A. Chitan ^{27b}, M. Chitishvili ¹⁶⁴, M.V. Chizhov ³⁸,
 K. Choi ¹¹, Y. Chou ¹³⁹, E.Y.S. Chow ¹¹⁴, K.L. Chu ¹⁷⁰, M.C. Chu ^{64a}, X. Chu ^{14a,14e},

J. Chudoba ¹³², J.J. Chwastowski ⁸⁷, D. Cieri ¹¹¹, K.M. Ciesla ^{86a}, V. Cindro ⁹⁴, A. Ciocio ^{17a},
 F. Cirotto ^{72a,72b}, Z.H. Citron ¹⁷⁰, M. Citterio ^{71a}, D.A. Ciubotaru ^{27b}, A. Clark ⁵⁶, P.J. Clark ⁵²,
 N. Clarke Hall ⁹⁷, C. Clarry ¹⁵⁶, J.M. Clavijo Columbie ⁴⁸, S.E. Clawson ⁴⁸, C. Clement ^{47a,47b},
 J. Clercx ⁴⁸, Y. Coadou ¹⁰³, M. Cobal ^{69a,69c}, A. Coccaro ^{57b}, R.F. Coelho Barrue ^{131a},
 R. Coelho Lopes De Sa ¹⁰⁴, S. Coelli ^{71a}, B. Cole ⁴¹, J. Collot ⁶⁰, P. Conde Muiño ^{131a,131g},
 M.P. Connell ^{33c}, S.H. Connell ^{33c}, E.I. Conroy ¹²⁷, F. Conventi ^{72a,ae}, H.G. Cooke ²⁰,
 A.M. Cooper-Sarkar ¹²⁷, F.A. Corchia ^{23b,23a}, A. Cordeiro Oudot Choi ¹²⁸, L.D. Corpe ⁴⁰,
 M. Corradi ^{75a,75b}, F. Corriveau ^{105,v}, A. Cortes-Gonzalez ¹⁸, M.J. Costa ¹⁶⁴, F. Costanza ⁴,
 D. Costanzo ¹⁴⁰, B.M. Cote ¹²⁰, G. Cowan ⁹⁶, K. Cranmer ¹⁷¹, D. Cremonini ^{23b,23a},
 S. Crépe-Renaudin ⁶⁰, F. Crescioli ¹²⁸, M. Cristinziani ¹⁴², M. Cristoforetti ^{78a,78b}, V. Croft ¹¹⁵,
 J.E. Crosby ¹²², G. Crosetti ^{43b,43a}, A. Cueto ¹⁰⁰, Z. Cui ⁷, W.R. Cunningham ⁵⁹, F. Curcio ¹⁶⁴,
 J.R. Curran ⁵², P. Czodrowski ³⁶, M.M. Czurylo ³⁶, M.J. Da Cunha Sargedas De Sousa ^{57b,57a},
 J.V. Da Fonseca Pinto ^{83b}, C. Da Via ¹⁰², W. Dabrowski ^{86a}, T. Dado ⁴⁹, S. Dahbi ¹⁴⁹,
 T. Dai ¹⁰⁷, D. Dal Santo ¹⁹, C. Dallapiccola ¹⁰⁴, M. Dam ⁴², G. D'amen ²⁹, V. D'Amico ¹¹⁰,
 J. Damp ¹⁰¹, J.R. Dandoy ³⁴, D. Dannheim ³⁶, M. Danninger ¹⁴³, V. Dao ³⁶, G. Darbo ^{57b},
 S.J. Das ^{29,af}, F. Dattola ⁴⁸, S. D'Auria ^{71a,71b}, A. D'avanzo ^{72a,72b}, C. David ^{33a}, T. Davidek ¹³⁴,
 I. Dawson ⁹⁵, H.A. Day-hall ¹³³, K. De ⁸, R. De Asmundis ^{72a}, N. De Biase ⁴⁸,
 S. De Castro ^{23b,23a}, N. De Groot ¹¹⁴, P. de Jong ¹¹⁵, H. De la Torre ¹¹⁶, A. De Maria ^{14c},
 A. De Salvo ^{75a}, U. De Sanctis ^{76a,76b}, F. De Santis ^{70a,70b}, A. De Santo ¹⁴⁷,
 J.B. De Vivie De Regie ⁶⁰, D.V. Dedovich ³⁸, J. Degens ⁹³, A.M. Deiana ⁴⁴, F. Del Corso ^{23b,23a},
 J. Del Peso ¹⁰⁰, F. Del Rio ^{63a}, L. Delagrangé ¹²⁸, F. Deliot ¹³⁶, C.M. Delitzsch ⁴⁹,
 M. Della Pietra ^{72a,72b}, D. Della Volpe ⁵⁶, A. Dell'Acqua ³⁶, L. Dell'Asta ^{71a,71b}, M. Delmastro ⁴,
 P.A. Delsart ⁶⁰, S. Demers ¹⁷³, M. Demichev ³⁸, S.P. Denisov ³⁷, L. D'Eramo ⁴⁰,
 D. Derendarz ⁸⁷, F. Derue ¹²⁸, P. Dervan ⁹³, K. Desch ²⁴, C. Deutsch ²⁴, F.A. Di Bello ^{57b,57a},
 A. Di Ciaccio ^{76a,76b}, L. Di Ciaccio ⁴, A. Di Domenico ^{75a,75b}, C. Di Donato ^{72a,72b},
 A. Di Girolamo ³⁶, G. Di Gregorio ³⁶, A. Di Luca ^{78a,78b}, B. Di Micco ^{77a,77b}, R. Di Nardo ^{77a,77b},
 K.F. Di Petrillo ³⁹, M. Diamantopoulou ³⁴, F.A. Dias ¹¹⁵, T. Dias Do Vale ¹⁴³,
 M.A. Diaz ^{138a,138b}, F.G. Diaz Capriles ²⁴, M. Didenko ¹⁶⁴, E.B. Diehl ¹⁰⁷, S. Díez Cornell ⁴⁸,
 C. Diez Pardos ¹⁴², C. Dimitriadi ^{162,24}, A. Dimitrievska ²⁰, J. Dingfelder ²⁴, I-M. Dinu ^{27b},
 S.J. Dittmeier ^{63b}, F. Dittus ³⁶, M. Divisek ¹³⁴, F. Djama ¹⁰³, T. Djobava ^{150b},
 C. Doglioni ^{102,99}, A. Dohalova ^{28a}, J. Dolejsi ¹³⁴, Z. Dolezal ¹³⁴, K. Domijan ^{86a},
 K.M. Dona ³⁹, M. Donadelli ^{83d}, B. Dong ¹⁰⁸, J. Donini ⁴⁰, A. D'Onofrio ^{72a,72b},
 M. D'Onofrio ⁹³, J. Dopke ¹³⁵, A. Doria ^{72a}, N. Dos Santos Fernandes ^{131a}, P. Dougan ¹⁰²,
 M.T. Dova ⁹¹, A.T. Doyle ⁵⁹, M.A. Draguet ¹²⁷, E. Dreyer ¹⁷⁰, I. Drivas-koulouris ¹⁰,
 M. Drnevich ¹¹⁸, M. Drozdova ⁵⁶, D. Du ^{62a}, T.A. du Pree ¹¹⁵, F. Dubinin ³⁷, M. Dubovsky ^{28a},
 E. Duchovni ¹⁷⁰, G. Duckeck ¹¹⁰, O.A. Ducu ^{27b}, D. Duda ⁵², A. Dudarev ³⁶, E.R. Duden ²⁶,
 M. D'uffizi ¹⁰², L. Duflo ⁶⁶, M. Dührssen ³⁶, I. Duminica ^{27g}, A.E. Dumitriu ^{27b},
 M. Dunford ^{63a}, S. Dungs ⁴⁹, K. Dunne ^{47a,47b}, A. Duperrin ¹⁰³, H. Duran Yildiz ^{3a},
 M. Düren ⁵⁸, A. Durglishvili ^{150b}, B.L. Dwyer ¹¹⁶, G.I. Dyckes ^{17a}, M. Dyndal ^{86a},
 B.S. Dziedzic ³⁶, Z.O. Earnshaw ¹⁴⁷, G.H. Eberwein ¹²⁷, B. Eckerova ^{28a}, S. Eggebrecht ⁵⁵,
 E. Egidio Purcino De Souza ¹²⁸, L.F. Ehrke ⁵⁶, G. Eigen ¹⁶, K. Einsweiler ^{17a}, T. Ekelof ¹⁶²,
 P.A. Ekman ⁹⁹, S. El Farkh ^{35b}, Y. El Ghazali ^{35b}, H. El Jarrari ³⁶, A. El Moussaouy ^{35a},
 V. Ellajosyula ¹⁶², M. Ellert ¹⁶², F. Ellinghaus ¹⁷², N. Ellis ³⁶, J. Elmsheuser ²⁹, M. Elsayy ^{117a},
 M. Elsing ³⁶, D. Emelianov ¹³⁵, Y. Enari ¹⁵⁴, I. Ene ^{17a}, S. Epari ¹³, P.A. Erland ⁸⁷,
 D. Ernani Martins Neto ⁸⁷, M. Errenst ¹⁷², M. Escalier ⁶⁶, C. Escobar ¹⁶⁴, E. Etzion ¹⁵²,
 G. Evans ^{131a}, H. Evans ⁶⁸, L.S. Evans ⁹⁶, A. Ezhilov ³⁷, S. Ezzarqtouni ^{35a}, F. Fabbri ^{23b,23a},
 L. Fabbri ^{23b,23a}, G. Facini ⁹⁷, V. Fadeyev ¹³⁷, R.M. Fakhruddinov ³⁷, D. Fakoudis ¹⁰¹,

S. Falciano ^{75a}, L.F. Falda Ulhoa Coelho ³⁶, F. Fallavollita ¹¹¹, J. Faltova ¹³⁴, C. Fan ¹⁶³,
 Y. Fan ^{14a}, Y. Fang ^{14a,14e}, M. Fanti ^{71a,71b}, M. Faraj ^{69a,69b}, Z. Farazpay ⁹⁸, A. Farbin ⁸,
 A. Farilla ^{77a}, T. Farooque ¹⁰⁸, S.M. Farrington ⁵², F. Fassi ^{35e}, D. Fassouliotis ⁹,
 M. Faucci Giannelli ^{76a,76b}, W.J. Fawcett ³², L. Fayard ⁶⁶, P. Federic ¹³⁴, P. Federicova ¹³²,
 O.L. Fedin ^{37,a}, M. Feickert ¹⁷¹, L. Feligioni ¹⁰³, D.E. Fellers ¹²⁴, C. Feng ^{62b}, M. Feng ^{14b},
 Z. Feng ¹¹⁵, M.J. Fenton ¹⁶⁰, L. Ferencz ⁴⁸, R.A.M. Ferguson ⁹², S.I. Fernandez Luengo ^{138f},
 P. Fernandez Martinez ¹³, M.J.V. Fernoux ¹⁰³, J. Ferrando ⁹², A. Ferrari ¹⁶², P. Ferrari ^{115,114},
 R. Ferrari ^{73a}, D. Ferrere ⁵⁶, C. Ferretti ¹⁰⁷, F. Fiedler ¹⁰¹, P. Fiedler ¹³³, A. Filipčič ⁹⁴,
 E.K. Filmer ¹, F. Filthaut ¹¹⁴, M.C.N. Fiolhais ^{131a,131c,c}, L. Fiorini ¹⁶⁴, W.C. Fisher ¹⁰⁸,
 T. Fitschen ¹⁰², P.M. Fitzhugh ¹³⁶, I. Fleck ¹⁴², P. Fleischmann ¹⁰⁷, T. Flick ¹⁷², M. Flores ^{33d,aa},
 L.R. Flores Castillo ^{64a}, L. Flores Sanz De Acedo ³⁶, F.M. Follega ^{78a,78b}, N. Fomin ¹⁶,
 J.H. Foo ¹⁵⁶, A. Formica ¹³⁶, A.C. Forti ¹⁰², E. Fortin ³⁶, A.W. Fortman ^{17a}, M.G. Foti ^{17a},
 L. Fountas ^{9,i}, D. Fournier ⁶⁶, H. Fox ⁹², P. Francavilla ^{74a,74b}, S. Francescato ⁶¹,
 S. Franchellucci ⁵⁶, M. Franchini ^{23b,23a}, S. Franchino ^{63a}, D. Francis ³⁶, L. Franco ¹¹⁴,
 V. Franco Lima ³⁶, L. Franconi ⁴⁸, M. Franklin ⁶¹, G. Frattari ²⁶, Y.Y. Frid ¹⁵², J. Friend ⁵⁹,
 N. Fritzsche ⁵⁰, A. Froch ⁵⁴, D. Froidevaux ³⁶, J.A. Frost ¹²⁷, Y. Fu ^{62a},
 S. Fuenzalida Garrido ^{138f}, M. Fujimoto ¹⁰³, K.Y. Fung ^{64a}, E. Furtado De Simas Filho ^{83e},
 M. Furukawa ¹⁵⁴, J. Fuster ¹⁶⁴, A. Gabrielli ^{23b,23a}, A. Gabrielli ¹⁵⁶, P. Gadow ³⁶,
 G. Gagliardi ^{57b,57a}, L.G. Gagnon ^{17a}, S. Gaid ¹⁶¹, S. Galantzan ¹⁵², E.J. Gallas ¹²⁷,
 B.J. Gallop ¹³⁵, K.K. Gan ¹²⁰, S. Ganguly ¹⁵⁴, Y. Gao ⁵², F.M. Garay Walls ^{138a,138b}, B. Garcia ²⁹,
 C. García ¹⁶⁴, A. Garcia Alonso ¹¹⁵, A.G. Garcia Caffaro ¹⁷³, J.E. García Navarro ¹⁶⁴,
 M. Garcia-Sciveres ^{17a}, G.L. Gardner ¹²⁹, R.W. Gardner ³⁹, N. Garelli ¹⁵⁹, D. Garg ⁸⁰,
 R.B. Garg ¹⁴⁴, J.M. Gargan ⁵², C.A. Garner ¹⁵⁶, C.M. Garvey ^{33a}, V.K. Gassmann ¹⁵⁹, G. Gaudio ^{73a},
 V. Gautam ¹³, P. Gauzzi ^{75a,75b}, I.L. Gavrilenko ³⁷, A. Gavriluk ³⁷, C. Gay ¹⁶⁵, G. Gaycken ⁴⁸,
 E.N. Gazis ¹⁰, A.A. Geanta ^{27b}, C.M. Gee ¹³⁷, A. Gekow ¹²⁰, C. Gemme ^{57b}, M.H. Genest ⁶⁰,
 A.D. Gentry ¹¹³, S. George ⁹⁶, W.F. George ²⁰, T. Geralis ⁴⁶, P. Gessinger-Befurt ³⁶,
 M.E. Geyik ¹⁷², M. Ghani ¹⁶⁸, K. Ghorbanian ⁹⁵, A. Ghosal ¹⁴², A. Ghosh ¹⁶⁰, A. Ghosh ⁷,
 B. Giacobbe ^{23b}, S. Giagu ^{75a,75b}, T. Giani ¹¹⁵, P. Giannetti ^{74a}, A. Giannini ^{62a}, S.M. Gibson ⁹⁶,
 M. Gignac ¹³⁷, D.T. Gil ^{86b}, A.K. Gilbert ^{86a}, B.J. Gilbert ⁴¹, D. Gillberg ³⁴, G. Gilles ¹¹⁵,
 L. Ginabat ¹²⁸, D.M. Gingrich ^{2,ad}, M.P. Giordani ^{69a,69c}, P.F. Giraud ¹³⁶, G. Giugliarelli ^{69a,69c},
 D. Giugni ^{71a}, F. Giuli ³⁶, I. Gkialas ^{9,i}, L.K. Gladilin ³⁷, C. Glasman ¹⁰⁰, G.R. Gledhill ¹²⁴,
 G. Glemža ⁴⁸, M. Glisic ¹²⁴, I. Gnesi ^{43b,e}, Y. Go ²⁹, M. Goblirsch-Kolb ³⁶, B. Gocke ⁴⁹,
 D. Godin ¹⁰⁹, B. Gokturk ^{21a}, S. Goldfarb ¹⁰⁶, T. Golling ⁵⁶, M.G.D. Gololo ^{33g}, D. Golubkov ³⁷,
 J.P. Gombas ¹⁰⁸, A. Gomes ^{131a,131b}, G. Gomes Da Silva ¹⁴², A.J. Gomez Delegido ¹⁶⁴,
 R. Gonçalves ^{131a}, L. Gonella ²⁰, A. Gongadze ^{150c}, F. Gonnella ²⁰, J.L. Gonski ¹⁴⁴,
 R.Y. González Andana ⁵², S. González de la Hoz ¹⁶⁴, R. Gonzalez Lopez ⁹³,
 C. Gonzalez Renteria ^{17a}, M.V. Gonzalez Rodrigues ⁴⁸, R. Gonzalez Suarez ¹⁶²,
 S. Gonzalez-Sevilla ⁵⁶, L. Goossens ³⁶, B. Gorini ³⁶, E. Gorini ^{70a,70b}, A. Gorišek ⁹⁴,
 T.C. Gosart ¹²⁹, A.T. Goshaw ⁵¹, M.I. Gostkin ³⁸, S. Goswami ¹²², C.A. Gottardo ³⁶,
 S.A. Gotz ¹¹⁰, M. Gouighri ^{35b}, V. Goumarre ⁴⁸, A.G. Goussiou ¹³⁹, N. Govender ^{33c},
 I. Grabowska-Bold ^{86a}, K. Graham ³⁴, E. Gramstad ¹²⁶, S. Grancagnolo ^{70a,70b}, C.M. Grant ^{1,136},
 P.M. Gravila ^{27f}, F.G. Gravili ^{70a,70b}, H.M. Gray ^{17a}, M. Greco ^{70a,70b}, C. Grefe ²⁴,
 A.S. Grefsrud ¹⁶, I.M. Gregor ⁴⁸, K.T. Greif ¹⁶⁰, P. Grenier ¹⁴⁴, S.G. Grewe ¹¹¹, A.A. Grillo ¹³⁷,
 K. Grimm ³¹, S. Grinstein ^{13,r}, J.-F. Grivaz ⁶⁶, E. Gross ¹⁷⁰, J. Grosse-Knetter ⁵⁵,
 J.C. Grundy ¹²⁷, L. Guan ¹⁰⁷, J.G.R. Guerrero Rojas ¹⁶⁴, G. Guerrieri ^{69a,69c}, R. Gugel ¹⁰¹,
 J.A.M. Guhit ¹⁰⁷, A. Guida ¹⁸, E. Guilloton ¹⁶⁸, S. Guindon ³⁶, F. Guo ^{14a,14e}, J. Guo ^{62c},
 L. Guo ⁴⁸, Y. Guo ¹⁰⁷, R. Gupta ¹³⁰, S. Gurbuz ²⁴, S.S. Gurdasani ⁵⁴, G. Gustavino ³⁶,

M. Guth ⁵⁶, P. Gutierrez ¹²¹, L.F. Gutierrez Zagazeta ¹²⁹, M. Gutsche ⁵⁰, C. Gutschow ⁹⁷,
C. Gwenlan ¹²⁷, C.B. Gwilliam ⁹³, E.S. Haaland ¹²⁶, A. Haas ¹¹⁸, M. Habedank ⁴⁸,
C. Haber ^{17a}, H.K. Hadavand ⁸, A. Hadeef ⁵⁰, S. Hadzic ¹¹¹, A.I. Hagan ⁹², J.J. Hahn ¹⁴²,
E.H. Haines ⁹⁷, M. Haleem ¹⁶⁷, J. Haley ¹²², J.J. Hall ¹⁴⁰, G.D. Hallewell ¹⁰³, L. Halser ¹⁹,
K. Hamano ¹⁶⁶, M. Hamer ²⁴, G.N. Hamity ⁵², E.J. Hampshire ⁹⁶, J. Han ^{62b}, K. Han ^{62a},
L. Han ^{14c}, L. Han ^{62a}, S. Han ^{17a}, Y.F. Han ¹⁵⁶, K. Hanagaki ⁸⁴, M. Hance ¹³⁷,
D.A. Hangal ⁴¹, H. Hanif ¹⁴³, M.D. Hank ¹²⁹, J.B. Hansen ⁴², P.H. Hansen ⁴², K. Hara ¹⁵⁸,
D. Harada ⁵⁶, T. Harenberg ¹⁷², S. Harkusha ³⁷, M.L. Harris ¹⁰⁴, Y.T. Harris ¹²⁷, J. Harrison ¹³,
N.M. Harrison ¹²⁰, P.F. Harrison ¹⁶⁸, N.M. Hartman ¹¹¹, N.M. Hartmann ¹¹⁰, R.Z. Hasan ^{96,135},
Y. Hasegawa ¹⁴¹, S. Hassan ¹⁶, R. Hauser ¹⁰⁸, C.M. Hawkes ²⁰, R.J. Hawkings ³⁶,
Y. Hayashi ¹⁵⁴, S. Hayashida ¹¹², D. Hayden ¹⁰⁸, C. Hayes ¹⁰⁷, R.L. Hayes ¹¹⁵, C.P. Hays ¹²⁷,
J.M. Hays ⁹⁵, H.S. Hayward ⁹³, F. He ^{62a}, M. He ^{14a,14e}, Y. He ¹⁵⁵, Y. He ⁴⁸, Y. He ⁹⁷,
N.B. Heatley ⁹⁵, V. Hedberg ⁹⁹, A.L. Heggelund ¹²⁶, N.D. Hehir ^{95,*}, C. Heidegger ⁵⁴,
K.K. Heidegger ⁵⁴, J. Heilman ³⁴, S. Heim ⁴⁸, T. Heim ^{17a}, J.G. Heinlein ¹²⁹, J.J. Heinrich ¹²⁴,
L. Heinrich ^{111,ab}, J. Hejbal ¹³², A. Held ¹⁷¹, S. Hellesund ¹⁶, C.M. Helling ¹⁶⁵,
S. Hellman ^{47a,47b}, R.C.W. Henderson ⁹², L. Henkelmann ³², A.M. Henriques Correia ³⁶, H. Herde ⁹⁹,
Y. Hernández Jiménez ¹⁴⁶, L.M. Herrmann ²⁴, T. Herrmann ⁵⁰, G. Herten ⁵⁴, R. Hertenberger ¹¹⁰,
L. Hervas ³⁶, M.E. Hesping ¹⁰¹, N.P. Hessey ^{157a}, M. Hidaoui ^{35b}, E. Hill ¹⁵⁶, S.J. Hillier ²⁰,
J.R. Hinds ¹⁰⁸, F. Hinterkeuser ²⁴, M. Hirose ¹²⁵, S. Hirose ¹⁵⁸, D. Hirschbuehl ¹⁷²,
T.G. Hitchings ¹⁰², B. Hiti ⁹⁴, J. Hobbs ¹⁴⁶, R. Hobincu ^{27c}, N. Hod ¹⁷⁰, M.C. Hodgkinson ¹⁴⁰,
B.H. Hodgkinson ¹²⁷, A. Hoecker ³⁶, D.D. Hofer ¹⁰⁷, J. Hofer ⁴⁸, T. Holm ²⁴, M. Holzbock ¹¹¹,
L.B.A.H. Hommels ³², B.P. Honan ¹⁰², J.J. Hong ⁶⁸, J. Hong ^{62c}, T.M. Hong ¹³⁰,
B.H. Hooberman ¹⁶³, W.H. Hopkins ⁶, M.C. Hoppesch ¹⁶³, Y. Horii ¹¹², S. Hou ¹⁴⁹,
A.S. Howard ⁹⁴, J. Howarth ⁵⁹, J. Hoya ⁶, M. Hrabovsky ¹²³, A. Hrynevich ⁴⁸, T. Hryn'ova ⁴,
P.J. Hsu ⁶⁵, S.-C. Hsu ¹³⁹, T. Hsu ⁶⁶, M. Hu ^{17a}, Q. Hu ^{62a}, S. Huang ^{64b}, X. Huang ^{14a,14e},
Y. Huang ¹⁴⁰, Y. Huang ¹⁰¹, Y. Huang ^{14a}, Z. Huang ¹⁰², Z. Hubacek ¹³³, M. Huebner ²⁴,
F. Huegging ²⁴, T.B. Huffman ¹²⁷, C.A. Hugli ⁴⁸, M. Huhtinen ³⁶, S.K. Huiberts ¹⁶,
R. Hulsken ¹⁰⁵, N. Huseynov ¹², J. Huston ¹⁰⁸, J. Huth ⁶¹, R. Hyneman ¹⁴⁴, G. Iacobucci ⁵⁶,
G. Iakovidis ²⁹, L. Iconomidou-Fayard ⁶⁶, J.P. Iddon ³⁶, P. Iengo ^{72a,72b}, R. Iguchi ¹⁵⁴,
Y. Iiyama ¹⁵⁴, T. Iizawa ¹²⁷, Y. Ikegami ⁸⁴, N. Ilic ¹⁵⁶, H. Imam ^{35a}, M. Ince Lezki ⁵⁶,
T. Ingebretsen Carlson ^{47a,47b}, G. Introzzi ^{73a,73b}, M. Iodice ^{77a}, V. Ippolito ^{75a,75b}, R.K. Irwin ⁹³,
M. Ishino ¹⁵⁴, W. Islam ¹⁷¹, C. Issever ^{18,48}, S. Istin ^{21a,ah}, H. Ito ¹⁶⁹, R. Iuppa ^{78a,78b},
A. Ivina ¹⁷⁰, J.M. Izen ⁴⁵, V. Izzo ^{72a}, P. Jacka ¹³², P. Jackson ¹, C.S. Jagfeld ¹¹⁰, G. Jain ^{157a},
P. Jain ⁴⁸, K. Jakobs ⁵⁴, T. Jakoubek ¹⁷⁰, J. Jamieson ⁵⁹, M. Javurkova ¹⁰⁴, L. Jeanty ¹²⁴,
J. Jejelava ^{150a,y}, P. Jenni ^{54,f}, C.E. Jessiman ³⁴, C. Jia ^{62b}, J. Jia ¹⁴⁶, X. Jia ⁶¹, X. Jia ^{14a,14e},
Z. Jia ^{14c}, C. Jiang ⁵², S. Jiggins ⁴⁸, J. Jimenez Pena ¹³, S. Jin ^{14c}, A. Jinaru ^{27b},
O. Jinnouchi ¹⁵⁵, P. Johansson ¹⁴⁰, K.A. Johns ⁷, J.W. Johnson ¹³⁷, D.M. Jones ¹⁴⁷, E. Jones ⁴⁸,
P. Jones ³², R.W.L. Jones ⁹², T.J. Jones ⁹³, H.L. Joos ^{55,36}, R. Joshi ¹²⁰, J. Jovicevic ¹⁵,
X. Ju ^{17a}, J.J. Junggeburth ¹⁰⁴, T. Junkermann ^{63a}, A. Juste Rozas ^{13,r}, M.K. Juzek ⁸⁷,
S. Kabana ^{138e}, A. Kaczmarska ⁸⁷, M. Kado ¹¹¹, H. Kagan ¹²⁰, M. Kagan ¹⁴⁴, A. Kahn ¹²⁹,
C. Kahra ¹⁰¹, T. Kaji ¹⁵⁴, E. Kajomovitz ¹⁵¹, N. Kakati ¹⁷⁰, I. Kalaitzidou ⁵⁴, C.W. Calderon ²⁹,
N.J. Kang ¹³⁷, D. Kar ^{33g}, K. Karava ¹²⁷, M.J. Kareem ^{157b}, E. Karentzos ⁵⁴, O. Karkout ¹¹⁵,
S.N. Karpov ³⁸, Z.M. Karpova ³⁸, V. Kartvelishvili ⁹², A.N. Karyukhin ³⁷, E. Kasimi ¹⁵³,
J. Katzy ⁴⁸, S. Kaur ³⁴, K. Kawade ¹⁴¹, M.P. Kawale ¹²¹, C. Kawamoto ⁸⁸, T. Kawamoto ^{62a},
E.F. Kay ³⁶, F.I. Kaya ¹⁵⁹, S. Kazakos ¹⁰⁸, V.F. Kazanin ³⁷, Y. Ke ¹⁴⁶, J.M. Keaveney ^{33a},
R. Keeler ¹⁶⁶, G.V. Kehris ⁶¹, J.S. Keller ³⁴, A.S. Kelly ⁹⁷, J.J. Kempster ¹⁴⁷, P.D. Kennedy ¹⁰¹,
O. Kepka ¹³², B.P. Kerridge ¹³⁵, S. Kersten ¹⁷², B.P. Kerševan ⁹⁴, L. Keszeghova ^{28a},

S. Ketabchi Haghighat [ID156](#), R.A. Khan [ID130](#), A. Khanov [ID122](#), A.G. Kharlamov [ID37](#), T. Kharlamova [ID37](#),
 E.E. Khoda [ID139](#), M. Kholodenko [ID37](#), T.J. Khoo [ID18](#), G. Khorauli [ID167](#), J. Khubua [ID150b](#),
 Y.A.R. Khwaira [ID128](#), B. Kibirige^{33g}, D.W. Kim [ID47a,47b](#), Y.K. Kim [ID39](#), N. Kimura [ID97](#),
 M.K. Kingston [ID55](#), A. Kirchhoff [ID55](#), C. Kirfel [ID24](#), F. Kirfel [ID24](#), J. Kirk [ID135](#), A.E. Kiryunin [ID111](#),
 C. Kitsaki [ID10](#), O. Kivernyk [ID24](#), M. Klassen [ID159](#), C. Klein [ID34](#), L. Klein [ID167](#), M.H. Klein [ID44](#),
 S.B. Klein [ID56](#), U. Klein [ID93](#), P. Klimek [ID36](#), A. Klimentov [ID29](#), T. Klioutchnikova [ID36](#), P. Kluit [ID115](#),
 S. Kluth [ID111](#), E. Kneringer [ID79](#), T.M. Knight [ID156](#), A. Knue [ID49](#), R. Kobayashi [ID88](#),
 D. Kobylanskii [ID170](#), S.F. Koch [ID127](#), M. Kocian [ID144](#), P. Kodyš [ID134](#), D.M. Koeck [ID124](#),
 P.T. Koenig [ID24](#), T. Koffas [ID34](#), O. Kolay [ID50](#), I. Koletsou [ID4](#), T. Komarek [ID123](#), K. Köneke [ID54](#),
 A.X.Y. Kong [ID1](#), T. Kono [ID119](#), N. Konstantinidis [ID97](#), P. Kontaxakis [ID56](#), B. Konya [ID99](#),
 R. Kopeliansky [ID41](#), S. Koperny [ID86a](#), K. Korcyl [ID87](#), K. Kordas [ID153,d](#), A. Korn [ID97](#), S. Korn [ID55](#),
 I. Korolkov [ID13](#), N. Korotkova [ID37](#), B. Kortman [ID115](#), O. Kortner [ID111](#), S. Kortner [ID111](#),
 W.H. Kostecka [ID116](#), V.V. Kostyukhin [ID142](#), A. Kotsokechagia [ID136](#), A. Kotwal [ID51](#), A. Koulouris [ID36](#),
 A. Kourkoumeli-Charalampidi [ID73a,73b](#), C. Kourkoumelis [ID9](#), E. Kourlitis [ID111,ab](#), O. Kovanda [ID124](#),
 R. Kowalewski [ID166](#), W. Kozanecki [ID136](#), A.S. Kozhin [ID37](#), V.A. Kramarenko [ID37](#), G. Kramberger [ID94](#),
 P. Kramer [ID101](#), M.W. Krasny [ID128](#), A. Krasznahorkay [ID36](#), A.C. Kraus [ID116](#), J.W. Kraus [ID172](#),
 J.A. Kremer [ID48](#), T. Kresse [ID50](#), J. Kretschmar [ID93](#), K. Kreul [ID18](#), P. Krieger [ID156](#),
 S. Krishnamurthy [ID104](#), M. Krivos [ID134](#), K. Krizka [ID20](#), K. Kroeninger [ID49](#), H. Kroha [ID111](#), J. Kroll [ID132](#),
 J. Kroll [ID129](#), K.S. Krowpman [ID108](#), U. Kruchonak [ID38](#), H. Krüger [ID24](#), N. Krumnack⁸¹, M.C. Kruse [ID51](#),
 O. Kuchinskaia [ID37](#), S. Kuday [ID3a](#), S. Kuehn [ID36](#), R. Kuesters [ID54](#), T. Kuhl [ID48](#), V. Kukhtin [ID38](#),
 Y. Kulchitsky [ID37,a](#), S. Kuleshov [ID138d,138b](#), M. Kumar [ID33g](#), N. Kumari [ID48](#), P. Kumari [ID157b](#),
 A. Kupco [ID132](#), T. Kupfer⁴⁹, A. Kupich [ID37](#), O. Kuprash [ID54](#), H. Kurashige [ID85](#), L.L. Kurchaninov [ID157a](#),
 O. Kurdysh [ID66](#), Y.A. Kurochkin [ID37](#), A. Kurova [ID37](#), M. Kuze [ID155](#), A.K. Kvam [ID104](#), J. Kvita [ID123](#),
 T. Kwan [ID105](#), N.G. Kyriacou [ID107](#), L.A.O. Laatu [ID103](#), C. Lacasta [ID164](#), F. Lacava [ID75a,75b](#),
 H. Lacker [ID18](#), D. Lacour [ID128](#), N.N. Lad [ID97](#), E. Ladygin [ID38](#), A. Lafarge [ID40](#), B. Laforge [ID128](#),
 T. Lagouri [ID173](#), F.Z. Lahbabi [ID35a](#), S. Lai [ID55](#), J.E. Lambert [ID166](#), S. Lammers [ID68](#), W. Lampl [ID7](#),
 C. Lampoudis [ID153,d](#), G. Lamprinoudis¹⁰¹, A.N. Lancaster [ID116](#), E. Lançon [ID29](#), U. Landgraf [ID54](#),
 M.P.J. Landon [ID95](#), V.S. Lang [ID54](#), O.K.B. Langrekken [ID126](#), A.J. Lankford [ID160](#), F. Lanni [ID36](#),
 K. Lantzsck [ID24](#), A. Lanza [ID73a](#), J.F. Laporte [ID136](#), T. Lari [ID71a](#), F. Lasagni Manghi [ID23b](#),
 M. Lassnig [ID36](#), V. Latonova [ID132](#), A. Laudrain [ID101](#), A. Laurier [ID151](#), S.D. Lawlor [ID140](#),
 Z. Lawrence [ID102](#), R. Lazaridou¹⁶⁸, M. Lazzaroni [ID71a,71b](#), B. Le¹⁰², E.M. Le Boulicaut [ID51](#),
 L.T. Le Pottier [ID17a](#), B. Leban [ID23b,23a](#), A. Lebedev [ID81](#), M. LeBlanc [ID102](#), F. Ledroit-Guillon [ID60](#),
 S.C. Lee [ID149](#), S. Lee [ID47a,47b](#), T.F. Lee [ID93](#), L.L. Leeuw [ID33c](#), H.P. Lefebvre [ID96](#), M. Lefebvre [ID166](#),
 C. Leggett [ID17a](#), G. Lehmann Miotto [ID36](#), M. Leigh [ID56](#), W.A. Leight [ID104](#), W. Leinonen [ID114](#),
 A. Leisos [ID153,q](#), M.A.L. Leite [ID83c](#), C.E. Leitgeb [ID18](#), R. Leitner [ID134](#), K.J.C. Leney [ID44](#), T. Lenz [ID24](#),
 S. Leone [ID74a](#), C. Leonidopoulos [ID52](#), A. Leopold [ID145](#), C. Leroy [ID109](#), R. Les [ID108](#), C.G. Lester [ID32](#),
 M. Levchenko [ID37](#), J. Levêque [ID4](#), L.J. Levinson [ID170](#), G. Levrini^{23b,23a}, M.P. Lewicki [ID87](#),
 C. Lewis [ID139](#), D.J. Lewis [ID4](#), A. Li [ID5](#), B. Li [ID62b](#), C. Li [ID62a](#), C-Q. Li [ID111](#), H. Li [ID62a](#), H. Li [ID62b](#),
 H. Li [ID14c](#), H. Li [ID14b](#), H. Li [ID62b](#), J. Li [ID62c](#), K. Li [ID139](#), L. Li [ID62c](#), M. Li [ID14a,14e](#), S. Li [ID14a,14e](#),
 S. Li [ID62d,62c](#), T. Li [ID5](#), X. Li [ID105](#), Z. Li [ID127](#), Z. Li [ID105](#), Z. Li [ID14a,14e](#), S. Liang^{14a,14e}, Z. Liang [ID14a](#),
 M. Liberatore [ID136](#), B. Liberti [ID76a](#), K. Lie [ID64c](#), J. Lieber Marin [ID83e](#), H. Lien [ID68](#), H. Lin [ID107](#),
 K. Lin [ID108](#), R.E. Lindley [ID7](#), J.H. Lindon [ID2](#), E. Lipeles [ID129](#), A. Lipniacka [ID16](#), A. Lister [ID165](#),
 J.D. Little [ID68](#), B. Liu [ID14a](#), B.X. Liu [ID14d](#), D. Liu [ID62d,62c](#), E.H.L. Liu [ID20](#), J.B. Liu [ID62a](#),
 J.K.K. Liu [ID32](#), K. Liu [ID62d](#), K. Liu [ID62d,62c](#), M. Liu [ID62a](#), M.Y. Liu [ID62a](#), P. Liu [ID14a](#), Q. Liu [ID62d,139,62c](#),
 X. Liu [ID62a](#), X. Liu [ID62b](#), Y. Liu [ID14d,14e](#), Y.L. Liu [ID62b](#), Y.W. Liu [ID62a](#), J. Llorente Merino [ID143](#),
 S.L. Lloyd [ID95](#), E.M. Lobodzinska [ID48](#), P. Loch [ID7](#), T. Lohse [ID18](#), K. Lohwasser [ID140](#), E. Loiacono [ID48](#),
 M. Lokajicek [ID132,*](#), J.D. Lomas [ID20](#), J.D. Long [ID163](#), I. Longarini [ID160](#), R. Longo [ID163](#),





















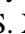

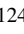


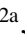

I. Lopez Paz ⁶⁷, A. Lopez Solis ⁴⁸, N. Lorenzo Martinez ⁴, A.M. Lory ¹¹⁰, M. Losada ^{117a},
 G. Lösckce Centeno ¹⁴⁷, O. Loseva ³⁷, X. Lou ^{47a,47b}, X. Lou ^{14a,14e}, A. Lounis ⁶⁶,
 P.A. Love ⁹², G. Lu ^{14a,14e}, M. Lu ⁶⁶, S. Lu ¹²⁹, Y.J. Lu ⁶⁵, H.J. Lubatti ¹³⁹, C. Luci ^{75a,75b},
 F.L. Lucio Alves ^{14c}, F. Luehring ⁶⁸, I. Luise ¹⁴⁶, O. Lukianchuk ⁶⁶, O. Lundberg ¹⁴⁵,
 B. Lund-Jensen ¹⁴⁵, N.A. Luongo ⁶, M.S. Lutz ³⁶, A.B. Lux ²⁵, D. Lynn ²⁹, R. Lysak ¹³²,
 E. Lytken ⁹⁹, V. Lyubushkin ³⁸, T. Lyubushkina ³⁸, M.M. Lyukova ¹⁴⁶, M.Firdaus M. Soberi ⁵²,
 H. Ma ²⁹, K. Ma ^{62a}, L.L. Ma ^{62b}, W. Ma ^{62a}, Y. Ma ¹²², J.C. MacDonald ¹⁰¹,
 P.C. Machado De Abreu Farias ^{83e}, R. Madar ⁴⁰, T. Madula ⁹⁷, J. Maeda ⁸⁵, T. Maeno ²⁹,
 H. Maguire ¹⁴⁰, V. Maiboroda ¹³⁶, A. Maio ^{131a,131b,131d}, K. Maj ^{86a}, O. Majersky ⁴⁸,
 S. Majewski ¹²⁴, N. Makovec ⁶⁶, V. Maksimovic ¹⁵, B. Malaescu ¹²⁸, Pa. Malecki ⁸⁷,
 V.P. Maleev ³⁷, F. Malek ^{60,m}, M. Mali ⁹⁴, D. Malito ⁹⁶, U. Mallik ⁸⁰, S. Maltezos ¹⁰,
 S. Malyukov ³⁸, J. Mamuzic ¹³, G. Mancini ⁵³, M.N. Mancini ²⁶, G. Manco ^{73a,73b},
 J.P. Mandalia ⁹⁵, I. Mandić ⁹⁴, L. Manhaes de Andrade Filho ^{83a}, I.M. Maniatis ¹⁷⁰,
 J. Manjarres Ramos ⁹⁰, D.C. Mankad ¹⁷⁰, A. Mann ¹¹⁰, S. Manzoni ³⁶, L. Mao ^{62c},
 X. Mapekula ^{33c}, A. Marantis ^{153,q}, G. Marchiori ⁵, M. Marcisovsky ¹³², C. Marcon ^{71a},
 M. Marinescu ²⁰, S. Marium ⁴⁸, M. Marjanovic ¹²¹, A. Markhoos ⁵⁴, M. Markovitch ⁶⁶,
 E.J. Marshall ⁹², Z. Marshall ^{17a}, S. Marti-Garcia ¹⁶⁴, J. Martin ⁹⁷, T.A. Martin ¹³⁵,
 V.J. Martin ⁵², B. Martin dit Latour ¹⁶, L. Martinelli ^{75a,75b}, M. Martinez ^{13,r},
 P. Martinez Agullo ¹⁶⁴, V.I. Martinez Outschoorn ¹⁰⁴, P. Martinez Suarez ¹³, S. Martin-Haugh ¹³⁵,
 G. Martinovicova ¹³⁴, V.S. Martoiu ^{27b}, A.C. Martyniuk ⁹⁷, A. Marzin ³⁶, D. Mascione ^{78a,78b},
 L. Masetti ¹⁰¹, T. Mashimo ¹⁵⁴, J. Masik ¹⁰², A.L. Maslennikov ³⁷, P. Massarotti ^{72a,72b},
 P. Mastrandrea ^{74a,74b}, A. Mastroberardino ^{43b,43a}, T. Masubuchi ¹⁵⁴, T. Mathisen ¹⁶²,
 J. Matousek ¹³⁴, N. Matsuzawa ¹⁵⁴, J. Maurer ^{27b}, A.J. Maury ⁶⁶, B. Maček ⁹⁴, D.A. Maximov ³⁷,
 A.E. May ¹⁰², R. Mazini ¹⁴⁹, I. Maznas ¹¹⁶, M. Mazza ¹⁰⁸, S.M. Mazza ¹³⁷, E. Mazzeo ^{71a,71b},
 C. Mc Ginn ²⁹, J.P. Mc Gowan ¹⁶⁶, S.P. Mc Kee ¹⁰⁷, C.C. McCracken ¹⁶⁵, E.F. McDonald ¹⁰⁶,
 A.E. McDougall ¹¹⁵, J.A. Mcfayden ¹⁴⁷, R.P. McGovern ¹²⁹, R.P. Mckenzie ^{33g},
 T.C. McLachlan ⁴⁸, D.J. McLaughlin ⁹⁷, S.J. McMahon ¹³⁵, C.M. Mcpartland ⁹³,
 R.A. McPherson ^{166,v}, S. Mehlhase ¹¹⁰, A. Mehta ⁹³, D. Melini ¹⁶⁴, B.R. Mellado Garcia ^{33g},
 A.H. Melo ⁵⁵, F. Meloni ⁴⁸, A.M. Mendes Jacques Da Costa ¹⁰², H.Y. Meng ¹⁵⁶, L. Meng ⁹²,
 S. Menke ¹¹¹, M. Mentink ³⁶, E. Meoni ^{43b,43a}, G. Mercado ¹¹⁶, S. Merianos ¹⁵³,
 C. Merlassino ^{69a,69c}, L. Merola ^{72a,72b}, C. Meroni ^{71a,71b}, J. Metcalfe ⁶, A.S. Mete ⁶,
 E. Meuser ¹⁰¹, C. Meyer ⁶⁸, J-P. Meyer ¹³⁶, R.P. Middleton ¹³⁵, L. Mijović ⁵²,
 G. Mikenberg ¹⁷⁰, M. Mikestikova ¹³², M. Mikuž ⁹⁴, H. Mildner ¹⁰¹, A. Milic ³⁶,
 D.W. Miller ³⁹, E.H. Miller ¹⁴⁴, L.S. Miller ³⁴, A. Milov ¹⁷⁰, D.A. Milstead ^{47a,47b}, T. Min ^{14c},
 A.A. Minaenko ³⁷, I.A. Minashvili ^{150b}, L. Mince ⁵⁹, A.I. Mincer ¹¹⁸, B. Mindur ^{86a},
 M. Mineev ³⁸, Y. Mino ⁸⁸, L.M. Mir ¹³, M. Miralles Lopez ⁵⁹, M. Mironova ^{17a}, A. Mishima ¹⁵⁴,
 M.C. Missio ¹¹⁴, A. Mitra ¹⁶⁸, V.A. Mitsou ¹⁶⁴, Y. Mitsumori ¹¹², O. Miu ¹⁵⁶,
 P.S. Miyagawa ⁹⁵, T. Mkrtchyan ^{63a}, M. Mlinarevic ⁹⁷, T. Mlinarevic ⁹⁷, M. Mlynarikova ³⁶,
 S. Mobius ¹⁹, P. Mogg ¹¹⁰, M.H. Mohamed Farook ¹¹³, A.F. Mohammed ^{14a,14e}, S. Mohapatra ⁴¹,
 G. Mokgatitwane ^{33g}, L. Moleri ¹⁷⁰, B. Mondal ¹⁴², S. Mondal ¹³³, K. Mönig ⁴⁸,
 E. Monnier ¹⁰³, L. Monsonis Romero ¹⁶⁴, J. Montejo Berlingen ¹³, M. Montella ¹²⁰,
 F. Montekali ^{77a,77b}, F. Monticelli ⁹¹, S. Monzani ^{69a,69c}, N. Morange ⁶⁶,
 A.L. Moreira De Carvalho ⁴⁸, M. Moreno Llácer ¹⁶⁴, C. Moreno Martinez ⁵⁶, P. Morettini ^{57b},
 S. Morgenstern ³⁶, M. Morii ⁶¹, M. Morinaga ¹⁵⁴, F. Morodei ^{75a,75b}, L. Morvaj ³⁶,
 P. Moschovakos ³⁶, B. Moser ³⁶, M. Mosidze ^{150b}, T. Moskalets ⁴⁴, P. Moskvitina ¹¹⁴,
 J. Moss ^{31,j}, P. Moszkowicz ^{86a}, A. Moussa ^{35d}, E.J.W. Moyse ¹⁰⁴, O. Mtintsilana ^{33g},
 S. Muanza ¹⁰³, J. Mueller ¹³⁰, D. Muenstermann ⁹², R. Müller ¹⁹, G.A. Mullier ¹⁶²,

A.J. Mullin³², J.J. Mullin¹²⁹, D.P. Mungo¹⁵⁶, D. Munoz Perez¹⁶⁴, F.J. Munoz Sanchez¹⁰²,
 M. Murin¹⁰², W.J. Murray^{168,135}, M. Muškinja⁹⁴, C. Mwewa²⁹, A.G. Myagkov^{37,a},
 A.J. Myers⁸, G. Myers¹⁰⁷, M. Myska¹³³, B.P. Nachman^{17a}, O. Nackenhorst⁴⁹, K. Nagai¹²⁷,
 K. Nagano⁸⁴, J.L. Nagle^{29,af}, E. Nagy¹⁰³, A.M. Nairz³⁶, Y. Nakahama⁸⁴, K. Nakamura⁸⁴,
 K. Nakkalil⁵, H. Nanjo¹²⁵, E.A. Narayanan¹¹³, I. Naryshkin³⁷, L. Nasella^{71a,71b},
 M. Naseri³⁴, S. Nasri^{117b}, C. Nass²⁴, G. Navarro^{22a}, J. Navarro-Gonzalez¹⁶⁴, R. Nayak¹⁵²,
 A. Nayaz¹⁸, P.Y. Nechaeva³⁷, S. Nechaeva^{23b,23a}, F. Nechansky⁴⁸, L. Nedic¹²⁷, T.J. Neep²⁰,
 A. Negri^{73a,73b}, M. Negrini^{23b}, C. Nellist¹¹⁵, C. Nelson¹⁰⁵, K. Nelson¹⁰⁷, S. Nemecek¹³²,
 M. Nessi^{36,g}, M.S. Neubauer¹⁶³, F. Neuhaus¹⁰¹, J. Neundorf⁴⁸, P.R. Newman²⁰,
 C.W. Ng¹³⁰, Y.W.Y. Ng⁴⁸, B. Ngair^{117a}, H.D.N. Nguyen¹⁰⁹, R.B. Nickerson¹²⁷,
 R. Nicolaidou¹³⁶, J. Nielsen¹³⁷, M. Niemeyer⁵⁵, J. Niermann⁵⁵, N. Nikiforou³⁶,
 V. Nikolaenko^{37,a}, I. Nikolic-Audit¹²⁸, K. Nikolopoulos²⁰, P. Nilsson²⁹, I. Ninca⁴⁸,
 G. Ninio¹⁵², A. Nisati^{75a}, N. Nishu², R. Nisius¹¹¹, J-E. Nitschke⁵⁰, E.K. Nkadimeng^{33g},
 T. Nobe¹⁵⁴, T. Nommensen¹⁴⁸, M.B. Norfolk¹⁴⁰, B.J. Norman³⁴, M. Noury^{35a}, J. Novak⁹⁴,
 T. Novak⁹⁴, L. Novotny¹³³, R. Novotny¹¹³, L. Nozka¹²³, K. Ntekas¹⁶⁰,
 N.M.J. Nunes De Moura Junior^{83b}, J. Ocariz¹²⁸, A. Ochi⁸⁵, I. Ochoa^{131a}, S. Oerdek^{48,s},
 J.T. Offermann³⁹, A. Ogrodnik¹³⁴, A. Oh¹⁰², C.C. Ohm¹⁴⁵, H. Oide⁸⁴, R. Oishi¹⁵⁴,
 M.L. Ojeda⁴⁸, Y. Okumura¹⁵⁴, L.F. Oleiro Seabra^{131a}, I. Oleksiyuk⁵⁶, S.A. Olivares Pino^{138d},
 G. Oliveira Correa¹³, D. Oliveira Damazio²⁹, D. Oliveira Goncalves^{83a}, J.L. Oliver¹⁶⁰,
 Ö.O. Öncel⁵⁴, A.P. O'Neill¹⁹, A. Onofre^{131a,131e}, P.U.E. Onyisi¹¹, M.J. Oreglia³⁹,
 G.E. Orellana⁹¹, D. Orestano^{77a,77b}, N. Orlando¹³, R.S. Orr¹⁵⁶, L.M. Osojnak¹²⁹,
 R. Ospanov^{62a}, G. Otero y Garzon³⁰, H. Otono⁸⁹, P.S. Ott^{63a}, G.J. Ottino^{17a}, M. Ouchrif^{35d},
 F. Ould-Saada¹²⁶, T. Ovsianikova¹³⁹, M. Owen⁵⁹, R.E. Owen¹³⁵, V.E. Ozcan^{21a},
 F. Ozturk⁸⁷, N. Ozturk⁸, S. Ozturk⁸², H.A. Pacey¹²⁷, A. Pacheco Pages¹³,
 C. Padilla Aranda¹³, G. Padovano^{75a,75b}, S. Pagan Griso^{17a}, G. Palacino⁶⁸, A. Palazzo^{70a,70b},
 J. Pampel²⁴, J. Pan¹⁷³, T. Pan^{64a}, D.K. Panchal¹¹, C.E. Pandini¹¹⁵, J.G. Panduro Vazquez¹³⁵,
 H.D. Pandya¹, H. Pang^{14b}, P. Pani⁴⁸, G. Panizzo^{69a,69c}, L. Panwar¹²⁸, L. Paolozzi⁵⁶,
 S. Parajuli¹⁶³, A. Paramonov⁶, C. Paraskevopoulos⁵³, D. Paredes Hernandez^{64b},
 A. Pareti^{73a,73b}, K.R. Park⁴¹, T.H. Park¹⁵⁶, M.A. Parker³², F. Parodi^{57b,57a}, E.W. Parrish¹¹⁶,
 V.A. Parrish⁵², J.A. Parsons⁴¹, U. Parzefall⁵⁴, B. Pascual Dias¹⁰⁹, L. Pascual Dominguez¹⁰⁰,
 E. Pasqualucci^{75a}, S. Passaggio^{57b}, F. Pastore⁹⁶, P. Patel⁸⁷, U.M. Patel⁵¹, J.R. Pater¹⁰²,
 T. Pauly³⁶, C.I. Pazos¹⁵⁹, J. Pearkes¹⁴⁴, M. Pedersen¹²⁶, R. Pedro^{131a}, S.V. Peleganchuk³⁷,
 O. Penc³⁶, E.A. Pender⁵², G.D. Penn¹⁷³, K.E. Penski¹¹⁰, M. Penzin³⁷, B.S. Peralva^{83d},
 A.P. Pereira Peixoto¹³⁹, L. Pereira Sanchez¹⁴⁴, D.V. Perpelitsa^{29,af}, E. Perez Codina^{157a},
 M. Perganti¹⁰, H. Pernegger³⁶, S. Perrella^{75a,75b}, O. Perrin⁴⁰, K. Peters⁴⁸, R.F.Y. Peters¹⁰²,
 B.A. Petersen³⁶, T.C. Petersen⁴², E. Petit¹⁰³, V. Petousis¹³³, C. Petridou^{153,d}, T. Petru¹³⁴,
 A. Petrukhin¹⁴², M. Pettee^{17a}, A. Petukhov³⁷, K. Petukhova¹³⁴, R. Pezoa^{138f}, L. Pezzotti³⁶,
 G. Pezzullo¹⁷³, T.M. Pham¹⁷¹, T. Pham¹⁰⁶, P.W. Phillips¹³⁵, G. Piacquadio¹⁴⁶,
 E. Pianori^{17a}, F. Piazza¹²⁴, R. Piegai³⁰, D. Pietreanu^{27b}, A.D. Pilkington¹⁰²,
 M. Pinamonti^{69a,69c}, J.L. Pinfeld², B.C. Pinheiro Pereira^{131a}, A.E. Pinto Pinoargote^{136,136},
 L. Pintucci^{69a,69c}, K.M. Piper¹⁴⁷, A. Pirttikoski⁵⁶, D.A. Pizzi³⁴, L. Pizzimento^{64b},
 A. Pizzini¹¹⁵, M.-A. Pleier²⁹, V. Pleskot¹³⁴, E. Plotnikova³⁸, G. Poddar⁹⁵, R. Poettgen⁹⁹,
 L. Poggioli¹²⁸, I. Pokharel⁵⁵, S. Polacek¹³⁴, G. Polesello^{73a}, A. Poley^{143,157a}, A. Polini^{23b},
 C.S. Pollard¹⁶⁸, Z.B. Pollock¹²⁰, E. Pompa Pacchi^{75a,75b}, N.I. Pond⁹⁷, D. Ponomarenko¹¹⁴,
 L. Pontecorvo³⁶, S. Popa^{27a}, G.A. Popeneciu^{27d}, A. Poreba³⁶, D.M. Portillo Quintero^{157a},
 S. Pospisil¹³³, M.A. Postill¹⁴⁰, P. Postolache^{27c}, K. Potamianos¹⁶⁸, P.A. Potepa^{86a},
 I.N. Potrap³⁸, C.J. Potter³², H. Potti¹, J. Poveda¹⁶⁴, M.E. Pozo Astigarraga³⁶,

A. Prades Ibanez [ID164](#), J. Pretel [ID54](#), D. Price [ID102](#), M. Primavera [ID70a](#), M.A. Principe Martin [ID100](#),
 R. Privara [ID123](#), T. Procter [ID59](#), M.L. Proffitt [ID139](#), N. Proklova [ID129](#), K. Prokofiev [ID64c](#), G. Proto [ID111](#),
 J. Proudfoot [ID6](#), M. Przybycien [ID86a](#), W.W. Przygoda [ID86b](#), A. Psallidas [ID46](#), J.E. Puddefoot [ID140](#),
 D. Pudzha [ID37](#), D. Pyatiizbyantseva [ID37](#), J. Qian [ID107](#), D. Qichen [ID102](#), Y. Qin [ID13](#), T. Qiu [ID52](#),
 A. Quadt [ID55](#), M. Queitsch-Maitland [ID102](#), G. Quetant [ID56](#), R.P. Quinn [ID165](#), G. Rabanal Bolanos [ID61](#),
 D. Rafanoharana [ID54](#), F. Raffaeli [ID76a,76b](#), F. Ragusa [ID71a,71b](#), J.L. Rainbolt [ID39](#), J.A. Raine [ID56](#),
 S. Rajagopalan [ID29](#), E. Ramakoti [ID37](#), I.A. Ramirez-Berend [ID34](#), K. Ran [ID48,14e](#), N.P. Rapheeha [ID33g](#),
 H. Rasheed [ID27b](#), V. Raskina [ID128](#), D.F. Rassloff [ID63a](#), A. Rastogi [ID17a](#), S. Rave [ID101](#), S. Ravera [ID57b,57a](#),
 B. Ravina [ID55](#), I. Ravinovich [ID170](#), M. Raymond [ID36](#), A.L. Read [ID126](#), N.P. Readioff [ID140](#),
 D.M. Rebuzzi [ID73a,73b](#), G. Redlinger [ID29](#), A.S. Reed [ID111](#), K. Reeves [ID26](#), J.A. Reidelsturz [ID172](#),
 D. Reikher [ID152](#), A. Rej [ID49](#), C. Rembser [ID36](#), M. Renda [ID27b](#), M.B. Rendel [ID111](#), F. Renner [ID48](#),
 A.G. Rennie [ID160](#), A.L. Rescia [ID48](#), S. Resconi [ID71a](#), M. Ressegotti [ID57b,57a](#), S. Rettie [ID36](#),
 J.G. Reyes Rivera [ID108](#), E. Reynolds [ID17a](#), O.L. Rezanova [ID37](#), P. Reznicek [ID134](#), H. Riani [ID35d](#),
 N. Ribaric [ID92](#), E. Ricci [ID78a,78b](#), R. Richter [ID111](#), S. Richter [ID47a,47b](#), E. Richter-Was [ID86b](#),
 M. Ridel [ID128](#), S. Ridouani [ID35d](#), P. Rieck [ID118](#), P. Riedler [ID36](#), E.M. Riefel [ID47a,47b](#), J.O. Rieger [ID115](#),
 M. Rijssenbeek [ID146](#), M. Rimoldi [ID36](#), L. Rinaldi [ID23b,23a](#), T.T. Rinn [ID29](#), M.P. Rinnagel [ID110](#),
 G. Ripellino [ID162](#), I. Riu [ID13](#), J.C. Rivera Vergara [ID166](#), F. Rizatdinova [ID122](#), E. Rizvi [ID95](#),
 B.R. Roberts [ID17a](#), S.H. Robertson [ID105,v](#), D. Robinson [ID32](#), C.M. Robles Gajardo [ID138f](#),
 M. Robles Manzano [ID101](#), A. Robson [ID59](#), A. Rocchi [ID76a,76b](#), C. Roda [ID74a,74b](#), S. Rodriguez Bosca [ID36](#),
 Y. Rodriguez Garcia [ID22a](#), A. Rodriguez Rodriguez [ID54](#), A.M. Rodríguez Vera [ID116](#), S. Roe [ID36](#),
 J.T. Roemer [ID160](#), A.R. Roepe-Gier [ID137](#), J. Roggel [ID172](#), O. Røhne [ID126](#), R.A. Rojas [ID104](#),
 C.P.A. Roland [ID128](#), J. Roloff [ID29](#), A. Romaniouk [ID37](#), E. Romano [ID73a,73b](#), M. Romano [ID23b](#),
 A.C. Romero Hernandez [ID163](#), N. Rompotis [ID93](#), L. Roos [ID128](#), S. Rosati [ID75a](#), B.J. Rosser [ID39](#),
 E. Rossi [ID127](#), E. Rossi [ID72a,72b](#), L.P. Rossi [ID61](#), L. Rossini [ID54](#), R. Rosten [ID120](#), M. Rotaru [ID27b](#),
 B. Rottler [ID54](#), C. Rougier [ID90](#), D. Rousseau [ID66](#), D. Rouso [ID48](#), A. Roy [ID163](#), S. Roy-Garand [ID156](#),
 A. Rozanov [ID103](#), Z.M.A. Rozario [ID59](#), Y. Rozen [ID151](#), A. Rubio Jimenez [ID164](#), A.J. Ruby [ID93](#),
 V.H. Ruelas Rivera [ID18](#), T.A. Ruggeri [ID1](#), A. Ruggiero [ID127](#), A. Ruiz-Martinez [ID164](#), A. Rummler [ID36](#),
 Z. Rurikova [ID54](#), N.A. Rusakovich [ID38](#), H.L. Russell [ID166](#), G. Russo [ID75a,75b](#), J.P. Rutherford [ID7](#),
 S. Rutherford Colmenares [ID32](#), M. Rybar [ID134](#), E.B. Rye [ID126](#), A. Ryzhov [ID44](#), J.A. Sabater Iglesias [ID56](#),
 P. Sabatini [ID164](#), H.F-W. Sadrozinski [ID137](#), F. Safai Tehrani [ID75a](#), B. Safarzadeh Samani [ID135](#), S. Saha [ID1](#),
 M. Sahinsoy [ID111](#), A. Saibel [ID164](#), M. Saimpert [ID136](#), M. Saito [ID154](#), T. Saito [ID154](#), A. Sala [ID71a,71b](#),
 D. Salamani [ID36](#), A. Salnikov [ID144](#), J. Salt [ID164](#), A. Salvador Salas [ID152](#), D. Salvatore [ID43b,43a](#),
 F. Salvatore [ID147](#), A. Salzburger [ID36](#), D. Sammel [ID54](#), E. Sampson [ID92](#), D. Sampsonidis [ID153,d](#),
 D. Sampsonidou [ID124](#), J. Sánchez [ID164](#), V. Sanchez Sebastian [ID164](#), H. Sandaker [ID126](#), C.O. Sander [ID48](#),
 J.A. Sandesara [ID104](#), M. Sandhoff [ID172](#), C. Sandoval [ID22b](#), L. Sanfilippo [ID63a](#), D.P.C. Sankey [ID135](#),
 T. Sano [ID88](#), A. Sansoni [ID53](#), L. Santi [ID36,75b](#), C. Santoni [ID40](#), H. Santos [ID131a,131b](#), A. Santra [ID170](#),
 E. Sanzani [ID23b,23a](#), K.A. Saoucha [ID161](#), J.G. Saraiva [ID131a,131d](#), J. Sardain [ID7](#), O. Sasaki [ID84](#),
 K. Sato [ID158](#), C. Sauer [ID63b](#), E. Sauvan [ID4](#), P. Savard [ID156,ad](#), R. Sawada [ID154](#), C. Sawyer [ID135](#),
 L. Sawyer [ID98](#), C. Sbarra [ID23b](#), A. Sbrizzi [ID23b,23a](#), T. Scanlon [ID97](#), J. Schaarschmidt [ID139](#),
 U. Schäfer [ID101](#), A.C. Schaffer [ID66,44](#), D. Schaile [ID110](#), R.D. Schamberger [ID146](#), C. Scharf [ID18](#),
 M.M. Schefer [ID19](#), V.A. Schegelsky [ID37](#), D. Scheirich [ID134](#), M. Schernau [ID160](#), C. Scheulen [ID55](#),
 C. Schiavi [ID57b,57a](#), M. Schioppa [ID43b,43a](#), B. Schlag [ID144,1](#), K.E. Schleicher [ID54](#), S. Schlenker [ID36](#),
 J. Schmeing [ID172](#), M.A. Schmidt [ID172](#), K. Schmieden [ID101](#), C. Schmitt [ID101](#), N. Schmitt [ID101](#),
 S. Schmitt [ID48](#), L. Schoeffel [ID136](#), A. Schoening [ID63b](#), P.G. Scholer [ID34](#), E. Schopf [ID127](#), M. Schott [ID24](#),
 J. Schovancova [ID36](#), S. Schramm [ID56](#), T. Schroer [ID56](#), H-C. Schultz-Coulon [ID63a](#), M. Schumacher [ID54](#),
 B.A. Schumm [ID137](#), Ph. Schune [ID136](#), A.J. Schuy [ID139](#), H.R. Schwartz [ID137](#), A. Schwartzman [ID144](#),
 T.A. Schwarz [ID107](#), Ph. Schwemling [ID136](#), R. Schwienhorst [ID108](#), A. Sciandra [ID29](#), G. Sciolla [ID26](#),

F. Scuri ^{74a}, C.D. Sebastiani ⁹³, K. Sedlaczek ¹¹⁶, S.C. Seidel ¹¹³, A. Seiden ¹³⁷,
 B.D. Seidlitz ⁴¹, C. Seitz ⁴⁸, J.M. Seixas ^{83b}, G. Sekhniadze ^{72a}, L. Selem ⁶⁰,
 N. Semprini-Cesari ^{23b,23a}, D. Sengupta ⁵⁶, V. Senthilkumar ¹⁶⁴, L. Serin ⁶⁶, M. Sessa ^{76a,76b},
 H. Severini ¹²¹, F. Sforza ^{57b,57a}, A. Sfyrta ⁵⁶, Q. Sha ^{14a}, E. Shabalina ⁵⁵, A.H. Shah ³²,
 R. Shaheen ¹⁴⁵, J.D. Shahinian ¹²⁹, D. Shaked Renous ¹⁷⁰, L.Y. Shan ^{14a}, M. Shapiro ^{17a},
 A. Sharma ³⁶, A.S. Sharma ¹⁶⁵, P. Sharma ⁸⁰, P.B. Shatalov ³⁷, K. Shaw ¹⁴⁷, S.M. Shaw ¹⁰²,
 Q. Shen ^{62c,5}, D.J. Sheppard ¹⁴³, P. Sherwood ⁹⁷, L. Shi ⁹⁷, X. Shi ^{14a}, C.O. Shimmin ¹⁷³,
 J.D. Shinner ⁹⁶, I.P.J. Shipsey ¹²⁷, S. Shirabe ⁸⁹, M. Shiyakova ^{38,t}, M.J. Shochet ³⁹,
 J. Shojaii ¹⁰⁶, D.R. Shope ¹²⁶, B. Shrestha ¹²¹, S. Shrestha ^{120,ag}, M.J. Shroff ¹⁶⁶, P. Sicho ¹³²,
 A.M. Sickles ¹⁶³, E. Sideras Haddad ^{33g}, A.C. Sidley ¹¹⁵, A. Sidoti ^{23b}, F. Siegert ⁵⁰,
 Dj. Sijacki ¹⁵, F. Sili ⁹¹, J.M. Silva ⁵², I. Silva Ferreira ^{83b}, M.V. Silva Oliveira ²⁹,
 S.B. Silverstein ^{47a}, S. Simion ⁶⁶, R. Simoniello ³⁶, E.L. Simpson ¹⁰², H. Simpson ¹⁴⁷,
 L.R. Simpson ¹⁰⁷, N.D. Simpson ⁹⁹, S. Simsek ⁸², S. Sindhu ⁵⁵, P. Sinervo ¹⁵⁶, S. Singh ¹⁵⁶,
 S. Sinha ⁴⁸, S. Sinha ¹⁰², M. Sioli ^{23b,23a}, I. Siral ³⁶, E. Sitnikova ⁴⁸, J. Sjölin ^{47a,47b},
 A. Skaf ⁵⁵, E. Skorda ²⁰, P. Skubic ¹²¹, M. Slawinska ⁸⁷, V. Smakhtin ¹⁷⁰, B.H. Smart ¹³⁵,
 S.Yu. Smirnov ³⁷, Y. Smirnov ³⁷, L.N. Smirnova ^{37,a}, O. Smirnova ⁹⁹, A.C. Smith ⁴¹,
 D.R. Smith ¹⁶⁰, E.A. Smith ³⁹, H.A. Smith ¹²⁷, J.L. Smith ¹⁰², R. Smith ¹⁴⁴, M. Smizanska ⁹²,
 K. Smolek ¹³³, A.A. Snesarev ³⁷, S.R. Snider ¹⁵⁶, H.L. Snoek ¹¹⁵, S. Snyder ²⁹, R. Sobie ^{166,v},
 A. Soffer ¹⁵², C.A. Solans Sanchez ³⁶, E.Yu. Soldatov ³⁷, U. Soldevila ¹⁶⁴, A.A. Solodkov ³⁷,
 S. Solomon ²⁶, A. Soloshenko ³⁸, K. Solovieva ⁵⁴, O.V. Solovyanov ⁴⁰, P. Sommer ³⁶,
 A. Sonay ¹³, W.Y. Song ^{157b}, A. Sopczak ¹³³, A.L. Soppio ⁹⁷, F. Sopkova ^{28b}, J.D. Sorenson ¹¹³,
 I.R. Sotarriva Alvarez ¹⁵⁵, V. Sothilingam ^{63a}, O.J. Soto Sandoval ^{138c,138b}, S. Sottocornola ⁶⁸,
 R. Soualah ¹⁶¹, Z. Soumami ^{35e}, D. South ⁴⁸, N. Soybelman ¹⁷⁰, S. Spagnolo ^{70a,70b},
 M. Spalla ¹¹¹, D. Sperlich ⁵⁴, G. Spigo ³⁶, S. Spinali ⁹², D.P. Spiteri ⁵⁹, M. Spousta ¹³⁴,
 E.J. Staats ³⁴, R. Stamen ^{63a}, A. Stampeki ²⁰, M. Standke ²⁴, E. Stanecka ⁸⁷,
 W. Stanek-Maslouska ⁴⁸, M.V. Stange ⁵⁰, B. Stanislaus ^{17a}, M.M. Stanitzki ⁴⁸, B. Stapf ⁴⁸,
 E.A. Starchenko ³⁷, G.H. Stark ¹³⁷, J. Stark ⁹⁰, P. Staroba ¹³², P. Starovoitov ^{63a}, S. Stärz ¹⁰⁵,
 R. Staszewski ⁸⁷, G. Stavropoulos ⁴⁶, J. Steentoft ¹⁶², P. Steinberg ²⁹, B. Stelzer ^{143,157a},
 H.J. Stelzer ¹³⁰, O. Stelzer-Chilton ^{157a}, H. Stenzel ⁵⁸, T.J. Stevenson ¹⁴⁷, G.A. Stewart ³⁶,
 J.R. Stewart ¹²², M.C. Stockton ³⁶, G. Stoicea ^{27b}, M. Stolarski ^{131a}, S. Stonjek ¹¹¹,
 A. Straessner ⁵⁰, J. Strandberg ¹⁴⁵, S. Strandberg ^{47a,47b}, M. Stratmann ¹⁷², M. Strauss ¹²¹,
 T. Strebler ¹⁰³, P. Strizenec ^{28b}, R. Ströhmer ¹⁶⁷, D.M. Strom ¹²⁴, R. Stroynowski ⁴⁴,
 A. Strubig ^{47a,47b}, S.A. Stucci ²⁹, B. Stugu ¹⁶, J. Stupak ¹²¹, N.A. Styles ⁴⁸, D. Su ¹⁴⁴,
 S. Su ^{62a}, W. Su ^{62d}, X. Su ^{62a}, D. Suchy ^{28a}, K. Sugizaki ¹⁵⁴, V.V. Sulin ³⁷, M.J. Sullivan ⁹³,
 D.M.S. Sultan ¹²⁷, L. Sultanaliyeva ³⁷, S. Sultansoy ^{3b}, T. Sumida ⁸⁸, S. Sun ¹⁷¹,
 O. Sunneborn Gudnadottir ¹⁶², N. Sur ¹⁰³, M.R. Sutton ¹⁴⁷, H. Suzuki ¹⁵⁸, M. Svatos ¹³²,
 M. Swiatlowski ^{157a}, T. Swirski ¹⁶⁷, I. Sykora ^{28a}, M. Sykora ¹³⁴, T. Sykora ¹³⁴, D. Ta ¹⁰¹,
 K. Tackmann ^{48,s}, A. Taffard ¹⁶⁰, R. Tafirout ^{157a}, J.S. Tafuya Vargas ⁶⁶, Y. Takubo ⁸⁴,
 M. Talby ¹⁰³, A.A. Talyshev ³⁷, K.C. Tam ^{64b}, N.M. Tamir ¹⁵², A. Tanaka ¹⁵⁴, J. Tanaka ¹⁵⁴,
 R. Tanaka ⁶⁶, M. Tanasini ¹⁴⁶, Z. Tao ¹⁶⁵, S. Tapia Araya ^{138f}, S. Tapprogge ¹⁰¹,
 A. Tarek Abouelfadl Mohamed ¹⁰⁸, S. Tarem ¹⁵¹, K. Tariq ^{14a}, G. Tarna ^{27b}, G.F. Tartarelli ^{71a},
 M.J. Tartarin ⁹⁰, P. Tas ¹³⁴, M. Tasevsky ¹³², E. Tassi ^{43b,43a}, A.C. Tate ¹⁶³, G. Tateno ¹⁵⁴,
 Y. Tayalati ^{35e,u}, G.N. Taylor ¹⁰⁶, W. Taylor ^{157b}, R. Teixeira De Lima ¹⁴⁴, P. Teixeira-Dias ⁹⁶,
 J.J. Teoh ¹⁵⁶, K. Terashi ¹⁵⁴, J. Terron ¹⁰⁰, S. Terzo ¹³, M. Testa ⁵³, R.J. Teuscher ^{156,v},
 A. Thaler ⁷⁹, O. Theiner ⁵⁶, N. Themistokleous ⁵², T. Thevenaux-Pelzer ¹⁰³, O. Thielmann ¹⁷²,
 D.W. Thomas ⁹⁶, J.P. Thomas ²⁰, E.A. Thompson ^{17a}, P.D. Thompson ²⁰, E. Thomson ¹²⁹,
 R.E. Thornberry ⁴⁴, C. Tian ^{62a}, Y. Tian ⁵⁵, V. Tikhomirov ^{37,a}, Yu.A. Tikhonov ³⁷,

S. Timoshenko³⁷, D. Timoshyn ¹³⁴, E.X.L. Ting ¹, P. Tipton ¹⁷³, A. Tishelman-Charny ²⁹, S.H. Tlou ^{33g}, K. Todome ¹⁵⁵, S. Todorova-Nova ¹³⁴, S. Todt⁵⁰, L. Toffolin ^{69a,69c}, M. Togawa ⁸⁴, J. Tojo ⁸⁹, S. Tokár ^{28a}, K. Tokushuku ⁸⁴, O. Toldaiev ⁶⁸, R. Tombs ³², M. Tomoto ^{84,112}, L. Tompkins ^{144,1}, K.W. Topolnicki ^{86b}, E. Torrence ¹²⁴, H. Torres ⁹⁰, E. Torr  Pastor ¹⁶⁴, M. Toscani ³⁰, C. Tosciri ³⁹, M. Tost ¹¹, D.R. Tovey ¹⁴⁰, I.S. Trandafir ^{27b}, T. Trefzger ¹⁶⁷, A. Tricoli ²⁹, I.M. Trigger ^{157a}, S. Trincaz-Duvoid ¹²⁸, D.A. Trischuk ²⁶, B. Trocm  ⁶⁰, L. Truong ^{33c}, M. Trzebinski ⁸⁷, A. Trzupke ⁸⁷, F. Tsai ¹⁴⁶, M. Tsai ¹⁰⁷, A. Tsiamis ^{153,d}, P.V. Tsiareshka³⁷, S. Tsigaridas ^{157a}, A. Tsirigotis ^{153,q}, V. Tsiskaridze ¹⁵⁶, E.G. Tskhadadze ^{150a}, M. Tsopoulou ¹⁵³, Y. Tsujikawa ⁸⁸, I.I. Tsukerman ³⁷, V. Tsulaia ^{17a}, S. Tsuno ⁸⁴, K. Tsurii ¹¹⁹, D. Tsybychev ¹⁴⁶, Y. Tu ^{64b}, A. Tudorache ^{27b}, V. Tudorache ^{27b}, A.N. Tuna ⁶¹, S. Turchikhin ^{57b,57a}, I. Turk Cakir ^{3a}, R. Turra ^{71a}, T. Turtuvshin ^{38,w}, P.M. Tuts ⁴¹, S. Tzamarias ^{153,d}, E. Tzovara ¹⁰¹, F. Ukegawa ¹⁵⁸, P.A. Ulloa Poblete ^{138c,138b}, E.N. Umaka ²⁹, G. Unal ³⁶, A. Undrus ²⁹, G. Unel ¹⁶⁰, J. Urban ^{28b}, P. Urrejola ^{138a}, G. Usai ⁸, R. Ushioda ¹⁵⁵, M. Usman ¹⁰⁹, Z. Uysal ⁸², V. Vacek ¹³³, B. Vachon ¹⁰⁵, T. Vafeiadis ³⁶, A. Vaitkus ⁹⁷, C. Valderanis ¹¹⁰, E. Valdes Santurio ^{47a,47b}, M. Valente ^{157a}, S. Valentinetti ^{23b,23a}, A. Valero ¹⁶⁴, E. Valiente Moreno ¹⁶⁴, A. Vallier ⁹⁰, J.A. Valls Ferrer ¹⁶⁴, D.R. Van Arneman ¹¹⁵, T.R. Van Daalen ¹³⁹, A. Van Der Graaf ⁴⁹, P. Van Gemmeren ⁶, M. Van Rijnbach ³⁶, S. Van Stroud ⁹⁷, I. Van Vulpen ¹¹⁵, P. Vana ¹³⁴, M. Vanadia ^{76a,76b}, W. Vandelli ³⁶, E.R. Vandewall ¹²², D. Vannicola ¹⁵², L. Vannoli ⁵³, R. Vari ^{75a}, E.W. Varnes ⁷, C. Varni ^{17b}, T. Varol ¹⁴⁹, D. Varouchas ⁶⁶, L. Varriale ¹⁶⁴, K.E. Varvell ¹⁴⁸, M.E. Vasile ^{27b}, L. Vaslin ⁸⁴, G.A. Vasquez ¹⁶⁶, A. Vasyukov ³⁸, L.M. Vaughan ¹²², R. Vavricka ¹⁰¹, T. Vazquez Schroeder ³⁶, J. Veatch ³¹, V. Vecchio ¹⁰², M.J. Veen ¹⁰⁴, I. Veliscek ²⁹, L.M. Veloce ¹⁵⁶, F. Veloso ^{131a,131c}, S. Veneziano ^{75a}, A. Ventura ^{70a,70b}, S. Ventura Gonzalez ¹³⁶, A. Verbytskyi ¹¹¹, M. Verducci ^{74a,74b}, C. Vergis ⁹⁵, M. Verissimo De Araujo ^{83b}, W. Verkerke ¹¹⁵, J.C. Vermeulen ¹¹⁵, C. Vernieri ¹⁴⁴, M. Vessella ¹⁰⁴, M.C. Vetterli ^{143,ad}, A. Vgenopoulos ^{153,d}, N. Viaux Maira ^{138f}, T. Vickey ¹⁴⁰, O.E. Vickey Boeriu ¹⁴⁰, G.H.A. Viehhauser ¹²⁷, L. Vigani ^{63b}, M. Villa ^{23b,23a}, M. Villaplana Perez ¹⁶⁴, E.M. Villhauer⁵², E. Vilucchi ⁵³, M.G. Vinciter ³⁴, A. Visibile¹¹⁵, C. Vittori ³⁶, I. Vivarelli ^{23b,23a}, E. Voevodina ¹¹¹, F. Vogel ¹¹⁰, J.C. Voigt ⁵⁰, P. Vokac ¹³³, Yu. Volkotrub ^{86b}, J. Von Ahnen ⁴⁸, E. Von Toerne ²⁴, B. Vormwald ³⁶, V. Vorobel ¹³⁴, K. Vorobev ³⁷, M. Vos ¹⁶⁴, K. Voss ¹⁴², M. Vozak ¹¹⁵, L. Vozdecky ¹²¹, N. Vranjes ¹⁵, M. Vranjes Milosavljevic ¹⁵, M. Vreeswijk ¹¹⁵, N.K. Vu ^{62d,62c}, R. Vuillermet ³⁶, O. Vujinovic ¹⁰¹, I. Vukotic ³⁹, S. Wada ¹⁵⁸, C. Wagner¹⁰⁴, J.M. Wagner ^{17a}, W. Wagner ¹⁷², S. Wahdan ¹⁷², H. Wahlberg ⁹¹, M. Wakida ¹¹², J. Walder ¹³⁵, R. Walker ¹¹⁰, W. Walkowiak ¹⁴², A. Wall ¹²⁹, E.J. Wallin ⁹⁹, T. Wamorkar ⁶, A.Z. Wang ¹³⁷, C. Wang ¹⁰¹, C. Wang ¹¹, H. Wang ^{17a}, J. Wang ^{64c}, P. Wang ⁹⁷, R. Wang ⁶¹, R. Wang ⁶, S.M. Wang ¹⁴⁹, S. Wang ^{62b}, T. Wang ^{62a}, W.T. Wang ⁸⁰, W. Wang ^{14a}, X. Wang ^{14c}, X. Wang ¹⁶³, X. Wang ^{62c}, Y. Wang ^{62d}, Y. Wang ^{14c}, Z. Wang ¹⁰⁷, Z. Wang ^{62d,51,62c}, Z. Wang ¹⁰⁷, A. Warburton ¹⁰⁵, R.J. Ward ²⁰, N. Warrack ⁵⁹, S. Waterhouse ⁹⁶, A.T. Watson ²⁰, H. Watson ⁵⁹, M.F. Watson ²⁰, E. Watton ^{59,135}, G. Watts ¹³⁹, B.M. Waugh ⁹⁷, J.M. Webb ⁵⁴, C. Weber ²⁹, H.A. Weber ¹⁸, M.S. Weber ¹⁹, S.M. Weber ^{63a}, C. Wei ^{62a}, Y. Wei ⁵⁴, A.R. Weidberg ¹²⁷, E.J. Weik ¹¹⁸, J. Weingarten ⁴⁹, C. Weiser ⁵⁴, C.J. Wells ⁴⁸, T. Wenaus ²⁹, B. Wendland ⁴⁹, T. Wengler ³⁶, N.S. Wenke¹¹¹, N. Wermes ²⁴, M. Wessels ^{63a}, A.M. Wharton ⁹², A.S. White ⁶¹, A. White ⁸, M.J. White ¹, D. Whiteson ¹⁶⁰, L. Wickremasinghe ¹²⁵, W. Wiedenmann ¹⁷¹, M. Wielers ¹³⁵, C. Wiglesworth ⁴², D.J. Wilbern¹²¹, H.G. Wilkens ³⁶, J.J.H. Wilkinson ³², D.M. Williams ⁴¹, H.H. Williams¹²⁹, S. Williams ³², S. Willocq ¹⁰⁴, B.J. Wilson ¹⁰², P.J. Windischhofer ³⁹, F.I. Winkel ³⁰, F. Winklmeier ¹²⁴, B.T. Winter ⁵⁴, J.K. Winter ¹⁰², M. Wittgen¹⁴⁴, M. Wobisch ⁹⁸, T. Wojtkowski⁶⁰, Z. Wolffs ¹¹⁵, J. Wollrath¹⁶⁰, M.W. Wolter ⁸⁷, H. Wolters ^{131a,131c}, M.C. Wong¹³⁷,

E.L. Woodward ⁴¹, S.D. Worm ⁴⁸, B.K. Wosiek ⁸⁷, K.W. Woźniak ⁸⁷, S. Wozniowski ⁵⁵, K. Wraight ⁵⁹, C. Wu ²⁰, M. Wu ^{14d}, M. Wu ¹¹⁴, S.L. Wu ¹⁷¹, X. Wu ⁵⁶, Y. Wu ^{62a}, Z. Wu ⁴, J. Wuerzinger ^{111,ab}, T.R. Wyatt ¹⁰², B.M. Wynne ⁵², S. Xella ⁴², L. Xia ^{14c}, M. Xia ^{14b}, J. Xiang ^{64c}, M. Xie ^{62a}, S. Xin ^{14a,14e}, A. Xiong ¹²⁴, J. Xiong ^{17a}, D. Xu ^{14a}, H. Xu ^{62a}, L. Xu ^{62a}, R. Xu ¹²⁹, T. Xu ¹⁰⁷, Y. Xu ^{14b}, Z. Xu ⁵², Z. Xu ^{14c}, B. Yabsley ¹⁴⁸, S. Yacoob ^{33a}, Y. Yamaguchi ¹⁵⁵, E. Yamashita ¹⁵⁴, H. Yamauchi ¹⁵⁸, T. Yamazaki ^{17a}, Y. Yamazaki ⁸⁵, J. Yan ^{62c}, S. Yan ⁵⁹, Z. Yan ¹⁰⁴, H.J. Yang ^{62c,62d}, H.T. Yang ^{62a}, S. Yang ^{62a}, T. Yang ^{64c}, X. Yang ³⁶, X. Yang ^{14a}, Y. Yang ⁴⁴, Y. Yang ^{62a}, Z. Yang ^{62a}, W.-M. Yao ^{17a}, H. Ye ^{14c}, H. Ye ⁵⁵, J. Ye ^{14a}, S. Ye ²⁹, X. Ye ^{62a}, Y. Yeh ⁹⁷, I. Yeletsikh ³⁸, B.K. Yeo ^{17b}, M.R. Yexley ⁹⁷, T.P. Yildirim ¹²⁷, P. Yin ⁴¹, K. Yorita ¹⁶⁹, S. Younas ^{27b}, C.J.S. Young ³⁶, C. Young ¹⁴⁴, C. Yu ^{14a,14e}, Y. Yu ^{62a}, M. Yuan ¹⁰⁷, R. Yuan ^{62d,62c}, L. Yue ⁹⁷, M. Zaazoua ^{62a}, B. Zabinski ⁸⁷, E. Zaid ⁵², Z.K. Zak ⁸⁷, T. Zakareishvili ¹⁶⁴, N. Zakharchuk ³⁴, S. Zambito ⁵⁶, J.A. Zamora Saa ^{138d,138b}, J. Zang ¹⁵⁴, D. Zanzi ⁵⁴, O. Zaplatilek ¹³³, C. Zeitnitz ¹⁷², H. Zeng ^{14a}, J.C. Zeng ¹⁶³, D.T. Zenger Jr ²⁶, O. Zenin ³⁷, T. Ženiš ^{28a}, S. Zenz ⁹⁵, S. Zerradi ^{35a}, D. Zerwas ⁶⁶, M. Zhai ^{14a,14e}, D.F. Zhang ¹⁴⁰, J. Zhang ^{62b}, J. Zhang ⁶, K. Zhang ^{14a,14e}, L. Zhang ^{62a}, L. Zhang ^{14c}, P. Zhang ^{14a,14e}, R. Zhang ¹⁷¹, S. Zhang ¹⁰⁷, S. Zhang ⁹⁰, T. Zhang ¹⁵⁴, X. Zhang ^{62c}, X. Zhang ^{62b}, Y. Zhang ^{62c}, Y. Zhang ⁹⁷, Y. Zhang ^{14c}, Z. Zhang ^{17a}, Z. Zhang ^{62b}, Z. Zhang ⁶⁶, H. Zhao ¹³⁹, T. Zhao ^{62b}, Y. Zhao ¹³⁷, Z. Zhao ^{62a}, Z. Zhao ^{62a}, A. Zhemchugov ³⁸, J. Zheng ^{14c}, K. Zheng ¹⁶³, X. Zheng ^{62a}, Z. Zheng ¹⁴⁴, D. Zhong ¹⁶³, B. Zhou ¹⁰⁷, H. Zhou ⁷, N. Zhou ^{62c}, Y. Zhou ^{14b}, Y. Zhou ^{14c}, Y. Zhou ⁷, C.G. Zhu ^{62b}, J. Zhu ¹⁰⁷, X. Zhu ^{62d}, Y. Zhu ^{62c}, Y. Zhu ^{62a}, X. Zhuang ^{14a}, K. Zhukov ³⁷, N.I. Zimine ³⁸, J. Zinsser ^{63b}, M. Ziolkowski ¹⁴², L. Živković ¹⁵, A. Zoccoli ^{23b,23a}, K. Zoch ⁶¹, T.G. Zorbas ¹⁴⁰, O. Zormpa ⁴⁶, W. Zou ⁴¹, L. Zwalinski ³⁶.

¹Department of Physics, University of Adelaide, Adelaide; Australia.

²Department of Physics, University of Alberta, Edmonton AB; Canada.

³(^a)Department of Physics, Ankara University, Ankara; (^b)Division of Physics, TOBB University of Economics and Technology, Ankara; Türkiye.

⁴LAPP, Université Savoie Mont Blanc, CNRS/IN2P3, Annecy; France.

⁵APC, Université Paris Cité, CNRS/IN2P3, Paris; France.

⁶High Energy Physics Division, Argonne National Laboratory, Argonne IL; United States of America.

⁷Department of Physics, University of Arizona, Tucson AZ; United States of America.

⁸Department of Physics, University of Texas at Arlington, Arlington TX; United States of America.

⁹Physics Department, National and Kapodistrian University of Athens, Athens; Greece.

¹⁰Physics Department, National Technical University of Athens, Zografou; Greece.

¹¹Department of Physics, University of Texas at Austin, Austin TX; United States of America.

¹²Institute of Physics, Azerbaijan Academy of Sciences, Baku; Azerbaijan.

¹³Institut de Física d'Altes Energies (IFAE), Barcelona Institute of Science and Technology, Barcelona; Spain.

¹⁴(^a)Institute of High Energy Physics, Chinese Academy of Sciences, Beijing; (^b)Physics Department, Tsinghua University, Beijing; (^c)Department of Physics, Nanjing University, Nanjing; (^d)School of Science, Shenzhen Campus of Sun Yat-sen University; (^e)University of Chinese Academy of Science (UCAS), Beijing; China.

¹⁵Institute of Physics, University of Belgrade, Belgrade; Serbia.

¹⁶Department for Physics and Technology, University of Bergen, Bergen; Norway.

¹⁷(^a)Physics Division, Lawrence Berkeley National Laboratory, Berkeley CA; (^b)University of California, Berkeley CA; United States of America.

- ¹⁸Institut für Physik, Humboldt Universität zu Berlin, Berlin; Germany.
- ¹⁹Albert Einstein Center for Fundamental Physics and Laboratory for High Energy Physics, University of Bern, Bern; Switzerland.
- ²⁰School of Physics and Astronomy, University of Birmingham, Birmingham; United Kingdom.
- ²¹(^a) Department of Physics, Bogazici University, Istanbul; (^b) Department of Physics Engineering, Gaziantep University, Gaziantep; (^c) Department of Physics, Istanbul University, Istanbul; Türkiye.
- ²²(^a) Facultad de Ciencias y Centro de Investigaciones, Universidad Antonio Nariño, Bogotá; (^b) Departamento de Física, Universidad Nacional de Colombia, Bogotá; Colombia.
- ²³(^a) Dipartimento di Fisica e Astronomia A. Righi, Università di Bologna, Bologna; (^b) INFN Sezione di Bologna; Italy.
- ²⁴Physikalisches Institut, Universität Bonn, Bonn; Germany.
- ²⁵Department of Physics, Boston University, Boston MA; United States of America.
- ²⁶Department of Physics, Brandeis University, Waltham MA; United States of America.
- ²⁷(^a) Transilvania University of Brasov, Brasov; (^b) Horia Hulubei National Institute of Physics and Nuclear Engineering, Bucharest; (^c) Department of Physics, Alexandru Ioan Cuza University of Iasi, Iasi; (^d) National Institute for Research and Development of Isotopic and Molecular Technologies, Physics Department, Cluj-Napoca; (^e) National University of Science and Technology Politehnica, Bucharest; (^f) West University in Timisoara, Timisoara; (^g) Faculty of Physics, University of Bucharest, Bucharest; Romania.
- ²⁸(^a) Faculty of Mathematics, Physics and Informatics, Comenius University, Bratislava; (^b) Department of Subnuclear Physics, Institute of Experimental Physics of the Slovak Academy of Sciences, Kosice; Slovak Republic.
- ²⁹Physics Department, Brookhaven National Laboratory, Upton NY; United States of America.
- ³⁰Universidad de Buenos Aires, Facultad de Ciencias Exactas y Naturales, Departamento de Física, y CONICET, Instituto de Física de Buenos Aires (IFIBA), Buenos Aires; Argentina.
- ³¹California State University, CA; United States of America.
- ³²Cavendish Laboratory, University of Cambridge, Cambridge; United Kingdom.
- ³³(^a) Department of Physics, University of Cape Town, Cape Town; (^b) iThemba Labs, Western Cape; (^c) Department of Mechanical Engineering Science, University of Johannesburg, Johannesburg; (^d) National Institute of Physics, University of the Philippines Diliman (Philippines); (^e) University of South Africa, Department of Physics, Pretoria; (^f) University of Zululand, KwaDlangezwa; (^g) School of Physics, University of the Witwatersrand, Johannesburg; South Africa.
- ³⁴Department of Physics, Carleton University, Ottawa ON; Canada.
- ³⁵(^a) Faculté des Sciences Ain Chock, Réseau Universitaire de Physique des Hautes Energies - Université Hassan II, Casablanca; (^b) Faculté des Sciences, Université Ibn-Tofail, Kénitra; (^c) Faculté des Sciences Semlalia, Université Cadi Ayyad, LPHEA-Marrakech; (^d) LPMR, Faculté des Sciences, Université Mohamed Premier, Oujda; (^e) Faculté des sciences, Université Mohammed V, Rabat; (^f) Institute of Applied Physics, Mohammed VI Polytechnic University, Ben Guerir; Morocco.
- ³⁶CERN, Geneva; Switzerland.
- ³⁷Affiliated with an institute covered by a cooperation agreement with CERN.
- ³⁸Affiliated with an international laboratory covered by a cooperation agreement with CERN.
- ³⁹Enrico Fermi Institute, University of Chicago, Chicago IL; United States of America.
- ⁴⁰LPC, Université Clermont Auvergne, CNRS/IN2P3, Clermont-Ferrand; France.
- ⁴¹Nevis Laboratory, Columbia University, Irvington NY; United States of America.
- ⁴²Niels Bohr Institute, University of Copenhagen, Copenhagen; Denmark.
- ⁴³(^a) Dipartimento di Fisica, Università della Calabria, Rende; (^b) INFN Gruppo Collegato di Cosenza, Laboratori Nazionali di Frascati; Italy.
- ⁴⁴Physics Department, Southern Methodist University, Dallas TX; United States of America.

- ⁴⁵Physics Department, University of Texas at Dallas, Richardson TX; United States of America.
- ⁴⁶National Centre for Scientific Research "Demokritos", Agia Paraskevi; Greece.
- ⁴⁷(^a) Department of Physics, Stockholm University; (^b) Oskar Klein Centre, Stockholm; Sweden.
- ⁴⁸Deutsches Elektronen-Synchrotron DESY, Hamburg and Zeuthen; Germany.
- ⁴⁹Fakultät Physik, Technische Universität Dortmund, Dortmund; Germany.
- ⁵⁰Institut für Kern- und Teilchenphysik, Technische Universität Dresden, Dresden; Germany.
- ⁵¹Department of Physics, Duke University, Durham NC; United States of America.
- ⁵²SUPA - School of Physics and Astronomy, University of Edinburgh, Edinburgh; United Kingdom.
- ⁵³INFN e Laboratori Nazionali di Frascati, Frascati; Italy.
- ⁵⁴Physikalisches Institut, Albert-Ludwigs-Universität Freiburg, Freiburg; Germany.
- ⁵⁵II. Physikalisches Institut, Georg-August-Universität Göttingen, Göttingen; Germany.
- ⁵⁶Département de Physique Nucléaire et Corpusculaire, Université de Genève, Genève; Switzerland.
- ⁵⁷(^a) Dipartimento di Fisica, Università di Genova, Genova; (^b) INFN Sezione di Genova; Italy.
- ⁵⁸II. Physikalisches Institut, Justus-Liebig-Universität Giessen, Giessen; Germany.
- ⁵⁹SUPA - School of Physics and Astronomy, University of Glasgow, Glasgow; United Kingdom.
- ⁶⁰LPSC, Université Grenoble Alpes, CNRS/IN2P3, Grenoble INP, Grenoble; France.
- ⁶¹Laboratory for Particle Physics and Cosmology, Harvard University, Cambridge MA; United States of America.
- ⁶²(^a) Department of Modern Physics and State Key Laboratory of Particle Detection and Electronics, University of Science and Technology of China, Hefei; (^b) Institute of Frontier and Interdisciplinary Science and Key Laboratory of Particle Physics and Particle Irradiation (MOE), Shandong University, Qingdao; (^c) School of Physics and Astronomy, Shanghai Jiao Tong University, Key Laboratory for Particle Astrophysics and Cosmology (MOE), SKLPPC, Shanghai; (^d) Tsung-Dao Lee Institute, Shanghai; (^e) School of Physics and Microelectronics, Zhengzhou University; China.
- ⁶³(^a) Kirchhoff-Institut für Physik, Ruprecht-Karls-Universität Heidelberg, Heidelberg; (^b) Physikalisches Institut, Ruprecht-Karls-Universität Heidelberg, Heidelberg; Germany.
- ⁶⁴(^a) Department of Physics, Chinese University of Hong Kong, Shatin, N.T., Hong Kong; (^b) Department of Physics, University of Hong Kong, Hong Kong; (^c) Department of Physics and Institute for Advanced Study, Hong Kong University of Science and Technology, Clear Water Bay, Kowloon, Hong Kong; China.
- ⁶⁵Department of Physics, National Tsing Hua University, Hsinchu; Taiwan.
- ⁶⁶IJCLab, Université Paris-Saclay, CNRS/IN2P3, 91405, Orsay; France.
- ⁶⁷Centro Nacional de Microelectrónica (IMB-CNM-CSIC), Barcelona; Spain.
- ⁶⁸Department of Physics, Indiana University, Bloomington IN; United States of America.
- ⁶⁹(^a) INFN Gruppo Collegato di Udine, Sezione di Trieste, Udine; (^b) ICTP, Trieste; (^c) Dipartimento Politecnico di Ingegneria e Architettura, Università di Udine, Udine; Italy.
- ⁷⁰(^a) INFN Sezione di Lecce; (^b) Dipartimento di Matematica e Fisica, Università del Salento, Lecce; Italy.
- ⁷¹(^a) INFN Sezione di Milano; (^b) Dipartimento di Fisica, Università di Milano, Milano; Italy.
- ⁷²(^a) INFN Sezione di Napoli; (^b) Dipartimento di Fisica, Università di Napoli, Napoli; Italy.
- ⁷³(^a) INFN Sezione di Pavia; (^b) Dipartimento di Fisica, Università di Pavia, Pavia; Italy.
- ⁷⁴(^a) INFN Sezione di Pisa; (^b) Dipartimento di Fisica E. Fermi, Università di Pisa, Pisa; Italy.
- ⁷⁵(^a) INFN Sezione di Roma; (^b) Dipartimento di Fisica, Sapienza Università di Roma, Roma; Italy.
- ⁷⁶(^a) INFN Sezione di Roma Tor Vergata; (^b) Dipartimento di Fisica, Università di Roma Tor Vergata, Roma; Italy.
- ⁷⁷(^a) INFN Sezione di Roma Tre; (^b) Dipartimento di Matematica e Fisica, Università Roma Tre, Roma; Italy.
- ⁷⁸(^a) INFN-TIFPA; (^b) Università degli Studi di Trento, Trento; Italy.
- ⁷⁹Universität Innsbruck, Department of Astro and Particle Physics, Innsbruck; Austria.

- ⁸⁰University of Iowa, Iowa City IA; United States of America.
- ⁸¹Department of Physics and Astronomy, Iowa State University, Ames IA; United States of America.
- ⁸²Istinye University, Sariyer, Istanbul; Türkiye.
- ⁸³(^a)Departamento de Engenharia Elétrica, Universidade Federal de Juiz de Fora (UFJF), Juiz de Fora;(^b)Universidade Federal do Rio De Janeiro COPPE/EE/IF, Rio de Janeiro;(^c)Instituto de Física, Universidade de São Paulo, São Paulo;(^d)Rio de Janeiro State University, Rio de Janeiro;(^e)Federal University of Bahia, Bahia; Brazil.
- ⁸⁴KEK, High Energy Accelerator Research Organization, Tsukuba; Japan.
- ⁸⁵Graduate School of Science, Kobe University, Kobe; Japan.
- ⁸⁶(^a)AGH University of Krakow, Faculty of Physics and Applied Computer Science, Krakow;(^b)Marian Smoluchowski Institute of Physics, Jagiellonian University, Krakow; Poland.
- ⁸⁷Institute of Nuclear Physics Polish Academy of Sciences, Krakow; Poland.
- ⁸⁸Faculty of Science, Kyoto University, Kyoto; Japan.
- ⁸⁹Research Center for Advanced Particle Physics and Department of Physics, Kyushu University, Fukuoka ; Japan.
- ⁹⁰L2IT, Université de Toulouse, CNRS/IN2P3, UPS, Toulouse; France.
- ⁹¹Instituto de Física La Plata, Universidad Nacional de La Plata and CONICET, La Plata; Argentina.
- ⁹²Physics Department, Lancaster University, Lancaster; United Kingdom.
- ⁹³Oliver Lodge Laboratory, University of Liverpool, Liverpool; United Kingdom.
- ⁹⁴Department of Experimental Particle Physics, Jožef Stefan Institute and Department of Physics, University of Ljubljana, Ljubljana; Slovenia.
- ⁹⁵School of Physics and Astronomy, Queen Mary University of London, London; United Kingdom.
- ⁹⁶Department of Physics, Royal Holloway University of London, Egham; United Kingdom.
- ⁹⁷Department of Physics and Astronomy, University College London, London; United Kingdom.
- ⁹⁸Louisiana Tech University, Ruston LA; United States of America.
- ⁹⁹Fysiska institutionen, Lunds universitet, Lund; Sweden.
- ¹⁰⁰Departamento de Física Teórica C-15 and CIAFF, Universidad Autónoma de Madrid, Madrid; Spain.
- ¹⁰¹Institut für Physik, Universität Mainz, Mainz; Germany.
- ¹⁰²School of Physics and Astronomy, University of Manchester, Manchester; United Kingdom.
- ¹⁰³CPPM, Aix-Marseille Université, CNRS/IN2P3, Marseille; France.
- ¹⁰⁴Department of Physics, University of Massachusetts, Amherst MA; United States of America.
- ¹⁰⁵Department of Physics, McGill University, Montreal QC; Canada.
- ¹⁰⁶School of Physics, University of Melbourne, Victoria; Australia.
- ¹⁰⁷Department of Physics, University of Michigan, Ann Arbor MI; United States of America.
- ¹⁰⁸Department of Physics and Astronomy, Michigan State University, East Lansing MI; United States of America.
- ¹⁰⁹Group of Particle Physics, University of Montreal, Montreal QC; Canada.
- ¹¹⁰Fakultät für Physik, Ludwig-Maximilians-Universität München, München; Germany.
- ¹¹¹Max-Planck-Institut für Physik (Werner-Heisenberg-Institut), München; Germany.
- ¹¹²Graduate School of Science and Kobayashi-Maskawa Institute, Nagoya University, Nagoya; Japan.
- ¹¹³Department of Physics and Astronomy, University of New Mexico, Albuquerque NM; United States of America.
- ¹¹⁴Institute for Mathematics, Astrophysics and Particle Physics, Radboud University/Nikhef, Nijmegen; Netherlands.
- ¹¹⁵Nikhef National Institute for Subatomic Physics and University of Amsterdam, Amsterdam; Netherlands.
- ¹¹⁶Department of Physics, Northern Illinois University, DeKalb IL; United States of America.

- ¹¹⁷(*a*) New York University Abu Dhabi, Abu Dhabi; (*b*) United Arab Emirates University, Al Ain; United Arab Emirates.
- ¹¹⁸Department of Physics, New York University, New York NY; United States of America.
- ¹¹⁹Ochanomizu University, Otsuka, Bunkyo-ku, Tokyo; Japan.
- ¹²⁰Ohio State University, Columbus OH; United States of America.
- ¹²¹Homer L. Dodge Department of Physics and Astronomy, University of Oklahoma, Norman OK; United States of America.
- ¹²²Department of Physics, Oklahoma State University, Stillwater OK; United States of America.
- ¹²³Palacký University, Joint Laboratory of Optics, Olomouc; Czech Republic.
- ¹²⁴Institute for Fundamental Science, University of Oregon, Eugene, OR; United States of America.
- ¹²⁵Graduate School of Science, Osaka University, Osaka; Japan.
- ¹²⁶Department of Physics, University of Oslo, Oslo; Norway.
- ¹²⁷Department of Physics, Oxford University, Oxford; United Kingdom.
- ¹²⁸LPNHE, Sorbonne Université, Université Paris Cité, CNRS/IN2P3, Paris; France.
- ¹²⁹Department of Physics, University of Pennsylvania, Philadelphia PA; United States of America.
- ¹³⁰Department of Physics and Astronomy, University of Pittsburgh, Pittsburgh PA; United States of America.
- ¹³¹(*a*) Laboratório de Instrumentação e Física Experimental de Partículas - LIP, Lisboa; (*b*) Departamento de Física, Faculdade de Ciências, Universidade de Lisboa, Lisboa; (*c*) Departamento de Física, Universidade de Coimbra, Coimbra; (*d*) Centro de Física Nuclear da Universidade de Lisboa, Lisboa; (*e*) Departamento de Física, Universidade do Minho, Braga; (*f*) Departamento de Física Teórica y del Cosmos, Universidad de Granada, Granada (Spain); (*g*) Departamento de Física, Instituto Superior Técnico, Universidade de Lisboa, Lisboa; Portugal.
- ¹³²Institute of Physics of the Czech Academy of Sciences, Prague; Czech Republic.
- ¹³³Czech Technical University in Prague, Prague; Czech Republic.
- ¹³⁴Charles University, Faculty of Mathematics and Physics, Prague; Czech Republic.
- ¹³⁵Particle Physics Department, Rutherford Appleton Laboratory, Didcot; United Kingdom.
- ¹³⁶IRFU, CEA, Université Paris-Saclay, Gif-sur-Yvette; France.
- ¹³⁷Santa Cruz Institute for Particle Physics, University of California Santa Cruz, Santa Cruz CA; United States of America.
- ¹³⁸(*a*) Departamento de Física, Pontificia Universidad Católica de Chile, Santiago; (*b*) Millennium Institute for Subatomic physics at high energy frontier (SAPHIR), Santiago; (*c*) Instituto de Investigación Multidisciplinario en Ciencia y Tecnología, y Departamento de Física, Universidad de La Serena; (*d*) Universidad Andres Bello, Department of Physics, Santiago; (*e*) Instituto de Alta Investigación, Universidad de Tarapacá, Arica; (*f*) Departamento de Física, Universidad Técnica Federico Santa María, Valparaíso; Chile.
- ¹³⁹Department of Physics, University of Washington, Seattle WA; United States of America.
- ¹⁴⁰Department of Physics and Astronomy, University of Sheffield, Sheffield; United Kingdom.
- ¹⁴¹Department of Physics, Shinshu University, Nagano; Japan.
- ¹⁴²Department Physik, Universität Siegen, Siegen; Germany.
- ¹⁴³Department of Physics, Simon Fraser University, Burnaby BC; Canada.
- ¹⁴⁴SLAC National Accelerator Laboratory, Stanford CA; United States of America.
- ¹⁴⁵Department of Physics, Royal Institute of Technology, Stockholm; Sweden.
- ¹⁴⁶Departments of Physics and Astronomy, Stony Brook University, Stony Brook NY; United States of America.
- ¹⁴⁷Department of Physics and Astronomy, University of Sussex, Brighton; United Kingdom.
- ¹⁴⁸School of Physics, University of Sydney, Sydney; Australia.

- ¹⁴⁹Institute of Physics, Academia Sinica, Taipei; Taiwan.
- ¹⁵⁰(^a) E. Andronikashvili Institute of Physics, Iv. Javakhishvili Tbilisi State University, Tbilisi; (^b) High Energy Physics Institute, Tbilisi State University, Tbilisi; (^c) University of Georgia, Tbilisi; Georgia.
- ¹⁵¹Department of Physics, Technion, Israel Institute of Technology, Haifa; Israel.
- ¹⁵²Raymond and Beverly Sackler School of Physics and Astronomy, Tel Aviv University, Tel Aviv; Israel.
- ¹⁵³Department of Physics, Aristotle University of Thessaloniki, Thessaloniki; Greece.
- ¹⁵⁴International Center for Elementary Particle Physics and Department of Physics, University of Tokyo, Tokyo; Japan.
- ¹⁵⁵Department of Physics, Tokyo Institute of Technology, Tokyo; Japan.
- ¹⁵⁶Department of Physics, University of Toronto, Toronto ON; Canada.
- ¹⁵⁷(^a) TRIUMF, Vancouver BC; (^b) Department of Physics and Astronomy, York University, Toronto ON; Canada.
- ¹⁵⁸Division of Physics and Tomonaga Center for the History of the Universe, Faculty of Pure and Applied Sciences, University of Tsukuba, Tsukuba; Japan.
- ¹⁵⁹Department of Physics and Astronomy, Tufts University, Medford MA; United States of America.
- ¹⁶⁰Department of Physics and Astronomy, University of California Irvine, Irvine CA; United States of America.
- ¹⁶¹University of Sharjah, Sharjah; United Arab Emirates.
- ¹⁶²Department of Physics and Astronomy, University of Uppsala, Uppsala; Sweden.
- ¹⁶³Department of Physics, University of Illinois, Urbana IL; United States of America.
- ¹⁶⁴Instituto de Física Corpuscular (IFIC), Centro Mixto Universidad de Valencia - CSIC, Valencia; Spain.
- ¹⁶⁵Department of Physics, University of British Columbia, Vancouver BC; Canada.
- ¹⁶⁶Department of Physics and Astronomy, University of Victoria, Victoria BC; Canada.
- ¹⁶⁷Fakultät für Physik und Astronomie, Julius-Maximilians-Universität Würzburg, Würzburg; Germany.
- ¹⁶⁸Department of Physics, University of Warwick, Coventry; United Kingdom.
- ¹⁶⁹Waseda University, Tokyo; Japan.
- ¹⁷⁰Department of Particle Physics and Astrophysics, Weizmann Institute of Science, Rehovot; Israel.
- ¹⁷¹Department of Physics, University of Wisconsin, Madison WI; United States of America.
- ¹⁷²Fakultät für Mathematik und Naturwissenschaften, Fachgruppe Physik, Bergische Universität Wuppertal, Wuppertal; Germany.
- ¹⁷³Department of Physics, Yale University, New Haven CT; United States of America.
- ^a Also Affiliated with an institute covered by a cooperation agreement with CERN.
- ^b Also at An-Najah National University, Nablus; Palestine.
- ^c Also at Borough of Manhattan Community College, City University of New York, New York NY; United States of America.
- ^d Also at Center for Interdisciplinary Research and Innovation (CIRI-AUTH), Thessaloniki; Greece.
- ^e Also at Centro Studi e Ricerche Enrico Fermi; Italy.
- ^f Also at CERN, Geneva; Switzerland.
- ^g Also at Département de Physique Nucléaire et Corpusculaire, Université de Genève, Genève; Switzerland.
- ^h Also at Departament de Física de la Universitat Autònoma de Barcelona, Barcelona; Spain.
- ⁱ Also at Department of Financial and Management Engineering, University of the Aegean, Chios; Greece.
- ^j Also at Department of Physics, California State University, Sacramento; United States of America.
- ^k Also at Department of Physics, King's College London, London; United Kingdom.
- ^l Also at Department of Physics, Stanford University, Stanford CA; United States of America.
- ^m Also at Department of Physics, Stellenbosch University; South Africa.
- ⁿ Also at Department of Physics, University of Fribourg, Fribourg; Switzerland.

- o* Also at Department of Physics, University of Thessaly; Greece.
- p* Also at Department of Physics, Westmont College, Santa Barbara; United States of America.
- q* Also at Hellenic Open University, Patras; Greece.
- r* Also at Institutio Catalana de Recerca i Estudis Avancats, ICREA, Barcelona; Spain.
- s* Also at Institut für Experimentalphysik, Universität Hamburg, Hamburg; Germany.
- t* Also at Institute for Nuclear Research and Nuclear Energy (INRNE) of the Bulgarian Academy of Sciences, Sofia; Bulgaria.
- u* Also at Institute of Applied Physics, Mohammed VI Polytechnic University, Ben Guerir; Morocco.
- v* Also at Institute of Particle Physics (IPP); Canada.
- w* Also at Institute of Physics and Technology, Mongolian Academy of Sciences, Ulaanbaatar; Mongolia.
- x* Also at Institute of Physics, Azerbaijan Academy of Sciences, Baku; Azerbaijan.
- y* Also at Institute of Theoretical Physics, Ilia State University, Tbilisi; Georgia.
- z* Also at Lawrence Livermore National Laboratory, Livermore; United States of America.
- aa* Also at National Institute of Physics, University of the Philippines Diliman (Philippines); Philippines.
- ab* Also at Technical University of Munich, Munich; Germany.
- ac* Also at The Collaborative Innovation Center of Quantum Matter (CICQM), Beijing; China.
- ad* Also at TRIUMF, Vancouver BC; Canada.
- ae* Also at Università di Napoli Parthenope, Napoli; Italy.
- af* Also at University of Colorado Boulder, Department of Physics, Colorado; United States of America.
- ag* Also at Washington College, Chestertown, MD; United States of America.
- ah* Also at Yeditepe University, Physics Department, Istanbul; Türkiye.
- * Deceased



Measurement of t -channel production of single top quarks and antiquarks in pp collisions at 13 TeV using the full ATLAS Run 2 data sample

The ATLAS Collaboration

The production of single top quarks and top antiquarks via the t -channel exchange of a virtual W boson is measured in proton–proton collisions at a centre-of-mass energy of 13 TeV at the LHC using 140 fb^{-1} of ATLAS data. The total cross-sections are determined to be $\sigma(tq) = 137_{-8}^{+8} \text{ pb}$ and $\sigma(\bar{t}q) = 84_{-5}^{+6} \text{ pb}$ for top-quark and top-antiquark production, respectively. The combined cross-section is found to be $\sigma(tq + \bar{t}q) = 221_{-13}^{+13} \text{ pb}$ and the cross-section ratio is $R_t = \sigma(tq)/\sigma(\bar{t}q) = 1.636_{-0.034}^{+0.036}$. The predictions at next-to-next-to-leading-order in quantum chromodynamics are in good agreement with these measurements. The predicted value of R_t using different sets of parton distribution functions is compared with the measured value, demonstrating the potential to further constrain the functions when using this result in global fits. The measured cross-sections are interpreted in an effective field theory approach, setting limits at the 95% confidence level on the strength of a four-quark operator and an operator coupling the third quark generation to the Higgs boson doublet: $-0.37 < C_{Qq}^{3,1}/\Lambda^2 < 0.06$ and $-0.87 < C_{\phi Q}^3/\Lambda^2 < 1.42$. The constraint $|V_{tb}| > 0.95$ at the 95% confidence level is derived from the measured value of $\sigma(tq + \bar{t}q)$. In a more general approach, pairs of CKM matrix elements involving top quarks are simultaneously constrained, leading to confidence contours in the corresponding two-dimensional parameter spaces.

Contents

1	Introduction	3
2	The ATLAS detector	4
3	Samples of data and simulated events	5
3.1	Simulation of $t\bar{t}$ and single-top-quark production	6
3.2	Simulation of W +jets, Z +jets and diboson production	7
3.3	Simulation and modelling of multijet production	8
3.4	Samples for the EFT and CKM interpretations	8
4	Object reconstruction and event selection	9
4.1	Object definitions	9
4.2	Modelling of non-prompt and fake leptons	11
4.3	Event selection and definition of signal regions	11
4.4	Control regions for the multijet background	12
5	Separation of signal from background events	12
6	Systematic uncertainties	15
6.1	Experimental uncertainties	18
6.2	Modelling uncertainties	19
7	Measurement results	21
8	Interpretation of the measurements	26
8.1	Sensitivity of R_t to PDF sets	26
8.2	EFT interpretation	26
8.3	Determination of $ V_{tb} $	29
8.4	Generalised CKM interpretation	30
9	Conclusions	31
	Appendix	34
	References	43

1 Introduction

During the 2015–2018 period of operation, known as Run 2, the Large Hadron Collider (LHC) [1] provided proton–proton (pp) collisions at a centre-of-mass energy of $\sqrt{s} = 13$ TeV, giving the collider experiments access to a previously unexplored kinematic range. By measuring top-quark production at this energy scale with high precision, theoretical predictions based on the Standard Model (SM) can be tested and deviations that might result from energy-dependent non-SM couplings can be searched for. Top quarks are produced singly in weak charged-current interactions. The dominant single-top-quark production process at the LHC is characterised by the t -channel exchange of a virtual W boson. Figure 1 depicts example Feynman diagrams of this process at leading order (LO) in perturbation theory. A light quark from one of the colliding protons interacts with a b -quark from another proton by exchanging a virtual W boson. Since the valence u -quark density of the proton is about twice as high as the valence d -quark density, the production cross-section of single top quarks, $\sigma(tq)$, is expected to be higher than the cross-section of top-antiquark production, $\sigma(\bar{t}q)$.

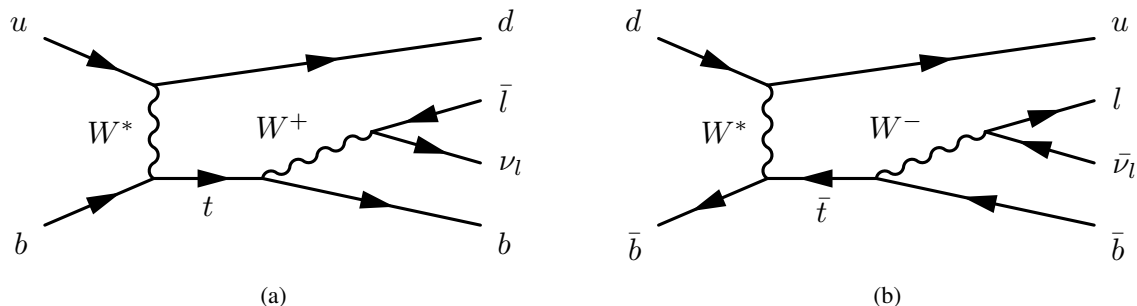


Figure 1: Example Feynman diagrams of (a) single top-quark and (b) single top-antiquark production via the t -channel exchange of a virtual W boson at LO in perturbation theory.

This document presents cross-section measurements of tq and $\bar{t}q$ production using the full data sample recorded with the ATLAS detector [2] during Run 2 of the LHC, corresponding to an integrated luminosity of 140 fb^{-1} . Separate measurements of tq and $\bar{t}q$ production provide sensitivity to the parton distribution functions (PDFs) of u - and d -quarks [3], exploiting the different initial states of the two processes shown in Figure 1. In addition, the combined cross-section $\sigma(tq + \bar{t}q)$ and the cross-section ratio $R_t = \sigma(tq)/\sigma(\bar{t}q)$ are measured. The ratio R_t has better precision than the individual cross-sections because of partial cancellations of common uncertainties. The measurements presented here supersede the results obtained by an ATLAS analysis of early Run 2 data corresponding to an integrated luminosity of 3.2 fb^{-1} [4], significantly improving the precision due to a larger data sample, better detector calibration, the use of more advanced object reconstruction [5, 6], and an improved statistical analysis based on profile maximum-likelihood fits which fully exploit the statistical power of the data sample. This analysis also features an improved treatment of systematic uncertainties related to the modelling of the hard partonic collision and the subsequent hadronisation with event generator programs based on the Monte Carlo (MC) method. The measurements are compared with fixed-order predictions made at next-to-next-to-leading-order (NNLO) in quantum chromodynamics (QCD). The measurement of R_t , in particular, is compared with predictions based on different PDFs.

The measurements are further interpreted in the context of effective field theory (EFT) to constrain the

Wilson coefficients associated with the four-quark operator $O_{Qq}^{3,1}$ and the operator $O_{\phi Q}^3$ that couples the third quark generation to the Higgs boson doublet. Both operators potentially contribute to t -channel single top-quark production in extensions of the SM. Existing limits on the coefficient of $O_{Qq}^{3,1}$ [7–9] are based on the combination of published measurements and do not account for reconstruction effects on EFT signal events, while the analysis presented here employs simulated signal samples and involves template fits to observed distributions. The operator $O_{\phi Q}^3$ features the same Lorentz structure as the Wtb vertex in the SM and limits on this operator are thus obtained from the measured value of $\sigma(tq + \bar{t}q)$. Another interpretation sets limits on the coupling strengths of Wtq vertices, constraining the products of a left-handed form factor f_{LV} and the absolute values of the Cabibbo–Kobayashi–Maskawa (CKM) matrix elements V_{tb} , V_{ts} and V_{td} . The form factor scales the cross-section of tq production with f_{LV}^2 , but leaves the Lorentz structure of the Wtq vertices unchanged; and thus the event kinematics remain unchanged. The SM has $f_{LV} = 1$.

The event selection of the analysis targets tq and $\bar{t}q$ events with leptonically decaying W bosons. Consequently, either one isolated electron or muon and high missing transverse momentum are required. In addition, there must be exactly two hadronic jets with high transverse momentum. Exactly one of these jets must be identified as originating from a b -quark and is hence labelled as a b -tagged jet, while the second jet is preferentially produced in the forward direction at high absolute values of pseudorapidity. The main background processes are top-quark–antiquark ($t\bar{t}$) pair production and $W+b\bar{b}$ production. Two other single top-quark production processes are also relevant: the associated production of a W boson and a top quark (tW production) and the production of $t\bar{b}$ or $\bar{t}b$ via the s -channel exchange of a virtual W boson. The selected signal and background events are further separated by constructing discriminants with an artificial neural network (NN). The output distributions of the NN are used in a maximum-likelihood fit to determine the signal yields and measure $\sigma(tq)$, $\sigma(\bar{t}q)$, $\sigma(tq + \bar{t}q)$, and R_t .

The CMS Collaboration measured tq and $\bar{t}q$ production at $\sqrt{s} = 13$ TeV using a partial Run 2 data sample, determining the total cross-sections [10], various differential cross-sections [11], and measuring CKM matrix elements [12].

2 The ATLAS detector

The ATLAS detector covers nearly the entire solid angle around the collision point.¹ It consists of an inner tracking detector surrounded by a thin superconducting solenoid, electromagnetic and hadronic calorimeters, and a muon spectrometer incorporating three large superconducting toroidal magnets.

The inner-detector system (ID) is immersed in a 2 T axial magnetic field and provides charged-particle tracking in the range of $|\eta| < 2.5$. The high-granularity silicon pixel detector covers the vertex region and typically provides four measurements per track, the first hit normally being in the insertable B-layer installed before Run 2 [13, 14]. It is followed by the silicon microstrip tracker, which usually provides eight measurements per track. These silicon detectors are complemented by the transition radiation tracker (TRT), which enables radially extended track reconstruction up to $|\eta| = 2.0$. The TRT also provides electron identification information based on the fraction of hits (typically 30 in total) above a higher energy-deposit threshold corresponding to transition radiation.

¹ ATLAS uses a right-handed coordinate system with its origin at the nominal interaction point (IP) in the centre of the detector and the z -axis along the beam pipe. The x -axis points from the IP to the centre of the LHC ring, and the y -axis points upwards. Cylindrical coordinates (r, ϕ) are used in the transverse plane, ϕ being the azimuthal angle around the z -axis. The pseudorapidity is defined in terms of the polar angle θ as $\eta = -\ln \tan(\theta/2)$. Angular distance is measured in units of $\Delta R \equiv \sqrt{(\Delta\eta)^2 + (\Delta\phi)^2}$.

The calorimeter system covers the pseudorapidity range $|\eta| < 4.9$. Within the region $|\eta| < 3.2$, electromagnetic calorimetry is provided by barrel and endcap high-granularity lead/liquid-argon (LAr) calorimeters, with an additional thin LAr presampler covering $|\eta| < 1.8$ to correct for energy loss in material upstream of the calorimeters. Hadronic calorimetry is provided by the steel/scintillator-tile calorimeter, segmented into three barrel structures within $|\eta| < 1.7$, and two copper/LAr hadronic endcap calorimeters. The solid angle coverage is completed with forward copper/LAr and tungsten/LAr calorimeter modules optimised for electromagnetic and hadronic measurements respectively.

The muon spectrometer (MS) comprises separate trigger and high-precision tracking chambers measuring the deflection of muons in a magnetic field generated by superconducting air-core toroids. The field integral of the toroids ranges between 2.0 and 6.0 Tm across most of the detector. A set of precision chambers covers the region $|\eta| < 2.7$ with three layers of monitored drift tubes, complemented by cathode-strip chambers in the forward region, where the background is highest. The muon trigger system covers the range $|\eta| < 2.4$ with resistive-plate chambers in the barrel, and thin-gap chambers in the endcap regions. Interesting events are selected to be recorded by the first-level trigger system implemented in custom hardware, followed by selections made by algorithms implemented in software in the high-level trigger [15]. The first-level trigger accepts events from the 40 MHz bunch crossings at a rate below 100 kHz, that the high-level trigger further reduces to record events to disk at about 1 kHz.

An extensive software suite [16] is used in the reconstruction and analysis of real and simulated data, in detector operations, and in the trigger and data acquisition systems of the experiment.

3 Samples of data and simulated events

The analysis uses proton–proton (pp) collision data recorded with the ATLAS detector in the years 2015 to 2018 at a centre-of-mass energy of 13 TeV. After applying data-quality requirements [17], the data set corresponds to an integrated luminosity of 140.1 fb^{-1} with a relative uncertainty of 0.83% [18]. The LUCID-2 detector [19] was used for the primary luminosity measurements, complemented by measurements using the inner detector and calorimeters.

Events were selected online during data taking by single-electron or single-muon triggers [20, 21]. Multiple triggers were combined in a logical OR to increase the selection efficiency. The lowest-threshold triggers utilised isolation requirements for reducing the trigger rate. The isolated-lepton triggers had thresholds in transverse momentum (p_T) of 20 GeV for muons and 24 GeV for electrons in 2015 data, and 26 GeV for both lepton types in 2016, 2017 and 2018 data. They were complemented by other triggers with higher p_T thresholds but no isolation requirements to increase the trigger efficiency.

Sets of simulated events from signal and background processes were produced with MC-based event generator programs to model the physics processes. After event generation, the response of the ATLAS detector was simulated using the GEANT4 toolkit [22] with a full detector model [23] or a fast simulation [24, 25] which employed a parameterisation of the calorimeter response. The fast simulation was used for samples that were employed to evaluate systematic uncertainties associated with the event generators and for samples used for the EFT interpretation. To account for additional inelastic pp collisions in the same and neighbouring bunch crossings (pile-up), minimum-bias interactions were overlaid on the hard-scattering events at the level of simulated energy depositions. The minimum-bias events were simulated using PYTHIA 8.186 [26] with the A3 [27] set of tuned parameters and the NNPDF2.3LO PDF set [28]. The

resulting events were weighted to reproduce the observed pile-up distribution. The average number of interactions per bunch crossing during the entire data-taking period from 2015 to 2018 is 33.7.

Finally, the simulated events were reconstructed using the same software as applied to the collision data. Except for events of the multijet background, the same event selection requirements were applied and the selected events were passed through the same analysis chain. Corrections are applied to simulated events such that the lepton trigger and reconstruction efficiencies, jet energy calibration and b -tagging efficiency are in better agreement with the response observed in data. More details of the simulated event samples are provided in the following subsections.

3.1 Simulation of $t\bar{t}$ and single-top-quark production

Samples of simulated events from $t\bar{t}$ and single-top-quark production were generated using the next-to-leading-order (NLO) matrix-element generator POWHEG Box v2 [29–35], setting the top-quark mass to $m_t = 172.5$ GeV. For $t\bar{t}$ and tW production as well as s -channel single-top-quark production ($t\bar{b}$ production) the NNPDF3.0_{NLO} PDF set [36] was used with the five-flavour scheme. Following a recommendation given in Ref. [35], single top-quark production in the t -channel (tq production) was simulated with the NNPDF3.0_{NLO_NF4} PDF set, which implements the four-flavour scheme. Parton showers, hadronisation, and the underlying event were modelled using PYTHIA 8.230 with the A14 [37] set of tuned parameters and the NNPDF2.3_{LO} PDF set. The POWHEG Box+PYTHIA generator setup applies a matching scheme to the modelling of hard emissions in the two programs. For $t\bar{t}$ production, the matrix-element-to-parton-shower matching is steered by the h_{damp} parameter, that controls the p_T of the first additional gluon emission beyond the LO Feynman diagram in the parton shower and therefore regulates the high- p_T emission against which the $t\bar{t}$ system recoils. Event generation was run with $h_{\text{damp}} = 1.5 \times m_t$ [38]. The renormalisation and factorisation scales were set dynamically on an event-by-event basis, namely to $\mu_r = \mu_f = \sqrt{m_t^2 + p_T^2(t)}$ for $t\bar{t}$ production and to $\mu_r = \mu_f = 4 \sqrt{m_b^2 + p_T^2(b)}$ for tq production, where $p_T(t)$ is the p_T of the top quark, m_b is the mass of the b -quark, and $p_T(b)$ is the p_T of the b -quark originating from the initial-state gluon that splits into a $b\bar{b}$ pair. The scale choice for tq production follows a recommendation in Ref. [35]. When generating tW events, the scales were set to $\mu_r = \mu_f = m_t$ and the diagram-removal scheme [39] was employed to treat the interference with $t\bar{t}$ production [38].

In the case of tq production, top-quark decays were modelled by MADSPIN [40, 41], while in the case of $t\bar{t}$, $t\bar{b}$ and tW production top-quark decays were handled by POWHEG Box directly. The decays of bottom and charm hadrons were simulated using the EVTGEN 1.6.0 program [42].

The sample of simulated $t\bar{t}$ events was normalised to a total cross-section of $\sigma(t\bar{t}) = 834 \pm 33$ pb (relative uncertainty: 4.0%), the value obtained from NNLO predictions from the TOP++ 2.0 program (see Ref. [43] and references therein), which includes the resummation of next-to-next-to-leading logarithmic (NNLL) soft-gluon terms. The predicted cross-sections of tq and $\bar{t}q$ production used to normalise the corresponding samples of simulated events are $\sigma(tq) = 134.2 \pm 2.2$ pb and $\sigma(\bar{t}q) = 80.0 \pm 1.6$ pb (relative uncertainties: 1.6% and 2.0%, respectively) and were calculated with the MCFM 10.1 program [44] at NNLO in QCD. The quoted uncertainties include the uncertainties related to a variation of μ_r and μ_f , the uncertainty in the PDFs and in the value of the strong coupling constant α_s . The scale uncertainty is determined by varying μ_r and μ_f independently up and down by a factor of two, whilst never allowing them to differ by a factor greater than two from each other. The combined PDF and α_s uncertainties were determined at the 68% confidence level (CL) according to the Hessian representation of the PDF4LHC21 PDF set [45]. The total

cross-section for $t\bar{b}$ production was computed at NLO in QCD with the HATHOR 2.1 program [46, 47] and the corresponding sample of simulated events was normalised to $\sigma(t\bar{b} + \bar{t}b) = 10.32 \pm 0.38$ pb (relative uncertainty: 3.7%). The cross-section used for normalising the tW sample is $\sigma(tW + \bar{t}W) = 79.3 \pm 2.9$ pb (relative uncertainty: 3.7%) [48]. All cross-section calculations assume $m_t = 172.5$ GeV.

3.2 Simulation of W +jets, Z +jets and diboson production

The production of W and Z bosons in association with jets, including heavy-flavour jets, was simulated with the SHERPA 2.2.1 generator [49]. In this setup, NLO-accurate matrix elements for up to two partons and LO-accurate matrix elements for up to four partons are calculated with the COMIX [50] and OPENLOOPS 1 [51–53] libraries. The default SHERPA parton shower [54] based on Catani–Seymour dipole factorisation and the cluster hadronisation model [55] were used. The generation employed the dedicated set of tuned parameters developed by the SHERPA authors and the NNPDF3.0_{NLO} PDF set.

The NLO matrix elements of a given jet multiplicity are matched to the parton shower using a colour-exact variant of the MC@NLO algorithm [56]. Different jet multiplicities are then merged into an inclusive sample using an improved CKKW matching procedure [57, 58] that is extended to NLO accuracy using the MEPS@NLO prescription [59]. The merging threshold was set to 20 GeV. The W +jets and Z +jets samples are normalised to NNLO predictions [60] of the total cross-sections, obtained with the FEWZ package [61].

After event generation and before detector simulation, the W +jets and Z +jets samples were subjected to hadron-flavour filters. Events in which at least one b -hadron is present were selected and form b -filtered samples. The production of a W boson in association with b -hadrons is dominated by processes in which a radiated high- p_T gluon splits into a $b\bar{b}$ pair. This class of background processes is thus called $W+b\bar{b}$ production. Samples with an applied c -filter were produced by vetoing events that pass the b -filter described above and requiring at least one c -hadron to be present. Two different classes of physics processes contribute to the c -filtered samples, flavour production via gluon splitting leading to $W+c\bar{c}$ and a second class of processes with a down-type quark and a gluon in the initial state, leading to the production of a single c -quark in the final state via $qg \rightarrow W+c$. To represent both classes of processes the associated production of a W boson and c -jets is denoted as $W+c(\bar{c})$ production. Generated events of W +jets production that remain after applying the b -filter and the c -filter as a veto constitute W +light-quark-jet production. The contribution of this process to the expected event yields is much smaller than the contributions of $W+b\bar{b}$ and $W+c(\bar{c})$ production due to the tight b -tagging requirement made, and therefore the W +light-quark-jet contribution is merged with the contribution of the $W+b\bar{b}$ process in the statistical analysis. The Z +jets samples are treated with the same hadron-flavour filtering scheme as the W +jets samples, leading to b -filtered, c -filtered and light-flavour samples. However, Z +jets production is a minor background in the analysis and therefore the flavour split is not used in the statistical analysis.

Samples of on-shell diboson production (WW , WZ and ZZ) were simulated with the same SHERPA setup as described above for W +jets and Z +jets production. The matrix elements considered contain all diagrams with four electroweak vertices and were calculated at NLO accuracy in QCD for up to one additional parton and at LO accuracy for up to three additional parton emissions. The diboson event samples are normalised to the total cross-sections provided by SHERPA.

3.3 Simulation and modelling of multijet production

Events featuring generic high- p_T multijet production may satisfy the event selection if a jet is misidentified as an electron or muon, or if real electrons or muons coming from hadron decays inside the jets satisfy the isolation requirements. The former are called *fake leptons*, the latter *non-prompt leptons*. In addition, non-prompt electrons occur as a result of photon conversions in the detector material. Multijet events with fake electrons or non-prompt electrons are modelled with a sample of simulated dijet events, while events with non-prompt muons are modelled with collision data, described in Section 4.2. The number of events with fake muons is negligible. The dijet event sample was generated using PYTHIA 8.186 with LO matrix elements for dijet production and interfaced to a p_T -ordered parton shower. The scales μ_r and μ_f were set to the square root of the geometric mean of the squared transverse masses of the two outgoing particles in the matrix element, $\mu_r = \mu_f = \sqrt{(p_{T,1}^2 + m_1^2)(p_{T,2}^2 + m_2^2)}$. At generator level, a filter was applied that required the existence of one particle-level jet with $p_T > 17$ GeV. The generation used the NNPDF2.3LO PDF set and the A14 set of tuned parameters. The generated sample of dijet events is used to model the kinematics of electron events of the multijet background when producing template distributions, while the rate of the multijet background is estimated in a data-driven way using dedicated control regions (CRs) described in Section 4.4.

3.4 Samples for the EFT and CKM interpretations

For interpreting the measurement in the framework of EFT, samples of tq (t -channel) and $t\bar{b}$ (s -channel) production were generated with MADGRAPH5_AMC@NLO 2.7.3 using the SMEFTatNLO-NLO model [62] with the five-flavour scheme and the NNPDF3.0NLO PDF set. The operator $O_{Qq}^{3,1}$ was activated, which introduces a four-quark contact interaction. Separate samples of simulated events were generated for each $C_{Qq}^{3,1}/\Lambda^2 \in \{-0.6, -0.2, 0.0, 0.4, 1.0\}$ for single top-quark and top-antiquark production. The setting $C_{Qq}^{3,1}/\Lambda^2 = 0.0$ corresponds to the SM. Each sample includes both tq and $t\bar{b}$ production. The SM production of the two processes is covered as well as the production via the four-quark operator $O_{Qq}^{3,1}$, and the interference of SM and non-SM amplitudes. The generated events were showered with PYTHIA 8.244 using the A14 set of tuned parameters and the NNPDF2.3LO PDF set. In these samples, the top-quark is assumed to decay to W^+b with a branching ratio of 100%.

The generalised CKM interpretation is based on samples of tq and $t\bar{q}$ events generated with MADGRAPH5_AMC@NLO 2.9.9 using the NNPDF3.0NLO PDF set. Eight samples were generated in which all different combinations of Wtq vertices with $q \in \{d, s, b\}$ are considered for the production and the decay vertex, except for the dominant mode that has a Wtb vertex on the production and the decay side. The four-flavour scheme was used for both samples in which the top quark originates from a b -quark. The other six samples were generated based on the five-flavour scheme. Parton showers were simulated with PYTHIA 8.307 using the A14 set of tuned parameters and the NNPDF2.3LO PDF set. The decay of top quarks was simulated with MADSPIN preserving all spin correlations, while W bosons coming from the top-quark decays were forced to decay leptonically. The samples are normalised to cross-sections calculated with MADGRAPH5_AMC@NLO assuming that the CKM matrix elements involved are equal to one, and were simulated with the full detector simulation.

The main background, $t\bar{t}$ production, also involves Wtq vertices when the top quark and antiquark decay. To facilitate a consistent treatment of the $t\bar{t}$ background eight additional samples were generated with POWHEG Box v2, implementing all combinations of Wtq decay vertices, except for the nominal channel that

involves two Wtb vertices. For the alternative samples, the parton shower was simulated with PYTHIA 8.307 using the A14 set of tuned parameters and the NNPDF2.3LO PDF set. The top-quark decay was handled with MADSPIN.

4 Object reconstruction and event selection

The partonic final state of the tq signal process comprises a charged lepton, a neutrino, a b -quark and a light quark (see Figure 1) and is reconstructed by identifying corresponding objects measured in the detector, such as electron and muon candidates, and hadronic jets. The presence of a high- p_T neutrino is indicated by large missing transverse momentum.

4.1 Object definitions

Events are required to have at least one vertex reconstructed from at least two ID tracks with transverse momenta of $p_T > 0.5$ GeV. The primary vertex of an event is defined as the vertex with the highest sum of p_T^2 over all associated ID tracks [63].

Electron candidates are reconstructed by matching a track in the ID to clusters of energy deposits in the electromagnetic calorimeter [64]. The pseudorapidity of clusters, η_{cluster} , is required to be in the range of $|\eta_{\text{cluster}}| < 2.47$. However, clusters are excluded if they are in the transition region $1.37 < |\eta_{\text{cluster}}| < 1.52$ between the barrel and endcap electromagnetic calorimeters. Electron candidates must have $p_T > 10$ GeV. A likelihood-based discriminant is constructed to simultaneously evaluate several properties of electron candidates, including shower shapes in the electromagnetic calorimeter, track quality, and the detection of transition radiation produced in the TRT. By placing a requirement on the discriminant, the selection of true electrons is enhanced, while photon conversions and hadrons misidentified as electrons are largely rejected. Two categories of electrons with different identification quality are defined [64]: the first category implements *Tight* identification criteria and features a high rejection of non-prompt or fake electrons, while the second category with *Loose* identification criteria has higher efficiency at the price of lower purity in prompt electrons. Electrons from decays of weak gauge bosons with $p_T(e) > 15$ GeV satisfy the *Tight* (*Loose*) criteria with an average efficiency of 80% (93%).

Muon candidates are reconstructed by combining tracks in the MS with tracks in the ID [65]. The tracks must be in the range of $|\eta| < 2.5$ and have $p_T > 10$ GeV. Similarly to electrons, two levels of identification criteria are applied, defining *Medium* and *Loose* quality categories of muon candidates [65]. Muons originating from W bosons in $t\bar{t}$ events with $p_T(\mu) > 10$ GeV satisfy the *Medium* (*Loose*) quality criteria with an efficiency of 97% (99%).

The tracks matched to electron and muon candidates must point to the primary vertex, which is ensured by requirements imposed on the transverse impact-parameter significance, $|d_0/\sigma(d_0)| < 5$ for electrons and $|d_0/\sigma(d_0)| < 3$ for muons, and on the longitudinal impact parameter, Δz_0 , for which $|\Delta z_0 \sin(\theta)| < 0.5$ mm must be satisfied for both of the lepton flavours. Non-prompt and fake leptons are efficiently rejected using multivariate discriminants [65] computed with boosted decision trees that combine electromagnetic shower shapes, track information from the ID, and a discriminant used to identify b -jets. Prompt muons with a p_T between 20 and 100 GeV satisfy the imposed isolation requirement with an efficiency of 87%, while the efficiency for muons from semileptonic decays of bottom or charm hadrons is 0.5%. Scale factors are

used to correct the efficiencies in simulation to match the efficiencies measured for the electron [20] and muon [21] triggers, and the reconstruction, identification and isolation criteria [64, 65].

Jets are reconstructed from particle-flow objects [66] with the anti- k_t clustering algorithm [67, 68] using a radius parameter of 0.4. This algorithm matches topological clusters [69] in the calorimeters to selected tracks in the ID. The energy of tracks is subtracted from the matched topological clusters and both the tracks and the energy-subtracted topological clusters are used as input to the clustering. The jet energy is calibrated by applying several simulation-based corrections and techniques correcting for differences between simulation and data [5]. The jets must fulfil $p_T > 30$ GeV and $|\eta| < 4.5$.

To suppress jets originating from pile-up collisions, several track-based variables are combined with a multivariate technique in the jet-vertex-tagger (JVT) discriminant [70]. Jets with $p_T < 60$ GeV and $|\eta| < 2.4$ are required to have a JVT-discriminant above 0.5, which corresponds to an efficiency of 92% for non-pile-up jets, while 98% of jets from pile-up events are rejected. For jets with $p_T < 60$ GeV and $|\eta| > 2.5$, the forward-jet-vertex-tagger (fJVT) [71] is used and an fJVT value below 0.4 is required. In addition, the jet must satisfy a timing condition. Differences in the efficiencies of the JVT and fJVT requirements between collision data and simulation are corrected by corresponding scale factors.

Jets containing b -hadrons are identified (b -tagged) with the DL1r algorithm, which uses a deep feed-forward neural network with several b -tagging algorithms as inputs [6]. These input algorithms exploit the impact parameters of charged-particle tracks, the properties of reconstructed secondary vertices and the topology of b - and c -hadron decays inside the jets. The requirement on the DL1r discriminant is chosen such that the efficiency of tagging b -jets with $p_T > 20$ GeV produced in simulated dileptonic $t\bar{t}$ events is 60%. Differences in the b -tagging efficiency between collision data and simulation are corrected with simulation-to-data scale factors derived from $t\bar{t}$ events. The scale factors are determined as a function of jet p_T and are found to be consistent with unity within uncertainties. The obtained scale factors depend on the parton-shower generator used to produce the $t\bar{t}$ samples. When using samples produced with a different parton-shower generator, for example SHERPA, to model W +jets events, or when evaluating systematic uncertainties with a setup based on HERWIG, additional correction factors called MC-to-MC scale factors are applied. Since the DL1r algorithm uses measurements from the ID, the identification of b -jets is limited to the region with $|\eta| < 2.5$.

To avoid double-counting objects satisfying more than one selection criterion, a procedure called *overlap removal* is applied. Reconstructed objects defined with *Loose* quality criteria are removed in the following order: electrons sharing an ID track with a muon; jets within $\Delta R = 0.2$ of an electron, thereby avoiding double-counting electron energy deposits as jets; electrons within $\Delta R = 0.4$ of a remaining jet, for reducing the impact of non-prompt electrons; jets within $\Delta R = 0.2$ of a muon if they have two or fewer associated tracks with $p_T > 0.5$ GeV; and muons within $\Delta R = 0.4$ of a remaining jet, reducing the rate of non-prompt muons.

The missing transverse momentum \vec{p}_T^{miss} is reconstructed as the negative vector sum of the p_T of the reconstructed leptons and jets, as well as ID tracks that point to the primary vertex but are not associated with a reconstructed object [72]. The latter contribution to \vec{p}_T^{miss} is named soft-track component. The magnitude of \vec{p}_T^{miss} is denoted by E_T^{miss} .

4.2 Modelling of non-prompt and fake leptons

Events of the multijet background with an identified electron candidate are modelled using the *jet-electron* method [73]. Simulated events from dijet production are selected if they contain a jet depositing a large fraction ($>80\%$) of its energy in the electromagnetic calorimeter. This jet is classified as an electron, labelled as the jet-electron, and is treated in the subsequent steps of the analysis in the same way as a properly identified prompt electron as defined in the previous section. The jet-electrons must satisfy the nominal p_T and $|\eta|$ requirements, but electron identification requirements are not applied.

Multijet events with non-prompt muons are modelled with collision events highly enriched in non-prompt muons [73]. Starting from the same sample of collision events as the nominal selection, a subset of events enriched in non-prompt muons is obtained by inverting or modifying some of the muon isolation requirements, such that the resulting sample does not overlap with the nominal sample. The kinematic requirements on p_T and $|\eta|$ are the same as for the nominal muon selection.

4.3 Event selection and definition of signal regions

Candidate events are required to have exactly one charged lepton (ℓ) with $p_T(\ell) > 28$ GeV, either an electron of *Tight* quality or a muon of *Medium* quality. The charged lepton is required to match the object that caused the event to pass a single-lepton trigger. To reduce contributions from $t\bar{t}$ events in the dilepton decay channel, any event with an additional lepton satisfying the *Loose* quality conditions with $p_T > 10$ GeV is rejected.

Multijet events containing fake or non-prompt leptons tend to have low E_T^{miss} and low W transverse mass, in contrast to events with prompt leptons from W and Z decays. The W transverse mass is defined as

$$m_T(W) = \sqrt{2p_T(\ell)E_T^{\text{miss}}(1 - \cos \Delta\phi(\vec{p}_T^{\text{miss}}, \ell))},$$

using the difference between the azimuthal angles of \vec{p}_T^{miss} and the charged lepton, $\Delta\phi(\vec{p}_T^{\text{miss}}, \ell)$. To reduce the multijet background, $E_T^{\text{miss}} > 30$ GeV and $m_T(W) > 50$ GeV are applied as selection requirements.

Exactly two jets with $p_T > 30$ GeV and $|\eta| < 4.5$ are required. Exactly one of these jets must be b -tagged, while the second jet must fail to meet the b -tagging requirement. The latter jet is therefore called the *untagged* jet. The b -tagged jet is explicitly required to have $|\eta| < 2.5$. Events with forward jets with $2.3 < |\eta| < 4.5$ are removed if at least one of the jets has $30 \text{ GeV} < p_T < 35 \text{ GeV}$, leading to an improved modelling of the $|\eta|$ distribution of untagged jets in the given regime.

To further suppress the multijet background and to remove poorly reconstructed leptons with low p_T , an additional requirement is applied based on the azimuthal angle between the charged lepton and the leading jet (j_1), i.e. the jet with the largest p_T . This quantity is denoted by $\Delta\phi(j_1, \ell)$. The imposed requirement is

$$p_T(\ell) > 40 \text{ GeV} \cdot \frac{|\Delta\phi(j_1, \ell)|}{\pi}, \quad (1)$$

which leads to a tighter p_T requirement on the charged lepton than the baseline definition if the leading jet and the charged lepton have a back-to-back topology, namely if $|\Delta\phi(j_1, \ell)| > 0.7\pi$. For the maximum separation $|\Delta\phi(j_1, \ell)| = \pi$ between the two objects, $p_T(\ell) > 40$ GeV must be satisfied.

Furthermore, an additional selection criterion is imposed on the invariant mass of the charged lepton and the b -tagged jet, $m(\ell b)$. Since the off-shell region for top-quark decays is not included in the calculation

CR name	Requirement
B-e-plus	$q_e/e = +1, \eta(e) < 1.37, E_T^{\text{miss}} < 30 \text{ GeV}$
B-e-minus	$q_e/e = -1, \eta(e) < 1.37, E_T^{\text{miss}} < 30 \text{ GeV}$
EC-e-plus	$q_e/e = +1, \eta(e) > 1.52, E_T^{\text{miss}} < 30 \text{ GeV}$
EC-e-minus	$q_e/e = -1, \eta(e) > 1.52, E_T^{\text{miss}} < 30 \text{ GeV}$
CR μ -plus	$q_\mu/e = +1, 28 \text{ GeV} < p_T(\mu) < 40 \text{ GeV} \cdot \frac{ \Delta\phi(j_1, \ell) }{\pi}$
CR μ -minus	$q_\mu/e = -1, 28 \text{ GeV} < p_T(\mu) < 40 \text{ GeV} \cdot \frac{ \Delta\phi(j_1, \ell) }{\pi}$

Table 1: Summary of the definition of the CRs.

of the matrix element of the event generator, it is not modelled well. Therefore, the tail of the $m(\ell b)$ distribution is removed by requiring $m(\ell b) < 160 \text{ GeV}$; this imposes a threshold that is slightly above the kinematic limit at LO, $m(\ell b)_{\text{limit}}^2 = m_t^2 - m_W^2$.

Two separate signal regions (SRs) are defined for events with a positively or a negatively charged lepton. These regions are denoted SR plus and SR minus, respectively.

4.4 Control regions for the multijet background

Since the misidentification of jets as electrons or muons are not well modelled by the detector simulation, the rate of the multijet background is determined in a data-driven way by including dedicated CRs in the fits of the statistical analysis. The rate of fake and non-prompt electrons is constrained in four CRs that are defined by the same selection criteria as the two SRs but inverting the E_T^{miss} requirement. Since the relative numbers of electrons detected in the barrel ($|\eta| < 1.37$) and endcap ($|\eta| > 1.52$) sections of the electromagnetic calorimeter are not modelled well enough by the sample of simulated dijet events, separate CRs are defined for the barrel and endcap regions and are denoted CR B-e-plus, CR B-e-minus, CR EC-e-plus and CR EC-e-minus. Only the event yields in these regions are included in the maximum-likelihood fit. The rate of non-prompt muons is constrained in two CRs defined by the same selection criteria as used for the two SRs but inverting the requirement on the p_T in Eq. 1. The two CRs are named CR μ -plus and CR μ -minus. The distributions of the difference in the azimuthal angles of \vec{p}_T^{miss} and the muon, $\Delta\phi(\vec{p}_T^{\text{miss}}, \mu)$, are included in the maximum-likelihood fits. Table 1 provides a summary of the definition of the CRs.

5 Separation of signal from background events

An artificial neural network is used to separate signal and background events in the two SRs by combining several kinematic variables into an optimised NN discriminant named D_{nn} . In addition to variables derived from the reconstructed objects, the NN builds on a reconstruction of the W boson and the top quark. The reconstruction of the leptonically decaying W boson requires the determination of the neutrino momentum.

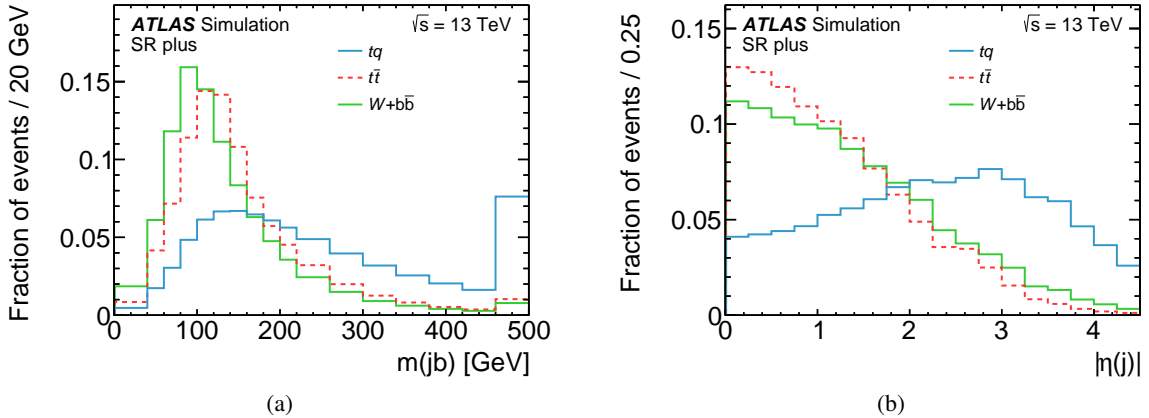


Figure 2: Probability densities of the two most discriminating input variables to the NN in SR plus. (a) The invariant mass $m(jb)$ of the untagged jet and the b -tagged jet and (b) the absolute value of the pseudorapidity of the untagged jet $|\eta(j)|$. The distributions are shown for the tq signal process, and the $t\bar{t}$ and the $W+b\bar{b}$ backgrounds. Events beyond the x -axis range are included in the last bin.

While the x - and y -components of the neutrino momentum, $p_x(\nu)$ and $p_y(\nu)$, are approximated by the components of \vec{p}_T^{miss} , the z -component, $p_z(\nu)$, is determined by constraining the mass of the reconstructed W boson to match the measured world average [74]. If the resulting quadratic equation has two real solutions, the one with the smallest $|p_z(\nu)|$ is chosen. In the case of complex solutions, which occur due to the limited E_T^{miss} resolution, a kinematic fit is performed that rescales the $p_x(\nu)$ and $p_y(\nu)$ such that the imaginary part vanishes and at the same time the distance between the transverse components of the neutrino momentum and \vec{p}_T^{miss} is minimised [75]. The W boson is formed by adding the four-vectors of the reconstructed neutrino and the charged lepton. The top quark is reconstructed by adding the four-vector of the W boson and the b -jet.

The NN is implemented using the NeuroBayes package [76, 77], which combines a three-layer feed-forward NN with a complex and robust preprocessing of the input variables before they are presented to the NN. The preprocessing produces a ranking of the input variables based on an algorithm employing the total correlation of a set of variables to the target function, which assumes the value 1 for signal and 0 for background events [78]. Utilising this ranking, NNs with different numbers of variables are trained, the full analysis is performed and the expected uncertainty of the measurement is determined. Networks using more input variables tend to result in measurements with lower uncertainties in $\sigma(tq)$, $\sigma(\bar{t}q)$, $\sigma(tq + \bar{t}q)$, and R_t . However, when employing 15–30 variables, only marginal further improvements are found if more variables are added. As a result, the 17 highest-ranking input variables are chosen for training the final NN. These input variables are listed and described in Table 2. The probability densities of the two most discriminating variables, $m(jb)$ and $|\eta(j)|$, are shown for the tq signal process, and the $t\bar{t}$ and the $W+b\bar{b}$ backgrounds in Figure 2 for SR plus. The symbol j represents the untagged jet.

A single NN is trained using a sample of simulated events comprising both the positively and negatively charged leptons, since the event kinematics of tq and $\bar{t}q$ production is very similar. This simple approach gives similar sensitivity as a scenario in which separate NNs are trained in the SR plus and SR minus. The NN is trained against all considered backgrounds with a fraction of 50% signal events and 50% background events. The different background processes are weighted relative to each other according to their expected numbers of events. NeuroBayes uses Bayesian regularisation techniques for the training process to improve

No.	Symbol	Description
1.	$m(jb)$	Invariant mass of the untagged jet (j) and the b -tagged jet (b)
2.	$ \eta(j) $	Absolute value of the pseudorapidity of the untagged jet
3.	$ \Delta p_T(W, jb) $	Absolute value of the difference in transverse momentum between the reconstructed W boson and the jet pair
4.	$ \Delta\phi(W, jb) $	Absolute value of the difference in azimuthal angle between the reconstructed W boson and the jet pair
5.	$m(t)$	Invariant mass of the reconstructed top quark
6.	$ \Delta\eta(\ell, j) $	Absolute value of the difference in pseudorapidity between the charged lepton (ℓ) and the untagged jet
7.	$\Delta R(\ell, j)$	Angular distance of the charged lepton and the untagged jet
8.	$ \Delta\eta(b, \ell) $	Absolute value of the difference in pseudorapidity between the b -tagged jet and the charged lepton
9.	$m_T(W)$	Transverse mass of the W boson
10.	$m(\ell b)$	Invariant mass of the charged lepton and the b -tagged jet
11.	$H_T(\ell, \text{jets}, E_T^{\text{miss}})$	Scalar sum of the transverse momenta of the charged lepton and the jets and E_T^{miss}
12.	$ \Delta\eta(b, j) $	Absolute value of the difference in the pseudorapidity of the two jets
13.	$ \Delta\phi(j, t) $	Absolute value of the difference in the azimuthal angle between the untagged jet and the reconstructed top quark
14.	$\cos\theta^*(\ell, j)$	Cosine of the angle θ^* between the charged lepton and the untagged jet in the rest frame of the reconstructed top quark
15.	$ \eta(\ell) $	Absolute value of the pseudorapidity of the charged lepton
16.	S	Sphericity defined as the sum of the 2nd and 3rd largest eigenvalues of the sphericity tensor multiplied by $3/2$
17.	$ \Delta p_T(\ell, j) $	Absolute value of the difference in transverse momentum of the charged lepton and the untagged jet

Table 2: The 17 variables used for the training of the NN ordered by their discriminating power. The sphericity tensor $S^{\alpha\beta}$ used to define the sphericity S is formed with the three-momenta \vec{p}_i of the reconstructed objects, namely the jets, the charged lepton and the reconstructed neutrino. The tensor is given by $S^{\alpha\beta} = \frac{\sum_i p_i^\alpha p_i^\beta}{\sum_i |\vec{p}_i|^2}$ where α and β correspond to the spatial components x , y and z .

the generalisation performance and to avoid overtraining. The network infrastructure consists of one input node for each input variable plus one bias node, followed by 22 nodes arranged in a single hidden layer, and one output node that gives a continuous output in the interval $(-1, +1)$. As a non-linear activation

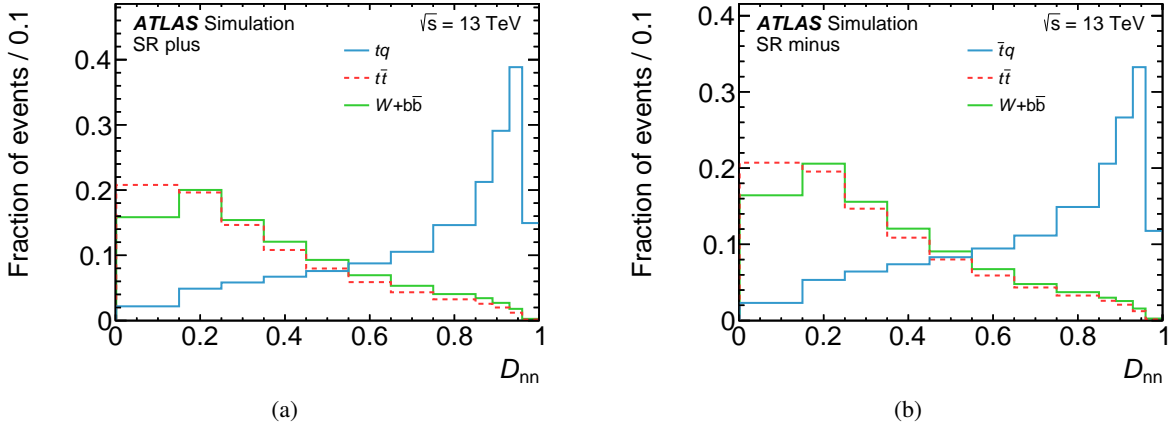


Figure 3: Probability densities of the NN discriminants for the tq and $\bar{t}q$ signal processes, and the $t\bar{t}$ and $W+b\bar{b}$ backgrounds in (a) SR plus and (b) SR minus.

function NeuroBayes uses the symmetric sigmoid function

$$S(x) = \frac{2}{1 + e^{-x}} - 1,$$

which maps the interval $(-\infty, +\infty)$ to the interval $(-1, +1)$. In the region close to zero, the sigmoid function has a linear response. The final discriminant D_{nn} is obtained by linearly scaling the output of the NN to the interval $(0, 1)$.

The probability densities of D_{nn} for the two SRs are shown in Figure 3 for the tq signal process and the main backgrounds, namely the $t\bar{t}$ and $W+b\bar{b}$ processes. Prior to the application of the NN to the observed collision data in the SRs, the modelling of the input variables is checked. For this purpose, a preliminary estimate of the rate of the multijet background is obtained by fitting the full E_T^{miss} distribution for electron events and fitting the $\Delta\phi(E_T^{\text{miss}}, \ell)$ distributions in CR μ -plus and CR μ -minus. Since the resulting estimate of the multijet background is only a preliminary step towards the final results, this fit is performed without using uncertainties other than the statistical data uncertainty and the MC statistical uncertainties. In the validation plots, the rates of all other processes including the signal process are set to their predicted values. The distributions of the eight most discriminating variables before performing the final maximum-likelihood fit (pre-fit) are shown in Figures 4 and 5 for SR plus. In all cases, the model describes the observed distributions within the estimated uncertainties. The pre-fit D_{nn} distributions are shown in Figure 6 for SR plus and SR minus.

6 Systematic uncertainties

Several sources of systematic uncertainty affect the expected event yield from signal and background processes, and the shape of the NN discriminants used in the maximum-likelihood fits. The systematic uncertainties are divided into two major categories. Experimental uncertainties are associated with the reconstruction of the four-momenta of final-state objects: electrons, muons, untagged jets, b -tagged jets, and E_T^{miss} . The second category of uncertainties is related to the modelling of scattering processes. All uncertainties are propagated through the analysis and their effects on the expected event yields and

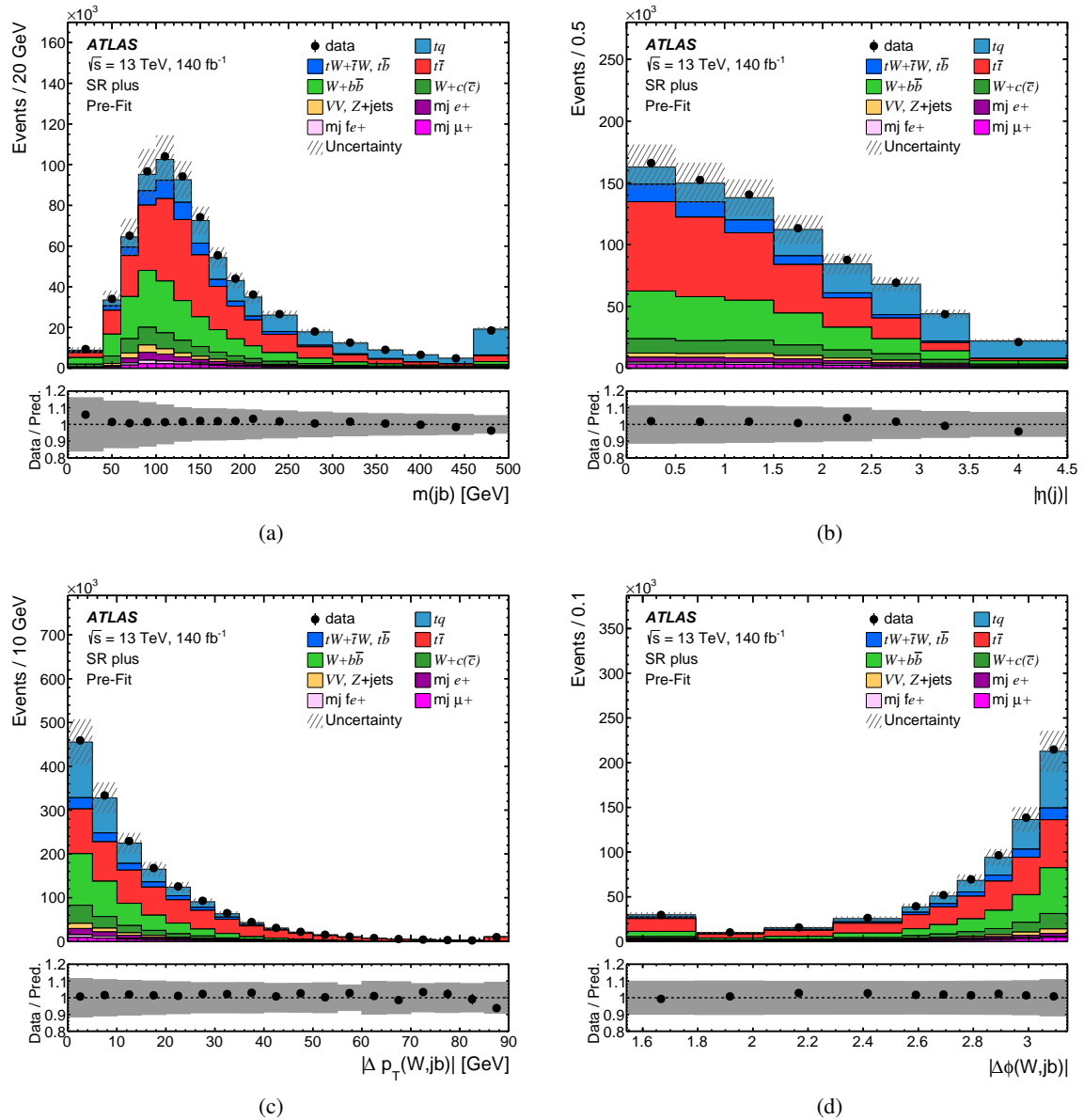


Figure 4: Pre-fit distributions of the four most discriminating input variables to the NN in SR plus: (a) the invariant mass $m(jb)$ of the untagged jet and the b -tagged jet, (b) the absolute value of the pseudorapidity of the untagged jet $|\eta(j)|$, (c) the absolute value of the difference in p_T between the reconstructed W boson and the jet pair, and (d) the difference in azimuth angle between the reconstructed W boson and the jet pair $|\Delta\phi(W, jb)|$. The observed distributions (dots) are compared with the expected distributions (histograms) from simulated events. In these distributions, the signal contribution is shown stacked on top of contributions from all considered background processes. All uncertainties considered in the analysis are included in the hatched uncertainty band. Events beyond the x -axis range are included in the last bin; the same applies to the first bin of the $|\Delta\phi(W, jb)|$ distribution in (d). The lower panel shows the ratio of data and the prediction; in this panel, the uncertainty is displayed as a grey band.

discriminant distributions are accounted for by including corresponding nuisance parameters in the fit. In the following, the estimation of experimental and modelling uncertainties is explained in more detail.

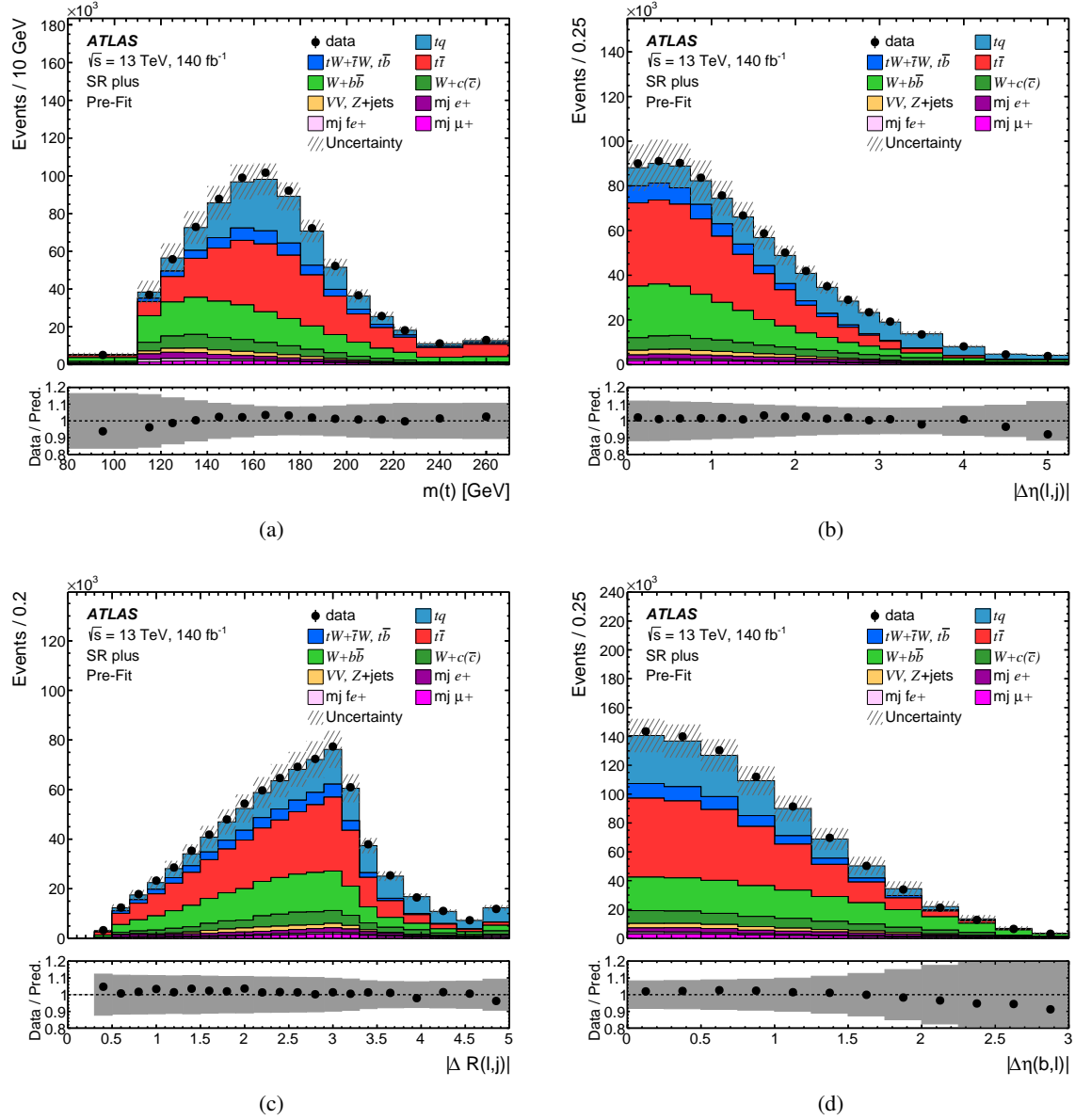


Figure 5: Pre-fit distributions of the four next most discriminating input variables to the NN in SR plus: (a) the invariant mass of the reconstructed top quark $m(t)$, (b) the absolute value of the difference in pseudorapidity between the charged lepton and the untagged jet $|\Delta\eta(\ell, j)|$, (c) the angular distance of the charged lepton and the untagged jet $\Delta R(\ell, j)$, and (d) the absolute value of the difference in pseudorapidity between the b -tagged jet and the charged lepton $|\Delta\eta(b, \ell)|$. The observed distributions (dots) are compared with the expected distributions (histograms) from simulated events. In these distributions, the signal contribution is shown stacked on top of contributions from all considered background processes. All uncertainties considered in the analysis are included in the hatched uncertainty band. Events beyond the x -axis range are included in the last bin. The lower panel shows the ratio of data and the prediction; in this panel, the uncertainty is displayed as a grey band.

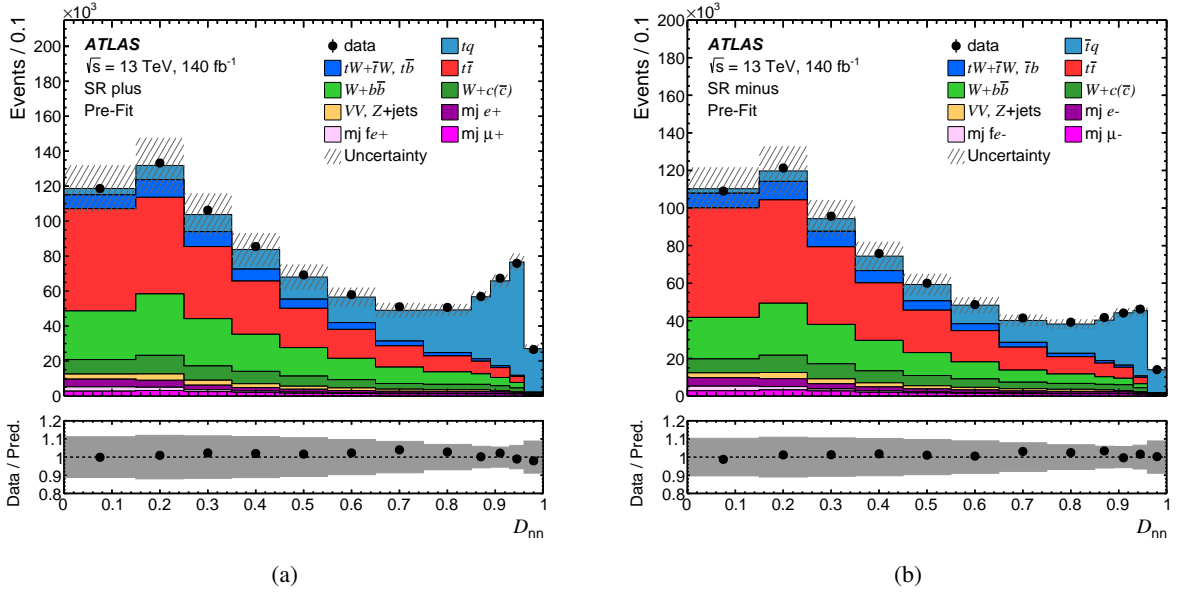


Figure 6: Pre-fit distributions of the D_{nn} in (a) SR plus and (b) SR minus. The observed distributions (dots) are compared with the expected distributions (histograms) from simulated events. In these distributions, the signal contribution is shown stacked on top of contributions from all considered background processes. All uncertainties considered in the analysis are included in the hatched uncertainty band. The lower panel shows the ratio of data and the prediction; in this panel, the uncertainty is displayed as a grey band.

6.1 Experimental uncertainties

The uncertainty in the integrated luminosity of the combined 2015–2018 data set is 0.83% and is based on a calibration of the luminosity scale using x – y beam-separation scans [18]. The luminosity uncertainty is applied to the expected signal and background event yields except for the multijet background, which is estimated in a data-driven way.

Scale factors are applied to simulated events to correct for reconstruction, identification, isolation and trigger performance differences between data and detector simulation for electrons and muons. These scale factors and their systematic uncertainties, as well as the lepton momentum scale and resolution, were assessed using $Z \rightarrow e^+e^-$ and $Z \rightarrow \mu^+\mu^-$ events in simulation and data [64, 65, 79, 80]. The probability of charge misidentification of reconstructed electrons is estimated from simulated events to be 1.9×10^{-3} . The net effect is a migration of events at the level of 6×10^{-4} from the SR plus to the SR minus (see Table 6). An uncertainty of 100% on this rate is applied in the maximum-likelihood fits and is taken to be anticorrelated between the tq and the $\bar{t}q$ processes.

The jet energy scale (JES) was calibrated using a combination of test-beam data, simulation and in situ techniques [5]. The JES is parameterised in bins of jet p_T and η . Its uncertainty is decomposed into a set of 30 uncorrelated components, of which 29 are non-zero in a given event depending on the type of simulation used. Sources of uncertainty contributing to the JES uncertainties computed using the detector position η_{det} include the η intercalibration of forward jets within $0.8 < |\eta_{\text{det}}| < 4.5$ with those in the central barrel region ($|\eta_{\text{det}}| < 0.8$), pile-up modelling, jet flavour composition and response, differences between jets induced by b -quarks and those from gluons or light-quarks, single-particle response, detector modelling, non-closure, and effects of jets not fully contained within the calorimeter.

The uncertainty of the jet energy resolution (JER) is evaluated by smearing jet energies according to a Gaussian function with width σ_{smear} [5]. Thirteen orthogonal components account for jet p_T - and η -dependent differences between simulation and data that were determined using dijet events and noise measurements based on random cones. The smearing is applied to simulated events, used to build the fit model, if the resolution in data is larger than in MC simulation, and to pseudo-data, obtained from simulated events, when the resolution is larger in simulation than in collision data. The JER uncertainties are defined by combining both variations and thereby taking the anticorrelation between different components into account. The nominal data remain unchanged. The uncertainty in the efficiency to satisfy the JVT requirement for pile-up suppression was derived in $Z(\rightarrow \mu^+ \mu^-)$ +jets events and is also considered [70]. The uncertainty in E_T^{miss} due to a possible miscalibration of its soft-track component was derived from data–simulation comparisons of the p_T balance between the hard and soft E_T^{miss} components [72].

The b -tagging requirement made in the measurement requires the consideration of uncertainties in the b -tagging efficiency of true b -jets and in the mistagging rates of light-quark jets and c -jets. The b -tagging efficiency is measured in dileptonic $t\bar{t}$ events. Differences between data and detector simulation are corrected by p_T -dependent scale factors applied to simulated events. The uncertainty in the scale factors is decomposed into 45 orthogonal components [81]. The uncertainties depend on the p_T of the b -jets and are propagated through the analysis as weights. The rate of mistagging c -jets as b -jets was measured in semileptonic $t\bar{t}$ events, where one of the W bosons decays into an electron or a muon and a neutrino and the other decays into a quark–antiquark pair [82]. This event sample allows the measurement to utilise the relatively large and known $W \rightarrow cs$ branching ratio. The mistagging rate of c -jets depends on the jet p_T and has a total uncertainty in the range of 3%-17%. The uncertainties are decomposed into 20 orthogonal components. The misidentification rate of light-quark jets was evaluated based on the techniques described in Ref. [83]. The resulting calibration factors are in the range of about 1.5 to 3 with uncertainties up to 50%. The uncertainties are decomposed into 20 independent eigenvectors.

6.2 Modelling uncertainties

Uncertainties in the theoretical cross-sections are evaluated for the top-quark background processes ($t\bar{t}$, tW and $t\bar{b}$) as quoted in Section 3.1. Due to the tight b -tagging requirement the largest contribution to the W +jets background comes from $W+b\bar{b}$ production in which the b -quarks are produced via gluon splitting ($g \rightarrow b\bar{b}$). An uncertainty of $\pm 40\%$ is assigned to the expected rate of this process, covering differences seen in previous measurements [84] between the SHERPA prediction and ATLAS collision data. The contribution of the associated production of a W boson and light-quark jets to the expected event yield is much smaller and therefore this contribution is merged with the $W+b\bar{b}$ process in the statistical analysis. The same uncertainty of $\pm 40\%$ is assigned to it. Events in which a W boson is produced in association with c -jets are mainly due to the $sg \rightarrow W^- c$ and $\bar{s}g \rightarrow W^+ \bar{c}$ scattering processes. An uncertainty of $\pm 20\%$ is assigned to the rate of $W+c$ -jets production. The same uncertainty is applied to the rate of the combined process of Z +jets and diboson production. The fit result and its uncertainty depend only marginally on the specific assignment of the uncertainties ($\pm 40\%$ and $\pm 20\%$, respectively) in the $W+b\bar{b}$, Z +jets, and diboson cross-sections. In the maximum-likelihood fit, separate nuisance parameters are used for the cross-section uncertainties of $W+b\bar{b}$ production and $W+c$ -jets production in the regions with positive and negative charge.

Uncertainties in modelling parton showers and hadronisation are assigned to the tq signal and the top-quark background processes ($t\bar{t}$, tW and $t\bar{b}$ production) by comparing the nominal samples with alternative samples for which POWHEG Box v2 was interfaced to HERWIG 7.2.1 [85, 86] (for $t\bar{t}$ production) or HERWIG 7.1.6 (for

tq , tW and $t\bar{b}$ production) instead of PYTHIA 8.230. The uncertainties are considered to be uncorrelated for the different scattering processes, namely the tq signal process and the three top-quark background processes. In the statistical analysis, normalisation and shape effects are decorrelated as well.

Uncertainties related to the choice of μ_r and μ_f for the matrix-element calculations are evaluated by varying the scales independently by factors of 2 and 0.5, separately for each of the top-quark production processes and for W +jets production. The scale variations are implemented as generator weights in the nominal sample. These weights are propagated through the entire analysis.

The uncertainty in matching the NLO matrix elements to the parton shower when generating $t\bar{t}$ and tq events is evaluated by comparing the nominal samples of simulated events to samples with an alternative setting of the p_T^{hard} parameter in the matching code, using 1 instead of the default setting of 0. This parameter regulates the definition of the vetoed region of the parton shower, important to avoid overlap in the phase space filled by POWHEG and PYTHIA. This estimate of the uncertainty follows the description in Ref. [87]. The uncertainty in the choice of the h_{damp} parameter for the $t\bar{t}$ event generation is estimated by using an additional $t\bar{t}$ sample produced with the h_{damp} parameter set to $3 \times m_t$, while keeping all other generator settings the same as for the nominal sample of events.

Uncertainties in the amount of initial-state and final-state radiation are assessed for the top-quark production processes by varying the parameter Var3c of the A14 parton-shower tune within the uncertainties of the tune and, for final-state radiation, by varying the renormalisation scale μ_r , at which the strong coupling constant α_s is evaluated, by factors of 0.5 and 2.0. The two variations are handled independently. The uncertainty due to the scheme for removing the overlap of the tW process with $t\bar{t}$ production is evaluated by comparing the nominal sample, using the diagram-removal scheme, with a sample produced with an alternative scheme (diagram subtraction) [39].

In all uncertainty evaluations mentioned above the alternative samples or reweighted samples are normalised to the total cross-section of the nominal samples.

Uncertainties in the PDFs are evaluated for the top-quark production processes using the PDF4LHC15 prescription with 30 eigenvectors [88]. Simulated events are reweighted to the central value and the eigenvectors of the combined PDF set. Systematically varied templates are constructed by taking the differences between the samples reweighted to the central value and those reweighted to the eigenvectors. In the likelihood fit, the PDF uncertainties are treated as correlated across the top-quark production processes.

The uncertainty in the multijet background is evaluated by modifying the selection criteria for jet-electron and non-prompt-muon candidates. Two alternative selections of jet-electron candidates are defined by varying the requirement on the energy fraction measured in the electromagnetic calorimeter, leading to two alternative shapes of the D_{nn} distributions for the multijet background in the SRs. In the statistical analysis, these shapes are used as “up” and “down” variations of a single nuisance parameter. For non-prompt-muon candidates a single variation is defined by varying the isolation criteria.

To account for differences in the pile-up distribution between simulation and data, the pile-up profile in the simulation is corrected to match the one in data. The uncertainty associated with the correction factor is applied in the measurement as a variation of the event weight.

The uncertainties due to the finite number of simulated events, also called the MC statistical uncertainty, is accounted for by adding a nuisance parameter for each bin of the D_{nn} distributions and the distributions in the CRs, implementing the Barlow–Beeston approach [89].

7 Measurement results

The cross-sections $\sigma(tq)$ and $\sigma(\bar{t}q)$ are determined in a simultaneous binned profile maximum-likelihood fit. To properly account for the correlations of systematic uncertainties when forming the sum and the ratio of $\sigma(tq)$ and $\sigma(\bar{t}q)$, $\sigma(tq + \bar{t}q)$ and R_t are measured in a second fit in which the parameterisation of the signal strength parameters is modified accordingly, while all other parameters of the fit setup are kept the same. The fitted distributions are the D_{nn} distributions in SR plus and SR minus, the $\Delta\phi(E_T^{\text{miss}}, \ell)$ distributions in the CR μ -plus and the CR μ -minus, and the event yields in the CR B-e-plus, the CR B-e-minus, the CR EC-e-plus and the CR EC-e-minus. In both fits, the event yields of the multijet background are left floating, while the yields of all other backgrounds are constrained to their predictions within the associated uncertainties.

The likelihood function is constructed as a product of Poisson probability terms over all considered bins. The fitted event yields in the bins depend on nuisance parameters that include the effects of systematic uncertainties. Each nuisance parameter, except those representing the MC statistical uncertainties, is constrained by a Gaussian term in the likelihood function. Some systematically varied discriminant distributions are smoothed and nuisance parameters of systematic uncertainties with negligible impact are entirely removed to reduce spurious effects in the minimisation, improve the convergence of the fit, and reduce the computing time. Normalisation and shape effects of a source of systematic uncertainty are treated separately in this removal process. Single-sided systematic variations are turned into symmetric variations by taking the full difference in event yield and shape between the nominal model and the alternative model and mirroring this difference in the opposite direction. For most sources with two variations, their effects are made symmetric by using the average deviation from the nominal prediction. Exceptions are the uncertainties in the JER and in the jet-electron model, for which the asymmetric variations are kept because the underlying effects are known to be asymmetric. No significant pulls of nuisance parameters are observed.

The total cross-sections for tq and $\bar{t}q$ production are measured to be

$$\sigma(tq) = 137^{+8}_{-8} \text{ pb} \quad \text{and} \quad \sigma(\bar{t}q) = 84^{+6}_{-5} \text{ pb}.$$

The NNLO predictions for these cross-sections (see Section 3.1) agree very well with the measurements. The relative precision reached is +5.9% and -5.5% for $\sigma(tq)$ and +6.6% and -6.2% for $\sigma(\bar{t}q)$. The fits to the observed data for the combined tq and $\bar{t}q$ cross-section and R_t give the following results:

$$\sigma(tq + \bar{t}q) = 221^{+13}_{-13} \text{ pb} \quad \text{and} \quad R_t = 1.636^{+0.036}_{-0.034}$$

with a relative precision of +6.1% and -5.7% for the combined cross-section and +2.2% and -2.1% for R_t . The global goodness of fit is evaluated with the saturated model [74] yielding a p -value of 76%. Table 3 provides a breakdown of the uncertainties categorised in groups according to different sources. The impact of a particular group of uncertainties is evaluated by performing an alternative likelihood fit in which the nuisance parameters related to the sources of uncertainty under investigation are fixed to their best-fit values as obtained from the nominal fit. The squared impact of the considered group of uncertainties is determined as the difference between the square of the nominal total uncertainty and the square of the uncertainty obtained from the alternative fit. For the measured cross-sections, the uncertainties in the signal modelling are the dominating ones, while they largely cancel out for the measurement of R_t . The data statistical uncertainty is very small compared with the systematic uncertainties. Since many uncertainties largely cancel out when forming the ratio, the uncertainty in R_t is much reduced compared with the uncertainties in the cross-sections.

Uncertainty group	$\Delta\sigma(tq)/\sigma(tq)$	$\Delta\sigma(\bar{t}q)/\sigma(\bar{t}q)$	$\Delta\sigma(tq + \bar{t}q)/\sigma(tq + \bar{t}q)$	$\Delta R_t/R_t$
Data statistics	+0.4 / -0.4	+0.5 / -0.5	+0.3 / -0.3	+0.6 / -0.6
Signal modelling	+4.9 / -4.5	+5.2 / -4.8	+5.0 / -4.6	+0.9 / -0.9
Background modelling	+1.8 / -1.6	+2.1 / -1.9	+1.8 / -1.6	+1.5 / -1.4
MC statistics	+1.0 / -1.0	+1.4 / -1.3	+1.1 / -1.0	+0.8 / -0.8
PDFs	+0.4 / -0.4	+1.2 / -1.0	+0.6 / -0.6	+0.9 / -0.8
Jets	+2.2 / -2.0	+3.0 / -2.7	+2.5 / -2.2	+1.0 / -0.9
<i>b</i> -tagging	+1.6 / -1.5	+1.7 / -1.5	+1.6 / -1.5	+0.2 / -0.1
Leptons	+1.1 / -1.0	+1.1 / -1.0	+1.1 / -1.0	+0.1 / -0.1
Luminosity	+0.9 / -0.8	+0.9 / -0.9	+0.9 / -0.8	< 0.1
Total	+5.9 / -5.5	+6.6 / -6.2	+6.1 / -5.7	+2.2 / -2.1

Table 3: The impact of different groups of systematic uncertainties on $\sigma(tq)$, $\sigma(\bar{t}q)$, $\sigma(tq + \bar{t}q)$ and R_t given in %.

Systematic uncertainty	$\Delta\sigma(tq)/\sigma(tq)$	$\Delta\sigma(\bar{t}q)/\sigma(\bar{t}q)$	$\Delta\sigma(tq + \bar{t}q)/\sigma(tq + \bar{t}q)$
<i>tq</i> matching scale definition, rate	-2.9 / +3.1	-2.6 / +2.8	-2.8 / +2.9
<i>tq</i> parton shower, rate	+2.6 / -2.5	+3.3 / -3.2	+2.9 / -2.8
<i>tq</i> final-state radiation	-2.0 / +2.1	-2.1 / +2.2	-2.0 / +2.1
<i>tq</i> matching scale definition, shape	-1.5 / +1.6	-1.2 / +1.2	-1.4 / +1.5
JES η intercalibration modelling	-1.2 / +1.2	-1.5 / +1.6	-1.3 / +1.4
<i>b</i> -tagging NP B1	+1.0 / -0.9	+1.0 / -1.0	+1.0 / -0.9
<i>b</i> -tagging NP B0	+1.0 / -0.9	+1.0 / -1.0	+1.0 / -0.9
Luminosity	-0.8 / +0.9	-0.9 / +0.9	-0.8 / +0.9

Table 4: The impact of the eight most important systematic uncertainties on $\sigma(tq)$, $\sigma(\bar{t}q)$ and $\sigma(tq + \bar{t}q)$ given in %. The sequence of the uncertainties is given by the impact on $\sigma(tq + \bar{t}q)$.

The eight single most important systematic uncertainties in the cross-section measurements are listed in Table 4. The four most important systematic uncertainties are due to the modelling of the *tq* process with an event generator. The single largest uncertainty is the rate effect due to the definition of the matching

Systematic uncertainty	$\Delta R_t / R_t$
$W^- + c(\bar{c})$ cross-section	+0.82 / -0.79
tq parton shower, rate	-0.68 / +0.65
$W^+ + c(\bar{c})$ cross-section	-0.47 / +0.46
PDF eigenvector 09	-0.45 / +0.46
MC statistical uncertainty in D_{nn} bin 10 of SR minus	+0.41 / -0.40
JES η intercalibration modelling	+0.36 / -0.38
tq matching scale definition, shape	-0.36 / +0.38
PDF eigenvector 05	+0.37 / -0.36

Table 5: The impact of the eight most important systematic uncertainties on R_t in %.

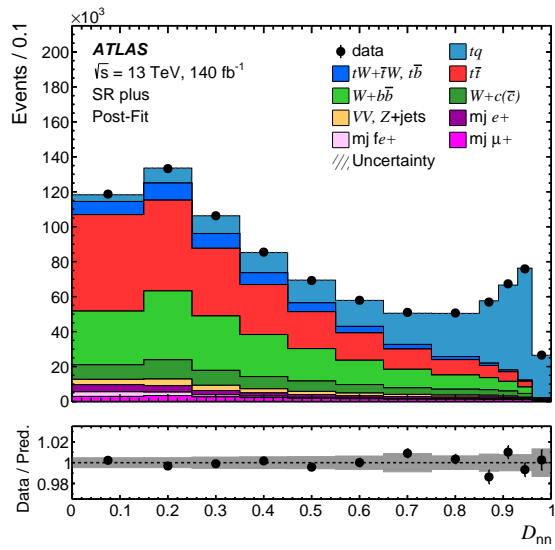
scale of the tq process. The eight most important systematic uncertainties in the R_t measurement are listed in Table 5. As a cross-check, the selected sample of events was split according to the lepton flavour into an electron and a muon sample and the measurements were repeated, leading to results compatible with the nominal analysis.

The D_{nn} distributions after performing the fit are shown for both of the SRs in Figure 7. The correlations induced by the maximum-likelihood fit are taken into account and lead to a large reduction in the size of the uncertainty band. The post-fit event yields of the different processes are provided in Table 6.

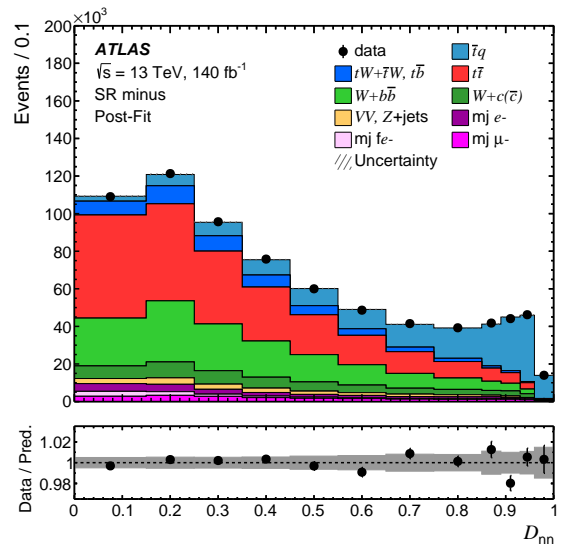
Dependence on m_t The cross-sections and the ratio R_t are determined at a fixed value of $m_t = 172.5$ GeV. The mass dependence of the measurements is determined by repeating the measurement with samples of simulated events produced with different values of m_t , namely $m_t = 171$ GeV and $m_t = 174$ GeV. The dependence of the resulting cross-sections on m_t is fitted with a first-order polynomial, for which the constant term is given by the central value at $m_t = 172.5$ GeV, namely

$$\sigma(m_t) = \sigma(172.5 \text{ GeV}) + a \cdot \Delta m_t [\text{GeV}],$$

where $\Delta m_t = m_t - 172.5$ GeV. The slopes are fitted to be $a = (-1.50 \pm 0.26)$ pb GeV⁻¹ for $\sigma(tq)$, $a = (-0.85 \pm 0.31)$ pb GeV⁻¹ for $\sigma(\bar{t}q)$, and $a = (-2.35 \pm 0.69)$ pb GeV⁻¹ for $\sigma(tq + \bar{t}q)$. For R_t the effect is found to be negligible.



(a)



(b)

Figure 7: The observed D_{nn} distributions (dots) for (a) SR plus and (b) SR minus are compared with the expected distributions (histograms) from simulated events after the fit (post-fit). In these distributions, the signal contribution is shown stacked on top of contributions from all contributing background processes. All uncertainties considered in the analysis are included in the hatched uncertainty band. The correlations induced by the fit are taken into account. The lower panel shows the ratio of data and the prediction; in this panel, the uncertainty is displayed as a grey band.

Process	SR plus	SR minus
tq	$169\,000 \pm 6\,000$	150 ± 150
$\bar{t}q$	90 ± 90	$109\,000 \pm 4\,000$
$tW + \bar{t}W, t\bar{b} + \bar{t}b$	$51\,000 \pm 4\,000$	$49\,000 \pm 4\,000$
$t\bar{t}$	$265\,000 \pm 14\,000$	$265\,000 \pm 14\,000$
$W+b\bar{b}$	$198\,000 \pm 21\,000$	$159\,000 \pm 17\,000$
$W+c(\bar{c})$	$60\,000 \pm 13\,000$	$49\,000 \pm 11\,000$
Z+jets, diboson	$21\,000 \pm 4\,000$	$19\,000 \pm 4\,000$
Multijet	$50\,000 \pm 10\,000$	$50\,000 \pm 10\,000$
Total	$814\,000 \pm 2\,100$	$698\,800 \pm 2\,000$
Observed	814 185	698 845

Table 6: The post-fit event yields in the two SRs. All uncertainties applied in the analysis are included. Correlations, including anticorrelations, among the nuisance parameters related to the uncertainties are taken into account as determined in the maximum-likelihood fit, leading to a reduction in the size of the uncertainties, in particular for the total prediction. The event yields of the different processes as quoted in the table do not add up to the total sum given because of rounding effects.

8 Interpretation of the measurements

The measurements of the tq production cross-sections presented in Section 7 are interpreted in different ways. Predictions based on different PDF sets are compared with the measured R_t value in Section 8.1. A search for a contribution of a four-quark EFT operator to tq production using the D_{nn} distributions in the SRs is presented in Section 8.2. The result of this search yields a confidence interval for the EFT coefficient $C_{Qq}^{3,1}/\Lambda^2$. In addition, the measurement of $\sigma(tq + \bar{t}q)$ is used to derive limits on the EFT coefficient $C_{\phi Q}^3/\Lambda^2$. The corresponding operator $O_{\phi Q}^3$ has the same Lorentz structure as the Wtb vertex in the SM, and thus simply scales the cross-section of tq production, while kinematic distributions are not altered by its presence. The CKM matrix element V_{tb} is extracted from the measurement of $\sigma(tq + \bar{t}q)$ (see Section 8.3). In a more general approach, confidence contours are determined in the $f_{LV}|V_{td}|$ -versus- $f_{LV}|V_{tb}|$, the $f_{LV}|V_{ts}|$ -versus- $f_{LV}|V_{tb}|$, and the $f_{LV}|V_{ts}|$ -versus- $f_{LV}|V_{td}|$ planes; the results are presented in Section 8.4.

8.1 Sensitivity of R_t to PDF sets

With an uncertainty of $+2.2\%$ / -2.1% , the measurement of R_t can potentially distinguish between different PDF sets. Predictions of R_t made with different PDF sets at NNLO, namely ABMP [90], ATLAS [91], CTEQ [92], MSHT [93], NNPDF [36, 94], and PDF4LHC [45], are compared with the measured value in Figure 8. The calculations were performed with the MCFM 10.1 program [44]. The differences between the R_t predictions are driven by differences between the u - and d -quark PDFs. The PDFs provided by the different groups differ in the data used, the value of α_s assumed, the values of quark masses used, and the treatment of heavy quarks. The scale uncertainties for the theoretical predictions are included in Figure 8. The scale uncertainties are determined by varying μ_r and μ_f independently up and down by a factor of two, whilst never allowing them to differ by a factor greater than two from each other. The scale uncertainty is defined as the envelope of the six resulting variations. The uncertainties in the predictions also include the uncertainties provided by the PDF set under investigation and, where possible, uncertainties in α_s .²

The prediction of ABMP is incompatible with the measurement of R_t at the level of approximately three standard deviations. All other predictions are in agreement with the measured value within the experimental and theoretical uncertainties. The predictions of ATLASpdf21 and NNPDF3.0 are the closest to the central value of the measurement; all other predictions are approximately one standard deviation above. The slightly higher uncertainty of the ATLASpdf21 prediction compared with those predictions based on other ATLAS PDF sets is attributed to the usage of a wider range of input data samples and, associated to that, a modified uncertainty definition.

8.2 EFT interpretation

The Standard Model Effective Field Theory (SMEFT) provides a model-independent framework for indirect searches for new physics. Within this framework, the SM is regarded as a low-energy approximation of a more fundamental theory involving interactions at an energy scale Λ . The impact of new physics is

² There is no functionality implemented to vary α_s for ATLAS (epWZ16). For MSHT the strong coupling constant is varied simultaneously with the PDF eigenvectors rather than independently.

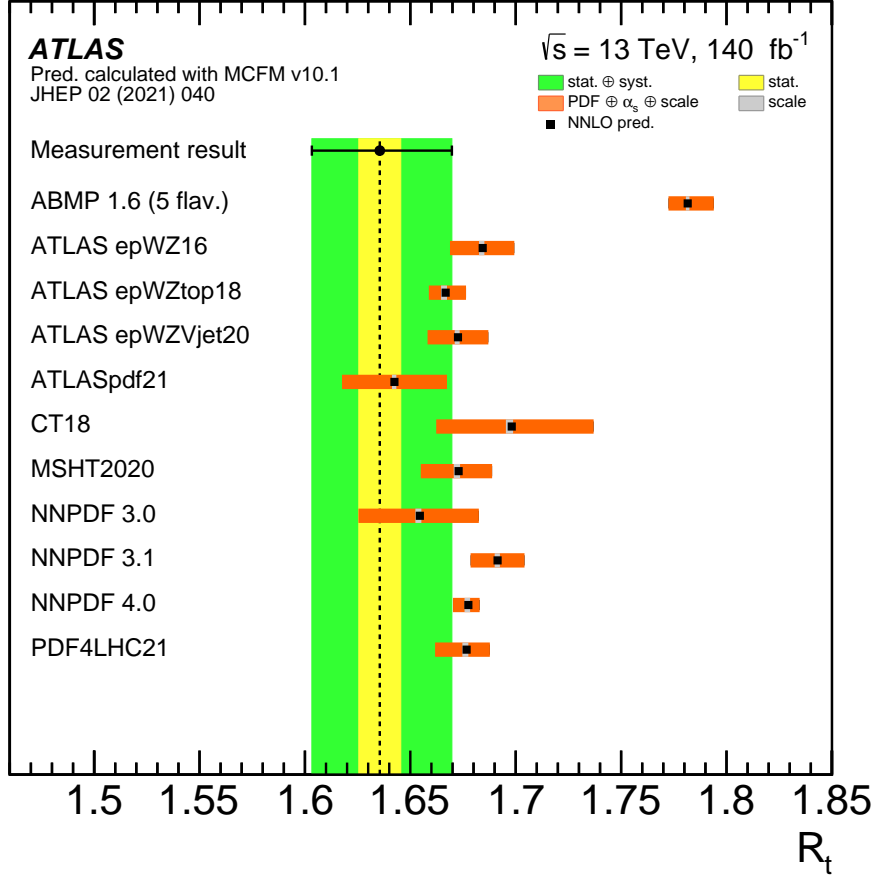


Figure 8: The measured value of R_t (dot). The yellow band represents the statistical uncertainty and the green band represents the total uncertainty of the measurement. For comparison, the NNLO predictions of MCFM based on different PDF sets are included: ABMP [90], ATLAS [91], CTEQ [92], MSHT [93], NNPDF [36, 94], and PDF4LHC [45]. The uncertainties in the theoretical predictions include PDF, scale and α_s uncertainties.

parameterised by higher-dimensional operators maintaining SM symmetries. The effective Lagrangian is given by

$$\mathcal{L}_{\text{eff}} = \mathcal{L}_{\text{SM}} + \sum_i \frac{C_i}{\Lambda^2} O_i + \text{Hermitian conjugate},$$

where \mathcal{L}_{SM} is the SM Lagrangian. The O_i are effective dimension-6 operators and the C_i are the associated Wilson coefficients. In this EFT interpretation, two operators are considered, the four-quark operator $O_{qq}^{3,1}$ and the operator $O_{\phi Q}^3$ coupling the third quark generation to the Higgs boson doublet Φ .

The relevant operators, expressed in the Warsaw basis, are

$$\begin{aligned} O_{qq}^{1(ijkl)} &= (\bar{q}_i \gamma^\mu q_j)(\bar{q}_k \gamma_\mu q_l), \\ O_{qq}^{3(ijkl)} &= (\bar{q}_i \gamma^\mu \tau^I q_j)(\bar{q}_k \gamma_\mu \tau^I q_l) \quad \text{and} \\ O_{\phi Q}^3 &= i(\Phi^\dagger \tau^I D_\mu \Phi)(\bar{Q} \gamma^\mu \tau^I Q). \end{aligned}$$

The q denote weak-isospin doublets with $ijkl \in 1, 2, 3$ as quark generation indices, while Q represents the doublet of the third quark generation. All contributing four-quark processes depend solely on a linear

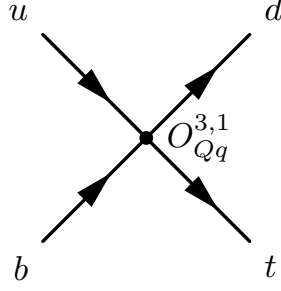


Figure 9: Representative LO Feynman diagram of a four-quark contact interaction leading to the production of a single top quark.

combination of Wilson coefficients

$$C_{Qq}^{3,1} = \sum_{i=1,2} C_{qq}^{3(ii33)} + \frac{1}{6} C_{qq}^{1(i33i)} - \frac{1}{6} C_{qq}^{3(i33i)},$$

therefore the four-quark interaction is fully characterised by $O_{Qq}^{3,1}$ [95].

The operator $O_{Qq}^{3,1}$ leads to non-SM single top-quark production, as illustrated in Figure 9, for example via the process $b + u \rightarrow t + d$. Top quarks produced in this way feature different angular distributions and kinematics than those produced via SM processes. A non-zero contribution from the operator $O_{\phi Q}^3$ does not alter the Lorentz structure of the Wtb vertex, it merely leads to a rescaling of the vertex strength, and thus changes the total cross-section, but it does not alter the shape of any kinematic distributions.

Events with single top quarks produced via SM vertices (tq and $t\bar{b}$ production) and via $O_{Qq}^{3,1}$ vertices were generated with MADGRAPH, as detailed in Section 3.4. These samples are subjected to the regular analysis chain, including the event selection and the processing of the NN analysis. Using the five different EFT samples, the single top-quark event yield ν_j in each bin j of the D_{nn} distributions in SR plus and SR minus is parameterised by a polynomial of second degree in the EFT coefficient $C_{Qq}^{3,1}$.

$$\nu_j = \nu_{0j} + a_{1j} \frac{C_{Qq}^{3,1}}{\Lambda^2} + a_{2j} \frac{(C_{Qq}^{3,1})^2}{\Lambda^4}.$$

The constant term ν_{0j} represents tq and $t\bar{b}$ production in the SM and is normalised to the SM cross-section predictions of both the processes, as reported in Section 3.1. The term linear in $C_{Qq}^{3,1}$ represents the effect of the interference of SM and non-SM amplitudes and the term proportional to $(C_{Qq}^{3,1})^2$ is entirely due to the four-quark operator. Based on a maximum-likelihood scan of the parameter $C_{Qq}^{3,1}/\Lambda^2$ the 95% CL interval is determined to be

$$-0.37 < C_{Qq}^{3,1}/\Lambda^2 < 0.06.$$

All SM processes are modelled in the same way as in the cross-section measurements presented in Section 7. The same systematic uncertainties are applied. The constraints presented improve the limits set by the ATLAS measurement of the charge asymmetry in $t\bar{t}$ production [96], which obtained a confidence interval of $[-0.70, 0.75]$. The interpretation of cross-section measurements of $t\bar{t}Z$ production by ATLAS [97] reaches the constraints $[-0.34, 0.23]$, similar to the ones presented above. Limits on the parameter $C_{Qq}^{3,1}/\Lambda^2$ were also set by global EFT fits that include inputs from measurements by the ATLAS and CMS

Collaborations. The results in Ref. [7] are based on various measurements of Higgs boson, diboson and top-quark production processes and lead to a confidence interval for $C_{Qq}^{3,1}/\Lambda^2$ of $[-0.088, 0.166]$ at the 95% CL when including terms of order Λ^{-4} . A similar approach by a different group of analysers [8] leads to a confidence interval of $[-0.043, 0.16]$. Using only top-quark measurements for the analysis, the authors of Ref. [9] obtain $C_{Qq}^{3,1}/\Lambda^2 \in [-0.39, 0.11]$. The comparison to these results of global EFT analyses demonstrates that the limits on $C_{Qq}^{3,1}/\Lambda^2$ obtained from the tq cross-section measurements presented in this document are quite competitive. An important difference to appreciate is that the results of Refs. [7–9] do not account for reconstruction effects on EFT signal events, while the results presented here are based on simulated samples that include detector effects.

Since the EFT operator $O_{\phi Q}^3$ has the same Lorentz structure as the Wtb vertex in the SM, and kinematic distributions of tq and $\bar{t}q$ events are thus not altered by contributions from $O_{\phi Q}^3$, limits on the corresponding Wilson coefficient $C_{\phi Q}^3/\Lambda^2$ are derived from the measured cross-section $\sigma(tq + \bar{t}q)$. The cross-section $\sigma(tq + \bar{t}q)$ is calculated for different values of $C_{\phi Q}^3/\Lambda^2$ with MADGRAPH5_AMC@NLO 2.7.3 using the SMEFTatNLO-NLO model [62] with the five-flavour scheme and the NNPDF3.0_{NLO} PDF set, and is obtained as the sum of $\sigma(tq)$ and $\sigma(\bar{t}q)$. The contribution of the quadratic term in $C_{\phi Q}^3/\Lambda^2$ is negligible in the relevant parameter range, and thus a linear function is fitted to the relative change in $\sigma(tq + \bar{t}q)$ as a function of $C_{\phi Q}^3/\Lambda^2$ relative to its value at $C_{\phi Q}^3/\Lambda^2 = 0$, resulting in a slope of 0.12 ± 0.02 . Based on this parameterisation, the 95% CL interval of $C_{\phi Q}^3/\Lambda^2$ is determined to be

$$-0.87 < C_{\phi Q}^3/\Lambda^2 < 1.42.$$

These constraints improve limits obtained by the interpretation of cross-section measurements of $t\bar{t}Z$ production that yielded the confidence interval $[-0.95, 2.0]$ [97]. However, the combined interpretation of Higgs boson, diboson, and top-quark measurements yielded a stronger limit of $[-0.375, 0.344]$ [7].

8.3 Determination of $|V_{tb}|$

Single top-quark production in the t -channel proceeds primarily via a Wtb vertex and the cross-section is proportional to $f_{LV}^2 \cdot |V_{tb}|^2$. In the SM, the left-handed form factor f_{LV} is exactly one and the CKM matrix is unitary. Assuming the unitarity relations, the measured values of other CKM matrix elements suggest that $|V_{tb}|$ is very close to one. However, new-physics contributions could alter the value of f_{LV} significantly. The determination of $f_{LV} \cdot |V_{tb}|$ based on single-top-quark cross-section measurements is independent of assumptions about the number of quark generations and the unitarity of the CKM matrix. The only assumptions made are that $|V_{tb}| \gg |V_{td}|, |V_{ts}|$ and that the Wtb interaction is a left-handed weak coupling, as in the SM.

The value of $f_{LV}^2 \cdot |V_{tb}|^2$ is extracted by dividing the measured value of $\sigma(tq + \bar{t}q)$ by the SM expectation of $214.2 \pm 3.4(\text{scale} + \text{PDF}) \pm 1.8(\Delta m_t)$ pb [44]. When calculating $f_{LV}^2 \cdot |V_{tb}|^2$, the experimental and theoretical uncertainties are added in quadrature. The uncertainty in m_t is also considered, assuming $\Delta m_t = \pm 1$ GeV. The result obtained is

$$f_{LV} \cdot |V_{tb}| = 1.015 \pm 0.031,$$

improving the precision by 30% compared with the combination of Run 1 measurements by ATLAS and CMS [98]. The Particle Data Group combined all available measurements performed at the Tevatron and the LHC to 1.014 ± 0.029 [74].

Restricting the range of $|V_{tb}|$ to the interval $[0, 1]$ and setting $f_{LV} = 1$, as required by the SM, a lower limit on $|V_{tb}|$ is extracted: $|V_{tb}| > 0.95$ at the 95% CL. In the Bayesian-style limit computation, it is assumed that the likelihood curve of $|V_{tb}|^2$ is a Gaussian function, centered at the measured value. A flat prior in $|V_{tb}|^2$ is applied, being one in the interval $[0, 1]$ and zero otherwise.

8.4 Generalised CKM interpretation

The interpretation of the tq cross-section measurements presented in Section 8.3 neglects the contributions due to Wts and Wtd vertices. In a more general approach, this caveat is avoided. Nine contributions to tq production are considered, differing in the combination of Wtq vertices for top-quark production and decay with $q \in \{d, s, b\}$. In $t\bar{t}$ production, Wtq vertices occur for the top-quark and top-antiquark decays. Again, nine different combinations of vertices are considered, thus treating the most important background process at the same level of modelling as the tq signal process. Including the effect of Wts and Wtd vertices for $t\bar{t}$ production improves the sensitivity of the measurement to $|V_{ts}|$ and $|V_{td}|$ by approximately 20%. The effects of Wts and Wtd vertices on the event yields of tW and $t\bar{b}$ production are neglected, since the corresponding event yields for these processes are much smaller than the yields for tq and $t\bar{t}$ production. Three different fit scenarios are investigated. In each scenario, two V_{tq} matrix elements are considered to be free parameters, while the third parameter is fixed to be either 0 or 1:

$$\text{Scenario 1} \quad |V_{tb}| \neq 0, |V_{td}| \neq 0 \text{ and } |V_{ts}| = 0,$$

$$\text{Scenario 2} \quad |V_{tb}| \neq 0, |V_{ts}| \neq 0 \text{ and } |V_{td}| = 0,$$

$$\text{Scenario 3} \quad |V_{td}| \neq 0, |V_{ts}| \neq 0 \text{ and } |V_{tb}| = 1.$$

The form factor f_{LV} is non-zero in all scenarios. For each scenario, a maximum-likelihood scan of the two non-zero CKM matrix elements is performed. As a result, confidence contours are determined at the 95% CL in the $f_{LV}|V_{td}|$ -versus- $f_{LV}|V_{tb}|$, the $f_{LV}|V_{ts}|$ -versus- $f_{LV}|V_{tb}|$, and the $f_{LV}|V_{ts}|$ -versus- $f_{LV}|V_{td}|$ planes. These contours are shown in Figure 10. The parameter $f_{LV}|V_{tb}|$ is constrained at the 95% CL to a range between 0.95 and 1.05, and $f_{LV}|V_{td}|$ and $f_{LV}|V_{ts}|$ are constrained to be < 0.23 and < 0.58 , respectively. The constraint on $|V_{td}|$ is stronger compared with the one on $|V_{ts}|$ because the d -quark is a valence quark of the proton, while s -quarks appear as sea-quarks only. The interpretation uses the nominal simulation-to-data corrections for the efficiency of tagging b -quark jets, which was determined with $t\bar{t}$ events in the dilepton channel assuming $|V_{tb}| = 1$ and thus $\mathcal{B}(t \rightarrow Wb) = 100\%$. This assumption is increasingly violated when moving to large values of $|V_{td}|$ and $|V_{ts}|$ and thus constitutes a caveat of the generalised CKM interpretation presented here.

The CKM matrix elements $|V_{td}|$ and $|V_{ts}|$ are determined very precisely using measurements of the mass differences Δm_d and Δm_s of the mass eigenstates of B_d^0 and B_s^0 mesons [74]. However, these determinations are based on $B-\bar{B}$ meson oscillations that are induced by box diagrams with top quarks, use lattice QCD results, and neglect corrections suppressed by $|V_{tb}| - 1$, and thus introduce a certain level of model dependence that is reduced in the studies presented here for tree-level processes, namely single top-quark production and decay. In addition, the top-quark processes give access to a much higher energy scale.

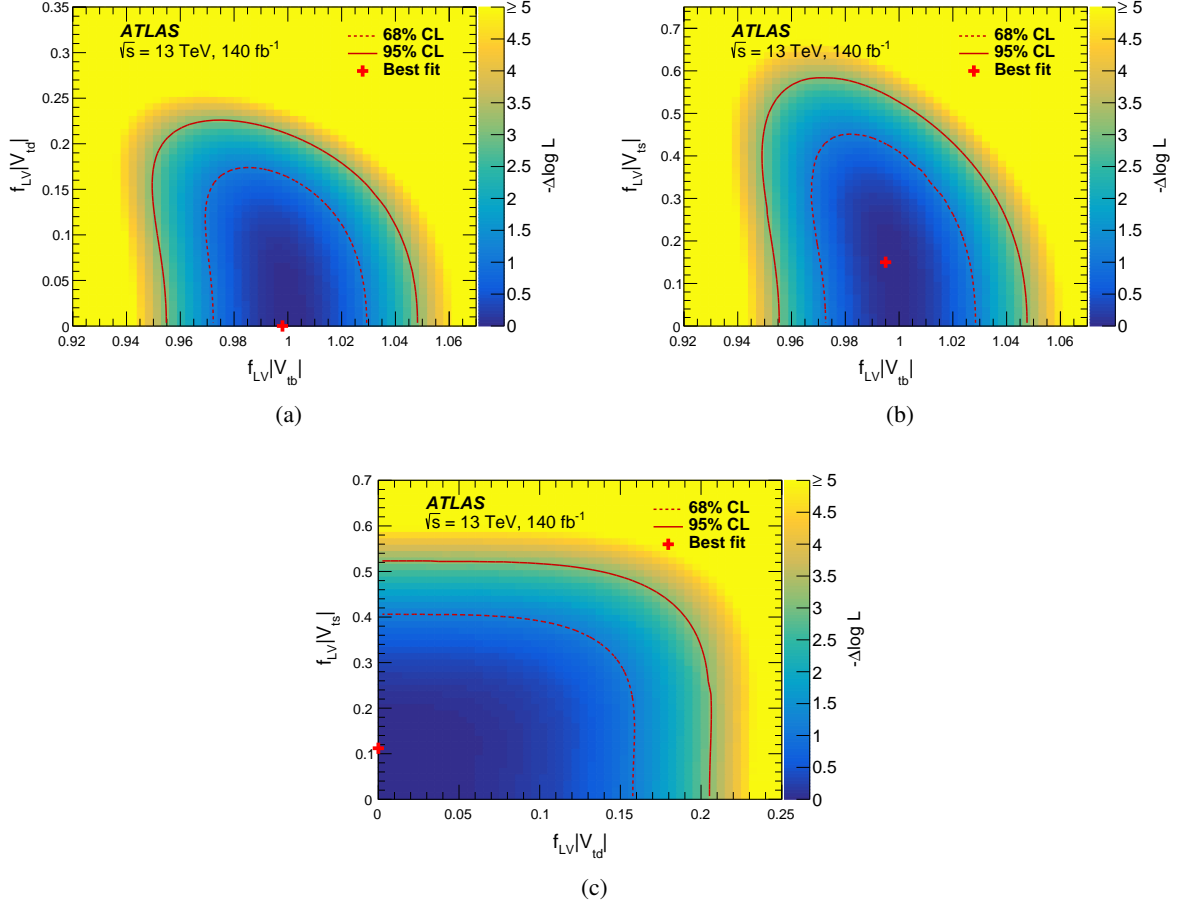


Figure 10: Confidence contours obtained from maximum-likelihood scans in (a) the $f_{LV}|V_{td}|$ -versus- $f_{LV}|V_{tb}|$ plane, (b) the $f_{LV}|V_{ts}|$ -versus- $f_{LV}|V_{tb}|$ plane, and (c) the $f_{LV}|V_{ts}|$ -versus- $f_{LV}|V_{td}|$ plane. Contours at the 68% and 95% confidence levels are shown. The two-dimensional histogram contains the values of the difference of the log-likelihood function at a certain point in the plane to the minimum of the log-likelihood function indicated by the red cross.

9 Conclusions

The production of single top quarks and top antiquarks via the t -channel exchange of a virtual W boson is measured in proton–proton collisions at the LHC at a centre-of-mass energy of 13 TeV, using the full Run 2 data sample of 140 fb^{-1} recorded with the ATLAS detector. Events are selected with either one isolated electron or muon, high E_T^{miss} , and exactly two hadronic jets with high p_T . Exactly one of these jets is required to be b -tagged. An artificial NN is used to construct a discriminant that separates signal and background events. The distributions of the discriminant are used in profile maximum-likelihood fits to determine the signal yields.

The total cross-sections are determined to be $\sigma(tq) = 137_{-8}^{+8} \text{ pb}$ and $\sigma(\bar{t}q) = 84_{-5}^{+6} \text{ pb}$ for top-quark and top-antiquark production, respectively. The combined cross-section is found to be $\sigma(tq + \bar{t}q) = 221_{-13}^{+13} \text{ pb}$ and the cross-section ratio is $R_t = \sigma(tq)/\sigma(\bar{t}q) = 1.636_{-0.034}^{+0.036}$. The predictions made at NNLO in perturbation theory are in good agreement with the measured cross-sections, which reach greater precision than previous measurements by the ATLAS and CMS Collaborations with partial Run 2 data samples at

$\sqrt{s} = 13$ TeV. The relative precision of the measurements presented also surpasses the precision reached in ATLAS Run 1 measurements at $\sqrt{s} = 7$ TeV and $\sqrt{s} = 8$ TeV. The new results are thus the most precise measurements of tq and $\bar{t}q$ production to date.

The predictions using various sets of PDFs are compared with the measured value of R_t , demonstrating the potential of further constraining the functions if the measurement is included into future fits. The measurements of $\sigma(tq)$, $\sigma(\bar{t}q)$, and $\sigma(tq + \bar{t}q)$ are interpreted in an EFT approach, setting limits at the 95% CL on the strength of the four-quark operator $O_{Qq}^{3,1}$ and the operator $C_{\phi Q}^3/\Lambda^2$: $-0.37 < C_{Qq}^{3,1}/\Lambda^2 < 0.06$ and $-0.87 < C_{\phi Q}^3/\Lambda^2 < 1.42$, respectively. The measured value of $\sigma(tq + \bar{t}q)$ is further used to derive the constraint $|V_{tb}| > 0.95$ at the 95% CL and determine $f_{LV} \cdot |V_{tb}| = 1.015 \pm 0.031$, improving by 30% the determination of this quantity based on a combination of Run 1 measurements by ATLAS and CMS. In a more general approach, confidence contours are determined in the $f_{LV}|V_{td}|$ -versus- $f_{LV}|V_{tb}|$, the $f_{LV}|V_{ts}|$ -versus- $f_{LV}|V_{tb}|$, and the $f_{LV}|V_{ts}|$ -versus- $f_{LV}|V_{td}|$ planes. The parameter $f_{LV}|V_{tb}|$ is constrained at the 95% CL to a range between 0.95 and 1.05, and $f_{LV}|V_{td}|$ and $f_{LV}|V_{ts}|$ are constrained to be < 0.23 and < 0.58 , respectively.

Acknowledgements

We thank CERN for the very successful operation of the LHC and its injectors, as well as the support staff at CERN and at our institutions worldwide without whom ATLAS could not be operated efficiently.

The crucial computing support from all WLCG partners is acknowledged gratefully, in particular from CERN, the ATLAS Tier-1 facilities at TRIUMF/SFU (Canada), NDGF (Denmark, Norway, Sweden), CC-IN2P3 (France), KIT/GridKA (Germany), INFN-CNAF (Italy), NL-T1 (Netherlands), PIC (Spain), RAL (UK) and BNL (USA), the Tier-2 facilities worldwide and large non-WLCG resource providers. Major contributors of computing resources are listed in Ref. [99].

We gratefully acknowledge the support of ANPCyT, Argentina; YerPhI, Armenia; ARC, Australia; BMWFW and FWF, Austria; ANAS, Azerbaijan; CNPq and FAPESP, Brazil; NSERC, NRC and CFI, Canada; CERN; ANID, Chile; CAS, MOST and NSFC, China; Minciencias, Colombia; MEYS CR, Czech Republic; DNRF and DNSRC, Denmark; IN2P3-CNRS and CEA-DRF/IRFU, France; SRNSFG, Georgia; BMBF, HGF and MPG, Germany; GSRI, Greece; RGC and Hong Kong SAR, China; ISF and Benoziyo Center, Israel; INFN, Italy; MEXT and JSPS, Japan; CNRST, Morocco; NWO, Netherlands; RCN, Norway; MEiN, Poland; FCT, Portugal; MNE/IFA, Romania; MESTD, Serbia; MSSR, Slovakia; ARRS and MIZŠ, Slovenia; DSI/NRF, South Africa; MICINN, Spain; SRC and Wallenberg Foundation, Sweden; SERI, SNSF and Cantons of Bern and Geneva, Switzerland; MOST, Taipei; TENMAK, Türkiye; STFC, United Kingdom; DOE and NSF, United States of America.

Individual groups and members have received support from BCKDF, CANARIE, CRC and DRAC, Canada; PRIMUS 21/SCI/017 and UNCE SCI/013, Czech Republic; COST, ERC, ERDF, Horizon 2020, ICSC-NextGenerationEU and Marie Skłodowska-Curie Actions, European Union; Investissements d’Avenir Labex, Investissements d’Avenir Idex and ANR, France; DFG and AvH Foundation, Germany; Herakleitos, Thales and Aristeia programmes co-financed by EU-ESF and the Greek NSRF, Greece; BSF-NSF and MINERVA, Israel; Norwegian Financial Mechanism 2014-2021, Norway; NCN and NAWA, Poland; La Caixa Banking Foundation, CERCA Programme Generalitat de Catalunya and PROMETEO and GenT Programmes Generalitat Valenciana, Spain; Göran Gustafssons Stiftelse, Sweden; The Royal Society and Leverhulme Trust, United Kingdom.

In addition, individual members wish to acknowledge support from Chile: Agencia Nacional de Investigación y Desarrollo (FONDECYT 1190886, FONDECYT 1210400, FONDECYT 1230987); China: National Natural Science Foundation of China (NSFC - 12175119, NSFC 12275265); European Union: European Research Council (ERC - 948254), Horizon 2020 Framework Programme (MUCCA - CHIST-ERA-19-XAI-00), Italian Center for High Performance Computing, Big Data and Quantum Computing (ICSC, NextGenerationEU), Marie Skłodowska-Curie Actions (EU H2020 MSC IF GRANT NO 101033496); France: Agence Nationale de la Recherche (ANR-20-CE31-0013, ANR-21-CE31-0022), Investissements d'Avenir IDEX (ANR-11-LABX-0012), Investissements d'Avenir Labex (ANR-11-LABX-0012); Germany: Baden-Württemberg Stiftung (BW Stiftung-Postdoc Eliteprogramme), Deutsche Forschungsgemeinschaft (DFG - CR 312/5-1); Italy: Istituto Nazionale di Fisica Nucleare (FELLINI G.A. n. 754496, ICSC, NextGenerationEU); Japan: Japan Society for the Promotion of Science (JSPS KAKENHI 22H01227, JSPS KAKENHI JP21H05085, JSPS KAKENHI JP22H04944); Netherlands: Netherlands Organisation for Scientific Research (NWO Veni 2020 - VI.Veni.202.179); Norway: Research Council of Norway (RCN-314472); Poland: Polish National Agency for Academic Exchange (PPN/PPO/2020/1/00002/U/00001), Polish National Science Centre (NCN 2021/42/E/ST2/00350, NCN UMO-2019/34/E/ST2/00393, UMO-2020/37/B/ST2/01043); Slovenia: Slovenian Research Agency (ARIS grant J1-3010); Spain: BBVA Foundation (LEO22-1-603), Generalitat Valenciana (Artemisa, FEDER, IDIFEDER/2018/048), La Caixa Banking Foundation (LCF/BQ/PI20/11760025), Ministry of Science and Innovation (RYC2019-028510-I, RYC2020-030254-I), PROMETEO and GenT Programmes Generalitat Valenciana (CIDEGENT/2019/023, CIDEGENT/2019/027); Sweden: Swedish Research Council (VR 2022-03845); Switzerland: Swiss National Science Foundation (SNSF - PCEFP2_194658); United Kingdom: Leverhulme Trust (Leverhulme Trust RPG-2020-004); United States of America: Neubauer Family Foundation.

Appendix

Figure 11 illustrates the fractions of selected events in the two SRs for the different scattering processes based on the post-fit event yields reported in Table 6.

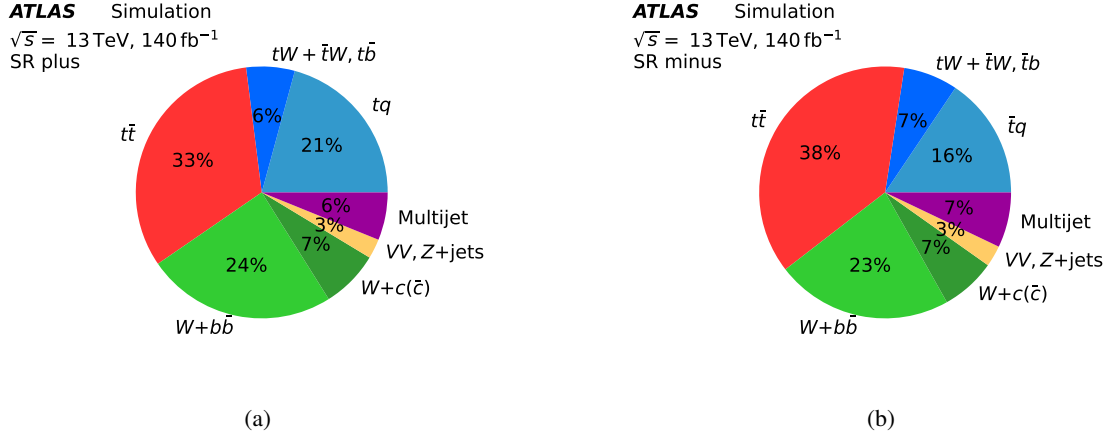


Figure 11: Pie chart of the composition of (a) the SR plus and (b) the SR minus in terms of the different scattering processes. The fractions are based on the post-fit event yields.

The rate of the multijet background is determined by including CRs enriched in this background in the maximum-likelihood fit. Figure 12 shows the post-fit distributions of the variable $\Delta\phi(\vec{p}_T^{\text{miss}}, \mu)$ in the CR μ -plus and CR μ -minus.

Figure 13 compares NNLO predictions obtained with different PDF sets with the measured values of $\sigma(tq)$ and $\sigma(\bar{t}q)$. The PDF sets used are ABMP [90], ATLAS [91], CTEQ [92], MSHT [93], NNPDF [36, 94], and PDF4LHC [45]. All predictions agree with the measurements within the uncertainties.

A 95% CL interval is determined for the EFT coefficient $C_{Qq}^{3,1}/\Lambda^2$ by scanning the likelihood function relative to this parameter. Figure 14 shows the difference between the natural logarithm of the likelihood function relative to its minimum as a function of $C_{Qq}^{3,1}/\Lambda^2$.

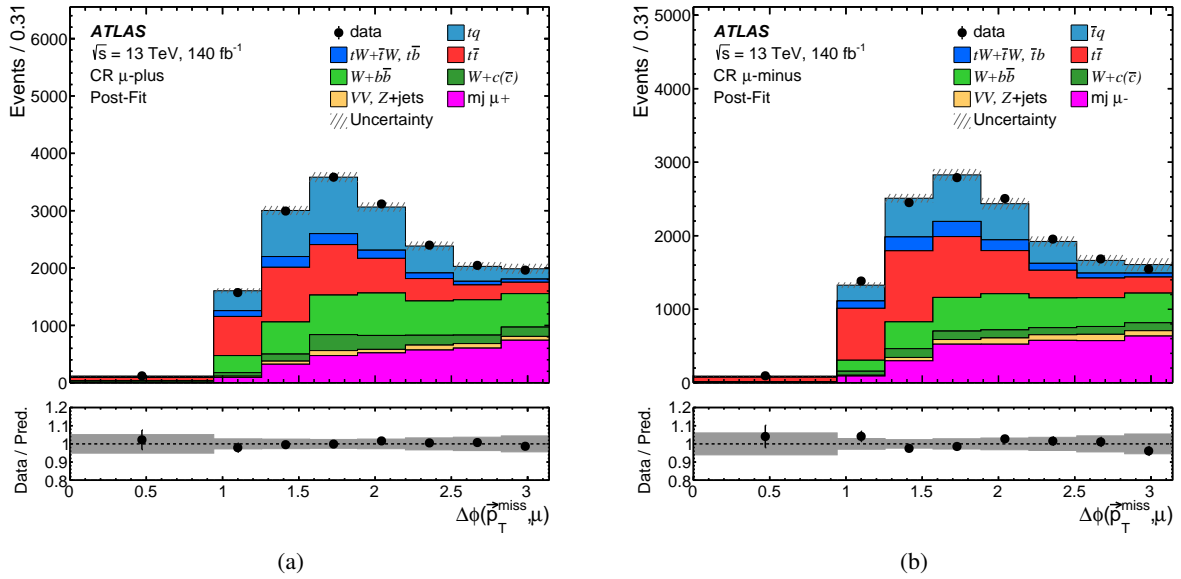


Figure 12: Distributions of the variable $\Delta\phi(\vec{p}_T^{\text{miss}}, \mu)$ in (a) the CR μ -plus and (b) the CR μ -minus after the maximum-likelihood fit is performed (post-fit). In these distributions, the signal contribution is shown stacked on top of contributions from all contributing background processes. All uncertainties considered in the analysis are included in the hatched uncertainty band. The correlations induced by the fit are taken into account. The lower panel shows the ratio of data and the prediction; in this panel, the uncertainty is displayed as a grey band.

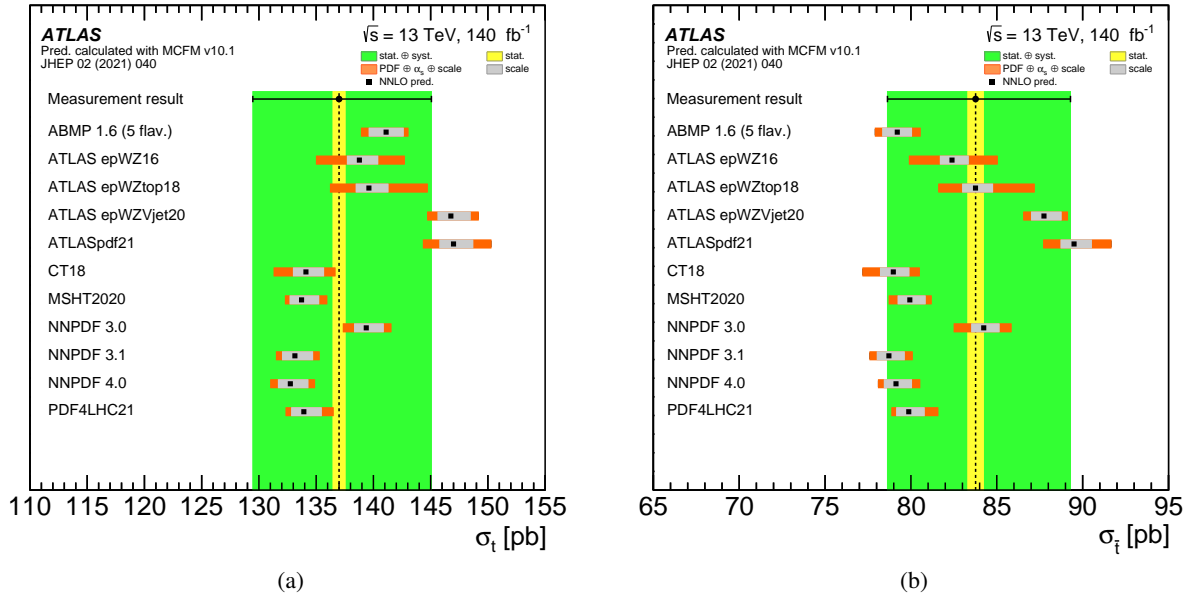


Figure 13: Comparison of NNLO predictions based on several different PDF sets with the measured values (dots) of (a) $\sigma(tq)$ and (b) $\sigma(\bar{t}q)$. The yellow band represents the statistical uncertainty and the green band the total uncertainty. The uncertainties in the theoretical predictions include PDF, scale and α_s uncertainties.

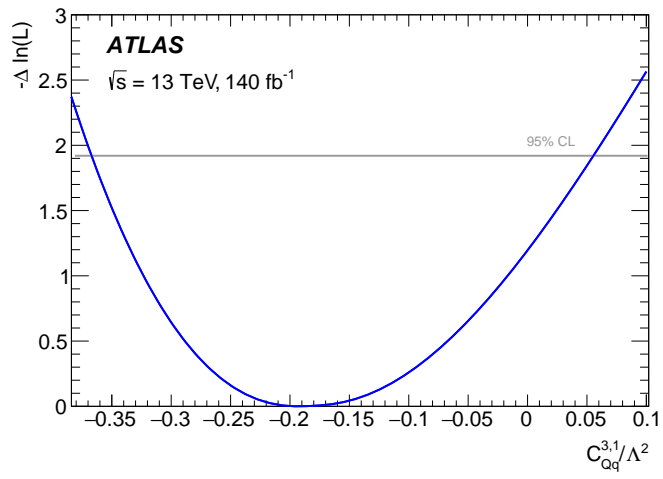


Figure 14: Likelihood scan of the EFT coefficient $C_{Qq}^{3,1}/\Lambda^2$.

References

- [1] L. Evans and P. Bryant, *LHC Machine*, **JINST** **3** (2008) S08001.
- [2] ATLAS Collaboration, *The ATLAS Experiment at the CERN Large Hadron Collider*, **JINST** **3** (2008) S08003.
- [3] E. R. Nocera, M. Ubiali and C. Voisey, *Single top production in PDF fits*, **JHEP** **05** (2020) 067, arXiv: [1912.09543 \[hep-ph\]](#).
- [4] ATLAS Collaboration, *Measurement of the inclusive cross-sections of single top-quark and top-antiquark t -channel production in pp collisions at $\sqrt{s} = 13$ TeV with the ATLAS detector*, **JHEP** **04** (2017) 086, arXiv: [1609.03920 \[hep-ex\]](#).
- [5] ATLAS Collaboration, *Jet energy scale and resolution measured in proton–proton collisions at $\sqrt{s} = 13$ TeV with the ATLAS detector*, **Eur. Phys. J. C** **81** (2021) 689, arXiv: [2007.02645 \[hep-ex\]](#).
- [6] ATLAS Collaboration, *ATLAS flavour-tagging algorithms for the LHC Run 2 pp collision dataset*, **Eur. Phys. J. C** **83** (2023) 681, arXiv: [2211.16345 \[physics.data-an\]](#).
- [7] SMEFT Collaboration, J. J. Ethier et al., *Combined SMEFT interpretation of Higgs, diboson, and top quark data from the LHC*, **JHEP** **11** (2021) 089, arXiv: [2105.00006 \[hep-ph\]](#).
- [8] J. Ellis, M. Madigan, K. Mimasu, V. Sanz and T. You, *Top, Higgs, diboson and electroweak fit to the Standard Model effective field theory*, **JHEP** **04** (2021) 279, arXiv: [2012.02779 \[hep-ph\]](#).
- [9] I. Brivio et al., *O new physics, where art thou? A global search in the top sector*, **JHEP** **02** (2020) 131, arXiv: [1910.03606 \[hep-ph\]](#).
- [10] CMS Collaboration, *Measurement of the single top quark and antiquark production cross sections in the t channel and their ratio in proton–proton collisions at $\sqrt{s} = 13$ TeV*, **Phys. Lett. B** **800** (2020) 135042, arXiv: [1812.10514 \[hep-ex\]](#).
- [11] CMS Collaboration, *Measurement of differential cross sections and charge ratios for t -channel single top quark production in proton–proton collisions at $\sqrt{s} = 13$ TeV*, **Eur. Phys. J. C** **80** (2020) 370, arXiv: [1907.08330 \[hep-ex\]](#).
- [12] CMS Collaboration, *Measurement of CKM matrix elements in single top quark t -channel production in proton–proton collisions at $\sqrt{s} = 13$ TeV*, **Phys. Lett. B** **808** (2020) 135609, arXiv: [2004.12181 \[hep-ex\]](#).
- [13] ATLAS Collaboration, *ATLAS Insertable B-Layer Technical Design Report*, ATLAS-TDR-19; CERN-LHCC-2010-013, 2010, URL: <https://cds.cern.ch/record/1291633>, Addendum: ATLAS-TDR-19-ADD-1; CERN-LHCC-2012-009, 2012, URL: <https://cds.cern.ch/record/1451888>.
- [14] B. Abbott et al., *Production and integration of the ATLAS Insertable B-Layer*, **JINST** **13** (2018) T05008, arXiv: [1803.00844 \[physics.ins-det\]](#).
- [15] ATLAS Collaboration, *Performance of the ATLAS trigger system in 2015*, **Eur. Phys. J. C** **77** (2017) 317, arXiv: [1611.09661 \[hep-ex\]](#).
- [16] ATLAS Collaboration, *The ATLAS Collaboration Software and Firmware*, ATL-SOFT-PUB-2021-001, 2021, URL: <https://cds.cern.ch/record/2767187>.

- [17] ATLAS Collaboration, *ATLAS data quality operations and performance for 2015–2018 data-taking*, *JINST* **15** (2020) P04003, arXiv: 1911.04632 [physics.ins-det].
- [18] ATLAS Collaboration, *Luminosity determination in pp collisions at $\sqrt{s} = 13$ TeV using the ATLAS detector at the LHC*, *Eur. Phys. J. C* **83** (2023) 982, arXiv: 2212.09379 [hep-ex].
- [19] G. Avoni et al., *The new LUCID-2 detector for luminosity measurement and monitoring in ATLAS*, *JINST* **13** (2018) P07017.
- [20] ATLAS Collaboration, *Performance of electron and photon triggers in ATLAS during LHC Run 2*, *Eur. Phys. J. C* **80** (2020) 47, arXiv: 1909.00761 [hep-ex].
- [21] ATLAS Collaboration, *Performance of the ATLAS muon triggers in Run 2*, *JINST* **15** (2020) P09015, arXiv: 2004.13447 [physics.ins-det].
- [22] S. Agostinelli et al., *GEANT4 – a simulation toolkit*, *Nucl. Instrum. Meth. A* **506** (2003) 250.
- [23] ATLAS Collaboration, *The ATLAS Simulation Infrastructure*, *Eur. Phys. J. C* **70** (2010) 823, arXiv: 1005.4568 [physics.ins-det].
- [24] ATLAS Collaboration, *The simulation principle and performance of the ATLAS fast calorimeter simulation FastCaloSim*, ATL-PHYS-PUB-2010-013, 2010, URL: <https://cds.cern.ch/record/1300517>.
- [25] ATLAS Collaboration, *Fast Simulation for ATLAS: Atfast-II and ISF*, ATL-SOFT-PROC-2012-065, 2012, URL: <http://cds.cern.ch/record/1458503>.
- [26] T. Sjöstrand, S. Mrenna and P. Skands, *A brief introduction to PYTHIA 8.1*, *Comput. Phys. Commun.* **178** (2008) 852, arXiv: 0710.3820 [hep-ph].
- [27] ATLAS Collaboration, *The Pythia 8 A3 tune description of ATLAS minimum bias and inelastic measurements incorporating the Donnachie–Landshoff diffractive model*, ATL-PHYS-PUB-2016-017, 2016, URL: <https://cds.cern.ch/record/2206965>.
- [28] NNPDF Collaboration, R. D. Ball et al., *Parton distributions with LHC data*, *Nucl. Phys. B* **867** (2013) 244, arXiv: 1207.1303 [hep-ph].
- [29] P. Nason, *A new method for combining NLO QCD with shower Monte Carlo algorithms*, *JHEP* **11** (2004) 040, arXiv: hep-ph/0409146.
- [30] S. Frixione, G. Ridolfi and P. Nason, *A positive-weight next-to-leading-order Monte Carlo for heavy flavour hadroproduction*, *JHEP* **09** (2007) 126, arXiv: 0707.3088 [hep-ph].
- [31] S. Frixione, P. Nason and C. Oleari, *Matching NLO QCD computations with parton shower simulations: the POWHEG method*, *JHEP* **11** (2007) 070, arXiv: 0709.2092 [hep-ph].
- [32] S. Alioli, P. Nason, C. Oleari and E. Re, *NLO single-top production matched with shower in POWHEG: s- and t-channel contributions*, *JHEP* **09** (2009) 111, arXiv: 0907.4076 [hep-ph], Erratum: *JHEP* **02** (2010) 011.
- [33] S. Alioli, P. Nason, C. Oleari and E. Re, *A general framework for implementing NLO calculations in shower Monte Carlo programs: the POWHEG BOX*, *JHEP* **06** (2010) 043, arXiv: 1002.2581 [hep-ph].
- [34] E. Re, *Single-top Wt-channel production matched with parton showers using the POWHEG method*, *Eur. Phys. J. C* **71** (2011) 1547, arXiv: 1009.2450 [hep-ph].

- [35] R. Frederix, E. Re and P. Torrielli, *Single-top t -channel hadroproduction in the four-flavour scheme with POWHEG and aMC@NLO*, *JHEP* **09** (2012) 130, arXiv: [1207.5391 \[hep-ph\]](#).
- [36] NNPDF Collaboration, R. D. Ball et al., *Parton distributions for the LHC run II*, *JHEP* **04** (2015) 040, arXiv: [1410.8849 \[hep-ph\]](#).
- [37] ATLAS Collaboration, *ATLAS Pythia 8 tunes to 7 TeV data*, ATL-PHYS-PUB-2014-021, 2014, URL: <https://cds.cern.ch/record/1966419>.
- [38] ATLAS Collaboration, *Studies on top-quark Monte Carlo modelling for Top2016*, ATL-PHYS-PUB-2016-020, 2016, URL: <https://cds.cern.ch/record/2216168>.
- [39] S. Frixione, E. Laenen, P. Motylinski, C. White and B. R. Webber, *Single-top hadroproduction in association with a W boson*, *JHEP* **07** (2008) 029, arXiv: [0805.3067 \[hep-ph\]](#).
- [40] S. Frixione, E. Laenen, P. Motylinski and B. R. Webber, *Angular correlations of lepton pairs from vector boson and top quark decays in Monte Carlo simulations*, *JHEP* **04** (2007) 081, arXiv: [hep-ph/0702198](#).
- [41] P. Artoisenet, R. Frederix, O. Mattelaer and R. Rietkerk, *Automatic spin-entangled decays of heavy resonances in Monte Carlo simulations*, *JHEP* **03** (2013) 015, arXiv: [1212.3460 \[hep-ph\]](#).
- [42] D. J. Lange, *The EvtGen particle decay simulation package*, *Nucl. Instrum. Meth. A* **462** (2001) 152.
- [43] M. Czakon and A. Mitov, *Top++: A program for the calculation of the top-pair cross-section at hadron colliders*, *Comput. Phys. Commun.* **185** (2014) 2930, arXiv: [1112.5675 \[hep-ph\]](#).
- [44] J. Campbell, T. Neumann and Z. Sullivan, *Single-top-quark production in the t -channel at NNLO*, *JHEP* **02** (2021) 040, arXiv: [2012.01574 \[hep-ph\]](#).
- [45] R. D. Ball et al., *The PDF4LHC21 combination of global PDF fits for the LHC Run III*, *J. Phys. G* **49** (2022) 080501, arXiv: [2203.05506 \[hep-ph\]](#).
- [46] M. Aliev et al., *HATHOR – HAdronic Top and Heavy quarks crOss section calculator*, *Comput. Phys. Commun.* **182** (2011) 1034, arXiv: [1007.1327 \[hep-ph\]](#).
- [47] P. Kant et al., *HatHor for single top-quark production: Updated predictions and uncertainty estimates for single top-quark production in hadronic collisions*, *Comput. Phys. Commun.* **191** (2015) 74, arXiv: [1406.4403 \[hep-ph\]](#).
- [48] N. Kidonakis and N. Yamanaka, *Higher-order corrections for tW production at high-energy hadron colliders*, *JHEP* **05** (2021) 278, arXiv: [2102.11300 \[hep-ph\]](#).
- [49] E. Bothmann et al., *Event generation with Sherpa 2.2*, *SciPost Phys.* **7** (2019) 034, arXiv: [1905.09127 \[hep-ph\]](#).
- [50] T. Gleisberg and S. Höche, *Comix, a new matrix element generator*, *JHEP* **12** (2008) 039, arXiv: [0808.3674 \[hep-ph\]](#).
- [51] F. Buccioni et al., *OpenLoops 2*, *Eur. Phys. J. C* **79** (2019) 866, arXiv: [1907.13071 \[hep-ph\]](#).
- [52] F. Cascioli, P. Maierhöfer and S. Pozzorini, *Scattering Amplitudes with Open Loops*, *Phys. Rev. Lett.* **108** (2012) 111601, arXiv: [1111.5206 \[hep-ph\]](#).

- [53] A. Denner, S. Dittmaier and L. Hofer, *COLLIER: A fortran-based complex one-loop library in extended regularizations*, *Comput. Phys. Commun.* **212** (2017) 220, arXiv: [1604.06792 \[hep-ph\]](#).
- [54] S. Schumann and F. Krauss, *A parton shower algorithm based on Catani–Seymour dipole factorisation*, *JHEP* **03** (2008) 038, arXiv: [0709.1027 \[hep-ph\]](#).
- [55] J.-C. Winter, F. Krauss and G. Soff, *A modified cluster-hadronisation model*, *Eur. Phys. J. C* **36** (2004) 381, arXiv: [hep-ph/0311085](#).
- [56] S. Höche, F. Krauss, M. Schönherr and F. Siegert, *A critical appraisal of NLO+PS matching methods*, *JHEP* **09** (2012) 049, arXiv: [1111.1220 \[hep-ph\]](#).
- [57] S. Catani, F. Krauss, B. R. Webber and R. Kuhn, *QCD Matrix Elements + Parton Showers*, *JHEP* **11** (2001) 063, arXiv: [hep-ph/0109231](#).
- [58] S. Höche, F. Krauss, S. Schumann and F. Siegert, *QCD matrix elements and truncated showers*, *JHEP* **05** (2009) 053, arXiv: [0903.1219 \[hep-ph\]](#).
- [59] S. Höche, F. Krauss, M. Schönherr and F. Siegert, *QCD matrix elements + parton showers. The NLO case*, *JHEP* **04** (2013) 027, arXiv: [1207.5030 \[hep-ph\]](#).
- [60] C. Anastasiou, L. Dixon, K. Melnikov and F. Petriello, *High-precision QCD at hadron colliders: Electroweak gauge boson rapidity distributions at next-to-next-to leading order*, *Phys. Rev. D* **69** (2004) 094008, arXiv: [hep-ph/0312266](#).
- [61] R. Gavin, Y. Li, F. Petriello and S. Quackenbush, *FEWZ 2.0: A code for hadronic Z production at next-to-next-to-leading order*, *Comput. Phys. Commun.* **182** (2011) 2388, arXiv: [1011.3540 \[hep-ph\]](#).
- [62] C. Degrande et al., *Automated one-loop computations in the standard model effective field theory*, *Phys. Rev. D* **103** (2021) 096024, arXiv: [2008.11743 \[hep-ph\]](#).
- [63] ATLAS Collaboration, *Vertex Reconstruction Performance of the ATLAS Detector at $\sqrt{s} = 13$ TeV*, ATL-PHYS-PUB-2015-026, 2015, URL: <https://cds.cern.ch/record/2037717>.
- [64] ATLAS Collaboration, *Electron and photon performance measurements with the ATLAS detector using the 2015–2017 LHC proton–proton collision data*, *JINST* **14** (2019) P12006, arXiv: [1908.00005 \[hep-ex\]](#).
- [65] ATLAS Collaboration, *Muon reconstruction and identification efficiency in ATLAS using the full Run 2 pp collision data set at $\sqrt{s} = 13$ TeV*, *Eur. Phys. J. C* **81** (2021) 578, arXiv: [2012.00578 \[hep-ex\]](#).
- [66] ATLAS Collaboration, *Jet reconstruction and performance using particle flow with the ATLAS Detector*, *Eur. Phys. J. C* **77** (2017) 466, arXiv: [1703.10485 \[hep-ex\]](#).
- [67] M. Cacciari, G. P. Salam and G. Soyez, *The anti- k_r jet clustering algorithm*, *JHEP* **04** (2008) 063, arXiv: [0802.1189 \[hep-ph\]](#).
- [68] M. Cacciari, G. P. Salam and G. Soyez, *FastJet user manual*, *Eur. Phys. J. C* **72** (2012) 1896, arXiv: [1111.6097 \[hep-ph\]](#).

- [69] ATLAS Collaboration, *Topological cell clustering in the ATLAS calorimeters and its performance in LHC Run 1*, *Eur. Phys. J. C* **77** (2017) 490, arXiv: [1603.02934 \[hep-ex\]](#).
- [70] ATLAS Collaboration, *Performance of pile-up mitigation techniques for jets in pp collisions at $\sqrt{s} = 8$ TeV using the ATLAS detector*, *Eur. Phys. J. C* **76** (2016) 581, arXiv: [1510.03823 \[hep-ex\]](#).
- [71] ATLAS Collaboration, *Identification and rejection of pile-up jets at high pseudorapidity with the ATLAS detector*, *Eur. Phys. J. C* **77** (2017) 580, arXiv: [1705.02211 \[hep-ex\]](#),
Erratum: *Eur. Phys. J. C* **77** (2017) 712.
- [72] ATLAS Collaboration, *Performance of missing transverse momentum reconstruction with the ATLAS detector using proton–proton collisions at $\sqrt{s} = 13$ TeV*, *Eur. Phys. J. C* **78** (2018) 903, arXiv: [1802.08168 \[hep-ex\]](#).
- [73] ATLAS Collaboration, *Estimation of non-prompt and fake lepton backgrounds in final states with top quarks produced in proton–proton collisions at $\sqrt{s} = 8$ TeV with the ATLAS Detector*, ATLAS-CONF-2014-058, 2014, URL: <https://cds.cern.ch/record/1951336>.
- [74] Particle Data Group, R. L. Workman et al., *Review of Particle Physics*, *PTEP* **2022** (2022) 083C01.
- [75] T. Chwalek, *Measurement of W-Boson Helicity-Fractions in Top-Quark Decays with the CDF II Experiment and Prospects for an Early $t\bar{t}$ Cross-Section Measurement with the CMS Experiment*, Ph.D. Thesis, Karlsruhe U., IEKP-KA-2010-05, FERMILAB-THESIS-2010-74, CERN-THESIS-2010-255, 2010, URL: <https://cds.cern.ch/record/1416031>.
- [76] M. Feindt, *A Neural Bayesian Estimator for Conditional Probability Densities*, IEKP-KA/04-05, 2004, arXiv: [physics/0402093 \[physics.data-an\]](#).
- [77] M. Feindt and U. Kerzel, *The NeuroBayes neural network package*, *Nucl. Instrum. Meth. A* **559** (2006) 190.
- [78] ATLAS Collaboration, *Measurement of the t-channel single top-quark production cross section in pp collisions at $\sqrt{s} = 7$ TeV with the ATLAS detector*, *Phys. Lett. B* **717** (2012) 330, arXiv: [1205.3130 \[hep-ex\]](#).
- [79] ATLAS Collaboration, *Electron and photon energy calibration with the ATLAS detector using LHC Run 2 data*, (2023), arXiv: [2309.05471 \[hep-ex\]](#).
- [80] ATLAS Collaboration, *Studies of the muon momentum calibration and performance of the ATLAS detector with pp collisions at $\sqrt{s} = 13$ TeV*, *Eur. Phys. J. C* **83** (2023) 686, arXiv: [2212.07338 \[hep-ex\]](#).
- [81] ATLAS Collaboration, *ATLAS b-jet identification performance and efficiency measurement with $t\bar{t}$ events in pp collisions at $\sqrt{s} = 13$ TeV*, *Eur. Phys. J. C* **79** (2019) 970, arXiv: [1907.05120 \[hep-ex\]](#).
- [82] ATLAS Collaboration, *Measurement of the c-jet mistagging efficiency in $t\bar{t}$ events using pp collision data at $\sqrt{s} = 13$ TeV collected with the ATLAS detector*, *Eur. Phys. J. C* **82** (2022) 95, arXiv: [2109.10627 \[hep-ex\]](#).

- [83] ATLAS Collaboration, *Calibration of the light-flavour jet mistagging efficiency of the b -tagging algorithms with Z +jets events using 139 fb^{-1} of ATLAS proton-proton collision data at $\sqrt{s} = 13 \text{ TeV}$, (2023), arXiv: [2301.06319 \[hep-ex\]](#).*
- [84] ATLAS Collaboration, *Search for flavour-changing neutral-current interactions of a top quark and a gluon in pp collisions at $\sqrt{s} = 13 \text{ TeV}$ with the ATLAS detector*, *Eur. Phys. J. C* **82** (2022) 334, arXiv: [2112.01302 \[hep-ex\]](#).
- [85] M. Bähr et al., *Herwig++ physics and manual*, *Eur. Phys. J. C* **58** (2008) 639, arXiv: [0803.0883 \[hep-ph\]](#).
- [86] J. Bellm et al., *Herwig 7.0/Herwig++ 3.0 release note*, *Eur. Phys. J. C* **76** (2016) 196, arXiv: [1512.01178 \[hep-ph\]](#).
- [87] S. Höche, S. Mrenna, S. Payne, C. T. Preuss and P. Skands, *A Study of QCD Radiation in VBF Higgs Production with Vincia and Pythia*, *SciPost Phys.* **12** (2022) 010, arXiv: [2106.10987 \[hep-ph\]](#).
- [88] J. Butterworth et al., *PDF4LHC recommendations for LHC Run II*, *J. Phys. G* **43** (2016) 023001, arXiv: [1510.03865 \[hep-ph\]](#).
- [89] R. Barlow and C. Beeston, *Fitting using finite Monte Carlo samples*, *Comput. Phys. Commun.* **77** (1993) 219.
- [90] S. Alekhin, J. Blümlein and S. Moch, *NLO PDFs from the ABMP16 fit*, *Eur. Phys. J. C* **78** (2018) 477, arXiv: [1803.07537 \[hep-ph\]](#).
- [91] ATLAS Collaboration, *Determination of the parton distribution functions of the proton using diverse ATLAS data from pp collisions at $\sqrt{s} = 7, 8$ and 13 TeV* , *Eur. Phys. J. C* **82** (2022) 438, arXiv: [2112.11266 \[hep-ex\]](#).
- [92] T.-J. Hou et al., *New CTEQ global analysis of quantum chromodynamics with high-precision data from the LHC*, *Phys. Rev. D* **103** (2021) 014013, arXiv: [1912.10053 \[hep-ph\]](#).
- [93] S. Bailey, T. Cridge, L. A. Harland-Lang, A. D. Martin and R. S. Thorne, *Parton distributions from LHC, HERA, Tevatron and fixed target data: MSHT20 PDFs*, *Eur. Phys. J. C* **81** (2021) 341, arXiv: [2012.04684 \[hep-ph\]](#).
- [94] NNPDF Collaboration, R. D. Ball et al., *The path to proton structure at 1% accuracy*, *Eur. Phys. J. C* **82** (2022) 428, arXiv: [2109.02653 \[hep-ph\]](#).
- [95] TopFitter Collaboration, A. Buckley et al., *Constraining top quark effective theory in the LHC Run II era*, *JHEP* **04** (2016) 015, arXiv: [1512.03360 \[hep-ph\]](#).
- [96] ATLAS Collaboration, *Evidence for the charge asymmetry in $pp \rightarrow t\bar{t}$ production at $\sqrt{s} = 13 \text{ TeV}$ with the ATLAS detector*, *JHEP* **08** (2023) 077, arXiv: [2208.12095 \[hep-ex\]](#).
- [97] ATLAS Collaboration, *Inclusive and differential cross-section measurements of $t\bar{t}Z$ production in pp collisions at $\sqrt{s} = 13 \text{ TeV}$ with the ATLAS detector, including EFT and spin-correlation interpretations*, 2023, arXiv: [2312.04450 \[hep-ex\]](#).

- [98] ATLAS and CMS Collaborations, *Combinations of single-top-quark production cross-section measurements and $|f_{LV}V_{tb}|$ determinations at $\sqrt{s} = 7$ and 8 TeV with the ATLAS and CMS experiments*, *JHEP* **05** (2019) 088, arXiv: [1902.07158](https://arxiv.org/abs/1902.07158) [[hep-ex](#)].
- [99] ATLAS Collaboration, *ATLAS Computing Acknowledgements*, ATL-SOFT-PUB-2023-001, 2023, URL: <https://cds.cern.ch/record/2869272>.

The ATLAS Collaboration

G. Aad ¹⁰², B. Abbott ¹²⁰, K. Abeling ⁵⁵, N.J. Abicht ⁴⁹, S.H. Abidi ²⁹, A. Aboulhorma ^{35e}, H. Abramowicz ¹⁵¹, H. Abreu ¹⁵⁰, Y. Abulaiti ¹¹⁷, A.C. Abusleme Hoffman ^{137a}, B.S. Acharya ^{69a,69b,n}, C. Adam Bourdarios ⁴, L. Adamczyk ^{86a}, L. Adamek ¹⁵⁵, S.V. Addepalli ²⁶, M.J. Addison ¹⁰¹, J. Adelman ¹¹⁵, A. Adiguzel ^{21c}, T. Auye ¹³⁴, A.A. Affolder ¹³⁶, Y. Afik ³⁶, M.N. Agaras ¹³, J. Agarwala ^{73a,73b}, A. Aggarwal ¹⁰⁰, C. Agheorghiesei ^{27c}, A. Ahmad ³⁶, F. Ahmadov ^{38,z}, W.S. Ahmed ¹⁰⁴, S. Ahuja ⁹⁵, X. Ai ^{62a}, G. Aielli ^{76a,76b}, A. Aikot ¹⁶³, M. Ait Tamlihat ^{35e}, B. Aitbenchikh ^{35a}, I. Aizenberg ¹⁶⁹, M. Akbiyik ¹⁰⁰, T.P.A. Åkesson ⁹⁸, A.V. Akimov ³⁷, D. Akiyama ¹⁶⁸, N.N. Akolkar ²⁴, K. Al Khoury ⁴¹, G.L. Alberghi ^{23b}, J. Albert ¹⁶⁵, P. Albicocco ⁵³, G.L. Albouy ⁶⁰, S. Alderweireldt ⁵², M. Aleksa ³⁶, I.N. Aleksandrov ³⁸, C. Alexa ^{27b}, T. Alexopoulos ¹⁰, F. Alfonsi ^{23b}, M. Algren ⁵⁶, M. Alhroob ¹²⁰, B. Ali ¹³², H.M.J. Ali ⁹¹, S. Ali ¹⁴⁸, S.W. Alibocus ⁹², M. Aliev ¹⁴⁵, G. Alimonti ^{71a}, W. Alkakh ⁵⁵, C. Allaire ⁶⁶, B.M.M. Allbrooke ¹⁴⁶, J.F. Allen ⁵², C.A. Allendes Flores ^{137f}, P.P. Allport ²⁰, A. Aloisio ^{72a,72b}, F. Alonso ⁹⁰, C. Alpigiani ¹³⁸, M. Alvarez Estevez ⁹⁹, A. Alvarez Fernandez ¹⁰⁰, M. Alves Cardoso ⁵⁶, M.G. Alviggi ^{72a,72b}, M. Aly ¹⁰¹, Y. Amaral Coutinho ^{83b}, A. Ambler ¹⁰⁴, C. Amelung ³⁶, M. Amerl ¹⁰¹, C.G. Ames ¹⁰⁹, D. Amidei ¹⁰⁶, S.P. Amor Dos Santos ^{130a}, K.R. Amos ¹⁶³, V. Ananiev ¹²⁵, C. Anastopoulos ¹³⁹, T. Andeen ¹¹, J.K. Anders ³⁶, S.Y. Andreev ^{47a,47b}, A. Andreatta ^{71a,71b}, S. Angelidakis ⁹, A. Angerami ^{41,ac}, A.V. Anisenkov ³⁷, A. Annovi ^{74a}, C. Antel ⁵⁶, M.T. Anthony ¹³⁹, E. Antipov ¹⁴⁵, M. Antonelli ⁵³, F. Anulli ^{75a}, M. Aoki ⁸⁴, T. Aoki ¹⁵³, J.A. Aparisi Pozo ¹⁶³, M.A. Aparo ¹⁴⁶, L. Aperio Bella ⁴⁸, C. Appelt ¹⁸, A. Apyan ²⁶, N. Aranzabal ³⁶, C. Arcangeletti ⁵³, A.T.H. Arce ⁵¹, E. Arena ⁹², J-F. Arguin ¹⁰⁸, S. Argyropoulos ⁵⁴, J.-H. Arling ⁴⁸, O. Arnaez ⁴, H. Arnold ¹¹⁴, G. Artoni ^{75a,75b}, H. Asada ¹¹¹, K. Asai ¹¹⁸, S. Asai ¹⁵³, N.A. Asbah ⁶¹, K. Assamagan ²⁹, R. Astalos ^{28a}, S. Atashi ¹⁶⁰, R.J. Atkin ^{33a}, M. Atkinson ¹⁶², H. Atmani ^{35f}, P.A. Atmasiddha ¹⁰⁶, K. Augsten ¹³², S. Auricchio ^{72a,72b}, A.D. Auriol ²⁰, V.A. Austrup ¹⁰¹, G. Avolio ³⁶, K. Axiotis ⁵⁶, G. Azuelos ^{108,ah}, D. Babal ^{28b}, H. Bachacou ¹³⁵, K. Bachas ^{152,q}, A. Bachi ³⁴, F. Backman ^{47a,47b}, A. Badea ⁶¹, P. Bagnaia ^{75a,75b}, M. Bahmani ¹⁸, A.J. Bailey ¹⁶³, V.R. Bailey ¹⁶², J.T. Baines ¹³⁴, L. Baines ⁹⁴, C. Bakalis ¹⁰, O.K. Baker ¹⁷², E. Bakos ¹⁵, D. Bakshi Gupta ⁸, V. Balakrishnan ¹²⁰, R. Balasubramanian ¹¹⁴, E.M. Baldin ³⁷, P. Balek ^{86a}, E. Ballabene ^{23b,23a}, F. Balli ¹³⁵, L.M. Baltes ^{63a}, W.K. Balunas ³², J. Balz ¹⁰⁰, E. Banas ⁸⁷, M. Bandieramonte ¹²⁹, A. Bandyopadhyay ²⁴, S. Bansal ²⁴, L. Barak ¹⁵¹, M. Barakat ⁴⁸, E.L. Barberio ¹⁰⁵, D. Barberis ^{57b,57a}, M. Barbero ¹⁰², K.N. Barends ^{33a}, T. Barillari ¹¹⁰, M-S. Barisits ³⁶, T. Barklow ¹⁴³, P. Baron ¹²², D.A. Baron Moreno ¹⁰¹, A. Baroncelli ^{62a}, G. Barone ²⁹, A.J. Barr ¹²⁶, J.D. Barr ⁹⁶, L. Barranco Navarro ^{47a,47b}, F. Barreiro ⁹⁹, J. Barreiro Guimarães da Costa ^{14a}, U. Barron ¹⁵¹, M.G. Barros Teixeira ^{130a}, S. Barsov ³⁷, F. Bartels ^{63a}, R. Bartoldus ¹⁴³, A.E. Barton ⁹¹, P. Bartos ^{28a}, A. Basan ¹⁰⁰, M. Baselga ⁴⁹, A. Bassalat ^{66,b}, M.J. Basso ^{156a}, C.R. Basson ¹⁰¹, R.L. Bates ⁵⁹, S. Batlamous ^{35e}, J.R. Batley ³², B. Batool ¹⁴¹, M. Battaglia ¹³⁶, D. Battulga ¹⁸, M. Bauge ^{75a,75b}, M. Bauer ³⁶, P. Bauer ²⁴, L.T. Bazzano Hurrell ³⁰, J.B. Beacham ⁵¹, T. Beau ¹²⁷, P.H. Beauchemin ¹⁵⁸, F. Becherer ⁵⁴, P. Bechtel ²⁴, H.P. Beck ^{19,p}, K. Becker ¹⁶⁷, A.J. Beddall ⁸², V.A. Bednyakov ³⁸, C.P. Bee ¹⁴⁵, L.J. Beamster ¹⁵, T.A. Beermann ³⁶, M. Begalli ^{83d}, M. Begel ²⁹, A. Behera ¹⁴⁵, J.K. Behr ⁴⁸, J.F. Beirer ⁵⁵, F. Beisiegel ²⁴, M. Belfkir ¹⁵⁹, G. Bella ¹⁵¹, L. Bellagamba ^{23b}, A. Bellerive ³⁴, P. Bellos ²⁰, K. Beloborodov ³⁷, N.L. Belyaev ³⁷, D. Bencheikroun ^{35a}, F. Bendebba ^{35a}, Y. Benhamou ¹⁵¹, M. Benoit ²⁹, J.R. Bensinger ²⁶, S. Bentvelsen ¹¹⁴,

L. Beresford ⁴⁸, M. Beretta ⁵³, E. Bergeaas Kuutmann ¹⁶¹, N. Berger ⁴, B. Bergmann ¹³²,
 J. Beringer ^{17a}, G. Bernardi ⁵, C. Bernius ¹⁴³, F.U. Bernlochner ²⁴, F. Bernon ^{36,102}, T. Berry ⁹⁵,
 P. Berta ¹³³, A. Berthold ⁵⁰, I.A. Bertram ⁹¹, O. Bessidskaia Bylund ¹⁷¹, S. Bethke ¹¹⁰,
 A. Betti ^{75a,75b}, A.J. Bevan ⁹⁴, M. Bhamjee ^{33c}, S. Bhatta ¹⁴⁵, D.S. Bhattacharya ¹⁶⁶,
 P. Bhattarai ¹⁴³, V.S. Bhopatkar ¹²¹, R. Bi ^{29,aj}, R.M. Bianchi ¹²⁹, G. Bianco ^{23b,23a}, O. Biebel ¹⁰⁹,
 R. Bielski ¹²³, M. Biglietti ^{77a}, T.R.V. Billoud ¹³², M. Bindi ⁵⁵, A. Bingul ^{21b}, C. Bini ^{75a,75b},
 A. Biondini ⁹², C.J. Birch-sykes ¹⁰¹, G.A. Bird ^{20,134}, M. Birman ¹⁶⁹, M. Biro ¹³³,
 S. Biryukov ¹⁴⁶, T. Bisanz ⁴⁹, E. Bisceglie ^{43b,43a}, J.P. Biswal ¹³⁴, D. Biswas ¹⁴¹, A. Bitadze ¹⁰¹,
 K. Bjørke ¹²⁵, I. Bloch ⁴⁸, C. Blocker ²⁶, A. Blue ⁵⁹, U. Blumenschein ⁹⁴, J. Blumenthal ¹⁰⁰,
 G.J. Bobbink ¹¹⁴, V.S. Bobrovnikov ³⁷, M. Boehler ⁵⁴, B. Boehm ¹⁶⁶, D. Bogavac ³⁶,
 A.G. Bogdanchikov ³⁷, C. Bohm ^{47a}, V. Boisvert ⁹⁵, P. Bokan ⁴⁸, T. Bold ^{86a}, M. Bomben ⁵,
 M. Bona ⁹⁴, M. Boonekamp ¹³⁵, C.D. Booth ⁹⁵, A.G. Borbély ⁵⁹, I.S. Bordulev ³⁷,
 H.M. Borecka-Bielska ¹⁰⁸, L.S. Borgna ⁹⁶, G. Borissov ⁹¹, D. Bortoletto ¹²⁶, D. Boscherini ^{23b},
 M. Bosman ¹³, J.D. Bossio Sola ³⁶, K. Bouaouda ^{35a}, N. Bouchhar ¹⁶³, J. Boudreau ¹²⁹,
 E.V. Bouhova-Thacker ⁹¹, D. Boumediene ⁴⁰, R. Bouquet ⁵, A. Boveia ¹¹⁹, J. Boyd ³⁶,
 D. Boye ²⁹, I.R. Boyko ³⁸, J. Bracik ²⁰, N. Brahimi ^{62d}, G. Brandt ¹⁷¹, O. Brandt ³²,
 F. Braren ⁴⁸, B. Brau ¹⁰³, J.E. Brau ¹²³, R. Brenner ¹⁶⁹, L. Brenner ¹¹⁴, R. Brenner ¹⁶¹,
 S. Bressler ¹⁶⁹, D. Britton ⁵⁹, D. Britzger ¹¹⁰, I. Brock ²⁴, G. Brooijmans ⁴¹, W.K. Brooks ^{137f},
 E. Brost ²⁹, L.M. Brown ¹⁶⁵, L.E. Bruce ⁶¹, T.L. Bruckler ¹²⁶, P.A. Bruckman de Renstrom ⁸⁷,
 B. Brüers ⁴⁸, A. Bruni ^{23b}, G. Bruni ^{23b}, M. Bruschi ^{23b}, N. Bruscinò ^{75a,75b}, T. Buanes ¹⁶,
 Q. Buat ¹³⁸, D. Buchin ¹¹⁰, A.G. Buckley ⁵⁹, O. Bulekov ³⁷, B.A. Bullard ¹⁴³, S. Burdin ⁹²,
 C.D. Burgard ⁴⁹, A.M. Burger ⁴⁰, B. Burghgrave ⁸, O. Burlayenko ⁵⁴, J.T.P. Burr ³²,
 C.D. Burton ¹¹, J.C. Burzynski ¹⁴², E.L. Busch ⁴¹, V. Büscher ¹⁰⁰, P.J. Bussey ⁵⁹,
 J.M. Butler ²⁵, C.M. Buttar ⁵⁹, J.M. Butterworth ⁹⁶, W. Buttinger ¹³⁴, C.J. Buxo Vazquez ¹⁰⁷,
 A.R. Buzykaev ³⁷, S. Cabrera Urbán ¹⁶³, L. Cadamuro ⁶⁶, D. Caforio ⁵⁸, H. Cai ¹²⁹,
 Y. Cai ^{14a,14e}, V.M.M. Cairo ³⁶, O. Cakir ^{3a}, N. Calace ³⁶, P. Calafiura ^{17a}, G. Calderini ¹²⁷,
 P. Calfayan ⁶⁸, G. Callea ⁵⁹, L.P. Caloba ^{83b}, D. Calvet ⁴⁰, S. Calvet ⁴⁰, T.P. Calvet ¹⁰²,
 M. Calvetti ^{74a,74b}, R. Camacho Toro ¹²⁷, S. Camarda ³⁶, D. Camarero Munoz ²⁶,
 P. Camarri ^{76a,76b}, M.T. Camerlingo ^{72a,72b}, D. Cameron ³⁶, C. Camincher ¹⁶⁵, M. Campanelli ⁹⁶,
 A. Camplani ⁴², V. Canale ^{72a,72b}, A. Canesse ¹⁰⁴, J. Cantero ¹⁶³, Y. Cao ¹⁶², F. Capocasa ²⁶,
 M. Capua ^{43b,43a}, A. Carbone ^{71a,71b}, R. Cardarelli ^{76a}, J.C.J. Cardenas ⁸, F. Cardillo ¹⁶³,
 T. Carli ³⁶, G. Carlino ^{72a}, J.I. Carlotto ¹³, B.T. Carlson ^{129,r}, E.M. Carlson ^{165,156a},
 L. Carminati ^{71a,71b}, A. Carnelli ¹³⁵, M. Carnesale ^{75a,75b}, S. Caron ¹¹³, E. Carquin ^{137f},
 S. Carrá ^{71a}, G. Carratta ^{23b,23a}, F. Carrio Argos ^{33g}, J.W.S. Carter ¹⁵⁵, T.M. Carter ⁵²,
 M.P. Casado ^{13,i}, M. Caspar ⁴⁸, E.G. Castiglia ¹⁷², F.L. Castillo ⁴, L. Castillo Garcia ¹³,
 V. Castillo Gimenez ¹⁶³, N.F. Castro ^{130a,130e}, A. Catinaccio ³⁶, J.R. Catmore ¹²⁵, V. Cavaliere ²⁹,
 N. Cavalli ^{23b,23a}, V. Cavalini ^{74a,74b}, Y.C. Cekmecelioglu ⁴⁸, E. Celebi ^{21a}, F. Celli ¹²⁶,
 M.S. Centonze ^{70a,70b}, V. Cepaitis ⁵⁶, K. Cerny ¹²², A.S. Cerqueira ^{83a}, A. Cerri ¹⁴⁶,
 L. Cerrito ^{76a,76b}, F. Cerutti ^{17a}, B. Cervato ¹⁴¹, A. Cervelli ^{23b}, G. Cesarini ⁵³, S.A. Cetin ⁸²,
 Z. Chadi ^{35a}, D. Chakraborty ¹¹⁵, J. Chan ¹⁷⁰, W.Y. Chan ¹⁵³, J.D. Chapman ³², E. Chapon ¹³⁵,
 B. Chargeishvili ^{149b}, D.G. Charlton ²⁰, T.P. Charman ⁹⁴, M. Chatterjee ¹⁹, C. Chauhan ¹³³,
 S. Chekanov ⁶, S.V. Chekulaev ^{156a}, G.A. Chelkov ^{38,a}, A. Chen ¹⁰⁶, B. Chen ¹⁵¹, B. Chen ¹⁶⁵,
 H. Chen ^{14c}, H. Chen ²⁹, J. Chen ^{62c}, J. Chen ¹⁴², M. Chen ¹²⁶, S. Chen ¹⁵³, S.J. Chen ^{14c},
 X. Chen ^{62c,135}, X. Chen ^{14b,ag}, Y. Chen ^{62a}, C.L. Cheng ¹⁷⁰, H.C. Cheng ^{64a}, S. Cheong ¹⁴³,
 A. Cheplakov ³⁸, E. Cheremushkina ⁴⁸, E. Cherepanova ¹¹⁴, R. Cherkaoui El Moursli ^{35e},
 E. Cheu ⁷, K. Cheung ⁶⁵, L. Chevalier ¹³⁵, V. Chiarella ⁵³, G. Chiarelli ^{74a}, N. Chiedde ¹⁰²,
 G. Chiodini ^{70a}, A.S. Chisholm ²⁰, A. Chitan ^{27b}, M. Chitishvili ¹⁶³, M.V. Chizhov ³⁸,

K. Choi ¹¹, A.R. Chomont ^{75a,75b}, Y. Chou ¹⁰³, E.Y.S. Chow ¹¹⁴, T. Chowdhury ^{33g},
 K.L. Chu ¹⁶⁹, M.C. Chu ^{64a}, X. Chu ^{14a,14e}, J. Chudoba ¹³¹, J.J. Chwastowski ⁸⁷, D. Cieri ¹¹⁰,
 K.M. Ciesla ^{86a}, V. Cindro ⁹³, A. Ciocio ^{17a}, F. Cirotto ^{72a,72b}, Z.H. Citron ^{169,1}, M. Citterio ^{71a},
 D.A. Ciubotaru ^{27b}, B.M. Ciungu ¹⁵⁵, A. Clark ⁵⁶, P.J. Clark ⁵², J.M. Clavijo Columbie ⁴⁸,
 S.E. Clawson ⁴⁸, C. Clement ^{47a,47b}, J. Clercx ⁴⁸, Y. Coadou ¹⁰², M. Cobal ^{69a,69c},
 A. Coccaro ^{57b}, R.F. Coelho Barrue ^{130a}, R. Coelho Lopes De Sa ¹⁰³, S. Coelli ^{71a}, H. Cohen ¹⁵¹,
 A.E.C. Coimbra ^{71a,71b}, B. Cole ⁴¹, J. Collot ⁶⁰, P. Conde Muiño ^{130a,130g}, M.P. Connell ^{33c},
 S.H. Connell ^{33c}, I.A. Connelly ⁵⁹, E.I. Conroy ¹²⁶, F. Conventi ^{72a,ai}, H.G. Cooke ²⁰,
 A.M. Cooper-Sarkar ¹²⁶, A. Cordeiro Oudot Choi ¹²⁷, F. Cormier ¹⁶⁴, L.D. Corpe ⁴⁰,
 M. Corradi ^{75a,75b}, F. Corriveau ^{104,x}, A. Cortes-Gonzalez ¹⁸, M.J. Costa ¹⁶³, F. Costanza ⁴,
 D. Costanzo ¹³⁹, B.M. Cote ¹¹⁹, G. Cowan ⁹⁵, K. Cranmer ¹⁷⁰, D. Cremonini ^{23b,23a},
 S. Crépe-Renaudin ⁶⁰, F. Crescioli ¹²⁷, M. Cristinziani ¹⁴¹, M. Cristoforetti ^{78a,78b}, V. Croft ¹¹⁴,
 J.E. Crosby ¹²¹, G. Crosetti ^{43b,43a}, A. Cueto ⁹⁹, T. Cuhadar Donszelmann ¹⁶⁰, H. Cui ^{14a,14e},
 Z. Cui ⁷, W.R. Cunningham ⁵⁹, F. Curcio ^{43b,43a}, P. Czodrowski ³⁶, M.M. Czurylo ^{63b},
 M.J. Da Cunha Sargedas De Sousa ^{57b,57a}, J.V. Da Fonseca Pinto ^{83b}, C. Da Via ¹⁰¹,
 W. Dabrowski ^{86a}, T. Dado ⁴⁹, S. Dahbi ^{33g}, T. Dai ¹⁰⁶, D. Dal Santo ¹⁹, C. Dallapiccola ¹⁰³,
 M. Dam ⁴², G. D'amen ²⁹, V. D'Amico ¹⁰⁹, J. Damp ¹⁰⁰, J.R. Dandoy ¹²⁸, M.F. Daneri ³⁰,
 M. Danninger ¹⁴², V. Dao ³⁶, G. Darbo ^{57b}, S. Darmora ⁶, S.J. Das ^{29,aj}, S. D'Auria ^{71a,71b},
 C. David ^{156b}, T. Davidek ¹³³, B. Davis-Purcell ³⁴, I. Dawson ⁹⁴, H.A. Day-hall ¹³², K. De ⁸,
 R. De Asmundis ^{72a}, N. De Biase ⁴⁸, S. De Castro ^{23b,23a}, N. De Groot ¹¹³, P. de Jong ¹¹⁴,
 H. De la Torre ¹¹⁵, A. De Maria ^{14c}, A. De Salvo ^{75a}, U. De Sanctis ^{76a,76b}, A. De Santo ¹⁴⁶,
 J.B. De Vivie De Regie ⁶⁰, D.V. Dedovich ³⁸, J. Degens ¹¹⁴, A.M. Deiana ⁴⁴, F. Del Corso ^{23b,23a},
 J. Del Peso ⁹⁹, F. Del Rio ^{63a}, F. Deliot ¹³⁵, C.M. Delitzsch ⁴⁹, M. Della Pietra ^{72a,72b},
 D. Della Volpe ⁵⁶, A. Dell'Acqua ³⁶, L. Dell'Asta ^{71a,71b}, M. Delmastro ⁴, P.A. Delsart ⁶⁰,
 S. Demers ¹⁷², M. Demichev ³⁸, S.P. Denisov ³⁷, L. D'Eramo ⁴⁰, D. Derendarz ⁸⁷, F. Derue ¹²⁷,
 P. Dervan ⁹², K. Desch ²⁴, C. Deutsch ²⁴, F.A. Di Bello ^{57b,57a}, A. Di Ciaccio ^{76a,76b},
 L. Di Ciaccio ⁴, A. Di Domenico ^{75a,75b}, C. Di Donato ^{72a,72b}, A. Di Girolamo ³⁶,
 G. Di Gregorio ⁵, A. Di Luca ^{78a,78b}, B. Di Micco ^{77a,77b}, R. Di Nardo ^{77a,77b}, C. Diaconu ¹⁰²,
 M. Diamantopoulou ³⁴, F.A. Dias ¹¹⁴, T. Dias Do Vale ¹⁴², M.A. Diaz ^{137a,137b},
 F.G. Diaz Capriles ²⁴, M. Didenko ¹⁶³, E.B. Diehl ¹⁰⁶, L. Diehl ⁵⁴, S. Díez Cornell ⁴⁸,
 C. Díez Pardos ¹⁴¹, C. Dimitriadi ^{161,24,161}, A. Dimitrievska ^{17a}, J. Dingfelder ²⁴, I-M. Dinu ^{27b},
 S.J. Dittmeier ^{63b}, F. Dittus ³⁶, F. Djama ¹⁰², T. Djobava ^{149b}, J.I. Djuvsland ¹⁶,
 C. Doglioni ^{101,98}, A. Dohnalova ^{28a}, J. Dolejsi ¹³³, Z. Dolezal ¹³³, K.M. Dona ³⁹,
 M. Donadelli ^{83c}, B. Dong ¹⁰⁷, J. Donini ⁴⁰, A. D'Onofrio ^{77a,77b}, M. D'Onofrio ⁹²,
 J. Dopke ¹³⁴, A. Doria ^{72a}, N. Dos Santos Fernandes ^{130a}, P. Dougan ¹⁰¹, M.T. Dova ⁹⁰,
 A.T. Doyle ⁵⁹, M.A. Draguet ¹²⁶, E. Dreyer ¹⁶⁹, I. Drivas-koulouris ¹⁰, A.S. Drobac ¹⁵⁸,
 M. Drozdova ⁵⁶, D. Du ^{62a}, T.A. du Pree ¹¹⁴, F. Dubinin ³⁷, M. Dubovsky ^{28a}, E. Duchovni ¹⁶⁹,
 G. Duckeck ¹⁰⁹, O.A. Ducu ^{27b}, D. Duda ⁵², A. Dudarev ³⁶, E.R. Duden ²⁶, M. D'uffizi ¹⁰¹,
 L. Duflot ⁶⁶, M. Dührssen ³⁶, C. Dülsen ¹⁷¹, A.E. Dumitriu ^{27b}, M. Dunford ^{63a}, S. Dungs ⁴⁹,
 K. Dunne ^{47a,47b}, A. Duperrin ¹⁰², H. Duran Yildiz ^{3a}, M. Düren ⁵⁸, A. Durglishvili ^{149b},
 B.L. Dwyer ¹¹⁵, G.I. Dyckes ^{17a}, M. Dyndal ^{86a}, S. Dysch ¹⁰¹, B.S. Dziedzic ⁸⁷,
 Z.O. Earnshaw ¹⁴⁶, G.H. Eberwein ¹²⁶, B. Eckerova ^{28a}, S. Eggebrecht ⁵⁵,
 E. Egidio Purcino De Souza ¹²⁷, L.F. Ehrke ⁵⁶, G. Eigen ¹⁶, K. Einsweiler ^{17a}, T. Ekelof ¹⁶¹,
 P.A. Ekman ⁹⁸, S. El Farkh ^{35b}, Y. El Ghazali ^{35b}, H. El Jarrari ^{35e,148}, A. El Moussaouy ^{35a},
 V. Ellajosyula ¹⁶¹, M. Ellert ¹⁶¹, F. Ellinghaus ¹⁷¹, A.A. Elliot ⁹⁴, N. Ellis ³⁶, J. Elmsheuser ²⁹,
 M. Elsing ³⁶, D. Emelianov ¹³⁴, Y. Enari ¹⁵³, I. Ene ^{17a}, S. Epari ¹³, J. Erdmann ⁴⁹,
 P.A. Erland ⁸⁷, M. Errenst ¹⁷¹, M. Escalier ⁶⁶, C. Escobar ¹⁶³, E. Etzion ¹⁵¹, G. Evans ^{130a},

H. Evans [id](#)⁶⁸, L.S. Evans [id](#)⁹⁵, M.O. Evans [id](#)¹⁴⁶, A. Ezhilov [id](#)³⁷, S. Ezzarqtouni [id](#)^{35a}, F. Fabbri [id](#)⁵⁹,
 L. Fabbri [id](#)^{23b,23a}, G. Facini [id](#)⁹⁶, V. Fadeyev [id](#)¹³⁶, R.M. Fakhrutdinov [id](#)³⁷, S. Falciano [id](#)^{75a},
 L.F. Falda Ulhoa Coelho [id](#)³⁶, P.J. Falke [id](#)²⁴, J. Faltova [id](#)¹³³, C. Fan [id](#)¹⁶², Y. Fan [id](#)^{14a}, Y. Fang [id](#)^{14a,14e},
 M. Fanti [id](#)^{71a,71b}, M. Faraj [id](#)^{69a,69b}, Z. Farazpay [id](#)⁹⁷, A. Farbin [id](#)⁸, A. Farilla [id](#)^{77a}, T. Farooque [id](#)¹⁰⁷,
 S.M. Farrington [id](#)⁵², F. Fassi [id](#)^{35e}, D. Fassouliotis [id](#)⁹, M. Faucci Giannelli [id](#)^{76a,76b}, W.J. Fawcett [id](#)³²,
 L. Fayard [id](#)⁶⁶, P. Federic [id](#)¹³³, P. Federicova [id](#)¹³¹, O.L. Fedin [id](#)^{37,a}, G. Fedotov [id](#)³⁷, M. Feickert [id](#)¹⁷⁰,
 L. Feligioni [id](#)¹⁰², D.E. Fellers [id](#)¹²³, C. Feng [id](#)^{62b}, M. Feng [id](#)^{14b}, Z. Feng [id](#)¹¹⁴, M.J. Fenton [id](#)¹⁶⁰,
 A.B. Fenyuk [id](#)³⁷, L. Ferencz [id](#)⁴⁸, R.A.M. Ferguson [id](#)⁹¹, S.I. Fernandez Luengo [id](#)^{137f}, M.J.V. Fernoux [id](#)¹⁰²,
 J. Ferrando [id](#)⁴⁸, A. Ferrari [id](#)¹⁶¹, P. Ferrari [id](#)^{114,113}, R. Ferrari [id](#)^{73a}, D. Ferrere [id](#)⁵⁶, C. Ferretti [id](#)¹⁰⁶,
 F. Fiedler [id](#)¹⁰⁰, A. Filipčić [id](#)⁹³, E.K. Filmer [id](#)¹, F. Filthaut [id](#)¹¹³, M.C.N. Fiolhais [id](#)^{130a,130c,c},
 L. Fiorini [id](#)¹⁶³, W.C. Fisher [id](#)¹⁰⁷, T. Fitschen [id](#)¹⁰¹, P.M. Fitzhugh [id](#)¹³⁵, I. Fleck [id](#)¹⁴¹, P. Fleischmann [id](#)¹⁰⁶,
 T. Flick [id](#)¹⁷¹, M. Flores [id](#)^{33d,ad}, L.R. Flores Castillo [id](#)^{64a}, L. Flores Sanz De Acedo [id](#)³⁶,
 F.M. Follega [id](#)^{78a,78b}, N. Fomin [id](#)¹⁶, J.H. Foo [id](#)¹⁵⁵, B.C. Forland [id](#)⁶⁸, A. Formica [id](#)¹³⁵, A.C. Forti [id](#)¹⁰¹,
 E. Fortin [id](#)³⁶, A.W. Fortman [id](#)⁶¹, M.G. Foti [id](#)^{17a}, L. Fountas [id](#)^{9j}, D. Fournier [id](#)⁶⁶, H. Fox [id](#)⁹¹,
 P. Francavilla [id](#)^{74a,74b}, S. Francescato [id](#)⁶¹, S. Franchellucci [id](#)⁵⁶, M. Franchini [id](#)^{23b,23a},
 S. Franchino [id](#)^{63a}, D. Francis [id](#)³⁶, L. Franco [id](#)¹¹³, L. Franconi [id](#)⁴⁸, M. Franklin [id](#)⁶¹, G. Frattari [id](#)²⁶,
 A.C. Freegard [id](#)⁹⁴, W.S. Freund [id](#)^{83b}, Y.Y. Frid [id](#)¹⁵¹, J. Friend [id](#)⁵⁹, N. Fritzsche [id](#)⁵⁰, A. Froch [id](#)⁵⁴,
 D. Froidevaux [id](#)³⁶, J.A. Frost [id](#)¹²⁶, Y. Fu [id](#)^{62a}, M. Fujimoto [id](#)^{118,ae}, E. Fullana Torregrosa [id](#)^{163,*},
 K.Y. Fung [id](#)^{64a}, E. Furtado De Simas Filho [id](#)^{83b}, M. Furukawa [id](#)¹⁵³, J. Fuster [id](#)¹⁶³, A. Gabrielli [id](#)^{23b,23a},
 A. Gabrielli [id](#)¹⁵⁵, P. Gadow [id](#)³⁶, G. Gagliardi [id](#)^{57b,57a}, L.G. Gagnon [id](#)^{17a}, E.J. Gallas [id](#)¹²⁶,
 B.J. Gallop [id](#)¹³⁴, K.K. Gan [id](#)¹¹⁹, S. Ganguly [id](#)¹⁵³, J. Gao [id](#)^{62a}, Y. Gao [id](#)⁵², F.M. Garay Walls [id](#)^{137a,137b},
 B. Garcia [id](#)²⁹, C. García [id](#)¹⁶³, A. Garcia Alonso [id](#)¹⁴, A.G. Garcia Caffaro [id](#)¹⁷², J.E. García Navarro [id](#)¹⁶³,
 M. Garcia-Sciveres [id](#)^{17a}, G.L. Gardner [id](#)¹²⁸, R.W. Gardner [id](#)³⁹, N. Garelli [id](#)¹⁵⁸, D. Garg [id](#)⁸⁰,
 R.B. Garg [id](#)^{143,o}, J.M. Gargan [id](#)⁵², C.A. Garner [id](#)¹⁵⁵, S.J. Gasiorowski [id](#)¹³⁸, P. Gaspar [id](#)^{83b}, G. Gaudio [id](#)^{73a},
 V. Gautam [id](#)¹³, P. Gauzzi [id](#)^{75a,75b}, I.L. Gavrilenko [id](#)³⁷, A. Gavrilyuk [id](#)³⁷, C. Gay [id](#)¹⁶⁴, G. Gaycken [id](#)⁴⁸,
 E.N. Gazis [id](#)¹⁰, A.A. Geanta [id](#)^{27b}, C.M. Gee [id](#)¹³⁶, C. Gemme [id](#)^{57b}, M.H. Genest [id](#)⁶⁰,
 S. Gentile [id](#)^{75a,75b}, A.D. Gentry [id](#)¹¹², S. George [id](#)⁹⁵, W.F. George [id](#)²⁰, T. Gerialis [id](#)⁴⁶,
 P. Gessinger-Befurt [id](#)³⁶, M.E. Geyik [id](#)¹⁷¹, M. Ghani [id](#)¹⁶⁷, M. Ghneimat [id](#)¹⁴¹, K. Ghorbanian [id](#)⁹⁴,
 A. Ghosal [id](#)¹⁴¹, A. Ghosh [id](#)¹⁶⁰, A. Ghosh [id](#)⁷, B. Giacobbe [id](#)^{23b}, S. Giagu [id](#)^{75a,75b}, T. Giani [id](#)¹¹⁴,
 P. Giannetti [id](#)^{74a}, A. Giannini [id](#)^{62a}, S.M. Gibson [id](#)⁹⁵, M. Gignac [id](#)¹³⁶, D.T. Gil [id](#)^{86b}, A.K. Gilbert [id](#)^{86a},
 B.J. Gilbert [id](#)⁴¹, D. Gillberg [id](#)³⁴, G. Gilles [id](#)¹¹⁴, N.E.K. Gillwald [id](#)⁴⁸, L. Ginabat [id](#)¹²⁷,
 D.M. Gingrich [id](#)^{2,ah}, M.P. Giordani [id](#)^{69a,69c}, P.F. Giraud [id](#)¹³⁵, G. Giugliarelli [id](#)^{69a,69c}, D. Giugni [id](#)^{71a},
 F. Giuli [id](#)³⁶, I. Gkialas [id](#)^{9j}, L.K. Gladilin [id](#)³⁷, C. Glasman [id](#)⁹⁹, G.R. Gledhill [id](#)¹²³, G. Glemža [id](#)⁴⁸,
 M. Glisic [id](#)¹²³, I. Gnesi [id](#)^{43b,f}, Y. Go [id](#)^{29,aj}, M. Goblirsch-Kolb [id](#)³⁶, B. Gocke [id](#)⁴⁹, D. Godin [id](#)¹⁰⁸,
 B. Gokturk [id](#)^{21a}, S. Goldfarb [id](#)¹⁰⁵, T. Golling [id](#)⁵⁶, M.G.D. Gololo [id](#)^{33g}, D. Golubkov [id](#)³⁷,
 J.P. Gombas [id](#)¹⁰⁷, A. Gomes [id](#)^{130a,130b}, G. Gomes Da Silva [id](#)¹⁴¹, A.J. Gomez Delegido [id](#)¹⁶³,
 R. Gonçalves [id](#)^{130a,130c}, G. Gonella [id](#)¹²³, L. Gonella [id](#)²⁰, A. Gongadze [id](#)^{149c}, F. Gonnella [id](#)²⁰,
 J.L. Gonski [id](#)⁴¹, R.Y. González Andana [id](#)⁵², S. González de la Hoz [id](#)¹⁶³, S. Gonzalez Fernandez [id](#)¹³,
 R. Gonzalez Lopez [id](#)⁹², C. Gonzalez Renteria [id](#)^{17a}, M.V. Gonzalez Rodrigues [id](#)⁴⁸,
 R. Gonzalez Suarez [id](#)¹⁶¹, S. Gonzalez-Sevilla [id](#)⁵⁶, G.R. Gonzalvo Rodriguez [id](#)¹⁶³, L. Goossens [id](#)³⁶,
 B. Gorini [id](#)³⁶, E. Gorini [id](#)^{70a,70b}, A. Gorišek [id](#)⁹³, T.C. Gosart [id](#)¹²⁸, A.T. Goshaw [id](#)⁵¹, M.I. Gostkin [id](#)³⁸,
 S. Goswami [id](#)¹²¹, C.A. Gottardo [id](#)³⁶, S.A. Gotz [id](#)¹⁰⁹, M. Goughri [id](#)^{35b}, V. Goumarre [id](#)⁴⁸,
 A.G. Goussiou [id](#)¹³⁸, N. Govender [id](#)^{33c}, I. Grabowska-Bold [id](#)^{86a}, K. Graham [id](#)³⁴, E. Gramstad [id](#)¹²⁵,
 S. Grancagnolo [id](#)^{70a,70b}, M. Grandi [id](#)¹⁴⁶, C.M. Grant [id](#)^{1,135}, P.M. Gravila [id](#)^{27f}, F.G. Gravili [id](#)^{70a,70b},
 H.M. Gray [id](#)^{17a}, M. Greco [id](#)^{70a,70b}, C. Grefe [id](#)²⁴, I.M. Gregor [id](#)⁴⁸, P. Grenier [id](#)¹⁴³, C. Grieco [id](#)¹³,
 A.A. Grillo [id](#)¹³⁶, K. Grimm [id](#)³¹, S. Grinstein [id](#)^{13,t}, J.-F. Grivaz [id](#)⁶⁶, E. Gross [id](#)¹⁶⁹,
 J. Grosse-Knetter [id](#)⁵⁵, C. Grud [id](#)¹⁰⁶, J.C. Grundy [id](#)¹²⁶, L. Guan [id](#)¹⁰⁶, W. Guan [id](#)²⁹, C. Gubbels [id](#)¹⁶⁴,

J.G.R. Guerrero Rojas ¹⁶³, G. Guerrieri ^{69a,69c}, F. Guescini ¹¹⁰, R. Gugel ¹⁰⁰, J.A.M. Guhit ¹⁰⁶, A. Guida ¹⁸, T. Guillemain ⁴, E. Guilloton ^{167,134}, S. Guindon ³⁶, F. Guo ^{14a,14e}, J. Guo ^{62c}, L. Guo ⁴⁸, Y. Guo ¹⁰⁶, R. Gupta ⁴⁸, S. Gurbuz ²⁴, S.S. Gurdasani ⁵⁴, G. Gustavino ³⁶, M. Guth ⁵⁶, P. Gutierrez ¹²⁰, L.F. Gutierrez Zagazeta ¹²⁸, C. Gutschow ⁹⁶, C. Gwenlan ¹²⁶, C.B. Gwilliam ⁹², E.S. Haaland ¹²⁵, A. Haas ¹¹⁷, M. Habedank ⁴⁸, C. Haber ^{17a}, H.K. Hadavand ⁸, A. Hadeef ¹⁰⁰, S. Hadzic ¹¹⁰, J.J. Hahn ¹⁴¹, E.H. Haines ⁹⁶, M. Haleem ¹⁶⁶, J. Haley ¹²¹, J.J. Hall ¹³⁹, G.D. Hallewell ¹⁰², L. Halser ¹⁹, K. Hamano ¹⁶⁵, M. Hamer ²⁴, G.N. Hamity ⁵², E.J. Hampshire ⁹⁵, J. Han ^{62b}, K. Han ^{62a}, L. Han ^{14c}, L. Han ^{62a}, S. Han ^{17a}, Y.F. Han ¹⁵⁵, K. Hanagaki ⁸⁴, M. Hance ¹³⁶, D.A. Hangal ^{41,ac}, H. Hanif ¹⁴², M.D. Hank ¹²⁸, R. Hankache ¹⁰¹, J.B. Hansen ⁴², J.D. Hansen ⁴², P.H. Hansen ⁴², K. Hara ¹⁵⁷, D. Harada ⁵⁶, T. Harenberg ¹⁷¹, S. Harkusha ³⁷, M.L. Harris ¹⁰³, Y.T. Harris ¹²⁶, J. Harrison ¹³, N.M. Harrison ¹¹⁹, P.F. Harrison ¹⁶⁷, N.M. Hartman ¹¹⁰, N.M. Hartmann ¹⁰⁹, Y. Hasegawa ¹⁴⁰, A. Hasib ⁵², S. Haug ¹⁹, R. Hauser ¹⁰⁷, C.M. Hawkes ²⁰, R.J. Hawkins ³⁶, Y. Hayashi ¹⁵³, S. Hayashida ¹¹¹, D. Hayden ¹⁰⁷, C. Hayes ¹⁰⁶, R.L. Hayes ¹¹⁴, C.P. Hays ¹²⁶, J.M. Hays ⁹⁴, H.S. Hayward ⁹², F. He ^{62a}, M. He ^{14a,14e}, Y. He ¹⁵⁴, Y. He ⁴⁸, N.B. Heatley ⁹⁴, V. Hedberg ⁹⁸, A.L. Heggelund ¹²⁵, N.D. Hehir ^{94,*}, C. Heidegger ⁵⁴, K.K. Heidegger ⁵⁴, W.D. Heidorn ⁸¹, J. Heilman ³⁴, S. Heim ⁴⁸, T. Heim ^{17a}, J.G. Heinlein ¹²⁸, J.J. Heinrich ¹²³, L. Heinrich ^{110,af}, J. Hejbal ¹³¹, L. Helary ⁴⁸, A. Held ¹⁷⁰, S. Hellesund ¹⁶, C.M. Helling ¹⁶⁴, S. Hellman ^{47a,47b}, R.C.W. Henderson ⁹¹, L. Henkelmann ³², A.M. Henriques Correia ³⁶, H. Herde ⁹⁸, Y. Hernández Jiménez ¹⁴⁵, L.M. Herrmann ²⁴, T. Herrmann ⁵⁰, G. Herten ⁵⁴, R. Hertenberger ¹⁰⁹, L. Hervas ³⁶, M.E. Hespings ¹⁰⁰, N.P. Hessey ^{156a}, H. Hibi ⁸⁵, S.J. Hillier ²⁰, J.R. Hinds ¹⁰⁷, F. Hinterkeuser ²⁴, M. Hirose ¹²⁴, S. Hirose ¹⁵⁷, D. Hirschbuehl ¹⁷¹, T.G. Hitchings ¹⁰¹, B. Hiti ⁹³, J. Hobbs ¹⁴⁵, R. Hobincu ^{27e}, N. Hod ¹⁶⁹, M.C. Hodgkinson ¹³⁹, B.H. Hodgkinson ³², A. Hoecker ³⁶, J. Hofer ⁴⁸, T. Holm ²⁴, M. Holzbock ¹¹⁰, L.B.A.H. Hommels ³², B.P. Honan ¹⁰¹, J. Hong ^{62c}, T.M. Hong ¹²⁹, B.H. Hooberman ¹⁶², W.H. Hopkins ⁶, Y. Horii ¹¹¹, S. Hou ¹⁴⁸, A.S. Howard ⁹³, J. Howarth ⁵⁹, J. Hoya ⁶, M. Hrabovsky ¹²², A. Hrynevich ⁴⁸, T. Hryn'ova ⁴, P.J. Hsu ⁶⁵, S.-C. Hsu ¹³⁸, Q. Hu ^{62a}, Y.F. Hu ^{14a,14e}, S. Huang ^{64b}, X. Huang ^{14c}, Y. Huang ¹³⁹, Y. Huang ^{14a}, Z. Huang ¹⁰¹, Z. Hubacek ¹³², M. Huebner ²⁴, F. Huegging ²⁴, T.B. Huffman ¹²⁶, C.A. Hugli ⁴⁸, M. Huhtinen ³⁶, S.K. Huiberts ¹⁶, R. Hulsken ¹⁰⁴, N. Huseynov ^{12,a}, J. Huston ¹⁰⁷, J. Huth ⁶¹, R. Hyneman ¹⁴³, G. Iacobucci ⁵⁶, G. Iakovidis ²⁹, I. Ibragimov ¹⁴¹, L. Iconomidou-Fayard ⁶⁶, P. Iengo ^{72a,72b}, R. Iguchi ¹⁵³, T. Iizawa ¹²⁶, Y. Ikegami ⁸⁴, N. Ilic ¹⁵⁵, H. Imam ^{35a}, M. Ince Lezki ⁵⁶, T. Ingebretsen Carlson ^{47a,47b}, G. Introzzi ^{73a,73b}, M. Iodice ^{77a}, V. Ippolito ^{75a,75b}, R.K. Irwin ⁹², M. Ishino ¹⁵³, W. Islam ¹⁷⁰, C. Issever ^{18,48}, S. Istin ^{21a,al}, H. Ito ¹⁶⁸, J.M. Iturbe Ponce ^{64a}, R. Iuppa ^{78a,78b}, A. Ivina ¹⁶⁹, J.M. Izen ⁴⁵, V. Izzo ^{72a}, P. Jacka ^{131,132}, P. Jackson ¹, R.M. Jacobs ⁴⁸, B.P. Jaeger ¹⁴², C.S. Jagfeld ¹⁰⁹, G. Jain ^{156a}, P. Jain ⁵⁴, G. Jäkel ¹⁷¹, K. Jakobs ⁵⁴, T. Jakoubek ¹⁶⁹, J. Jamieson ⁵⁹, K.W. Janas ^{86a}, M. Javurkova ¹⁰³, F. Jeanneau ¹³⁵, L. Jeanty ¹²³, J. Jejelava ^{149a,aa}, P. Jenni ^{54,g}, C.E. Jessiman ³⁴, S. Jézéquel ⁴, C. Jia ^{62b}, J. Jia ¹⁴⁵, X. Jia ⁶¹, X. Jia ^{14a,14e}, Z. Jia ^{14c}, Y. Jiang ^{62a}, S. Jiggins ⁴⁸, J. Jimenez Pena ¹³, S. Jin ^{14c}, A. Jinaru ^{27b}, O. Jinnouchi ¹⁵⁴, P. Johansson ¹³⁹, K.A. Johns ⁷, J.W. Johnson ¹³⁶, D.M. Jones ³², E. Jones ⁴⁸, P. Jones ³², R.W.L. Jones ⁹¹, T.J. Jones ⁹², H.L. Joos ^{55,36}, R. Joshi ¹¹⁹, J. Jovicevic ¹⁵, X. Ju ^{17a}, J.J. Junggeburth ¹⁰³, T. Junkermann ^{63a}, A. Juste Rozas ^{13,t}, M.K. Juzek ⁸⁷, S. Kabana ^{137e}, A. Kaczmarska ⁸⁷, M. Kado ¹¹⁰, H. Kagan ¹¹⁹, M. Kagan ¹⁴³, A. Kahn ⁴¹, A. Kahn ¹²⁸, C. Kahra ¹⁰⁰, T. Kaji ¹⁵³, E. Kajomovitz ¹⁵⁰, N. Kakati ¹⁶⁹, I. Kalaitzidou ⁵⁴, C.W. Kalderon ²⁹, A. Kamenshchikov ¹⁵⁵, N.J. Kang ¹³⁶, D. Kar ^{33g}, K. Karava ¹²⁶, M.J. Kareem ^{156b}, E. Karentzos ⁵⁴, I. Karknias ¹⁵², O. Karkout ¹¹⁴, S.N. Karpov ³⁸, Z.M. Karpova ³⁸, V. Kartvelishvili ⁹¹, A.N. Karyukhin ³⁷,

E. Kasimi ¹⁵², J. Katzy ⁴⁸, S. Kaur ³⁴, K. Kawade ¹⁴⁰, M.P. Kawale ¹²⁰, T. Kawamoto ¹³⁵,
 E.F. Kay ³⁶, F.I. Kaya ¹⁵⁸, S. Kazakos ¹⁰⁷, V.F. Kazanin ³⁷, Y. Ke ¹⁴⁵, J.M. Keaveney ^{33a},
 R. Keeler ¹⁶⁵, G.V. Kehris ⁶¹, J.S. Keller ³⁴, A.S. Kelly ⁹⁶, J.J. Kempster ¹⁴⁶, K.E. Kennedy ⁴¹,
 P.D. Kennedy ¹⁰⁰, O. Kepka ¹³¹, B.P. Kerridge ¹⁶⁷, S. Kersten ¹⁷¹, B.P. Kerševan ⁹³,
 S. Keshri ⁶⁶, L. Keszeghova ^{28a}, S. Ketabchi Haghghat ¹⁵⁵, M. Khandoga ¹²⁷, A. Khanov ¹²¹,
 A.G. Kharlamov ³⁷, T. Kharlamova ³⁷, E.E. Khoda ¹³⁸, T.J. Khoo ¹⁸, G. Khorauli ¹⁶⁶,
 J. Khubua ^{149b}, Y.A.R. Khwaira ⁶⁶, A. Kilgallon ¹²³, D.W. Kim ^{47a,47b}, Y.K. Kim ³⁹,
 N. Kimura ⁹⁶, M.K. Kingston ⁵⁵, A. Kirchhoff ⁵⁵, C. Kirfel ²⁴, F. Kirfel ²⁴, J. Kirk ¹³⁴,
 A.E. Kiryunin ¹¹⁰, C. Kitsaki ¹⁰, O. Kivernyk ²⁴, M. Klassen ^{63a}, C. Klein ³⁴, L. Klein ¹⁶⁶,
 M.H. Klein ¹⁰⁶, M. Klein ⁹², S.B. Klein ⁵⁶, U. Klein ⁹², P. Klimek ³⁶, A. Klimentov ²⁹,
 T. Klioutchnikova ³⁶, P. Kluit ¹¹⁴, S. Kluth ¹¹⁰, E. Kneringer ⁷⁹, T.M. Knight ¹⁵⁵, A. Knue ⁴⁹,
 R. Kobayashi ⁸⁸, D. Kobylanski ¹⁶⁹, S.F. Koch ¹²⁶, M. Kocian ¹⁴³, P. Kodyš ¹³³,
 D.M. Koeck ¹²³, P.T. Koenig ²⁴, T. Koffas ³⁴, M. Kolb ¹³⁵, I. Koletsou ⁴, T. Komarek ¹²²,
 K. Köneke ⁵⁴, A.X.Y. Kong ¹, T. Kono ¹¹⁸, N. Konstantinidis ⁹⁶, B. Konya ⁹⁸,
 R. Kopeliansky ⁶⁸, S. Koperny ^{86a}, K. Korcyl ⁸⁷, K. Kordas ^{152,e}, G. Koren ¹⁵¹, A. Korn ⁹⁶,
 S. Korn ⁵⁵, I. Korolkov ¹³, N. Korotkova ³⁷, B. Kortman ¹¹⁴, O. Kortner ¹¹⁰, S. Kortner ¹¹⁰,
 W.H. Kostecka ¹¹⁵, V.V. Kostyukhin ¹⁴¹, A. Kotsokechagia ¹³⁵, A. Kotwal ⁵¹, A. Koulouris ³⁶,
 A. Kourkoumeli-Charalampidi ^{73a,73b}, C. Kourkoumelis ⁹, E. Kourlitis ^{110,af}, O. Kovanda ¹⁴⁶,
 R. Kowalewski ¹⁶⁵, W. Kozanecki ¹³⁵, A.S. Kozhin ³⁷, V.A. Kramarenko ³⁷, G. Kramberger ⁹³,
 P. Kramer ¹⁰⁰, M.W. Krasny ¹²⁷, A. Krasznahorkay ³⁶, J.W. Kraus ¹⁷¹, J.A. Kremer ¹⁰⁰,
 T. Kresse ⁵⁰, L. Kretschmann ¹⁷¹, J. Kretzschmar ⁹², K. Kreul ¹⁸, P. Krieger ¹⁵⁵,
 S. Krishnamurthy ¹⁰³, M. Krivos ¹³³, K. Krizka ²⁰, K. Kroeninger ⁴⁹, H. Kroha ¹¹⁰, J. Kroll ¹³¹,
 J. Kroll ¹²⁸, K.S. Krowpman ¹⁰⁷, U. Kruchonak ³⁸, H. Krüger ²⁴, N. Krumnack ⁸¹, M.C. Kruse ⁵¹,
 J.A. Krzysiak ⁸⁷, O. Kuchinskaia ³⁷, S. Kuday ^{3a}, S. Kuehn ³⁶, R. Kuesters ⁵⁴, T. Kuhl ⁴⁸,
 V. Kukhtin ³⁸, Y. Kulchitsky ^{37,a}, S. Kuleshov ^{137d,137b}, M. Kumar ^{33g}, N. Kumari ⁴⁸,
 A. Kupco ¹³¹, T. Kupfer ⁴⁹, A. Kupich ³⁷, O. Kuprash ⁵⁴, H. Kurashige ⁸⁵, L.L. Kurchaninov ^{156a},
 O. Kurdysh ⁶⁶, Y.A. Kurochkin ³⁷, A. Kurova ³⁷, M. Kuze ¹⁵⁴, A.K. Kvam ¹⁰³, J. Kvitá ¹²²,
 T. Kwan ¹⁰⁴, N.G. Kyriacou ¹⁰⁶, L.A.O. Laatu ¹⁰², C. Lacasta ¹⁶³, F. Lacava ^{75a,75b},
 H. Lacker ¹⁸, D. Lacour ¹²⁷, N.N. Lad ⁹⁶, E. Ladygin ³⁸, B. Laforge ¹²⁷, T. Lagouri ^{137e},
 F.Z. Lahbabi ^{35a}, S. Lai ⁵⁵, I.K. Lakomic ^{86a}, N. Lalloue ⁶⁰, J.E. Lambert ¹⁶⁵, S. Lammers ⁶⁸,
 W. Lampl ⁷, C. Lampoudis ^{152,e}, A.N. Lancaster ¹¹⁵, E. Lançon ²⁹, U. Landgraf ⁵⁴,
 M.P.J. Landon ⁹⁴, V.S. Lang ⁵⁴, R.J. Langenberg ¹⁰³, O.K.B. Langrekken ¹²⁵, A.J. Lankford ¹⁶⁰,
 F. Lanni ³⁶, K. Lantzsch ²⁴, A. Lanza ^{73a}, A. Lapertosa ^{57b,57a}, J.F. Laporte ¹³⁵, T. Lari ^{71a},
 F. Lasagni Manghi ^{23b}, M. Lassnig ³⁶, V. Latonova ¹³¹, A. Laudrain ¹⁰⁰, A. Laurier ¹⁵⁰,
 S.D. Lawlor ⁹⁵, Z. Lawrence ¹⁰¹, M. Lazzaroni ^{71a,71b}, B. Le ¹⁰¹, E.M. Le Boulicaut ⁵¹,
 B. Leban ⁹³, A. Lebedev ⁸¹, M. LeBlanc ¹⁰¹, F. Ledroit-Guillon ⁶⁰, A.C.A. Lee ⁹⁶, S.C. Lee ¹⁴⁸,
 S. Lee ^{47a,47b}, T.F. Lee ⁹², L.L. Leeuw ^{33c}, H.P. Lefebvre ⁹⁵, M. Lefebvre ¹⁶⁵, C. Leggett ^{17a},
 G. Lehmann Miotto ³⁶, M. Leigh ⁵⁶, W.A. Leight ¹⁰³, W. Leinonen ¹¹³, A. Leisos ^{152,s},
 M.A.L. Leite ^{83c}, C.E. Leitgeb ⁴⁸, R. Leitner ¹³³, K.J.C. Leney ⁴⁴, T. Lenz ²⁴, S. Leone ^{74a},
 C. Leonidopoulos ⁵², A. Leopold ¹⁴⁴, C. Leroy ¹⁰⁸, R. Les ¹⁰⁷, C.G. Lester ³²,
 M. Levchenko ³⁷, J. Levêque ⁴, D. Levin ¹⁰⁶, L.J. Levinson ¹⁶⁹, M.P. Lewicki ⁸⁷, D.J. Lewis ⁴,
 A. Li ⁵, B. Li ^{62b}, C. Li ^{62a}, C-Q. Li ^{62c}, H. Li ^{62a}, H. Li ^{62b}, H. Li ^{14c}, H. Li ^{14b}, H. Li ^{62b},
 K. Li ¹³⁸, L. Li ^{62c}, M. Li ^{14a,14e}, Q.Y. Li ^{62a}, S. Li ^{14a,14e}, S. Li ^{62d,62c,d}, T. Li ⁵, X. Li ¹⁰⁴,
 Z. Li ¹²⁶, Z. Li ¹⁰⁴, Z. Li ⁹², Z. Li ^{14a,14e}, S. Liang ^{14a,14e}, Z. Liang ^{14a}, M. Liberatore ¹³⁵,
 B. Liberti ^{76a}, K. Lie ^{64c}, J. Lieber Marin ^{83b}, H. Lien ⁶⁸, K. Lin ¹⁰⁷, R.E. Lindley ⁷,
 J.H. Lindon ², E. Lipeles ¹²⁸, A. Lipniacka ¹⁶, A. Lister ¹⁶⁴, J.D. Little ⁴, B. Liu ^{14a},
 B.X. Liu ¹⁴², D. Liu ^{62d,62c}, J.B. Liu ^{62a}, J.K.K. Liu ³², K. Liu ^{62d,62c}, M. Liu ^{62a},

M.Y. Liu ^{62a}, P. Liu ^{14a}, Q. Liu ^{62d,138,62c}, X. Liu ^{62a}, Y. Liu ^{14d,14e}, Y.L. Liu ^{62b}, Y.W. Liu ^{62a},
J. Llorente Merino ¹⁴², S.L. Lloyd ⁹⁴, E.M. Lobodzinska ⁴⁸, P. Loch ⁷, S. Loffredo ^{76a,76b},
T. Lohse ¹⁸, K. Lohwasser ¹³⁹, E. Loiacono ⁴⁸, M. Lokajicek ^{131,*}, J.D. Lomas ²⁰,
J.D. Long ¹⁶², I. Longarini ¹⁶⁰, L. Longo ^{70a,70b}, R. Longo ¹⁶², I. Lopez Paz ⁶⁷,
A. Lopez Solis ⁴⁸, J. Lorenz ¹⁰⁹, N. Lorenzo Martinez ⁴, A.M. Lory ¹⁰⁹,
G. Löschcke Centeno ¹⁴⁶, O. Loseva ³⁷, X. Lou ^{47a,47b}, X. Lou ^{14a,14e}, A. Lounis ⁶⁶, J. Love ⁶,
P.A. Love ⁹¹, G. Lu ^{14a,14e}, M. Lu ⁸⁰, S. Lu ¹²⁸, Y.J. Lu ⁶⁵, H.J. Lubatti ¹³⁸, C. Luci ^{75a,75b},
F.L. Lucio Alves ^{14c}, A. Lucotte ⁶⁰, F. Luehring ⁶⁸, I. Luise ¹⁴⁵, O. Lukianchuk ⁶⁶,
O. Lundberg ¹⁴⁴, B. Lund-Jensen ¹⁴⁴, N.A. Luongo ¹²³, M.S. Lutz ¹⁵¹, D. Lynn ²⁹, H. Lyons ⁹²,
R. Lysak ¹³¹, E. Lytken ⁹⁸, V. Lyubushkin ³⁸, T. Lyubushkina ³⁸, M.M. Lyukova ¹⁴⁵, H. Ma ²⁹,
K. Ma ^{62a}, L.L. Ma ^{62b}, Y. Ma ¹²¹, D.M. Mac Donell ¹⁶⁵, G. Maccarrone ⁵³, J.C. MacDonald ¹⁰⁰,
P.C. Machado De Abreu Farias ^{83b}, R. Madar ⁴⁰, W.F. Mader ⁵⁰, T. Madula ⁹⁶, J. Maeda ⁸⁵,
T. Maeno ²⁹, M. Maerker ⁵⁰, H. Maguire ¹³⁹, V. Maiboroda ¹³⁵, A. Maio ^{130a,130b,130d},
K. Maj ^{86a}, O. Majersky ⁴⁸, S. Majewski ¹²³, N. Makovec ⁶⁶, V. Maksimovic ¹⁵,
B. Malaescu ¹²⁷, Pa. Malecki ⁸⁷, V.P. Maleev ³⁷, F. Malek ⁶⁰, M. Mali ⁹³, D. Malito ⁹⁵,
U. Mallik ⁸⁰, S. Maltezos ¹⁰, S. Malyukov ³⁸, J. Mamuzic ¹³, G. Mancini ⁵³, G. Manco ^{73a,73b},
J.P. Mandalia ⁹⁴, I. Mandić ⁹³, L. Manhaes de Andrade Filho ^{83a}, I.M. Maniatis ¹⁶⁹,
J. Manjarres Ramos ^{102,ab}, D.C. Mankad ¹⁶⁹, A. Mann ¹⁰⁹, B. Mansoulie ¹³⁵, S. Manzoni ³⁶,
A. Marantis ^{152,s}, G. Marchiori ⁵, M. Marcisovsky ¹³¹, C. Marcon ^{71a}, M. Marinescu ²⁰,
M. Marjanovic ¹²⁰, E.J. Marshall ⁹¹, Z. Marshall ^{17a}, S. Marti-Garcia ¹⁶³, T.A. Martin ¹⁶⁷,
V.J. Martin ⁵², B. Martin dit Latour ¹⁶, L. Martinelli ^{75a,75b}, M. Martinez ^{13,t},
P. Martinez Agullo ¹⁶³, V.I. Martinez Outschoorn ¹⁰³, P. Martinez Suarez ¹³, S. Martin-Haugh ¹³⁴,
V.S. Martoiu ^{27b}, A.C. Martyniuk ⁹⁶, A. Marzin ³⁶, D. Mascione ^{78a,78b}, L. Masetti ¹⁰⁰,
T. Mashimo ¹⁵³, J. Masik ¹⁰¹, A.L. Maslennikov ³⁷, L. Massa ^{23b}, P. Massarotti ^{72a,72b},
P. Mastrandrea ^{74a,74b}, A. Mastroberardino ^{43b,43a}, T. Masubuchi ¹⁵³, T. Mathisen ¹⁶¹,
J. Matousek ¹³³, N. Matsuzawa ¹⁵³, J. Maurer ^{27b}, B. Maček ⁹³, D.A. Maximov ³⁷, R. Mazini ¹⁴⁸,
I. Maznas ¹⁵², M. Mazza ¹⁰⁷, S.M. Mazza ¹³⁶, E. Mazzeo ^{71a,71b}, C. Mc Ginn ²⁹,
J.P. Mc Gowan ¹⁰⁴, S.P. Mc Kee ¹⁰⁶, E.F. McDonald ¹⁰⁵, A.E. McDougall ¹¹⁴, J.A. Mcfayden ¹⁴⁶,
R.P. McGovern ¹²⁸, G. Mchedlidze ^{149b}, R.P. Mckenzie ^{33g}, T.C. Mclachlan ⁴⁸,
D.J. McLaughlin ⁹⁶, K.D. McLean ¹⁶⁵, S.J. McMahan ¹³⁴, P.C. McNamara ¹⁰⁵,
C.M. Mcpartland ⁹², R.A. McPherson ^{165,x}, S. Mehlhase ¹⁰⁹, A. Mehta ⁹², D. Melini ¹⁵⁰,
B.R. Mellado Garcia ^{33g}, A.H. Melo ⁵⁵, F. Meloni ⁴⁸, A.M. Mendes Jacques Da Costa ¹⁰¹,
H.Y. Meng ¹⁵⁵, L. Meng ⁹¹, S. Menke ¹¹⁰, M. Mentink ³⁶, E. Meoni ^{43b,43a}, C. Merlassino ¹²⁶,
L. Merola ^{72a,72b}, C. Meroni ^{71a,71b}, G. Merz ¹⁰⁶, O. Meshkov ³⁷, J. Metcalfe ⁶, A.S. Mete ⁶,
C. Meyer ⁶⁸, J-P. Meyer ¹³⁵, R.P. Middleton ¹³⁴, L. Mijović ⁵², G. Mikenberg ¹⁶⁹,
M. Mkestikova ¹³¹, M. Mikuž ⁹³, H. Mildner ¹⁰⁰, A. Milic ³⁶, C.D. Milke ⁴⁴, D.W. Miller ³⁹,
L.S. Miller ³⁴, A. Milov ¹⁶⁹, D.A. Milstead ^{47a,47b}, T. Min ^{14c}, A.A. Minaenko ³⁷,
I.A. Minashvili ^{149b}, L. Mince ⁵⁹, A.I. Mincer ¹¹⁷, B. Mindur ^{86a}, M. Mineev ³⁸, Y. Mino ⁸⁸,
L.M. Mir ¹³, M. Miralles Lopez ¹⁶³, M. Mironova ^{17a}, A. Mishima ¹⁵³, M.C. Missio ¹¹³,
A. Mitra ¹⁶⁷, V.A. Mitsou ¹⁶³, Y. Mitsumori ¹¹¹, O. Miu ¹⁵⁵, P.S. Miyagawa ⁹⁴,
T. Mkrtchyan ^{63a}, M. Mlinarevic ⁹⁶, T. Mlinarevic ⁹⁶, M. Mlynarikova ³⁶, S. Mobius ¹⁹,
P. Moder ⁴⁸, P. Mogg ¹⁰⁹, A.F. Mohammed ^{14a,14e}, S. Mohapatra ⁴¹, G. Mokgatitwane ^{33g},
L. Moleri ¹⁶⁹, B. Mondal ¹⁴¹, S. Mondal ¹³², K. Mönig ⁴⁸, E. Monnier ¹⁰²,
L. Monsonis Romero ¹⁶³, J. Montejo Berlingen ¹³, M. Montella ¹¹⁹, F. Montekali ^{77a,77b},
F. Monticelli ⁹⁰, S. Monzani ^{69a,69c}, N. Morange ⁶⁶, A.L. Moreira De Carvalho ^{130a},
M. Moreno Llácer ¹⁶³, C. Moreno Martinez ⁵⁶, P. Moretini ^{57b}, S. Morgenstern ³⁶, M. Morii ⁶¹,
M. Morinaga ¹⁵³, A.K. Morley ³⁶, F. Morodei ^{75a,75b}, L. Morvaj ³⁶, P. Moschovakos ³⁶,

B. Moser ³⁶, M. Mosidze ^{149b}, T. Moskalets ⁵⁴, P. Moskvitina ¹¹³, J. Moss ^{31,m},
 E.J.W. Moyse ¹⁰³, O. Mtintsilana ^{33g}, S. Muanza ¹⁰², J. Mueller ¹²⁹, D. Muenstermann ⁹¹,
 R. Müller ¹⁹, G.A. Mullier ¹⁶¹, A.J. Mullin³², J.J. Mullin¹²⁸, D.P. Mungo ¹⁵⁵, D. Munoz Perez ¹⁶³,
 F.J. Munoz Sanchez ¹⁰¹, M. Murin ¹⁰¹, W.J. Murray ^{167,134}, A. Murrone ^{71a,71b}, J.M. Muse ¹²⁰,
 M. Muškinja ^{17a}, C. Mwewa ²⁹, A.G. Myagkov ^{37,a}, A.J. Myers ⁸, A.A. Myers¹²⁹, G. Myers ⁶⁸,
 M. Myska ¹³², B.P. Nachman ^{17a}, O. Nackenhorst ⁴⁹, A. Nag ⁵⁰, K. Nagai ¹²⁶, K. Nagano ⁸⁴,
 J.L. Nagle ^{29,aj}, E. Nagy ¹⁰², A.M. Nairz ³⁶, Y. Nakahama ⁸⁴, K. Nakamura ⁸⁴, K. Nakkalil ⁵,
 H. Nanjo ¹²⁴, R. Narayan ⁴⁴, E.A. Narayanan ¹¹², I. Naryshkin ³⁷, M. Naseri ³⁴, S. Nasri ¹⁵⁹,
 C. Nass ²⁴, G. Navarro ^{22a}, J. Navarro-Gonzalez ¹⁶³, R. Nayak ¹⁵¹, A. Nayaz ¹⁸,
 P.Y. Nechaeva ³⁷, F. Nechansky ⁴⁸, L. Nedic ¹²⁶, T.J. Neep ²⁰, A. Negri ^{73a,73b}, M. Negrini ^{23b},
 C. Nellist ¹¹⁴, C. Nelson ¹⁰⁴, K. Nelson ¹⁰⁶, S. Nemecek ¹³¹, M. Nessi ^{36,h}, M.S. Neubauer ¹⁶²,
 F. Neuhaus ¹⁰⁰, J. Neundorf ⁴⁸, R. Newhouse ¹⁶⁴, P.R. Newman ²⁰, C.W. Ng ¹²⁹, Y.W.Y. Ng ⁴⁸,
 B. Ngair ^{35e}, H.D.N. Nguyen ¹⁰⁸, R.B. Nickerson ¹²⁶, R. Nicolaidou ¹³⁵, J. Nielsen ¹³⁶,
 M. Niemeyer ⁵⁵, J. Niermann ^{55,36}, N. Nikiforou ³⁶, V. Nikolaenko ^{37,a}, I. Nikolic-Audit ¹²⁷,
 K. Nikolopoulos ²⁰, P. Nilsson ²⁹, I. Ninca ⁴⁸, H.R. Nindhito ⁵⁶, G. Ninio ¹⁵¹, A. Nisati ^{75a},
 N. Nishu ², R. Nisius ¹¹⁰, J-E. Nitschke ⁵⁰, E.K. Nkadimeng ^{33g}, T. Nobe ¹⁵³, D.L. Noel ³²,
 T. Nommensen ¹⁴⁷, M.B. Norfolk ¹³⁹, R.R.B. Norisam ⁹⁶, B.J. Norman ³⁴, J. Novak ⁹³,
 T. Novak ⁴⁸, L. Novotny ¹³², R. Novotny ¹¹², L. Nozka ¹²², K. Ntekas ¹⁶⁰,
 N.M.J. Nunes De Moura Junior ^{83b}, E. Nurse⁹⁶, J. Ocariz ¹²⁷, A. Ochi ⁸⁵, I. Ochoa ^{130a},
 S. Oerdek ^{48,u}, J.T. Offermann ³⁹, A. Ogrodnik ¹³³, A. Oh ¹⁰¹, C.C. Ohm ¹⁴⁴, H. Oide ⁸⁴,
 R. Oishi ¹⁵³, M.L. Ojeda ⁴⁸, M.W. O'Keefe⁹², Y. Okumura ¹⁵³, L.F. Oleiro Seabra ^{130a},
 S.A. Olivares Pino ^{137d}, D. Oliveira Damazio ²⁹, D. Oliveira Goncalves ^{83a}, J.L. Oliver ¹⁶⁰,
 A. Olszewski ⁸⁷, Ö.O. Öncel ⁵⁴, A.P. O'Neill ¹⁹, A. Onofre ^{130a,130e}, P.U.E. Onyisi ¹¹,
 M.J. Oreglia ³⁹, G.E. Orellana ⁹⁰, D. Orestano ^{77a,77b}, N. Orlando ¹³, R.S. Orr ¹⁵⁵,
 V. O'Shea ⁵⁹, L.M. Osojnak ¹²⁸, R. Ospanov ^{62a}, G. Otero y Garzon ³⁰, H. Otono ⁸⁹,
 P.S. Ott ^{63a}, G.J. Ottino ^{17a}, M. Ouchrif ^{35d}, J. Ouellette ²⁹, F. Ould-Saada ¹²⁵, M. Owen ⁵⁹,
 R.E. Owen ¹³⁴, K.Y. Oyulmaz ^{21a}, V.E. Ozcan ^{21a}, N. Ozturk ⁸, S. Ozturk ⁸², H.A. Pacey ³²,
 A. Pacheco Pages ¹³, C. Padilla Aranda ¹³, G. Padovano ^{75a,75b}, S. Pagan Griso ^{17a},
 G. Palacino ⁶⁸, A. Palazzo ^{70a,70b}, S. Palestini ³⁶, J. Pan ¹⁷², T. Pan ^{64a}, D.K. Panchal ¹¹,
 C.E. Pandini ¹¹⁴, J.G. Panduro Vazquez ⁹⁵, H.D. Pandya ¹, H. Pang ^{14b}, P. Pani ⁴⁸,
 G. Panizzo ^{69a,69c}, L. Paolozzi ⁵⁶, C. Papadatos ¹⁰⁸, S. Parajuli ⁴⁴, A. Paramonov ⁶,
 C. Paraskevopoulos ¹⁰, D. Paredes Hernandez ^{64b}, T.H. Park ¹⁵⁵, M.A. Parker ³², F. Parodi ^{57b,57a},
 E.W. Parrish ¹¹⁵, V.A. Parrish ⁵², J.A. Parsons ⁴¹, U. Parzefall ⁵⁴, B. Pascual Dias ¹⁰⁸,
 L. Pascual Dominguez ¹⁵¹, E. Pasqualucci ^{75a}, S. Passaggio ^{57b}, F. Pastore ⁹⁵, P. Pasuwan ^{47a,47b},
 P. Patel ⁸⁷, U.M. Patel ⁵¹, J.R. Pater ¹⁰¹, T. Pauly ³⁶, J. Parkes ¹⁴³, M. Pedersen ¹²⁵,
 R. Pedro ^{130a}, S.V. Peleganchuk ³⁷, O. Penc ³⁶, E.A. Pender ⁵², H. Peng ^{62a}, K.E. Pensi ¹⁰⁹,
 M. Penzin ³⁷, B.S. Peralva ^{83d}, A.P. Pereira Peixoto ⁶⁰, L. Pereira Sanchez ^{47a,47b},
 D.V. Perepelitsa ^{29,aj}, E. Perez Codina ^{156a}, M. Perganti ¹⁰, L. Perini ^{71a,71b,*}, H. Pernegger ³⁶,
 O. Perrin ⁴⁰, K. Peters ⁴⁸, R.F.Y. Peters ¹⁰¹, B.A. Petersen ³⁶, T.C. Petersen ⁴², E. Petit ¹⁰²,
 V. Petousis ¹³², C. Petridou ^{152,e}, A. Petrukhin ¹⁴¹, M. Pettee ^{17a}, N.E. Pettersson ³⁶,
 A. Petukhov ³⁷, K. Petukhova ¹³³, R. Pezoa ^{137f}, L. Pezzotti ³⁶, G. Pezzullo ¹⁷², T.M. Pham ¹⁷⁰,
 T. Pham ¹⁰⁵, P.W. Phillips ¹³⁴, G. Piacquadio ¹⁴⁵, E. Pianori ^{17a}, F. Piazza ^{71a,71b}, R. Piegai ³⁰,
 D. Pietreanu ^{27b}, A.D. Pilkington ¹⁰¹, M. Pinamonti ^{69a,69c}, J.L. Pinfeld ²,
 B.C. Pinheiro Pereira ^{130a}, A.E. Pinto Pinoargote ^{100,135}, L. Pintucci ^{69a,69c}, K.M. Piper ¹⁴⁶,
 A. Pirttikoski ⁵⁶, D.A. Pizzi ³⁴, L. Pizzimento ^{64b}, A. Pizzini ¹¹⁴, M.-A. Pleier ²⁹, V. Plesanovs⁵⁴,
 V. Pleskot ¹³³, E. Plotnikova³⁸, G. Poddar ⁴, R. Poettgen ⁹⁸, L. Poggioli ¹²⁷, I. Pokharel ⁵⁵,
 S. Polacek ¹³³, G. Polesello ^{73a}, A. Poley ^{142,156a}, R. Polifka ¹³², A. Polini ^{23b}, C.S. Pollard ¹⁶⁷,

Z.B. Pollock ¹¹⁹, V. Polychronakos ²⁹, E. Pompa Pacchi ^{75a,75b}, D. Ponomarenko ¹¹³,
L. Pontecorvo ³⁶, S. Popa ^{27a}, G.A. Popeneciu ^{27d}, A. Poreba ³⁶, D.M. Portillo Quintero ^{156a},
S. Pospisil ¹³², M.A. Postill ¹³⁹, P. Postolache ^{27c}, K. Potamianos ¹⁶⁷, P.A. Potepa ^{86a},
I.N. Potrap ³⁸, C.J. Potter ³², H. Potti ¹, T. Poulsen ⁴⁸, J. Poveda ¹⁶³, M.E. Pozo Astigarraga ³⁶,
A. Prades Ibanez ¹⁶³, J. Pretel ⁵⁴, D. Price ¹⁰¹, M. Primavera ^{70a}, M.A. Principe Martin ⁹⁹,
R. Privara ¹²², T. Procter ⁵⁹, M.L. Proffitt ¹³⁸, N. Proklova ¹²⁸, K. Prokofiev ^{64c}, G. Proto ¹¹⁰,
S. Protopopescu ²⁹, J. Proudfoot ⁶, M. Przybycien ^{86a}, W.W. Przygoda ^{86b}, J.E. Puddefoot ¹³⁹,
D. Pudzha ³⁷, D. Pyatiizbyantseva ³⁷, J. Qian ¹⁰⁶, D. Qichen ¹⁰¹, Y. Qin ¹⁰¹, T. Qiu ⁵²,
A. Quadt ⁵⁵, M. Queitsch-Maitland ¹⁰¹, G. Quetant ⁵⁶, R.P. Quinn ¹⁶⁴, G. Rabanal Bolanos ⁶¹,
D. Rafanoharana ⁵⁴, F. Ragusa ^{71a,71b}, J.L. Rainbolt ³⁹, J.A. Raine ⁵⁶, S. Rajagopalan ²⁹,
E. Ramakoti ³⁷, K. Ran ^{48,14e}, N.P. Rapheeha ^{33g}, H. Rasheed ^{27b}, V. Raskina ¹²⁷,
D.F. Rassloff ^{63a}, S. Rave ¹⁰⁰, B. Ravina ⁵⁵, I. Ravinovich ¹⁶⁹, M. Raymond ³⁶, A.L. Read ¹²⁵,
N.P. Readioff ¹³⁹, D.M. Rebutzi ^{73a,73b}, G. Redlinger ²⁹, A.S. Reed ¹¹⁰, K. Reeves ²⁶,
J.A. Reidelsturz ¹⁷¹, D. Reikher ¹⁵¹, A. Rej ¹⁴¹, C. Rembser ³⁶, A. Renardi ⁴⁸, M. Renda ^{27b},
M.B. Rendel ¹¹⁰, F. Renner ⁴⁸, A.G. Rennie ¹⁶⁰, A.L. Rescia ⁴⁸, S. Resconi ^{71a},
M. Ressegotti ^{57b,57a}, S. Rettie ³⁶, J.G. Reyes Rivera ¹⁰⁷, E. Reynolds ^{17a}, O.L. Rezanova ³⁷,
P. Reznicek ¹³³, N. Ribaric ⁹¹, E. Ricci ^{78a,78b}, R. Richter ¹¹⁰, S. Richter ^{47a,47b},
E. Richter-Was ^{86b}, M. Ridel ¹²⁷, S. Ridouani ^{35d}, P. Rieck ¹¹⁷, P. Riedler ³⁶,
M. Rijssenbeek ¹⁴⁵, A. Rimoldi ^{73a,73b}, M. Rimoldi ⁴⁸, L. Rinaldi ^{23b,23a}, T.T. Rinn ²⁹,
M.P. Rinnagel ¹⁰⁹, G. Ripellino ¹⁶¹, I. Riu ¹³, P. Rivadeneira ⁴⁸, J.C. Rivera Vergara ¹⁶⁵,
F. Rizatdinova ¹²¹, E. Rizvi ⁹⁴, B.A. Roberts ¹⁶⁷, B.R. Roberts ^{17a}, S.H. Robertson ^{104,x},
D. Robinson ³², C.M. Robles Gajardo ^{137f}, M. Robles Manzano ¹⁰⁰, A. Robson ⁵⁹, A. Rocchi ^{76a,76b},
C. Roda ^{74a,74b}, S. Rodriguez Bosca ^{63a}, Y. Rodriguez Garcia ^{22a}, A. Rodriguez Rodriguez ⁵⁴,
A.M. Rodríguez Vera ^{156b}, S. Roe ³⁶, J.T. Roemer ¹⁶⁰, A.R. Roepe-Gier ¹³⁶, J. Roggel ¹⁷¹,
O. Røhne ¹²⁵, R.A. Rojas ¹⁰³, C.P.A. Roland ⁶⁸, J. Roloff ²⁹, A. Romaniouk ³⁷,
E. Romano ^{73a,73b}, M. Romano ^{23b}, A.C. Romero Hernandez ¹⁶², N. Rompotis ⁹², L. Roos ¹²⁷,
S. Rosati ^{75a}, B.J. Rosser ³⁹, E. Rossi ¹²⁶, E. Rossi ^{72a,72b}, L.P. Rossi ^{57b}, L. Rossini ⁵⁴,
R. Rosten ¹¹⁹, M. Rotaru ^{27b}, B. Rottler ⁵⁴, C. Rougier ^{102,ab}, D. Rousseau ⁶⁶, D. Rousso ³²,
A. Roy ¹⁶², S. Roy-Garand ¹⁵⁵, A. Rozanov ¹⁰², Y. Rozen ¹⁵⁰, X. Ruan ^{33g},
A. Rubio Jimenez ¹⁶³, A.J. Ruby ⁹², V.H. Ruelas Rivera ¹⁸, T.A. Ruggeri ¹, A. Ruggiero ¹²⁶,
A. Ruiz-Martinez ¹⁶³, A. Rummler ³⁶, Z. Rurikova ⁵⁴, N.A. Rusakovich ³⁸, H.L. Russell ¹⁶⁵,
G. Russo ^{75a,75b}, J.P. Rutherford ⁷, S. Rutherford Colmenares ³², K. Rybacki ⁹¹, M. Rybar ¹³³,
E.B. Rye ¹²⁵, A. Ryzhov ⁴⁴, J.A. Sabater Iglesias ⁵⁶, P. Sabatini ¹⁶³, L. Sabetta ^{75a,75b},
H.F-W. Sadrozinski ¹³⁶, F. Safai Tehrani ^{75a}, B. Safarzadeh Samani ¹⁴⁶, M. Safdari ¹⁴³,
S. Saha ¹⁶⁵, M. Sahinsoy ¹¹⁰, M. Saimpert ¹³⁵, M. Saito ¹⁵³, T. Saito ¹⁵³, D. Salamani ³⁶,
A. Salnikov ¹⁴³, J. Salt ¹⁶³, A. Salvador Salas ¹³, D. Salvatore ^{43b,43a}, F. Salvatore ¹⁴⁶,
A. Salzburger ³⁶, D. Sammel ⁵⁴, D. Sampsonidis ^{152,e}, D. Sampsonidou ¹²³, J. Sánchez ¹⁶³,
A. Sanchez Pineda ⁴, V. Sanchez Sebastian ¹⁶³, H. Sandaker ¹²⁵, C.O. Sander ⁴⁸,
J.A. Sandesara ¹⁰³, M. Sandhoff ¹⁷¹, C. Sandoval ^{22b}, D.P.C. Sankey ¹³⁴, T. Sano ⁸⁸,
A. Sansoni ⁵³, L. Santi ^{75a,75b}, C. Santoni ⁴⁰, H. Santos ^{130a,130b}, S.N. Santpur ^{17a}, A. Santra ¹⁶⁹,
K.A. Saoucha ^{116b}, J.G. Saraiva ^{130a,130d}, J. Sardain ⁷, O. Sasaki ⁸⁴, K. Sato ¹⁵⁷, C. Sauer ^{63b},
F. Sauerburger ⁵⁴, E. Sauvan ⁴, P. Savard ^{155,ah}, R. Sawada ¹⁵³, C. Sawyer ¹³⁴, L. Sawyer ⁹⁷,
I. Sayago Galvan ¹⁶³, C. Sbarra ^{23b}, A. Sbrizzi ^{23b,23a}, T. Scanlon ⁹⁶, J. Schaarschmidt ¹³⁸,
P. Schacht ¹¹⁰, D. Schaefer ³⁹, U. Schäfer ¹⁰⁰, A.C. Schaffer ^{66,44}, D. Schaile ¹⁰⁹,
R.D. Schamberger ¹⁴⁵, C. Scharf ¹⁸, M.M. Schefer ¹⁹, V.A. Schegelsky ³⁷, D. Scheirich ¹³³,
F. Schenck ¹⁸, M. Schernau ¹⁶⁰, C. Scheulen ⁵⁵, C. Schiavi ^{57b,57a}, E.J. Schioppa ^{70a,70b},
M. Schioppa ^{43b,43a}, B. Schlag ^{143,o}, K.E. Schleicher ⁵⁴, S. Schlenker ³⁶, J. Schmeing ¹⁷¹,

M.A. Schmidt [ID171](#), K. Schmieden [ID100](#), C. Schmitt [ID100](#), S. Schmitt [ID48](#), L. Schoeffel [ID135](#),
A. Schoening [ID63b](#), P.G. Scholer [ID54](#), E. Schopf [ID126](#), M. Schott [ID100](#), J. Schovancova [ID36](#),
S. Schramm [ID56](#), F. Schroeder [ID171](#), T. Schroer [ID56](#), H-C. Schultz-Coulon [ID63a](#), M. Schumacher [ID54](#),
B.A. Schumm [ID136](#), Ph. Schune [ID135](#), A.J. Schuy [ID138](#), H.R. Schwartz [ID136](#), A. Schwartzman [ID143](#),
T.A. Schwarz [ID106](#), Ph. Schwemling [ID135](#), R. Schwienhorst [ID107](#), A. Sciandra [ID136](#), G. Sciolla [ID26](#),
F. Scuri [ID74a](#), C.D. Sebastiani [ID92](#), K. Sedlaczek [ID115](#), P. Seema [ID18](#), S.C. Seidel [ID112](#), A. Seiden [ID136](#),
B.D. Seidlitz [ID41](#), C. Seitz [ID48](#), J.M. Seixas [ID83b](#), G. Sekhniaidze [ID72a](#), S.J. Sekula [ID44](#), L. Selem [ID60](#),
N. Semprini-Cesari [ID23b,23a](#), D. Sengupta [ID56](#), V. Senthilkumar [ID163](#), L. Serin [ID66](#), L. Serkin [ID69a,69b](#),
M. Sessa [ID76a,76b](#), H. Severini [ID120](#), F. Sforza [ID57b,57a](#), A. Sfyrta [ID56](#), E. Shabalina [ID55](#), R. Shaheen [ID144](#),
J.D. Shahinian [ID128](#), D. Shaked Renous [ID169](#), L.Y. Shan [ID14a](#), M. Shapiro [ID17a](#), A. Sharma [ID36](#),
A.S. Sharma [ID164](#), P. Sharma [ID80](#), S. Sharma [ID48](#), P.B. Shatalov [ID37](#), K. Shaw [ID146](#), S.M. Shaw [ID101](#),
A. Shcherbakova [ID37](#), Q. Shen [ID62c,5](#), P. Sherwood [ID96](#), L. Shi [ID96](#), X. Shi [ID14a](#), C.O. Shimmin [ID172](#),
J.D. Shinner [ID95](#), I.P.J. Shipsey [ID126](#), S. Shirabe [ID56,h](#), M. Shiyakova [ID38,v](#), J. Shlomi [ID169](#),
M.J. Shochet [ID39](#), J. Shojaii [ID105](#), D.R. Shope [ID125](#), B. Shrestha [ID120](#), S. Shrestha [ID119,ak](#),
E.M. Shrif [ID33g](#), M.J. Shroff [ID165](#), P. Sicho [ID131](#), A.M. Sickles [ID162](#), E. Sideras Haddad [ID33g](#),
A. Sidoti [ID23b](#), F. Siegert [ID50](#), Dj. Sijacki [ID15](#), R. Sikora [ID86a](#), F. Sili [ID90](#), J.M. Silva [ID20](#),
M.V. Silva Oliveira [ID29](#), S.B. Silverstein [ID47a](#), S. Simion [ID66](#), R. Simoniello [ID36](#), E.L. Simpson [ID59](#),
H. Simpson [ID146](#), L.R. Simpson [ID106](#), N.D. Simpson [ID98](#), S. Simsek [ID82](#), S. Sindhu [ID55](#), P. Sinervo [ID155](#),
S. Singh [ID155](#), S. Sinha [ID48](#), S. Sinha [ID101](#), M. Sioli [ID23b,23a](#), I. Siral [ID36](#), E. Sitnikova [ID48](#),
S.Yu. Sivoklov [ID37,*](#), J. Sjölin [ID47a,47b](#), A. Skaf [ID55](#), E. Skorda [ID20](#), P. Skubic [ID120](#), M. Slawinska [ID87](#),
V. Smakhtin [ID169](#), B.H. Smart [ID134](#), J. Smiesko [ID36](#), S.Yu. Smirnov [ID37](#), Y. Smirnov [ID37](#),
L.N. Smirnova [ID37,a](#), O. Smirnova [ID98](#), A.C. Smith [ID41](#), E.A. Smith [ID39](#), H.A. Smith [ID126](#),
J.L. Smith [ID92](#), R. Smith [ID143](#), M. Smizanska [ID91](#), K. Smolek [ID132](#), A.A. Snesarev [ID37](#), S.R. Snider [ID155](#),
H.L. Snoek [ID114](#), S. Snyder [ID29](#), R. Sobie [ID165,x](#), A. Soffer [ID151](#), C.A. Solans Sanchez [ID36](#),
E.Yu. Soldatov [ID37](#), U. Soldevila [ID163](#), A.A. Solodkov [ID37](#), S. Solomon [ID26](#), A. Soloshenko [ID38](#),
K. Solovieva [ID54](#), O.V. Solovyanov [ID40](#), V. Solovyev [ID37](#), P. Sommer [ID36](#), A. Sonay [ID13](#),
W.Y. Song [ID156b](#), J.M. Sonneveld [ID114](#), A. Sopczak [ID132](#), A.L. Sopio [ID96](#), F. Sopkova [ID28b](#),
V. Sothilingam [ID63a](#), S. Sottocornola [ID68](#), R. Soualah [ID116b](#), Z. Soumami [ID35e](#), D. South [ID48](#),
N. Soybelman [ID169](#), S. Spagnolo [ID70a,70b](#), M. Spalla [ID110](#), D. Sperlich [ID54](#), G. Spigo [ID36](#), S. Spinali [ID91](#),
D.P. Spiteri [ID59](#), M. Spousta [ID133](#), E.J. Staats [ID34](#), A. Stabile [ID71a,71b](#), R. Stamen [ID63a](#), A. Stampekis [ID20](#),
M. Standke [ID24](#), E. Stanecka [ID87](#), M.V. Stange [ID50](#), B. Stanislaus [ID17a](#), M.M. Stanitzki [ID48](#), B. Stapf [ID48](#),
E.A. Starchenko [ID37](#), G.H. Stark [ID136](#), J. Stark [ID102,ab](#), D.M. Starke [ID156b](#), P. Staroba [ID131](#),
P. Starovoitov [ID63a](#), S. Stärz [ID104](#), R. Staszewski [ID87](#), G. Stavropoulos [ID46](#), J. Steentoft [ID161](#),
P. Steinberg [ID29](#), B. Stelzer [ID142,156a](#), H.J. Stelzer [ID129](#), O. Stelzer-Chilton [ID156a](#), H. Stenzel [ID58](#),
T.J. Stevenson [ID146](#), G.A. Stewart [ID36](#), J.R. Stewart [ID121](#), M.C. Stockton [ID36](#), G. Stoicea [ID27b](#),
M. Stolarski [ID130a](#), S. Stonjek [ID110](#), A. Straessner [ID50](#), J. Strandberg [ID144](#), S. Strandberg [ID47a,47b](#),
M. Stratmann [ID171](#), M. Strauss [ID120](#), T. Strebler [ID102](#), P. Strizenec [ID28b](#), R. Ströhmer [ID166](#),
D.M. Strom [ID123](#), L.R. Strom [ID48](#), R. Stroynowski [ID44](#), A. Strubig [ID47a,47b](#), S.A. Stucci [ID29](#),
B. Stugu [ID16](#), J. Stupak [ID120](#), N.A. Styles [ID48](#), D. Su [ID143](#), S. Su [ID62a](#), W. Su [ID62d](#), X. Su [ID62a,66](#),
K. Sugizaki [ID153](#), V.V. Sulin [ID37](#), M.J. Sullivan [ID92](#), D.M.S. Sultan [ID78a,78b](#), L. Sultanaliyeva [ID37](#),
S. Sultansoy [ID3b](#), T. Sumida [ID88](#), S. Sun [ID106](#), S. Sun [ID170](#), O. Sunneborn Gudnadottir [ID161](#), N. Sur [ID102](#),
M.R. Sutton [ID146](#), H. Suzuki [ID157](#), M. Svatos [ID131](#), M. Swiatlowski [ID156a](#), T. Swirski [ID166](#),
I. Sykora [ID28a](#), M. Sykora [ID133](#), T. Sykora [ID133](#), D. Ta [ID100](#), K. Tackmann [ID48,u](#), A. Taffard [ID160](#),
R. Tafirout [ID156a](#), J.S. Tafoya Vargas [ID66](#), E.P. Takeva [ID52](#), Y. Takubo [ID84](#), M. Talby [ID102](#),
A.A. Talyshev [ID37](#), K.C. Tam [ID64b](#), N.M. Tamir [ID151](#), A. Tanaka [ID153](#), J. Tanaka [ID153](#), R. Tanaka [ID66](#),
M. Tanasini [ID57b,57a](#), Z. Tao [ID164](#), S. Tapia Araya [ID137f](#), S. Tapprogge [ID100](#),
A. Tarek Abouelfadl Mohamed [ID107](#), S. Tarem [ID150](#), K. Tariq [ID14a](#), G. Tarna [ID102,27b](#), G.F. Tartarelli [ID71a](#),

P. Tas ¹³³, M. Tasevsky ¹³¹, E. Tassi ^{43b,43a}, A.C. Tate ¹⁶², G. Tateno ¹⁵³, Y. Tayalati ^{35e,w},
 G.N. Taylor ¹⁰⁵, W. Taylor ^{156b}, H. Teagle ⁹², A.S. Tee ¹⁷⁰, R. Teixeira De Lima ¹⁴³,
 P. Teixeira-Dias ⁹⁵, J.J. Teoh ¹⁵⁵, K. Terashi ¹⁵³, J. Terron ⁹⁹, S. Terzo ¹³, M. Testa ⁵³,
 R.J. Teuscher ^{155,x}, A. Thaler ⁷⁹, O. Theiner ⁵⁶, N. Themistokleous ⁵², T. Thevenaux-Pelzer ¹⁰²,
 O. Thielmann ¹⁷¹, D.W. Thomas ⁹⁵, J.P. Thomas ²⁰, E.A. Thompson ^{17a}, P.D. Thompson ²⁰,
 E. Thomson ¹²⁸, Y. Tian ⁵⁵, V. Tikhomirov ^{37,a}, Yu.A. Tikhonov ³⁷, S. Timoshenko ³⁷,
 D. Timoshyn ¹³³, E.X.L. Ting ¹, P. Tipton ¹⁷², S.H. Tlou ^{33g}, A. Tnourji ⁴⁰, K. Todome ¹⁵⁴,
 S. Todorova-Nova ¹³³, S. Todt ⁵⁰, M. Togawa ⁸⁴, J. Tojo ⁸⁹, S. Tokár ^{28a}, K. Tokushuku ⁸⁴,
 O. Toldaiev ⁶⁸, R. Tombs ³², M. Tomoto ^{84,111}, L. Tompkins ^{143,o}, K.W. Topolnicki ^{86b},
 E. Torrence ¹²³, H. Torres ^{102,ab}, E. Torró Pastor ¹⁶³, M. Toscani ³⁰, C. Tosciri ³⁹, M. Tost ¹¹,
 D.R. Tovey ¹³⁹, A. Traeet ¹⁶, I.S. Trandafir ^{27b}, T. Trefzger ¹⁶⁶, A. Tricoli ²⁹, I.M. Trigger ^{156a},
 S. Trincaz-Duvoid ¹²⁷, D.A. Trischuk ²⁶, B. Trocmé ⁶⁰, C. Troncon ^{71a}, L. Truong ^{33c},
 M. Trzebinski ⁸⁷, A. Trzupiek ⁸⁷, F. Tsai ¹⁴⁵, M. Tsai ¹⁰⁶, A. Tsiamis ^{152,e}, P.V. Tsiareshka ³⁷,
 S. Tsigaridas ^{156a}, A. Tsirigotis ^{152,s}, V. Tsiskaridze ¹⁵⁵, E.G. Tskhadadze ^{149a},
 M. Tsopoulou ^{152,e}, Y. Tsujikawa ⁸⁸, I.I. Tsukerman ³⁷, V. Tsulaia ^{17a}, S. Tsuno ⁸⁴, O. Tsur ¹⁵⁰,
 K. Tsuru ¹¹⁸, D. Tsybychev ¹⁴⁵, Y. Tu ^{64b}, A. Tudorache ^{27b}, V. Tudorache ^{27b}, A.N. Tuna ³⁶,
 S. Turchikhin ^{57b,57a}, I. Turk Cakir ^{3a}, R. Turra ^{71a}, T. Turtuvshin ^{38,y}, P.M. Tuts ⁴¹,
 S. Tzamarias ^{152,e}, P. Tzani ¹⁰, E. Tzovara ¹⁰⁰, F. Ukegawa ¹⁵⁷, P.A. Ulloa Poblete ^{137c,137b},
 E.N. Umaka ²⁹, G. Unal ³⁶, M. Unal ¹¹, A. Undrus ²⁹, G. Unel ¹⁶⁰, J. Urban ^{28b},
 P. Urquijo ¹⁰⁵, G. Usai ⁸, R. Ushioda ¹⁵⁴, M. Usman ¹⁰⁸, Z. Uysal ^{21b}, L. Vacavant ¹⁰²,
 V. Vacek ¹³², B. Vachon ¹⁰⁴, K.O.H. Vadla ¹²⁵, T. Vafeiadis ³⁶, A. Vaitkus ⁹⁶, C. Valderanis ¹⁰⁹,
 E. Valdes Santurio ^{47a,47b}, M. Valente ^{156a}, S. Valentinetti ^{23b,23a}, A. Valero ¹⁶³,
 E. Valiente Moreno ¹⁶³, A. Vallier ^{102,ab}, J.A. Valls Ferrer ¹⁶³, D.R. Van Arneeman ¹¹⁴,
 T.R. Van Daalen ¹³⁸, A. Van Der Graaf ⁴⁹, P. Van Gemmeren ⁶, M. Van Rijnbach ^{125,36},
 S. Van Stroud ⁹⁶, I. Van Vulpen ¹¹⁴, M. Vanadia ^{76a,76b}, W. Vandelli ³⁶, M. Vandenbroucke ¹³⁵,
 E.R. Vandewall ¹²¹, D. Vannicola ¹⁵¹, L. Vannoli ^{57b,57a}, R. Vari ^{75a}, E.W. Varnes ⁷,
 C. Varni ^{17b}, T. Varol ¹⁴⁸, D. Varouchas ⁶⁶, L. Varriale ¹⁶³, K.E. Varvell ¹⁴⁷, M.E. Vasile ^{27b},
 L. Vaslin ⁴⁰, G.A. Vasquez ¹⁶⁵, A. Vasyukov ³⁸, F. Vazeille ⁴⁰, T. Vazquez Schroeder ³⁶,
 J. Veatch ³¹, V. Vecchio ¹⁰¹, M.J. Veen ¹⁰³, I. Veliscek ¹²⁶, L.M. Veloce ¹⁵⁵, F. Veloso ^{130a,130c},
 S. Veneziano ^{75a}, A. Ventura ^{70a,70b}, S. Ventura Gonzalez ¹³⁵, A. Verbytskyi ¹¹⁰,
 M. Verducci ^{74a,74b}, C. Vergis ²⁴, M. Verissimo De Araujo ^{83b}, W. Verkerke ¹¹⁴,
 J.C. Vermeulen ¹¹⁴, C. Vernieri ¹⁴³, M. Vessella ¹⁰³, M.C. Vetterli ^{142,ah}, A. Vgenopoulos ^{152,e},
 N. Viaux Maira ^{137f}, T. Vickey ¹³⁹, O.E. Vickey Boeriu ¹³⁹, G.H.A. Viehhauser ¹²⁶, L. Vignani ^{63b},
 M. Villa ^{23b,23a}, M. Villaplana Perez ¹⁶³, E.M. Villhauer ⁵², E. Vilucchi ⁵³, M.G. Vincter ³⁴,
 G.S. Virdee ²⁰, A. Vishwakarma ⁵², A. Visibile ¹¹⁴, C. Vittori ³⁶, I. Vivarelli ¹⁴⁶, V. Vladimirov ¹⁶⁷,
 E. Voevodina ¹¹⁰, F. Vogel ¹⁰⁹, P. Vokac ¹³², Yu. Volkotrub ^{86a}, J. Von Ahnen ⁴⁸,
 E. Von Toerne ²⁴, B. Vormwald ³⁶, V. Vorobel ¹³³, K. Vorobev ³⁷, M. Vos ¹⁶³, K. Voss ¹⁴¹,
 J.H. Vossebeld ⁹², M. Vozak ¹¹⁴, L. Vozdecky ⁹⁴, N. Vranjes ¹⁵, M. Vranjes Milosavljevic ¹⁵,
 M. Vreeswijk ¹¹⁴, R. Vuillermet ³⁶, O. Vujanovic ¹⁰⁰, I. Vukotic ³⁹, S. Wada ¹⁵⁷, C. Wagner ¹⁰³,
 J.M. Wagner ^{17a}, W. Wagner ¹⁷¹, S. Wahdan ¹⁷¹, H. Wahlberg ⁹⁰, M. Wakida ¹¹¹, J. Walder ¹³⁴,
 R. Walker ¹⁰⁹, W. Walkowiak ¹⁴¹, A. Wall ¹²⁸, T. Wamorkar ⁶, A.Z. Wang ¹⁷⁰, C. Wang ¹⁰⁰,
 C. Wang ^{62c}, H. Wang ^{17a}, J. Wang ^{64a}, R.-J. Wang ¹⁰⁰, R. Wang ⁶¹, R. Wang ⁶,
 S.M. Wang ¹⁴⁸, S. Wang ^{62b}, T. Wang ^{62a}, W.T. Wang ⁸⁰, W. Wang ^{14a}, X. Wang ^{14c},
 X. Wang ¹⁶², X. Wang ^{62c}, Y. Wang ^{62d}, Y. Wang ^{14c}, Z. Wang ¹⁰⁶, Z. Wang ^{62d,51,62c},
 Z. Wang ¹⁰⁶, A. Warburton ¹⁰⁴, R.J. Ward ²⁰, N. Warrack ⁵⁹, A.T. Watson ²⁰, H. Watson ⁵⁹,
 M.F. Watson ²⁰, E. Watton ^{59,134}, G. Watts ¹³⁸, B.M. Waugh ⁹⁶, C. Weber ²⁹, H.A. Weber ¹⁸,
 M.S. Weber ¹⁹, S.M. Weber ^{63a}, C. Wei ^{62a}, Y. Wei ¹²⁶, A.R. Weidberg ¹²⁶, E.J. Weik ¹¹⁷,

J. Weingarten ⁴⁹, M. Weirich ¹⁰⁰, C. Weiser ⁵⁴, C.J. Wells ⁴⁸, T. Wenaus ²⁹, B. Wendland ⁴⁹, T. Wengler ³⁶, N.S. Wenke ¹¹⁰, N. Wermes ²⁴, M. Wessels ^{63a}, A.M. Wharton ⁹¹, A.S. White ⁶¹, A. White ⁸, M.J. White ¹, D. Whiteson ¹⁶⁰, L. Wickremasinghe ¹²⁴, W. Wiedenmann ¹⁷⁰, C. Wiel ⁵⁰, M. Wielers ¹³⁴, C. Wiglesworth ⁴², D.J. Wilbern ¹²⁰, H.G. Wilkens ³⁶, D.M. Williams ⁴¹, H.H. Williams ¹²⁸, S. Williams ³², S. Willocq ¹⁰³, B.J. Wilson ¹⁰¹, P.J. Windischhofer ³⁹, F.I. Winkel ³⁰, F. Winklmeier ¹²³, B.T. Winter ⁵⁴, J.K. Winter ¹⁰¹, M. Wittgen ¹⁴³, M. Wobisch ⁹⁷, Z. Wolfs ¹¹⁴, J. Wollrath ¹⁶⁰, M.W. Wolter ⁸⁷, H. Wolters ^{130a,130c}, A.F. Wongel ⁴⁸, S.D. Worm ⁴⁸, B.K. Wosiek ⁸⁷, K.W. Woźniak ⁸⁷, S. Wozniwski ⁵⁵, K. Wraight ⁵⁹, C. Wu ²⁰, J. Wu ^{14a,14e}, M. Wu ^{64a}, M. Wu ¹¹³, S.L. Wu ¹⁷⁰, X. Wu ⁵⁶, Y. Wu ^{62a}, Z. Wu ¹³⁵, J. Wuerzinger ^{110,af}, T.R. Wyatt ¹⁰¹, B.M. Wynne ⁵², S. Xella ⁴², L. Xia ^{14c}, M. Xia ^{14b}, J. Xiang ^{64c}, M. Xie ^{62a}, X. Xie ^{62a}, S. Xin ^{14a,14e}, J. Xiong ^{17a}, D. Xu ^{14a}, H. Xu ^{62a}, L. Xu ^{62a}, R. Xu ¹²⁸, T. Xu ¹⁰⁶, Y. Xu ^{14b}, Z. Xu ⁵², Z. Xu ^{14a}, B. Yabsley ¹⁴⁷, S. Yacoub ^{33a}, Y. Yamaguchi ¹⁵⁴, E. Yamashita ¹⁵³, H. Yamauchi ¹⁵⁷, T. Yamazaki ^{17a}, Y. Yamazaki ⁸⁵, J. Yan ^{62c}, S. Yan ¹²⁶, Z. Yan ²⁵, H.J. Yang ^{62c,62d}, H.T. Yang ^{62a}, S. Yang ^{62a}, T. Yang ^{64c}, X. Yang ^{62a}, X. Yang ^{14a}, Y. Yang ⁴⁴, Y. Yang ^{62a}, Z. Yang ^{62a}, W.-M. Yao ^{17a}, Y.C. Yap ⁴⁸, H. Ye ^{14c}, H. Ye ⁵⁵, J. Ye ^{14a}, S. Ye ²⁹, X. Ye ^{62a}, Y. Yeh ⁹⁶, I. Yeletsikh ³⁸, B.K. Yeo ^{17b}, M.R. Yexley ⁹⁶, P. Yin ⁴¹, K. Yorita ¹⁶⁸, S. Younas ^{27b}, C.J.S. Young ³⁶, C. Young ¹⁴³, C. Yu ^{14a,14e}, Y. Yu ^{62a}, M. Yuan ¹⁰⁶, R. Yuan ^{62b,k}, L. Yue ⁹⁶, M. Zaazoua ^{62a}, B. Zabinski ⁸⁷, E. Zaid ⁵², T. Zakareishvili ^{149b}, N. Zakharchuk ³⁴, S. Zambito ⁵⁶, J.A. Zamora Saa ^{137d,137b}, J. Zang ¹⁵³, D. Zanzi ⁵⁴, O. Zaplatilek ¹³², C. Zeitnitz ¹⁷¹, H. Zeng ^{14a}, J.C. Zeng ¹⁶², D.T. Zenger Jr ²⁶, O. Zenin ³⁷, T. Ženiš ^{28a}, S. Zenz ⁹⁴, S. Zerradi ^{35a}, D. Zerwas ⁶⁶, M. Zhai ^{14a,14e}, B. Zhang ^{14c}, D.F. Zhang ¹³⁹, J. Zhang ^{62b}, J. Zhang ⁶, K. Zhang ^{14a,14e}, L. Zhang ^{14c}, P. Zhang ^{14a,14e}, R. Zhang ¹⁷⁰, S. Zhang ¹⁰⁶, T. Zhang ¹⁵³, X. Zhang ^{62c}, X. Zhang ^{62b}, Y. Zhang ^{62c,5}, Y. Zhang ⁹⁶, Z. Zhang ^{17a}, Z. Zhang ⁶⁶, H. Zhao ¹³⁸, P. Zhao ⁵¹, T. Zhao ^{62b}, Y. Zhao ¹³⁶, Z. Zhao ^{62a}, A. Zhemchugov ³⁸, J. Zheng ^{14c}, K. Zheng ¹⁶², X. Zheng ^{62a}, Z. Zheng ¹⁴³, D. Zhong ¹⁶², B. Zhou ¹⁰⁶, H. Zhou ⁷, N. Zhou ^{62c}, Y. Zhou ⁷, C.G. Zhu ^{62b}, J. Zhu ¹⁰⁶, Y. Zhu ^{62c}, Y. Zhu ^{62a}, X. Zhuang ^{14a}, K. Zhukov ³⁷, V. Zhulanov ³⁷, N.I. Zimine ³⁸, J. Zinsser ^{63b}, M. Ziolkowski ¹⁴¹, L. Živković ¹⁵, A. Zoccoli ^{23b,23a}, K. Zoch ⁵⁶, T.G. Zorbas ¹³⁹, O. Zormpa ⁴⁶, W. Zou ⁴¹, L. Zwalinski ³⁶.

¹Department of Physics, University of Adelaide, Adelaide; Australia.

²Department of Physics, University of Alberta, Edmonton AB; Canada.

³(^a)Department of Physics, Ankara University, Ankara; (^b)Division of Physics, TOBB University of Economics and Technology, Ankara; Türkiye.

⁴LAPP, Université Savoie Mont Blanc, CNRS/IN2P3, Annecy; France.

⁵APC, Université Paris Cité, CNRS/IN2P3, Paris; France.

⁶High Energy Physics Division, Argonne National Laboratory, Argonne IL; United States of America.

⁷Department of Physics, University of Arizona, Tucson AZ; United States of America.

⁸Department of Physics, University of Texas at Arlington, Arlington TX; United States of America.

⁹Physics Department, National and Kapodistrian University of Athens, Athens; Greece.

¹⁰Physics Department, National Technical University of Athens, Zografou; Greece.

¹¹Department of Physics, University of Texas at Austin, Austin TX; United States of America.

¹²Institute of Physics, Azerbaijan Academy of Sciences, Baku; Azerbaijan.

¹³Institut de Física d'Altes Energies (IFAE), Barcelona Institute of Science and Technology, Barcelona; Spain.

¹⁴(^a)Institute of High Energy Physics, Chinese Academy of Sciences, Beijing; (^b)Physics Department,

Tsinghua University, Beijing;^(c)Department of Physics, Nanjing University, Nanjing;^(d)School of Science, Shenzhen Campus of Sun Yat-sen University;^(e)University of Chinese Academy of Science (UCAS), Beijing; China.

¹⁵Institute of Physics, University of Belgrade, Belgrade; Serbia.

¹⁶Department for Physics and Technology, University of Bergen, Bergen; Norway.

¹⁷(^a)Physics Division, Lawrence Berkeley National Laboratory, Berkeley CA;^(b)University of California, Berkeley CA; United States of America.

¹⁸Institut für Physik, Humboldt Universität zu Berlin, Berlin; Germany.

¹⁹Albert Einstein Center for Fundamental Physics and Laboratory for High Energy Physics, University of Bern, Bern; Switzerland.

²⁰School of Physics and Astronomy, University of Birmingham, Birmingham; United Kingdom.

²¹(^a)Department of Physics, Bogazici University, Istanbul;^(b)Department of Physics Engineering, Gaziantep University, Gaziantep;^(c)Department of Physics, Istanbul University, Istanbul; Türkiye.

²²(^a)Facultad de Ciencias y Centro de Investigaciones, Universidad Antonio Nariño,

Bogotá;^(b)Departamento de Física, Universidad Nacional de Colombia, Bogotá; Colombia.

²³(^a)Dipartimento di Fisica e Astronomia A. Righi, Università di Bologna, Bologna;^(b)INFN Sezione di Bologna; Italy.

²⁴Physikalisches Institut, Universität Bonn, Bonn; Germany.

²⁵Department of Physics, Boston University, Boston MA; United States of America.

²⁶Department of Physics, Brandeis University, Waltham MA; United States of America.

²⁷(^a)Transilvania University of Brasov, Brasov;^(b)Horia Hulubei National Institute of Physics and Nuclear Engineering, Bucharest;^(c)Department of Physics, Alexandru Ioan Cuza University of Iasi, Iasi;^(d)National Institute for Research and Development of Isotopic and Molecular Technologies, Physics Department, Cluj-Napoca;^(e)National University of Science and Technology Politehnica, Bucharest;^(f)West University in Timisoara, Timisoara;^(g)Faculty of Physics, University of Bucharest, Bucharest; Romania.

²⁸(^a)Faculty of Mathematics, Physics and Informatics, Comenius University, Bratislava;^(b)Department of Subnuclear Physics, Institute of Experimental Physics of the Slovak Academy of Sciences, Kosice; Slovak Republic.

²⁹Physics Department, Brookhaven National Laboratory, Upton NY; United States of America.

³⁰Universidad de Buenos Aires, Facultad de Ciencias Exactas y Naturales, Departamento de Física, y CONICET, Instituto de Física de Buenos Aires (IFIBA), Buenos Aires; Argentina.

³¹California State University, CA; United States of America.

³²Cavendish Laboratory, University of Cambridge, Cambridge; United Kingdom.

³³(^a)Department of Physics, University of Cape Town, Cape Town;^(b)iThemba Labs, Western

Cape;^(c)Department of Mechanical Engineering Science, University of Johannesburg,

Johannesburg;^(d)National Institute of Physics, University of the Philippines Diliman

(Philippines);^(e)University of South Africa, Department of Physics, Pretoria;^(f)University of Zululand, KwaDlangezwa;^(g)School of Physics, University of the Witwatersrand, Johannesburg; South Africa.

³⁴Department of Physics, Carleton University, Ottawa ON; Canada.

³⁵(^a)Faculté des Sciences Ain Chock, Réseau Universitaire de Physique des Hautes Energies - Université Hassan II, Casablanca;^(b)Faculté des Sciences, Université Ibn-Tofail, Kénitra;^(c)Faculté des Sciences Semlalia, Université Cadi Ayyad, LPHEA-Marrakech;^(d)LPMR, Faculté des Sciences, Université Mohamed Premier, Oujda;^(e)Faculté des sciences, Université Mohammed V, Rabat;^(f)Institute of Applied Physics, Mohammed VI Polytechnic University, Ben Guerir; Morocco.

³⁶CERN, Geneva; Switzerland.

³⁷Affiliated with an institute covered by a cooperation agreement with CERN.

³⁸Affiliated with an international laboratory covered by a cooperation agreement with CERN.

- ³⁹Enrico Fermi Institute, University of Chicago, Chicago IL; United States of America.
- ⁴⁰LPC, Université Clermont Auvergne, CNRS/IN2P3, Clermont-Ferrand; France.
- ⁴¹Nevis Laboratory, Columbia University, Irvington NY; United States of America.
- ⁴²Niels Bohr Institute, University of Copenhagen, Copenhagen; Denmark.
- ⁴³(^a) Dipartimento di Fisica, Università della Calabria, Rende; (^b) INFN Gruppo Collegato di Cosenza, Laboratori Nazionali di Frascati; Italy.
- ⁴⁴Physics Department, Southern Methodist University, Dallas TX; United States of America.
- ⁴⁵Physics Department, University of Texas at Dallas, Richardson TX; United States of America.
- ⁴⁶National Centre for Scientific Research "Demokritos", Agia Paraskevi; Greece.
- ⁴⁷(^a) Department of Physics, Stockholm University; (^b) Oskar Klein Centre, Stockholm; Sweden.
- ⁴⁸Deutsches Elektronen-Synchrotron DESY, Hamburg and Zeuthen; Germany.
- ⁴⁹Fakultät Physik, Technische Universität Dortmund, Dortmund; Germany.
- ⁵⁰Institut für Kern- und Teilchenphysik, Technische Universität Dresden, Dresden; Germany.
- ⁵¹Department of Physics, Duke University, Durham NC; United States of America.
- ⁵²SUPA - School of Physics and Astronomy, University of Edinburgh, Edinburgh; United Kingdom.
- ⁵³INFN e Laboratori Nazionali di Frascati, Frascati; Italy.
- ⁵⁴Physikalisches Institut, Albert-Ludwigs-Universität Freiburg, Freiburg; Germany.
- ⁵⁵II. Physikalisches Institut, Georg-August-Universität Göttingen, Göttingen; Germany.
- ⁵⁶Département de Physique Nucléaire et Corpusculaire, Université de Genève, Genève; Switzerland.
- ⁵⁷(^a) Dipartimento di Fisica, Università di Genova, Genova; (^b) INFN Sezione di Genova; Italy.
- ⁵⁸II. Physikalisches Institut, Justus-Liebig-Universität Giessen, Giessen; Germany.
- ⁵⁹SUPA - School of Physics and Astronomy, University of Glasgow, Glasgow; United Kingdom.
- ⁶⁰LPSC, Université Grenoble Alpes, CNRS/IN2P3, Grenoble INP, Grenoble; France.
- ⁶¹Laboratory for Particle Physics and Cosmology, Harvard University, Cambridge MA; United States of America.
- ⁶²(^a) Department of Modern Physics and State Key Laboratory of Particle Detection and Electronics, University of Science and Technology of China, Hefei; (^b) Institute of Frontier and Interdisciplinary Science and Key Laboratory of Particle Physics and Particle Irradiation (MOE), Shandong University, Qingdao; (^c) School of Physics and Astronomy, Shanghai Jiao Tong University, Key Laboratory for Particle Astrophysics and Cosmology (MOE), SKLPPC, Shanghai; (^d) Tsung-Dao Lee Institute, Shanghai; China.
- ⁶³(^a) Kirchhoff-Institut für Physik, Ruprecht-Karls-Universität Heidelberg, Heidelberg; (^b) Physikalisches Institut, Ruprecht-Karls-Universität Heidelberg, Heidelberg; Germany.
- ⁶⁴(^a) Department of Physics, Chinese University of Hong Kong, Shatin, N.T., Hong Kong; (^b) Department of Physics, University of Hong Kong, Hong Kong; (^c) Department of Physics and Institute for Advanced Study, Hong Kong University of Science and Technology, Clear Water Bay, Kowloon, Hong Kong; China.
- ⁶⁵Department of Physics, National Tsing Hua University, Hsinchu; Taiwan.
- ⁶⁶IJCLab, Université Paris-Saclay, CNRS/IN2P3, 91405, Orsay; France.
- ⁶⁷Centro Nacional de Microelectrónica (IMB-CNM-CSIC), Barcelona; Spain.
- ⁶⁸Department of Physics, Indiana University, Bloomington IN; United States of America.
- ⁶⁹(^a) INFN Gruppo Collegato di Udine, Sezione di Trieste, Udine; (^b) ICTP, Trieste; (^c) Dipartimento Politecnico di Ingegneria e Architettura, Università di Udine, Udine; Italy.
- ⁷⁰(^a) INFN Sezione di Lecce; (^b) Dipartimento di Matematica e Fisica, Università del Salento, Lecce; Italy.
- ⁷¹(^a) INFN Sezione di Milano; (^b) Dipartimento di Fisica, Università di Milano, Milano; Italy.
- ⁷²(^a) INFN Sezione di Napoli; (^b) Dipartimento di Fisica, Università di Napoli, Napoli; Italy.
- ⁷³(^a) INFN Sezione di Pavia; (^b) Dipartimento di Fisica, Università di Pavia, Pavia; Italy.
- ⁷⁴(^a) INFN Sezione di Pisa; (^b) Dipartimento di Fisica E. Fermi, Università di Pisa, Pisa; Italy.
- ⁷⁵(^a) INFN Sezione di Roma; (^b) Dipartimento di Fisica, Sapienza Università di Roma, Roma; Italy.

- ^{76(a)}INFN Sezione di Roma Tor Vergata;^(b)Dipartimento di Fisica, Università di Roma Tor Vergata, Roma; Italy.
- ^{77(a)}INFN Sezione di Roma Tre;^(b)Dipartimento di Matematica e Fisica, Università Roma Tre, Roma; Italy.
- ^{78(a)}INFN-TIFPA;^(b)Università degli Studi di Trento, Trento; Italy.
- ⁷⁹Universität Innsbruck, Department of Astro and Particle Physics, Innsbruck; Austria.
- ⁸⁰University of Iowa, Iowa City IA; United States of America.
- ⁸¹Department of Physics and Astronomy, Iowa State University, Ames IA; United States of America.
- ⁸²Istinye University, Sariyer, Istanbul; Türkiye.
- ^{83(a)}Departamento de Engenharia Elétrica, Universidade Federal de Juiz de Fora (UFJF), Juiz de Fora;^(b)Universidade Federal do Rio De Janeiro COPPE/EE/IF, Rio de Janeiro;^(c)Instituto de Física, Universidade de São Paulo, São Paulo;^(d)Rio de Janeiro State University, Rio de Janeiro; Brazil.
- ⁸⁴KEK, High Energy Accelerator Research Organization, Tsukuba; Japan.
- ⁸⁵Graduate School of Science, Kobe University, Kobe; Japan.
- ^{86(a)}AGH University of Krakow, Faculty of Physics and Applied Computer Science, Krakow;^(b)Marian Smoluchowski Institute of Physics, Jagiellonian University, Krakow; Poland.
- ⁸⁷Institute of Nuclear Physics Polish Academy of Sciences, Krakow; Poland.
- ⁸⁸Faculty of Science, Kyoto University, Kyoto; Japan.
- ⁸⁹Research Center for Advanced Particle Physics and Department of Physics, Kyushu University, Fukuoka ; Japan.
- ⁹⁰Instituto de Física La Plata, Universidad Nacional de La Plata and CONICET, La Plata; Argentina.
- ⁹¹Physics Department, Lancaster University, Lancaster; United Kingdom.
- ⁹²Oliver Lodge Laboratory, University of Liverpool, Liverpool; United Kingdom.
- ⁹³Department of Experimental Particle Physics, Jožef Stefan Institute and Department of Physics, University of Ljubljana, Ljubljana; Slovenia.
- ⁹⁴School of Physics and Astronomy, Queen Mary University of London, London; United Kingdom.
- ⁹⁵Department of Physics, Royal Holloway University of London, Egham; United Kingdom.
- ⁹⁶Department of Physics and Astronomy, University College London, London; United Kingdom.
- ⁹⁷Louisiana Tech University, Ruston LA; United States of America.
- ⁹⁸Fysiska institutionen, Lunds universitet, Lund; Sweden.
- ⁹⁹Departamento de Física Teórica C-15 and CIAFF, Universidad Autónoma de Madrid, Madrid; Spain.
- ¹⁰⁰Institut für Physik, Universität Mainz, Mainz; Germany.
- ¹⁰¹School of Physics and Astronomy, University of Manchester, Manchester; United Kingdom.
- ¹⁰²CPPM, Aix-Marseille Université, CNRS/IN2P3, Marseille; France.
- ¹⁰³Department of Physics, University of Massachusetts, Amherst MA; United States of America.
- ¹⁰⁴Department of Physics, McGill University, Montreal QC; Canada.
- ¹⁰⁵School of Physics, University of Melbourne, Victoria; Australia.
- ¹⁰⁶Department of Physics, University of Michigan, Ann Arbor MI; United States of America.
- ¹⁰⁷Department of Physics and Astronomy, Michigan State University, East Lansing MI; United States of America.
- ¹⁰⁸Group of Particle Physics, University of Montreal, Montreal QC; Canada.
- ¹⁰⁹Fakultät für Physik, Ludwig-Maximilians-Universität München, München; Germany.
- ¹¹⁰Max-Planck-Institut für Physik (Werner-Heisenberg-Institut), München; Germany.
- ¹¹¹Graduate School of Science and Kobayashi-Maskawa Institute, Nagoya University, Nagoya; Japan.
- ¹¹²Department of Physics and Astronomy, University of New Mexico, Albuquerque NM; United States of America.
- ¹¹³Institute for Mathematics, Astrophysics and Particle Physics, Radboud University/Nikhef, Nijmegen;

Netherlands.

¹¹⁴Nikhef National Institute for Subatomic Physics and University of Amsterdam, Amsterdam; Netherlands.

¹¹⁵Department of Physics, Northern Illinois University, DeKalb IL; United States of America.

¹¹⁶(^a)New York University Abu Dhabi, Abu Dhabi;(^b)University of Sharjah, Sharjah; United Arab Emirates.

¹¹⁷Department of Physics, New York University, New York NY; United States of America.

¹¹⁸Ochanomizu University, Otsuka, Bunkyo-ku, Tokyo; Japan.

¹¹⁹Ohio State University, Columbus OH; United States of America.

¹²⁰Homer L. Dodge Department of Physics and Astronomy, University of Oklahoma, Norman OK; United States of America.

¹²¹Department of Physics, Oklahoma State University, Stillwater OK; United States of America.

¹²²Palacký University, Joint Laboratory of Optics, Olomouc; Czech Republic.

¹²³Institute for Fundamental Science, University of Oregon, Eugene, OR; United States of America.

¹²⁴Graduate School of Science, Osaka University, Osaka; Japan.

¹²⁵Department of Physics, University of Oslo, Oslo; Norway.

¹²⁶Department of Physics, Oxford University, Oxford; United Kingdom.

¹²⁷LPNHE, Sorbonne Université, Université Paris Cité, CNRS/IN2P3, Paris; France.

¹²⁸Department of Physics, University of Pennsylvania, Philadelphia PA; United States of America.

¹²⁹Department of Physics and Astronomy, University of Pittsburgh, Pittsburgh PA; United States of America.

¹³⁰(^a)Laboratório de Instrumentação e Física Experimental de Partículas - LIP, Lisboa;(^b)Departamento de Física, Faculdade de Ciências, Universidade de Lisboa, Lisboa;(^c)Departamento de Física, Universidade de Coimbra, Coimbra;(^d)Centro de Física Nuclear da Universidade de Lisboa, Lisboa;(^e)Departamento de Física, Universidade do Minho, Braga;(^f)Departamento de Física Teórica y del Cosmos, Universidad de Granada, Granada (Spain);(^g)Departamento de Física, Instituto Superior Técnico, Universidade de Lisboa, Lisboa; Portugal.

¹³¹Institute of Physics of the Czech Academy of Sciences, Prague; Czech Republic.

¹³²Czech Technical University in Prague, Prague; Czech Republic.

¹³³Charles University, Faculty of Mathematics and Physics, Prague; Czech Republic.

¹³⁴Particle Physics Department, Rutherford Appleton Laboratory, Didcot; United Kingdom.

¹³⁵IRFU, CEA, Université Paris-Saclay, Gif-sur-Yvette; France.

¹³⁶Santa Cruz Institute for Particle Physics, University of California Santa Cruz, Santa Cruz CA; United States of America.

¹³⁷(^a)Departamento de Física, Pontificia Universidad Católica de Chile, Santiago;(^b)Millennium Institute for Subatomic physics at high energy frontier (SAPHIR), Santiago;(^c)Instituto de Investigación Multidisciplinario en Ciencia y Tecnología, y Departamento de Física, Universidad de La Serena;(^d)Universidad Andres Bello, Department of Physics, Santiago;(^e)Instituto de Alta Investigación, Universidad de Tarapacá, Arica;(^f)Departamento de Física, Universidad Técnica Federico Santa María, Valparaíso; Chile.

¹³⁸Department of Physics, University of Washington, Seattle WA; United States of America.

¹³⁹Department of Physics and Astronomy, University of Sheffield, Sheffield; United Kingdom.

¹⁴⁰Department of Physics, Shinshu University, Nagano; Japan.

¹⁴¹Department Physik, Universität Siegen, Siegen; Germany.

¹⁴²Department of Physics, Simon Fraser University, Burnaby BC; Canada.

¹⁴³SLAC National Accelerator Laboratory, Stanford CA; United States of America.

¹⁴⁴Department of Physics, Royal Institute of Technology, Stockholm; Sweden.

- ¹⁴⁵Departments of Physics and Astronomy, Stony Brook University, Stony Brook NY; United States of America.
- ¹⁴⁶Department of Physics and Astronomy, University of Sussex, Brighton; United Kingdom.
- ¹⁴⁷School of Physics, University of Sydney, Sydney; Australia.
- ¹⁴⁸Institute of Physics, Academia Sinica, Taipei; Taiwan.
- ¹⁴⁹^(a)E. Andronikashvili Institute of Physics, Iv. Javakhishvili Tbilisi State University, Tbilisi;^(b)High Energy Physics Institute, Tbilisi State University, Tbilisi;^(c)University of Georgia, Tbilisi; Georgia.
- ¹⁵⁰Department of Physics, Technion, Israel Institute of Technology, Haifa; Israel.
- ¹⁵¹Raymond and Beverly Sackler School of Physics and Astronomy, Tel Aviv University, Tel Aviv; Israel.
- ¹⁵²Department of Physics, Aristotle University of Thessaloniki, Thessaloniki; Greece.
- ¹⁵³International Center for Elementary Particle Physics and Department of Physics, University of Tokyo, Tokyo; Japan.
- ¹⁵⁴Department of Physics, Tokyo Institute of Technology, Tokyo; Japan.
- ¹⁵⁵Department of Physics, University of Toronto, Toronto ON; Canada.
- ¹⁵⁶^(a)TRIUMF, Vancouver BC;^(b)Department of Physics and Astronomy, York University, Toronto ON; Canada.
- ¹⁵⁷Division of Physics and Tomonaga Center for the History of the Universe, Faculty of Pure and Applied Sciences, University of Tsukuba, Tsukuba; Japan.
- ¹⁵⁸Department of Physics and Astronomy, Tufts University, Medford MA; United States of America.
- ¹⁵⁹United Arab Emirates University, Al Ain; United Arab Emirates.
- ¹⁶⁰Department of Physics and Astronomy, University of California Irvine, Irvine CA; United States of America.
- ¹⁶¹Department of Physics and Astronomy, University of Uppsala, Uppsala; Sweden.
- ¹⁶²Department of Physics, University of Illinois, Urbana IL; United States of America.
- ¹⁶³Instituto de Física Corpuscular (IFIC), Centro Mixto Universidad de Valencia - CSIC, Valencia; Spain.
- ¹⁶⁴Department of Physics, University of British Columbia, Vancouver BC; Canada.
- ¹⁶⁵Department of Physics and Astronomy, University of Victoria, Victoria BC; Canada.
- ¹⁶⁶Fakultät für Physik und Astronomie, Julius-Maximilians-Universität Würzburg, Würzburg; Germany.
- ¹⁶⁷Department of Physics, University of Warwick, Coventry; United Kingdom.
- ¹⁶⁸Waseda University, Tokyo; Japan.
- ¹⁶⁹Department of Particle Physics and Astrophysics, Weizmann Institute of Science, Rehovot; Israel.
- ¹⁷⁰Department of Physics, University of Wisconsin, Madison WI; United States of America.
- ¹⁷¹Fakultät für Mathematik und Naturwissenschaften, Fachgruppe Physik, Bergische Universität Wuppertal, Wuppertal; Germany.
- ¹⁷²Department of Physics, Yale University, New Haven CT; United States of America.
- ^a Also Affiliated with an institute covered by a cooperation agreement with CERN.
- ^b Also at An-Najah National University, Nablus; Palestine.
- ^c Also at Borough of Manhattan Community College, City University of New York, New York NY; United States of America.
- ^d Also at Center for High Energy Physics, Peking University; China.
- ^e Also at Center for Interdisciplinary Research and Innovation (CIRI-AUTH), Thessaloniki; Greece.
- ^f Also at Centro Studi e Ricerche Enrico Fermi; Italy.
- ^g Also at CERN, Geneva; Switzerland.
- ^h Also at Département de Physique Nucléaire et Corpusculaire, Université de Genève, Genève; Switzerland.
- ⁱ Also at Departament de Física de la Universitat Autònoma de Barcelona, Barcelona; Spain.
- ^j Also at Department of Financial and Management Engineering, University of the Aegean, Chios; Greece.

^k Also at Department of Physics and Astronomy, Michigan State University, East Lansing MI; United States of America.

^l Also at Department of Physics, Ben Gurion University of the Negev, Beer Sheva; Israel.

^m Also at Department of Physics, California State University, Sacramento; United States of America.

ⁿ Also at Department of Physics, King's College London, London; United Kingdom.

^o Also at Department of Physics, Stanford University, Stanford CA; United States of America.

^p Also at Department of Physics, University of Fribourg, Fribourg; Switzerland.

^q Also at Department of Physics, University of Thessaly; Greece.

^r Also at Department of Physics, Westmont College, Santa Barbara; United States of America.

^s Also at Hellenic Open University, Patras; Greece.

^t Also at Institutio Catalana de Recerca i Estudis Avancats, ICREA, Barcelona; Spain.

^u Also at Institut für Experimentalphysik, Universität Hamburg, Hamburg; Germany.

^v Also at Institute for Nuclear Research and Nuclear Energy (INRNE) of the Bulgarian Academy of Sciences, Sofia; Bulgaria.

^w Also at Institute of Applied Physics, Mohammed VI Polytechnic University, Ben Guerir; Morocco.

^x Also at Institute of Particle Physics (IPP); Canada.

^y Also at Institute of Physics and Technology, Mongolian Academy of Sciences, Ulaanbaatar; Mongolia.

^z Also at Institute of Physics, Azerbaijan Academy of Sciences, Baku; Azerbaijan.

^{aa} Also at Institute of Theoretical Physics, Ilia State University, Tbilisi; Georgia.

^{ab} Also at L2IT, Université de Toulouse, CNRS/IN2P3, UPS, Toulouse; France.

^{ac} Also at Lawrence Livermore National Laboratory, Livermore; United States of America.

^{ad} Also at National Institute of Physics, University of the Philippines Diliman (Philippines); Philippines.

^{ae} Also at Ochanomizu University, Otsuka, Bunkyo-ku, Tokyo; Japan.

^{af} Also at Technical University of Munich, Munich; Germany.

^{ag} Also at The Collaborative Innovation Center of Quantum Matter (CICQM), Beijing; China.

^{ah} Also at TRIUMF, Vancouver BC; Canada.

^{ai} Also at Università di Napoli Parthenope, Napoli; Italy.

^{aj} Also at University of Colorado Boulder, Department of Physics, Colorado; United States of America.

^{ak} Also at Washington College, Chestertown, MD; United States of America.

^{al} Also at Yeditepe University, Physics Department, Istanbul; Türkiye.

* Deceased

Observation of $\psi(3686) \rightarrow 3\phi$

M. Ablikim¹, M. N. Achasov^{4,c}, P. Adlarson⁷⁵, O. Afedulidis³, X. C. Ai⁸⁰, R. Aliberti³⁵, A. Amoroso^{74A,74C}, Q. An^{71,58,a}, Y. Bai⁵⁷, O. Bakina³⁶, I. Balossino^{29A}, Y. Ban^{46,h}, H.-R. Bao⁶³, V. Batzskaya^{1,44}, K. Begzsuren³², N. Berger³⁵, M. Berlowski⁴⁴, M. Bertani^{28A}, D. Bettoni^{29A}, F. Bianchi^{74A,74C}, E. Bianco^{74A,74C}, A. Bortone^{74A,74C}, I. Boyko³⁶, R. A. Briere⁵, A. Brueggemann⁶⁸, H. Cai⁷⁶, X. Cai^{1,58}, A. Calcaterra^{28A}, G. F. Cao^{1,63}, N. Cao^{1,63}, S. A. Cetin^{62A}, J. F. Chang^{1,58}, G. R. Che⁴³, G. Chelkov^{36,b}, C. Chen⁴³, C. H. Chen⁹, Chao Chen⁵⁵, G. Chen¹, H. S. Chen^{1,63}, H. Y. Chen²⁰, M. L. Chen^{1,58,63}, S. J. Chen⁴², S. L. Chen⁴⁵, S. M. Chen⁶¹, T. Chen^{1,63}, X. R. Chen^{31,63}, X. T. Chen^{1,63}, Y. B. Chen^{1,58}, Y. Q. Chen³⁴, Z. J. Chen^{25,i}, Z. Y. Chen^{1,63}, S. K. Choi^{10A}, G. Cibinetto^{29A}, F. Cossio^{74C}, J. J. Cui⁵⁰, H. L. Dai^{1,58}, J. P. Dai⁷⁸, A. Dbeyssi¹⁸, R. E. de Boer³, D. Dedovich³⁶, C. Q. Deng⁷², Z. Y. Deng¹, A. Denig³⁵, I. Denysenko³⁶, M. Destefanis^{74A,74C}, F. De Mori^{74A,74C}, B. Ding^{66,1}, X. X. Ding^{46,h}, Y. Ding³⁴, Y. Ding⁴⁰, J. Dong^{1,58}, L. Y. Dong^{1,63}, M. Y. Dong^{1,58,63}, X. Dong⁷⁶, M. C. Du¹, S. X. Du⁸⁰, Y. Y. Duan⁵⁵, Z. H. Duan⁴², P. Egorov^{36,b}, Y. H. Fan⁴⁵, J. Fang^{1,58}, J. Fang⁵⁹, S. S. Fang^{1,63}, W. X. Fang¹, Y. Fang¹, Y. Q. Fang^{1,58}, R. Farinelli^{29A}, L. Fava^{74B,74C}, F. Feldbauer³, G. Felici^{28A}, C. Q. Feng^{71,58}, J. H. Feng⁵⁹, Y. T. Feng^{71,58}, M. Fritsch³, C. D. Fu¹, J. L. Fu⁶³, Y. W. Fu^{1,63}, H. Gao⁶³, X. B. Gao⁴¹, Y. N. Gao^{46,h}, Yang Gao^{71,58}, S. Garbolino^{74C}, I. Garzia^{29A,29B}, L. Ge⁸⁰, P. T. Ge⁷⁶, Z. W. Ge⁴², C. Geng⁵⁹, E. M. Gersabeck⁶⁷, A. Gilman⁶⁹, K. Goetzen¹³, L. Gong⁴⁰, W. X. Gong^{1,58}, W. Gradl³⁵, S. Gramigna^{29A,29B}, M. Greco^{74A,74C}, M. H. Gu^{1,58}, Y. T. Gu¹⁵, C. Y. Guan^{1,63}, A. Q. Guo^{31,63}, L. B. Guo⁴¹, M. J. Guo⁵⁰, R. P. Guo⁴⁹, Y. P. Guo^{12,g}, A. Guskov^{36,b}, J. Gutierrez²⁷, K. L. Han⁶³, T. T. Han¹, F. Hanisch³, X. Q. Hao¹⁹, F. A. Harris⁶⁵, K. K. He⁵⁵, K. L. He^{1,63}, F. H. Heinsius³, C. H. Heinz³⁵, Y. K. Heng^{1,58,63}, C. Herold⁶⁰, T. Holtmann³, P. C. Hong³⁴, G. Y. Hou^{1,63}, X. T. Hou^{1,63}, Y. R. Hou⁶³, Z. L. Hou¹, B. Y. Hu⁵⁹, H. M. Hu^{1,63}, J. F. Hu^{56,j}, S. L. Hu^{12,g}, T. Hu^{1,58,63}, Y. Hu¹, G. S. Huang^{71,58}, K. X. Huang⁵⁹, L. Q. Huang^{31,63}, X. T. Huang⁵⁰, Y. P. Huang¹, Y. S. Huang⁵⁹, T. Hussain⁷³, F. Hölzken³, N. Hüskens³⁵, N. in der Wiesche⁶⁸, J. Jackson²⁷, S. Janchiv³², J. H. Jeong^{10A}, Q. Ji¹, Q. P. Ji¹⁹, W. Ji^{1,63}, X. B. Ji^{1,63}, X. L. Ji^{1,58}, Y. Y. Ji⁵⁰, X. Q. Jia⁵⁰, Z. K. Jia^{71,58}, D. Jiang^{1,63}, H. B. Jiang⁷⁶, P. C. Jiang^{46,h}, S. S. Jiang³⁹, T. J. Jiang¹⁶, X. S. Jiang^{1,58,63}, Y. Jiang⁶³, J. B. Jiao⁵⁰, J. K. Jiao³⁴, Z. Jiao²³, S. Jin⁴², Y. Jin⁶⁶, M. Q. Jing^{1,63}, X. M. Jing⁶³, T. Johansson⁷⁵, S. Kabana³³, N. Kalantar-Nayestanaki⁶⁴, X. L. Kang⁹, X. S. Kang⁴⁰, M. Kavatsyuk⁶⁴, B. C. Ke⁸⁰, V. Khachatryan²⁷, A. Khoukaz⁶⁸, R. Kiuchi¹, O. B. Kolcu^{62A}, B. Kopf³, M. Kuessner³, X. Kui^{1,63}, N. Kumar²⁶, A. Kupsc^{44,75}, W. Kühn³⁷, J. J. Lane⁶⁷, P. Larin¹⁸, L. Lavezzi^{74A,74C}, T. T. Lei^{71,58}, Z. H. Lei^{71,58}, M. Lellmann³⁵, T. Lenz³⁵, C. Li⁴⁷, C. Li⁴³, C. H. Li³⁹, Cheng Li^{71,58}, D. M. Li⁸⁰, F. Li^{1,58}, G. Li¹, H. B. Li^{1,63}, H. J. Li¹⁹, H. N. Li^{56,j}, Hui Li⁴³, J. R. Li⁶¹, J. S. Li⁵⁹, K. Li¹, L. J. Li^{1,63}, L. K. Li¹, Lei Li⁴⁸, M. H. Li⁴³, P. R. Li^{38,k,l}, Q. M. Li^{1,63}, Q. X. Li⁵⁰, R. Li^{17,31}, S. X. Li¹², T. Li⁵⁰, W. D. Li^{1,63}, W. G. Li^{1,a}, X. Li^{1,63}, X. H. Li^{71,58}, X. L. Li⁵⁰, X. Y. Li^{1,63}, X. Z. Li⁵⁹, Y. G. Li^{46,h}, Z. J. Li⁵⁹, Z. Y. Li⁷⁸, C. Liang⁴², H. Liang^{1,63}, H. Liang^{71,58}, Y. F. Liang⁵⁴, Y. T. Liang^{31,63}, G. R. Liao¹⁴, Y. L. Liao⁵⁰, Y. P. Liao^{1,63}, J. Libby²⁶, A. Limphirat⁶⁰, C. C. Lin⁵⁵, D. X. Lin^{31,63}, T. Lin¹, B. J. Liu¹, B. X. Liu⁷⁶, C. Liu³⁴, C. X. Liu¹, F. Liu¹, F. H. Liu⁵³, Feng Liu⁶, G. M. Liu^{56,j}, H. Liu^{38,k,l}, H. B. Liu¹⁵, H. H. Liu¹, H. M. Liu^{1,63}, Huihui Liu²¹, J. B. Liu^{71,58}, J. Y. Liu^{1,63}, K. Liu^{38,k,l}, K. Y. Liu⁴⁰, Ke Liu²², L. Liu^{71,58}, L. C. Liu⁴³, Lu Liu⁴³, M. H. Liu^{12,g}, P. L. Liu¹, Q. Liu⁶³, S. B. Liu^{71,58}, T. Liu^{12,g}, W. K. Liu⁴³, W. M. Liu^{71,58}, X. Liu^{38,k,l}, X. Liu³⁹, Y. Liu⁸⁰, Y. Liu^{38,k,l}, Y. B. Liu⁴³, Z. A. Liu^{1,58,63}, Z. D. Liu⁹, Z. Q. Liu⁵⁰, X. C. Lou^{1,58,63}, F. X. Lu⁵⁹, H. J. Lu²³, J. G. Lu^{1,58}, X. L. Lu¹, Y. Lu⁷, Y. P. Lu^{1,58}, Z. H. Lu^{1,63}, C. L. Luo⁴¹, J. R. Luo⁵⁹, M. X. Luo⁷⁹, T. Luo^{12,g}, X. L. Luo^{1,58}, X. R. Lyu⁶³, Y. F. Lyu⁴³, F. C. Ma⁴⁰, H. Ma⁷⁸, H. L. Ma¹, J. L. Ma^{1,63}, L. L. Ma⁵⁰, M. M. Ma^{1,63}, Q. M. Ma¹, R. Q. Ma^{1,63}, T. Ma^{71,58}, X. T. Ma^{1,63}, X. Y. Ma^{1,58}, Y. Ma^{46,h}, Y. M. Ma³¹, F. E. Maas¹⁸, M. Maggiora^{74A,74C}, S. Malde⁶⁹, Y. J. Mao^{46,h}, Z. P. Mao¹, S. Marcello^{74A,74C}, Z. X. Meng⁶⁶, J. G. Messchendorp^{13,64}, G. Mezzadri^{29A}, H. Miao^{1,63}, T. J. Min⁴², R. E. Mitchell²⁷, X. H. Mo^{1,58,63}, B. Moses²⁷, N. Yu. Muchnoi^{4,c}, J. Muskalla³⁵, Y. Nefedov³⁶, F. Nerling^{18,e}, L. S. Nie²⁰, I. B. Nikolaev^{4,c}, Z. Ning^{1,58}, S. Nisar^{11,m}, Q. L. Niu^{38,k,l}, W. D. Niu⁵⁵, Y. Niu⁵⁰, S. L. Olsen⁶³, Q. Ouyang^{1,58,63}, S. Pacetti^{28B,28C}, X. Pan⁵⁵, Y. Pan⁵⁷, A. Pathak³⁴, P. Patteri^{28A}, Y. P. Pei^{71,58}, M. Pelizaeus³, H. P. Peng^{71,58}, Y. Y. Peng^{38,k,l}, K. Peters^{13,e}, J. L. Ping⁴¹, R. G. Ping^{1,63}, S. Plura³⁵, V. Prasad³³, F. Z. Qi¹, H. Qi^{71,58}, H. R. Qi⁶¹, M. Qi⁴², T. Y. Qi^{12,g}, S. Qian^{1,58}, W. B. Qian⁶³, C. F. Qiao⁶³, X. K. Qiao⁸⁰, J. J. Qin⁷², L. Q. Qin¹⁴, L. Y. Qin^{71,58}, X. S. Qin⁵⁰, Z. H. Qin^{1,58}, J. F. Qiu¹, Z. H. Qu⁷², C. F. Redmer³⁵, K. J. Ren³⁹, A. Rivetti^{74C}, M. Rolo^{74C}, G. Rong^{1,63}, Ch. Rosner¹⁸, S. N. Ruan⁴³, N. Salone⁴⁴, A. Sarantsev^{36,d}, Y. Schelhaas³⁵, K. Schoenning⁷⁵, M. Scodeggio^{29A}, K. Y. Shan^{12,g}, W. Shan²⁴, X. Y. Shan^{71,58}, Z. J. Shang^{38,k,l}, L. G. Shao^{1,63}, M. Shao^{71,58}, C. P. Shen^{12,g}, H. F. Shen^{1,8}, W. H. Shen⁶³, X. Y. Shen^{1,63}, B. A. Shi⁶³, H. Shi^{71,58}, H. C. Shi^{71,58}, J. L. Shi^{12,g}, J. Y. Shi¹, Q. Q. Shi⁵⁵, S. Y. Shi⁷², X. Shi^{1,58}, J. J. Song¹⁹, T. Z. Song⁵⁹, W. M. Song^{34,1}, Y. J. Song^{12,g}, Y. X. Song^{46,h,n}, S. Sosio^{74A,74C}, S. Spataro^{74A,74C}, F. Stielers³⁵, Y. J. Su⁶³, G. B. Sun⁷⁶, G. X. Sun¹, H. Sun⁶³, H. K. Sun¹, J. F. Sun¹⁹, K. Sun⁶¹, L. Sun⁷⁶, S. S. Sun^{1,63}, T. Sun^{51,f}, W. Y. Sun³⁴, Y. Sun⁹, Y. J. Sun^{71,58}, Y. Z. Sun¹, Z. Q. Sun^{1,63}, Z. T. Sun⁵⁰, C. J. Tang⁵⁴, G. Y. Tang¹, J. Tang⁵⁹, M. Tang^{71,58}, Y. A. Tang⁷⁶, L. Y. Tao⁷², Q. T. Tao^{25,i}, M. Tat⁶⁹, J. X. Teng^{71,58}, V. Thoren⁷⁵, W. H. Tian⁵⁹, Y. Tian^{31,63}, Z. F. Tian⁷⁶, I. Uman^{62B}, Y. Wan⁵⁵, S. J. Wang⁵⁰, B. Wang¹, B. L. Wang⁶³, Bo Wang^{71,58}, D. Y. Wang^{46,h}, F. Wang⁷², H. J. Wang^{38,k,l}, J. J. Wang⁷⁶, J. P. Wang⁵⁰, K. Wang^{1,58}, L. L. Wang¹, M. Wang⁵⁰, N. Y. Wang⁶³, S. Wang^{38,k,l}, S. Wang^{12,g}, T. Wang^{12,g}, T. J. Wang⁴³, W. Wang⁵⁹, W. Wang⁷², W. P. Wang^{35,71,o}, X. Wang^{46,h}, X. F. Wang^{38,k,l}, X. J. Wang³⁹, X. L. Wang^{12,g}, X. N. Wang¹, Y. Wang⁶¹, Y. D. Wang⁴⁵, Y. F. Wang^{1,58,63}, Y. L. Wang¹⁹, Y. N. Wang⁴⁵, Y. Q. Wang¹, Yaqian Wang¹⁷, Yi Wang⁶¹, Z. Wang^{1,58}, Z. L. Wang⁷², Z. Y. Wang^{1,63}, Ziyi Wang⁶³, D. H. Wei¹⁴, F. Weidner⁶⁸, S. P. Wen¹, Y. R. Wen³⁹, U. Wiedner³, G. Wilkinson⁶⁹, M. Wolke⁷⁵, L. Wollenberg³, C. Wu³⁹, J. F. Wu^{1,8}, L. H. Wu¹, L. J. Wu^{1,63}, X. Wu^{12,g}, X. H. Wu³⁴, Y. Wu^{71,58}, Y. H. Wu⁵⁵, Y. J. Wu³¹, Z. Wu^{1,58}, L. Xia^{71,58}, X. M. Xian³⁹, B. H. Xiang^{1,63}, T. Xiang^{46,h}, D. Xiao^{38,k,l}, G. Y. Xiao⁴², S. Y. Xiao¹, Y. L. Xiao^{12,g}, Z. J. Xiao⁴¹, C. Xie⁴², X. H. Xie^{46,h}, Y. Xie⁵⁰, Y. G. Xie^{1,58}, Y. H. Xie⁶, Z. P. Xie^{71,58}, T. Y. Xing^{1,63}, C. F. Xu^{1,63}, C. J. Xu⁵⁹, G. F. Xu¹, H. Y. Xu^{66,2,p}, M. Xu^{71,58}, Q. J. Xu¹⁶, Q. N. Xu³⁰, W. Xu¹, W. L. Xu⁶⁶, X. P. Xu⁵⁵, Y. C. Xu⁷⁷, Z. P. Xu⁴², Z. S. Xu⁶³, F. Yan^{12,g}, L. Yan^{12,g}, W. B. Yan^{71,58}, W. C. Yan⁸⁰,

X. Q. Yan¹, H. J. Yang^{51,f}, H. L. Yang³⁴, H. X. Yang¹, T. Yang¹, Y. Yang^{12,g}, Y. F. Yang^{1,63}, Y. F. Yang⁴³, Y. X. Yang^{1,63},
 Z. W. Yang^{38,k,l}, Z. P. Yao⁵⁰, M. Ye^{1,58}, M. H. Ye⁸, J. H. Yin¹, Z. Y. You⁵⁹, B. X. Yu^{1,58,63}, C. X. Yu⁴³, G. Yu^{1,63},
 J. S. Yu^{25,i}, T. Yu⁷², X. D. Yu^{46,h}, Y. C. Yu⁸⁰, C. Z. Yuan^{1,63}, J. Yuan³⁴, J. Yuan⁴⁵, L. Yuan², S. C. Yuan^{1,63}, Y. Yuan^{1,63},
 Z. Y. Yuan⁵⁹, C. X. Yue³⁹, A. A. Zafar⁷³, F. R. Zeng⁵⁰, S. H. Zeng⁷², X. Zeng^{12,g}, Y. Zeng^{25,i}, Y. J. Zeng⁵⁹, Y. J. Zeng^{1,63},
 X. Y. Zhai³⁴, Y. C. Zhai⁵⁰, Y. H. Zhan⁵⁹, A. Q. Zhang^{1,63}, B. L. Zhang^{1,63}, B. X. Zhang¹, D. H. Zhang⁴³, G. Y. Zhang¹⁹,
 H. Zhang^{71,58}, H. Zhang⁸⁰, H. C. Zhang^{1,58,63}, H. H. Zhang³⁴, H. H. Zhang⁵⁹, H. Q. Zhang^{1,58,63}, H. R. Zhang^{71,58},
 H. Y. Zhang^{1,58}, J. Zhang⁸⁰, J. Zhang⁵⁹, J. J. Zhang⁵², J. L. Zhang²⁰, J. Q. Zhang⁴¹, J. S. Zhang^{12,g}, J. W. Zhang^{1,58,63},
 J. X. Zhang^{38,k,l}, J. Y. Zhang¹, J. Z. Zhang^{1,63}, Jianyu Zhang⁶³, L. M. Zhang⁶¹, Lei Zhang⁴², P. Zhang^{1,63}, Q. Y. Zhang³⁴,
 R. Y. Zhang^{38,k,l}, S. H. Zhang^{1,63}, Shulei Zhang^{25,i}, X. D. Zhang⁴⁵, X. M. Zhang¹, X. Y. Zhang⁵⁰, Y. Zhang⁷², Y. Zhang¹,
 Y. T. Zhang⁸⁰, Y. H. Zhang^{1,58}, Y. M. Zhang³⁹, Yan Zhang^{71,58}, Z. D. Zhang¹, Z. H. Zhang¹, Z. L. Zhang³⁴, Z. Y. Zhang⁷⁶,
 Z. Y. Zhang⁴³, Z. Z. Zhang⁴⁵, G. Zhao¹, J. Y. Zhao^{1,63}, J. Z. Zhao^{1,58}, L. Zhao¹, Lei Zhao^{71,58}, M. G. Zhao⁴³, N. Zhao⁷⁸,
 R. P. Zhao⁶³, S. J. Zhao⁸⁰, Y. B. Zhao^{1,58}, Y. X. Zhao^{31,63}, Z. G. Zhao^{71,58}, A. Zhemchugov^{36,b}, B. Zheng⁷², B. M. Zheng³⁴,
 J. P. Zheng^{1,58}, W. J. Zheng^{1,63}, Y. H. Zheng⁶³, B. Zhong⁴¹, X. Zhong⁵⁹, H. Zhou⁵⁰, J. Y. Zhou³⁴, L. P. Zhou^{1,63}, S. Zhou⁶,
 X. Zhou⁷⁶, X. K. Zhou⁶, X. R. Zhou^{71,58}, X. Y. Zhou³⁹, Y. Z. Zhou^{12,g}, J. Zhu⁴³, K. Zhu¹, K. J. Zhu^{1,58,63}, K. S. Zhu^{12,g},
 L. Zhu³⁴, L. X. Zhu⁶³, S. H. Zhu⁷⁰, S. Q. Zhu⁴², T. J. Zhu^{12,g}, W. D. Zhu⁴¹, Y. C. Zhu^{71,58}, Z. A. Zhu^{1,63}, J. H. Zou¹,
 J. Zu^{71,58}

(BESIII Collaboration)

¹ Institute of High Energy Physics, Beijing 100049, People's Republic of China

² Beihang University, Beijing 100191, People's Republic of China

³ Bochum Ruhr-University, D-44780 Bochum, Germany

⁴ Budker Institute of Nuclear Physics SB RAS (BINP), Novosibirsk 630090, Russia

⁵ Carnegie Mellon University, Pittsburgh, Pennsylvania 15213, USA

⁶ Central China Normal University, Wuhan 430079, People's Republic of China

⁷ Central South University, Changsha 410083, People's Republic of China

⁸ China Center of Advanced Science and Technology, Beijing 100190, People's Republic of China

⁹ China University of Geosciences, Wuhan 430074, People's Republic of China

¹⁰ Chung-Ang University, Seoul, 06974, Republic of Korea

¹¹ COMSATS University Islamabad, Lahore Campus, Defence Road, Off Raiwind Road, 54000 Lahore, Pakistan

¹² Fudan University, Shanghai 200433, People's Republic of China

¹³ GSI Helmholtzcentre for Heavy Ion Research GmbH, D-64291 Darmstadt, Germany

¹⁴ Guangxi Normal University, Guilin 541004, People's Republic of China

¹⁵ Guangxi University, Nanning 530004, People's Republic of China

¹⁶ Hangzhou Normal University, Hangzhou 310036, People's Republic of China

¹⁷ Hebei University, Baoding 071002, People's Republic of China

¹⁸ Helmholtz Institute Mainz, Staudinger Weg 18, D-55099 Mainz, Germany

¹⁹ Henan Normal University, Xinxiang 453007, People's Republic of China

²⁰ Henan University, Kaifeng 475004, People's Republic of China

²¹ Henan University of Science and Technology, Luoyang 471003, People's Republic of China

²² Henan University of Technology, Zhengzhou 450001, People's Republic of China

²³ Huangshan College, Huangshan 245000, People's Republic of China

²⁴ Hunan Normal University, Changsha 410081, People's Republic of China

²⁵ Hunan University, Changsha 410082, People's Republic of China

²⁶ Indian Institute of Technology Madras, Chennai 600036, India

²⁷ Indiana University, Bloomington, Indiana 47405, USA

²⁸ INFN Laboratori Nazionali di Frascati, (A)INFN Laboratori Nazionali di Frascati, I-00044, Frascati, Italy; (B)INFN Sezione di Perugia, I-06100, Perugia, Italy; (C)University of Perugia, I-06100, Perugia, Italy

²⁹ INFN Sezione di Ferrara, (A)INFN Sezione di Ferrara, I-44122, Ferrara, Italy; (B)University of Ferrara, I-44122, Ferrara, Italy

³⁰ Inner Mongolia University, Hohhot 010021, People's Republic of China

³¹ Institute of Modern Physics, Lanzhou 730000, People's Republic of China

³² Institute of Physics and Technology, Peace Avenue 54B, Ulaanbaatar 13330, Mongolia

³³ Instituto de Alta Investigación, Universidad de Tarapacá, Casilla 7D, Arica 1000000, Chile

³⁴ Jilin University, Changchun 130012, People's Republic of China

³⁵ Johannes Gutenberg University of Mainz, Johann-Joachim-Becher-Weg 45, D-55099 Mainz, Germany

³⁶ Joint Institute for Nuclear Research, 141980 Dubna, Moscow region, Russia

³⁷ Justus-Liebig-Universität Giessen, II. Physikalisches Institut, Heinrich-Buff-Ring 16, D-35392 Giessen, Germany

³⁸ Lanzhou University, Lanzhou 730000, People's Republic of China

³⁹ Liaoning Normal University, Dalian 116029, People's Republic of China

⁴⁰ Liaoning University, Shenyang 110036, People's Republic of China

⁴¹ Nanjing Normal University, Nanjing 210023, People's Republic of China

⁴² Nanjing University, Nanjing 210093, People's Republic of China

⁴³ Nankai University, Tianjin 300071, People's Republic of China

- ⁴⁴ National Centre for Nuclear Research, Warsaw 02-093, Poland
- ⁴⁵ North China Electric Power University, Beijing 102206, People's Republic of China
- ⁴⁶ Peking University, Beijing 100871, People's Republic of China
- ⁴⁷ Qufu Normal University, Qufu 273165, People's Republic of China
- ⁴⁸ Renmin University of China, Beijing 100872, People's Republic of China
- ⁴⁹ Shandong Normal University, Jinan 250014, People's Republic of China
- ⁵⁰ Shandong University, Jinan 250100, People's Republic of China
- ⁵¹ Shanghai Jiao Tong University, Shanghai 200240, People's Republic of China
- ⁵² Shanxi Normal University, Linfen 041004, People's Republic of China
- ⁵³ Shanxi University, Taiyuan 030006, People's Republic of China
- ⁵⁴ Sichuan University, Chengdu 610064, People's Republic of China
- ⁵⁵ Soochow University, Suzhou 215006, People's Republic of China
- ⁵⁶ South China Normal University, Guangzhou 510006, People's Republic of China
- ⁵⁷ Southeast University, Nanjing 211100, People's Republic of China
- ⁵⁸ State Key Laboratory of Particle Detection and Electronics, Beijing 100049, Hefei 230026, People's Republic of China
- ⁵⁹ Sun Yat-Sen University, Guangzhou 510275, People's Republic of China
- ⁶⁰ Suranaree University of Technology, University Avenue 111, Nakhon Ratchasima 30000, Thailand
- ⁶¹ Tsinghua University, Beijing 100084, People's Republic of China
- ⁶² Turkish Accelerator Center Particle Factory Group, (A)Istinye University, 34010, Istanbul, Turkey; (B)Near East University, Nicosia, North Cyprus, 99138, Mersin 10, Turkey
- ⁶³ University of Chinese Academy of Sciences, Beijing 100049, People's Republic of China
- ⁶⁴ University of Groningen, NL-9747 AA Groningen, The Netherlands
- ⁶⁵ University of Hawaii, Honolulu, Hawaii 96822, USA
- ⁶⁶ University of Jinan, Jinan 250022, People's Republic of China
- ⁶⁷ University of Manchester, Oxford Road, Manchester, M13 9PL, United Kingdom
- ⁶⁸ University of Muenster, Wilhelm-Klemm-Strasse 9, 48149 Muenster, Germany
- ⁶⁹ University of Oxford, Keble Road, Oxford OX13RH, United Kingdom
- ⁷⁰ University of Science and Technology Liaoning, Anshan 114051, People's Republic of China
- ⁷¹ University of Science and Technology of China, Hefei 230026, People's Republic of China
- ⁷² University of South China, Hengyang 421001, People's Republic of China
- ⁷³ University of the Punjab, Lahore-54590, Pakistan
- ⁷⁴ University of Turin and INFN, (A)University of Turin, I-10125, Turin, Italy; (B)University of Eastern Piedmont, I-15121, Alessandria, Italy; (C)INFN, I-10125, Turin, Italy
- ⁷⁵ Uppsala University, Box 516, SE-75120 Uppsala, Sweden
- ⁷⁶ Wuhan University, Wuhan 430072, People's Republic of China
- ⁷⁷ Yantai University, Yantai 264005, People's Republic of China
- ⁷⁸ Yunnan University, Kunming 650500, People's Republic of China
- ⁷⁹ Zhejiang University, Hangzhou 310027, People's Republic of China
- ⁸⁰ Zhengzhou University, Zhengzhou 450001, People's Republic of China
- ^a Deceased
- ^b Also at the Moscow Institute of Physics and Technology, Moscow 141700, Russia
- ^c Also at the Novosibirsk State University, Novosibirsk, 630090, Russia
- ^d Also at the NRC "Kurchatov Institute", PNPI, 188300, Gatchina, Russia
- ^e Also at Goethe University Frankfurt, 60323 Frankfurt am Main, Germany
- ^f Also at Key Laboratory for Particle Physics, Astrophysics and Cosmology, Ministry of Education; Shanghai Key Laboratory for Particle Physics and Cosmology; Institute of Nuclear and Particle Physics, Shanghai 200240, People's Republic of China
- ^g Also at Key Laboratory of Nuclear Physics and Ion-beam Application (MOE) and Institute of Modern Physics, Fudan University, Shanghai 200443, People's Republic of China
- ^h Also at State Key Laboratory of Nuclear Physics and Technology, Peking University, Beijing 100871, People's Republic of China
- ⁱ Also at School of Physics and Electronics, Hunan University, Changsha 410082, China
- ^j Also at Guangdong Provincial Key Laboratory of Nuclear Science, Institute of Quantum Matter, South China Normal University, Guangzhou 510006, China
- ^k Also at MOE Frontiers Science Center for Rare Isotopes, Lanzhou University, Lanzhou 730000, People's Republic of China
- ^l Also at Lanzhou Center for Theoretical Physics, Lanzhou University, Lanzhou 730000, People's Republic of China
- ^m Also at the Department of Mathematical Sciences, IBA, Karachi 75270, Pakistan
- ⁿ Also at Ecole Polytechnique Federale de Lausanne (EPFL), CH-1015 Lausanne, Switzerland
- ^o Also at Helmholtz Institute Mainz, Staudinger Weg 18, D-55099 Mainz, Germany
- ^p Also at School of Physics, Beihang University, Beijing 100191, China

(Dated: March 5, 2024)

Using $(2.712 \pm 0.014) \times 10^9$ $\psi(3686)$ events collected by the BESIII detector operating at the BEPCII collider, we report the first observation of $\psi(3686) \rightarrow 3\phi$ decay with a significance larger

than 10σ . The branching fraction of this decay is determined to be $(1.46 \pm 0.05 \pm 0.17) \times 10^{-5}$, where the first uncertainty is statistical and the second is systematic. No significant structure is observed in the $\phi\phi$ invariant mass spectra.

I. INTRODUCTION

Charmonium resonances lie in between the perturbative and non-perturbative regimes of Quantum Chromodynamics (QCD) [1–3], which describes the strong interaction. Below the open charm threshold, both J/ψ and $\psi(3686)$ mainly decay into light hadrons through the annihilation of the $c\bar{c}$ pair into three gluons or one single virtual photon, with the decay width proportional to the modules of the charmonium wave function [4]. QCD has been tested thoroughly at high energy region where the strong interaction coupling constant is small. However, in the low energy region, theoretical calculations based on first principles of QCD are still unreliable since the non-perturbative contribution is significant, and various effective field theories are introduced [5–7] to approximate these non-perturbative contributions. The study of charmonium decays can provide valuable insights to improve the understanding of the inner charmonium structure and test phenomenological mechanisms of non-perturbative QCD.

In recent years, significant progress has been made in experimental studies of multi-body J/ψ and $\psi(3686)$ decays. Previously, the $\psi(3686) \rightarrow PPP$, $\psi(3686) \rightarrow VPP$, and $\psi(3686) \rightarrow VVP$ decays have been extensively studied, as summarized in Ref. [1], where P and V denote pseudoscalar and vector mesons, respectively. To date, no study of $\psi(3686) \rightarrow VVV$ has been reported. In this paper, we present the first observation of the $\psi(3686) \rightarrow 3\phi$ decay. This analysis is based on $(2.712 \pm 0.014) \times 10^9$ $\psi(3686)$ events collected at the center-of-mass energy of 3.686 GeV by the BESIII detector in 2009, 2012 and 2021 [8].

II. BESIII EXPERIMENT AND MONTE CARLO SIMULATION

The BESIII detector [9] records symmetric e^+e^- collisions provided by the BEPCII storage ring [10] in the center-of-mass energy (\sqrt{s}) range from 2.0 to 4.95 GeV, with a peak luminosity (\mathcal{L}) of $1 \times 10^{33} \text{ cm}^{-2}\text{s}^{-1}$ achieved at $\sqrt{s} = 3.77$ GeV. BESIII has collected large data samples in this energy region [1, 11, 12]. The cylindrical core of the BESIII detector covers 93% of the full solid angle and consists of a helium-based multilayer drift chamber (MDC), a plastic scintillator time-of-flight system (TOF), and a CsI(Tl) electromagnetic calorimeter (EMC), which are all enclosed in a superconducting solenoidal magnet providing a 1.0 T magnetic field. The solenoid is supported by an octagonal flux-return yoke with resistive plate counter muon identification modules interleaved with steel. The charged-particle momentum

resolution at 1 GeV/ c is 0.5%, and the dE/dx resolution is 6% for electrons from Bhabha scattering. The EMC measures photon energies with a resolution of 2.5% (5%) at 1 GeV in the barrel (end-cap) region. The time resolution in the TOF barrel region is 68 ps, while that in the end-cap region was 110 ps. The end-cap TOF system was upgraded in 2015 using multigap resistive plate chamber technology, providing a time resolution of 60 ps, which benefits about 85% of the data used in this analysis [13].

Simulated data samples are produced with a GEANT4-based [14] Monte Carlo (MC) package, which includes the geometric description of the BESIII detector and the detector response. The simulations model the beam energy spread and initial state radiation (ISR) in the e^+e^- annihilations with the generator KKMC [15]. To estimate backgrounds, an inclusive MC sample is generated including the production of the $\psi(3686)$ resonance, the ISR production of the J/ψ , and the continuum processes incorporated in KKMC [15]. All particle decays are modelled with EVTGEN [16] using branching fractions either taken from the Particle Data Group (PDG) [17], when available, or otherwise estimated with LUNDCHARM [18]. Final state radiation from charged final state particles is incorporated using the PHOTOS package [19]. The detection efficiency of the $\psi(3686) \rightarrow 3\phi$ decay is determined using the signal MC samples containing 5×10^5 events, where the $\psi(3686) \rightarrow 3\phi$ and $\phi \rightarrow K^+K^-$ decays are generated with PHSP and VSS models, respectively. The PHSP model represents the generic phase space for n-body decays, averaging over the spins of initial and final state particles. The VSS model describes the decay of a vector particle (ϕ) into two scalar particles.

In addition, the data sample collected at the center-of-mass energy of 3.773 GeV with an integrated luminosity of 7.93 fb^{-1} [20] is used to estimate the contribution from continuum process.

III. EVENT SELECTION

In this analysis, candidate events for $\psi(3686) \rightarrow 3\phi$ are selected by reconstructing three or two ϕ candidates. The two reconstruction methods are hereafter referred to as “full reconstruction” for the three ϕ case and “partial reconstruction” for the two ϕ case. A ϕ candidate is reconstructed by the decay $\phi \rightarrow K^+K^-$.

Each kaon candidate must satisfy $|\cos\theta| < 0.93$, where θ is the polar angle defined with respect to the z -axis, which is the symmetry axis of the MDC. Additionally, each kaon candidate must originate within 1 cm (10 cm) of the interaction point in the plane transverse to the beam direction (in the beam direction).

Particle identification (PID) is performed on kaon candidates using the dE/dx and TOF information. The

charged kaons are identified by comparing the likelihoods for the kaon and pion hypotheses and requiring $\mathcal{L}(K) > \mathcal{L}(\pi)$.

A. Full reconstruction sample

A four-constraint (4C) kinematic fit, ensuring energy and momentum conservation, is performed under the hypothesis of $e^+e^- \rightarrow 3(K^+K^-)$ with at least six good kaon candidates. The helix parameters of charged tracks in the MC simulations are corrected to improve the χ^2 distribution consistency between data and MC simulation using the method described in Ref. [21]. Events satisfying $\chi_{4C}^2 < 50$ are retained for further analysis. If there are multiple combinations in an event, the combination with the lowest χ_{4C}^2 is kept for further analysis.

The three K^+K^- pairs result in six combinations to form the three different ϕ candidates. The best combination of three ϕ candidates is selected by minimizing

$$\Delta = \sqrt{\sum_{i=a,b,c} (M_{K^+K^-}^i - m_\phi)^2}, \quad (1)$$

where m_ϕ is the nominal ϕ mass [17]. The three ϕ candidates are randomly labeled by using the Knuth-Durstenfeld shuffle algorithm [22, 23], since they are identical in the reconstruction procedure.

B. Partial reconstruction sample

To improve the detection efficiency, we employ the partial reconstruction strategy when six kaon candidates cannot be reconstructed. The reconstruction of the $\psi(3686) \rightarrow 3\phi$ decay is performed by selecting exactly five kaon candidates from six charged tracks in each event, with at least two kaons of each charge. Events with less than five identified kaons are not used because of the very high combinatorial background.

The two K^+K^- pairs along with one K^\pm result in six combinations to form the two ϕ candidates. The best combination of two ϕ candidates is selected by minimizing

$$\Delta = \sqrt{\sum_{i=a,b} (M_{K^+K^-}^i - m_\phi)^2 + (M_\phi^{\text{rec}} - m_\phi)^2}, \quad (2)$$

where M_ϕ^{rec} is defined as

$$M_\phi^{\text{rec}} = \sqrt{(\sqrt{s} - E_{\phi\phi})^2 - p_{\phi\phi}^2}, \quad (3)$$

in which $E_{\phi\phi}$ and $p_{\phi\phi}$ are the energy and momentum of the two ϕ system, respectively. Additionally, to further improve the purity of the signal sample, the recoil mass of the $2(K^+K^-)K^\pm$ combination is required to be in the mass interval of (0.4746, 0.5145) GeV/ c^2 . This range

corresponds to about $\pm 3\sigma$ around the kaon mass, where σ is the resolution on the $2(K^+K^-)K^\pm$ recoil mass. Similar to the full reconstruction case, the two reconstructed ϕ candidates are randomly labeled.

C. Background analysis

Potential background components are investigated by analyzing the inclusive MC sample of $\psi(3686)$ decays with the generic event type analysis tool, TopoAna [24]. The study shows that only a very small background contribution survives the event selection. After imposing all selection criteria, the three dimensional (3D) distributions of the invariant masses of the three ϕ candidates in the data are shown in Fig. 1 for both full and partial reconstruction cases. In both cases, a distinct cluster around the ϕ mass is evident.

IV. RESULTS

A. Fitting of data

The signal yield of the $\psi(3686) \rightarrow 3\phi$ decay is determined through a simultaneous unbinned maximum likelihood fit to the 3D distribution of $M_{K^+K^-}^a : M_{K^+K^-}^b : M_{K^+K^-}^c$ for the full reconstruction case, and to the 3D distribution of $M_{K^+K^-}^a : M_{K^+K^-}^b : M_\phi^{\text{rec}}$ for the partial reconstruction case. In the simultaneous fit, the branching fractions of $\psi(3686) \rightarrow 3\phi$ measured with the different reconstruction cases are constrained to be equal. Events are divided into four cases based on the source of the K^+K^- pairs: the ‘Signal’ describes candidates where all three pairs of K^+K^- originate from ϕ mesons; the ‘BKGI’ denotes candidates where two pairs of K^+K^- originate from ϕ mesons and one pair from combinatorial backgrounds; the ‘BKGII’ describes candidates where only one pair of K^+K^- comes from the ϕ meson and the remaining two pairs are from combinatorial backgrounds; the ‘BKGIII’ encompasses candidates where all three pairs of K^+K^- come from combinatorial backgrounds, as well as the incorrectly reconstructed events with different final states.

So, the probability density functions (PDFs) of Signal, BKGI, BKGII, and BKGIII are constructed as follows:

- Signal: $\mathcal{S}_x \times \mathcal{S}_y \times \mathcal{S}_z$,
- BKGI: $f_1 \cdot \mathcal{S}_x \times \mathcal{S}_y \times \mathcal{A}_z + \mathcal{S}_x \times \mathcal{A}_y \times \mathcal{S}_z + \mathcal{A}_x \times \mathcal{S}_y \times \mathcal{S}_z$,
- BKGII: $\mathcal{S}_x \times \mathcal{A}_y \times \mathcal{A}_z + \mathcal{A}_x \times \mathcal{S}_y \times \mathcal{A}_z + f_2 \cdot \mathcal{A}_x \times \mathcal{A}_y \times \mathcal{S}_z$,
- BKGIII: $\mathcal{A}_x \times \mathcal{A}_y \times \mathcal{A}_z$.

Here, x , y , and z correspond to the three dimensions of the 3D fit. The \mathcal{S}_i are the signal shapes derived from signal MC simulations, while \mathcal{A}_i are the reversed ARGUS

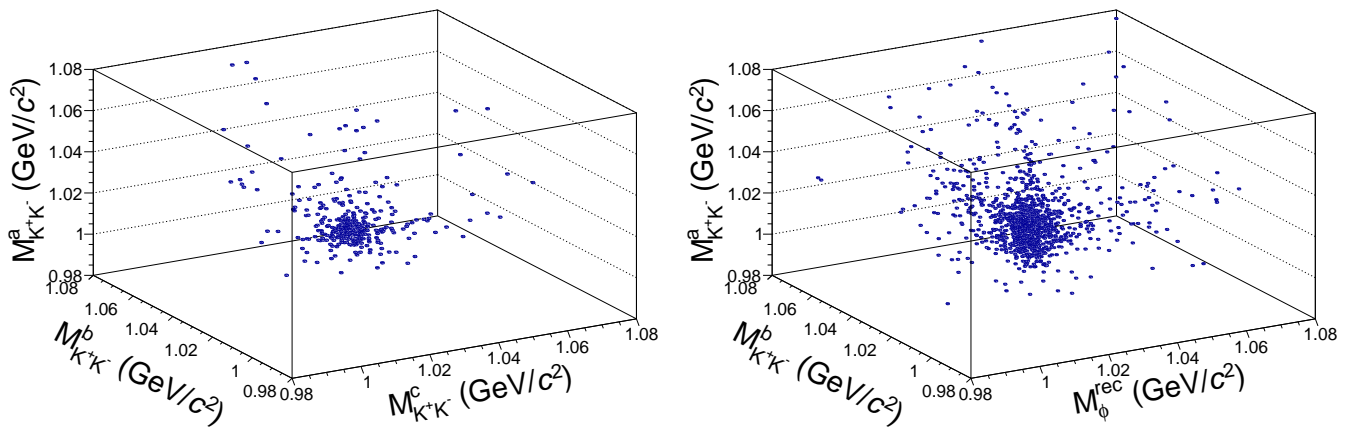


Fig. 1. The $M_{K^+K^-}^a : M_{K^+K^-}^b : M_{K^+K^-}^c (M_\phi^{\text{rec}})$ distributions of the (left) full and (right) partial reconstructed candidates for $\psi(3686) \rightarrow 3\phi$.

functions [25] that characterize the combinatorial background shape in the K^+K^- invariant mass spectrum, where i denotes the different dimensions. The parameters f_1 and f_2 describe the distinct PDFs resulting from the non-identical ϕ reconstructions in the partial reconstruction sample. This disparity is attributed to the resolution differences between the full and partial reconstructions. While f_1 and f_2 are fixed to 1 for the full reconstruction sample, they are treated as free fit parameters for the partial reconstruction sample to incorporate the resolution variation.

For the full reconstruction case, the \mathcal{S}_i are identical and determined from the ϕ candidates of signal MC. Additionally, \mathcal{A}_i are identical reversed ARGUS functions with starting points fixed at the K^+K^- mass threshold.

For the partial reconstruction case, we specify the z as the recoil dimension. \mathcal{S}_x and \mathcal{S}_y are identical PDFs derived from the two fully reconstructed ϕ candidates and \mathcal{S}_z is derived from the line shape of M_ϕ^{rec} of signal MC. \mathcal{A}_x and \mathcal{A}_y share the same parameters, while the parameters of \mathcal{A}_z are independently determined. The starting points of all \mathcal{A}_i are fixed at the K^+K^- mass threshold.

B. Detection efficiency

The detection efficiency of the $\psi(3686) \rightarrow 3\phi$ decay is evaluated by analyzing the signal MC samples. Figure 2 shows the Dalitz plots of the $\psi(3686) \rightarrow 3\phi$ candidates selected in data and signal MC samples. Figures 3 and 4 show the comparisons of the momenta and cosines of polar angles of each ϕ candidate, as well as the K^+K^- invariant mass spectra between data and MC simulation. The consistency between data and MC simulation is good. The detection efficiencies of $\psi(3686) \rightarrow 3\phi$ is determined to be $(6.13 \pm 0.04)\%$ and $(20.58 \pm 0.08)\%$ for full and partial reconstruction samples, respectively. An

efficiency correction factor is applied to account for the data-MC deviation arising from tracking and PID efficiencies for K^\pm , as listed in Sec. V.

C. Branching fraction

Under the assumption that there is no interference between the $\psi(3686)$ and continuum amplitudes, the branching fraction of the $\psi(3686) \rightarrow 3\phi$ decay is determined as follows:

$$\mathcal{B}_{\psi(3686) \rightarrow 3\phi} = \frac{N_{\psi(3686) \rightarrow 3\phi} - f_c \times N_{e^+e^-(3773) \rightarrow 3\phi}}{N_{\psi(3686)} \mathcal{B}_{\phi \rightarrow K^+K^-}^3 \epsilon_{\psi(3686) \rightarrow 3\phi}}, \quad (4)$$

where $N_{\psi(3686) \rightarrow 3\phi}$ and $N_{e^+e^-(3773) \rightarrow 3\phi}$ are the numbers of $\psi(3686) \rightarrow 3\phi$ and $e^+e^-(3773) \rightarrow 3\phi$ events extracted from the data sample taken at $\sqrt{s} = 3.686$ GeV and 3.773 GeV. They are determined to be 1319 ± 43 and 138 ± 15 , also the fractions of full reconstructed events out of total events are 23% and 27%. Figures 5 and 6 show the fit results on the selected candidates. Meanwhile the fitted event numbers of BKGI, BKGII and BKGIII are 74 ± 24 , 30 ± 16 and 48 ± 16 . The factor f_c is introduced to propagate the number of continuum events observed at 3.773 GeV to the 3.686 GeV energy point taking into account luminosities [8] $\mathcal{L}_{3.686(3.773)}$ and cross sections at different energies. It is calculated as $f_c = \frac{\epsilon_{\psi(3686) \rightarrow 3\phi}}{\epsilon_{e^+e^-(3773) \rightarrow 3\phi}} \times \frac{\mathcal{L}_{3.686}}{\mathcal{L}_{3.773}} \times \frac{(3.773 \text{ GeV})^{2n}}{(3.686 \text{ GeV})^{2n}}$, where n is the power of the $\frac{1}{s}$ dependence of the cross section. We take $n = 1$ [26] and obtain $f_c = 0.49$. The total number of $\psi(3686)$ events is labeled as $N_{\psi(3686)}$ and $\mathcal{B}_{\phi \rightarrow K^+K^-}$ is the world average value of the branching fraction of $\phi \rightarrow K^+K^-$ taken from the PDG [17]. The detection efficiencies for $\psi(3686) \rightarrow 3\phi$ and the continuum process $e^+e^-(3773) \rightarrow 3\phi$ are labeled as $\epsilon_{\psi(3686) \rightarrow 3\phi}$ and $\epsilon_{e^+e^-(3773) \rightarrow 3\phi}$. The branching fraction of the $\psi(3686) \rightarrow 3\phi$ decay is determined to be $(1.46 \pm 0.05) \times 10^{-5}$, where

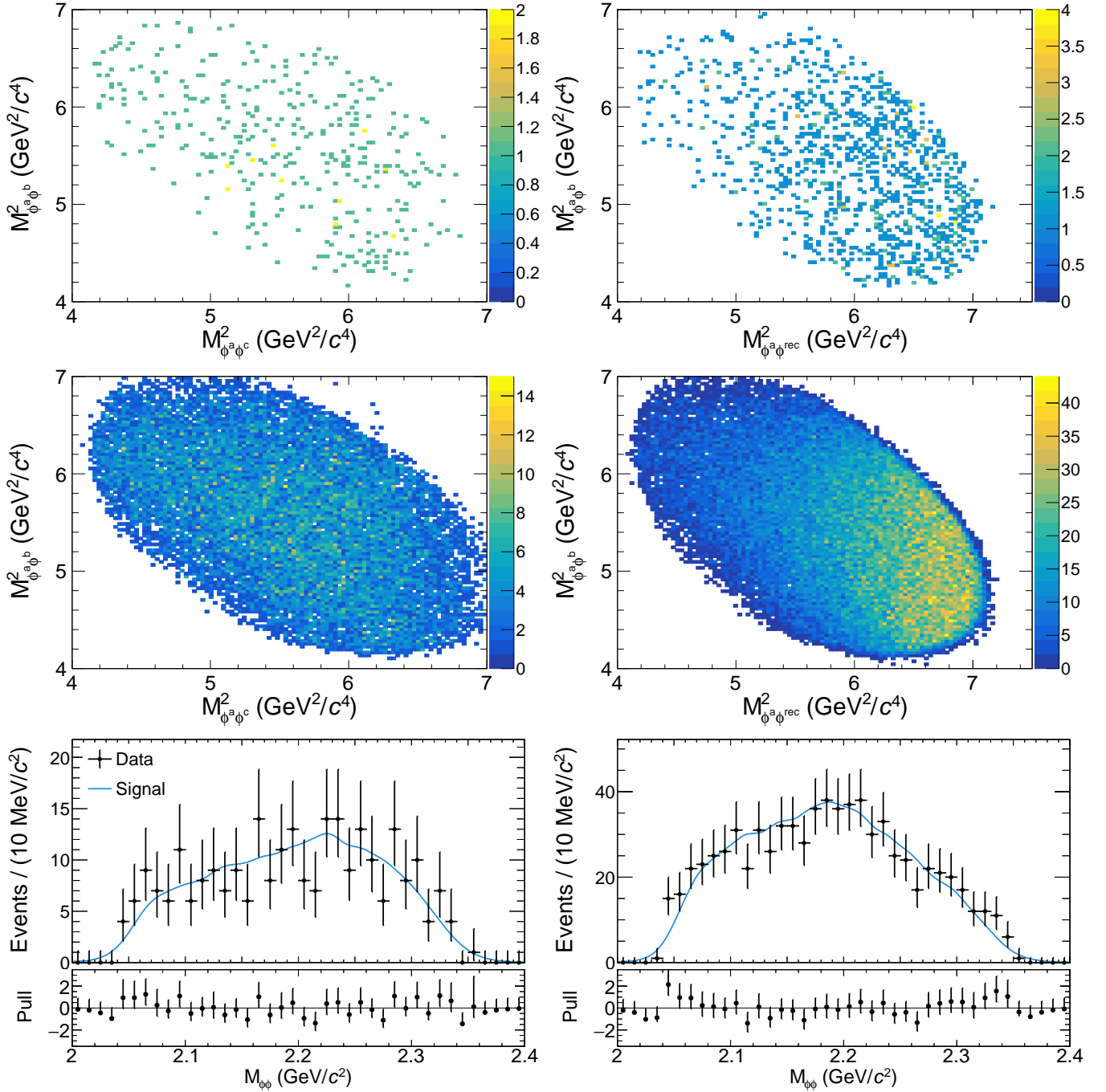


Fig. 2. Dalitz plots of $M_{\phi^a\phi^b}^2$ vs $M_{\phi^a\phi^c}^2$ of the (left) full and (right) partial reconstructed candidates. The first row indicates data and the second row indicates signal MC events. In the third row, the distributions of the invariant masses of the two lowest momentum ϕ candidates are shown. The black points with error bars are data. The blue curves represent the signal component of the fit.

the uncertainty is statistical only.

The statistical significance is estimated by examining the probability of the change in negative log-likelihood values when the signal is included or excluded in the fits. This probability is calculated under the χ^2 distribution hypothesis taking into account the change in the number of degrees of freedom. Consequently, the significance is

determined to be greater than 10σ .

We have also examined the Dalitz plot and $\phi\phi$ invariant mass spectra, as shown in Fig. 2, and no obvious structure is found.

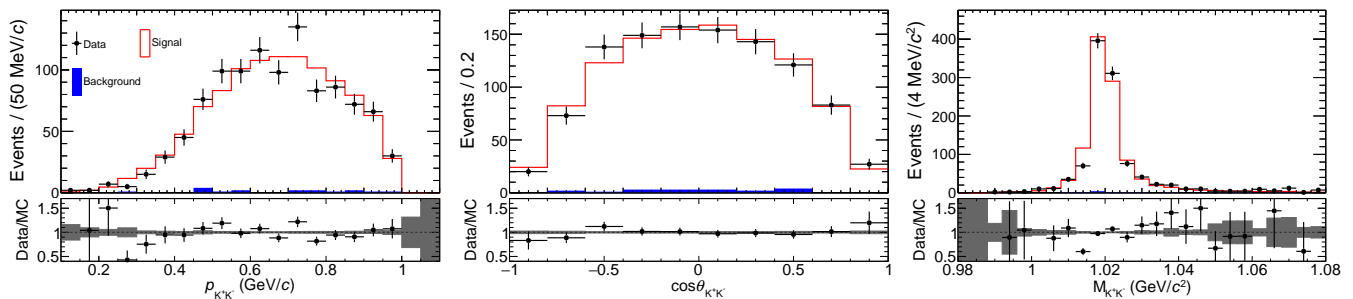


Fig. 3. Distributions of the momentum, cosines of polar angle and mass spectra of the ϕ candidates for full reconstructed candidates, all reconstructed ϕ candidates are filled in the same histogram. The black points with error bars are data, the solid red lines show the signal MC simulation which is scaled to the total number of events of data, and the blue solid-filled histograms are the background contribution of the inclusive MC sample. The bottom panels show the data and MC comparison, where the error bands indicate the MC statistical uncertainty only.

V. SYSTEMATIC UNCERTAINTIES

The systematic uncertainties in the measurement of the branching fraction of the $\psi(3686) \rightarrow 3\phi$ are discussed below.

The total number of $\psi(3686)$ events has been determined to be $N_{\psi(3686)} = (2.712 \pm 0.014) \times 10^9$ with inclusive hadronic events as described in Ref. [8]. This measurement contributes 0.5% to the systematic uncertainty of the branching fraction.

The systematic uncertainties of K^\pm tracking and PID are studied with the control sample of $e^+e^- \rightarrow \pi^+\pi^-J/\psi$ ($J/\psi \rightarrow K^+K^-K^+K^-$). The differences of K^\pm tracking and PID efficiencies between data and MC simulation are obtained in different transverse momentum intervals. The data-MC differences are then weighted according to the distribution of the transverse momentum of kaon in the signal decay. The data to MC ratios of the re-weighted tracking and PID efficiencies are $(98.86 \pm 0.55)\%$ and $(99.50 \pm 0.05)\%$, respectively. Here the errors originate mainly from the limited statistics of the control sample. The detection efficiency estimated from the MC is corrected with the data to MC ratios, and the rounded uncertainties of the ratios, 0.6% and 0.1%, are taken as the systematic uncertainty of the tracking and PID efficiencies per K^\pm , respectively.

The systematic uncertainty of the 3D fit is considered in three aspects. The background shape is changed from the reversed ARGUS function to a second-order polynomial function. The signal shape is changed from the simulated MC shape to the shape used by BaBar [27], written as

$$\sigma(s) = \frac{1}{s^{5/2}} \frac{q_{K^+K^-}^3(s)}{q_{K^+K^-}^3(m_\phi^2)} \left| \frac{\Gamma_\phi m_\phi^3 \sqrt{m_\phi \sigma_{\phi \rightarrow K^+K^-} / C}}{s - m_\phi^2 + i\sqrt{s} \Gamma_\phi \frac{q_{K^+K^-}^3(s)}{q_{K^+K^-}^3(m_\phi^2)}} \right|^2, \quad (5)$$

where $q_{K^+K^-}(s) = \sqrt{s - 4m_{K^\pm}^2}$ is a threshold term; $\sigma_{\phi \rightarrow K^+K^-}$ is a normalization factor obtained from the fit; $C = 0.389 \times 10^{12}$ nb MeV²/c⁴; m_ϕ and Γ_ϕ are the mass

and width of the ϕ meson. The alternative fit ranges are chosen as [0.98, 1.09], [0.98, 1.07], [0.97, 1.08], and [0.99, 1.08] GeV/c². The quadratic sum of the signal yield variations, 5.7%, is assigned as the corresponding systematic uncertainty.

The effect of the misidentification of the potential backgrounds from $\psi(3686) \rightarrow 2\phi K^+K^-$, $\psi(3686) \rightarrow \phi 2(K^+K^-)$ and $\psi(3686) \rightarrow 3(K^+K^-)$ to signal are found to be less than 0.1% and are thereby ignored in the systematic uncertainty.

In the nominal analysis, the helix parameters of charged tracks in the 4C kinematic fit have been corrected with the parameters derived with the control sample of $e^+e^- \rightarrow K^*(892)K\pi \rightarrow KK\pi\pi$ in Ref. [21]. The difference of detection efficiencies with and without helix parameter correction, 1.7%, is assigned as the corresponding systematic uncertainty.

In the nominal analysis, the M_{rec}^K is required to be within the $\pm 3\sigma$ interval around the kaon mass. Changing this interval to $\pm 2\sigma$ or $\pm 4\sigma$ results in a relative change of the measured signal by 1.0%, which is taken as a systematic uncertainty.

Another source of the systematic uncertainty is the limited MC statistics. This contribution is evaluated as

$$\frac{1}{\sqrt{N}} \sqrt{\frac{(1-\epsilon)}{\epsilon}}, \quad (6)$$

where ϵ is the detection efficiency and N is total number of signal MC events. The corresponding number, 0.4%, is assigned as the systematic uncertainty.

The branching fraction $(49.1 \pm 0.5)\%$ of $\phi \rightarrow K^+K^-$ is quoted from the PDG [17], contributing a relative uncertainty of 1.0%.

In the nominal analysis, we determine the branching fraction without considering the interference between $\psi(3686)$ and continuum amplitudes. The systematic uncertainty due to this effect is estimated by introducing an interference term between $\psi(3686)$ and continuum amplitudes. The largest relative change of the signal yield, 9.0%, which is observed for $\pm 90^\circ$ phase between the two amplitudes, is taken as the systematic error.

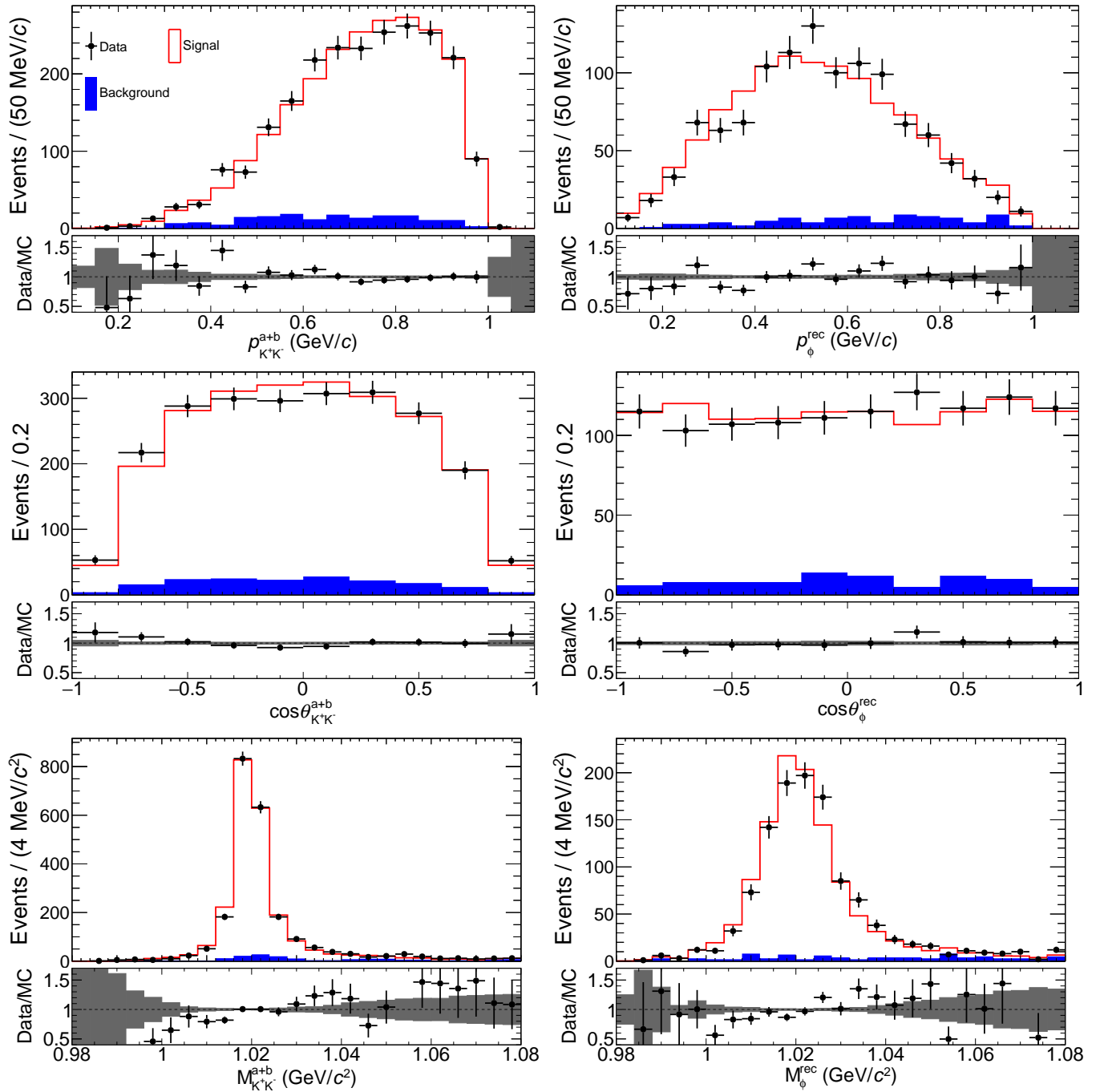


Fig. 4. Distributions of the momentum, cosines of polar angle and mass spectra of the ϕ candidates for partial candidates, two reconstructed ϕ candidates are filled in the same histogram (first column). The black points with error bars are data, the solid red lines show the signal MC simulation which is scaled to the total number of events of data, and the blue solid-filled histograms are the background contribution of the inclusive MC sample. The bottom panels show the data and MC comparison, where the error bands indicate the MC statistical uncertainty only.

All the systematic uncertainties are summarized in Table 1. The total uncertainty for each reconstruction case in the Table 1 is calculated as a quadratic sum of all contributions, which are assumed to be independent within each case. The total systematic uncertainty is calculated using the method described in [28], which takes

into account the correlations of systematic uncertainties between the different reconstruction cases. The uncertainties from the 4C kinematic fit, the M_{rec}^K requirement and MC statistics are taken as uncorrelated and all other contributions are assumed to be fully correlated between the two reconstruction cases. The total systematic un-

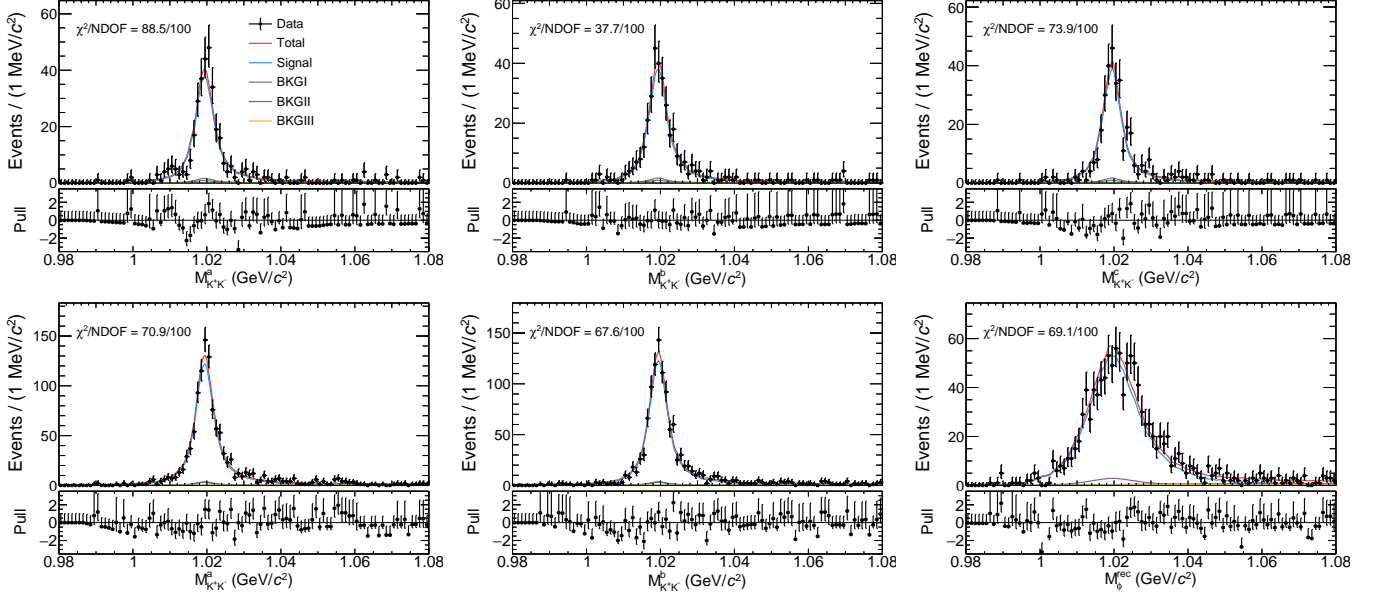


Fig. 5. One-dimensional projections of the simultaneous fit to the $M_{K^+K^-}^a : M_{K^+K^-}^b : M_{K^+K^-}^c (M_\phi^{\text{rec}})$ distribution of the (top row) full and (bottom row) partial reconstructed candidate events of $\psi(3686) \rightarrow 3\phi$ for $\psi(3686)$ data (shown as the dots with error bars). The red solid curves are the total fit results, while the blue curves are the signal contributions of the fit and other curves represent the different background contributions. For each projection, the χ^2/NDOF are provided, with χ^2 being calculated from the difference between the binned data points and the total fit projection, and the NDOF representing the number of bins.

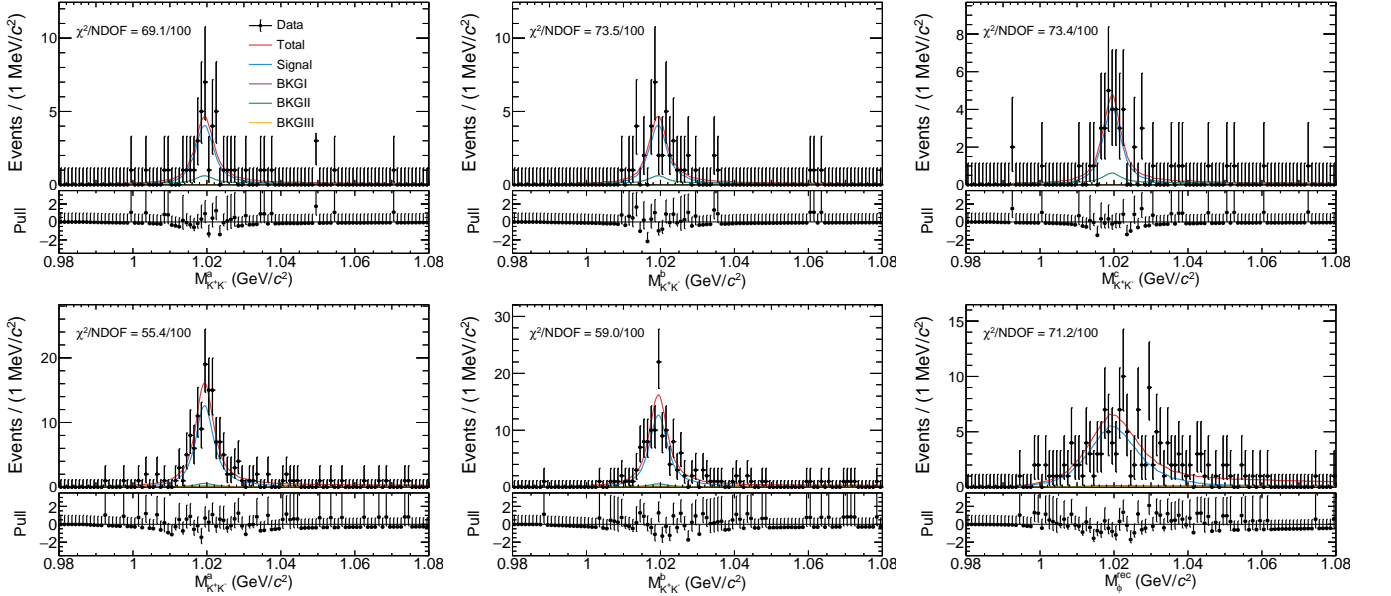


Fig. 6. One-dimensional projections of the simultaneous fit to the $M_{K^+K^-}^a : M_{K^+K^-}^b : M_{K^+K^-}^c (M_\phi^{\text{rec}})$ distribution of the (top row) full and (bottom row) partial reconstructed candidate events of $e^+e^- \rightarrow 3\phi$ for data taken at 3.773 GeV (shown as the dots with error bars). The red solid curves are the total fit results, while the blue curves are the signal contributions of the fit and other curves represent the different background contributions. For each projection, the χ^2/NDOF are given, with χ^2 being calculated from the difference between the binned data points and the total fit projection, and the NDOF representing the number of bins.

certainty is determined to be 11.5%.

Table 1. Systematic uncertainties in the branching fraction measurement.

Source	full (%)	partial (%)
$N_{\psi(3686)}$	0.5	0.5
Tracking	3.6	3.0
PID	0.6	0.5
3D fit	5.7	5.7
4C kinematic fit	1.7	none
M_{rec}^K requirement	none	1.0
MC statistics	0.4	0.4
$\mathcal{B}(\phi \rightarrow K^+ K^-)$	3.0	3.0
Interference	9.0	9.0
Total	11.8	11.5

VI. SUMMARY

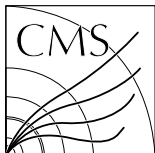
By analyzing $(2.712 \pm 0.014) \times 10^9$ events collected with the BESIII detector operating at the BEPCII collider, we report the first observation of the $\psi(3686) \rightarrow 3\phi$ decay. The branching fraction of this decay is determined to be $(1.46 \pm 0.05 \pm 0.17) \times 10^{-5}$, with the first uncertainty being statistical and the second one systematic. Furthermore, we have examined the Dalitz plots and found no obvious structure. Further studies with high statistics data taken at the future super tau-charm factory [29] will be valuable to deeply understand the decay mechanisms of these types of decays and to seek potential new structures in the $\phi\phi$ mass spectrum.

ACKNOWLEDGMENTS

The BESIII Collaboration thanks the staff of BEPCII and the IHEP computing center for their strong support. This work is supported in part by National Key R&D Program of China under Contracts Nos. 2020YFA0406300, 2020YFA0406400; National Natural Science Foundation of China (NSFC) under Contracts Nos. 11635010, 11735014, 11835012, 11935015, 11935016, 11935018, 11961141012, 12025502, 12035009, 12035013, 12061131003, 12192260, 12192261, 12192262, 12192263, 12192264, 12192265, 12221005, 12225509, 12235017; the Chinese Academy of Sciences (CAS) Large-Scale Scientific Facility Program; the CAS Center for Excellence in Particle Physics (CCEPP); Joint Large-Scale Scientific Facility Funds of the NSFC and CAS under Contract No. U1832207; CAS Key Research Program of Frontier Sciences under Contracts Nos. QYZDJ-SSW-SLH003, QYZDJ-SSW-SLH040; 100 Talents Program of CAS; The Institute of Nuclear and Particle Physics (INPAC) and Shanghai Key Laboratory for Particle Physics and Cosmology; European Union's Horizon 2020 research and innovation programme under Marie Skłodowska-Curie grant agreement under Contract No. 894790; German Research Foundation DFG under Contracts Nos. 455635585, Collaborative Research Center CRC 1044, FOR5327, GRK 2149; Istituto Nazionale di Fisica Nucleare, Italy; Ministry of Development of Turkey under Contract No. DPT2006K-120470; National Research Foundation of Korea under Contract No. NRF-2022R1A2C1092335; National Science and Technology fund of Mongolia; National Science Research and Innovation Fund (NSRF) via the Program Management Unit for Human Resources & Institutional Development, Research and Innovation of Thailand under Contract No. B16F640076; Polish National Science Centre under Contract No. 2019/35/O/ST2/02907; The Swedish Research Council; U. S. Department of Energy under Contract No. DE-FG02-05ER41374.

-
- [1] M. Ablikim *et al.* (BESIII Collaboration), *Chin. Phys. C* **44**, 040001 (2020).
- [2] W. Kwong, J. L. Rosner and C. Quigg, *Ann. Rev. Nucl. Part. Sci.* **37**, 325 (1987).
- [3] E. Eichten, S. Godfrey, H. Mahlke and J. L. Rosner, *Rev. Mod. Phys.* **80**, 1161 (2008).
- [4] T. Appelquist and H. D. Politzer, *Phys. Rev. Lett.* **34**, 43 (1975); A. De Rujula and S. L. Glashow, *Phys. Rev. Lett.* **34**, 46 (1975).
- [5] E. Eichten and K. Gottfried, *Phys. Lett. B.* **66**, 286-290 (1977).
- [6] J. M. Drouffe and J. B. Zuber, *Phys. Rep.* **102**, 1-119 (1983).
- [7] V. L. Chernyak and A.R. Zhitnitsky, *Phys. Rep.* **112**, 173-318 (1984).
- [8] M. Ablikim *et al.* (BESIII Collaboration), *Chin. Phys. C* **42**, 023001 (2018). With the same method, the total number of $\psi(3686)$ events collected in 2009, 2012 and 2021 is determined to be $(2.712 \pm 0.014) \times 10^9$ with an uncertainty of 0.5% as a preliminary result.
- [9] M. Ablikim *et al.* (BESIII Collaboration), *Nucl. Instrum. Methods Phys. Res., Sec. A* **614**, 345 (2010); *Chin. Phys. C* **44**, 040001 (2020).
- [10] C. H. Yu *et al.*, in *Proceedings of IPAC 2016, Busan, Korea, 2016*, ISBN 978-3-95450-147-2.
- [11] J. Lu, Y. Xiao, X. Ji, *Radiat. Detect. Technol. Methods* **4**, 337-344 (2020).
- [12] J. W. Zhang, L. H. Wu, S. S. Sun *et al.*, *Radiat. Detect. Technol. Methods* **6**, 289-293 (2022).
- [13] X. Li *et al.*, *Radiat. Detect. Technol. Methods* **1**, 13 (2017); Y. X. Guo *et al.*, *Radiat. Detect. Technol. Meth-*

- ods **1**, 15 (2017); P. Cao *et al.*, *Nucl. Instrum. Meth. A* **953**, 163053 (2020).
- [14] S. Agostinelli *et al.* (GEANT4 Collaboration), *Nucl. Instrum. Meth. A* **506**, 250 (2003).
- [15] S. Jadach, B. F. L. Ward and Z. Was, *Phys. Rev. D* **63**, 113009 (2001); *Comput. Phys. Commun.* **130**, 260 (2000).
- [16] D. J. Lange, *Nucl. Instrum. Meth. A* **462**, 152 (2001); R. G. Ping, *Chin. Phys. C* **32**, 599 (2008).
- [17] R. L. Workman *et al.* (Particle Data Group), *Prog. Theor. Exp. Phys.* **2022**, 083C01 (2022).
- [18] J. C. Chen, G. S. Huang, X. R. Qi., D. H. Zhang, and Y. S. Zhu, *Phys. Rev. D* **62**, 034003 (2000); R. L. Yang, R. G. Ping and H. Chen, *Chin. Phys. Lett.* **31**, 061301 (2014).
- [19] E. Richter-Was, *Phys. Lett. B* **303**, 163 (1993).
- [20] M. Ablikim *et al.* (BESIII Collaboration), *Chin. Phys. C* **37**, 123001 (2013); *Phys. Lett. B* **753**, 629 (2016). With the same method, the total luminosity of $\psi(3773)$ data sample collected in 2009, 2010 and 2022 is determined to be 7.93 fb^{-1} as a preliminary result.
- [21] M. Ablikim *et al.* (BESIII Collaboration), *Phys. Rev. D* **87**, 012002 (2013).
- [22] R. Durstenfield, *Algorithm 235: Random Permutation*, Communications of the ACM **7**, 420 (1964), DOI: 10.1145/364520.364540.
- [23] D. E. Knuth, *Seminumerical algorithms. The Art of Computer Programming, Vol. 2*, Addison-Wesley, Reading, MA, 1969, pp. 139-140, OCLC 85975465.
- [24] X. Y. Zhou, S. X. Du, G. Li and C. P. Shen, *Comput. Phys. Commun.* **258**, 107540 (2021).
- [25] H. Albrecht *et al.* (ARGUS Collaboration), *Phys. Lett. B* **241**, 278 (1990).
- [26] M. Ablikim *et al.* (BESIII Collaboration), *Phys. Rev. D* **108**, 052001 (2023).
- [27] J. P. Lees *et al.* (BaBar Collaboration), *Phys. Rev. D* **89**, 092002 (2014).
- [28] Michael Schmelling, *Physica Scripta* **51**, 676 (1995).
- [29] M. Achasov *et al.*, [arXiv:2303.15790](https://arxiv.org/abs/2303.15790).



Search for new physics with emerging jets in proton-proton collisions at $\sqrt{s} = 13$ TeV

The CMS Collaboration*

Abstract

A search for “emerging jets” produced in proton-proton collisions at a center-of-mass energy of 13 TeV is performed using data collected by the CMS experiment corresponding to an integrated luminosity of 138 fb^{-1} . This search examines a hypothetical dark quantum chromodynamics (QCD) sector that couples to the standard model (SM) through a scalar mediator. The scalar mediator decays into an SM quark and a dark sector quark. As the dark sector quark showers and hadronizes, it produces long-lived dark mesons that subsequently decay into SM particles, resulting in a jet, known as an emerging jet, with multiple displaced vertices. This search looks for pair production of the scalar mediator at the LHC, which yields events with two SM jets and two emerging jets at leading order. The results are interpreted using two dark sector models with different flavor structures, and exclude mediator masses up to 1950 (1850) GeV for an unflavored (flavor-aligned) dark QCD model. The unflavored results surpass a previous search for emerging jets by setting the most stringent mediator mass exclusion limits to date, while the flavor-aligned results provide the first direct mediator mass exclusion limits to date.

Submitted to the Journal of High Energy Physics

1 Introduction

Although there is a preponderance of evidence from astronomical and cosmological observations [1–5] for the existence of dark matter (DM), it has not yet been detected in laboratories, suggesting that its origin may be associated with as-of-yet unobserved physics processes beyond the standard model (SM). As experimental searches have excluded a large portion of the phase space of DM models with weakly interacting massive particles, alternative theoretical models have been developed with a hidden gauge sector, similar to quantum chromodynamics (QCD), which can result in strongly self-interacting DM particles [6–9]. Dark matter of this type could interact with SM particles through so-called mediator particles and potentially be produced at colliders, producing signatures such as semivisible jets [10] or emerging jets (EJs) [11].

The search described in this paper is motivated by the models proposed in Refs. [11–13]. A composite dark sector, which has a QCD-like non-Abelian gauge symmetry $SU(N_{\text{color}}^{\text{dark}})$, where $N_{\text{color}}^{\text{dark}}$ is the number of dark colors, is added to the SM gauge group. We consider the case where fermions in the dark sector (dark quarks Q_{dark}) communicate with the SM quarks through a scalar mediator X_{dark} , which is charged under both SM QCD and dark QCD and which couples to a quark and a dark quark via Yukawa interactions with coupling strength $\kappa_{\alpha i}$, where the subscript α (i) denotes flavors of dark (SM) quarks. The mediator can be pair produced through gluon splitting at the LHC, similar to the pair production of a single type of squark in supersymmetry [14]. In fact, the production cross section is the same as for pair production of right-handed top squarks [15, 16] multiplied by $N_{\text{color}}^{\text{dark}}$. Each mediator decays into a quark and a dark quark, as shown in Fig. 1. The dark quarks hadronize into dark hadrons. Of the dark hadrons, either the lightest dark baryon or dark meson is stable and therefore a good DM candidate, escaping the detector without leaving a signal. The unstable dark hadrons have lifetimes and branching fractions to SM particles that depend on the masses of the dark mesons, the mediator mass, the coupling strength $\kappa_{\alpha i}$, along with phase-space and spin considerations.

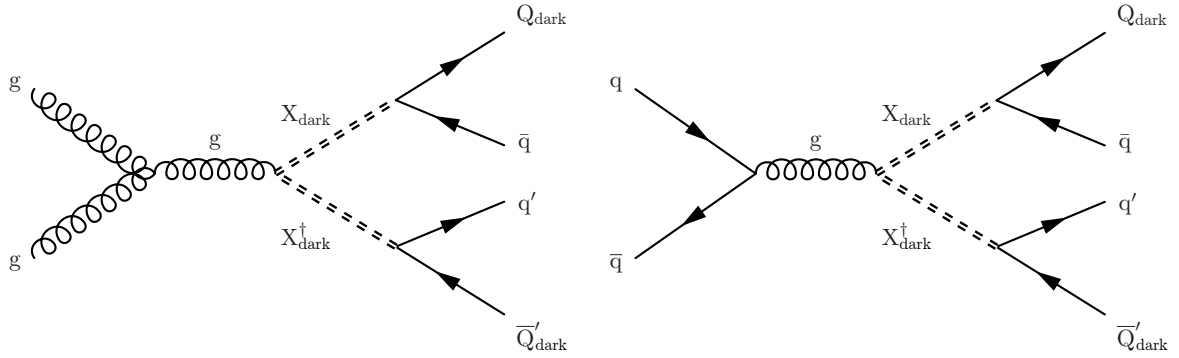


Figure 1: Feynman diagrams for pair production of dark mediator particles via gluon-gluon fusion (left) and quark-antiquark annihilation (right), with each mediator decaying to an SM quark and a dark quark.

The first version of this model that we consider, referred to as “unflavored”, has a simplified flavor structure in the coupling of the dark sector to SM particles, such that only the Yukawa coupling to the d quark is non-negligible [11]. Equation (1), taken from Ref. [11], gives the average decay length of a dark pion in this model:

$$c\tau_{\pi_{\text{dark}}} = 80 \text{ mm} \left(\frac{1}{\kappa^4} \right) \left(\frac{2 \text{ GeV}}{f_{\pi_{\text{dark}}}} \right)^2 \left(\frac{100 \text{ MeV}}{m_d} \right)^2 \left(\frac{2 \text{ GeV}}{m_{\pi_{\text{dark}}}} \right) \left(\frac{m_{X_{\text{dark}}}}{1 \text{ TeV}} \right)^4, \quad (1)$$

where κ is the coupling between dark quarks and the SM down quark, $f_{\pi_{\text{dark}}}$ is the dark pion decay constant, m_d is the mass of the SM down quark, and $m_{\pi_{\text{dark}}}$ is the dark pion mass.

If instead multiple Yukawa couplings $\kappa_{\alpha i}$ have non-negligible values, the average decay length for dark mesons composed of dark quarks of flavor indices α and β is given by Eq. (2) from Ref. [13]:

$$c\tau_{\pi_{\text{dark}}}^{\alpha\beta} = \frac{8\pi m_{\chi_{\text{dark}}}^4}{N_c m_{\pi_{\text{dark}}} f_{\pi_{\text{dark}}}^2 \sum_{i,j} |\kappa_{\alpha i} \kappa_{\beta j}^*|^2 (m_i^2 + m_j^2) \sqrt{\left(1 - \frac{(m_i + m_j)^2}{m_{\pi_{\text{dark}}}^2}\right) \left(1 - \frac{(m_i - m_j)^2}{m_{\pi_{\text{dark}}}^2}\right)}}, \quad (2)$$

where $m_{\chi_{\text{dark}}}$ is the mediator particle mass, N_c is the SM color factor, and m_i, m_j are the masses of the SM quarks with flavor indices i, j , respectively. Within this model, we focus on the “flavor-aligned” scenario, with three dark quark flavors that couple to the SM down-type quarks (d, s, b) via a diagonal matrix $\kappa_{\alpha i} = \kappa_0 \delta_{\alpha i}$. Because of spin considerations, dark hadron decays to heavier SM particles are favored, typically resulting in a large number of b quarks in the decays when kinematically allowed. We characterize the flavor-aligned model in terms of the maximum lifetime for any dark pion, $c\tau_{\pi_{\text{dark}}}^{\text{max}}$. When the lifetimes are long enough to give macroscopic decay distances, the resulting signature from either model is two SM jets and two EJs containing multiple displaced vertices. Alternative dark sector models with short dark hadron lifetimes can produce “semivisible” jets that each contain a mixture of promptly produced SM particles and invisible DM particles.

Previous experimental searches for strongly self-interacting DM have been made using proton-proton (pp) collision data collected at the CERN LHC at $\sqrt{s} = 13$ TeV and corresponding to about 140 fb^{-1} . This includes a search for semivisible jets by the CMS Collaboration [17], a search for semivisible jets by the ATLAS Collaboration [18], and a search for dark quarks in a dijet final state by ATLAS [19]. In addition, a previous search for EJs interpreted with an unflavored dark sector model was performed by the CMS Collaboration using a data sample collected in 2016, corresponding to an integrated luminosity of 16.1 fb^{-1} [20].

In this paper, we present a search for the emerging jet signatures of the unflavored and the flavor-aligned dark sector models, using the data set collected by the CMS Collaboration in 2016–2018 using pp collisions at a center-of-mass energy of 13 TeV and corresponding to 138 fb^{-1} . The search strategy first identifies EJs by exploiting their topological differences relative to SM jets using selection criteria optimized separately for each model. Then, the probability for an SM jet to be misidentified as an EJ is measured, and the background is estimated using control samples in data. The main background comes from SM multijet production where SM jets are misidentified as EJs.

Compared to the previous analysis [20], we have extended the unflavored EJ model search to a wider parameter space. This study also includes the first dedicated search for a flavored dark QCD sector. We have implemented a number of important changes that considerably increase the sensitivity of the search, including the incorporation of a novel machine learning (ML) technique, which significantly enhances the EJ identification (tagging) performance. The tabulated results are provided as a HEPData record [21].

This paper is organized as follows. In Section 2 we give an introduction of the CMS detector, followed in Section 3 by a detailed description of the simulated data used in this search. The event reconstruction and triggering algorithms are discussed in Section 4. In Section 5 we present the analysis strategy, two independent EJ tagging methods, and the background

estimation method. The treatment of uncertainties is detailed in Section 6. The results are presented in Section 7 and summarized in Section 8.

2 The CMS detector

The central feature of the CMS apparatus is a superconducting solenoid of 6 m internal diameter, providing a magnetic field of 3.8 T. Located within the solenoid volume are a silicon pixel and strip tracker, a lead tungstate crystal electromagnetic calorimeter (ECAL), and a brass and scintillator hadron calorimeter (HCAL), each composed of a barrel and two endcap sections. Forward calorimeters extend the pseudorapidity (η) coverage provided by the barrel and endcap detectors. Muons are measured in gas-ionization detectors embedded in the steel flux-return yoke outside the solenoid.

The silicon tracker used in 2016 measured charged particles within the range $|\eta| < 2.5$. For non-isolated particles of $1 < p_T < 10$ GeV and $|\eta| < 1.4$, the track resolutions were typically 1.5% in p_T and 25–90 (45–150) μm in the transverse (longitudinal) impact parameter d_{xy} (d_z) [22]. At the start of 2017, a new pixel detector was installed [23]; the upgraded tracker measured particles up to $|\eta| < 3.0$ with typical resolutions of 1.5% in p_T and 20–75 μm in d_{xy} for nonisolated particles of $1 < p_T < 10$ GeV [24].

Physics events of interest are selected using a two-tiered trigger system. The first level, called the level-1 trigger, is composed of custom hardware processors and uses information from the calorimeters and muon detectors to select events at a rate of around 100 kHz within a fixed latency of about 4 μs [25]. The second level, known as the high-level trigger, consists of a farm of processors running a version of the full event reconstruction software optimized for fast processing, and reduces the event rate to around 1 kHz before data storage [26]. A more detailed description of the CMS detector, together with a definition of the coordinate system used and the relevant kinematic variables, can be found in Ref. [27].

3 Event simulation

Monte Carlo (MC) events are used to evaluate the signal acceptance, optimize selection criteria, and test the closure of the background estimation methods.

The signal process is generated using the Hidden Valley module [28, 29] in PYTHIA version 8.240 [30], based on Ref. [11]. In the unflavored scenario, we choose the number of mass degenerate dark quark flavors to be $N_{\text{flavor}}^{\text{dark}} = 7$, following Ref. [11]. The running of the dark coupling constant with Q^2 , where Q is the momentum transfer, is faster for smaller $N_{\text{flavor}}^{\text{dark}}$, and the resulting showers have fewer dark mesons. In the flavor-aligned scenario, $N_{\text{flavor}}^{\text{dark}} = 3$ is used, and κ_{ai} is set to be diagonal, with all diagonal elements having the value κ_0 . For this scenario, the PYTHIA Hidden Valley module is modified to produce the different dark hadron species at the desired occurrence frequencies based on the dark quark flavors. For both cases, we consider a representation similar to QCD with $N_{\text{color}}^{\text{dark}} = 3$. The dark quark masses are degenerate and equal to the confinement scale Λ_{dark} . The dark pion mass is set to be half of Λ_{dark} , and the dark ρ meson mass four times the dark pion mass. The natural width of X_{dark} is set to 10 GeV, a relatively small value compared to the detector resolution. Under these assumptions, the free parameters of the model are limited to the mediator mass $m_{X_{\text{dark}}}$, the dark pion mass $m_{\pi_{\text{dark}}}$, and the dark pion lifetime $c\tau_{\pi_{\text{dark}}}$. Tables 1 and 2 summarize the signal model parameters used in this search. The signal cross section, described in Section 1, is computed at next-to-leading order (NLO), with the resummation of soft gluon emission included at next-to-

leading-logarithmic accuracy.

Table 1: Model parameters for the unflavored model.

Model parameter	List of values
$m_{\chi_{\text{dark}}}$ [GeV]	1000, 1200, 1400, 1500, 1600, 1800, 2000, 2200, 2400, 2500
$m_{\pi_{\text{dark}}}$ [GeV]	10, 20
$c\tau_{\pi_{\text{dark}}}$ [mm]	1, 2, 5, 25, 45, 60, 100, 150, 225, 300, 500, 1000

We simulate SM QCD multijet events and γ +jets events using the MADGRAPH5_aMC@NLO 2.6.5 event generator [31] at leading order with the MLM matching procedure [32].

In all cases parton showering and hadronization is performed using PYTHIA8 with the CP5 underlying event tune [33] and the NNPDF3.1 next-to-NLO parton distribution functions (PDFs) [34]. The response of the CMS detector is modeled using GEANT4 [35], and corrections are applied to the simulated samples to account for the differences in resolutions and efficiencies between the data and the simulation.

4 Event reconstruction and triggering

A global “particle-flow” (PF) algorithm [36] aims to reconstruct all individual particles in an event, combining information provided by the tracker, calorimeters, and muon system. The reconstructed information from the different subsystems is used to build physics objects such as photons, leptons, jets, and missing transverse momentum [37–39].

Jets are reconstructed from the PF particles using the anti- k_T algorithm [40, 41] with a distance parameter of 0.4. The jet momentum (energy) is calculated as the vectorial (scalar) sum of the momenta (energies) of all clustered particles. Corrections derived from data and simulation are applied to the jet energy. Jets that are consistent with the fragmentation of b quarks (b jets) are identified using the DEEPJET discriminator [42–44]. Both the medium and loose working points are used; the medium (loose) working point has an 85% (90%) probability of correctly identifying b jets with $p_T > 90$ GeV and a 1% (10%) probability of misidentifying light-flavor jets as b jets. The scalar p_T sum of all jets within an event (H_T) is used to select energetic events.

The pp interaction vertices are reconstructed by clustering tracks on the basis of their z coordinates along the beamline at their points of closest approach to the beam axis using a deterministic annealing algorithm [45]. The position of each vertex is estimated with an adaptive vertex fit [46].

Multiple vertex candidates can be reconstructed because of additional pp interactions in a bunch crossing (pileup). The primary vertex (PV) is taken to be the vertex corresponding to the hardest scattering in the event, evaluated using tracking information alone, as described in Section 9.4.1 of Ref. [47]. The contribution from charged-particle tracks from pileup interactions is reduced by rejecting those associated with other vertices [48]. The PV is required to be within 15 cm of the CMS detector center in the z direction to ensure optimal reconstruction efficiency.

The analysis considers data collected using triggers based on jet p_T and on H_T calculated from the summed p_T of online-reconstructed jets. The trigger used for the data collected in 2016 requires at least one jet with $p_T > 450$ GeV or $H_T > 900$ GeV, while for 2017–2018, the H_T threshold is increased to 1050 GeV and there is no p_T requirement. The inclusion of a jet p_T trigger requirement for 2016 was necessary because, in part of the 2016 data taking period, some

Table 2: Parameters used for the flavor-aligned model. In order to probe a range of lifetimes, the values of κ_0 listed in columns 3–7 are tuned to give the desired $c\tau_{\pi_{\text{dark}}}^{\text{max}}$ values of 5, 25, 45, 100, and 500 mm. In addition, samples were made with fixed $\kappa_0 = 1$, with a resultant value of $c\tau_{\pi_{\text{dark}}}^{\text{max}}$ that depends on the other model parameters.

$m_{\chi_{\text{dark}}}$ [GeV]	$m_{\pi_{\text{dark}}}$ [GeV]	κ_0 value				
1000	6	0.92	0.61	0.53	0.43	0.29
	10	0.62	0.42	0.36	0.30	0.20
	20	0.37	0.25	0.21	0.18	0.12
1200	6	1.10	0.73	0.63	0.52	0.35
	10	0.75	0.50	0.43	0.35	0.24
	20	0.45	0.30	0.26	0.21	0.14
1400	6	1.28	0.86	0.74	0.61	0.41
	10	0.87	0.58	0.50	0.41	0.28
	20	0.52	0.35	0.30	0.25	0.16
1600	6	1.47	0.98	0.85	0.69	0.46
	10	1.00	0.67	0.58	0.47	0.32
	20	0.59	0.40	0.34	0.28	0.19
1800	6	1.65	1.10	0.95	0.78	0.52
	10	1.12	0.75	0.65	0.53	0.36
	20	0.67	0.45	0.39	0.32	0.21
2000	6	1.83	1.23	1.06	0.87	0.58
	10	1.25	0.84	0.72	0.59	0.40
	20	0.74	0.50	0.43	0.35	0.23
2200	6	2.02	1.35	1.16	0.95	0.64
	10	1.37	0.92	0.79	0.65	0.43
	20	0.82	0.55	0.47	0.39	0.26
2400	6	2.20	1.47	1.27	1.04	0.70
	10	1.50	1.00	0.87	0.71	0.47
	20	0.89	0.60	0.51	0.42	0.28
2500	6	2.29	1.53	1.32	1.08	0.72
	10	1.56	1.04	0.90	0.74	0.49
	20	0.93	0.62	0.54	0.44	0.29

jets reaching the saturation energy for the level-1 trigger were mistakenly dropped from the H_T sum, resulting in a significant loss of efficiency. This loss was recovered by including the single-jet trigger requirement. The H_T threshold was increased in 2017 to compensate for the higher instantaneous luminosity. The efficiencies for an event to pass any of these trigger conditions in both data and simulation are measured from data sets collected with an independent trigger that requires a muon with $p_T > 50$ GeV. In both cases, the efficiencies are close to unity above the signal selection H_T thresholds, and the difference between the efficiencies as measured in simulation and data is applied as a correction to the simulation.

5 Analysis

The offline analysis selects energetic events with at least four jets. Jets are classified as EJ candidates using information from tracks associated with the jets. An overview of the event selection strategy is given in Section 5.1. Descriptions of the “candidate” EJ identification criteria (“tagging”) is given in Section 5.2. The algorithms used to optimize the selection criteria to maximize signal sensitivity, and the resulting event selection requirements are described in Section 5.3. Section 5.4 describes the procedure used to estimate the background from control regions in data.

5.1 Event and physics object selection

While some SM hadrons, such as those containing b quarks, have macroscopic decay lengths, tracks associated with SM jets mainly come from particles produced promptly (close to the collision primary vertex). In EJs, when the lifetime of one or more of the dark mesons is long, a substantial fraction of the tracks can emerge from displaced vertices. In addition, in the flavor-aligned scenario, most of the dark pion decay products are b quarks, which results in displaced tracks even when the dark pion decays immediately. We use as our displacement measure the d_{xy} (d_z), measured from the PV to the point of closest approach on the track trajectory, as this gives better sensitivity than reconstructing individual decay vertices. Jets used in this analysis are required to have $p_T > 100$ GeV, as we are looking for EJs originating from a heavy-mediator decay, and $|\eta| < 2$, to ensure that they are well contained in the tracker. Jet candidates are also required to pass a set of quality criteria to reject spurious jets from instrumental sources [49]. High-purity tracks, as defined in Ref. [22], with $p_T > 1$ GeV are associated with jets by requiring the angular separation between the jet direction and the track direction, $\Delta R = \sqrt{(\Delta\eta)^2 + (\Delta\phi)^2} < R_{\max}$, where $\Delta\eta$ is the η separation between the jet and the track, and $\Delta\phi$ is the separation in the azimuthal direction. We also reject tracks with $|d_z| > d_z^{\max}$ to suppress jets from pileup interactions. The values of R_{\max} and d_z^{\max} are optimized for each signal model. If a track can be assigned to multiple jets, it is assigned to the jet with the smallest ΔR separation. Jets are required to have at least one associated track so that the jet displacement measure can be calculated. To suppress events with a poorly reconstructed PV, we require that at least 10% of associated tracks have a longitudinal displacement from the PV less than 0.01 cm.

Candidate signal events are required to have high H_T and at least four jets passing the criteria above. At least two of these four jets must be tagged as EJs. If more than four jets are found, the four jets with the largest p_T are used. The H_T and EJ criteria are optimized for each signal model.

5.2 EJ tagging

Two EJ tagging strategies are used in this analysis. The first selects candidate EJs via requirements on jet-level variables using track displacement measures (“model-agnostic selection”). The second uses a graph neural network trained on specific signal models to determine an EJ tagging score (“machine learning or ML-based selection”). The model-agnostic method allows for a simpler reinterpretation of the results for alternate theoretical models not considered in this paper, while the ML-based approach achieves the best possible sensitivity for the specific models studied here.

The model-agnostic EJ tagger uses different input features for the unflavored and flavor-aligned dark sector models, while the ML-based EJ tagger is trained separately for each class of model.

5.2.1 Model-agnostic EJ tagging

For the EJ tagging that targets the unflavored dark-sector models, $R_{\max} = 0.4$ is used. The following variables, which were also used in Ref. [20], are used for the EJ tagging:

- $\langle d_{xy} \rangle$: this is the median d_{xy} of tracks associated with a jet.
- α_{3D} : this is defined as

$$\alpha_{3D} = \frac{\sum_{D_N < D_N^{\max}} p_T^{\text{track}}}{\sum p_T^{\text{track}}},$$

which is the ratio between the scalar p_T sum of the associated tracks with a pseudo-significance D_N smaller than the selection value D_N^{\max} and the scalar p_T sum of all the associated tracks. The pseudo-significance D_N is defined as:

$$D_N = \sqrt{\left(\frac{d_z}{0.01 \text{ cm}}\right)^2 + \left(\frac{d_{xy}}{\sigma(d_{xy})}\right)^2},$$

where $\sigma(d_{xy})$ is the d_{xy} uncertainty calculated from the covariance matrix of the fitted track trajectory. The d_z significance is based on the PV z resolution.

The distributions of these variables are presented in Fig. 2 for data events and for simulated signal and multijet background events. The data and simulated events shown require $H_T > 1200 \text{ GeV}$ and at least four jets with $p_T > 100 \text{ GeV}$ and $|\eta| < 2$, which is much less restrictive than the final signal selection requirements.

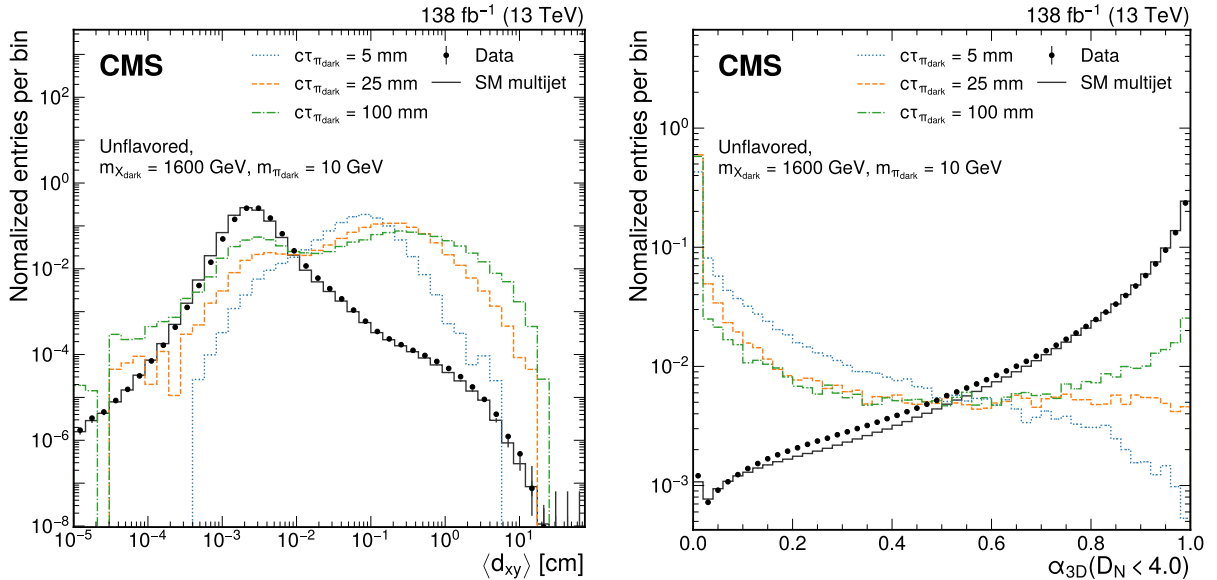


Figure 2: Distributions of the jet variables $\langle d_{xy} \rangle$ (left) and α_{3D} with $D_N^{\max} = 4$ (right) used for the model-agnostic EJ tagging that targets the unflavored dark sector models are shown for data (points), SM multijet simulation (gray line), and signal jets in simulation (colored lines). The sums of the entries are normalized to unity.

The flavor-aligned dark-sector model has three different dark meson lifetime ranges: long-lived dark mesons (up to 50 cm for the κ_0 parameters considered in this search), dark mesons with a b-hadron-like displacement from prompt dark meson decays into b quarks, and dark mesons that decay promptly into light SM quarks. In addition, since at least one dark quark in the

flavor-aligned model couples to the b quark, the jets often contain heavy-flavor hadrons, and the resulting EJ is wider than that of the unflavored model. Because of this, the tagging of EJs in the flavor-aligned model associates tracks with a jet using a proximity measure of $R_{\max} = 0.8$. The selection for candidate flavor-aligned EJs is based on the following variables:

- $n_{\text{track}}^{d_{xy} > d_{xy}^{\min}}$, the number of tracks with d_{xy} greater than a threshold d_{xy}^{\min} : this quantity exploits the tendency of the flavor-aligned dark sector to generate multiple long-lived SM mesons in the particle shower, resulting in a large number of displaced tracks.
- Jet girth: this is defined as the p_T -weighted ΔR separation of tracks from the jet direction:

$$\text{Jet girth} = \frac{\sum_i p_T^i \Delta R(i, \text{jet})}{\sum_i p_T^i},$$

where the index i runs over all tracks associated with the jet of interest. This variable exploits the feature that particles in EJs tend to have a wider angular separation than SM jets because of the large mass of the dark mesons.

Figure 3 shows the distributions of the tagging variables used in the flavor-aligned analysis for data, simulated signal, and multijet background events. The data and simulated events follow the same requirements as those appearing in Fig. 2.

As the jet-track association radius $R_{\max} = 0.8$ is larger than the $R = 0.4$ value used to perform jet clustering, jets that have nearby soft jets can be misidentified as EJs. To remove these candidates, a modified N -subjettiness variable $\bar{\tau}_n$ is calculated as follows:

1. For each of the four candidate high- p_T jets, we consider all jets within $\Delta R < 0.8$ of the selected jets that have $p_T > 30$ GeV in decreasing order of jet p_T . These will be used as the “subjett” collection to calculate $\bar{\tau}_n$. Using this definition, all candidate jets will have at least one subjett: the candidate jet itself.
2. After determining the subjett collection assigned to each candidate jet, the computation of $\bar{\tau}_n$ is then carried out up to the leading n subjett:

$$\bar{\tau}_n = \frac{\sum_i p_T^i \min\{\Delta R_{ij}\}}{\sum_i 0.8 p_T^i},$$

similar to the definition of the original N -subjettiness [50]. The index i runs over the tracks associated with the candidate jet, and j runs from 1 up to n for the subjett collection assigned to the selected jet.

The requirement that $\bar{\tau}_{2/1} = \bar{\tau}_2/\bar{\tau}_1 > 0.5$ is applied to all EJ candidates and is found to reliably suppress the misidentification of SM jets with nearby soft jets as EJs.

5.2.2 The ML-based EJ tagging

The ML-based tagger uses a graph neural network (GNN) based on PARTICLENET [51] to directly incorporate the track information. Two separate GNNs are trained to classify EJs: one for the unflavored model (uGNN) and the other for the flavor-aligned model (aGNN). Each is trained using all of the samples from its class of model, weighted equally. A validation data set is used to monitor potential bias and overtraining. The output of each GNN is a score ranging from 0 to 1, which is a measure of the probability that the jet is an EJ. Tracks are associated with

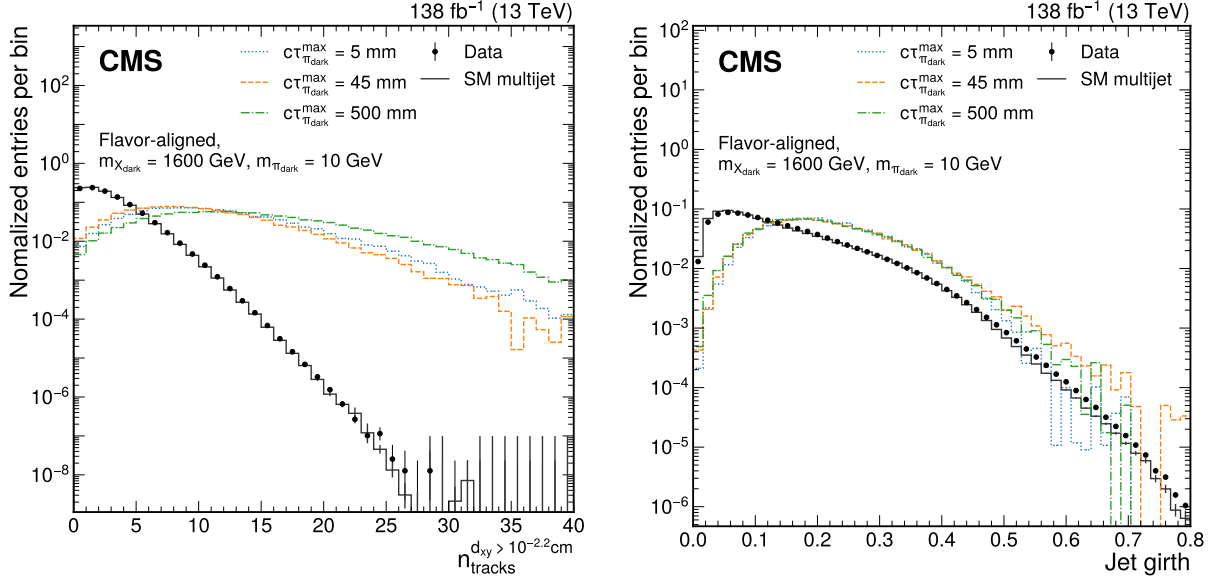


Figure 3: Distributions of the jet variables used for the model-agnostic EJ tagging targeting flavor-aligned dark sector models for jets obtained in data (points), SM multijet simulation (gray line), and simulated signal jets (colored lines). The distribution of the number of tracks with $d_{xy} > 10^{-2.2}$ cm (jet girth) is shown on the left (right). The sums of the entries are normalized to unity.

a jet using $R_{\max} = 0.8$. To maximize the available information for the ML training, the tracks are not required to satisfy a d_z^{\max} requirement. Each network is trained on all jets originating from a dark quark in the signal models of interest, and an equal number of jets taken from SM QCD simulation as the background sample.

The $\Delta\eta$ and $\Delta\phi$ between each track and its associated jet are used as the track coordinate variables in the jet space. Each track in the jet is represented by a 5-feature vector containing:

- $\Delta R(\text{track}, \text{jet})$, as particles in EJs tend to have a wider angular separation than in the SM jets because of the heaviness of the dark mesons.
- $\ln(p_T^{\text{track}}/1 \text{ GeV})$, $\ln(p_T^{\text{track}}/\sum_i p_T^i)$, as the combination of the dark shower and the decay of the mesons back to the SM sector causes the p_T of tracks to be smaller on average for EJs than for SM jets.
- $T(d_{xy})$, $T(d_z)$. The transformation function $T(x)$ is applied to the track displacement variables, to reduce the range of values input to the GNN while preserving the variables' sign and continuity. It is defined as:

$$T(x) = \text{sign}(x) \ln \left(\left| \frac{x}{1 \text{ cm}} \right| + 1 \right).$$

This transformation was found to give comparable or better performance than a standard scaling.

The impact parameter d_{xy} is the most influential feature. Figure 4 shows the output score distributions for signal and background, demonstrating good separation. The signal distributions are similar despite the wide range of dark meson $c\tau$ values.

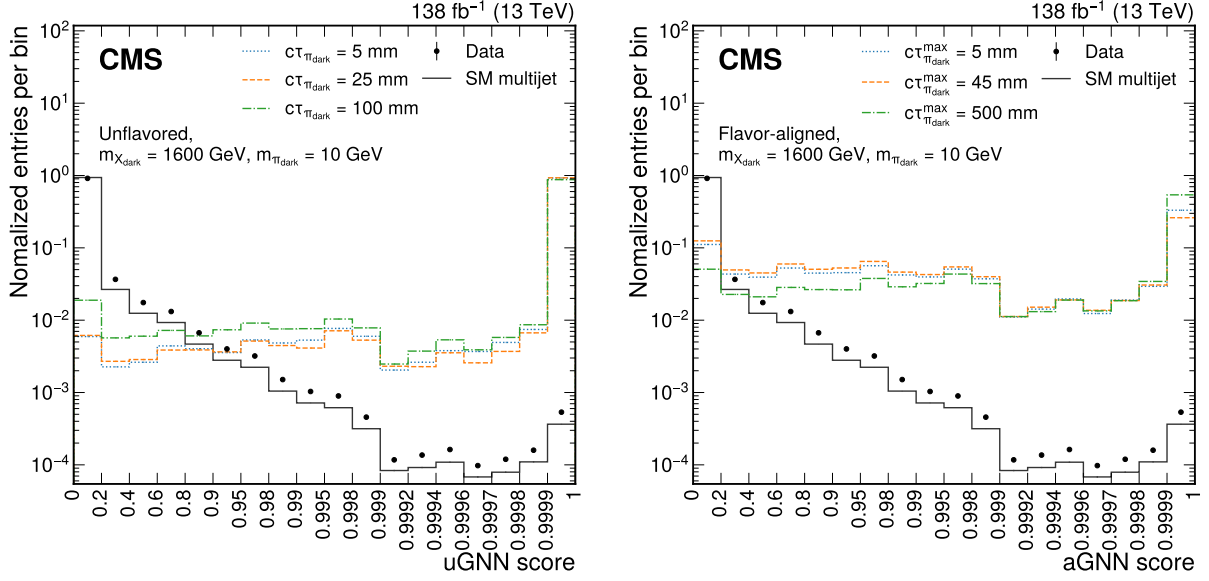


Figure 4: Distributions of the output score of the uGNN (left) and aGNN (right) for the data (points with error bars), SM multijet simulation (dark gray line), and signal simulation (colored lines). The signal distributions in the left (right) plot are generated from the unflavored (flavor-aligned) model. Bins are chosen to correspond to the jet selection criteria defined in Table 5. The sums of the entries are normalized to unity.

5.3 Determining the EJ tagging and event selection criteria

An optimization procedure is performed for each signal model to determine the best threshold on the event H_T , jet p_T , and the EJ tagging variables by maximizing σ_{opt} , defined as:

$$\sigma_{\text{opt}} = \frac{S}{\sqrt{S + B + \beta^2 B^2}}, \quad (3)$$

where S (B) is the number of simulated signal (background multijet) events passing the selection thresholds and β is the estimated relative systematic uncertainty in the background, taken to be 10%. To reduce the number of sets of selection criteria, similar selection sets are grouped, and a representative set that gives at least 90% of the original best significance value is used for all the models in the group. Additional selection sets with higher background selection efficiencies are used to validate the background estimation calculations. Their selection criteria are detailed in Section 5.4.

The selection criteria used for EJ tagging are shown in Tables 3–5, and those for the event selection in Table 6. For the unflavored model, at $c\tau_{\pi_{\text{dark}}} = 45$ mm, the model-agnostic taggers yield a maximum signal selection efficiency of $\approx 40\%$, while the ML-based taggers yield a maximum signal selection efficiency of $\approx 60\%$. The signal selection efficiency of the model-agnostic taggers drops to a few percent for very short-lived (≈ 1 mm) dark pions, and the efficiency of both taggers drops to a few percent for very long-lived (≈ 1000 mm) dark pions. For the flavor-aligned model, at $c\tau_{\pi_{\text{dark}}}^{\text{max}} = 45$ mm, the model-agnostic taggers yield a maximum signal selection efficiency of $\approx 25\%$, while the ML-based taggers yield a maximum signal selection efficiency of $\approx 40\%$. This efficiency remains fairly stable along the full maximum lifetime range for both taggers.

Table 3: Emerging jet selection criteria for the model-agnostic analysis designed for the unflavored scenario. The validation regions are discussed in Section 5.4. The symbols in parentheses indicate a minimum ($>$) or maximum ($<$) requirement.

Tag name	d_z [cm] ($<$)	$\langle d_{xy} \rangle$ [cm] ($>$)	D_N ($<$)	a_{3D} ($<$)
u-tag 1	0.5	$10^{-1.6}$	4.0	0.25
u-tag 2	1.0	$10^{-1.4}$	8.0	0.25
u-tag 3	5.0	$10^{-1.2}$	8.0	0.25
u-tag 4	5.0	$10^{-1.2}$	12.0	0.15
u-tag 5	5.0	$10^{-1.0}$	12.0	0.15
validation u-tag	0.5	$10^{-1.6}$	4.0	0.40

Table 4: Emerging jet selection criteria for the model-agnostic analysis designed for the flavor-aligned scenario. The validation tag is described in Section 5.4. The symbols in parentheses indicate a minimum ($>$) or maximum ($<$) requirement.

Tag name	d_z [cm] ($<$)	d_{xy}^{\min} [cm]	$n_{\text{track}}^{d_{xy} > d_{xy}^{\min}}$ ($>$)	Jet girth ($>$)
a-tag 1	0.5	$10^{-2.2}$	12	0.05
a-tag 2	0.5	$10^{-2.2}$	12	0.1
a-tag 3	0.5	$10^{-2.3}$	14	0.0
a-tag 4	0.5	$10^{-2.4}$	14	0.1
validation a-tag	0.5	$10^{-2.4}$	12	0.0

5.4 Background estimation

The signal region (SR) for this analysis is constructed from events with two or more tagged EJs. The main source of background for this analysis is the production of four SM jets, where two or more of these jets are misidentified as EJs. We estimate the number of SM events passing the selection criteria in the SR by constructing a control region (CR) with identical event and jet kinematic requirements, but where exactly one jet is tagged as an EJ. We estimate the fraction of signal events in the CR to be no more than 10^{-5} . The probability of an SM jet being misidentified as an EJ (mistag rate) is heavily dependent on the underlying jet flavor, as SM jets containing b hadrons also have displaced tracks. We therefore estimate the misidentification probability $\epsilon(f, p_T)$ as a function of the underlying jet flavor f , where f is b for b jets and q for other jet flavors, and the jet p_T .

Table 5: The GNN score range used to identify a jet as an EJ. The uGNN (aGNN) tag indicates that the tagger uses the output score of the GNN trained on the unflavored (flavor-aligned) simulated signal samples. The validation tags are described in Section 5.4.

Tag name	Score min.	Score max.
uGNN tag 1	0.9997	1
uGNN tag 2	0.9998	1
uGNN tag 3	0.9996	1
uGNN validation tag	0.998	0.9995
aGNN tag 1	0.9953	1
aGNN tag 2	0.9993	1
aGNN tag 3	0.9983	1
aGNN validation tag	0.99	0.995

Table 6: Event selection criteria used for the analysis. The validation selection criteria are described in Section 5.4.

Selection set	H_T [GeV]	Jet p_T [GeV] (>)				EJ tagger
u-set 1	>1600	275	250	250	150	u-tag 1
u-set 2	>1600	200	200	150	150	u-tag 2
u-set 3	>1600	200	150	100	100	u-tag 3
u-set 4	>1500	200	150	100	100	u-tag 4
u-set 5	>1200	200	150	100	100	u-tag 5
u-set validation	1000–1200	100	100	100	100	validation u-tag
a-set 1	>1500	200	150	100	100	a-tag 1
a-set 2	>1800	250	250	200	200	a-tag 2
a-set 3	>1200	275	250	250	200	a-tag 2
a-set 4	>1500	275	250	250	100	a-tag 3
a-set 5	>1800	200	150	100	100	a-tag 4
a-set validation	1000–1200	100	100	100	100	validation a-tag
uGNN set 1	>1350	170	120	120	100	uGNN tag 1
uGNN set 2	>1750	300	260	250	250	uGNN tag 2
uGNN set 3	>1800	240	180	180	100	uGNN tag 3
uGNN validation	>1000	100	100	100	100	uGNN validation tag
aGNN set 1	>1300	200	140	120	100	aGNN tag 1
aGNN set 2	>1650	300	250	200	200	aGNN tag 2
aGNN set 3	>1400	270	220	220	120	aGNN tag 3
aGNN validation	>1000	100	100	100	100	aGNN validation tag

Assuming that the probability of a jet being misidentified as an EJ is independent of the multiplicity and properties of other jets in the event, the number of background events in the SR is estimated using counts in the CR and the mistag rate according to the following formula:

$$N_{\text{SR}} = \sum_{\text{events} \in \text{CR}} \frac{\frac{1}{2!} \left(\sum_i \epsilon_i \prod_{j \neq i} (1 - \epsilon_j) \right) + \frac{1}{3!} \left(\sum_{i \neq j} \epsilon_i \epsilon_j \prod_{k \neq i, j} (1 - \epsilon_k) \right) + \frac{1}{4!} \left(\sum_{i \neq j \neq k} \epsilon_i \epsilon_j \epsilon_k \right)}{\prod_i (1 - \epsilon_i)}, \quad (4)$$

where ϵ_i is an abbreviation of $\epsilon(f_i, p_T^i)$, the estimated mistag rate of jet i in each event. The jet indices in the summations and products run over all jets that are not EJ tagged. Because the underlying flavor of each jet is difficult to determine, we approximate ϵ_i in Eq.(4) using a flavor-fraction-averaged misidentification rate $\epsilon^{\text{avg}}(p_T)$ and the estimated b jet fraction F_b^{CR} of all non EJ-tagged jets in the CR:

$$\epsilon^{\text{avg}}(p_T) = F_b^{\text{CR}} \epsilon(\text{b}, p_T) + (1 - F_b^{\text{CR}}) \epsilon(\text{q}, p_T). \quad (5)$$

The value of F_b^{CR} is estimated by fitting the CMS DEEPJET discriminator [42] spectrum of the non EJ-tagged jets in the CR to two template distributions obtained from SM multijet MC events. One template contains the discriminator value for jets identified using generator-level information as containing a b quark, and the complement template is used for the other jets. The template distributions are varied within the measured uncertainties [43, 44]. The fit is performed for each of the selection criteria listed in Table 6. Figure 5 gives an example of the fit performance for the ‘‘u-set validation’’ selection criteria, defined in Table 6.

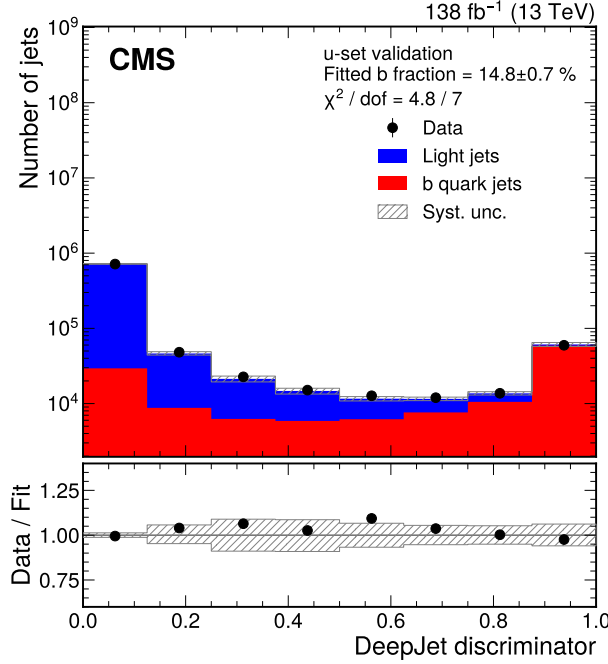


Figure 5: Template fit of the DEEPJET discriminator used to determine the b jet fraction of the non-EJ tagged jets for data events that pass the “u-set validation” selection criteria, except with the requirement on the number of EJ-tagged jets changed from 2 to 1. The lower panel shows the ratio of the number of jets in the data compared to the sum of the fitted template distributions.

The evaluation of the mistag rate is performed in a signal-free region (FR) that consists of events passing a high- p_T photon trigger and containing an isolated photon in the ECAL barrel with $p_T > 200$ GeV. The FR events are required to have either one or two jets passing the jet selection criteria described in Section 5.1. To obtain the misidentification probability for different jet flavors, we further divide the FR into a b-enriched region (ER) and a b-depleted region (DR) by imposing b tagging requirements on an additional jet with $p_T > 50$ GeV and $|\eta| < 2.4$ that passes a set of noise-rejection criteria [49]. As a significant fraction of heavy-flavored jets originate from gluon splitting in this event sample, b tagging requirements on this extra jet will change the b jet fraction of the selected jets. Events are classified as ER if the additional jet passes DEEPJET b tagging at the medium working point, and are classified as DR if the additional jet fails DEEPJET b tagging at the loose working point. Assuming that the ER and DR have the same mistag probabilities for the selected jets, and the only difference between these regions is the overall b jet fraction, the misidentification rate for all the selected jets in a specific region XR, $\epsilon^{XR}(p_T)$, can be expressed as a linear combination of $\epsilon(b, p_T)$ and $\epsilon(q, p_T)$:

$$\begin{aligned} \epsilon^{ER}(p_T) &= F_b^{ER}(p_T)\epsilon(b, p_T) + (1 - F_b^{ER}(p_T))\epsilon(q, p_T), \\ \epsilon^{DR}(p_T) &= F_b^{DR}(p_T)\epsilon(b, p_T) + (1 - F_b^{DR}(p_T))\epsilon(q, p_T), \end{aligned} \quad (6)$$

where $F_b^{XR}(p_T)$ is the estimated b jet fraction of region XR in bins of jet p_T . The b jet fraction is obtained by fitting the DEEPJET b discriminator distribution to templates obtained using jets from a simulated γ +jets sample. On average, the selected jets in the ER and DR have b jet fractions of 15% and 4%, respectively. The linear relation in Eq. (6) can then be inverted to obtain the mistag rates for different underlying jet flavors $\epsilon(f, p_T)$, which is used in Eq. (5) to estimate the misidentification rate of jets in the CR. Figure 6 gives examples of the estimated

EJ tagger misidentification probabilities for “u-tag 1” and “uGNN tag 1” taggers, defined in Tables 3 and 5.

Because the Phase 1 upgrade of the pixel detector [23] improved the track reconstruction performance, the evaluation of the expected background is performed separately for the pixel Phase 0 geometry (2016) and Phase 1 geometry (2017–2018).

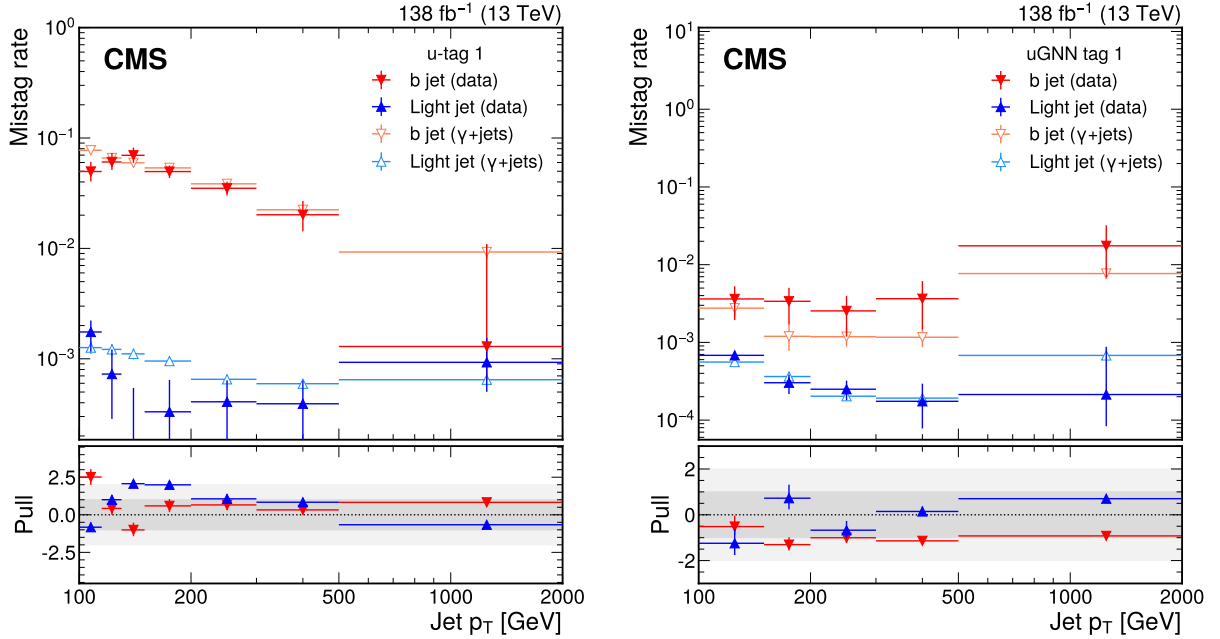


Figure 6: The EJ tagger misidentification probability for b quark jets (red, orange) and light jets (light blue, dark blue) as a function of jet p_T for the model-agnostic tagger “u-tag 1” (left) and the ML-based tagger “uGNN tag 1” (right), as defined in Tables 3 and 5, evaluated using data (red, dark blue) and generator-level flavor information from simulated samples (orange, light blue) in events containing a high- p_T photon. The lower panel shows the pull, defined as the difference between the mistag rate calculated in simulation and mistag rate measured in data divided by the uncertainty measured in data.

To validate the background estimation, closure tests are performed in validation regions (VRs) that use selection criteria that are orthogonal to the SRs. The VRs are defined using signal-like selection criteria that require at least two jets passing a validation EJ tagger. The observed number of events in the VR is compared to the number predicted using our background estimation technique. For the model-agnostic EJ tagging VR, the H_T requirement of the validation event selection is inverted to ensure orthogonality with the SRs and small signal contamination. The EJ identification requirements for the validation EJ tagger are based on the u-tag 1 and a-tag 1 requirements for unflavored and flavor-aligned models, respectively, with one jet-variable selection requirement relaxed to further reduce the effect of any small signal contamination. The VR for the ML-based EJ tagging uses a validation tagger that selects jets with GNN scores in a region disjoint from the SRs. To further increase the number of events that pass the ML-based VR, we relax the H_T and jet p_T requirements. The full list of the selection criteria used for the VRs is given in Tables 3–6. The signal contamination in these VRs is less than 1% for all surveyed signal models.

The number of events passing the VR selection criteria with at least two jets passing the validation jet tag, as well as the predicted number using the estimation described in Eq. (4), is given in Table 7. No significant deviation between the observed and the estimation results is observed,

indicating that the background estimation calculation is robust.

Table 7: The observed yield of events in data satisfying the validation selection criteria with at least two jets passing the corresponding validation tag, and the estimation based on the misidentification rate calculated using validation events with exactly one jet passing the validation tagger scaled by the factor given in Eq. (4). The statistical and systematic uncertainties are reported for the estimated yields.

Selection set	Estimation \pm stat. \pm syst.	Observed yield
u-set validation	1220 \pm $\frac{80}{80}$ \pm 210	1484
a-set validation	77 \pm $\frac{4}{4}$ \pm 15	118
uGNN validation	29.3 \pm $\frac{7.0}{3.4}$ \pm 8.2	21
aGNN validation	29.1 \pm $\frac{6.1}{2.6}$ \pm 5.2	37

6 Systematic uncertainties

6.1 Background uncertainties

The main sources of systematic uncertainty in this search arise from the background estimation method based on control samples in data. The kinematic differences between the SM jets in the CR photon-triggered data used for the misidentification rate calculation and the SM jets in the H_T -triggered data used in the SR may lead to slightly different misidentification rates. We estimate the corresponding uncertainties by applying the background prediction method in Eq. (4) to simulated SM multijets events, using either the mistag rate from the SM multijet simulation or from the γ +jets simulation. The uncertainty is taken as the difference in the background predictions obtained with the two mistag rates. There is also an uncertainty in the flavor composition used in the misidentification rate estimations. This uncertainty is estimated from simulated background events by comparing the flavor-decomposition estimate described in Section 5.4 with one derived from generator-level flavor information. Finally, there is the uncertainty associated with the choice of variables used to parameterize the mistag rate. This uncertainty is estimated by comparing the estimation results when parameterizing the mistag rate as a function of jet p_T versus track multiplicity, as these are the variables for which the mistag rate shows the most significant dependence. The selection variables $\langle d_{xy} \rangle$ and α_{3D} used in the model-agnostic taggers have an intrinsic dependence on the track multiplicity, making the mistag rate parameterization uncertainty more pronounced in the model-agnostic method. These three uncertainty sources are considered to be uncorrelated and summed in quadrature. The resulting uncertainties are given in Tables 7 and 9.

6.2 Signal uncertainties

Various sources of uncertainty affecting the signal yields are also considered. The integrated luminosity uncertainties for the 2016, 2017, and 2018 data-taking periods are 1.2, 2.3, and 2.5%, respectively [52–54]. The trigger efficiency is slightly different in data and simulation. A correction factor compensates for this difference, and its statistical uncertainty is propagated to an uncertainty in the signal acceptance. The evaluation of jet energy correction uncertainties is performed as a function of jet p_T and η , propagated to all jet-related kinematic variables, and then to an uncertainty in the signal acceptance. Uncertainty sources are treated as fully

correlated across the years for the jet energy scale (JES), and uncorrelated for the jet energy resolution (JER). While the pileup distribution in the simulation is reweighted to match the data, there is a 4.6% uncertainty in the total inelastic cross section [55], which is treated as fully correlated across the years. The impact parameter distribution is slightly broader in the data CRs than in simulation. A smearing function that corrects this is applied to tracks in the simulated samples, and the resulting changes to the signal acceptances are used to estimate the modeling uncertainty. The corrected values are also used to recompute the GNN score. The uncertainty in the acceptance from the uncertainties in the PDFs is evaluated by reweighting events with different PDF variations [34, 56]. As reconstruction efficiency differences between data and simulation for displaced tracks are difficult to evaluate, we varied the reconstruction efficiency for tracks with $d_{xy} > 4$ cm (approximately the distance to the second layer of the pixel detector) by 10% and found an $\approx 1\%$ overall change in signal acceptance. As the measured difference in reconstruction efficiency in data and MC is expected to be much smaller (on the order of 1–2% [57]), no uncertainty is assigned. The uncertainty from the factorization scale (μ_F) and renormalization scale (μ_R) choices is estimated by independently varying μ_F and μ_R by factors of 2 and 0.5 [58, 59]. A summary of the estimated uncertainties for the various signal model acceptances is given in Table 8.

Table 8: Mean and standard deviation (std.) of the relative uncertainty calculated on the unflavored and flavor-aligned samples, by source, in percent.

Uncertainty source	Model-agnostic taggers				ML-based taggers			
	Unflavored		Flavor-aligned		Unflavored		Flavor-aligned	
	mean	std.	mean	std.	mean	std.	mean	std.
Integrated luminosity	1.8	0.6	1.8	0.6	1.8	0.6	1.8	0.6
Trigger efficiency	0.3	0.1	0.3	0.1	0.3	0.1	0.3	0.1
JES	1.0	1.3	0.8	0.7	1.3	0.9	0.7	0.4
JER	0.3	0.4	0.3	0.3	0.2	0.3	0.2	0.1
Pileup reweighting	1.6	1.4	1.4	1.2	0.9	0.8	1.0	0.9
Track modeling in sim.	0.2	0.3	1.4	1.8	0.3	0.8	0.5	0.6
PDF	<0.1	<0.1	<0.1	<0.1	<0.1	<0.1	<0.1	<0.1
μ_F, μ_R	<0.1	<0.1	<0.1	<0.1	<0.1	<0.1	<0.1	<0.1

7 Results

After the full event selection, the observed and expected event yields corresponding to each selection set are shown in Table 9. No statistically significant deviation from the SM background prediction is observed. The observation is used to set upper limits on the various signal parameter models considered using the CL_s criterion [60, 61]. The test statistic is defined as the likelihood ratio employed in Higgs boson analyses in ATLAS and CMS, as elaborated in Ref. [62]. Upper limits at the 95% confidence level (CL) on the production cross section in the 2-dimensional plane defined by the signal parameters are shown in Figs. 7 ($m_{\pi_{\text{dark}}} = 10$ GeV) and 8 ($m_{\pi_{\text{dark}}} = 20$ GeV) for both the unflavored and the flavor-aligned scenarios, and in Fig. 9 ($m_{\pi_{\text{dark}}} = 6$ GeV) for the flavor-aligned scenario. These excluded cross sections are compared to the theoretical prediction to derive the exclusion regions shown as red and black curves for the expected and observed 95% CL limit, respectively. The red curves also have an associated red band to indicate the 68% CL variation on the expected exclusion limit.

In the unflavored coupling model, the key tagging variable for the model-agnostic method is the mean d_{xy} of the associated tracks in the jet. In the case where the dark pion lifetime is too

Table 9: The estimated number of events from the background prediction based on control samples in data and the observed event yields. Statistical and systematic uncertainties in the estimated background are provided.

Selection set	Estimation \pm stat. \pm syst.	Observed yield
u-set 1	56 \pm $\frac{9}{5}$ \pm 20	67
u-set 2	20.0 \pm $\frac{4.3}{2.5}$ \pm 7.0	21
u-set 3	22.9 \pm $\frac{7.3}{2.1}$ \pm 4.9	24
u-set 4	7.9 \pm $\frac{2.0}{1.6}$ \pm 2.2	10
u-set 5	11.3 \pm $\frac{2.7}{1.9}$ \pm 2.0	13
a-set 1	8.8 \pm $\frac{2.4}{1.0}$ \pm 2.0	16
a-set 2	1.67 \pm $\frac{0.49}{0.23}$ \pm 0.38	3
a-set 3	1.97 \pm $\frac{0.47}{0.22}$ \pm 0.37	2
a-set 4	2.30 \pm $\frac{0.81}{0.30}$ \pm 0.39	3
a-set 5	10.2 \pm $\frac{2.3}{1.1}$ \pm 3.4	16
uGNN set 1	15.6 \pm $\frac{5.4}{1.9}$ \pm 3.8	18
uGNN set 2	0.73 \pm $\frac{0.44}{0.16}$ \pm 0.27	0
uGNN set 3	7.6 \pm $\frac{3.5}{1.3}$ \pm 2.3	9
aGNN set 1	45 \pm $\frac{18}{8}$ \pm 16	59
aGNN set 2	0.30 \pm $\frac{0.23}{0.07}$ \pm 0.18	1
aGNN set 3	3.8 \pm $\frac{2.2}{0.7}$ \pm 2.0	5

short, the displaced tracks from the dark pion decay products will be very similar to prompt SM tracks. In the opposite case, where the dark pion lifetime is very large, the dark pions increasingly decay outside the tracker. Thus, this search method is less sensitive to these two cases, giving reduced performance, as shown in the upper-left plots of Figs. 7 and 8. In contrast, the GNN method performs well even at low dark pion lifetimes, as the signal acceptance remains high. However, signal sensitivity is still limited for long dark pion lifetimes, as shown in the upper-right plots of Figs. 7 and 8.

In the flavor-aligned scenario, the differentiating power for the model-agnostic method comes mainly from the multiplicity of associated tracks with large displacements. Unlike d_{xy} , the multiplicity distribution is more uniform for different dark pion lifetimes (as we only consider $c\tau_{\pi_{\text{dark}}}^{\text{max}}$ above the typical b hadron lifetime) leading to less dependence on $c\tau_{\pi_{\text{dark}}}^{\text{max}}$ as seen in the lower-left plots of Figs. 7 and 8. Similarly, the GNN is also not sensitive to changes in lifetime, resulting in a stable signal acceptance across the $c\tau_{\pi_{\text{dark}}}^{\text{max}}$ range. In the flavor-aligned models where $m_{\pi_{\text{dark}}} = 6$ GeV, the dark pions decay predominantly to light SM quarks because of mass constraints, resulting in fewer displaced tracks in the events. This reduces the selection efficiencies for these signal models, leading to the model-agnostic method having less sensitivity compared to models with larger $m_{\pi_{\text{dark}}}$, as shown in Fig. 9.

The ML-based EJ tagging methods yield more stringent limits on the surveyed models. In the

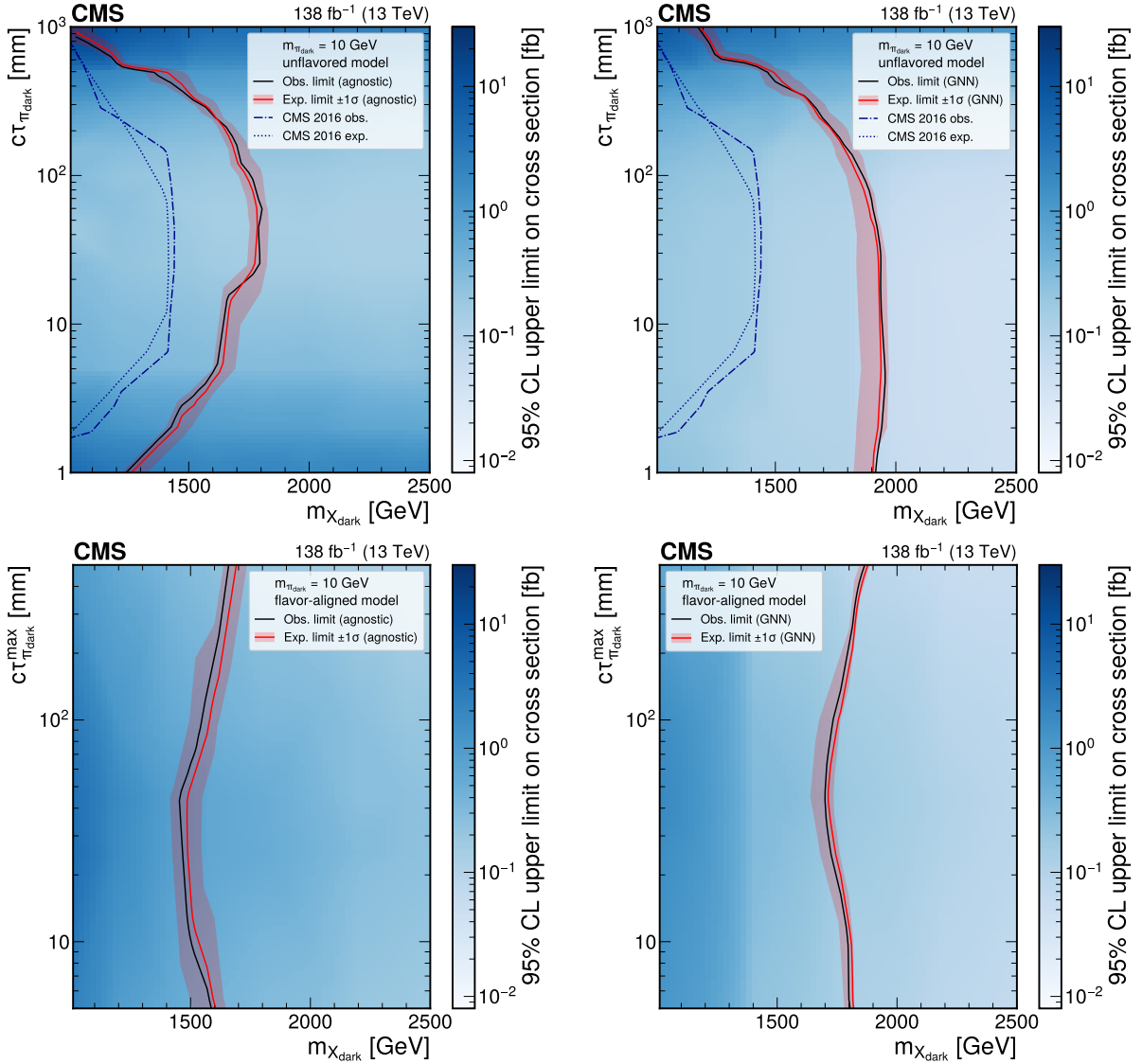


Figure 7: The 95% CL upper limits on the production cross section for various signal models in the unflavored scenario (upper plots) and the flavor-aligned scenario (lower plots) with $m_{\pi_{\text{dark}}} = 10$ GeV using the model-agnostic (GNN) EJ tagging method, on the left (right). The red curve is the expected exclusion limit, with the band representing its 68% CL variation. The black curve is the observed limit. The dark blue dotted curves in the upper plots are the expected and observed limits previously obtained by CMS [20].

unflavored model, X_{dark} masses up to 1900 and 1950 GeV are excluded at 95% CL for $m_{\pi_{\text{dark}}}$ of 10 and 20 GeV, respectively, closely matching the expected limits. For the flavor-aligned models, the X_{dark} mass exclusion at 95% CL increases to 1950, 1850, and 1900 GeV for $m_{\pi_{\text{dark}}}$ of 6, 10, and 20 GeV, respectively, again matching well the expected limits. Relative to the model-agnostic tagger, the greatest increase in sensitivity is for the unflavored signal models with short lifetimes, where the dark showers generate nearly prompt tracks that are difficult to tag using simple requirements on the track displacement variables.

The GNN-based limits for the flavor-aligned models that utilize the aGNN set 2 selection have a narrow expected band, as shown in the lower right plots of Figs. 7–8 and the right plot of Fig. 9. For that selection set, 0.3 background events are predicted, which implies that the most frequent

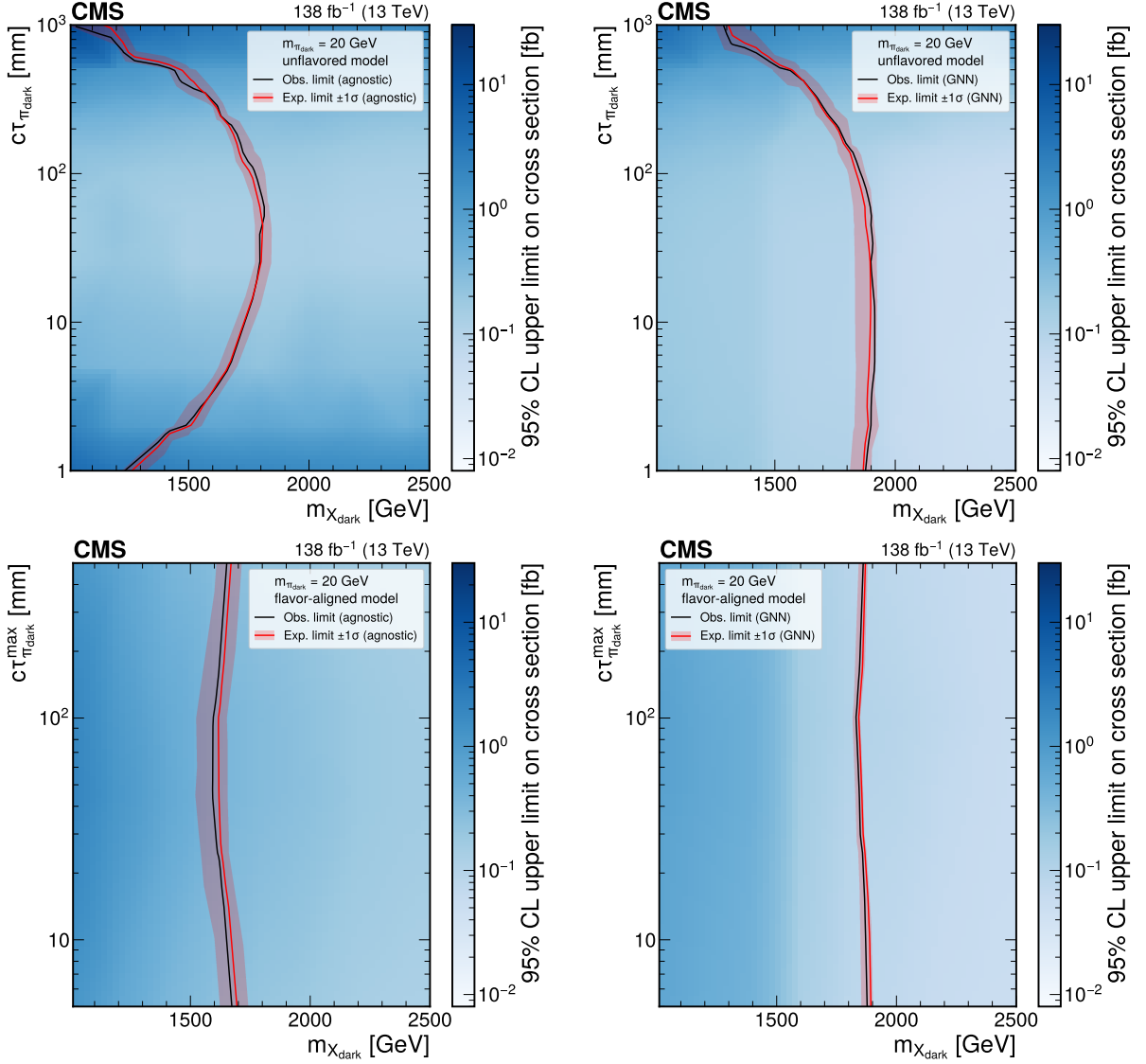


Figure 8: The 95% CL upper limits on the production cross section for various signal models in the unflavored scenario (upper plots) and the flavor-aligned scenario (lower plots) with $m_{\pi_{\text{dark}}} = 20$ GeV using the model-agnostic (GNN) EJ tagging method, on the left (right). The red curve is the expected exclusion limit, with the band representing its 68% CL variation. The black curve is the observed limit.

observation will be exactly zero events if the background-only hypothesis is correct. Because the likelihood function is constructed from Poisson probabilities, this leads to the background-only test statistic distribution exhibiting discrete, narrow peaks. With a free-floating signal strength, the test statistic distribution for the signal plus background hypothesis shares similar features. As a result, only a small change in the signal strength is required to obtain a CL_s value of 0.05 when going from 95 to 68% CL to the expected median of the background expectation. The resulting expected limit bands in this region are narrow and asymmetrical.

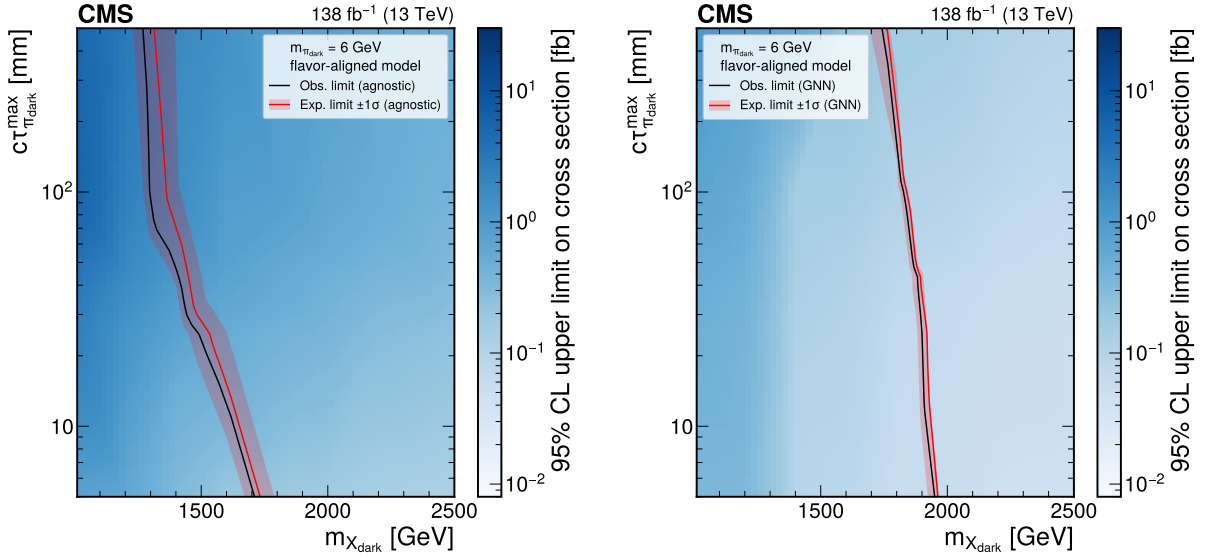


Figure 9: The 95% CL upper limits on the production cross section for various signal models in the flavor-aligned scenario with $m_{\pi_{\text{dark}}} = 6$ GeV using the model-agnostic (GNN) EJ tagging method, on the left (right). The red curve is the expected exclusion limit, with the band representing its 68% CL variation. The black curve is the observed limit.

8 Summary

A search for emerging jet signatures arising from a strongly interacting dark sector produced in proton-proton collisions has been presented, using data corresponding to an integrated luminosity of 138 fb^{-1} at $\sqrt{s} = 13$ TeV. The signal model contains a family of dark quarks that couple to the standard model (SM) quarks via a scalar mediator χ_{dark} . Dark pions (π_{dark}) with a significant lifetime ($c\tau_{\pi_{\text{dark}}}$) are produced by the hadronization of the dark quarks; these then decay to SM particles at vertices displaced from the proton-proton interaction point. As the scalar mediator is assumed to be produced in pairs, and each decays to an SM quark and a dark quark, the signature of this process is two SM jets plus two jets of particles with constituents emerging from displaced vertices.

Both unflavored and flavor-aligned couplings between the SM quarks and the dark quarks are examined in the search. Events are selected using either a traditional cut-based approach or a graph neural network to identify emerging jets, in combination with other event-level selection criteria. The overall selection requirements are optimized for each coupling scenario and for different combinations of the mediator particle mass, dark pion mass, and dark pion lifetime. No excess of events beyond the SM expectations is found, and the observed 95% confidence level exclusion limits agree with the expected limits. For the unflavored model, dark mediator masses $m_{\chi_{\text{dark}}} < 1950$ GeV are excluded for $c\tau_{\pi_{\text{dark}}} \approx 100$ mm and $m_{\pi_{\text{dark}}} = 10$ GeV, while the flavor-aligned model result excludes $m_{\chi_{\text{dark}}} < 1850$ GeV at $c\tau_{\pi_{\text{dark}}}^{\text{max}} \approx 500$ mm for $m_{\pi_{\text{dark}}} = 10$ GeV. This result surpasses the previous search for emerging jets in the unflavored scenario, increasing the experimental limit of the dark mediator particle by ≈ 500 GeV to set the most stringent limits to date, and provides the first direct exclusion of the flavor-aligned scenario.

Acknowledgments

We congratulate our colleagues in the CERN accelerator departments for the excellent performance of the LHC and thank the technical and administrative staffs at CERN and at other CMS institutes for their contributions to the success of the CMS effort. In addition, we gratefully acknowledge the computing centers and personnel of the Worldwide LHC Computing Grid and other centers for delivering so effectively the computing infrastructure essential to our analyses. Finally, we acknowledge the enduring support for the construction and operation of the LHC, the CMS detector, and the supporting computing infrastructure provided by the following funding agencies: SC (Armenia), BMBWF and FWF (Austria); FNRS and FWO (Belgium); CNPq, CAPES, FAPERJ, FAPERGS, and FAPESP (Brazil); MES and BNSF (Bulgaria); CERN; CAS, MoST, and NSFC (China); MINCIENCIAS (Colombia); MSES and CSF (Croatia); RIF (Cyprus); SENESCYT (Ecuador); ERC PRG, RVTT3 and MoER TK202 (Estonia); Academy of Finland, MEC, and HIP (Finland); CEA and CNRS/IN2P3 (France); SRNSF (Georgia); BMBF, DFG, and HGF (Germany); GSRI (Greece); NKFIH (Hungary); DAE and DST (India); IPM (Iran); SFI (Ireland); INFN (Italy); MSIP and NRF (Republic of Korea); MES (Latvia); LMTLT (Lithuania); MOE and UM (Malaysia); BUAP, CINVESTAV, CONACYT, LNS, SEP, and UASLP-FAI (Mexico); MOS (Montenegro); MBIE (New Zealand); PAEC (Pakistan); MES and NSC (Poland); FCT (Portugal); MESTD (Serbia); MCIN/AEI and PCTI (Spain); MOSTR (Sri Lanka); Swiss Funding Agencies (Switzerland); MST (Taipei); MHESI and NSTDA (Thailand); TUBITAK and TENMAK (Turkey); NASU (Ukraine); STFC (United Kingdom); DOE and NSF (USA).

Individuals have received support from the Marie-Curie program and the European Research Council and Horizon 2020 Grant, contract Nos. 675440, 724704, 752730, 758316, 765710, 824093, 101115353, and COST Action CA16108 (European Union); the Leventis Foundation; the Alfred P. Sloan Foundation; the Alexander von Humboldt Foundation; the Science Committee, project no. 22r1-037 (Armenia); the Belgian Federal Science Policy Office; the Fonds pour la Formation à la Recherche dans l'Industrie et dans l'Agriculture (FRIA-Belgium); the Agentschap voor Innovatie door Wetenschap en Technologie (IWT-Belgium); the F.R.S.-FNRS and FWO (Belgium) under the "Excellence of Science – EOS" – be.h project n. 30820817; the Beijing Municipal Science & Technology Commission, No. Z191100007219010 and Fundamental Research Funds for the Central Universities (China); the Ministry of Education, Youth and Sports (MEYS) of the Czech Republic; the Shota Rustaveli National Science Foundation, grant FR-22-985 (Georgia); the Deutsche Forschungsgemeinschaft (DFG), under Germany's Excellence Strategy – EXC 2121 "Quantum Universe" – 390833306, and under project number 400140256 - GRK2497; the Hellenic Foundation for Research and Innovation (HFRI), Project Number 2288 (Greece); the Hungarian Academy of Sciences, the New National Excellence Program - ÚNKP, the NKFIH research grants K 124845, K 124850, K 128713, K 128786, K 129058, K 131991, K 133046, K 138136, K 143460, K 143477, 2020-2.2.1-ED-2021-00181, and TKP2021-NKTA-64 (Hungary); the Council of Science and Industrial Research, India; ICSC – National Research Center for High Performance Computing, Big Data and Quantum Computing, funded by the EU NexGeneration program (Italy); the Latvian Council of Science; the Ministry of Education and Science, project no. 2022/WK/14, and the National Science Center, contracts Opus 2021/41/B/ST2/01369 and 2021/43/B/ST2/01552 (Poland); the Fundação para a Ciência e a Tecnologia, grant CEECIND/01334/2018 (Portugal); the National Priorities Research Program by Qatar National Research Fund; MCIN/AEI/10.13039/501100011033, ERDF "a way of making Europe", and the Programa Estatal de Fomento de la Investigación Científica y Técnica de Excelencia María de Maeztu, grant MDM-2017-0765 and Programa Severo Ochoa del Principado de Asturias (Spain); the Chulalongkorn Academic into Its 2nd Century Project Advance-

ment Project, and the National Science, Research and Innovation Fund via the Program Management Unit for Human Resources & Institutional Development, Research and Innovation, grant B37G660013 (Thailand); the Kavli Foundation; the Nvidia Corporation; the SuperMicro Corporation; the Welch Foundation, contract C-1845; and the Weston Havens Foundation (USA).

References

- [1] V. C. Rubin, N. Thonnard, and W. K. Ford, Jr., “Rotational properties of 21 SC galaxies with a large range of luminosities and radii, from NGC 4605 ($R = 4$ kpc) to UGC 2885 ($R = 122$ kpc)”, *Astrophys. J.* **238** (1980) 471, doi:10.1086/158003.
- [2] M. Persic, P. Salucci, and F. Stel, “The universal rotation curve of spiral galaxies: I. The dark matter connection”, *Mon. Not. Roy. Astron. Soc.* **281** (1996) 27, doi:10.1093/mnras/278.1.27, arXiv:astro-ph/9506004.
- [3] D. Clowe et al., “A direct empirical proof of the existence of dark matter”, *Astrophys. J.* **648** (2006) L109, doi:10.1086/508162, arXiv:astro-ph/0608407.
- [4] DES Collaboration, “Dark Energy Survey year 1 results: curved-sky weak lensing mass map”, *Mon. Not. Roy. Astron. Soc.* **475** (2018) 3165, doi:10.1093/mnras/stx3363, arXiv:1708.01535.
- [5] Planck Collaboration, “Planck 2018 results. VI. Cosmological parameters”, *Astron. Astrophys.* **641** (2020) A6, doi:10.1051/0004-6361/201833910, arXiv:1807.06209. [Erratum: doi:10.1051/0004-6361/201833910e].
- [6] M. J. Strassler and K. M. Zurek, “Echoes of a hidden valley at hadron colliders”, *Phys. Lett. B* **651** (2007) 374, doi:10.1016/j.physletb.2007.06.055, arXiv:hep-ph/0604261.
- [7] K. Petraki and R. R. Volkas, “Review of asymmetric dark matter”, *Int. J. Mod. Phys. A* **28** (2013) 1330028, doi:10.1142/S0217751X13300287, arXiv:1305.4939.
- [8] H. Beauchesne, E. Bertuzzo, and G. Grilli di Cortona, “Dark matter in Hidden Valley models with stable and unstable light dark mesons”, *JHEP* **04** (2019) 118, doi:10.1007/JHEP04(2019)118, arXiv:1809.10152.
- [9] Y. Bai and P. Schwaller, “Scale of dark QCD”, *Phys. Rev. D* **89** (2014) 063522, doi:10.1103/PhysRevD.89.063522, arXiv:1306.4676.
- [10] T. Cohen, M. Lisanti, and H. K. Lou, “Semi-visible jets: Dark matter undercover at the LHC”, *Phys. Rev. Lett.* **115** (2015) 171804, doi:10.1103/PhysRevLett.115.171804, arXiv:1503.00009.
- [11] P. Schwaller, D. Stolarski, and A. Weiler, “Emerging jets”, *JHEP* **05** (2015) 059, doi:10.1007/JHEP05(2015)059, arXiv:1502.05409.
- [12] P. Agrawal, M. Blanke, and K. Gemmler, “Flavored dark matter beyond Minimal Flavor Violation”, *JHEP* **10** (2014) 072, doi:10.1007/JHEP10(2014)072, arXiv:1405.6709.
- [13] S. Renner and P. Schwaller, “A flavoured dark sector”, *JHEP* **08** (2018) 052, doi:10.1007/JHEP08(2018)052, arXiv:1803.08080.

- [14] P. Fayet and S. Ferrara, “Supersymmetry”, *Phys. Rept.* **32** (1977) 249, doi:10.1016/0370-1573(77)90066-7.
- [15] C. Borschensky et al., “Squark and gluino production cross sections in pp collisions at $\sqrt{s} = 13, 14, 33$ and 100 TeV”, *Eur. Phys. J. C* **74** (2014) 3174, doi:10.1140/epjc/s10052-014-3174-y, arXiv:1407.5066.
- [16] W. Beenakker et al., “NNLL-fast: predictions for coloured supersymmetric particle production at the LHC with threshold and Coulomb resummation”, *JHEP* **12** (2016) 133, doi:10.1007/JHEP12(2016)133, arXiv:1607.07741.
- [17] CMS Collaboration, “Search for resonant production of strongly coupled dark matter in proton-proton collisions at 13 TeV”, *JHEP* **06** (2022) 156, doi:10.1007/JHEP06(2022)156, arXiv:2112.11125.
- [18] ATLAS Collaboration, “Search for non-resonant production of semi-visible jets using Run 2 data in ATLAS”, *Phys. Lett. B* **848** (2024) 138324, doi:10.1016/j.physletb.2023.138324, arXiv:2305.18037.
- [19] ATLAS Collaboration, “Search for resonant production of dark quarks in the dijet final state with the ATLAS detector”, *JHEP* **02** (2024) 128, doi:10.1007/JHEP02(2024)128, arXiv:2311.03944.
- [20] CMS Collaboration, “Search for new particles decaying to a jet and an emerging jet”, *JHEP* **02** (2019) 179, doi:10.1007/JHEP02(2019)179, arXiv:1810.10069.
- [21] HEPData record for this analysis, 2024. doi:10.17182/hepdata.147271.
- [22] CMS Collaboration, “Description and performance of track and primary-vertex reconstruction with the CMS tracker”, *JINST* **9** (2014) P10009, doi:10.1088/1748-0221/9/10/P10009, arXiv:1405.6569.
- [23] Tracker Group of the CMS Collaboration, “The CMS phase-1 pixel detector upgrade”, *JINST* **16** (2021) P02027, doi:10.1088/1748-0221/16/02/P02027, arXiv:2012.14304.
- [24] CMS Collaboration, “Track impact parameter resolution for the full pseudo rapidity coverage in the 2017 dataset with the CMS phase-1 pixel detector”, CMS Detector Performance Note CMS-DP-2020-049, 2020.
- [25] CMS Collaboration, “Performance of the CMS Level-1 trigger in proton-proton collisions at $\sqrt{s} = 13$ TeV”, *JINST* **15** (2020) P10017, doi:10.1088/1748-0221/15/10/P10017, arXiv:2006.10165.
- [26] CMS Collaboration, “The CMS trigger system”, *JINST* **12** (2017) P01020, doi:10.1088/1748-0221/12/01/P01020, arXiv:1609.02366.
- [27] CMS Collaboration, “The CMS experiment at the CERN LHC”, *JINST* **3** (2008) S08004, doi:10.1088/1748-0221/3/08/S08004.
- [28] L. Carloni and T. Sjöstrand, “Visible effects of invisible hidden valley radiation”, *JHEP* **09** (2010) 105, doi:10.1007/JHEP09(2010)105, arXiv:1006.2911.
- [29] L. Carloni, J. Rathsmann, and T. Sjöstrand, “Discerning secluded sector gauge structures”, *JHEP* **04** (2011) 091, doi:10.1007/JHEP04(2011)091, arXiv:1102.3795.


-
- [30] T. Sjöstrand et al., “An introduction to PYTHIA 8.2”, *Comput. Phys. Commun.* **191** (2015) 159, doi:10.1016/j.cpc.2015.01.024, arXiv:1410.3012.
- [31] J. Alwall et al., “The automated computation of tree-level and next-to-leading order differential cross sections, and their matching to parton shower simulations”, *JHEP* **07** (2014) 079, doi:10.1007/JHEP07(2014)079, arXiv:1405.0301.
- [32] J. Alwall et al., “Comparative study of various algorithms for the merging of parton showers and matrix elements in hadronic collisions”, *Eur. Phys. J. C* **53** (2008) 473, doi:10.1140/epjc/s10052-007-0490-5, arXiv:0706.2569.
- [33] CMS Collaboration, “Extraction and validation of a new set of CMS PYTHIA8 tunes from underlying-event measurements”, *Eur. Phys. J. C* **80** (2020) 4, doi:10.1140/epjc/s10052-019-7499-4, arXiv:1903.12179.
- [34] NNPDF Collaboration, “Parton distributions from high-precision collider data”, *Eur. Phys. J. C* **77** (2017) 663, doi:10.1140/epjc/s10052-017-5199-5, arXiv:1706.00428.
- [35] GEANT4 Collaboration, “GEANT4—a simulation toolkit”, *Nucl. Instrum. Meth. A* **506** (2003) 250, doi:10.1016/S0168-9002(03)01368-8.
- [36] CMS Collaboration, “Particle-flow reconstruction and global event description with the CMS detector”, *JINST* **12** (2017) P10003, doi:10.1088/1748-0221/12/10/P10003, arXiv:1706.04965.
- [37] CMS Collaboration, “Performance of reconstruction and identification of τ leptons decaying to hadrons and ν_τ in pp collisions at $\sqrt{s} = 13$ TeV”, *JINST* **13** (2018) P10005, doi:10.1088/1748-0221/13/10/P10005, arXiv:1809.02816.
- [38] CMS Collaboration, “Jet energy scale and resolution in the CMS experiment in pp collisions at 8 TeV”, *JINST* **12** (2017) P02014, doi:10.1088/1748-0221/12/02/P02014, arXiv:1607.03663.
- [39] CMS Collaboration, “Performance of missing transverse momentum reconstruction in proton-proton collisions at $\sqrt{s} = 13$ TeV using the CMS detector”, *JINST* **14** (2019) P07004, doi:10.1088/1748-0221/14/07/P07004, arXiv:1903.06078.
- [40] M. Cacciari, G. P. Salam, and G. Soyez, “The anti- k_T jet clustering algorithm”, *JHEP* **04** (2008) 063, doi:10.1088/1126-6708/2008/04/063, arXiv:0802.1189.
- [41] M. Cacciari, G. P. Salam, and G. Soyez, “FastJet user manual”, *Eur. Phys. J. C* **72** (2012) 1896, doi:10.1140/epjc/s10052-012-1896-2, arXiv:1111.6097.
- [42] E. Bols et al., “Jet flavour classification using DeepJet”, *JINST* **15** (2020) P12012, doi:10.1088/1748-0221/15/12/P12012, arXiv:2008.10519.
- [43] CMS Collaboration, “Identification of heavy-flavour jets with the CMS detector in pp collisions at 13 TeV”, *JINST* **13** (2018) P05011, doi:10.1088/1748-0221/13/05/P05011, arXiv:1712.07158.
- [44] CMS Collaboration, “Performance summary of AK4 jet b tagging with data from proton-proton collisions at 13 TeV with the CMS detector”, CMS Detector Performance Note CMS-DP-2023-005, 2023.

- [45] K. Rose, “Deterministic annealing for clustering, compression, classification, regression, and related optimization problems”, *IEEE Proc.* **86** (1998) 2210, doi:10.1109/5.726788.
- [46] R. Fruhwirth, W. Waltenberger, and P. Vanlaer, “Adaptive vertex fitting”, *J. Phys. G* **34** (2007) N343, doi:10.1088/0954-3899/34/12/N01.
- [47] CMS Collaboration, “Technical proposal for the Phase-II upgrade of the Compact Muon Solenoid”, CMS Technical Proposal CERN-LHCC-2015-010, CMS-TDR-15-02, 2015.
- [48] CMS Collaboration, “Pileup mitigation at CMS in 13 TeV data”, *JINST* **15** (2020) P09018, doi:10.1088/1748-0221/15/09/P09018, arXiv:2003.00503.
- [49] CMS Collaboration, “Jet algorithms performance in 13 TeV data”, CMS Physics Analysis Summary CMS-PAS-JME-16-003, 2017.
- [50] J. Thaler and K. Van Tilburg, “Identifying boosted objects with N-subjettiness”, *JHEP* **03** (2011) 015, doi:10.1007/JHEP03(2011)015, arXiv:1011.2268.
- [51] H. Qu and L. Gouskos, “Jet tagging via particle clouds”, *Phys. Rev. D* **101** (2020) 056019, doi:10.1103/PhysRevD.101.056019, arXiv:1902.08570.
- [52] CMS Collaboration, “Precision luminosity measurement in proton-proton collisions at $\sqrt{s} = 13$ TeV in 2015 and 2016 at CMS”, *Eur. Phys. J. C* **81** (2021) 800, doi:10.1140/epjc/s10052-021-09538-2, arXiv:2104.01927.
- [53] CMS Collaboration, “CMS luminosity measurement for the 2017 data-taking period at $\sqrt{s} = 13$ TeV”, CMS Physics Analysis Summary CMS-PAS-LUM-17-004, 2018.
- [54] CMS Collaboration, “CMS luminosity measurement for the 2018 data-taking period at $\sqrt{s} = 13$ TeV”, CMS Physics Analysis Summary CMS-PAS-LUM-18-002, 2019.
- [55] CMS Collaboration, “Measurement of the inelastic proton-proton cross section at $\sqrt{s} = 13$ TeV”, *JHEP* **07** (2018) 161, doi:10.1007/JHEP07(2018)161, arXiv:1802.02613.
- [56] NNPDF Collaboration, “Parton distributions with QED corrections”, *Nucl. Phys. B* **877** (2013) 290, doi:10.1016/j.nuclphysb.2013.10.010, arXiv:1308.0598.
- [57] CMS Collaboration, “Muon tracking performance in the CMS Run-2 Legacy data using the tag-and-probe technique”, CMS Detector Performance Note CMS-DP-2020-035, 2020.
- [58] M. Cacciari et al., “The t anti- t cross-section at 1.8-TeV and 1.96-TeV: A study of the systematics due to parton densities and scale dependence”, *JHEP* **04** (2004) 068, doi:10.1088/1126-6708/2004/04/068, arXiv:hep-ph/0303085.
- [59] S. Catani, D. de Florian, M. Grazzini, and P. Nason, “Soft gluon resummation for Higgs boson production at hadron colliders”, *JHEP* **07** (2003) 028, doi:10.1088/1126-6708/2003/07/028, arXiv:hep-ph/0306211.
- [60] T. Junk, “Confidence level computation for combining searches with small statistics”, *Nucl. Instrum. Meth. A* **434** (1999) 435, doi:10.1016/S0168-9002(99)00498-2, arXiv:hep-ex/9902006.
- [61] A. L. Read, “Presentation of search results: the CL_s technique”, *J. Phys. G* **28** (2002) 2693, doi:10.1088/0954-3899/28/10/313.






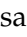


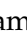


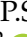


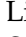
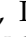


- [62] ATLAS and CMS Collaborations, and LHC Higgs Combination Group, "Procedure for the LHC Higgs boson search combination in Summer 2011", Technical Report CMS-NOTE-2011-005, ATL-PHYS-PUB-2011-11, 2011.

A The CMS Collaboration




Yerevan Physics Institute, Yerevan, Armenia

A. Hayrapetyan, A. Tumasyan¹ 





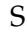
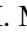






Institut für Hochenergiephysik, Vienna, Austria

W. Adam , J.W. Andrejkovic, T. Bergauer , S. Chatterjee , K. Damanakis , M. Dragicevic , P.S. Hussain , M. Jeitler² , N. Krammer , A. Li , D. Liko , I. Mikulec , J. Schieck² , R. Schöfbeck , D. Schwarz , M. Sonawane , S. Templ , W. Waltenberger , C.-E. Wulz² 









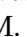


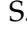
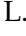

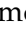
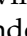
Universiteit Antwerpen, Antwerpen, Belgium

M.R. Darwish³ , T. Janssen , P. Van Mechelen 













Vrije Universiteit Brussel, Brussel, Belgium

N. Breugelmans, J. D'Hondt , S. Dansana , A. De Moor , M. Delcourt , F. Heyen, S. Lowette , I. Makarenko , D. Müller , S. Tavernier , M. Tytgat⁴ , G.P. Van Onsem , S. Van Putte , D. Vannerom 



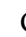



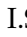







Université Libre de Bruxelles, Bruxelles, Belgium

B. Clerbaux , A.K. Das, G. De Lentdecker , H. Evard , L. Favart , P. Gianneios , D. Hohov , J. Jaramillo , A. Khalilzadeh, F.A. Khan , K. Lee , M. Mahdavihorrani , A. Malara , S. Paredes , L. Thomas , M. Vanden Bemden , C. Vander Velde , P. Vanlaer 








Ghent University, Ghent, Belgium

M. De Coen , D. Dobur , G. Gokbulut , Y. Hong , J. Knolle , L. Lambrecht , D. Marckx , G. Mestdach, K. Mota Amarilo , C. Rendón, A. Samalan, K. Skovpen , N. Van Den Bossche , J. van der Linden , L. Wezenbeek 








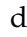






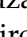

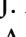

Université Catholique de Louvain, Louvain-la-Neuve, Belgium

A. Benecke , A. Bethani , G. Bruno , C. Caputo , J. De Favereau De Jeneret , C. Delaere , I.S. Donertas , A. Giammanco , A.O. Guzel , Sa. Jain , V. Lemaitre, J. Lidrych , P. Mastrapasqua , T.T. Tran , S. Wertz 




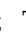





Centro Brasileiro de Pesquisas Fisicas, Rio de Janeiro, Brazil

G.A. Alves , E. Coelho , C. Hensel , T. Menezes De Oliveira , A. Moraes , P. Rebello Teles , M. Soeiro, A. Vilela Pereira⁵ 

Universidade do Estado do Rio de Janeiro, Rio de Janeiro, Brazil

W.L. Aldá Júnior , M. Alves Gallo Pereira , M. Barroso Ferreira Filho , H. Brandao Malbouisson , W. Carvalho , J. Chinellato⁶, E.M. Da Costa , G.G. Da Silveira⁷ , D. De Jesus Damiao , S. Fonseca De Souza , R. Gomes De Souza, M. Macedo , J. Martins⁸ , C. Mora Herrera , L. Mundim , H. Nogima , J.P. Pinheiro , A. Santoro , A. Sznajder , M. Thiel 

Universidade Estadual Paulista, Universidade Federal do ABC, São Paulo, Brazil

C.A. Bernardes⁷ , L. Calligaris , T.R. Fernandez Perez Tomei , E.M. Gregores , I. Maitto Silverio , P.G. Mercadante , S.F. Novaes , B. Orzari , Sandra S. Padula 

Institute for Nuclear Research and Nuclear Energy, Bulgarian Academy of Sciences, Sofia, Bulgaria

A. Aleksandrov , G. Antchev , R. Hadjiiska , P. Iaydjiev , M. Misheva , M. Shopova , G. Sultanov 




University of Sofia, Sofia, Bulgaria

A. Dimitrov , L. Litov , B. Pavlov , P. Petkov , A. Petrov , E. Shumka 



Instituto De Alta Investigación, Universidad de Tarapacá, Casilla 7 D, Arica, Chile

S. Keshri , S. Thakur 



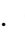







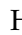

Beihang University, Beijing, China

T. Cheng , T. Javaid , L. Yuan 

Department of Physics, Tsinghua University, Beijing, China

Z. Hu , Z. Liang, J. Liu, K. Yi^{9,10} 


Institute of High Energy Physics, Beijing, China

G.M. Chen¹¹ , H.S. Chen¹¹ , M. Chen¹¹ , F. Iemmi , C.H. Jiang, A. Kapoor¹² , H. Liao , Z.-A. Liu¹³ , R. Sharma¹⁴ , J.N. Song¹³, J. Tao , C. Wang¹¹, J. Wang , Z. Wang¹¹, H. Zhang , J. Zhao 

State Key Laboratory of Nuclear Physics and Technology, Peking University, Beijing, China

A. Agapitos , Y. Ban , S. Deng , B. Guo, C. Jiang , A. Levin , C. Li , Q. Li , Y. Mao, S. Qian, S.J. Qian , X. Qin, X. Sun , D. Wang , H. Yang, L. Zhang , Y. Zhao, C. Zhou 

Guangdong Provincial Key Laboratory of Nuclear Science and Guangdong-Hong Kong Joint Laboratory of Quantum Matter, South China Normal University, Guangzhou, China

S. Yang 


Sun Yat-Sen University, Guangzhou, China

Z. You 

University of Science and Technology of China, Hefei, China

K. Jaffel , N. Lu 

Nanjing Normal University, Nanjing, China

G. Bauer¹⁵, B. Li, J. Zhang 

Institute of Modern Physics and Key Laboratory of Nuclear Physics and Ion-beam Application (MOE) - Fudan University, Shanghai, China

X. Gao¹⁶ 

Zhejiang University, Hangzhou, Zhejiang, China

Z. Lin , C. Lu , M. Xiao 





Universidad de Los Andes, Bogota, Colombia

C. Avila , D.A. Barbosa Trujillo, A. Cabrera , C. Florez , J. Fraga , J.A. Reyes Vega


Universidad de Antioquia, Medellin, Colombia

F. Ramirez , M. Rodriguez , A.A. Ruales Barbosa, J.D. Ruiz Alvarez 

University of Split, Faculty of Electrical Engineering, Mechanical Engineering and Naval Architecture, Split, Croatia

D. Giljanovic , N. Godinovic , D. Lelas , A. Sculac 








University of Split, Faculty of Science, Split, Croatia

M. Kovac , A. Petkovic, T. Sculac 




Institute Rudjer Boskovic, Zagreb, Croatia

P. Bargassa , V. Brigljevic , B.K. Chitroda , D. Ferencek , K. Jakovic, S. Mishra , A. Starodumov¹⁷ , T. Susa 

University of Cyprus, Nicosia, Cyprus

A. Attikis , K. Christoforou , A. Hadjiagapiou, C. Leonidou, J. Mousa , C. Nicolaou, L. Paizanos, F. Ptochos , P.A. Razis , H. Rykaczewski, H. Saka , A. Stepennov 

Charles University, Prague, Czech Republic

M. Finger , M. Finger Jr. , A. Kveton 

Universidad San Francisco de Quito, Quito, Ecuador

E. Carrera Jarrin 





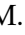



Academy of Scientific Research and Technology of the Arab Republic of Egypt, Egyptian Network of High Energy Physics, Cairo, Egypt

Y. Assran^{18,19}, B. El-mahdy, S. Elgammal¹⁹

Center for High Energy Physics (CHEP-FU), Fayoum University, El-Fayoum, Egypt

M.A. Mahmoud , Y. Mohammed 







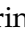







National Institute of Chemical Physics and Biophysics, Tallinn, Estonia

K. Ehataht , M. Kadastik, T. Lange , S. Nandan , C. Nielsen , J. Pata , M. Raidal , L. Tani , C. Veelken 

Department of Physics, University of Helsinki, Helsinki, Finland

H. Kirschenmann , K. Osterberg , M. Voutilainen 










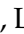







Helsinki Institute of Physics, Helsinki, Finland

S. Bharthuar , E. Brücken , F. Garcia , P. Inkaew , K.T.S. Kallonen , R. Kinnunen, T. Lampén , K. Lassila-Perini , S. Lehti , T. Lindén , L. Martikainen , M. Myllymäki , M.m. Rantanen , H. Siikonen , J. Tuominiemi 



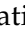




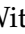















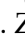

Lappeenranta-Lahti University of Technology, Lappeenranta, Finland

P. Luukka , H. Petrow 







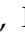







IRFU, CEA, Université Paris-Saclay, Gif-sur-Yvette, France

M. Besancon , F. Couderc , M. Dejardin , D. Denegri, J.L. Faure, F. Ferri , S. Ganjour , P. Gras , G. Hamel de Monchenault , V. Lohezic , J. Malcles , F. Orlandi , L. Portales , J. Rander, A. Rosowsky , M.Ö. Sahin , A. Savoy-Navarro²⁰ , P. Simkina , M. Titov , M. Tornago 




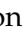
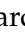




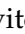


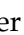
Laboratoire Leprince-Ringuet, CNRS/IN2P3, Ecole Polytechnique, Institut Polytechnique de Paris, Palaiseau, France

F. Beaudette , P. Busson , A. Cappati , C. Charlot , M. Chiusi , F. Damas , O. Davignon , A. De Wit , I.T. Ehle , B.A. Fontana Santos Alves , S. Ghosh , A. Gilbert , R. Granier de Cassagnac , A. Hakimi , B. Harikrishnan , L. Kalipoliti , G. Liu , M. Nguyen , C. Ochando , R. Salerno , J.B. Sauvan , Y. Sirois , E. Vernazza , A. Zabi , A. Zghiche 

Université de Strasbourg, CNRS, IPHC UMR 7178, Strasbourg, France




J.-L. Agram²¹ , J. Andrea , D. Apparú , D. Bloch , J.-M. Brom , E.C. Chabert , C. Collard , S. Falke , U. Goerlach , R. Haeberle , A.-C. Le Bihan , M. Meena , O. Poncet , G. Saha , M.A. Sessini , P. Van Hove , P. Vaucelle 

Institut de Physique des 2 Infinis de Lyon (IP2I), Villeurbanne, France

D. Amram, S. Beauceron , B. Blancon , G. Boudoul , N. Chanon , D. Contardo , P. Depasse , C. Dozen²² , H. El Mamouni, J. Fay , S. Gascon , M. Gouzevitch , C. Greenberg, G. Grenier , B. Ille , E. Jourdhuy, I.B. Laktineh, M. Lethuillier , L. Mirabito,

S. Perries, A. Purohit , M. Vander Donckt , P. Verdier , J. Xiao 






























Georgian Technical University, Tbilisi, Georgia

D. Chokheli , I. Lomidze , Z. Tsamalaidze¹⁷ 









RWTH Aachen University, I. Physikalisches Institut, Aachen, Germany

V. Botta , L. Feld , K. Klein , M. Lipinski , D. Meuser , A. Pauls , N. Röwert ,
M. Teroerde 






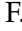




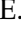

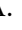
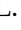

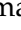

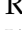





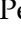

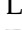
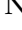


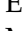
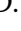



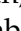

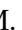







RWTH Aachen University, III. Physikalisches Institut A, Aachen, Germany

S. Diekmann , A. Dodonova , N. Eich , D. Eliseev , F. Engelke , J. Erdmann , M. Erdmann , P. Fackeldey , B. Fischer , T. Hebbeker , K. Hoepfner , F. Ivone , A. Jung ,
M.y. Lee , F. Mausolf , M. Merschmeyer , A. Meyer , S. Mukherjee , D. Noll ,
F. Nowotny, A. Pozdnyakov , Y. Rath, W. Redjeb , F. Rehm, H. Reithler , V. Sarkisovi ,
A. Schmidt , A. Sharma , J.L. Spah , A. Stein , F. Torres Da Silva De Araujo²³ ,
S. Wiedenbeck , S. Zaleski















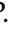


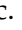



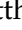
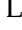

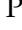
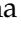






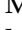

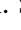



RWTH Aachen University, III. Physikalisches Institut B, Aachen, Germany

C. Dziwok , G. Flügge , T. Kress , A. Nowack , O. Pooth , A. Stahl , T. Ziemons ,
A. Zotz 


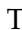


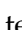
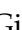

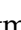
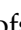

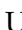

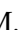
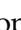



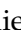

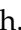

Deutsches Elektronen-Synchrotron, Hamburg, Germany



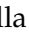





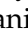





H. Aarup Petersen , M. Aldaya Martin , J. Alimena , S. Amoroso, Y. An , J. Bach ,
S. Baxter , M. Bayatmakou , H. Becerril Gonzalez , O. Behnke , A. Belvedere ,
S. Bhattacharya , F. Blekman²⁴ , K. Borrás²⁵ , A. Campbell , A. Cardini , C. Cheng,
F. Colombina , S. Consuegra Rodríguez , G. Correia Silva , M. De Silva , G. Eckerlin,
D. Eckstein , L.I. Estevez Banos , O. Filatov , E. Gallo²⁴ , A. Geiser , V. Guglielmi ,
M. Guthoff , A. Hinzmänn , L. Jeppe , B. Kaech , M. Kasemann , C. Kleinwort ,
R. Kogler , M. Komm , D. Krücker , W. Lange, D. Leyva Pernia , K. Lipka²⁶ ,
W. Lohmann²⁷ , F. Lorkowski , R. Mankel , I.-A. Melzer-Pellmann , M. Mendizabal Morentin ,
A.B. Meyer , G. Milella , K. Moral Figueroa , A. Mussgiller ,
L.P. Nair , J. Niedziela , A. Nürnberg , Y. Otariid, J. Park , D. Pérez Adán ,
E. Ranken , A. Raspereza , D. Rastorguev , J. Rübenach, L. Rygaard, A. Saggio ,
M. Scham^{28,25} , S. Schnake²⁵ , P. Schütze , C. Schwanenberger²⁴ , D. Selivanova ,
K. Sharko , M. Shchedrolosiev , D. Stafford, F. Vazzoler , A. Ventura Barroso ,
R. Walsh , D. Wang , Q. Wang , Y. Wen , K. Wichmann, L. Wiens²⁵ , C. Wissing ,
Y. Yang , A. Zimmermann Castro Santos 

University of Hamburg, Hamburg, Germany

A. Albrecht , S. Albrecht , M. Antonello , S. Bein , L. Benato , S. Bollweg,
M. Bonanomi , P. Connor , K. El Morabit , Y. Fischer , E. Garutti , A. Grohsjean ,
J. Haller , H.R. Jabusch , G. Kasieczka , P. Keicher, R. Klanner , W. Korcari ,
T. Kramer , C.c. Kuo, V. Kutzner , F. Labe , J. Lange , A. Lobanov , C. Matthies ,
L. Moureaux , M. Mrowietz, A. Nigamova , Y. Nissan, A. Paasch , K.J. Pena Rodriguez ,
T. Quadfasel , B. Raciti , M. Rieger , D. Savoii , J. Schindler , P. Schleper ,
M. Schröder , J. Schwandt , M. Sommerhalder , H. Stadie , G. Steinbrück , A. Tews,
M. Wolf 

Karlsruher Institut fuer Technologie, Karlsruhe, Germany

S. Brommer , M. Burkart, E. Butz , T. Chwalek , A. Dierlamm , A. Droll, N. Faltermann ,
M. Giffels , A. Gottmann , F. Hartmann²⁹ , R. Hofsaess , M. Horzela ,
U. Husemann , J. Kieseler , M. Klute , R. Koppenhöfer , J.M. Lawhorn , M. Link,
A. Lintuluoto , B. Maier , S. Maier , S. Mitra , M. Mormile , Th. Müller , M. Neukum,

M. Oh , E. Pfeffer , M. Presilla , G. Quast , K. Rabbertz , B. Regnery , N. Shadskiy , I. Shvetsov , H.J. Simonis , L. Sowa, L. Stockmeier, K. Tauqeer, M. Toms , N. Trevisani , R.F. Von Cube , M. Wassmer , S. Wieland , F. Wittig, R. Wolf , X. Zuo 

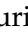
Institute of Nuclear and Particle Physics (INPP), NCSR Demokritos, Aghia Paraskevi, Greece

G. Anagnostou, G. Daskalakis , A. Kyriakis, A. Papadopoulos²⁹, A. Stakia 

National and Kapodistrian University of Athens, Athens, Greece

P. Kontaxakis , G. Melachroinos, Z. Painesis , A. Panagiotou, I. Papavergou , I. Paraskevas , N. Saoulidou , K. Theofilatos , E. Tziaferi , K. Vellidis , I. Zisopoulos 







National Technical University of Athens, Athens, Greece

G. Bakas , T. Chatzistavrou, G. Karapostoli , K. Kousouris , I. Papakrivopoulos , E. Siamarkou, G. Tsiolitis, A. Zacharopoulou

University of Ioánnina, Ioánnina, Greece

K. Adamidis, I. Bestintzanos, I. Evangelou , C. Foudas, C. Kamtsikis, P. Katsoulis, P. Kokkas , P.G. Kosmoglou Kioseoglou , N. Manthos , I. Papadopoulos , J. Strologas 



HUN-REN Wigner Research Centre for Physics, Budapest, Hungary

M. Bartók³⁰ , C. Hajdu , D. Horvath^{31,32} , K. Márton, A.J. Rádli³³ , F. Sikler , V. Veszpremi 

MTA-ELTE Lendület CMS Particle and Nuclear Physics Group, Eötvös Loránd University, Budapest, Hungary

M. Csanád , K. Farkas , A. Fehérkuti³⁴ , M.M.A. Gadallah³⁵ , Á. Kadlecik , P. Major , G. Pásztor , G.I. Veres 

Faculty of Informatics, University of Debrecen, Debrecen, Hungary

P. Raics, B. Ujvari , G. Zilizi 






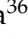


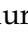





Institute of Nuclear Research ATOMKI, Debrecen, Hungary

G. Bencze, S. Czellar, J. Molnar, Z. Szillasi

Karoly Robert Campus, MATE Institute of Technology, Gyongyos, Hungary

T. Csorgo³⁴ , T. Novak 

Panjab University, Chandigarh, India

J. Babbar , S. Bansal , S.B. Beri, V. Bhatnagar , G. Chaudhary , S. Chauhan , N. Dhingra³⁶ , A. Kaur , A. Kaur , H. Kaur , M. Kaur , S. Kumar , K. Sandeep , T. Sheokand, J.B. Singh , A. Singla 


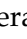

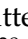
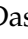










University of Delhi, Delhi, India

A. Ahmed , A. Bhardwaj , A. Chhetri , B.C. Choudhary , A. Kumar , A. Kumar , M. Naimuddin , K. Ranjan , M.K. Saini, S. Saumya 

Saha Institute of Nuclear Physics, HBNI, Kolkata, India

S. Baradia , S. Barman³⁷ , S. Bhattacharya , S. Das Gupta, S. Dutta , S. Dutta, S. Sarkar










Indian Institute of Technology Madras, Madras, India

M.M. Ameen , P.K. Behera , S.C. Behera , S. Chatterjee , G. Dash , P. Jana , P. Kalbhor , S. Kamble , J.R. Komaragiri³⁸ , D. Kumar³⁸ , P.R. Pujahari , N.R. Saha , A. Sharma , A.K. Sikdar , R.K. Singh, P. Verma, S. Verma , A. Vijay












Tata Institute of Fundamental Research-A, Mumbai, India

S. Dugad, M. Kumar , G.B. Mohanty , B. Parida , M. Shelake, P. Suryadevara

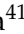






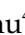

Tata Institute of Fundamental Research-B, Mumbai, India

A. Bala , S. Banerjee , R.M. Chatterjee, M. Guchait , Sh. Jain , A. Jaiswal, S. Kumar , G. Majumder , K. Mazumdar , S. Parolia , A. Thachayath 

National Institute of Science Education and Research, An OCC of Homi Bhabha National Institute, Bhubaneswar, Odisha, India

S. Bahinipati³⁹ , C. Kar , D. Maity⁴⁰ , P. Mal , T. Mishra , V.K. Muraleedharan Nair Bindhu⁴⁰ , K. Naskar⁴⁰ , A. Nayak⁴⁰ , S. Nayak, K. Pal, P. Sadangi, S.K. Swain , S. Varghese⁴⁰ , D. Vats⁴⁰ 

Indian Institute of Science Education and Research (IISER), Pune, India

S. Acharya⁴¹ , A. Alpana , S. Dube , B. Gomber⁴¹ , P. Hazarika , B. Kansal , A. Laha , B. Sahu⁴¹ , S. Sharma , K.Y. Vaish

Isfahan University of Technology, Isfahan, Iran

H. Bakhshiansohi⁴² , A. Jafari⁴³ , M. Zeinali⁴⁴ 



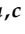
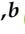







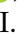

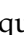
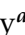
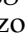



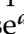
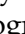





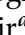


Institute for Research in Fundamental Sciences (IPM), Tehran, Iran

S. Bashiri, S. Chenarani⁴⁵ , S.M. Etesami , Y. Hosseini , M. Khakzad , E. Khazaie⁴⁶ , M. Mohammadi Najafabadi , S. Tizchang 














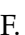

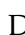

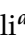












University College Dublin, Dublin, Ireland

M. Felcini , M. Grunewald 

INFN Sezione di Bari^a, Università di Bari^b, Politecnico di Bari^c, Bari, Italy

M. Abbrescia^{a,b} , A. Colaleo^{a,b} , D. Creanza^{a,c} , B. D'Anzi^{a,b} , N. De Filippis^{a,c} , M. De Palma^{a,b} , A. Di Florio^{a,c} , L. Fiore^a , G. Iaselli^{a,c} , M. Louka^{a,b}, G. Maggi^{a,c} , M. Maggi^a , I. Margjeka^{a,b} , V. Mastrapasqua^{a,b} , S. My^{a,b} , S. Nuzzo^{a,b} , A. Pellecchia^{a,b} , A. Pompili^{a,b} , G. Pugliese^{a,c} , R. Radogna^a , D. Ramos^a , A. Ranieri^a , L. Silvestris^a , F.M. Simone^{a,b} , Ü. Sözbilir^a , A. Stamerra^a , D. Troiano^a , R. Venditti^a , P. Verwilligen^a , A. Zaza^{a,b} 











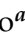


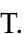

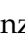
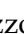
INFN Sezione di Bologna^a, Università di Bologna^b, Bologna, Italy

G. Abbiendi^a , C. Battilana^{a,b} , D. Bonacorsi^{a,b} , L. Borghonovi^a , P. Capiluppi^{a,b} , A. Castro^{a,b} , F.R. Cavallo^a , M. Cuffiani^{a,b} , G.M. Dallavalle^a , T. Diotallevi^{a,b} , F. Fabbri^a , A. Fanfani^{a,b} , D. Fasanella^{a,b} , P. Giacomelli^a , L. Giommi^{a,b} , C. Grandi^a , L. Guiducci^{a,b} , S. Lo Meo^{a,47} , M. Lorusso^{a,b} , L. Lunerti^a , S. Marcellini^a , G. Masetti^a , F.L. Navarria^{a,b} , G. Paggi^a , A. Perrotta^a , F. Primavera^{a,b} , A.M. Rossi^{a,b} , S. Rossi Tisbeni^{a,b} , T. Rovelli^{a,b} , G.P. Siroli^{a,b} 

INFN Sezione di Catania^a, Università di Catania^b, Catania, Italy

S. Costa^{a,b,48} , A. Di Mattia^a , R. Potenza^{a,b}, A. Tricomi^{a,b,48} , C. Tuve^{a,b} 

INFN Sezione di Firenze^a, Università di Firenze^b, Firenze, Italy

P. Assiouras^a , G. Barbagli^a , G. Bardelli^{a,b} , B. Camaiani^{a,b} , A. Cassese^a , R. Ceccarelli^a , V. Ciulli^{a,b} , C. Civinini^a , R. D'Alessandro^{a,b} , E. Focardi^{a,b} , T. Kello^a, G. Latino^{a,b} , P. Lenzi^{a,b} , M. Lizzo^a , M. Meschini^a , S. Paoletti^a , A. Papanastassiou^{a,b}, G. Sguazzoni^a , L. Viliani^a 





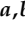
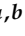








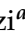




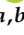
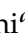



INFN Laboratori Nazionali di Frascati, Frascati, Italy

L. Benussi , S. Bianco , S. Meola⁴⁹ , D. Piccolo 


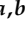





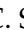

INFN Sezione di Genova^a, Università di Genova^b, Genova, Italy

P. Chatagnon^a , F. Ferro^a , E. Robutti^a , S. Tosi^{a,b} 





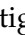

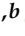

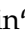



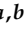
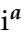

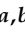

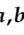
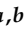




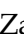
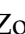



INFN Sezione di Milano-Bicocca^a, Università di Milano-Bicocca^b, Milano, Italy

A. Benaglia^a , G. Boldrini^{a,b} , F. Brivio^a , F. Cetorelli^a , F. De Guio^{a,b} , M.E. Dinardo^{a,b} , P. Dini^a , S. Gennai^a , R. Gerosa^{a,b} , A. Ghezzi^{a,b} , P. Govoni^{a,b} , L. Guzzi^a , M.T. Lucchini^{a,b} , M. Malberti^a , S. Malvezzi^a , A. Massironi^a , D. Menasce^a , L. Moroni^a , M. Paganoni^{a,b} , S. Palluotto^{a,b} , D. Pedrini^a , A. Perego^a , B.S. Pinolini^a, G. Pizzati^{a,b}, S. Ragazzi^{a,b} , T. Tabarelli de Fatis^{a,b} 











INFN Sezione di Napoli^a, Università di Napoli 'Federico II'^b, Napoli, Italy; Università della Basilicata^c, Potenza, Italy; Scuola Superiore Meridionale (SSM)^d, Napoli, Italy

S. Buontempo^a , A. Cagnotta^{a,b} , F. Carnevali^{a,b}, N. Cavallo^{a,c} , F. Fabozzi^{a,c} , A.O.M. Iorio^{a,b} , L. Lista^{a,b,50} , P. Paolucci^{a,29} , B. Rossi^a , C. Sciacca^{a,b} 





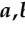


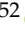

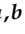


INFN Sezione di Padova^a, Università di Padova^b, Padova, Italy; Università di Trento^c, Trento, Italy

R. Ardino^a , P. Azzi^a , N. Bacchetta^{a,51} , M. Bellato^a , D. Bisello^{a,b} , P. Bortignon^a , G. Bortolato^{a,b}, A. Bragagnolo^{a,b} , A.C.M. Bulla^a , R. Carlin^{a,b} , P. Checchia^a , T. Dorigo^a , F. Gasparini^{a,b} , U. Gasparini^{a,b} , E. Lusiani^a , M. Margoni^{a,b} , M. Migliorini^{a,b} , J. Pazzini^{a,b} , P. Ronchese^{a,b} , R. Rossin^{a,b} , F. Simonetto^{a,b} , G. Strong^a , M. Tosi^{a,b} , A. Triossi^{a,b} , S. Ventura^a , M. Zanetti^{a,b} , P. Zotto^{a,b} , A. Zucchetta^{a,b} , G. Zumerle^{a,b} 





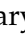
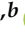

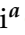
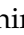

















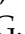





INFN Sezione di Pavia^a, Università di Pavia^b, Pavia, Italy

C. Aimè^a , A. Braghieri^a , S. Calzaferri^a , D. Fiorina^a , P. Montagna^{a,b} , V. Re^a , C. Riccardi^{a,b} , P. Salvini^a , I. Vai^{a,b} , P. Vitulo^{a,b} 



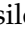









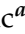
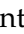
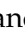


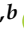



INFN Sezione di Perugia^a, Università di Perugia^b, Perugia, Italy

S. Ajmal^{a,b} , M.E. Ascioti^{a,b}, G.M. Bilei^a , C. Carrivale^{a,b}, D. Ciangottini^{a,b} , L. Fanò^{a,b} , M. Magherini^{a,b} , V. Mariani^{a,b} , M. Menichelli^a , F. Moscatelli^{a,52} , A. Rossi^{a,b} , A. Santocchia^{a,b} , D. Spiga^a , T. Tedeschi^{a,b} 

INFN Sezione di Pisa^a, Università di Pisa^b, Scuola Normale Superiore di Pisa^c, Pisa, Italy; Università di Siena^d, Siena, Italy


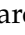
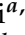


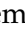
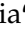




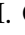
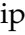
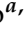


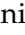

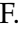

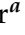




C.A. Alexe^{a,c} , P. Asenov^{a,b} , P. Azzurri^a , G. Bagliesi^a , R. Bhattacharya^a , L. Bianchini^{a,b} , T. Boccali^a , E. Bossini^a , D. Bruschini^{a,c} , R. Castaldi^a , M.A. Ciocci^{a,b} , M. Cipriani^{a,b} , V. D'Amante^{a,d} , R. Dell'Orso^a , S. Donato^a , A. Giassi^a , F. Ligabue^{a,c} , D. Matos Figueiredo^a, A. Messineo^{a,b} , M. Musich^{a,b} , F. Palla^a , A. Rizzi^{a,b} , G. Rolandi^{a,c} , S. Roy Chowdhury^a , T. Sarkar^a , A. Scribano^a , P. Spagnolo^a , R. Tenchini^a , G. Tonelli^{a,b} , N. Turini^{a,d} , F. Vaselli^{a,c} , A. Venturi^a , P.G. Verdini^a 

INFN Sezione di Roma^a, Sapienza Università di Roma^b, Roma, Italy




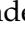


C. Baldenegro Barrera^{a,b} , P. Barria^a , C. Basile^{a,b} , M. Campana^{a,b} , F. Cavallari^a , L. Cunqueiro Mendez^{a,b} , D. Del Re^{a,b} , E. Di Marco^a , M. Diemoz^a , F. Errico^{a,b} , E. Longo^{a,b} , P. Meridiani^a , J. Mijuskovic^{a,b} , G. Organtini^{a,b} , F. Pandolfi^a , R. Paramatti^{a,b} , C. Quaranta^{a,b} , S. Rahatlou^{a,b} , C. Rovelli^a , F. Santanastasio^{a,b} , L. Soffi^a 

INFN Sezione di Torino^a, Università di Torino^b, Torino, Italy; Università del Piemonte Orientale^c, Novara, Italy

N. Amapane^{a,b} , R. Arcidiacono^{a,c} , S. Argiro^{a,b} , M. Arneodo^{a,c} , N. Bartosik^a , R. Bellan^{a,b} , A. Bellora^{a,b} , C. Biino^a , C. Borca^{a,b} , N. Cartiglia^a , M. Costa^{a,b} 

R. Covarelli^{a,b} , N. Demaria^a , L. Finco^a , M. Grippo^{a,b} , B. Kiani^{a,b} , F. Legger^a , F. Luongo^{a,b} , C. Mariotti^a , L. Markovic^{a,b} , S. Maselli^a , A. Mecca^{a,b} , L. Menzio^{a,b}, E. Migliore^{a,b} , M. Monteno^a , R. Mulargia^a , M.M. Obertino^{a,b} , G. Ortona^a , L. Pacher^{a,b} , N. Pastrone^a , M. Pelliccioni^a , M. Ruspa^{a,c} , F. Siviero^{a,b} , V. Sola^{a,b} , A. Solano^{a,b} , A. Staiano^a , C. Tarricone^{a,b} , D. Trocino^a , G. Umoret^{a,b} , E. Vlasov^{a,b} , R. White^{a,b}

INFN Sezione di Trieste^a, Università di Trieste^b, Trieste, Italy

S. Belforte^a , V. Candelise^{a,b} , M. Casarsa^a , F. Cossutti^a , K. De Leo^a , G. Della Ricca^{a,b} 

Kyungpook National University, Daegu, Korea

S. Dogra , J. Hong , C. Huh , B. Kim , J. Kim, D. Lee, H. Lee, S.W. Lee , C.S. Moon , Y.D. Oh , M.S. Ryu , S. Sekmen , B. Tae, Y.C. Yang 

Department of Mathematics and Physics - GWNNU, Gangneung, Korea

M.S. Kim 






Chonnam National University, Institute for Universe and Elementary Particles, Kwangju, Korea

G. Bak , P. Gwak , H. Kim , D.H. Moon 

Hanyang University, Seoul, Korea

E. Asilar , J. Choi , D. Kim , T.J. Kim , J.A. Merlin, Y. Ryou

Korea University, Seoul, Korea

S. Choi , S. Han, B. Hong , K. Lee, K.S. Lee , S. Lee , S.K. Park, J. Yoo 

Kyung Hee University, Department of Physics, Seoul, Korea

J. Goh , S. Yang 








Sejong University, Seoul, Korea

H. S. Kim , Y. Kim, S. Lee



Seoul National University, Seoul, Korea

J. Almond, J.H. Bhyun, J. Choi , J. Choi, W. Jun , J. Kim , S. Ko , H. Kwon , H. Lee , J. Lee , J. Lee , B.H. Oh , S.B. Oh , H. Seo , U.K. Yang, I. Yoon 

University of Seoul, Seoul, Korea

W. Jang , D.Y. Kang, Y. Kang , S. Kim , B. Ko, J.S.H. Lee , Y. Lee , I.C. Park , Y. Roh, I.J. Watson 

Yonsei University, Department of Physics, Seoul, Korea

S. Ha , H.D. Yoo 

Sungkyunkwan University, Suwon, Korea

M. Choi , M.R. Kim , H. Lee, Y. Lee , I. Yu 


College of Engineering and Technology, American University of the Middle East (AUM), Dasman, Kuwait

T. Beyrouthy

Riga Technical University, Riga, Latvia

K. Dreimanis , A. Gaile , G. Pikurs, A. Potrebko , M. Seidel , D. Sidiropoulos Kontos

University of Latvia (LU), Riga, Latvia

N.R. Strautnieks 







Vilnius University, Vilnius, Lithuania

M. Ambrozas , A. Juodagalvis , A. Rinkevicius , G. Tamulaitis 








National Centre for Particle Physics, Universiti Malaya, Kuala Lumpur, Malaysia

N. Bin Norjoharuddeen , I. Yusuff⁵³ , Z. Zolkapli



Universidad de Sonora (UNISON), Hermosillo, Mexico

J.F. Benitez , A. Castaneda Hernandez , H.A. Encinas Acosta, L.G. Gallegos Maríñez, M. León Coello , J.A. Murillo Quijada , A. Sehrawat , L. Valencia Palomo 

Centro de Investigacion y de Estudios Avanzados del IPN, Mexico City, Mexico

G. Ayala , H. Castilla-Valdez , H. Crotte Ledesma, E. De La Cruz-Burelo , I. Heredia-De La Cruz⁵⁴ , R. Lopez-Fernandez , J. Mejia Guisao , C.A. Mondragon Herrera, A. Sánchez Hernández 

Universidad Iberoamericana, Mexico City, Mexico

C. Oropeza Barrera , D.L. Ramirez Guadarrama, M. Ramírez García 


Benemerita Universidad Autonoma de Puebla, Puebla, Mexico

I. Bautista , I. Pedraza , H.A. Salazar Ibarguen , C. Uribe Estrada 

University of Montenegro, Podgorica, Montenegro

I. Bubanja, N. Raicevic 

University of Canterbury, Christchurch, New Zealand

P.H. Butler 

National Centre for Physics, Quaid-I-Azam University, Islamabad, Pakistan

A. Ahmad , M.I. Asghar, A. Awais , M.I.M. Awan, H.R. Hoorani , W.A. Khan 







AGH University of Krakow, Faculty of Computer Science, Electronics and Telecommunications, Krakow, Poland

V. Avati, L. Grzanka , M. Malawski 

National Centre for Nuclear Research, Swierk, Poland

H. Bialkowska , M. Bluj , M. Górski , M. Kazana , M. Szleper , P. Zalewski 



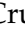













Institute of Experimental Physics, Faculty of Physics, University of Warsaw, Warsaw, Poland

K. Bunkowski , K. Doroba , A. Kalinowski , M. Konecki , J. Krolikowski , A. Muhammad 



Warsaw University of Technology, Warsaw, Poland

K. Pozniak , W. Zabolotny 

Laboratório de Instrumentação e Física Experimental de Partículas, Lisboa, Portugal

M. Araujo , D. Bastos , C. Beirão Da Cruz E Silva , A. Boletti , M. Bozzo , T. Camporesi , G. Da Molin , P. Faccioli , M. Gallinaro , J. Hollar , N. Leonardo , G.B. Marozzo, T. Niknejad , A. Petrilli , M. Pisano , J. Seixas , J. Varela , J.W. Wulff












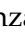


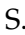














Faculty of Physics, University of Belgrade, Belgrade, Serbia

P. Adzic , P. Milenovic 

VINCA Institute of Nuclear Sciences, University of Belgrade, Belgrade, Serbia

M. Dordevic , J. Milosevic , L. Nadderd , V. Rekovic





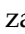









Centro de Investigaciones Energéticas Medioambientales y Tecnológicas (CIEMAT), Madrid, Spain

J. Alcaraz Maestre , Cristina F. Bedoya , Oliver M. Carretero , M. Cepeda , M. Cerrada , N. Colino , B. De La Cruz , A. Delgado Peris , A. Escalante Del Valle , D. Fernández Del Val , J.P. Fernández Ramos , J. Flix , M.C. Fouz , O. Gonzalez Lopez , S. Goy Lopez , J.M. Hernandez , M.I. Josa , E. Martin Viscasillas , D. Moran , C.M. Morcillo Perez , Á. Navarro Tobar , C. Perez Dengra , A. Pérez-Calero Yzquierdo , J. Puerta Pelayo , I. Redondo , S. Sánchez Navas , J. Sastre , L. Urda Gómez , J. Vazquez Escobar 












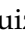







Universidad Autónoma de Madrid, Madrid, Spain

J.F. de Trocóniz 

Universidad de Oviedo, Instituto Universitario de Ciencias y Tecnologías Espaciales de Asturias (ICTEA), Oviedo, Spain

B. Alvarez Gonzalez , J. Cuevas , J. Fernandez Menendez , S. Folgueras , I. Gonzalez Caballero , J.R. González Fernández , P. Leguina , E. Palencia Cortezon , C. Ramón Álvarez , V. Rodríguez Bouza , A. Soto Rodríguez , A. Trapote , C. Vico Villalba , P. Vischia 

Instituto de Física de Cantabria (IFCA), CSIC-Universidad de Cantabria, Santander, Spain

S. Bhowmik , S. Blanco Fernández , J.A. Brochero Cifuentes , I.J. Cabrillo , A. Calderon , J. Duarte Campderros , M. Fernandez , G. Gomez , C. Lasiosa García , R. Lopez Ruiz , C. Martinez Rivero , P. Martinez Ruiz del Arbol , F. Matorras , P. Matorras Cuevas , E. Navarrete Ramos , J. Piedra Gomez , L. Scodellaro , I. Vila , J.M. Vizan Garcia 














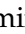





























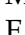
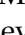




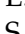


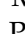


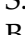


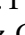

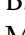
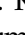

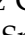


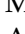
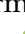

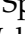
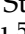

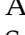

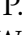
University of Colombo, Colombo, Sri Lanka

B. Kailasapathy⁵⁵ , D.D.C. Wickramarathna 









University of Ruhuna, Department of Physics, Matara, Sri Lanka

W.G.D. Dharmaratna⁵⁶ , K. Liyanage , N. Perera 


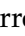







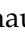




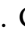



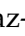



CERN, European Organization for Nuclear Research, Geneva, Switzerland

D. Abbaneo , C. Amendola , E. Auffray , G. Auzinger , J. Baechler, D. Barney , A. Bermúdez Martínez , M. Bianco , B. Bilin , A.A. Bin Anuar , A. Bocci , C. Botta , E. Brondolin , C. Caillol , G. Cerminara , N. Chernyavskaya , D. d'Enterria , A. Dabrowski , A. David , A. De Roeck , M.M. Defranchis , M. Deile , M. Dobson , G. Franzoni , W. Funk , S. Giani, D. Gigi, K. Gill , F. Glege , L. Gouskos , J. Hegeman , J.K. Heikkilä , B. Huber, V. Innocente , T. James , P. Janot , O. Kaluzinska , S. Laurila , P. Lecoq , E. Leutgeb , C. Lourenço , L. Malgeri , M. Mannelli , A.C. Marini , M. Matthewman, A. Mehta , F. Meijers , S. Mersi , E. Meschi , V. Milosevic , F. Monti , F. Moortgat , M. Mulders , I. Neutelings , S. Orfanelli, F. Pantaleo , G. Petrucciani , A. Pfeiffer , M. Pierini , H. Qu , D. Rabaday , B. Ribeiro Lopes , M. Rovere , H. Sakulin , S. Sanchez Cruz , S. Scarfi , C. Schwick, M. Selvaggi , A. Sharma , K. Shchelina , P. Silva , P. Sphicas⁵⁷ , A.G. Stahl Leitner , A. Steen , S. Summers , D. Treille , P. Tropea , D. Walter , J. Wanczyk⁵⁸ , J. Wang, S. Wuchterl , P. Zehetner , P. Zejdl , W.D. Zeuner


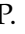
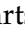






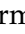


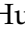






Paul Scherrer Institut, Villigen, Switzerland

T. Bevilacqua⁵⁹ , L. Caminada⁵⁹ , A. Ebrahimi , W. Erdmann , R. Horisberger , Q. Ingram , H.C. Kaestli , D. Kotlinski , C. Lange , M. Missiroli⁵⁹ , L. Noehte⁵⁹ , T. Rohe 





ETH Zurich - Institute for Particle Physics and Astrophysics (IPA), Zurich, Switzerland

T.K. Aarrestad , K. Androsov⁵⁸ , M. Backhaus , G. Bonomelli, A. Calandri , C. Cazaniga , K. Datta , P. De Bryas Dexmiers D'archiac⁵⁸ , A. De Cosa , G. Dissertori , M. Dittmar, M. Donegà , F. Eble , M. Galli , K. Gedia , F. Glessgen , C. Grab , N. Härringer , T.G. Harte, D. Hits , W. Lustermann , A.-M. Lyon , R.A. Manzoni , M. Marchegiani , L. Marchese , C. Martin Perez , A. Mascellani⁵⁸ , F. Nessi-Tedaldi , F. Pauss , V. Perovic , S. Pigazzini , C. Reissel , T. Reitenspiess , B. Ristic , F. Riti , R. Seidita , J. Steggemann⁵⁸ , A. Tarabini , D. Valsecchi , R. Wallny

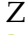

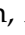



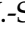
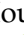

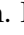
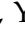
Universität Zürich, Zurich, Switzerland

C. Amsler⁶⁰ , P. Bärtshi , M.F. Canelli , K. Cormier , M. Huwiler , W. Jin , A. Jofrehei , B. Kilminster , S. Leontsinis , S.P. Liehti , A. Macchiolo , P. Meiring , F. Meng , U. Molinatti , J. Motta , A. Reimers , P. Robmann, M. Senger , E. Shokr, F. Stäger , R. Tramontano 


National Central University, Chung-Li, Taiwan

C. Adloff⁶¹ , D. Bhowmik, C.M. Kuo, W. Lin, P.K. Rout , P.C. Tiwari³⁸ , S.S. Yu 


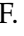
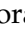

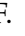



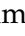


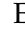
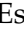


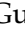
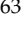

National Taiwan University (NTU), Taipei, Taiwan

L. Ceard, K.F. Chen , P.s. Chen, Z.g. Chen, A. De Iorio , W.-S. Hou , T.h. Hsu, Y.w. Kao, S. Karmakar , G. Kole , Y.y. Li , R.-S. Lu , E. Paganis , X.f. Su , J. Thomas-Wilsker , L.s. Tsai, H.y. Wu, E. Yazgan 


High Energy Physics Research Unit, Department of Physics, Faculty of Science, Chulalongkorn University, Bangkok, Thailand

C. Asawatangtrakuldee , N. Srimanobhas , V. Wachirapusanand 

Çukurova University, Physics Department, Science and Art Faculty, Adana, Turkey

D. Agyel , F. Boran , F. Dolek , I. Dumanoglu⁶² , E. Eskut , Y. Guler⁶³ , E. Gurpinar Guler⁶³ , C. Isik , O. Kara, A. Kayis Topaksu , U. Kiminsu , G. Onengut , K. Ozdemir⁶⁴ , A. Polatoz , B. Tali⁶⁵ , U.G. Tok , S. Turkcapar , E. Uslan , I.S. Zorbakir 

Middle East Technical University, Physics Department, Ankara, Turkey

G. Sokmen, M. Yalvac⁶⁶ 

Bogazici University, Istanbul, Turkey

B. Akgun , I.O. Atakisi , E. Gülmez , M. Kaya⁶⁷ , O. Kaya⁶⁸ , S. Tekten⁶⁹ 





Istanbul Technical University, Istanbul, Turkey

A. Cakir , K. Cankocak^{62,70} , G.G. Dincer⁶² , Y. Komurcu , S. Sen⁷¹ 

Istanbul University, Istanbul, Turkey

O. Aydilek⁷² , V. Epshteyn , B. Hacisahinoglu , I. Hos⁷³ , B. Kaynak , S. Ozkorucuklu , O. Potok , H. Sert , C. Simsek , C. Zorbilmez 

Yildiz Technical University, Istanbul, Turkey

S. Cerci⁶⁵ , B. Isildak⁷⁴ , D. Sunar Cerci , T. Yetkin 







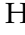
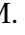
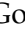
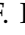
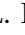
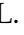

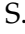

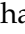

Institute for Scintillation Materials of National Academy of Science of Ukraine, Kharkiv, Ukraine

A. Boyaryntsev , B. Grynyov 


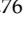






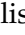


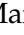



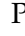

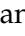






National Science Centre, Kharkiv Institute of Physics and Technology, Kharkiv, Ukraine

L. Levchuk 






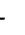

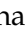

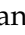











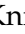

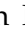

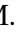

















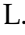
University of Bristol, Bristol, United Kingdom

D. Anthony , J.J. Brooke , A. Bundock , F. Bury , E. Clement , D. Cussans , H. Flacher , M. Glowacki , J. Goldstein , H.F. Heath , M.-L. Holmberg , L. Kreczko , S. Paramesvaran , L. Robertshaw , S. Seif El Nasr-Storey , V.J. Smith , N. Stylianou⁷⁵ , K. Walkingshaw Pass






Rutherford Appleton Laboratory, Didcot, United Kingdom

A.H. Ball , K.W. Bell , A. Belyaev⁷⁶ , C. Brew , R.M. Brown , D.J.A. Cockerill , C. Cooke , A. Elliot , K.V. Ellis , K. Harder , S. Harper , J. Linacre , K. Manolopoulos , D.M. Newbold , E. Olaiya , D. Petyt , T. Reis , A.R. Sahasransu , G. Salvi , T. Schuh , C.H. Shepherd-Themistocleous , I.R. Tomalin , K.C. Whalen , T. Williams 

Imperial College, London, United Kingdom

R. Bainbridge , P. Bloch , C.E. Brown , O. Buchmuller , V. Cacchio , C.A. Carrillo Montoya , G.S. Chahal⁷⁷ , D. Colling , J.S. Dancu , I. Das , P. Dauncey , G. Davies , J. Davies , M. Della Negra , S. Fayer , G. Fedi , G. Hall , M.H. Hassanshahi , A. Howard , G. Iles , M. Knight , J. Langford , J. León Holgado , L. Lyons , A.-M. Magnan , S. Mallios , M. Mieskolainen , J. Nash⁷⁸ , M. Pesaresi , P.B. Pradeep , B.C. Radburn-Smith , A. Richards , A. Rose , K. Savva , C. Seez , R. Shukla , A. Tapper , K. Uchida , G.P. Uttley , L.H. Vage , T. Virdee²⁹ , M. Vojinovic , N. Wardle , D. Winterbottom 



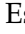

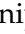
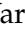
Brunel University, Uxbridge, United Kingdom

K. Coldham , J.E. Cole , A. Khan , P. Kyberd , I.D. Reid 








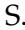



Baylor University, Waco, Texas, USA

S. Abdullin , A. Brinkerhoff , B. Caraway , E. Collins , J. Dittmann , K. Hatakeyama , J. Hiltbrand , B. McMaster , J. Samudio , S. Sawant , C. Sutantawibul , J. Wilson 



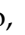










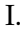
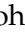





Catholic University of America, Washington, DC, USA

R. Bartek , A. Dominguez , C. Huerta Escamilla , A.E. Simsek , R. Uniyal , A.M. Vargas Hernandez 



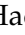
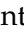
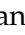






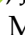








The University of Alabama, Tuscaloosa, Alabama, USA

B. Bam , A. Buchot Perraguin , R. Chudasama , S.I. Cooper , C. Crovella , S.V. Gleyzer , E. Pearson , C.U. Perez , P. Rumerio⁷⁹ , E. Usai , R. Yi 






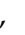


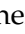
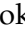







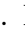


Boston University, Boston, Massachusetts, USA

A. Akpınar , C. Cosby , G. De Castro , Z. Demiragli , C. Erice , C. Fangmeier , C. Fernandez Madrazo , E. Fontanesi , D. Gastler , F. Golf , S. Jeon , J. O'cain , I. Reed , J. Rohlf , K. Salyer , D. Sperka , D. Spitzbart , I. Suarez , A. Tsatsos , A.G. Zecchinelli 










Brown University, Providence, Rhode Island, USA

G. Benelli , X. Coubez²⁵ , D. Cutts , M. Hadley , U. Heintz , J.M. Hogan⁸⁰ , T. Kwon , G. Landsberg , K.T. Lau , D. Li , J. Luo , S. Mondal , M. Narain[†] , N. Pervan , S. Sagir⁸¹ , F. Simpson , M. Stamenkovic , N. Venkatasubramanian , X. Yan , W. Zhang 

University of California, Davis, Davis, California, USA

S. Abbott , J. Bonilla , C. Brainerd , R. Breedon , H. Cai , M. Calderon De La Barca Sanchez , M. Chertok , M. Citron , J. Conway , P.T. Cox , R. Erbacher , F. Jensen , O. Kukral , G. Mocellin , M. Mulhearn , S. Ostrom , W. Wei , Y. Yao , S. Yoo , F. Zhang 


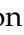


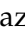















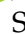



University of California, Los Angeles, California, USA

M. Bachtis , R. Cousins , A. Datta , G. Flores Avila, J. Hauser , M. Ignatenko , M.A. Iqbal , T. Lam , E. Manca , A. Nunez Del Prado, D. Saltzberg , V. Valuev 

University of California, Riverside, Riverside, California, USA

R. Clare , J.W. Gary , M. Gordon, G. Hanson , W. Si , S. Wimpenny[†] 

University of California, San Diego, La Jolla, California, USA

A. Aportela, A. Arora , J.G. Branson , S. Cittolin , S. Cooperstein , D. Diaz , J. Duarte , L. Giannini , Y. Gu, J. Guiang , R. Kansal , V. Krutelyov , R. Lee , J. Letts , M. Masciovecchio , F. Mokhtar , S. Mukherjee , M. Pieri , M. Quinnan , B.V. Sathia Narayanan , V. Sharma , M. Tadel , E. Vourliotis , F. Würthwein , Y. Xiang , A. Yagil 











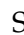
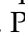

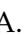


University of California, Santa Barbara - Department of Physics, Santa Barbara, California, USA

A. Barzdukas , L. Brennan , C. Campagnari , K. Downham , C. Grieco , J. Incandela , J. Kim , A.J. Li , P. Masterson , H. Mei , J. Richman , S.N. Santpur , U. Sarica , R. Schmitz , F. Setti , J. Sheplock , D. Stuart , T.Á. Vámi , S. Wang , D. Zhang



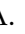
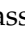
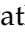










California Institute of Technology, Pasadena, California, USA

A. Bornheim , O. Cerri, A. Latorre, J. Mao , H.B. Newman , G. Reales Gutiérrez, M. Spiropulu , J.R. Vlimant , C. Wang , S. Xie , R.Y. Zhu 



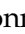












Carnegie Mellon University, Pittsburgh, Pennsylvania, USA

J. Alison , S. An , M.B. Andrews , P. Bryant , M. Cremonesi, V. Dutta , T. Ferguson , T.A. Gómez Espinosa , A. Harilal , A. Kallil Tharayil, C. Liu , T. Mudholkar , S. Murthy , P. Palit , K. Park, M. Paulini , A. Roberts , A. Sanchez , W. Terrill 



















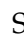









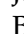
















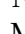
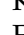
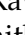



University of Colorado Boulder, Boulder, Colorado, USA

J.P. Cumalat , W.T. Ford , A. Hart , A. Hassani , G. Karathanasis , N. Manganelli , J. Pearkes , A. Perloff , C. Savard , N. Schonbeck , K. Stenson , K.A. Ulmer , S.R. Wagner , N. Zipper , D. Zuolo 







Cornell University, Ithaca, New York, USA

J. Alexander , S. Bright-Thonney , X. Chen , D.J. Cranshaw , J. Fan , X. Fan , S. Hogan , P. Kotamnives, J. Monroy , M. Oshiro , J.R. Patterson , M. Reid , A. Ryd , J. Thom , P. Wittich , R. Zou 

Fermi National Accelerator Laboratory, Batavia, Illinois, USA







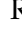



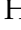
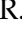



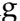
M. Albrow , M. Alyari , O. Amram , G. Apollinari , A. Apresyan , L.A.T. Bauerdick , D. Berry , J. Berryhill , P.C. Bhat , K. Burkett , J.N. Butler , A. Canepa , G.B. Cerati , H.W.K. Cheung , F. Chlebana , G. Cummings , J. Dickinson , I. Dutta , V.D. Elvira , Y. Feng , J. Freeman , A. Gandrakota , Z. Gecse , L. Gray , D. Green, A. Grummer , S. Grünendahl , D. Guerrero , O. Gutsche , R.M. Harris , R. Heller , T.C. Herwig , J. Hirschauer , B. Jayatilaka , S. Jindariani , M. Johnson , U. Joshi , T. Klijnsma , B. Klima , K.H.M. Kwok , S. Lammel , D. Lincoln , R. Lipton , T. Liu , C. Madrid , K. Maeshima , C. Mantilla , D. Mason , P. McBride , P. Merkel , S. Mrenna , S. Nahn , J. Ngadiuba , D. Noonan , S. Norberg, V. Papadimitriou , N. Pastika , K. Pedro , C. Pena⁸² , F. Ravera , A. Reinsvold Hall⁸³ , L. Ristori , M. Safdari , E. Sexton-Kennedy , N. Smith , A. Soha , L. Spiegel , S. Stoynev , J. Strait , L. Taylor , S. Tkaczyk , N.V. Tran , L. Uplegger , E.W. Vaandering , I. Zoi 

University of Florida, Gainesville, Florida, USA









C. Aruta , P. Avery , D. Bourilkov , P. Chang , V. Cherepanov , R.D. Field, E. Koenig 

M. Kolosova , J. Konigsberg , A. Korytov , K. Matchev , N. Menendez , G. Mitselmakher , K. Mohrman , A. Muthirakalayil Madhu , N. Rawal , S. Rosenzweig , Y. Takahashi , J. Wang 








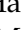
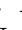
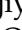
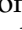
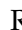



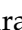











Florida State University, Tallahassee, Florida, USA

T. Adams , A. Al Kadhim , A. Askew , S. Bower , R. Habibullah , V. Hagopian , R. Hashmi , R.S. Kim , S. Kim , T. Kolberg , G. Martinez , H. Prosper , P.R. Prova , M. Wulansatiti , R. Yohay , J. Zhang 






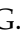


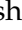
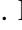



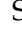
Florida Institute of Technology, Melbourne, Florida, USA

B. Alsufyani , M.M. Baarmand , S. Butalla , S. Das , T. Elkafrawy⁸⁴ , M. Hohlmann , M. Rahmani , E. Yanes 







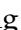

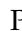

University of Illinois Chicago, Chicago, USA, Chicago, USA

M.R. Adams , A. Baty , C. Bennett , R. Cavanaugh , R. Escobar Franco , O. Evdokimov , C.E. Gerber , M. Hawksworth , A. Hingrajiya , D.J. Hofman , J.h. Lee , D. S. Lemos , A.H. Merrit , C. Mills , S. Nanda , G. Oh , B. Ozek , D. Pilipovic , R. Pradhan , E. Prifti , T. Roy , S. Rudrabhatla , M.B. Tonjes , N. Varelas , M.A. Wadud , Z. Ye , J. Yoo 








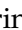
















The University of Iowa, Iowa City, Iowa, USA

M. Alhousseini , D. Blend , K. Dilsiz⁸⁵ , L. Emediato , G. Karaman , O.K. Köseyan , J.-P. Merlo , A. Mestvirishvili⁸⁶ , O. Neogi , H. Ogul⁸⁷ , Y. Onel , A. Penzo , C. Snyder , E. Tiras⁸⁸ 






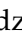
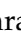

Johns Hopkins University, Baltimore, Maryland, USA

B. Blumenfeld , L. Corcodilos , J. Davis , A.V. Gritsan , L. Kang , S. Kyriacou , P. Maksimovic , M. Roguljic , J. Roskes , S. Sekhar , M. Swartz 



















The University of Kansas, Lawrence, Kansas, USA

A. Abreu , L.F. Alcerro Alcerro , J. Anguiano , S. Arteaga Escatel , P. Baringer , A. Bean , Z. Flowers , D. Grove , J. King , G. Krintiras , M. Lazarovits , C. Le Mahieu , J. Marquez , N. Minafra , M. Murray , M. Nickel , M. Pitt , S. Popescu⁸⁹ , C. Rogan , C. Royon , R. Salvatico , S. Sanders , C. Smith , G. Wilson 




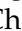
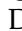


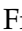














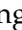




Kansas State University, Manhattan, Kansas, USA

B. Allmond , R. Gujju Gurunadha , A. Ivanov , K. Kaadze , Y. Maravin , J. Natoli , D. Roy , G. Sorrentino 

University of Maryland, College Park, Maryland, USA

A. Baden , A. Belloni , J. Bistany-riebman , Y.M. Chen , S.C. Eno , N.J. Hadley , S. Jabeen , R.G. Kellogg , T. Koeth , B. Kronheim , Y. Lai , S. Lascio , A.C. Mignerey , S. Nabili , C. Palmer , C. Papageorgakis , M.M. Paranjpe , L. Wang 


Massachusetts Institute of Technology, Cambridge, Massachusetts, USA

J. Bendavid , I.A. Cali , P.c. Chou , M. D'Alfonso , J. Eysermans , C. Freer , G. Gomez-Ceballos , M. Goncharov , G. Grosso , P. Harris , D. Hoang , D. Kovalskyi , J. Krupa , L. Lavezzo , Y.-J. Lee , K. Long , C. Mcginn , A. Novak , C. Paus , D. Rankin , C. Roland , G. Roland , S. Rothman , G.S.F. Stephans , Z. Wang , B. Wyslouch , T. J. Yang 











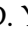

University of Minnesota, Minneapolis, Minnesota, USA

B. Crossman , B.M. Joshi , C. Kapsiak , M. Krohn , D. Mahon , J. Mans , B. Marzocchi , M. Revering , R. Rusack , R. Saradhy , N. Strobbe 

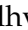









University of Mississippi, Oxford, Mississippi, USA

L.M. Cremaldi 












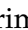



University of Nebraska-Lincoln, Lincoln, Nebraska, USA

K. Bloom , D.R. Claes , G. Haza , J. Hossain , C. Joo , I. Kravchenko , J.E. Siado ,
W. Tabb , A. Vagnerini , A. Wightman , F. Yan , D. Yu 








State University of New York at Buffalo, Buffalo, New York, USA

H. Bandyopadhyay , L. Hay , H.w. Hsia, I. Iashvili , A. Kalogeropoulos ,
A. Kharchilava , M. Morris , D. Nguyen , S. Rappoccio , H. Rejeb Sfar, A. Williams ,
P. Young 






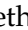





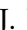








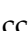





Northeastern University, Boston, Massachusetts, USA

G. Alverson , E. Barberis , J. Dervan, Y. Haddad , Y. Han , A. Krishna , J. Li ,
M. Lu , G. Madigan , R. Mccarthy , D.M. Morse , V. Nguyen , T. Orimoto ,
A. Parker , L. Skinnari , D. Wood 



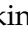


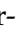
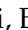

Northwestern University, Evanston, Illinois, USA

J. Bueghly, S. Dittmer , K.A. Hahn , Y. Liu , Y. Miao , D.G. Monk , M.H. Schmitt ,
A. Taliercio , M. Velasco

















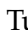
University of Notre Dame, Notre Dame, Indiana, USA

G. Agarwal , R. Band , R. Bucci, S. Castells , A. Das , R. Goldouzian , M. Hildreth ,
K.W. Ho , K. Hurtado Anampa , T. Ivanov , C. Jessop , K. Lannon , J. Lawrence ,
N. Loukas , L. Lutton , J. Mariano, N. Marinelli, I. Mcalister, T. McCauley , C. Mcgrady ,
C. Moore , Y. Musienko¹⁷ , H. Nelson , M. Osherson , A. Piccinelli , R. Ruchti ,
A. Townsend , Y. Wan, M. Wayne , H. Yockey, M. Zarucki , L. Zygalá 

The Ohio State University, Columbus, Ohio, USA

A. Basnet , B. Bylsma, M. Carrigan , L.S. Durkin , C. Hill , M. Joyce , M. Nunez Ornelas ,
K. Wei, B.L. Winer , B. R. Yates 







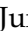
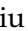
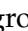
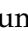
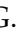







Princeton University, Princeton, New Jersey, USA

H. Bouchamaoui , P. Das , G. Dezoort , P. Elmer , A. Frankenthal , B. Greenberg ,
N. Haubrich , K. Kennedy, G. Kopp , S. Kwan , D. Lange , A. Loeliger , D. Marlow ,
I. Ojalvo , J. Olsen , A. Shevelev , D. Stickland , C. Tully 




University of Puerto Rico, Mayaguez, Puerto Rico, USA

G. Fidalgo , S. Malik , C. Suarez

Purdue University, West Lafayette, Indiana, USA

A.S. Bakshi , V.E. Barnes , S. Chandra , R. Chawla , A. Gu , L. Gutay, M. Jones ,
A.W. Jung , A.M. Koshy, M. Liu , G. Negro , N. Neumeister , G. Paspalaki ,
S. Piperov , V. Scheurer, J.F. Schulte , M. Stojanovic , J. Thieman , A. K. Viridi ,
F. Wang , W. Xie 

Purdue University Northwest, Hammond, Indiana, USA

J. Dolen , N. Parashar , A. Pathak 


Rice University, Houston, Texas, USA

D. Acosta , T. Carnahan , K.M. Ecklund , P.J. Fernández Manteca , S. Freed, P. Gardner,
F.J.M. Geurts , W. Li , J. Lin , O. Miguel Colin , B.P. Padley , R. Redjimi, J. Rotter ,
E. Yigitbasi , Y. Zhang 




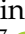






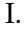
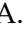
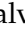

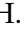


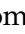

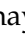

University of Rochester, Rochester, New York, USA

A. Bodek , P. de Barbaro , R. Demina , J.L. Dulemba , A. Garcia-Bellido , O. Hindrichs , A. Khukhunaishvili , N. Parmar, P. Parygin⁹⁰ , E. Popova⁹⁰ , R. Taus 




The Rockefeller University, New York, New York, USA

K. Goulianos 






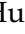

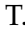






Rutgers, The State University of New Jersey, Piscataway, New Jersey, USA

B. Chiarito, J.P. Chou , S.V. Clark , D. Gadkari , Y. Gershtein , E. Halkiadakis , M. Heindl , C. Houghton , D. Jaroslowski , O. Karacheban²⁷ , S. Konstantinou , I. Laflotte , A. Lath , R. Montalvo, K. Nash, J. Reichert , H. Routray , P. Saha , S. Salur , S. Schnetzer, S. Somalwar , R. Stone , S.A. Thayil , S. Thomas, J. Vora , H. Wang 

University of Tennessee, Knoxville, Tennessee, USA

H. Acharya, D. Ally , A.G. Delannoy , S. Fiorendi , S. Higginbotham , T. Holmes , A.R. Kanuganti , N. Karunarathna , L. Lee , E. Nibigira , S. Spanier 





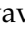






Texas A&M University, College Station, Texas, USA

D. Aebi , M. Ahmad , T. Akhter , O. Bouhali⁹¹ , R. Eusebi , J. Gilmore , T. Huang , T. Kamon⁹² , H. Kim , S. Luo , R. Mueller , D. Overton , D. Rathjens , A. Safonov 







Texas Tech University, Lubbock, Texas, USA

N. Akchurin , J. Damgov , N. Gogate , V. Hegde , A. Hussain , Y. Kazhykarim, K. Lamichhane , S.W. Lee , A. Mankel , T. Peltola , I. Volobouev 

Vanderbilt University, Nashville, Tennessee, USA

E. Appelt , Y. Chen , S. Greene, A. Gurrola , W. Johns , R. Kunnawalkam Elayavalli , A. Melo , F. Romeo , P. Sheldon , S. Tuo , J. Velkovska , J. Viinikainen 



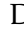

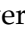



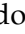



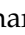






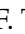


University of Virginia, Charlottesville, Virginia, USA

B. Cardwell , B. Cox , J. Hakala , R. Hirosky , A. Ledovskoy , C. Neu 

Wayne State University, Detroit, Michigan, USA












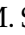

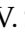
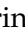



S. Bhattacharya , P.E. Karchin 

University of Wisconsin - Madison, Madison, Wisconsin, USA

A. Aravind, S. Banerjee , K. Black , T. Bose , S. Dasu , I. De Bruyn , P. Everaerts , C. Galloni, H. He , M. Herndon , A. Herve , C.K. Koraka , A. Lanaro, R. Loveless , J. Madhusudanan Sreekala , A. Mallampalli , A. Mohammadi , S. Mondal, G. Parida , L. Pétré , D. Pinna, A. Savin, V. Shang , V. Sharma , W.H. Smith , D. Teague, H.F. Tsoi , W. Vetens , A. Warden 

Authors affiliated with an institute or an international laboratory covered by a cooperation agreement with CERN

S. Afanasiev , V. Alexakhin , V. Andreev , Yu. Andreev , T. Aushev , M. Azarkin , A. Babaev , V. Blinov⁹³, E. Boos , V. Borshch , D. Budkouski , V. Bunichev , M. Chadeeva⁹³ , V. Chekhovsky, R. Chistov⁹³ , A. Dermenev , T. Dimova⁹³ , D. Druzhkin⁹⁴ , M. Dubinin⁸² , L. Dudko , A. Ershov , G. Gavrilov , V. Gavrilov , S. Gninenko , V. Golovtcov , N. Golubev , I. Golutvin , I. Gorbunov , A. Gribushin , Y. Ivanov , V. Kachanov , V. Karjavine , A. Karneyeu , V. Kim⁹³ , M. Kirakosyan, D. Kirpichnikov , M. Kirsanov , V. Klyukhin , O. Kodolova⁹⁵ , D. Konstantinov , V. Korenkov , A. Kozyrev⁹³ , N. Krasnikov , A. Lanev , P. Levchenko⁹⁶ , N. Lychkovskaya , V. Makarenko , A. Malakhov , V. Matveev⁹³ , V. Murzin , A. Nikitenko^{97,95} , S. Obraztsov , V. Oreshkin , V. Palichik , V. Perelygin 

S. Petrushanko , S. Polikarpov⁹³ , V. Popov , O. Radchenko⁹³ , M. Savina , V. Savrin , V. Shalaev , S. Shmatov , S. Shulha , Y. Skovpen⁹³ , S. Slabospitskii , V. Smirnov , A. Snigirev , D. Sosnov , V. Sulimov , E. Tcherniaev , A. Terkulov , O. Teryaev , I. Tlisova , A. Toropin , L. Uvarov , A. Uzunian , A. Vorobyev[†], N. Voytishin , B.S. Yuldashev⁹⁸, A. Zarubin , I. Zhizhin , A. Zhokin

†: Deceased

¹Also at Yerevan State University, Yerevan, Armenia

²Also at TU Wien, Vienna, Austria

³Also at Institute of Basic and Applied Sciences, Faculty of Engineering, Arab Academy for Science, Technology and Maritime Transport, Alexandria, Egypt

⁴Also at Ghent University, Ghent, Belgium

⁵Also at Universidade do Estado do Rio de Janeiro, Rio de Janeiro, Brazil

⁶Also at Universidade Estadual de Campinas, Campinas, Brazil

⁷Also at Federal University of Rio Grande do Sul, Porto Alegre, Brazil

⁸Also at UFMS, Nova Andradina, Brazil

⁹Also at Nanjing Normal University, Nanjing, China

¹⁰Now at The University of Iowa, Iowa City, Iowa, USA

¹¹Also at University of Chinese Academy of Sciences, Beijing, China

¹²Also at China Center of Advanced Science and Technology, Beijing, China

¹³Also at University of Chinese Academy of Sciences, Beijing, China

¹⁴Also at China Spallation Neutron Source, Guangdong, China

¹⁵Now at Henan Normal University, Xinxiang, China

¹⁶Also at Université Libre de Bruxelles, Bruxelles, Belgium

¹⁷Also at an institute or an international laboratory covered by a cooperation agreement with CERN

¹⁸Also at Suez University, Suez, Egypt

¹⁹Now at British University in Egypt, Cairo, Egypt

²⁰Also at Purdue University, West Lafayette, Indiana, USA

²¹Also at Université de Haute Alsace, Mulhouse, France

²²Also at Department of Physics, Tsinghua University, Beijing, China

²³Also at The University of the State of Amazonas, Manaus, Brazil

²⁴Also at University of Hamburg, Hamburg, Germany

²⁵Also at RWTH Aachen University, III. Physikalisches Institut A, Aachen, Germany

²⁶Also at Bergische University Wuppertal (BUW), Wuppertal, Germany

²⁷Also at Brandenburg University of Technology, Cottbus, Germany

²⁸Also at Forschungszentrum Jülich, Juelich, Germany

²⁹Also at CERN, European Organization for Nuclear Research, Geneva, Switzerland

³⁰Also at Institute of Physics, University of Debrecen, Debrecen, Hungary

³¹Also at Institute of Nuclear Research ATOMKI, Debrecen, Hungary

³²Now at Universitatea Babeş-Bolyai - Facultatea de Fizica, Cluj-Napoca, Romania

³³Also at MTA-ELTE Lendület CMS Particle and Nuclear Physics Group, Eötvös Loránd University, Budapest, Hungary

³⁴Also at HUN-REN Wigner Research Centre for Physics, Budapest, Hungary

³⁵Also at Physics Department, Faculty of Science, Assiut University, Assiut, Egypt

³⁶Also at Punjab Agricultural University, Ludhiana, India

³⁷Also at University of Visva-Bharati, Santiniketan, India

³⁸Also at Indian Institute of Science (IISc), Bangalore, India

³⁹Also at IIT Bhubaneswar, Bhubaneswar, India

⁴⁰Also at Institute of Physics, Bhubaneswar, India

- ⁴¹Also at University of Hyderabad, Hyderabad, India
- ⁴²Also at Deutsches Elektronen-Synchrotron, Hamburg, Germany
- ⁴³Also at Isfahan University of Technology, Isfahan, Iran
- ⁴⁴Also at Sharif University of Technology, Tehran, Iran
- ⁴⁵Also at Department of Physics, University of Science and Technology of Mazandaran, Behshahr, Iran
- ⁴⁶Also at Department of Physics, Isfahan University of Technology, Isfahan, Iran
- ⁴⁷Also at Italian National Agency for New Technologies, Energy and Sustainable Economic Development, Bologna, Italy
- ⁴⁸Also at Centro Siciliano di Fisica Nucleare e di Struttura Della Materia, Catania, Italy
- ⁴⁹Also at Università degli Studi Guglielmo Marconi, Roma, Italy
- ⁵⁰Also at Scuola Superiore Meridionale, Università di Napoli 'Federico II', Napoli, Italy
- ⁵¹Also at Fermi National Accelerator Laboratory, Batavia, Illinois, USA
- ⁵²Also at Consiglio Nazionale delle Ricerche - Istituto Officina dei Materiali, Perugia, Italy
- ⁵³Also at Department of Applied Physics, Faculty of Science and Technology, Universiti Kebangsaan Malaysia, Bangi, Malaysia
- ⁵⁴Also at Consejo Nacional de Ciencia y Tecnología, Mexico City, Mexico
- ⁵⁵Also at Trincomalee Campus, Eastern University, Sri Lanka, Nilaveli, Sri Lanka
- ⁵⁶Also at Saegis Campus, Nugegoda, Sri Lanka
- ⁵⁷Also at National and Kapodistrian University of Athens, Athens, Greece
- ⁵⁸Also at Ecole Polytechnique Fédérale Lausanne, Lausanne, Switzerland
- ⁵⁹Also at Universität Zürich, Zurich, Switzerland
- ⁶⁰Also at Stefan Meyer Institute for Subatomic Physics, Vienna, Austria
- ⁶¹Also at Laboratoire d'Annecy-le-Vieux de Physique des Particules, IN2P3-CNRS, Annecy-le-Vieux, France
- ⁶²Also at Near East University, Research Center of Experimental Health Science, Mersin, Turkey
- ⁶³Also at Konya Technical University, Konya, Turkey
- ⁶⁴Also at Izmir Bakircay University, Izmir, Turkey
- ⁶⁵Also at Adiyaman University, Adiyaman, Turkey
- ⁶⁶Also at Bozok Universitetesi Rektörlüğü, Yozgat, Turkey
- ⁶⁷Also at Marmara University, Istanbul, Turkey
- ⁶⁸Also at Milli Savunma University, Istanbul, Turkey
- ⁶⁹Also at Kafkas University, Kars, Turkey
- ⁷⁰Now at Istanbul Okan University, Istanbul, Turkey
- ⁷¹Also at Hacettepe University, Ankara, Turkey
- ⁷²Also at Erzincan Binali Yildirim University, Erzincan, Turkey
- ⁷³Also at Istanbul University - Cerrahpasa, Faculty of Engineering, Istanbul, Turkey
- ⁷⁴Also at Yildiz Technical University, Istanbul, Turkey
- ⁷⁵Also at Vrije Universiteit Brussel, Brussel, Belgium
- ⁷⁶Also at School of Physics and Astronomy, University of Southampton, Southampton, United Kingdom
- ⁷⁷Also at IPPP Durham University, Durham, United Kingdom
- ⁷⁸Also at Monash University, Faculty of Science, Clayton, Australia
- ⁷⁹Also at Università di Torino, Torino, Italy
- ⁸⁰Also at Bethel University, St. Paul, Minnesota, USA
- ⁸¹Also at Karamanoğlu Mehmetbey University, Karaman, Turkey
- ⁸²Also at California Institute of Technology, Pasadena, California, USA
- ⁸³Also at United States Naval Academy, Annapolis, Maryland, USA

⁸⁴Also at Ain Shams University, Cairo, Egypt

⁸⁵Also at Bingol University, Bingol, Turkey

⁸⁶Also at Georgian Technical University, Tbilisi, Georgia

⁸⁷Also at Sinop University, Sinop, Turkey

⁸⁸Also at Erciyes University, Kayseri, Turkey

⁸⁹Also at Horia Hulubei National Institute of Physics and Nuclear Engineering (IFIN-HH), Bucharest, Romania

⁹⁰Now at an institute or an international laboratory covered by a cooperation agreement with CERN

⁹¹Also at Texas A&M University at Qatar, Doha, Qatar

⁹²Also at Kyungpook National University, Daegu, Korea

⁹³Also at another institute or international laboratory covered by a cooperation agreement with CERN

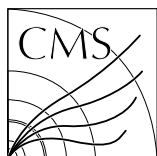
⁹⁴Also at Universiteit Antwerpen, Antwerpen, Belgium

⁹⁵Also at Yerevan Physics Institute, Yerevan, Armenia

⁹⁶Also at Northeastern University, Boston, Massachusetts, USA

⁹⁷Also at Imperial College, London, United Kingdom

⁹⁸Also at Institute of Nuclear Physics of the Uzbekistan Academy of Sciences, Tashkent, Uzbekistan



Review of top quark mass measurements in CMS

The CMS Collaboration*

Abstract

The top quark mass is one of the most intriguing parameters of the standard model (SM). Its value indicates a Yukawa coupling close to unity, and the resulting strong ties to the Higgs physics make the top quark mass a crucial ingredient for understanding essential aspects of the electroweak sector of the SM. While it is such an important parameter of the SM, its measurement and interpretation in terms of the Lagrangian parameter are challenging. The CMS Collaboration has performed multiple measurements of the top quark mass, addressing these challenges from different angles: highly precise ‘direct’ measurements, using the top quark decay products, as well as ‘indirect’ measurements aiming at accurate interpretations in terms of the Lagrangian parameter. Recent mass measurements using Lorentz-boosted top quarks are particularly promising, opening a new avenue of measurements based on top quark decay products contained in a single particle jet, with superior prospects for accurate theoretical interpretations. Moreover, dedicated studies of the dominant uncertainties in the modelling of the signal processes have been performed. This review offers the first comprehensive overview of these measurements performed by the CMS Collaboration using the data collected at centre-of-mass energies of 7, 8, and 13 TeV.

To be submitted to Physics Reports

Contents

1	Introduction	2
1.1	Early top quark studies	2
1.2	Role of the top quark mass in the standard model and beyond	3
1.3	Scope of the review	5
2	Conceptual and experimental aspects of top quark mass measurements	8
2.1	Top quark production and decay	8
2.2	Reconstruction of physics objects in CMS	10
2.3	Kinematic reconstruction of the $t\bar{t}$ system	11
2.4	Monte Carlo simulations and modelling uncertainties	20
2.5	Experimental uncertainties	31
2.6	General aspects of unfolding	32
2.7	Particle- and parton-level top quark definitions	33
2.8	Top quark mass definitions	35
3	Direct measurements from top quark decays	37
3.1	Top quark mass measurements in top quark pair events	37
3.2	Measurement of the top quark mass in single top quark events	48
3.3	Status of the interpretation of top quark Monte Carlo mass	57
4	Extraction of the Lagrangian top quark mass	59
4.1	Measurements of m_t^{pole} from inclusive $t\bar{t}$ cross sections	61
4.2	Mitigating the dependence of the measured cross section on m_t^{MC}	65
4.3	The first measurement of the running of the top quark mass	70
4.4	Resolving correlations of m_t , $\alpha_S(m_Z)$, and PDFs	73
4.5	Top quark pole mass extracted from $t\bar{t}$ +jet events	78
4.6	Problems and prospects for Lagrangian top quark mass extraction	81
5	Measurements in the Lorentz-boosted regime	82
5.1	Overview of existing jet mass measurements	83
5.2	The jet mass	84
5.3	Optimising the jet definition for jet mass measurements	88
5.4	Reconstruction effects in the jet mass	89
5.5	Uncertainties from the modelling of the jet mass	91
5.6	Aspects in the unfolding of the data	92
5.7	Top quark mass from jet mass	92
6	Summary and outlook	94
6.1	Summary of the top quark mass results	94
6.2	Evolution of analysis methods in CMS	96
6.3	Prospects at the HL-LHC	97
6.4	Conclusions	103
A	Glossary of acronyms	127
B	The CMS Collaboration	129

1 Introduction

In the exploration of the fundamental building blocks of the universe, the study of the top quark, the most massive elementary particle yet known, has emerged as a key area of research at the Large Hadron Collider (LHC) at CERN. At the Compact Muon Solenoid (CMS) experiment, the properties of this particle have been studied in great detail.

With a multitude of unique features that set it apart from other elementary particles, the top quark plays a crucial role in the standard model (SM) of particle physics. In the SM, the large mass of the top quark (m_t) results in its Higgs Yukawa coupling being close to unity. This leads to a particular significance of the top quark in the context of vacuum stability and cosmology, as well as in alternative models of spontaneous electroweak (EW) symmetry breaking.

The top quark has an extremely short lifetime of approximately 5×10^{-25} s [1]. Therefore it decays through the weak interaction before it would undergo hadronisation (happening at the time scale of $\sim 10^{-23}$ s) and before the strong interaction could affect its spin properties. Therefore, spin information of the top quark is transmitted to the particles that result from its decay [2]. This distinct property entails that the top quark exhibits features of a quasi-free observable particle with a Breit–Wigner distributed mass and grants a direct access to its fundamental properties, enabling precise measurements of its mass and polarisation. This picture of the top quark is the basis of state-of-the-art experimental measurements. The analogous concept does not apply to any other quark, for which spin and mass are always masked by colour confinement. However, this picture is only an approximation. With growing precision in the measured top quark properties, in particular m_t , the quantum aspects of the top quark related to its short lifetime and colour charge can not be ignored. These subtle issues entail for example that the top quark is considered as a coherent quantum state which is defined only through the analysis strategy, or that top quark final states can interfere with some of the background processes. The limitations of the picture of the top quark as a free particle lead to ambiguities in the theoretical interpretation [3]. For the m_t measurements, this can generally result in uncertainties of up to 1 GeV.

1.1 Early top quark studies

In 1972, Kobayashi and Maskawa predicted the existence of a third generation of fermions in the SM [4] as an explanation for the violation of the charge conjugation parity (CP) symmetry, and more precise measurements of this effect pointed towards a large value of the mass of the hypothetical top quark already in the mid 1980s [5, 6]. Experimental hints to the existence of the top quark emerged in measurements of the b quark isospin from the forward-backward asymmetry in $e^+e^- \rightarrow b\bar{b}$ processes at the DESY PETRA collider [7], and in the suppression of flavour-changing neutral current decays of B mesons through the Glashow–Iliopoulos–Maiani (GIM) mechanism [8]. The absence of a narrow top quark-antiquark resonance in direct searches at the e^+e^- colliders PETRA [9] and KEK TRISTAN [10] meant that m_t had to be substantially higher than that of the other quarks, setting a lower limit at 23.3 and 30.2 GeV, respectively. The hadron collider experiments UA1 and UA2 at the $Sp\bar{p}$ S at CERN did not find evidence of the top quark in W boson decays $\bar{p}p \rightarrow W \rightarrow t\bar{b}$, excluding $m_t < 60$ [11] and 69 GeV [12] at 95% confidence level (CL), respectively. More evidence for a very massive top quark accumulated from measurements of $B^0-\bar{B}^0$ mixing by the ARGUS [13] and CLEO [14] Collaborations, where lower bounds on m_t between 45 and 90 GeV were obtained by exploiting the features of the GIM mechanism [15]. In the early 1990s, when the CERN LEP and SLC colliders started operating at the energy of the Z resonance, no evidence was found for the decay $Z \rightarrow t\bar{t}$, excluding $m_t < 45.8$ GeV [16, 17]. Precise measurements of the Z boson mass,

partial decay widths, and forward-backward asymmetries were made at the LEP and SLAC SLC colliders. Since the relation between these quantities and the weak mixing angle is affected by the value of m_t via radiative EW corrections, these measurements at the Z pole could be used to indirectly constrain the value of m_t . Initial constraints indicated m_t to be in the range of 64–169 GeV at 68% CL [18]. With more data, the range narrowed down to 158–199 GeV at 68% CL [19] in the year of the discovery of the top quark, where the extent of this range came mainly from the unknown Higgs boson (H) mass. At the same time, the experimental determinations of the Cabibbo–Kobayashi–Maskawa (CKM) matrix elements had been considerably improved and progress had been made in calculating B meson form factors, such that more reliable bounds from CP violation in $B^0\text{--}\bar{B}^0$ and $K^0\text{--}\bar{K}^0$ systems could be calculated [20, 21], resulting in lower limits on m_t of about 100 GeV. Finally, in 1995, Fermilab experiments CDF and D0, operating at Tevatron proton-antiproton ($p\bar{p}$) collider, announced the discovery of the top quark at $m_t = 175 \pm 8$ GeV [22, 23]. In the following years, the properties of the top quark were measured with ever-increasing accuracy by the CDF and D0 Collaborations. While most measurements were done with $t\bar{t}$ pairs, which are copiously produced by the strong interaction, the production of single top quarks through the EW interaction was also observed for the first time during the Tevatron Run II [24, 25]. Combining all m_t measurements performed at the Tevatron, a final result of $m_t = 174.30 \pm 0.65$ GeV was obtained [26]. A more detailed discussion can be found in Ref. [27] and references therein.

When the Tevatron shut down in 2011, the CERN LHC became the only collider facility in the world capable of producing top quarks in large quantities. The LHC increased the number of produced top quarks by orders of magnitude as compared to the Tevatron.

1.2 Role of the top quark mass in the standard model and beyond

The SM does not predict a specific value of m_t . It does, however, provide relations between m_t and other quantities. The value of m_t needs to be determined experimentally, either through a direct reconstruction of the invariant mass of its final state, or by measuring m_t -sensitive observables and extracting m_t indirectly.

The value of m_t influences the top quark decay modes and production rates, which are essential for understanding top quark properties and dynamics. Apart from being a reflection of our ability to describe the dynamics of the strong and EW interactions using quantum-field theoretical methods, accurate measurements of m_t provide critical tests of the SM and its extensions. In this context, it needs to be recalled that the quantum aspects of the top quark associated with its colour charge and its finite lifetime imply that m_t is not a directly measurable physical parameter like the masses of hadrons. The value of m_t can only be inferred indirectly through observables that depend on it. Since quantum effects affect this dependence, m_t measurements are only possible on the basis of theoretical predictions of these observables. In these theoretical predictions, it is mandatory to account for the fact that m_t is not a unique physical parameter, but needs to be defined through a certain renormalisation scheme within quantum field theory. Defined this way, m_t plays a role of a SM coupling and is a renormalisation scheme dependent quantity, as discussed in Section 2.8.

The top quark appears in quantum loop corrections to various processes, and depending on its mass, it can have a substantial impact on the behaviour of other particles, particularly in rare production processes and precision EW measurements. One example is the $B^0\text{--}\bar{B}^0$ mixing mentioned earlier. Another example is the ratio of direct to indirect CP violation size in kaon decays [28, 29].

Further, m_t enters into loop corrections that contribute to the masses of the W and Z bosons,

and therefore indirectly affects the weak mixing angle. Since the sensitivity of EW precision observables to m_t arises through radiative corrections, the choice of the renormalisation scheme for m_t is essential for the precise theoretical description of the EW observables [30]. The uncertainty in m_t is among the leading uncertainties in the predictions of the W and H boson masses [31], which are crucial for testing the internal consistency of the SM.

The SM Higgs mechanism endows fermions, including the top quark, with mass through their interaction with the Higgs field. The mass of a fermion, m_f , emerges from a Yukawa interaction with coupling strength $Y_f = \sqrt{2}(m_f/v)$, where $v = 246.22$ GeV [1] is the vacuum expectation value of the Higgs field. The top quark has the largest Yukawa coupling in the SM, with a value close to unity. This can be compared to a direct measurement of the Yukawa coupling strength from the production cross section of final states involving top quarks and the Higgs boson, mostly from $t\bar{t}H$ production, with further contributing processes, $Y_t = 0.95^{+0.07}_{-0.08}$ [32, 33]. Kinematic distributions in $t\bar{t}$ production can also be used to probe the top-quark Yukawa coupling through loop-induced corrections from the Higgs field. The most precise such measurement was performed by the CMS experiment, resulting in $Y_t = 1.16^{+0.24}_{-0.35}$ [34], consistent with the value obtained from m_t and the direct measurement. The top quark Yukawa coupling significantly affects the shape of the Higgs potential. The value of m_t is linked to the Higgs boson mass through quantum loop corrections and enhances the quantum contributions to the Higgs potential. Therefore, the value of m_t has a direct impact on the stability of the EW vacuum [35, 36]. In particular, if the potential energy of the Higgs field is too shallow, it could lead to vacuum instability. In such a scenario, the EW vacuum may not be the true minimum of the potential, and the Higgs field could eventually undergo a phase transition to a deeper minimum at very high energies. This transition would have profound consequences, leading to the collapse of the vacuum and changing the fundamental properties of all particles, which could drastically affect the structure of the universe. Since this sensitivity is generated through quantum effects, accurate control of the renormalisation scheme of m_t is essential.

A deviation of the measured m_t from the prediction using a SM fit when all other free parameters are constrained to their measured values could indicate the presence of new physics beyond the SM (BSM), such as supersymmetry [37] or the existence of additional Higgs bosons. Further, m_t is related to the evolution of the early universe, and its precise value has implications for cosmology [38] and our understanding of dark matter [39].

With the data provided by the LHC so far, there has been no observation of BSM effects in direct searches for new resonant states, which could either point to new physics processes coupling very weakly to the SM sector, or appearing only at energy scales higher than what experiments can probe to date. In the latter case, the BSM contributions can be described by e.g. an effective field theory (EFT). In the EFT-extended SM (SMEFT), BSM contributions are parametrised in a model-independent way through higher-dimensional operators [40–42]. These operators involve the known SM particle fields, while their Wilson coefficients, playing a role of couplings, encode the effects of potential BSM particles and interactions. The value of m_t plays a crucial role in SMEFT interpretations, since it affects the behaviour of higher-dimensional operators and their interplay with known SM interactions. An illustrative example given in Ref. [43] is the invariant mass of the $t\bar{t}$ pair, $m_{t\bar{t}}$, being sensitive to the effective couplings c_{tG} and c_{tq}^8 , which depend on the value of m_t . In addition, precise knowledge of m_t is essential for reducing uncertainties in theoretical calculations of B meson decays [44–46].

1.3 Scope of the review

The focus of this review is on the measurements of m_t carried out by the CMS Collaboration, based on data collected during the LHC Run 1 at $\sqrt{s} = 7$ and 8 TeV in 2010–2012, and Run 2 at $\sqrt{s} = 13$ TeV in 2015–2018. Since the initial top quark mass analyses performed at the Tevatron, experimental methods, theoretical calculations, and Monte Carlo (MC) models have evolved in sophistication and accuracy. Modern detector technologies, increased computing power, optimised reconstruction algorithms, and above all the higher centre-of-mass energies and integrated luminosities delivered by the LHC have allowed for the development of an array of novel top quark mass analyses, exploring new aspects of top quark phenomenology and reaching unprecedented levels of detail and precision.

While all the results included in this review have been published before, it is the first time that a comprehensive overview is presented by the CMS Collaboration, detailing and contrasting the leading approaches and discussing aspects of the theoretical interpretation of the results. To illustrate the broadness of the top mass measurement program of CMS, the summary of the relevant publications to date is given in Table 1, with the details to be discussed in the course of the review. These investigations have been classified as either direct measurements or indirect extractions of the Lagrangian mass of the top quark, defined in a particular renormalisation scheme.

The direct measurements are based on the picture of the top quark as a free particle and make the fundamental assumption that the invariant mass of the top quark decay products is directly related to the mass of the original top quark particle. In this picture, the main challenge is to identify the top quark decay products and reconstruct their invariant mass with the best possible experimental resolution. The direct measurements rely on MC simulations for the precise modelling of the event decay topologies and experimental effects, but also for the calibration of the analysis in terms of a built-in m_t parameter that is extracted from the simulation. Such measurements have the smallest experimental uncertainties. However, due to limitations of the current theoretical knowledge, an additional conceptual uncertainty has to be accounted for when the result is interpreted in terms of m_t defined in the field theory of quantum chromodynamics (QCD). The measurements in this category typically employ a full reconstruction of the top quark and are performed by analysing top quark-antiquark pair ($t\bar{t}$) events in multiple decay channels. In the dilepton channel, a full kinematic analysis (KINb) [47], the analytical matrix weighting technique (AMWT) [47, 49, 53], an $M_{b\ell} + M_{T2}^{bb}$ hybrid fit, taking into account external constraints on the jet energy scale (hybrid) [60], as well as an $m_{b\ell}$ fit [63] have been employed. In the lepton+jets and all-jets channels the techniques have evolved from a simultaneous fit of m_t and the jet energy scale (2D ideogram) [48, 51] to the hybrid ideogram method [53, 61, 62] and, in the most recent measurement [71], to a 5D profile likelihood fit. Template fits were used to extract m_t in single top quark [58, 67] events. While the single top quark analyses currently have relatively large uncertainties compared to the analyses using $t\bar{t}$ events, they offer complementary information and have an excellent potential for improvement with the large data sets expected in future LHC runs.

The extraction of the Lagrangian m_t , clearly defined in a given renormalisation scheme, is realised through comparison of the measured inclusive or differential cross sections of $t\bar{t}$ production with the respective theoretical predictions at least at the next-to-leading-order (NLO) accuracy in QCD perturbation theory. The Lagrangian m_t extractions provide better control of the relevant quantum effects than direct measurements, but currently have larger uncertainties, since the m_t -dependence of an observable arises from kinematic features and $t\bar{t}$ production rates, which are subject to additional uncertainties. Lagrangian m_t extractions were performed

Table 1: List of all CMS m_t measurements by using different analysis methods in chronological order of publication. The summary of these measurements is also depicted in Fig. 54. The analyses are categorised as direct mass measurements (a), indirect extraction of the Lagrangian mass (b), or boosted measurements (c), as explained in the text. The analysis methods of the publications marked with a star (*) are covered in the following sections of this review. All acronyms are defined in Appendix A.

Year	Channel	\sqrt{s} [TeV]	Analysis method	m_t [GeV]	δm_t^{stat} [GeV]	δm_t^{sys} [GeV]	Ref.
2011	Dilepton	7	^a KINb and AMWT	175.5	4.6	4.6	[47]
2012	Lepton+jets	7	^a 2D ideogram	173.49	0.43	0.98	[48]*
2012	Dilepton	7	^a AMWT	172.5	0.4	1.5	[49]
2013	Dilepton	7	^a Kinematic endpoints	173.9	0.9	$^{+1.7}_{-2.1}$	[50]
2013	All-jets	7	^a 2D ideogram	173.54	0.33	0.96	[51]*
2014	Dilepton	7	^b Cross section	177.0	—	$^{+3.6}_{-3.3}$	[52]*
2015	Lepton+jets	8	^a Hybrid ideogram	172.35	0.16	0.48	[53]*
	All-jets	8	^a Hybrid ideogram	172.32	0.25	0.59	[53]*
	Dilepton	8	^a AMWT	172.82	0.19	1.22	[53]
	Combination	7, 8	^a CMS 7 inputs	172.44	0.13	0.47	[53]
2016	Dilepton	7, 8	^b Cross section	174.3	—	$^{+2.1}_{-2.2}$	[54]*
2016	1+2 leptons	8	^a Lepton + secondary vertex	173.68	0.20	$^{+1.58}_{-0.97}$	[55]
2016	1+2 leptons	8	^a Lepton + J/ψ meson	173.5	3.0	0.9	[56]
2017	Lepton+jets	13	^b Cross section	170.6	—	2.7	[57]
2017	Single top quark	8	^a Template fit	172.95	0.77	$^{+0.97}_{-0.93}$	[58]*
2017	Boosted	8	^c CA jet mass unfolded	170.9	6.0	6.7	[59]*
2017	Dilepton	8	^a $M_{b\ell} + M_{T2}^{\text{bb}}$ hybrid fit	172.22	0.18	$^{+0.89}_{-0.93}$	[60]
2018	Lepton+jets	13	^a Hybrid ideogram	172.25	0.08	0.62	[61]*
2018	All-jets	13	^a Hybrid ideogram	172.34	0.20	0.70	[62]*
	Combination	13	^a Combined likelihood	172.26	0.07	0.61	[62]
2018	Dilepton	13	^a $m_{b\ell}$ fit	172.33	0.14	$^{+0.66}_{-0.72}$	[63]*
	Dilepton	13	^b Cross section	173.7	—	$^{+2.1}_{-2.3}$	[63]*
2019	Dilepton	13	^b Multi-differential cross section	170.5	—	0.8	[64]*
2019	Dilepton	13	^b Running mass	—	—	—	[65]*
2019	Boosted	13	^c XCone jet mass unfolded	172.6	0.4	2.4	[66]*
2021	Single top quark	13	^a $\ln(m_t/1 \text{ GeV})$ fit	172.13	0.32	$^{+0.69}_{-0.71}$	[67]*
2022	Dilepton	7, 8	^b ATLAS+CMS cross section	173.4	—	$^{+1.8}_{-2.0}$	[68]
2022	Dilepton	13	^b $t\bar{t}$ +jet differential cross section	172.13	—	1.43	[69]*
2022	Boosted	13	^c XCone jet mass unfolded	173.06	0.24	0.80	[70]*
2023	Lepton+jets	13	^a Profile likelihood	171.77	0.04	0.37	[71]*
2024	Combination	7, 8	^a CMS 9 inputs	172.52	0.14	0.39	[72]
	Combination	7, 8	^a ATLAS+CMS 15 inputs	172.52	0.14	0.30	[72]

using the $t\bar{t}$ inclusive [52, 54, 57, 63, 68] and differential [64], as well as $t\bar{t}$ +jet differential [69] production cross sections.

Recently, m_t measurements were also carried out focusing particularly on events where the top quarks are produced with a high Lorentz boost [59, 66, 70]. These boosted top quark events are characterised by the top quark decay products being collimated within a single jet. These measurements are complementary to both the direct measurements and extraction of Lagrangian m_t , and may be used to establish a clear relation between these two classes of m_t results in the future. The boosted topology combines a kinematic m_t sensitivity and the ability to make systematic theoretical predictions at the experimentally observable level, namely quantum-field theoretical predictions of the invariant mass of top quark jets consisting of stable particles.

Finally, CMS conducted an extensive program of measurements using alternative methods. These are conceptually close to the direct measurements but were designed aiming at reduced or orthogonal systematic uncertainties. The m_t measurements from kinematic endpoints [50] and from b hadron decay products [55, 56] are considered the most promising. The first two employ the lepton+jets channel, while the latter combines the lepton+jets and dilepton channels. The J/ψ method [56] had been proposed already in the CMS technical design report [73] as a particularly clean method, relying only on the reconstruction of three leptons in the final state: one lepton from the W boson decay, and two from the decay of a J/ψ produced in the decay of the b-flavoured hadron in the b jet. The results have demonstrated the viability of the method, however its full potential can only be reached with the much larger data sets expected at the High-Luminosity LHC (HL-LHC) (as discussed in Section 6.3). The secondary vertex method [55] uses a similar approach, but replaces the leptonic decay of the J/ψ particle by the secondary vertex of the decay of the b hadron in the b jet, thus obtaining a much larger selection of events, and still only using tracking information, however sacrificing the much cleaner experimental signature of the leptonic J/ψ meson decay.

Measurements performed using alternative methods or in single top quark enriched topologies, despite reaching lower precision compared to standard measurement with the current data sets, can already have a beneficial effect in m_t combinations. These measurements, in fact, have different sensitivity to systematic uncertainties both from the experimental and modelling points of view, and therefore provide independent information. For example, measurements based on the reconstruction of b-hadron decay products do not rely on the precise calibration of the b jet energy, at the cost of a stronger dependence on the modelling of the b quark fragmentation. This can be seen explicitly in the updated CMS Run 1 combination presented in Ref. [72] and resulting in a value of $m_t = 172.52 \pm 0.42$ GeV. By performing the combination of CMS inputs excluding the single top quark and alternative measurements of Refs. [55, 56, 58], a total uncertainty of 0.44 GeV is obtained, which corresponds to adding in quadrature an extra uncertainty of about 0.15 GeV. This is equivalent to more than half the size of the leading systematic uncertainty in the combination, i.e. the jet energy response of b quark jets. The work of Ref. [72] also provides the combination of ATLAS and CMS measurements in Run 1, resulting in a value of $m_t = 172.52 \pm 0.33$ GeV, with a precision demonstrating the importance of combination of results obtained at different experiments.

The focus of this review is the development of analysis strategies in CMS leading to the high-precision m_t results in direct determination, extraction of the Lagrangian m_t , and measurements in boosted topologies. Before highlighting recent examples of the major approaches to measure m_t in Sections 3–5, the general aspects in common between the different analyses are discussed in Section 2. The measurements are summarised and the future perspectives are given in Section 6.

2 Conceptual and experimental aspects of top quark mass measurements

Measurements of the top quark mass rely on the detection and accurate reconstruction of events containing a $t\bar{t}$ pair or a single top quark. Depending on the final state formed in the top quark decay, as described in Section 2.1, the details of the event reconstruction may differ. Sophisticated algorithms have been developed to identify final-state particles and their momenta with optimal efficiency and resolution, as described in Section 2.2. In many of the analyses discussed in this review, it is advantageous to use a kinematic reconstruction of the full event, using the laws of energy and momentum conservation to improve the knowledge of the final state objects beyond the detector resolution. This is particularly important for final states that contain an energetic neutrino. The approaches used in the reconstruction of $t\bar{t}$ events are described in Section 2.3. The full event reconstruction also aims to resolve ambiguities in the assignment of final-state objects as decay products of a given top quark. This task becomes more challenging in the presence of energetic gluon radiation creating additional jets, and the presence of remnants of the colliding protons (underlying event, UE) as well as multiple simultaneous proton collisions (pileup, PU). In order to account for these effects, all analyses rely on MC simulation programs, tuned to describe the event properties as accurately as possible, as reported in Section 2.4. Besides uncertainties in the MC models, the analyses are also affected by experimental uncertainties, briefly summarised in Section 2.5. Finally, to perform a measurement of m_t , the features of the events observed in data are compared with the theoretical predictions or MC simulations, for a range of hypothetical m_t values, and a fit is performed to extract the best fit m_t , and uncertainties are evaluated. This procedure can be based on distributions reconstructed at the detector level (via a so-called ‘template fit’) or by comparing theoretical predictions to the distributions corrected for experimental effects using unfolding techniques as discussed in Section 2.6. The unfolding procedure can rely on the MC generator to correct back to a hypothetical picture of on-shell top quarks (‘parton level’) or to reproduce the event distributions at the level of stable particles in the final state (‘particle level’). The latter approach is particularly useful to provide experimental distributions that can be compared to new MC generator predictions for the purpose of MC tuning, as discussed in Section 2.7. To interpret the measured m_t as a parameter of the SM, quantum aspects related to the short lifetime and colour charge of the top quark must be considered, as outlined in Section 2.8.

2.1 Top quark production and decay

At the LHC, top quarks can either be produced in $t\bar{t}$ pairs, via the strong interaction, or as single top quarks through the EW interaction. Enhanced by the strong coupling, the rate of $t\bar{t}$ production is significantly larger than that of the single top quark process.

In leading order (LO) in QCD, hadronic collisions at higher energies produce $t\bar{t}$ pairs through quark-antiquark ($q\bar{q}$) annihilation or gluon-gluon (gg) fusion. In contrast to $p\bar{p}$ collisions at the Tevatron, where $t\bar{t}$ production is dominated by $q\bar{q}$ annihilation, in proton-proton (pp) collisions at the LHC, the gg fusion process is dominant. The QCD predictions for $t\bar{t}$ production are available at next-to-next-to leading order (NNLO) also including next-to-next-to-leading-logarithmic (NNLL) soft-gluon resummation [74–81]. The cross section of $t\bar{t}$ production has been studied by the experiments at the Tevatron and the LHC at different centre-of-mass energies and is found to be well described by the QCD predictions, as shown in Fig. 1.

Single top quark production is mediated by virtual W bosons in s - and t -channels, with the latter being kinematically enhanced and resulting in a sizeable cross section both at the Tevatron and the LHC [83, 84]. The cross sections for single top quark production in s - and t -channels

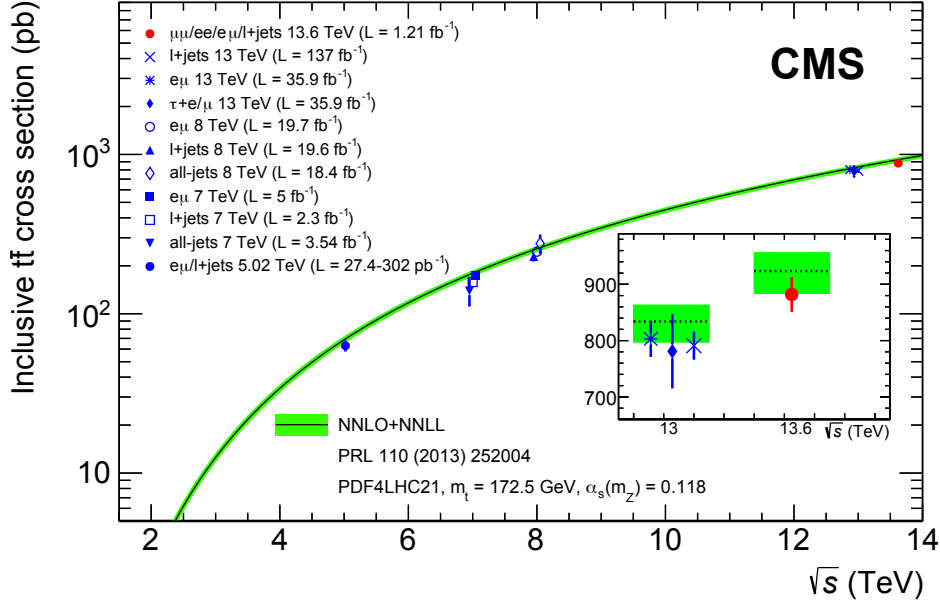


Figure 1: Summary of CMS measurements of the $t\bar{t}$ production cross section as a function of \sqrt{s} compared to the NNLO QCD calculation complemented with NNLL resummation (TOP++ v2.0 [77]). The theory band represents uncertainties due to the renormalisation and factorisation scales, parton distribution functions, and the strong coupling. The measurements and the theoretical calculation are quoted at $m_t = 172.5$ GeV. Measurements made at the same \sqrt{s} are slightly offset for clarity. An enlarged inset is included to highlight the difference between 13 and 13.6 TeV predictions and results. Figure taken from Ref. [82].

are calculated at NNLO [85–88]. In $p\bar{p}$ collisions at the Tevatron, the t and \bar{t} quarks are produced with identical cross sections in each channel. In contrast, in pp collisions at the LHC these differ because of the charge-asymmetric initial state. Furthermore, at the LHC, the W -associated production (tW) becomes relevant, with the cross section predicted at approximate NNLO [89]. In Fig. 2, the CMS measurements of single top quark production cross sections in different channels are presented as functions of the centre-of-mass energy in comparison to the theoretical predictions.

The decay width of the top quark is predicted [90] at NLO as 1.35 GeV [1] at $m_t = 173.3$ GeV and $\alpha_s(m_Z) = 0.118$, and increases with m_t . With the correspondingly short lifetime of about 5×10^{-25} s, the top quark decays before forming top-flavoured hadrons or $t\bar{t}$ quarkonium-bound states [91]. Instead, the top quark decays weakly into a W boson and a down-type quark, most probably a b quark. The branching fraction is given by $\mathcal{B}_{bW} = |V_{tb}|^2 / (|V_{tb}|^2 + |V_{ts}|^2 + |V_{td}|^2)$, with V_{tq} ($q = d, s, b$) denoting the elements of the CKM matrix, in particular $V_{tb} = 0.998$ [1].

Events with $t\bar{t}$ production are categorised by the final states of the W bosons emitted in the decays of t and \bar{t} quarks. In the *dilepton* channel, both W bosons decay leptonically, i.e. into a charged lepton and neutrino; in the *lepton+jets* channel one W boson decays leptonically while the other one decays to a $q\bar{q}$ pair; in the *all-jets* channel, both W bosons decay into $q\bar{q}$, forming hadronic jets in the final state:

- dilepton (10.5%), $t\bar{t} \rightarrow W^+bW^- \rightarrow \ell^+\nu\ell^-\bar{\nu}\bar{b}$,
- lepton+jets (43.8%), $t\bar{t} \rightarrow W^+bW^- \rightarrow q\bar{q}'b\ell^-\bar{\nu}\bar{b}$ or $\ell^+\nu bq\bar{q}'\bar{b}$,
- all-jets (45.7%), $t\bar{t} \rightarrow W^+bW^- \rightarrow q\bar{q}'bq\bar{q}'\bar{b}$.

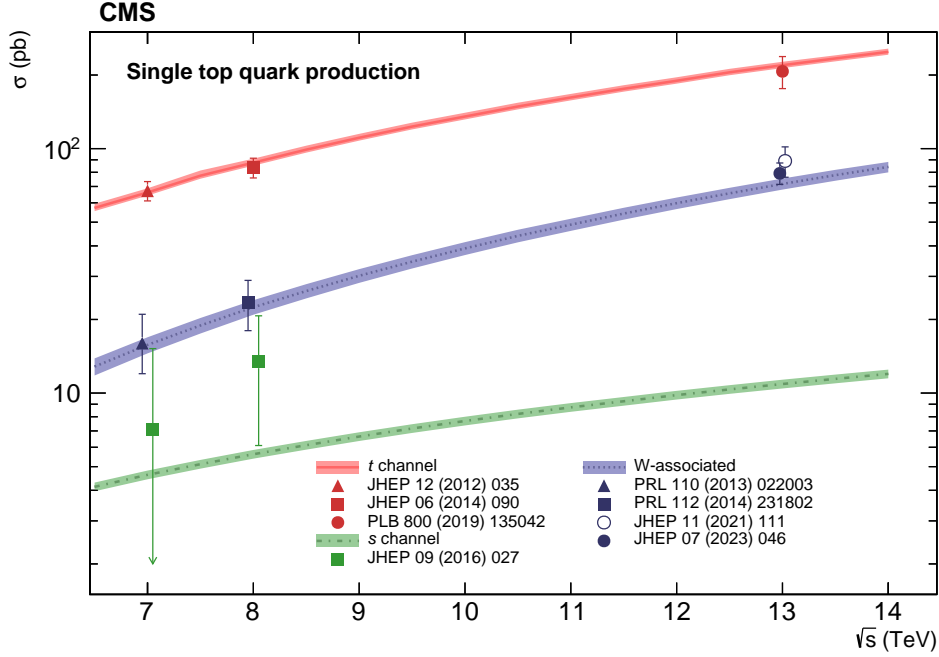


Figure 2: Summary of single top quark production cross section measurements by CMS. Theoretical calculations for t -channel, s -channel, and W -associated production are courtesy of N. Kidonakis [88, 89].

For each channel, the relative contributions are indicated in parentheses and include hadronic corrections and assume lepton universality [1]. The charged leptons ℓ denote electrons e , muons μ , or tau leptons τ . Since τ leptons are more difficult to reconstruct experimentally compared to e or μ , these are implicitly included in the experimental measurements via their leptonic decays. Further in this review, the notation ‘lepton’ refers to e and μ if not specified otherwise.

Despite the lowest relative contribution, top quark dilepton decays are widely used in physics analyses since they can be experimentally identified with the highest purity. While the all-jets channel accounts for almost half of the $t\bar{t}$ decays, it is difficult to distinguish those from QCD multijet production. The lepton+jets channel has intermediate properties, with moderate background contamination and large relative contribution.

In addition to the quarks resulting from the top quark decays, extra QCD radiation can lead to additional jets. Although the neutrinos remain undetected, their transverse momenta p_T are obtained from the imbalance in the transverse momentum measured in each event.

2.2 Reconstruction of physics objects in CMS

All top quark measurements rely on the efficient reconstruction of its decay products from electrical signals in the detector. A detailed description of the CMS detector, together with a definition of its coordinate system, can be found in Ref. [92]. Particles are reconstructed using the particle-flow (PF) algorithm [93], which follows the trajectory of particles through the various detector systems of the CMS experiment and combines the measurements in the tracking system, calorimeters, and muon system in order to achieve an optimised reconstruction. For each event, the PF algorithm returns a list of PF candidates that are categorised either as electron, muon, photon, neutral hadron, or charged hadron, depending on their signature in the detector systems. Electrons are identified by combining hits in the silicon tracker, the energy

measured in a corresponding cluster in the electromagnetic calorimeter (ECAL), and the sum of all bremsstrahlung photons compatible with the electron trajectory. Muons are reconstructed from hits in the tracker and muon system. Charged hadrons are measured by a combination of tracker and the connected energy clusters in the ECAL and hadronic calorimeter (HCAL). Photons and neutral hadrons are reconstructed from energy clusters in the ECAL and a combination of ECAL and HCAL, respectively.

The primary pp interaction vertex is taken to be the vertex corresponding to the hardest scattering in the event, evaluated using tracking information alone, as described in Section 9.4.1 of Ref. [94]. In order to reduce effects from additional pp collisions in each event, we use pileup mitigation tools that act on the list and remove PF candidates that can be associated with a pileup vertex. The CMS Collaboration uses two algorithms for pileup mitigation. The charge-hadron subtraction (CHS) [95] technique removes charged hadrons that are associated with a pileup vertex by calculating the distance of closest approach of each track to the reconstructed primary vertices. The PU-per-particle identification (PUPPI) [96, 97] algorithm goes one step further and also acts on neutral PF candidates. Each PF candidate is assigned a weight between 0 and 1 that scales the four-momentum according to the probability of the particle to originate from a pileup interaction. The weight is calculated as a function of a variable defined by the energy deposits in the vicinity of the PF candidate. The PUPPI algorithm makes the additional pileup corrections to jets unnecessary, and has improved the performance and pileup stability of jet substructure tagging.

The modified list of PF candidates is subsequently used as input for jet clustering algorithms, such that hadronic decay products of the top quark can be identified with jets. In CMS, the anti- k_T [98] jet clustering algorithm is commonly used, as implemented in the FASTJET software package [99] using a distance parameter of $R = 0.4$. The missing transverse momentum vector \vec{p}_T^{miss} is computed as the negative vector sum of the transverse momenta of all the PF candidates in an event, and its magnitude is denoted as p_T^{miss} [100]. The jet energy scale (JES) [101] is corrected for pileup effects, detector effects, and residual differences between data and simulation. The jet energy resolution (JER) [101] is smeared in simulated events in order to match the resolution observed in data. Both corrections are propagated to p_T^{miss} in each event.

Jets originating from b quarks are identified (tagged) with multivariate approaches that make use of global event, secondary vertex, displaced track, and jet constituent information [102].

2.3 Kinematic reconstruction of the $t\bar{t}$ system

The top quarks are investigated experimentally by measuring their decay products and their kinematic properties. In the all-jets decay channel, all decay products are reconstructed. In the dilepton channel, however, the two neutrinos from the W boson decay are not measured, thus leading to ambiguities in the reconstruction of neutrino momenta. The lepton+jets channel exhibits intermediate properties with only one neutrino in the final state, leading to fewer ambiguities. Several methods of kinematic reconstruction of $t\bar{t}$ pairs have been developed, which are described in the following.

2.3.1 Reconstruction in the lepton+jets and all-jets channels

In the lepton+jets and all-jets channels, kinematic fits [103, 104] are employed to check the compatibility of an event with the $t\bar{t}$ hypothesis and to improve the resolution of the reconstructed quantities. The fit parameters are the three-vectors of the momenta of the six decay products resulting in 18 unknowns. The following constraints are applied in the fit: the invariant masses of the two top quark candidates should be the same and the invariant masses of both W boson

candidates should be 80.4 GeV [1].

In the lepton+jets channel, the four-momenta of the lepton and the four highest- p_T (leading) jets, and \vec{p}_T^{miss} are the inputs that are fed together with their resolutions to the fit algorithm [103]. With these input values, the fit has two degrees of freedom. In the all-jets channel, the momenta and resolutions of the six leading jets are the inputs to the fitter [104] resulting in a fit with three degrees of freedom. The kinematic fit then minimises $\chi^2 \equiv (\mathbf{x} - \mathbf{x}^m)^T G (\mathbf{x} - \mathbf{x}^m)$, where \mathbf{x}^m and \mathbf{x} are the vectors of the measured and fitted momenta, respectively, and G is the inverse covariance matrix, which is constructed from the uncertainties in the measured momenta. The above-mentioned constraints are added to the minimisation procedure with Lagrange multipliers.

The fit is performed for all possible assignments of the jets to the decay products. To reduce combinatorics, exactly two of the selected leading jets are required to be identified as originating from a b quark (b tagged). In the lepton+jets channel, the two b-tagged jets are candidates for the b quarks in the $t\bar{t}$ hypothesis, while the two jets that are not b tagged serve as candidates for the light quarks from the hadronically decaying W boson. In addition, there are two solutions for the start value of the longitudinal component of the neutrino momentum per parton-jet assignment. Hence, the fit is performed for four different permutations per event. In the all-jets channel, the two b-tagged jets are the candidates for the b quarks and the four jets that are not b tagged serve as candidates for the light quarks from the hadronically decaying W bosons. Hence, the fit is performed for six different permutations.

The χ^2 probability P_{gof} of the kinematic fits is used to rank the permutations, since the permutations with wrongly assigned jets typically have very low P_{gof} values. For simulated $t\bar{t}$ events, the parton-jet assignments can be classified as correct, wrong, and unmatched permutations. In the first case, all quarks from the $t\bar{t}$ decay are matched within a distance of $\Delta R = \sqrt{(\Delta\eta)^2 + (\Delta\phi)^2} < 0.3$, where ϕ is the azimuthal angle and η is the pseudorapidity, to a selected jet and assigned with the correct flavour assumption to the correct top quark. If all quarks are matched to a selected jet, but the wrong permutation is chosen, it is labelled ‘wrong’, while ‘unmatched’ indicates that not all quarks are matched unambiguously to a selected jet.

Due to the constraints, the kinematic fits improve the resolution of the reconstructed mass of the top quark candidates. The resolution of the reconstructed mass of the top quark with and without applying the kinematic fit is presented in Fig. 3 for the lepton+jets (multiple permutations) and all-jets channels (permutation with lowest χ^2). In the all-jets channel, only the permutation with the lowest χ^2 in each event is considered for further analysis. The resolution σ^{peak} is extracted by fitting a Gaussian distribution within the range $-40 < m_t^{\text{rec}} - m_t^{\text{gen}} < +40$ GeV. Without a kinematic fit, the resolution of the reconstructed top quark mass is relatively poor in the case of the lepton+jets channel, while the peak is hardly discernible at all in the all-jets channel. In both $t\bar{t}$ decay channels, the kinematic fit improves the resolution using either all jet-parton permutations or the one with the lowest χ^2 . Finally, a cut on $P_{\text{gof}} > 0.2$ (0.1) is used in the lepton+jets (all-jets) channel, which matches the resolution of the case where only correct permutations are considered with their pre-fit momenta. The selection efficiency of the P_{gof} cut is 27.4 (5.3)% in the lepton+jets (all-jets) channel. Besides the mass, the kinematic fits can also improve the reconstruction of other kinematic variables of the $t\bar{t}$ system, such as its invariant mass $m_{t\bar{t}}$. The bias and resolution of the reconstructed $m_{t\bar{t}}^{\text{rec}}$ with regard to the generated $m_{t\bar{t}}^{\text{gen}}$ is shown for the lepton+jets channel in Fig. 4 and for the all-jets channel in Fig. 5. The resolution is defined as the root-mean-square (RMS) of the difference between the reconstructed and the generated parton-level quantity, and the bias as its mean. The kinematic fit with a P_{gof} cutoff improves the resolution and is almost free of bias over the examined range in $m_{t\bar{t}}^{\text{gen}}$.

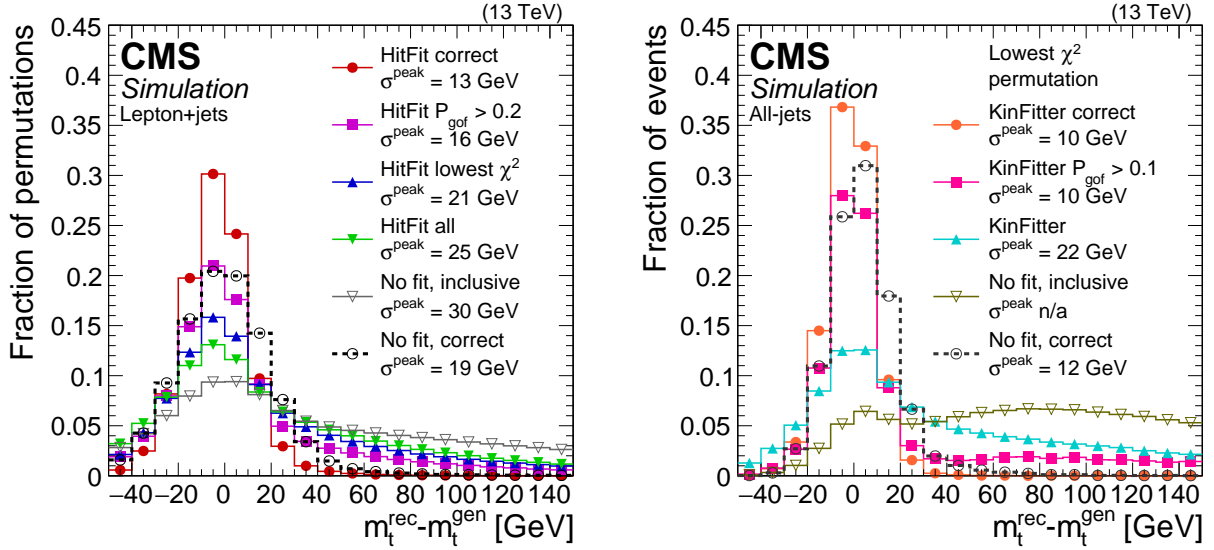


Figure 3: Reconstructed top quark mass resolution with and without the HITFIT/KINFITTER kinematic reconstruction in the lepton+jets (left) and all-jets (right) channels. Multiple reconstruction options with and without kinematic fit are represented by lines of different colour, and “correct” denotes the correct parton-jet assignments as discussed in the text. The HITFIT/KINFITTER reconstruction with a cutoff on P_{gof} is used for measuring the top quark mass [61, 62].

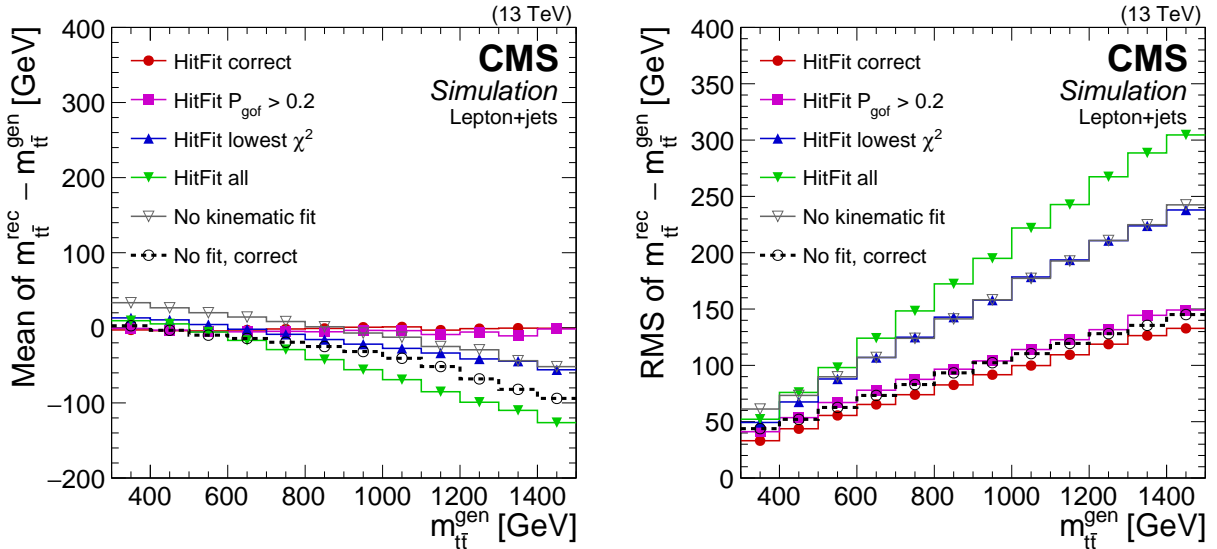


Figure 4: Reconstructed $t\bar{t}$ mass bias (left) and resolution (right) with and without the HITFIT kinematic reconstruction in the lepton+jets channel, as functions of the $t\bar{t}$ invariant mass at generator level. Multiple reconstruction options with and without kinematic fit are represented by lines of different colour, and “correct” denotes the correct parton-jet assignments as discussed in the text. The HITFIT reconstruction with a cutoff on P_{gof} is used for measuring the top quark mass [61].

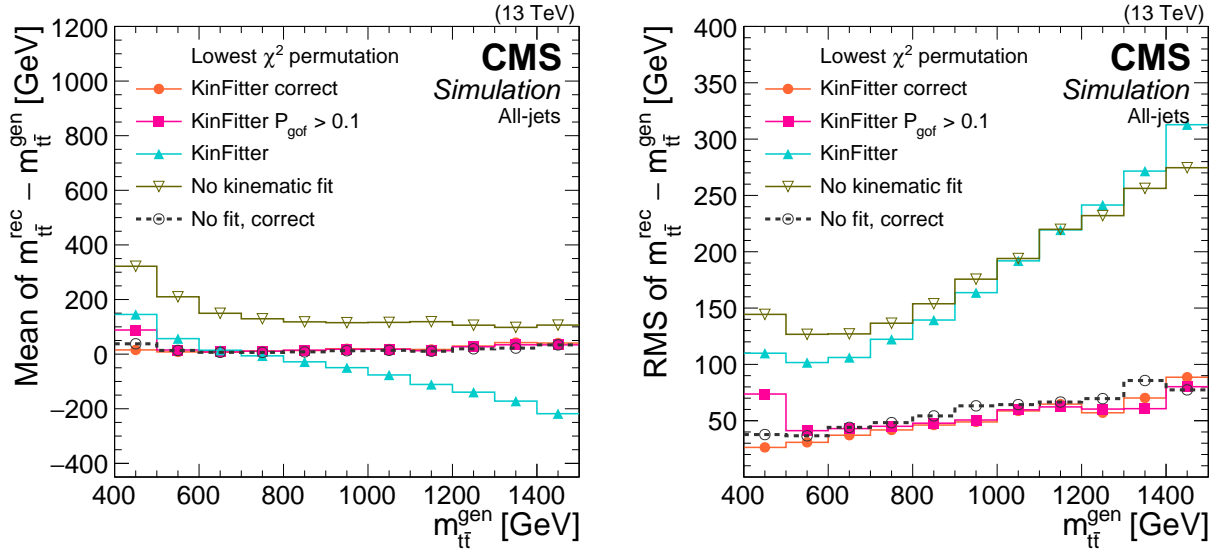


Figure 5: Reconstructed $t\bar{t}$ mass bias (left) and resolution (right) with and without the KINFITTER kinematic reconstruction in the all-jet channel, as functions of the $t\bar{t}$ invariant mass at generator level. Multiple reconstruction options with and without kinematic fit are represented by lines of different colour, and “correct” denotes the correct parton-jet assignments as discussed in the text. The KINFITTER reconstruction with a cutoff on P_{gof} is used for measuring the top quark mass [62].

2.3.2 Reconstruction in the dilepton channel

In contrast to the lepton+jets channel, direct measurements of m_t in the dilepton channel are challenging because of the ambiguity due to the two neutrinos in the final state, reconstructed as \vec{p}_T^{miss} . Therefore, the dilepton $t\bar{t}$ events are mostly used for extraction of the Lagrangian m_t through comparisons of the measurements of inclusive or differential $t\bar{t}$ cross sections [64, 65, 69] to the theoretical predictions, as explained in Section 4. In this case, the reconstruction method aims to obtain good resolution of the observable of interest and a high reconstruction efficiency.

For the $t\bar{t}$ reconstruction in the dilepton channel, several methods have been developed, with the primary task of obtaining solutions for the two unknown neutrino momenta. Depending on the observable of interest, either the individual top quark and antiquark, e.g. in the measurement of single-particle kinematics, or only the $t\bar{t}$ system, e.g. in the measurement of $m_{t\bar{t}}$ distribution, are reconstructed.

The **full kinematic reconstruction** (FKR) of the $t\bar{t}$ pair is based on the algebraic approach suggested in Ref. [105]. A system of kinematic equations describing the $t\bar{t}$ system is solved using the four-momenta of the six final-state particles, i.e. two leptons, two b jets, and the two neutrinos. It is assumed that the total measured missing transverse momentum is due to the two neutrinos and can be decomposed as follows:

$$p_x^{\text{miss}} = p_{x,\nu} + p_{x,\bar{\nu}}, \quad p_y^{\text{miss}} = p_{y,\nu} + p_{y,\bar{\nu}}. \quad (1)$$

The invariant mass of the lepton and the neutrino from the same top quark should correspond to the mass of the W boson, resulting in the following equations:

$$m_{W^+}^2 = (E_{\ell^+} + E_\nu)^2 - (p_{x,\ell^+} + p_{x,\nu})^2 - (p_{y,\ell^+} + p_{y,\nu})^2 - (p_{z,\ell^+} + p_{z,\nu})^2, \quad (2)$$

$$m_{W^-}^2 = (E_{\ell^-} + E_{\bar{\nu}})^2 - (p_{x,\ell^-} + p_{x,\bar{\nu}})^2 - (p_{y,\ell^-} + p_{y,\bar{\nu}})^2 - (p_{z,\ell^-} + p_{z,\bar{\nu}})^2. \quad (3)$$

Finally, the masses of the top quark and antiquark are given, respectively, by:

$$m_t^2 = (E_{\ell^+} + E_\nu + E_b)^2 - (p_{x,\ell^+} + p_{x,\nu} + p_{x,b})^2 - (p_{y,\ell^+} + p_{y,\nu} + p_{y,b})^2 - (p_{z,\ell^+} + p_{z,\nu} + p_{z,b})^2, \quad (4)$$

$$m_{\bar{t}}^2 = (E_{\ell^-} + E_{\bar{\nu}} + E_{\bar{b}})^2 - (p_{x,\ell^-} + p_{x,\bar{\nu}} + p_{x,\bar{b}})^2 - (p_{y,\ell^-} + p_{y,\bar{\nu}} + p_{y,\bar{b}})^2 - (p_{z,\ell^-} + p_{z,\bar{\nu}} + p_{z,\bar{b}})^2. \quad (5)$$

The masses of the b quarks are set to the values used in the simulation, while lepton masses are assumed to be negligible. The masses of the top quark and of the W boson need to be fixed in order to solve the system of equations (1)–(5). For analyses where the choice does not directly affect the result of the measurement, they are typically fixed to the default values of $m_t = 172.5 \text{ GeV}$ and $m_W = 80.4 \text{ GeV}$. The equation system can then be solved analytically with a maximum four-fold ambiguity. Selected is the solution which yields the minimum invariant mass of the $t\bar{t}$ system, as it was shown that this choice provides the best solution in most cases. In analyses that target direct reconstruction of m_t in the dilepton channel, a dedicated method [47, 49, 53] is used that tests different m_t hypotheses. In contrast, in differential measurements of the $t\bar{t}$ cross section, the dependence on the choice of m_t in the reconstruction is usually estimated by varying the top quark mass assumption in the MC simulation.

To capture the effects of the finite detector resolution, the kinematic reconstruction is repeated 100 times, each time randomly smearing the measured energies and directions of the reconstructed leptons and jets within their resolutions. This smearing procedure recovers events that initially yielded no solution because of limited experimental resolution. Further, in the same smearing procedure, the mass of the W boson is varied according to a relativistic Breit–Wigner function, estimated using the generator-level W boson mass distribution. For each solution, a weight is calculated based on the expected true spectrum of the invariant mass of a lepton and a b jet ($m_{\ell b}$) stemming from the decay of a top quark and taking the product of the two weights for the top quark and antiquark decay chains: $w = w_{m_{\ell b}} w_{m_{\ell \bar{b}}}$. The final three-momenta of the top quarks j and k are then determined as a weighted average over all smeared solutions summing over all 100 kinematic reconstructions:

$$\langle \vec{p}_t^{k,j} \rangle = \frac{1}{w_s} \sum_{i=1}^{100} w_i \vec{p}_{t,i}^{k,j}, \quad \text{with} \quad w_s = \sum_{i=1}^{100} w_i. \quad (6)$$

All possible lepton-jet combinations in the event that satisfy the requirement for the invariant mass of the lepton and jet $m_{\ell b} < 180 \text{ GeV}$ are considered. Combinations are ranked, based on the presence of b-tagged jets in the assignments, i.e. a combination with both leptons assigned to b-tagged jets is preferred over those with one or zero b-tagged jet. Among assignments with an equal number of b-tagged jets, the one with the highest sum of weights is chosen. Events with no solution after smearing are discarded. The four-momentum vector of the top quark is determined by its energy, which is calculated from $\langle \vec{p}_t \rangle$, and the top quark mass of 172.5 GeV . The kinematic properties of the top antiquark are determined analogously. The efficiency of the kinematic reconstruction, defined as the number of events where a solution is found divided by the total number of selected $t\bar{t}$ events, is studied in data and simulation, and consistent results of about 90% are found in analyses at $\sqrt{s} = 13 \text{ TeV}$.

The value of the invariant mass $m_{t\bar{t}}$ of the $t\bar{t}$ pair obtained using FKR is highly sensitive to the predefined value of the top quark mass used as a kinematic constraint. However, the objective of the analyses described in this paper is the extraction of m_t , in some cases exploiting the $m_{t\bar{t}}$ distribution or related observables. For such cases, the **loose kinematic reconstruction** (LKR)

was developed [64], where the value of the top quark mass is not constrained. In this algorithm, the $\nu\bar{\nu}$ system is reconstructed, rather than the individual ν and $\bar{\nu}$. As a consequence, only the $t\bar{t}$ system can be reconstructed in LKR, but not the individual top quark and antiquark. As in FKR, all possible lepton-jet combinations in the event that satisfy the requirement for the invariant mass of the lepton and jet $m_{\ell b} < 180 \text{ GeV}$ are considered. Combinations are ranked, based on the presence of b-tagged jets in the assignments, but from all the combinations with an equal number of the b-tagged jets, the ones with the highest p_T jets are chosen. The kinematic variables of the $\nu\bar{\nu}$ system are derived as follows:

1. the transverse momentum \vec{p}_T of the $\nu\bar{\nu}$ system is set equal to \vec{p}_T^{miss} ;
2. the $\nu\bar{\nu}$ longitudinal momentum $p_{z,\nu\bar{\nu}}$ is set to that of the lepton pair, $p_{z,\nu\bar{\nu}} = p_{z,\ell\bar{\ell}}$, for $p_{T,\nu\bar{\nu}} < E_{\ell\bar{\ell}}$, and to zero otherwise;
3. the energy of the $\nu\bar{\nu}$ system $E_{\nu\bar{\nu}}$ is defined as $E_{\nu\bar{\nu}} = E_{\ell\bar{\ell}}$ for $p_{\nu\bar{\nu}} < E_{\ell\bar{\ell}}$, and $E_{\nu\bar{\nu}} = p_{\ell\bar{\ell}}$ otherwise, ensuring that $m_{\nu\bar{\nu}} \geq 0$;
4. the four-momentum sum of $\ell\bar{\ell}\nu\bar{\nu}$ is calculated;
5. for $m_{\ell\bar{\ell}\nu\bar{\nu}} < 2m_W = 2 \times 80.4 \text{ GeV}$, the mass component of the four-momentum of $\ell\bar{\ell}\nu\bar{\nu}$ is set to $2m_W$, ensuring that $m_{W+W-} \geq 2m_W$;
6. the four-momentum of the $t\bar{t}$ system is calculated by using the four-momenta of the $\ell\bar{\ell}\nu\bar{\nu}$ system and of the two b jets as $\ell\bar{\ell}\nu\bar{\nu}+b\bar{b}$.

The additional constraints that are applied on the invariant mass of the neutrino pair, $m_{\nu\bar{\nu}} \geq 0$ (item 3) and on the invariant mass of the W bosons, $m_{W+W-} \geq 2m_W$ (item 5) have only minor effects on the performance of the reconstruction. The method yields similar $t\bar{t}$ kinematic resolutions and reconstruction efficiency as for the FKR method. In the CMS analysis [64], the LKR was exclusively used to measure triple-differential $t\bar{t}$ cross sections as functions of the invariant mass and rapidity of the $t\bar{t}$ system, and the additional-jet multiplicity.

For the presented performance studies, the POWHEG+PYTHIA8 [106–110] $t\bar{t}$ simulated samples are used, which are explained in detail in Section 2.4. The reconstruction efficiency for both methods is shown in Fig. 6 as a function of the reconstructed $t\bar{t}$ kinematic variables $m_{t\bar{t}}$, $p_{T,t\bar{t}}$, and $y_{t\bar{t}}$. An event is considered as reconstructed if the reconstruction method yields at least one solution as described above. The overall efficiency for the LKR is about 4% higher than for the FKR, and shows the same kinematic properties. The maximum efficiency is achieved for low $m_{t\bar{t}}$, central $y_{t\bar{t}}$, and low $p_{T,t\bar{t}}$. The efficiency drops rapidly with increasing $p_{T,t\bar{t}}$ as the leptons and jets become less separated. For Lorentz-boosted configurations with $p_{T,t\bar{t}} > 700 \text{ GeV}$, the reconstruction fails in 20% of the cases.

The resolution and bias for both algorithms are shown in Figs. 7 and 8, respectively, as functions of the same three observables at the generator level. As described above for the lepton+jets decay channel, the resolution is defined as the RMS of the difference between the reconstructed and the parton-level quantity, and the bias as its mean. As in the case of the efficiencies, the LKR shows better performance. Its bias is often closer to zero in the low- $m_{t\bar{t}}$ regime, but becomes larger than in the case of the FKR for very large values of $m_{t\bar{t}}$. The LKR shows better resolution over the whole spectra, but it should be noted that the resolution definition is sensitive to outliers, e.g. in the tails of the distribution, affecting the performance of the FKR, e.g. in the low- $m_{t\bar{t}}$ region. For probing m_t in the dilepton channel, the resolution at low $m_{t\bar{t}}$, close to the

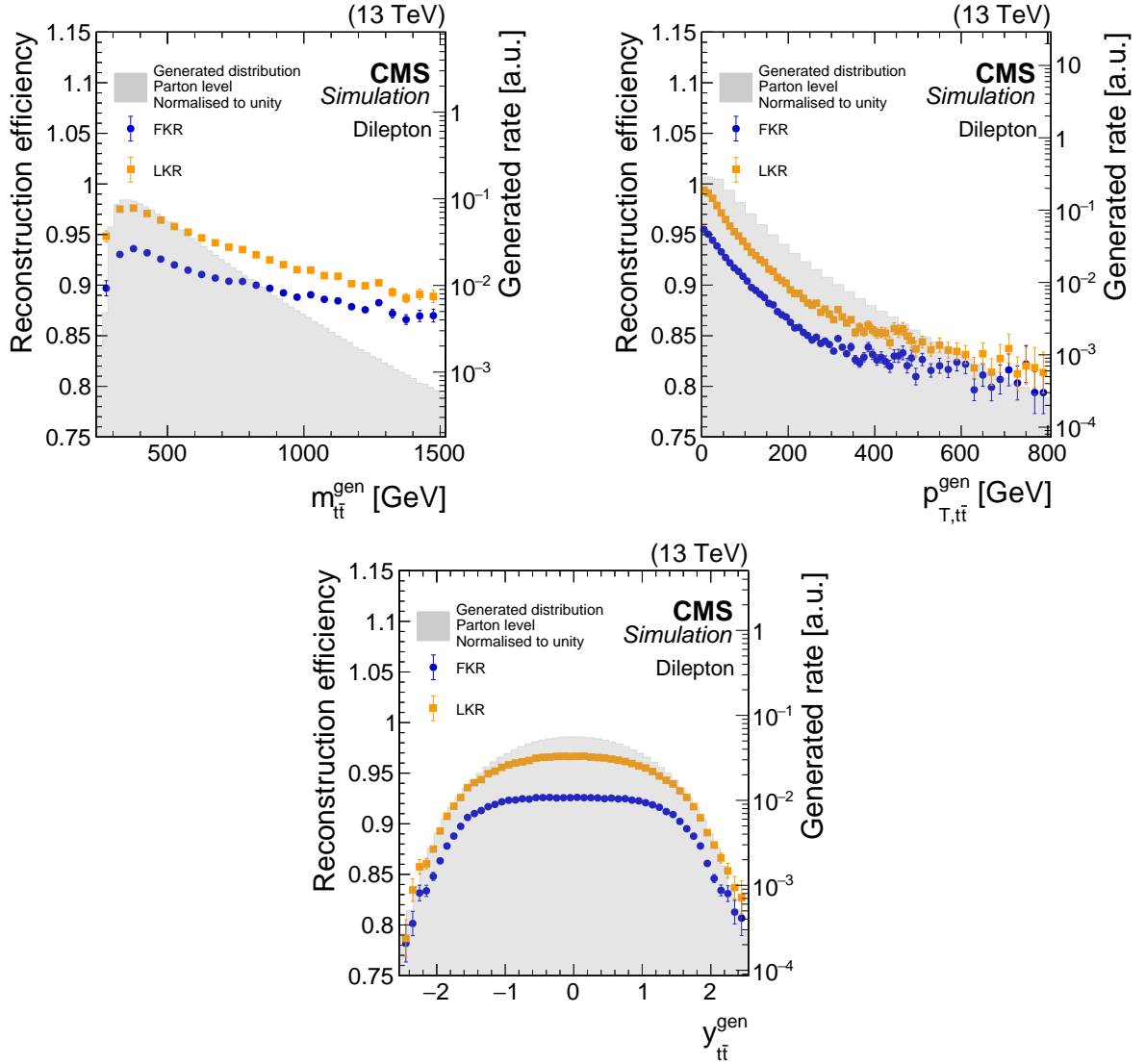


Figure 6: The reconstruction efficiencies for the full kinematic reconstruction (FKR, blue circles) and loose kinematic reconstruction (LKR, orange squares) are shown as functions of the invariant mass, transverse momentum, and rapidity of the reconstructed $t\bar{t}$ system. The averaged efficiencies are 92 (96)% for the FKR (LKR). The corresponding parton-generator-level distributions, normalised to unit area, for $t\bar{t}$ production are represented by the grey shaded areas, shown on the logarithmic scale (right y axis). The POWHEG+PYTHIA8 $t\bar{t}$ simulated samples are used.

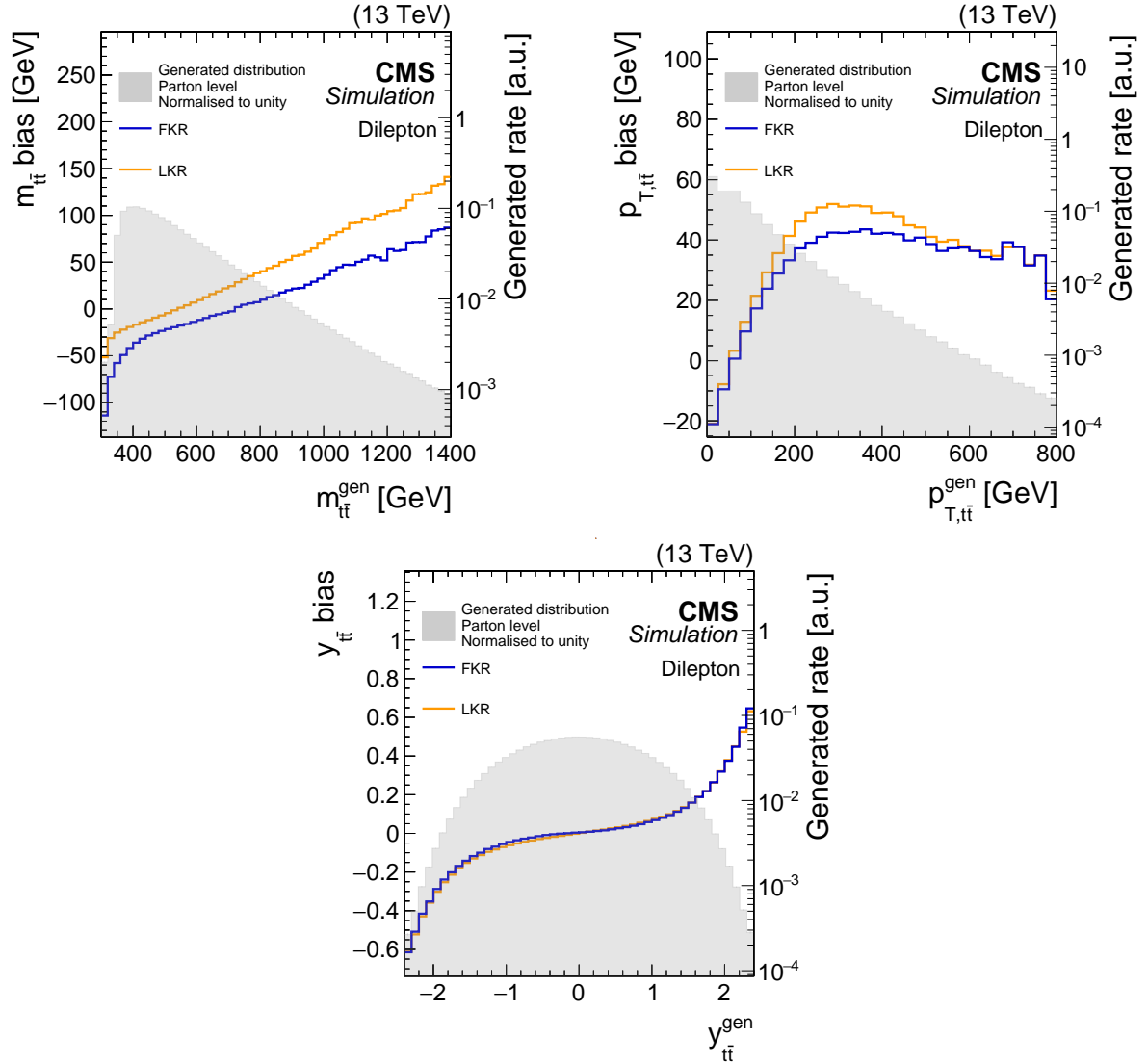


Figure 7: The biases (solid lines), as defined in the text, for the full kinematic reconstruction (FKR, blue) and loose kinematic reconstruction (LKR, orange) are shown for the invariant mass, transverse momentum, and rapidity of the $t\bar{t}$ system, as a function of the same variables at the generator level. The corresponding parton-generator-level distributions, normalised to unit area, for $t\bar{t}$ production are represented by the grey shaded areas, shown on the logarithmic scale (right y axis). The POWHEG+PYTHIA8 $t\bar{t}$ simulated samples are used.

production threshold, is of key importance. The resolution is about 100–150 GeV, which defines the minimal bin width in the differential $m_{t\bar{t}}$ measurement.

Since the FKR and LKR methods are developed to be agnostic to additional radiation for $t\bar{t}$ production, a multivariate method was developed in CMS [69] to optimise the resolution for an observable related to the invariant mass of the $t\bar{t}$ +jet system, denoted as ρ , which is defined for $t\bar{t}$ events with at least one additional jet:

$$\rho = \frac{340 \text{ GeV}}{m_{t\bar{t}+\text{jet}}}. \quad (7)$$

In the definition of ρ , the leading jet is considered and $m_{t\bar{t}+\text{jet}}$ is the invariant mass of the $t\bar{t}$ +jet system. This observable shows a large m_t sensitivity and is measured in a CMS analysis [69]

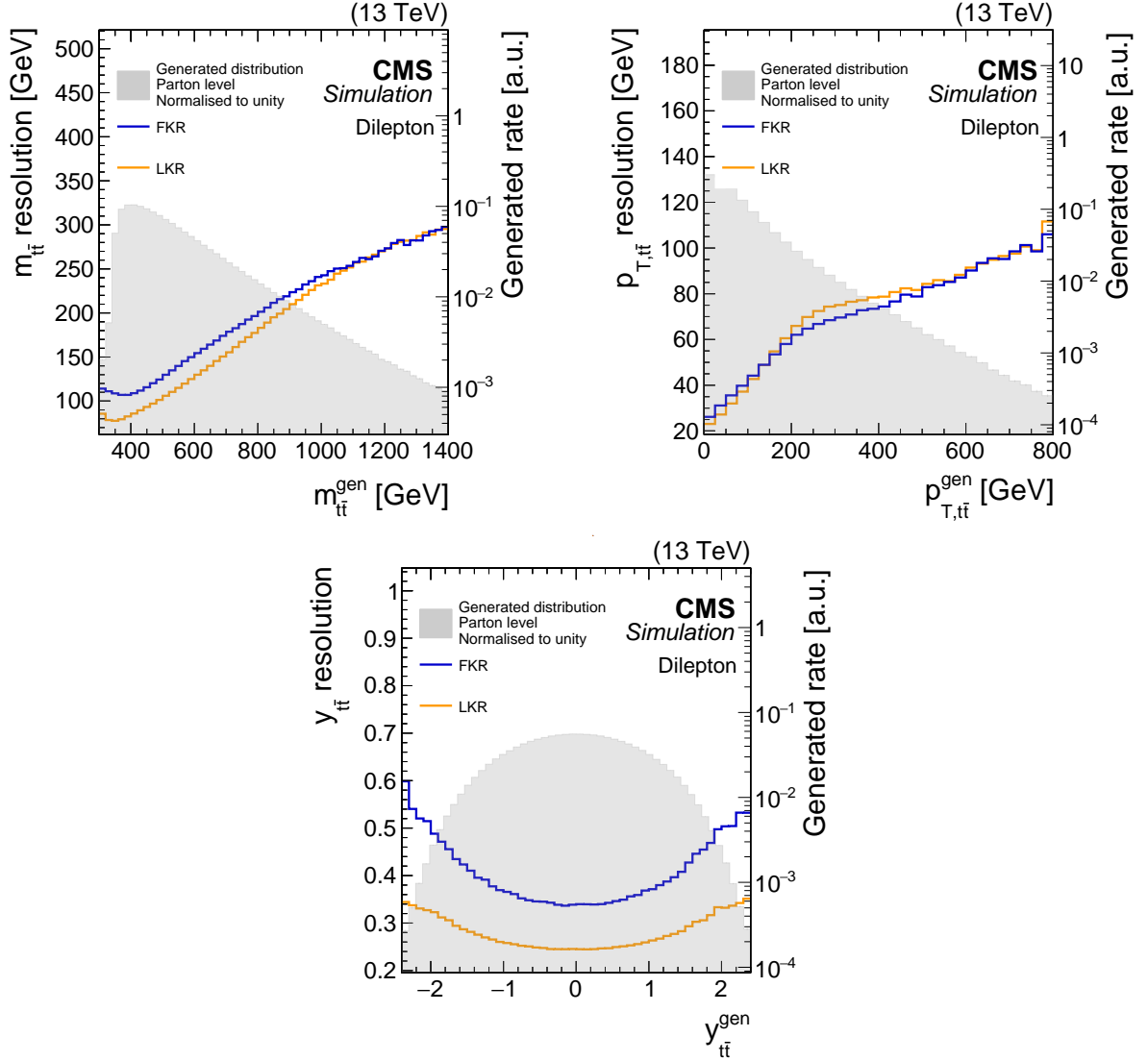


Figure 8: The resolutions (solid lines), as defined in the text, for the full kinematic reconstruction (FKR, blue) and loose kinematic reconstruction (LKR, orange) are shown as functions of the invariant mass, transverse momentum, and rapidity of the $t\bar{t}$ system at the generator level. The corresponding parton-generator-level distributions, normalised to unit area, for $t\bar{t}$ production are represented by the grey shaded areas, shown on the logarithmic scale (right y axis). The POWHEG+PYTHIA8 $t\bar{t}$ simulated samples are used.

described in Section 4.5 to extract m_t^{pole} . The result of the measurement is independent of the choice of the scaling constant in the numerator, which is introduced to define ρ dimensionless, and is on the order of two times m_t . Set up as a regressional neural network (NN), a fully connected feed-forward NN is trained. The benefit of using a regression NN is the maximised reconstruction efficiency, increasing the acceptance of the measurement, as it yields a solution for every event. The NN uses a set of low-level inputs, e.g. particle four-momenta, and high-level input variables, such as geometric and kinematic properties of the systems of the final-state objects. Starting from a set of 100 variables, the ten variables with the highest impact on the output of the NN are selected. These also include solutions of the LKR and FKR algorithms. Simulated events are used for the training of the regression NN if they contain at least three reconstructed jets with $p_T > 30 \text{ GeV}$ and $|\eta| < 2.4$. The ten input variables, ordered by their impact, used for the regression NN are:

- the calculation for ρ using the LKR;
- the calculation for ρ using the FKR;
- the invariant mass of the dilepton and subleading jet system;
- the invariant mass of the leading lepton and subleading jet system;
- the p_T of the subleading lepton;
- the invariant mass of the dilepton system;
- the invariant mass of the subleading lepton and subleading jet system;
- the invariant mass of the subleading lepton and leading jet system;
- the invariant mass of the dilepton and leading jet system;
- p_T^{miss} .

The training is performed using an independent data set, which is produced with the MADGRAPH5_aMC@NLO [111] event generator at NLO accuracy, interfaced with PYTHIA8 [110]. Afterwards, the resulting performance is also evaluated using the POWHEG+PYTHIA8 simulation, and is checked for possible overtraining.

The performance of the NN regression is shown in Fig. 9. The left plot shows the correlation between the parton-level value (ρ_{gen}) and the reconstructed value (ρ_{reco}). The correlation coefficient for the regression is 0.87, compared to 0.78 (0.84) for the loose (full) kinematic reconstruction.

The resolution of the regression NN is compared to that of the FKR and LKR in Fig. 9 (right). The resolution is defined as the RMS of the difference between the true value ρ_{gen} at parton level and the reconstructed value ρ_{reco} of the regression NN in a given ρ_{gen} bin, divided by $1 + \langle \rho_{\text{gen}} - \rho_{\text{reco}} \rangle$ to account for the bias in the reconstruction and to evaluate the response corrected resolution. The advantage of the multivariate method is the final resolution ranging between 0.05 and 0.08 in the full spectrum, which is an improvement by as much as a factor of two with respect to earlier approaches. The most significant improvement is achieved for the values of ρ_{gen} close to unity. Since this kinematic regime corresponds to small values for the invariant mass of the $t\bar{t}$ +jet system, it is the most sensitive region for the m_t measurement. An additional advantage is the 10–15% higher reconstruction efficiency since the described method is 100% efficient.

2.4 Monte Carlo simulations and modelling uncertainties

Physics generator configurations for top quark mass measurements Proton-proton collisions are modelled and studied using MC event generators, which split the prediction into

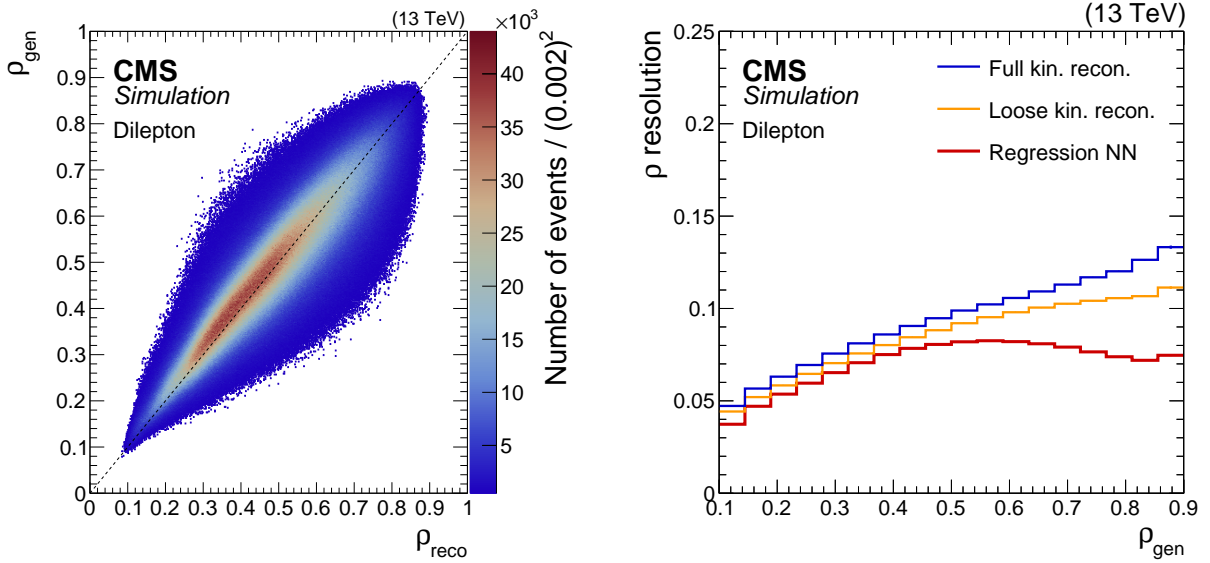


Figure 9: The correlation between ρ_{gen} and ρ_{reco} is shown for the regression NN reconstruction method (left). The ρ_{reco} resolution, defined in the text, as a function of ρ_{gen} (right) for the full (blue line) and loose (orange line) kinematic reconstructions and the regression NN (red line) methods. The number of events per bin in the left plot is shown by the colour scale. Figure taken from Ref. [69].

several steps, each tackled with different techniques, depending on the typical energies involved: the hard scattering, computed with a pure perturbative approach; the parton shower (PS), evolving the partons emerging from the hard scattering down to energies where the perturbative approach is no longer viable; the hadronisation, which is based on phenomenological models; UE, and the decays of unstable hadrons. The UE is composed of the beam-beam remnants (BBR), the particles from multiple-parton interactions (MPI), and their corresponding initial-state radiation (ISR) and final-state radiation (FSR). The BBR are the relics after the hard scattering of the initial beam hadrons. The hard scattering is calculated perturbatively using matrix element (ME) codes such as MADGRAPH [111], and ISR and FSR are simulated with shower algorithms with general-purpose MC codes such as PYTHIA8. Hadronisation, underlying event, colour reconnection (CR), and MPI can only be calculated nonperturbatively, and require tuning of the involved phenomenological parameters to describe the data reliably. Another nonperturbative ingredient to event generators is given by the parton distribution functions (PDFs) used in the hard partonic ME calculation, the PS simulation, and the MPI model. Typically, the generated events were processed with the CMS detector simulation based on GEANT4 [112] using the conditions appropriate for each period of data taking. As a convention among the Tevatron and LHC experiments and the theory community, from the beginning of the LHC running, the reference value for the top quark mass in the MC simulations is set to $m_t^{\text{MC}} = 172.5 \text{ GeV}$ [113].

In the LHC Run 1, $t\bar{t}$ signal samples were generated at LO in QCD with up to three additional partons using the MADGRAPH5.1 ME generator [111]. The top quark decays were treated without spin correlations in the samples produced for the analysis of the 7 TeV dataset. The 8 TeV CMS samples employed MADSPIN [114] to improve the description of angular correlations between the top quark decay products. For parton showering, hadronisation, and underlying event simulation, PYTHIA6.4 [115] was used with the Z2 [116] and Z2* tunes [117] at 7 and 8 TeV, respectively. The tune Z2* is a result of retuning a subset of the parameters of the Z2 tune using the automated PROFESSOR tuning package [118].

The top quark MC samples produced for the analyses of LHC Run 2 data, in particular those used in the analyses of data taken at 13 TeV and collected during the years 2015 and 2016, were generated with the POWHEG v2 [106–109] NLO generator interfaced with PYTHIA8.2 [110] using the CUETP8M2T4 tune [119]. This tune included a fit to CMS $t\bar{t}$ +jet data taken at $\sqrt{s} = 8$ TeV to obtain an improved description of ISR in $t\bar{t}$ events.

Later Run 2 samples (so-called “legacy” samples, referring to the updated data reconstruction and calibrations) were produced with the CP5 tune [120], which for the first time incorporated fits to data taken at 13 TeV and employed an identical NNLO PDF set and the corresponding value of the strong coupling α_S at NNLO for both the POWHEG ME generator and the PYTHIA8 components, i.e. ISR, FSR, and MPI.

In the measurements of the top quark mass, the uncertainties related to simulations need to be considered. Ideally, different MC generators and implied setups should provide an adequate description of the observables of interest. In practice, the default MC setups were validated most extensively in CMS analyses. The modelling uncertainties are factorised into individual components associated with the aforementioned setups, as summarised in Table 2, and are discussed in more detail in the following.

Table 2: Overview of CMS MC setups for $t\bar{t}$ production used in analyses of Run 1 and Run 2 data, and their associated modelling uncertainties. Variations marked with a dagger (\dagger) are evaluated via event weights, which mitigates the uncertainty associated with the size of MC samples without the need for additional simulations.

	Run 1	Early Run 2	Run 2 legacy
Default setup			
ME generator	MADGRAPH5 $t\bar{t} + \leq 3$ jets @ LO	POWHEG v2 $t\bar{t}$ @ NLO	POWHEG v2 $t\bar{t}$ @ NLO
PDF	CT10 NLO	NNPDF3.0 NLO	NNPDF3.1 NNLO
PS/UE generator	PYTHIA6.4	PYTHIA8.2	PYTHIA8.2
PS/UE tune	Z2(*)	CUETP8M2T4	CP5
Uncertainties			
PDF	CT10 eigenvectors, MSTW08, NNPDF2.3 \dagger	NNPDF replicas \dagger	NNPDF eigenvectors, CT14, MMHT14 \dagger
ME scales	$\mu_r \oplus \mu_f$ up/down	$\mu_r \oplus \mu_f$ 7-point \dagger	$\mu_r \oplus \mu_f$ 7-point \dagger
ME-PS matching	threshold up/down	h_{damp} up/down	h_{damp} up/down
Alternative ME	POWHEG v1	MADGRAPH5_aMC@NLO	MADGRAPH5_aMC@NLO
Top quark p_T	ratio to 7/8 TeV data	ratio to 13 TeV data	ratio to 13 TeV data
ISR	μ_r^{ISR} up/down (correlated with ME)	μ_r^{ISR} up/down	μ_r^{ISR} up/down \dagger
FSR	—	μ_r^{FSR} up/down	μ_r^{FSR} up/down \dagger
UE	P11, P11 mpiHi/TeV	CUETP8M2T4 up/down	CP5 up/down
CR	P11, P11noCR	ERD on/off, CR1 (ERD on), CR2 (ERD off)	ERD on/off, CR1, CR2 (both ERD off)
b fragmentation	r_b up/down \dagger	r_b up/down, Peterson \dagger	r_b up/down, un/tuned, Peterson \dagger

PDF uncertainties PDF uncertainties are evaluated through reweighting, without the need of generating additional MC samples. The MADGRAPH5 LO samples used in analyses of Run 1

data were reweighted a posteriori using LHAPDF5.6 [121–123] following the formula

$$w^{\text{new}} = \frac{f_1^{\text{new}}(x_1; Q^2) f_2^{\text{new}}(x_2; Q^2)}{f_1^{\text{ref}}(x_1; Q^2) f_2^{\text{ref}}(x_2; Q^2)}. \quad (8)$$

Here, f_i refers to the distribution of the interacting parton i in each of the two colliding protons and is a function of the fraction x_i of the proton momentum carried by that parton, and of the factorisation scale denoted here as Q . The PDF uncertainty was evaluated as an envelope of the individual uncertainties encoded in Hessian CT10 NLO [124] and MSWT2008 [125] eigenvectors, and in NNPDF2.3 NLO [126] replicas.

Since Run 2, PDF weights are calculated directly during the POWHEG v2 NLO event generation and stored in the event. In particular, in early Run 2 analyses, the PDF uncertainty was evaluated using replicas of the NNPDF3.0 NLO PDF set [127]. The Run 2 legacy setup includes the Hessian eigenvectors of NNPDF3.1 NNLO by default, and, alternatively, of CT14 NNLO [128] and MMHT2014 NNLO [129].

Matrix element scales For the Run 1 MADGRAPH5 predictions, additional samples were generated varying the renormalisation (μ_r) and factorisation (μ_f) scales in the matrix element by factors of 1/2 and 2, in parallel with the ISR renormalisation scale prefactor and the FSR Λ_{QCD} (outside resonance decays) in PYTHIA6. The POWHEG v2 samples in Run 2 include weights for variations of μ_r and μ_f that allow for independent, simultaneous, or full 7-point scale variations, avoiding the cases in which $\mu_r/\mu_f = 1/4$ or 4, following Ref. [130].

Parton shower matching The Run 1 samples were generated with MLM matching [131] to interface the MADGRAPH5 matrix elements with the PYTHIA6 PS. The matching threshold was varied from a default of 40 GeV to 30 and 60 GeV, respectively. For the early Run 2 POWHEG+PYTHIA8 samples, the POWHEG h_{damp} parameter, regulating the high- p_T radiation, and the value of α_S^{ISR} were tuned to CMS $t\bar{t}$ +jets data in the dilepton channel at 8 TeV [119, 132], yielding $h_{\text{damp}} = 1.58^{+0.66}_{-0.59} m_t$ and $\alpha_S^{\text{ISR}} = 0.111^{+0.014}_{-0.014}$. For the Run 2 legacy samples, α_S^{ISR} was fixed to 0.118 and only the damping parameter was retuned to $h_{\text{damp}} = 1.38^{+0.93}_{-0.51} m_t$.

Initial-state radiation In Run 1 simulations, the ISR renormalisation scale in PYTHIA6 was varied simultaneously with the matrix-element scales in dedicated samples by factors of 1/2 and 2. For the early Run 2 analyses, additional samples were produced with the ISR scale in PYTHIA8 varied by the same factors, to approximate the α_S^{ISR} variations found in the tuning to $t\bar{t}$ data. For production of Run 2 legacy samples and later, ISR scale variations are included as weights [133], providing reduced (factor $f_{\mu_r} = \sqrt{2}$ and $1/\sqrt{2}$), default ($f_{\mu_r} = 2$ and $1/2$), and conservative ($f_{\mu_r} = 4$ and $1/4$) variations. In addition, $f_{\mu_r} = 2$ (and $1/2$) and nonsingular term variations [133] are available for each ISR splitting $g \rightarrow gg$, $g \rightarrow q\bar{q}$, $q \rightarrow qg$, and $b \rightarrow bg$ separately. The nonsingular terms are ambiguous terms that appear away from the soft collinear singular infrared limits. These terms are sensitive to missing higher-order ME corrections, the effect of which could be ameliorated by NLO scale compensation terms, as discussed in Ref. [133].

Final-state radiation Both PYTHIA6 and PYTHIA8 include NLO matrix-element corrections for the top quark and W boson decays so that the leading gluon emission has LO precision. There was no variation for FSR from the top quark and W boson decay products in the Run 1 samples. For early Run 2, additional samples were produced with the FSR scale in PYTHIA8 varied by factors of 1/2 and 2. The Run 2 legacy samples include weights providing reduced

(factor $f_{\mu_r} = \sqrt{2}$), default ($f_{\mu_r} = 2$), and conservative ($f_{\mu_r} = 4$) variations for FSR. As for ISR, $f_{\mu_r} = 2$ and nonsingular term variations are available for each FSR splitting $g \rightarrow gg$, $g \rightarrow q\bar{q}$, $q \rightarrow qg$, and $b \rightarrow bg$ separately. In particular, this allows for a decorrelation of radiation from the quarks within the W boson decay (which typically is constrained by the reconstructed W boson mass) and the radiation from b quarks in the top quark decay.

Figure 10 shows the evolution of central prediction and radiation uncertainties from Run 1 to Run 2 compared to measurements at 13 TeV. The jet multiplicity N_{jets} [134] is sensitive to ME scale, ME-PS matching, and ISR uncertainties, while the angle between groomed subjects ΔR_g [135] strongly depends on the FSR and its uncertainties. The FSR uncertainty in the Run 2 legacy sample is significantly reduced due to an NLO scale compensation term [133].

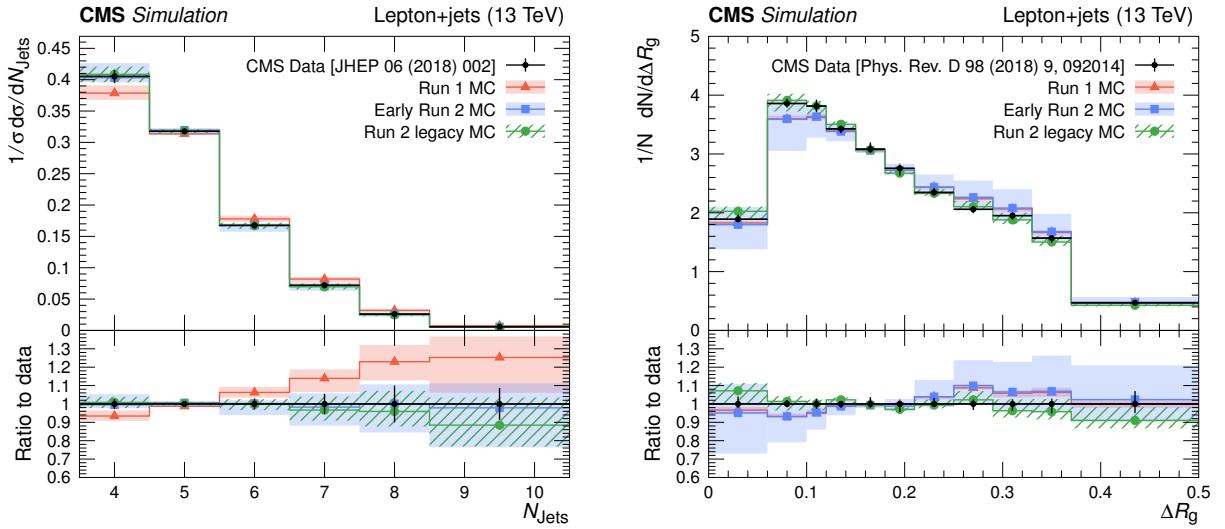


Figure 10: Distributions of the jet multiplicity N_{jets} [134] (left) and the jet substructure observable ΔR_g , the angle between the groomed subjects, normalised to the number of jets [135] (right) in $t\bar{t}$ events at 13 TeV (black symbols). The data are compared to the MC simulation setups used in Run 1, early Run 2, and Run 2 legacy analyses, presented by bands of different style and colour. The uncertainty bands include ME scale, ME-PS matching, ISR, and FSR uncertainties.

Alternative ME generators Alternative MC samples were generated in Run 1 using the POWHEG v1 NLO generator, and their difference was included as a systematic uncertainty. In Run 2, alternative samples have been produced with MADGRAPH5_aMC@NLO and FxFx merging [136], including up to three additional partons at NLO. As these samples were missing matrix-element corrections to the top quark decays [137], they were not suitable for the top quark mass measurements and were not included in systematic uncertainty estimation.

Top quark p_T In the context of Run 1 analyses, it was observed that the p_T spectra of top quarks in data are considerably softer than predicted by the then available NLO MC generators. While the central MC prediction was not altered, an additional uncertainty was introduced to cover this difference, derived from the ratio of data to NLO MC prediction. In Fig. 11, this ratio is shown for 2015 data and POWHEG+PYTHIA8 simulation used in early Run 2, in dilepton and lepton+jets [138] events. To evaluate the systematic uncertainty, the fitted exponential function $\exp(0.0615 - 0.0005p_T)$ is applied to p_T of each top quark at the parton level. Also shown is the top quark p_T measurement using 13 TeV data recorded in 2016 [139], compared to the predictions of the generator setups used in Run 1, early Run 2, and Run 2 legacy samples with ME scale, ME-PS matching, and ISR/FSR uncertainties. The Run 2 POWHEG simulation shows an improved agreement with the data.

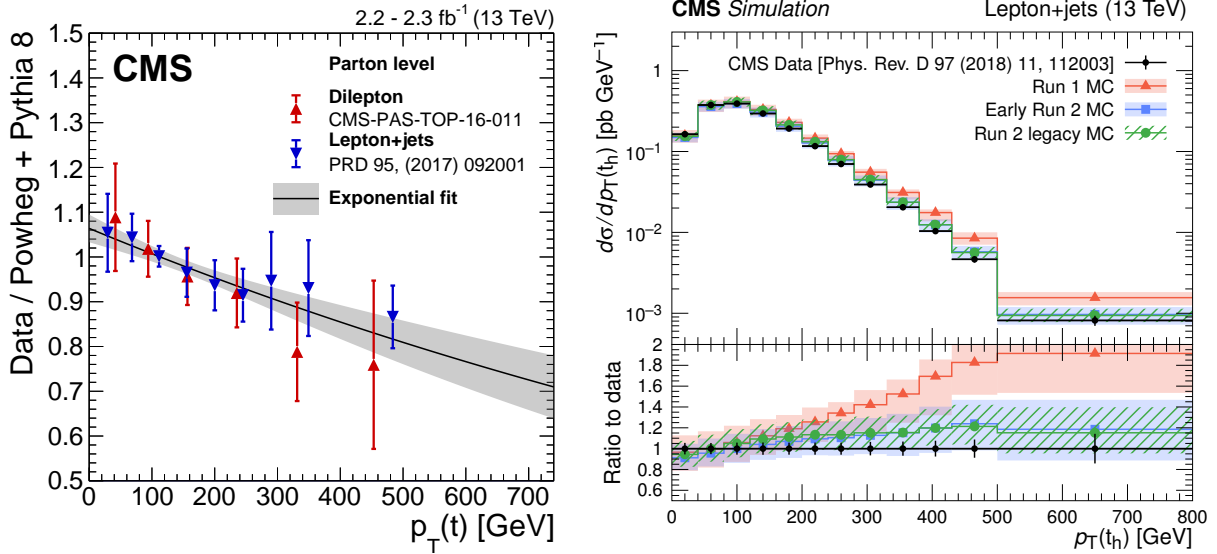


Figure 11: Left: Ratio of data to POWHEG+PYTHIA8 (early Run 2) predictions for top quark p_T in the dilepton (red symbols) and lepton+jets (blue symbols) channels along with an exponential fit (solid line). Right: Distribution of the transverse momentum of hadronically decaying top quark as measured by CMS [139] (black symbols) compared to MC simulations for the generator setups used in Run 1, early Run 2, and Run 2 legacy analyses, presented by bands of different styles. The uncertainty bands include ME scale, ME-PS matching, ISR, and FSR uncertainties.

Underlying event For the simulations used in CMS Run 1 measurements, the PYTHIA6 Z2 tune [116] was employed. This tune is obtained by fitting 900 GeV and 7 TeV CMS UE data and is based on the CTEQ6L PDF set and uses p_T -ordered showers. The variations for the Z2 tune have not been provided, therefore corresponding UE uncertainties are estimated by comparing the Perugia 2011 (P11) tune to the P11 mpiHi, and P11 Tevatron tunes [140]. The Perugia Tevatron tunes family is derived using hadronic Z boson decays at LEP, Tevatron minimum bias (MB) data taken at $\sqrt{s} = 0.63$ TeV, Tevatron MB and Drell–Yan data at 1.8 TeV and 1.96 TeV, and SPS MB data taken at 0.2, 0.546, and 0.9 TeV. As in the Z2 tune, it is based on p_T -ordered showers. The Perugia tunes and their corresponding variations were updated in 2011 [140] to use the same value of Λ_{QCD} for both ISR and FSR in the shower and to take into account the early 0.9 and 7 TeV LHC MB and UE data. With this update, a variant, called P11 mpiHi, with MPI that also uses the same Λ_{QCD} used for ISR and FSR is also provided.

In the m_t analyses in Run 2 the differences between the nominal tunes and their corresponding variations, obtained by their eigentunes, are considered as the UE uncertainty. In early Run 2 top quark analyses, the simulations employ the CUETP8M2T4 tune [119], which is derived using $\alpha_S^{\text{ISR}}(m_Z)$ constrained by the $t\bar{t}$ kinematic properties of the jet (also using the ISR rapidity ordering [120] to cure the overestimation of high jet multiplicities). In legacy Run 2 analyses, the PYTHIA8 UE tune CP5 [120] is used. This tune is based on an NNLO version of the NNPDF3.1 set (NNPDF31_nnlo.as_0118) [141], and the strong coupling evolution at NLO. The CP5 consistently uses the same value of $\alpha_S(m_Z) = 0.118$ in various components of the parton shower: initial and final state radiation, and MPI. The tune uses the MPI-based CR model. The CMS UE tunes are detailed in Table 2.

In Fig. 12, a minimum bias observable is displayed, the pseudorapidity density of charged hadrons ($dN_{\text{ch}}/d\eta$) from inelastic pp collisions, within $|\eta| = 2$ using both hit pairs and reconstructed tracks by the CMS experiment at $\sqrt{s} = 13$ TeV [142] operated at zero magnetic

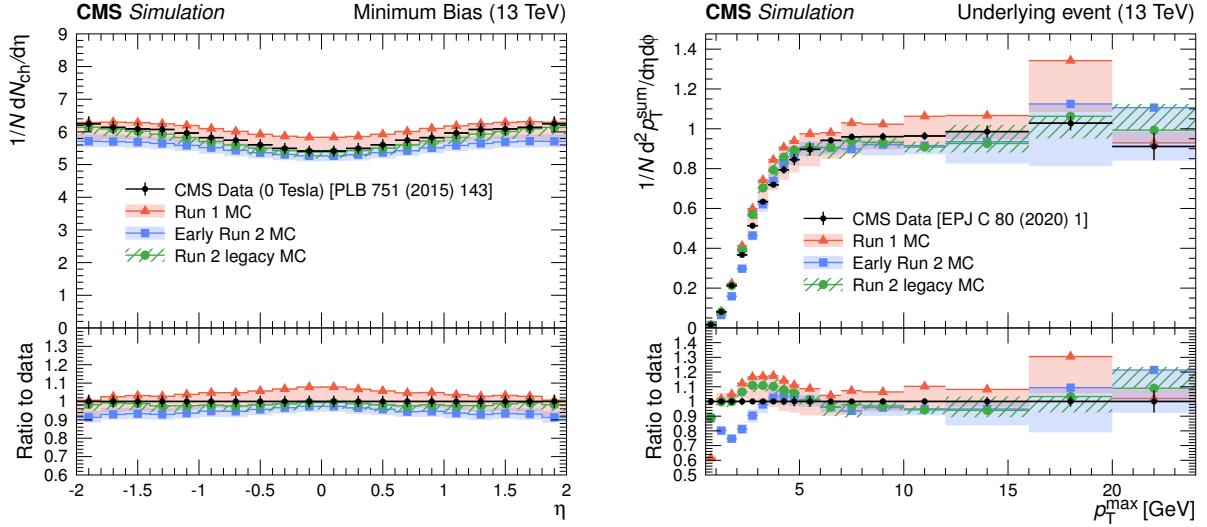


Figure 12: Left: The pseudorapidity density of charged hadrons, $dN_{ch}/d\eta$, using data from about 170 000 MB events from inelastic pp collisions using both hit pairs and reconstructed tracks by the CMS experiment [142] at $\sqrt{s} = 13$ TeV. Right: The charged-particle p_T^{sum} density in the azimuthal region transverse to the direction of the leading charged particle as a function of the p_T of the leading charged particle, p_T^{max} , measured by the CMS experiment [143] at $\sqrt{s} = 13$ TeV. The predictions of the CMS UE tunes from Run 1 to Run 2 legacy evaluated at 13 TeV are compared with data. The coloured bands represent the variations of the tunes, and error bars on the data points represent the total experimental uncertainty in the data including the model uncertainty. Both distributions are normalised to the total number of events.

field (left diagram). Also an UE observable is shown, the density of the scalar sum of p_T of charged particles (p_T^{sum} density) in the azimuthal region transverse to the direction of the leading charged particle as a function of the p_T of the same particle, p_T^{max} , measured by the CMS experiment at $\sqrt{s} = 13$ TeV [143] compared with different UE predictions simulated by PYTHIA8. The leading charged particle is required to be produced in the central region $|\eta| < 2$ with transverse momentum $p_T > 0.5$ GeV. The coloured band in these plots represents the variations of the tunes. For the Run 1 predictions, uncertainties are estimated from the envelope of the three tunes Z2*, P11, and P11 mpiHi, since Z2* eigentune variations were not available. This causes the one-sided variation in the Run 1 sample in the left diagram of Fig. 12. For the early Run 2 and Run 2 legacy predictions, the uncertainties are estimated from the eigentune variations provided by the PROFESSOR tuning package. For practical purposes, the eigentune variations are condensed in two effective variations: “up” and “down”. The “up” (“down”) variation is calculated using the positive (negative) differences in each bin between each eigentune and the central prediction of the nominal tune for the distributions used in the tuning procedure, added in quadrature. The resulting “up” and “down” variations are fit using the same fitting procedure that is used to obtain the nominal tune to obtain parameter sets for “up” and “down” that can be used in the uncertainty estimation in the nominal tune.

The underlying event, together with CR, has been one of the dominant systematic uncertainties for the most precise CMS top quark measurements. Therefore, more dedicated studies have been performed. UE activity in $t\bar{t}$ dilepton events is measured, for the first time, by CMS at $\sqrt{s} = 13$ TeV [144]. This is achieved by removing charged particles associated with the decay products of the $t\bar{t}$ event candidates as well as with removing pileup interactions for each event. Normalised differential cross sections in bins of the multiplicity and kinematic variables of charged-particle tracks from the UE in $t\bar{t}$ events are studied. The observables and categories

chosen for the measurements enhance the sensitivity to $t\bar{t}$ modelling, MPI, CR, and $\alpha_S(m_Z)$ in PYTHIA8. The normalised differential cross section measured as a function of $\sum p_T$ in the UE of $t\bar{t}$ -dilepton events is shown in Fig. 13 (left). The distribution is obtained after unfolding the background-subtracted data and normalising the result to unity. The ratio between different predictions and the data is shown in Fig. 13 (right). The comparisons indicate a fair agreement between the data and POWHEG [107–109] matched with PYTHIA8 using the CUETP8M2T4 tune, but disfavour the setups in which MPI and CR is switched off or the default configurations of POWHEG+HERWIG++ with the EE5C UE tune [145] and the CTEQ6 (L1) [146] PDF set, POWHEG+HERWIG7 [147, 148] with its default tune and the MMHT2014 (LO) [129] PDF set and SHERPA 2.2.4 [149] + OPENLOOPS (v1.3.1) [150] with a PS-based on the Catani–Seymour dipole subtraction scheme [151]. It has been furthermore verified that, as expected, the choice of the NLO ME generator does not impact significantly the expected characteristics of the UE by comparing predictions from POWHEG and MADGRAPH5_aMC@NLO, both interfaced with PYTHIA8. The UE measurements in $t\bar{t}$ events test the hypothesis of universality of UE at an energy scale of two times m_t , considerably higher than the ones at which UE models have been studied in detail. The results also show that a value of $\alpha_S(m_Z)^{\text{FSR}} = 0.120 \pm 0.006$ is consistent with these data.

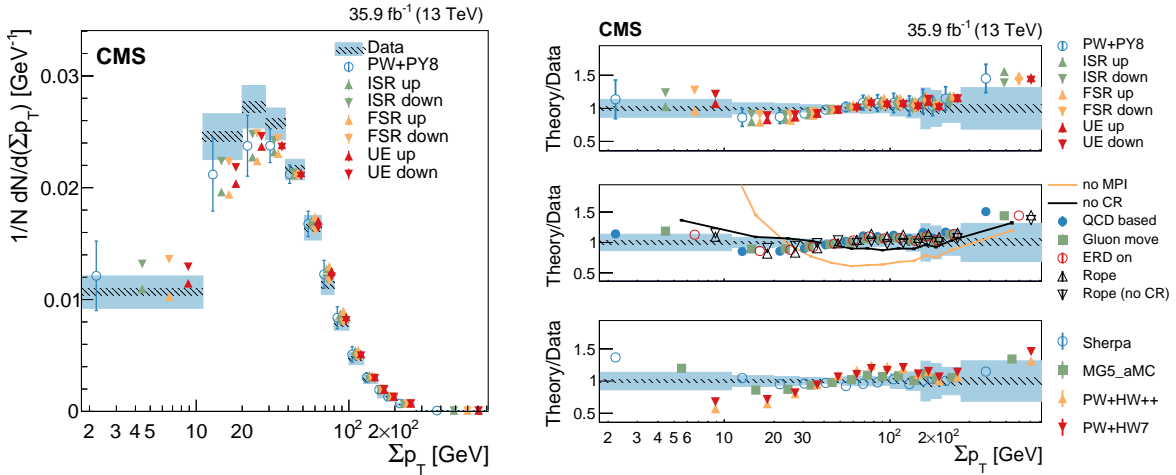


Figure 13: Left: Normalised differential cross section as a function of $\sum p_T$ of charged particles in the UE in $t\bar{t}$ events, compared to the predictions of different models. The data (coloured boxes) are compared to the nominal POWHEG+PYTHIA8 predictions and to the expectations obtained from varied $\alpha_S^{\text{ISR}}(m_Z)$ or $\alpha_S^{\text{FSR}}(m_Z)$ POWHEG+PYTHIA8 setups (markers). In the case of the POWHEG+PYTHIA8 setup, the error bar represents the envelope obtained by varying the main parameters of the CEUP8M2T4 tune, according to their uncertainties. This envelope includes the variation of the CR model, $\alpha_S^{\text{ISR}}(m_Z)$, $\alpha_S^{\text{FSR}}(m_Z)$, the h_{damp} parameter, and the μ_r/μ_f scales at the ME level. Right: The different panels show the ratio between each model tested and the data. The shaded (hatched) band represents the total (statistical) uncertainty of the data, while the error bars represent either the total uncertainty of the POWHEG+PYTHIA8 setup, or the statistical uncertainty of the other MC simulation setups. Figures taken from Ref. [144].

Colour reconnection In the limit of large number of colours N_c , quarks and gluons are assigned unique colour charges during the parton shower stage, and Lund string hadronisation describes the formation of hadrons from the colour string formed between each colour and anti-colour pair. Colour reconnection (CR) is a reconfiguration of the colour assignments, finding states with lower potential energy and allowing interactions between the partons from the hard collision and the UE, independent of their history of production. The CR uncertainty in

the Run 1 (2009–2013) analyses at $\sqrt{s} = 7$ and 8 TeV was calculated comparing two values of m_t , using predictions with the same UE tune with and without CR effects using the P11 tune [53]. However, the data completely disfavours the setups in which CR is switched off (as discussed, e.g. in Ref. [144]). Because of this, comparing setups with CR switched on and off may be nonoptimal for uncertainty calculations. Instead, a more realistic estimation of the CR uncertainty may be obtained by comparing different CR models that describe the data. In order to do this, we compare MPI-based, QCD-inspired, and gluon-move models in PYTHIA8 for which the details, and further references, can be found in Ref. [152]. In addition, the early resonance decay (ERD) [153], which allows top quark decay products to take part in CR, was investigated. This was first done in Ref. [61] for m_t measurements with $t\bar{t}$ events, and in Refs. [58, 67] with single top quark events, using the CUETP8M2T4 tune and the QCD-inspired and gluon-move CR models compared to the default CR model. New sets of tunes for two of the CR models implemented in PYTHIA8, QCD-inspired (CR1) and gluon-move (CR2), have been derived by CMS [152]. The new CMS CR tunes are based on $\sqrt{s} = 1.96$ TeV CDF, and 7 and 13 TeV CMS data. They are obtained by changing the CR model in the default CMS CP5 tune and retuning. These new CR tunes are tested against a wide range of measurements from LEP, CDF, and CMS. The new CMS CR tunes for MB and UE describe the data significantly better than the ones with the default parameters.

Figure 14 shows the evolution of colour reconnection uncertainties from Run 1 to Run 2 compared to the ATLAS measurement of the colour flow in $t\bar{t}$ events at 8 TeV [154]. Colour flow is measured using the jet pull angle, $\theta_p(j_1, j_2)/\pi$ where the jets j_1 and j_2 originate from the W boson decays and reconstructed using only charged constituents. Figure 15 (left) displays the colour flow in $t\bar{t}$ events measured in data, compared to POWHEG+PYTHIA8 predictions using different tune configurations: CP5, CP5-CR1, CP5-CR2, and these three tunes with the ERD option. Colour flow exhibits a high degree of sensitivity to the ERD option. Without ERD, W boson decay products are not colour reconnected, therefore the predictions of the tunes are closer to each other compared to the tunes with ERD for which CR modifies the angle between the

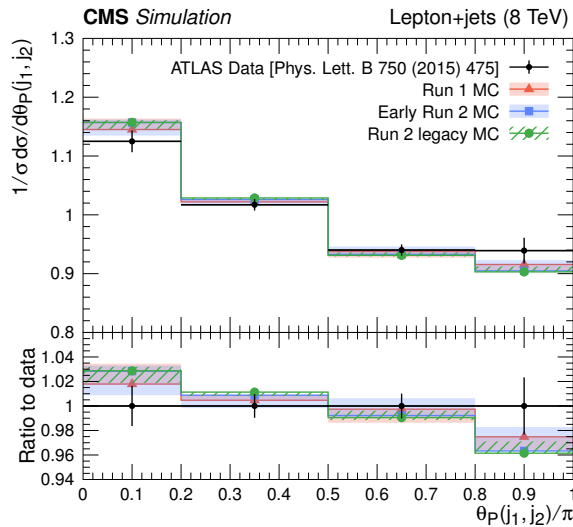


Figure 14: Measured distribution of the pull angle in $t\bar{t}$ events taken at 8 TeV recorded by ATLAS [154] (points with vertical error bars) compared to MC simulations for the generator setups used in Run 1, early Run 2, and Run 2 legacy analyses, presented by bands of different styles. The uncertainty bands illustrate the uncertainties resulting from colour reconnection effects, as estimated by variations described in the main text. The same variations are applied in CMS top quark mass measurements.

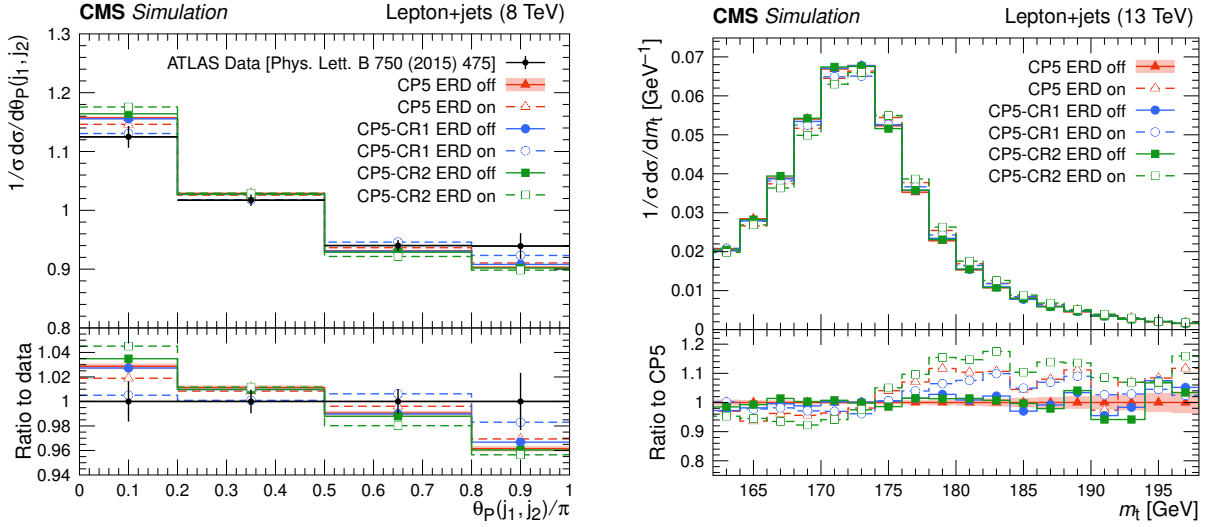


Figure 15: Normalised $t\bar{t}$ differential cross section for the pull angle between jets from the W boson in hadronic top quark decays, calculated from the charged constituents of the jets, measured by the ATLAS experiment using $\sqrt{s} = 8$ TeV data [154] to investigate colour flow (left). The predictions from POWHEG+PYTHIA8 using different tune configurations are compared with data. The statistical uncertainties in the predictions are represented by the coloured band and the vertical bars. The coloured band and error bars on the data points represent the total experimental uncertainty in the data. The invariant mass reconstructed from the hadronically decaying top quark candidates at the generator level (right). The coloured band and the vertical bars represent the statistical uncertainty in the predictions. Figures adapted from Ref. [152].

two jets visibly in Fig. 15. It can also be observed from this figure that CP5-CR1 (QCD-inspired) tune with ERD provides the best description of colour flow, and CP5-CR2 (gluon-move) tune with ERD displays the largest deviation from the data.

Figure 15 (right) displays the invariant mass of the hadronically decaying top quark constructed at the particle level, comparing theoretical predictions with different tunes. Although CR is one of the dominant uncertainties in top quark mass measurements, it is difficult to demonstrate its direct effect on the measurements. Therefore, here, we show comparisons at the particle level for which the differences are not diluted by detector and reconstruction effects. As for colour flow, the largest deviation from the prediction of the default CP5 tune is by the CP5-CR2 (gluon-move) tune with ERD. The deviation visible here is consistent with what is found in the top quark mass measurement at $\sqrt{s} = 13$ TeV [144] using the CUETP8M2T4 tune.

b quark fragmentation and semileptonic b hadron decays

In the Bowler–Lund fragmentation function [155] used in PYTHIA,

$$f(z) \propto \frac{1}{z^{1+r_b} m_T^2} (1-z)^a \exp\left(\frac{-bm_T^2}{z}\right), \quad (9)$$

the parameter r_b steers the distribution of the momentum fraction z carried by the b quark containing hadron (b hadron), defined as $z = E_{\text{b hadron}}/E_{\text{quark}}$. The parameter r_b is tuned to the distribution of $x_b = E_{\text{b hadron}}/E_{\text{beam}}$ measured in $Z \rightarrow b\bar{b}$ events at the LEP and SLC colliders [156–159] as a proxy for z . The parameter m_T is the transverse mass defined by $m_T = \sqrt{m^2 + p_T^2}$, where m is the mass and p_T is the transverse momentum of the b hadron. The

resulting modelling of the b quark fragmentation is compared to ALEPH data [156] in Fig. 16 (left) and described in more detail in the following paragraphs.

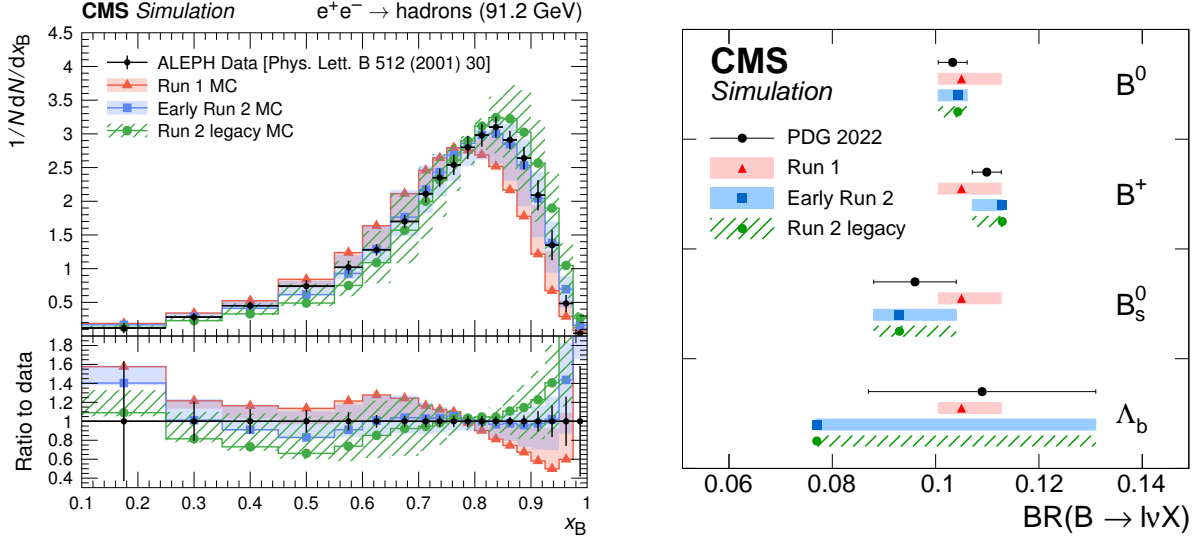


Figure 16: Distribution of the b quark fragmentation function normalised to the number of b hadrons measured by ALEPH in e^+e^- collisions at $\sqrt{s} = 91.2$ GeV [156] (black symbols with vertical error bars showing the total measurement uncertainties) compared to e^+e^- MC simulations for the generator setups used in Run 1, early Run 2, and Run 2 legacy analyses, presented by bands of different styles (left). The uncertainty bands are constructed around the default prediction and illustrate the b quark fragmentation uncertainties. The measured semileptonic branching ratios of b hadrons [1] (black symbols) compared to the values in the generator setups (coloured symbols) and their uncertainties, illustrated by shaded bands (right).

For the PYTHIA6 setup used in Run 1, the default value $r_b = 1.0$ leads to b quark fragmentation which appeared too soft, and was subsequently tuned to the x_b data provided by the ALEPH and DELPHI experiments. While the central Z2* prediction was left unchanged, the difference to the tuned $r_b = 0.591^{+0.216}_{-0.275}$ was taken as the systematic uncertainty, as it was larger than the uncertainties in the retuning.

In early Run 2, the PYTHIA8 fragmentation function was pre-tuned by the PYTHIA authors to $r_b = 0.855$, and only a minor change in the central value was found by tuning to ALEPH, DELPHI, OPAL, and SLD data: $r_b = 0.895^{+0.184}_{-0.197}$. In addition to the uncertainties in r_b , the Peterson fragmentation function [160]

$$f(z) \propto \frac{1}{z} \left(1 - \frac{1}{z} - \frac{\varepsilon_b}{1-z} \right)^{-2}, \quad (10)$$

with the tuned $\varepsilon_b = 3.27^{+3.98}_{-2.06} \times 10^{-3}$, was considered as an alternative parameterisation of the b quark fragmentation.

The CP5 tune used for Run 2 legacy samples featured a lower value of α_S for FSR which resulted in the prediction of a harder b quark fragmentation compared to the x_b data when using the default value of $r_b = 0.855$. While the central prediction was again left unchanged, the difference between the default value and the newly tuned $r_b = 1.056^{+0.193}_{-0.196}$ is considered as an uncertainty in addition to the variations of r_b and of the tuned parameter of Peterson fragmentation ($\varepsilon_b = 6.038^{+4.382}_{-2.466} \times 10^{-3}$), thus covering the data as well.

Semileptonic b hadron decays These constitute a source of unobservable neutrinos inside b jets, lowering the jet response with respect to the original b quark. For the Run 1 PYTHIA6 samples, a common semileptonic branching fraction was used for multiple b hadron species. The uncertainty in this was estimated from the envelope of the measured values and uncertainties for charged and neutral B mesons (B^\pm and B^0) reported by the PDG [1], and propagated to all b hadron species. For Run 2, PYTHIA8 includes decay tables specific to B^0 , B^\pm , B_s^0 , and Λ_b . These are simultaneously reweighted within their respective PDG uncertainties. By construction, the uncertainty bands become highly asymmetric in cases where the generator value is outside the PDG value with its uncertainty range. The values and uncertainties used for semileptonic branching fractions are shown in Fig. 16 (right).

2.5 Experimental uncertainties

The observables used in top quark mass measurements are sensitive to systematic effects related to the uncertainties in the calibration of the final-state objects used in the physics analyses. These include for example the calibration of the JES and JER, the measurement of the missing transverse momentum in the event, the efficiency in reconstructing and identifying leptons and jets originating from b quarks, the integrated luminosity of the considered data set (mostly relevant in absolute cross section measurements), and the average number of PU interactions. Correction factors are obtained by comparing data with simulation, and are used to correct the relevant quantities in simulated events.

The JES and JER corrections are derived as functions of the jet transverse momentum and pseudorapidity [101]. The measurements are obtained by exploiting momentum balance in dijet, γ +jet, Z+jet, and multijet events, and take into account systematic dependencies related to uniformity of the detector response, the number of pileup interactions, and residual differences between data and simulation. The absolute JES calibration is determined with the highest precision in Z+jet events at $p_T = 200$ GeV, where approximately 20% of the jets stem from gluons, 70% from light (u, d, s) quarks, and 10% from heavy (c and b) quarks. In order to extrapolate to different flavour compositions, notably pure b jets, the PYTHIA and HERWIG parton-shower generators are used with their respective hadronisation models, resulting in additional flavour-dependent jet energy uncertainties. The energy scale of central-rapidity jets with $p_T > 30$ GeV, which are the most relevant in the context of m_t measurements, is measured with a precision better than 1%, excluding the flavour-dependent components, while the total uncertainty varies between 1 and 3.5%, depending on the jet kinematics [101]. The energy resolution of particles that are not clustered in jets is also taken into account in the estimate of the missing transverse momentum in the event [161].

The efficiencies of electron and muon identification algorithms are corrected as functions of the lepton's (ℓ) kinematic quantities, making use of $Z \rightarrow \ell\ell$ events. This is commonly achieved by means of the so-called 'tag-and-probe' method, where one of the leptons is used to tag the $Z \rightarrow \ell\ell$ event, while the other is used as a probe to estimate the efficiency. In order to achieve a pure sample of neutral Drell–Yan events, the invariant mass of the lepton pair is required to be compatible with that of the Z boson. The corresponding uncertainties lie in the range 0.5–1.5% for muons and 2–5% for electrons [162, 163]. The energy scale of the leptons is also calibrated using $Z \rightarrow \ell\ell$ events and the corresponding uncertainty is propagated to the analyses. Typical values of the lepton scale uncertainties are 0.1 (0.3)% for electrons and 0.2 (0.3)% for muons in the barrel (endcap) [162, 163]. Leptons are also reconstructed at the trigger level and are used to pre-select events during data taking [164]. The trigger efficiencies are often estimated by each individual analysis, and are derived as functions of the lepton kinematics making use of an orthogonal data set. The corresponding uncertainty is then propagated to the final result,

and is often dominated by the statistical uncertainty of the utilised data set.

To select b jets, three working points are defined based on fixed light-quark jet misidentification probabilities of 10, 1, and 0.1%. Correction factors for the b tagging efficiencies and light jet misidentification probabilities are derived as functions of the jet kinematic properties and the generator-level flavour of the jet. Different calibration methods make use of independent b jet and light jet enriched regions, e.g. in muon-enriched inclusive jet production or $t\bar{t}$ phase spaces. The resulting corrections have uncertainties of 1–5% and 5–10% for b jets and light jets, respectively [102].

The PU in an event can also affect the calibration of the final-state objects. Simulated PU events are weighted according to Ref. [96] in order to match the PU distribution observed in data. For the reweighting procedure, PU-sensitive distributions, such as the number of vertices (N_{vtx}) are used to determine an effective value for the inelastic cross section. The remaining disagreement between data and MC simulation in the PU-sensitive observables is accounted for by an uncertainty, determined by varying the average number of PU interactions.

In the measurements, the uncertainty due to the integrated luminosity is also taken into account. The expected signal and background yields in simulation are normalised to the measured integrated luminosity and the related uncertainty is accounted for. For this purpose, the simulated distributions are obtained by varying the yields within the uncertainty in the integrated luminosity, which in Run 1 ranges between 2.2 and 2.6% [165, 166], and in Run 2 ranges between 1.2 and 2.5%, depending on the year of data taking [167–169]. The uncertainty in the integrated luminosity is particularly relevant in the context of indirect m_t extraction based on the measurements of the absolute $t\bar{t}$ cross sections.

2.6 General aspects of unfolding

The MC simulations described in Section 2.4 are generally processed through the CMS detector simulation based on GEANT4 [112] so that predicted and observed distributions for observables such as the reconstructed top quark mass can be compared at the reconstructed detector level. In order to compare to theoretical calculations at the parton or particle level (Section 2.7), an unfolding procedure has to be applied in order to remove experimental effects from the measured detector-level distributions. This is the case also for the Lagrangian top quark mass extraction, where m_t is obtained by comparing measured (differential) cross sections to standalone calculations.

Depending on the purpose of the measurement and on the details of the theoretical calculation, the unfolding can be performed to the particle or the parton level, discussed in detail in Section 2.7. Once the generator level in the simulation is defined, the unfolding procedure to either particle or parton level is identical. However, unfolding to parton level requires a larger degree of extrapolation from the measured distributions, and often comes at the cost of increased dependence on the modelling uncertainties. On the other hand, unfolding to particle level does not allow for a comparison of the obtained results to fixed-order calculations. In the following, general aspects of the unfolding problem are discussed, while the details of the unfolding methods are presented in the context of each particular analysis in the following sections. In the following, “generator level” refers to both parton and particle levels.

The goal of unfolding is the inference of a distribution corrected for experimental effects, such as resolution, misreconstruction, inefficiencies, and detector acceptance. The problem can be formulated as a maximum likelihood estimate. A generator-level distribution \mathbf{g} can be mapped to the corresponding detector-level distribution \mathbf{d} using the so-called response matrix R as

$\mathbf{d} = R\mathbf{g}$. The elements of the response matrix R_{ij} represent the probabilities to observe in bin i an event generated in bin j . The response matrices are typically obtained by using the simulated events and incorporate all experimental effects.

Assuming a Poisson distribution of the observed yields \mathbf{d}' , the likelihood for the unfolding problem can be written as

$$L = \prod_i \text{Poisson}\left(d'_i, \sum_j R_{ij}g'_j\right). \quad (11)$$

The maximum likelihood estimate for the unfolded distribution \mathbf{g}' can then be obtained as $\mathbf{g}' = R^{-1}\mathbf{d}'$. When detector resolution effects are larger or of comparable size to the desired binning in the unfolded distribution, the unfolding problem can become ill-conditioned. This means that small differences in \mathbf{d}' can lead to large effects on the evaluated \mathbf{g}' . In such cases, the statistical fluctuations in \mathbf{d}' can result in extremely large variances in estimates of \mathbf{g}' . However, in cases where R is sufficiently diagonal, this simple approach is the preferred method, as it provides an unbiased estimate of \mathbf{g}' .

When the approach described above is found to be ill-conditioned, the likelihood function in Eq. (11) can be extended by adding to $\chi^2 = -2\ln L$ a so-called regularisation term, such as [170, 171]

$$\tau^2(\mathbf{g}' - \mathbf{b})^T D^T D (\mathbf{g}' - \mathbf{b}), \quad (12)$$

where the quantity \mathbf{b} is set to the expected \mathbf{g} as estimated in the simulation, and the matrix D is the discrete second-order derivative operator. In this way, the regularisation term penalises solutions whose curvatures deviate from the expectation. The regularisation strength is controlled by the parameter τ , which is then optimised, e.g. by minimising the average global correlation coefficient or using the so-called L-curve scan [170, 171]. While such an approach prefers solutions that do not suffer from large oscillations, the obtained solution can be biased towards the simulation. Analyses making use of this approach therefore perform dedicated tests in order to verify that biases from regularisation are covered by the measurement uncertainties.

The unfolding procedure, especially in the presence of large off-diagonal components in the response matrix, can introduce large statistical correlations among the bins of the unfolded distribution. To take this into account, the statistical uncertainties in \mathbf{d}' and the systematic uncertainties in R are propagated to the final result in order to obtain the full covariance matrix of the measured \mathbf{g}' . Whenever a χ^2 is calculated between unfolded distributions and a theoretical prediction, e.g. for a fit extracting m_t , the full covariance matrix with all bin-to-bin correlations is utilised.

Several unfolding and regularisation procedures were proposed [170–177], which are not reviewed in the scope of this work. Different procedures may lead to differences in the unfolded results, and the most appropriate method is chosen in each analysis based on the nature of the unfolding problem to solve.

2.7 Particle- and parton-level top quark definitions

In the simulations at NLO, a finite width of the top quark is assumed. This is important for accurate modelling of the off-shell top quark production and the interference with background processes. However, in such simulations, the concept of a top quark particle is not precisely defined and is model-dependent. An unambiguous object can be constructed only using the kinematic quantities of the final-state particles without extra assumptions. A particle-level

top quark (or pseudo-top quark) can be defined using the final-state objects after hadronisation and is less affected by nonperturbative effects or acceptance corrections. Similar phase space definitions at the particle and detector levels lead to mitigation of the model dependence. More details of particle-level top quark definitions, maximising the correlation of reconstructed quantities with the parton-level definition, are discussed in Ref. [178] as a fundamental aspect of top quark measurements. The algorithms implemented in RIVET routines [179] that describe the measurements at particle level allow for testing the quality of top-quark modelling. The results reported in Ref. [178] suggest that the choice of a particle-level top quark definition is not universal and should be optimised depending on the production mode, the final state, or the variable and the phase space under study. Below, a typical particle-level definition used in the CMS top quark mass measurements is described.

Pseudo-top quarks are reconstructed from a sample of simulated lepton+jets $t\bar{t}$ events using a RIVET routine. These events fulfil specific criteria for leptons and jets to define top quarks at the particle level, similar to the ones described in Ref. [178] and summarised in Table 3. Using these definitions, the invariant mass of the charged lepton and neutrino is required to be within $75.4 < m_{\ell\nu} < 85.4$ GeV. In the jet clustering process, hadrons stemming from charm and bottom quark fragmentation, and regardless of the decay channel τ leptons are included, with their momenta scaled by a factor 10^{-20} in order for the jet properties to be preserved. These objects are referred to as “ghost” particles. A jet can encompass one or more “ghost” particles, which can be utilised for the purpose of flavour assignment and are included in the list of constituents of the jet. The events are required to include a minimum of four jets, which are defined in Table 3. Among these jets, at least two must be unequivocally associated to the fragmentation of bottom quarks, while the remaining two jets, i.e. light-quark jets, must not stem from the bottom quarks. A leptonically decaying top quark is reconstructed by combining the lepton, the neutrino, and one of the jets originating from a bottom quark in the event. A hadronically decaying top quark candidate is reconstructed by combining the other jet originating from a bottom quark with two remaining jets. Typically, it is required that the difference between the invariant masses of top quark reconstructed in the leptonic leg and the hadronic leg in an event must not exceed 20 GeV. Additionally, the invariant mass of the system of the two light-quark jets should fall within a window of 10 GeV, centred at 80.4 GeV. In situations where multiple combinations of jets satisfy these criteria, along with the charged lepton and neutrino, we employ a selection process to choose the most appropriate combination. This selection is based on two factors: the closeness of the invariant masses of the two top quark candidates to each other, and the closeness of the invariant mass of the light-quark jets to the W boson mass value of 80.4 GeV.

Parton-level object definitions allow for direct comparisons to fixed-order theoretical calculations and extractions of SM parameters. The kinematic properties of the top quarks and the $t\bar{t}$ system are defined with respect to the on-shell top quark and antiquark before decay, as given by the MC generator. The used definitions vary for Run 2 with respect to Run 1 analyses. For Run 1 analyses, top quarks were typically defined at the matrix-element level before radiation was added by the parton-shower algorithms. For measurements described in this review, the parton definition takes QED and QCD emissions as described by the parton shower generator and the intrinsic transverse momentum of the initial-state partons into account. As a consequence, the description depends on the generator used and is model-dependent. Measurements are usually performed in the visible phase space (within acceptance) and are extrapolated to the full (not measured) phase space using the MC simulation. In this procedure, the results are corrected for detector and hadronisation effects. Unless further specified, all presented parton-level results use the given Run 2 definition.

Table 3: Typical object definitions, and configuration parameters used for defining top quarks at the particle level (pseudo-top candidate). The pseudo-top candidate definition is not universal and may be optimised for the production mode, final state, the variable, and the phase space being studied. The details of particle-level top quark definitions adopted in the RIVET [179, 180] framework by CMS codes are described in Ref. [178] as a fundamental aspect for current and future measurements of differential production cross sections in both $t\bar{t}$ and single-top quark production.

Requirement	Comment
	<i>All final-state particles</i>
$ \eta < 5.0$	matching the detector coverage
	<i>Charged leptons, neutrinos, photons</i>
usePrompt=True	exclude those stemming from hadron decays
	<i>Leptons</i>
$R_\ell = 0.1$	radius in η - ϕ , used to dress the leptons
$p_T(\ell) > 15 \text{ GeV}, \eta(\ell) < 2.5$	matching the tracker coverage (e/μ from $\tau \rightarrow e/\mu$ are also accepted)
	<i>Jets</i>
excludePromptLeptons=True	use leptons only from hadron decays
$R = 0.4 (0.8)$	anti- k_T jet cone parameter for resolved (boosted) jets
$p_T > 30 (400) \text{ GeV}, \eta < 2.4 (2.4)$	selection for resolved (boosted) jets

2.8 Top quark mass definitions

Due to the quantum aspects of the top quark related to its colour and short lifetime, m_t is not a unique physical parameter but needs to be defined through renormalisation schemes within quantum field theory. The top quark mass (and likewise the masses of all other quarks) therefore plays a role similar to the couplings of the SM Lagrangian. There are many possibilities to define m_t , but theoretical control can be maintained only when renormalisation schemes, defined in perturbation theory, are employed such that the values of m_t in different schemes can be related to each other reliably [181, 182] and m_t -dependent perturbative cross section predictions can be expressed in these schemes. Formally, theoretical predictions for (differential) cross sections are independent of a choice of renormalisation scheme. However, the fact that these theoretical predictions can be made only at some finite truncation order in perturbation theory entails that for a particular observable only certain scheme choices are adequate, so that the scheme provides an absorption of sizeable quantum corrections in the m_t dependence. For example, the impact of the choice of renormalisation scheme for m_t is very large in the theoretical predictions for single Higgs boson or Higgs boson pair production [183], expected to be measured with high precision in the upcoming HL-LHC era.

Top quark mass renormalisation schemes, defined within perturbation theory, include the pole mass scheme, the modified minimal-subtraction ($\overline{\text{MS}}$) scheme, and the low-scale short-distance mass (MSR) scheme [184]. The $\overline{\text{MS}}$ and MSR schemes furthermore depend on the renormalisation scales μ_m and R , respectively.

The pole mass m_t^{pole} is defined as the pole of the top quark propagator in the approximation of a free particle. It is used most frequently for theoretical calculations of the top quark production cross sections in fixed-order perturbation theory. The $\overline{\text{MS}}$ scheme implies m_t as a function of the mass-renormalisation scale μ_m , $m_t(\mu_m)$, sometimes also denoted as $\overline{m}_t(\mu_m)$. At the scale of

the mass itself, $\overline{m}_t(\overline{m}_t)$ is also referred to as $m_t(m_t)$. The MSR scheme operates with $m_t^{\text{MSR}}(R)$.

Because its colour does not prohibit the definition of the top quark as an asymptotic state within perturbation theory, m_t^{pole} can be formally defined at any order [185, 186]. However, the concept of an asymptotic “top particle” is unphysical because it assumes that the virtual QCD self energy quantum corrections (absorbed into the mass) can be distinguished from the real radiation effects at arbitrarily small scales μ , as shown in the very left part of Fig. 17. This unphysical aspect entails that m_t^{pole} suffers from an intrinsic renormalon ambiguity of 110–250 MeV [187, 188]. The $\overline{\text{MS}}$ and MSR masses do not have this ambiguity. Their scales μ_m and R represent the energy scales, above which the self-energy corrections are absorbed into the mass parameter. Below these scales, the real and virtual quantum corrections are treated as unresolved, as shown by the other parts of Fig. 17. This more physical treatment of QCD self-energy corrections avoids the renormalon ambiguity.

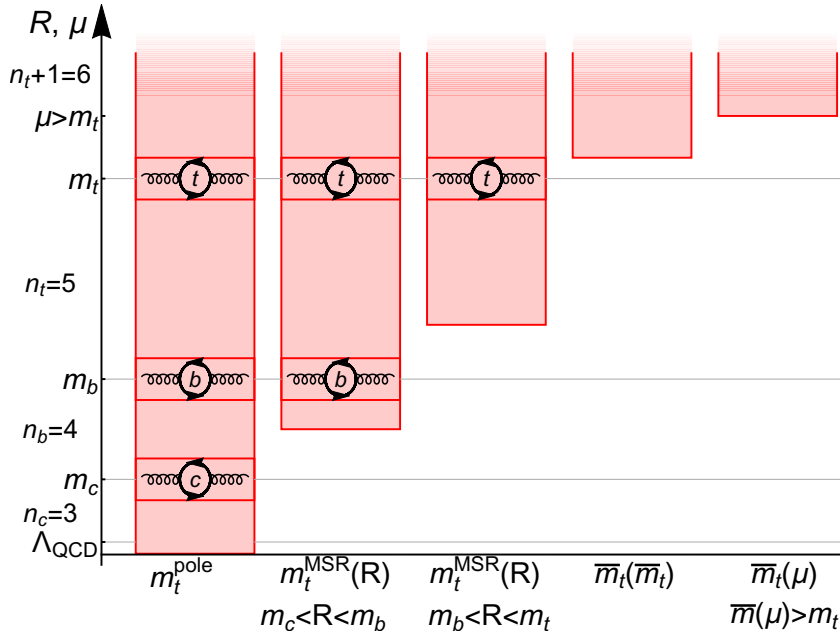


Figure 17: Momenta of the self-energy quantum corrections in the top quark rest frame (red segments), absorbed into the top quark mass parameter in the pole (very left), MSR and $\overline{\text{MS}}$ schemes for different mass renormalisation scales with respect to the charm and bottom quark masses. The red segments extend to infinite momenta for all top quark mass schemes. The loops inside the red segments illustrate contributions of the virtual top, charm, or bottom quark loops, and n_q stands for the number of quarks lighter than quark q , indicating that the MSR and the $\overline{\text{MS}}$ masses run with different flavour numbers between flavour thresholds, as does the strong coupling constant α_s . Figure taken from Ref. [188].

The freedom in the choice of μ_m or R allows to set them equal to the dynamical momentum scale of the m_t dependence of an observable. This dynamical scale is related to the size of the typical momenta involved in the quantum corrections to this m_t dependence. For example, in the case of a reconstructed top quark invariant mass resonance, where the m_t sensitivity arises from the shape and position of the peak, this dynamical scale can be as small as the top quark width Γ_t , depending on the reconstruction procedure. On the other hand, for an inclusive total cross section, the dynamical scale is at least of the order of m_t or the energy of the hard interaction. In general, the more inclusive the observable, the larger the dynamical

scale of the m_t dependence. An adequate choice of μ_m or R can reduce the size of higher order perturbative corrections and make the theoretical predictions, which are always based on truncated perturbative expansions, more reliable. As far as QCD corrections are concerned, m_t^{pole} is about 9 GeV larger than the $\overline{\text{MS}}$ mass $m_t(m_t)$, which is a quite sizeable effect. This conversion, however, suffers from the renormalon ambiguity mentioned in the previous paragraph. The renormalon-free mass schemes MSR and $\overline{\text{MS}}$, for any choice of their renormalisation scales, can be related to each other with a precision of about 10–20 MeV [184]. Libraries for numerical conversion of different top quark mass schemes are provided in Refs. [181, 182].

While the $\overline{\text{MS}}$ mass $\overline{m}_t(\mu_m)$ is suitable for dynamical scales $\mu_m > m_t$, the choice of $m_t^{\text{MSR}}(R)$ is preferred for smaller dynamical scales $R < m_t$. For $R = m_t(m_t)$ the MSR mass is approximately equal to $m_t(m_t)$, and in the limit of vanishing R , the MSR mass approaches the pole mass, $m_t^{\text{MSR}}(R) \xrightarrow{R \rightarrow 0} m_t^{\text{pole}}$. However, this limit is formal since the MSR mass can only be used for R scales that are still in the realm of perturbation theory. For small R values of 1–3 GeV, shown by the second bin in Fig. 17, the MSR mass can serve as a renormalon-free proxy for the pole mass. A proper choice of the scheme or of the renormalisation scales is straightforward in the context of analytic theoretical predictions, e.g. through the analysis of logarithmic terms in the perturbative coefficients and convergence studies (as demonstrated, e.g. in Refs. [189, 190]). However, corresponding analyses in the context of purely numerical predictions, which is the case for the calculations for top quark production at the LHC, are more involved and also need to account for correlations with other input quantities and renormalisation scales related, e.g. to the strong coupling and PDFs.

In the experimental measurements that rely entirely on MC simulations, such as the direct m_t measurements, indeed the top quark mass parameter m_t^{MC} of the MC generator is measured. For an ideal MC generator, having at least a next-to-leading-logarithmic parton shower and a hadronisation description determined rigorously from QCD, m_t^{MC} would constitute a well-defined mass scheme that depends on the parton shower implementation and the value of the infrared cutoff scale of the parton shower evolution [191]. However, due to the theoretical limitations of state-of-the-art MC generators, the interpretation of m_t^{MC} in terms of Lagrangian m_t is still limited and contains perturbative as well as nonperturbative uncertainties, as discussed in more detail in Section 3.3.

With the continuously increasing precision of the experimental analyses, the subtle aspects of a scheme choice for m_t , its proper interpretation and respective consistency of the results become increasingly relevant. In the works on m_t determination carried out by the CMS Collaboration so far, measurements of m_t^{MC} , m_t^{pole} , and $\overline{m}_t(\mu_m)$ have been provided.

3 Direct measurements from top quark decays

The top quark mass can be measured directly using the top quark decay products. This section focuses mainly on two direct measurements. One is performed in the lepton+jets channel of $t\bar{t}$ production using a profile likelihood method and the other analyses single top final states using a template method.

3.1 Top quark mass measurements in top quark pair events

In the direct mass measurements, m_t -dependent templates are fit to data to measure m_t directly. These templates are derived from simulations of different top quark mass values. They are described by probability density functions $p(x|m_t, \vec{\theta})$, where x is an observable and $\vec{\theta}$ a list

of possible additional fit parameters. The considered observable should have a strong dependence on m_t . In the CMS measurements, this is usually the invariant mass of the top quark decay products in the lepton+jets and all-jets channels and the invariant mass of a lepton and a b-tagged jet in the dilepton channel.

In the lepton+jets channel, a second observable was already used in the measurements at the Tevatron: the invariant mass of the two jets assigned to the decay products of hadronically decaying W bosons. In $t\bar{t}$ events, the position of the maximum of the invariant mass distribution is expected to be near the precisely known W boson mass and depends strongly on the calibration of the reconstructed jets. This allows the introduction of an additional jet energy scale factor (JSF) in the probability density function to reduce the impact of the uncertainty in the the JES corrections on the measurement. An ideogram method was utilised in the Run 1 and early Run 2 measurements, while a profile likelihood method was applied in the latest CMS measurement using lepton+jets final states.

3.1.1 Ideogram method in the lepton+jets channel

Besides the JES, the statistical uncertainty was a major uncertainty in the measurement of m_t due to the limited data sample sizes in the measurements at the Tevatron and the early CMS measurements. Hence, a couple of steps were taken to get the best m_t sensitivity from each $t\bar{t}$ candidate event, as described in the following.

At first, the kinematic fit described in the previous chapter is employed. The W boson mass constraint enforced in the fit drastically improves the estimates of the momenta of the two quarks from the W boson decay. In addition, the top quark mass from the kinematic fit, m_t^{fit} , includes information from the lepton+jets decay branch due to the requirement of equal invariant masses for both top quark candidates. An alternative to the kinematic fit and m_t^{fit} is to compute the invariant mass of the hadronically decaying top quark, m_t^{reco} , from the reconstructed momenta, i.e. before the kinematic fit, of the assigned jets. For correct permutations, where the jets can be matched to corresponding partons, the resolution of m_t^{fit} is 30% better than the resolution of m_t^{reco} . For the measurements discussed in this section, only permutations with a χ^2 goodness-of-fit probability $P_{\text{gof}} > 0.2$ are used to increase the fraction of well-reconstructed and correctly assigned jets. Figure 18 shows the improvements in the mass resolution and the fraction of permutations with correctly assigned jets obtained for the measurement using data collected at $\sqrt{s} = 7$ TeV in Run 1 [48], corresponding to an integrated luminosity of 5.0 fb^{-1} .

If one assumes that the peak position or the average is used as an estimator of m_t , the statistical uncertainty in the measurement scales with σ/\sqrt{N} where σ is the standard deviation of the observable and N is the number of events. Hence, an improvement in the resolution by 30% is equivalent to an increase in the number of events in the peak by a factor of two. However, this simplistic approach only works if the jets are correctly assigned to the decay products. As illustrated in Fig. 18 (left), a large fraction of the events are in the unmatched category, i.e. at least one of the selected jets cannot be matched to a parton from the top quark decay. These unmatched permutations dilute the measurement and are the reason for the $P_{\text{gof}} > 0.2$ selection, which helps to effectively suppress their contribution.

The use of the ideogram method [48, 192] was the second step in order to reduce the statistical uncertainty in the direct m_t measurements. The details of the procedure outlined below are identical with the approach taken in the Run 1 CMS measurement [53] and the first Run 2 CMS measurement [61]. The observable used to measure m_t is the mass m_t^{fit} evaluated after applying the kinematic fit. It takes the reconstructed W boson mass m_W^{reco} , before it is constrained

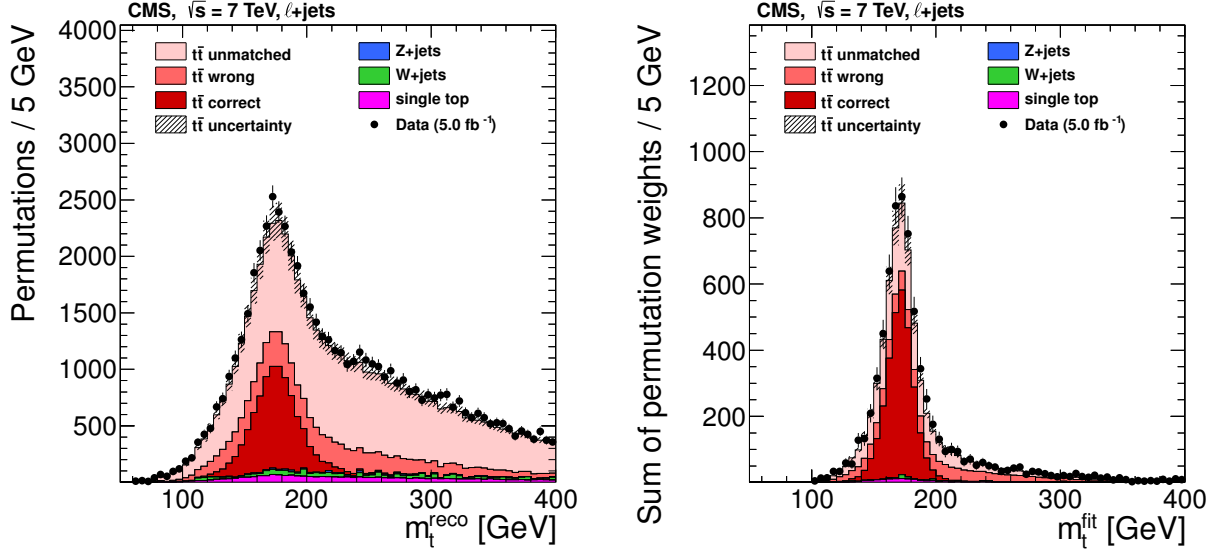


Figure 18: Left: The distribution of the reconstructed top quark mass m_t^{reco} using the jet assignment from the kinematic fit, but the reconstructed jet momenta and no addition selection. Right: The distribution of the top quark mass from the kinematic fit m_t^{fit} with the $P_{\text{gof}} > 0.2$ selection. Data are shown as points with vertical error bars showing the statistical uncertainties. The coloured histograms show the simulated signal and background contributions. The simulated signal is decomposed into the contributions from correct, wrong, or unmatched permutations as introduced in Section 2.3. The uncertainty in the predicted $t\bar{t}$ cross section is indicated by the hatched area. In the figures, the default value of $m_t^{\text{gen}} = 172.5$ GeV is used. The reduction of permutations with wrongly assigned jets and the much narrower peak are clearly visible in the m_t^{fit} measurement. Figures taken from Ref. [48].

by the kinematic fit, as an estimator for measuring the additional JES factor to be applied in addition to the standard CMS JES corrections. An ideogram is the likelihood per event for certain values of m_t and JSF. It is the weighted sum of the probabilities of all selected permutations of an event: $\sum_i P_{\text{gof},i} p(m_{t,i}^{\text{fit}}, m_{W,i}^{\text{reco}} | m_t, \text{JSF})$, where $p(m_{t,i}^{\text{fit}}, m_{W,i}^{\text{reco}} | m_t, \text{JSF})$ is a probability density function obtained from simulation and $P_{\text{gof},i}$, $m_{t,i}^{\text{fit}}$, and $m_{W,i}^{\text{reco}}$ are the values of the respective variable of the i -th permutation. As the momenta of the jets from the W boson decay are strongly modified in the kinematic fit by the mass constraint $m_W^{\text{fit}} = 80.4$ GeV, m_t^{fit} and m_W^{reco} can be assumed as independent random variables and the ansatz $P(m_{t,i}^{\text{fit}}, m_{W,i}^{\text{reco}} | m_t, \text{JSF}) = P(m_{t,i}^{\text{fit}} | m_t, \text{JSF}) P(m_{W,i}^{\text{reco}} | m_t, \text{JSF})$ is used. The distributions of m_t^{fit} and m_W^{reco} are obtained from simulation for different m_t and JSF values. From these distributions, the probability density functions $P(m_{t,i}^{\text{fit}} | m_t, \text{JSF})$ and $P(m_{W,i}^{\text{reco}} | m_t, \text{JSF})$ are derived separately for the three permutation cases, i.e. correct, wrong, and unmatched. Analytical functions are used to describe the shape of the distributions. The parameters of these functions are themselves linear functions of m_t and JSF and the product of the two.

The most likely m_t and JSF values are obtained by minimising $-2 \ln[\mathcal{L}(\text{sample} | m_t, \text{JSF})]$. With an additional probability density function $P(\text{JSF})$, the likelihood $\mathcal{L}(\text{sample} | m_t, \text{JSF})$ is defined as:

$$\mathcal{L}(\text{sample} | m_t, \text{JSF}) = P(\text{JSF}) \times \prod_{\text{events}} \left(\sum_{i=1}^n P_{\text{gof}}(i) \left(\sum_j f_j P_j(m_{t,i}^{\text{fit}} | m_t, \text{JSF}) P_j(m_{W,i}^{\text{reco}} | m_t, \text{JSF}) \right) \right)^{w_{\text{evt}}}, \quad (13)$$

where n denotes the number of the (at most four) permutations in each event, j labels the permutation cases, and f_j represents their relative fractions. The event weight $w_{\text{evt}} = c \sum_{i=1}^n P_{\text{gof}}(i)$ is introduced to reduce the impact of events without correct permutations, where c normalises the average w_{evt} to 1. Examples of ideograms from the Run 1 CMS measurement [53] can be seen in Fig. 19.

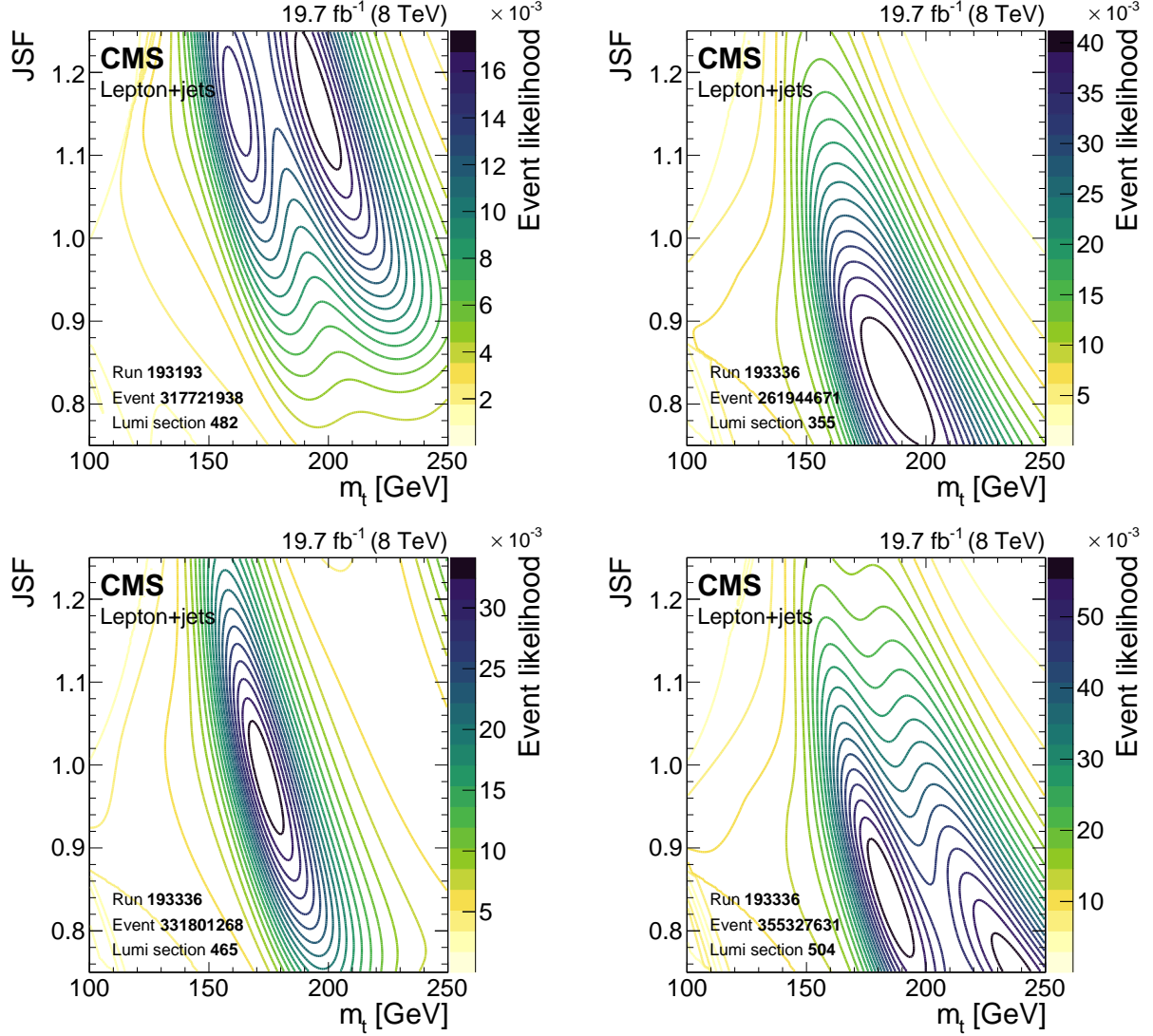


Figure 19: Contours of the likelihood of m_t and JSF values for single events in the Run 1 CMS measurement [53].

As background contributions are neglected in the derivation of the probability density functions, the measurement needs to be calibrated. This is done with pseudo-experiments where events are drawn from signal samples generated for different top quark mass values, m_t^{gen} , and background samples according to their expected occurrence in data. Usually, the corrected bias amounts to 0.5 GeV for m_t . Corrections for the statistical uncertainty reported by the method are also derived from pseudo-experiments and have a size of 5%.

The systematic uncertainties in the final measurement are determined from pseudo-experiments. Events are drawn from samples where the parameters in the simulation that are related to a systematic uncertainty are changed by ± 1 standard deviation. Then, the pseudo-data is fit with the ideogram method yielding m_t and JSF values for the up and down varied samples

for each systematic uncertainty source. These values are compared to the values for the default simulation and the absolute value of the largest observed shifts in m_t and JSF are assigned as systematic uncertainties. The only exception to this is if the statistical uncertainty in the observed shift is larger than the value of the calculated shift. In this case the statistical uncertainty is taken as the best estimate of the uncertainty in the parameter. This (over)cautious approach guarantees that systematic effects that are known from particle-level studies to have a sizeable impact on m_t are not underestimated because of finite sample sizes.

Different choices are made for the probability density function $P(\text{JSF})$ in the fit. When the JSF is fixed to unity, the $P_j(m_{W,i}^{\text{reco}}|m_t, \text{JSF})$ can be approximated by a constant, as they barely depend on m_t . Hence, only the m_t^{fit} observable is used in the fit, and this approach is called the 1D analysis. The approach with an unconstrained JSF is called the 2D analysis. Finally, in the hybrid analysis, the prior $P(\text{JSF})$ is a Gaussian centred at one. Its width depends on the relative weight w_{hyb} that is assigned to the prior knowledge on the JSF, $\sigma_{\text{prior}} = \delta\text{JSF}_{\text{stat}}^{2\text{D}} \sqrt{1/w_{\text{hyb}} - 1}$, where $\delta\text{JSF}_{\text{stat}}^{2\text{D}}$ is the statistical uncertainty in the 2D result of the JSF.

The optimal value of w_{hyb} is determined from pseudo-experiments. The constraint on the JSF gets stronger, the lower the experimental uncertainty in the JES is. However, it is important to note that the introduction of the JSF reduces not only experimental uncertainties, but also all modelling uncertainties that affect the m_t^{fit} and m_W^{reco} distributions similarly to a JES change. In other words, the effects of these uncertainties would shift the position of the W boson and top quark peaks in the same direction, and are mitigated by a corresponding change in the JSF. Hence, the optimisation of the hybrid approach also results in a strong reduction of most modelling uncertainties. This approach leads to the most precise single measurement of m_t with Run 1 data of $m_t = 172.35 \pm 0.16$ (stat+JSF) ± 0.48 (syst) GeV [53]. Its application to Run 2 data resulted in $m_t = 172.25 \pm 0.08$ (stat+JSF) ± 0.62 (syst) GeV [61] where the larger systematic uncertainty stems from the changes in the evaluation of the modelling uncertainties described in Section 2.4.

Although the ideogram method has proven itself to be very successful, its implementation has some drawbacks: the neglect of the background in the probability density function and the way the ideograms are constructed require an iterative calibration of estimated mass values with pseudo-experiments. In addition, the evaluation of the systematic uncertainties via pseudo-experiments is computationally challenging with the growing number of considered sources. However, the main concern is the choice of the hybrid weight and the fact that the JSF parameter reduces not just the jet energy correction uncertainties but also many modelling uncertainties in an opaque way. The large data sample collected during Run 2 makes the use of complicated ideograms that achieve the best statistical precision unnecessary.

3.1.2 Profile likelihood method

To overcome the shortcomings of the ideogram method, a profile likelihood method with nuisance parameters was chosen for the latest top quark mass measurement [71]. The incorporation of all systematic effects via nuisance parameters has multiple advantages. There is no need anymore to perform dedicated pseudo-experiments for each systematic effect. All parameters are determined by the fit to give the best agreement with data and precision and, hence, no additional optimisation of an external parameter such as the hybrid weight in the ideogram method is needed. The nuisance parameter values and uncertainties after the fit show directly how each uncertainty is constrained by the measurement procedure.

However, there are some differences between a direct top quark mass measurement and the

application of the profile likelihood method in other analyses. The main difference is that m_t is estimated from the shape of the data distributions and not from the rate in distinct phase space regions as is done to measure cross sections. The most characteristic feature of the m_t^{fit} distribution is the position of the top quark mass peak and this is not easily described by changes in the content of coarse bins in m_t^{fit} . Instead of the (linear) interpolation of bin contents, i.e. vertical morphing, used in most implementations of the profile likelihood method, it is desirable to still use analytic functions to describe the m_t^{fit} distribution where one parameter is directly the peak position. The probability density function for the m_t^{fit} histograms is approximated by the sum of a Voigt profile (the convolution of a relativistic Breit–Wigner distribution and a Gaussian distribution) for the correctly reconstructed $t\bar{t}$ candidates and Chebyshev polynomials for the remaining event contributions. Unlike the previous measurements with the ideogram method, this ansatz includes the effect of backgrounds and does not need an iterative calibration of the estimator with pseudo-experiments. For other distributions, which do not feature a narrow peak, a binned probability density function is used that returns the relative fraction of events per histogram bin. Here, eight bins are used for each observable and the widths of the bins are chosen so that each bin has a similar number of selected events for the default simulation ($m_t^{\text{gen}} = 172.5 \text{ GeV}$). The dependence of bin contents of the first seven bins on m_t and the nuisance parameters is implemented with vertical morphing. The content of the eighth bin is given by the normalisation to data.

A custom implementation was also developed for the inclusion of the effects of finite sample sizes [193, 194]. Random fluctuations in the shapes predicted for a systematic variation can cause overly strong constraints on the corresponding nuisance parameter. This was seen in the first application of a profile likelihood method for a direct m_t measurement in the dilepton channel [63]. Already in the measurements with the ideogram method, the statistical uncertainties in the samples used for estimation of the systematic effects were sizeable, and a special treatment was introduced to include them to avoid a possible underestimation of the systematic uncertainties. However, the profile likelihood method introduces a clear bias towards too small systematic uncertainties from finite sample sizes. In the dilepton analysis described in Ref. [63], the size of this effect is estimated by repeating the measurement with alternative simulation templates representing ± 1 standard deviation variations of a systematic source that are varied within their Poisson uncertainties. In the lepton+jets analysis, additional nuisance parameters were introduced directly into the likelihood that account for the statistical uncertainty. The implementation is different from the approach of Refs. [193, 194] and the formulas can be found in Ref. [71]. This approach is validated with pseudo-experiments. Here, multiple steps are performed for each pseudo-experiment. At first, new probability density functions that describe how the observables depend on m_t and the nuisance parameters are derived using templates from simulated samples that are varied within their statistical uncertainties. Then m_t is drawn from a uniform distribution with a mean of 172.5 GeV and a standard deviation of 1 GeV. The values of the nuisance parameters for systematic effects are drawn from standard normal distributions. For these parameter values, pseudo-data are generated from the new probability density functions. Then, a fit with the same probability density functions that are applied to the collider data is performed on the pseudo-data. The fit is performed twice, once with and once without the additional nuisance parameters that account for the finite sample sizes. Figure 20 shows the distribution of the differences between the measured and generated m_t values, divided by the uncertainty reported by the fit for both cases. A nearly 40% underestimation of the measurement uncertainty can be seen for the case without the additional nuisance parameters, while consistency is observed for the method that is employed on data. This demonstrates that the limited sample sizes have a big effect on the total uncertainty of the measurement and that the additional nuisance parameters can account for these effects.

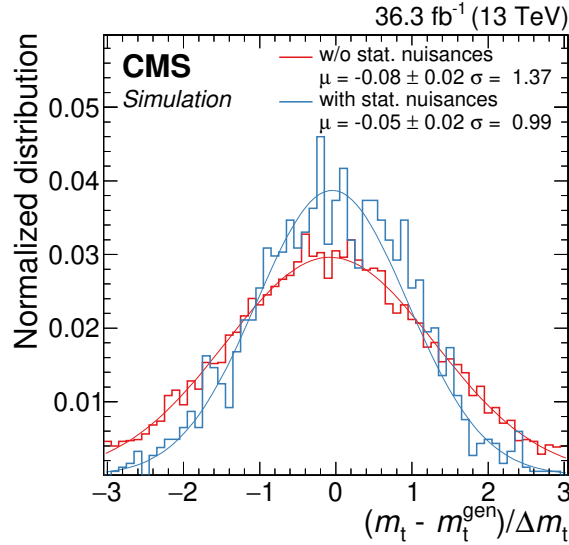


Figure 20: The difference between the measured and generated m_t values, divided by the uncertainty reported by the fit from pseudo-experiments without (red) or with (blue) the additional nuisance parameters for the finite sample sizes. Also included in the legend are the μ and σ parameters of Gaussian functions (red and blue lines) fit to the histograms. Figure taken from Ref. [71].

3.1.3 Observables and systematic uncertainties

In the lepton+jets channel, events are selected with exactly one isolated electron or muon and at least four jets. Only the four jets with the highest transverse momentum are used in the kinematic fit. Exactly two b-tagged jets are required among the four selected jets. In the latest CMS measurement [71] using a data set corresponding to an integrated luminosity of 36.3 fb^{-1} at $\sqrt{s} = 13 \text{ TeV}$ [167], this yields 287 842 (451 618) candidate events in the electron+jets (muon+jets) decay channel.

The goodness-of-fit probability, P_{gof} , computed from the χ^2 value of the kinematic fit is used to determine the most likely parton-jet assignment. For each event, the observables from the permutation with the highest P_{gof} value are the input to the m_t measurement. In addition, the events are categorised as either $P_{\text{gof}} < 0.2$ or $P_{\text{gof}} > 0.2$, matching the value chosen in Ref. [61]. Requiring $P_{\text{gof}} > 0.2$ yields 87 265 (140 362) $t\bar{t}$ candidate events in the electron+jets (muon+jets) decay channel and has a predicted signal fraction of 95%. This selection improves the expected fraction of correctly reconstructed events from 20 to 47%.

The distributions of the two main observables for the m_t measurement in the lepton+jets channel are shown in Fig. 21. A large part of the depicted uncertainties in the expected event yields are correlated. Hence, the overall normalisation of the simulation agrees with the data within the uncertainties, although the simulation predicts 10% more events in all distributions. For the final measurement, the simulation is normalised to the number of events observed in data.

For events with $P_{\text{gof}} > 0.2$, the mass of the top quark candidates from the kinematic fit, m_t^{fit} , shows a very strong dependence on m_t and is the main observable in this analysis. For events with $P_{\text{gof}} < 0.2$, the invariant mass of the lepton and the b-tagged jet assigned to the top quark, decaying in lepton+jets channel, $m_{\ell b}^{\text{reco}}$ is used. For most $t\bar{t}$ events, a low P_{gof} value is caused by assigning a wrong jet to the W boson candidate, while the two b-tagged jets are the correct candidates for the b quarks. Hence, $m_{\ell b}^{\text{reco}}$ preserves a good m_t dependence and adds

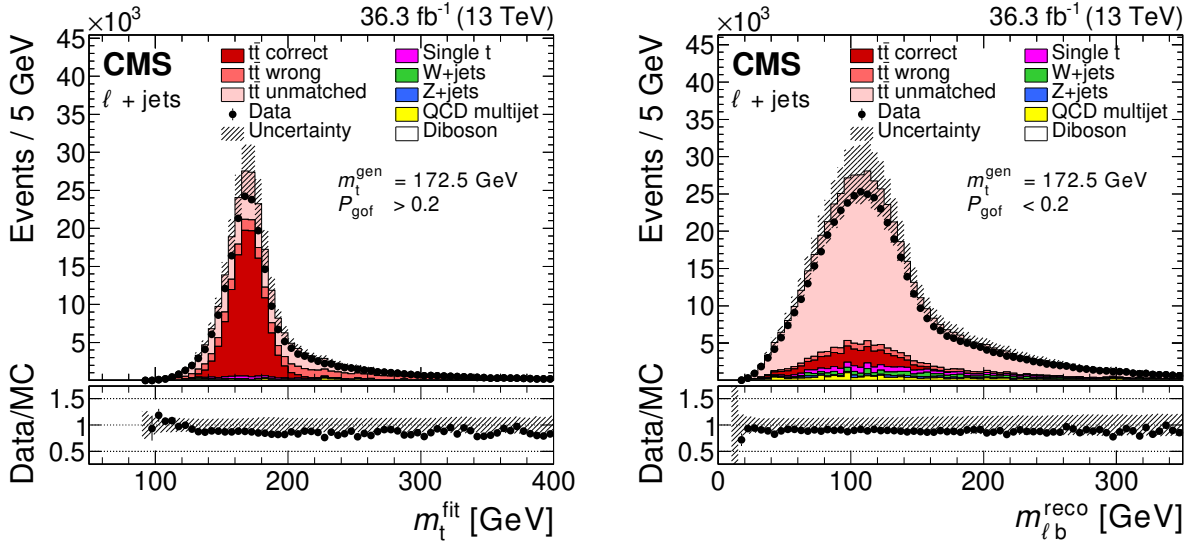


Figure 21: The distributions of the top quark mass from the kinematic fit for the $P_{\text{gof}} > 0.2$ category (left) and of the invariant mass of the lepton and the jet assigned to the top quark decaying in the lepton+jets channel for the $P_{\text{gof}} < 0.2$ category (right). Data are shown as points with vertical error bars showing the statistical uncertainties. The coloured histograms show the simulated signal and background contributions. The simulated signal is decomposed into the contributions from correct, wrong, or unmatched permutations, as introduced in Section 2.3. The uncertainty bands contain statistical uncertainties in the simulation, normalisation uncertainties due to the integrated luminosity and cross section, JES correction, and all uncertainties that are evaluated from event-based weights. A large part of the depicted uncertainties in the expected event yields are correlated. The lower panels show the ratio of data to the prediction. In the figures, the default value of $m_t^{\text{gen}} = 172.5 \text{ GeV}$ is used. Figures taken from Ref. [71].

additional sensitivity to the measurement. While a similar observable has routinely been used in m_t measurements in the dilepton channel [63, 195], this is the first application by CMS of this observable in the lepton+jets channel.

Additional observables are used in parallel for the mass extraction to constrain systematic uncertainties. In previous analyses by the CMS Collaboration in the lepton+jets channel [53, 61], the invariant mass of the two non-b-tagged jets before the kinematic fit, m_W^{reco} , has been used together with m_t^{fit} , mainly to reduce the uncertainty in the JES and the jet modelling. As m_W^{reco} is only sensitive to the energy scale and modelling of light-flavour jets, two additional observables are employed to improve sensitivity to the scale and modelling of jets originating from b quarks. These are the ratio $m_{\ell b}^{\text{reco}}/m_t^{\text{fit}}$ as well as the ratio of the scalar sum of the transverse momenta of the two b-tagged jets (b_1, b_2) and the two non-b-tagged jets (q_1, q_2), $R_{bq}^{\text{reco}} = (p_T^{b_1} + p_T^{b_2}) / (p_T^{q_1} + p_T^{q_2})$. The distributions of all three additional observables are shown in Fig. 22. While m_t^{fit} and m_W^{reco} have been used by the CMS Collaboration in previous analyses in the lepton+jets channel, $m_{\ell b}^{\text{reco}}/m_t^{\text{fit}}$ and R_{bq}^{reco} are new additions. However, R_{bq}^{reco} has been used in the lepton+jets channel by the ATLAS Collaboration [196, 197].

The value of m_t is determined with the profile likelihood fit for different sets of data histograms. As shown in Table 4, the 1D measurement set fits just the m_t^{fit} distribution for events with $P_{\text{gof}} > 0.2$ and the 2D measurement set simultaneously fits this distribution and the m_W^{reco} for events with $P_{\text{gof}} > 0.2$. These sets allow the comparison with the analyses using the ideogram

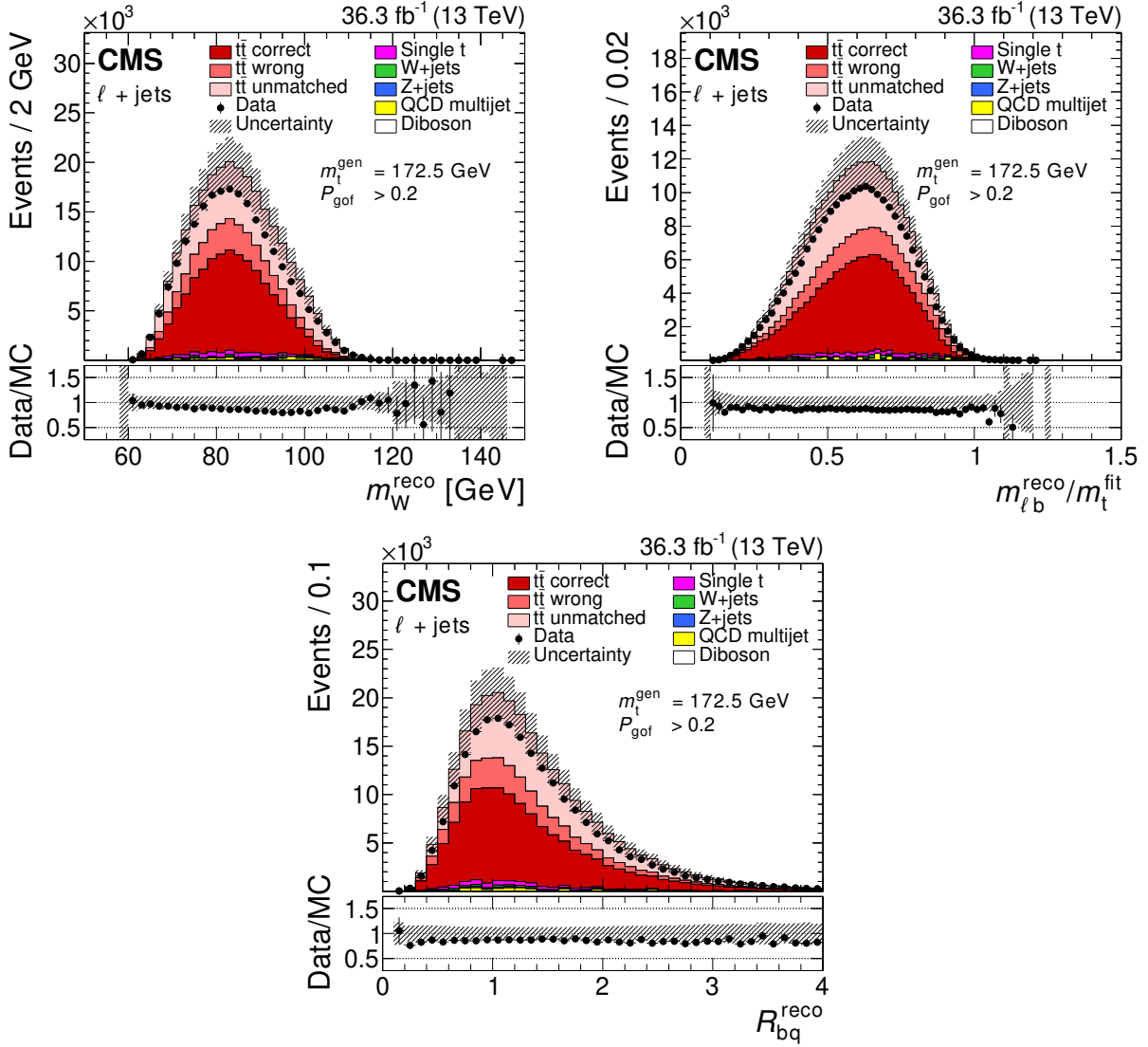


Figure 22: The distributions of m_W^{reco} (upper left), $m_{\ell b}^{\text{reco}}/m_t^{\text{fit}}$ (upper right), and R_{bq}^{reco} (lower) for the $P_{\text{gof}} > 0.2$ category. Symbols and patterns are the same as in Fig. 21. In the figures, the default value of $m_t^{\text{gen}} = 172.5$ GeV is used. Figures taken from Ref. [71].

Table 4: The overall list of different input histograms and their inclusion in a certain histogram set. A histogram marked with “ \times ” is included in a set (measurement).

Histogram		Set label				
Observable	Category	1D	2D	3D	4D	5D
m_t^{fit}	$P_{\text{gof}} > 0.2$	\times	\times	\times	\times	\times
m_W^{reco}	$P_{\text{gof}} > 0.2$		\times	\times	\times	\times
$m_{\ell b}^{\text{reco}}$	$P_{\text{gof}} < 0.2$			\times	\times	\times
$m_{\ell b}^{\text{reco}}/m_t^{\text{fit}}$	$P_{\text{gof}} > 0.2$				\times	\times
R_{bq}^{reco}	$P_{\text{gof}} > 0.2$					\times

method. The $5D$ measurement performs a simultaneous fit of the m_t^{fit} , m_W^{reco} , $m_{\ell b}^{\text{reco}}/m_t^{\text{fit}}$, and R_{bq}^{reco} distributions for $P_{\text{gof}} > 0.2$ and the $m_{\ell b}^{\text{reco}}$ distribution for $P_{\text{gof}} < 0.2$.

The expected total uncertainty in m_t is evaluated for each set defined in Table 4 with pseudo-experiments using the default simulation. The results of the pseudo-experiments are shown in Fig. 23. The improvements in the data reconstruction and calibration, event selection, simulation, and mass extraction method reduce the uncertainty in the $1D$ measurement from 1.09 to 0.63 GeV, when compared to the previous measurement [61], which used the same data set. The uncertainty in the $2D$ measurement improves from 0.63 to 0.51 GeV. The additional observables and the split into categories further reduce the expected uncertainty down to 0.37 GeV for the $5D$ set.

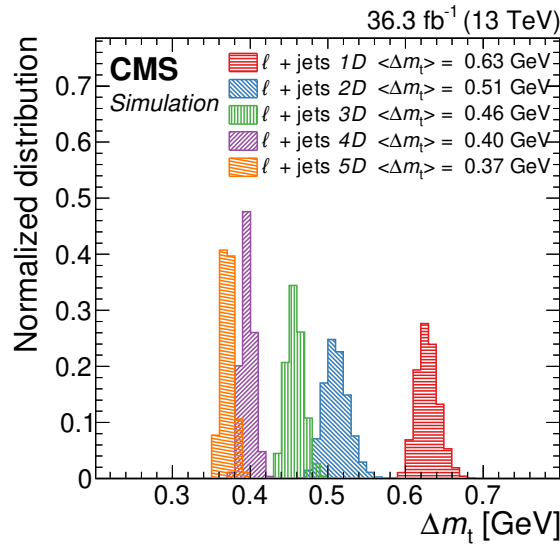


Figure 23: Comparison of the expected total uncertainty in m_t in the combined lepton+jets channel and for different observable categories defined in Table 4. Figure taken from Ref. [71].

The statistical uncertainty is obtained from fits that only have m_t as a free parameter. From studies on simulation, it is expected to be 0.07, 0.06, and 0.04 GeV in the electron+jets, muon+jets, and the combined (lepton+jets) channels, respectively.

3.1.4 Mass extraction method and results

The result of the $5D$ fit to data [71] and the previous direct m_t measurements in the lepton+jets channel [48, 53, 61] are displayed in Fig. 24. The uncertainties in the measurements are broken down into statistical, experimental, and modelling uncertainties.

For the statistical uncertainty in the three ideogram measurements, the expected reduction is observed, proportional to the inverse of the square root of the number of selected $t\bar{t}$ candidates. The increase in the number of candidates stems not only from the increase in the recorded luminosity from 5.0 to 36.3 fb^{-1} , but also in the increased $t\bar{t}$ production cross section from $\sqrt{s} = 7$ TeV to 13 TeV. While the statistical uncertainty for the three ideogram measurements is obtained from a fit with two free parameters, m_t and JSF, the statistical uncertainty for the profile likelihood method is derived when only m_t is free in the fit. This explains a large part of the difference in the statistical uncertainty in the ideogram and the profile likelihood ($5D$) measurements on the same data, but with slightly different reconstruction and calibration. However, the m_t -only fit with the ideogram method [61] yields still a roughly 50% larger statistical uncertainty of 0.06 GeV compared to 0.04 GeV in the $5D$ method. This remaining re-

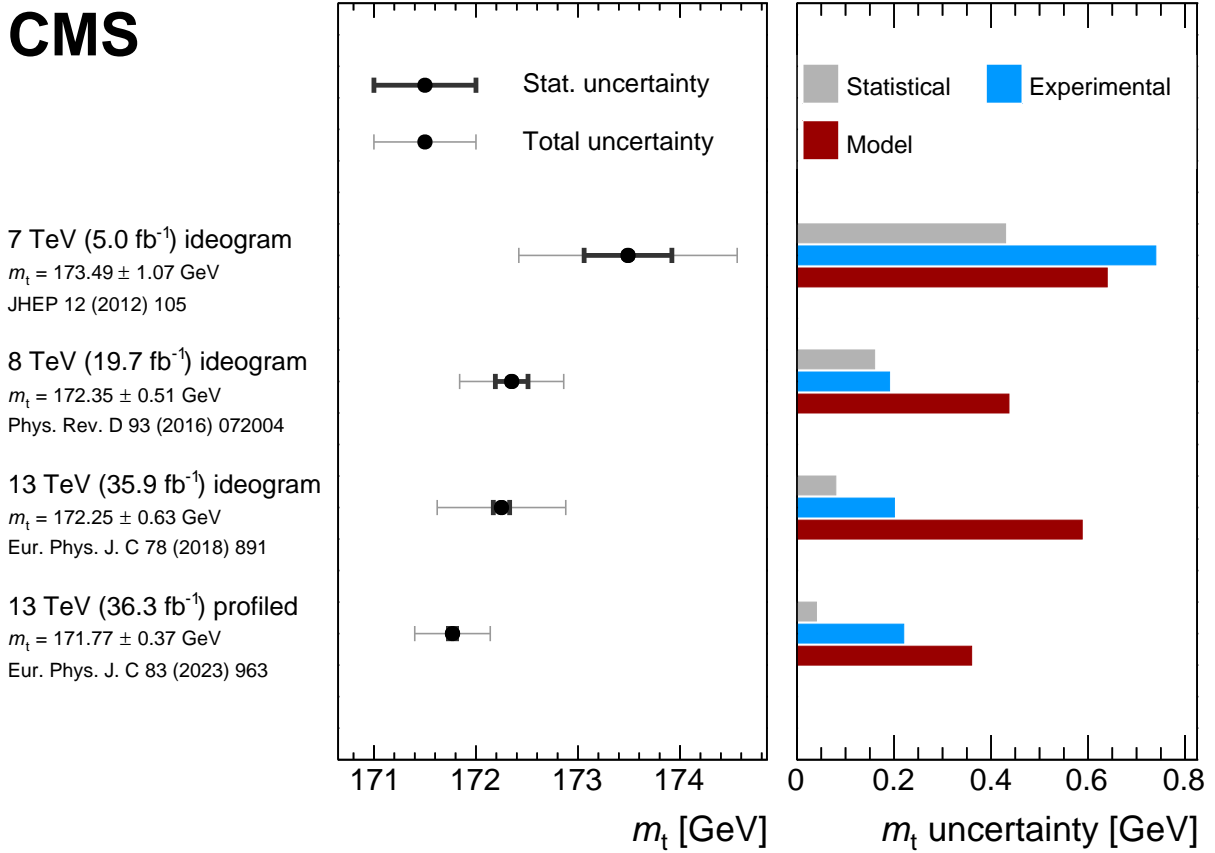
CMS

Figure 24: Summary of the direct m_t measurements in the lepton+jets channel by the CMS Collaboration. The left panel shows the measured value of m_t (marker) with statistical (black bars) and total (grey bars) uncertainties. The right panel displays a breakdown of contributing uncertainty groups and their impact on the uncertainty in the measurement. The two results at 13 TeV are derived from the same data. The figure is compiled from Refs. [48, 53, 61, 71].

duction stems from the inclusion of previously discarded events that fail the P_{gof} criterion via the $m_{\text{tb}}^{\text{reco}}$ observable in the $5D$ measurement.

The main experimental uncertainties are in the JES and JER. The energy scale and resolution corrections are mainly derived from QCD dijet events. Due to the high cross section for these processes for the relatively soft jets ($p_T \lesssim 100$ GeV) from top quark decays, the sample size is not limited by the integrated luminosity but by the bandwidth allocated to the dijet triggers. Hence, one cannot expect an improvement with rising integrated luminosity or centre-of-mass energy. A lot of time and effort was invested after the end of the Run 1 data taking to reduce the uncertainty in the JES corrections for the legacy Run 1 measurement at $\sqrt{s} = 8$ TeV [101], and, hence, this measurement has the smallest experimental uncertainty. Similarly, the second measurement using the 13 TeV data with the profile likelihood method [71] should profit from the improved JES corrections that were used in comparison to the ideogram measurement on the same data. Nevertheless, the ideogram measurement has a slightly smaller experimental uncertainty. For the profile likelihood measurement, the JES uncertainties are split in many categories and the FSR PS scale is varied independently for different emission processes. The latter reduces the constraint from the W boson peak position on the JES as out-of-cone radiation from the quarks of the W boson decay has a stronger impact on the m_W^{reco} distribution than a single JES variation. In addition, the non- $t\bar{t}$ background, which is included in the experimental

uncertainties, has become more important by the inclusion of events that fail the P_{gof} criterion, which have a higher contribution from background processes.

The main modelling uncertainties are related to b jets, FSR, and CR. The small experimental uncertainties, especially in the JES corrections, in the legacy Run 1 measurement also lead to reduced modelling uncertainties with the hybrid approach. For the Run 2 measurements, new procedures for the CR and FSR uncertainty lead to larger modelling uncertainties. In part, this is just caused by the increase in the number of alternative signal samples for CR/ERD modelling from one to three samples and, hence, more statistical effects on the size of the uncertainty. In contrast, weights are used to vary parameters of the FSR modelling in the profile likelihood measurement removing the statistical component on the size of the FSR uncertainty. While this reduces the estimated uncertainty, the introduction of separate scales per splitting type leads to an overall increase in the size of the FSR uncertainty. The introduction of $m_{\text{tb}}^{\text{reco}}/m_{\text{t}}^{\text{fit}}$ and $R_{\text{bq}}^{\text{reco}}$ reduces the impact of the b jet modelling on the m_{t} measurement by 30% comparing the ideogram and the profile likelihood measurements with 2016 data.

3.1.5 Other channels and outlook

Besides the lepton+jets channel, also the dilepton and the all-jets channels can be used to measure m_{t} using its decay products. Figure 25 compares the best CMS measurements from $\sqrt{s} = 8$ TeV Run 1 data for each channel with the corresponding $\sqrt{s} = 13$ TeV Run 2 data collected in 2016.

In contrast to the lepton+jets channel, both Run 2 measurements in the dilepton channel [63, 69] utilise a profile likelihood approach and, hence, surpass the Run 1 precision. The later measurement [69] has the same tendency to lower m_{t} values as the latest measurement in the lepton+jets channel. Both analyses were derived on simulated Run 2 legacy samples described in Section 2.4 and the lower m_{t} value might be a consequence of the specific parameters used in these simulated samples.

The all-jets channel requires a very pure event selection to suppress QCD multijet background and, hence, suffers from low event count. This is partly compensated by the two fully reconstructed top quark candidates and superior resolution in the predicted top quark mass from the kinematic fit. The only published analysis with Run 2 data in this channel [62] still employed the ideogram method derived on early Run 2 simulation and could not improve on the Run 1 result.

Measurements of m_{t} for different phase space regions allow us to experimentally test the universality of the m_{t} values measured by direct methods and appraise the quality of the modelling by simulation. The results obtained in Ref. [61] and depicted in Fig. 26 show the difference between the measured m_{t} value in a particular bin and m_{t} from the inclusive sample in bins of the invariant mass of the $\text{t}\bar{\text{t}}$ system, $m_{\text{t}\bar{\text{t}}}$, and the ΔR between the light-quark jets, $\Delta R_{\text{qq}'}$, with comparisons to four generator models. The models use either POWHEG or MADGRAPH for the hard interaction interfaced into either PYTHIA8 or HERWIG++. The data and models that use PYTHIA8 show agreement within 0.5 GeV, while the model using HERWIG++ shows variations of several GeV.

3.2 Measurement of the top quark mass in single top quark events

3.2.1 Motivation

At the LHC, single top quark production occurs through charged-current electroweak (EW) interactions. The different production modes can be distinguished at the tree level, depending

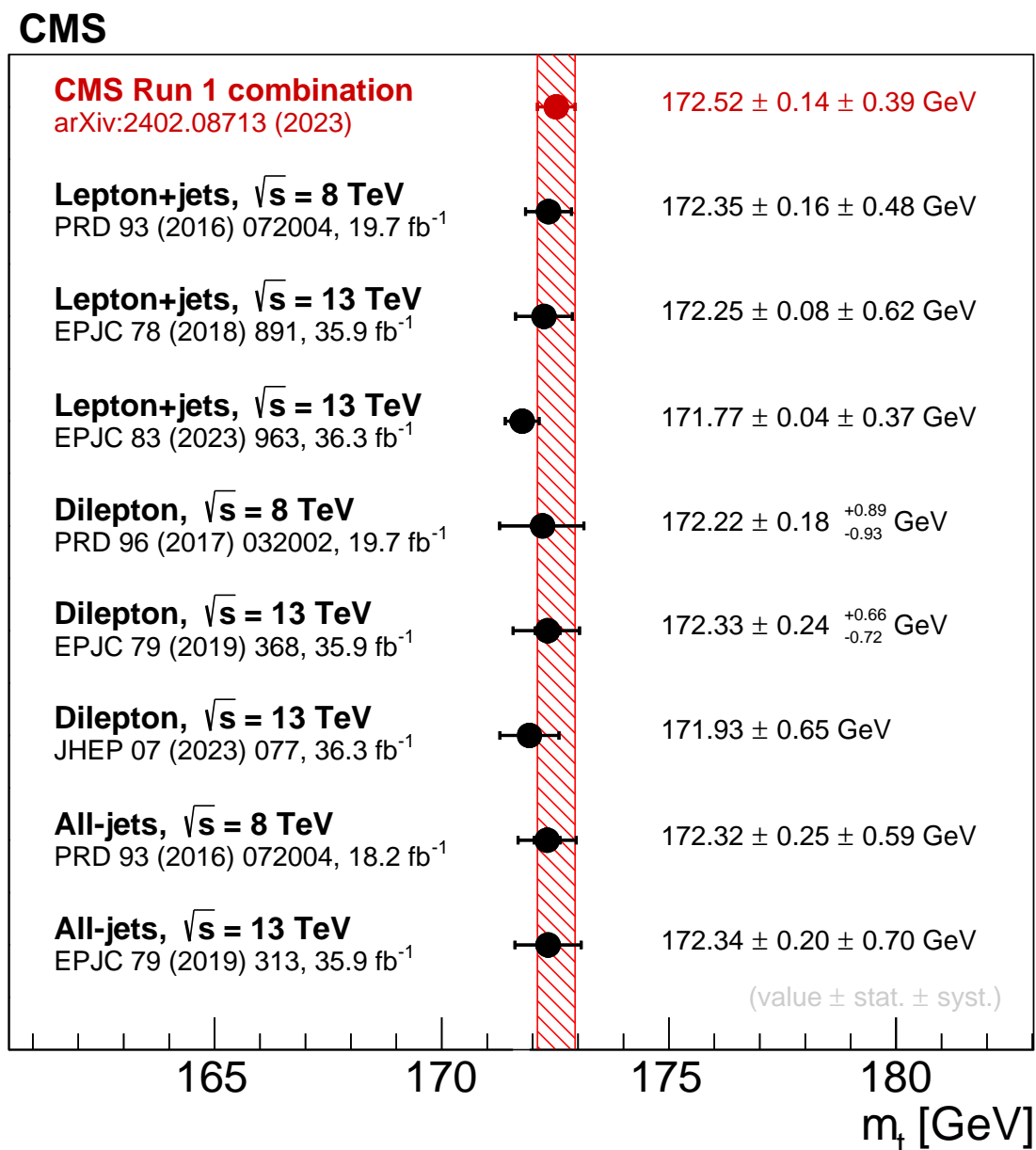


Figure 25: Comparison of the CMS direct m_t measurements from the Run 2 data collected in 2016 at $\sqrt{s} = 13$ TeV to the best Run 1 measurements at $\sqrt{s} = 8$ TeV in each channel. The horizontal bars display the total uncertainty in the measurements and the red band shows the uncertainty in the Run 1 combination [72]. The figure is compiled from Refs. [53, 60–63, 69, 71, 72].

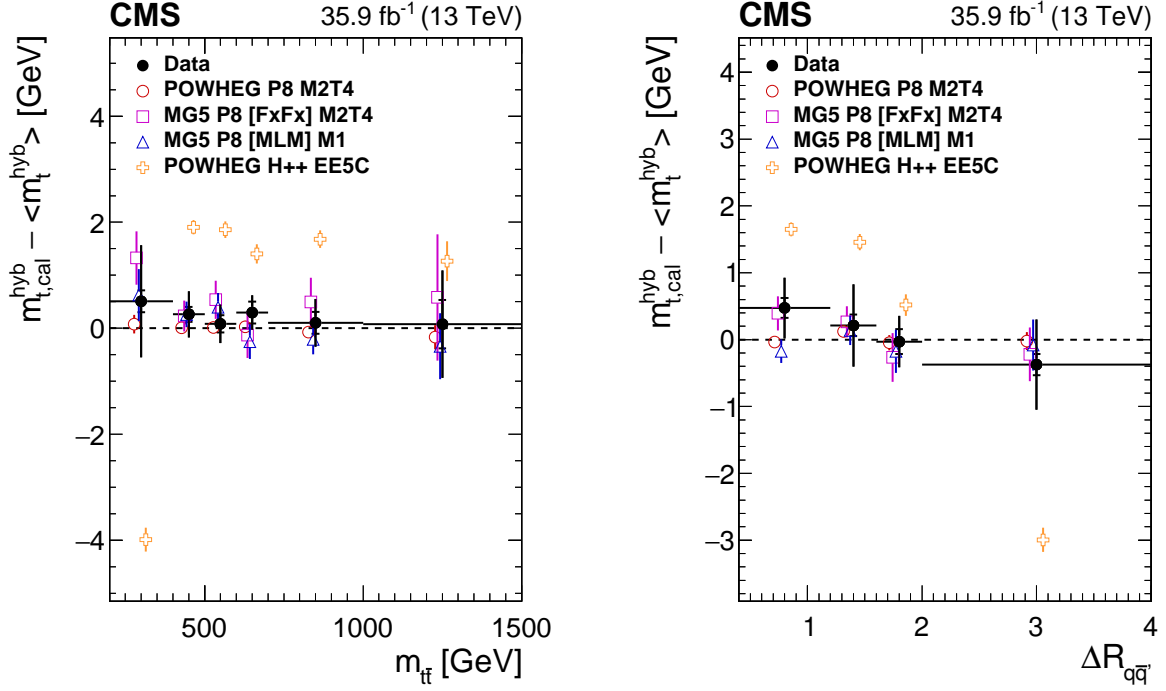


Figure 26: Difference of the m_t extracted after calibration in each bin and from the inclusive sample as a function of the invariant mass of the $t\bar{t}$ system $m_{t\bar{t}}$ (left) and the ΔR between the light-quark jets $\Delta R_{q\bar{q}'}$ (right), obtained from the hybrid fit [61], compared to different generator models. The filled circles represent the data, and the other symbols are for the simulations. For reasons of clarity, the horizontal bars indicating the bin widths are shown only for the data points and each of the simulations is shown as a single offset point with a vertical error bar representing its statistical uncertainty. The statistical uncertainty of the data is displayed by the inner error bars. For the outer error bars, the systematic uncertainties are added in quadrature. Figures taken from Ref. [61].

on the virtuality of the W boson: the t -channel (spacelike), the W-associated or tW channel (on-shell), and the s -channel (timelike). In Fig. 27, the Feynman diagrams for the t -channel, which is the dominant mode for single top quark production in pp collisions at the LHC, are shown. The total production cross section for this process as calculated at NLO in QCD is 217^{+9}_{-8} pb at 13 TeV [198, 199], in good agreement with the experimentally measured values [200].

The t -channel single top quark production offers a partially independent event sample for m_t measurements in a complementary region of phase space as compared to $t\bar{t}$ events. It also allows to extract the value of m_t at lower energy scales, and provides different sensitivity to systematic and modelling effects, such as PDFs and CR. In fact, in the case of $t\bar{t}$, both top quarks, as well as their decay products, are colour connected to the colliding protons, which complicates the modelling of the colour reconnection of final-state particles. On the contrary, in single-top events, the top quark is colour connected only to the parton that participated in the tWb vertex.

The t -channel single top quark production is simulated with POWHEG 2.0 in the four-flavour number scheme (4FS) [201], where b quarks are produced via gluon splitting, as shown in Fig. 27 (right). This scheme is expected to yield a better description of the kinematic properties of the top quark and its decay products for the t -channel events, as compared to the five-flavour

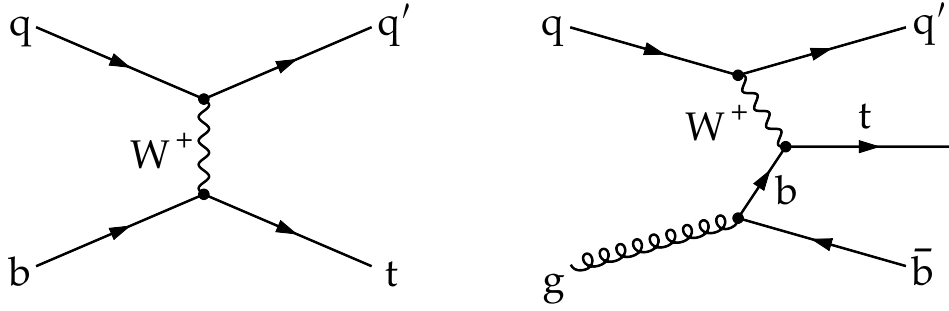


Figure 27: Feynman diagrams of the t -channel single top quark production at LO corresponding to five- (left) and four-flavour (right) schemes, assuming five (u, d, s, c, b) or four (u, d, s, c) active quark flavours in the proton, respectively. At NLO in perturbative QCD, the right diagram is also part of the five-flavour scheme.

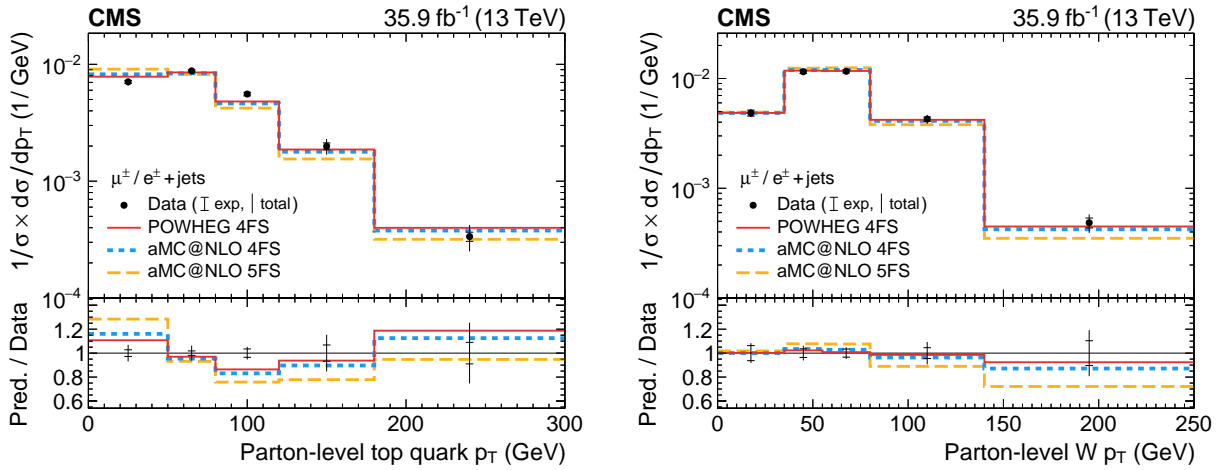


Figure 28: Normalised differential cross section of the t -channel single top quark production as a function of the p_T of the parton-level top quark (left) and the W boson (right). Figures taken from Ref. [204].

number scheme (5FS) [202–204] shown in Fig. 27 (left), since it accounts for the mass of the b quark. This is illustrated in Fig. 28, presenting the differential cross section measurements at 13 TeV [204], together with the 4FS and 5FS predictions. On the other hand, 5FS predictions provide more accurate calculations of the total cross section. Therefore, the simulated samples are normalised using the total cross section calculated at NLO in the 5FS using the HATHOR 2.1 package [198, 199].

3.2.2 Event selection and categorisation

The considered final-state signature of t -channel single top quark production used for m_t measurement consists of an isolated high-momentum charged muon or electron, a neutrino from the W boson decay, which results in an overall transverse momentum imbalance, a light-quark jet often produced in the forward direction, and another jet arising from the hadronisation of a b quark from the top quark decay. The second b jet arising from the initial-state gluon splitting, as shown in Fig. 27 (right), is found to have a softer p_T spectrum and a broader η distribution compared to the b jet originating from the top quark. Therefore these jets often escape the final-state object selection or lie outside the detector acceptance.

Based on the above considerations, candidate events are required to contain one isolated electron or muon with $p_T > 20$ or 30 GeV, respectively, and $|\eta| < 2.4$, exactly two jets with

$p_T > 40 \text{ GeV}$, and $|\eta| < 4.7$, one of which is b tagged and has $|\eta| < 2.5$. The b-tagged jet is required to satisfy a stringent identification criterion corresponding to approximately 0.1% misidentification probability for light-quark or gluon jets. Additionally, the transverse mass of the charged lepton and neutrino system is required to exceed 50 GeV to further suppress the QCD multijet background.

The selected events are then assigned to two categories (labelled $nJmT$), depending on the number of jets (n) and number of b-tagged jets (m). The 2J1T category has the largest contribution from t -channel single top quark production events and is referred to as the signal category for the measurement. The contribution from the QCD multijet background is determined from a side-band in data, by inverting the isolation (identification) criteria of the charged muons (electrons) [67].

3.2.3 Single top quark reconstruction

The top quark mass and four-momentum are reconstructed by combining the momenta of its decay products. The transverse momentum of the neutrino, $p_{T,\nu}$, is inferred from p_T^{miss} , while the momenta of the lepton and b-tagged jet are measured in the detector. The longitudinal momentum of the neutrino, $p_{z,\nu}$, can be calculated by imposing energy-momentum conservation at the $W \rightarrow \ell\nu$ vertex while assuming $m_W = 80.4 \text{ GeV}$ [1]:

$$m_W^2 = \left(E_\ell + \sqrt{(p_T^{\text{miss}})^2 + p_{z,\nu}^2} \right)^2 - (\vec{p}_{T,\ell} + \vec{p}_T^{\text{miss}})^2 - (p_{z,\ell} + p_{z,\nu})^2. \quad (14)$$

Here, $p_{z,\ell}$ is the z component of the charged-lepton momentum and E_ℓ is its energy. Two possible solutions for $p_{z,\nu}$ can be obtained from Eq. (14):

$$p_{z,\nu} = \frac{\Lambda p_{z,\ell}}{(p_{T,\ell})^2} \pm \frac{1}{(p_{T,\ell})^2} \sqrt{\Lambda^2 p_{z,\ell}^2 - (p_{T,\ell})^2 [E_\ell^2 (p_T^{\text{miss}})^2 - \Lambda^2]}, \quad (15)$$

with $\Lambda = m_W^2/2 + \vec{p}_{T,\ell} \cdot \vec{p}_T^{\text{miss}}$.

The finite resolution of p_T^{miss} can lead to negative values in the radical of Eq. (15), giving rise to complex solutions. In the case of real solutions, the one with the smaller magnitude is retained [24, 25]. This choice is found to have higher accuracy of the inferred values of $p_{z,\nu}$ when compared to the true values in simulated events. If complex solutions are obtained, the radical in Eq. (15) is set to zero, and the value of $p_{T,\nu}$ satisfying Eq. (14) and with the smallest $|\Delta\phi|$ with respect to p_T^{miss} is chosen.

This reconstruction method, however, leads to a softer reconstructed spectrum compared to the true spectrum in simulation. This leads to a bias in the reconstructed m_t spectrum, which is one of the reasons that the mass extraction needs to be calibrated a posteriori. The value of the extracted m_t from the final fit, when applied to a sample of simulated t -channel single top quark and $t\bar{t}$ simulations with a given m_t^{MC} , is plotted for a range of m_t^{MC} values, and fitted with a linear dependence [67]. The uncertainty in the calibration is then propagated to the final result as an additional systematic uncertainty [58, 67].

3.2.4 Top quark mass extraction

The primary challenge in measuring m_t in single top quark events lies in controlling the large irreducible $t\bar{t}$ background. Improved analysis techniques, such as multivariate and likelihood approaches, have contributed to significant reduction of the impact of the $t\bar{t}$ background and

to improvement of precision of single top quark mass measurements [67]. The main changes with respect to the corresponding Run 1 analysis are summarised in Table 5. In this section, the main aspects of such improvements are discussed.

Table 5: Advancement in analysis strategies between Run 1 [58] and Run 2 [67] measurements of m_t in single top events. Primary improvements that resulted in a higher precision in the Run 2 measurement are highlighted in bold.

	Run 1	Run 2
Final state	μ +jets	μ +jets and e +jets
Strategy	Cutoff-based: untagged jet $ \eta > 2.5$ μ charge = +1	Multivariate: Boosted decision tree (BDT) per lepton flavour Any lepton charge Optimised thresholds on BDT responses
Fit observable	Reconstructed m_t ($m_{\mu\nu b}$)	$\zeta = \ln(m_t/1 \text{ GeV})$
Signal and background norm.	No constraints	Constrained in final fit
QCD multijet background	Absorbed into EW (V+jets and VV) category during final fit	Subtracted from data before final fit; separate systematic uncertainty for its modelling
Fit model validation	Using events with μ charge = -1	Using orthogonal region based on the BDT values

In the analysis of Ref. [67], a boosted decision tree (BDT) is trained in each lepton flavour in the 2J1T event category in order to separate t -channel single top quark production from a combination of other top quark ($t\bar{t}$, tW , and s -channel), EW, and QCD multijet processes. A minimal set of observables that provide good discrimination power while being loosely correlated with the reconstructed m_t is used in the BDT training [67]. The correlation between the BDT score and the reconstructed m_t is found to be 13%, which ensures that the selection based on the BDT score does not significantly affect the reconstructed mass spectrum. The value of the BDT cut-off that minimises the calibration uncertainty mentioned in Section 3.2.3 is used in the analysis (Fig. 29). This cutoff corresponds to an expected signal purity of 65 (60)% in the muon (electron) channels.

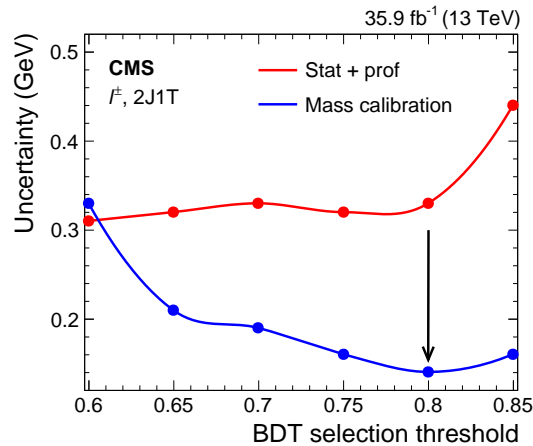


Figure 29: The uncertainty in m_t from the statistical and profiled systematic components (red) and uncertainty in the m_t calibration (blue) as a function of the cutoff on the BDT score. Figure taken from Ref. [67].

The asymmetric shape of the reconstructed m_t distribution (Fig. 30, left) makes it challenging to obtain an accurate analytic description of signal and background shapes, which is desirable when the position of the peak of a distribution has to be determined. This can be solved by introducing the variable $\zeta = \ln(m_t/1 \text{ GeV})$, which exhibits a more symmetric distribution

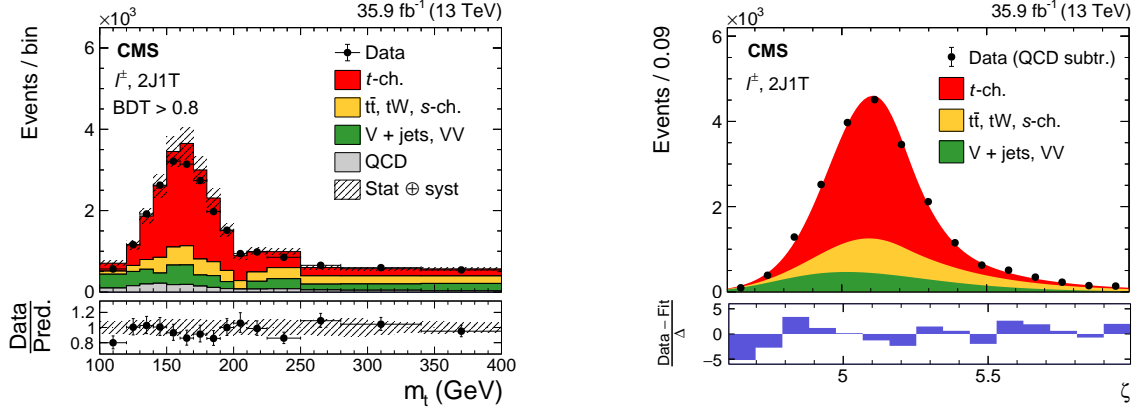


Figure 30: Data-to-simulation comparison of the reconstructed top quark mass (left) and postfit $\zeta = \ln(m_t/1 \text{ GeV})$ (right) distributions after BDT selection. The lower panel in the left plot shows the data-to-simulation ratios for each bin, while the lower panel in the right plot shows the normalised residuals or pulls, determined using the bin contents of the data distributions (after background QCD subtraction) and the $F(\zeta)$ values evaluated at the centre of the bins. Figures taken from Ref. [67].

around the peak (Fig. 30, right). A simultaneous maximum likelihood fit is performed with the ζ distributions obtained from the muon and electron channels. The fit is carried out separately for a positively charged lepton (ℓ^+), negatively charged lepton (ℓ^-), as well as inclusive in lepton charge (ℓ^\pm) in the final state. The estimated QCD multijet contribution is subtracted from data before the fit in the absence of a reliable analytic shape to model this background. A separate systematic uncertainty is assigned due to the QCD multijet background, by conservatively varying its per-bin contribution independently by 50%. The binned ζ distribution, obtained after the QCD background subtraction, is parameterised with an analytic function $F_\ell(\zeta)$ for each lepton flavour ($\ell = \mu$ or e). The total likelihood is given by

$$\mathcal{L}_{\text{tot}} = \prod_{\ell=\mu,e} \mathcal{L}_\ell \quad \text{with} \quad \mathcal{L}_\ell = \prod_{i,j} \mathcal{P} \left[N_{i,\ell}^{\text{obs}} | F_\ell(\zeta; \zeta_0, f_j) \right] \Theta(f_j), \quad (16)$$

where i is the bin index, ζ_0 represents the value of ζ corresponding to the true value of m_t , \mathcal{P} denotes the Poisson probability of the analytic model, $F_\ell(\zeta; \zeta_0, f_j)$, to describe the observed ζ distribution, and Θ represents penalty terms for the normalisation parameters f_j . These parameters are defined for the rates of various processes denoted by j , namely t -channel signal, $t\bar{t}$, and EW backgrounds, as

$$f_j = \frac{N_j^{\text{obs}}}{N_j^{\text{exp}}}, \quad j \in \{t\text{-ch.}, t\bar{t}, \text{EW}\}, \quad (17)$$

where N_j^{obs} (N_j^{exp}) is the observed (expected) yield for the process j . The function $F_\ell(\zeta; \zeta_0, f_j)$ is then expressed as

$$F_\ell(\zeta; \zeta_0, f_j) = f_{\text{sig}} F_{\text{sig}}(\zeta; \zeta_0) + f_{t\bar{t}} F_{t\bar{t}}(\zeta; \zeta_0) + f_{\text{EW}} F_{\text{EW}}(\zeta), \quad (18)$$

where F_{sig} , $F_{t\bar{t}}$, and F_{EW} represent the analytic shapes for the signal, $t\bar{t}$, and EW background, respectively.

The F_{sig} shape is described by a sum of an asymmetric Gaussian (ζ_0) function convolved with a Landau distribution to account for asymmetry at higher ζ , while the $F_{t\bar{t}}$ shape is modelled by a

Crystal Ball function [205]. The tW and s -channel single top quark processes are absorbed into the dominant $t\bar{t}$ component. The F_{EW} shape comprises contributions from the W +jets, Z +jets, and diboson processes and is modelled with a Novosibirsk function [206]. The parameter ζ_0 is then treated as a free parameter of the fit, and is used to directly extract the fitted m_t . Other parameters that alter the analytic shapes of the signal and background models are fixed to their estimated values from simulated events, around their estimated values and are considered as sources of systematic uncertainties. The parameters f_{sig} , $f_{t\bar{t}}$, and f_{EW} are constrained in the fit within their corresponding uncertainties of 15, 6, and 10%, respectively. The postfit ζ distributions for the ℓ^\pm case are shown in Fig. 30 (right). The fit model described above is validated in a control sample obtained using an orthogonal cutoff in the BDT score.

3.2.5 Systematic uncertainties and results

All relevant sources of systematic uncertainties described in Section 2 are considered. Similarly to the measurements in $t\bar{t}$ events, the dominant sources of systematic uncertainties are those related to the JES, the signal modelling, the colour reconnection, and b quark hadronisation model. The largest impact originates from the JES calibration, and can be attributed to the requirement of a jet in the endcap region of the detector. In fact, the jet energy calibrations are known to have large uncertainties in the endcap regions, because of their coarse granularity [207].

In the Run 2 simulation, the models of CR (Section 2.4) have evolved in sophistication, as compared to those used in Run 1 analyses, and correspond to larger estimated uncertainties. The uncertainty associated with the b quark hadronisation is also increased with respect to Run 1, since alternative fragmentation functions are considered (Section 2.4).

Similar to the case of the $t\bar{t}$ analyses, the impact due to the possible mismodelling of the signal process is determined by considering the variation of parton-shower and matrix element scales, and by varying the PDF within uncertainties, for which NNPDF3.0 NLO set [127] is used. In addition, NNPDF3.0 sets with the value of the strong coupling constant changed from the default value 0.118 to 0.117 and 0.119 are evaluated and the observed mass difference is added in quadrature. In the case of single top quark, the matrix-element renormalisation and factorisation scales are set to a nominal value of $m_t = 172.5$ GeV, and are varied up and down by a factor of two.

As a cross check, the value of m_t is also extracted using alternative MC models for the parton shower (HERWIG++), the matrix element generator (MADGRAPH5_aMC@NLO), the flavour scheme, and the underlying event tune. Resulting changes in the value of m_t are found to be covered by the signal modelling uncertainties used in the fit.

The fit in the ℓ^\pm inclusive channel yields

$$m_t = 172.13^{+0.76}_{-0.77} \text{ GeV}, \quad (19)$$

resulting in the first m_t measurement in the t -channel with sub-GeV precision. The result is consistent with the CMS 8 TeV measurement in single top quark events [58], as shown in Fig. 31. Thanks to the improvements in the analysis techniques, the larger data set, and the inclusion of the electron channel in the fit, the Run 2 measurement improves the precision by about 30% compared to the Run 1 result, despite the fact that the impact of the signal modelling uncertainties has remained mostly unchanged. Therefore, this class of measurements can benefit significantly from future advancements in the modelling of the signal process.

CMS

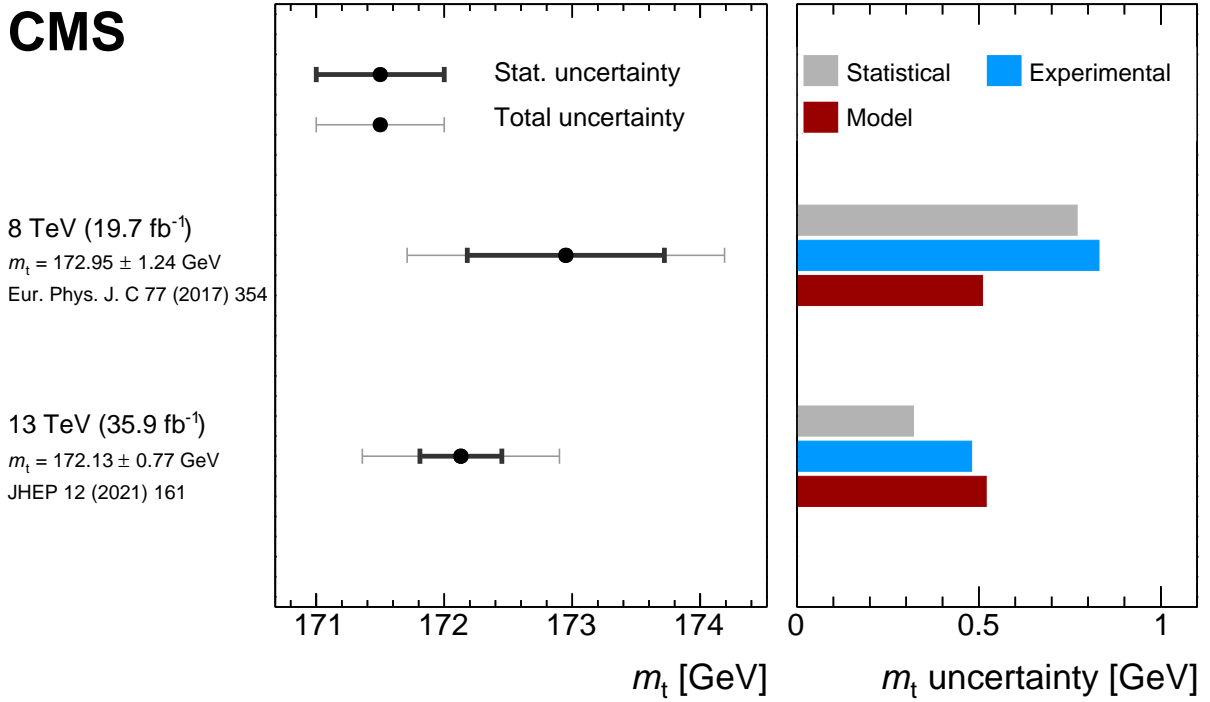


Figure 31: Summary of m_t measurements in single top quark events. The left panel shows the measured value of m_t (marker) with statistical (thick bars) and total (thin bars) uncertainties. In the case of the 13 TeV measurement [67], the statistical component of the uncertainty includes contributions from the statistical and profiled systematic uncertainties. The right panel displays a breakdown of contributing uncertainty groups and their impact on the uncertainty in the measurement. The figure is compiled from Refs. [58, 67].

3.2.6 Top quark-antiquark mass difference and ratio

In quantum field theory, the equality of the mass of a particle and its antiparticle is a consequence of the *CPT* theorem, according to which all Lorentz-invariant local gauge theories are invariant under a *CPT* transformation [208]. Therefore, the validity of the *CPT* theorem can be tested experimentally by measuring the mass of a particle and its antiparticle.

In CMS, the mass of the top quark and antiquark are independently determined by performing the fit described in Section 3.2.4 in the ℓ^+ and ℓ^- final states, respectively, resulting in

$$\begin{aligned} m_t &= 172.62^{+1.04}_{-0.75} \text{ GeV}, \\ m_{\bar{t}} &= 171.79^{+1.44}_{-1.51} \text{ GeV}, \end{aligned} \quad (20)$$

in good agreement with each other and with the result of the combined-channel fit. The uncertainty in $m_{\bar{t}}$ is found to be larger due to a lower production rate of top antiquarks compared to top quarks in single top quark production in pp collisions.

The mass ratio and the mass difference are then derived accounting for the correlation between the systematic uncertainties in the two cases, resulting in:

$$\begin{aligned} R_{m_t} &= \frac{m_{\bar{t}}}{m_t} = 0.9952^{+0.0079}_{-0.0104}, \\ \Delta m_t &= m_t - m_{\bar{t}} = 0.83^{+1.79}_{-1.35} \text{ GeV}. \end{aligned} \quad (21)$$

The estimated values of R_{m_t} and Δm_t are consistent with unity and zero, respectively, within

uncertainties, showing no evidence for violation of CPT invariance. In Fig. 32, the result for Δm_t is compared to those of previous CMS measurements in $t\bar{t}$ events [209, 210], which were based on a modified ideogram analysis method in the lepton+jets channel, allowing m_t and $m_{\bar{t}}$ to have different values, and separating the event samples using the lepton charge. The results in $t\bar{t}$ events are of better precision compared to single top quark results. All measurements of Δm_t are compatible with zero. Currently, the most stringent test of CPT invariance is obtained from the measurements of the antiproton to proton mass ratio in so-called Penning-trap experiments [211, 212]. However, the CMS 8 TeV result from $t\bar{t}$ events [210] remains the most precise measurement of the mass ratio for the top quark to antiquark.

CMS

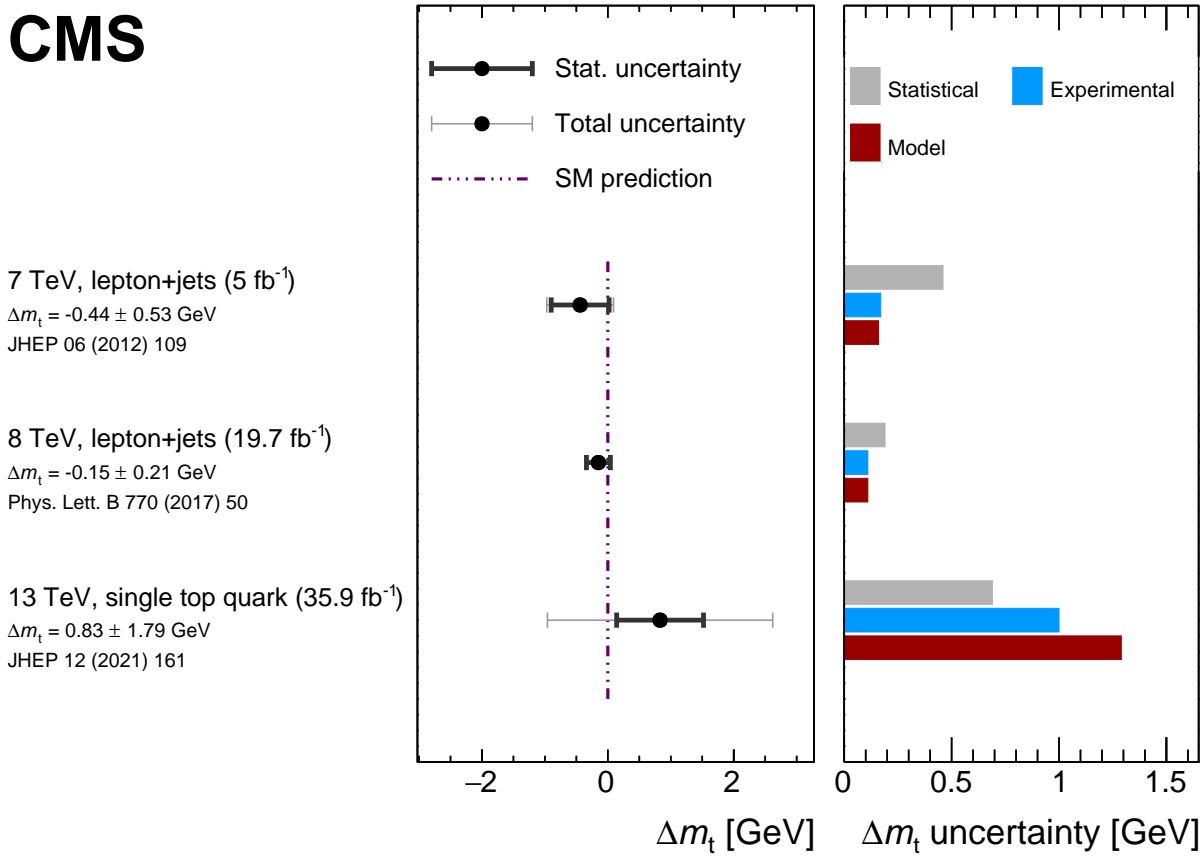


Figure 32: Summary of Δm_t measurements in $t\bar{t}$ and single top quark events. The left panel shows the measured value of Δm_t (marker) with statistical (thick bars) and total (thin bars) uncertainties. In the case of the single top quark measurement [67], the statistical component of the uncertainty includes contributions from the statistical and profiled systematic uncertainties. The right panel displays a breakdown of contributing uncertainty groups and their impact on the uncertainty in the measurement. The figure is compiled from Refs. [67, 209, 210].

3.3 Status of the interpretation of top quark Monte Carlo mass

The direct m_t measurements rely on particle-level kinematic observables, which exhibit high sensitivity to the value of m_t . To date, such observables can not be calculated in the SM, and in particular in QCD higher-order perturbation theory, from first principles. The direct measurements imply comparison of measurements with simulations based on general-purpose MC event generators and therefore constrain the top quark mass parameter of the corresponding MC event generator m_t^{MC} .

However, for the SM and BSM theory predictions or EW precision fits beyond LO, m_t as a parameter of the Lagrangian in a well-defined renormalisation scheme is required. Even though the available multipurpose MC generators contain hard ME at LO or NLO, and collinear and soft radiation is simulated by applying parton showering, the precise interpretation of m_t^{MC} in terms of a renormalised Lagrangian mass is difficult, due to the limited theoretical precision of the individual components and the modelling aspects of the MC event generators. The experimental results for m_t^{MC} have frequently been identified with m_t^{pole} . This association is adequate within uncertainties of 0.5–1 GeV [3, 213]. A level of precision below 400 MeV, reached recently in the m_t^{MC} measurements, demands significantly higher precision in the relation of m_t^{MC} to m_t in well-defined renormalisation schemes. It should be noted, that the MC simulations based on NLO ME matched to PS used in the experimental analyses do not resolve the issue of the m_t^{MC} interpretation. Although the matching improves the description of hard gluon radiation, the observables used in the direct measurement are dominated by soft, collinear, and in particular nonperturbative dynamics associated to the reconstructed final-state objects. In the following, the current status of knowledge concerning the interpretation of m_t^{MC} is briefly reviewed.

From the first-principle QCD perspective, the theoretical meaning of m_t^{MC} is tied to the accuracy and implementation of the PS algorithms and the top quark decay matrix elements, which are the primary partonic components of the MC generators relevant for the direct m_t measurement. In order to control m_t^{MC} at NLO [191] for the direct measurement, at least NLL precision for the PS evolution and NLO for the description of the top quark decay are necessary. For the coherent branching (angular ordered) PS algorithm and the 2-jettiness event-shape distribution in e^+e^- annihilation (which is top quark decay-insensitive and where coherent branching is NLL precise), it was demonstrated [191] that m_t^{MC} and m_t^{pole} satisfy the relation $m_t^{\text{MC}} - m_t^{\text{pole}} = -(2/3)Q_0\alpha_S(Q_0^2)$. Here, Q_0 is the transverse momentum shower cutoff of the coherent branching algorithm. For the shower cutoff values Q_0 of about 1 GeV, used in the state-of-the-art MC simulations, this difference amounts to up to 0.5 GeV. Since any practical PS implementation requires a finite shower cutoff, a similar relation holds for any PS [214, 215] and numerical evidence supporting this view for the dipole shower has been provided in Ref. [216].

Physically, the shower cutoff Q_0 acts as an infrared resolution scale, which means that partonic real and virtual (soft) radiation below Q_0 is unresolved and cancels. In general, any linear dependence of an observable on the shower cutoff Q_0 signals a sizeable contribution of hadronisation effects, with related studies for $t\bar{t}$ production initiated recently in Ref. [217]. This is, however, not the case for the linear dependence that can be associated with the top quark mass parameter, since the top quark does not hadronise. The above relation between m_t^{MC} and m_t^{pole} may be therefore interpreted within perturbation theory, with Q_0 adopting the role of an infrared factorisation scale that is still perturbative. In this context, m_t^{MC} has a closer numerical relation to low-scale short-distance masses with a low-energy renormalisation scale, such as $m_t^{\text{MSR}}(R = Q_0)$ [184]. Indeed, the relation between m_t^{MC} and $m_t^{\text{MSR}}(R = Q_0)$ obtained from Ref. [191] reads $m_t^{\text{MC}} - m_t^{\text{MSR}}(Q_0) = -0.24Q_0\alpha_S(Q_0^2)$, which amounts to much less than 0.5 GeV. These insights allow to circumvent the use of m_t^{pole} , which conceptually suffers from the renormalon problem. The renormalon degrades the theoretical predictions for the cross section and also appears in the relation of the pole-mass to high-energy m_t schemes, such as $\overline{\text{MS}}$.

Alternatively to the conceptual insights, a number of studies to quantify the difference between m_t^{MC} and m_t have been carried out. In Ref. [218], a simultaneous extraction of m_t^{MC} and of $\sigma_{t\bar{t}}$ was suggested. This method allowed for an m_t^{MC} -independent measurement of $\sigma_{t\bar{t}}$

and in turn for an m_t^{MC} -independent extraction of m_t . This way, the relation between m_t^{MC} in the MC generator used in $\sigma_{t\bar{t}}$ measurement and the extracted value of m_t could be obtained. Given the precision of inclusive $\sigma_{t\bar{t}}$ to that date, an uncertainty in such a relation of about 2 GeV was achieved. A more precise direct calibration was performed in Ref. [219], where logarithmically resummed NNLL and matched to NLO fixed-order theoretical calculations for the $e^+e^- \rightarrow t\bar{t}$ 2-jettiness distribution in the highly m_t -sensitive resonance region for boosted top quark production, also used in the aforementioned study of Ref. [191], were fitted to pseudo-data obtained by using PYTHIA v8.205 [110]. Since the theoretical prediction of the 2-jettiness distribution allows for a rigorous particle-level description, where nonperturbative effects can be parameterised by a shape function [220, 221], the calibration is based on fits involving m_t as well as the shape function. In this analysis, the numerical relations $m_t^{\text{MC}} - m_t^{\text{pole}} = 0.57 \pm 0.29 \text{ GeV}$ and $m_t^{\text{MC}} - m_t^{\text{MSR}}(1 \text{ GeV}) = 0.18 \pm 0.23 \text{ GeV}$ were obtained. A similar analysis for the LHC scenario was performed by the ATLAS Collaboration in Ref. [222] using soft-drop groomed [223] boosted top quark jet mass distributions based on the NLL+LO hadron level theoretical description, developed in Refs. [189, 224]. The findings of Ref. [222] are compatible with the calibration results, but are much less precise. The result of Ref. [219] was recently updated in Ref. [225], where calibrations for PYTHIA v8.305, HERWIG v7.2, and SHERPA v2.2.11 were performed, considering different m_t -sensitive event shape distributions and accounting for m_t -suppressed power corrections. Consistent m_t calibration results among the three generators were obtained. For PYTHIA v8.305, these read $m_t^{\text{MC}} - m_t^{\text{pole}} = 0.35 \pm 0.30 \text{ GeV}$ and $m_t^{\text{MC}} - m_t^{\text{MSR}}(1 \text{ GeV}) = 0.03 \pm 0.21 \text{ GeV}$.

The current theoretical knowledge concerning the interpretation of m_t^{MC} described above does not yet allow to relate the direct measurements of m_t^{MC} to well-defined Lagrangian m_t with a small uncertainty. The reason is that the direct measurements are based on top quark decay-sensitive observables, mostly considering non-boosted top quarks, and are affected by UE and initial-state MPIs. Nevertheless, it is quite unlikely that the aspects that have not yet been investigated will lead to sizeable additional corrections substantially beyond the level of 0.5 GeV. Therefore, m_t^{MC} can be assumed to be numerically close to m_t defined in a renormalisation scheme compatible with the top Breit–Wigner resonance, e.g. m_t^{pole} or $m_t^{\text{MSR}}(R)$ at R close to Q_0 or Γ_t , within 0.5–1.0 GeV [3, 213].

4 Extraction of the Lagrangian top quark mass

An alternative to the direct measurement of m_t^{MC} is the extraction of m_t from the measured cross section of $t\bar{t}$ pair production $\sigma_{t\bar{t}}$. There, the m_t dependence of $\sigma_{t\bar{t}}$ is used to determine m_t in a given top quark mass renormalisation scheme by comparing the theoretical predictions to the corresponding measured $t\bar{t}$ cross section. The theoretical predictions for $\sigma_{t\bar{t}}$, which require NLO or higher precision, describe the production of the on-shell top quark and antiquark and are inclusive with respect to other radiation in the event, therefore an unfolding procedure from the detector to the parton level needs to be employed in the experimental data analysis. First measurements of this kind, sometimes referred to as “indirect” top quark mass determinations, were performed at the Tevatron [226] using the inclusive $\sigma_{t\bar{t}}$. In this approach, m_t can in principle be determined in any renormalisation scheme, but suitable choices of mass schemes are tied to convergence properties of the respective prediction, in close analogy to suitable renormalisation scale choices of the strong coupling α_s . The values of m_t , obtained by using this approach, are less precise than the direct m_t^{MC} measurements. This is because the $\sigma_{t\bar{t}}$ is more sensitive to the hard production mechanism and, in general, less sensitive to the kinematic dependence on

m_t than the observables in direct measurements (discussed in Section 3.3). The analyses, where the Lagrangian mass is extracted, are affected by very different systematic uncertainties, and therefore represent important alternatives to direct m_t^{MC} determinations.

The first extraction of the Lagrangian top quark mass using inclusive $\sigma_{t\bar{t}}$ in proton-proton collisions at the LHC was performed by the CMS Collaboration at $\sqrt{s} = 7$ TeV [52]. This analysis identified a general issue of such determinations, that is the further dependence of the $\sigma_{t\bar{t}}$ prediction on $\alpha_S(m_Z)$ and the PDFs. Another problem was represented by the remaining dependence of the measured $\sigma_{t\bar{t}}$ on the value of m_t^{MC} , inherited from the extrapolation of the fiducial measurement to the full phase space, which relies on the simulation of the final state. These problems were addressed by the CMS Collaboration in a series of follow-up studies [63, 64, 69, 227], where novel experimental analyses techniques have been developed, and specific observables in $t\bar{t}$ and $t\bar{t}$ +jet production have been measured.

To assure the highest purity of the $t\bar{t}$ signal, most of the $\sigma_{t\bar{t}}$ measurements used to extract m_t have been performed in the dilepton channel. The experimental techniques of the cross section measurements have constantly been improved. More recent measurements use template fits to multi-differential distributions in the selected final state, taking into account features of the topology of the $t\bar{t}$ signal and the background. As a result, the systematic uncertainties were further reduced and correlations between systematic uncertainties were treated consistently, resulting in a significantly improved experimental precision of the cross section measurements [54, 63]. Since the first m_t measurement in CMS, also the technique of reconstructing the $t\bar{t}$ pairs in dilepton final states have experienced significant developments. As detailed in Section 2, the determination of the momenta of the two neutrinos in the dilepton channel required assumptions on the masses of the W boson and the top quark. Releasing these requirements in m_t measurements has triggered methodical improvements, such as the so-called loose kinematic reconstruction and the DNN-based reconstruction of $t\bar{t}$ pairs, discussed in details in Section 2.3.

Further, novel observables in top quark production and decay have been explored, as suggested by theoretical investigations. The inverse of the invariant mass of the $t\bar{t}$ +jet system, ρ , in events where the $t\bar{t}$ pair is produced with an associated energetic jet, and the invariant mass of the b quark and the lepton from the W boson decay, $m_{\ell b}$ [228], exhibit a strong dependence on m_t^{pole} . In particular, by considering the $m_{\ell b}^{\text{min}}$ distribution in the $\sigma_{t\bar{t}}$ measurement, its dependence on m_t^{MC} is used for the simultaneous extraction of $\sigma_{t\bar{t}}$ and m_t^{MC} . This way, the remaining dependence of $\sigma_{t\bar{t}}$ on m_t^{MC} is mitigated and one of the major problems of m_t extractions via inclusive or differential $\sigma_{t\bar{t}}$ measurements is resolved. This approach made it possible to extract m_t^{pole} and $m_t(m_t)$ without an additional uncertainty related to the prior assumption of m_t^{MC} in inclusive and differential measurements, leading to the first experimental confirmation of the running of the scale dependent $\overline{\text{MS}}$ top quark mass [65].

The 3-fold correlations of m_t^{pole} , PDFs, and α_S in the QCD prediction of $\sigma_{t\bar{t}}$ was further investigated by the CMS Collaboration [64] using multi-differential $\sigma_{t\bar{t}}$ measurements. In particular, by including the measurements of $m_{t\bar{t}}$ and $y_{t\bar{t}}$ in a comprehensive QCD analysis at NLO, the PDFs, $\alpha_S(m_Z)$, and m_t^{pole} could be extracted simultaneously and their correlations were demonstrated to significantly reduce. This analysis resulted in the most precise value of m_t^{pole} at NLO to that date, with simultaneously reduced uncertainty in the gluon PDF. At the same time, a low value of $\alpha_S(m_Z)$ was obtained, in tension with the results of other measurements at the LHC. In a follow-up analysis [227], this issue was resolved by including the CMS jet production

measurements which have additional strong sensitivity to PDFs and $\alpha_S(m_Z)$.

In the following, the aforementioned analyses are discussed in more details, with the emphasis on the progress of analysis strategies with respect to the state-of-the-art at the time of the measurements. In each of the mentioned analyses, the extraction of m_t is performed under the assumption that the measured $t\bar{t}$ cross sections are not affected by physics phenomena beyond the SM.

4.1 Measurements of m_t^{pole} from inclusive $t\bar{t}$ cross sections

In the CMS work [52], the predicted inclusive $\sigma_{t\bar{t}}$ at NNLO+NNLL [77] was compared to the most precise single measurement at $\sqrt{s} = 7$ TeV at CMS to that date [229], using an integrated luminosity of 2.3 fb^{-1} of the data in the dilepton decay channel. The values of m_t^{pole} and, alternatively, of $\alpha_S(m_Z)$ were determined. In Fig. 33, the dependence of the predicted $\sigma_{t\bar{t}}$ cross section on the value of m_t^{pole} is shown.

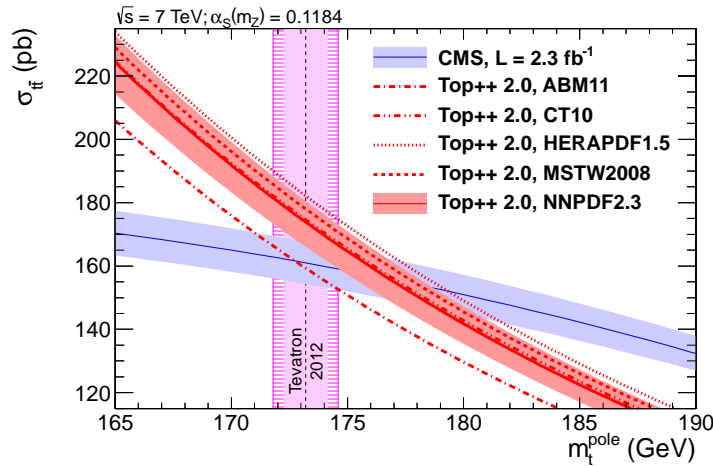


Figure 33: Predicted $\sigma_{t\bar{t}}$ as a function of the top quark pole mass, using different PDF sets (red shaded band and red lines of different styles), compared to the cross section measured by CMS assuming $m_t^{\text{MC}} = m_t^{\text{pole}}$ (blue shaded band). The uncertainties in the measured $\sigma_{t\bar{t}}$ as well as the scale and PDF uncertainties in the prediction with NNPDF2.3 [126] are illustrated by the filled band. The m_t^{MC} result obtained in direct measurements to that date is shown as hatched area. The inner (solid) area of the vertical band corresponds to the quoted experimental uncertainty in m_t^{MC} , while the outer (hatched) area additionally accounts for a possible difference between this value and m_t^{pole} . Figure taken from Ref. [52].

Besides the value of m_t^{pole} , the predicted cross section depends on the value of α_S . A simultaneous extraction of m_t and $\alpha_S(m_Z)$ from the inclusive $\sigma_{t\bar{t}}$ alone is not possible since both parameters alter the predicted $\sigma_{t\bar{t}}$ in such a way that any variation of one parameter can be compensated by a variation of the other. In cross section calculations, $\alpha_S(m_Z)$ appears not only in the expression for the parton-parton interaction but also in the QCD evolution of the PDFs. Varying the value of $\alpha_S(m_Z)$ in the $\sigma_{t\bar{t}}$ calculation therefore requires a consistent modification of the PDFs. Consequently, to extract the value of m_t^{pole} , a choice of the PDFs and of $\alpha_S(m_Z)$ has to be made. The interplay of m_t , $\alpha_S(m_Z)$, and the proton PDFs in the predicted $\sigma_{t\bar{t}}$ was studied for the first time by using 5 different PDF sets available to that date at NNLO, and for each set a series of different choices of $\alpha_S(m_Z)$ was considered.

The cross section was measured to be $\sigma_{t\bar{t}} = 161.9 \pm 2.5$ (stat) $_{-5.0}^{+5.1}$ (syst) ± 3.6 (lumi) pb [229] using the profile likelihood ratio method, where the minimum value of a function $-2 \ln[R(\sigma_{t\bar{t}})]$ is determined. The ratio R is composed of the likelihood functions depending on $\sigma_{t\bar{t}}$ and the maximum likelihood estimates of $\sigma_{t\bar{t}}$, as well as the sets of nuisance parameters describing the systematic uncertainties in the measurement. The likelihoods are defined by a probability density function binned in a 2-dimensional space of jet multiplicity and the multiplicity of b-tagged jets [229]. The acceptance for $t\bar{t}$ and, in turn, the measured $\sigma_{t\bar{t}}$ depend on the value of m_t^{MC} that is used to simulate $t\bar{t}$ events. The central value of $\sigma_{t\bar{t}}$ is obtained by assuming $m_t^{\text{MC}} = 172.5$ GeV, while the dependence of $\sigma_{t\bar{t}}$ on m_t^{MC} is studied by varying m_t^{MC} in the MC simulation in the range 160–185 GeV and parameterised, as shown in Fig. 33 by a blue shaded band.

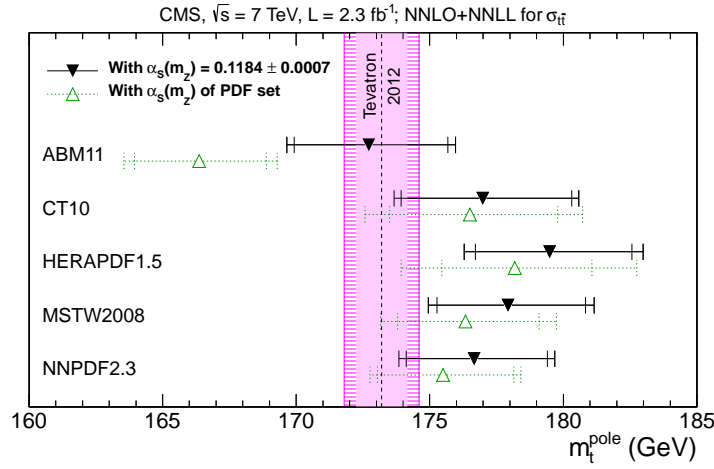


Figure 34: Values of m_t^{pole} obtained by using measured $\sigma_{t\bar{t}}$ together with the prediction at NNLO+NNLL using different NNLO PDF sets. The filled symbols represent the results obtained when using the world average of $\alpha_s(m_Z)$, while the open symbols indicate the results obtained with the default $\alpha_s(m_Z)$ value of the respective PDF set. The inner error bars include the uncertainties in the measured cross section and in the LHC beam energy, as well as the PDF and scale uncertainties in the predicted cross section. The outer error bars additionally account for the uncertainty in the $\alpha_s(m_Z)$ value used for a specific prediction. For comparison, the most precise m_t^{MC} to that date is shown as vertical band, where the inner (solid) area corresponds to the original uncertainty of the direct m_t average, while the outer (hatched) area additionally accounts for the possible difference between m_t^{MC} and m_t^{pole} . Figure taken from Ref. [52].

The extraction of m_t^{pole} was performed through the so-called probabilistic approach by maximising the marginalised posterior

$$P(m_t^{\text{pole}}) = \int_{m_t^{\text{pole}}} f_{\text{exp}}(\sigma_{t\bar{t}}(m_t^{\text{pole}})) f_{\text{th}}(\sigma_{t\bar{t}}(m_t^{\text{pole}})). \quad (22)$$

The measured cross section and its uncertainty are represented by a Gaussian probability $f_{\text{exp}}(\sigma_{t\bar{t}})$. The probability function for the predicted cross section, $f_{\text{th}}(\sigma_{t\bar{t}})$, was obtained through an analytic convolution of two probability distributions, one accounting for the PDF uncertainty and the other for scale uncertainties. A Gaussian distribution is used to describe the PDF uncertainty. Given that no particular probability distribution is known to be adequate for the confidence interval obtained from the variation of the factorisation, μ_f , and renormalisation, μ_r , scales, the corresponding uncertainty in the $\sigma_{t\bar{t}}$ prediction is approximated using a flat prior. The posterior $P(m_t^{\text{pole}})$ is marginalised by integration over $\sigma_{t\bar{t}}$ and a Bayesian credible

interval for m_t^{pole} is computed, based on the external constraint for $\alpha_S(m_Z)$. The results using different sets of PDF are presented in Fig. 34. The top quark pole mass is determined to be $m_t^{\text{pole}} = 176.7^{+3.0}_{-2.8}$ GeV using the theoretical prediction based on the NNPDF2.3 PDF [52]. The experimental and theoretical uncertainties equally contribute to the final precision of 1.7%. The theoretical precision is limited by the PDF uncertainties (0.8%) and the variation of the QCD scales in the theoretical prediction at NNLO+NLL (0.5%), followed by the uncertainty in the assumption $m_t^{\text{pole}} = m_t^{\text{MC}}$, for which 1 GeV was assumed. This first LHC measurement of m_t^{pole} , although inferior in precision compared to the direct measurements, has set an important milestone in the extraction of the Lagrangian mass of the top quark. The correlations between m_t^{pole} , $\alpha_S(m_Z)$, and PDFs were for the first time quantified and the remaining dependence of $\sigma_{t\bar{t}}$ on m_t^{MC} was pointed out.

In a later work [54], the analysis strategy to measure the $\sigma_{t\bar{t}}$ was significantly improved. The cross sections were measured through a template fit of the signal and background contributions to multi-differential distributions, binned in the multiplicity of b quark jets and the multiplicity of the other jets in the event. First, the cross section in a fiducial region, $\sigma_{t\bar{t}}^{\text{vis}}$, was determined, defined by the requirements on the transverse momenta and pseudorapidities of the final-state leptons. The expected signal and background distributions were modelled in the fit by template histograms, constructed from the simulated samples. The free parameters in the fit were $\sigma_{t\bar{t}}^{\text{vis}}$, the normalisation for different background contributions, and the nuisance parameters representing other sources of systematic uncertainties, such as the JES and the trigger efficiency. All systematic uncertainties were implemented in the likelihood as nuisance parameters with Gaussian constraints. Each systematic uncertainty was assessed individually by relevant variations in MC simulations or by varying parameter values within their estimated uncertainties in the analysis. Each source was represented by a nuisance parameter, which was fitted together with $\sigma_{t\bar{t}}^{\text{vis}}$. The impact of theoretical assumptions in the modelling was determined by repeating the analysis and replacing the signal $t\bar{t}$ simulation by dedicated simulation samples with varied parameters affecting, e.g. the scales for the hard process and for matching to the parton shower, the hadronisation, the colour-reconnection, the underlying event, and PDFs.

The fiducial results were then extrapolated to obtain the value of $\sigma_{t\bar{t}}$ in the full phase space, by dividing $\sigma_{t\bar{t}}^{\text{vis}}$ by the acceptance, determined from the $t\bar{t}$ signal MC simulation. Since the acceptance depends on the theoretical model used in the MC event generator, it was parameterised as a function of the same nuisance parameters that were used for the modelling uncertainties in the binned likelihood fit of $\sigma_{t\bar{t}}^{\text{vis}}$. For the extrapolation of the fitted $\sigma_{t\bar{t}}^{\text{vis}}$ to the full phase space, the full unconstrained variations of the relevant modelling uncertainties were applied.

The $\sigma_{t\bar{t}}$ measurements at 7 and 8 TeV centre-of-mass energies were simultaneously used to extract m_t^{pole} while the correlation between the two measurements for the systematic uncertainties was taken into account. The cross section fit and the extrapolation to the full phase space were repeated for $m_t^{\text{MC}} = 169.5, 172.5, \text{ and } 175.5$ GeV. For each case, a sample of simulated $t\bar{t}$ events, generated with the corresponding m_t^{MC} value, was used in the fit as a signal model. The dependence of the distributions used in the fit on detector effects and model variations was evaluated individually and the parameterisation of $\sigma_{t\bar{t}}$ dependence on m_t^{MC} was obtained. To express the measured dependence as a function of m_t^{pole} instead of m_t^{MC} , an additional uncertainty in the measured cross section, $\Delta_{m_t^{\pm}}$, was evaluated by varying m_t^{MC} by ± 1 GeV and reevaluating $\sigma_{t\bar{t}}$.

The dependence of the $\sigma_{t\bar{t}}$ measurements on m_t^{pole} was modelled by Gaussian likelihoods as

$$L_{\text{exp}}(m_t^{\text{pole}}, \sigma_{t\bar{t}}) = \exp \left[\frac{(\sigma_{t\bar{t}}(m_t) - \sigma_{t\bar{t}})^2}{-2(\Delta^2 + \Delta_{m_t^\pm}^2)} \right], \quad (23)$$

where Δ is the total uncertainty in each of the $\sigma_{t\bar{t}}$ measurements, considering the measured dependence of $\sigma_{t\bar{t}}(m_t^{\text{pole}})$.

The predicted dependence of $\sigma_{t\bar{t}}$ on m_t^{pole} at NNLO+NNLL was determined with TOP++ [77], employing 3 different PDF sets and $\alpha_S(m_Z) = 0.118 \pm 0.001$. The predicted $\sigma_{t\bar{t}}$ was represented by an asymmetric Gaussian function with width $\Delta_{p,\pm}$, comprising uncertainties in PDF, $\alpha_S(m_Z)$, and the uncertainty in the LHC beam energy, summed in quadrature. This function is convolved with a box function to account for the uncertainty arising from variations of μ_r and μ_f in the theoretical prediction,

$$L_{\text{pred}}(m_t^{\text{pole}}, \sigma_{t\bar{t}}) = \frac{1}{C(m_t^{\text{pole}})} \left(\text{erf} \left[\frac{\sigma_{t\bar{t}}^{(h)}(m_t^{\text{pole}}) - \sigma_{t\bar{t}}}{\sqrt{2}\Delta_{p,+}} \right] - \text{erf} \left[\frac{\sigma_{t\bar{t}}^{(l)}(m_t^{\text{pole}}) - \sigma_{t\bar{t}}}{\sqrt{2}\Delta_{p,-}} \right] \right). \quad (24)$$

Here, $\sigma_{t\bar{t}}^{(h)}$ and $\sigma_{t\bar{t}}^{(l)}$ denote the upper and lower predicted cross section values, respectively, from variations of μ_r and μ_f . The normalisation factor $C(m_t^{\text{pole}})$ assures that $\max(L_{\text{pred}}) = 1$ for any fixed m_t^{pole} . The value of m_t^{pole} is extracted by using the product of the two likelihoods, L_{exp} and L_{pred} , maximised simultaneously with respect to m_t^{pole} and $\sigma_{t\bar{t}}$. The likelihoods for the predicted $\sigma_{t\bar{t}}$ obtained using the NNPDF3.0 PDF set, and the measurement of $\sigma_{t\bar{t}}$ at $\sqrt{s} = 7$ and 8 TeV as a function of m_t^{pole} are shown in Fig. 35. As a result, the value of $m_t^{\text{pole}} = 173.8^{+1.7}_{-1.8}$ GeV was obtained [54], with the uncertainty of 1%.

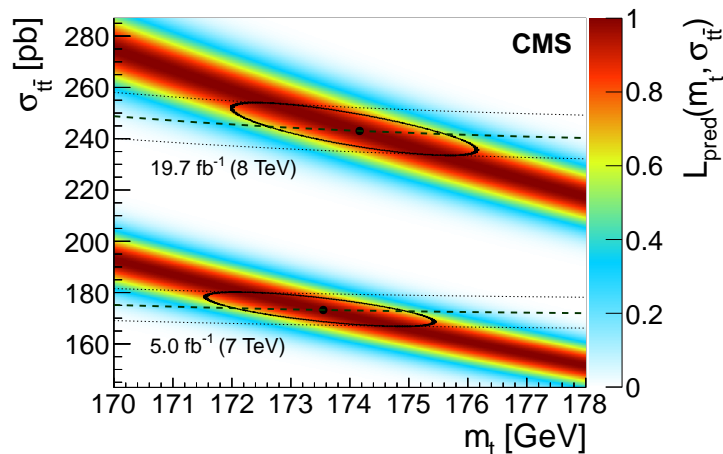


Figure 35: Likelihood for the predicted dependence of $\sigma_{t\bar{t}}$ on m_t^{pole} for 7 and 8 TeV determined with TOP++, using the NNPDF3.0 PDF set. The measured dependencies on the mass are given by the dashed lines, their 1σ uncertainties are represented by the dotted lines. The extracted mass at each value of \sqrt{s} is indicated by a black point, with its ± 1 standard deviation uncertainty constructed from the continuous contour, corresponding to $-2\Delta \log(L_{\text{pred}}L_{\text{exp}}) = 1$. Figure taken from Ref. [54].

From the experimental perspective, the remaining dependence of $\sigma_{t\bar{t}}$ on the assumed m_t^{MC} and the related additional uncertainty in m_t^{pole} seemed yet unsatisfactory. This issue was addressed in later analyses by introducing novel observables in $t\bar{t}$ production, sensitive to m_t^{MC} , into the template fit in the $\sigma_{t\bar{t}}$ measurement.

4.2 Mitigating the dependence of the measured cross section on m_t^{MC}

Beyond the inclusive cross section, the top quark mass can be extracted from m_t -sensitive kinematic distributions. However, the reliability of the precision of the respective results obtained using parton-shower event generators suffers from the aforementioned m_t^{MC} interpretation. Alternative ways to estimate theoretical uncertainties in the description of relevant kinematic distributions and specific observables were investigated. Several kinematic distributions, typically involving top quark decay products were suggested, e.g. in Ref. [228]. The NLO QCD corrections to $t\bar{t}$ production and decay considering the spin correlations became available at the same time, e.g. Refs. [230, 231]. In particular, the higher order corrections were important since those allow the distinction between the mass parameters defined in different renormalisation schemes. In Ref. [228], several observables relevant for the m_t extraction at LO and NLO QCD were studied, and their sensitivity to input parameters was investigated. One of the most promising observables was found to be the invariant mass of the lepton and the b jet, $m_{\ell b}$, in dilepton $t\bar{t}$ events. Considering the top quark decay $t \rightarrow bW$, $W \rightarrow \ell\nu$ at LO and neglecting the masses of leptons and b quark,

$$m_{\ell b}^2 = \frac{m_t^2 - m_W^2}{2}(1 - \cos\theta_{\ell b}), \quad (25)$$

so the dependence of $m_{\ell b}$ on m_t is precisely known, given a value of the W boson mass m_W . Here, $\theta_{\ell b}$ is the angle between the lepton and the b quark in the W boson rest frame. At maximum, the value of $m_{\ell b}$ approaches $\sqrt{m_t^2 - m_W^2}$. Experimentally, there is an ambiguity in which of the two b jets should be combined with the chosen lepton of a certain charge. Therefore, the lepton is associated with the b jet resulting in the smallest value of $m_{\ell b}$, $m_{\ell b}^{\text{min}}$. The $m_{\ell b}^{\text{min}}$ distribution was shown to be under good theoretical control, but the way higher-order effects are considered appeared important [232, 233]. For the experimental extraction of m_t using $m_{\ell b}^{\text{min}}$, however, the respective NLO calculation would need to be implemented in the MC simulations used in the measurement of $\sigma_{t\bar{t}}$. In the absence of those, $m_{\ell b}^{\text{min}}$ appeared to be a promising observable in the determination of m_t^{MC} and in the mitigation of the m_t^{MC} -dependence of the $\sigma_{t\bar{t}}$ measurement.

The $m_{\ell b}^{\text{min}}$ distribution provides strong sensitivity to the choice of m_t^{MC} at values of $m_{\ell b}^{\text{min}}$ close to the top quark mass, as demonstrated in Fig. 36.

A generic approach to measure any observed distribution ξ sensitive to m_t in a particular renormalisation scheme without any prior assumptions on m_t^{MC} , or its relation to m_t , was suggested in Ref. [218]. The method employs a simultaneous likelihood fit of m_t^{MC} and ξ , comparing an observed distribution in data to its MC prediction. In later CMS analyses, $m_{\ell b}^{\text{min}}$ is chosen as such an observable.

In the view of precision measurements of m_t , the fundamental issue of m_t^{pole} is the infrared-sensitivity, also known as the renormalon problem, which leads to poor perturbative behavior. Alternative renormalisation schemes [184, 234] were explored in the context of m_t measurements at the LHC, and better perturbative convergence by using the $\overline{\text{MS}}$ scheme was demon-

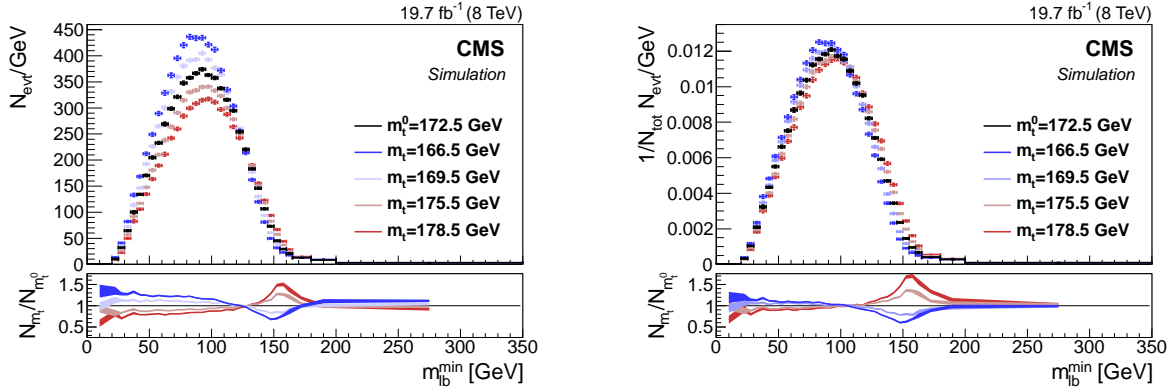


Figure 36: Absolute (left) and shape (right) distributions of m_{lb}^{\min} for $t\bar{t}$ production at the LHC at $\sqrt{s} = 8$ TeV after detector simulation and event selection in the $e\mu$ channel. The central prediction (black symbols) is obtained at the value of m_t^{MC} of 172.5 GeV, denoted as m_t^0 . Predictions assuming different m_t^{MC} values are shown by different colours.

strated [234]. Using the higher-order calculations for inclusive and differential $\sigma_{t\bar{t}}$ in the $\overline{\text{MS}}$ scheme, extraction of the running mass of the top quark, $m_t(m_t)$, and of its scale-dependence becomes possible.

In the CMS analysis [63] based on the LHC data collected at a centre-of-mass energy of 13 TeV, the top quark mass is extracted in both the on-shell and the $\overline{\text{MS}}$ mass schemes. In Ref. [63], the $\sigma_{t\bar{t}}$ measurement was performed using a template fit to multidifferential distributions, similar to the measurement [54] at $\sqrt{s} = 7$ and 8 TeV. First, a visible $t\bar{t}$ cross section $\sigma_{t\bar{t}}^{\text{vis}}$ in the experimentally accessible fiducial volume is determined, using the fit to constrain the systematic uncertainties from the data. The measured $\sigma_{t\bar{t}}^{\text{vis}}$ is then extrapolated to the full phase space to obtain $\sigma_{t\bar{t}}$, which introduces a residual dependence of $\sigma_{t\bar{t}}$ on m_t^{MC} , due to the impact of m_t^{MC} on the simulated detector acceptance. In contrast to previous measurements, where this dependence was determined by repeating the analysis with varied m_t^{MC} , the approach of Ref. [218] is followed and m_t^{MC} is introduced in the fit as an additional free parameter. The sensitivity to m_t^{MC} is enhanced by introducing the m_{lb}^{\min} distribution in the fit. In the simultaneous fit, $\sigma_{t\bar{t}}$ and m_t^{MC} are directly constrained from the data. The resulting $\sigma_{t\bar{t}}$ and its uncertainty therefore account for the dependence on m_t^{MC} , irrespective of its physics interpretation, and are used for the extraction of m_t^{pole} and $m_t(m_t)$, or alternatively, of $\alpha_s(m_Z)$.

While Ref. [63] contains $\sigma_{t\bar{t}}$ measurements obtained in the e^+e^- , $\mu^+\mu^-$, and $e^\pm\mu^\mp$ channels, to minimise the impact from background, only the $e^\pm\mu^\mp$ channel was used for the simultaneous $\sigma_{t\bar{t}}$ and m_t^{MC} measurement. The templates describing the distributions for the signal and background events were taken from the simulation and their statistical uncertainty was accounted for by using pseudo-experiments. To construct the templates describing the dependence of the final-state distributions on m_t^{MC} , separate MC simulation samples of $t\bar{t}$ and tW production were used, in which m_t^{MC} is varied in the range 169.5–175.5 GeV.

The fit was performed in twelve mutually exclusive categories, according to the number of b-tagged jets and of additional non-b-tagged jets in the event. Categorising the events by their b-tagged jet multiplicity allows to constrain the efficiency to select and identify a b jet. Besides $\sigma_{t\bar{t}}^{\text{vis}}$, the free parameters of the fit are the nuisance parameters $\vec{\lambda}$ corresponding to the various sources of systematic uncertainty. The function $-2\ln(L)$ was minimised, with likelihood L

based on Poisson statistics:

$$L = \prod_i \frac{e^{-v_i} v_i^{n_i}}{n_i!} \prod_j \pi(\lambda_j). \quad (26)$$

Here, i denotes the bin of the respective final-state distribution, while v_i and n_i are the expected and observed number of events in bin i , respectively. The terms $\pi(\lambda_j)$ account for deviations of the nuisance parameters λ_j from their nominal values according to their prior density distributions, which are assumed to be Gaussian. In the fit, the expected number of events in each bin i , v_i , is parameterised as

$$v_i = s_i(\sigma_{t\bar{t}}^{\text{vis}}, \vec{\lambda}) + \sum_k b_{k,i}^{\text{MC}}(\vec{\lambda}), \quad (27)$$

where s_i is the expected number of $t\bar{t}$ signal events in bin i , and $b_{k,i}^{\text{MC}}$ represents the predicted number of background events in bin i from a source k . Comparisons of the data and the prediction from the MC simulation before and after the fit are presented in Fig. 37 for the $m_{\ell b}^{\text{min}}$ distribution.

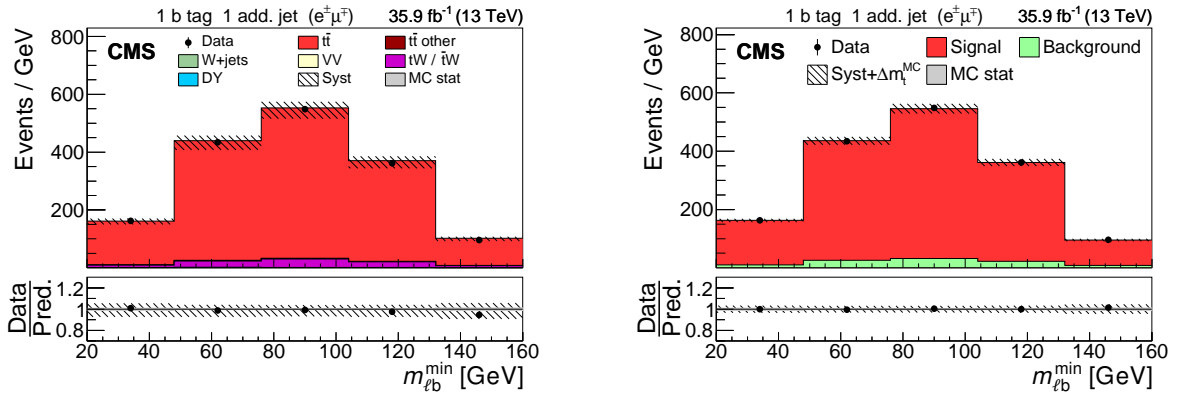


Figure 37: Data (points) compared to pre-fit (left) and post-fit (right) $m_{\ell b}^{\text{min}}$ distributions of the expected signal and backgrounds from simulation (shaded histograms) used in the simultaneous fit of $\sigma_{t\bar{t}}$ and m_t^{MC} . Events with exactly one b-tagged jets are shown. The hatched bands correspond to the total uncertainty in the sum of the predicted yields. The ratios of data to the sum of the predicted yields are shown in the lower panel. Here, the solid grey band represents the contribution of the statistical uncertainty. Figures taken from Ref. [63].

The fit impact on the uncertainties can be quantified by the pulls and constraints of the corresponding nuisance parameters. The constraint is defined as the ratio of the post-fit uncertainty to the pre-fit uncertainty of a given nuisance parameter, while the normalised pull is the difference between the post-fit and the pre-fit values of the nuisance parameter normalised to its pre-fit uncertainty. The normalised pulls and constraints of the nuisance parameters related to the modelling uncertainties for the simultaneous fit of $\sigma_{t\bar{t}}$ and m_t^{MC} in the CMS analysis [63] are shown in Fig. 38.

As a result of the simultaneous fit, the values of $\sigma_{t\bar{t}} = 815 \pm 2$ (stat) ± 29 (syst) ± 20 (lumi) pb, and $m_t^{\text{MC}} = 172.33 \pm 0.14$ (stat) $^{+0.66}_{-0.72}$ (syst) GeV are obtained [63], with 12% correlation between the two.

The result on $\sigma_{t\bar{t}}$ is used together with the QCD prediction [198] at NNLO in the $\overline{\text{MS}}$ scheme to extract the value of $m_t(m_t)$. For this purpose, the measured and the predicted cross sections are compared via a χ^2 minimisation, using the open-source QCD analysis framework xFITTER [235]. For a measurement μ , a corresponding theoretical prediction m , and the set of

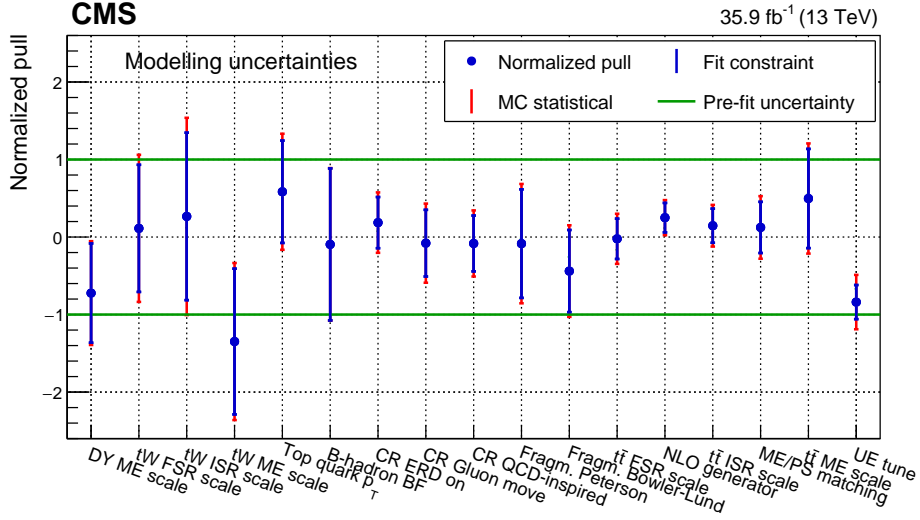


Figure 38: Normalised pulls and constraints of the nuisance parameters related to the modelling uncertainties for the simultaneous fit of $\sigma_{t\bar{t}}$ and m_t^{MC} . The markers denote the fitted value, while the inner vertical bars represent the constraint and the outer vertical bars denote the additional uncertainty as determined from pseudo-experiments. The constraint is defined as the ratio of the post-fit uncertainty to the pre-fit uncertainty of a given nuisance parameter, while the normalised pull is the difference between the post-fit and the pre-fit values of the nuisance parameter normalised to its pre-fit uncertainty. The horizontal lines at ± 1 represent the pre-fit uncertainty. Figure taken from Ref. [63].

systematic nuisance parameters \vec{b} , the following χ^2 definition is used:

$$\chi^2(m, \vec{b}) = \frac{[\mu - m(1 - \sum_j \gamma_j b_j)]^2}{\delta_{\text{unc}}^2 m^2 + \delta_{\text{stat}}^2 \mu m(1 - \sum_j \gamma_j b_j)} + \sum_j b_j^2. \quad (28)$$

Here, δ_{stat} and δ_{unc} are relative statistical and uncorrelated systematic uncertainties of the measurement, γ_j quantifies the sensitivity of the measurement to the correlated systematic source j . This definition of the χ^2 function assumes that systematic uncertainties are proportional to the values of the central prediction (multiplicative uncertainties, $m_i(1 - \sum_j \gamma_j b_j)$), whereas the statistical uncertainties scale with the square root of the expected number of events.

The four most recent PDF sets available at NNLO to that date were used: ABMP16nnlo, CT14nnlo, MMHT14nnlo, and NNPDF3.1nnlo. Unlike other PDF sets, the ABMP16nnlo employs the $\overline{\text{MS}}$ scheme for the heavy quarks in the theoretical predictions used in the PDF determination. For the other PDFs, values of m_t^{pole} are assumed and are converted to $m_t(m_t)$ using the number of α_s loops according to the individual prescription by the corresponding PDF group (as shown in Table 4 of Ref. [63]). Because of the strong correlation between $\alpha_s(m_Z)$ and $m_t(m_t)$ in the prediction of $\sigma_{t\bar{t}}$, for the $m_{t\bar{t}}$ extraction, the value of $\alpha_s(m_Z)$ in the theoretical prediction is set to that of the particular PDF set.

The fit is performed by varying $m_t(m_t)$ in the theoretical prediction in the range $158 < m_t(m_t) < 163$ GeV for ABMP16nnlo PDF and in the range $162 < m_t(m_t) < 167$ GeV for the other PDFs. The uncertainties related to the variation of $\alpha_s(m_Z)$ in the PDFs are estimated by repeating the fit using the PDF eigenvectors with $\alpha_s(m_Z)$ varied within its uncertainty as provided by each PDF, except for ABMP16nnlo, where the value of $\alpha_s(m_Z)$ is a free parameter in the PDF fit and its uncertainty is included in the eigenvectors.

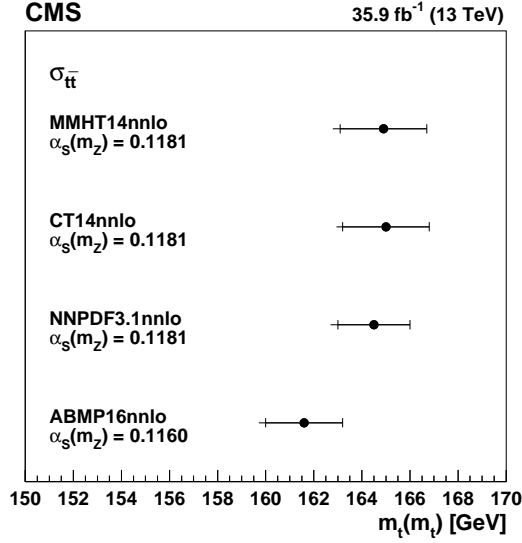


Figure 39: Values of $m_t(m_t)$ obtained from comparing the $\sigma_{t\bar{t}}$ measurement to the theoretical NNLO predictions using different PDF sets. The inner horizontal bars on the points represent the quadratic sum of the experimental, PDF, and $\alpha_s(m_Z)$ uncertainties, while the outer horizontal bars give the total uncertainties. Figure taken from Ref. [63].

Instead of assuming a prior for the scale variation uncertainty, in the analysis [63], the variation of μ_r and μ_f was externalised, by repeating the χ^2 fit independently for different choices of the μ_r and μ_f in the predicted $\sigma_{t\bar{t}}$. The nominal values of these scales were set to $m_t(m_t)$ and varied by a factor of two up and down, independently. The largest differences of the results to the nominal one was considered as scale uncertainty. The results on $m_t(m_t)$ are illustrated in Fig. 39.

The results obtained with different PDF sets are in agreement, although the ABMP16nnlo PDF set yields a systematically lower value. This difference is expected and has its origin in a larger value of $\alpha_s(m_Z) = 0.118$ assumed in the NNPDF3.1, MMHT2014, and CT14 PDFs. The result obtained by using ABMP16 PDF, $m_t(m_t) = 161.6 \pm 1.6$ (fit+PDF+ α_s) $^{+0.1}_{-1.0}$ (scale) GeV [63], with its total uncertainty of about 1.2%, should be considered as the most theoretically consistent, since only ABMP16 PDF implies a heavy quark treatment in the $\overline{\text{MS}}$ scheme and considers the correlation between the $\alpha_s(m_Z)$ and PDF. Using the same theoretical prediction consistently in the pole mass scheme, results in $m_t^{\text{pole}} = 169.1 \pm 1.8$ (fit+PDF+ α_s) $^{+1.3}_{-1.9}$ (scale) GeV [63] using the ABMP16 PDF. The shift between the pole and the running mass values is expected, but the significantly smaller scale uncertainties in the case of the $\overline{\text{MS}}$ scheme arises from significantly better perturbative convergence in this scheme.

While higher experimental precision is achieved in the 13 TeV analysis as compared to 7 and 8 TeV measurements, the full consideration of the PDF eigenvectors in $\sigma_{t\bar{t}}$ calculation and, in turn, in the χ^2 minimisation procedure, and externalising the scale variations leads to an increased uncertainty with respect to the combined 7 and 8 TeV result. Therefore, the extraction of m_t through comparison of measured and predicted $\sigma_{t\bar{t}}$ has the limitation by the PDF uncertainty, and aforementioned correlation of PDF, α_s , and m_t in the prediction of $\sigma_{t\bar{t}}$. The correlations between the $m_t(m_t)$ with the assumption on $\alpha_s(m_Z)$ was investigated in detail for each PDF by performing a χ^2 scan in $\alpha_s(m_Z)$ for ten different assumptions of $m_t(m_t)$, varied from 160.5 to 165.0 GeV. A linear dependence is observed, as shown in Fig. 40, illustrating the strong

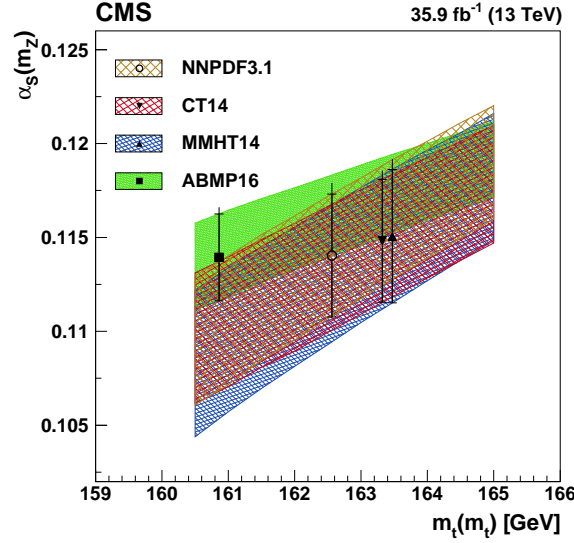


Figure 40: Values of $\alpha_S(m_Z)$ obtained in the comparison of the $\sigma_{t\bar{t}}$ measurement to the NNLO prediction using different PDFs, as functions of the $m_t(m_t)$ value used in the theoretical calculation. The results from using the different PDFs are shown by the bands with different shadings, with the band width corresponding to the quadratic sum of the experimental and PDF uncertainties in $\alpha_S(m_Z)$. The resulting measured values of $\alpha_S(m_Z)$ are shown by the different style points at the $m_t(m_t)$ values used for each PDF. The inner vertical bars on the points represent the quadratic sum of the experimental and PDF uncertainties in $\alpha_S(m_Z)$, while the outer vertical bars show the total uncertainties. Figure taken from Ref. [63].

correlation of the PDF, $\alpha_S(m_Z)$ and $m_t(m_t)$ in the $\sigma_{t\bar{t}}$ prediction and the related ambiguity in the extraction of one parameter by fixing the others.

4.3 The first measurement of the running of the top quark mass

In Section 4.2, the inclusive measurement of the $t\bar{t}$ production cross section is used to extract the value of the top quark mass in the $\overline{\text{MS}}$ scheme at the top quark mass scale, $m_t(m_t)$. In the $\overline{\text{MS}}$ scheme, which is the standard scheme used to renormalise α_S , the top quark mass depends on an additional scale μ_m . As already mentioned in Section 2.8, the scale μ_m sets the lower bound of the self-energy contributions absorbed in the $\overline{\text{MS}}$ mass and should be chosen close to the dynamical scale governing the m_t sensitivity of the cross section. This scale setting ensures the absence of large logarithmic corrections as far as the mass dependence of the theoretical prediction is concerned and thus ensures an adequate treatment of quantum corrections related to the mass sensitivity. The $\overline{\text{MS}}$ mass is adequate for cross sections where this dynamical scale is close to or larger than the top quark mass, i.e. $\mu_m \gtrsim m_t$. For the inclusive cross section measurement described in Section 4.2 this dynamical scale is set by typical transverse momentum of the produced top quarks which is around the top quark mass, justifying the use of $m_t(m_t)$.

As in the case of α_S , the scale evolution (often referred to as “running”) of $m_t(\mu_m)$ is described by the renormalisation group equation (RGE):

$$\mu_m^2 \frac{dm_t(\mu_m)}{d\mu_m^2} = -\gamma(\alpha_S(\mu_m)) m_t(\mu_m), \quad (29)$$

where $\gamma(\alpha_S(\mu_m))$ is known as the mass anomalous dimension. This quantity can be calculated in perturbation theory, and the coefficients are currently known up to order α_S^5 [236, 237].

Measuring the running of $m_t(\mu)$ is not only a fundamental test of the validity of perturbative QCD, but also an indirect probe of BSM physics scenarios that can modify the RGE running, e.g. supersymmetric theories [238] or models based on the dynamic mass generation of fermions [239].

Measuring cross sections where the top quark mass sensitivity is governed at widely different energy scales Q allows the running of the $\overline{\text{MS}}$ top quark mass to be measured by extracting the value of $m_t(\mu_m = Q)$. This is in close analogy to measurements of the running strong coupling α_s . In Ref. [65], where the first measurement of the running of the top quark mass is presented, this is achieved by comparing a measurement of the $t\bar{t}$ production cross section as a function of $m_{t\bar{t}}$ to the QCD predictions at NLO. The analysis of Ref. [65] makes use of the same data as in Ref. [63], addressing the $t\bar{t}$ production with the $e^\pm\mu^\mp$ final state. The differential cross section, $d\sigma_{t\bar{t}}/dm_{t\bar{t}}$, is measured by means of a profile likelihood unfolding of multi-differential distributions, extending the method of Ref. [63] presented in Section 4.1. The investigation of the $\overline{\text{MS}}$ mass running adopts $m_{t\bar{t}}/2$ as the scale μ_m , which quantifies the energy scale of the hard $t\bar{t}$ production process.

In order to measure the $t\bar{t}$ cross section differentially, the $t\bar{t}$ simulation is split into bins of $m_{t\bar{t}}$ at the generator level, and each sub-sample is treated as an independent signal process in the likelihood fit, while preserving the correlation between the systematic uncertainties. This procedure is commonly known as maximum likelihood unfolding. The expected number of events in each bin is parameterised as:

$$\nu_i = \sum_{k=1}^4 s_i^k(\sigma_{t\bar{t}}^k, m_t^{\text{MC}}, \vec{\lambda}) + \sum_j b_i^j(m_t^{\text{MC}}, \vec{\lambda}), \quad (30)$$

where $\sigma_{t\bar{t}}^k$ is the total cross $t\bar{t}$ cross section in bin k of $m_{t\bar{t}}$, s_i^k represents the contribution of bin k in $m_{t\bar{t}}$ to bin i , b_i^j is the contamination from background j in that bin, and $\vec{\lambda}$ are the nuisance parameters that parameterise the effects of the systematic uncertainties. As in the analysis of Ref. [63], the effect of m_t^{MC} is profiled in the likelihood. This expression incorporates the effect of the detector response and of the signal acceptance, and directly connects parton-level quantities to measurable detector-level distributions. Therefore, the likelihood fit provides directly the unfolded results at the parton level. In order to allow for a comparison to fixed-order theoretical predictions, in this analysis the parton level is defined as the matrix-element level, i.e. before parton showering, assuming stable top quarks. Details on the MC simulation are given in Section 2.4.

In order to enhance the sensitivity to each individual bin of $m_{t\bar{t}}$, the invariant mass of the $t\bar{t}$ system is reconstructed at the detector level ($m_{t\bar{t}}^{\text{reco}}$) using the full kinematic reconstruction described in Section 2.3. The additional dependence on the value of m_t assumed in the kinematic reconstruction is fully parameterised in the likelihood via the parameter m_t^{MC} . As in Ref. [63], this parameter is treated as freely floating in the fit, and is constrained via the $m_{\ell b}^{\text{min}}$ distribution.

The fit is performed in categories of b-tagged jet multiplicity and in bins of $m_{t\bar{t}}^{\text{reco}}$, while all events with less than two jets in the final state, for which no kinematic reconstruction is possible, are assigned to separate categories. The $m_{t\bar{t}}^{\text{reco}}$ distribution after the fit to the data, which illustrates the likelihood unfolding procedure, is shown in Fig. 41 (left). In Fig. 41 (right), instead, the unfolded $d\sigma_{t\bar{t}}/dm_{t\bar{t}}$ is compared to the NLO theoretical predictions used in Ref. [65] to extract the running of m_t . The bin centers are chosen as the average value of $m_{t\bar{t}}$ in each bin according to the POWHEG+PYTHIA8 simulation, and are considered as the representative en-

ergy scale of each $m_{t\bar{t}}$ bin. As illustrated in Fig. 41 (right), the dependence of the $t\bar{t}$ production cross section on the value of m_t decreases rapidly with increasing $m_{t\bar{t}}$.

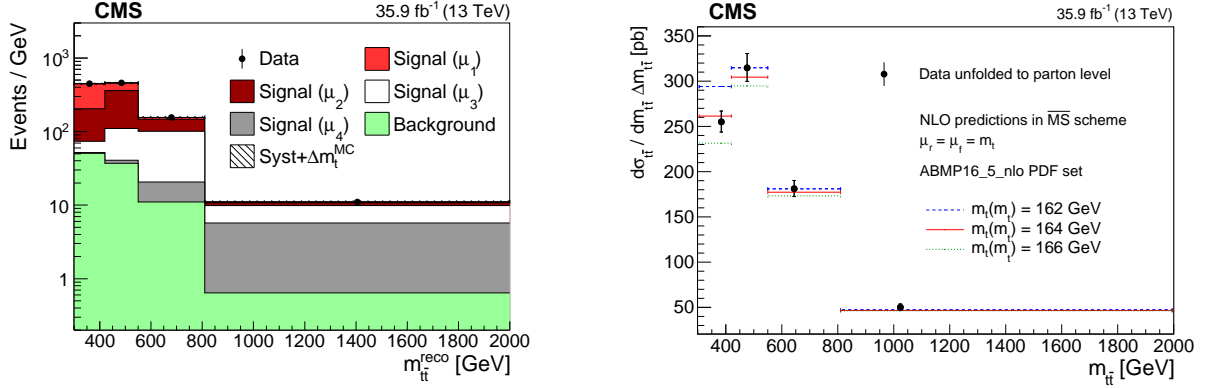


Figure 41: Left: profile likelihood unfolding of the $m_{t\bar{t}}$ distribution. The signal sample is split into subprocesses in bins of parton-level $m_{t\bar{t}}$, and the signal corresponding to bin k in $m_{t\bar{t}}$ is denoted with “Signal (μ_k)”. The vertical bars represent the statistical uncertainty in the data, while the hashed band is the total uncertainty in the MC simulation. Right: unfolded $t\bar{t}$ cross section as a function of $m_{t\bar{t}}$, compared to theoretical predictions in the $\overline{\text{MS}}$ scheme for different values of $m_t(m_t)$. The vertical bars correspond to the total uncertainty in the unfolded cross section. Here, the bin centres for the unfolded cross section are defined as the average $m_{t\bar{t}}$ in the POWHEG+PYTHIA8 simulation. Figures taken from Ref. [65].

An updated extraction of the running of m_t is obtained in the scope of this article, with a similar theoretical setup as the one suggested in Ref. [240], where differential calculations in the $\overline{\text{MS}}$ scheme are obtained at NNLO and compared to the results of Ref. [65]. Here, unlike in the original result of Ref. [65], a bin-by-bin dynamic scale is implemented in the NLO calculation, which allows the direct extraction of the value of $m_t(\mu_m)$. A dynamic scale choice is also favoured from the theoretical point of view, as it accounts for the summation of higher-order QCD corrections. This approach has also been used in the improved analysis of Ref. [241], where the running of m_t is extracted at NNLO in QCD.

The measured cross section of Ref. [65] is also updated according to the new luminosity measurement of the 2016 data set [167], which leads to a significant improvement in the uncertainty in the measured cross section. Following the approach of Ref. [65], the value of $m_t(\mu_m)$ is extracted in each bin of $m_{t\bar{t}}$ separately. Here, μ_m is chosen to be $\mu_k/2$, where μ_k is the representative scale of bin k in $m_{t\bar{t}}$, corresponding to the bin centre in Fig. 41 (right). The measured values of $m_t(\mu_m)$ are normalised to the value of $m_t(\mu_{\text{ref}})$, where μ_{ref} is arbitrarily chosen as the scale of the second bin in $m_{t\bar{t}}$, in order to profit from the cancellation of correlated systematic uncertainties.

The result is shown in Fig. 42, where it is compared to the one-loop solution of the QCD RGE, to the original result of Ref. [65], and to the more recent re-interpretation at NNLO in QCD described in Ref. [241]. However, it has to be noted that the results are not directly comparable to each other, as they differ not only for the perturbative order in QCD, but also for the choice of the renormalisation and factorisation scales in the fixed-order calculations, as summarised in Table 6. Nonetheless, in all cases the RGE running scenario is favoured by the data compared to a hypothetical no-running scenario in which $dm_t(\mu_m)/d\mu_m = 0$.

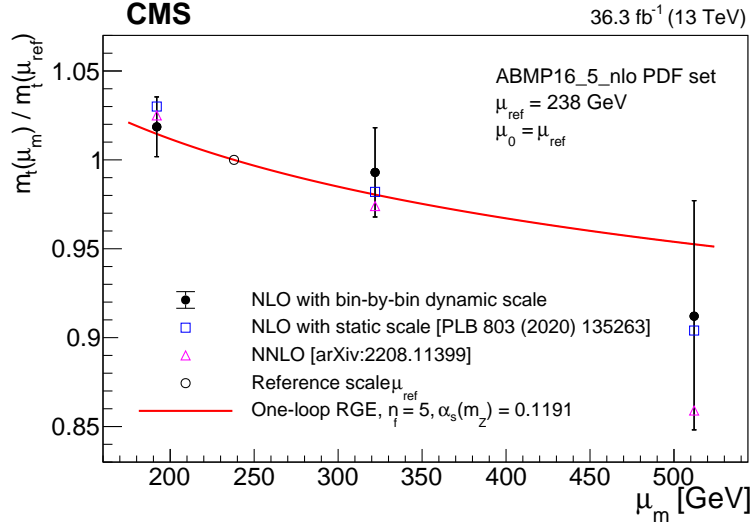


Figure 42: Running of the top quark mass as a function of $\mu_m = m_{t\bar{t}}/2$ obtained with a bin-by-bin dynamic scale $\mu_k/2$ (full circles), compared to the central values of the results of Ref. [65] obtained with a constant scale $\mu_m = \mu_k$ (hollow squares) and to those of the NNLO results of Ref. [241] (hollow triangles). As in Ref. [65], the error bars indicate the combination of experimental, extrapolation, and PDF uncertainties in the NLO extraction with bin-by-bin dynamic scale. The full treatment of the QCD scale variations can be found in Ref. [241]. The assumptions on the renormalisation and factorisation scales adopted in the different interpretations are summarised in Table 6. The uncertainties in the three results, which are mostly correlated, are given in the respective references and are of comparable size.

Table 6: Summary of scale choices for μ_r , μ_f , and μ_m for the three different extractions of the running of the top quark mass. The NLO fixed scale corresponds to the result of Ref. [65], while the NNLO result is described in Ref. [241]. The NLO bin-by-bin dynamic result, instead, is obtained in the scope of this review work.

Fixed-order theory model	μ_m [GeV]	μ_r, μ_f [GeV]
NLO fixed scales	m_t	$m_t(m_t)$
NLO bin-by-bin dynamic scale	$m_{t\bar{t}}/2$	$m_t(\mu_m)$
NNLO bin-by-bin dynamic scale	$m_{t\bar{t}}/2$	μ_m

4.4 Resolving correlations of m_t , $\alpha_S(m_Z)$, and PDFs

The correlation among PDFs, $\alpha_S(m_Z)$, and m_t in the QCD prediction of $\sigma_{t\bar{t}}$ was already mentioned in the context of the extraction of m_t using the inclusive $\sigma_{t\bar{t}}$. The origin of this correlation is the fact that $t\bar{t}$ production in pp collisions is dominated by the gluon-gluon fusion process (to about 90%), so that the gluon PDF, $\alpha_S(m_Z)$, and m_t alter the normalisation and shape of the $\sigma_{t\bar{t}}$ prediction. At the same time, it means that any of these parameters can be extracted individually, by using the $t\bar{t}$ cross sections, only once the other two are fixed. Therefore, besides extraction of m_t or $\alpha_S(m_Z)$ by using the measurements of inclusive cross section of $t\bar{t}$ production, the same measurements can be used to constrain the proton PDFs, by fixing m_t and $\alpha_S(m_Z)$. Due to the large scale, provided by the top quark mass, the $t\bar{t}$ production is sensitive to the gluon distribution $g(x)$ at large fractions x of the proton momentum, carried by the gluon. Due to lack of other experimental data constraining the gluon distribution at high x , $g(x)$ has large uncertainties in this region.

An illustrative example of PDF constraints using the inclusive $\sigma_{t\bar{t}}$ is the result of the CMS analysis [242]. In this work, the $\sigma_{t\bar{t}}$ measurement at $\sqrt{s} = 5.02$ TeV based on the integrated luminosity of 24.4 pb^{-1} was included in a PDF fit at NNLO together with the cross sections of ep deep inelastic scattering (DIS) at HERA [243], and the CMS muon charge asymmetry measurements in W boson production [244]. In the fit, performed by using the open-source QCD analysis platform xFITTER [235], the values of $\alpha_S(m_Z) = 0.118$ and $m_t^{\text{pole}} = 172.5$ GeV are assumed. Already by including a single measurement of $\sigma_{t\bar{t}}$ at 5.02 TeV, the reduction of the uncertainty in $g(x)$ is observed, as shown in Fig. 43.

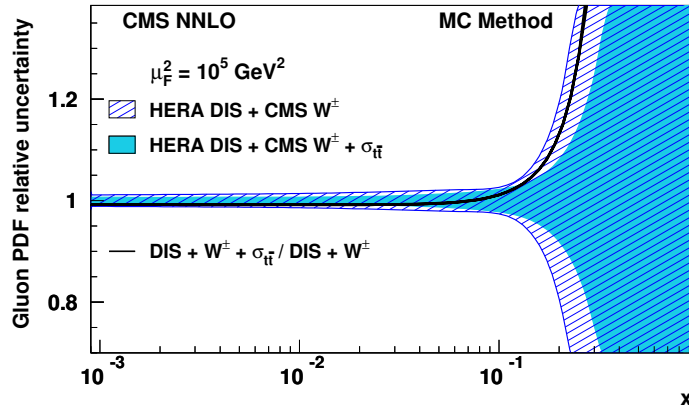


Figure 43: The fractional uncertainties in the gluon distribution function of the proton as a function of x at factorisation scale $\mu_f^2 = 10^5 \text{ GeV}^2$ from a QCD analysis using the DIS and CMS muon charge asymmetry measurements (hatched area), and also including the CMS $\sigma_{t\bar{t}}$ results at $\sqrt{s} = 5.02$ TeV (solid area). The relative uncertainties are found after the two gluon distributions have been normalised to unity. The solid line shows the ratio of the gluon distribution function found from the fit with the CMS $\sigma_{t\bar{t}}$ measurements included to that found without. Figure taken from Ref. [242].

While the PDF constraints by using inclusive $\sigma_{t\bar{t}}$ are achieved only through the global normalisation, differential cross sections provide further information about the PDFs, α_S , and m_t . This was investigated in Ref. [245], where the differential cross sections were suggested to be used in a QCD analyses to extract PDFs, $\alpha_S(m_Z)$, and m_t . In particular, the invariant mass $m_{t\bar{t}}$ and rapidity $y_{t\bar{t}}$ of the $t\bar{t}$ pair are directly related to x as $x = (m_{t\bar{t}}/\sqrt{s}) \exp[\pm y(t\bar{t})]$ at LO QCD. In the CMS work [246], measurements of double-differential $t\bar{t}$ cross sections as functions of $m_{t\bar{t}}$ and $y_{t\bar{t}}$ were demonstrated to be most sensitive to $g(x)$, providing more significant constraints than inclusive or single-differential cross sections.

By using multi-differential $t\bar{t}$ cross sections, it is possible to obtain a good overall constraint on the PDFs, $\alpha_S(m_Z)$, and m_t , simultaneously, since the $m_{t\bar{t}}$ distribution is driven by the value of m_t . To better access the $t\bar{t}$ threshold in the final states with two leptons, the LKR algorithm, discussed in Section 2.3, was developed, probing $m_{t\bar{t}}$ in a less biased way compared to FKR. However, the limited resolution in $m_{t\bar{t}}$ mentioned in Section 2.3.2, prevents splitting the $m_{t\bar{t}}$ distribution in bins narrower than 100–150 GeV, in particular close to the threshold. Further, production of $t\bar{t}$ associated with jets brings in additional sensitivity to $\alpha_S(m_Z)$ at the scale of m_t , and enhances sensitivity to m_t , since the gluon radiation depends on m_t through threshold and cone effects [247].

First simultaneous determination of the PDFs, $\alpha_S(m_Z)$, and m_t^{pole} by using multi-differential $t\bar{t}$ cross sections were carried out by CMS in Ref. [64]. In particular, double-differential $t\bar{t}$ cross sections as functions of $m_{t\bar{t}}$ and $y_{t\bar{t}}$ were measured in different categories with respect to the number of associated additional particle-level jets in the event, N_{jet} , using two ($N_{\text{jet}} = 0$ and $N_{\text{jet}} \geq 1$) and three ($N_{\text{jet}} = 0$, $N_{\text{jet}} = 1$, and $N_{\text{jet}} \geq 2$) bins of N_{jet} . These cross sections are denoted as $[N_{\text{jet}}^{0,1+}, m_{t\bar{t}}, y_{t\bar{t}}]$ and $[N_{\text{jet}}^{0,1,2+}, m_{t\bar{t}}, y_{t\bar{t}}]$, respectively. To correct for the detector resolution and inefficiency, a regularised unfolding was performed simultaneously in bins of the observables in which $\sigma_{t\bar{t}}$ were measured. To compare the measured cross sections for $t\bar{t}$ production with additional jets to NLO QCD predictions, the measured cross sections were further corrected from particle to parton level for MPI, hadronisation, and top quark decay effects, by using the MC simulation. The measured triple-differential cross sections are compared to calculations of the order in α_S required for NLO accuracy: the inclusive $t\bar{t}$ production at $O(\alpha_S^3)$ [248]; $t\bar{t}$ production with one jet at $O(\alpha_S^4)$ [249]; and $t\bar{t}$ production with two additional jets at $O(\alpha_S^5)$ [250, 251]. In particular, the cross sections for inclusive $t\bar{t}$ production are calculated from the sum of the measured $\sigma_{t\bar{t}}$ in the $N_{\text{jet}} = 0$ and $N_{\text{jet}} \geq 1$ bins. Thus, the cross sections obtained for inclusive $t\bar{t}$ and $t\bar{t} + 1$ jet production are compared to the NLO $O(\alpha_S^3)$ and NLO $O(\alpha_S^4)$ calculations, respectively. Similarly, cross sections for inclusive $t\bar{t}$, $t\bar{t} + 1$, and $t\bar{t} + 2$ jets production are obtained using the $[N_{\text{jet}}^{0,1,2+}, m_{t\bar{t}}, y_{t\bar{t}}]$ measurement and compared to the NLO $O(\alpha_S^3)$, NLO $O(\alpha_S^4)$, and NLO $O(\alpha_S^5)$ calculations, respectively.

Using the normalised cross sections results in the partial cancellation of experimental and theoretical uncertainties. To demonstrate the sensitivity to m_t^{pole} , in Fig. 44, the data are compared to the predictions obtained with different values of m_t^{pole} . The largest sensitivity to m_t^{pole} is observed at lower $m_{t\bar{t}}$ (indicated as $M_{t\bar{t}}$ in Fig. 44 and Fig. 45), closest to the $t\bar{t}$ production threshold, while the sensitivity at higher $m_{t\bar{t}}$ occurs mainly because of the cross section normalisation. To further demonstrate the sensitivity of the theoretical predictions for the measured $[N_{\text{jet}}^{0,1+}, m_{t\bar{t}}, y_{t\bar{t}}]$ cross sections to different input parameters, in Fig. 45, the contributions arising from the PDF, $\alpha_S(m_Z)$ (± 0.005), and m_t^{pole} (± 1 GeV) uncertainties are shown separately. The total theoretical uncertainties are obtained by adding the uncertainties originating from PDF, $\alpha_S(m_Z)$, m_t^{pole} , and variations of μ_r and μ_f , in quadrature.

The normalised triple-differential $[N_{\text{jet}}^{0,1+}, m_{t\bar{t}}, y_{t\bar{t}}]$ cross sections are used together with the combined HERA DIS data [243] in a QCD analysis, where PDF, $\alpha_S(m_Z)$, and m_t^{pole} are extracted at NLO, using the xFITTER program [235]. The resulting NLO values of $\alpha_S(m_Z)$ and m_t^{pole} are obtained [64] as follows:

$$\begin{aligned} \alpha_S(m_Z) &= 0.1135 \pm 0.0016 \text{ (fit)} \begin{matrix} +0.0002 \\ -0.0004 \end{matrix} \text{ (model)} \begin{matrix} +0.0008 \\ -0.0001 \end{matrix} \text{ (param)} \begin{matrix} +0.0011 \\ -0.0005 \end{matrix} \text{ (scale)} \\ &= 0.1135 \begin{matrix} +0.0021 \\ -0.0017 \end{matrix} \end{aligned} \quad (31)$$

$$\begin{aligned} m_t^{\text{pole}} &= 170.5 \pm 0.7 \text{ (fit)} \pm 0.1 \text{ (model)} \begin{matrix} +0.0 \\ -0.1 \end{matrix} \text{ (param)} \pm 0.3 \text{ (scale)} \text{ GeV} \\ &= 170.5 \pm 0.8 \text{ GeV.} \end{aligned} \quad (32)$$

Here ‘fit’, ‘model’, and ‘param’ denote the fit, model, and parameterisation uncertainties. The fit uncertainties were obtained using the criterion of $\Delta\chi^2 = 1$. The model uncertainties arise from the variations of assumptions on theoretical inputs, such as masses of c and b quarks or the value of the starting evolution scale. The parameterisation uncertainties originate from the variations of the functional form for the PDFs at the starting scale. In addition, ‘scale’ denotes the uncertainties arising from the scale variations in $\sigma_{t\bar{t}}$ predictions, which are estimated by

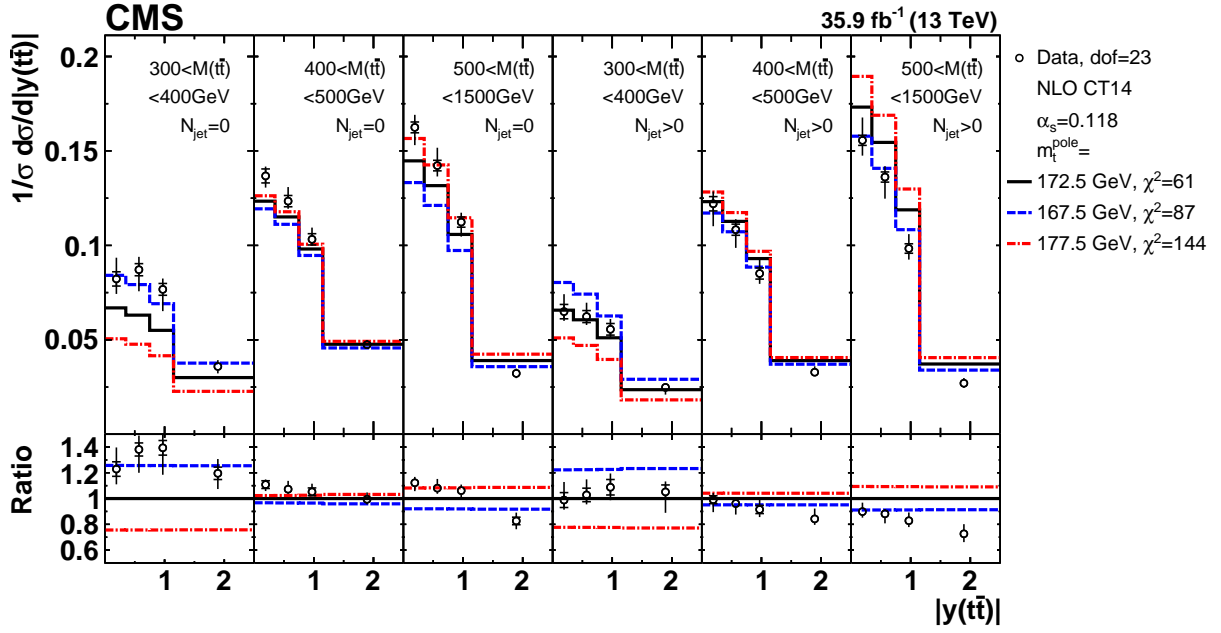


Figure 44: Comparison of the measured $[N_{\text{jet}}^{0,1+}, m_{t\bar{t}}, y_{t\bar{t}}]$ cross sections to NLO predictions obtained using different m_t^{pole} values. For each theoretical prediction, values of χ^2 and dof for the comparison to the data are reported. Figure taken from Ref. [64].

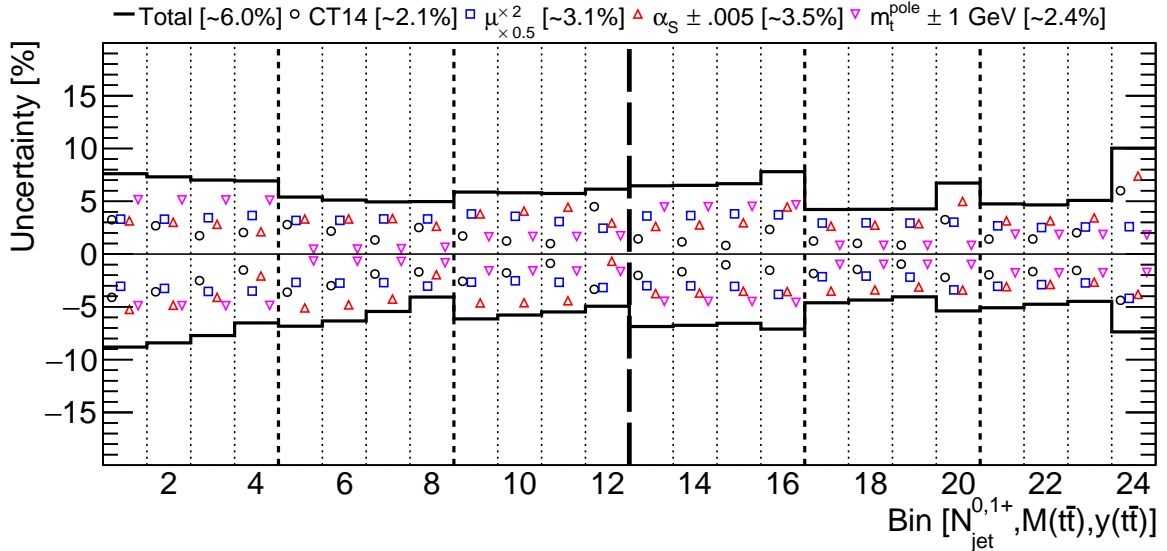


Figure 45: The theoretical uncertainties for $[N_{\text{jet}}^{0,1+}, m_{t\bar{t}}, y_{t\bar{t}}]$ cross sections, arising from the scale, PDF, $\alpha_S(m_Z)$, and m_t variations, as well as the total theoretical uncertainties obtained from variations in μ_r and μ_f , with their bin-averaged values shown in brackets. The bins are the same as in Fig. 44. Figure taken from Ref. [64].

repeating the fit using predictions where the values of μ_r and μ_f are varied by a factor of 2, independently up and down, and taking the differences with respect to the nominal result.

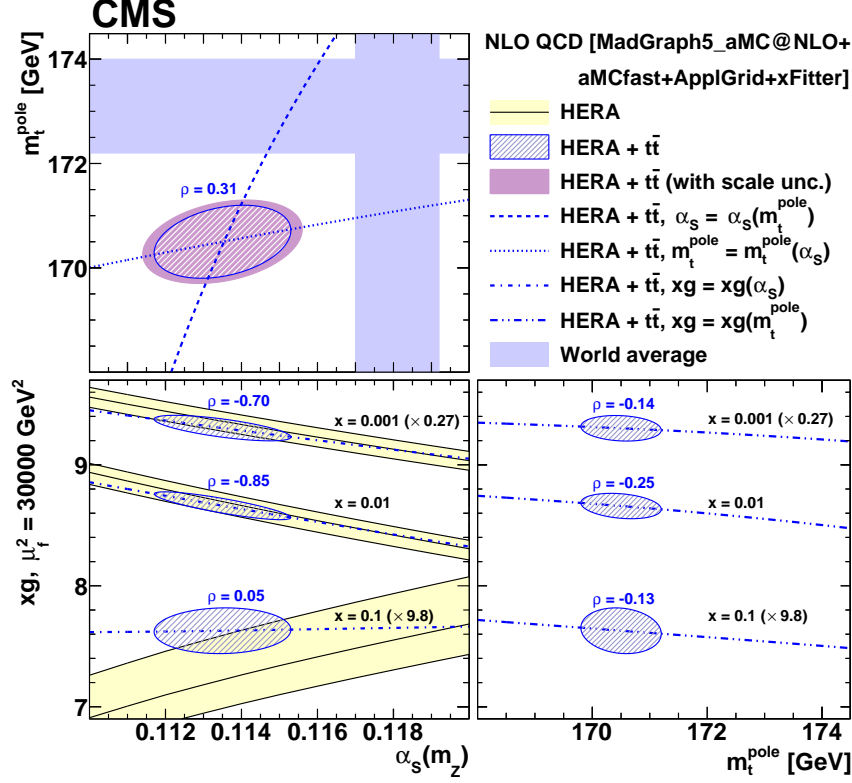


Figure 46: The extracted values and their correlations for α_S and m_t^{pole} (upper left), α_S and gluon PDF (lower left), and m_t^{pole} and gluon PDF (lower, right). The gluon PDF is shown at the scale $\mu_f^2 = 30\,000\text{ GeV}^2$ for several values of x . For the extracted values of α_S and m_t^{pole} , the additional uncertainties arising from the dependence on the scale are shown. The correlation coefficients ρ as defined in Ref. [64] are displayed. Furthermore, values of α_S (m_t^{pole} , gluon PDF) extracted using fixed values of m_t^{pole} (α_S) are displayed as dashed, dotted, or dash-dotted lines. The world average values $\alpha_S(m_Z) = 0.1181 \pm 0.0011$ and $m_t^{\text{pole}} = 173.1 \pm 0.9\text{ GeV}$ from Ref. [252] are shown for reference. Figure taken from Ref. [64].

In Fig. 46 the extracted $\alpha_S(m_Z)$, m_t^{pole} , and gluon PDF at the scale $\mu_f^2 = 30\,000\text{ GeV}^2$ for several values of x are shown, together with their correlations. When using only DIS data, the largest correlation to $\alpha_S(m_Z)$ is observed in the gluon PDF. Once included in the fit, measurement of the $t\bar{t}$ production resolves this correlation in the relevant kinematic range, because of its sensitivity to both $g(x)$ and $\alpha_S(m_Z)$. In addition, the multi-differential $[N_{\text{jet}}^{0,1+}, m_{t\bar{t}}, y_{t\bar{t}}]$ cross sections provide constraints on m_t^{pole} . As a result, the correlations between $g(x)$, $\alpha_S(m_Z)$, and m_t^{pole} are significantly reduced in the kinematic range of $t\bar{t}$ production. This way, the simultaneous QCD analysis of PDFs, $\alpha_S(m_Z)$, and m_t^{pole} has highest potential to extract m_t^{pole} with best precision through mitigating uncertainties in $\alpha_S(m_Z)$ and $g(x)$. However, an additional theoretical uncertainty in the extracted m_t^{pole} value is expected, due to the gluon resummation corrections, and in particular the Coulomb gluon exchange contributions arising from the toponium quasi bound state dynamics in the small- $m_{t\bar{t}}$ region [253, 254]. These corrections

are not yet implemented in a form suitable for the $\sigma_{t\bar{t}}$ analysis in pp collisions, as discussed in Section 4.6. It was estimated in Ref. [64] that this could result in an uncertainty of +1 GeV in m_t^{pole} , in addition to the one quoted in Eq. (31). Note that the uncertainty in m_t due to the missing Coulomb quasi bound state effects would be considerably smaller, once instead of the pole mass scheme, a renormalisation scheme is chosen, where these Coulomb corrections can be partially absorbed into m_t itself. As shown in Ref. [255], this can be achieved by using the MSR mass $m_t^{\text{MSR}}(R)$ for a scale $R \approx 80$ GeV.

While the resulting values of m_t^{pole} and $\alpha_s(m_Z)$ in Ref. [64] are very precise, the central value of $\alpha_s(m_Z)$ is small in comparison to other extractions at NLO, and to the world average result. In the CMS work [227], the normalised triple-differential $t\bar{t}$ cross sections of Ref. [64] and further data sets used therein, were included in the QCD fit together with the double-differential cross section of inclusive jet production at \sqrt{s} of 13 TeV. With increased sensitivity to $g(x)$ and the value of $\alpha_s(m_Z)$, provided by the jet production measurements, the simultaneous extraction of PDFs, $\alpha_s(m_Z)$, and m_t^{pole} could be further refined. The value $\alpha_s(m_Z) = 0.1188 \pm 0.0031$ is obtained at NLO [227], in good agreement with the world average, and the value of $m_t^{\text{pole}} = 170.4 \pm 0.7$ GeV is obtained with improved precision.

4.5 Top quark pole mass extracted from $t\bar{t}$ +jet events

Alternatively to the m_t extraction using inclusive $t\bar{t}$ production, a novel observable was suggested in Ref. [247] to extract m_t using events where the $t\bar{t}$ pair is produced in association with at least one energetic jet ($t\bar{t}$ +jet). Here, the dependence of the gluon radiation on m_t through threshold and cone effects is explored. The observable of interest ρ is defined¹ as

$$\rho = \frac{340 \text{ GeV}}{m_{t\bar{t}+\text{jet}}}, \quad (33)$$

where $m_{t\bar{t}+\text{jet}}$ is the invariant mass of the $t\bar{t}$ +jet system using the leading additional jet. By using the $t\bar{t}$ +jet normalised differential cross section as a function of ρ , m_t can be extracted. The result of the measurement is independent of the choice of the scaling constant in the numerator, which is introduced to define ρ dimensionless, and is on the order of two times m_t .

A high sensitivity to m_t is expected close to the production threshold, for $\rho > 0.65$, while for high $m_{t\bar{t}+\text{jet}}$, e.g. $\rho < 0.55$, this sensitivity is small. The sensitivity \mathcal{S} is defined as [247]

$$\mathcal{S}(\rho) = \sum_{\Delta m_t^{\text{pole}} = \pm 3 \text{ GeV}} \frac{\mathcal{R}(\rho, m_t^{\text{pole}}) - \mathcal{R}(\rho, m_t^{\text{pole}} + \Delta m_t^{\text{pole}})}{2|\Delta m_t^{\text{pole}}| \mathcal{R}(\rho, m_t^{\text{pole}})}, \quad (34)$$

where \mathcal{R} is the normalised differential cross section of $t\bar{t}$ +jet production as a function of ρ and Δm_t^{pole} the variation of m_t^{pole} . The value of \mathcal{S} quantifies how the differential cross section changes, as a result of the variation in m_t^{pole} and is studied in Ref. [247] by using the POWHEG generator. In Fig. 47 (left), the m_t sensitivities are compared for $t\bar{t}$ +jet and inclusive $t\bar{t}$ production. For the latter, in the definition of ρ , the invariant mass of $t\bar{t}$ +jet is replaced by the invariant mass of the $t\bar{t}$ pair, $m_{t\bar{t}}$. For both processes, the sensitivity is largest close to the threshold of the $t\bar{t}$ production, however in the case of $t\bar{t}$ +jet this sensitivity is significantly increased due to the presence of additional gluon radiation. The infrared safety is assured through the requirement

¹Should not to be confused with correlation coefficients of Ref. [64].

for the additional jet in $t\bar{t}$ +jet to have a transverse momentum of at least 30 GeV. As compared to the $t\bar{t}$ production, the kinematic range accessed by $t\bar{t}$ +jet is shifted further away from the threshold region, where the highest sensitivity to m_t is expected, as shown in Fig. 47 (right). On the other hand, the reliable theoretical prediction in this region would require resummation of threshold effects and soft-gluon emission, not yet fully available for $t\bar{t}$ production in pp collisions.

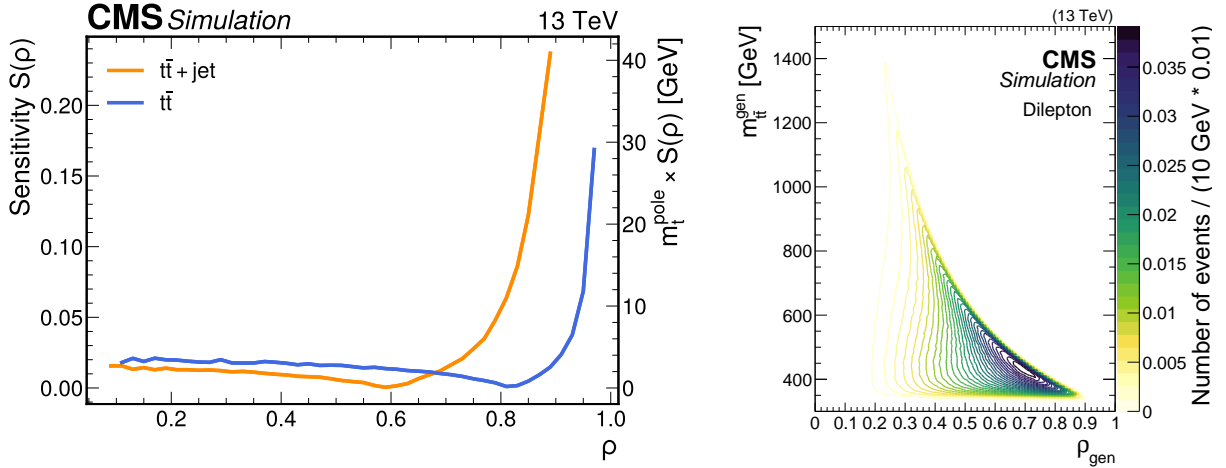


Figure 47: Left: Sensitivity \mathcal{S} to the value of m_t^{pole} for $t\bar{t}$ (blue) and $t\bar{t}$ +jet production (orange). Figure taken from Ref. [69]. Right: The distribution of $m_{t\bar{t}}$ at the parton level as given by the POWHEG+PYTHIA8 $t\bar{t}$ simulation as a function of ρ at parton level, obtained in Ref. [69].

The first extraction of m_t^{pole} using $t\bar{t}$ +jet events in CMS [69] was performed at $\sqrt{s} = 13$ TeV, using pp collision data collected by the CMS experiment in 2016 and corresponding to an integrated luminosity of 36.3 fb^{-1} . Dilepton decays of $t\bar{t}$ are used, and a novel method of kinematic reconstruction, based on a NN regression, developed for the purpose of this measurement, is applied, as discussed in details in Section 2.3. By using a maximum likelihood fit to the final-state distributions of $t\bar{t}$ and $t\bar{t}$ +jet events, the differential cross section of $t\bar{t}$ +jet production as a function of ρ is measured. The method of Refs. [63, 65], as described above, is extended in order to constrain systematic uncertainties in the visible phase space together with the differential cross section. To mitigate the correlation between the extracted cross section and m_t^{MC} , the latter is treated as an additional free parameter in the fit, by considering the $m_{t\bar{t}}^{\text{min}}$ distribution.

The cross section is measured at the parton level, as defined in Section 2.7. Additional jets are reconstructed using the anti- k_T algorithm with a distance parameter of 0.4, and jets originating from the top quark decay products are removed. At least one such additional jet at the parton level with $p_T > 30 \text{ GeV}$ and $|\eta| < 2.4$ is required. This definition allows for the direct comparison of the measurement to the fixed-order theoretical predictions. The measurement [69] is performed in four bins of ρ_{gen} and ρ_{reco} : 0–0.3, 0.3–0.45, 0.45–0.7, and 0.7–1.0. Eleven exclusive event categories are introduced, based on the number of b-tagged jets ($N_{\text{bjet}} = 1, N_{\text{bjet}} \geq 2$), jets ($N_{\text{jet}} = 1, N_{\text{jet}} = 2, N_{\text{jet}} \geq 3$), and the four bins in ρ_{reco} , as listed in Table 7. In the ρ_{reco} categories, a discriminating variable (R_{NN}) originating from a NN-based multiclassifier is fitted to maximise the signal sensitivity. The classifier aims to separate events originating from the $t\bar{t}$ +jet, $t\bar{t}$ +0 jet, and Z+jets processes, and R_{NN} is defined such to optimise the $t\bar{t}$ +jet over $t\bar{t}$ +0 jet separation. The systematic uncertainties related to the calibration of the JES are constrained by fitting jet p_T distributions.

The resulting $t\bar{t}$ +jet cross section is shown in Fig. 48. It is compared to fixed-order theoretical

Table 7: A list of the event categories and distributions used in the maximum likelihood fit.

	Reconstructed ρ				No reconstructed ρ	
	$\rho < 0.3$	$0.3 < \rho < 0.45$	$0.45 < \rho < 0.7$	$\rho > 0.7$	$N_{\text{jet}} = 1$	$N_{\text{jet}} = 2$
$N_{\text{b jet}} = 1$	R_{NN}	R_{NN}	R_{NN}	R_{NN}	$p_{\text{T}}^{\text{leading jet}}$	$p_{\text{T}}^{\text{subleading jet}}$
$N_{\text{b jet}} \geq 2$	R_{NN}	R_{NN}	R_{NN}	R_{NN}	—	$m_{\ell\text{b}}^{\text{min}}$

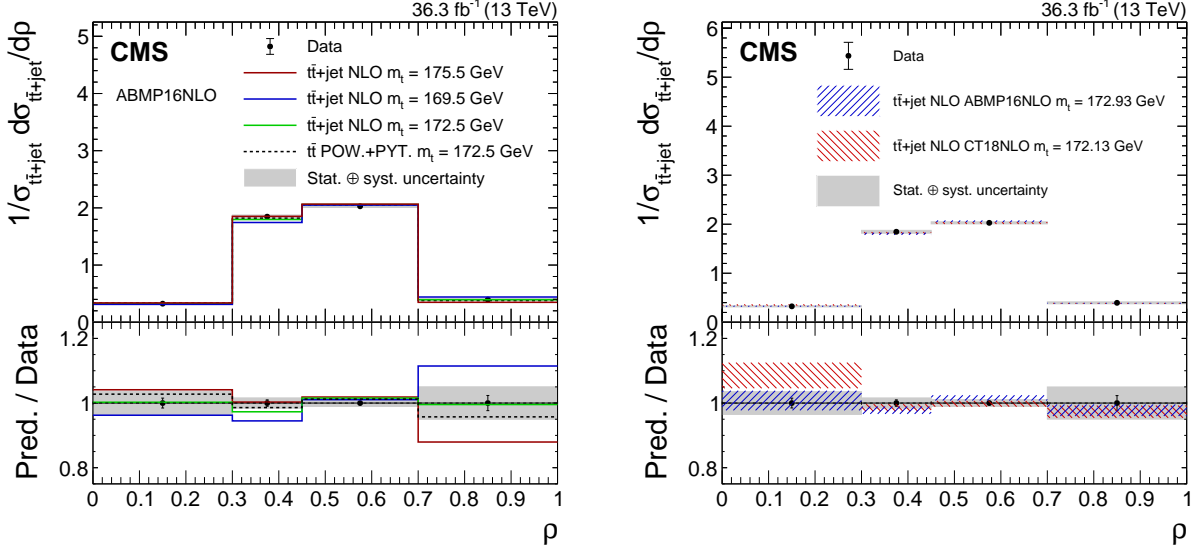


Figure 48: The measured normalised $t\bar{t}$ +jet differential cross section (closed symbols) as a function of ρ . The vertical error bars (shaded areas) show the statistical (statistical plus systematic) uncertainty. The data are compared to theoretical predictions and the POWHEG+PYTHIA8 simulation, either using alternative values of m_t^{pole} (left panel), shown by the solid lines, or two alternative PDF sets (right), shown by the hatched areas. In the lower panels, the ratio of the predictions to the measurement is shown. Figures taken from Ref. [69].

calculations obtained using the $t\bar{t}$ +jet process implemented in POWHEG-BOX [256] at NLO, with the ABMP16NLO [257] PDF set, and assuming m_t^{pole} values of 169.5, 172.5, and 175.5 GeV. Alternatively, the CT18NLO PDF set [258] is considered. The NLO calculation benefits from the implementation of a dynamical scale, as discussed in Ref. [259], which depends on the scalar sum of the top quark and antiquark transverse masses and the p_{T} of the additional jet.

The value for m_t^{pole} is extracted using a χ^2 fit of the theoretical predictions to the measured normalised $t\bar{t}$ +jet cross section, taking into account its full covariance obtained from the likelihood fit. The PDF uncertainties are evaluated in each bin and included in the total covariance matrix. For CT18NLO, the uncertainties evaluated at 90% confidence level (CL), are symmetrised and rescaled to the 68% CL to be consistent with the precision of the ABMP16NLO PDF. To estimate the scale variation uncertainty, the fit is repeated for each choice of μ_r and μ_f and the maximum difference in the results to the nominal one was considered as the total uncertainty. Using the ABMP16NLO PDF set, the resulting m_t^{pole} value is obtained as

$$m_t^{\text{pole}} = 172.93 \pm 1.26 (\text{fit})^{+0.51}_{-0.43} (\text{scale}) \text{ GeV}. \quad (35)$$

Using the CT18NLO PDF set instead, this results in

$$m_t^{\text{pole}} = 172.13 \pm 1.34 (\text{fit})^{+0.50}_{-0.40} (\text{scale}) \text{ GeV}. \quad (36)$$

The total uncertainty in m_t^{pole} corresponds to 1.37 (1.44) GeV for the ABMP16NLO (CT18NLO) PDF set. The comparison of the predictions using the best fit top quark mass value to the unfolded data is shown in the right panel of Fig. 48. The impact of the individual PDF uncertainties is estimated to be 0.35 (0.27) GeV for the CT18NLO (ABMP16NLO) PDF set by excluding the effect of the PDF uncertainties in a χ^2 fit and replacing the central values of the measured cross section with the ones obtained from the theoretical prediction.

4.6 Problems and prospects for Lagrangian top quark mass extraction

The described methods to extract the Lagrangian m_t from pp collision data using $t\bar{t}$ and $t\bar{t}+\text{jet}$ production result in an uncertainty of about 1 GeV.

The experimental uncertainties in Lagrangian m_t , obtained by using inclusive $\sigma_{t\bar{t}}$ are limited by the uncertainty associated with the integrated luminosity, which itself is a subject of careful refinements and improvements [260]. The main limitation of such measurements, however, arises from the correlations of PDFs, $\alpha_S(m_Z)$, and m_t in the theoretical predictions for $\sigma_{t\bar{t}}$ and resulting theoretical uncertainty.

Therefore, the most precise m_t results are obtained in analyses, where together with m_t , the PDFs and α_S are extracted, based on normalised multi-differential $\sigma_{t\bar{t}}$ measurements, so that the respective correlations are mitigated. To ensure minimal uncertainty in the theoretical prediction, calculations at NNLO or higher order are of an advantage. The presence of a reconstructed jet in the final state makes the computation of NNLO QCD correction more involved so that in the foreseeable future only theoretical predictions at NLO may be available for the $m_{t\bar{t}+\text{jet}}$ analysis. Therefore, the extraction of m_t by using $t\bar{t}$ production seems currently more preferable, which makes $m_{t\bar{t}}$ and $y_{t\bar{t}}$ most promising observables of interest. In the HL-LHC scenario, improvements in experimental precision in the measurement of $m_{t\bar{t}}$ or $y_{t\bar{t}}$ distributions, and in turn of m_t or $m_t(\mu)$ are expected from better population of the respective spectra [213].

Further improvements in the precision in m_t would require several important developments in the theoretical predictions that can be used for the experimental analyses: improved description of the threshold of $t\bar{t}$ production; implementation of scale-dependent and renormalon-free mass schemes with suitable scale choice prescriptions for the different observables; availability of open-source, fast, and numerically precise multi-differential calculations of $t\bar{t}$ and $t\bar{t}+\text{jet}$ production to at least NNLO in QCD with fast-grid interface to PDF convolution; and availability of electroweak corrections to at least NLO with a systematic treatment of finite-width and off-shell effects. In the following, the need for these improvements is discussed in more details.

In $t\bar{t}$ production, calculated recently at NNLO in QCD [74–76, 78–81], the strongest sensitivity to m_t arises from the threshold $t\bar{t}$ region, i.e. where $m_{t\bar{t}}$ is in the range from 340 to 360 GeV. However, in this region, the fixed-order perturbative calculations become insufficient and the theoretical uncertainty can not be estimated reliably through the common normalisation scale variations. Here, nonrelativistic quasi-bound state QCD corrections become important since the produced top quarks attain small nonrelativistic velocities in the $t\bar{t}$ centre-of-mass frame, and the dynamics of the $t\bar{t}$ system is governed by m_t , relative momentum, and kinetic energy of the top quark. Appearance of ratios involving the masses, momenta, and kinetic energy of the top quark makes the standard fixed-order expansion in powers of α_S unreliable and, in contrast to the simpler situation at e^+e^- linear colliders [261], colour singlet as well as colour octet $t\bar{t}$ states need to be described systematically. The most pronounced quasi-bound state effects arise from the Coulomb corrections due to the exchange of gluons between the produced t and \bar{t} . There are a number of predictions available for the Coulomb corrections [253, 262, 263],

suitable for the threshold region and provided in the pole mass scheme. It was shown in the NLO analysis of Ref. [255] that the fixed-order corrections in the threshold region are significantly smaller if the MSR mass at an intermediate scale $R \approx 80$ GeV is employed, since this choice partially sums bound state binding energy effects that lower the threshold value of $m_{t\bar{t}}$. However, none of the current theoretical predictions provides an adequate description of the entire lowest $m_{t\bar{t}}$ interval between 300 GeV and the quasi-bound state region, where the imaginary energy and the optical theorem approach to account for the top quark width [261] used in Refs. [253, 262, 263] is not adequate and yields an unreliable description of the $t\bar{t}$ production rate (as shown in Ref. [263]). Here, a matching to nonresonant production of the top quark related final states as well as a careful account for definition of the reconstructed experimental final state needs to be implemented. Furthermore, a systematic treatment of the intermediate region for $m_{t\bar{t}}$ above 360 GeV has to be devised, where the nonrelativistic and relativistic calculations are matched, such that the reliable uncertainty estimates in this region are possible. It should also be mentioned that the foundation of the particle to parton unfolding procedure to determine the momenta of the top quarks and antiquarks in the on-shell approximation that is used in the theoretical differential $t\bar{t}$ cross section predictions deserves some scrutiny from the theoretical perspective because it is based entirely on the particle picture of the top quark implemented in the simulations.

An important further desired theoretical improvement concerns the implementation of top quark mass renormalisation schemes for the differential cross section, most notably the $\overline{\text{MS}}$ mass $m_t(\mu_m)$ (suitable for scales above m_t) or the MSR mass $m_t^{\text{MSR}}(R)$ (suitable for scales below m_t) with adaptable choice of the mass renormalisation scales μ_m and R , to allow for flexible dynamical scale settings. This also avoids the impact of the pole mass renormalon problem already mentioned in Section 3.3, which will become increasingly relevant for improving precision. Currently, no open-source code for calculation of differential cross sections at NNLO using an arbitrary short-distance mass scheme is yet available. Further, to perform a full QCD analysis with simultaneous extraction of $m_t(m_t)$, $\alpha_s(m_Z)$, and PDFs, the interpolation of fast-grid techniques (e.g. FASTNLO [264], APPLGRID [265] or APPLFAST [266]) to such a theoretical calculation would be necessary. It should also be mentioned that eventually electroweak corrections should be provided in the cross section predictions used for the experimental analyses. This also entails the treatment of off-shell and nonresonant effects and the dependence on the definition of the electroweak vacuum expectation value [267, 268] that affects the relation of the pole or the MSR mass, both of which can be defined in theories where all massive boson effects are integrated out, with the $\overline{\text{MS}}$ mass and the top quark Yukawa coupling relevant for applications at the electroweak scale and above. Furthermore, the availability of off-shell theoretical calculations, implying only top quark decay products in the final state, would imply changes in the experimental analysis strategy, since no unfolding to the parton level would be required.

5 Measurements in the Lorentz-boosted regime

Measurements of the jet mass in decays of Lorentz-boosted top quarks provide an alternative approach to m_t measurements in a phase space region where the top quarks are produced at very high p_T , dominated by different systematic uncertainties than direct m_t measurements and extractions of the Lagrangian top quark mass. The generator-based extraction of m_t^{MC} from the invariant mass of a single jet, containing the entire top quark decay, relies on reconstruction techniques and modelling aspects in the simulation that are very distinct from direct measurements, where the top quark decay can be resolved in separate jets. Thus, this approach offers an important consistency check of the m_t^{MC} measurements discussed in Sec. 3. In addition, the

boosted topology where the top quark and antiquark decay products are well separated offers the possibility of analytic and resummed particle-level theory predictions that may eventually lead to alternative measurements of m_t in a well-defined renormalisation scheme. In this regime, Coulomb effects modifying predictions in the $t\bar{t}$ threshold region, important for the Lagrangian top quark mass extraction, are irrelevant. The sensitivity to the top quark mass predominantly comes from the inclusive kinematic properties of the jet initiated by a boosted top quark and its decay products, and subtle effects from the modelling of the inclusive and differential $t\bar{t}$ production cross sections have a negligible impact.

Although top quarks are dominantly produced at lower p_T , top quarks with large p_T are still abundantly produced at the LHC. Their decay products receive large Lorentz boosts and are thus strongly collimated, such that the fully hadronic decay $t \rightarrow bq\bar{q}'$ can be reconstructed with a single large- R jet, where R is the jet distance parameter and usually lies in the range 0.8–1.2. The distribution in the invariant mass (m_{jet}) of these jets features a distinct peak, the position of which is closely related to the value of m_t . The m_{jet} measurement is robust against typical uncertainties affecting $t\bar{t}$ production close to the threshold, such as uncertainties in the proton PDFs, resummation effects, and Coulomb corrections. In addition to having complementary uncertainties, this measurement is based on high-energy events that have a negligible impact on direct measurements, and thus constitutes an additional independent method, which can readily be combined with other measurements of m_t .

An analysis of the measured distribution of m_{jet} allows for a precise determination of m_t , which can be m_t^{MC} in a generator-based analysis or the top quark mass in a well-defined renormalisation scheme in an analysis based on analytic theory calculations. The jet mass distribution of boosted top quarks has good prospects for systematic analytical first-principle QCD predictions at the particle level. The boosted topology allows the application of factorisation and effective theory methods for hadron-level descriptions that do not rely on multipurpose MC event generators. Theoretical studies in this direction are based on the strong collimation of the top quark decay products, such that all relevant QCD radiation can be classified into factorisable soft, collinear, or collinear-soft radiation (in the directions of the top quark and antiquark) where also jet grooming techniques can be accounted for [189, 220, 221, 224]. As for observables related to global event shapes used in the conceptual studies of Refs. [191, 219], and discussed in Section 3.3, these analytic computations allow for a consistent implementation of the top quark mass in well-defined renormalisation schemes. Unfortunately, because of very limited statistical precision, the phase space with jet $p_T > 750$ GeV, for which the theoretical results [189, 224] are currently available, is not experimentally accessible with the LHC Run 2 data. Still, we perform the extraction of m_t^{MC} based on the predicted m_{jet} distributions from simulations by MC event generators in analogy to the direct measurements. This measurement of m_t^{MC} is, however, quite uncorrelated from direct measurements and demonstrates the principle capability and precision of this method. For the time being, this approach also provides an important consistency check of the direct measurements of m_t^{MC} within the MC simulation framework. Once the theoretical calculations and experimental measurements are carried out in a comparable kinematic phase space, the measurement of m_{jet} may turn into a precision measurement of a top quark mass in a well-defined mass scheme, which does not rely on the picture of a top quark particle with a Breit–Wigner distributed mass.

5.1 Overview of existing jet mass measurements

All the jet mass measurements by CMS have been performed in the lepton+jets channel of $t\bar{t}$ production, where the semi-leptonic top quark decay $t \rightarrow bW \rightarrow b\ell\nu_\ell$ is used to identify $t\bar{t}$ events, and the measurement is performed on the fully hadronic decay $t \rightarrow bW \rightarrow bq\bar{q}'$. The

single lepton in this decay mode of the $t\bar{t}$ system allows the selection of a pure sample with a small background contribution, and is required to be an electron or muon carrying a minimum p_T of approximately 50 GeV. We require each event to have exactly two large- R jets with high p_T , aiming at reconstructing the hadronic top quark decay $t \rightarrow bq\bar{q}'$ in one jet, and the b jet of the leptonic top quark decay in a separate jet with large angular separation. The jet containing the hadronic top quark decay is identified by the larger distance to the single lepton and is required to have $p_T > 400$ GeV. In addition, m_{jet} has to exceed the invariant mass of the system composed of the second jet and the single lepton. The latter criterion should always hold true if all products of the hadronic decay are within the selected jet, since the neutrino from the leptonic decay is not reconstructed.

The CMS Collaboration has carried out three measurements of the jet mass in decays of boosted top quarks. The first measurement has been performed using 8 TeV data corresponding to an integrated luminosity of 19.7 fb^{-1} [59]. This measurement has large statistical and modelling uncertainties, with a total uncertainty in the extracted value of m_t of 9 GeV. Nevertheless, it was the first measurement of this kind and showed the possibility of a determination of m_t from the jet mass. The first m_{jet} measurement at $\sqrt{s} = 13$ TeV used data corresponding to an integrated luminosity of 35.9 fb^{-1} [66]. The increase in centre-of-mass energy, together with the larger data set, resulted in an increase in the number of selected events by more than a factor of ten with respect to the 8 TeV measurement. The use of a novel jet reconstruction resulted in a decreased width of the m_{jet} distribution at the particle level and better experimental resolution in m_{jet} , which subsequently improved the sensitivity to m_t . Furthermore, the optimised jet clustering led to a significant reduction in the experimental and modelling uncertainties, resulting in a total uncertainty of 2.5 GeV in m_t . The most recent measurement used the Run 2 data set corresponding to an integrated luminosity of 138 fb^{-1} [70]. For this measurement, CMS has developed a new method for calibrating the jet mass, and an auxiliary measurement of the jet substructure of large- R jets has resulted in a smaller uncertainty from the modelling of final state radiation. These improvements, together with the larger data set, result in an uncertainty of 0.84 GeV in m_t .

5.2 The jet mass

The jet mass is defined as the invariant mass of the sum of all jet constituent four-momenta,

$$m_{\text{jet}}^2 = \left(\sum_i^N p_i \right)^2, \quad (37)$$

where p_i is the four-momentum of constituent i from N jet constituents. In gluon and light-quark jets, the jet mass is dominantly generated by a series of collinear $1 \rightarrow 2$ splittings. The invariant mass of two massless particles i and j can be approximated by $m^2 \approx p_{T,i} p_{T,j} \Delta R_{ij}^2$ [269] and depends on the p_T of both particles and their angular separation ΔR_{ij} . This causes p_T -dependent Sudakov peaks [270] in the m_{jet} distribution in light-quark and gluon jets. In the case of on-shell decays of top quarks, the dominant part of the jet mass is generated by the resonance decay, with corrections from additional radiation. In order to have a reliable correlation between the peak in the m_{jet} distribution and the value of m_t , the precise knowledge of which constituents produced in the event are included in the calculation of m_{jet} is mandatory. Ideally, within the picture of an on-shell decay of a top quark, all particles from the top quark decay would be included in the large- R jet. This would only be possible if the size of the jet cone is equal to or larger than the largest angular distance between the decay products of the top quark, which depends on the top quark p_T . In the following discussion and in the evaluation of suitable jet algorithms, we use the picture of an on-shell top quark particle decaying via

$t \rightarrow bq\bar{q}'$, as it is implemented in event generators simulating $t\bar{t}$ production, where we use the generator information of the three decay quarks at the parton level before PS. Even though this simplified picture is used to find an optimal jet reconstruction algorithm, the analysis does not rely on this simplified picture, since the jet mass is defined by the jet constituents at the particle level as discussed below. After the unfolding to the particle level, the data include effects not accounted for in event generators, such as gluons that provide colour neutralisation and off-shell contributions beyond the Breit–Wigner mass distribution. For the m_t^{MC} measurement it is implicitly assumed that these effects are small.

Figure 49 shows the most probable region of maximum distance of the three partons from the decay $t \rightarrow bq\bar{q}'$, as a function of the top quark p_T . At p_T larger than 800 GeV, a distance parameter of $R = 0.8$ is sufficient to fully reconstruct the decay products of the top quark in about 80% of the time. In order to obtain a similar coverage at lower p_T , the value of R has to be increased proportionally to approximately $1/p_T$.

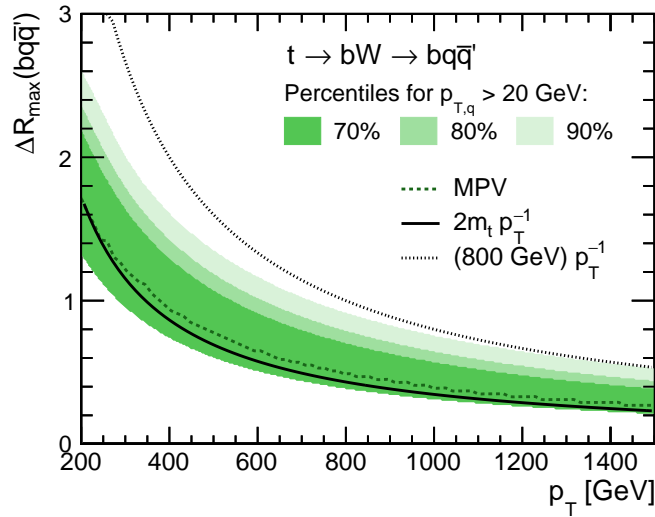


Figure 49: Percentiles of maximum angular distance between the top quark decay partons as a function of the top quark p_T obtained from $t\bar{t}$ simulation. The filled bands indicate the areas that are populated by 70, 80, and 90% of all simulated $t\bar{t}$ events, where the decay partons have at least $p_T > 20$ GeV. The most probable value (MPV) is shown as a dashed line, and two functional forms are shown that approximate the p_T -dependence of ΔR_{max} . Figure taken from Ref. [271].

The jet mass is affected by additional effects, some of which are not correlated to the top quark decay. At the particle level, the jet mass receives contributions from ISR, the underlying event, and multi-particle interactions. Since these processes are not correlated with the production and decay of the top quark, their effect is independent of the top quark kinematics and scales with $p_T R^4$ because it depends quadratically on the active area of the jet. The linear dependence in p_T stems from the fact that these contributions increase the jet p_T , but the leading effect comes from the size of the jet distance parameter. Since including more particles can only increase the jet mass, the peak position in the m_{jet} distribution is shifted towards higher values, and a tail is introduced at large $m_{\text{jet}} \gg m_t$. The leading power corrections to the jet mass from hadronisation scale as $p_T R$, and are more than a factor of ten smaller than the effects from the underlying event. At the detector level, contributions from pileup have a similar effect as the underlying event, but the effect is larger because of the high energy density of pileup at high instantaneous luminosities. In the data analysis, several corrections are applied to remove the

effects of pileup, enabled by the possibility to distinguish pileup particles from particles from the hard scattering and by subtracting on average the pileup contributions from jets, such that the measured distribution in m_{jet} at the particle level is free of pileup effects.

The correlation of m_{jet} to the mass of the particle initiating the jet makes m_{jet} an important observable for jet tagging algorithms, where jet substructure information is used for large- R jet identification [271–273]. In order to increase the tagging performance, grooming or trimming algorithms are used to remove wide-angle and soft radiation from the jet before calculating m_{jet} . Depending on the strength of the grooming algorithm, this largely removes the p_{T} -dependent Sudakov peaks in light-quark and gluon jets and leads to a steeply falling m_{jet} spectrum with a peak at very small values [274]. In top quark decays, grooming removes additional particles in the jet from ISR, the underlying event and pileup, and subsequently improves the jet mass resolution at the detector level and reduces the width of the lineshape of the m_{jet} distribution at the particle level, and thus increases the sensitivity to m_{t} . For top quark tagging this is an essential tool to increase the separating power of m_{jet} in the categorisation into jets initiated by top quarks or light quarks and gluons. In measurements of m_{jet} , grooming not only enhances the sensitivity to m_{t} , but also removes a large fraction of the nonperturbative effects, particularly arising from ISR and underlying event. We note that there is no algorithm that removes all nonperturbative effects, such that these still have to be accounted for in the description of m_{jet} .

5.2.1 Theoretical considerations

The large angular separation between the decay products of the top quark and antiquarks at high top quark boosts allows for the derivation of factorisation formulae for differential cross sections, where the scales of the hard interaction, collinear and soft radiation within the jets, and nonperturbative effects can be separated [220]. Previous calculations for e^+e^- collisions [221], based on soft-collinear effective theory (SCET) [275–279] and boosted heavy-quark effective theory [220, 221], have been extended to pp collisions with the help of light soft-drop grooming [189, 224] to reduce the impact of ISR and the underlying event. Light soft-drop grooming is a less restrictive version of the soft-drop grooming algorithm [270, 280] so that the top quark decay products are not affected. The presented calculation considers top quark jets with $p_{\text{T}} > 750 \text{ GeV}$, where soft-drop grooming enables the factorisation between the top quark and antiquark, by removing soft-wide angle radiation, such that the analysis can be carried out in the lepton+jets channel. The groomed jet mass is measured on the fully hadronic decay leg of the $t\bar{t}$ decay, which has a large angular separation from the semi-leptonic top quark decay, thanks to the large Lorentz boost. Light soft-drop grooming, with the soft-drop parameters $z_{\text{cut}} = 0.01$ and $\beta = 2$ [189], removes significant nonperturbative contamination from the top quark jet while retaining collinear radiation associated with the top quark decay products within the cone defined by the hard jets from the top quark decay. This allows for a treatment of the top quark and antiquark as individual radiators and a clear interpretation in terms of a short-distance mass scheme since all radiation that is soft in the top quark (or antiquark) rest frame (called ultracollinear in the laboratory frame) remains ungroomed and is treated inclusively. A stronger soft-drop grooming, for example with $z_{\text{cut}} = 0.1$ and $\beta = 0$ as used in many CMS analyses, would result in a breakdown of the validity of the factorisation formulae since parts of the ultracollinear radiation would be restricted. The calculation predicts the jet mass distribution in the MSR and the pole mass schemes, such that it can be used to determine the MSR mass from a corresponding measurement. Since nonperturbative effects are not fully removed by the light soft-drop grooming, a free parameter is introduced in the particle level factorisation formulae to account for the shift of the m_{jet} distribution because of the underlying event. This parameter needs to be obtained from data and shows a correlation with the value

of the top quark mass, which can impact the accuracy of the m_t determination if not accounted for. While the requirement of top quark $p_T > 750$ GeV is not yet experimentally accessible with the present 13 TeV data set because of the small $t\bar{t}$ production cross section at high p_T , this measurement will become feasible at the HL-LHC. We also note that the effects from multi-particle interactions and the underlying event are still significant despite grooming, such that a first-principle description of these effects would be desirable. The existing calculations provide a tool for the calibration of the top quark mass parameter in the event generator used for the simulation of $t\bar{t}$ production, such that a numerical relation between m_t^{MC} and the MSR (or the pole) mass can be determined [222]. This is in close analogy to the m_t^{MC} calibration framework proposed in Refs. [219, 225] based on global event shapes in e^+e^- collisions. Calculations for moderate top quark p_T starting at 400 GeV will need considerable theoretical work, because the three decay quarks cannot be considered as a single radiator anymore, but a factorisation theorem needs to be developed taking into account the dynamics of three separate colour-charged radiators.

Finally we note that the m_{jet} distribution in boosted top quark decays shares many physical aspects with the e^+e^- shape observables mentioned in Section 3.3—such as the 2-jettiness—for which some concrete insights concerning the interpretation of the MC top quark mass parameter m_t^{MC} exist. Similar insights do not yet exist for observables close to the ones used for the direct m_t^{MC} measurements.

5.2.2 Experimental methods

The most important experimental elements of this measurement are well reconstructed and calibrated large- R jets. Jets are clustered from the list of PF candidates as described in Section 2.2. In addition to the commonly used anti- k_T jets, large- R jets are clustered for measurements of boosted heavy objects.

In the presented m_{jet} measurements, all ingredients to jet clustering play a crucial role since the width of the peak in the m_{jet} distribution, possible shifts from pileup and the underlying event, and the jet mass scale (JMS) and resolution directly translate to the sensitivity to m_t . All three existing measurements of m_{jet} [59, 66, 70] make use of jets clustered from a list of PF particles. The 8 TeV measurement [59] did not use any pileup mitigation technique, while the measurements at 13 TeV [66, 70] use the CHS algorithm. A specialised two-step jet clustering was introduced with the first measurement at 13 TeV [66], using the XCone algorithm [281]. The clustering procedure acts as a grooming algorithm on the large- R jets. It improves both the peak width and the jet mass resolution by factors of two compared to the initial measurement at 8 TeV [59] and reduces the shift of the peak due to additional particles from pileup and the underlying event. In the future, the measurement of m_{jet} will also profit from studies in the context of jet substructure tagging, where PUPPI and soft-drop grooming have been calibrated with sufficient precision.

Another crucial aspect of the m_{jet} measurement regards an optimal selection of the jet including the hadronic top quark decay. High-energy ISR and FSR can not only affect the m_{jet} distribution of the top quark jet, but can also lead to the selection of a wrong jet that reconstructs radiation uncorrelated with the top quark decay. This leads to enhanced tails to both sides of the m_{jet} peak and degrades the sensitivity to m_t by shifting the peak position. Thus, the jet definition and the selection of the jet that fully contains the $t \rightarrow b\bar{q}\bar{q}'$ decay has to be carefully optimised in order to reduce the influence of radiation not connected with the top quark decay.

5.3 Optimising the jet definition for jet mass measurements

Measurements of the jet mass aim to reconstruct all particles associated with the top quark decay in a single large- R jet. In pp collisions at the LHC, additional particles arise from various sources such as pileup, underlying event, and final-state radiation. Since all these effects can change the jet mass and might even affect the identification of the jet that contains the hadronic top quark decay, a suitable jet algorithm is crucial for measurements of m_{jet} . In commonly used jet clustering algorithms the distance parameter R controls the largest distance at which particles are combined to form a jet. The Lorentz boost that subsequently defines the opening angle of the decay in the lab frame depends on the top quark p_T . Thus, an optimal value of R has to be chosen such that the jet cone is large enough for a given top quark momentum in order to catch all products of the hadronic top quark decay. On the other hand, effects from pileup and the underlying event are enhanced with a larger jet size, such that a compromise needs to be made for R sufficiently large, but just large enough.

In the measurement using the LHC 8 TeV data [59], Cambridge–Aachen (CA) [282, 283] jets with $R = 1.2$ were chosen. At 8 TeV, this decision was driven by the available size of the selected data set. A smaller value of R would have improved the experimental resolution but also leads to a larger fraction of top quark decays that are not fully reconstructed within the jet or the need to require a minimum jet p_T larger than 400 GeV. While the former would have decreased the sensitivity to the top quark mass, the latter would have drastically reduced the already limited statistical precision of the measurement because of the steeply falling top quark p_T spectrum. No grooming was applied in this measurement and although the statistical uncertainty dominates the extraction of m_t , the effects of additional particles from the underlying event and pileup are visible in a p_T -dependent shift of the peak in the m_{jet} distribution.

For the first m_{jet} measurement with 13 TeV data [66], the jet reconstruction was changed from CA jets to a two-step clustering [284] using XCone [281]. First, XCone is run with $R = 1.2$ and $N = 2$ using all CHS PF candidates as input particles. As an exclusive jet algorithm, XCone returns exactly two large- R jets, where the jet axes are found by minimising the N -jettiness [285]. This setup is optimised to include all partons from the two top quark decays in a phase space where the jet p_T is larger than 400 GeV. Subsequently, XCone is run again separately for the constituents of each large- R jet, now with $R = 0.4$ and $N = 3$, which aims at reconstructing the three-prong top quark decay. All particles that are not part of one of the three subjets are removed from the jet. In this way, the two-step procedure acts as a grooming algorithm and the effects of additional and soft radiation are mitigated. A display of the clustering procedure in a simulated $t\bar{t}$ event is shown in Fig. 50. In this example, the first clustering step reconstructs both top quarks. In the next step, soft and wide angle radiation is removed by reconstructing three subjets. Ideally, the subjets match the three-prong structure of the hadronic top quark decay. On the leptonic side, we aim at a two-prong decay and run XCone with $N = 2$, since the lepton is part of the clustering and the neutrino cannot be detected. However, the measurement is performed using the hadronic jet only and it was verified that the details of the clustering procedure of the leptonic side do not change the measurement. In Fig. 50 another feature of the XCone algorithm becomes visible. The XCone subjets can be arbitrarily close and form a straight border separating the jets. In contrast, the anti- k_T algorithm commonly used in other analyses would result in an approximately circular high-energy jet at the centre of the overlap of two jets and lower-energy jets clustering the remnants around the jet in the centre. This feature of the XCone algorithm allows a reconstruction of the three-prong structure of the top quark decay despite an angular overlap of size $R = 0.4$ of the subjets at large Lorentz boosts. A distinct advantage of this approach is that the two-prong W boson decay can be identified and reconstructed from two XCone subjets, which is subsequently used in the calibration of the

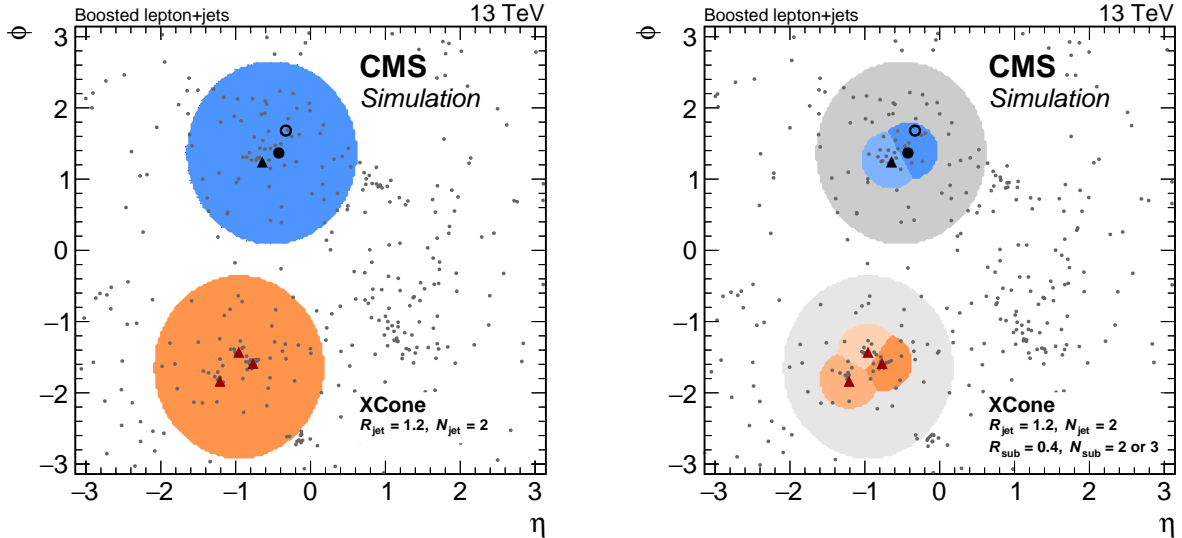


Figure 50: Display of a simulated $t\bar{t}$ event. Each point marks the position of a particle at the particle level in the η - ϕ plane. Decay products of the top quarks are highlighted with triangles or larger circles. The red triangles mark the three quarks from the hadronic decay; the black triangle, black circle, and open circle correspond to the b quark, charged lepton, and neutrino from the leptonic top quark decay, respectively. The jet areas are shown as coloured shapes. The left panel shows the first clustering step with $N = 2$ and $R = 1.2$, while the right panel shows the subjet clustering.

JMS.

A comparison of this approach to the CA jets used for the 8 TeV measurement is shown in Fig. 51, displaying the normalised m_{jet} distribution for the fraction of “matched” events. The width of the distribution around the peak in m_{jet} reduces by a factor of two with the two-step clustering, and the shift of the peak position towards larger values is strongly reduced. While the performance is comparable to jets with $R = 0.8$, the first step in the X Cone clustering with $R = 1.2$ maintains high reconstruction efficiencies also for jets close to the selection threshold of 400 GeV and improves the statistical precision in the measurement. In this way, the two-step clustering allows a smoother transition between moderately and highly boosted top quark jets.

5.4 Reconstruction effects in the jet mass

The event selection at the detector level is very similar to the particle level phase space detailed above in order to minimise migrations in the detector response matrix used in the unfolding, such that the respective corrections are small. The data are selected with a single-lepton trigger, which usually provides high efficiency in the selection of high-energy $t\bar{t}$ events in the lepton+jets channel. Moreover, a few well known and understood selection criteria, such as b jet tagging, a customised lepton isolation, and a cut on $p_{\text{T}}^{\text{miss}}$, are used in order to reduce backgrounds and select a pure $t\bar{t}$ sample.

Pileup effects play a role at the detector level, but are absent at the particle level. Together with detector resolution effects, this leads to a finite jet mass resolution that highly depends on the jet reconstruction. Here we define the resolution as the width of the distribution in $(m_{\text{jet}}^{\text{rec}} - m_{\text{jet}}^{\text{gen}})/m_{\text{jet}}^{\text{gen}}$, where $m_{\text{jet}}^{\text{rec}}$ and $m_{\text{jet}}^{\text{gen}}$ are the jet mass at the detector and particle levels, respectively. The specialised X Cone reconstruction, because of its grooming, results in a resolution of 7–8%. This translates to an improvement by a factor of 2 compared to 14%, obtained

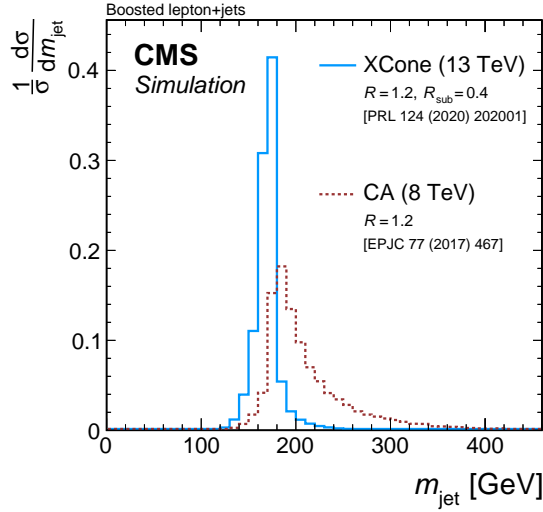


Figure 51: Normalised jet mass distribution at the particle level for the two-step X Cone clustering (blue solid) used in Ref. [66, 70] and CA jets with $R = 1.2$ (red dotted) used in Ref. [59]. Only events where all top quark decay products are within $\Delta R = 0.4$ to any X Cone subjet or within $\Delta R = 1.2$ to the CA jet are shown.

for nongroomed CA jets. Furthermore, we only observe a very small dependence on the number of reconstructed primary vertices, which indicates a significant reduction of pileup effects.

At detector level, the calibration of physics objects is a crucial aspect of the measurement. The connected uncertainties are grouped into experimental uncertainties and are dominated by uncertainties in the jet calibration. Variations in the JES shift the peak in the m_{jet} distribution and thus lead to large uncertainties in the extraction of m_t . At 8 TeV, the statistical uncertainty was very large, such that a reduction of the JES uncertainty would not have improved the measurement precision. For the first measurement at 13 TeV [66], a dedicated calibration for X Cone subjets was derived to correct for differences in the reconstruction compared to anti- k_T jets with $R = 0.4$, which are used to derive JES corrections. The improvements introduced with the first measurement at 13 TeV, most importantly the two-step jet clustering with X Cone which results in an improved line shape of the m_{jet} distribution, improved jet mass resolution, and pileup stability, and the large gain in statistical precision, resulted in the JES uncertainty becoming the dominant experimental uncertainty. Therefore, in the measurement with the full Run 2 data set [70], a dedicated calibration of the JMS was introduced. The centrally provided JES corrections are derived by calibrating the jet with p_T - and η -dependent correction factors that scale the full jet four-momentum. However, the jet mass is not necessarily affected in the same way as the jet three-momentum, calling for a technique to calibrate the JMS. The method developed for this measurement uses the distribution in the reconstructed W boson mass for the JMS calibration, similar to JEC constraints from m_W in direct measurements of m_t^{MC} . The W boson decay is reconstructed by selecting the two X Cone subjets that are not associated with the b quark from the top quark decay, which is identified by using the b tagging score. The JMS response is parameterised as a function of two parameters, which affect the JES and X Cone corrections. These parameters are obtained from a fit to data in the reconstructed m_W distributions. The jet four-momentum is then constructed such that the JES only changes the jet three-momentum, while the JMS acts on m_{jet} . Since the W boson decay results in a sample of light-flavour jets, there is an additional uncertainty connected to the jet response to heavy-flavour jets, estimated from a comparison of PYTHIA and HERWIG. The dedicated JMS calibration reduces the effect of the uncertainty in the JES from $\Delta m_t = 1.47$ GeV in the m_t

extraction to $\Delta m_t = 0.37 \oplus 0.26 \oplus 0.07 \text{ GeV} = 0.46 \text{ GeV}$, where the uncertainty is split into the contributions from the JMS, JMS flavour, and JES, respectively.

5.5 Uncertainties from the modelling of the jet mass

Modelling uncertainties arise from potential differences of the data compared to the simulation used to construct the response matrix in the unfolding. These differences can introduce a model dependence in the unfolding and subsequently lead to a bias in the unfolded distribution. Thus, all theoretical uncertainties enter this measurement twice: as biases in the unfolding and through the prediction of the m_{jet} distribution when extracting the top quark mass. The modelling uncertainties are estimated by varying the simulation within theoretical uncertainties, unfolding the detector level distribution of the varied simulation and comparing the unfolded result to the true particle-level distribution. Any difference points to a potential bias due to the modelling and is accounted for as a model uncertainty. A full list of modelling uncertainties that are considered in top quark mass measurements in CMS can be found in Section 2.4.

By focusing on the jet mass in hadronic decays of boosted top quarks rather than on the reconstructed top quark mass in resolved decays or on $t\bar{t}$ production rates, many uncertainties relevant for the latter are small in jet mass measurements. This includes uncertainties in the factorisation and renormalisation scales, choice of PDFs, and b fragmentation model. The uncertainty in the colour reconnection model is estimated as non-negligible in the latest measurements at 13 TeV, but includes a significant statistical uncertainty due to the limited statistical precision in the simulated samples that are used for these variations. In addition, our studies show that uncertainties in the underlying event tune are small in m_{jet} measurements when using the X Cone jet clustering. This can be understood by the jet grooming properties of the two-step X Cone clustering, which removes additional particles in the large- R jet that are not connected to the top quark decay.

However, uncertainties in the parton shower model are very relevant for the measurement of m_{jet} . Since the precision in the m_t extraction at 8 TeV was limited by the statistical uncertainty, a simple comparison of the m_{jet} distribution between simulated $t\bar{t}$ samples using POWHEG+PYTHIA and POWHEG+HERWIG was used as an estimate of the uncertainty in the parton shower and hadronisation modelling. With increasing precision in the first measurement at 13 TeV, the parton shower uncertainty was studied in more detail by evaluating variations of single model parameters that vary ISR, FSR, and the parameter h_{damp} , that steers the matching between matrix element and parton shower. The uncertainties in the scale choice of FSR modelling turned out to be the dominant modelling uncertainty in the 13 TeV measurement using data collected in 2016 [66]. Already then it was assumed that the variations by a factor of 2 in the FSR energy scale in the CUETP8M2T4 [120] tune was overestimating this uncertainty. With the switch to the CP5 [120] tune for the simulated samples for the data-taking periods of 2017 and 2018, this uncertainty is already much reduced, which is directly visible in the decreasing theoretical uncertainties of the latest Run 2 measurement [70] compared to the measurement with 2016 data [66], where the FSR uncertainty is the dominant source. In addition, the latest m_{jet} measurement makes use of jet substructure observables in order to constrain the FSR modelling uncertainty. The N -subjettiness ratio $\tau_{32} = \tau_3/\tau_2$ [286, 287] is sensitive to the amount of additional radiation that affects the three-prong top quark decay and is thus used to tune the FSR modelling in $t\bar{t}$ simulation and consequently reduce the corresponding uncertainties.

With the FSR uncertainty being under control, the uncertainty in the choice of m_t^{MC} is the dominant modelling uncertainty. This uncertainty reproduces a possible bias when unfolding a

distribution that corresponds to a different value of m_t compared to the one used in the simulation that populates the response matrix. In order to estimate this effect, we unfold the m_{jet} distribution of alternative simulated samples with different m_t^{MC} with the nominal response matrix and compare the result to the m_{jet} particle-level distribution of the alternative samples. Unfortunately, the available simulated samples with different values of m_t^{MC} are very limited in statistical precision, especially at high top quark energies. Thus, a substantial fraction of this estimated uncertainty is caused by statistical effects.

5.6 Aspects in the unfolding of the data

The data are unfolded using regularised unfolding as implemented in the TUNFOLD software package [170]. We unfold the data to the particle level, which differs from the procedure in Lagrangian top quark mass extractions, where one unfolds to the level of stable on-shell top quarks. The response matrix, which contains the information about the transition from the particle to the detector levels, is filled using simulated $t\bar{t}$ events, where each event contributes with the value of m_{jet} at the particle level and the m_{jet} at the detector level. Although the response matrix is created from a $t\bar{t}$ sample that simulates on-shell top quarks that further decay, the unfolding procedure in this measurement does not rely on a definition of an on-shell top quark, since all information is extracted from jets at the particle and detector level.

Another key feature of the unfolding setup in the jet mass measurement is the inclusion of events into and out of the measured phase space by adding multiple sideband regions to the response matrix. Furthermore, the response matrix is built differentially in jet mass and jet p_T . The high granularity is crucial in order to make the unfolding more independent from the model chosen in the simulation and subsequently reduce modelling uncertainties. Thus, the increase in the number of selected events by collecting more data and the growth of the $t\bar{t}$ production cross section—especially at high top quark energies—with the LHC upgrade from $\sqrt{s} = 8$ to 13 TeV did not only increase the statistical precision but also allowed the response matrix to be more granular and reduced modelling uncertainties. The smaller jet mass resolution in the two-step X Cone jet clustering enables smaller bin sizes at the particle level that help the unfolding to disentangle modelling differences and increases sensitivity to the later extracted top quark mass. Furthermore, the binning is set up such that the purity and stability—defined as the fraction of events that are reconstructed in the same bin as they are generated and the fraction of events that are generated in the same bin as they are reconstructed—surpass 40% over the full range of the particle-level phase space. We also split the m_{jet} bins in the peak region in the unfolding in order to increase the sensitivity to model differences and retain the statistical precision by recombining them after the procedure. With the currently available data set after Run 2, this results in a response matrix consisting of 200 bins at the detector level and 72 bins at the particle level.

5.7 Top quark mass from jet mass

The top quark mass has been extracted from the normalised differential $t\bar{t}$ cross section as a function of m_{jet} in order to be insensitive to normalisation effects. Figure 52 shows the normalised measurement with the full Run 2 data set [70]. So far, no analytical calculations are available for the selected phase space, thus we have extracted m_t using the POWHEG+PYTHIA simulation (detailed in Section 2.4), resulting in a value of $m_t^{\text{MC}} = 173.06 \pm 0.84$ GeV, which is compatible with direct measurements at moderate top quark energies.

The resulting values and uncertainties in the extraction of m_t in the three m_{jet} measurements [59, 66, 70] are summarised in Fig. 53. The uncertainties are broken down into statistical, experi-

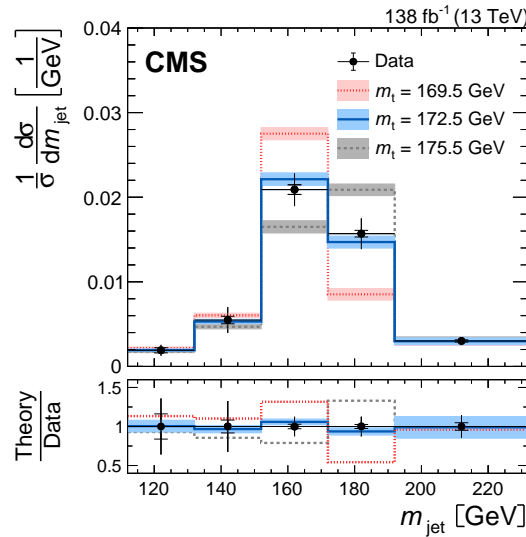


Figure 52: Normalised differential $t\bar{t}$ production cross section as a function of m_{jet} . Data (markers) are compared to predictions for different m_t obtained from simulation (lines). The bars on the markers display the statistical (inner bars) and total (outer bars) uncertainties. The theoretical uncertainty is shown as coloured area. Figure taken from Ref. [70].

CMS

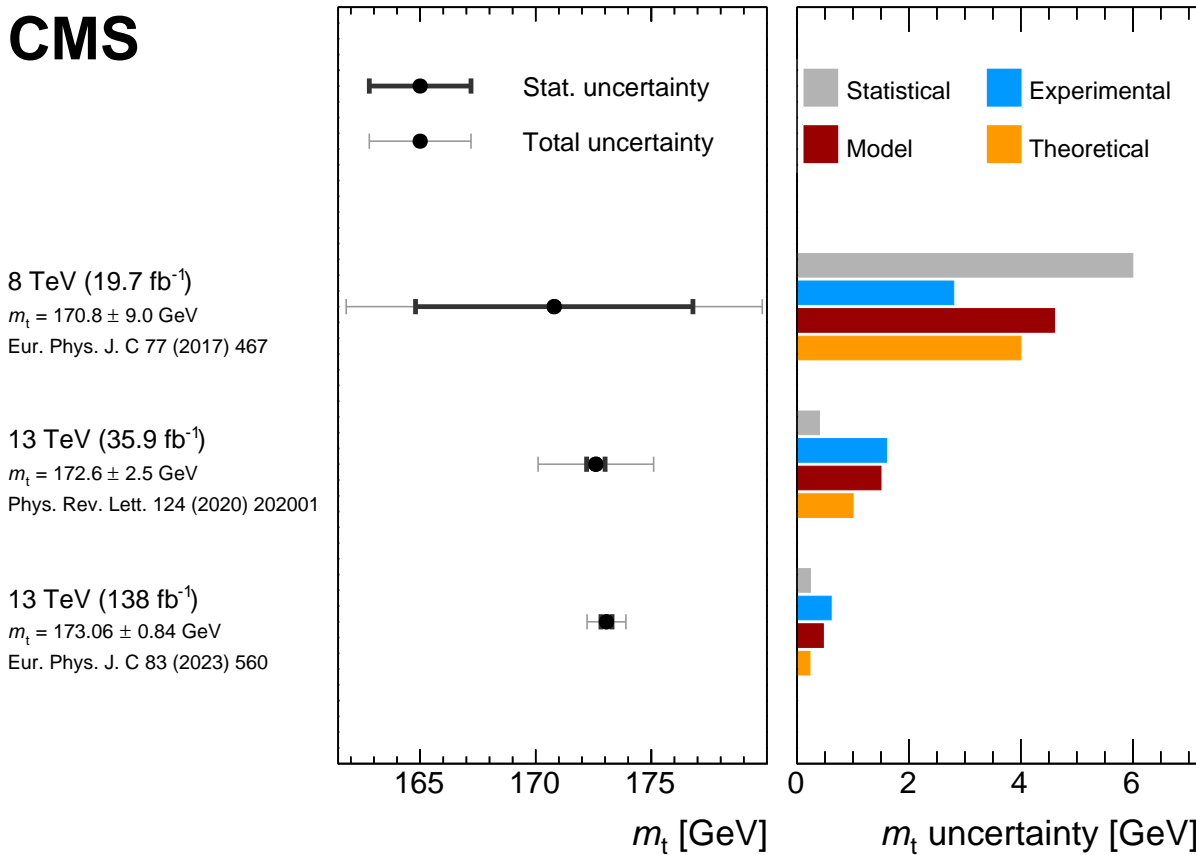


Figure 53: Summary of the m_t extraction in m_{jet} measurements. The left panel shows the extracted value of m_t (marker) with statistical (thick bars) and total (thin bars) uncertainties. The right panel displays a breakdown of contributing uncertainty groups and their impact on the uncertainty in the m_t extraction. The figure is compiled from Refs. [59, 66, 70].

mental, model, and theoretical contributions. The statistical uncertainty accounts for the finite statistical precision in the available data set. Experimental uncertainties arise from the calibration of physics objects. Model uncertainties and theoretical uncertainties both originate from choices of modelling parameters in the simulation. While theoretical uncertainties are taken into account on the particle-level predictions for the m_t hypotheses, model uncertainties arise from the potential bias in the unfolding that can be introduced by differences between data and the $t\bar{t}$ simulation.

After the first measurement at $\sqrt{s} = 8$ TeV with an initial statistical uncertainty of 6 GeV, the extraction of the top quark mass from the jet mass has largely profited from the increased production cross section of boosted top quarks at $\sqrt{s} = 13$ TeV and the vast amount of data collected during Run 2. Already with the data collected during 2016, the statistical uncertainty was no longer dominant. The sensitivity to m_t was improved by the specialised two-step jet clustering procedure using X Cone. The width of the peak in the m_{jet} distribution and jet mass resolution could both be reduced by a factor of two. The significantly larger data set allowed the use of a much more granular response matrix that leads to smaller biases in the unfolding and subsequently reduced modelling uncertainties. Better knowledge of the data also led to improved $t\bar{t}$ modelling through constraining the variations in the choice of tuning parameters, which reduced the size of modelling variations and theoretical uncertainties. Furthermore, parton shower uncertainties were no longer estimated by a comparison of PYTHIA to HERWIG but by a variation of dedicated parameters, which allows for a more detailed breakdown of systematic sources. With the full Run 2 data set and dedicated calibrations of the JMS and FSR modelling in $t\bar{t}$ simulation, the dominant sources of experimental and modelling uncertainties were reduced. In addition, the newly introduced CP5 tune (see Section 2.4) featured reduced variations of the value of α_s that controls the amount of FSR, which directly translates to reduced theoretical uncertainties. For the increased data set also the number of simulated events was substantially increased. This led to a decrease of the statistical part in the estimation of modelling and theoretical uncertainties. Especially the estimation of uncertainties that rely on an additional sample and led to artificially large theoretical uncertainties in the first measurement at 13 TeV are now reduced with the increased statistical precision in the simulation for the full Run 2 data.

6 Summary and outlook

To date, the most precise measurements of the mass of the top quark m_t reach a relative precision of approximately 0.2%. And still, the value of m_t and its uncertainty remain a focal point in particle physics, because of the central role of m_t in the electroweak symmetry breaking and fermion mass generation, and in probing physics beyond the standard model, where it enters as an essential parameter for the theoretical predictions and their quantum corrections. This makes the determination of m_t a compelling topic for both experimental and theory communities.

6.1 Summary of the top quark mass results

The CMS Collaboration embarked on an extensive and diverse program of m_t measurements. Some of the most recent results were highlighted in Sections 3, 4, and 5, for direct measurements, extractions of the Lagrangian m_t in different renormalisation schemes, and analyses in the boosted top quark regime, respectively, together with their historical development. In Fig. 54, the summary of m_t results published by the CMS Collaboration to date, also listed in Table 1, is shown. The measurements are presented in different groups, according to the ap-

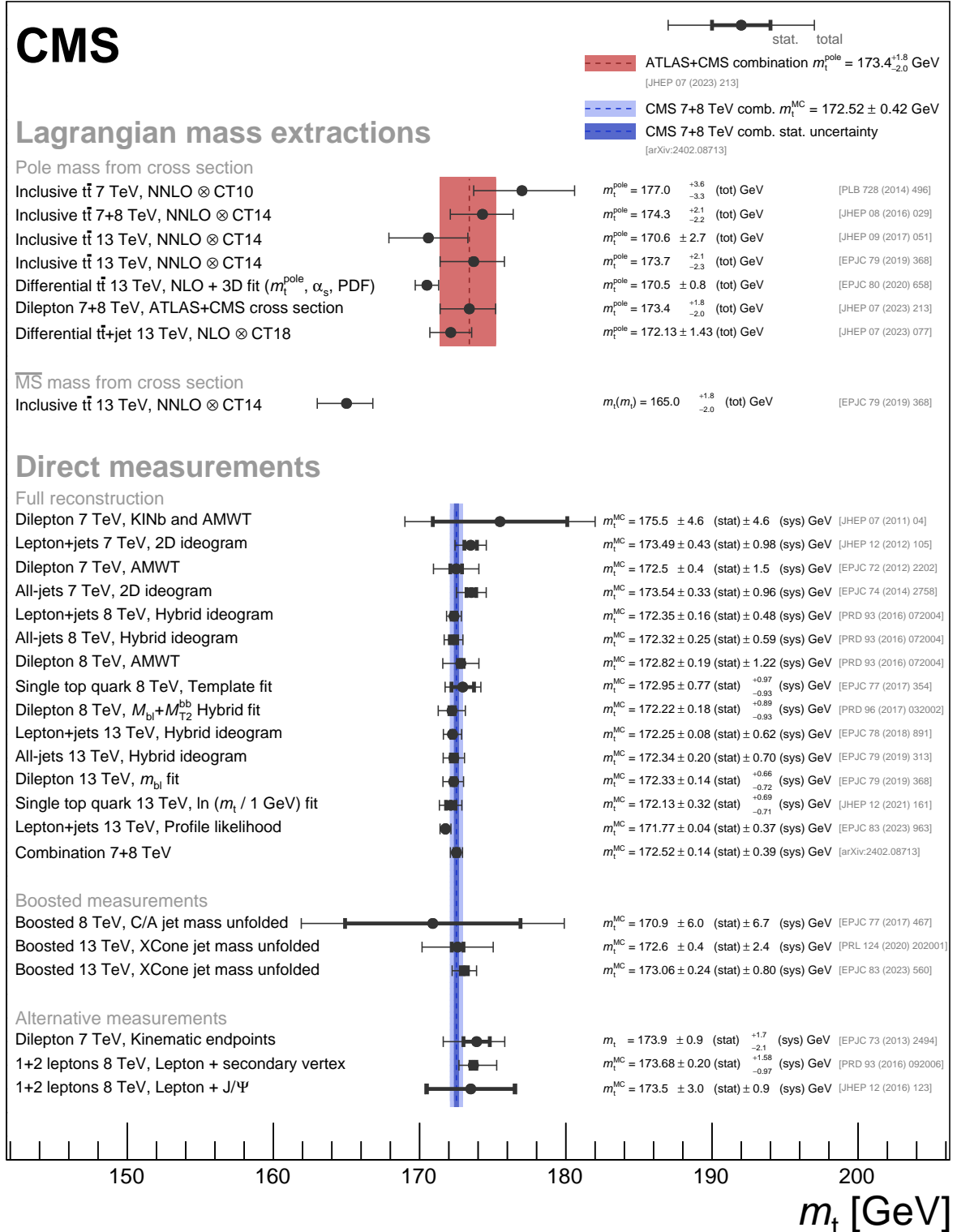


Figure 54: Overview of top quark mass measurement results published by the CMS Collaboration. The markers display the respective measured value of m_t with the statistical (inner) and total (outer) uncertainties shown as horizontal error bars. The measurements are categorised into Lagrangian mass extractions from cross section measurements and direct measurements of m_t^{MC} and are compared to the combined cross section measurement of the ATLAS and CMS Collaborations (red) and a CMS combination of Run 1 results (blue). Similar labelling as in Table 1 is used. The figure is compiled from Refs. [47–64, 66–72].

proaches and m_t definitions used. Note that the QCD conversion between the pole mass and the $\overline{\text{MS}}$ mass schemes yields a value of $m_t(m_t)$ of about 9 GeV lower than corresponding m_t^{pole} , as discussed in Section 2.8, which is consistent with the difference found between the m_t^{pole} and $m_t(m_t)$ determinations. Although the results obtained in direct measurements of the top quark mass m_t^{MC} and from extractions of the Lagrangian parameter m_t might be numerically similar, it is important to consider ambiguities in the relation between them, originating from theoretical uncertainties and limitations of the current Monte Carlo (MC) simulations.

The measurements collectively indicate results that are consistent with each other, whether considering top quark pole mass m_t^{pole} or direct m_t^{MC} measurements. Nevertheless, it is crucial to acknowledge that while the methods employed may vary, there are notable correlations of systematic and statistical nature among many of the measurements. These correlations arise from common sources of systematic uncertainties and, in certain instances, event overlap. To accurately assess compatibility and to consolidate results into a unified top quark mass extraction, it is essential to consider these correlations. However, this detailed task falls beyond the scope of the present review.

6.2 Evolution of analysis methods in CMS

The development of the analysis strategies for the m_t measurements at the LHC in the last decade has resulted in significant advancements in precision.

In the case of direct m_t measurements using $t\bar{t}$ production, the evolution of the analysis methods has led to a yet unprecedented experimental precision of less than 400 MeV. Direct measurements of m_t using single top quark production allow for probing lower energy scales compared to $t\bar{t}$ events in a different process and event topology, and thus provide different sensitivity to systematic uncertainties which can be beneficial in mass combinations [72]. However, any of these direct m_t measurements rely to large extent on MC simulations. This fact complicates the interpretation of the resulting MC parameter, m_t^{MC} , in terms of a Lagrangian m_t defined in a certain renormalisation scheme of Quantum Chromodynamics (QCD). In the face of the high experimental precision, the adequate theoretical interpretation of m_t^{MC} remains an active area of research. In fact, a deeper understanding of both perturbative and nonperturbative effects in MC simulations is required in order to relate the value of m_t^{MC} to that of a Lagrangian mass m_t with reliable uncertainty estimates.

For the Lagrangian m_t extractions, performed by comparing the measured cross sections of top quark-antiquark pair ($t\bar{t}$) production or $t\bar{t}$ +jet to theoretical predictions obtained in perturbative QCD, the current uncertainties in m_t are larger by a factor of about two, as compared to direct measurements. The theoretical uncertainty is dominated by the missing higher-order corrections, estimated by variation of the renormalisation and factorisation scales, and the uncertainties in the strong coupling constant $\alpha_s(m_Z)$ and parton distribution functions (PDFs). Experimentally, an unfolding procedure is necessary in order to relate observed detector-level variables with the theoretical calculations involving on-shell top quarks and antiquarks. Analysis strategies for measurements of cross sections of $t\bar{t}$ and $t\bar{t}$ +jet production, $\sigma_{t\bar{t}}$ and $\sigma_{t\bar{t}+\text{jet}}$, have seen improvements both from the experimental and phenomenological side. Template fits to multidifferential distributions considering both signal and background topologies are utilised. Techniques for the reconstruction of $t\bar{t}$ pairs have also been substantially advanced. Conceptually, using normalised multidifferential cross sections in an analysis, where $\alpha_s(m_Z)$, PDFs and m_t can be extracted simultaneously, helps to mitigate their correlation in the theoretical predictions of $\sigma_{t\bar{t}}$ and leads to reduction of the uncertainties due to missing higher-order corrections.

All these improvements lead to a precision in the Lagrangian m_t of about 1 GeV. These results must be further refined by improvements in theoretical calculations, e.g. consideration of the Coulomb and off-shell effects.

Boosted topology measurements make use of top quarks that are produced at transverse momenta higher than about 400 GeV, where the decay products can be reconstructed in single jets of large distance parameter R , and m_t can be extracted from the mass of the jet m_{jet} . This is in contrast to both of the aforementioned approaches, dominated by events where the $t\bar{t}$ system is produced at transverse momenta of about 100 GeV, and with top quark decay products that are well resolved in the measurement. Significant progress has been made experimentally in boosted measurements, achieving sub-GeV precision in m_t . This progress involves a dedicated calibration of the jet mass scale and a thorough investigation of the impact of final-state radiation within large- R jets. Measurements utilising boosted topologies are of particular interest, as the m_{jet} distribution is calculable within the framework of soft collinear effective theories. When such theoretical calculations become available, they can be used for Lagrangian m_t measurements, with the unfolded m_{jet} distribution serving as a means to extract m_t in a well-defined renormalisation scheme. Such measurements could be compared to those of m_t^{MC} obtained using the same data, offering not only an alternative method for measuring m_t but also an experimental input for the interpretation of m_t^{MC} . The precision of these measurements is anticipated to improve further with a larger number of $t\bar{t}$ events at high transverse momenta.

As discussed in Section 2, studies are in progress to further refine the understanding of the systematic uncertainties related to experimental effects, the modelling of $t\bar{t}$ events in MC simulation using the latest generators and tunes, and theoretical calculations of differential $t\bar{t}$ cross sections. Further improvements in precision can therefore be expected from new m_t measurements in the coming years, based on full Run 2 and Run 3 data. Early data from the Run 3 of the LHC has already led to the first inclusive $\sigma_{t\bar{t}}$ measurement [82], also shown in Fig. 1. Moreover, the forthcoming full Run 3 holds the promise of increasing the recorded top quark data set by more than twice its current size. This increase in the size of the data set, together with improvements in systematic treatment should allow for relevant advances in all the top quark studies.

In the following section, the prospects for the future m_t measurements beyond Run 3 are discussed in the context of the upcoming HL-LHC, which will bring the next big step in integrated luminosity and detector performance improvements.

6.3 Prospects at the HL-LHC

The High-Luminosity LHC (HL-LHC) upgrade [288] has the goal of accumulating data corresponding to an integrated luminosity of up to 3 ab^{-1} at a centre-of-mass energy of 14 TeV. The average number of simultaneous pp collisions bunch crossings is expected to reach nominal values up to 200. To mitigate the effect of this challenging environment, and since some detector components will have suffered from too much radiation damage, several detector components will be replaced, introducing new technology and capability into the CMS detector (Phase-2 upgrade). Among these upgrades, significant improvements are being made in the tracker and muon resolution and coverage [289, 290], dedicated timing detectors [291], and highly granular endcap calorimeters [292], as well as improved barrel calorimeters [293].

Measurements of m_t will profit twofold from the HL-LHC upgrade. The larger data sample will enable measurements in currently less populated areas of the phase space, and will allow the application of methods exploiting processes with small branching fractions. Also, the de-

ector upgrades can lead to more accurate measurements of the physics objects, subsequently providing the basis for higher precision m_t measurements. An illustrative example is m_t extraction from J/ψ meson decays inside b jets [56] accompanied by a lepton from the W boson decay. This measurement is less affected by the jet energy scale uncertainty than classical direct m_t measurements, but suffers from large statistical uncertainties and uncertainties in b quark fragmentation. The core of this analysis relies on an accurately measurable peak in the $J/\psi \rightarrow \mu\mu$ invariant mass distribution, and subsequent determination of the $\mu + J/\psi$ mass. With the new higher-resolution tracker and with the improvements in the muon system for the HL-LHC, the resolution of this peak will improve by almost a factor of two, as shown in Fig. 55.

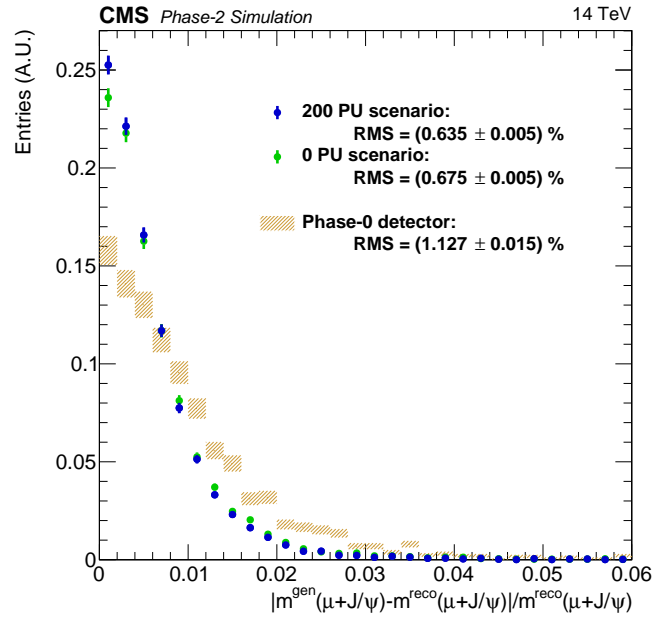


Figure 55: The resolution of the $\mu + J/\psi$ mass for the CMS Phase-2 upgraded detector, for the two PU scenarios, and for the Run 2 (Phase-0) detector. Figure taken from Ref. [290].

Most m_t measurements are limited by the systematic uncertainties. Approximate studies to obtain HL-LHC projections for the m_t measurements were performed and are shown in Fig. 56. These do not fully account for improvements in the performance of the upgraded CMS detector. An ultimate relative precision of direct m_t measurement better than 0.1% is expected. But also other methods profit significantly from the HL-LHC data and will continue to provide complementary information. To estimate the HL-LHC prospects for these analyses, the systematic uncertainties are assumed to decrease, as expected considering the detector upgrades, developments of the reconstruction algorithms, refinements in the theoretical predictions, and improvements in the modelling from ancillary measurements [294]. In particular, the effect of the increased pileup is expected to be controllable for all objects, given higher detector granularity, timing capabilities of subdetectors, dedicated timing detectors, and exploiting the potential of pileup mitigation algorithms such as PUPPI [97]. A moderate increase in the production cross section is expected to compensate possible losses in selection and trigger efficiencies. Furthermore, an increase in the acceptance of the upgraded detectors is expected.

Significant reduction of the systematic uncertainties in the signal modelling is expected too. Ancillary studies are being performed for the modelling of colour reconnection and the underlying event tunes, as outlined in previous sections. These are partially limited by statistical effects, and are therefore assumed to improve under HL-LHC conditions. These improvements are expected to reduce the corresponding uncertainties by about a factor of two. Further, the

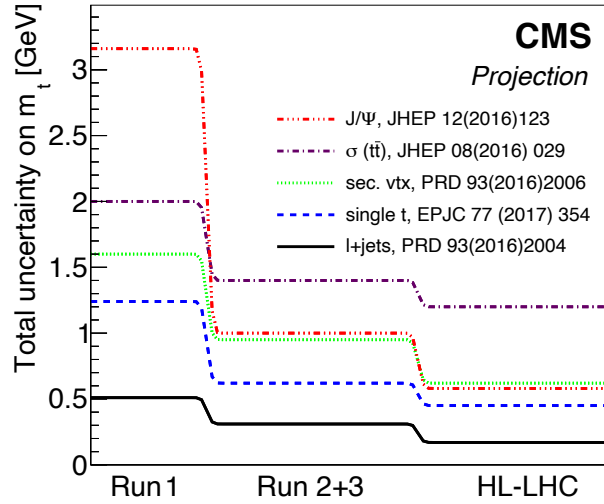


Figure 56: Total uncertainty in m_t obtained with a selection of different measurement methods and their projections for expected running conditions in Run 2 + Run 3 and at the HL-LHC. The projections are based on m_t measurements performed during the LHC Run 1, also listed in Table 1: the J/ψ [56], total $t\bar{t}$ cross section [54] in the dilepton channel, secondary vertex [55], single top quark [58], and lepton+jets direct [53] measurements. These projections do not fully account for improvements in the performance of the upgraded CMS detector. Figure taken from Ref. [294].

precision of modelling QCD and fragmentation effects is expected to increase, by using new MC generators at next-to-leading (NLO) and next-to-next-to-leading order (NNLO) QCD, improvements in the parton-shower simulation, and a fine-grained tuning of their parameters by exploiting larger data sets. While the choice of the PDF set and the PDF uncertainties typically only have a small effect in direct m_t measurements, these are of high importance in the extraction of the Lagrangian m_t using QCD predictions in well-defined renormalisation schemes. For the HL-LHC projections, the contribution of the PDF uncertainty is usually assumed to be reduced by a factor of two. The experimental uncertainties, often dominated by the jet energy scale, are also expected to be reduced by approximately a factor of two by the end of the HL-LHC running. However, the relative importance of the individual effects differs between the various m_t measurement methods [294, 295]. The flavour-dependent components of the jet energy scale and the corresponding modelling of the b quark fragmentation and the hadronisation model limit the precision of the direct measurements of m_t in $t\bar{t}$ production. With dedicated measurements and improvements in the modelling, these contributions are expected to reduce. The projected uncertainty reduction does not yet account for in-situ constraints for fits to multi-dimensional final-state distributions, introduced in Refs. [63, 65, 218] and used successfully for the most precise single measurement to date [71].

In measurements that exploit the electroweak production modes in single top quark events, the background modelling is among the dominant sources of systematic uncertainties. With increasing centre-of-mass energy, the cross section of the leading contributions from W +jets production increases more slowly than for top quark production, in particular compared to Run 1. Moreover, due to the large data sample, fine-grained regions can be used to constrain the background processes, which is why finally their contribution to the uncertainty is expected to be reduced by a factor of three with respect to Run 1.

As mentioned earlier, m_t analyses relying on secondary vertices in the b jets or a full reconstruction of particles therein, e.g. the J/ψ meson, will profit from the upgraded tracking detector. The dominant systematic uncertainties remain related to the modelling of the b quark hadronisation. These effects are studied through dedicated analyses, and could be constrained in situ, given the improved vertex resolution, leading to the assumption that their impact on the precision of m_t will be reduced significantly.

Also the measurements of the Lagrangian m_t , such as the extraction from the inclusive $t\bar{t}$ production cross section, are expected to become more precise. Besides the conceptual issue of correlation of PDF, $\alpha_S(m_Z)$ and m_t in the $\sigma_{t\bar{t}}$ prediction, the extraction of m_t^{pole} from the inclusive $\sigma_{t\bar{t}}$ is limited in almost equal parts by uncertainties in the theoretical prediction, currently available up to NNLO in QCD, and the experimental precision of the $\sigma_{t\bar{t}}$ measurement. With several improvements in the analysis techniques [54, 63], the experimental precision of the inclusive $\sigma_{t\bar{t}}$ measurement is already mostly limited by the uncertainty in the integrated luminosity. A projection [63] of the Run 2 measurement is shown in Fig. 57. It has been obtained in the context of the CMS beam and radiation monitoring system upgrade studies [296]. The systematic uncertainties are scaled according to the assumptions outlined above, and the fit to the measured distributions has been repeated. In order to show their impact, the uncertainties in the NNLO prediction are assumed to remain at the current level and compared to a scenario with no uncertainties. Depending on the scenario, a precision of up to 1.3 GeV in the m_t^{pole} can be reached.

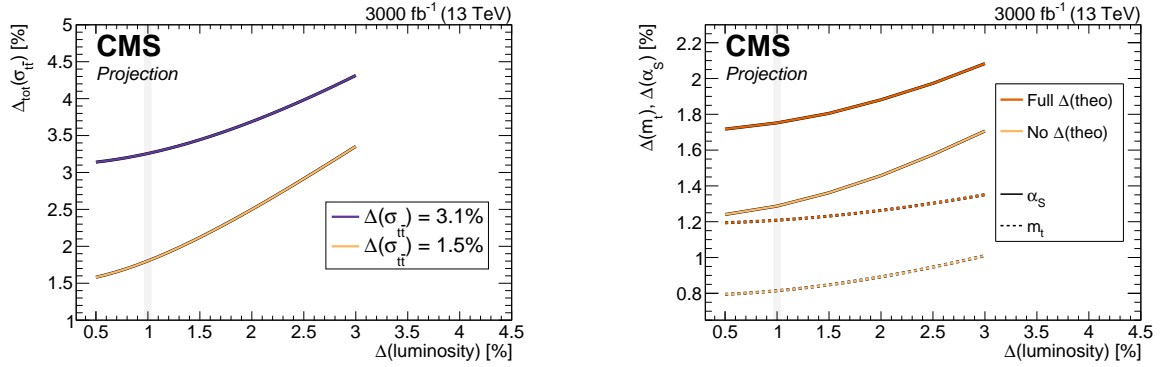


Figure 57: Left: The projected total experimental uncertainty in the top quark pair production cross section as a function of the uncertainty in the integrated luminosity, for two experimental scenarios, assuming no reduction of the experimental uncertainties with respect to Run 2 and a reduction of the uncertainties following the recommendations outlined in Ref [295]. Right: The projected relative uncertainties in the extracted values of m_t (dotted lines) and α_S (solid lines) as a function of the uncertainty in the integrated luminosity, comparing the case of the full uncertainty in the prediction and no uncertainty in the prediction. The results are obtained assuming a reduction of the uncertainties in the measurement to 1.5%. Figure taken from Ref. [296].

This is approximately consistent with the projection from Ref. [294] shown in Fig. 56, where a reduction of the uncertainty in the integrated luminosity down to 0.5% is expected. Furthermore, a reduction of theoretical uncertainties in $\sigma_{t\bar{t}}$ is assumed, originating from uncertainties in PDFs, $\alpha_S(m_Z)$, and from missing higher-order corrections. With additional measurements, the PDF and α_S uncertainty are assumed to be reduced by a factor of two by the end of the HL-LHC phase. However, it is uncertain whether QCD predictions beyond NNLO will become available. Therefore, the uncertainties from the scale variations are assumed to be constant.

In the HL-LHC phase, the precision of the differential $t\bar{t}$ cross section measurements and, in

turn, the experimental accuracy of extraction of m_t , $\alpha_S(m_Z)$ and of PDFs will profit from both the increased amount of data and the extended rapidity reach of the HL-LHC CMS detector. The projection study of Ref. [297] demonstrated that despite the significantly higher pileup, the performance of the $t\bar{t}$ reconstruction in the HL-LHC phase is expected to remain similar to the one of analyses based on data taken in 2016. The measurable phase space will increase due to the extended rapidity range, allowing for finer binning of double-differential measurements of $m_{t\bar{t}}$ and $y_{t\bar{t}}$ in a phase space not accessible in current measurements, as illustrated in Fig. 58.

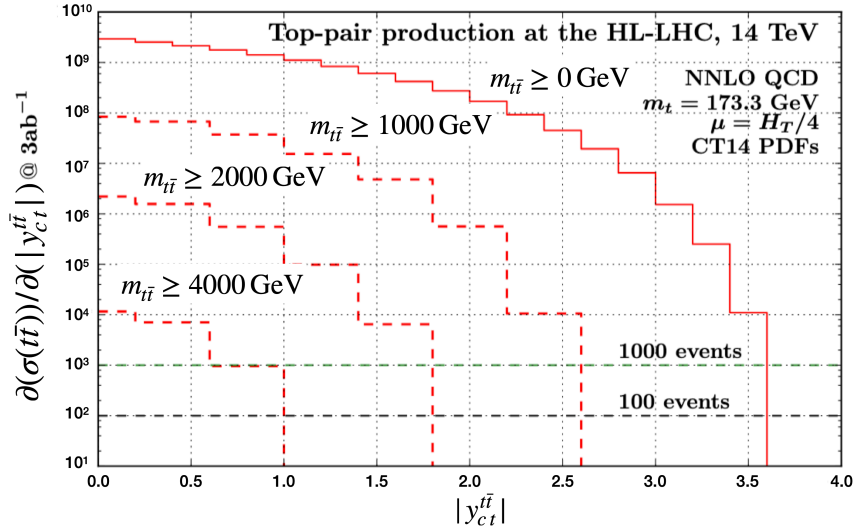


Figure 58: Projected cumulative differential $t\bar{t}$ distributions for HL-LHC scenario as functions of rapidity and invariant mass of the $t\bar{t}$ pair. Figure taken from Ref. [297].

While no projection is available for the precision of m_t when extracted from the differential cross sections, the projected precision in the PDF extraction from $t\bar{t}$ multi-differential measurements is investigated in Ref. [297]. The inclusion of $t\bar{t}$ cross section measurements is found to significantly improve the precision in PDF extraction. In particular, the uncertainties in $g(x)$ could be reduced by a factor of 5–10 at high x , as illustrated in Fig. 59, obtained using a profiling technique [298]. The latter is based on minimising the χ^2 function between the data and theoretical predictions using available PDFs and taking into account both experimental and theoretical uncertainties arising from the PDF variations. As discussed in Section 4.4, this significant reduction in the $g(x)$ would immediately translate in reduction of related uncertainty in m_t due to large correlations of both in theoretical predictions of $\sigma_{t\bar{t}}$. Beyond these projections, further improvement is expected from higher-order calculations of double-differential distributions, which should be provided with fast interpolation grids in the future. By performing the full QCD analysis of PDFs, m_t and $\alpha_S(m_Z)$, the correlation between those is expected to be diminished, so that ultimate precision in the Lagrangian m_t can be achieved. Furthermore, QCD corrections from resummations beyond the fixed-order approach and off-shell corrections, which are currently missing in these analyses, should be accounted for, once available, to achieve the ultimate theoretical accuracy.

The extraction of m_t from the m_{jet} distribution in decays of Lorentz-boosted top quarks will also benefit from the increased centre-of-mass energy and the large data set expected after the HL-LHC upgrade. While the possibility of a precision m_t measurement from high-energy top quarks has been demonstrated with the data collected already today, the full potential of this measurement is not reached yet. Already for the generator based extraction of m_t^{MC} more data will allow to make the unfolding more granular and even to perform the measurement differentially in jet p_T . With the CMS Run 2 data set, corresponding to an integrated luminosity

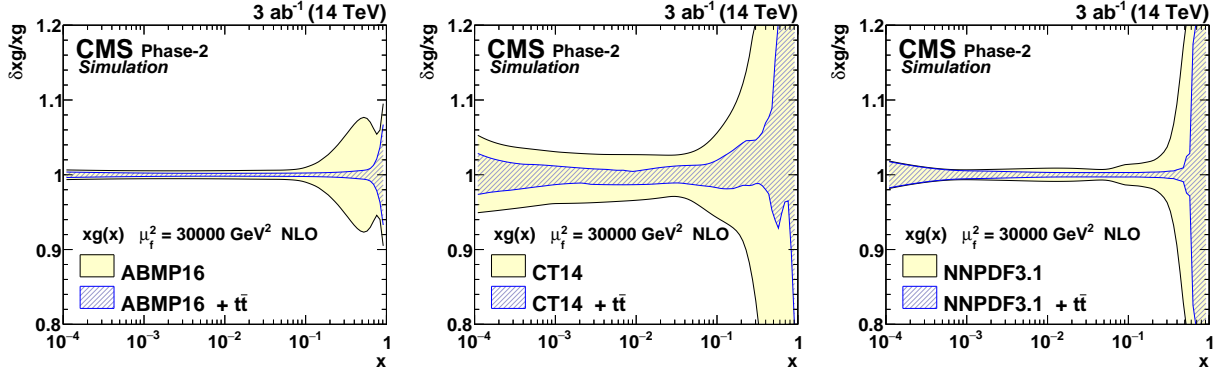


Figure 59: The relative gluon PDF uncertainties of the original and profiled ABMP16 (left), CT14 (middle), and NNPDF3.1 (right) sets. Figure taken from Ref. [297].

of 138 fb^{-1} , about 52 000 events were selected in the measurement region. This number is reduced to 21 500 when requiring jets to have $p_T > 500 \text{ GeV}$ and even drops to below 3000 events for $p_T > 750 \text{ GeV}$, which would coincide with the space for which analytical calculations exist. Figure 60 shows a study where the possible jet p_T threshold is calculated as a function of integrated luminosity in order to achieve the same statistical precision as in the latest Run 2 measurement [70]. After the HL-LHC upgrade, a data set corresponding to 3000 fb^{-1} in combination with a slightly increased $t\bar{t}$ production cross section at higher \sqrt{s} is expected. Thus, the phase space at very high p_T becomes available experimentally.

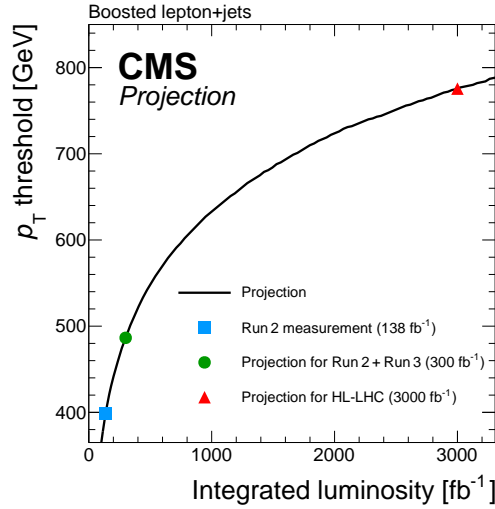


Figure 60: Scan of the jet p_T threshold in the measurements of the jet mass against integrated luminosity resulting in the same event yield in data after the full selection as in the most recent measurement [70]. The projection is obtained by scanning the jet p_T spectrum observed in data. The markers correspond to 138 fb^{-1} of LHC Run 2 data used in Ref. [70], to an estimated data set for the combination of Run 2 and Run 3, and to the HL-LHC scenario. For simplicity a constant centre-of-mass energy of 13 TeV and a similar detector acceptance to Run 2 are assumed in all scenarios.

In addition, systematic uncertainties can be further reduced. On the experimental side, the calibration of the jet mass scale can be extended to include a measurement of the jet mass resolution in order to constrain this dominant uncertainty and become independent from the p_T driven calibration of the jet energy resolution. Modelling uncertainties will benefit from

a more granular unfolding process. This involves increasing the number of bins in the m_{jet} and jet p_T measurements, as well as incorporating additional observables. These steps will help to separate the model dependencies more effectively. This is particularly relevant for reducing uncertainties related to the choice of m_t^{MC} in simulations. By adopting a more detailed approach, we can better distinguish between the correlations of jet p_T and m_{jet} , thus reducing this uncertainty. With more data available, one cannot only increase the jet p_T threshold to a higher value but also perform the m_{jet} measurement differentially in jet p_T . This could be used to dampen any p_T -dependent effects in the m_{jet} distribution and further increase the sensitivity to m_t . Furthermore, a precise test of p_T independence of the measured m_t^{MC} would provide an important consistency check of the generator-based measurement.

Already now, the measurement of m_{jet} provides a precise determination of m_t^{MC} at energy scales not probed before. However, the full potential of these measurements can only be reached once the definitions in calculations and the experimental analysis are brought into concordance, requiring developments from both sides. At this point, these will become a powerful tool not only for precisely measuring m_t in a well-defined theoretical scheme but also for resolving the ambiguities in relation to m_t^{MC} .

6.4 Conclusions

Measurements of the top quark mass have been an essential part of the CMS research programme since the first data were recorded in 2010, with more than 20 journal publications that reveal different aspects related to this fundamental parameter of the standard model. A growing understanding of theoretical and experimental issues on the way towards increasing precision in m_t , demanded by matching the accuracy of other electroweak parameters, were followed by steady improvements in analysis techniques. Different complementary methods have been used for measurements of m_t , affected by different sources of theoretical and experimental systematic uncertainties. An impressive sub-GeV precision has been achieved, despite the challenging environment of high-energy pp collisions at the LHC, where events are affected by QCD and electroweak radiation, the underlying event and an unprecedented level of pileup interactions.

This success, and a clear perspective of experimental improvements envisaged for the HL-LHC, give confidence in reaching the ultimate precision in m_t achievable at a hadron collider in the next decade. This experimental goal requires that the necessary theoretical developments will take place, including advancements in the description of the top quark beyond the picture of a free particle, matching higher-order calculations to resummations and hadronisation models, and calculating corrections at the threshold of $t\bar{t}$ production. The precise determination of m_t is an ongoing endeavor that fosters a close collaboration of the experimental and theoretical communities, with bright prospects in the coming years.

Acknowledgments

We congratulate our colleagues in the CERN accelerator departments for the excellent performance of the LHC and thank the technical and administrative staffs at CERN and at other CMS institutes for their contributions to the success of the CMS effort. In addition, we gratefully acknowledge the computing centres and personnel of the Worldwide LHC Computing Grid and other centres for delivering so effectively the computing infrastructure essential to our analyses. Finally, we acknowledge the enduring support for the construction and operation of the LHC, the CMS detector, and the supporting computing infrastructure provided

by the following funding agencies: the Armenian Science Committee, project no. 22rl-037; the Austrian Federal Ministry of Education, Science and Research and the Austrian Science Fund; the Belgian Fonds de la Recherche Scientifique, and Fonds voor Wetenschappelijk Onderzoek; the Brazilian Funding Agencies (CNPq, CAPES, FAPERJ, FAPERGS, and FAPESP); the Bulgarian Ministry of Education and Science, and the Bulgarian National Science Fund; CERN; the Chinese Academy of Sciences, Ministry of Science and Technology, the National Natural Science Foundation of China, and Fundamental Research Funds for the Central Universities; the Ministerio de Ciencia Tecnología e Innovación (MINCIENCIAS), Colombia; the Croatian Ministry of Science, Education and Sport, and the Croatian Science Foundation; the Research and Innovation Foundation, Cyprus; the Secretariat for Higher Education, Science, Technology and Innovation, Ecuador; the Estonian Research Council via PRG780, PRG803, RVTT3 and the Ministry of Education and Research TK202; the Academy of Finland, Finnish Ministry of Education and Culture, and Helsinki Institute of Physics; the Institut National de Physique Nucléaire et de Physique des Particules / CNRS, and Commissariat à l'Énergie Atomique et aux Énergies Alternatives / CEA, France; the Shota Rustaveli National Science Foundation, Georgia; the Bundesministerium für Bildung und Forschung, the Deutsche Forschungsgemeinschaft (DFG), under Germany's Excellence Strategy – EXC 2121 “Quantum Universe” – 390833306, and under project number 400140256 - GRK2497, and Helmholtz-Gemeinschaft Deutscher Forschungszentren, Germany; the General Secretariat for Research and Innovation and the Hellenic Foundation for Research and Innovation (HFRI), Project Number 2288, Greece; the National Research, Development and Innovation Office (NKFIH), Hungary; the Department of Atomic Energy and the Department of Science and Technology, India; the Institute for Studies in Theoretical Physics and Mathematics, Iran; the Science Foundation, Ireland; the Istituto Nazionale di Fisica Nucleare, Italy; the Ministry of Science, ICT and Future Planning, and National Research Foundation (NRF), Republic of Korea; the Ministry of Education and Science of the Republic of Latvia; the Research Council of Lithuania, agreement No. VS-19 (LMTLT); the Ministry of Education, and University of Malaya (Malaysia); the Ministry of Science of Montenegro; the Mexican Funding Agencies (BUAP, CINEVESTAV, CONACYT, LNS, SEP, and UASLP-FAI); the Ministry of Business, Innovation and Employment, New Zealand; the Pakistan Atomic Energy Commission; the Ministry of Education and Science and the National Science Centre, Poland; the Fundação para a Ciência e a Tecnologia, grants CERN/FIS-PAR/0025/2019 and CERN/FIS-INS/0032/2019, Portugal; JINR, Dubna; the Ministry of Education and Science of the Russian Federation, the Federal Agency of Atomic Energy of the Russian Federation, Russian Academy of Sciences, the Russian Foundation for Basic Research, and the National Research Center “Kurchatov Institute”; the Ministry of Education, Science and Technological Development of Serbia; MCIN/AEI/10.13039/501100011033, ERDF “a way of making Europe”, Programa Estatal de Fomento de la Investigación Científica y Técnica de Excelencia María de Maeztu, grant MDM-2017-0765, projects PID2020-113705RB, PID2020-113304RB, PID2020-116262RB and PID2020-113341RB-I00, and Plan de Ciencia, Tecnología e Innovación de Asturias, Spain; the Ministry of Science, Technology and Research, Sri Lanka; the Swiss Funding Agencies (ETH Board, ETH Zurich, PSI, SNF, UniZH, Canton Zurich, and SER); the Ministry of Science and Technology, Taipei; the Ministry of Higher Education, Science, Research and Innovation, and the National Science and Technology Development Agency of Thailand; the Scientific and Technical Research Council of Turkey, and Turkish Energy, Nuclear and Mineral Research Agency; the National Academy of Sciences of Ukraine; the Science and Technology Facilities Council, UK; the US Department of Energy, and the US National Science Foundation.

Individuals have received support from the Marie-Curie programme and the European Research Council and Horizon 2020 Grant, contract Nos. 675440, 724704, 752730, 758316, 765710,

824093, 101115353, and COST Action CA16108 (European Union) the Leventis Foundation; the Alfred P. Sloan Foundation; the Alexander von Humboldt Foundation; the Belgian Federal Science Policy Office; the Fonds pour la Formation à la Recherche dans l'Industrie et dans l'Agriculture (FRIA-Belgium); the Agentschap voor Innovatie door Wetenschap en Technologie (IWT-Belgium); the F.R.S.-FNRS and FWO (Belgium) under the "Excellence of Science – EOS" – be.h project n. 30820817; the Beijing Municipal Science & Technology Commission, No. Z191100007219010; the Ministry of Education, Youth and Sports (MEYS) of the Czech Republic; the Shota Rustaveli National Science Foundation, grant FR-22-985 (Georgia); the Hungarian Academy of Sciences, the New National Excellence Program - ÚNKP, the NKFIH research grants K 124845, K 124850, K 128713, K 128786, K 129058, K 131991, K 133046, K 138136, K 143460, K 143477, 2020-2.2.1-ED-2021-00181, and TKP2021-NKTA-64 (Hungary); the Council of Scientific and Industrial Research, India; ICSC – National Research Centre for High Performance Computing, Big Data and Quantum Computing, funded by the EU NexGeneration program, Italy; the Latvian Council of Science; the Ministry of Education and Science, project no. 2022/WK/14, and the National Science Center, contracts Opus 2021/41/B/ST2/01369 and 2021/43/B/ST2/01552 (Poland); the Fundação para a Ciência e a Tecnologia, grant FCT CEECIND/01334/2018; the National Priorities Research Program by Qatar National Research Fund; the Ministry of Science and Higher Education, projects no. FSWU-2023-0073 and no. FSWW-2020-0008 (Russia); the Programa Estatal de Fomento de la Investigación Científica y Técnica de Excelencia María de Maeztu, grant MDM-2017-0765 and projects PID2020-113705RB, PID2020-113304RB, PID2020-116262RB and PID2020-113341RB-I00, and Programa Severo Ochoa del Principado de Asturias (Spain); the Chulalongkorn Academic into Its 2nd Century Project Advancement Project, and the National Science, Research and Innovation Fund via the Program Management Unit for Human Resources & Institutional Development, Research and Innovation, grant B37G660013 (Thailand); the Kavli Foundation; the Nvidia Corporation; the SuperMicro Corporation; the Welch Foundation, contract C-1845; and the Weston Havens Foundation (USA).

References

- [1] Particle Data Group, R. L. Workman et al., "Review of particle physics", *Prog. Theor. Exp. Phys.* **2022** (2022) 083C01, doi:10.1093/ptep/ptac097.
- [2] G. Mahlon and S. J. Parke, "Spin correlation effects in top quark pair production at the LHC", *Phys. Rev. D* **81** (2010) 074024, doi:10.1103/PhysRevD.81.074024, arXiv:1001.3422.
- [3] A. H. Hoang, "What is the top quark mass?", *Ann. Rev. Nucl. Part. Sci.* **70** (2020) 225, doi:10.1146/annurev-nucl-101918-023530, arXiv:2004.12915.
- [4] M. Kobayashi and T. Maskawa, "CP-violation in the renormalizable theory of weak interaction", *Prog. Theor. Phys.* **49** (1973) 652, doi:10.1143/PTP.49.652.
- [5] P. H. Ginsparg, S. L. Glashow, and M. B. Wise, "Top-quark mass and bottom-quark decay", *Phys. Rev. Lett.* **50** (1983) 1415, doi:10.1103/PhysRevLett.50.1415. [Erratum: doi:10.1103/PhysRevLett.51.1395.2].
- [6] A. J. Buras, W. Slominski, and H. Steger, "B meson decay, CP violation, mixing angles and the top quark mass", *Nucl. Phys. B* **238** (1984) 529, doi:10.1016/0550-3213(84)90334-1.

- [7] JADE Collaboration, "A measurement of the electroweak induced charge asymmetry in $e^+e^- \rightarrow b\bar{b}$ ", *Phys. Lett. B* **146** (1984) 437, doi:10.1016/0370-2693(84)90156-4.
- [8] S. L. Glashow, J. Iliopoulos, and L. Maiani, "Weak interactions with lepton-hadron symmetry", *Phys. Rev. D* **2** (1970) 1285, doi:10.1103/PhysRevD.2.1285.
- [9] B. Adeva et al., "Search for top quark and a test of models without top quark up to 38.54 GeV at PETRA", *Phys. Rev. Lett.* **50** (1983) 799, doi:10.1103/PhysRevLett.50.799.
- [10] TOPAZ Collaboration, "Search for top quark in e^+e^- collisions at $\sqrt{s} = 52$ GeV", *Phys. Rev. Lett.* **60** (1988) 97, doi:10.1103/PhysRevLett.60.97.
- [11] UA1 Collaboration, "Search for new heavy quarks in proton-antiproton collisions at $\sqrt{s} = 0.63$ TeV", *Z. Phys. C* **48** (1990) 1, doi:10.1007/BF01565600.
- [12] UA2 Collaboration, "Search for top quark production at the CERN $\bar{p}p$ collider", *Z. Phys. C* **46** (1990) 179, doi:10.1007/BF01555995.
- [13] ARGUS Collaboration, "Observation of $B^0\bar{B}^0$ mixing", *Phys. Lett. B* **192** (1987) 245, doi:10.1016/0370-2693(87)91177-4.
- [14] CLEO Collaboration, " $B^0\bar{B}^0$ mixing at the $Y(4s)$ ", *Phys. Rev. Lett.* **62** (1989) 2233, doi:10.1103/PhysRevLett.62.2233.
- [15] G. Altarelli and P. J. Franzini, " $B^0\bar{B}^0$ mixing within and beyond the standard model", *Z. Phys. C* **37** (1988) 271, doi:10.1007/BF01579913.
- [16] ALEPH Collaboration, "A search for new quarks and leptons from Z^0 decay", *Phys. Lett. B* **236** (1990) 511, doi:10.1016/0370-2693(90)90392-J.
- [17] OPAL Collaboration, "A search for the top and b' quarks in hadronic Z^0 decays", *Phys. Lett. B* **236** (1990) 364, doi:10.1016/0370-2693(90)90999-M.
- [18] ALEPH, DELPHI, L3, and OPAL Collaborations, "Electroweak parameters of the Z^0 resonance and the standard model", *Phys. Lett. B* **276** (1992) 247, doi:10.1016/0370-2693(92)90572-L.
- [19] ALEPH, DELPHI, L3, and OPAL Collaborations, and LEP Electroweak Working Group, "A combination of preliminary LEP electroweak measurements and constraints on the standard model", LEP Note CERN-PPE-95-172, 1995.
- [20] M. Lusignoli, L. Maiani, G. Martinelli, and L. Reina, "Mixing and CP violation in K- and B-mesons: a lattice QCD point of view", *Nucl. Phys. B* **369** (1992) 139, doi:10.1016/0550-3213(92)90381-K.
- [21] A. J. Buras, "A 1993 look at the lower bound on the top quark mass from CP violation", *Phys. Lett. B* **317** (1993) 449, doi:10.1016/0370-2693(93)91023-G, arXiv:hep-ph/9307318.
- [22] CDF Collaboration, "Observation of top quark production in $\bar{p}p$ collisions with the Collider Detector at Fermilab", *Phys. Rev. Lett.* **74** (1995) 2626, doi:10.1103/PhysRevLett.74.2626, arXiv:hep-ex/9503002.
- [23] D0 Collaboration, "Observation of the top quark", *Phys. Rev. Lett.* **74** (1995) 2632, doi:10.1103/PhysRevLett.74.2632, arXiv:hep-ex/9503003.

- [24] D0 Collaboration, “Observation of single top-quark production”, *Phys. Rev. Lett.* **103** (2009) 092001, doi:10.1103/PhysRevLett.103.092001, arXiv:0903.0850.
- [25] CDF Collaboration, “Observation of electroweak single top-quark production”, *Phys. Rev. Lett.* **103** (2009) 092002, doi:10.1103/PhysRevLett.103.092002, arXiv:0903.0885.
- [26] CDF and D0 Collaborations, “Combination of CDF and D0 results on the mass of the top quark using up to 9.7 fb^{-1} at the Tevatron”, 2016. arXiv:1608.01881.
- [27] C. Campagnari and M. Franklin, “The discovery of the top quark”, *Rev. Mod. Phys.* **69** (1997) 137, doi:10.1103/RevModPhys.69.137, arXiv:hep-ex/9608003.
- [28] J. M. Flynn and L. Randall, “The electromagnetic penguin contribution to ϵ'/ϵ for large top quark mass”, *Phys. Lett. B* **224** (1989) 221, doi:10.1016/0370-2693(89)91078-2. [Erratum: doi:10.1016/0370-2693(90)91986-L].
- [29] G. Buchalla, A. J. Buras, and M. K. Harlander, “The anatomy of ϵ'/ϵ in the standard model”, *Nucl. Phys. B* **337** (1990) 313, doi:10.1016/0550-3213(90)90275-I.
- [30] J. Erler and M. Schott, “Electroweak precision tests of the standard model after the discovery of the Higgs boson”, *Prog. Part. Nucl. Phys.* **106** (2019) 68, doi:10.1016/j.pnpnp.2019.02.007, arXiv:1902.05142.
- [31] J. Haller et al., “Update of the global electroweak fit and constraints on two-Higgs-doublet models”, *Eur. Phys. J. C* **78** (2018) 675, doi:10.1140/epjc/s10052-018-6131-3, arXiv:1803.01853.
- [32] ATLAS Collaboration, “A detailed map of Higgs boson interactions by the ATLAS experiment ten years after the discovery”, *Nature* **607** (2022) 52, doi:10.1038/s41586-022-04893-w, arXiv:2207.00092. [Publisher correction: doi:10.1038/s41586-022-05581-5, author correction: doi:10.1038/s41586-023-06248-5].
- [33] CMS Collaboration, “A portrait of the Higgs boson by the CMS experiment ten years after the discovery”, *Nature* **607** (2022) 60, doi:10.1038/s41586-022-04892-x, arXiv:2207.00043. [Author correction: doi:10.1038/s41586-023-06164-8].
- [34] CMS Collaboration, “Measurement of the top quark Yukawa coupling from $t\bar{t}$ kinematic distributions in the dilepton final state in proton-proton collisions at $\sqrt{s} = 13 \text{ TeV}$ ”, *Phys. Rev. D* **102** (2020) 092013, doi:10.1103/PhysRevD.102.092013, arXiv:2009.07123.
- [35] G. Degrandi et al., “Higgs mass and vacuum stability in the standard model at NNLO”, *JHEP* **08** (2012) 098, doi:10.1007/JHEP08(2012)098, arXiv:1205.6497.
- [36] S. Alekhin, A. Djouadi, and S. Moch, “The top quark and Higgs boson masses and the stability of the electroweak vacuum”, *Phys. Lett. B* **716** (2012) 214, doi:10.1016/j.physletb.2012.08.024, arXiv:1207.0980.
- [37] S. Heinemeyer, W. Hollik, G. Weiglein, and L. Zeune, “Implications of LHC search results on the W boson mass prediction in the MSSM”, *JHEP* **12** (2013) 084, doi:10.1007/JHEP12(2013)084, arXiv:1311.1663.

- [38] F. Bezrukov, M. Y. Kalmykov, B. A. Kniehl, and M. Shaposhnikov, “Higgs boson mass and new physics”, *JHEP* **10** (2012) 140, doi:10.1007/JHEP10(2012)140, arXiv:1205.2893.
- [39] D. Dunsy, L. J. Hall, and K. Harigaya, “Dark matter detection, standard model parameters and intermediate scale supersymmetry”, *JHEP* **04** (2021) 052, doi:10.1007/JHEP04(2021)052, arXiv:2011.12302.
- [40] W. Buchmuller and D. Wyler, “Effective Lagrangian analysis of new interactions and flavour conservation”, *Nucl. Phys. B* **268** (1986) 621, doi:10.1016/0550-3213(86)90262-2.
- [41] G. F. Giudice, C. Grojean, A. Pomarol, and R. Rattazzi, “The strongly-interacting light Higgs”, *JHEP* **06** (2007) 045, doi:10.1088/1126-6708/2007/06/045, arXiv:hep-ph/0703164.
- [42] B. Grzadkowski, M. Iskrzynski, M. Misiak, and J. Rosiek, “Dimension-six terms in the standard model Lagrangian”, *JHEP* **10** (2010) 085, doi:10.1007/JHEP10(2010)085, arXiv:1008.4884.
- [43] J. Gao et al., “Simultaneous CTEQ-TEA extraction of PDFs and SMEFT parameters from jet and $t\bar{t}$ data”, *JHEP* **05** (2023) 003, doi:10.1007/JHEP05(2023)003, arXiv:2211.01094.
- [44] A. J. Buras, J. Girrbach, D. Guadagnoli, and G. Isidori, “On the standard model prediction for $\mathcal{B}(B_{s,d} \rightarrow \mu^+ \mu^-)$ ”, *Eur. Phys. J. C* **72** (2012) 2172, doi:10.1140/epjc/s10052-012-2172-1, arXiv:1208.0934.
- [45] M. Misiak et al., “Updated next-to-next-to-leading-order QCD predictions for the weak radiative B-meson decays”, *Phys. Rev. Lett.* **114** (2015) 221801, doi:10.1103/PhysRevLett.114.221801, arXiv:1503.01789.
- [46] M. Czakon et al., “The $(Q_7, Q_{1,2})$ contribution to $\bar{B} \rightarrow X_s \gamma$ at $\mathcal{O}(\alpha_s^2)$ ”, *JHEP* **04** (2015) 168, doi:10.1007/JHEP04(2015)168, arXiv:1503.01791.
- [47] CMS Collaboration, “Measurement of the $t\bar{t}$ production cross section and the top quark mass in the dilepton channel in pp collisions at $\sqrt{s} = 7$ TeV”, *JHEP* **07** (2011) 049, doi:10.1007/JHEP07(2011)049, arXiv:1105.5661.
- [48] CMS Collaboration, “Measurement of the top-quark mass in $t\bar{t}$ events with lepton+jets final states in pp collisions at $\sqrt{s} = 7$ TeV”, *JHEP* **12** (2012) 105, doi:10.1007/JHEP12(2012)105, arXiv:1209.2319.
- [49] CMS Collaboration, “Measurement of the top-quark mass in $t\bar{t}$ events with dilepton final states in pp collisions at $\sqrt{s} = 7$ TeV”, *Eur. Phys. J. C* **72** (2012) 2202, doi:10.1140/epjc/s10052-012-2202-z, arXiv:1209.2393.
- [50] CMS Collaboration, “Measurement of masses in the $t\bar{t}$ system by kinematic endpoints in pp collisions at $\sqrt{s} = 7$ TeV”, *Eur. Phys. J. C* **73** (2013) 2494, doi:10.1140/epjc/s10052-013-2494-7, arXiv:1304.5783.
- [51] CMS Collaboration, “Measurement of the top-quark mass in all-jets $t\bar{t}$ events in pp collisions at $\sqrt{s} = 7$ TeV”, *Eur. Phys. J. C* **74** (2014) 2758, doi:10.1140/epjc/s10052-014-2758-x, arXiv:1307.4617.

- [52] CMS Collaboration, “Determination of the top-quark pole mass and strong coupling constant from the $t\bar{t}$ production in pp collisions at $\sqrt{s} = 7$ TeV”, *Phys. Lett. B* **728** (2014) 496, doi:10.1016/j.physletb.2013.12.009, arXiv:1307.1907.
[Corrigendum: doi:10.1016/j.physletb.2014.08.040].
- [53] CMS Collaboration, “Measurement of the top quark mass using proton-proton data at $\sqrt{s} = 7$ and 8 TeV”, *Phys. Rev. D* **93** (2016) 072004, doi:10.1103/PhysRevD.93.072004, arXiv:1509.04044.
- [54] CMS Collaboration, “Measurement of the $t\bar{t}$ production cross section in the $e\mu$ channel in proton-proton collisions at $\sqrt{s} = 7$ and 8 TeV”, *JHEP* **08** (2016) 029, doi:10.1007/JHEP08(2016)029, arXiv:1603.02303.
- [55] CMS Collaboration, “Measurement of the top quark mass using charged particles in pp collisions at $\sqrt{s} = 8$ TeV”, *Phys. Rev. D* **93** (2016) 092006, doi:10.1103/PhysRevD.93.092006, arXiv:1603.06536.
- [56] CMS Collaboration, “Measurement of the mass of the top quark in decays with a J/ψ meson in pp collisions at 8 TeV”, *JHEP* **12** (2016) 123, doi:10.1007/JHEP12(2016)123, arXiv:1608.03560.
- [57] CMS Collaboration, “Measurement of the $t\bar{t}$ production cross section using events with one lepton and at least one jet in pp collisions at $\sqrt{s} = 13$ TeV”, *JHEP* **09** (2017) 051, doi:10.1007/JHEP09(2017)051, arXiv:1701.06228.
- [58] CMS Collaboration, “Measurement of the top quark mass using single top quark events in proton-proton collisions at $\sqrt{s} = 8$ TeV”, *Eur. Phys. J. C* **77** (2017) 354, doi:10.1140/epjc/s10052-017-4912-8, arXiv:1703.02530.
- [59] CMS Collaboration, “Measurement of the jet mass in highly boosted $t\bar{t}$ events from pp collisions at $\sqrt{s} = 8$ TeV”, *Eur. Phys. J. C* **77** (2017) 467, doi:10.1140/epjc/s10052-017-5030-3, arXiv:1703.06330.
- [60] CMS Collaboration, “Measurement of the top quark mass in the dileptonic $t\bar{t}$ decay channel using the mass observables $M_{b\ell}$, M_{T2} , and $m_{b\ell\nu}$ in pp collisions at $\sqrt{s} = 8$ TeV”, *Phys. Rev. D* **96** (2017) 032002, doi:10.1103/PhysRevD.96.032002, arXiv:1704.06142.
- [61] CMS Collaboration, “Measurement of the top quark mass with lepton+jets final states using pp collisions at $\sqrt{s} = 13$ TeV”, *Eur. Phys. J. C* **78** (2018) 891, doi:10.1140/epjc/s10052-018-6332-9, arXiv:1805.01428.
- [62] CMS Collaboration, “Measurement of the top quark mass in the all-jets final state at $\sqrt{s} = 13$ TeV and combination with the lepton+jets channel”, *Eur. Phys. J. C* **79** (2019) 313, doi:10.1140/epjc/s10052-019-6788-2, arXiv:1812.10534.
- [63] CMS Collaboration, “Measurement of the $t\bar{t}$ production cross section, the top quark mass, and the strong coupling constant using dilepton events in pp collisions at $\sqrt{s} = 13$ TeV”, *Eur. Phys. J. C* **79** (2019) 368, doi:10.1140/epjc/s10052-019-6863-8, arXiv:1812.10505.
- [64] CMS Collaboration, “Measurement of $t\bar{t}$ normalised multi-differential cross sections in pp collisions at $\sqrt{s} = 13$ TeV, and simultaneous determination of the strong coupling strength, top quark pole mass, and parton distribution functions”, *Eur. Phys. J. C* **80** (2020) 658, doi:10.1140/epjc/s10052-020-7917-7, arXiv:1904.05237.

- [65] CMS Collaboration, “Running of the top quark mass from proton-proton collisions at $\sqrt{s} = 13$ TeV”, *Phys. Lett. B* **803** (2020) 135263, doi:10.1016/j.physletb.2020.135263, arXiv:1909.09193.
- [66] CMS Collaboration, “Measurement of the jet mass distribution and top quark mass in hadronic decays of boosted top quarks in pp collisions at $\sqrt{s} = 13$ TeV”, *Phys. Rev. Lett.* **124** (2020) 202001, doi:10.1103/PhysRevLett.124.202001, arXiv:1911.03800.
- [67] CMS Collaboration, “Measurement of the top quark mass using events with a single reconstructed top quark in pp collisions at $\sqrt{s} = 13$ TeV”, *JHEP* **12** (2021) 161, doi:10.1007/JHEP12(2021)161, arXiv:2108.10407.
- [68] ATLAS and CMS Collaborations, “Combination of inclusive top-quark pair production cross-section measurements using ATLAS and CMS data at $\sqrt{s} = 7$ and 8 TeV”, *JHEP* **07** (2023) 213, doi:10.1007/JHEP07(2023)213, arXiv:2205.13830.
- [69] CMS Collaboration, “Measurement of the top quark pole mass using $t\bar{t}$ +jet events in the dilepton final state in proton-proton collisions at $\sqrt{s} = 13$ TeV”, *JHEP* **07** (2023) 077, doi:10.1007/JHEP07(2023)077, arXiv:2207.02270.
- [70] CMS Collaboration, “Measurement of the differential $t\bar{t}$ production cross section as a function of the jet mass and extraction of the top quark mass in hadronic decays of boosted top quarks”, *Eur. Phys. J. C* **83** (2023) 560, doi:10.1140/epjc/s10052-023-11587-8, arXiv:2211.01456.
- [71] CMS Collaboration, “Measurement of the top quark mass using a profile likelihood approach with the lepton+jets final states in proton-proton collisions at $\sqrt{s} = 13$ TeV”, *Eur. Phys. J. C* **83** (2023) 963, doi:10.1140/epjc/s10052-023-12050-4, arXiv:2302.01967.
- [72] ATLAS and CMS Collaborations, “Combination of measurements of the top quark mass from data collected by the ATLAS and CMS experiments at $\sqrt{s} = 7$ and 8 TeV”, 2024. arXiv:2402.08713. Submitted to *Phys. Rev. Lett.*
- [73] CMS Collaboration, “CMS physics technical design report, volume I: Detector performance and software”, CMS Technical Proposal CERN-LHCC-2006-001, CMS-TDR-8.1, 2006.
- [74] N. Kidonakis, “NNNLO soft-gluon corrections for the top-quark p_T and rapidity distributions”, *Phys. Rev. D* **91** (2015) 031501, doi:10.1103/PhysRevD.91.031501, arXiv:1411.2633.
- [75] N. Kidonakis, “Top-quark double-differential distributions at approximate N³LO”, *Phys. Rev. D* **101** (2020) 074006, doi:10.1103/PhysRevD.101.074006, arXiv:1912.10362.
- [76] M. Czakon, D. Heymes, and A. Mitov, “High-precision differential predictions for top-quark pairs at the LHC”, *Phys. Rev. Lett.* **116** (2016) 082003, doi:10.1103/PhysRevLett.116.082003, arXiv:1511.00549.
- [77] M. Czakon and A. Mitov, “TOP++: a program for the calculation of the top-pair cross-section at hadron colliders”, *Comput. Phys. Commun.* **185** (2014) 2930, doi:10.1016/j.cpc.2014.06.021, arXiv:1112.5675.

- [78] M. Czakon et al., “Top-pair production at the LHC through NNLO QCD and NLO EW”, *JHEP* **10** (2017) 186, doi:10.1007/JHEP10(2017)186, arXiv:1705.04105.
- [79] M. Czakon et al., “Resummation for (boosted) top-quark pair production at NNLO+NNLL’ in QCD”, *JHEP* **05** (2018) 149, doi:10.1007/JHEP05(2018)149, arXiv:1803.07623.
- [80] S. Catani et al., “Top-quark pair production at the LHC: fully differential QCD predictions at NNLO”, *JHEP* **07** (2019) 100, doi:10.1007/JHEP07(2019)100, arXiv:1906.06535.
- [81] M. Czakon, A. Mitov, and R. Poncelet, “NNLO QCD corrections to leptonic observables in top-quark pair production and decay”, *JHEP* **05** (2021) 212, doi:10.1007/JHEP05(2021)212, arXiv:2008.11133.
- [82] CMS Collaboration, “First measurement of the top quark pair production cross section in proton-proton collisions at $\sqrt{s} = 13.6$ TeV”, *JHEP* **08** (2023) 204, doi:10.1007/JHEP08(2023)204, arXiv:2303.10680.
- [83] S. Cortese and R. Petronzio, “The single top production channel at Tevatron energies”, *Phys. Lett. B* **253** (1991) 494, doi:10.1016/0370-2693(91)91758-N.
- [84] S. S. D. Willenbrock and D. A. Dicus, “Production of heavy quarks from W-gluon fusion”, *Phys. Rev. D* **34** (1986) 155, doi:10.1103/PhysRevD.34.155.
- [85] J. Campbell, T. Neumann, and Z. Sullivan, “Single-top-quark production in the t -channel at NNLO”, *JHEP* **02** (2021) 040, doi:10.1007/JHEP02(2021)040, arXiv:2012.01574.
- [86] M. Brucherseifer, F. Caola, and K. Melnikov, “On the NNLO QCD corrections to single-top production at the LHC”, *Phys. Lett. B* **736** (2014) 58, doi:10.1016/j.physletb.2014.06.075, arXiv:1404.7116.
- [87] E. L. Berger, J. Gao, and H. X. Zhu, “Differential distributions for t -channel single top-quark production and decay at next-to-next-to-leading order in QCD”, *JHEP* **11** (2017) 158, doi:10.1007/JHEP11(2017)158, arXiv:1708.09405.
- [88] N. Kidonakis, “Next-to-next-to-leading logarithm resummation for s -channel single top quark production”, *Phys. Rev. D* **81** (2010) 054028, doi:10.1103/PhysRevD.81.054028, arXiv:1001.5034.
- [89] N. Kidonakis, “Two-loop soft anomalous dimensions for single top quark associated production with a W^- or H^- ”, *Phys. Rev. D* **82** (2010) 054018, doi:10.1103/PhysRevD.82.054018, arXiv:1005.4451.
- [90] M. Jezabek and J. H. Kühn, “QCD corrections to semileptonic decays of heavy quarks”, *Nucl. Phys. B* **314** (1989) 1, doi:10.1016/0550-3213(89)90108-9.
- [91] I. Bigi et al., “Production and decay properties of ultra-heavy quarks”, *Phys. Lett. B* **181** (1986) 157, doi:10.1016/0370-2693(86)91275-X.
- [92] CMS Collaboration, “The CMS experiment at the CERN LHC”, *JINST* **3** (2008) S08004, doi:10.1088/1748-0221/3/08/S08004.

-
- [93] CMS Collaboration, “Particle-flow reconstruction and global event description with the CMS detector”, *JINST* **12** (2017) P10003, doi:10.1088/1748-0221/12/10/P10003, arXiv:1706.04965.
- [94] CMS Collaboration, “Technical proposal for the Phase-II upgrade of the Compact Muon Solenoid”, CMS Technical Proposal CERN-LHCC-2015-010, CMS-TDR-15-02, 2015.
- [95] CMS Collaboration, “Pileup removal algorithms”, CMS Physics Analysis Summary CMS-PAS-JME-14-001, 2014.
- [96] CMS Collaboration, “Pileup mitigation at CMS in 13 TeV data”, *JINST* **15** (2020) P09018, doi:10.1088/1748-0221/15/09/P09018, arXiv:2003.00503.
- [97] D. Bertolini, P. Harris, M. Low, and N. Tran, “Pileup per particle identification”, *JHEP* **10** (2014) 059, doi:10.1007/JHEP10(2014)059, arXiv:1407.6013.
- [98] M. Cacciari, G. P. Salam, and G. Soyez, “The anti- k_T jet clustering algorithm”, *JHEP* **04** (2008) 063, doi:10.1088/1126-6708/2008/04/063, arXiv:0802.1189.
- [99] M. Cacciari, G. P. Salam, and G. Soyez, “FASTJET user manual”, *Eur. Phys. J. C* **72** (2012) 1896, doi:10.1140/epjc/s10052-012-1896-2, arXiv:1111.6097.
- [100] CMS Collaboration, “Performance of missing transverse momentum reconstruction in proton-proton collisions at $\sqrt{s} = 13$ TeV using the CMS detector”, *JINST* **14** (2019) P07004, doi:10.1088/1748-0221/14/07/P07004, arXiv:1903.06078.
- [101] CMS Collaboration, “Jet energy scale and resolution in the CMS experiment in pp collisions at 8 TeV”, *JINST* **12** (2017) P02014, doi:10.1088/1748-0221/12/02/P02014, arXiv:1607.03663.
- [102] CMS Collaboration, “Identification of heavy-flavour jets with the CMS detector in pp collisions at 13 TeV”, *JINST* **13** (2018) P05011, doi:10.1088/1748-0221/13/05/P05011, arXiv:1712.07158.
- [103] D0 Collaboration, “Direct measurement of the top quark mass at D0”, *Phys. Rev. D* **58** (1998) 052001, doi:10.1103/PhysRevD.58.052001, arXiv:hep-ex/9801025.
- [104] J. D’Hondt et al., “Fitting of event topologies with external kinematic constraints in CMS”, CMS Note CMS-NOTE-2006-023, 2006.
- [105] L. Sonnenschein, “Analytical solution of $t\bar{t}$ dilepton equations”, *Phys. Rev. D* **73** (2006) 054015, doi:10.1103/PhysRevD.73.054015, arXiv:hep-ph/0603011. [Erratum: doi:10.1103/PhysRevD.78.079902].
- [106] S. Frixione, G. Ridolfi, and P. Nason, “A positive-weight next-to-leading-order Monte Carlo for heavy flavour hadroproduction”, *JHEP* **09** (2007) 126, doi:10.1088/1126-6708/2007/09/126, arXiv:0707.3088.
- [107] P. Nason, “A new method for combining NLO QCD with shower Monte Carlo algorithms”, *JHEP* **11** (2004) 040, doi:10.1088/1126-6708/2004/11/040, arXiv:hep-ph/0409146.
- [108] S. Alioli, P. Nason, C. Oleari, and E. Re, “A general framework for implementing NLO calculations in shower Monte Carlo programs: the POWHEG BOX”, *JHEP* **06** (2010) 043, doi:10.1007/JHEP06(2010)043, arXiv:1002.2581.

- [109] S. Frixione, P. Nason, and C. Oleari, “Matching NLO QCD computations with parton shower simulations: the POWHEG method”, *JHEP* **11** (2007) 070, doi:10.1088/1126-6708/2007/11/070, arXiv:0709.2092.
- [110] T. Sjöstrand et al., “An introduction to PYTHIA 8.2”, *Comput. Phys. Commun.* **191** (2015) 159, doi:10.1016/j.cpc.2015.01.024, arXiv:1410.3012.
- [111] J. Alwall et al., “MADGRAPH5: going beyond”, *JHEP* **06** (2011) 128, doi:10.1007/JHEP06(2011)128, arXiv:1106.0522.
- [112] GEANT4 Collaboration, “GEANT4—a simulation toolkit”, *Nucl. Instrum. Meth. A* **506** (2003) 250, doi:10.1016/S0168-9002(03)01368-8.
- [113] Particle Data Group, W. M. Yao et al., “Review of particle physics”, *J. Phys. G.* **33** (2006) 1, doi:10.1088/0954-3899/33/1/001.
- [114] P. Artoisenet, R. Frederix, O. Mattelaer, and R. Rietkerk, “Automatic spin-entangled decays of heavy resonances in Monte Carlo simulations”, *JHEP* **03** (2013) 015, doi:10.1007/JHEP03(2013)015, arXiv:1212.3460.
- [115] T. Sjöstrand, S. Mrenna, and P. Z. Skands, “PYTHIA 6.4 physics and manual”, *JHEP* **05** (2006) 026, doi:10.1088/1126-6708/2006/05/026, arXiv:hep-ph/0603175.
- [116] CMS Collaboration, “Measurement of the underlying event activity at the LHC with $\sqrt{s} = 7$ TeV and comparison with $\sqrt{s} = 0.9$ TeV”, *JHEP* **09** (2011) 109, doi:10.1007/JHEP09(2011)109, arXiv:1107.0330.
- [117] CMS Collaboration, “Event generator tunes obtained from underlying event and multiparton scattering measurements”, *Eur. Phys. J. C* **76** (2016) 155, doi:10.1140/epjc/s10052-016-3988-x, arXiv:1512.00815.
- [118] A. Buckley et al., “Systematic event generator tuning for the LHC”, *Eur. Phys. J. C* **65** (2010) 331, doi:10.1140/epjc/s10052-009-1196-7, arXiv:0907.2973.
- [119] CMS Collaboration, “Investigations of the impact of the parton shower tuning in PYTHIA 8 in the modelling of $t\bar{t}$ at $\sqrt{s} = 8$ and 13 TeV”, CMS Physics Analysis Summary CMS-PAS-TOP-16-021, 2016.
- [120] CMS Collaboration, “Extraction and validation of a new set of CMS PYTHIA 8 tunes from underlying-event measurements”, *Eur. Phys. J. C* **80** (2020) 4, doi:10.1140/epjc/s10052-019-7499-4, arXiv:1903.12179.
- [121] W. Giele et al., “The QCD/SM working group: Summary report”, in *Proc. 2nd Les Houches Workshop on Physics at TeV Colliders (PhysTeV 2001): Les Houches, France, May 21–June 01, 2001*, p. 275. 2002. arXiv:hep-ph/0204316.
- [122] M. R. Whalley, D. Bourilkov, and R. C. Group, “The Les Houches accord PDFs (LHAPDF) and LHAGLUE”, in *Proc. HERA and the LHC: A Workshop on the Implications of HERA and LHC Physics: Meyrin, Switzerland, March 26–27 and October 11–13, 2004*, p. 575. 2005. arXiv:hep-ph/0508110.
- [123] D. Bourilkov, R. C. Group, and M. R. Whalley, “LHAPDF: PDF use from the Tevatron to the LHC”, in *Proc. TeV4LHC Workshop, 4th Meeting: Batavia IL, USA, October 20–22, 2005*. 2006. arXiv:hep-ph/0605240.

- [124] H.-L. Lai et al., “New parton distributions for collider physics”, *Phys. Rev. D* **82** (2010) 074024, doi:10.1103/PhysRevD.82.074024, arXiv:1007.2241.
- [125] A. D. Martin, W. J. Stirling, R. S. Thorne, and G. Watt, “Parton distributions for the LHC”, *Eur. Phys. J. C* **63** (2009) 189, doi:10.1140/epjc/s10052-009-1072-5, arXiv:0901.0002.
- [126] NNPDF Collaboration, “Parton distributions with LHC data”, *Nucl. Phys. B* **867** (2013) 244, doi:10.1016/j.nuclphysb.2012.10.003, arXiv:1207.1303.
- [127] NNPDF Collaboration, “Parton distributions for the LHC run II”, *JHEP* **04** (2015) 040, doi:10.1007/JHEP04(2015)040, arXiv:1410.8849.
- [128] S. Dulat et al., “New parton distribution functions from a global analysis of quantum chromodynamics”, *Phys. Rev. D* **93** (2016) 033006, doi:10.1103/PhysRevD.93.033006, arXiv:1506.07443.
- [129] L. A. Harland-Lang, A. D. Martin, P. Motylinski, and R. S. Thorne, “Parton distributions in the LHC era: MMHT 2014 PDFs”, *Eur. Phys. J. C* **75** (2015) 204, doi:10.1140/epjc/s10052-015-3397-6, arXiv:1412.3989.
- [130] M. Cacciari et al., “The $t\bar{t}$ cross-section at 1.8 and 1.96 TeV: a study of the systematics due to parton densities and scale dependence”, *JHEP* **04** (2004) 068, doi:10.1088/1126-6708/2004/04/068, arXiv:hep-ph/0303085.
- [131] J. Alwall et al., “Comparative study of various algorithms for the merging of parton showers and matrix elements in hadronic collisions”, *Eur. Phys. J. C* **53** (2008) 473, doi:10.1140/epjc/s10052-007-0490-5, arXiv:0706.2569.
- [132] CMS Collaboration, “Measurement of $t\bar{t}$ production with additional jet activity, including b quark jets, in the dilepton decay channel using pp collisions at $\sqrt{s} = 8$ TeV”, *Eur. Phys. J. C* **76** (2016) 379, doi:10.1140/epjc/s10052-016-4105-x, arXiv:1510.03072.
- [133] S. Mrenna and P. Skands, “Automated parton-shower variations in PYTHIA 8”, *Phys. Rev. D* **94** (2016) 074005, doi:10.1103/PhysRevD.94.074005, arXiv:1605.08352.
- [134] CMS Collaboration, “Measurements of differential cross sections of top quark pair production as a function of kinematic event variables in proton-proton collisions at $\sqrt{s} = 13$ TeV”, *JHEP* **06** (2018) 002, doi:10.1007/JHEP06(2018)002, arXiv:1803.03991.
- [135] CMS Collaboration, “Measurement of jet substructure observables in $t\bar{t}$ events from proton-proton collisions at $\sqrt{s} = 13$ TeV”, *Phys. Rev. D* **98** (2018) 092014, doi:10.1103/PhysRevD.98.092014, arXiv:1808.07340.
- [136] R. Frederix and S. Frixione, “Merging meets matching in MC@NLO”, *JHEP* **12** (2012) 061, doi:10.1007/JHEP12(2012)061, arXiv:1209.6215.
- [137] S. Frixione, S. Amoroso, and S. Mrenna, “Matrix element corrections in the PYTHIA 8 parton shower in the context of matched simulations at next-to-leading order”, *Eur. Phys. J. C* **83** (2023) 970, doi:10.1140/epjc/s10052-023-12154-x, arXiv:2308.06389.

- [138] CMS Collaboration, “Measurement of differential cross sections for top quark pair production using the lepton+jets final state in proton-proton collisions at 13 TeV”, *Phys. Rev. D* **95** (2017) 092001, doi:10.1103/PhysRevD.95.092001, arXiv:1610.04191.
- [139] CMS Collaboration, “Measurement of differential cross sections for the production of top quark pairs and of additional jets in lepton+jets events from pp collisions at $\sqrt{s} = 13$ TeV”, *Phys. Rev. D* **97** (2018) 112003, doi:10.1103/PhysRevD.97.112003, arXiv:1803.08856.
- [140] P. Z. Skands, “Tuning Monte Carlo generators: The Perugia tunes”, *Phys. Rev. D* **82** (2010) 074018, doi:10.1103/PhysRevD.82.074018, arXiv:1005.3457.
- [141] NNPDF Collaboration, “Parton distributions from high-precision collider data”, *Eur. Phys. J. C* **77** (2017) 663, doi:10.1140/epjc/s10052-017-5199-5, arXiv:1706.00428.
- [142] CMS Collaboration, “Pseudorapidity distribution of charged hadrons in proton-proton collisions at $\sqrt{s} = 13$ TeV”, *Phys. Lett. B* **751** (2015) 143, doi:10.1016/j.physletb.2015.10.004, arXiv:1507.05915.
- [143] CMS Collaboration, “Underlying event measurements with leading particles and jets in pp collisions at $\sqrt{s} = 13$ TeV”, CMS Physics Analysis Summary CMS-PAS-FSQ-15-007, 2015.
- [144] CMS Collaboration, “Study of the underlying event in top quark pair production in pp collisions at 13 TeV”, *Eur. Phys. J. C* **79** (2019) 123, doi:10.1140/epjc/s10052-019-6620-z, arXiv:1807.02810.
- [145] M. H. Seymour and A. Siódmok, “Constraining MPI models using σ_{eff} and recent Tevatron and LHC underlying event data”, *JHEP* **10** (2013) 113, doi:10.1007/JHEP10(2013)113, arXiv:1307.5015.
- [146] J. Pumplin et al., “New generation of parton distributions with uncertainties from global QCD analysis”, *JHEP* **07** (2002) 012, doi:10.1088/1126-6708/2002/07/012, arXiv:hep-ph/0201195.
- [147] M. Bähr et al., “HERWIG++ physics and manual”, *Eur. Phys. J. C* **58** (2008) 639, doi:10.1140/epjc/s10052-008-0798-9, arXiv:0803.0883.
- [148] J. Bellm et al., “HERWIG 7.0/HERWIG++ 3.0 release note”, *Eur. Phys. J. C* **76** (2016) 196, doi:10.1140/epjc/s10052-016-4018-8, arXiv:1512.01178.
- [149] T. Gleisberg et al., “Event generation with SHERPA 1.1”, *JHEP* **02** (2009) 007, doi:10.1088/1126-6708/2009/02/007, arXiv:0811.4622.
- [150] F. Cascioli, P. Maierhöfer, and S. Pozzorini, “Scattering amplitudes with open loops”, *Phys. Rev. Lett.* **108** (2012) 111601, doi:10.1103/PhysRevLett.108.111601, arXiv:1111.5206.
- [151] S. Schumann and F. Krauss, “A parton shower algorithm based on Catani–Seymour dipole factorisation”, *JHEP* **03** (2008) 038, doi:10.1088/1126-6708/2008/03/038, arXiv:0709.1027.

- [152] CMS Collaboration, “CMS PYTHIA 8 colour reconnection tunes based on underlying-event data”, *Eur. Phys. J. C* **83** (2023) 587, doi:10.1140/epjc/s10052-023-11630-8, arXiv:2205.02905.
- [153] S. Argyropoulos and T. Sjöstrand, “Effects of color reconnection on $t\bar{t}$ final states at the LHC”, *JHEP* **11** (2014) 043, doi:10.1007/JHEP11(2014)043, arXiv:1407.6653.
- [154] ATLAS Collaboration, “Measurement of colour flow with the jet pull angle in $t\bar{t}$ events using the ATLAS detector at $\sqrt{s} = 8$ TeV”, *Phys. Lett. B* **750** (2015) 475, doi:10.1016/j.physletb.2015.09.051, arXiv:1506.05629.
- [155] M. G. Bowler, “ e^+e^- production of heavy quarks in the string model”, *Z. Phys. C* **11** (1981) 169, doi:10.1007/BF01574001.
- [156] ALEPH Collaboration, “Study of the fragmentation of b quarks into B mesons at the Z peak”, *Phys. Lett. B* **512** (2001) 30, doi:10.1016/S0370-2693(01)00690-6, arXiv:hep-ex/0106051.
- [157] DELPHI Collaboration, “A study of the b-quark fragmentation function with the DELPHI detector at LEP I and an averaged distribution obtained at the Z pole”, *Eur. Phys. J. C* **71** (2011) 1557, doi:10.1140/epjc/s10052-011-1557-x, arXiv:1102.4748.
- [158] OPAL Collaboration, “Inclusive analysis of the b quark fragmentation function in Z decays at LEP”, *Eur. Phys. J. C* **29** (2003) 463, doi:10.1140/epjc/s2003-01229-x, arXiv:hep-ex/0210031.
- [159] SLD Collaboration, “Measurement of the b-quark fragmentation function in Z^0 decays”, *Phys. Rev. D* **65** (2002) 092006, doi:10.1103/PhysRevD.65.092006, arXiv:hep-ex/0202031. [Erratum: doi:10.1103/PhysRevD.66.079905].
- [160] C. Peterson, D. Schlatter, I. Schmitt, and P. M. Zerwas, “Scaling violations in inclusive e^+e^- annihilation spectra”, *Phys. Rev. D* **27** (1983) 105, doi:10.1103/PhysRevD.27.105.
- [161] CMS Collaboration, “Performance of the CMS missing transverse momentum reconstruction in pp data at $\sqrt{s} = 8$ TeV”, *JINST* **10** (2015) P02006, doi:10.1088/1748-0221/10/02/P02006, arXiv:1411.0511.
- [162] CMS Collaboration, “Electron and photon reconstruction and identification with the CMS experiment at the CERN LHC”, *JINST* **16** (2021) P05014, doi:10.1088/1748-0221/16/05/P05014, arXiv:2012.06888.
- [163] CMS Collaboration, “Performance of the CMS muon detector and muon reconstruction with proton-proton collisions at $\sqrt{s} = 13$ TeV”, *JINST* **13** (2018) P06015, doi:10.1088/1748-0221/13/06/P06015, arXiv:1804.04528.
- [164] CMS Collaboration, “The CMS trigger system”, *JINST* **12** (2017) P01020, doi:10.1088/1748-0221/12/01/P01020, arXiv:1609.02366.
- [165] CMS Collaboration, “Absolute calibration of the luminosity measurement at CMS: Winter 2012 update”, CMS Physics Analysis Summary CMS-PAS-SMP-12-008, 2012.
- [166] CMS Collaboration, “CMS luminosity based on pixel cluster counting—Summer 2013 update”, CMS Physics Analysis Summary CMS-PAS-LUM-13-001, 2013.

- [167] CMS Collaboration, “Precision luminosity measurement in proton-proton collisions at $\sqrt{s} = 13$ TeV in 2015 and 2016 at CMS”, *Eur. Phys. J. C* **81** (2021) 800, doi:10.1140/epjc/s10052-021-09538-2, arXiv:2104.01927.
- [168] CMS Collaboration, “CMS luminosity measurement for the 2017 data-taking period at $\sqrt{s} = 13$ TeV”, CMS Physics Analysis Summary CMS-PAS-LUM-17-004, 2018.
- [169] CMS Collaboration, “CMS luminosity measurement for the 2018 data-taking period at $\sqrt{s} = 13$ TeV”, CMS Physics Analysis Summary CMS-PAS-LUM-18-002, 2019.
- [170] S. Schmitt, “TUNFOLD, an algorithm for correcting migration effects in high energy physics”, *JINST* **7** (2012) T10003, doi:10.1088/1748-0221/7/10/T10003, arXiv:1205.6201.
- [171] S. Schmitt, “Data unfolding methods in high energy physics”, in *Proc. 12th Conference on Quark Confinement and the Hadron Spectrum (Confinement XII): Thessaloniki, Greece, August 28–September 04, 2016*. 2017. arXiv:1611.01927. [EPJ Web Conf. 137 (2017) 11008]. doi:10.1051/epjconf/201713711008.
- [172] G. D’Agostini, “A multidimensional unfolding method based on Bayes’ theorem”, *Nucl. Instrum. Meth. A* **362** (1995) 487, doi:10.1016/0168-9002(95)00274-X.
- [173] G. D’Agostini, “Improved iterative Bayesian unfolding”, in *Proc. Alliance Workshop on Unfolding and Data Correction: Hamburg, Germany, May 27–28, 2010*. 2010. arXiv:1010.0632.
- [174] A. Höcker and V. Kartvelishvili, “SVD approach to data unfolding”, *Nucl. Instrum. Meth. A* **372** (1996) 469, doi:10.1016/0168-9002(95)01478-0, arXiv:hep-ph/9509307.
- [175] A. N. Tikhonov, “On the solution of ill-posed problems and the method of regularization”, *Dokl. Akad. Nauk SSSR* **151** (1963) 3.
- [176] L. Brenner et al., “Comparison of unfolding methods using ROOFITUNFOLD”, *Int. J. Mod. Phys. A* **35** (2020) 2050145, doi:10.1142/S0217751X20501456, arXiv:1910.14654.
- [177] M. Stanley, P. Patil, and M. Kuusela, “Uncertainty quantification for wide-bin unfolding: one-at-a-time strict bounds and prior-optimized confidence intervals”, *JINST* **17** (2022) P10013, doi:10.1088/1748-0221/17/10/P10013, arXiv:2111.01091.
- [178] CMS Collaboration, “Object definitions for top quark analyses at the particle level”, CMS Note CMS-NOTE-2017-004, 2017.
- [179] A. Buckley et al., “RIVET user manual”, *Comput. Phys. Commun.* **184** (2013) 2803, doi:10.1016/j.cpc.2013.05.021, arXiv:1003.0694.
- [180] C. Bierlich et al., “Robust independent validation of experiment and theory: RIVET version 3”, *SciPost Phys.* **8** (2020) 026, doi:10.21468/SciPostPhys.8.2.026, arXiv:1912.05451.
- [181] F. Herren and M. Steinhauser, “Version 3 of RUNDEC and CRUNDEC”, *Comput. Phys. Commun.* **224** (2018) 333, doi:10.1016/j.cpc.2017.11.014, arXiv:1703.03751.

- [182] A. H. Hoang, C. Lepenik, and V. Mateu, “REVOLVER: Automated running and matching of couplings and masses in QCD”, *Comput. Phys. Commun.* **270** (2022) 108145, doi:10.1016/j.cpc.2021.108145, arXiv:2102.01085.
- [183] J. Mazitelli, “NNLO study of top-quark mass renormalization scheme uncertainties in Higgs boson production”, *JHEP* **09** (2022) 065, doi:10.1007/JHEP09(2022)065, arXiv:2206.14667.
- [184] A. H. Hoang et al., “The MSR mass and the $\mathcal{O}(\Lambda_{\text{QCD}})$ renormalon sum rule”, *JHEP* **04** (2018) 003, doi:10.1007/JHEP04(2018)003, arXiv:1704.01580.
- [185] R. Tarrach, “The pole mass in perturbative QCD”, *Nucl. Phys. B* **183** (1981) 384, doi:10.1016/0550-3213(81)90140-1.
- [186] A. S. Kronfeld, “Perturbative pole mass in QCD”, *Phys. Rev. D* **58** (1998) 051501, doi:10.1103/PhysRevD.58.051501, arXiv:hep-ph/9805215.
- [187] M. Beneke, P. Marquard, P. Nason, and M. Steinhauser, “On the ultimate uncertainty of the top quark pole mass”, *Phys. Lett. B* **775** (2017) 63, doi:10.1016/j.physletb.2017.10.054, arXiv:1605.03609.
- [188] A. H. Hoang, C. Lepenik, and M. Preisser, “On the light massive flavor dependence of the large order asymptotic behavior and the ambiguity of the pole mass”, *JHEP* **09** (2017) 099, doi:10.1007/JHEP09(2017)099, arXiv:1706.08526.
- [189] A. H. Hoang, S. Mantry, A. Pathak, and I. W. Stewart, “Extracting a short distance top mass with light grooming”, *Phys. Rev. D* **100** (2019) 074021, doi:10.1103/PhysRevD.100.074021, arXiv:1708.02586.
- [190] B. Bachu et al., “Boosted top quarks in the peak region with N³LL resummation”, *Phys. Rev. D* **104** (2021) 014026, doi:10.1103/PhysRevD.104.014026, arXiv:2012.12304.
- [191] A. H. Hoang, S. Plätzer, and D. Samitz, “On the cutoff dependence of the quark mass parameter in angular ordered parton showers”, *JHEP* **10** (2018) 200, doi:10.1007/JHEP10(2018)200, arXiv:1807.06617.
- [192] DELPHI Collaboration, “Measurement of the mass and width of the W boson in e^+e^- collisions at $\sqrt{s} = 161\text{--}209\text{ GeV}$ ”, *Eur. Phys. J. C* **55** (2008) 1, doi:10.1140/epjc/s10052-008-0585-7, arXiv:0803.2534.
- [193] R. Barlow and C. Beeston, “Fitting using finite Monte Carlo samples”, *Comput. Phys. Commun.* **77** (1993) 219, doi:10.1016/0010-4655(93)90005-w.
- [194] J. S. Conway, “Incorporating nuisance parameters in likelihoods for multisource spectra”, in *Proc. 2011 Workshop on Statistical Issues Related to Discovery Claims in Search Experiments and Unfolding (PHYSTAT 2011): Geneva, Switzerland, January 17–20, 2011*. 2011. arXiv:1103.0354. doi:10.5170/CERN-2011-006.115.
- [195] ATLAS Collaboration, “Measurement of the top quark mass in the $t\bar{t} \rightarrow$ dilepton channel from $\sqrt{s} = 8\text{ TeV}$ ”, *Phys. Lett. B* **761** (2016) 350, doi:10.1016/j.physletb.2016.08.042, arXiv:1606.02179.

- [196] ATLAS Collaboration, “Measurement of the top quark mass in the $t\bar{t} \rightarrow$ lepton+jets and $t\bar{t} \rightarrow$ dilepton channels using $\sqrt{s} = 7$ TeV ATLAS data”, *Eur. Phys. J. C* **75** (2015) 330, doi:10.1140/epjc/s10052-015-3544-0, arXiv:1503.05427.
- [197] ATLAS Collaboration, “Measurement of the top quark mass in the $t\bar{t} \rightarrow$ lepton+jets channel from $\sqrt{s} = 8$ TeV ATLAS data and combination with previous results”, *Eur. Phys. J. C* **79** (2019) 290, doi:10.1140/epjc/s10052-019-6757-9, arXiv:1810.01772.
- [198] M. Aliev et al., “HATHOR: Hadronic top and heavy quarks cross section calculator”, *Comput. Phys. Commun.* **182** (2011) 1034, doi:10.1016/j.cpc.2010.12.040, arXiv:1007.1327.
- [199] P. Kant et al., “HATHOR for single top-quark production: Updated predictions and uncertainty estimates for single top-quark production in hadronic collisions”, *Comput. Phys. Commun.* **191** (2015) 74, doi:10.1016/j.cpc.2015.02.001, arXiv:1406.4403.
- [200] CMS Collaboration, “Measurement of the single top quark and antiquark production cross sections in the t channel and their ratio in proton-proton collisions at $\sqrt{s} = 13$ TeV”, *Phys. Lett. B* **800** (2020) 135042, doi:10.1016/j.physletb.2019.135042, arXiv:1812.10514.
- [201] S. Alioli, P. Nason, C. Oleari, and E. Re, “NLO single-top production matched with shower in POWHEG: s - and t -channel contributions”, *JHEP* **09** (2009) 111, doi:10.1088/1126-6708/2009/09/111, arXiv:0907.4076. [Erratum: doi:10.1007/JHEP02(2010)011].
- [202] R. Frederix, E. Re, and P. Torrielli, “Single-top t -channel hadroproduction in the four-flavors scheme with POWHEG and aMC@NLO”, *JHEP* **09** (2012) 130, doi:10.1007/JHEP09(2012)130, arXiv:1207.5391.
- [203] ATLAS Collaboration, “Fiducial, total and differential cross-section measurements of t -channel single top-quark production in pp collisions at 8 TeV using data collected by the ATLAS detector”, *Eur. Phys. J. C* **77** (2017) 531, doi:10.1140/epjc/s10052-017-5061-9, arXiv:1702.02859.
- [204] CMS Collaboration, “Measurement of differential cross sections and charge ratios for t -channel single top quark production in proton-proton collisions at $\sqrt{s} = 13$ TeV”, *Eur. Phys. J. C* **80** (2020) 370, doi:10.1140/epjc/s10052-020-7858-1, arXiv:1907.08330.
- [205] M. J. Oreglia, “A study of the reactions $\psi' \rightarrow \gamma\gamma\psi$ ”. PhD thesis, Stanford University, 1980. SLAC-R-236.
- [206] Belle Collaboration, “A detailed test of the CsI($T\ell$) calorimeter for BELLE with photon beams of energy between 20 MeV and 5.4 GeV”, *Nucl. Instrum. Meth. A* **441** (2000) 401, doi:10.1016/S0168-9002(99)00992-4.
- [207] CMS Collaboration, “Determination of jet energy calibration and transverse momentum resolution in CMS”, *JINST* **6** (2011) P11002, doi:10.1088/1748-0221/6/11/P11002, arXiv:1107.4277.

- [208] O. W. Greenberg, “CPT violation implies violation of Lorentz invariance”, *Phys. Rev. Lett.* **89** (2002) 231602, doi:10.1103/PhysRevLett.89.231602, arXiv:hep-ph/0201258.
- [209] CMS Collaboration, “Measurement of the mass difference between top and antitop quarks”, *JHEP* **06** (2012) 109, doi:10.1007/JHEP06(2012)109, arXiv:1204.2807.
- [210] CMS Collaboration, “Measurement of the mass difference between top quark and antiquark in pp collisions at $\sqrt{s} = 8$ TeV”, *Phys. Lett. B* **770** (2017) 50, doi:10.1016/j.physletb.2017.04.028, arXiv:1610.09551.
- [211] BASE Collaboration, “A 16-parts-per-trillion measurement of the antiproton-to-proton charge-mass ratio”, *Nature* **601** (2022) 53, doi:10.1038/s41586-021-04203-w.
- [212] T. Cheng, M. Lindner, and M. Sen, “Implications of a matter-antimatter mass asymmetry in Penning-trap experiments”, *Phys. Lett. B* **844** (2023) 138068, doi:10.1016/j.physletb.2023.138068, arXiv:2210.10819.
- [213] P. Azzi et al., “Report from working group 1: Standard model physics at the HL-LHC and HE-LHC”, CERN Report CERN-LPCC-2018-03, 2019. doi:10.23731/CYRM-2019-007.1, arXiv:1902.04070.
- [214] A. H. Hoang and I. W. Stewart, “Top mass measurements from jets and the Tevatron top-quark mass”, in *Proc. 2nd International Workshop on Top-Quark Physics (TOP2008): La Biodola, Italy, May 18–24, 2008*. 2008. arXiv:0808.0222. [*Nucl. Phys. B Proc. Suppl.* **185** (2008) 220]. doi:10.1016/j.nuclphysbps.2008.10.028.
- [215] A. H. Hoang, “The top mass: interpretation and theoretical uncertainties”, in *Proc. 7th International Workshop on Top Quark Physics (TOP2014): Cannes, France, September 28–October 03, 2014*. 2014. arXiv:1412.3649.
- [216] R. Baumeister and S. Weinzierl, “Cutoff dependence of the thrust peak position in the dipole shower”, *Eur. Phys. J. C* **80** (2020) 843, doi:10.1140/epjc/s10052-020-8425-5, arXiv:2004.01657.
- [217] S. Makarov, K. Melnikov, P. Nason, and M. A. Ozelik, “Linear power corrections to top quark pair production in hadron collisions”, *JHEP* **01** (2024) 074, doi:10.1007/JHEP01(2024)074, arXiv:2308.05526.
- [218] J. Kieseler, K. Lipka, and S.-O. Moch, “Calibration of the top-quark Monte Carlo mass”, *Phys. Rev. Lett.* **116** (2016) 162001, doi:10.1103/PhysRevLett.116.162001, arXiv:1511.00841.
- [219] M. Butenschoen et al., “Top quark mass calibration for Monte Carlo event generators”, *Phys. Rev. Lett.* **117** (2016) 232001, doi:10.1103/PhysRevLett.117.232001, arXiv:1608.01318.
- [220] S. Fleming, A. H. Hoang, S. Mantry, and I. W. Stewart, “Jets from massive unstable particles: Top-mass determination”, *Phys. Rev. D* **77** (2008) 074010, doi:10.1103/PhysRevD.77.074010, arXiv:hep-ph/0703207.
- [221] S. Fleming, A. H. Hoang, S. Mantry, and I. W. Stewart, “Top jets in the peak region: Factorization analysis with next-to-leading-log resummation”, *Phys. Rev. D* **77** (2008) 114003, doi:10.1103/PhysRevD.77.114003, arXiv:0711.2079.

- [222] ATLAS Collaboration, “Towards a precise interpretation for the top quark mass parameter in ATLAS Monte Carlo samples”, ATLAS PUB Note ATL-PHYS-PUB-2021-034, 2021.
- [223] D. Krohn, J. Thaler, and L.-T. Wang, “Jet trimming”, *JHEP* **02** (2010) 084, doi:10.1007/JHEP02(2010)084, arXiv:0912.1342.
- [224] A. H. Hoang, S. Mantry, A. Pathak, and I. W. Stewart, “Nonperturbative corrections to soft drop jet mass”, *JHEP* **12** (2019) 002, doi:10.1007/JHEP12(2019)002, arXiv:1906.11843.
- [225] B. Dehnadi, A. H. Hoang, O. L. Jin, and V. Mateu, “Top quark mass calibration for Monte Carlo event generators—an update”, *JHEP* **12** (2023) 065, doi:10.1007/JHEP12(2023)065, arXiv:2309.00547.
- [226] D0 Collaboration, “Determination of the pole and \overline{MS} masses of the top quark from the $t\bar{t}$ cross section”, *Phys. Lett. B* **703** (2011) 422, doi:10.1016/j.physletb.2011.08.015, arXiv:1104.2887.
- [227] CMS Collaboration, “Measurement and QCD analysis of double-differential inclusive jet cross sections in proton-proton collisions at $\sqrt{s} = 13$ TeV”, *JHEP* **02** (2022) 142, doi:10.1007/JHEP02(2022)142, arXiv:2111.10431. [Addendum: doi:10.1007/JHEP12(2022)035].
- [228] S. Biswas, K. Melnikov, and M. Schulze, “Next-to-leading order QCD effects and the top quark mass measurements at the LHC”, *JHEP* **08** (2010) 048, doi:10.1007/JHEP08(2010)048, arXiv:1006.0910.
- [229] CMS Collaboration, “Measurement of the $t\bar{t}$ production cross section in the dilepton channel in pp collisions at $\sqrt{s} = 7$ TeV”, *JHEP* **11** (2012) 067, doi:10.1007/JHEP11(2012)067, arXiv:1208.2671.
- [230] K. Melnikov and M. Schulze, “NLO QCD corrections to top quark pair production and decay at hadron colliders”, *JHEP* **08** (2009) 049, doi:10.1088/1126-6708/2009/08/049, arXiv:0907.3090.
- [231] W. Bernreuther and Z.-G. Si, “Distributions and correlations for top quark pair production and decay at the Tevatron and LHC”, *Nucl. Phys. B* **837** (2010) 90, doi:10.1016/j.nuclphysb.2010.05.001, arXiv:1003.3926.
- [232] S. Moch et al., “High precision fundamental constants at the TeV scale”, 2014. arXiv:1405.4781.
- [233] G. Heinrich et al., “NLO QCD corrections to $W^+W^-b\bar{b}$ production with leptonic decays in the light of top quark mass and asymmetry measurements”, *JHEP* **06** (2014) 158, doi:10.1007/JHEP06(2014)158, arXiv:1312.6659.
- [234] M. Dowling and S.-O. Moch, “Differential distributions for top-quark hadro-production with a running mass”, *Eur. Phys. J. C* **74** (2014) 3167, doi:10.1140/epjc/s10052-014-3167-x, arXiv:1305.6422.
- [235] S. Alekhin et al., “HERAFitter: Open source QCD fit project”, *Eur. Phys. J. C* **75** (2015) 304, doi:10.1140/epjc/s10052-015-3480-z, arXiv:1410.4412.

- [236] P. A. Baikov, K. G. Chetyrkin, and J. H. Kühn, “Quark mass and field anomalous dimensions to $\mathcal{O}(\alpha_S^5)$ ”, *JHEP* **10** (2014) 076, doi:10.1007/JHEP10(2014)076, arXiv:1402.6611.
- [237] T. Luthe, A. Maier, P. Marquard, and Y. Schröder, “Five-loop quark mass and field anomalous dimensions for a general gauge group”, *JHEP* **01** (2017) 081, doi:10.1007/JHEP01(2017)081, arXiv:1612.05512.
- [238] L. Mihaila, “Precision calculations in supersymmetric theories”, *Adv. High Energy Phys.* **2013** (2013) 607807, doi:10.1155/2013/607807, arXiv:1310.6178.
- [239] N. D. Christensen and R. Shrock, “Implications of dynamical generation of standard-model fermion masses”, *Phys. Rev. Lett.* **94** (2005) 241801, doi:10.1103/PhysRevLett.94.241801, arXiv:hep-ph/0501294.
- [240] S. Catani et al., “Top-quark pair hadroproduction at NNLO: differential predictions with the $\overline{\text{MS}}$ mass”, *JHEP* **08** (2020) 027, doi:10.1007/JHEP08(2020)027, arXiv:2005.00557.
- [241] M. M. Defranichis, J. Kieseler, K. Lipka, and J. Mazzitelli, “Running of the top quark mass at NNLO in QCD”, 2022. arXiv:2208.11399.
- [242] CMS Collaboration, “Measurement of the inclusive $t\bar{t}$ cross section in pp collisions at $\sqrt{s} = 5.02$ TeV using final states with at least one charged lepton”, *JHEP* **03** (2018) 115, doi:10.1007/JHEP03(2018)115, arXiv:1711.03143.
- [243] H1 and ZEUS Collaborations, “Combination of measurements of inclusive deep inelastic $e^\pm p$ scattering cross sections and QCD analysis of HERA data”, *Eur. Phys. J. C* **75** (2015) 580, doi:10.1140/epjc/s10052-015-3710-4, arXiv:1506.06042.
- [244] CMS Collaboration, “Measurement of the differential cross section and charge asymmetry for inclusive $pp \rightarrow W^\pm + X$ production at $\sqrt{s} = 8$ TeV”, *Eur. Phys. J. C* **76** (2016) 469, doi:10.1140/epjc/s10052-016-4293-4, arXiv:1603.01803.
- [245] M. Guzzi, K. Lipka, and S.-O. Moch, “Top-quark pair production at hadron colliders: differential cross section and phenomenological applications with DIFFTOP”, *JHEP* **01** (2015) 082, doi:10.1007/JHEP01(2015)082, arXiv:1406.0386.
- [246] CMS Collaboration, “Measurement of double-differential cross sections for top quark pair production in pp collisions at $\sqrt{s} = 8$ TeV and impact on parton distribution functions”, *Eur. Phys. J. C* **77** (2017) 459, doi:10.1140/epjc/s10052-017-4984-5, arXiv:1703.01630.
- [247] S. Alioli et al., “A new observable to measure the top-quark mass at hadron colliders”, *Eur. Phys. J. C* **73** (2013) 2438, doi:10.1140/epjc/s10052-013-2438-2, arXiv:1303.6415.
- [248] M. L. Mangano, P. Nason, and G. Ridolfi, “Heavy-quark correlations in hadron collisions at next-to-leading order”, *Nucl. Phys. B* **373** (1992) 295, doi:10.1016/0550-3213(92)90435-E.
- [249] S. Dittmaier, P. Uwer, and S. Weinzierl, “NLO QCD corrections to $t\bar{t} + \text{jet}$ production at hadron colliders”, *Phys. Rev. Lett.* **98** (2007) 262002, doi:10.1103/PhysRevLett.98.262002, arXiv:hep-ph/0703120.

- [250] G. Bevilacqua, M. Czakon, C. G. Papadopoulos, and M. Worek, “Dominant QCD backgrounds in Higgs boson analyses at the LHC: A study of $pp \rightarrow t\bar{t} + 2$ jets at next-to-leading order”, *Phys. Rev. Lett.* **104** (2010) 162002, doi:10.1103/PhysRevLett.104.162002, arXiv:1002.4009.
- [251] G. Bevilacqua, M. Czakon, C. G. Papadopoulos, and M. Worek, “Hadronic top-quark pair production in association with two jets at next-to-leading order QCD”, *Phys. Rev. D* **84** (2011) 114017, doi:10.1103/PhysRevD.84.114017, arXiv:1108.2851.
- [252] Particle Data Group, M. Tanabashi et al., “Review of particle physics”, *Phys. Rev. D* **98** (2018) 030001, doi:10.1103/PhysRevD.98.030001.
- [253] Y. Kiyo et al., “Top-quark pair production near threshold at LHC”, *Eur. Phys. J. C* **60** (2009) 375, doi:10.1140/epjc/s10052-009-0892-7, arXiv:0812.0919.
- [254] J. Piclum and C. Schwinn, “Soft-gluon and Coulomb corrections to hadronic top-quark pair production beyond NNLO”, *JHEP* **03** (2018) 164, doi:10.1007/JHEP03(2018)164, arXiv:1801.05788.
- [255] T. Mäkelä, A. Hoang, K. Lipka, and S.-O. Moch, “Investigation of the scale dependence in the MSR and $\overline{\text{MS}}$ top quark mass schemes for the $t\bar{t}$ invariant mass differential cross section using LHC data”, *JHEP* **09** (2023) 037, doi:10.1007/JHEP09(2023)037, arXiv:2301.03546.
- [256] S. Alioli, S.-O. Moch, and P. Uwer, “Hadronic top-quark pair-production with one jet and parton showering”, *JHEP* **01** (2012) 137, doi:10.1007/JHEP01(2012)137, arXiv:1110.5251.
- [257] S. Alekhin, J. Blümlein, and S. Moch, “NLO PDFs from the ABMP16 fit”, *Eur. Phys. J. C* **78** (2018) 477, doi:10.1140/epjc/s10052-018-5947-1, arXiv:1803.07537.
- [258] T.-J. Hou et al., “Progress in the CTEQ-TEA NNLO global QCD analysis”, 2019. arXiv:1908.11394.
- [259] S. Alioli et al., “Phenomenology of $t\bar{t}j + X$ production at the LHC”, *JHEP* **05** (2022) 146, doi:10.1007/JHEP05(2022)146, arXiv:2202.07975.
- [260] A. Babaev et al., “Impact of beam-beam effects on absolute luminosity calibrations at the CERN Large Hadron Collider”, *Eur. Phys. J. C* **84** (2024) 17, doi:10.1140/epjc/s10052-023-12192-5, arXiv:2306.10394.
- [261] A. H. Hoang et al., “Top-antitop pair production close to threshold: Synopsis of recent NNLO results”, in *Proc. 4th Workshop of the 2nd ECFA/DESY Study on Physics and Detectors for a Linear Electron-Positron Collider: Oxford, UK, March 20–23, 1999*. 2000. arXiv:hep-ph/0001286. [*Eur. Phys. J. direct* **2** (2000) 1]. doi:10.1007/s1010500c0003.
- [262] K. Hagiwara, Y. Sumino, and H. Yokoya, “Bound-state effects on top quark production at hadron colliders”, *Phys. Lett. B* **666** (2008) 71, doi:10.1016/j.physletb.2008.07.006, arXiv:0804.1014.
- [263] W.-L. Ju et al., “Top quark pair production near threshold: single/double distributions and mass determination”, *JHEP* **06** (2020) 158, doi:10.1007/JHEP06(2020)158, arXiv:2004.03088.

- [264] fastNLO Collaboration, D. Britzger, K. Rabbertz, F. Stober, and M. Wobisch, “New features in version 2 of the fastNLO project”, in *Proc. 20th International Workshop on Deep-Inelastic Scattering and Related Subjects (DIS2012): Bonn, Germany, March 26–30, 2012*. 2012. arXiv:1208.3641. doi:10.3204/DESY-PROC-2012-02/165.
- [265] T. Carli et al., “A posteriori inclusion of parton density functions in NLO QCD final-state calculations at hadron colliders: the APPLGRID project”, *Eur. Phys. J. C* **66** (2010) 503, doi:10.1140/epjc/s10052-010-1255-0, arXiv:0911.2985.
- [266] D. Britzger et al., “NNLO interpolation grids for jet production at the LHC”, *Eur. Phys. J. C* **82** (2022) 930, doi:10.1140/epjc/s10052-022-10880-2, arXiv:2207.13735.
- [267] A. L. Kataev and V. S. Molokoedov, “Notes on interplay between the QCD and EW perturbative corrections to the pole-running-to-top-quark mass ratio”, *JETP Lett.* **115** (2022) 704, doi:10.1134/S0021364022600902, arXiv:2201.12073.
- [268] S. Dittmaier and H. Rzehak, “Electroweak renormalization based on gauge-invariant vacuum expectation values of non-linear Higgs representations. Part I. Standard model”, *JHEP* **05** (2022) 125, doi:10.1007/JHEP05(2022)125, arXiv:2203.07236.
- [269] G. P. Salam, “Towards jetography”, *Eur. Phys. J. C* **67** (2010) 637, doi:10.1140/epjc/s10052-010-1314-6, arXiv:0906.1833.
- [270] M. Dasgupta, A. Fregoso, S. Marzani, and G. P. Salam, “Towards an understanding of jet substructure”, *JHEP* **09** (2013) 029, doi:10.1007/JHEP09(2013)029, arXiv:1307.0007.
- [271] R. Kogler, “Advances in jet substructure at the LHC: Algorithms, measurements and searches for new physical phenomena”. Springer Cham, 2021. ISBN 978-3-030-72858-8. doi:10.1007/978-3-030-72858-8.
- [272] A. J. Larkoski, I. Moult, and B. Nachman, “Jet substructure at the Large Hadron Collider: A review of recent advances in theory and machine learning”, *Phys. Rept.* **841** (2020) 1, doi:10.1016/j.physrep.2019.11.001, arXiv:1709.04464.
- [273] R. Kogler et al., “Jet substructure at the Large Hadron Collider”, *Rev. Mod. Phys.* **91** (2019) 045003, doi:10.1103/RevModPhys.91.045003, arXiv:1803.06991.
- [274] CMS Collaboration, “Measurements of the differential jet cross section as a function of the jet mass in dijet events from proton-proton collisions at $\sqrt{s} = 13$ TeV”, *JHEP* **11** (2018) 113, doi:10.1007/JHEP11(2018)113, arXiv:1807.05974.
- [275] C. W. Bauer, S. Fleming, and M. E. Luke, “Summing Sudakov logarithms in $B \rightarrow X_s \gamma$ in effective field theory”, *Phys. Rev. D* **63** (2000) 014006, doi:10.1103/PhysRevD.63.014006, arXiv:hep-ph/0005275.
- [276] C. W. Bauer, S. Fleming, D. Pirjol, and I. W. Stewart, “An effective field theory for collinear and soft gluons: Heavy to light decays”, *Phys. Rev. D* **63** (2001) 114020, doi:10.1103/PhysRevD.63.114020, arXiv:hep-ph/0011336.
- [277] C. W. Bauer and I. W. Stewart, “Invariant operators in collinear effective theory”, *Phys. Lett. B* **516** (2001) 134, doi:10.1016/S0370-2693(01)00902-9, arXiv:hep-ph/0107001.

- [278] C. W. Bauer, D. Pirjol, and I. W. Stewart, “Soft-collinear factorization in effective field theory”, *Phys. Rev. D* **65** (2002) 054022, doi:10.1103/PhysRevD.65.054022, arXiv:hep-ph/0109045.
- [279] C. W. Bauer et al., “Hard scattering factorization from effective field theory”, *Phys. Rev. D* **66** (2002) 014017, doi:10.1103/PhysRevD.66.014017, arXiv:hep-ph/0202088.
- [280] A. J. Larkoski, S. Marzani, G. Soyez, and J. Thaler, “Soft drop”, *JHEP* **05** (2014) 146, doi:10.1007/JHEP05(2014)146, arXiv:1402.2657.
- [281] I. W. Stewart et al., “XCone: N -jettiness as an exclusive cone jet algorithm”, *JHEP* **11** (2015) 072, doi:10.1007/JHEP11(2015)072, arXiv:1508.01516.
- [282] Y. L. Dokshitzer, G. D. Leder, S. Moretti, and B. R. Webber, “Better jet clustering algorithms”, *JHEP* **08** (1997) 001, doi:10.1088/1126-6708/1997/08/001, arXiv:hep-ph/9707323.
- [283] M. Wobisch and T. Wengler, “Hadronization corrections to jet cross sections in deep-inelastic scattering”, in *Proc. Workshop on Monte Carlo Generators for HERA Physics: Hamburg, Germany, April 27–30, 1998*. 1999. arXiv:hep-ph/9907280.
- [284] J. Thaler and T. F. Wilkason, “Resolving boosted jets with XCone”, *JHEP* **12** (2015) 051, doi:10.1007/JHEP12(2015)051, arXiv:1508.01518.
- [285] I. W. Stewart, F. J. Tackmann, and W. J. Waalewijn, “ N jettiness: An inclusive event shape to veto jets”, *Phys. Rev. Lett.* **105** (2010) 092002, doi:10.1103/PhysRevLett.105.092002, arXiv:1004.2489.
- [286] J. Thaler and K. Van Tilburg, “Identifying boosted objects with N -subjettiness”, *JHEP* **03** (2011) 015, doi:10.1007/JHEP03(2011)015, arXiv:1011.2268.
- [287] J. Thaler and K. Van Tilburg, “Maximizing boosted top identification by minimizing N -subjettiness”, *JHEP* **02** (2012) 093, doi:10.1007/JHEP02(2012)093, arXiv:1108.2701.
- [288] G. Apollinari et al., “High-Luminosity Large Hadron Collider (HL-LHC): Preliminary design report”, CERN Technical Proposal CERN-2015-005, 2015. doi:10.5170/CERN-2015-005.
- [289] CMS Collaboration, “The Phase-2 upgrade of the CMS tracker”, CMS Technical Proposal CERN-LHCC-2017-009, CMS-TDR-014, 2017. doi:10.17181/CERN.QZ28.FLHW.
- [290] CMS Collaboration, “The Phase-2 upgrade of the CMS muon detectors”, CMS Technical Proposal CERN-LHCC-2017-012, CMS-TDR-016, 2017.
- [291] CMS Collaboration, “A MIP timing detector for the CMS Phase-2 upgrade”, CMS Technical Proposal CERN-LHCC-2019-003, CMS-TDR-020, 2019.
- [292] CMS Collaboration, “The Phase-2 upgrade of the CMS endcap calorimeter”, CMS Technical Proposal CERN-LHCC-2017-023, CMS-TDR-019, 2017.
- [293] CMS Collaboration, “The Phase-2 upgrade of the CMS barrel calorimeters”, CMS Technical Proposal CERN-LHCC-2017-011, CMS-TDR-015, 2017.

- [294] CMS Collaboration, “ECFA 2016: Prospects for selected standard model measurements with the CMS experiment at the High-Luminosity LHC”, CMS Physics Analysis Summary CMS-PAS-FTR-16-006, 2017.
- [295] CMS Collaboration, “Expected performance of the physics objects with the upgraded CMS detector at the HL-LHC”, CMS Note CMS-NOTE-2018-006, 2018.
- [296] CMS Collaboration, “The Phase-2 upgrade of the CMS beam radiation, instrumentation, and luminosity detectors”, CMS Technical Proposal CERN-LHCC-2021-008, CMS-TDR-023, 2021.
- [297] A. Dainese et al., “Physics at the HL-LHC, and perspectives at the HE-LHC”, CERN Report CERN-2019-007, 2019. doi:10.23731/CYRM-2019-007.
- [298] H. Paukkunen and P. Zurita, “PDF reweighting in the Hessian matrix approach”, *JHEP* **12** (2014) 100, doi:10.1007/JHEP12(2014)100, arXiv:1402.6623.


A Glossary of acronyms

AMWT	Analytical matrix weighting technique
BBR	Beam-beam remnants
BDT	Boosted decision tree
BSM	Beyond the standard model
CA	Cambridge–Aachen
CHS	Charged hadron subtraction
CKM	Cabibbo–Kobayashi–Maskawa
CL	Confidence level
CMS	Compact Muon Solenoid
CP	Charge conjugation parity
CR	Colour reconnection
DIS	Deep inelastic scattering
ECAL	Electromagnetic calorimeter
EFT	Effective field theory
ERD	Early resonance decay
EW	Electroweak
FKR	Full kinematic reconstruction
FSR	Final-state radiation
GIM	Glashow–Iliopoulos–Maiani
HCAL	Hadronic calorimeter
HL-LHC	High-Luminosity Large Hadron Collider
ISR	Initial-state radiation
JER	Jet energy resolution
JES	Jet energy scale
JMS	Jet mass scale
JSF	Jet scale factor
KIN b	Kinematic method using b tagging
LHC	Large Hadron Collider
LKR	Loose kinematic reconstruction
LO	Leading order
MB	Minimum bias
MC	Monte Carlo
ME	Matrix element
MPI	Multiple-parton interactions
MPV	Most probable value
\overline{MS}	Modified minimal subtraction
MSR	Low-scale short-distance mass scheme derived from the \overline{MS} mass
NLO	Next-to-leading order
NN	Neural network
NNLL	Next-to-next-to-leading logarithm
NNLO	Next-to-next-to-leading order
PDF	Parton distribution function
PF	Particle flow
PS	Parton shower
PU	Pileup
PUPPI	Pileup-per-particle identification
QCD	Quantum chromodynamics





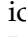




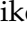

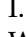




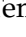


RGE	Renormalisation group equation
RMS	Root mean square
SCET	Soft-collinear effective theory
SM	Standard model
SMEFT	Standard model effective field theory
UE	Underlying event
2D	Two-dimensional
4FS	Four-flavour number scheme
5FS	Five-flavour number scheme

B The CMS Collaboration




Yerevan Physics Institute, Yerevan, Armenia

A. Hayrapetyan, A. Tumasyan¹ 





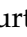



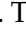
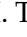

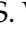

Institut für Hochenergiephysik, Vienna, Austria

W. Adam , J.W. Andrejkovic, T. Bergauer , S. Chatterjee , K. Damanakis , M. Dragicevic , A. Hoang , P.S. Hussain , M. Jeitler² , N. Krammer , A. Li , D. Liko , I. Mikulec , J. Schieck² , R. Schöffbeck , D. Schwarz , M. Sonawane , S. Templ , W. Waltenberger , C.-E. Wulz² 

















Universiteit Antwerpen, Antwerpen, Belgium

M.R. Darwish³ , T. Janssen , P. Van Mechelen 











Vrije Universiteit Brussel, Brussel, Belgium

E.S. Bols , J. D'Hondt , S. Dansana , A. De Moor , M. Delcourt , S. Lowette , I. Makarenko , D. Müller , S. Tavernier , M. Tytgat⁴ , G.P. Van Onsem , S. Van Putte , D. Vannerom 




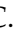
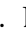
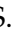




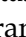

Université Libre de Bruxelles, Bruxelles, Belgium

B. Clerbaux , A.K. Das, G. De Lentdecker , H. Evard , L. Favart , P. Gianneios , D. Hohov , J. Jaramillo , A. Khalilzadeh, F.A. Khan , K. Lee , M. Mahdavihorrani , A. Malara , S. Paredes , L. Thomas , M. Vanden Bemden , C. Vander Velde , P. Vanlaer 



Ghent University, Ghent, Belgium

M. De Coen , D. Dobur , Y. Hong , J. Knolle , L. Lambrecht , G. Mestdach, K. Mota Amarilo , C. Rendón, A. Samalan, K. Skovpen , N. Van Den Bossche , J. van der Linden , L. Wezenbeek 




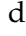
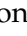

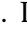


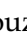








Université Catholique de Louvain, Louvain-la-Neuve, Belgium

A. Benecke , A. Bethani , G. Bruno , C. Caputo , C. Delaere , I.S. Donertas , A. Giammanco , Sa. Jain , V. Lemaitre, J. Lidrych , P. Mastrapasqua , T.T. Tran , S. Wertz 

Centro Brasileiro de Pesquisas Físicas, Rio de Janeiro, Brazil

G.A. Alves , E. Coelho , C. Hensel , T. Menezes De Oliveira , A. Moraes , P. Rebello Teles , M. Soeiro

Universidade do Estado do Rio de Janeiro, Rio de Janeiro, Brazil
























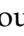

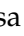




W.L. Aldá Júnior , M. Alves Gallo Pereira , M. Barroso Ferreira Filho , H. Brandao Malbouisson , W. Carvalho , J. Chinellato⁵, E.M. Da Costa , G.G. Da Silveira⁶ , D. De Jesus Damiao , S. Fonseca De Souza , R. Gomes De Souza, J. Martins⁷ , C. Mora Herrera , L. Mundim , H. Nogima , J.P. Pinheiro , A. Santoro , A. Sznajder , M. Thiel , A. Vilela Pereira 


































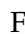
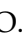



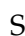







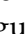





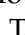

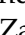



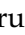
















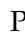






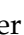




Universidade Estadual Paulista, Universidade Federal do ABC, São Paulo, Brazil

C.A. Bernardes⁶ , L. Calligaris , T.R. Fernandez Perez Tomei , E.M. Gregores , P.G. Mercadante , S.F. Novaes , B. Orzari , Sandra S. Padula 

Institute for Nuclear Research and Nuclear Energy, Bulgarian Academy of Sciences, Sofia, Bulgaria







A. Aleksandrov , G. Antchev , R. Hadjiiska , P. Iaydjiev , M. Misheva , M. Shopova , G. Sultanov 

University of Sofia, Sofia, BulgariaA. Dimitrov , L. Litov , B. Pavlov , P. Petkov , A. Petrov , E. Shumka **Instituto De Alta Investigación, Universidad de Tarapacá, Casilla 7 D, Arica, Chile**S. Keshri , S. Thakur **Beihang University, Beijing, China**T. Cheng , T. Javaid , L. Yuan **Department of Physics, Tsinghua University, Beijing, China**Z. Hu , J. Liu, K. Yi^{8,9} **Institute of High Energy Physics, Beijing, China**G.M. Chen¹⁰ , H.S. Chen¹⁰ , M. Chen¹⁰ , F. Iemmi , C.H. Jiang, A. Kapoor¹¹ , H. Liao , Z.-A. Liu¹² , R. Sharma¹³ , J.N. Song¹², J. Tao , C. Wang¹⁰, J. Wang , Z. Wang¹⁰, H. Zhang **State Key Laboratory of Nuclear Physics and Technology, Peking University, Beijing, China**A. Agapitos , Y. Ban , A. Levin , C. Li , Q. Li , Y. Mao, S.J. Qian , X. Sun , D. Wang , H. Yang, L. Zhang , C. Zhou **Sun Yat-Sen University, Guangzhou, China**Z. You **University of Science and Technology of China, Hefei, China**K. Jaffel , N. Lu **Nanjing Normal University, Nanjing, China**G. Bauer¹⁴**Institute of Modern Physics and Key Laboratory of Nuclear Physics and Ion-beam Application (MOE) - Fudan University, Shanghai, China**X. Gao¹⁵ **Zhejiang University, Hangzhou, Zhejiang, China**Z. Lin , C. Lu , M. Xiao **Universidad de Los Andes, Bogota, Colombia**C. Avila , D.A. Barbosa Trujillo, A. Cabrera , C. Florez , J. Fraga , J.A. Reyes Vega**Universidad de Antioquia, Medellin, Colombia**J. Mejia Guisao , F. Ramirez , M. Rodriguez , J.D. Ruiz Alvarez **University of Split, Faculty of Electrical Engineering, Mechanical Engineering and Naval Architecture, Split, Croatia**D. Giljanovic , N. Godinovic , D. Lelas , A. Sculac **University of Split, Faculty of Science, Split, Croatia**M. Kovac , T. Sculac **Institute Rudjer Boskovic, Zagreb, Croatia**P. Bargassa , V. Brigljevic , B.K. Chitroda , D. Ferencek , K. Jakovcic, S. Mishra , A. Starodumov¹⁶ , T. Susa **University of Cyprus, Nicosia, Cyprus**A. Attikis , K. Christoforou , A. Hadjiagapiou, S. Konstantinou , J. Mousa , C. Nicolaou, F. Ptochos , P.A. Razis , H. Rykaczewski, H. Saka , A. Stepennov 


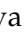



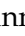



















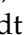




Charles University, Prague, Czech RepublicM. Finger , M. Finger Jr. , A. Kveton **Escuela Politecnica Nacional, Quito, Ecuador**E. Ayala **Universidad San Francisco de Quito, Quito, Ecuador**E. Carrera Jarrin **Academy of Scientific Research and Technology of the Arab Republic of Egypt, Egyptian Network of High Energy Physics, Cairo, Egypt**A.A. Abdelalim^{17,18} , E. Salama^{19,20} **Center for High Energy Physics (CHEP-FU), Fayoum University, El-Fayoum, Egypt**A. Lotfy , M.A. Mahmoud **National Institute of Chemical Physics and Biophysics, Tallinn, Estonia**K. Ehataht , M. Kadastik, T. Lange , S. Nandan , C. Nielsen , J. Pata , M. Raidal , L. Tani , C. Veelken **Department of Physics, University of Helsinki, Helsinki, Finland**H. Kirschenmann , K. Osterberg , M. Voutilainen **Helsinki Institute of Physics, Helsinki, Finland**S. Bharthuar , E. Brücken , F. Garcia , K.T.S. Kallonen , R. Kinnunen, T. Lampén , K. Lassila-Perini , S. Lehti , T. Lindén , L. Martikainen , M. Myllymäki , M.m. Rantanen , H. Siikonen , E. Tuominen , J. Tuominiemi **Lappeenranta-Lahti University of Technology, Lappeenranta, Finland**P. Luukka , H. Petrow **IRFU, CEA, Université Paris-Saclay, Gif-sur-Yvette, France**M. Besancon , F. Couderc , M. Dejardin , D. Denegri, J.L. Faure, F. Ferri , S. Ganjour , P. Gras , G. Hamel de Monchenault , V. Lohezic , J. Malcles , J. Rander, A. Rosowsky , M.Ö. Sahin , A. Savoy-Navarro²¹ , P. Simkina , M. Titov , M. Tornago **Laboratoire Leprince-Ringuet, CNRS/IN2P3, Ecole Polytechnique, Institut Polytechnique de Paris, Palaiseau, France**F. Beaudette , A. Buchot Perraguin , P. Busson , A. Cappati , C. Charlot , M. Chiusi , F. Damas , O. Davignon , A. De Wit , I.T. Ehle , B.A. Fontana Santos Alves , S. Ghosh , A. Gilbert , R. Granier de Cassagnac , A. Hakimi , B. Harikrishnan , L. Kalipoliti , G. Liu , J. Motta , M. Nguyen , C. Ochando , L. Portales , R. Salerno , J.B. Sauvan , Y. Sirois , A. Tarabini , E. Vernazza , A. Zabi , A. Zghiche **Université de Strasbourg, CNRS, IPHC UMR 7178, Strasbourg, France**J.-L. Agram²² , J. Andrea , D. Apparú , D. Bloch , J.-M. Brom , E.C. Chabert , C. Collard , S. Falke , U. Goerlach , C. Grimault, R. Haeberle , A.-C. Le Bihan , M. Meena , G. Saha , M.A. Sessini , P. Van Hove **Institut de Physique des 2 Infinis de Lyon (IP2I), Villeurbanne, France**S. Beauceron , B. Blancon , G. Boudoul , N. Chanon , J. Choi , D. Contardo , P. Depasse , C. Dozen²³ , H. El Mamouni, J. Fay , S. Gascon , M. Gouzevitch , C. Greenberg, G. Grenier , B. Ille , I.B. Laktineh, M. Lethuillier , L. Mirabito, S. Perries, A. Purohit , M. Vander Donckt , P. Verdier , J. Xiao **Georgian Technical University, Tbilisi, Georgia**

G. Adamov, I. Lomidze , Z. Tsamalaidze¹⁶ 

RWTH Aachen University, I. Physikalisches Institut, Aachen, Germany

V. Botta , L. Feld , K. Klein , M. Lipinski , D. Meuser , A. Pauls , N. Röwert ,
M. Teroerde 





RWTH Aachen University, III. Physikalisches Institut A, Aachen, Germany

S. Diekmann , A. Dodonova , N. Eich , D. Eliseev , F. Engelke , J. Erdmann ,
M. Erdmann , P. Fackeldey , B. Fischer , T. Hebbeker , K. Hoepfner , F. Ivone ,
A. Jung , M.y. Lee , F. Mausolf , M. Merschmeyer , A. Meyer , S. Mukherjee ,
D. Noll , F. Nowotny, A. Pozdnyakov , Y. Rath, W. Redjeb , F. Rehm, H. Reithler ,
U. Sarkar , V. Sarkisovi , A. Schmidt , A. Sharma , J.L. Spah , A. Stein ,
F. Torres Da Silva De Araujo²⁴ , S. Wiedenbeck , S. Zaleski













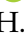



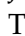


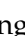
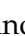



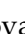
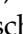

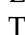











RWTH Aachen University, III. Physikalisches Institut B, Aachen, Germany

C. Dziwok , G. Flügge , W. Haj Ahmad²⁵ , T. Kress , A. Nowack , O. Pooth ,
A. Stahl , T. Ziemons , A. Zotz 




















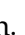

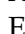

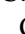




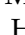




Deutsches Elektronen-Synchrotron, Hamburg, Germany


H. Aarup Petersen , M. Aldaya Martin , J. Alimena , S. Amoroso, Y. An , S. Baxter ,
M. Bayatmakou , H. Becerril Gonzalez , O. Behnke , A. Belvedere , S. Bhattacharya ,
F. Blekman²⁶ , K. Borras²⁷ , A. Campbell , A. Cardini , C. Cheng, F. Colombina ,
S. Consuegra Rodríguez , G. Correia Silva , M. De Silva , G. Eckerlin, D. Eckstein ,
L.I. Estevez Banos , O. Filatov , E. Gallo²⁶ , A. Geiser , A. Giraldi , V. Guglielmi ,
M. Guthoff , A. Hinzmann , A. Jafari²⁸ , L. Jeppe , N.Z. Jomhari , B. Kaech ,
M. Kasemann , C. Kleinwort , R. Kogler , M. Komm , D. Krücker , W. Lange,
D. Leyva Pernia , K. Lipka²⁹ , W. Lohmann³⁰ , R. Mankel , I.-A. Melzer-Pellmann ,
M. Mendizabal Morentin , A.B. Meyer , G. Milella , A. Mussgiller , L.P. Nair ,
A. Nürnberg , Y. Otarid, J. Park , D. Pérez Adán , E. Ranken , A. Raspereza ,
B. Ribeiro Lopes , J. Rübenach, A. Saggio , M. Scham^{31,27} , S. Schnake²⁷ , P. Schütze ,
C. Schwanenberger²⁶ , D. Selivanova , K. Sharko , M. Shchedrolosiev , R.E. Sosa Ric-
cardo , D. Stafford, F. Vazzoler , A. Ventura Barroso , R. Walsh , Q. Wang , Y. Wen ,
K. Wichmann, L. Wiens²⁷ , C. Wissing , Y. Yang , O. Zenaiev , A. Zimmermann Castro Santos 

University of Hamburg, Hamburg, Germany

A. Albrecht , S. Albrecht , M. Antonello , S. Bein , L. Benato , S. Bollweg,
M. Bonanomi , P. Connor , K. El Morabit , Y. Fischer , E. Garutti , A. Grohsjean ,
J. Haller , H.R. Jabusch , G. Kasieczka , P. Keicher, R. Klanner , W. Korcari ,
T. Kramer , V. Kutzner , F. Labe , J. Lange , A. Lobanov , C. Matthies , A. Mehta ,
L. Moureaux , M. Mrowietz, A. Nigamova , Y. Nissan, A. Paasch , K.J. Pena Rodriguez ,
T. Quadfasel , B. Raciti , M. Rieger , D. Savoio , J. Schindler , P. Schleper ,
M. Schröder , J. Schwandt , M. Sommerhalder , H. Stadie , G. Steinbrück , A. Tews,
M. Wolf 

Karlsruher Institut fuer Technologie, Karlsruhe, Germany

S. Brommer , M. Burkart, E. Butz , T. Chwalek , A. Dierlamm , A. Droll, N. Fal-
termann , M. Giffels , A. Gottmann , F. Hartmann³² , R. Hofsaess , M. Horzela ,
U. Husemann , J. Kieseler , M. Klute , R. Koppenhöfer , J.M. Lawhorn , M. Link,
A. Lintuluoto , S. Maier , S. Mitra , M. Mormile , Th. Müller , M. Neukum, M. Oh ,
E. Pfeffer , M. Presilla , G. Quast , K. Rabbertz , B. Regnery , N. Shadskiy ,
I. Shvetsov , H.J. Simonis , M. Toms , N. Trevisani , R.F. Von Cube , M. Wassmer 

S. Wieland , F. Wittig, R. Wolf , X. Zuo 





Institute of Nuclear and Particle Physics (INPP), NCSR Demokritos, Aghia Paraskevi, Greece

G. Anagnostou, G. Daskalakis , A. Kyriakis, A. Papadopoulos³², A. Stakia 

National and Kapodistrian University of Athens, Athens, Greece

P. Kontaxakis , G. Melachroinos, Z. Painesis , A. Panagiotou, I. Papavergou , I. Paraskevas , N. Saoulidou , K. Theofilatos , E. Tziaferi , K. Vellidis , I. Zisopoulos 







National Technical University of Athens, Athens, Greece

G. Bakas , T. Chatzistavrou, G. Karapostoli , K. Kousouris , I. Papakrivopoulos , E. Siamarkou, G. Tsipolitis, A. Zacharopoulou

University of Ioánnina, Ioánnina, Greece

K. Adamidis, I. Bestintzanos, I. Evangelou , C. Foudas, C. Kamtsikis, P. Katsoulis, P. Kokkas , P.G. Kosmoglou Kioseoglou , N. Manthos , I. Papadopoulos , J. Strogas 

HUN-REN Wigner Research Centre for Physics, Budapest, Hungary

M. Bartók³³ , C. Hajdu , D. Horvath^{34,35} , K. Márton, A.J. Rádl³⁶ , F. Sikler , V. Veszpremi 

MTA-ELTE Lendület CMS Particle and Nuclear Physics Group, Eötvös Loránd University, Budapest, Hungary

M. Csanád , K. Farkas , M.M.A. Gadallah³⁷ , Á. Kadlecik , P. Major , K. Mandal , G. Pásztor , G.I. Veres 




Faculty of Informatics, University of Debrecen, Debrecen, Hungary

P. Raics, B. Ujvari , G. Zilizi 















Institute of Nuclear Research ATOMKI, Debrecen, Hungary

G. Bencze, S. Czellar, J. Molnar, Z. Szillasi

Karoly Robert Campus, MATE Institute of Technology, Gyongyos, Hungary

T. Csorgo³⁸ , F. Nemes³⁸ , T. Novak 


Panjab University, Chandigarh, India

J. Babbar , S. Bansal , S.B. Beri, V. Bhatnagar , G. Chaudhary , S. Chauhan , N. Dhingra³⁹ , A. Kaur , A. Kaur , H. Kaur , M. Kaur , S. Kumar , K. Sandeep , T. Sheokand, J.B. Singh , A. Singla 














University of Delhi, Delhi, India

A. Ahmed , A. Bhardwaj , A. Chhetri , B.C. Choudhary , A. Kumar , A. Kumar , M. Naimuddin , K. Ranjan , S. Saumya 



Saha Institute of Nuclear Physics, HBNI, Kolkata, India

S. Baradia , S. Barman⁴⁰ , S. Bhattacharya , S. Dutta , S. Dutta, S. Sarkar












Indian Institute of Technology Madras, Madras, India

M.M. Ameen , P.K. Behera , S.C. Behera , S. Chatterjee , P. Jana , P. Kalbhor , J.R. Komaragiri⁴¹ , D. Kumar⁴¹ , P.R. Pujahari , N.R. Saha , A. Sharma , A.K. Sikdar , S. Verma 

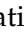










Tata Institute of Fundamental Research-A, Mumbai, India

S. Dugad, M. Kumar , G.B. Mohanty , P. Suryadevara








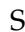
Tata Institute of Fundamental Research-B, Mumbai, India

A. Bala , S. Banerjee , R.M. Chatterjee, R.K. Dewanjee⁴² , M. Guchait , Sh. Jain ,
A. Jaiswal, S. Karmakar , S. Kumar , G. Majumder , K. Mazumdar , S. Parolia ,
A. Thachayath 




National Institute of Science Education and Research, An OCC of Homi Bhabha National Institute, Bhubaneswar, Odisha, India

S. Bahinipati⁴³ , C. Kar , D. Maity⁴⁴ , P. Mal , T. Mishra , V.K. Muraleedharan Nair Bindhu⁴⁴ , K. Naskar⁴⁴ , A. Nayak⁴⁴ , P. Sadangi, S.K. Swain , S. Varghese⁴⁴ ,
D. Vats⁴⁴ 





Indian Institute of Science Education and Research (IISER), Pune, India

S. Acharya⁴⁵ , A. Alpana , S. Dube , B. Gomber⁴⁵ , B. Kansal , A. Laha , B. Sahu⁴⁵ ,
S. Sharma , K.Y. Vaish


Isfahan University of Technology, Isfahan, Iran

H. Bakhshiansohi⁴⁶ , E. Khazaie⁴⁷ , M. Zeinali⁴⁸ 












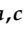



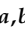















Institute for Research in Fundamental Sciences (IPM), Tehran, Iran

S. Chenarani⁴⁹ , S.M. Etesami , M. Khakzad , M. Mohammadi Najafabadi 





















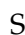





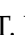
University College Dublin, Dublin, Ireland

M. Grunewald 





INFN Sezione di Bari^a, Università di Bari^b, Politecnico di Bari^c, Bari, Italy

M. Abbrescia^{a,b} , R. Aly^{a,c,17} , A. Colaleo^{a,b} , D. Creanza^{a,c} , B. D'Anzi^{a,b} ,
N. De Filippis^{a,c} , M. De Palma^{a,b} , A. Di Florio^{a,c} , W. Elmetenawee^{a,b,17} ,
L. Fiore^a , G. Iaselli^{a,c} , M. Louka^{a,b}, G. Maggi^{a,c} , M. Maggi^a , I. Margjeka^{a,b} ,
V. Mastrapasqua^{a,b} , S. My^{a,b} , S. Nuzzo^{a,b} , A. Pellicchia^{a,b} , A. Pompili^{a,b} ,
G. Pugliese^{a,c} , R. Radogna^a , G. Ramirez-Sanchez^{a,c} , D. Ramos^a , A. Ranieri^a ,
L. Silvestris^a , F.M. Simone^{a,b} , Ü. Sözbilir^a , A. Stamerra^a , R. Venditti^a ,
P. Verwilligen^a , A. Zaza^{a,b} 



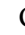
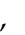



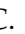


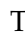

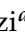



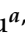
INFN Sezione di Bologna^a, Università di Bologna^b, Bologna, Italy

G. Abbiendi^a , C. Battilana^{a,b} , D. Bonacorsi^{a,b} , L. Borgonovi^a , R. Campanini^{a,b} ,
P. Capiluppi^{a,b} , A. Castro^{a,b} , F.R. Cavallo^a , M. Cuffiani^{a,b} , G.M. Dallavalle^a ,
T. Diotallevi^{a,b} , F. Fabbri^a , A. Fanfani^{a,b} , D. Fasanella^{a,b} , P. Giacomelli^a ,
L. Giommi^{a,b} , C. Grandi^a , L. Guiducci^{a,b} , S. Lo Meo^{a,50} , L. Lunerti^{a,b} ,
S. Marcellini^a , G. Masetti^a , F.L. Navarria^{a,b} , A. Perrotta^a , F. Primavera^{a,b} ,
A.M. Rossi^{a,b} , T. Rovelli^{a,b} 

INFN Sezione di Catania^a, Università di Catania^b, Catania, Italy

S. Costa^{a,b,51} , A. Di Mattia^a , R. Potenza^{a,b}, A. Tricomi^{a,b,51} , C. Tuve^{a,b} 

INFN Sezione di Firenze^a, Università di Firenze^b, Firenze, Italy

P. Assiouras^a , G. Barbagli^a , G. Bardelli^{a,b} , B. Camaiani^{a,b} , A. Cassese^a ,
R. Ceccarelli^a , V. Ciulli^{a,b} , C. Civinini^a , R. D'Alessandro^{a,b} , E. Focardi^{a,b} ,
T. Kello^a, G. Latino^{a,b} , P. Lenzi^{a,b} , M. Lizzo^a , M. Meschini^a , S. Paoletti^a ,
A. Papanastassiou^{a,b}, G. Sguazzoni^a , L. Viliani^a 
















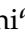



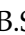



INFN Laboratori Nazionali di Frascati, Frascati, Italy

L. Benussi , S. Bianco , S. Meola⁵² , D. Piccolo 

INFN Sezione di Genova^a, Università di Genova^b, Genova, Italy

P. Chatagnon^a , F. Ferro^a , E. Robutti^a , S. Tosi^{a,b} 




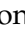



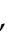






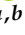
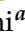
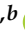
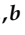

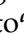


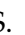



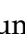

INFN Sezione di Milano-Bicocca^a, Università di Milano-Bicocca^b, Milano, Italy

A. Benaglia^a , G. Boldrini^{a,b} , F. Brivio^a , F. Cetorelli^a , F. De Guio^{a,b} , M.E. Dinardo^{a,b} , P. Dini^a , S. Gennai^a , R. Gerosa^{a,b} , A. Ghezzi^{a,b} , P. Govoni^{a,b} , L. Guzzi^a , M.T. Lucchini^{a,b} , M. Malberti^a , S. Malvezzi^a , A. Massironi^a , D. Menasce^a , L. Moroni^a , M. Paganoni^{a,b} , D. Pedrini^a , B.S. Pinolini^a, S. Ragazzi^{a,b} , T. Tabarelli de Fatis^{a,b} , D. Zuolo^a 




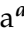




INFN Sezione di Napoli^a, Università di Napoli 'Federico II'^b, Napoli, Italy; Università della Basilicata^c, Potenza, Italy; Scuola Superiore Meridionale (SSM)^d, Napoli, Italy

S. Buontempo^a , A. Cagnotta^{a,b} , F. Carnevali^{a,b}, N. Cavallo^{a,c} , F. Fabozzi^{a,c} , A.O.M. Iorio^{a,b} , L. Lista^{a,b,53} , P. Paolucci^{a,32} , B. Rossi^a , C. Sciacca^{a,b} 



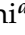
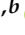
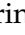

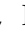

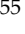



INFN Sezione di Padova^a, Università di Padova^b, Padova, Italy; Università di Trento^c, Trento, Italy

R. Ardino^a , P. Azzi^a , N. Bacchetta^{a,54} , P. Bortignon^a , G. Bortolato^{a,b}, A. Bragagnolo^{a,b} , R. Carlin^{a,b} , P. Checchia^a , T. Dorigo^a , F. Gasparini^{a,b} , U. Gasparini^{a,b} , F. Gonella^a , E. Lusiani^a , M. Margoni^{a,b} , F. Marini^a , A.T. Meneguzzo^{a,b} , M. Migliorini^{a,b} , J. Pazzini^{a,b} , P. Ronchese^{a,b} , R. Rossin^{a,b} , F. Simonetto^{a,b} , G. Strong^a , M. Tosi^{a,b} , A. Triossi^{a,b} , S. Ventura^a , H. Yarar^{a,b}, M. Zanetti^{a,b} , P. Zotto^{a,b} , A. Zucchetta^{a,b} , G. Zumerle^{a,b} 

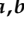



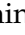


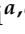


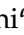




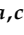













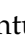


INFN Sezione di Pavia^a, Università di Pavia^b, Pavia, Italy

S. Abu Zeid^{a,20} , C. Aimè^{a,b} , A. Braghieri^a , S. Calzaferri^a , D. Fiorina^a , P. Montagna^{a,b} , V. Re^a , C. Riccardi^{a,b} , P. Salvini^a , I. Vai^{a,b} , P. Vitulo^{a,b} 




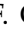

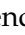

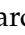




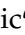


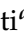





INFN Sezione di Perugia^a, Università di Perugia^b, Perugia, Italy

S. Ajmal^{a,b} , G.M. Bilei^a , D. Ciangottini^{a,b} , L. Fanò^{a,b} , M. Magherini^{a,b} , G. Mantovani^{a,b}, V. Mariani^{a,b} , M. Menichelli^a , F. Moscatelli^{a,55} , A. Rossi^{a,b} , A. Santocchia^{a,b} , D. Spiga^a , T. Tedeschi^{a,b} 


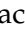
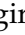





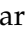


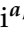
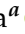

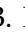
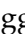

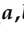




INFN Sezione di Pisa^a, Università di Pisa^b, Scuola Normale Superiore di Pisa^c, Pisa, Italy; Università di Siena^d, Siena, Italy








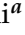








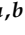

P. Asenov^{a,b} , P. Azzurri^a , G. Bagliesi^a , R. Bhattacharya^a , L. Bianchini^{a,b} , T. Boccali^a , E. Bossini^a , D. Bruschini^{a,c} , R. Castaldi^a , M.A. Ciocci^{a,b} , M. Cipriani^{a,b} , V. D'Amante^{a,d} , R. Dell'Orso^a , S. Donato^a , A. Giassi^a , F. Ligabue^{a,c} , D. Matos Figueiredo^a , A. Messineo^{a,b} , M. Musich^{a,b} , F. Palla^a , A. Rizzi^{a,b} , G. Rolandi^{a,c} , S. Roy Chowdhury^a , T. Sarkar^a , A. Scribano^a , P. Spagnolo^a , R. Tenchini^a , G. Tonelli^{a,b} , N. Turini^{a,d} , F. Vaselli^{a,c} , A. Venturi^a , P.G. Verdini^a 

INFN Sezione di Roma^a, Sapienza Università di Roma^b, Roma, Italy


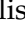




C. Baldenegro Barrera^{a,b} , P. Barria^a , C. Basile^{a,b} , M. Campana^{a,b} , F. Cavallari^a , L. Cunqueiro Mendez^{a,b} , D. Del Re^{a,b} , E. Di Marco^a , M. Diemoz^a , F. Errico^{a,b} , E. Longo^{a,b} , P. Meridiani^a , J. Mijuskovic^{a,b} , G. Organtini^{a,b} , F. Pandolfi^a , R. Paramatti^{a,b} , C. Quaranta^{a,b} , S. Rahatlou^{a,b} , C. Rovelli^a , F. Santanastasio^{a,b} , L. Soffi^a 

INFN Sezione di Torino^a, Università di Torino^b, Torino, Italy; Università del Piemonte Orientale^c, Novara, Italy










N. Amapane^{a,b} , R. Arcidiacono^{a,c} , S. Argiro^{a,b} , M. Arneodo^{a,c} , N. Bartosik^a , R. Bellan^{a,b} , A. Bellora^{a,b} , C. Biino^a , C. Borca^{a,b} , N. Cartiglia^a , M. Costa^{a,b} , R. Covarelli^{a,b} , N. Demaria^a , L. Finco^a , M. Grippo^{a,b} , B. Kiani^{a,b} , F. Legger^a , F. Luongo^{a,b} , C. Mariotti^a , L. Markovic^{a,b} , S. Maselli^a , A. Mecca^{a,b} 

E. Migliore^{a,b} , M. Monteno^a , R. Mulargia^a , M.M. Obertino^{a,b} , G. Ortona^a ,
L. Pacher^{a,b} , N. Pastrone^a , M. Pelliccioni^a , M. Ruspa^{a,c} , F. Siviero^{a,b} ,
V. Sola^{a,b} , A. Solano^{a,b} , A. Staiano^a , C. Tarricone^{a,b} , D. Trocino^a , G. Umoret^{a,b} ,
E. Vlasov^{a,b} , R. White^a 


INFN Sezione di Trieste^a, Università di Trieste^b, Trieste, Italy

S. Belforte^a , V. Candelise^{a,b} , M. Casarsa^a , F. Cossutti^a , K. De Leo^a ,
G. Della Ricca^{a,b} 

Kyungpook National University, Daegu, Korea

S. Dogra , J. Hong , C. Huh , B. Kim , D.H. Kim , J. Kim, H. Lee, S.W. Lee ,
C.S. Moon , Y.D. Oh , M.S. Ryu , S. Sekmen , Y.C. Yang 

Department of Mathematics and Physics - GWNNU, Gangneung, Korea

M.S. Kim 


Chonnam National University, Institute for Universe and Elementary Particles, Kwangju, Korea

G. Bak , P. Gwak , H. Kim , D.H. Moon 

Hanyang University, Seoul, Korea

E. Asilar , D. Kim , T.J. Kim , J.A. Merlin

Korea University, Seoul, Korea

S. Choi , S. Han, B. Hong , K. Lee, K.S. Lee , S. Lee , J. Park, S.K. Park, J. Yoo 


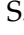

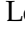




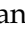
Kyung Hee University, Department of Physics, Seoul, Korea

J. Goh , S. Yang 




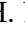

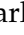

Sejong University, Seoul, Korea

H. S. Kim , Y. Kim, S. Lee



Seoul National University, Seoul, Korea

J. Almond, J.H. Bhyun, J. Choi , W. Jun , J. Kim , S. Ko , H. Kwon , H. Lee , J. Lee ,
J. Lee , B.H. Oh , S.B. Oh , H. Seo , U.K. Yang, I. Yoon 

University of Seoul, Seoul, Korea

W. Jang , D.Y. Kang, Y. Kang , S. Kim , B. Ko, J.S.H. Lee , Y. Lee , I.C. Park , Y. Roh,
I.J. Watson 

Yonsei University, Department of Physics, Seoul, Korea

S. Ha , H.D. Yoo 





Sungkyunkwan University, Suwon, Korea

M. Choi , M.R. Kim , H. Lee, Y. Lee , I. Yu 


**College of Engineering and Technology, American University of the Middle East (AUM),
Dasman, Kuwait**

T. Beyrouthy

Riga Technical University, Riga, Latvia

K. Dreimanis , A. Gaile , G. Pikurs, A. Potrebko , M. Seidel 

University of Latvia (LU), Riga, Latvia

N.R. Strautnieks 



Vilnius University, Vilnius, Lithuania

M. Ambrozias , A. Juodagalvis , A. Rinkevicius , G. Tamulaitis 







National Centre for Particle Physics, Universiti Malaya, Kuala Lumpur, Malaysia

N. Bin Norjoharuddeen , I. Yusuff⁵⁶ , Z. Zolkapli

Universidad de Sonora (UNISON), Hermosillo, Mexico

J.F. Benitez , A. Castaneda Hernandez , H.A. Encinas Acosta, L.G. Gallegos Maríñez, M. León Coello , J.A. Murillo Quijada , A. Sehwat , L. Valencia Palomo 

Centro de Investigacion y de Estudios Avanzados del IPN, Mexico City, Mexico

G. Ayala , H. Castilla-Valdez , H. Crotte Ledesma, E. De La Cruz-Burelo , I. Heredia-De La Cruz⁵⁷ , R. Lopez-Fernandez , C.A. Mondragon Herrera, A. Sánchez Hernández 

Universidad Iberoamericana, Mexico City, Mexico

C. Oropeza Barrera , M. Ramírez García 

Benemerita Universidad Autonoma de Puebla, Puebla, Mexico

I. Bautista , I. Pedraza , H.A. Salazar Ibarguen , C. Uribe Estrada 

University of Montenegro, Podgorica, Montenegro

I. Bubanja, N. Raicevic 

University of Canterbury, Christchurch, New Zealand

P.H. Butler 

National Centre for Physics, Quaid-I-Azam University, Islamabad, Pakistan

A. Ahmad , M.I. Asghar, A. Awais , M.I.M. Awan, H.R. Hoorani , W.A. Khan 







AGH University of Krakow, Faculty of Computer Science, Electronics and Telecommunications, Krakow, Poland

V. Avati, L. Grzanka , M. Malawski 

National Centre for Nuclear Research, Swierk, Poland

H. Bialkowska , M. Bluj , B. Boimska , M. Górski , M. Kazana , M. Szeper , P. Zalewski 

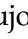















Institute of Experimental Physics, Faculty of Physics, University of Warsaw, Warsaw, Poland

K. Bunkowski , K. Doroba , A. Kalinowski , M. Konecki , J. Krolikowski , A. Muhammad 



Warsaw University of Technology, Warsaw, Poland

K. Pozniak , W. Zabolotny 

Laboratório de Instrumentação e Física Experimental de Partículas, Lisboa, Portugal

M. Araujo , D. Bastos , C. Beirão Da Cruz E Silva , A. Boletti , M. Bozzo , T. Camporesi , G. Da Molin , P. Faccioli , M. Gallinaro , J. Hollar , N. Leonardo , T. Niknejad , A. Petrilli , M. Pisano , J. Seixas , J. Varela , J.W. Wulff

Faculty of Physics, University of Belgrade, Belgrade, Serbia


























P. Adzic , P. Milenovic 

VINCA Institute of Nuclear Sciences, University of Belgrade, Belgrade, Serbia

M. Dordevic , J. Milosevic , V. Rekovic

Centro de Investigaciones Energéticas Medioambientales y Tecnológicas (CIEMAT), Madrid, Spain









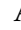





M. Aguilar-Benitez, J. Alcaraz Maestre , Cristina F. Bedoya , Oliver M. Carretero 

M. Cepeda , M. Cerrada , N. Colino , B. De La Cruz , A. Delgado Peris , A. Escalante Del Valle , D. Fernández Del Val , J.P. Fernández Ramos , J. Flix , M.C. Fouz , O. Gonzalez Lopez , S. Goy Lopez , J.M. Hernandez , M.I. Josa , D. Moran , C. M. Morcillo Perez , Á. Navarro Tobar , C. Perez Dengra , A. Pérez-Calero Yzquierdo , J. Puerta Pelayo , I. Redondo , D.D. Redondo Ferrero , L. Romero, S. Sánchez Navas , L. Urda Gómez , J. Vazquez Escobar , C. Willmott








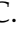

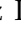

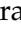






Universidad Autónoma de Madrid, Madrid, Spain

J.F. de Trocóniz 

Universidad de Oviedo, Instituto Universitario de Ciencias y Tecnologías Espaciales de Asturias (ICTEA), Oviedo, Spain

B. Alvarez Gonzalez , J. Cuevas , J. Fernandez Menendez , S. Folgueras , I. Gonzalez Caballero , J.R. González Fernández , P. Leguina , E. Palencia Cortezon , C. Ramón Álvarez , V. Rodríguez Bouza , A. Soto Rodríguez , A. Trapote , C. Vico Villalba , P. Vischia 





Instituto de Física de Cantabria (IFCA), CSIC-Universidad de Cantabria, Santander, Spain

S. Bhowmik , S. Blanco Fernández , J.A. Brochero Cifuentes , I.J. Cabrillo , A. Calderon , J. Duarte Campderros , M. Fernandez , G. Gomez , C. Lasaosa García , C. Martinez Rivero , P. Martinez Ruiz del Arbol , F. Matorras , P. Matorras Cuevas , E. Navarrete Ramos , J. Piedra Gomez , L. Scodellaro , I. Vila , J.M. Vizan Garcia 

University of Colombo, Colombo, Sri Lanka

M.K. Jayananda , B. Kailasapathy⁵⁸ , D.U.J. Sonnadara , D.D.C. Wickramarathna 










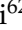


University of Ruhuna, Department of Physics, Matara, Sri Lanka

W.G.D. Dharmaratna⁵⁹ , K. Liyanage , N. Perera , N. Wickramage 

CERN, European Organization for Nuclear Research, Geneva, Switzerland














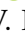










D. Abbaneo , C. Amendola , E. Auffray , G. Auzinger , J. Baechler, D. Barney , A. Bermúdez Martínez , M. Bianco , B. Bilin , A.A. Bin Anuar , A. Bocci , C. Botta , E. Brondolin , C. Caillol , G. Cerminara , N. Chernyavskaya , D. d'Enterria , A. Dabrowski , A. David , A. De Roeck , M.M. Defranchis , M. Deile , M. Dobson , L. Forthomme , G. Franzoni , W. Funk , S. Giani, D. Gigi, K. Gill , F. Glege , L. Gouskos , M. Haranko , J. Hegeman , B. Huber, V. Innocente , T. James , P. Janot , O. Kaluzinska , S. Laurila , P. Lecoq , E. Leutgeb , C. Lourenço , B. Maier , L. Malgeri , M. Mannelli , A.C. Marini , M. Matthewman, F. Meijers , S. Mersi , E. Meschi , V. Milosevic , F. Monti , F. Moortgat , M. Mulders , I. Neutelings , S. Orfanelli, F. Pantaleo , G. Petrucciani , A. Pfeiffer , M. Pierini , D. Piparo , H. Qu , D. Rabady , G. Reales Gutiérrez, M. Rovere , H. Sakulin , S. Scarfi , C. Schwick, M. Selvaggi , A. Sharma , K. Shchelina , P. Silva , P. Sphicas⁶⁰ , A.G. Stahl Leitner , A. Steen , S. Summers , D. Treille , P. Tropea , A. Tsiros, D. Walter , J. Wanczyk⁶¹ , J. Wang, S. Wuchterl , P. Zehetner , P. Zejdl , W.D. Zeuner

Paul Scherrer Institut, Villigen, Switzerland














T. Bevilacqua⁶² , L. Caminada⁶² , A. Ebrahimi , W. Erdmann , R. Horisberger , Q. Ingram , H.C. Kaestli , D. Kotlinski , C. Lange , M. Missiroli⁶² , L. Noehte⁶² , T. Rohe 

ETH Zurich - Institute for Particle Physics and Astrophysics (IPA), Zurich, Switzerland








T.K. Aarrestad , K. Androsova⁶¹ , M. Backhaus , A. Calandri , C. Cazzaniga , K. Datta , A. De Cosa , G. Dissertori , M. Dittmar, M. Donegà , F. Eble , M. Galli 

K. Gedia , F. Glessgen , C. Grab , N. Härringer , D. Hits , W. Luster , A.-M. Lyon , R.A. Manzoni , M. Marchegiani , L. Marchese , C. Martin Perez , A. Mascellani⁶¹ , F. Nessi-Tedaldi , F. Pauss , V. Perovic , S. Pigazzini , C. Reissel , T. Reitenspiess , B. Ristic , F. Riti , R. Seidita , J. Steggemann⁶¹ , D. Valsecchi , R. Wallny 



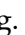



Universität Zürich, Zurich, Switzerland

C. Amsler⁶³ , P. Bäertschi , M.F. Canelli , K. Cormier , J.K. Heikkilä , M. Huwiler , W. Jin , A. Jofrehei , B. Kilminster , S. Leontsinis , S.P. Liechti , A. Macchiolo , P. Meiring , U. Molinatti , A. Reimers , P. Robmann , S. Sanchez Cruz , M. Senger , F. Stäger , Y. Takahashi , R. Tramontano

National Central University, Chung-Li, Taiwan

C. Adloff⁶⁴ , D. Bhowmik , C.M. Kuo , W. Lin , P.K. Rout , P.C. Tiwari⁴¹ , S.S. Yu 














National Taiwan University (NTU), Taipei, Taiwan

L. Ceard , Y. Chao , K.F. Chen , P.s. Chen , Z.g. Chen , A. De Iorio , W.-S. Hou , T.h. Hsu , Y.w. Kao , R. Khurana , G. Kole , Y.y. Li , R.-S. Lu , E. Paganis , X.f. Su , J. Thomas-Wilsker , L.s. Tsai , H.y. Wu , E. Yazgan


High Energy Physics Research Unit, Department of Physics, Faculty of Science, Chulalongkorn University, Bangkok, Thailand

C. Asawatangtrakuldee , N. Srimanobhas , V. Wachirapusanand 

Çukurova University, Physics Department, Science and Art Faculty, Adana, Turkey

D. Agyel , F. Boran , Z.S. Demiroglu , F. Dolek , I. Dumanoglu⁶⁵ , E. Eskut , Y. Guler⁶⁶ , E. Gurpinar Guler⁶⁶ , C. Isik , O. Kara , A. Kayis Topaksu , U. Kiminsu , G. Onengut , K. Ozdemir⁶⁷ , A. Polatoz , B. Tali⁶⁸ , U.G. Tok , S. Turkcapar , E. Uslan , I.S. Zorbakir

Middle East Technical University, Physics Department, Ankara, Turkey

M. Yalvac⁶⁹ 

Bogazici University, Istanbul, Turkey

B. Akgun , I.O. Atakisi , E. Gülmez , M. Kaya⁷⁰ , O. Kaya⁷¹ , S. Tekten⁷² 



Istanbul Technical University, Istanbul, Turkey

A. Cakir , K. Cankocak^{65,73} , G.G. Dincer , Y. Komurcu , S. Sen⁷⁴ 

Istanbul University, Istanbul, Turkey

O. Aydılek²⁵ , S. Cerci⁶⁸ , V. Epshteyn , B. Hacisahinoglu , I. Hos⁷⁵ , B. Kaynak , S. Ozkorucuklu , O. Potok , H. Sert , C. Simsek , C. Zorbilmez

Yildiz Technical University, Istanbul, Turkey

B. Isildak⁷⁶ , D. Sunar Cerci⁶⁸ 

Institute for Scintillation Materials of National Academy of Science of Ukraine, Kharkiv, Ukraine




A. Boyaryntsev , B. Grynyov 

National Science Centre, Kharkiv Institute of Physics and Technology, Kharkiv, Ukraine


















L. Levchuk 

University of Bristol, Bristol, United Kingdom






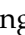










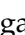

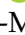





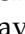









D. Anthony , J.J. Brooke , A. Bundock , F. Bury , E. Clement , D. Cussans , H. Flacher , M. Glowacki , J. Goldstein , H.F. Heath , M.-L. Holmberg , L. Kreczko

S. Paramesvaran , L. Robertshaw, S. Seif El Nasr-Storey, V.J. Smith , N. Stylianou⁷⁷ ,
K. Walkingshaw Pass




Rutherford Appleton Laboratory, Didcot, United Kingdom

A.H. Ball, K.W. Bell , A. Belyaev⁷⁸ , C. Brew , R.M. Brown , D.J.A. Cockerill ,
C. Cooke , K.V. Ellis, K. Harder , S. Harper , J. Linacre , K. Manolopoulos,
D.M. Newbold , E. Olaiya, D. Petyt , T. Reis , A.R. Sahasransu , G. Salvi , T. Schuh,
C.H. Shepherd-Themistocleous , I.R. Tomalin , T. Williams 

Imperial College, London, United Kingdom

R. Bainbridge , P. Bloch , C.E. Brown , O. Buchmuller, V. Cacchio, C.A. Carrillo Mon-
toya , G.S. Chahal⁷⁹ , D. Colling , J.S. Dancu, I. Das , P. Dauncey , G. Davies ,
J. Davies, M. Della Negra , S. Fayer, G. Fedi , G. Hall , M.H. Hassanshahi , A. Howard,
G. Iles , M. Knight , J. Langford , J. León Holgado , L. Lyons , A.-M. Magnan ,
S. Malik, M. Mieskolainen , J. Nash⁸⁰ , M. Pesaresi , B.C. Radburn-Smith , A. Richards,
A. Rose , K. Savva , C. Seez , R. Shukla , A. Tapper , K. Uchida , G.P. Uttley ,
L.H. Vage, T. Virdee³² , M. Vojinovic , N. Wardle , D. Winterbottom 




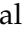

Brunel University, Uxbridge, United Kingdom

K. Coldham, J.E. Cole , A. Khan, P. Kyberd , I.D. Reid 

Baylor University, Waco, Texas, USA

S. Abdullin , A. Brinkerhoff , B. Caraway , E. Collins , J. Dittmann , K. Hatakeyama ,
J. Hiltbrand , B. McMaster , M. Saunders , S. Sawant , C. Sutantawibul , J. Wilson 



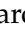






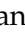

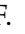




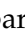



Catholic University of America, Washington, DC, USA

R. Bartek , A. Dominguez , C. Huerta Escamilla, A.E. Simsek , R. Uniyal , A.M. Var-
gas Hernandez 


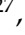





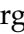
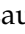








The University of Alabama, Tuscaloosa, Alabama, USA

B. Bam , R. Chudasama , S.I. Cooper , S.V. Gleyzer , C.U. Perez , P. Rumerio⁸¹ ,
E. Usai , R. Yi 







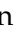
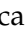









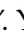

Boston University, Boston, Massachusetts, USA

A. Akpinar , D. Arcaro , C. Cosby , Z. Demiragli , C. Erice , C. Fangmeier ,
C. Fernandez Madrazo , E. Fontanesi , D. Gastler , F. Golf , S. Jeon , I. Reed ,
J. Rohlf , K. Salyer , D. Sperka , D. Spitzbart , I. Suarez , A. Tsatsos , S. Yuan ,
A.G. Zecchinelli 




Brown University, Providence, Rhode Island, USA

G. Benelli , X. Coubez²⁷, D. Cutts , M. Hadley , U. Heintz , J.M. Hogan⁸² , T. Kwon ,
G. Landsberg , K.T. Lau , D. Li , J. Luo , S. Mondal , M. Narain[†] , N. Pervan ,
S. Sagir⁸³ , F. Simpson , M. Stamenkovic , X. Yan , W. Zhang

University of California, Davis, Davis, California, USA

S. Abbott , J. Bonilla , C. Brainerd , R. Breedon , H. Cai ,
M. Calderon De La Barca Sanchez , M. Chertok , M. Citron , J. Conway , P.T. Cox ,
R. Erbacher , F. Jensen , O. Kukral , G. Mocellin , M. Mulhearn , D. Pellett ,
W. Wei , Y. Yao , F. Zhang 




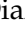

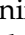
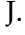



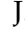
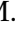
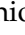
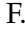
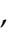


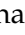
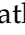
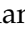



University of California, Los Angeles, California, USA

M. Bachtis , R. Cousins , A. Datta , G. Flores Avila, J. Hauser , M. Ignatenko ,
M.A. Iqbal , T. Lam , E. Manca , A. Nunez Del Prado, D. Saltzberg , V. Valuev 

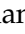



University of California, Riverside, Riverside, California, USA

R. Clare , J.W. Gary , M. Gordon, G. Hanson , W. Si , S. Wimpenny[†] 



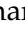



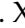

University of California, San Diego, La Jolla, California, USA

J.G. Branson , S. Cittolin , S. Cooperstein , D. Diaz , J. Duarte , L. Giannini , J. Guiang , R. Kansal , V. Krutelyov , R. Lee , J. Letts , M. Masciovecchio , F. Mokhtar , S. Mukherjee , M. Pieri , M. Quinnan , B.V. Sathia Narayanan , V. Sharma , M. Tadel , E. Vourliotis , F. Würthwein , Y. Xiang , A. Yagil 




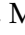











University of California, Santa Barbara - Department of Physics, Santa Barbara, California, USA

A. Barzdukas , L. Brennan , C. Campagnari , J. Incandela , J. Kim , A.J. Li , P. Masterson , H. Mei , J. Richman , U. Sarica , R. Schmitz , F. Setti , J. Sheplock , D. Stuart , T.Á. Vami , S. Wang 

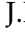
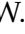
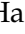

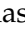
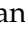


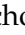




California Institute of Technology, Pasadena, California, USA

A. Bornheim , O. Cerri, A. Latorre, J. Mao , H.B. Newman , M. Spiropulu , J.R. Vlimant , C. Wang , S. Xie , R.Y. Zhu 


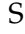



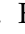
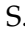









Carnegie Mellon University, Pittsburgh, Pennsylvania, USA

J. Alison , S. An , M.B. Andrews , P. Bryant , M. Cremonesi, V. Dutta , T. Ferguson , A. Harilal , C. Liu , T. Mudholkar , S. Murthy , P. Palit , M. Paulini , A. Roberts , A. Sanchez , W. Terrill 


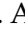
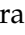
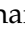
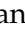
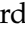

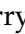
















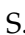











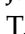

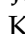
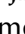








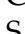
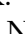
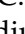



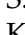
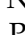
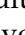
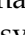
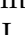
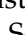
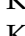
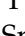


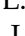

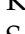
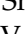


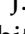



University of Colorado Boulder, Boulder, Colorado, USA

J.P. Cumalat , W.T. Ford , A. Hart , A. Hassani , G. Karathanasis , N. Manganelli , A. Perloff , C. Savard , N. Schonbeck , K. Stenson , K.A. Ulmer , S.R. Wagner , N. Zipper 





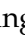
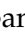



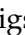









Cornell University, Ithaca, New York, USA

J. Alexander , S. Bright-Thonney , X. Chen , D.J. Cranshaw , J. Fan , X. Fan , S. Hogan , P. Kotamnives, J. Monroy , M. Oshiro , J.R. Patterson , J. Reichert , M. Reid , A. Ryd , J. Thom , P. Wittich , R. Zou 











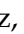




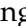
Fermi National Accelerator Laboratory, Batavia, Illinois, USA

M. Albrow , M. Alyari , O. Amram , G. Apollinari , A. Apresyan , L.A.T. Bauerdick , D. Berry , J. Berryhill , P.C. Bhat , K. Burkett , J.N. Butler , A. Canepa , G.B. Cerati , H.W.K. Cheung , F. Chlebana , G. Cummings , J. Dickinson , I. Dutta , V.D. Elvira , Y. Feng , J. Freeman , A. Gandrakota , Z. Gecse , L. Gray , D. Green, A. Grummer , S. Grünendahl , D. Guerrero , O. Gutsche , R.M. Harris , R. Heller , T.C. Herwig , J. Hirschauer , L. Horyn , B. Jayatilaka , S. Jindariani , M. Johnson , U. Joshi , T. Klijnsma , B. Klima , K.H.M. Kwok , S. Lammel , D. Lincoln , R. Lipton , T. Liu , C. Madrid , K. Maeshima , C. Mantilla , D. Mason , P. McBride , P. Merkel , S. Mrenna , S. Nahn , J. Ngadiuba , D. Noonan , V. Papadimitriou , N. Pastika , K. Pedro , C. Pena⁸⁴ , F. Ravera , A. Reinsvold Hall⁸⁵ , L. Ristori , E. Sexton-Kennedy , N. Smith , A. Soha , L. Spiegel , S. Stoynev , J. Strait , L. Taylor , S. Tkaczyk , N.V. Tran , L. Uplegger , E.W. Vaandering , A. Whitbeck , I. Zoi 










University of Florida, Gainesville, Florida, USA

C. Aruta , P. Avery , D. Bourilkov , L. Cadamuro , P. Chang , V. Cherepanov , R.D. Field, E. Koenig , M. Kolosova , J. Konigsberg , A. Korytov , K. Matchev , N. Menendez , G. Mitselmakher , K. Mohrman , A. Muthirakalayil Madhu , N. Rawal , D. Rosenzweig , S. Rosenzweig , J. Wang 






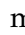













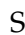





Florida State University, Tallahassee, Florida, USA

T. Adams , A. Al Kadhim , A. Askew , S. Bower , R. Habibullah , V. Hagopian , R. Hashmi , R.S. Kim , S. Kim , T. Kolberg , G. Martinez , H. Prosper , P.R. Prova , M. Wulansatiti , R. Yohay , J. Zhang 


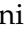







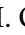
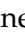




Florida Institute of Technology, Melbourne, Florida, USA

B. Alsufyani , M.M. Baarmand , S. Butalla , S. Das , T. Elkafrawy²⁰ , M. Hohlmann , R. Kumar Verma , M. Rahmani , E. Yanes 












University of Illinois Chicago, Chicago, USA, Chicago, USA

M.R. Adams , A. Baty , C. Bennett , R. Cavanaugh , R. Escobar Franco , O. Evdokimov , C.E. Gerber , A. Hingrajiya , D.J. Hofman , J.h. Lee , D. S. Lemos , A.H. Merrit , C. Mills , S. Nanda , G. Oh , B. Ozek , D. Pilipovic , R. Pradhan , E. Prifti , T. Roy , S. Rudrabhatla , M.B. Tonjes , N. Varelas , Z. Ye , J. Yoo 

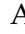
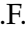
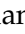














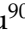



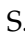
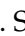

The University of Iowa, Iowa City, Iowa, USA

M. Alhusseini , D. Blend , K. Dilsiz⁸⁶ , L. Emediato , G. Karaman , O.K. Köseyan , J.-P. Merlo , A. Mestvirishvili⁸⁷ , J. Nachtman , O. Neogi , H. Ogul⁸⁸ , Y. Onel , A. Penzo , C. Snyder , E. Tiras⁸⁹ 


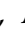

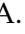
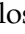




Johns Hopkins University, Baltimore, Maryland, USA

B. Blumenfeld , L. Corcodilos , J. Davis , A.V. Gritsan , L. Kang , S. Kyriacou , P. Maksimovic , M. Roguljic , J. Roskes , S. Sekhar , M. Swartz 

The University of Kansas, Lawrence, Kansas, USA

A. Abreu , L.F. Alcerro Alcerro , J. Anguiano , P. Baringer , A. Bean , Z. Flowers , D. Grove , J. King , G. Krintiras , M. Lazarovits , C. Le Mahieu , J. Marquez , N. Minafra , M. Murray , M. Nickel , M. Pitt , S. Popescu⁹⁰ , C. Rogan , C. Royon , R. Salvatico , S. Sanders , C. Smith , Q. Wang , G. Wilson 

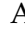


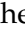
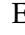

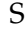









Kansas State University, Manhattan, Kansas, USA

B. Allmond , A. Ivanov , K. Kaadze , A. Kalogeropoulos , D. Kim , Y. Maravin , J. Natoli , D. Roy , G. Sorrentino 

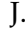

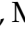

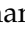

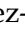



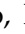



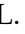










Lawrence Livermore National Laboratory, Livermore, California, USA

F. Rebassoo , D. Wright 















University of Maryland, College Park, Maryland, USA

A. Baden , A. Belloni , Y.M. Chen , S.C. Eno , N.J. Hadley , S. Jabeen , R.G. Kellogg , T. Koeth , Y. Lai , S. Lascio , A.C. Mignerey , S. Nabili , C. Palmer , C. Papageorgakis , M.M. Paranjpe , L. Wang 

Massachusetts Institute of Technology, Cambridge, Massachusetts, USA

J. Bendavid , I.A. Cali , M. D'Alfonso , J. Eysermans , C. Freer , G. Gomez-Ceballos , M. Goncharov , G. Grosso , P. Harris , D. Hoang , D. Kovalskyi , J. Krupa , L. Lavezzo , Y.-J. Lee , K. Long , A. Novak , C. Paus , D. Rankin , C. Roland , G. Roland , S. Rothman , G.S.F. Stephans , Z. Wang , B. Wyslouch , T. J. Yang 











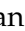

University of Minnesota, Minneapolis, Minnesota, USA

B. Crossman , B.M. Joshi , C. Kapsiak , M. Krohn , D. Mahon , J. Mans , B. Marzocchi , S. Pandey , M. Revering , R. Rusack , R. Saradhy , N. Schroeder , N. Strobbe , M.A. Wadud 

University of Mississippi, Oxford, Mississippi, USA

L.M. Cremaldi 


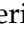



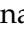

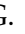


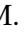





University of Nebraska-Lincoln, Lincoln, Nebraska, USA

K. Bloom , D.R. Claes , G. Haza , J. Hossain , C. Joo , I. Kravchenko , J.E. Siado , W. Tabb , A. Vagnerini , A. Wightman , F. Yan , D. Yu 




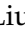



State University of New York at Buffalo, Buffalo, New York, USA

H. Bandyopadhyay , L. Hay , I. Iashvili , A. Kharchilava , M. Morris , D. Nguyen , S. Rappoccio , H. Rejeb Sfar, A. Williams 






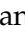


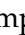
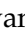










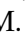





Northeastern University, Boston, Massachusetts, USA

G. Alverson , E. Barberis , J. Dervan, Y. Haddad , Y. Han , A. Krishna , J. Li , M. Lu , G. Madigan , R. Mccarthy , D.M. Morse , V. Nguyen , T. Orimoto , A. Parker , L. Skinnari , B. Wang , D. Wood 


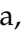
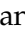
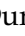




Northwestern University, Evanston, Illinois, USA

S. Bhattacharya , J. Bueghly, Z. Chen , S. Dittmer , K.A. Hahn , Y. Liu , Y. Miao , D.G. Monk , M.H. Schmitt , A. Taliercio , M. Velasco


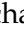
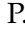
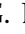
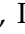
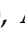


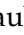









University of Notre Dame, Notre Dame, Indiana, USA

G. Agarwal , R. Band , R. Bucci, S. Castells , A. Das , R. Goldouzian , M. Hildreth , K.W. Ho , K. Hurtado Anampa , T. Ivanov , C. Jessop , K. Lannon , J. Lawrence , N. Loukas , L. Lutton , J. Mariano, N. Marinelli, I. Mcalister, T. McCauley , C. Mcgrady , C. Moore , Y. Musienko¹⁶ , H. Nelson , M. Osherson , A. Piccinelli , R. Ruchti , A. Townsend , Y. Wan, M. Wayne , H. Yockey, M. Zarucki , L. Zygala 


The Ohio State University, Columbus, Ohio, USA

A. Basnet , B. Bylsma, M. Carrigan , L.S. Durkin , C. Hill , M. Joyce , M. Nunez Ornelas , K. Wei, B.L. Winer , B. R. Yates 


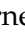



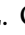




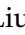








Princeton University, Princeton, New Jersey, USA

F.M. Addesa , H. Bouchamaoui , P. Das , G. Dezoort , P. Elmer , A. Frankenthal , B. Greenberg , N. Haubrich , G. Kopp , S. Kwan , D. Lange , A. Loeliger , D. Marlow , I. Ojalvo , J. Olsen , A. Shevelev , D. Stickland , C. Tully 




University of Puerto Rico, Mayaguez, Puerto Rico, USA

S. Malik 





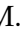






Purdue University, West Lafayette, Indiana, USA

A.S. Bakshi , V.E. Barnes , S. Chandra , R. Chawla , A. Gu , L. Gutay, M. Jones , A.W. Jung , D. Kondratyev , A.M. Koshy, M. Liu , G. Negro , N. Neumeister , G. Paspalaki , S. Piperov , V. Scheurer, J.F. Schulte , M. Stojanovic , J. Thieman , A. K. Viridi , F. Wang , W. Xie 

Purdue University Northwest, Hammond, Indiana, USA

J. Dolen , N. Parashar , A. Pathak 


Rice University, Houston, Texas, USA

D. Acosta , T. Carnahan , K.M. Ecklund , P.J. Fernández Manteca , S. Freed, P. Gardner, F.J.M. Geurts , W. Li , O. Miguel Colin , B.P. Padley , R. Redjimi, J. Rotter , E. Yigitbasi , Y. Zhang 


















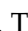

University of Rochester, Rochester, New York, USA

A. Bodek , P. de Barbaro , R. Demina , J.L. Dulemba , A. Garcia-Bellido , O. Hindrichs , A. Khukhunaishvili , N. Parmar, P. Parygin⁹¹ , E. Popova⁹¹ , R. Taus 

The Rockefeller University, New York, New York, USA

K. Goulianos 



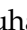










Rutgers, The State University of New Jersey, Piscataway, New Jersey, USA

B. Chiarito, J.P. Chou , S.V. Clark , D. Gadkari , Y. Gershtein , E. Halkiadakis , M. Heindl , C. Houghton , D. Jaroslowski , O. Karacheban³⁰ , I. Laflotte , A. Lath , R. Montalvo, K. Nash, H. Routray , P. Saha , S. Salur , S. Schnetzer, S. Somalwar , R. Stone , S.A. Thayil , S. Thomas, J. Vora , H. Wang 










University of Tennessee, Knoxville, Tennessee, USA

H. Acharya, D. Ally , A.G. Delannoy , S. Fiorendi , S. Higginbotham , T. Holmes , A.R. Kanuganti , N. Karunarathna , L. Lee , E. Nibigira , S. Spanier 

Texas A&M University, College Station, Texas, USA

D. Aebi , M. Ahmad , O. Bouhali⁹² , R. Eusebi , J. Gilmore , T. Huang , T. Kamon⁹³ , H. Kim , S. Luo , R. Mueller , D. Overton , D. Rathjens , A. Safonov 








Texas Tech University, Lubbock, Texas, USA

N. Akchurin , J. Damgov , V. Hegde , A. Hussain , Y. Kazhykarim, K. Lamichhane , S.W. Lee , A. Mankel , T. Peltola , I. Volobouev 

Vanderbilt University, Nashville, Tennessee, USA

E. Appelt , Y. Chen , S. Greene, A. Gurrola , W. Johns , R. Kunnawalkam Elayavalli , A. Melo , F. Romeo , P. Sheldon , S. Tuo , J. Velkovska , J. Viinikainen 

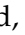



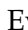


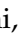

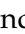

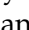








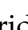

University of Virginia, Charlottesville, Virginia, USA

B. Cardwell , B. Cox , J. Hakala , R. Hirosky , A. Ledovskoy , C. Neu , C.E. Perez Lara 

Wayne State University, Detroit, Michigan, USA





P.E. Karchin 

University of Wisconsin - Madison, Madison, Wisconsin, USA

A. Aravind, S. Banerjee , K. Black , T. Bose , S. Dasu , I. De Bruyn , P. Everaerts , C. Galloni, H. He , M. Herndon , A. Herve , C.K. Koraka , A. Lanaro, R. Loveless , J. Madhusudanan Sreekala , A. Mallampalli , A. Mohammadi , S. Mondal, G. Parida , L. Pétré , D. Pinna, A. Savin, V. Shang , V. Sharma , W.H. Smith , D. Teague, H.F. Tsoi , W. Vetens , A. Warden 

Authors affiliated with an institute or an international laboratory covered by a cooperation agreement with CERN

S. Afanasiev , V. Andreev , Yu. Andreev , T. Aushev , M. Azarkin , I. Azhgirey , A. Babaev , A. Belyaev , V. Blinov⁹⁴, E. Boos , V. Borshch , D. Budkouski , V. Bunichev , M. Chadeeva⁹⁴ , V. Chekhovsky, R. Chistov⁹⁴ , A. Dermenev , T. Dimova⁹⁴ , D. Druzhkin⁹⁵ , M. Dubinin⁸⁴ , L. Dudko , A. Ershov , G. Gavrilo , V. Gavrilo , S. Gninenko , V. Golovtcov , N. Golubev , I. Golutvin , I. Gorbunov , Y. Ivanov , V. Kachanov , V. Karjavine , A. Karneyeu , V. Kim⁹⁴ , M. Kirakosyan, D. Kirpichnikov , M. Kirsanov , V. Klyukhin , O. Kodolova⁹⁶ , D. Konstantinov , V. Korenkov , A. Kozyrev⁹⁴ , N. Krasnikov , A. Lanev , P. Levchenko⁹⁷ , N. Lychkovskaya , V. Makarenko , A. Malakhov , V. Matveev⁹⁴ , V. Murzin , A. Nikitenko^{98,96} , S. Obraztsov , V. Oreshkin , V. Palichik , V. Perelygin , M. Perfilov, S. Polikarpov⁹⁴ , V. Popov , O. Radchenko⁹⁴ , R. Ryutin, M. Savina , V. Savrin , V. Shalaev , S. Shmatov , S. Shulha , Y. Skovpen⁹⁴ , S. Slabospitskii , V. Smirnov , D. Sosnov , V. Sulimov , E. Tcherniaev , A. Terkulov , O. Teryaev , I. Tlisova , A. Toropin , L. Uvarov , A. Uzunian , P. Volkov , A. Vorobyev[†], G. Vorochnikov 

N. Voytishin , B.S. Yuldashev⁹⁹, A. Zarubin , I. Zhizhin , A. Zhokin 

†: Deceased

¹Also at Yerevan State University, Yerevan, Armenia

²Also at TU Wien, Vienna, Austria

³Also at Institute of Basic and Applied Sciences, Faculty of Engineering, Arab Academy for Science, Technology and Maritime Transport, Alexandria, Egypt

⁴Also at Ghent University, Ghent, Belgium

⁵Also at Universidade Estadual de Campinas, Campinas, Brazil

⁶Also at Federal University of Rio Grande do Sul, Porto Alegre, Brazil

⁷Also at UFMS, Nova Andradina, Brazil

⁸Also at Nanjing Normal University, Nanjing, China

⁹Now at The University of Iowa, Iowa City, Iowa, USA

¹⁰Also at University of Chinese Academy of Sciences, Beijing, China

¹¹Also at China Center of Advanced Science and Technology, Beijing, China

¹²Also at University of Chinese Academy of Sciences, Beijing, China

¹³Also at China Spallation Neutron Source, Guangdong, China

¹⁴Now at Henan Normal University, Xinxiang, China

¹⁵Also at Université Libre de Bruxelles, Bruxelles, Belgium

¹⁶Also at an institute or an international laboratory covered by a cooperation agreement with CERN

¹⁷Also at Helwan University, Cairo, Egypt

¹⁸Now at Zewail City of Science and Technology, Zewail, Egypt

¹⁹Also at British University in Egypt, Cairo, Egypt

²⁰Now at Ain Shams University, Cairo, Egypt

²¹Also at Purdue University, West Lafayette, Indiana, USA

²²Also at Université de Haute Alsace, Mulhouse, France

²³Also at Department of Physics, Tsinghua University, Beijing, China

²⁴Also at The University of the State of Amazonas, Manaus, Brazil

²⁵Also at Erzincan Binali Yildirim University, Erzincan, Turkey

²⁶Also at University of Hamburg, Hamburg, Germany

²⁷Also at RWTH Aachen University, III. Physikalisches Institut A, Aachen, Germany

²⁸Also at Isfahan University of Technology, Isfahan, Iran

²⁹Also at Bergische University Wuppertal (BUW), Wuppertal, Germany

³⁰Also at Brandenburg University of Technology, Cottbus, Germany

³¹Also at Forschungszentrum Jülich, Juelich, Germany

³²Also at CERN, European Organization for Nuclear Research, Geneva, Switzerland

³³Also at Institute of Physics, University of Debrecen, Debrecen, Hungary

³⁴Also at Institute of Nuclear Research ATOMKI, Debrecen, Hungary

³⁵Now at Universitatea Babeş-Bolyai - Facultatea de Fizica, Cluj-Napoca, Romania

³⁶Also at MTA-ELTE Lendület CMS Particle and Nuclear Physics Group, Eötvös Loránd University, Budapest, Hungary

³⁷Also at Physics Department, Faculty of Science, Assiut University, Assiut, Egypt

³⁸Also at HUN-REN Wigner Research Centre for Physics, Budapest, Hungary

³⁹Also at Punjab Agricultural University, Ludhiana, India

⁴⁰Also at University of Visva-Bharati, Santiniketan, India

⁴¹Also at Indian Institute of Science (IISc), Bangalore, India

⁴²Also at Birla Institute of Technology, Mesra, Mesra, India

⁴³Also at IIT Bhubaneswar, Bhubaneswar, India

⁴⁴Also at Institute of Physics, Bhubaneswar, India

- ⁴⁵Also at University of Hyderabad, Hyderabad, India
- ⁴⁶Also at Deutsches Elektronen-Synchrotron, Hamburg, Germany
- ⁴⁷Also at Department of Physics, Isfahan University of Technology, Isfahan, Iran
- ⁴⁸Also at Sharif University of Technology, Tehran, Iran
- ⁴⁹Also at Department of Physics, University of Science and Technology of Mazandaran, Behshahr, Iran
- ⁵⁰Also at Italian National Agency for New Technologies, Energy and Sustainable Economic Development, Bologna, Italy
- ⁵¹Also at Centro Siciliano di Fisica Nucleare e di Struttura Della Materia, Catania, Italy
- ⁵²Also at Università degli Studi Guglielmo Marconi, Roma, Italy
- ⁵³Also at Scuola Superiore Meridionale, Università di Napoli 'Federico II', Napoli, Italy
- ⁵⁴Also at Fermi National Accelerator Laboratory, Batavia, Illinois, USA
- ⁵⁵Also at Consiglio Nazionale delle Ricerche - Istituto Officina dei Materiali, Perugia, Italy
- ⁵⁶Also at Department of Applied Physics, Faculty of Science and Technology, Universiti Kebangsaan Malaysia, Bangi, Malaysia
- ⁵⁷Also at Consejo Nacional de Ciencia y Tecnología, Mexico City, Mexico
- ⁵⁸Also at Trincomalee Campus, Eastern University, Sri Lanka, Nilaveli, Sri Lanka
- ⁵⁹Also at Saegis Campus, Nugegoda, Sri Lanka
- ⁶⁰Also at National and Kapodistrian University of Athens, Athens, Greece
- ⁶¹Also at Ecole Polytechnique Fédérale Lausanne, Lausanne, Switzerland
- ⁶²Also at Universität Zürich, Zurich, Switzerland
- ⁶³Also at Stefan Meyer Institute for Subatomic Physics, Vienna, Austria
- ⁶⁴Also at Laboratoire d'Annecy-le-Vieux de Physique des Particules, IN2P3-CNRS, Annecy-le-Vieux, France
- ⁶⁵Also at Near East University, Research Center of Experimental Health Science, Mersin, Turkey
- ⁶⁶Also at Konya Technical University, Konya, Turkey
- ⁶⁷Also at Izmir Bakircay University, Izmir, Turkey
- ⁶⁸Also at Adiyaman University, Adiyaman, Turkey
- ⁶⁹Also at Bozok Universiteleri Rektörlüğü, Yozgat, Turkey
- ⁷⁰Also at Marmara University, Istanbul, Turkey
- ⁷¹Also at Milli Savunma University, Istanbul, Turkey
- ⁷²Also at Kafkas University, Kars, Turkey
- ⁷³Now at Istanbul Okan University, Istanbul, Turkey
- ⁷⁴Also at Hacettepe University, Ankara, Turkey
- ⁷⁵Also at Istanbul University - Cerrahpasa, Faculty of Engineering, Istanbul, Turkey
- ⁷⁶Also at Yildiz Technical University, Istanbul, Turkey
- ⁷⁷Also at Vrije Universiteit Brussel, Brussel, Belgium
- ⁷⁸Also at School of Physics and Astronomy, University of Southampton, Southampton, United Kingdom
- ⁷⁹Also at IPPP Durham University, Durham, United Kingdom
- ⁸⁰Also at Monash University, Faculty of Science, Clayton, Australia
- ⁸¹Also at Università di Torino, Torino, Italy
- ⁸²Also at Bethel University, St. Paul, Minnesota, USA
- ⁸³Also at Karamanoğlu Mehmetbey University, Karaman, Turkey
- ⁸⁴Also at California Institute of Technology, Pasadena, California, USA
- ⁸⁵Also at United States Naval Academy, Annapolis, Maryland, USA
- ⁸⁶Also at Bingöl University, Bingöl, Turkey
- ⁸⁷Also at Georgian Technical University, Tbilisi, Georgia

⁸⁸Also at Sinop University, Sinop, Turkey

⁸⁹Also at Erciyes University, Kayseri, Turkey

⁹⁰Also at Horia Hulubei National Institute of Physics and Nuclear Engineering (IFIN-HH), Bucharest, Romania

⁹¹Now at an institute or an international laboratory covered by a cooperation agreement with CERN

⁹²Also at Texas A&M University at Qatar, Doha, Qatar

⁹³Also at Kyungpook National University, Daegu, Korea

⁹⁴Also at another institute or international laboratory covered by a cooperation agreement with CERN

⁹⁵Also at Universiteit Antwerpen, Antwerpen, Belgium

⁹⁶Also at Yerevan Physics Institute, Yerevan, Armenia

⁹⁷Also at Northeastern University, Boston, Massachusetts, USA

⁹⁸Also at Imperial College, London, United Kingdom

⁹⁹Also at Institute of Nuclear Physics of the Uzbekistan Academy of Sciences, Tashkent, Uzbekistan

Angular analyses of rare decays at the LHC

Biplab Dey, on behalf of the LHCb collaboration^{a,*}

^a*Eotvos University,
Budapest, Hungary*

E-mail: biplab.dey@cern.ch

Loop-suppressed penguin $b \rightarrow s$ transitions are sensitive to heavy New Physics particles propagating inside the loops. Thanks to the large sample sizes from the LHC, we are able to perform multidimensional angular analyses that are sensitive to interferences between the Standard Model and New Physics terms. This article surveys the latest results, primarily from LHCb, on $b \rightarrow s\mu^+\mu^-$ electroweak and $b \rightarrow s\gamma$ radiative penguins.

*16th International Conference on Heavy Quarks and Leptons (HQL2023)
28 November-2 December 2023
TIFR, Mumbai, Maharashtra, India*

*Speaker

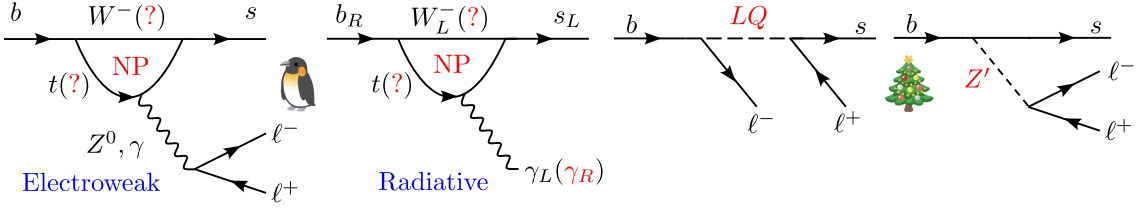


Figure 1: Flavor-changing neutral currents occur only at the loop-level in the SM but can be enhanced by NP effects, both in loop (penguin) and tree-level diagrams.

1. Introduction and theory

In the Standard Model (SM), the flavor-changing neutral current process $b \rightarrow s$ is forbidden at the tree-level and proceeds only via loop-suppressed diagrams as shown in Fig. 1. These provide excellent avenues to probe New Physics (NP) contributions that can enter either in loop- or tree-level processes such as via Leptoquarks (LQ) or heavy Z' boson, as shown in Fig. 1. This article focuses on the electroweak (EWP) and radiative (Rad) penguin diagrams, but gluonic penguins can also be an important NP source. A convenient theoretical formalism to study such decays is to regard the SM as a low energy effective field theory containing dimension $d \leq 4$ local operators from renormalizability requirements. Higher dimensional operators can be added with an appropriate cutoff scale Λ , as

$$\mathcal{L}_{\text{eff}}(x) = \mathcal{L}_{\text{SM}}(x) + \sum_{d>4} \frac{C_i}{\Lambda^{d-4}} \mathcal{O}_i^{(d)}(x) \quad (1)$$

whereby the NP amplitudes have $(E/\Lambda)^{d-4}$ behavior in the energy, E : divergent at high energies, but suppressed at $E \ll \Lambda$. Most relevant for rare $b \rightarrow s$ decays are $d = 6$ operators that yield $\mathcal{A}_{\text{eff}} \sim C^{\text{SM}}/m_W^2 + C^{\text{NP}}/\Lambda_{\text{NP}}^2$. The basis comprises 10 operators [1]: $\mathcal{O}_{1,2}$ (4-quark tree), \mathcal{O}_{3-6} (4-quark penguins) and \mathcal{O}_8 (gluonic penguin) that are suppressed for the EWP/Rad modes. The dominant left-handed contributions are from the electromagnetic dipole and weak vector (axialvector) operators

$$\mathcal{O}_{7\gamma} = \frac{e}{16\pi^2} m_b (\bar{s} \sigma_{\mu\nu} P_R b) F^{\mu\nu}, \quad \mathcal{O}_{9V(10A)} = \frac{e^2}{16\pi^2} (\bar{s} \gamma_\mu P_L b) (\bar{\ell} \gamma^\mu (\gamma_5) \ell). \quad (2)$$

The corresponding right-handed (quark side) operators are suppressed in the SM, but can be enhanced in NP scenarios. The dimensionless couplings (Wilson coefficients) associated with the operators in Eq. 2 encode the short distance physics. They are calculated at the m_W scale by integrating out the heavy degrees of freedom from the full theory and evolving to the m_b scale using renormalization group equations. The total amplitudes $\mathcal{A}(i \rightarrow f) = C_n(m_b) \langle f | \mathcal{O}_n(m_b) | i \rangle_{\text{had}}$ also contains the long-distance physics (QCD/hadronization) which mostly comes from *local* form-factors (FFs) that are computed from lattice QCD and other theory tools, but can get important non-local contributions (rescattering, charm loops) that are hard to estimate theoretically.

Thanks to the large $b\bar{b}$ samples available at the LHC, a comprehensive effort on multidimensional angular analyses in $b \rightarrow s\ell^+\ell^-$ and $b \rightarrow s\vec{\gamma}$ is ongoing. These offer a rich set of angular observables sensitive to $\Delta C_i \equiv C_i^{\text{SM}} - C_i^{\text{NP}}$. The thrust has been to identify and probe “theoretically clean observables” with reduced dependence on the QCD contributions that often form the

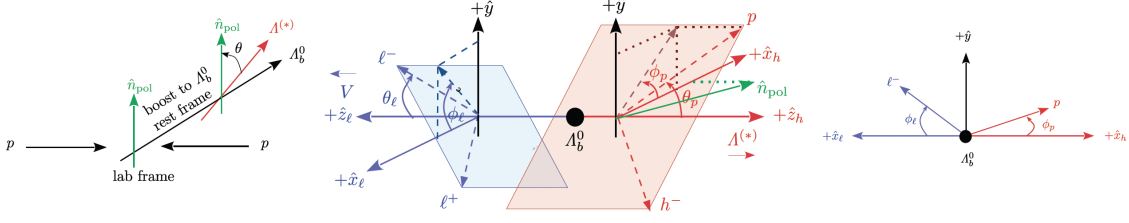


Figure 2: The four angular variables for the decay of a polarized Λ_b^0 decaying to a 4-body final state, $pK^-\ell^+\ell^-$: θ_l (θ_p) is the ℓ^- (proton) helicity angle. The beam direction, Λ^* flight direction and the Λ_b^0 polarization defines a coordinate system relative to which the dilepton and dihadron azimuthal angles can be defined as ϕ_ℓ and ϕ_p .

largest theory uncertainties. The angles for a typical 4-body final state decay is shown in Fig. 2 for $\Lambda_b^0 \rightarrow pK^-\ell^+\ell^-$; the two other kinematic variables being $q^2 \equiv m_{\ell^+\ell^-}^2$ and $k^2 \equiv m_{pK}^2$. For an unpolarized parent Λ_b^0 (or spin-0 $B_{(s)}$ mesons), ϕ_ℓ is set to 0 and $\chi = \phi_p$ is the single azimuthal angle between the dilepton and dihadron decay planes. Equivalent variables apply for $B \rightarrow K\pi\ell^+\ell^-$ and $B_s^0 \rightarrow K^+K^-\ell^+\ell^-$.

2. Electroweak penguins

2.1 The golden channel: $B^0 \rightarrow K^{*0}\ell^+\ell^-$

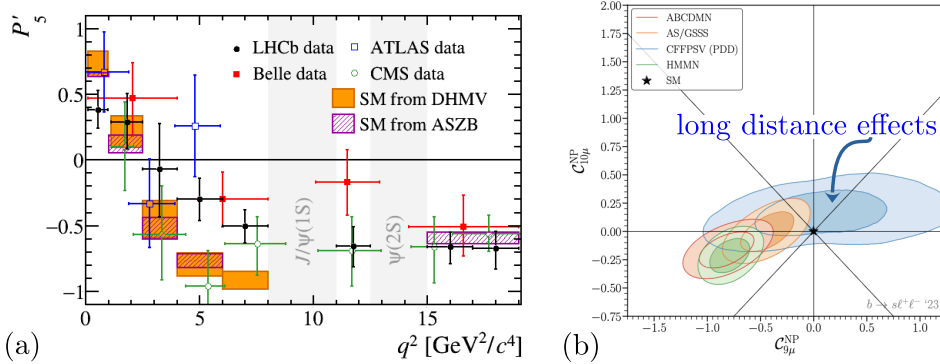


Figure 3: $B^0 \rightarrow K^{*0}\mu^+\mu^-$: (a) world-average of the P'_5 measurements compared to theory (filled/hatched boxes). The situation is representative after publication of the LHCb Run 1 results. (b) effect on $C_{9,10}^{\text{NP}}$ from a recent global fit in Ref. [2].

$B^0 \rightarrow K^{*0}\ell^+\ell^-$ has been a gold-plated channel [1] since the B -factory era due to the relatively narrow K^{*0} (892) resonance. Especially in the low q^2 regime, where the recoiling K^{*0} has a large γ -factor in the parent B^0 frame, QCD sum rules on the light-cone (LCSR) affords control over the FF calculations. However, with the BaBar/Belle statistics, only 1-dimensional angular analyses in either the lepton or hadron helicity angles ($\cos\theta_l$ or $\cos\theta_K$) were possible [3]. Full 3-dimensional analysis in $d\theta_l d\theta_K d\chi$ in q^2 bins was possible only with the advent of LHCb. For instance, while the full BaBar dataset had $\mathcal{O}(50)$ $B^0 \rightarrow K^{*0}(\rightarrow K^+\pi^-)\mu^+\mu^-$ events, the existing Run1+2 LHCb dataset already includes $\mathcal{O}(10^4)$ clean signal events for this muonic mode. On the other hand,

B -factories, including Belle II, have complementary advantages, with better reconstruction for the π^0 isospin modes as well the dielectron channels.

An important result from the muonic analyses at LHCb is tension with SM predictions in the angular observable P'_5 [4] (see Fig. 3a). Similar tensions have also been seen in $B^+ \rightarrow K^{*+} \mu^+ \mu^-$ [5] and $B_s^0 \rightarrow \phi \mu^+ \mu^-$ [6]. A related tension is observed in the overall branching fractions in several $b \rightarrow s \mu^+ \mu^-$ modes which tend to consistently lie lower than the SM predictions [7–9]. Competitive results have also come from ATLAS/CMS [10–12] where the advantage is higher overall luminosity, but the disadvantage is the limited B -physics trigger bandwidth and lack of a RICH detector for $K^+/\pi^+/p$ separation. Numerous global fits with different data subsets, statistical methods and theory priors have been performed [2] pointing to a preferred negative C_9^{NP} . The major point of contention, however, has been the effect of non-factorizable long-distance contributions due to soft+hard gluons from charm-loops that can mimic NP effects (see Fig. 3b). To constrain the non-factorizable part in a data-driven fashion, LHCb has performed an unbinned angular analysis [13, 14] using the same dataset as in Ref. [5]. The underlying transversity amplitudes are

$$\mathcal{A}_{\lambda=0,\parallel,\perp}^{L,R} = N_\lambda \left\{ [(C_9 \pm C'_9) \mp (C_{10} \pm C'_{10})] \mathcal{F}_\lambda + \frac{2m_b M_B}{q^2} [(C_7 \pm C'_7) \mathcal{F}_\lambda^T - 16\pi^2 \frac{M_B}{m_b} \mathcal{H}_\lambda] \right\}, \quad (3)$$

where \mathcal{F}_λ are the usual local FFs (taken from LCSR and lattice QCD) and \mathcal{H}_λ are the new non-factorizable part which are extracted from a q^2 -dependent parameterization. The values of C_i^{SM} are taken from theory, while allowing for $C_{9,10}^{\text{NP}}$ to be floated. The results of the fit are shown in Fig. 4. Good consistency is found in the extracted binned observables compared to Ref. [5]. The overall tension with the SM is reduced to $\sim 1.8\sigma$ in C_9 , and $\sim 1.4\sigma$ in global fits. The full Run 1+2 analysis and more precise theory FFs will improve upon these results.

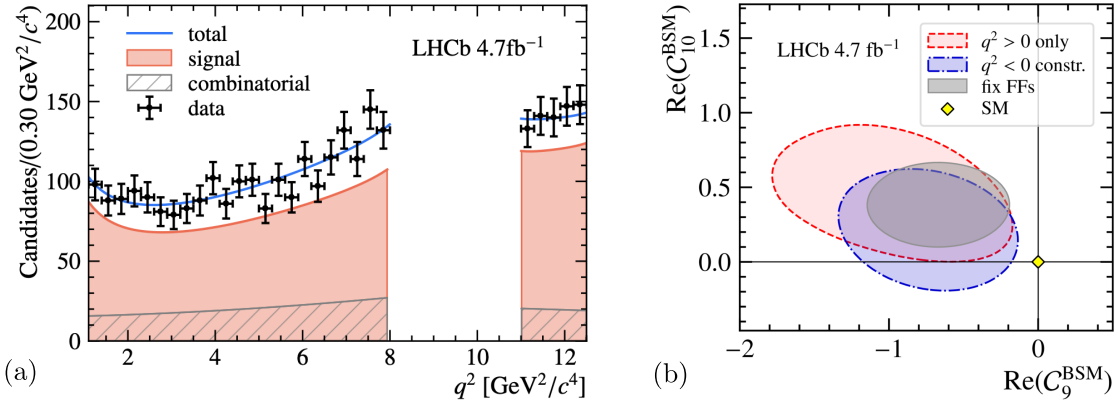


Figure 4: $B^0 \rightarrow K^{*0} \mu^+ \mu^-$ long-distance contribution fits [13, 14]: (a) q^2 projections; (b) effect on $\text{Re}(C_{9,10}^{\text{NP}})$.

2.2 Access to tensor states in $B \rightarrow X_s \mu^+ \mu^-$

While most of the theory and experimental investigations have focused on the ground state vector states $K^*(892)$ and $\phi(1020)$ in B -meson decays, LHCb has also probed the excited $K_{0,2}^*(1430) \rightarrow K^+ \pi^-$ [15] and $f_2'(1525) \rightarrow K^+ K^-$ [7], including an angular moments analysis [16] for the former, to separate the S -, P - and D -wave $K\pi$ states. The results are shown in Fig. 5. The theory interpretation however will require reliable FFs for B decays to these excited states.

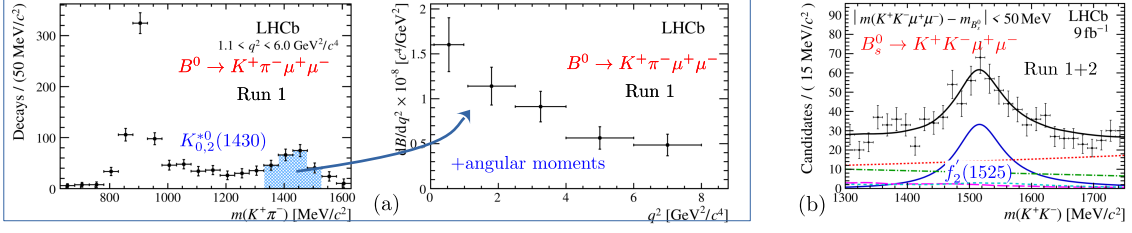


Figure 5: Tensor states in (a) $B^0 \rightarrow K^+\pi^-\mu^+\mu^-$, (b) $B_s^0 \rightarrow K^+K^-\mu^+\mu^-$ decays.

2.3 Angular analysis of $B \rightarrow K\mu^+\mu^-$

For the 3-body final state $B \rightarrow K\mu^+\mu^-$, only the lepton helicity angle, θ_ℓ , can be defined and the SM predicts an almost pure $\sin^2\theta_\ell$ distribution save for small effects due to the muon mass. The angular distribution is sensitive to new scalar and tensor operators via the new terms A_{FB} and F_{H} :

$$d\Gamma/d\cos\theta_\ell \propto \frac{3}{4}(1 - F_{\text{H}})\sin^2\theta_\ell + \frac{1}{2}F_{\text{H}} + A_{\text{FB}}\cos\theta_\ell. \quad (4)$$

Figure 6 shows the results of the fit to Run 1 data for both B^{+0} [17], subject to the constraints $|A_{\text{FB}}| \leq F_{\text{H}}/2$, $0 \leq F_{\text{H}} \leq 3$, such that the rate in Eq. 4 is positive. The extracted A_{FB} and F_{H} in different q^2 bins are also consistent with SM.

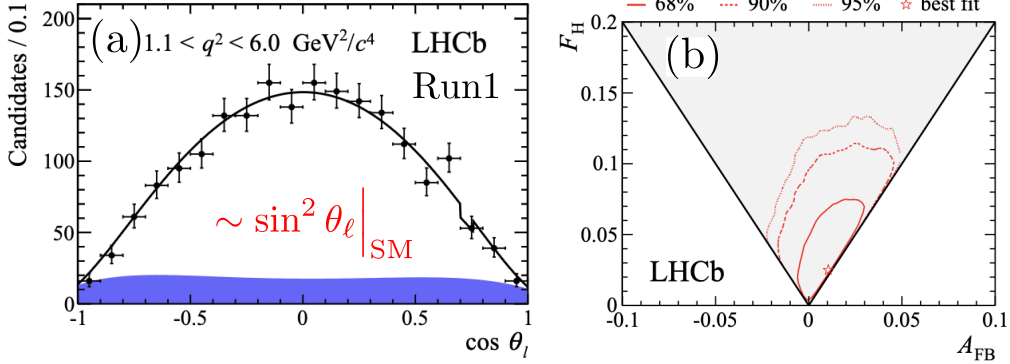


Figure 6: Charged and neutral $B \rightarrow K\mu^+\mu^-$ angular analysis [17]: (a) projection in $\cos\theta_\ell$ showing the expected $\sin^2\theta_\ell$ distribution. (b) extracted A_{FB} and F_{H} with uncertainty contours.

2.4 $\Lambda_b^0 \rightarrow \Lambda\mu^+\mu^-$ moments analysis

LHCb is unique among the B -factories to have access to all b -hadron species, including large samples of Λ_b^0 baryons. Therefore it is possible to probe $b \rightarrow s$ penguin decays in the baryonic sector as well. For $\Lambda_b^0 \rightarrow \Lambda^0$ transition, the narrow Λ^0 state allows lattice QCD calculations [18] for the FFs. For a given value of q^2 , the decay rate for polarized $\vec{\Lambda}_b^0$ and $\vec{\Lambda}^0$ depends on five angles, $\vec{Q} = \{\theta, \theta_\ell, \phi_\ell, \theta_h, \phi_h\}$ (see Fig. 2) and is expanded in an orthonormal angular basis as

$$\frac{d^5\Gamma(q^2)}{d\vec{Q}} = \frac{3}{32\pi^2} \sum_{i=1}^{34} K_i(q^2) f_i(\vec{Q}). \quad (5)$$

The K_i moments can be related to more familiar observables such as forward-backward asymmetries in the angles: $A_{\text{FB}}^{\ell} = [\frac{3}{2}K_3](\rightarrow \cos \theta_l)$, $A_{\text{FB}}^h = [K_4 + \frac{1}{2}K_5](\rightarrow \cos \theta_h)$, $A_{\text{FB}}^{\ell h} = [\frac{3}{4}K_6](\rightarrow \cos \theta_l \cos \theta_h)$. If the Λ_b^0 is unpolarized, only the first 10 moments are non-zero [19]. Due to the long-lived nature of the Λ^0 , its reconstruction in LHCb is somewhat non-trivial. At low q^2 , the Run 1 analysis [8] found very few events. Therefore the analysis using Run 1 + partial Run 2 (collected between 2011-16) [20] focused on the high- q^2 region, $q^2 \in [15, 20]$ GeV². The results are shown in Fig. 7. The SM predictions are taken from the EOS [19] software package and show a slight tension with the data in the K_6 observable.

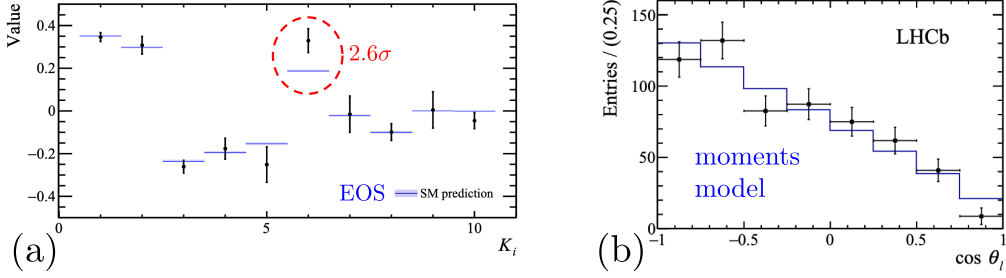


Figure 7: $\Lambda_b^0 \rightarrow \Lambda^0 \mu^+ \mu^-$ angular analysis in $q^2 \in [15, 20]$ GeV² [20]: (a) first 10 moments from Eq. 5; (b) comparison of the background-subtracted data and angular moments model.

2.5 Differential cross-sections for $\Lambda_b^0 \rightarrow \Lambda(1520) \mu^+ \mu^-$

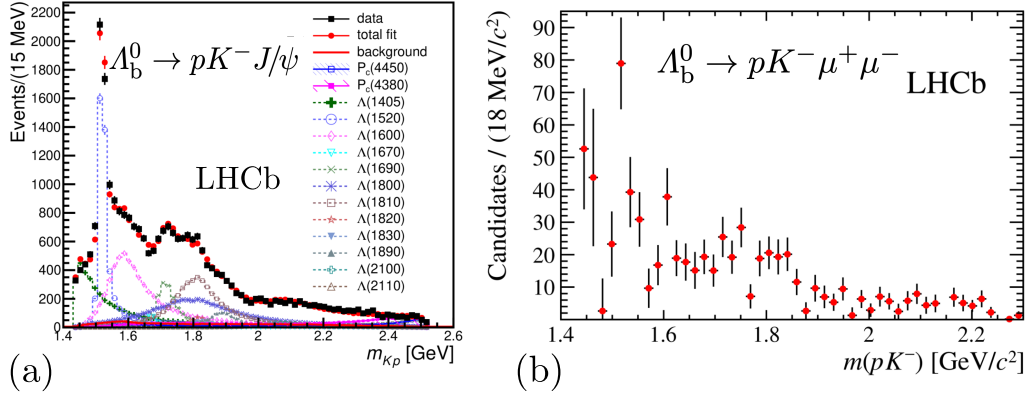


Figure 8: $m(pK^-)$ spectrum from Run 1 $\Lambda_b^0 \rightarrow pK^- \mu^+ \mu^-$ LHCb data: (a) at the J/ψ resonance [21]; (b) in the non-resonant region [22].

The first observation of $\Lambda_b^0 \rightarrow pK^- \mu^+ \mu^-$ decay using LHCb Run 1 data [22] demonstrated a rich $m(pK^-)$ spectrum. The comparison between the resonant and non-resonant spectra is shown in Fig. 8. Employing the full Run 1+2 datasets, LHCb has examined the $m(pK^-)$ region around the narrow $\Lambda(1520)$ resonance. Integrating over the angles and including the resonances $\Lambda(1405)(\frac{1}{2}^-)$, $\Lambda(1520)(\frac{3}{2}^-)$, $\Lambda(1600)(\frac{1}{2}^+)$ and $\Lambda(1800)(\frac{1}{2}^-)$, 1-dimensional fits are performed in $m(pK^-)$. Differential cross-sections for the $\Lambda_b^0 \rightarrow \Lambda(1520) \mu^+ \mu^-$ decay are also provided [23] that show large discrepancies with theory calculations in the low q^2 region (see Fig. 9).

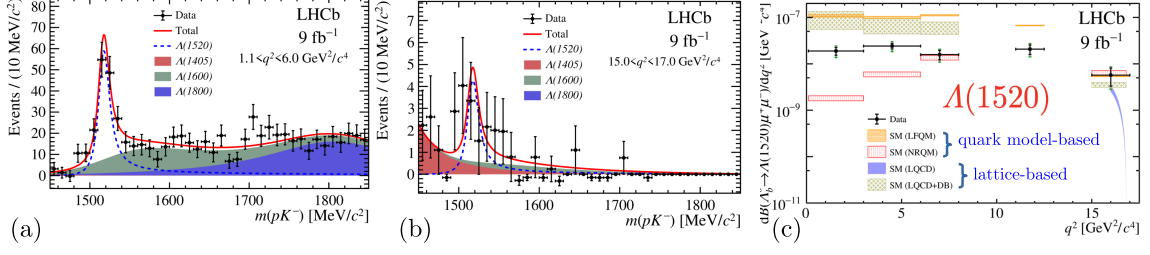


Figure 9: $\Lambda_b^0 \rightarrow \Lambda(1520)\mu^+\mu^-$ [23]: (a) low q^2 , (b) high q^2 , (c) $d\Gamma/dq^2$.

3. Radiative penguins

In the SM, due to the left-handed nature of the weak interaction, the photon from a $b \rightarrow s\gamma$ is almost purely left-handed; the right-handed component is suppressed ($C_7' \sim \frac{m_s}{m_b} C_7$) and is a sensitive NP probe. However, one needs angular analyses to extract the interferences. LHCb probes this in several ways: very low q^2 angular analysis of $B^0 \rightarrow K^{*0}e^+e^-$ [24] and $B_s^0 \rightarrow \phi e^+e^-$; angular analysis of $B^+ \rightarrow K^+\pi^+\pi^-\gamma$ [25]; time-dependent CP violation of $B_s^0 \rightarrow \phi\gamma$ [26] and $B^0 \rightarrow K_S^0\pi^+\pi^-\gamma$; angular analyses of $\Lambda_b^0 \rightarrow \Lambda^{0(*)}\gamma$ [27].

3.1 Angular analysis of $\Lambda_b^0 \rightarrow \Lambda^0\gamma$

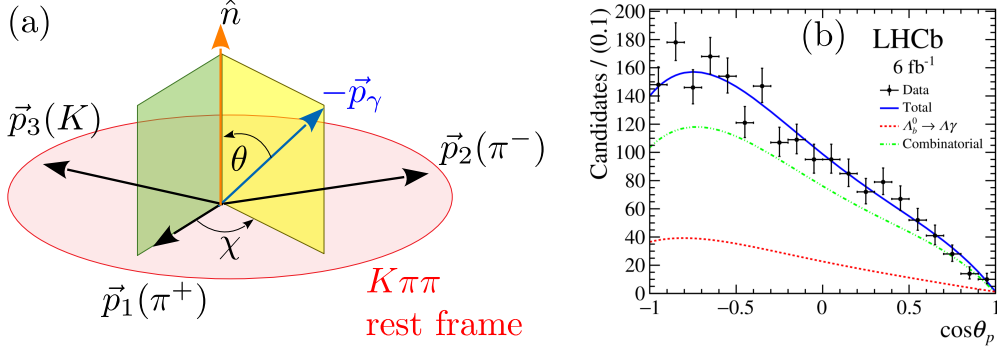


Figure 10: (a) If the hadronic system has a 3-body decay, the normal to the plane defines a preferred direction to extract the photon polarization from the up-down asymmetry in $\cos\theta$ [25]. (b) An exception is the 2-body decay of $\vec{\Lambda} \rightarrow p\pi^-$ where the measurable polarization of the Λ^0 provides the preferred direction.

To measure the photon polarization in $H_b \rightarrow H_s\vec{\gamma}$, the hadronic system must undergo a 3-body decay, so that the normal to the plane defines a preferred direction and the up-down asymmetry is proportional to the photon polarization, λ_γ . For example, this has been utilized in $B^+ \rightarrow K^+\pi^+\pi^-\gamma$ [25] as shown in Fig 10a. In such cases, due to poor knowledge of the resonant structures in the H_s system and thereby the hadronic current $\mathcal{J}_\mu^{\text{had}}$, the proportionality factor remains unknown and λ_γ can still not be extracted out. An exception is the 2-body decay of $\vec{\Lambda}^0 \rightarrow p\pi^-$, where the self-analyzing nature of the Λ^0 polarization provides the preferred direction. Moreover, the differential rate is $d\Gamma/d\cos\theta_p \propto (1 - \alpha_\Lambda\lambda_\gamma\cos\theta)$ where the Λ^0 decay asymmetry parameter α_Λ is known quite precisely [28] and thereby λ_γ can be extracted from a fit to the $\cos\theta_p$ slope, as shown in Fig 10b. Experimentally, $\Lambda_b^0 \rightarrow \Lambda^0\gamma$ is challenging due to lack of a reconstructible secondary

vertex for the Λ_b^0 decay. Employing dedicated reconstruction to reject the high background, the first observation with Run 2 2016 data was reported in Ref. [29] and the polarization measurement with full Run 2 was reported in Ref. [27]. The measured value of $\alpha_\gamma = 0.82^{+0.17}_{-0.26}(\text{stat.})^{+0.04}_{-0.13}(\text{syst.})$ is compatible with the SM expectation of 1 and from global $C_7^{(\prime)}$ fits, reducing a 4-fold ambiguity in the C_7^{NP} phase to a 2-fold ambiguity.

3.2 Angular analysis of $\Lambda_b^0 \rightarrow pK^- \gamma$

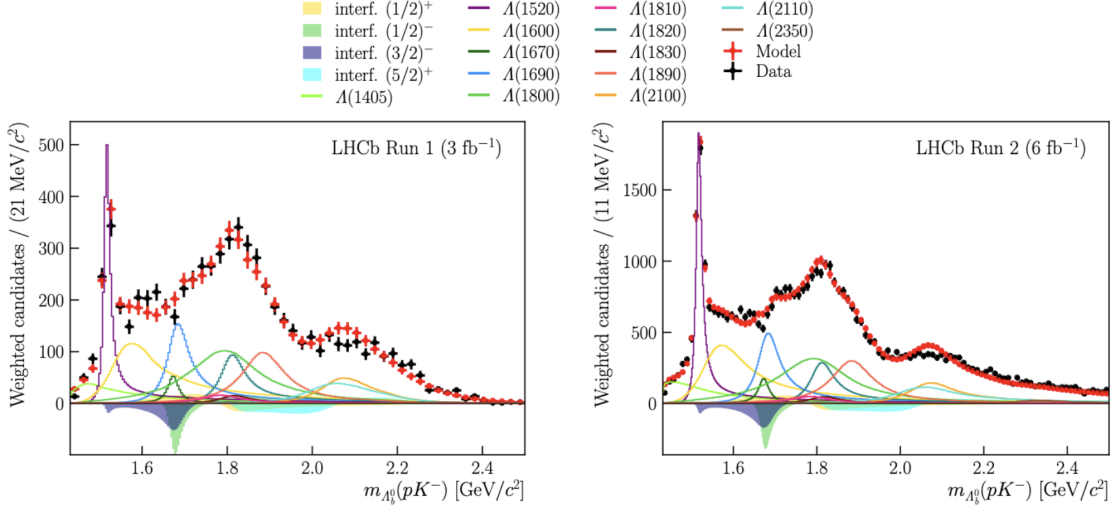


Figure 11: Fit projections for $\Lambda_b^0 \rightarrow pK^- \gamma$ in the $m(pK)$ variable. The shaded areas depict interferences between Λ^* states with the same spin-parity.

As for the electroweak penguin case in Sec. 2.5, for the radiative $\Lambda_b^0 \rightarrow \Lambda^*(pK^-)\gamma$ decay, the $[pK^-]$ system is dominated by a large number of overlapping resonances. Employing the full Run1+2 data, LHCb has performed a 2-dimensional angular analysis of this mode in $\{m(pK), \cos \theta_p\}$. All well-established Λ^* states [28] are included in an isobar model with Breit-Wigner lineshapes incorporating mass-dependent widths. The only exception is the $\Lambda(1405)$ resonance where a two-pole Flatte-form is used. To reduce the large set of parameters, the maximum orbital angular momentum of the $\Lambda^* \rightarrow pK^-$ decay is taken to be $L = 3$. The result from such a *reduced* model is shown in Fig. 11. The fit fractions and interference fit fractions are reported from the amplitude analysis.

4. Summary and outlook

The large existing Run 1+2 data samples at the LHC has already allowed the hitherto (pre-LHC) “rare” $b \rightarrow s$ decays to be probed in an unprecedented fashion. This will continue into the LHCb upgrade era, with Run 3 having already commenced. Multi-dimensional angular analyses in both the electroweak and radiative penguin sectors have given rise to surprising tensions. A large and mature angular analysis effort exists at LHCb which will continue to evolve. The thrust will be to include time-dependent CP violation [30] in more rare decay angular analyses, as well as to probe the further Cabibbo-suppressed $b \rightarrow d$ transitions [31, 32].

References

- [1] W. Altmannshofer, P. Ball, A. Bharucha, A.J. Buras, D.M. Straub and M. Wick, *Symmetries and Asymmetries of $B \rightarrow K^* \mu^+ \mu^-$ Decays in the Standard Model and Beyond*, *JHEP* **01** (2009) 019 [[0811.1214](#)].
- [2] B. Capdevila, A. Crivellin and J. Matias, *Review of Semileptonic B Anomalies*, *Eur. Phys. J. ST* **1** (2023) 20 [[2309.01311](#)].
- [3] BABAR collaboration, *Measurement of Branching Fractions and Rate Asymmetries in the Rare Decays $B \rightarrow K^{(*)} l^+ l^-$* , *Phys. Rev. D* **86** (2012) 032012 [[1204.3933](#)].
- [4] LHCb collaboration, *Measurement of CP-Averaged Observables in the $B^0 \rightarrow K^{*0} \mu^+ \mu^-$ Decay*, *Phys. Rev. Lett.* **125** (2020) 011802 [[2003.04831](#)].
- [5] LHCb collaboration, *Angular Analysis of the $B^+ \rightarrow K^{*+} \mu^+ \mu^-$ Decay*, *Phys. Rev. Lett.* **126** (2021) 161802 [[2012.13241](#)].
- [6] LHCb collaboration, *Angular analysis of the rare decay $B_s^0 \rightarrow \phi \mu^+ \mu^-$* , *JHEP* **11** (2021) 043 [[2107.13428](#)].
- [7] LHCb collaboration, *Branching Fraction Measurements of the Rare $B_s^0 \rightarrow \phi \mu^+ \mu^-$ and $B_s^0 \rightarrow f_2'(1525) \mu^+ \mu^-$ Decays*, *Phys. Rev. Lett.* **127** (2021) 151801 [[2105.14007](#)].
- [8] LHCb collaboration, *Differential branching fraction and angular analysis of $\Lambda_b^0 \rightarrow \Lambda \mu^+ \mu^-$ decays*, *JHEP* **06** (2015) 115 [[1503.07138](#)].
- [9] LHCb collaboration, *Differential branching fractions and isospin asymmetries of $B \rightarrow K^{(*)} \mu^+ \mu^-$ decays*, *JHEP* **06** (2014) 133 [[1403.8044](#)].
- [10] ATLAS collaboration, *Angular analysis of $B_d^0 \rightarrow K^* \mu^+ \mu^-$ decays in pp collisions at $\sqrt{s} = 8$ TeV with the ATLAS detector*, *JHEP* **10** (2018) 047 [[1805.04000](#)].
- [11] CMS collaboration, *Measurement of angular parameters from the decay $B^0 \rightarrow K^{*0} \mu^+ \mu^-$ in proton-proton collisions at $\sqrt{s} = 8$ TeV*, *Phys. Lett. B* **781** (2018) 517 [[1710.02846](#)].
- [12] CMS collaboration, *Angular analysis of the decay $B^+ \rightarrow K^*(892)^+ \mu^+ \mu^-$ in proton-proton collisions at $\sqrt{s} = 8$ TeV*, *JHEP* **04** (2021) 124 [[2010.13968](#)].
- [13] LHCb collaboration, *Amplitude analysis of the $B^0 \rightarrow K^{*0} \mu^+ \mu^-$ decay*, [2312.09115](#).
- [14] LHCb collaboration, *Determination of short- and long-distance contributions in $B^0 \rightarrow K^{*0} \mu^+ \mu^-$ decays*, [2312.09102](#).
- [15] LHCb collaboration, *Differential branching fraction and angular moments analysis of the decay $B^0 \rightarrow K^+ \pi^- \mu^+ \mu^-$ in the $K_{0,2}^*(1430)^0$ region*, *JHEP* **12** (2016) 065 [[1609.04736](#)].
- [16] B. Dey, *Angular analyses of exclusive $\bar{B} \rightarrow X \ell_1 \ell_2$ with complex helicity amplitudes*, *Phys. Rev. D* **92** (2015) 033013 [[1505.02873](#)].

- [17] LHCb collaboration, *Angular analysis of charged and neutral $B \rightarrow K\mu^+\mu^-$ decays*, *JHEP* **05** (2014) 082 [[1403.8045](#)].
- [18] W. Detmold and S. Meinel, *$\Lambda_b \rightarrow \Lambda\ell^+\ell^-$ form factors, differential branching fraction, and angular observables from lattice QCD with relativistic b quarks*, *Phys. Rev. D* **93** (2016) 074501 [[1602.01399](#)].
- [19] D. van Dyk et al., *Eos – a hep program for flavor observables*, 2016. 10.5281/zenodo.886055.
- [20] LHCb collaboration, *Angular moments of the decay $\Lambda_b^0 \rightarrow \Lambda\mu^+\mu^-$ at low hadronic recoil*, *JHEP* **09** (2018) 146 [[1808.00264](#)].
- [21] LHCb collaboration, *Observation of $J/\psi p$ Resonances Consistent with Pentaquark States in $\Lambda_b^0 \rightarrow J/\psi K^- p$ Decays*, *Phys. Rev. Lett.* **115** (2015) 072001 [[1507.03414](#)].
- [22] LHCb collaboration, *Observation of the decay $\Lambda_b^0 \rightarrow pK^-\mu^+\mu^-$ and a search for CP violation*, *JHEP* **06** (2017) 108 [[1703.00256](#)].
- [23] LHCb collaboration, *Measurement of the $\Lambda_b^0 \rightarrow \Lambda(1520)\mu^+\mu^-$ differential branching fraction*, *Phys. Rev. Lett.* **131** (2023) 151801 [[2302.08262](#)].
- [24] LHCb collaboration, *Strong constraints on the $b \rightarrow s\gamma$ photon polarisation from $B^0 \rightarrow K^{*0}e^+e^-$ decays*, *JHEP* **12** (2020) 081 [[2010.06011](#)].
- [25] LHCb collaboration, *Observation of Photon Polarization in the $b \rightarrow s\gamma$ Transition*, *Phys. Rev. Lett.* **112** (2014) 161801 [[1402.6852](#)].
- [26] LHCb collaboration, *First experimental study of photon polarization in radiative B_s^0 decays*, *Phys. Rev. Lett.* **118** (2017) 021801 [[1609.02032](#)].
- [27] LHCb collaboration, *Measurement of the photon polarization in $\Lambda_b^0 \rightarrow \Lambda\gamma$ decays*, *Phys. Rev. D* **105** (2022) L051104 [[2111.10194](#)].
- [28] PARTICLE DATA GROUP collaboration, *Review of Particle Physics*, *PTEP* **2022** (2022) 083C01.
- [29] LHCb collaboration, *First Observation of the Radiative Decay $\Lambda_b^0 \rightarrow \Lambda\gamma$* , *Phys. Rev. Lett.* **123** (2019) 031801 [[1904.06697](#)].
- [30] LHCb collaboration, *Measurement of CP-violating and mixing-induced observables in $B_s^0 \rightarrow \phi\gamma$ decays*, *Phys. Rev. Lett.* **123** (2019) 081802 [[1905.06284](#)].
- [31] LHCb collaboration, *Observation of the suppressed decay $\Lambda_b^0 \rightarrow p\pi^-\mu^+\mu^-$* , *JHEP* **04** (2017) 029 [[1701.08705](#)].
- [32] LHCb collaboration, *First measurement of the differential branching fraction and CP asymmetry of the $B^\pm \rightarrow \pi^\pm\mu^+\mu^-$ decay*, *JHEP* **10** (2015) 034 [[1509.00414](#)].

Determination of the resonant parameters of $\chi_{c0}(3915)$ with global fit

Chunhua Li^{1,2*} and Xijun Wang^{1,2}, Chen Wu^{1,2}

¹*Department of physics and electronic technology,*

²*Center for Theoretical and Experimental High Energy Physics,
Liaoning Normal University
Dalian, 116029, P.R.China*

The $\chi_{c0}(3915)$ was observed firstly by the Belle experiment in the $\omega J/\psi$ invariant mass spectrum in the process $B \rightarrow K\omega J/\psi$, and then confirmed by the Babar experiment. The two experiments reported the resonant parameters of this particle in the both processes $\gamma\gamma \rightarrow \omega J/\psi$ and $B \rightarrow K\omega J/\psi$ by assuming $\chi_{c0}(3915)$ as a S-wave Breit-Wigner resonance. We perform a global fit to the distributions of invariant mass of $\omega J/\psi$ measured by the Belle and Babar experiments, and incorporate the measurement by the LHCb experiment additionally to extract the mass and width of $\chi_{c0}(3915)$. We obtain $M = 3921.0 \pm 0.9$ MeV/ c^2 and $\Gamma = 17.9 \pm 2.2$ MeV which are in good agreement with the values on PDG but with higher precision.

I. INTRODUCTION

Since the first charmonium-like state $X(3872)$ was discovered by Belle experiment via the process $e^+e^- \rightarrow \gamma_{ISR}\pi^+\pi^-J/\psi$, a new era of the study of charmonium-like states was triggered [1]. A series of mesons comprised of charmed and anticharmed quark pairs, such as the $Y(4260)$, $X(3915)$, and $Z_c(3900)$, were subsequently discovered, and most of them were confirmed by different experiments [2–11]. The understanding of the nature of these particles has turned out to be quite a challenge. Many of them have properties that are quite different from the conventional charmonium, e.g. low open-charm decay rate or absence of hadronic transitions to other charmonium states. To explain these anomalous features, many models have been proposed by theorists, including charmonium molecule mixed states [12, 13], $c\bar{c}g$ hybrid states [15], and tetra-quarks [14]. In addition, the production rates for some of these charmonium-like states are quite low in most experiments which limits the measurement precision of the resonant parameters and the determination of the corresponding quantum numbers, which make the interpretation of these particles difficult. Particle Data Group (PDG) [16] has assigned the $X(3915)$ and $X(3872)$ as the excited spin-triplet charmonium states $\chi_{c0}(2P)$ and $\chi_{c1}(2P)$ named $\chi_{c0}(3915)$ and $\chi_{c1}(3915)$, respectively. We just follow the PDG name convention in the article.

As a member of charmonium-like family of states, the $\chi_{c0}(3915)$ was first observed by the Belle experiment in the process $B \rightarrow KJ/\psi\omega$ in a data sample containing 275×10^6 $B\bar{B}$ pairs [9]. The measured mass and width were determined to be $3943 \pm 11 \pm 13$ MeV/ c^2 and $87 \pm 22 \pm 26$ MeV with the assumption that the $\chi_{c0}(3915)$ is an S-wave Breit-Wigner (BW) resonance. The particle was confirmed by Babar experiment in the same decay mode with a 383×10^6 $B\bar{B}$ event data sample [10], their reported mass and width were $3914.6^{+3.8}_{-3.4} \pm 2.0$ MeV/ c^2 and $34^{+12}_{-8} \pm 5$ MeV. Babar experiment subsequently updated their measurements with a larger data sample of 467×10^6 $B\bar{B}$ events and looser $M(\pi^+\pi^-\pi^0)$ requirements that revealed a $X(3872)$ signal as well [11]; the updated mass and width were $3919.1^{+3.8}_{-3.4} \pm 2.0$ MeV/ c^2 and $31^{+10}_{-8} \pm 5$ MeV. In addition, the $\chi_{c0}(3915)$ was also observed in the two-photon collision process $\gamma\gamma \rightarrow \omega J/\psi$ by both the Babar and Belle experiments [7, 8]. Their measured masses and widths are listed in Table I. Babar did a spin-parity analysis in their analysis and obtained the quantum number to be $J^P = 0^+$, and identified the $\chi_{c0}(3915)$ as the $\chi_{c0}(2P)$ charmonium state. However, this assignment was disputed because of the large rate for $\chi_{c0}(3915) \rightarrow \omega J/\psi$ decay and the absence of $\chi_{c0}(3915) \rightarrow D\bar{D}$ decays [17, 18]. Moreover, the mass difference between the $\chi_{c2}(2P)$ and $\chi_{c0}(3915)$ is only about 10 MeV, which is too small for the fine splitting of P -wave charmonia [17]. In 2020, LHCb experiment made an amplitude analysis of the $B^+ \rightarrow D^+D^-K^+$ decay [19], and reported that the spin-0 resonance is of necessity to describe the data well and determined its mass and width to be $2923.8 \pm 1.5 \pm 0.4$ MeV/ c^2 and $17.4 \pm 5.1 \pm 0.8$ MeV, respectively.

In this article, we perform a simultaneous χ^2 fit to the distributions of invariant mass of $\omega J/\psi$ in the processes of $\gamma\gamma \rightarrow \omega J/\psi$ measured by Belle [denoted as (a)], $\gamma\gamma \rightarrow \omega J/\psi$ by Babar [(b)], $B^0 \rightarrow \omega J/\psi K^0$ by Babar [(c)], $B^+ \rightarrow \omega J/\psi K^+(d)$ by Babar, and $B \rightarrow \omega J/\psi K$ by Belle [(e)] to extract the mass and width of $\chi_{c0}(3915)$. The distributions of $M(\omega J/\psi)$ for these processes are shown in Figure 1. Furthermore, LHCb's results are taken into

* chunhua@lnnu.edu.cn

account as an additional component in the χ^2 calculation. Compared to the values on PDG who also gives the $\chi_{c0}(3915)$ mass and width by combining the measurements by these experiments, we use more detailed information of the $\omega J/\psi$ invariant mass spectrum which expect to provide a result of higher precision.

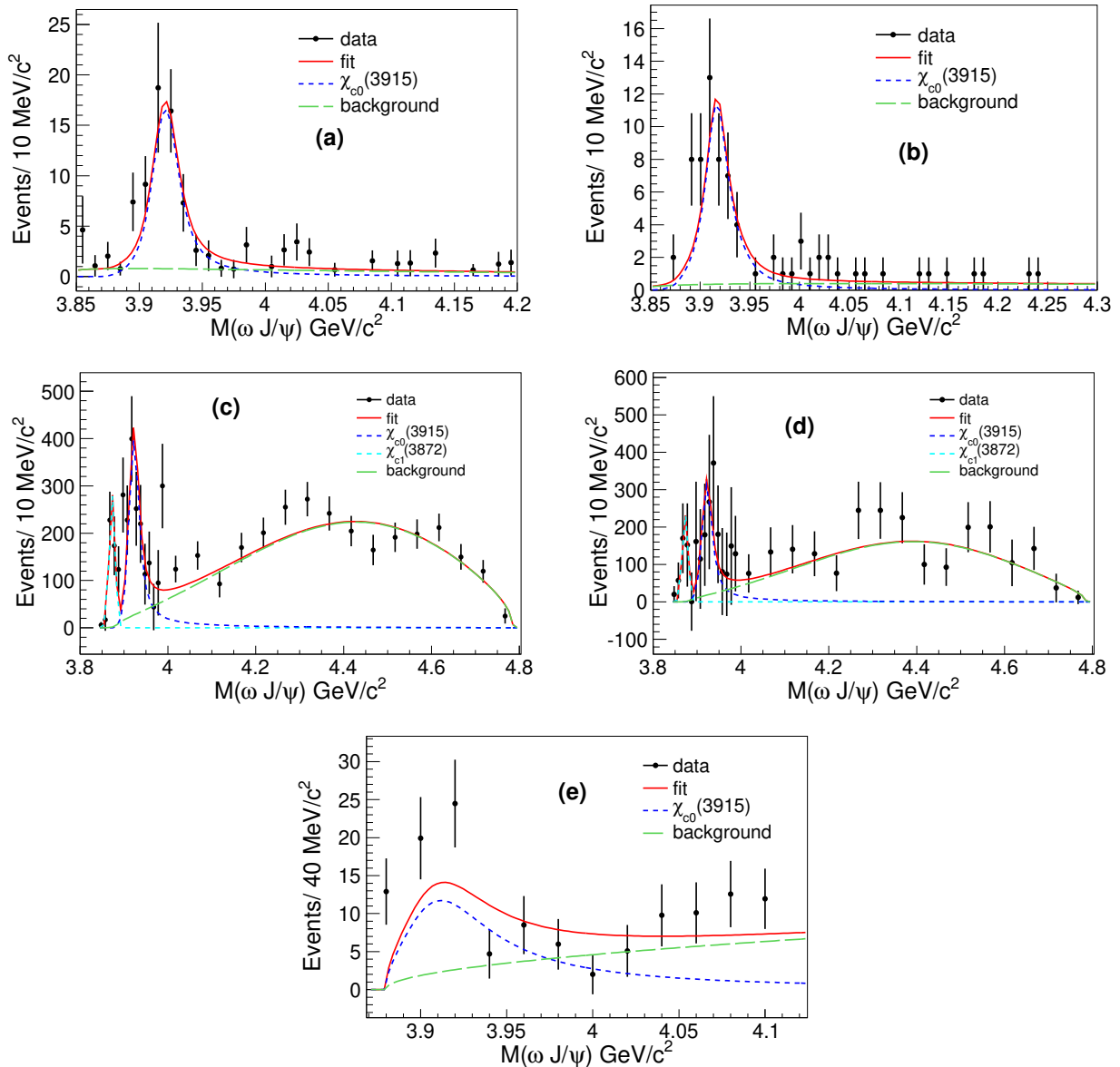


FIG. 1. Fit to the distributions of the $\omega J/\psi$ invariant mass. The black dots with error bars are the data mentioned in the main text. The red solid curves are the fit results, the cyan/blue dashed curves indicate the $\chi_{c1}(3872)/\chi_{c0}(3915)$ signals, and the green dashed curves show the backgrounds.

II. SIMULTANEOUS χ^2 FIT

In the simultaneous χ^2 fit, the functions used to fit the $M(\omega J/\psi)$ spectra in Fig. 1 are similar to those applied in their corresponding publications. The fit function is comprised of signal and background components. The $\chi_{c0}(3915)$ signal shape is described by a S-wave BW function convoluted with the detector resolutions. The BW is $\frac{\Gamma(p^*/p_0)}{(m^2 - M^2)^2 + (M\Gamma(p^*/p_0))^2}$, where M is the peak mass, p^* is the momentum of J/ψ momentum in the rest frame of a $\omega J/\psi$ system, and $p_0 = p^*$ when $m = M$ [20]. M and Γ are common parameters for the four measurements that are

allowed float in the fitting. The contributions of the $\chi_{c1}(3872)$ are needed for the measurements (c) and (d) as shown in Fig. 1. The signal shape of the $\chi_{c1}(3872)$ is described with a simple BW function with a fixed mass and width of 3871.69 MeV/ c^2 and 1.2 MeV, respectively. The detector resolution of $\gamma\gamma \rightarrow \omega J/\psi$ for Belle is described by a double Gaussian function, one Gaussian has the mean and deviation values of 4.5 MeV and 0 MeV, respectively, with a coefficient of 0.59, and the other one has 16 MeV and -4.0 MeV with a coefficient of 0.41 [7]. The resolution for the process $\gamma\gamma \rightarrow \omega J/\psi$ by Babar is described by a single Gaussian with a deviation of 6.7 MeV and a mean value of zero. The resolution for the measurement $B \rightarrow K\omega J/\psi$ by Babar is described by a single Gaussian function with a deviation of 5.7 MeV and a mean value of zero. All of the resolution information is from the corresponding publications. The non-resonance background shapes for the measurement (a) and (b) are both described as $p^*(m)\exp(-\delta p^*(m))$, where δ is a parameter that is allowed to float in the fitting, and $m = m(J/\psi\omega)$ [8]. The background shapes of the measurement (c) and (d) are described with a Gaussian function with parameters that float in the fitting [11]. The shape of the background in the measurement (e) is described with the J/ψ momentum in the rest frame of a $\omega J/\psi$ system, $p^*(M)$. The mass and width are the common parameters in all the $\chi_{c0}(3915)$ BW functions and allowed to be free in the fit.

The χ^2 is defined as

$$\chi^2 = \sum_{i=1}^5 \sum_{j=1}^{N_i} \left(\frac{x_{ij} - \mu_{ij}}{\sigma_{ij}} \right)^2 + \left(\frac{M_h - M}{\sigma_{M_h}} \right)^2 + \left(\frac{\Gamma_h - \Gamma}{\sigma_{\Gamma_h}} \right)^2 \quad (1)$$

where i have values from 1 to 5, corresponding to the measurements (a) to (e), x_{ij} and σ_{ij} are the observed signals and corresponding errors in each bin as shown in Fig. 1, μ_{ij} is the expected value in each bin calculated with the fitting shape mentioned above, and N_i is the number of bins in each measurement. The bin width of the measurements (a) and (b), shown in the published papers [7, 8], is 10 MeV, however, the number of observed events in each bin in the mass region of 3.95 GeV to 4.3 GeV is very small, so the bin width is reset to be 50 MeV in this region to ensure that statistics in each bin are large enough to make a meaningful calculation of their contribution to the χ^2 value. The numbers of bins in the measurement (a) and (b) are $N_1=19$ and $N_2=15$. For the measurements (c) and (d), the bin width in the mass region of 3.8425 to 3.9925 GeV/ c^2 is 10 MeV/ c^2 , and 50 MeV/ c^2 in the region beyond 3.9925 GeV/ c^2 as shown in Fig. 1. The bin numbers N_3 and N_4 are both 31. For the measurement (e), $N_5=12$. The rest two components of the χ^2 formula, $\frac{M_h - M}{\sigma_{M_h}}$ and $\frac{\Gamma_h - \Gamma}{\sigma_{\Gamma_h}}$, are the measurements from the LHCb experiment, where M_h and Γ_h are the measured mass and width, and σ_{M_h} and σ_{Γ_h} the corresponding statistical uncertainties.

By minimizing the χ^2 with MINUIT [21], we obtained the fit results with $M = 3921.0 \pm 0.8$ MeV/ c^2 and $\Gamma = 17.9 \pm 2.1$ MeV. The goodness of fit is $\chi^2/ndf = 113.1/87$ where ndf is the number of degree of freedom in the fit. The fit results are also shown in Fig. 1.

The total systematic uncertainty of the mass and width, σ_{sum} , is obtained with the formula $\frac{1}{\sigma_{\text{sum}}^2} = \sum_{i=1}^5 \frac{1}{\sigma_i^2}$, where the i has a value from 1 to 5 corresponding to each measurement listed in Table I, and σ_i is the systematic uncertainty of the i -th measurement. Combining with the statistical uncertainties from the previous fit, we finally get the results of $M = 3921.0 \pm 0.9$ MeV/ c^2 and $\Gamma = 17.9 \pm 2.2$ MeV.

TABLE I. Mass (M) and width (Γ) of the $\chi_{c0}(3915)$ measured by the different experiments, where the first uncertainty is the statistical and the second is systematic. The results from PDG and this work are listed in the last two rows.

Experiment	Production	M (MeV/ c^2)	Γ (MeV)
Belle [9]	$B \rightarrow \omega J/\psi K$	$3943 \pm 11 \pm 13$	$87 \pm 22 \pm 26$
Babar [11]	$B \rightarrow \omega J/\psi K$	$3919.1_{-3.4}^{+3.8} \pm 2.0$	$31_{-8}^{+10} \pm 5$
Belle [7]	$\gamma\gamma \rightarrow \omega J/\psi$	$3915 \pm 3 \pm 2$	$13 \pm 6 \pm 3$
Babar [8]	$\gamma\gamma \rightarrow \omega J/\psi$	$3919.4 \pm 2.2 \pm 1.6$	$17 \pm 10 \pm 3$
LHCb [19]	$B^+ \rightarrow D^+ D^- K^+$	$2923.8 \pm 1.5 \pm 0.4$	$17.4 \pm 5.1 \pm 0.8$
PDG [16]		3921.7 ± 1.8	18.8 ± 3.5
This work		3921.0 ± 0.9	17.9 ± 2.2

III. SUMMARY

In summary, we determine the resonant parameters of $\chi_{c0}(3915)$ by simultaneously fitting the measurements provided by the Belle, Babar, and LHCb experiments. The mass and width are determined to be $M = 3921.0 \pm 0.9$ MeV/ c^2 and $\Gamma = 17.9 \pm 2.2$ MeV, respectively, which are in good agreement the average values in PDG but with higher precision.

ACKNOWLEDGMENTS

This work is supported by National Natural Science Foundation of China (NSFC) under contract No. 11805090.

- [1] S. K. Choi *et al.* [Belle], Phys. Rev. Lett. **91**, 262001 (2003).
- [2] B. Auber *et al.* [BaBar] Phys. Rev. Lett. **95**, 042001 (2005).
- [3] Q. He *et al.* [CLEO], Phys. Rev. D **74**, 091104 (2006).
- [4] C. Z. Yuan *et al.* [Belle], Phys. Rev. Lett. **99**, 0182004 (2007).
- [5] M. Ablikim *et al.* [BESIII], Phys. Rev. Lett. **110**, 252001 (2013).
- [6] Z. Q. Liu *et al.* [Belle], Phys. Rev. Lett. **110**, 252002 (2013).
- [7] S. Uehara *et al.* [Belle], Phys. Rev. Lett. **104**, 092001 (2010).
- [8] J. P. Lees *et al.* [BaBar], Phys. Rev. D **86**, 072002 (2012).
- [9] K. Abe *et al.* [Belle], Phys. Rev. Lett. **94**, 182002 (2005).
- [10] B. Aubert *et al.* [BaBar], Phys. Rev. Lett. **101**, 082001 (2008).
- [11] P. del Amo Sanchez *et al.* [BaBar], Phys. Rev. D **82**, 011101 (2010).
- [12] R. D. Matheus, F. S. Navarra, M. Nielsen and C. M. Zanetti, Phys. Rev. D **80**, 056002 (2009).
- [13] W. Chen, H. y. Jin, R. T. Kleiv, T. G. Steele, M. Wang and Q. Xu, Phys. Rev. D **88**, no.4, 045027 (2013).
- [14] L. Maiani, F. Piccinini, A. D. Polosa and V. Riquer, Phys. Rev. D **71**, 014028 (2005).
- [15] B. A. Li, Phys. Lett. B **605**, 306-310 (2005).
- [16] R. L. Workman *et al.* (Particle Data Group), PTEP, 2022, 083C01 (2022).
- [17] F. K. Guo and U. G. Meissner, Phys. Rev. D **86**, 091501 (2012).
- [18] S. L. Olsen, Phys. Rev. D **91**, no.5, 057501 (2015).
- [19] R. Aaij *et al.* [LHCb], Phys. Rev. D **102** (2020), 112003.
- [20] K. Abe *et al.* [Belle], Phys. Rev. Lett. **94**, 182002 (2005).
- [21] F. James and M. Roos, Comput. Phys. Commun. **10**, 343 (1975).

Strangeness plus-one ($S = +1$) resonance-state P_0^{+*} via $K^+n \rightarrow K^{*0}p$

Dayoung Lee^{1,2,*} and Seung-il Nam^{1,2,3,†}

¹*Department of Physics, Pukyong National University (PKNU), Busan 48513, Korea*

²*Center for Extreme Nuclear Matters (CENuM), Korea University, Seoul 02841, Korea*

³*Asia Pacific Center for Theoretical Physics (APCTP), Pohang 37673, Korea*

(Dated: March 5, 2024)

In our current study, we delve into the peak-like structure observed during the reaction process of $K^+n \rightarrow K^0p$ at approximately $\sqrt{s} \sim 2.5$ GeV. Our focus centers on exploring the potential $S = +1$ resonance $P_0^{+*} \equiv P_0^*$ as an excited state within the extended vector-meson and baryon (VB) antidecuplet. To achieve this aim, we employ the effective Lagrangian method in conjunction with the (u, t) -channel Regge approach, operating within the tree-level Born approximation. We thoroughly examine various spin-parity quantum numbers for the resonance, resulting in a compelling description of the data, where $M_{P_0^*} \approx 2.5$ GeV and $\Gamma_{P_0^*} \approx 100$ MeV. Furthermore, we propose an experimental technique to amplify the signal-to-noise ratio (S/N) for accurately measuring the resonance. Notably, our findings reveal that background interference diminishes significantly within the K^* forward-scattering region in the center-of-mass frame when the K^* is perpendicularly polarized to the reaction plane. Additionally, we explore the recoil-proton spin asymmetry to definitively determine the spin and parity of the resonance. This study stands to serve as a valuable reference for designing experimental setups aimed at investigating and comprehending exotic phenomena in QCD. Specifically, our insights will inform future J-PARC experiments, particularly those employing higher kaon beam energies.

Keywords: Pentaquark, vector-meson and baryon interaction, $S = +1$ production process, effective Lagrangian method, Regge approach, polarization, resonance, forward-scattering cross-section.

I. INTRODUCTION

Quantum Chromodynamics (QCD) stands as the foundational principle governing the strong interactions among standard-model particles, portraying various hadrons through the non-perturbative interactions of quarks and gluons. It showcases confinement and asymptotic freedom within the framework of non-Abelian color-SU(3) gauge theory. While the minimal composition for baryons is represented by qqq and for mesons by $q\bar{q}$, QCD does not forbid more intricate compositions such as $qqqq\bar{q}$ (pentaquark) and $q\bar{q}q\bar{q}$ (tetraquark), termed *Exotics*. Experimental evidence supporting these exotics has accumulated over decades. The initial observation of the tetraquark meson $X(3872)$, which defies the simple quark model, dates back to 2003, reported by the Belle experiment [1]. Recently, its existence was reaffirmed by the LHCb [2] and CMS [3] experiments, specifying $J^{PS} = 1^{++}$. Additionally, the Belle experiments reported evidence for $Y(4660)$ and $Z(4430)$ in 2007 [4]. Further tetraquark states have been identified via experiments conducted by LHCb, Belle, BES III, Fermilab, and others [5]. Regarding baryons, LHCb reported the $P_c^+(4312, 4440, 4457)$, observed in decay into J/ψ and p [6]. Recently, the same facility detected a novel pentaquark state with the strange-quark s ($udsc\bar{c}$) in the decay of $B^- \rightarrow J/\psi\Lambda\bar{p}$ [7]. While not yet definitively confirmed, these pentaquarks can potentially be understood as bound states of vector-meson and baryon (VB), denoted as $P_c^+ \sim D^*\Sigma_c$.

Remarkably, all experimentally observed and confirmed exotics exhibit heavy (charm) flavor. A theoretical rationale for this peculiarity concerning the stability of heavy pentaquarks was elucidated through color-spin interactions among quarks, contrasting with colorless hadronic interactions [8]. While the $S = +1$ light-pentaquark $\Theta^+ \sim uud\bar{s}$ was reported by the LEPs collaboration [9], supported by the non-topological chiral-quark soliton model [10], its existence remains disputed and unresolved due to varied outcomes across experimental facilities [11]. Furthermore, generating the $S = +1$ resonance dynamically proves challenging within the framework of Weinberg-Tomozawa (WT) type chiral interactions, primarily due to their repulsive nature. Nevertheless, the suggestion of an $S = 0$ pentaquark-like bound-state $P_s^+ \sim uuds\bar{s} \sim K^*\Sigma$, akin to P_c^+ in heavy flavor, was put forth by one of the present authors and collaborators [12, 13], aiming to elucidate the bump structure observed near $\sqrt{s} \approx 2.1$ GeV in $\gamma p \rightarrow \phi p$ [14]. In Ref. [14], the existence of P_s^+ was found to be crucial for reproducing the nontrivial structure observed in the spin-density matrix elements (SDMEs), in addition to successfully describing the angular-dependent cross-sections.

*E-mail: ldyoung0421@pukyong.ac.kr

†E-mail: sinam@pknu.ac.kr (corresponding author)

Given the current circumstances outlined above, it becomes of paramount importance to explore the potential for observing evidence of light-pentaquark states, either as bound states or resonances within the VB framework, to further enhance our understanding of QCD regarding exotic particles. Additionally, even in the $S = +1$ channel, there may exist a resonance or bound-state pentaquark, despite the lack of support from chiral dynamics [15]. Hence, in the present study, we undertake a theoretical examination of relatively aged data pertaining to the $S = +1$ channel reaction process, such as $K^+n \rightarrow K^{*0}p$ [16]. Intriguingly, this reaction process exhibits a peak-like structure around $\sqrt{s} = 2.5$ GeV, potentially indicative of an $S = +1$ resonance state, which we provisionally designate as $P_0^{+*} \equiv P_0^*$. We aim to elucidate this hypothetical pentaquark resonance P_0^* in our current investigation. Drawing upon our previous work [13], where we assigned the light-flavor VB pentaquark as $P_s \sim qqqs\bar{s}$, assuming it as a member of the extended VB antidecuplet flavor structure akin to Θ^+ , we can extend this assignment to other possible states: $P_0 \sim qqqs\bar{s}$, $P_1 \equiv P_s \sim qqqs\bar{s}$, $P_2 \equiv P_{ss} \sim qqss\bar{s}$, and $P_3 \equiv P_{sss} \sim qsss\bar{s}$, where q represents the flavor-SU(2) light quarks (u and d), being categorized by the numbers of the strange quarks they include.

In our previous study [13], we set the mass of P_s to be approximately 2.071 GeV, guided by the chiral-unitary approach [12]. Assuming $P_s(2071)$ as the $S = 0$ ground-state pentaquark of the extended VB antidecuplet and considering the mass difference between antidecuplets due to the inertia moment of the non-topological chiral soliton, approximately ~ 180 MeV [10], the ground-state P_0 mass is estimated to be around 1.890 GeV. Consequently, we regard the hypothetical resonance in the vicinity of the bump structure at 2.5 GeV as a resonance state of P_0 , denoted as $P_0^*(2500)$. Furthermore, we highlight several advantageous features of the chosen process: Firstly, since all hadrons in the final state of $K^+n \rightarrow K^{*0}p \rightarrow \pi^\mp K^\pm p$ can be measured experimentally in principle, the Fermi-motion effects of the deuteron-target experiment can be minimized. Secondly, in the s channel, it is possible to measure the resonance simultaneously coupling to PB and VB channels, allowing for the study of its production mechanism in two distinct dynamics. Lastly, this process involves the vector meson with polarizations, enabling the selection of specific quantum numbers for the resonance and control over its production mechanism.

To achieve this objective, we employ a straightforward tree-level Born approximation calculation utilizing the effective Lagrangian method. We account for the Regge trajectories in the t and u channels, incorporating phenomenological form factors to characterize the spatial extension of the hadrons. To replicate the observed peak-like structure in the total cross-section, potentially indicative of the $S = +1$ VB resonance ($\equiv P_0^{+*}$), we introduce a relativistic Breit-Wigner type contribution with $M_R = 2.5$ GeV and $\Gamma_R = 100$ MeV. Our numerical calculations reveal that, alongside the resonance contribution in the s channel, Reggeized π -exchange in the t channel and $\Lambda(1116)$ one in the u channel dominate the reaction process. We explore various spin-parity quantum numbers theoretically ($J^P = 1/2^\pm, 3/2^\pm$) since experimental data to determine them precisely are lacking. Notably, all tested spin-parity quantum numbers qualitatively reproduce the data well. To mitigate the signal-to-noise (S/N) ratio, we propose a specific combination of scattering angle and polarization ($\theta_{K^*} \sim 0$ and $k_K \cdot \epsilon_{K^*} \sim 0$) for future experiments, surpassing current programs like the K1.8 beam-line at J-PARC, which require a kaon beam energy of approximately 3.0 GeV to access the P_0^* region. Additionally, we recommend utilizing the recoil-proton spin asymmetry to ascertain the spin parity of the resonance.

The current study is structured as follows: Section II presents the theoretical framework. In Section III, we present the numerical results along with detailed explanations and discussions. Finally, the concluding section provides a summary and outlines future directions.

II. THEORETICAL FRAMEWORK

In this section, we will provide a concise overview of the theoretical framework governing the present reaction process. Relevant Feynman diagrams for the process are illustrated in Fig. 1, where the four momenta of the particles involved are also defined. The Yukawa interaction vertices are described as follows:

$$\begin{aligned}
\mathcal{L}_{PBB'} &= \frac{g_{PBB'}}{M_K} \bar{B}'^\mu \Theta_{\mu\nu}(X) (\partial^\nu K) \Gamma_5 B + \text{h.c.}, \\
\mathcal{L}_{VBB'} &= -\frac{ig_{VBB'}}{M_{K^*}} \bar{B}'^\mu \gamma^\nu (\partial_\mu K_\nu^* - \partial_\nu K_\mu^*) \Gamma_5 \gamma_5 B + \text{h.c.}, \\
\mathcal{L}_{PBB} &= ig_{PBB} \bar{B} \Gamma_5 \gamma_5 K^\dagger B + \text{h.c.}, \\
\mathcal{L}_{VBB} &= g_{VBB} \bar{B} \gamma^\mu \Gamma_5 V_\mu^\dagger B + \text{h.c.}, \\
\mathcal{L}_{PPV} &= ig_{PPV} V^\mu [P \partial_\mu P^\dagger - P^\dagger \partial_\mu P] + \text{h.c.}, \\
\mathcal{L}_{PBB} &= \left(\frac{f_{PBB}}{M_P} \right) \bar{B} \gamma_5 (\not{\partial} P) B.
\end{aligned} \tag{1}$$

In this context, B' , B , P , and V denote the fields corresponding to spin-3/2, spin-1/2 baryons, pseudoscalar, and vector mesons, respectively. We utilize the notation $\Gamma_5 = (I_{4 \times 4}, \gamma_5)$ to represent the parity (+, -) of B' . The term

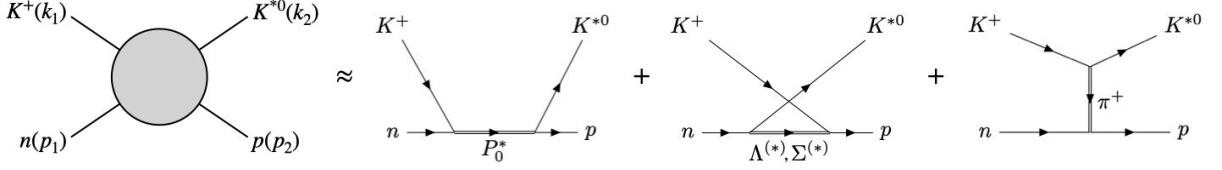


FIG. 1: Feynman diagrams pertinent to the process $K^+ n \rightarrow K^{*0} p$ within the tree-level Born approximation are presented.

$\Theta_{\mu\nu}(X)$ signifies the off-shell parameter X -dependent term within the Rarita-Schwinger formalism [17].

$$\Theta_{\mu\nu}(X) = g_{\mu\nu} + X\gamma_\mu\gamma_\nu. \quad (2)$$

As illustrated in Fig. 1, our analysis encompasses the P_0^* diagram in the s channel, hyperon ($\Lambda^{(*)}$, $\Sigma^{(*)}$) exchange in the u channel, and π exchange in the t channel. Given the absence of experimentally confirmed $S = +1$ baryon states to date, we exclusively focus on the hypothetical VB pentaquark P_0^* . Concerning the t channel, while there could be additional meson exchanges, such as the axial-vector meson $b_1(1235)$, we exclude them due to the scant information available regarding their decays [11].

Following straightforward calculations, the invariant amplitudes for the Feynman diagrams depicted in Fig. 1 are presented as follows:

$$\begin{aligned} i\mathcal{M}_{P_0^*(s=1/2)}^s &= -g_{K^*NP_0^*}g_{KNP_0^*}\bar{u}(p_2)\Gamma_5\not{\epsilon}_s\frac{\not{\epsilon}_s + M_{P_0^*}}{s - M_{P_0^*}^2 - iM_{P_0^*}\Gamma_{P_0^*}}\gamma_5\Gamma_5u(p_1), \\ i\mathcal{M}_{P_0^*(s=3/2)}^s &= -\frac{ig_{K^*NP_0^*}g_{KNP_0^*}}{M_{K^*}M_K}\bar{u}(p_2)\gamma_5\Gamma_5(k_{2\mu}\epsilon_\nu - k_{2\nu}\epsilon_\mu)\gamma^\nu\frac{(\not{\epsilon}_s + M_{P_0^*})\bar{g}^{\mu\alpha}(q_s)}{s - M_{P_0^*}^2 + iM_{P_0^*}\Gamma_{P_0^*}}(g_{\alpha\beta} + X\gamma_\alpha\gamma_\beta)k_1^\beta\Gamma_5u(p_1), \\ i\mathcal{M}_Y^u &= -\frac{i}{2}g_{KNY}g_{K^*NY}\bar{u}(p_2)\Gamma_5\frac{(\not{\epsilon}_u + M_Y)\not{\epsilon}_u}{u - M_Y^2 - iM_Y\Gamma_Y}\Gamma_5\gamma_5u(p_1), \\ i\mathcal{M}_{\Sigma^*(1385)}^u &= \frac{i}{2}\frac{g_{K^*N\Sigma^*}}{M_{K^*}}\frac{g_{KN\Sigma^*}}{M_K}\bar{u}(p_2)k_1^\nu(g_{\mu\nu} + X\gamma_\mu\gamma_\nu)\frac{\bar{g}^{\mu\alpha}(q_u)(\not{\epsilon}_u + M_{\Sigma^*})}{u - M_{\Sigma^*}^2 + iM_{\Sigma^*}\Gamma_{\Sigma^*}}\gamma^\beta(k_{2\alpha}\epsilon_\beta - k_{2\beta}\epsilon_\alpha)\gamma_5u(p_1), \\ i\mathcal{M}_\pi^t &= -\frac{2if_{\pi NN}}{M_\pi}g_{PPV}\bar{u}(p_2)\gamma_5\frac{\not{\epsilon}_t(\epsilon \cdot k_1)}{t - M_\pi^2}u(p_1). \end{aligned} \quad (3)$$

Here, the notation $(s, u, t) = (q_s^2, q_u^2, q_t^2)$ denotes the Mandelstam variables. In our calculations, we utilize the spin-1/2 hyperons $Y = \Lambda(1116, 1/2^+)$, $\Sigma(1192, 1/2^+)$, $\Lambda(1405, 1/2^-)$, and $\Lambda(1670, 1/2^-)$, along with the hyperon resonance $\Sigma^*(1385, 3/2^+)$. The polarization vector of K^* is represented by ϵ_μ . The spin sum of the Rarita-Schwinger field yields the following expression:

$$\bar{g}^{\mu\nu}(q) = g^{\mu\nu} - \frac{1}{3}\gamma^\mu\gamma^\nu - \frac{2}{3M^2}q^\mu q^\nu + \frac{q^\mu\gamma^\nu + q^\nu\gamma^\mu}{3M}. \quad (4)$$

Here, M and Γ represent the mass and full decay width of the particle corresponding to the field. All relevant couplings are established based on experimental data and theoretical frameworks [11, 12, 18], as summarized in Table I, except for those for P_0^* . To streamline our analysis, we denote the combined coupling as $g_{P^*0} \equiv g_{K^*NP_0^*}g_{KNP_0^*}$ hereafter.

To account for the spatial extension of the hadrons, we incorporate a phenomenological form factor, defined as follows:

$$F(x) = \frac{\Lambda^4}{\Lambda^4 + (x - M_x^2)}. \quad (5)$$

Hyperon (Y)	g_{K^*NY}	g_{KNY}	Combined
$\Lambda(1116, 1/2^+)$	-4.26	-13.4	57.08
$\Lambda^*(1405, 1/2^-)$	$0.2 - 2.7i$	$2.5 + 0.9i$	$2.93 - 6.57i$
$\Lambda^*(1670, 1/2^-)$	$-0.2 + 0.8i$	$0.2 - 0.6i$	$-0.52 - 0.04i$
$\Sigma(1192, 1/2^+)$	-2.46	4.09	-10.06
$\Sigma^*(1385, 3/2^+)$	-5.48	-6.94	38.03
π	$f_{\pi NN} = 0.989$	$g_{\pi KK^*} = 3.76$	3.72

TABLE I: Strong couplings for the hyperon and pion vertices and their combinations derived from theoretical models and experimental data [11, 12, 18].

In this expression, x represents the Mandelstam variable, and M_x denotes the off-shell mass of the corresponding particle. The cutoff parameter Λ will be adjusted to accurately reproduce the experimental data.

Given that the available data from Ref. [16] extends up to $\sqrt{s} \sim 5$ GeV, which approaches the asymptotic limit $s \rightarrow \infty$, it becomes imperative to account for the higher-spin states of the exchange particles. To address this, we incorporate the t - and u -channel Regge trajectories. Following the methodology outlined in Ref. [19], the u -channel amplitudes for the $\Lambda(1116)$, $\Sigma(1192)$, and $\Sigma^*(1385)$ are adjusted using the Regge approach, wherein each trajectory $\alpha(x)$ is characterized by the intercept α' .

$$\begin{aligned}\tilde{\mathcal{M}}_{\Lambda,\Sigma}^u(s,u) &= C_{\Lambda,\Sigma}(u)\mathcal{M}_{\Lambda,\Sigma}^{\prime u}\left(\frac{s}{s_{\Lambda,\Sigma}}\right)^{\alpha_{\Lambda,\Sigma}(u)-\frac{1}{2}}\Gamma\left[\frac{1}{2}-\alpha_{\Lambda,\Sigma}(u)\right]\alpha'_{\Lambda}, \\ \tilde{\mathcal{M}}_{\Sigma^*}^u(s,u) &= C_{\Sigma^*}(u)\mathcal{M}_{\Sigma^*}^{\prime u}\left(\frac{s}{s_{\Sigma^*}}\right)^{\alpha_{\Sigma^*}(u)-\frac{3}{2}}\Gamma\left[\frac{3}{2}-\alpha_{\Sigma^*}(u)\right]\alpha'_{\Sigma^*}.\end{aligned}\quad (6)$$

Note that the amplitude \mathcal{M}' represents the expression in Eq. (3) after removing the denominator part of the propagator. The trajectories are specified as $\alpha_{\Lambda}(u) = -0.65 + 0.94u$, $\alpha_{\Sigma}(u) = -0.79 + 0.87u$, and $\alpha_{\Sigma^*}(u) = -0.27 + 0.9u$. Additionally, the phenomenological momentum-dependent hadronic coefficient is defined as follows:

$$C_Y(u) = \left[\frac{\epsilon_Y \Lambda_Y^2}{\Lambda_Y^2 - u}\right]^2. \quad (7)$$

Finally, the t -channel Reggeized amplitude for the π reads

$$\tilde{\mathcal{M}}_{\pi}^t(s,u) = C_{\pi}(u)\mathcal{M}_{\pi}^{\prime t}\left(\frac{s}{s_{\pi}}\right)^{\alpha_{\pi}(t)}\frac{\pi\alpha'_{\pi}}{\Gamma[\alpha_X(t)+1]\sin[\pi\alpha_{\pi}(t)]}. \quad (8)$$

Here, $C_{\pi}(t) = a_{\pi}/(1-t/\Lambda_{\pi}^2)^2$. The Regge parameters and cutoffs for the form factors are provided in Table II. It is important to mention that we adopt $X = 0$ for simplicity in our analysis.

III. NUMERICAL RESULTS AND DISCUSSIONS

In this section, we present the numerical results for the reaction process along with detailed discussions. The cutoffs for the form factors in Eq. (5) are chosen to be 1.0 GeV and 0.45 GeV for the (s, t) and u channels, respectively, by fitting the data as shown in Table II. Firstly, in panel (a) of Fig. 2, we depict the total cross-sections as functions of the center-of-mass energy (cm)(E_{cm}), showcasing the non-resonant u - and t -channel contributions separately. The lines represent contributions from the total (solid), π (dotted), $\Lambda(1116)$ (dashed), $\Lambda(1670)$ (long-dashed), $\Lambda(1670)$ (dot-dashed), $\Sigma(1192)$ (long-short-dashed), and $\Sigma^*(1385)$ (long-dot-dashed). Experimental data are obtained from both charged (circle) and neutral (square) channels [16, 20–25]. We observe that the $\Lambda(1116)$ exchange in the u -channel is crucial for reproducing the strength of the cross-section near the threshold, while the contributions from other hyperons are almost negligible, as inferred from their coupling strengths with the Regge coefficients, as depicted in Tables I and II. Conversely, the π -exchange contribution in the t channel is significant for describing the relatively higher-energy region. However, these non-resonant contributions fail to explain the peak-like structure at $E_{\text{cm}} \approx 2.5$ GeV. In the figure, data points beyond the description provided by the background (BKG) are denoted with a hollow circle. Several explanations can potentially account for the observed peak-like structure in the cross-sections: 1) Single or combinations of resonances, which are the focus of our current investigation; 2) Opening of meson-baryon scattering channels [26]; 3) Interferences of scattering amplitudes [27]; and 4) Non-trivial kinematic singularities [28].

Considering the scattering of ground-state vector-meson and baryon multiplets ($8, 10, \bar{10}$) in the $S = +1$ channel, the possibility of channel opening appears less likely due to their masses, which are approximately $M_{\text{max}} = M_{K^*} + M_{\Delta} \approx$

Hyperon (Y)	η_Y	s_Y [GeV ²]	Λ_Y [GeV]
$\Lambda(1116, 1/2^+)$	2.60	1.10	0.45
$\Sigma(1192, 1/2^+)$	0.66	1.10	0.45
$\Sigma^*(1385, 3/2^+)$	0.66	1.10	0.45
π	$\alpha_{\pi} = 0.53$	$s_{\pi} = 1.00$	$\Lambda_{\pi} = 1.00$

TABLE II: Parameters for the Regge approach and cutoffs in the present work [19].

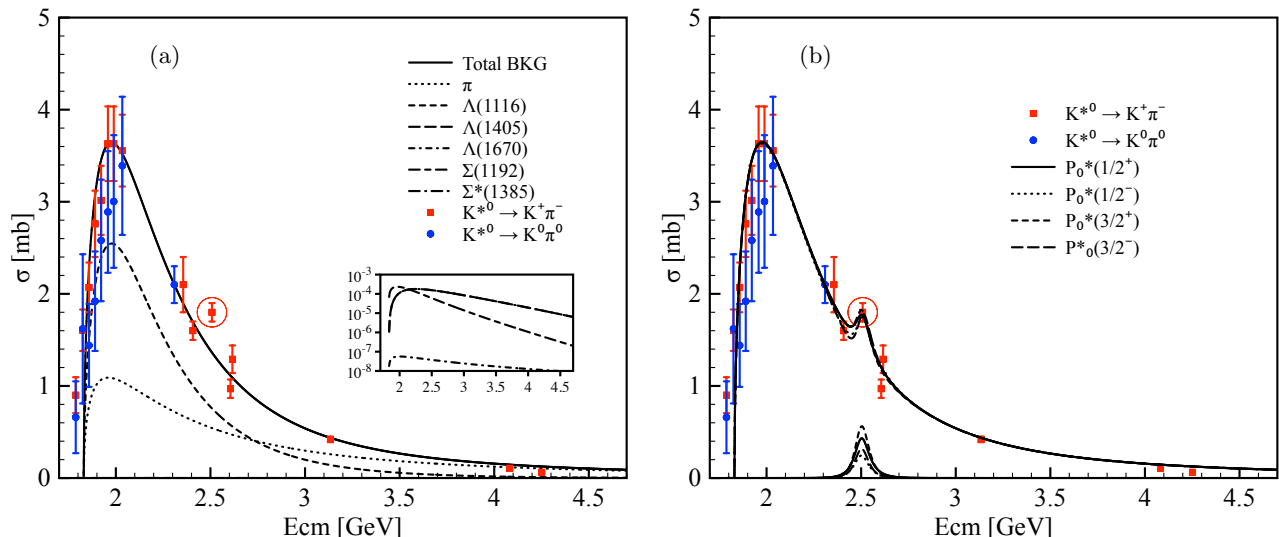


FIG. 2: (a) Total cross-sections for the non-resonant contributions as functions of E_{cm} , serving as the background (BKG), including the total (solid), π (dotted), $\Lambda(1116)$ (dashed), $\Lambda(1405)$ (long-dashed), $\Lambda(1670)$ (dot-dashed), $\Sigma(1192)$ (long-short-dashed), and $\Sigma^*(1385)$ (long-dot-dashed) components. (b) Total cross-sections with four different spin-parity quantum numbers of the P_0^* : $J^P = 1/2^+$ (solid), $J^P = 1/2^-$ (dotted), $J^P = 3/2^+$ (dashed), and $J^P = 3/2^-$ (long-dashed). Experimental data are obtained from various sources, including Refs. [16, 20–25]. Data points that deviate from the background description are marked with hollow circles.

2.12 GeV. Although scatterings involving higher multiplets may contribute, this possibility is beyond the scope of our current investigation. We also explore the interferences between the u - and t -channel amplitudes with various phase factors, yielding no significant structures. Another potential source of interference could arise from crossing the invariant-mass bands on the Dalitz plot for $K^+n \rightarrow \pi^+K^-p$, as a function of $M_{\pi^+K^-}$ and M_{K^-p} , for instance. It's worth noting that similar considerations regarding interference possibilities have been explored theoretically and experimentally for $\gamma p \rightarrow \pi^+K^-p$, with a focus on ϕ production [27]. It was found that interference effects were negligible. Nontrivial effects, such as the triangle singularity [28], could also be introduced. For example, one might consider a triangle diagram consisting of the P - V - B internal lines in the present work, where higher-mass meson-baryon cuts can lead to singularities. However, achieving a peak at $E_{\text{cm}} \approx 2.5$ GeV would require very high-mass hadrons. Nonetheless, this remains an intriguing subject for future exploration, and we leave it for subsequent studies.

Therefore, our focus lies in identifying the presence of a resonance within the observed structure. It's important to note that we explore four different spin-parity scenarios for P_0^* , namely $J^P = 1/2^\pm$, $3/2^\pm$, as there is currently no experimental data available for reference. It has been verified that all these scenarios can qualitatively reproduce the peak-like structure effectively by adjusting the combined couplings as follows:

$$g_{P_0^*}^{1/2^+} = 0.65, \quad g_{P_0^*}^{1/2^-} = 0.15, \quad g_{P_0^*}^{3/2^+} = 0.70, \quad g_{P_0^*}^{3/2^-} = 0.23. \quad (9)$$

It's worth noting that the full decay width of P_0^* remains consistent across all spin-parity quantum numbers, set at $\Gamma_{P_0^*} = 100$ MeV. In panel (b) of Fig. 2, we present the total cross-sections for each case separately: $J^P = 1/2^+$ (solid line), $J^P = 1/2^-$ (dotted line), $J^P = 3/2^+$ (dashed line), and $J^P = 3/2^-$ (long-dashed line).

In Fig. 3, the numerical results for the differential cross-sections for the angular dependence $d\sigma/d\cos\theta$ are presented for $E_{\text{cm}} = (2.0, 2.5, 3.0)$ GeV in panels (a), (b), and (c), respectively, illustrating each contribution. Here, θ denotes the scattering angle of the final state K^* in the cm frame. Notably, strong forward and backward scatterings are observed from the hyperons in the u channel and from π in the t channel, respectively. Conversely, the s -channel contribution yields almost flat curves, as anticipated. Around $E_{\text{cm}} = 2.5$ GeV, corresponding to the resonance region (where we use $3/2^-$), a slight yet discernible angular dependence emerges. As the energy surpasses the resonance region, the angular dependence markedly separates into forward- and backward-scattering regions. Panel (d) presents the angular dependence as a function of E_{cm} and $\cos\theta$. Notably, the resonance signal becomes more pronounced around $\cos\theta = 0$, where the contributions from the t and u channels are diminished or negligible. These observations suggest a potential method for experimentally isolating the resonance P_0^* contribution, which we will discuss below.

Now, we are in a position to discuss how to enhance the S/N for the P_0^* resonance. As previously illustrated, the dominant contributions in the present reaction process originate from the u - and t -channel interactions. Therefore, by focusing solely on the forward-scattering region, where the hyperon-induced backward scattering is negligible, we

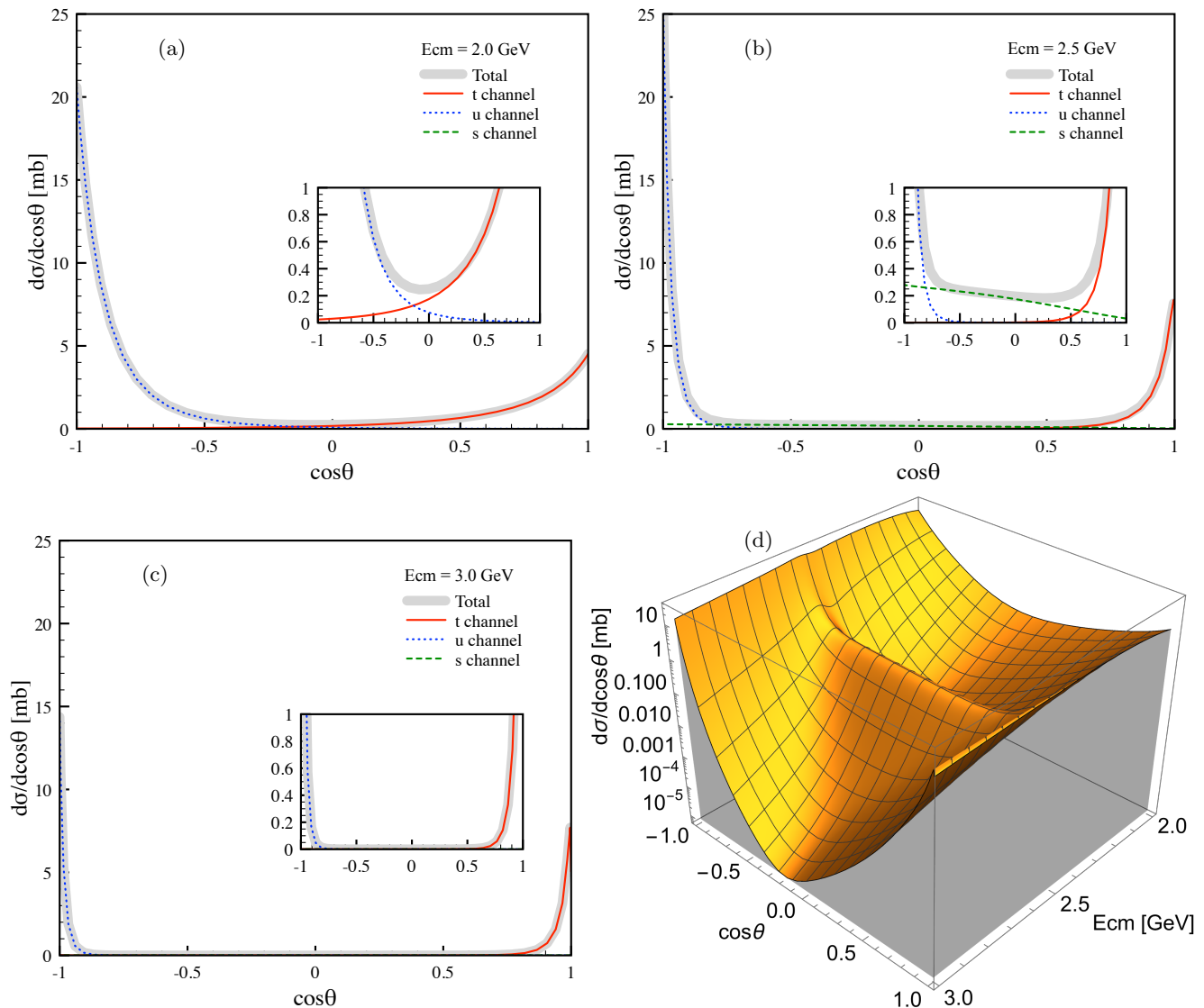


FIG. 3: The differential cross-sections for the angular dependence $d\sigma/d\cos\theta$ [mb] at $E_{\text{cm}} = (2.0, 2.5, 3.0)$ GeV are depicted in panels (a), (b), and (c) as functions of $\cos\theta$, illustrating each contribution. Here, θ represents the scattering angle of the final state K^* in the cm frame. Panel (d) displays $d\sigma/d\cos\theta$ as a function of E_{cm} and $\cos\theta$. In this panel, we exclusively showcase the results for $P_0^*(3/2^-)$, as other quantum-number states exhibit negligible differences.

can effectively eliminate this background. The subsequent step involves reducing the contribution from the t -channel π -exchange. Remarkably, due to its vector-meson nature, the invariant amplitude for the π exchange in Eq. (3) is directly proportional to $\mathbf{k}_K \cdot \boldsymbol{\epsilon}_{K^*}$, where \mathbf{k}_K represents the three-momentum of the initial K^+ meson. Consequently, when the polarization of K^* is fixed perpendicular to the reaction plane, where all particle momenta are defined, the π -exchange contribution diminishes. In panel (a) of Fig. 4, we display the differential cross-sections $d\sigma/d\cos\theta$ as a function of E_{cm} for $\mathbf{k}_K \cdot \boldsymbol{\epsilon}_{K^*} = 0$ at $\theta = 0$ (solid), $\pi/4$ (dotted), and $\pi/2$ (dashed) in the cm frame. Here, we specifically focus on the result for the $P_0^*(3/2^-)$, as other quantum-number states exhibit minimal variation. At $\theta = 0$, where K^* is scattered forwardly, the P_0^* signal is isolated with minimal background contamination. As the angle increases, the S/N value worsens, particularly at $\theta = \pi/4$. Further increasing it to $\theta = \pi/2$ enhances the peak due to interference between the resonance and the u -channel contribution, although the background contamination also increases. In panel (b) of Fig. 4, we plot the differential cross-section as a function of $\cos\theta$ and E_{cm} . Across a wide range of angles ($-0.5 \lesssim \cos\theta \leq 1$), clear resonance signals are observed, facilitating their measurement in experiments. Additionally, we confirm that the *unpolarized* cross-sections exhibit minimal dependence on the spin-parity quantum numbers. Therefore, the discussions provided for Figs. 3 and 4 remain applicable to other quantum-number cases without loss of generality.

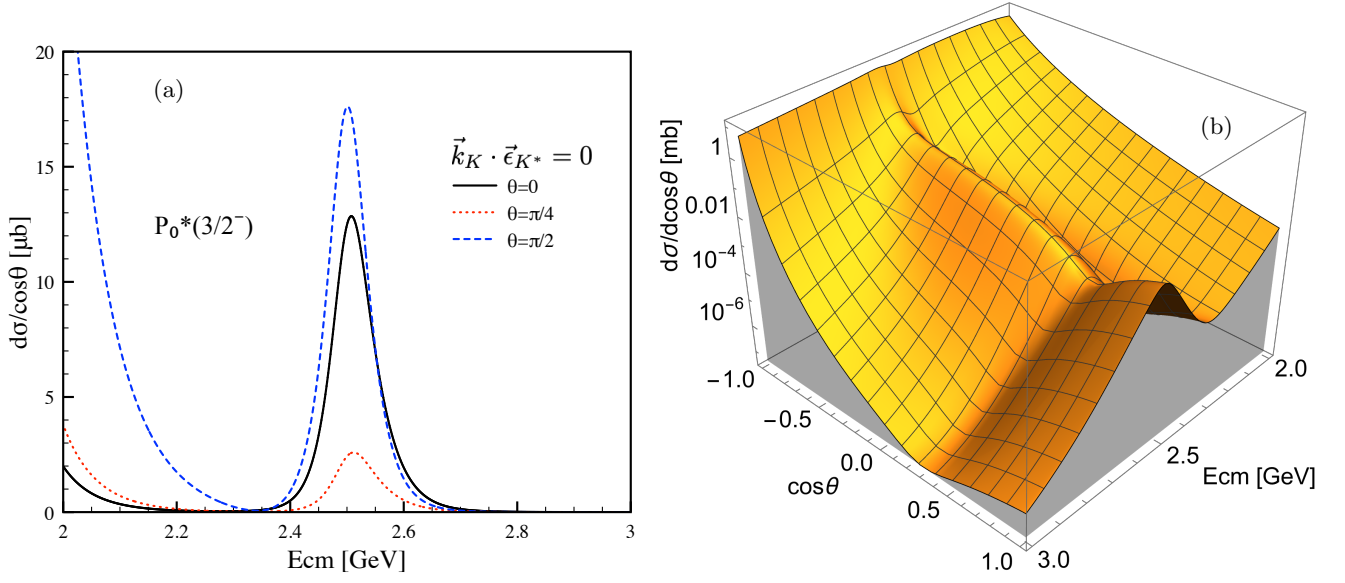


FIG. 4: (a) Differential cross-sections $d\sigma/d\cos\theta$ for $\mathbf{k}_K \cdot \boldsymbol{\epsilon}_{K^*} = 0$ for $\theta = 0$ (solid), $\pi/4$ (dotted), and $\pi/2$ (dashed) in the cm frame. Here, we only present the results for the $P_0^*(3/2^-)$, as other quantum-number states do not significantly differ. (b) The same as (a), plotted as a function of $\cos\theta$ and E_{cm} for $\mathbf{k}_K \cdot \boldsymbol{\epsilon}_{K^*} = 0$ at $\theta = 0$.

Finally, we would like to propose a physical observable for determining the spin-parity quantum number of the P_0^* resonance. The polarizations of the involved particles, such as the target and recoil nucleons, and K^* , are invaluable for this determination. However, achieving a definite neutron polarization inside the deuteron target poses challenges in experimental setups. As discussed earlier, to maximize the S/N , it's advantageous to set the K^* polarization as $\mathbf{k}_K \cdot \boldsymbol{\epsilon}_{K^*} = 0$ (perpendicular configuration). Consequently, we rely on controlling the recoil-proton polarization for quantum-number determination. Hence, we introduce the recoil-proton spin asymmetry (RSA) defined as follows, with $\boldsymbol{\epsilon}_{K^*}$ perpendicular to the reaction plane:

$$\Sigma_{\perp} \equiv \frac{d\sigma_{\uparrow}/d\cos\theta - d\sigma_{\downarrow}/d\cos\theta}{d\sigma_{\uparrow}/d\cos\theta + d\sigma_{\downarrow}/d\cos\theta} \Big|_{\mathbf{k}_K \cdot \boldsymbol{\epsilon}_{K^*} = 0}, \quad (10)$$

where the notation (\uparrow, \downarrow) denotes the (up, down)-spin polarization of the recoil proton, respectively. In panel (a) of Fig. 5, we illustrate the RSAs as functions of $\cos\theta$ at $E_{\text{cm}} = 2.5$ GeV. Note that the curves mainly comprise contributions from the s -channel and u -channel, as the t -channel contribution is eliminated by fixing the polarization as $\mathbf{k}_K \cdot \boldsymbol{\epsilon}_{K^*} = 0$. The spin-1/2 cases exhibit much smaller asymmetry compared to the spin-3/2 ones. The $P_0^*(1/2^{\pm})$ amplitudes show weak angular dependence and are relatively small due to their Lorentz structures in the vicinity of $E_{\text{cm}} = 2.5$ GeV as follows:

$$u^{\dagger}(p_2)\gamma_0\gamma_2(E_{\text{cm}}\gamma_0 \pm M_{P_0^*})\gamma_5 u(p_1) \sim A(E_{\text{cm}} \pm M_{P_0^*}) + B(E_{\text{cm}} \mp M_{P_0^*})(\cos\theta, \sin\theta), \quad (A, B) \in R. \quad (11)$$

On the contrary, the $P_0^*(3/2^{\pm})$ amplitudes exhibit highly nontrivial angular dependencies arising from the spin-sum of the Rarita-Schwinger field and the kinematic factor $\mathbf{k}_K \cdot \mathbf{k}_{K^*} \propto t$, as shown in Eq. (3). Consequently, the spin-parity quantum numbers can be determined from $\Sigma_{\perp}(\cos\theta)$ for the spin-3/2 cases, whereas fixing the parity for the spin-1/2 cases proves to be more challenging. In panel (b) of Fig. 5, the numerical results for the RSA as functions of E_{cm} are presented. Each spin-parity case exhibits a distinctive curve shape above $E_{\text{cm}} \approx 2.2$ GeV. Once more, the spin-3/2 cases demonstrate different energy dependence, whereas the spin-1/2 ones remain small and flat due to the same reasons as discussed above.

IV. SUMMARY AND FUTURE PERSPECTIVES

In our current study, we delve into the peak-like structure observed around $\sqrt{s} \sim 2.5$ GeV in the reaction $K^+n \rightarrow K^{*0}p$. We consider the potential $S = +1$ resonance $P_0^{+*} \equiv P_0^*$ as an excited state within the extended vector-meson and baryon (VB) antidecuplet, particularly in the s channel. To explore this, we employ the effective Lagrangian

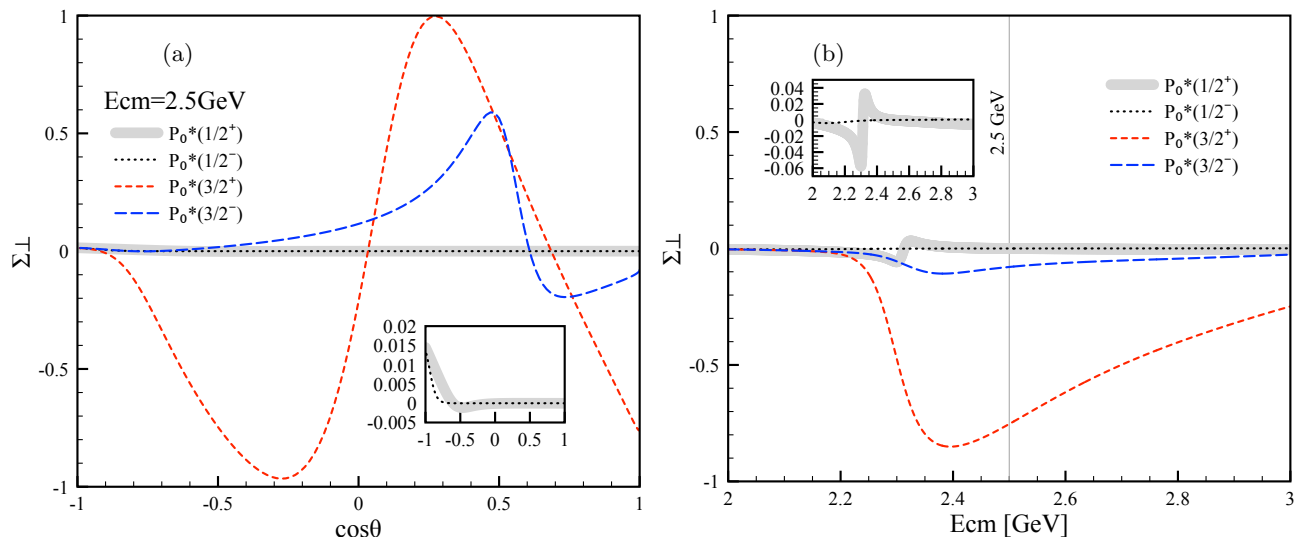


FIG. 5: (a) Recoil-proton spin asymmetry (RSA) in Eq. (10) as functions of E_{cm} for different spin-parity quantum numbers of P_0^* , with ϵ_{K^*} perpendicular to the reaction plane. (b) Σ_{\perp} as functions of $\cos\theta$ at $E_{\text{cm}} = 2.5$ GeV following the same approach.

method in conjunction with the Regge approach at the tree-level Born approximation. We examine various hyperon (Y) exchanges in the u channel and pion (π) ones in the t channel. Below, we list important findings of the present studies:

- We find that the currently available experimental data around $E_{\text{cm}} = 2.5$ GeV cannot be adequately explained solely by the tree-level Born diagrams incorporating Regge contributions as the background (BKG). However, they are well accounted for by a resonance state characterized by $M_{P_0^*} = 2.5$ GeV and $\Gamma_{P_0^*} = 100$ MeV, alongside its spin-parity quantum numbers $J^P = 1/2^{\pm}$ and $3/2^{\pm}$. To further elucidate this, we estimate the combined coupling constants for the resonance, denoted as $g_{P_0^*} \equiv g_{KNP_0^*}g_{K^*NP_0^*}$, by fitting the data, paving the way for future theoretical studies.
- The angular dependence of the reaction process, represented by $d\sigma/d\cos\theta$, is primarily influenced by the contributions from the t -channel π and u -channel $\Lambda(1116)$. These contributions result in significant enhancements of both forward and backward scattering in the center-of-mass (cm) frame, which gradually diminish as E_{cm} increases. However, in contrast, for all spin-parity states of P_0^* , it becomes evident that the resonance contribution is comparatively smaller than the background (BKG) and only becomes notable around $E_{\text{cm}} = 2.5$ GeV, particularly in the vicinity of $\cos\theta = 0$.
- To accurately study the resonance contribution, we have devised an experimental approach aimed at enhancing the signal-to-noise ratio (S/N) by taking into account the structure of the predominant background signals (BKGs). By concentrating on the forward-scattering region and orienting the polarization of the K^* perpendicular to the reaction plane, it becomes feasible to effectively circumvent the effects originating from the u channel and deactivate those from the t channel, respectively. This strategy yields a S/N value close to unity. As the scattering angle increases towards $\cos\theta \approx 0$, the contamination stemming from the u -channel becomes more pronounced, yet the S/N value remains reasonably high.
- Considering the ongoing reaction process, we delve into exploring a polarized observable known as the recoil-proton spin asymmetry (RSA) with $\mathbf{k}_K \cdot \epsilon_{K^*} = 0$ to discern the spin-parity quantum numbers of the P_0^* . We discern distinctive angular dependencies of the RSAs for the $J^P = 3/2^{\pm}$ states. However, determining the parity for the spin-1/2 states proves to be challenging due to their weak and minimal angular dependencies at $E_{\text{cm}} = 2.5$ GeV. Furthermore, we analyze the energy dependencies of the RSA for prospective experiments.

We wish to underscore that the potential $S = +1$ resonance state P_0^* , proposed to account for the currently available data on $K^+n \rightarrow K^{*0}p$, holds promise for illuminating our understanding of exotic phenomena in QCD, surpassing traditional chiral interaction theories. The conjecture that P_0^* pertains to the resonance of the extended VB antidecuplet, akin to the PB antidecuplet for Θ^+ , remains inadequately elucidated within existing theories. Nevertheless, ongoing discourse contemplates plausible explanations for these antidecuplet resonances [29]. Furthermore, more

realistic theoretical studies will be conducive to future experimental analyses, i.e., $K^+n \rightarrow K^{*0}p \rightarrow \pi^0 \mp K^{0,\pm}p$ for instance. Such endeavors will yield valuable insights into P_0^* , particularly in the K^0p invariant-mass domain. Relevant investigations are underway and will be detailed elsewhere.

Acknowledgment

The authors extend their gratitude for the fruitful discussions with Jung Keun Ahn (Korea University), Shin Hyung Kim (Kyungpook National University), Ghil-Seok Yang (Hoseo University), Kanchan Pradeepkumar Khemchandani (Federal University of São Paulo), and Alberto Martinez Torres (University of São Paulo). This work received support from the National Research Foundation of Korea (NRF) grants funded by the Korean government (MSIT) (2018R1A5A1025563, 2022R1A2C1003964, and 2022K2A9A1A06091761).

-
- [1] S. K. Choi *et al.* [Belle], Phys. Rev. Lett. **91**, 262001 (2003).
 - [2] R. Aaij *et al.* [LHCb], Phys. Rev. Lett. **110**, 222001 (2013).
 - [3] A. M. Sirunyan *et al.* [CMS], Phys. Rev. Lett. **128**, no.3, 032001 (2022).
 - [4] G. Cotugno, R. Faccini, A. D. Polosa and C. Sabelli, Phys. Rev. Lett. **104**, 132005 (2010).
 - [5] H. X. Chen, W. Chen, X. Liu, Y. R. Liu and S. L. Zhu, Rept. Prog. Phys. **86**, no.2, 026201 (2023).
 - [6] R. Aaij *et al.* [LHCb], Phys. Rev. Lett. **115**, 072001 (2015).
 - [7] R. Aaij *et al.* [LHCb], Phys. Rev. Lett. **131**, no.3, 031901 (2023).
 - [8] W. Park, S. Cho and S. H. Lee, Phys. Rev. D **99**, no.9, 094023 (2019).
 - [9] T. Nakano *et al.* [LEPS], Phys. Rev. C **79**, 025210 (2009).
 - [10] D. Diakonov, V. Petrov and M. V. Polyakov, Z. Phys. A **359**, 305-314 (1997).
 - [11] P.A. Zyla *et al.* (Particle Data Group), Prog. Theor. Exp. Phys. 2020, 083C01 (2020).
 - [12] K. P. Khemchandani, H. Kaneko, H. Nagahiro and A. Hosaka, Phys. Rev. D **83**, 114041 (2011).
 - [13] S. i. Nam, Phys. Rev. D **103**, no.5, 054040 (2021).
 - [14] S. I. Shim, Y. Kim and S. i. Nam, [arXiv:2402.07392 [hep-ph]].
 - [15] Private communications with Kanchan P. Khemchandani (Federal University of São Paulo).
 - [16] G. Giacomelli *et al.* [Bologna-Glasgow-Rome-Trieste], Nucl. Phys. B **111**, 365-396 (1976).
 - [17] W. Rarita and J. Schwinger, Phys. Rev. **60**, 61 (1941).
 - [18] V. G. J. Stoks and T. A. Rijken, AIP Conf. Proc. **334**, 379-382 (1995).
 - [19] S. H. Kim, J. K. Ahn, S. H. Kim, S. i. Nam and M. K. Cheoun, Phys. Rev. C **107**, no.6, 065202 (2023).
 - [20] D. Cords *et al.*, Phys. Rev. D **4**, 1974 (1971).
 - [21] S. L. Baker *et al.*, Nucl. Phys. B **99**, 211-231 (1975).
 - [22] S. Goldhaber *et al.*, Phys. Rev. L **15**, 737 (1965).
 - [23] K. Buchner *et al.*, Nucl. Phys. B **45**, 333-378 (1972).
 - [24] G. Bassompierre *et al.*, Nucl. Phys. B **16**, 125-154 (1970).
 - [25] K. Hendrickx *et al.*, Nucl. Phys. B **112**, 189-212 (1976).
 - [26] J. K. Ahn, S. Yang and S. i. Nam, Phys. Rev. D **100**, no.3, 034027 (2019).
 - [27] S. Y. Ryu *et al.* [LEPS], Phys. Rev. Lett. **116**, no.23, 232001 (2016).
 - [28] A. P. Szczepaniak, Phys. Lett. B **747**, 410-416 (2015).
 - [29] G. S. Yang, S. i. Nam, in progress.

Quantum-number projected generator coordinate method for ^{21}Ne with a chiral two-nucleon-plus-three-nucleon interaction

W. Lin

School of Physics and Astronomy, Sun Yat-sen University, Zhuhai 519082, P.R. China

E. F. Zhou

School of Physics and Astronomy, Sun Yat-sen University, Zhuhai 519082, P.R. China

J. M. Yao*

School of Physics and Astronomy, Sun Yat-sen University, Zhuhai 519082, P.R. China

H. Hergert

Facility for Rare Isotope Beams, Michigan State University,

East Lansing, Michigan 48824-1321, USA. and

Department of Physics & Astronomy, Michigan State University,

East Lansing, Michigan 48824-1321, USA.

Abstract

In this paper, we report a study of the low-lying states of deformed ^{21}Ne within the framework of quantum-number projected generator coordinate method (PGCM), starting from a chiral two-nucleon-plus-three-nucleon (NN+3N) interaction. The wave functions of states are constructed as a linear combination of a set of axially-deformed Hartree-Fock-Bogoliubov (HFB) wave functions with different quadrupole deformations. These HFB wave functions are projected onto different angular momenta and the correct neutron and proton numbers for ^{21}Ne . The results of calculations based on the effective Hamiltonians derived by normal-ordering the 3N interaction with respect to three different reference states, including the quantum-number projected HFB wave functions for ^{20}Ne , ^{22}Ne , and an ensemble of them with equal weights, are compared. This study serves as a key step towards ab initio calculations of odd-mass deformed nuclei with the in-medium GCM.

PACS numbers:

*Electronic address: yaojm8@sysu.edu.cn

I. INTRODUCTION

Studying nuclear low-lying states, including energy spectra and electroweak transition strengths, is crucial for advancing our understanding of nuclear physics [1, 2]. It also plays a key role in exploring new physics at the high-precision frontier, such as nonzero electric dipole moments [3, 4], single- β decay [5], and neutrinoless double- β decay [6]. Modeling the low-lying states of light to heavy atomic nuclei directly from the fundamental interactions between nucleons is of great interest for this purpose. Compared to even-even nuclei, the low-lying states of odd-mass nuclei contain richer nuclear structure information because of the interplay of single-particle and collective motions, presenting a considerable challenge for nuclear theory.

The generator coordinate method (GCM) provides an efficient and flexible framework to describe the wave function of a quantum many-body system, represented as a superposition of a set of nonorthogonal basis functions, such as Slater determinants, generated by continuously changing parameters called generator coordinates [7, 8]. In nuclear physics, the quantum-number projected GCM (PGCM) has been extensively employed in studies of the energies and transition rates of low-lying states. See, for instance, Refs. [9–11]). In the recent decade, the PGCM has been implemented into ab initio methods for atomic nuclei. This idea has given birth to a new generation of ab initio methods, including the no-core Monte Carlo shell model [12], the in-medium generator coordinate method (IM-GCM) [13, 14] and perturbative PGCM with second-order perturbation theory [15–17].

In this paper, we extend the PGCM for the low-lying states of an odd-mass deformed nucleus ^{21}Ne , starting from a Hamiltonian composed of two-nucleon-plus-three-nucleon (NN+3N) interaction derived from chiral effective field theory (EFT). The PGCM has been extended for odd-mass nuclei based on different energy density functionals (EDFs)[18–26]. It is known that EDF-based PGCM approaches may suffer from spurious divergences and discontinuities [26–28]. In this work, we examine that this Hamiltonian-based framework is free of those problems as the same interaction is applied to both the particle-hole and particle-particle channels when computing the energy overlaps of Hamiltonian kernels. Additionally, we compare the energy spectra of the low-lying states from the PGCM calculations using the effective Hamiltonian normal-ordered with respect to three different reference states, i.e., particle-number projected Hartree-Fock-Bogoliubov (PNP-HFB) wave functions for ^{20}Ne , ^{22}Ne , and an ensemble of them with equal weights.

The article is arranged as follows. In Sec.II, we present the main formulas of PGCM for an

odd-mass nucleus, including the generation of an effective Hamiltonian in the normal-ordering two-body (NO2B) approximation, and the construction of nuclear wave functions in the PGCM. The results of calculations for ^{21}Ne are presented in Sec. III. A short summary and outlook are provided in Sec. IV.

II. THE PGCM FOR AN ODD-MASS NUCLEUS

A. Nuclear Hamiltonian

We employ an intrinsic nuclear A -body Hamiltonian containing both NN and $3N$ interactions,

$$\hat{H}_0 = \left(1 - \frac{1}{A}\right)T^{[1]} + \frac{1}{A}T^{[2]} + \sum_{i<j} V_{ij}^{[2]} + \sum_{i<j<k} W_{ijk}^{[3]}, \quad (1)$$

where the kinetic term is composed of one- and two-body pieces,

$$T^{[1]} = \sum_{i=1}^A \frac{\mathbf{p}_i^2}{2m_N}, \quad T^{[2]} = - \sum_{i<j} \frac{\mathbf{p}_i \cdot \mathbf{p}_j}{m_N}, \quad (2)$$

with m_N being the mass of nucleon and \mathbf{p}_i the momentum of the i -th nucleon.

The above Hamiltonian is normal-ordered with respect to a symmetr-conserving reference state $|\Psi\rangle$, and truncated up to NO2B terms. The resultant Hamiltonian $\hat{\mathcal{H}}_0$ in the NO2B approximation can be written as

$$\hat{\mathcal{H}}_0 = E_0 + \sum_{pq} f_q^p :A_q^p: + \frac{1}{4} \sum_{pqrs} \Gamma_{rs}^{pq} :A_{rs}^{pq}:. \quad (3)$$

The strings of creation and annihilation operators are defined as

$$A_{stu\dots}^{pqr\dots} = a_p^\dagger a_q^\dagger a_r^\dagger \dots a_u a_t a_s. \quad (4)$$

The expectation values of the normal-ordered operators, indicated by $:A_{q\dots}^p:$, with respect to the reference state are zero. The zero-body piece of the \mathcal{H}_0 is just the energy of the reference state

$$E_0 \equiv \langle \Psi | \hat{H}_0 | \Psi \rangle = \sum_{pq} \bar{t}_q^p \gamma_q^p + \frac{1}{4} \sum_{pqrs} \bar{v}_{rs}^{pq} \gamma_{rs}^{pq} + \frac{1}{36} \sum_{pqrstu} w_{sttu}^{pqr} \gamma_{stu}^{pqr}. \quad (5)$$

The matrix element of the normal-ordered one-body operator (NO1B) is given by

$$f_q^p = \bar{t}_q^p + \sum_{rs} \bar{v}_{rs}^{pq} \gamma_s^r + \frac{1}{4} \sum_{rstu} w_{qtuu}^{prs} \gamma_{tu}^{rs}, \quad (6)$$

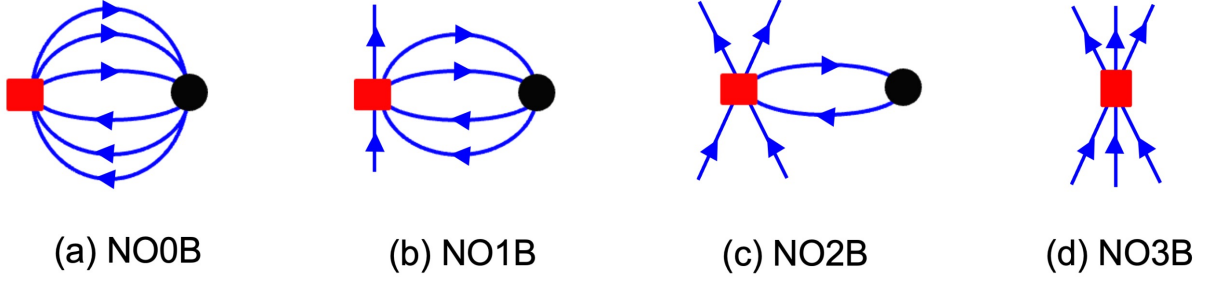


FIG. 1: Schematic illustration of the three-nucleon interaction W (red squares), normal-ordered to (a) zero-body, (b) one-body, (c) two-body and (d) three-body terms with a reference state. The n -bdy density matrices $\gamma^{[n]}$ of the reference state, defined in (8), are represented with black circles.

and that of the NO2B operator,

$$\Gamma_{rs}^{pq} = \bar{v}_{rs}^{pq} + \sum_{tu} w_{rsu}^{pqt} \gamma_u^t. \quad (7)$$

The last terms in (5), (6) and (7) contributed by the 3N interaction are depicted schematically in Fig. 1(a), (b), and (c), respectively. Here, we have introduced the density matrices of the (symmetry-conserving) correlated reference state $|\Psi\rangle$,

$$\gamma_q^p \equiv \langle \Psi | A_q^p | \Psi \rangle, \quad (8a)$$

$$\gamma_{rs}^{pq} \equiv \langle \Psi | A_{rs}^{pq} | \Psi \rangle, \quad (8b)$$

$$\gamma_{stu}^{pqr} \equiv \langle \Psi | A_{stu}^{pqr} | \Psi \rangle. \quad (8c)$$

Static correlations within the reference state are encoded in the corresponding *irreducible* density matrices

$$\lambda_q^p \equiv \gamma_q^p, \quad (9a)$$

$$\lambda_{rs}^{pq} \equiv \gamma_{rs}^{pq} - \mathcal{A}(\lambda_r^p \lambda_s^q) = \gamma_{rs}^{pq} - \lambda_r^p \lambda_s^q + \lambda_s^p \lambda_r^q, \quad (9b)$$

$$\lambda_{stu}^{pqr} \equiv \gamma_{stu}^{pqr} - \mathcal{A}(\lambda_s^p \lambda_{tu}^{qr} + \lambda_s^q \lambda_{tu}^{pr}), \quad (9c)$$

where the antisymmetrization operator \mathcal{A} generates all possible permutations (each only once) of upper indices and lower indices. For a single-reference state, the two-body and three-body irreducible densities λ_{rs}^{pq} and λ_{stu}^{pqr} vanish.

The Hamiltonian $\hat{\mathcal{H}}_0$ is subsequently rewritten into the unnormal-ordered form as follows,

$$\hat{\mathcal{H}}_0 = \mathcal{E}_0 + \sum_{pq} \mathcal{F}_q^p A_q^p + \frac{1}{4} \sum_{pqrs} \mathcal{V}_{rs}^{pq} A_{rs}^{pq}, \quad (10)$$

where the zero-body term is given by

$$\begin{aligned}
\mathcal{E}_0 &= E_0 - \sum_{pq} \left(f_q^p - \sum_{rs} \Gamma_{qs}^{pr} \gamma_s^r \right) \gamma_q^p - \frac{1}{4} \sum_{pqrs} \Gamma_{qs}^{pr} \gamma_{qs}^{pr} \\
&= \frac{1}{36} \sum_{pqrst} w_{st}^{pqr} (\gamma_{st}^{pqr} + 36 \gamma_s^p \gamma_t^q \gamma_u^r - 18 \gamma_{st}^{pq} \gamma_u^r) \\
&= \frac{1}{36} \sum_{pqrst} w_{st}^{pqr} \left(6 \lambda_s^p \lambda_t^q \lambda_u^r - 9 \lambda_{st}^{pq} \lambda_u^r + \lambda_{st}^{pqr} \right).
\end{aligned} \tag{11a}$$

The matrix elements of one-body read

$$\begin{aligned}
\mathcal{F}_q^p &= f_q^p - \sum_{rs} \Gamma_{qs}^{pr} \gamma_s^r \\
&= \bar{f}_q^p + \frac{1}{4} \sum_{rstu} w_{qt}^{prs} \left(\lambda_{tu}^{rs} - 2 \lambda_t^r \lambda_u^s \right),
\end{aligned} \tag{11b}$$

and those of two-body terms

$$\mathcal{V}_{rs}^{pq} = \Gamma_{rs}^{pq} = \bar{v}_{rs}^{pq} + \sum_{tu} w_{rstu}^{pqt} \lambda_u^t. \tag{11c}$$

In this work, the reference state $|\Psi\rangle$ is chosen as a PNP-HFB state for ^{20}Ne , ^{22}Ne and an ensemble of them with equal weights, which are labeled with `magic-Ne20`, `magic-Ne22`, and `magic-ENO/EW`, respectively. The obtained effective Hamiltonians \mathcal{H}_0 are labeled as `H0`. For comparison, we also derive the Hamiltonian without the $3N$ interaction term in (1), and this Hamiltonian is labeled as `H0 (w/o 3N)`. The expressions for the one-, two-, and three-body density matrices of a spherical PNP-HFB state have been given in Ref. [29]. Subsequently, these Hamiltonians are employed into the PGCM calculations.

B. Nuclear wave functions

The wave functions of low-lying states for an odd-mass nucleus are constructed with the PGCM as follows,

$$|\Psi_\alpha^{J\pi}\rangle = \sum_c f_c^{J\alpha\pi} |NZJ\pi; c\rangle, \tag{12}$$

Here, α distinguishes the states with the same angular momentum J , and the symbol c is a collective label for the indices (K, κ, \mathbf{q}) . The basis function with correct quantum numbers $(NZJ\pi)$ is given by

$$|NZJ\pi; c\rangle = \hat{P}_{MK}^J \hat{P}^N \hat{P}^Z |\Phi_\kappa^{(\text{OA})}(\mathbf{q})\rangle, \tag{13}$$

where \hat{P}_{MK}^J and $\hat{P}^{N,Z}$ are projection operators that select components with the angular momentum J , neutron number N and proton number Z [2],

$$\hat{P}_{MK}^J = \frac{2J+1}{8\pi^2} \int d\Omega D_{MK}^{J*}(\Omega) \hat{R}(\Omega), \quad (14a)$$

$$\hat{P}^{N_\tau} = \frac{1}{2\pi} \int_0^{2\pi} d\varphi_\tau e^{i\varphi_\tau(\hat{N}_\tau - N_\tau)}. \quad (14b)$$

The operator \hat{P}_{MK}^J extracts the component of angular momentum along the intrinsic axis z defined by K . The Wigner D -function is defined as $D_{MK}^J(\Omega) \equiv \langle JM | \hat{R}(\Omega) | JK \rangle = \langle JM | e^{i\phi\hat{J}_z} e^{i\theta\hat{J}_y} e^{i\psi\hat{J}_z} | JK \rangle$, where $\Omega = (\phi, \theta, \psi)$ represents the three Euler angles. The $\hat{N} = \sum_k a_k^\dagger a_k$ is particle-number operator. The mean-field configurations $|\Phi_k^{(\text{OA})}(\mathbf{q})\rangle$ for odd-mass nuclei can be constructed as one-quasiparticle excitations on even-even vacua [2],

$$|\Phi_k^{(\text{OA})}(\mathbf{q})\rangle = \alpha_k^\dagger |\Phi_{(k)}(\mathbf{q})\rangle, \quad \alpha_k |\Phi_{(k)}(\mathbf{q})\rangle = 0, \quad (15)$$

where $|\Phi_{(k)}(\mathbf{q})\rangle$ is a HFB state with even-number parity labeled with the collective coordinate \mathbf{q} . The quasiparticle operators (α, α^\dagger) are connected to single-particle operators (a, a^\dagger) via the Bogoliubov transformation [2],

$$\begin{pmatrix} \alpha \\ \alpha^\dagger \end{pmatrix} = \begin{pmatrix} U^\dagger & V^\dagger \\ V^T & U^T \end{pmatrix} \begin{pmatrix} a \\ a^\dagger \end{pmatrix}, \quad (16)$$

where the U, V matrices are determined by the minimization of particle-number projected energy,

$$\delta \frac{\langle \Phi_k^{(\text{OA})}(\mathbf{q}) | \hat{\mathcal{H}} \hat{P}^N \hat{P}^Z | \Phi_k^{(\text{OA})}(\mathbf{q}) \rangle}{\langle \Phi_k^{(\text{OA})}(\mathbf{q}) | \hat{P}^N \hat{P}^Z | \Phi_k^{(\text{OA})}(\mathbf{q}) \rangle} = 0. \quad (17)$$

Different from the recent study based on a covariant EDF in Ref.[26], where three different schemes were employed to construct the configurations for odd-mass nuclei within the BCS ansatz, in this work we obtain the configurations of one-quasiparticle states with odd-number parity self-consistently by simply exchanging the k -column of the U and V matrices in the HFB wave function [2]:

$$(U_{pk}, V_{pk}) \longleftrightarrow (V_{pk}^*, U_{pk}^*), \quad (18)$$

where the index $p = (\tau n \ell j m)_p \equiv (n_p, \xi_p)$ is a label for the spherical harmonic oscillator basis, and k the label for a quasiparticle state. For simplicity, axial symmetry is assumed. In this case, quasiparticle states are labeled with quantum numbers K^π , where $K = |m_p|$ with m_p being the

projection of angular momentum j_p along z -axis, and parity $\pi = (-1)^{\ell_p}$. The collective coordinate \mathbf{q} is replaced with the dimensionless quadrupole deformation β_2 ,

$$\beta_2 = \frac{4\pi}{3AR^2} \langle \Phi_\kappa^{(\text{OA})}(\mathbf{q}) | r^2 Y_{20} | \Phi_\kappa^{(\text{OA})}(\mathbf{q}) \rangle. \quad (19)$$

The U and V matrices are determined from the HFB calculation within the scheme of variation after particle-number projection(VAPNP). For details, see, for instance, Ref. [30]. We note that the Kramer's degeneracy is lifted due to the breaking of time-reversal invariance in the self-consistent HFB calculation.

The weight function $f_c^{J\alpha\pi}$ of the state (12) is determined by the variational principle, which leads to the following Hill-Wheeler-Griffin (HWG) equation [2, 7],

$$\sum_{c'} \left[\mathcal{H}_{cc'}^{NZJ\pi} - E_\alpha^J \mathcal{N}_{cc'}^{NZJ\pi} \right] f_{c'}^{J\alpha\pi} = 0, \quad (20)$$

where the Hamiltonian kernel and norm kernel are defined by

$$\begin{aligned} \mathcal{O}_{cc'}^{NZJ\pi} &= \langle NZJ\pi; c | \hat{O} | NZJ\pi; c' \rangle \\ &= \frac{2J+1}{8\pi^2} \int d\Omega D_{KK'}^*(\Omega) \int_0^{2\pi} d\varphi_n \frac{e^{-iN\varphi_n}}{2\pi} \int_0^{2\pi} d\varphi_p \frac{e^{-iZ\varphi_p}}{2\pi} \\ &\quad \times \langle \Phi_\kappa^{(\text{OA})}(\mathbf{q}) | \hat{O} \hat{R}(\Omega) e^{iZ\varphi_p} e^{iN\varphi_n} | \Phi_{\kappa'}^{(\text{OA})}(\mathbf{q}') \rangle, \end{aligned} \quad (21)$$

with the operator \hat{O} representing $\hat{\mathcal{H}}$ and 1, respectively. The parity π is defined by the quasiparticle configurations $|\Phi_\kappa^{(\text{OA})}(\mathbf{q})\rangle$.

The HWG equation (20) for a given set of quantum numbers (NZJ) is solved in the standard way as discussed in Refs.[2, 31]. It is accomplished by diagonalizing the norm kernel $\mathcal{N}_{cc'}^{NZJ\pi}$ first. A new set of basis is constructed using the eigenfunctions of the norm kernel with eigenvalue larger than a pre-chosen cutoff value to remove possible redundancy in the original basis. The Hamiltonian is diagonalized in this new basis. In this way, one is able to obtain the energies E_α^J and the mixing weights $f_c^{J\alpha\pi}$ of nuclear states $|\Psi_\alpha^{J\pi}\rangle$. Since the basis functions $|NZJ; c\rangle$ are nonorthogonal to each other, one usually introduces the collective wave function $g_\alpha^{J\pi}(K, \mathbf{q})$ as below

$$g_\alpha^{J\pi}(K, \mathbf{q}) = \sum_{c'} (\mathcal{N}^{1/2})_{c,c'}^{NZJ\pi} f_{c'}^{J\alpha\pi}, \quad (22)$$

which fulfills the normalization condition. The distribution of $g_\alpha^{J\pi}(K, \mathbf{q})$ over K and \mathbf{q} reflects the contribution of each basis function to the nuclear state $|\Psi_\alpha^{J\pi}\rangle$.

C. Evaluation of norm and Hamiltonian overlaps

The energy overlap is defined as the ratio of Hamiltonian overlap to the norm overlap,

$$\begin{aligned}
E(\kappa\mathbf{q}, \kappa'\mathbf{q}'; g) &\equiv \frac{\langle \Phi_{\kappa}^{(\text{OA})}(\mathbf{q}) | \hat{\mathcal{H}} \hat{R}(\Omega) e^{i\hat{Z}\varphi_p} e^{i\hat{N}\varphi_n} | \Phi_{\kappa'}^{(\text{OA})}(\mathbf{q}') \rangle}{\langle \Phi_{\kappa}^{(\text{OA})}(\mathbf{q}) | \hat{R}(\Omega) e^{i\hat{Z}\varphi_p} e^{i\hat{N}\varphi_n} | \Phi_{\kappa'}^{(\text{OA})}(\mathbf{q}') \rangle} \\
&= \mathcal{E} + \sum_{pq} \mathcal{F}_q^p \tilde{\rho}_q^p(\kappa\mathbf{q}, \kappa'\mathbf{q}'; g) + \frac{1}{4} \sum_{pqrs} \gamma_{rs}^{pq} \tilde{\rho}_{rs}^{pq}(\kappa\mathbf{q}, \kappa'\mathbf{q}'; g), \tag{23}
\end{aligned}$$

where g stands for the set of parameters $\{\Omega, \varphi_n, \varphi_p\}$. The matrix elements of the mixed one-body densities and pairing tensors, hatted with the symbol \sim , are defined as

$$\tilde{\rho}_q^p(\kappa\mathbf{q}, \kappa'\mathbf{q}'; g) \equiv \frac{\langle \Phi_{\kappa}^{(\text{OA})}(\mathbf{q}) | a_p^\dagger a_q \hat{R}(\Omega) e^{i\hat{Z}\varphi_p} e^{i\hat{N}\varphi_n} | \Phi_{\kappa'}^{(\text{OA})}(\mathbf{q}') \rangle}{\langle \Phi_{\kappa}^{(\text{OA})}(\mathbf{q}) | \hat{R}(\Omega) e^{i\hat{Z}\varphi_p} e^{i\hat{N}\varphi_n} | \Phi_{\kappa'}^{(\text{OA})}(\mathbf{q}') \rangle}, \tag{24}$$

$$\tilde{\kappa}^{pq}(\kappa\mathbf{q}, \kappa'\mathbf{q}'; g) \equiv \frac{\langle \Phi_{\kappa}^{(\text{OA})}(\mathbf{q}) | a_p^\dagger a_q^\dagger \hat{R}(\Omega) e^{i\hat{Z}\varphi_p} e^{i\hat{N}\varphi_n} | \Phi_{\kappa'}^{(\text{OA})}(\mathbf{q}') \rangle}{\langle \Phi_{\kappa}^{(\text{OA})}(\mathbf{q}) | \hat{R}(\Omega) e^{i\hat{Z}\varphi_p} e^{i\hat{N}\varphi_n} | \Phi_{\kappa'}^{(\text{OA})}(\mathbf{q}') \rangle}, \tag{25}$$

$$\tilde{\kappa}_{rs}(\kappa\mathbf{q}, \kappa'\mathbf{q}'; g) \equiv \frac{\langle \Phi_{\kappa}^{(\text{OA})}(\mathbf{q}) | a_s a_r \hat{R}(\Omega) e^{i\hat{Z}\varphi_p} e^{i\hat{N}\varphi_n} | \Phi_{\kappa'}^{(\text{OA})}(\mathbf{q}') \rangle}{\langle \Phi_{\kappa}^{(\text{OA})}(\mathbf{q}) | \hat{R}(\Omega) e^{i\hat{Z}\varphi_p} e^{i\hat{N}\varphi_n} | \Phi_{\kappa'}^{(\text{OA})}(\mathbf{q}') \rangle}. \tag{26}$$

The matrix elements of the mixed two-body density are determined by the generalized Wick theorem [32],

$$\begin{aligned}
\tilde{\rho}_{rs}^{pq}(\kappa\mathbf{q}, \kappa'\mathbf{q}'; g) &\equiv \frac{\langle \Phi_{\kappa}^{(\text{OA})}(\mathbf{q}) | a_p^\dagger a_q^\dagger a_s a_r \hat{R}(\Omega) e^{i\hat{Z}\varphi_p} e^{i\hat{N}\varphi_n} | \Phi_{\kappa'}^{(\text{OA})}(\mathbf{q}') \rangle}{\langle \Phi_{\kappa}^{(\text{OA})}(\mathbf{q}) | \hat{R}(\Omega) e^{i\hat{Z}\varphi_p} e^{i\hat{N}\varphi_n} | \Phi_{\kappa'}^{(\text{OA})}(\mathbf{q}') \rangle} \\
&= \tilde{\rho}_r^p \tilde{\rho}_s^q - \tilde{\rho}_s^p \tilde{\rho}_r^q + \tilde{\kappa}^{pq} \tilde{\kappa}_{rs}. \tag{27}
\end{aligned}$$

With the above relation, the energy overlap can be rewritten as below,

$$E(\kappa\mathbf{q}, \kappa'\mathbf{q}'; g) = \mathcal{E} + \sum_{pq} \mathcal{F}_q^p \tilde{\rho}_q^p + \frac{1}{2} \sum_{pq} \left(\tilde{\Gamma}_q^p \tilde{\rho}_q^p + \tilde{\Delta}^{pq} \tilde{\kappa}_{pq} \right), \tag{28}$$

where the matrix elements of the mixed particle-hole field $\tilde{\Gamma}$ and particle-particle field $\tilde{\Delta}$ are defined as

$$\tilde{\Gamma}_q^p \equiv \sum_{pqrs} \gamma_{qs}^{pr} \tilde{\rho}_s^r, \quad \tilde{\Delta}^{pq} \equiv \frac{1}{2} \sum_{rs} \gamma_{pq}^{rs} \tilde{\kappa}^{rs}. \tag{29}$$

It is efficient to compute the energy overlap directly in the J -coupled scheme.

- The contribution of the one-body term is simply given by

$$E^{(1B)} = \sum_{pq} \delta_{j_p j_q} \hat{J}_p \mathcal{F}_{(qp)}^0 \tilde{\rho}_{(qp)00}, \tag{30}$$

where $\hat{j}_p \equiv \sqrt{2j_p + 1}$. The reduced matrix element is defined as $\mathcal{F}_{qp}^0 = \langle q | \mathcal{F}_0 | p \rangle$, and the one-body density operator with the two angular momenta coupled to zero [13]

$$\hat{\rho}_{(qp)00} \equiv \frac{[a_q^\dagger \tilde{a}_p]_{00}}{\sqrt{2j_q + 1}} \delta_{\xi_q \xi_p} \quad (31)$$

with $\tilde{a}_{nljm} \equiv (-1)^{j+m} a_{nlj-m}$.

- The energy by the two-body term consists of pp term

$$E_{pp}^{(2B)} = -\frac{1}{4} \sum_{abcd,L} \mathcal{V}_{(ab)(cd)}^L \sum_{M_L} (-1)^{L-M_L} \tilde{\kappa}_{(ab)LM_L}^{(01)} \tilde{\kappa}_{(cd)L-M_L}^{(10)} \quad (32)$$

and ph term

$$E_{ph}^{(2B)} = \frac{1}{2} \sum_{abcd,L} \mathcal{V}_{(a\bar{b})(c\bar{d})}^L \sum_{M_L} \tilde{\rho}_{(ba)LM_L} \tilde{\rho}_{(dc)L-M_L}^\dagger \quad (33)$$

where the J -coupled mixed density and pairing density are defined as,

$$\tilde{\rho}_{(ba)LM_L} = \sum_{m_a m_b} s_b \langle j_a m_a j_b - m_b | LM_L \rangle \tilde{\rho}_b^a, \quad (34a)$$

$$\tilde{\rho}_{(dc)L-M_L}^\dagger = \sum_{m_c m_d} s_d \langle j_c m_c j_d - m_d | L - M_L \rangle (\tilde{\rho}_d^c)^\dagger, \quad (34b)$$

$$\tilde{\kappa}_{(ab)LM_L}^{(01)} = \sum_{m_a m_b} \langle j_a m_a j_b m_b | LM_L \rangle \tilde{\kappa}^{ab}, \quad (34c)$$

$$\tilde{\kappa}_{(cd)L-M_L}^{(10)} = (-1)^{L+M_L} \sum_{m_c m_d} \langle j_c m_c j_d m_d | LM_L \rangle (\tilde{\kappa}_{cd})^\dagger. \quad (34d)$$

Here, we introduce the symbol $s_b \equiv (-1)^{j_b - m_b}$. The symmetry of Clebsch–Gordan coefficient $\langle j_a m_a j_b - m_b | LM_L \rangle$ implies the relation $\tilde{\rho}_{(ba)LM_L} = (-1)^{L-(j_a+j_b)+1} \tilde{\rho}_{(ab)LM_L}$. The ph -type two-body interaction matrix elements in the J -coupled form are related to those of pp -type by Pandya transformation [33],

$$\mathcal{V}_{(i\bar{j})(k\bar{l})}^J = - \sum_L \hat{L}^2 \begin{Bmatrix} j_i & j_j & J \\ j_k & j_l & L \end{Bmatrix} \mathcal{V}_{(i)(k,j)}^L, \quad (35)$$

where the unnormalized pp -type two-body matrix elements in the J -coupled form are related to those in M -scheme as follows

$$\mathcal{V}_{(ij)(kl)}^J = \sum_{m_i m_j m_k m_l} \langle j_i m_i j_j m_j | JM \rangle \langle j_k m_k j_l m_l | JM \rangle \mathcal{V}_{kl}^{ij}. \quad (36)$$

The norm overlap of the HFB wave functions with odd-number parity is computed with the Pfaffian formula in Ref. [34].

III. RESULTS AND DISCUSSION

A. Effective Hamiltonians

In this work, the NN interaction $V_{ij}^{(2)}$ in Eq.(1) is chosen as the chiral $N^3\text{LO}$ interaction by Entem and Machleidt [35], denoted as "EM". We utilize the free-space SRG [36] to evolve the EM interaction to a resolution scale of $\lambda = 1.8 \text{ fm}^{-1}$. The $3N$ interaction $W_{ijk}^{(3)}$ is directly constructed with a cutoff of $\Lambda = 2.0 \text{ fm}^{-1}$. The Hamiltonian is referred to as $\text{EM}\lambda/\Lambda$, i.e., $\text{EM}1.8/2.0$, which was fitted to NN scattering phase shifts, the binding energy of ^3H , and the charge radius of ^4He . See Ref.[37] for details. For the $3N$ interaction, we discard all matrix elements involving states with $e_1 + e_2 + e_3 > 14$, where $e_i = 2n_i + \ell_i$ denotes the number of harmonic oscillator major shells for the i -th state. The maximal value of e_i is labeled with e_{\max} , and the frequency of the harmonic oscillator basis is chosen as $\hbar\omega = 20 \text{ MeV}$. In this work, $e_{\max} = 6$, and $\hbar\omega = 20 \text{ MeV}$ are employed. Starting from the chiral $NN+3N$ interaction, we produce three sets of effective Hamiltonians labeled as **magic-Ne20**, **magic-Ne22**, and **magic-ENO/EW**, respectively. These Hamiltonians are generated by normal-ordering the $3N$ interaction with respect to the reference states of spherical PNP-HFB states for ^{20}Ne , ^{22}Ne , and their ensemble with equal weights, respectively. The residual normal-ordered three-body term, c.f. Fig. 1(d), is neglected. Table I lists the expectation value of each term in the three types of effective Hamiltonians \mathcal{H}_0 in (10) with respect to the corresponding reference state. One can see that in the case without the $3N$ interaction, the unnormal-ordering form of the Hamiltonian \mathcal{H}_0 returns back to the original Hamiltonian \hat{H}_0 .

The relative contribution of each term in different effective Hamiltonians to the energy is compared in Tab I. The contribution of the $3N$ interaction to energy, c.f. Fig. 1(a), is given by

$$E_0^{(3)} = \frac{1}{36} \sum_{pqrst} w_{rsu}^{pqt} \left(6\lambda_s^p \lambda_t^q \lambda_u^r + 9\lambda_s^p \lambda_{tu}^{qr} + \lambda_{rsu}^{pqt} \right). \quad (37)$$

Comparing the E_0 value in the third row of Tab I, labeled by **Ne20** with the E_0 value in the last row, labeled by **Ne20 (w/o 3N)**, one finds the contribution of the $3N$ interaction to the energy $E_0^{(3)} = 80.338 \text{ MeV}$. On the other hand, the zero-point energy \mathcal{E}_0 in (11a) of the unnormal-ordered Hamiltonian in the first row

$$\mathcal{E}_0 = \frac{1}{36} \sum_{pqrst} w_{stu}^{pqr} \left(6\lambda_s^p \lambda_t^q \lambda_u^r - 9\lambda_{st}^{pq} \lambda_u^r + \lambda_{stu}^{pqr} \right) \quad (38)$$

TABLE I: The expectation value (in MeV) of each term in the three different effective Hamiltonians \mathcal{H}_0 with respect to corresponding reference state.

Interactions	E_0	$\langle \mathcal{F} \rangle$	$\langle \mathcal{V} \rangle$	\mathcal{E}_0
magic-Ne20	-96.931	211.205	-358.229	50.093
magic-ENO/EW	-101.781	225.067	-381.555	54.706
magic-Ne22	-109.034	242.241	-408.614	57.339
magic-Ne20(w/o 3N)	-177.269	506.122	-683.391	0

is 50.093 MeV. Their difference gives

$$\frac{1}{2} \sum_{pqrstu} w_{stu}^{pqr} \lambda_{st}^{pq} \lambda_u^r = 30.245 \quad \text{MeV.} \quad (39)$$

Since the term depending on λ_{stu}^{pqr} is much smaller than the other terms, we drop this term out and find the term,

$$\frac{1}{6} \sum_{pqrstu} w_{rsu}^{pqt} \lambda_s^p \lambda_t^q \lambda_u^r = 65.215 \quad \text{MeV,} \quad (40)$$

which depends solely on the one-body density, provides the predominant contribution to energies $E_0^{(3)}$ and \mathcal{E}_0 . It implies that the terms depend on higher-order of irreducible densities λ are less important. Subsequently, we carry out PGCM calculations for low-lying states of ^{21}Ne using the above effective Hamiltonians.

Both Fig. 2 and Fig. 3 show the change of the effective single-particle energies (ESPEs) with the quadrupole deformation β_2 from the PNP-HFB (VAPNP) calculation for the HFB states with different K^π , where the PNP is carried before variation. The ESPE is obtained from the diagonalization of the single-particle Hamiltonian,

$$\begin{aligned} h_q^p &= \mathcal{F}_q^p + \sum_{rs} \mathcal{V}_{qs}^{pr} \rho_s^r \\ &= \bar{t}_q^p + \sum_{rs} \bar{v}_{qs}^{pr} \rho_s^r + \frac{1}{4} \sum_{rstu} w_{qsu}^{prt} \gamma_{su}^{rt} + \sum_{rstu} w_{qsu}^{prt} \gamma_s^r (\rho_u^t - \gamma_u^t), \end{aligned} \quad (41)$$

where γ_u^t is the one-body density of the correlated state, and ρ_s^r is the one-body density of mean-field state $|\Phi_\kappa^{(\text{OA})}(\mathbf{q})\rangle$ defined by

$$\rho_s^r \equiv \langle \Phi_\kappa^{(\text{OA})}(\mathbf{q}) | a_r^\dagger a_s | \Phi_\kappa^{(\text{OA})}(\mathbf{q}) \rangle. \quad (42)$$

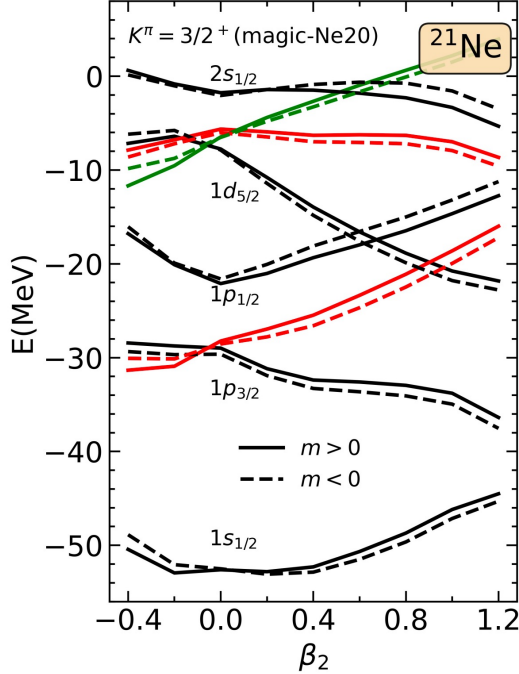


FIG. 2: The effective single-particle energies of neutron states with $m > 0$ (solid lines) and $m < 0$ (dashed lines) as a function of quadrupole deformation β_2 from the PNP-HFB (VAPNP) calculation for the HFB states with $K^\pi = 3/2^+$ using the effective Hamiltonians `magic-Ne20`.

It is shown in Fig. 2 that the neutron partner states with the same value of $|m|$, related by the time-reversal operator, are not degenerate in the HFB states for ^{21}Ne with odd-number parity. A comparison is made between the ESPEs obtained by the effective Hamiltonians `magic-Ne20` and `magic-Ne22`. The lifting of Kramers's degeneracy in the HFB states for ^{21}Ne results in non-degeneracy among time-reversal states with identical values of $|m|$. For clarity, only the energy of one of the time-reversal states with $m > 0$ is depicted in Fig. 3. It is observed that the ESPEs from the two effective Hamiltonians are difficult to distinguish.

Before presenting the projected energy curves with different angular momenta, we examine the issues of singularity and finite steps found in the MR-EDF [27, 28]. Figure 4 displays the energies (normalized to the converged values) of PNP-HFB states for ^{21}Ne with $K^\pi = 1/2^+$ and quadrupole deformation $\beta_2 = 0.0$, as a function of the number N_φ of meshpoints in the gauge angle φ . The Fomenko expansion method [38] is used for the particle-number projection, where the k -th gauge angle φ_k is chosen as $2\pi(k/N_\varphi)$. It is observed that the energy remains constant for $N_\varphi \geq 5$, regardless of whether N_φ is an even or odd number. For comparison, we also show the results from calculations by artificially multiplying a factor of 1.1 to the two-body interaction

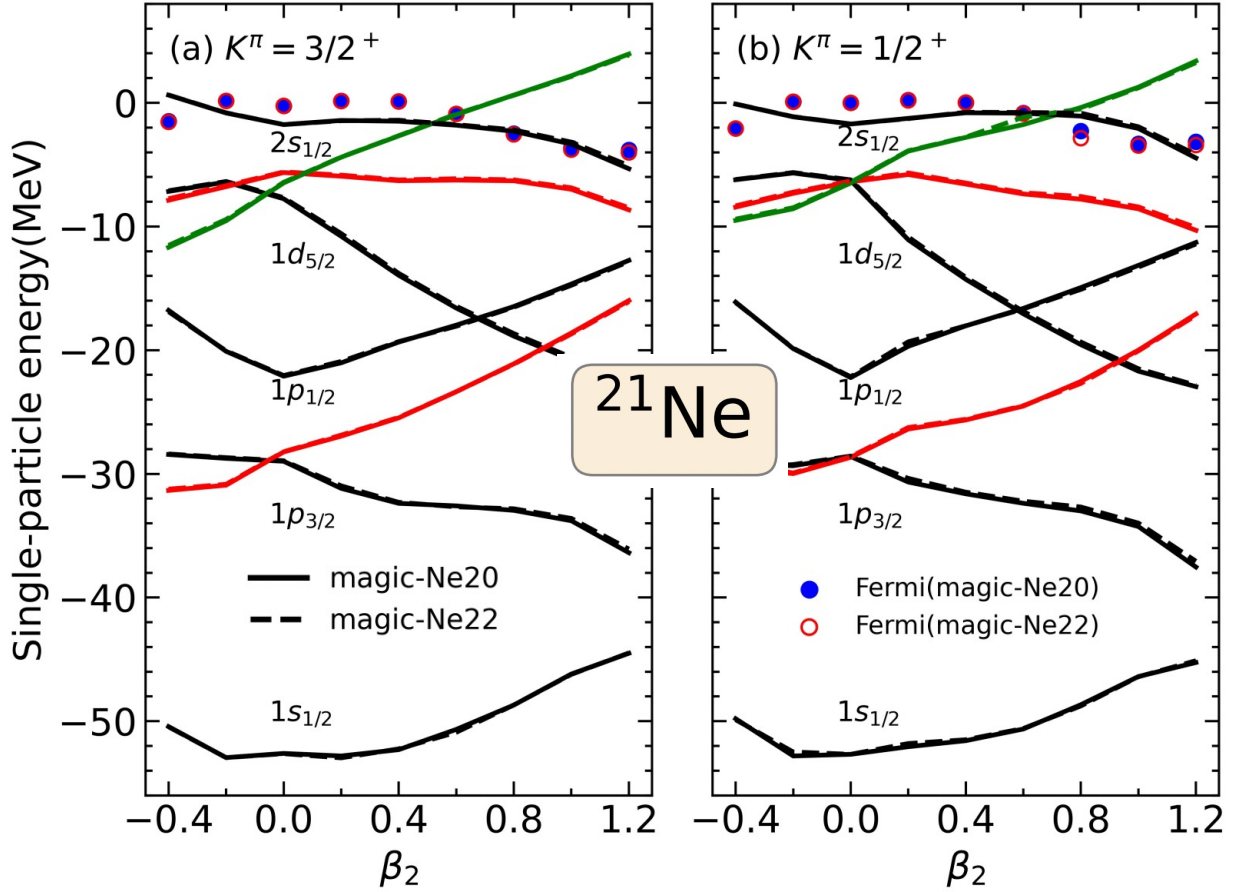


FIG. 3: The effective single-particle energies of neutron states (with $m > 0$) from the PNP-HFB (VAPNP) calculation for the HFB states with $K^\pi = 3/2^+$ (a) and $K^\pi = 1/2^+$ (b), where the effective Hamiltonians magic-Ne20 (solid) and magic-Ne22 (dashed lines) are employed, respectively. The Fermi energies are indicated with dots.

matrix elements \mathcal{V} for the mixed particle-hole field $\tilde{\Gamma}$. In this case, dips are indeed observed at $N_\varphi = 20, 40, 60, \dots$, corresponding to the situation where the gauge angle $\varphi_k = \pi/2$ is chosen at the meshpoints with $k = 5, 10, 15, \dots$, respectively. It demonstrates numerically that one should use the same interaction matrix elements for both the particle-hole and particle-particle channels in which case one is free of the problem of singularity.

Figure 5 displays the energy curves of particle-number projected HFB states for ^{21}Ne with $K^\pi = 3/2^+$ and $1/2^+$, respectively. The HFB wave functions are obtained from the PNP-HFB (VAPNP) calculations using the Hamiltonian $\hat{\mathcal{H}}_0$, with the $3N$ interaction normal-ordered with respect to the references of ^{20}Ne , ^{22}Ne , and their ensemble with equal weights, respectively. It

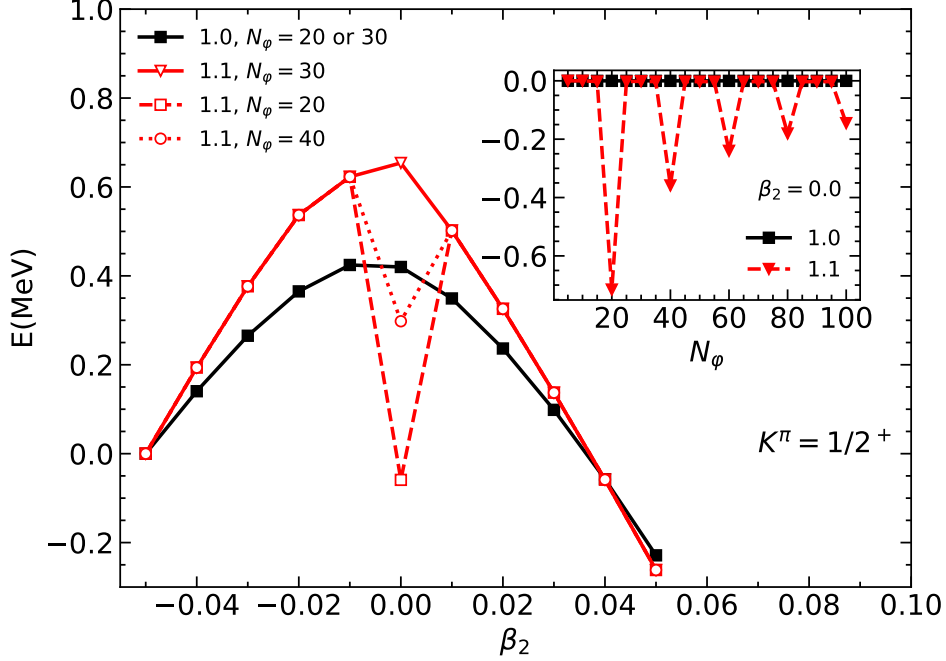


FIG. 4: The energies of PNP-HFB (VAPNP) states for ^{21}Ne with $K^\pi = 1/2^+$ as a function of quadrupole deformation β_2 , where the number N_φ of meshpoint in the gauge angle φ is chosen as 20, 30, and 40, respectively. The results from the calculations by multiplying a factor of 1.1 artificially to the two-body interaction matrix elements for the mixed field $\tilde{\Gamma}$ are given for comparison. The inset shows the energy of spherical state normalized to the converged value as a function of N_φ .

can be observed that the global energy minima of all three curves are located in prolate states with quadrupole deformation β_2 between 0.4 and 0.5. The configurations with $K^\pi = 3/2^+$ are globally lower than those with $K^\pi = 1/2^+$. Furthermore, the configurations based on different Hamiltonians are systematically shifted from each other in energy by less than one MeV.

Figure 6 displays the energies of states with projection onto correct particle numbers and $J^\pi = 3/2^+$, $5/2^+$, and $7/2^+$ for ^{21}Ne with $K^\pi = 3/2^+$ and $K^\pi = 1/2^+$, respectively. The effective Hamiltonians used are H_0 with and without the $3N$ interaction. It is shown that the quadrupole deformation parameter β_2 of the prolate energy-minimal state by the H_0 (w/o $3N$) is smaller than the other two cases. Additionally, the energy curve with the increase of β_2 is also stiffer than that with the $3N$ interaction. In other words, the $3N$ interaction helps the development of quadrupole collectivity in ^{21}Ne .

Figure 7 shows a comparison of the energy spectra for ^{21}Ne from configuration-mixing calculations with different Hamiltonians. The states with the same K^π are grouped into the same

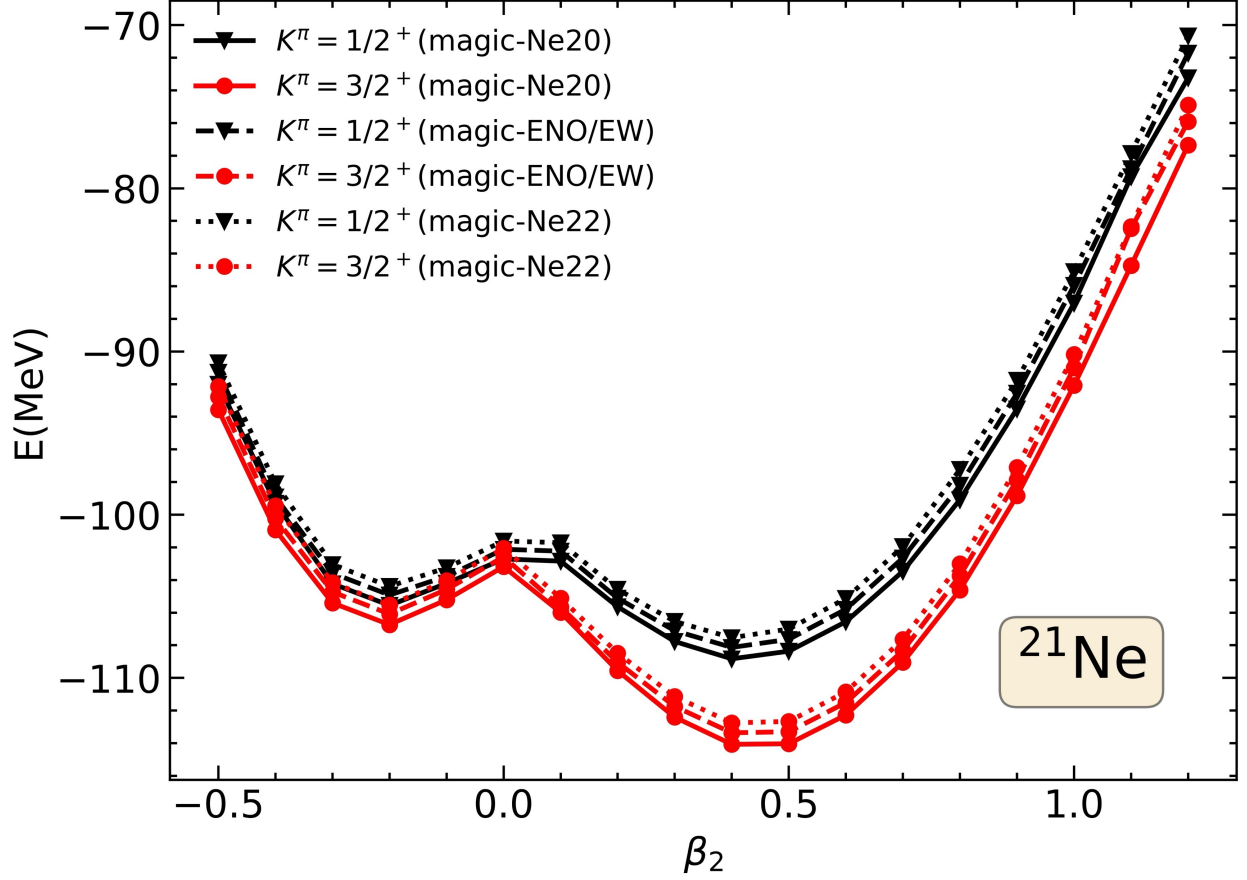


FIG. 5: The energies of mean-field states $|\Phi_k^{(OA)}(\mathbf{q})\rangle$ for ^{21}Ne with $K^\pi = 1/2^+, 3/2^+$ as a function of intrinsic quadrupole deformation β_2 from the PNP-HFB (VAPNP) calculation using the three effective Hamiltonians.

column. The main features of the two bands with $K^\pi = 3/2^+$ and $1/2^+$ are reproduced, although the excitation energies of the states belonging to the $1/2^+$ band are systematically overestimated. The mixing of quasiparticle excitation configurations is expected to lower the entire $K^\pi = 1/2^+$ band. In Fig.7(c), one can observe that the energy spectra from the Hamiltonians `magic-Ne20` and `magic-Ne22` are very close to each other. The high-lying states from `magic-Ne22` are slightly lower than those from `magic-Ne20`. In Fig.7(b), the energy spectra become more stretched when the $3N$ interaction is turned off.

The collective wave functions of the low-lying states with different J^π , and $K^\pi = 3/2^+$ and $1/2^+$, by the `magic-Ne20` effective Hamiltonian, are displayed in Fig. 8. It is shown that in all cases, the wave functions are peaked around $\beta_2 = 0.4$ and do not change significantly with the increase of angular momentum, implying the stability of the shapes in the low-lying states.

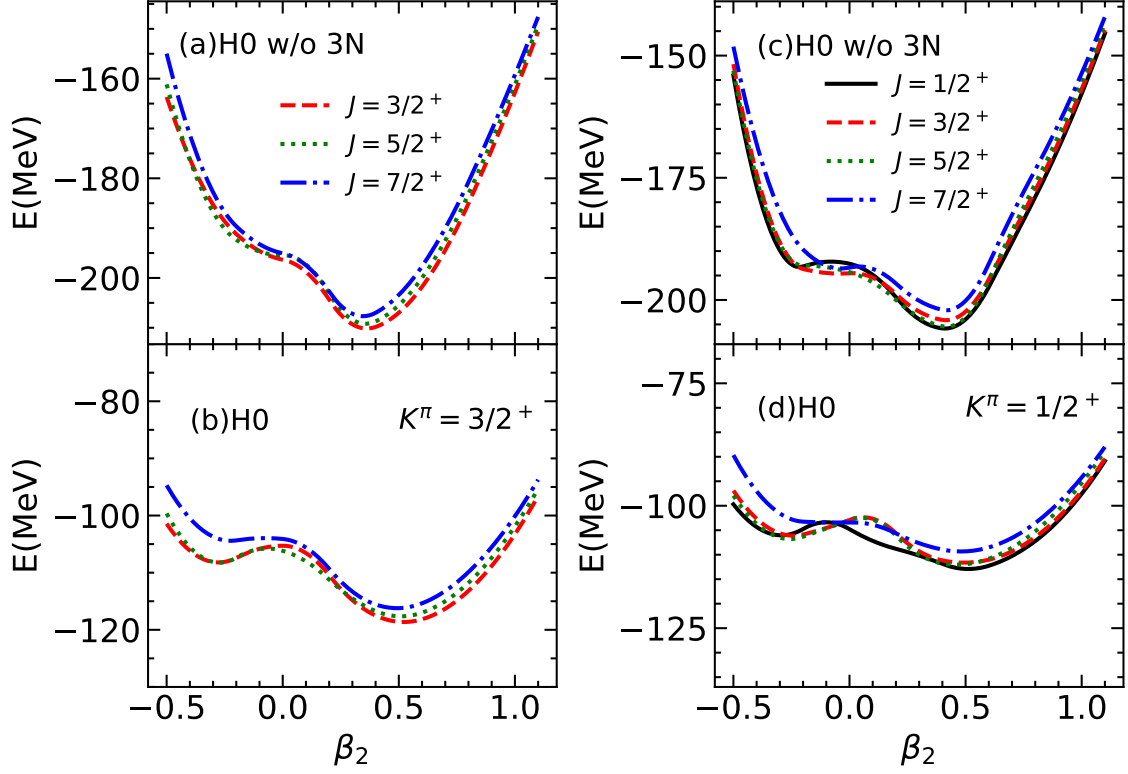


FIG. 6: The energies of states with projection onto particle numbers ($N = 11, Z = 10$) and spin-parity $J^\pi = 3/2^+, 5/2^+$ and $7/2^+$ for ^{21}Ne with quantum numbers $K^\pi = 3/2^+$ (left panels) and $K^\pi = 1/2^+$ (right panels) as a function of the quadrupole deformation parameter β_2 by the Hamiltonians `magic-Ne20` (b, d) and `magic-Ne20 (w/o 3N)` (a, c).

IV. CONCLUSIONS

We have extended PGCM for the low-lying states of ^{21}Ne starting from a chiral two-nucleon-plus-three-nucleon interaction, and compared the results obtained using effective Hamiltonians derived with the three-nucleon interaction normal-ordered with three different reference states: spherical particle-number projected HFB states for ^{20}Ne , ^{22}Ne , and an ensemble of them with equal weights. The topology of the potential energy surfaces (PES) shows no significant differences among the results by the three effective Hamiltonians, even though the PESs exhibit a systematic energy shift of less than one MeV. The excitation energies of the low-lying states of ^{21}Ne by the effective Hamiltonian based on the reference state of ^{20}Ne are slightly larger than those by the effective Hamiltonian of ^{22}Ne . Furthermore, we demonstrate that the three-nucleon interaction notably affects the low-lying states, i.e., the energy spectrum becomes stretched and

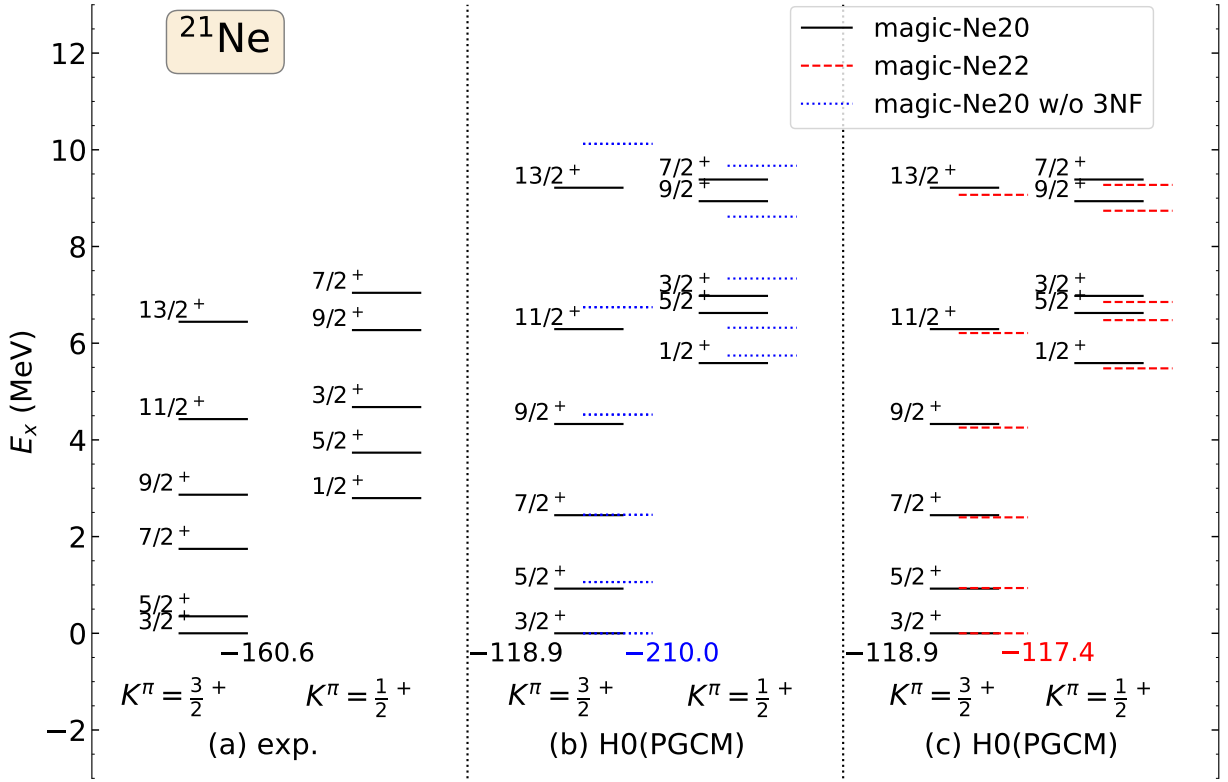


FIG. 7: The energy spectra of low-lying states in ^{21}Ne with $K^\pi = 3/2^+$ and $1/2^+$. The corresponding data from Ref. [39] are shown in (a). The results by the Hamiltonians `magic-Ne20` and `magic-Ne20 (w/o 3N)` are displayed in (b). The results by the Hamiltonians `magic-Ne20` and `magic-Ne22` are compared in (c).

quadrupole collectivity is reduced.

This study provides a solid basis to extend the framework of IM-GCM [13, 14], namely, the combination of PGCM with ab initio method of multi-reference in-medium similarity renormalization group (MR-IMSRG) [40], for the low-lying states of odd-mass nuclei based on consistently-evolved operators. The results of this study will be published elsewhere, separately.

Acknowledgments

This research was funded in part by the National Natural Science Foundation of China (Grant Nos. 12375119, 12141501, and 12005804), Guangdong Basic and Applied Basic Research Foundation (2023A1515010936) and the Fundamental Research Funds for the Central Universities, Sun Yat-sen University. H.H. was funded by the U.S. Department of Energy, Office of Science, Office

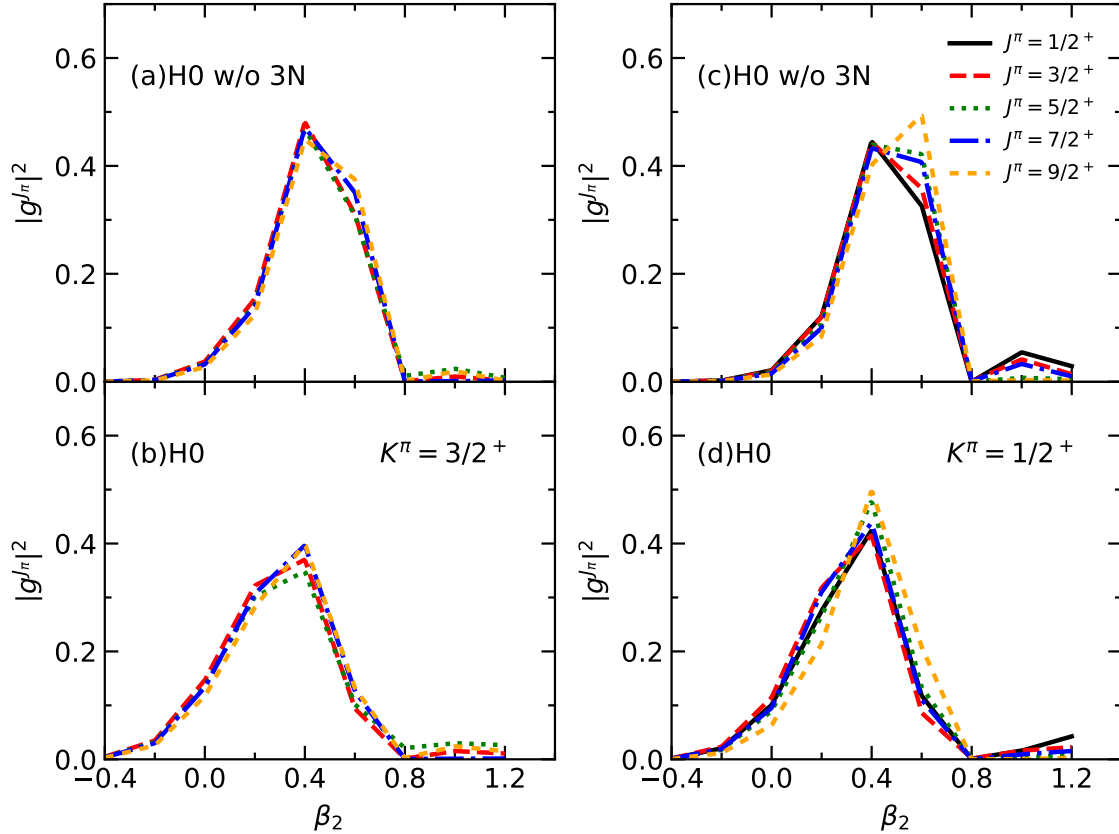


FIG. 8: The distribution of collective wave functions $|g_{\alpha}^{J\pi}|^2$, defined in (22), as a function of quadrupole deformation β_2 for the low-lying states of ^{21}Ne with $K^{\pi} = 3/2^+$ (left panels) and $K^{\pi} = 1/2^+$ (right panels), respectively. The energy of the ground-state in each case is also provided.

of Nuclear Physics DE-SC0017887, DE-SC0023516, as well as DE-SC0018083, DE-SC0023175 (SciDAC NUCLEI Collaboration).

-
- [1] Bohr, A.; Mottelson, B.R. *Nuclear structure. Volume II. Nuclear deformations*; Word Scientific: Singapore, 1998.
 - [2] Ring, P.; Schuck, P. *The nuclear many-body problem*; Springer-Verlag: New York, 1980.
 - [3] Engel, J.; Ramsey-Musolf, M.J.; van Kolck, U. Electric Dipole Moments of Nucleons, Nuclei, and Atoms: The Standard Model and Beyond. *Prog. Part. Nucl. Phys.* **2013**, *71*, 21–74, [arXiv:nucl-th/1303.2371]. <https://doi.org/10.1016/j.ppnp.2013.03.003>.
 - [4] Arrowsmith-Kron, G.; et al. Opportunities for Fundamental Physics Research with Radioactive

- Molecules **2023**. [arXiv:nucl-ex/2302.02165].
- [5] Brodeur, M.; et al. Nuclear β decay as a probe for physics beyond the Standard Model. 1 2023, [arXiv:nucl-ex/2301.03975].
- [6] Yao, J.M.; Meng, J.; Niu, Y.F.; Ring, P. Beyond-mean-field approaches for nuclear neutrinoless double beta decay in the standard mechanism. *Prog. Part. Nucl. Phys.* **2022**, *126*, 103965, [arXiv:nucl-th/2111.15543]. <https://doi.org/10.1016/j.pnpnp.2022.103965>.
- [7] Hill, D.L.; Wheeler, J.A. Nuclear constitution and the interpretation of fission phenomena. *Phys. Rev.* **1953**, *89*, 1102–1145. <https://doi.org/10.1103/PhysRev.89.1102>.
- [8] Griffin, J.J.; Wheeler, J.A. Collective Motions in Nuclei by the Method of Generator Coordinates. *Phys. Rev.* **1957**, *108*, 311–327. <https://doi.org/10.1103/PhysRev.108.311>.
- [9] Bender, M.; Heenen, P.H.; Reinhard, P.G. Self-consistent mean-field models for nuclear structure. *Rev. Mod. Phys.* **2003**, *75*, 121–180. <https://doi.org/10.1103/RevModPhys.75.121>.
- [10] Niksic, T.; Vretenar, D.; Ring, P. Relativistic Nuclear Energy Density Functionals: Mean-Field and Beyond. *Prog. Part. Nucl. Phys.* **2011**, *66*, 519–548, [arXiv:nucl-th/1102.4193]. <https://doi.org/10.1016/j.pnpnp.2011.01.055>.
- [11] Sheikh, J.A.; Dobaczewski, J.; Ring, P.; Robledo, L.M.; Yannouleas, C. Symmetry restoration in mean-field approaches. *J. Phys. G* **2021**, *48*, 123001, [arXiv:nucl-th/1901.06992]. <https://doi.org/10.1088/1361-6471/ac288a>.
- [12] Liu, L.; Otsuka, T.; Shimizu, N.; Utsuno, Y.; Roth, R. No-core Monte Carlo shell-model calculation for ^{10}Be and ^{12}Be low-lying spectra. *Phys. Rev. C* **2012**, *86*, 014302. <https://doi.org/10.1103/PhysRevC.86.014302>.
- [13] Yao, J.M.; Engel, J.; Wang, L.J.; Jiao, C.F.; Hergert, H. Generator-coordinate reference states for spectra and $0\nu\beta\beta$ decay in the in-medium similarity renormalization group. *Phys. Rev. C* **2018**, *98*, 054311, [arXiv:nucl-th/1807.11053]. <https://doi.org/10.1103/PhysRevC.98.054311>.
- [14] Yao, J.M.; Bally, B.; Engel, J.; Wirth, R.; Rodríguez, T.R.; Hergert, H. Ab Initio Treatment of Collective Correlations and the Neutrinoless Double Beta Decay of ^{48}Ca . *Phys. Rev. Lett.* **2020**, *124*, 232501. <https://doi.org/10.1103/PhysRevLett.124.232501>.
- [15] Frosini, M.; Duguet, T.; Ebran, J.P.; Somà, V. Multi-reference many-body perturbation theory for nuclei: I. Novel PGCM-PT formalism. *Eur. Phys. J. A* **2022**, *58*, 62, [arXiv:nucl-th/2110.15737]. <https://doi.org/10.1140/epja/s10050-022-00692-z>.
- [16] Frosini, M.; Duguet, T.; Ebran, J.P.; Bally, B.; Mongelli, T.; Rodríguez, T.R.; Roth, R.; Somà, V.

- Multi-reference many-body perturbation theory for nuclei: II. Ab initio study of neon isotopes via PGCM and IM-NCSM calculations. *Eur. Phys. J. A* **2022**, 58, 63, [arXiv:nucl-th/2111.00797]. <https://doi.org/10.1140/epja/s10050-022-00693-y>.
- [17] Frosini, M.; Duguet, T.; Ebran, J.P.; Bally, B.; Hergert, H.; Rodríguez, T.R.; Roth, R.; Yao, J.; Somà, V. Multi-reference many-body perturbation theory for nuclei: III. Ab initio calculations at second order in PGCM-PT. *Eur. Phys. J. A* **2022**, 58, 64, [arXiv:nucl-th/2111.01461]. <https://doi.org/10.1140/epja/s10050-022-00694-x>.
- [18] Kimura, M. The Intruder feature of Mg-31 and the coexistence of many particle and many hole states. *Phys. Rev. C* **2007**, 75, 041302, [nucl-th/0702012]. <https://doi.org/10.1103/PhysRevC.75.041302>.
- [19] Kimura, M. Spectroscopy and intruder configurations of ^{33}Mg and ^{31}Ne studied with antisymmetrized molecular dynamics **2011**. [arXiv:nucl-th/1105.3281].
- [20] Bally, B.; Avez, B.; Bender, M.; Heenen, P.H. Beyond Mean-Field Calculations for Odd-Mass Nuclei. *Phys. Rev. Lett.* **2014**, 113, 162501, [arXiv:nucl-th/1406.5984]. <https://doi.org/10.1103/PhysRevLett.113.162501>.
- [21] Bally, B.; Giacalone, G.; Bender, M. Structure of $^{128,129,130}\text{Xe}$ through multi-reference energy density functional calculations. *Eur. Phys. J. A* **2022**, 58, 187, [arXiv:nucl-th/2207.13576]. <https://doi.org/10.1140/epja/s10050-022-00833-4>.
- [22] Bally, B.; Giacalone, G.; Bender, M. The shape of gold. *Eur. Phys. J. A* **2023**, 59, 58, [arXiv:nucl-th/2301.02420]. <https://doi.org/10.1140/epja/s10050-023-00955-3>.
- [23] Borrajo, M.; Egido, J.L. A symmetry-conserving description of odd nuclei with the Gogny force. *Eur. Phys. J. A* **2016**, 52, 277, [arXiv:nucl-th/1609.02472]. [Erratum: *Eur.Phys.J.A* 53, 38 (2017)], <https://doi.org/10.1140/epja/i2016-16277-8>.
- [24] Borrajo, M.; Egido, J.L. Ground-state properties of even and odd Magnesium isotopes in a symmetry-conserving approach. *Phys. Lett. B* **2017**, 764, 328–334, [arXiv:nucl-th/1611.06982]. <https://doi.org/10.1016/j.physletb.2016.11.037>.
- [25] Borrajo, M.; Egido, J.L. Symmetry Conserving Configuration Mixing description of odd mass nuclei. *Phys. Rev. C* **2018**, 98, 044317, [arXiv:nucl-th/1809.04287]. <https://doi.org/10.1103/PhysRevC.98.044317>.
- [26] Zhou, E.F.; Wu, X.Y.; Yao, J.M. Multireference covariant density-functional theory for the low-lying states of odd-mass nuclei **2023**. [arXiv:nucl-th/2311.15305].

- [27] Bender, M.; Duguet, T.; Lacroix, D. Particle-number restoration within the energy density functional formalism. *Phys. Rev. C* **2009**, *79*, 044319. <https://doi.org/10.1103/PhysRevC.79.044319>.
- [28] Duguet, T.; Bender, M.; Bennaceur, K.; Lacroix, D.; Lesinski, T. Particle-number restoration within the energy density functional formalism: Nonviability of terms depending on noninteger powers of the density matrices. *Phys. Rev. C* **2009**, *79*, 044320. <https://doi.org/10.1103/PhysRevC.79.044320>.
- [29] Hergert, H. In-Medium Similarity Renormalization Group for Closed and Open-Shell Nuclei. *Phys. Scripta* **2017**, *92*, 023002, [arXiv:nucl-th/1607.06882]. <https://doi.org/10.1088/1402-4896/92/2/023002>.
- [30] Bally, B.; Sánchez-Fernández, A.; Rodríguez, T.R. Symmetry-projected variational calculations with the numerical suite TAURUS: I. Variation after particle-number projection. *Eur. Phys. J. A* **2021**, *57*, 69, [arXiv:nucl-th/2010.14169]. [Erratum: *Eur.Phys.J.A* 57, 124 (2021)], <https://doi.org/10.1140/epja/s10050-021-00369-z>.
- [31] Yao, J.M.; Meng, J.; Ring, P.; Vretenar, D. Configuration mixing of angular-momentum projected triaxial relativistic mean-field wave functions. *Phys. Rev. C* **2010**, *81*, 044311, [arXiv:nucl-th/0912.2650]. <https://doi.org/10.1103/PhysRevC.81.044311>.
- [32] Balian, R.; Brezin, E. Nonunitary bogoliubov transformations and extension of wick's theorem. *Nuovo Cim. B* **1969**, *64*, 37–55. <https://doi.org/10.1007/BF02710281>.
- [33] Pandya, S.P. Nucleon-Hole Interaction in jj Coupling. *Phys. Rev.* **1956**, *103*, 956–957. <https://doi.org/10.1103/PhysRev.103.956>.
- [34] Avez, B.; Bender, M. Evaluation of overlaps between arbitrary fermionic quasiparticle vacua. *Phys. Rev. C* **2012**, *85*, 034325. <https://doi.org/10.1103/PhysRevC.85.034325>.
- [35] Entem, D.R.; Machleidt, R. Accurate charge-dependent nucleon-nucleon potential at fourth order of chiral perturbation theory. *Phys. Rev. C* **2003**, *68*, 041001. <https://doi.org/10.1103/PhysRevC.68.041001>.
- [36] Bogner, S.K.; Furnstahl, R.J.; Schwenk, A. From low-momentum interactions to nuclear structure. *Prog. Part. Nucl. Phys.* **2010**, *65*, 94–147, [arXiv:nucl-th/0912.3688]. <https://doi.org/10.1016/j.ppnp.2010.03.001>.
- [37] Hebeler, K.; Bogner, S.K.; Furnstahl, R.J.; Nogga, A.; Schwenk, A. Improved nuclear matter calculations from chiral low-momentum interactions. *Phys. Rev. C* **2011**, *83*, 031301. <https://doi.org/10.1103/PhysRevC.83.031301>.

- [38] Fomenko, V.N. Projection in the occupation-number space and the canonical transformation. *J. Phys. A: General Physics* **1970**, *3*, 8–20. <https://doi.org/10.1088/0305-4470/3/1/002>.
- [39] Firestone, R. Nuclear Data Sheets for A = 21. *Nuclear Data Sheets* **2015**, *127*, 1–68. <https://doi.org/https://doi.org/10.1016/j.nds.2015.07.001>.
- [40] Hergert, H.; Bogner, S.K.; Morris, T.D.; Schwenk, A.; Tsukiyama, K. The In-Medium Similarity Renormalization Group: A Novel Ab Initio Method for Nuclei. *Phys. Rept.* **2016**, *621*, 165–222, [arXiv:nucl-th/1512.06956]. <https://doi.org/10.1016/j.physrep.2015.12.007>.

Abatement of Ionizing Radiation for Superconducting Quantum Devices

**B. Loer,^{a,1} P. M. Harrington,^b B. Archambault,^a E. Fuller,^a B. Pierson,^a I. Arnquist,^a
K. Harouaka,^a T. D. Schlieder,^a D. K. Kim,^c A. J. Melville,^c B. M. Niedzielski,^c J. L. Yoder,^c
K. Serniak,^{b,c} W. D. Oliver,^{b,c} J. L. Orrell,^a R. Bunker,^a B. A. VanDevender,^a M. Warner^a**

^a*Pacific Northwest National Laboratory,
902 Battelle Boulevard, Richland, WA, USA*

^b*Research Laboratory of Electronics, Massachusetts Institute of Technology, Cambridge, MA 02139, USA*

^c*MIT Lincoln Laboratory,
244 Wood Street, Lexington, MA, USA*

E-mail: ben.loer@pnnl.gov

ABSTRACT: Ionizing radiation has been shown to reduce the performance of superconducting quantum circuits. In this report, we evaluate the expected contributions of different sources of ambient radioactivity for typical superconducting qubit experiment platforms. Our assessment of radioactivity inside a typical cryostat highlights the importance of selecting appropriate materials for the experiment components nearest to qubit devices, such as packaging and electrical interconnects. We present a shallow underground facility (30-meter water equivalent) to reduce the flux of cosmic rays and a lead shielded cryostat to abate the naturally occurring radiogenic gamma-ray flux in the laboratory environment. We predict that superconducting qubit devices operated in this facility could experience a reduced rate of correlated multi-qubit errors by a factor of approximately 20 relative to the rate in a typical above-ground, unshielded facility. Finally, we outline overall design improvements that would be required to further reduce the residual ionizing radiation rate, down to the limit of current generation direct detection dark matter experiments.

KEYWORDS: Interaction of radiation with matter; Superconducting devices and qubits; Detector modeling and simulations

¹Corresponding author.

Contents

1	Introduction	1
2	Estimating the radiation environment	2
2.1	Monte Carlo simulation	2
2.2	Cosmic-ray secondaries	3
2.3	Laboratory gamma flux	6
2.4	Internal sources of radiation	9
2.5	Total radiation budget	13
3	Abatement of ionizing radiation	16
3.1	The Low Background Cryogenic Facility (LBCF)	16
3.2	Expected performance of superconducting qubits in the LBCF	19
4	Discussion and conclusions	20
4.1	Further reduction in ionizing radiation	20
4.2	Conclusion	23
A	Variance Reduction Techniques	24
B	Procedure for fitting HPGe measurements	25
C	Variation of ambient gamma flux in different laboratories	27
D	Radiation transport hit efficiencies	27
E	Transmon qubit device fabrication and assay methodology	28
E.1	Fabrication	28
E.2	Assay	30

1 Introduction

Quantum technologies that leverage entanglement between multiple sensors or computing elements (qubits) have the potential to dramatically advance a range of computing and sensing applications [1–5]. Many different technologies are being investigated for the physical implementation of qubits, but much focus has been placed on superconducting qubits due, in part, to their ease of manufacturing with standard semiconductor fabrication techniques as well as control and readout with microwave pulses [6–8]. A key characteristic affecting the real-world computing potential of qubits of any modality is the coherence time—how long on average a qubit will remain in a given quantum state.

Improving the coherence time of superconducting qubits has been a major research focus for the past several years [8].

Recent experiments have demonstrated that ionizing radiation can directly lead to superconducting qubit decoherence [9]. Notably, error “bursts” that are correlated in time across multiple qubits and extending over entire device substrates have been observed with characteristics consistent with the production of nonequilibrium quasiparticles by ionizing radiation [10–15]. Correlated error events have been shown to occur in part from cosmic-ray impacts [16, 17]. This poses a challenge for the implementation of many proposed quantum error correction techniques, such as the surface code, which rely on an assumption of random and uncorrelated errors in space and time [18–21].

In this report, we present an estimate of the rate of energy injections from sources of ionizing radiation into a typical device operating inside a dilution refrigerator, followed by a specific approach to reducing that rate. Ionizing radiation sources are separated into three components based on effective techniques for mitigation: (1) cosmic-ray-induced radiation, which can be reduced by operating in an underground location; (2) terrestrial gamma rays in the laboratory environment, which can be mitigated by surrounding the dilution refrigerator with a lead radiation shield; and (3) naturally-occurring radioactive isotopes in materials inside the dilution refrigerator, which can be abated by replacing with more radiopure alternatives and by an internal gamma shield.

We address the first two sources of radiation with a design for a Low Background Cryogenic Facility (LBCF), a radiation-shielded dilution refrigerator sited in a shallow underground laboratory at Pacific Northwest National Laboratory (PNNL), which will allow operation of superconducting devices, such as qubits, with reduced ionizing radiation exposure. This concept represents one mitigation strategy among many that could work in concert with device design improvements (“radiation-hardening”) to realize superconducting qubits that are less impacted by the effects of ionizing radiation. This facility provides a near-term opportunity for research into ionizing radiation effects within a controlled environment. In particular we highlight the potential to quantify the effects of radiation on superconducting qubit performance, such as the average decoherence rate [9], the rate of spatiotemporally correlated qubit errors [12, 13, 16], reconfiguration of two-level systems (TLS) [15], and performance of error correction codes [11, 14]. The facility will also enable testing the efficacy of design modifications intended to mitigate the impact of ionizing radiation on device performance, such as the use of normal metals for phonon downconversion [22, 23] or detecting and “vetoing” likely error states using classical sensors [24] or spectator qubits not directly participating in the quantum computation [14].

2 Estimating the radiation environment

2.1 Monte Carlo simulation

We employ a Monte Carlo radiation-transport simulation to estimate how radiation fluxes measured in the laboratory interacts with devices inside a dilution refrigerator, with the goal of creating a radiation budget for a typical cryogenic device. The simulation uses the GEANT4 [25–27] toolkit, version 10.7.p03. We simulate a generic laboratory space as a $8 \times 8 \times 4$ m³ box. In this space various models of radiation-sensitive devices are simulated: a NaI detector used to measure the

cosmic-ray muon flux (Section 2.2), a high purity germanium (HPGe) detector used to measure the environmental gamma flux (Section 2.3), and an array of silicon chips representing the substrates of superconducting quantum circuits in a simplified model of a dilution refrigerator.

We use a $2.5 \times 5 \times 0.38 \text{ mm}^3$ silicon chip as a qubit substrate. We simulate the effect of radiation on 144 identical silicon chips within the cryostat to increase the computational efficiency of the radiation transport simulation, given the low probability of radiation interactions with any given chip. Groups of nine chips are placed on a 0.5 mm polyimide¹ “interposer” inside a $3 \times 3 \times 2 \text{ cm}^3$ copper box with 0.5 cm thick sides that would act as an RF shielding package for typical microwave-addressed qubits. Sixteen of these units are attached to a 6.35 mm thick copper plate, 18 cm per side, hanging vertically from the dilution refrigerator mixing chamber stage. A 1.59 cm thick cylindrical aluminum cylinder with inner diameter 180.1 mm (just large enough to contain the plate) surrounds this plate (not shown in Figure 1). This cylinder is a placeholder for additional copper, aluminum, and mumetal shielding often included in superconducting qubit setups. The simulated dilution refrigerator is based approximately on the dimensions of a Bluefors LD-400 system, the dimensions of which are given in Table 1. Because cosmic-ray secondaries (primarily muons but also neutrons, protons, and gammas) are highly directional downward, the orientation of the silicon chips may have a significant effect on the interaction rate. Therefore when evaluating cosmic-ray effects, we perform separate simulations with the packages oriented either vertically (i.e., with the normal to the chip face along the horizon) or horizontally (with the normal vector pointed up toward the zenith). Figure 1 shows the simulated dilution refrigerator and array of chips.

For each radiation source, we calculate three quantities for the qubit chips: the rate of interactions depositing greater than 3 eV into the silicon substrate, the rate of interactions depositing greater than 1 MeV, and the total absorbed dose (interaction rate times average interaction energy with no threshold) from all interactions. Each of these measures is normalized per unit mass of substrate. The lower threshold for counting interactions roughly corresponds to the silicon bandgap, and the precise value has negligible effect on the results presented. We expect the minimum energy injection required to observe a response to be highly device-dependent. The very low threshold we have adopted is supported by measurements with SuperCDMS detectors in which eV-scale energy deposits excite sensors spread over a square centimeter on a gram-scale device [28]², and by simulations with the GEANT4 Condensed Matter Physics (G4CMP) toolkit [29].

2.2 Cosmic-ray secondaries

For both external sources of radiation (cosmic-ray secondaries and environmental gammas), we use the same basic approach to estimate interaction rates in superconducting device substrates. First, we measure the energy spectrum of interactions with a commercial radiation detector. Then we simulate the appropriate particle fluxes interacting with a model of that detector in our radiation transport code and compare with the measured data to obtain an overall normalization constant for

¹Although polyimide is not typically used for this purpose for microwave frequency superconducting devices, it was convenient to implement because it is common in simulations of lower-frequency devices such as transition edge sensors. Due to the small mass, the details of this material choice will have negligible impact on the radiation transport.

²Note that SuperCDMS detectors have a substantially different aspect ratio ($\sim 1:3$ vs. $\sim 1:10$ or smaller for a typical qubit chip) and are intentionally thermally isolated. Both of these features may lead to a more uniform phonon population in the substrate and thus greater sensitivity to energy deposits.

Table 1. Dimensions of stages and cans for the simulated dilution refrigerator. All dimensions are in millimeters. All copper materials are assumed to be gold-plated. For simplicity in the simulation, gold-plated copper is modeled as copper with 0.1% bulk admixture of gold.

Cooling stages

Stage	Vertical Offset	Radius	Thickness	Material
Vacuum Flange	0	261	12	stainless steel
50K	191	223.5	12	aluminum
4K	480	176	10	copper
Still	730	153	9	copper
Cold Plate (CP)	829	140	6	copper
Mixing Chamber (MXC)	997	142.3	8	copper

Cans

Can	Vertical Offset	Radius	Height	Thickness	Material
Vacuum top	12	230	486	3.2	aluminum
Vacuum bottom	498	207.65	840	3.2	aluminum
50K top	203	204	286.5	1	aluminum
50K bottom	489.5	182	793	1	aluminum
4K	490	160	774	1.5	aluminum
Still	739	151.5	500	0.5	copper

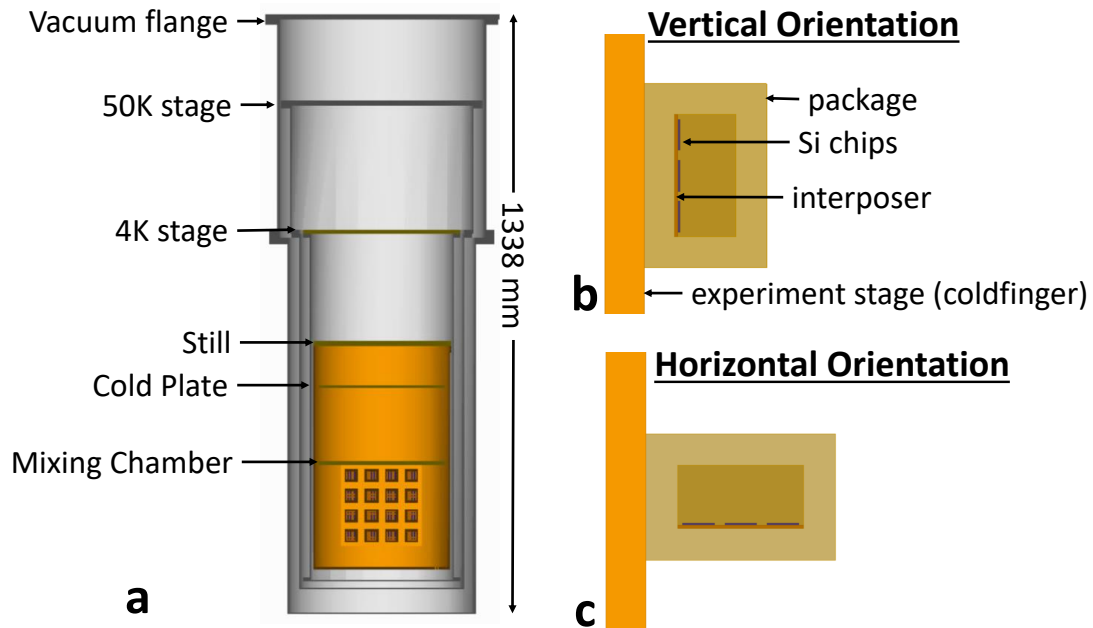


Figure 1. Cross-sectional view of the dilution refrigerator simulated in GEANT4 showing the 16 device packages attached to a coldfinger experiment stage, and detailed views of the package in the (b) vertical and (c) horizontal orientations.

the absolute particle flux. Finally, we use the estimated absolute particle flux to simulate the rate of interactions in the simulated silicon chips. A similar procedure was previously used to estimate the ionizing radiation environment for a superconducting qubit chip [9].

The flux of cosmic-ray secondary particles depends strongly on atmospheric depth (or elevation relative to sea level) and any overburden (including upper building floors), and weakly on latitude and solar cycle [30]. For this study, we employ the CRY cosmic-ray shower generator software [31] to generate distributions of cosmic-ray secondary particles that are then propagated in our GEANT4 model. To validate and normalize the simulations, we measured the spectrum of cosmic-ray muon interactions in two laboratories at PNNL: a surface laboratory and the shallow underground laboratory (SUL) [32]. Spectra were acquired with a 3 inch (7.62 cm) diameter and height NaI(Tl) scintillator attached to a photomultiplier tube (PMT) read out by a Mirion Osprey integrated base and multichannel analyzer (MCA) [33]. The PMT was operated with lower-than-nominal high voltage to bring the ~ 40 MeV minimum ionizing muon peak into the range of the MCA. Data was acquired for 92 hours in the surface laboratory and 410 hours in the SUL.

To compare CRY simulation results to the measurements, we add a simplified model of the NaI detector to our simulation described in Section 2.1. The simulated detector is a NaI cylinder with 3 inch diameter and height enclosed in a 0.5 mm thick aluminum oxide “reflector” and 0.8 mm thick aluminum case; the PMT is not modeled. The simulated detector is placed in the center of the laboratory model volume, 1.5 m from the floor. cosmic-ray secondary particles generated by CRY are propagated, and the energy deposited in the simulated NaI volume is recorded and normalized to counts per second using the live time reported by CRY. For the surface measurement, no walls or ceiling are modeled in the simulation, and the CRY-generated cosmic-ray secondaries are produced from a square plane 20 m on a side, 4 m above the floor (2.5 m above the detector), which accounts for $\sim 95\%$ of the total cosmic-ray muon flux assuming a $\cos^2 \theta$ zenith angle dependence [30].

For the underground estimate, the simulated laboratory space is surrounded by 1.2 m thick concrete walls and a 19 m overburden (above and extending on all sides) composed of calcium carbonate (limestone) with a density of 2.8 g/cm^3 . The simulation geometry is shown in Figure 2. This simplified model does not include any vertical access shafts, near which there is significantly higher muon and neutron flux, nor does it account for the “heaped” profile of the SUL overburden, which affects the muon flux particularly at high zenith angles. We compensate for this lack of fidelity in the simulation model by normalizing to *in situ* measurement. Only secondary muons are generated from a 38 m square plane just at the top of the overburden (see Fig. 2); all other cosmic-ray secondary particles contribute negligibly. To speed up the simulation, we employ a biasing technique where we immediately discard before propagation any initial muon whose momentum direction points more than 3 m from the NaI detector. This biasing technique was compared to a full simulation, and the results agreed to within statistical uncertainty (as described in Section A).

Figure 3 shows the measured data compared to the scaled simulation output. A simple two-parameter fit is performed to align the simulated data with measurement: a linear scale factor to convert from the arbitrary detector energy scale to energy deposited and a linear amplitude scale. The data measured at surface agree with the CRY-simulated rate within 20%, which we consider reasonable agreement for comparison to an altitude, geomagnetic-latitude, and solar-cycle dependent estimate of the absolute rate of cosmic-ray secondaries at any specific location on the surface of the Earth. However, the rate measured underground is more than 4 times the

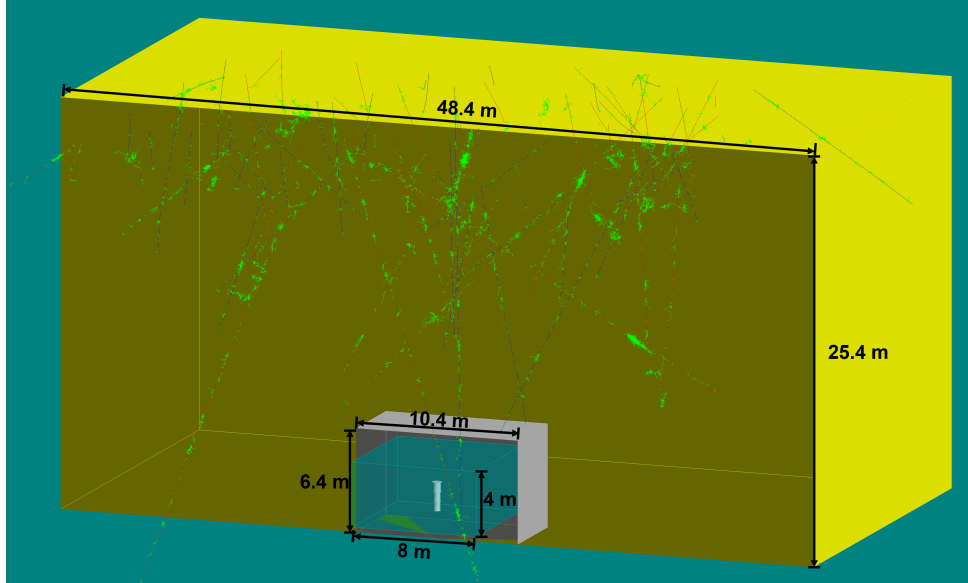


Figure 2. A GEANT4 model cross-section rendering of a dilution fridge (cylinders) within a concrete cavity (grey) beneath a 19 m overburden (yellow) representing the PNNL Shallow Underground Laboratory (SUL). Some simulated cosmic-ray muon tracks are rendered in red and blue with tertiary ionized electron tracks shown in bright green.

simulated rate, most likely due to the simplified model with flat overburden and the proximity of the measurement detector to a vertical access shaft. The measured rate underground in the 30-50 MeV peak region is reduced by a factor of 6 relative to surface, in good agreement with prior measurements [32]. The excess event rate in the measured spectra below 3 MeV is due to environmental gammas which are not included in the cosmic-ray simulations. The additional, smaller excess in the surface measurements up to ~ 12 MeV are most likely due to details of the actual cosmic-ray secondary interactions with the surface laboratory building and detector effects such as quenching of neutron-induced scintillation, neither of which are modeled.

To estimate the interaction rate and dose from cosmic-ray secondaries in superconducting qubit chips, we perform essentially the same procedure as for simulating the NaI detector. Particles are generated by CRY, propagated by GEANT4 through our model of a laboratory containing a dilution refrigerator and array of silicon chips (including walls and overburden for the SUL), and then normalized by the equivalent live time as reported by CRY and scaled by the correction factors obtained from the NaI measurements. Respectively, the measurement determined normalization factors are 1.19 for the surface laboratory and 4.36 for the SUL.

2.3 Laboratory gamma flux

Estimating the radiation dose absorbed in superconducting devices from the ambient flux of gammas in the laboratory follows a similar procedure as for the cosmic-ray secondaries. We measure the spectrum of energy deposited in a radiation detector, simulate gammas from the laboratory walls interacting with the detector, and compare measurement to simulation to determine the absolute flux of gammas and to normalize subsequent simulations of superconducting devices.

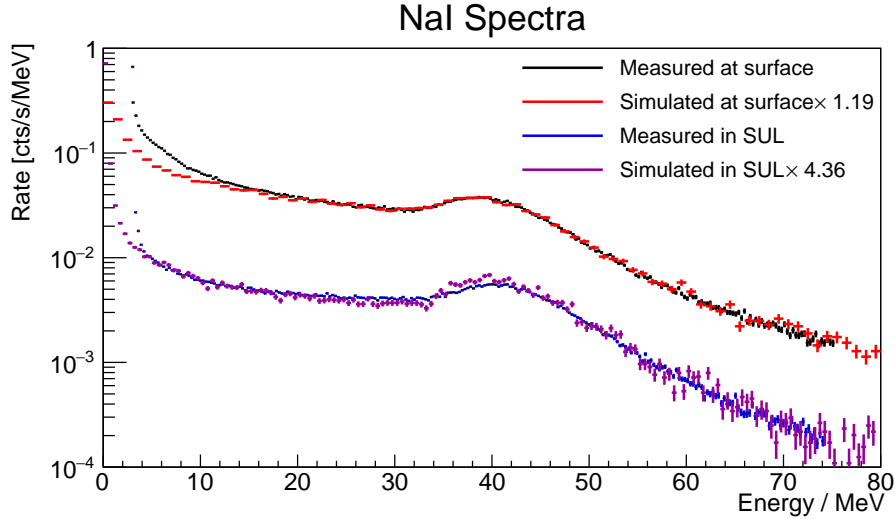


Figure 3. Comparison of cosmic-ray simulations to data collected from a 3 inch NaI detector operated in the PNNL SUL with ~ 19 m overburden (blue, bottom) and a surface laboratory (black, top). The simulated spectra are linearly scaled horizontally and vertically to match the energy scale and amplitude, respectively.

The measured gamma-ray spectrum was obtained with an unshielded high purity germanium (HPGe) detector. The Mirion GC14022 HPGe detector used for these measurements was a *p*-type coaxial design with a vendor-specified 140% relative efficiency at 1.33 MeV. The detector was placed near the center of one of the SUL labs, away from walls. Collected data were analyzed using PeakEasy v4.86 to identify key terrestrial background gamma-ray emitters. The most prominent isotopes (and their decay chain) identified were ^{40}K (K), ^{214}Pb (U), ^{214}Bi (U), ^{228}Ac (Th), ^{212}Pb (Th), ^{212}Bi (Th), and ^{208}Tl (Th), which accounted for 93.5% of the total terrestrial gamma background spectrum.

For the simulation, the identified isotopes are distributed uniformly throughout a 1.2 m concrete wall around the laboratory model and the characteristic gamma- and x-ray emissions are generated using GEANT4’s radioactive decay module [34, 35]. The energy, position, and direction of each photon passing the surface of a 145 cm radius sphere (just large enough to contain the dilution refrigerator model) centered on the HPGe are recorded. An analysis, not presented here (see Ref. [36]), showed that the radiation emissions crossing the 145 cm radius sphere have an angular distribution consistent with an isotropic flux. This permitted “re-throwing” (i.e., generation of new simulation primaries) of the gamma- and x-ray flux uniformly and isotropically from a smaller simulated sphere inside the room, substantially reducing the number of primaries required to parametrically explore specific shield design thicknesses and event rates at the location of the superconducting devices.

To determine the total gamma flux, separate simulations of the isotropic flux from each of the seven identified radionuclides are performed, and the energies deposited in a simulated HPGe detector are recorded. The simulated data are then fit to the measured data to determine the relative amplitude of each component. Details of the fitting procedure are provided in Appendix B. The fit to the measured data and the total gamma flux spectrum resulting from the fit are presented in Figure 4. The total integrated flux is approximately $7 \text{ cm}^{-2}\text{s}^{-1}(4\pi \text{ sr})^{-1}$. Although this flux

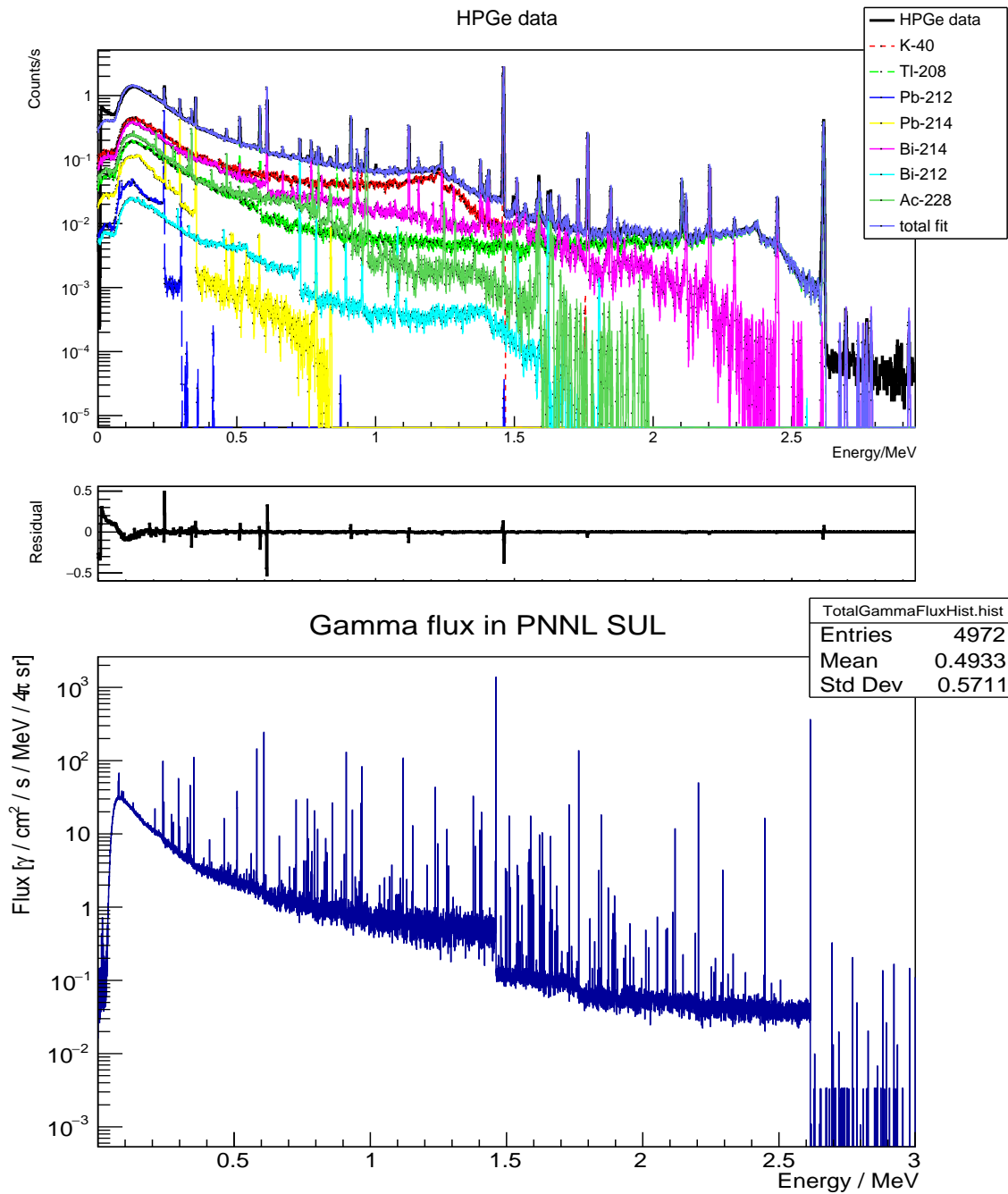


Figure 4. Top: spectrum recorded with an unshielded HPGe detector in the SUL and corresponding best fit produced from simulation data. Middle: Fit residual, normalized to the measured value at each energy. Bottom: The total flux of ambient gammas in the PNNL SUL estimated by the fit.

spectrum is specific to the SUL, experience suggests that the ambient radiogenic gamma flux in most laboratories will be within a factor of a few of this result. Measurements taken with a NaI detector in various labs at PNNL and MIT presented in Appendix C support this assertion.

2.4 Internal sources of radiation

To estimate the radiation dose from radioactive contaminants in materials inside the dilution refrigerator, we need two pieces of information for each component: (1) the total decay rate of radionuclides in that component and (2) the probability for a radioactive decay at the component’s location to result in energy deposited into the superconducting quantum circuit device substrates, which we call the “hit efficiency.” To address the second requirement, we simulate radioactive decay emissions using our GEANT4 simulation. The most common radioactive isotopes—namely ^{238}U , ^{232}Th , ^{40}K , ^{60}Co , ^{137}Cs and ^{210}Pb —are distributed throughout each volume (excluding the silicon chip itself) in the simulation and allowed to decay via GEANT4’s Radioactive Decay Module. ^{238}U and ^{232}Th are allowed to decay through their entire chains (to stable ^{206}Pb and ^{208}Pb respectively), assuming secular equilibrium for simplicity. The resulting energy depositions in the silicon chips are recorded, and normalized to the silicon mass and total number of decays simulated. This creates the hit efficiency lookup table (Appendix D). The total interaction rate or dose for a given component is then equal to the component’s mass times the differential contamination level (typically expressed in Bq/kg, i.e., decays per second per kilogram) times the entry in the corresponding table for the isotope of interest and the component’s location.

The level of radioactivity in different materials varies by several orders of magnitude, from 10’s of Bq/kg in many common materials down to $\mu\text{Bq/kg}$ in the purest materials such as silicon and OFHC copper. Different samples of the same material may have significant variation due to differences in manufacturing and handling, although we assume for simplicity that all instances of a given material have the same level of radioactivity. Thus, the radiation levels to which a device is exposed may vary substantially among laboratories and depend on the specific hardware and materials used in an experiment apparatus. For this estimate, radioactivity measurements for most materials are selected from references in the literature that are representative of the most common fabrication processes. In the remainder of this section, we present radioactivity assay results for some key components and materials used in superconducting qubit experiments: qubits, microwave printed circuit board (PCB) substrates, and cryogenic coaxial cables and connectors. The levels of radioactivity we have assumed for all materials considered are presented in Table 5.

2.4.1 Transmon qubit assay

Superconducting qubits typically comprise crystalline dielectric substrates and superconducting thin films. For these devices, distributed circuit elements are constructed using standard nano- and micro-fabrication techniques. Josephson junctions (almost exclusively Al/AlOx/Al heterostructures) are formed using double-angle electron-beam shadow evaporation through a resist mask. In order to reduce energy loss at the microwave frequencies at which superconducting qubits (transmons in this case) operate, high-purity materials are consistently chosen and fabrication recipes are optimized to reduce process-induced contamination.

In this study, we screened transmon-based devices fabricated at MIT Lincoln Laboratory (MIT LL) for the presence of residual radioisotopes. Details of the fabrication process for these devices are presented in Appendix E.1. Three substrates containing transmon qubit circuits were assayed for ^{232}Th and ^{238}U content at the PNNL’s Ultra-Low Background Detection facility, which specializes

Table 2. Assay results of the superconducting qubit chips and, for comparison, pure silicon and sapphire, which are commonly used for superconducting circuit substrates. The provided values for sapphire were measured on sapphire rods; we were unable to locate measurements for sapphire wafers. The fabricated qubit chips have similar levels of radiopurity as pure substrates.

Sample	^{232}Th (mBq/kg)	^{238}U (mBq/kg)	Ref.
Superconducting qubit chip	0.0065 ± 0.0012	0.014 ± 0.003	This work
Silicon	<0.0073	<0.011	[43]
Sapphire	0.024 ± 0.004	<0.11	[44]

in highly sensitive radiopurity assays of materials [37–42]. Details of the measurement are reported in Appendix E.2.

Of the three transmon qubit chips assayed, only one replicate value was above the detection limit and is reported in Table 2. The error on the single measurement is the instrumental error. Detection limits were 0.003 and 0.009 mBq/kg for ^{232}Th and ^{238}U , respectively. For comparison, we also provide in Table 2 assay results of pure silicon and sapphire found in literature.

The measured activity levels of the assayed devices are similar to those of pure silicon, which indicates that neither the transmon qubit fabrication process, nor the additional materials applied in the circuitry, elevate the trace levels of ^{232}Th and ^{238}U above the purity of the substrate. The qubit chip radiopurity is comparable to or better than OFHC copper, commonly used in device packages, which can be one of the purest materials available commercially, with uranium and thorium levels typically ranging from $\sim 0.1\text{--}50 \mu\text{Bq/kg}$ [45–47]. In contrast, external materials such as the surrounding readout wiring can have as much as one to six orders of magnitude higher activity than the qubits themselves.

2.4.2 Interposer laminate assay

Frequently, qubits are packaged with an “interposer:” a printed circuit board (PCB) to which the qubit device is connected by wirebonds and which brings the RF and DC connections for the qubit to discrete connectors outside the package. The bulk material of the interposer is often a composite dielectric. The interposer may have metallization layers that are gold, copper, tin, or aluminum. Typical choices for the interposer bulk material include Rogers TMM10, Rogers “RO series”, and alumina, although more radiopure materials such as silicon and sapphire may also be used. As a general rule, ceramics often have above-average levels of radioactivity. This, coupled with their close proximity to the qubit, suggests that the interposer may be a significant source of radiation events in the chip. In Table 3, we report the radionuclide assay of samples of Rogers TMM10 and RO4350B PCB substrates, each counted for approximately 5 days in a high purity germanium (HPGe) system. As can be seen in Table 5, these ceramic substrates do indeed have substantially higher levels of radioactivity than other materials in the dilution refrigerator. FR4, another common PCB substrate, has similarly high levels of radioactivity [48, 49].

Table 3. Radioactive isotopes measured in Bq/kg in Rogers ceramic PCBs by HPGe counting. Only isotopes identified with >90% confidence are reported. The uncertainty in the final digit is reported in parentheses.

Sample	Mass	⁴⁰ K	²⁰⁸ Tl	²¹² Pb	²¹⁴ Bi	²¹⁴ Pb	²²⁶ Ra	²¹⁰ Pb
TMM10	200 g	17.3(9)	1.51(6)	5.5(3)	28.9(4)	25.4(8)	29(2)	-
RO4350B	30 g	9.1(8)	4.9(2)	15.1(9)	-	11.2(4)	8(4)	11(2)

Table 4. ICP-MS assay results for SMA connectors and hand-flex 086 coaxial cable. Reported uncertainties are given by the instrumental precision. Detection limits are calculated as three times the standard deviation of process blanks.

Sample		Total Sample Mass (g)	Assayed Mass (g)	Mass Fraction Assayed	²³² Th (mBq/kg)	²³⁸ U (mBq/kg)
connector	1	2.9040	2.6336	0.907	1430 ± 20	21000 ± 2000
	2	2.8953	2.6432	0.913	2240 ± 140	25000 ± 2000
cable	1	0.1429	0.1056	0.739	< 0.130	< 0.39
	2	0.1872	0.1334	0.713	< 0.152	< 0.42
	3	0.1552	0.1111	0.716	< 0.16	< 0.49

2.4.3 SMA connector and coaxial cable assay

Because superconducting qubits are generally sensitive to magnetic fields, non-magnetic materials, such as BeCu, are often selected for the package and nearby interconnects. Device packages often have non-magnetic (BeCu) coaxial connectors attached to the package perimeter. The coaxial cables that mate to these package connectors are also selected as non-magnetic. The proximity and relatively high activity of BeCu may produce a significant interaction rate in the nearby superconducting devices. We assayed two SMA connectors, one from each of two cables supplied by Bluefors and from Crystek, both 50 Ohm, 0.086 inch (2.2 mm) OD hand-formable coaxial cable. We also assayed three sections of the Crystek cable with braided tinned copper outer conductor. Measurements followed the dissolution and ICP-MS technique described in Appendix E.2. Before dissolution, the cables and connectors were cleaned by sonication at room temperature, first with a 2% Micro90 solution, then MilliQ water, for 15 minutes each with a triple rinse in MilliQ water after each sonication step. Only the metals in each part were dissolved in a mixture of HNO₃ and HCl and sampled. The results reported in Table 4 are normalized only to the sampled mass fraction. The remaining materials were primarily the PTFE dielectric and silicone o-ring in the connector, both of which materials are typically low in radioactivity. As Table 4 shows, the body of the SMA connector has high levels of ²³⁸U and ²³²Th, most likely due to BeCu, while the cable body is much more radiopure.

Table 5. Radio-contaminant levels of materials and small parts used to estimate the ionizing radiation interaction rate and dose generated by materials inside the dilution refrigerator. Where a range of reported values exists, we choose values roughly consistent with the distribution median.

Material	Isotope concentrations (mBq/kg)						Act. ^b	Ref.
	²³⁸ U	²³² Th	⁴⁰ K	⁶⁰ Co	¹³⁷ Cs	²¹⁰ Pb ^a		
copper	0.070	0.021	0.023	0.002	-	40	6.6	[46, 50, 51]
lead	0.04	0.005	0.1	-	-	200000	-	[45, 52, 53]
steel	130	2.4	10	8.5	0.9	-	-	[46]
aluminum	66	200	2100	-	-	-	-	[46]
gold	74	19	150	-	-	-	-	[45, 54]
brass	4.9	3.5	40	-	2.6	40	6.6	[49, 55]
Kapton	10	20	60	3	-	-	-	[47, 55]
Al bonding wire	110	370	100	-	-	-	-	[45]
mumetal	20	7	15	-	-	-	-	[56]
isolator	240	190	2000	-	50	-	-	[48]
HEMT	1000	890	10000	-	210	-	-	[48]
K&L filter	9	23	100	5	1.9	-	-	[48]
attenuator	200	52	140	-	13	-	-	[48]
alumina	5000	66	600	-	-	-	-	[56]
Rogers TMM10	29000	5500	17000	-	-	-	-	this work
Rogers RO4350B	11000	15000	9000	-	-	-	-	this work
SMA connector	23000	1800	-	-	-	-	-	this work
coaxial cable	0.4	0.15	-	-	-	-	-	this work
qubit chip	0.014	0.0065	-	-	-	-	-	this work
Indium	¹¹⁵ In: 250000							

^a ²¹⁰Pb is not typically measured, however there is evidence that commercial OFHC copper contains bulk ²¹⁰Pb contamination at the ~10's of mBq/kg level, several orders of magnitude out of equilibrium with ancestor ²³⁸U [50, 57].

^b Copper and its alloys are assumed to have the following radioactive isotopes from cosmogenic activation in equilibrium (rates in mBq/kg): ⁶⁰Co (2.1), ⁵⁹Fe (0.5), ⁵⁸Co (1.7), ⁵⁷Co (1.8), ⁵⁶Co (0.2), ⁵⁴Mn (0.2), ⁴⁸V (0.1), ⁴⁶Sc (0.05) [51]. These rates are appropriate for sea level altitude and will increase at higher elevation. Other materials, such as mumetal which is primarily nickel, may also have significant rates of activation-maintained radioactivity but are not modeled here.

2.5 Total radiation budget

Table 6 lists the average interaction rates and doses from different sources of ionizing radiation for a typical superconducting device in a laboratory near sea level. Figure 5 (top) shows the integrated interaction rate above a given energy threshold. Figure 5 (bottom) summarizes the contributions from each major source in a bar chart. The rate of interactions depositing greater than 1 MeV of energy into the chip substrate is much lower than the total rate for sources without line-of-sight to the device. Excluding line-of-sight sources, the total interaction rate is driven roughly equally by the ambient gamma flux and by cosmic rays. In most cases, the ratio between the dose rate and the interaction rate is roughly constant across sources, with the principle exceptions of cosmic rays and indium bump bonds. Indium emits only relatively low energy betas, unlike other radio-contaminants that emit gammas. The dose rate for cosmic rays is largely independent of orientation, whereas the interaction rates, both total and greater than 1 MeV, vary with orientation. A simple test comparing the induced error rates of a superconducting chip in horizontal versus vertical orientation may shed light on whether errors scale with interaction rate or with dose, which would provide insight on the possible underlying mechanisms.

Typical variation across different locations will be within a factor of ~ 3 for both the ambient gamma flux (see Appendix C) and for cosmic-ray muons [30]. The level of radioactive contamination in materials inside the dilution refrigerator may easily vary by one to two orders of magnitude compared to our estimates. However, to be significant compared to rates from the ambient gamma and muon fluxes, internal sources would need to be either massive (kg) or very close to the device (cm). Several interesting conclusions can be drawn, as described in the next three paragraphs.

Ambient gammas and cosmic-ray muons contribute roughly equally. This statement holds if the effective threshold energy is below ~ 0.5 MeV. Each of these sources produces an event rate on the order of 0.3 counts/s/g, or around 1 count/minute for a cm^2 chip. If the rate of ionizing radiation events must be reduced for a device, both shielding (for ambient gammas) and operating in an underground facility (for cosmogenic muons) are required. In an above-ground laboratory, shielding alone would reduce the overall rate by no more than about 70%.

Nearly ceramics, BeCu, and indium dominate internal sources. Although only roughly a gram in mass, ceramic PCB interposers and BeCu SMA connectors contribute over two orders of magnitude more than all other internal components combined. This is due to their relatively high radioactivity content and close proximity to devices. This situation is exemplified when we consider two different locations for SMA connectors, either directly outside the copper package or inside with direct line-of-sight to the device of interest. In the latter case, the contributed event rate (assuming near-zero threshold) is over 20 times higher. SMA connectors located at the mixing chamber (MXC) plate contribute 100 times less. We note that the pieces assayed were male SMA connectors on cables, whereas a typical part with line-of-sight to the device would be the inner pin of a bulkhead solder receptacle, which may have significantly lower radioactivity. On the other hand, the inner pin is usually BeCu, which is the most likely source of contamination in the male SMA connector. These two sources also contribute at similar levels to the environmental sources, which suggests that any shielded and underground operation will benefit only marginally unless these materials are also addressed. Indium has by far the highest specific activity of all materials

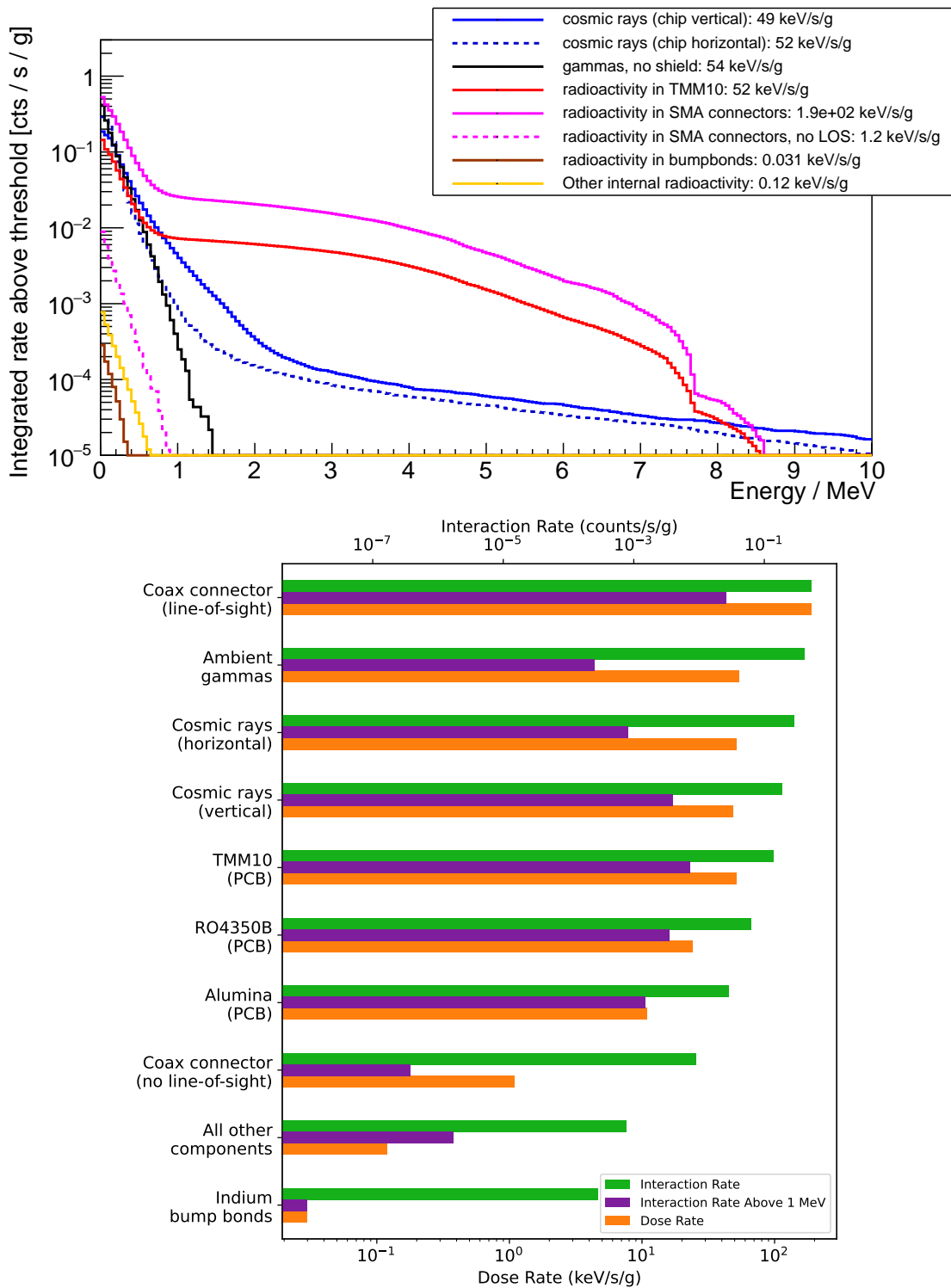


Figure 5. Top: Total rate of ionizing radiation events depositing energy greater than a threshold (horizontal axis) in a silicon substrate inside a dilution refrigerator operating at sea level. Bottom: Bar chart summary of spectra comparing total interaction rate, interaction rate of events depositing >1 MeV, and average dose rate (total interaction rate times the average energy deposited per interaction).

Table 6. Simulated interaction rate for all events and for events that deposit greater than 1 MeV in a silicon chip from environmental gammas, cosmic rays, and trace radioactivity inside an unshielded dilution refrigerator at sea level. Upper limits due to finite simulation statistics are reported at 90% confidence level.

Component	Material	Mass (kg)	Interaction rate (10^{-3} counts/s/g)	Rate >1 MeV (10^{-3} counts/s/g)
Cosmic rays (chip horizontal)			290	0.81
Cosmic rays (chip vertical)			190	4.0
Ambient Gammas			420	< 0.025
Ceramic PCB interposers				
	alumina	780 mg	29	1.5
	RO4350B	370 mg	63	3.5
	TMM10	550 mg	140	7.2
Coax connectors on package				
inside (line-of-sight)	SMA	10×2.3 g	530	26
outside (no line-of-sight)	SMA	10×2.3 g	8.9	3.8×10^{-4}
Bump bonds	indium	$20 \mu\text{g}$	0.28	$< 1 \times 10^{-5}$
All other components (itemized below)			0.72	0.0017
Fridge stages and shields			0.23	4.4×10^{-5}
MXC stage	Cu	4.6	0.0027	3.9×10^{-7}
CP stage	Cu	3.3	2.9×10^{-4}	1.5×10^{-7}
Still stage	Cu	5.9	2.1×10^{-4}	2.1×10^{-8}
4K stage	Cu	8.7	8.6×10^{-5}	1.5×10^{-8}
50K stage	Cu	5.1	1.6×10^{-5}	$< 2 \times 10^{-6}$
Vacuum flange	steel	21	7.9×10^{-4}	$< 4 \times 10^{-5}$
Still can	Cu	6.3	0.0019	2.9×10^{-7}
4K can	Al	4.1	0.058	4.2×10^{-6}
50K can	Al	5.7	0.047	2.5×10^{-5}
Vacuum can	Al	21	0.11	1.2×10^{-5}
Gold plating	gold	0.5	0.010	1.7×10^{-6}
Experiment readout			0.49	0.0017
Wirebonds	Al/Si	10×0.1 mg	0.0029	1.8×10^{-4}
Package	Cu	0.1	0.042	0.0013
Package Fasteners	brass	10×0.3 g	0.0045	8.9×10^{-5}
Cryo filters	K&L	10×15 g	0.10	2.8×10^{-5}
Closest coax cable	semirigid	10×10 cm	4.5×10^{-6}	$< 9 \times 10^{-9}$
Coldfinger	Cu	1.8	0.0065	1.1×10^{-6}
Inner shield			0.11	1.4×10^{-7}
	Cu	1	9.9×10^{-4}	1.4×10^{-7}
	Al	1	0.098	$< 3 \times 10^{-3}$
	mumetal	1	0.0065	$< 4 \times 10^{-5}$
MXC DC feedthroughs	BeCu	100 pins	4.0×10^{-5}	9.2×10^{-9}
MXC RF feedthroughs	SMA	10×2.3 g	0.082	4.0×10^{-5}
MXC RF attenuators		10×5 g	0.0018	7.9×10^{-7}
MXC isolators		10×145 g	0.14	3.9×10^{-5}
4K HEMT amplifiers		10×17 g	8.6×10^{-4}	$< 2 \times 10^{-5}$

considered in this study and the closest proximity to the chips. Only the extremely small mass (10's of μg) prevent it from being a more significant contributor. We estimate that indium bump bonds contribute 3×10^{-4} counts/s/g (~ 1 count/10 hours for a cm^2 chip) to the total interaction rate, which is comparable to the sum of all other internal components considered excluding ceramic and BeCu parts (7×10^{-4} counts/s/g).

Alphas and cosmic-ray secondaries can produce high energy events, unlike gammas. In Table 6, when enumerating the “total interaction rate,” we consider all interactions that inject energy above the silicon bandgap energy. Data from microcalorimeter detectors instrumented with multiple sensors [58] and from energy transport simulations [29] suggest that this could be enough energy to produce a phonon cloud subsequently filling the entire substrate and therefore have high probability to be detected (or generate an error in a superconducting qubit). However, if the phonons are efficiently absorbed or converted to low energy, (*e.g.*, by superconducting or normal-metal ground planes [22, 23]), then the size of the phonon cloud and the probability to reach the active device elements may exhibit some energy dependence. A 5 MeV energy deposit will raise the temperature of a 10 mm^3 silicon chip to ~ 150 mK, which may affect devices regardless of how effectively the initial athermal phonon population is downshifted. If there is a significant threshold effect, gammas become much less of a concern, and the error-inducing event rate will be dominated almost entirely by line-of-sight alpha emission. High energy alpha, proton, and neutron interactions can also produce dislocations in the crystal, which may, for example, affect local two-level systems over long timescales [15].

3 Abatement of ionizing radiation

In this section, we consider steps to reduce the rate of ionizing radiation interactions within superconducting devices. The three major background contributors (cosmic-ray muons, external gammas, and internal contamination) must be reduced with different methods: shielding cosmic-ray particles with overburden (going underground), gamma shielding (usually lead or tungsten), and replacement of relevant materials with lower-radioactivity alternatives. We begin by describing the design and predicted ionizing radiation rates in the Low Background Cryogenic Facility (LBCF) at PNNL: a dilution refrigerator operating in PNNL's Shallow Underground Laboratory (SUL) outfitted with a lead gamma shield. In Section 3.2 we predict how superconducting qubit devices might perform in the reduced radiation environment of the LBCF. In Section 4.1, conclude with a discussion of how one would further reduce the rate of ionizing radiation-induced interactions in superconducting devices, eventually adopting techniques used in ultra low background experiments such as those searching for dark matter, which target ionizing interaction rates on the order of 1 event per gram per month [59].

3.1 The Low Background Cryogenic Facility (LBCF)

The LBCF is designed to enable the study of superconducting device performance in a low ionizing radiation environment, limited by the residual cosmic-ray muon flux in the PNNL SUL. A Bluefors LD-400 dilution refrigerator has been operating in the SUL space since 2023. The SUL is described in Ref. [32]. The entire SUL including the LBCF laboratory is operated as a class 10,000 or better

cleanroom with focus on controlling radioactivity-bearing particulates. The 30 m.w.e overburden reduces the cosmic-ray muon flux by a factor of ~ 6 and the cosmic-ray neutron and proton fluxes by > 100 [32]. Our simple simulation model is described in Section 2.2 and depicted in Figure 2. In addition to the overall reduction in total muon flux, the muon angular distribution is slightly more downward-going than at surface, which has a small effect on the relative interaction rates for horizontally- versus vertically-oriented chips. The interaction rate for a 12.5 mm^2 chip in the SUL oriented horizontally is roughly twice that for a vertically oriented chip, compared to a ratio of ~ 1.5 at surface. The muon spectrum underground also has higher average energy because lower-energy muons are attenuated more efficiently, but this does not significantly affect the results.

The residual muon flux determines the required efficiency of the gamma shield: reducing the gamma-induced rate below a few percent of the muon-induced rate is unproductive. From Table 6, the optimal residual gamma rate, accounting for the factor 6 reduction in muon flux, is ~ 0.001 to 0.01 counts/s/g, or a reduction factor of ~ 100 to 1000 .

Designing the lead gamma shield proceeds in two stages. First, we simulate a 4π fully-enclosing shield of varying thickness around the dilution refrigerator and record the residual rate from environmental gammas to determine the required thickness. Then we introduce gaps into the shield model to account for practical considerations such as mechanical supports and interfaces, penetrations for cooling and signal lines, and gaps from finite mechanical tolerances, and evaluate how these modifications reduce the effective shielding rate.

To simplify the large possible parameter space for the specific shield design, we assume the shield is built primarily from “standard” $2 \times 4 \times 8 \text{ in}^3$ lead bricks. This sets a natural step size (2 in) for considering variations in the shield thickness. We also use this assumption to simplify modeling gaps in the shield to set extremely conservative tolerances (i.e., the possibility for gaps between lead shield bricks). In the simulation, bricks are arranged with an edge parallel to the shield’s thickness, such that any gaps between bricks become direct holes in the shield. We then add gaps of the specified tolerance around each individual brick and evaluate the effect. Our simulations suggest that gaps up to $1/8 \text{ in}$ ($\sim 3 \text{ mm}$) thickness have negligible impact on shielding performance. In the actual design, the bricks are arranged with overlapping gaps to prevent such direct lines of sight, and the only full gaps would be at the seams where movable sections meet. These full gaps are mitigated in the design with stepped faces at the seams.

Figure 6 shows the simulated rate of ionizing interactions above a set threshold in the silicon substrates for cosmic rays and for the unshielded and residual ambient gamma flux. Table 7 summarizes the results and additionally presents residual gamma-induced rates for fully-enclosed ideal shields of varying thickness. As discussed previously, the details of the overburden profile affect the cosmic-ray angular distribution and therefore the spectrum in the silicon. In particular, more flux at higher zenith angle (closer to the horizon) would lead to higher average energy deposition for horizontally-oriented chips and conversely lower average energy deposited for vertically-oriented chips. This is likely the case in the PNNL SUL because we used a flat overburden in our simulation unlike the true heaped profile. The total ionizing radiation interaction rate decreases with additional shielding, but with significantly diminishing returns as the residual gamma rate becomes much less than the cosmic-ray rate. With 4 inches of lead shielding, the simulated gamma rate reaches about 2% of the cosmic-ray rate for a vertically-oriented chip.

Figure 7 shows a CAD rendering of the shield design. The shield is separated into bottom and

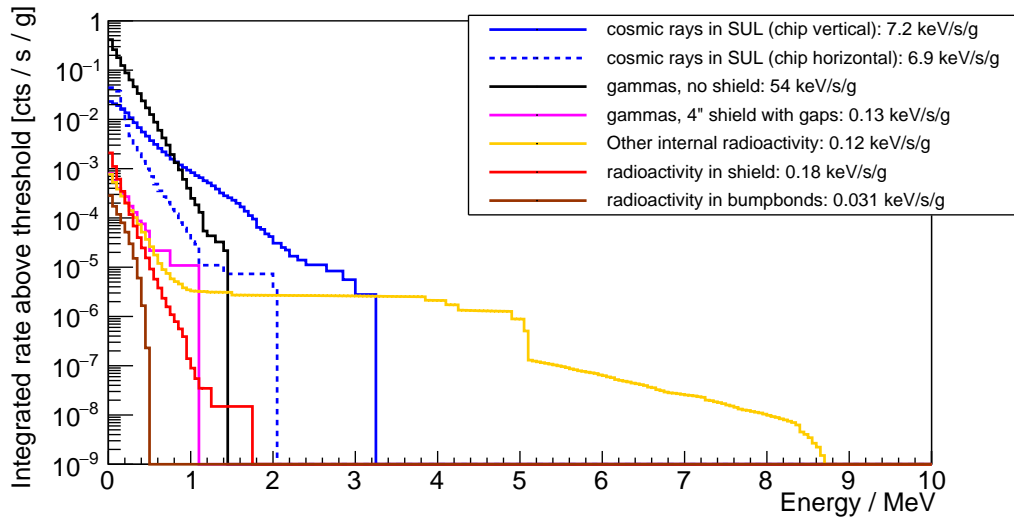


Figure 6. Simulated rate of ionization interactions depositing energy greater than a threshold (horizontal axis) in silicon substrates located in the PNNL SUL, for cosmic rays, ambient gammas, residual gammas for a 4" thick lead shield with penetrations (for mechanical supports, vacuum and helium connections, and instrumentation), radioactivity inside the dilution refrigerator, and radioactivity from the shield itself.

Table 7. Simulated interaction rate and dose in silicon chips from cosmic-ray and ambient gamma-ray sources vs. various design configurations. The final detailed shield includes holes in the shield for cryogenic and power service (see text body).

Source, Configuration	Interaction rate (10^{-3} cts/s/g)	Rate >1 MeV (10^{-3} cts/s/g)	Dose rate (keV/s/g)
cosmic-ray muons in SUL			
Chip vertical	22	1.0	7.4
Chip horizontal	44	0.033	6.9
Residual environmental gammas			
2" (5.08 cm) enclosed lead shield	11	0.033	2
4" (10.16 cm) enclosed lead shield	0.54	< 0.03	0.10
6" (15.24 cm) enclosed lead shield	0.043	< 0.03	0.010
4" (10.16 cm) lead shield with gaps	0.80	0.011	0.13
Internal radioactivity	0.72	0.0017	0.11
Gammas from shield	2.1	9.0×10^{-5}	0.18
^{210}Pb in lead	1.7	1.5×10^{-7}	0.12
Aluminum support	0.41	9.0×10^{-5}	0.05

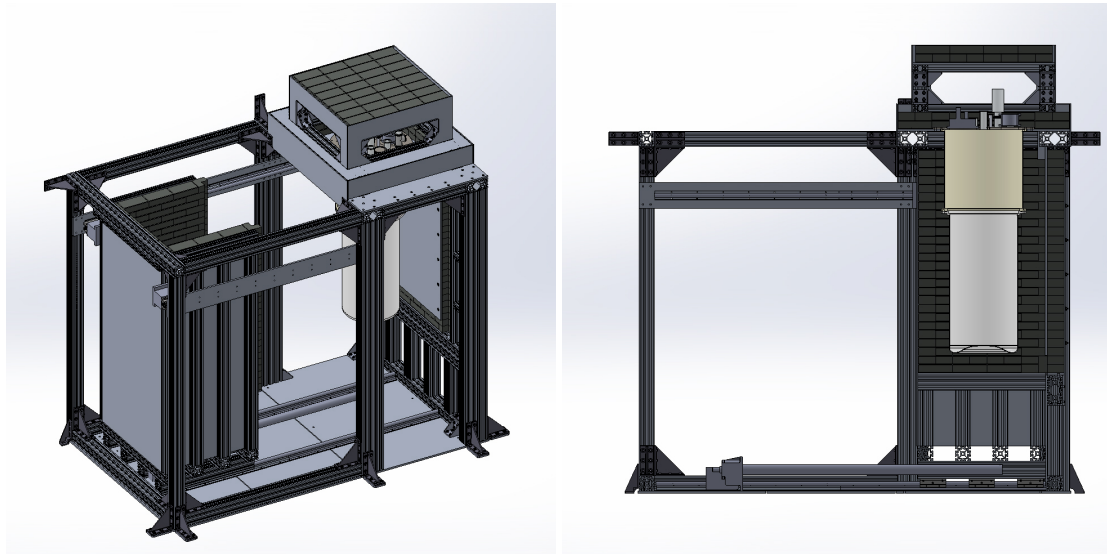


Figure 7. Draft renderings of the lead shield around the dilution refrigerator in open (left) and closed with cutaway (right) configurations.

top sections to accommodate the section of frame from which the dilution refrigerator hangs. The top is further separated into two sections, an upper roof and a lower skirt, with the gap between allowing for the fridge pulse tube and vacuum connections as well as experiment cabling. The upper sections create “shadow shielding” so that any straight ray drawn from the mixing chamber volume to the large gaps in the shield intersect with the top portion. The shield bottom consists of a single fixed wall attached to the dilution refrigerator frame, with the other four sides mounted to a linear motion system that allows access to the vacuum and IR shield cans and interior space and enables rapid shielded vs. unshielded comparison measurements. The lead is stepped where the two parts of the bottom shield meet to prevent line-of-sight gaps.

Figure 6 also shows the estimated rate from radioactivity inside the dilution refrigerator already reported (assuming that the most significant sources, i.e. nearby PCBs and BeCu coaxial connectors, have been removed) and an estimate of the contribution from the shield itself, namely the aluminum support structure and ^{210}Pb in the lead bricks. As Table 7 shows, the expected contribution from ^{210}Pb is greater than the expected residual environmental gamma flux, assuming a level of 200 Bq/kg.

3.2 Expected performance of superconducting qubits in the LBCF

The combination of overburden and lead shielding described in this work should reduce the total ionizing radiation interaction rate for devices inside the dilution refrigerator by approximately 95% compared to an unshielded system operating at sea level. We assume some care is taken to avoid introducing items with high radioactivity into the fridge such as ceramic PCBs. The primary purpose of this design is to enable the study of superconducting devices in a controlled radiation environment, in particular, testing of superconducting qubits and quasiparticle sensitive detectors for the effects of ionizing radiation. The simplest use case of the design includes A/B comparison

testing of device performance between an above-ground, unshielded laboratory and the LBCF. PNNL has a similar model dilution refrigerator available on campus, above ground for such studies.

McEwen et. al. report time-correlated events of energy-relaxation errors for multiple qubits simultaneously across a qubit array, occurring at an average rate of $\lambda \sim 1/(10 \text{ s})$ [13]. If the reported multi-qubit correlated error rate is directly proportional to the average ionizing radiation interaction rate, such a device in our shielded underground system would observe a burst rate of $\lambda \sim 1/(200 \text{ s})$. This estimate assumes that the radiation environment in their laboratory is similar to ours when unshielded and that there is essentially zero threshold energy to produce correlated error bursts. If instead there is a strong energy dependence, the rate reduction could be much less significant, as the reduction in cosmic-ray muons in the LBCF is modest and gammas cannot efficiently inject high energy into small pieces of silicon. For example, if the effective threshold for multi-qubit correlated error bursts is 1 MeV, the reduction in rate would be roughly a factor of 4 only. These two contrasting scenarios create an opportunity to directly investigate details of the underlying mechanisms leading to ionizing radiation sensitivity for specific device designs.

We note the title of the McEwen et. al. report suggestively attributes the observed correlated error bursts to cosmic rays, though the authors do make clear that gamma rays from naturally occurring radioactivity in the environment can also contribute. Determining the relative influence of cosmic-ray secondary interactions and interactions from gamma-ray radiation is one of the goals enabled by the LBCF. By comparing measurements taken with the gamma shield open vs. closed, the contributions from gammas and from cosmic rays plus internal radioactivity can be cleanly separated.

Harrington et. al. determined multi-qubit correlated error event rates from cosmic rays (at surface) and other sources separately by correlating a $5 \times 5 \times 0.35 \text{ mm}^3$ qubit device with a muon tracker [16]. They measure a total error event rate of $\sim 1/(100 \text{ s})$ and estimate the cosmic-ray-induced contribution is $\sim 1/(600 \text{ s})$ for their 20 mg, vertically-oriented chip. Our model suggests a cosmic-ray threshold of $\sim 200 \text{ keV}$, with significant uncertainty given that we have simulated a device substrate with different dimensions (i.e., $2.5 \times 5 \times 0.38 \text{ mm}^3$) which will have a strong effect on cosmic-ray interaction rates. The total reported rate suggests a lower energy-threshold ($\lesssim 50 \text{ keV}$) for gamma-rays, which is determined based on the mass of the qubit chip substrate and not the specific geometry. If the reported event rate in the Harrington et. al. device is dominated by external gamma rays (rather than some internal source, such as a PCB), the expected event rate in the LBCF would be $\sim 1/\text{hour}$ and dominated by cosmic-ray-induced events.

4 Discussion and conclusions

4.1 Further reduction in ionizing radiation

In this section we examine what steps would be required to further reduce ionizing radiation relative to the LBCF. For each successive reduction step, we target and mitigate the highest remaining source. Eventually we reach the background limits achieved by advanced fundamental physics detectors searching for neutrinoless double-beta decay events or interactions with galactic-halo dark matter particles.

Cosmic-ray muons Cosmic-ray muons are the dominant source of ionizing radiation in devices operating in the underground shielded system. Further reduction would require a site that is located deeper underground with greater overburden. A further reduction factor of 1000, at which point the residual muon-induced event rate would be a few percent of the rate from the fridge itself, would require a depth of roughly 1 kilometer water equivalent [60]. This depth is achievable in some of the shallower deep underground laboratories such as KURF (1450 m.w.e.) [61] and WIPP (1585 m.w.e.) [62].

Depending on device and use case, an alternative to operating at a deeper site may be to employ a muon veto system as is commonly done for sensitive radiation detectors [63]. A muon veto would detect whenever a muon passed through some “shell” surrounding the device of interest, allowing for the rejection of any data generated during that time, or, alternatively, better characterizing device response to cosmic-ray interactions [16, 17]. However, a veto system would not prevent errors in a superconducting qubit. While a veto system could provide a trigger to apply quantum fault mitigation [24], for very long computational duration, such methods may still prove ineffective. This is another open research question that is intended for study at the LBCF.

Improved low background shielding After cosmic rays, three sources contribute roughly equally: residual external gammas, gammas from ^{210}Pb in the shield lead [53], and radioactivity inside the dilution refrigerator. Further reducing the ambient gamma flux is not as straightforward as increasing the shield thickness. As Table 7 shows, the effect of the open top of the shield that allows free access to the vacuum flange is a significant source of the residual flux. Closing all of those openings would require a substantially more complex shield design. Eventually, small gaps between lead bricks would become significant, requiring multiple layers to be staggered or redesigned with curved or “chevron” interfaces to remove any line-of-sight openings through the shield.

Reducing the contribution from the shield itself is straightforward but costly. ^{210}Pb is present at high levels in all recently-manufactured lead. There exist stockpiles of “low background” lead (often synonymous with “Doe Run” lead, the primary ore source) with ^{210}Pb levels roughly an order of magnitude lower [52]. To further reduce this source, the innermost several centimeters would have to be replaced with so-called ancient lead, refined a sufficiently long time ago that most of the ^{210}Pb , with 22 year half-life, has decayed away [63]. Because ancient lead is most often obtained from ancient shipwrecks, it is a very limited and correspondingly expensive commodity. To reach the lowest levels, an additional inner liner of several centimeters of copper is common. Once the ^{210}Pb is reduced by a factor of ~ 10 , the aluminum plates supporting the fridge and lead that are inside the shield become dominant.³ These would need to be removed from the design or, if not possible, replaced with a lower background material such as copper.

Radiation sources inside the dilution refrigerator Further reducing the ionizing radiation event rate would require either an internal high density (e.g., tungsten or lead) shield, or modification of the instrument packaging and readout and the dilution refrigerator itself. From Table 6, the most significant sources, assuming we have already removed ceramic interposers and BeCu coaxial connections on the device package, are:

³Note that aluminum and steel plates and structural framing outside the shield are not included in our presented simulations as they contribute insignificantly to the total environmental gamma flux.

- Indium bump bonds. These are required for certain device designs (such as flip-chip connections). Should this become a hard limit, alternative designs not requiring bump bonds may be favored.
- Aluminum IR shields and vacuum can. These could be replaced with copper straightforwardly.
- Aluminum and mumetal experiment shields. Here aluminum is chosen as a superconductor, so copper would not be a suitable replacement. A study would be required to evaluate the tradeoffs between residual radiation rate vs. lack of a superconducting shield, or identifying a suitable superconducting replacement with lower radioactivity than aluminum. We estimate the mumetal to contribute roughly an order of magnitude less than aluminum.
- Cryogenic filters. If lower-background alternatives cannot be identified, a tradeoff study to evaluate the device performance with the filters moved further from the device could be beneficial.
- Isolators located at the MXC plate. The assumed contamination level is derived from a measurement that yielded upper limits only [48]. A more sensitive assay is required to determine the true contribution.
- BeCu in feedthroughs at the MXC plate. Moving the package as far as possible from the plate would have some benefit, otherwise custom feedthroughs without BeCu would be required. The research physics community has developed low-voltage, low-radioactivity connectors [64] and cables [65]. However, such connectors and cables are likely not suitable for the cryogenic and RF-signal applications required for the case studied in this report. Further R&D on material and instrumentation could likely address this need.
- Copper instrument package. The dominant contributors are ^{210}Pb (out of equilibrium with ^{238}U) with direct line-of-sight to the device and cosmogenic activation, both present in commercial copper. Both sources would be reduced significantly by replacing the package with electroformed copper [66].

These items account for $\sim 90\%$ of the estimated internal radioactivity. Significant further reduction would require construction of the experiment setup (including the dilution refrigerator unit) with ultra low-background materials and techniques similar to a dark matter experiment. For example, the SuperCDMS experiment locates the cooling elements of the dilution fridge outside the ionizing radiation shields, connected to the experiment volume by long tails [59]. This separates the devices from uncontrolled sources of radioactivity, with the tradeoff of significantly increased complexity and reduction in effective cooling power.

As a partial alternative to complete redesign, an internal radiation shield may reduce the ionizing radiation backgrounds from the dilution refrigerator. Based on a prior, unpublished study, we estimate that a 5 cm thick tungsten shield placed around the qubit package, with slits to allow cable connections, would attenuate the environmental gamma flux by a factor of ~ 50 . A similar reduction factor is expected for the residual flux after the steps above have been implemented. The addition of the shield mass to the mixing chamber stage would increase cooldown times. We also did not consider the intrinsic radioactivity of the tungsten itself in this estimate. A recent report

evaluates the levels of achievable purity in tungsten [67]. In the prior study we chose tungsten over lead due to its higher gamma attenuation coefficient per unit thickness than lead. An ancient lead inner shield would have similar performance while being less massive and easier to machine.

Current state-of-the-art limits The next generation of dark matter detectors expect to attain sufficient shielding and background reduction efficiency that they will be limited by ^{32}Si in the silicon substrate [68–70]. ^{32}Si has been measured in silicon CCDs to be approximately 10–100 /kg/day [43, 71], corresponding to a reduction factor of $\sim 10^{-6}$ to 10^{-7} compared to our estimates for unshielded surface operation. The feasibility to produce isotopically pure ^{28}Si for ultra-low background detectors has been explored [69], and other substrates without any long-lived isotopes, such as sapphire, might achieve even lower rates. Attaining these levels of backgrounds requires tens of millions of dollars for shielding and custom ultra low-background components. These experiments operate in dedicated underground laboratories at depths of several kilometers water equivalent to obtain the necessary reduction in cosmic-ray muon fluence [72].

4.2 Conclusion

In this report we have estimated the rate of ionizing radiation interactions in superconducting qubit devices⁴ from environmental sources and from internal radioactivity in a typical dilution refrigerator. We conclude that the rate of high energy interactions is strongly dominated by materials with high levels of radioactivity and within direct line-of-sight to the devices such as interposers composed of ceramic laminates and coaxial connectors containing BeCu. Other internal sources are subdominant regardless of effective energy threshold to typical laboratory gamma-ray and cosmic-ray secondary fluxes, which contribute roughly equally. We have presented the design methodology for a gamma-ray shield for the Low Background Cryogenic Facility in PNNL’s 30 meters-water-equivalent Shallow Underground Laboratory. The shield and overburden combined reduce the total ionizing radiation interaction rate by approximately 95% compared to an unshielded dilution refrigerator on the surface at sea level. Assuming multi-qubit correlated error event rates scale linearly with the ionizing radiation interaction rate, we expect that a representative superconducting quantum processor (estimates based on a Google Sycamore device [13]) operated in the LBCF would exhibit error burst rates less than $\sim 1/200\text{s}$, and a qubit device on a smaller, 20 mg substrate could experience error burst rates less than $\sim 1/\text{hour}$ [16]. Further reduction by a factor of ~ 10 could be achieved with the same design operated at a deeper ($\sim 1 \text{ km.w.e}$) site. Even further reduction would require a substantially more complex shield design and replacing some elements of the dilution refrigerator such as the aluminum IR shields due to relatively high naturally-occurring quantities of trace radionuclides in these materials. The methods outlined in this work and the simulated hit efficiency tables can be applied to quickly produce rough estimates of the rate of ionizing radiation-induced interactions for arbitrary materials inside a dilution refrigerator, given some knowledge of the level of intrinsic radionuclide contamination in that material.

We believe this design concept provides utility for mitigation of highly-correlated catastrophic error bursts [12, 13, 16] as well as suppression of quasiparticle poisoning that reduces individual qubit coherence times [9, 10]. Both of these effects are associated with ionizing radiation interactions

⁴Although we have simulated a silicon substrate in this work, the general conclusions should be largely independent of the substrate material, so long as the substrate itself has comparably low levels of intrinsic radioactive contaminants.

in superconducting quantum devices. The analysis presented in this report suggests that modest-sized shields located in shallow underground facilities are sufficient for providing an ionizing-radiation-reduced environment for the advancement and study of another 10- to 100-fold increase beyond current state-of-the-art superconducting quantum device coherence times [73, 74], assuming all other sources of decoherence are reduced commensurately. Such a facility also enables more controlled study of the characteristics of correlated errors and of tertiary effects of ionizing radiation such as its effect on two-level systems.

Acknowledgments

The authors would like to thank Joe Formaggio, Doug Pinckney, Mollie Schwartz, and Michael Kelsey for helpful discussions.

The authors acknowledge support from the Pacific Northwest National Laboratory (PNNL) Laboratory Directed Research and Development (LDRD) program. The LDRD effort was responsible for the modeling and simulation efforts which resulted in a previous report (PNNL-31996) [36], the results of which were adapted for this report. The LBCF dilution refrigerator was provided by a PNNL institutional investment. This work was supported by grants from the US Department of Energy Office of Nuclear Physics, and Office of High Energy Physics Quantum Information Science Enabled Discovery (QuantISED) program. Pacific Northwest National Laboratory is operated by Battelle Memorial Institute under contract no. DE-AC05-76RL01830 for the US Department of Energy. This research was supported by an appointment to the Intelligence Community Postdoctoral Research Fellowship Program at Massachusetts Institute of Technology administered by Oak Ridge Institute for Science and Education (ORISE) through an interagency agreement between the U.S. DOE and the Office of the Director of National Intelligence (ODNI). Work at MIT Lincoln Laboratory is supported under Air Force Contract No. FA8702-15-D-0001. Any opinions, findings, conclusions or recommendations expressed in this material are those of the authors and do not necessarily reflect the views of the U.S. Government.

A Variance Reduction Techniques

Monte Carlo methods are, inherently, computationally and time intensive; so much so that obtaining statistically relevant results with singular compute nodes within days to weeks is challenging. This complication has been encountered in other cosmic background simulations; thus, highlighting the need to accelerate the simulation process. Variance reduction is the most common method of mitigating this problem.

Two methods of variance reduction were explored: one proposed by Battistoni in [75] which makes use of repeated geometries to increase the simulated count rate, and source biasing. Figure 2 depicts the model configuration of a dilution refrigerator housing sensitive instruments within a concrete shell and 19-m soil overburden.

The muon source term relative to a small object can be treated as an anisotropic plane source. As noted by Battistoni and Bielajew, repeated structures at a constant altitude are effectively equivalent because of the translation invariance of the problem. No impact on the angular or energy dependence of the incident particle counts was observed using this method.

The second method, source biasing, makes use of a maximum radial acceptance criterion whereby the direction of primaries at birth, \hat{u} , must be towards the recording volume. Using the center point of the tally volume, v_t , initial starting point of the primary, v_p , and a radial point perpendicular to the vector between the center of the tally volume and initial primary position $\hat{u}_t = v_t - v_p$ at a user specified distance, the maximum possible angular difference between the direction of the primary and \hat{u}_t is computed as θ_a along with the angle between \hat{u} and \hat{u}_t as θ_u . Only particles with $\theta_h \leq \theta_a$ are emitted and tracked. Unlike Battistoni’s method, this technique was expected to reduce the number of low energy events. This bias was verified by applying the variance reduction technique to a simulated PVT muon counter, which was used in an earlier iteration of this study. Although the PVT panel itself is no longer used in this analysis, the derived geometric acceptance factor was carried forward.

The radial acceptance range was evaluated at 1, 2, 3, 4 and ∞ meters. A “good” variance reduction technique produces results identical to the full, unbiased simulation within statistical uncertainties but with lower variance for the same processing time. The comparison of results is provided in Figure 8. Virtually no impact to the muon peak or high-energy tail was observed, but a significant reduction in low-energy events (80% reduction in the lowest energy bin) was observed using a 1-m acceptance criteria applied to a 76-cm square PVT panel, as expected. This discrepancy was quickly reduced, however, by expanding the radial acceptance window; the 4-m window achieved 80% of the value observed with an open acceptance window in the lowest energy bin. An improvement in events processed per CPU-hours of a factor of ≈ 170 was observed with a 1-m acceptance window and reducing inversely to the square of radius. We applied a radial acceptance cut of 3 m to all simulations of cosmic rays in the SUL for this analysis. The simulated energy deposition spectrum in the unbiased simulation was equal to that obtained from the 3-m cut simulation within statistical fluctuations.

B Procedure for fitting HPGe measurements

To determine the relative weights of the environmental sources in the simulation, we compared to the measurements taken with the HPGe detector in the SUL. We determined the individual nuclide concentrations that minimized the chi-squared of the fit of the simulated HPGe response to the collected data. The fit was performed using CERN ROOT’s Minuit2 solver [76, 77] with 11 free parameters: an offset (pedestal) and linear scale factor to convert from energy to arbitrary analog to digital converter (ADC) counts, constant and square-root proportional terms for the energy resolution ($\sigma_E^2 = \sigma_0^2 + \sigma_1^2 E$), and linear scale factors for each of the seven isotopes listed above. Accurate simulation of a HPGe detector requires the optimization of several parameters. These parameters consist of values supplied by the vendor on detector design, consideration of detector aging features, and incomplete charge collection in portions of the crystal. The optimization of the dead layer thickness on the Ge crystal is particularly important, which strongly affects the HPGe response at low photon energies.

The final optimized HPGe parameters used for this simulation are shown in Table 8 and the final resultant simulated spectrum along with the measured HPGe spectrum is shown in Figure 4. The data presented in Figure 4 were normalized using the 63.9 live hours collection time (i.e., 99.4% live during the data collection period) and results are reported in counts/second for each 0.36-keV-wide

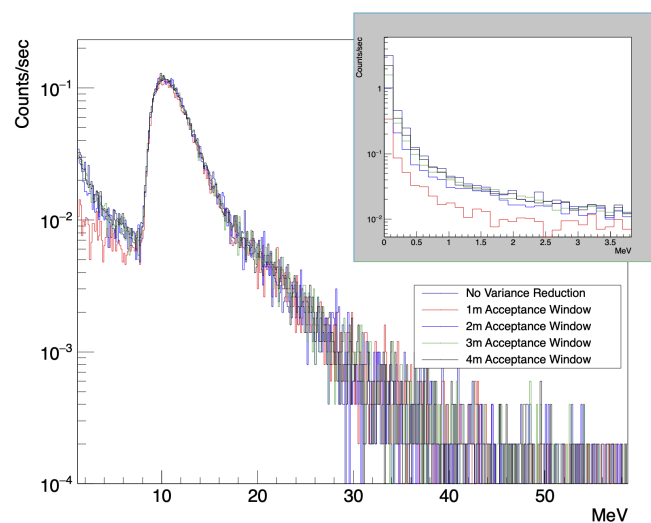


Figure 8. Comparison of the simulated muon spectrum interacting with a PVT scintillator panel as a function of the acceptance radius cut employed for variance reduction. A 1-meter cut shows significant divergence from the uncut spectrum at low energies, indicating that such a cut would introduce significant bias in the result. A 3-m cut was used for this analysis.

Table 8. Optimized and vendor provided parameters for Mirion GC14022 HPGe detector used in this work. The associated data is plotted in Figure 4.

HPGe configuration	Vendor Specified	Optimized
Ge crystal		
Diameter	-	84 mm
Length	-	84 mm
Outer dead layer thickness	0.5 mm	1.2 mm
Inner dead layer thickness	0.3 μm	0.6 μm
Crystal holder (copper)		
Thickness	-	7.5 mm
End cap (aluminum)		
Thickness	-	0.5 mm
Diameter	108 mm	108 mm
Length	-	159 mm
Ge front to endcap distance	-	7.5 mm
Performance (at 1.33 MeV)	140%	136%

energy bin. The simulated fluxes recorded for each isotope are scaled by the corresponding fit amplitude and combined to produce a single reference for the total gamma flux in the SUL, which is then used as the input to estimate the gamma contribution to devices in the dilution refrigerator and evaluate shielding efficiency.

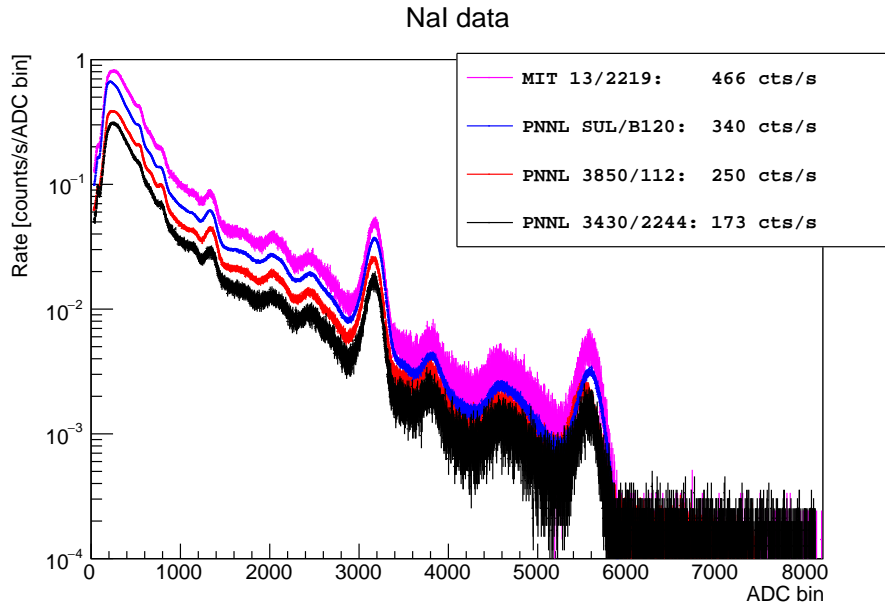


Figure 9. Comparison of background gamma spectra measured with a 3 inch NaI detector at various laboratories, demonstrating the fairly small variation between different sites. The gains (horizontal axis) were adjusted manually to align the prominent 1.4 MeV ^{40}K peak.

C Variation of ambient gamma flux in different laboratories

In this work, we conclude that the radiation budget for superconducting devices is dominated by cosmic-ray secondaries and gammas from radioactivity in the surrounding laboratory. This conclusion is based on a single measurement of gammas in the SUL at PNNL. Figure 9 shows measurements of ambient backgrounds in several locations using an NaI detector: one laboratory at MIT and three at PNNL, two at the surface and one in the SUL. The total interaction rate for each location is presented in the legend. Of the labs in the survey, the highest measured rate (at MIT) was 2.7 times larger than the smallest measured rate (in one of the PNNL surface laboratories).

D Radiation transport hit efficiencies

We anticipate there are some researchers in the superconducting device community who do not have ready-built radiation transport Monte Carlo simulation models of their dilution refrigerator systems. However, they may nonetheless wish to answer specific questions of the following nature: *If some device component might be radioactive at an estimated (or measured) level, then what is the potential impact on the superconducting device?* A full model and simulation is required to answer the question in an absolute sense. However, the *relative* impact between different materials, at different locations, and of different radioactive background content, can be determined *if and only if* a set of self-consistent radiation transport “hit efficiencies” is available. A hit efficiency is defined as the probability of radiation emitted from a given location and source in secular equilibrium to strike the device of interest. In other words, the contribution to the total ionizing radiation event (or

dose) rate R for a given component is given by

$$R = M \sum_{\text{all } i} A_i E_{i,L}$$

where M is the component's mass, A_i is the specific activity of contaminant i (e.g., ^{238}U , ^{232}Th) in the component, L is the location of the component, and $E_{i,L}$ is the hit efficiency for contaminant i at location L .

Table 9 provides the hit efficiencies derived for locations throughout the dilution refrigerator. The ‘‘Activation’’ column in Table 9 refers to cosmogenic activation of copper at sea level as presented in Table 5. See the table notes for the relative activities of the isotopes considered. An example of how one may use Table 9 is as follows. To estimate the contribution of an alumina interposer board, we take the radioactive assay values from Table 5 to get:

$$\begin{array}{r} 0.00078 \text{ kg} \times 5 \text{ Bq/kg} \times 7.3/\text{g} = 0.028 \text{ cts/s/g} \quad ^{238}\text{U} \\ 0.00078 \text{ kg} \times 0.066 \text{ Bq/kg} \times 5.2/\text{g} = 0.00027 \text{ cts/s/g} \quad ^{232}\text{Th} \\ 0.00078 \text{ kg} \times 0.6 \text{ Bq/kg} \times 1.5/\text{g} = 0.00070 \text{ cts/s/g} \quad ^{40}\text{K} \\ \hline \text{Total } 0.029 \text{ cts/s/g} \end{array}$$

which matches the value reported in Table 6.

As a second example, we can evaluate the contribution to the total background rate from 10 SMA connectors located at the CP stage to compare with the same number of connectors at the device package and at the MXC stage presented in Table 5.

$$\begin{array}{r} 0.023 \text{ kg} \times 23 \text{ Bq/kg} \times 1.7 \times 10^{-5}/\text{g} = 9.0 \times 10^{-6} \text{ cts/s/g} \quad ^{238}\text{U} \\ 0.023 \text{ kg} \times 1.8 \text{ Bq/kg} \times 2.3 \times 10^{-5}/\text{g} = 0.95 \times 10^{-6} \text{ cts/s/g} \quad ^{232}\text{Th} \\ \hline \text{Total } 1.0 \times 10^{-5} \text{ cts/s/g} \end{array}$$

One can see a factor of 10 less than the same components located at the MXC plate, which we could infer directly by the ratio of the relevant entries in Table 9, showing the utility of Table 9 for making quick, order-of-magnitude relative assessments.

E Transmon qubit device fabrication and assay methodology

E.1 Fabrication

In fabrication of the assayed transmon qubit device, Al base metallization was grown via thermal evaporation from an effusion cell in an ultra-high-vacuum (UHV) molecular-beam epitaxy (MBE) system on a high-purity, single-crystal silicon wafer. Embedding circuitry (feedlines, readout resonators, bias lines, etc.) was patterned using optical lithography and wet-etched with Aluminum Etchant Type A (Transene Company, Inc.). Josephson junctions (JJs) were fabricated using the Dolan-bridge technique, in which a suspended bridge produces shadows from two angled-evaporation steps [78]. In the MIT LL process, this is achieved with a mask stack consisting of ZEP520A resist (ZEONREX Electronic Chemicals) on a thin layer of Ge, supported by a sacrificial layer of electron-beam resist copolymer MMA(8.5)/MAA EL9 (MicroChem). The ZEP520A is exposed by a Vistec EBPG-5200 electron beam pattern generator and developed, after which the

Table 9. For a radioactive isotope (and its progeny in secular equilibrium in the case of ^{238}U and ^{232}Th) at a given location, average number “hits” depositing greater than 3 eV in the silicon substrates per equilibrium decay (top) and average energy deposited per decay (bottom). Equivalently, conversion factors from decay rate to hit rate or dose. Values derived from Monte Carlo simulation.

Source location	^{238}U	^{232}Th	^{40}K	^{60}Co	^{137}Cs	^{210}Pb	Activation
	Hit efficiency, 1/g/s/Bq						
Bump bonds	8.3E+2	6.6E+2	5.4E+1	5.6E+1	6.4E+1	^{115}In : 5.7E+1	
Interposer board	7.3E+0	5.2E+0	1.5E+0	3.1E-1	8.3E-1	1.5E+0	4.2E-1
Package	7.3E-2	6.0E-2	1.2E-2	2.1E-2	9.8E-3	8.0E-3	1.4E-2
Package Connector Inside	8.4E-1	5.2E-1	1.8E-1	5.3E-2	7.5E-2		
Package Connector Outside	1.4E-2	1.7E-2	9.4E-4	1.4E-2	4.8E-3		
Experiment stage	7.3E-4	1.0E-3	4.5E-5	9.1E-4	2.3E-4	2.5E-6	5.2E-4
Experiment shield	2.2E-4	2.8E-4	1.3E-5	2.5E-4	8.1E-5	0.0E+0	1.5E-4
Mixing Chamber Stage	1.2E-4	1.6E-4	8.8E-6	1.5E-4	4.4E-5	1.8E-7	8.7E-5
Cold Plate Stage	1.7E-5	2.3E-5	1.1E-6	2.3E-5	6.8E-6	1.4E-8	1.3E-5
Still Stage	7.3E-6	9.3E-6	5.8E-7	9.5E-6	2.6E-6	4.8E-9	5.4E-6
4K Stage	1.6E-6	2.3E-6	1.3E-7	2.7E-6	4.1E-7	0.0E+0	1.5E-6
50K Stage	4.6E-7	7.4E-7	2.1E-8	8.2E-7	1.9E-7	3.1E-9	4.4E-7
Vacuum Flange	2.6E-7	3.3E-7	1.5E-8	4.0E-7	8.6E-8	0.0E+0	2.3E-7
Still Can	6.0E-5	8.1E-5	4.3E-6	7.4E-5	2.1E-5	7.5E-8	4.4E-5
4K Can	3.0E-5	3.9E-5	2.1E-6	3.6E-5	1.1E-5	9.7E-9	2.1E-5
Lower 50K Can	2.5E-5	3.1E-5	1.8E-6	2.9E-5	9.1E-6	9.7E-9	1.7E-5
Upper 50K Can	9.3E-7	1.3E-6	3.6E-8	1.5E-6	4.4E-7	0.0E+0	7.9E-7
Lower Vacuum Can	1.7E-5	2.3E-5	1.4E-6	2.1E-5	7.6E-6	0.0E+0	1.2E-5
Upper Vacuum Can	6.3E-7	1.0E-6	8.7E-8	1.1E-6	2.1E-7	0.0E+0	5.7E-7
	Dose efficiency, keV/g/s/Bq						
Bump bonds	1.9E+6	1.6E+6	1.3E+4	4.0E+3	8.9E+3	^{115}In : 6.0E+3	
Interposer board	2.7E+3	2.3E+3	3.3E+2	3.7E+1	1.3E+2	4.2E+2	2.8E+1
Package Inner Surface	2.3E+4	1.9E+4	1.9E+2	3.6E+1	7.6E+1	1.7E+3	2.2E+1
Package	2.0E+1	1.8E+1	2.6E+0	3.6E+0	1.3E+0	2.7E+0	2.0E+0
Package Connector Inside	3.0E+2	2.3E+2	3.7E+1	8.4E+0	1.1E+1		
Experiment stage	1.0E-1	1.4E-1	7.8E-3	1.5E-1	2.5E-2	1.5E-4	7.9E-2
Experiment shield	2.9E-2	3.8E-2	1.5E-3	4.2E-2	9.6E-3	0.0E+0	2.3E-2
Mixing Chamber Stage	1.6E-2	2.1E-2	1.4E-3	2.4E-2	4.7E-3	9.8E-6	1.3E-2
Cold Plate Stage	2.2E-3	2.9E-3	1.9E-4	3.3E-3	6.4E-4	7.5E-7	1.8E-3
Still Stage	9.6E-4	1.2E-3	9.7E-5	1.4E-3	2.4E-4	1.4E-7	7.2E-4
4K Stage	2.1E-4	3.2E-4	2.3E-5	3.7E-4	4.0E-5	0.0E+0	1.9E-4
50K Stage	6.8E-5	1.0E-4	4.7E-6	1.2E-4	1.4E-5	1.3E-8	5.8E-5
Vacuum Flange	3.0E-5	5.8E-5	2.1E-6	6.2E-5	9.6E-6	0.0E+0	3.2E-5
Still Can	7.9E-3	1.0E-2	6.6E-4	1.2E-2	2.4E-3	3.3E-6	6.3E-3
4K Can	3.8E-3	5.2E-3	3.5E-4	5.6E-3	1.3E-3	4.2E-7	3.0E-3
Lower 50K Can	3.0E-3	4.3E-3	3.1E-4	4.7E-3	9.5E-4	2.2E-7	2.5E-3
Upper 50K Can	1.2E-4	1.7E-4	8.0E-6	2.3E-4	4.3E-5	0.0E+0	1.2E-4
Lower Vacuum Can	2.1E-3	3.1E-3	2.4E-4	3.2E-3	8.7E-4	0.0E+0	1.7E-3
Upper Vacuum Can	8.7E-5	1.4E-4	1.2E-5	1.7E-4	2.0E-5	0.0E+0	8.2E-5

pattern is transferred to the Ge via a CF_4 reactive-ion etch. The MMA/MAA layer is then cleared in the vicinity of the pattern by an O_2 plasma. An *in situ* Ar ion-milling was performed before angled deposition of the first Al electrode of the Josephson junctions. Thermal oxidation in a dedicated chamber grew the junction barrier prior to a final angled deposition of Al to create the second junction electrode. Finally, airbridge crossovers to link ground planes in coplanar waveguide structures were added using optical lithography and electron-beam evaporation of Al. The wafers were then coated with protective organic photoresist for dicing into 2.5x5 mm chips. The chips are finally cleaned with ACS-grade solvents and mounted into packages for testing.

E.2 Assay

Measurements were conducted using an Agilent 8900 triple quadrupole inductively coupled plasma mass spectrometer (QQQ-ICP-MS; Agilent Technologies, Santa Clara, CA, USA) with integrated autosampler, Pt skimmer and sampler cones, s-lens, and standard electron multiplier detector. A quartz double-pass spray chamber and a $100 \mu\text{L}\cdot\text{min}^{-1}$ microflow perfluoroalkoxy alkane (PFA) nebulizer (Elemental Scientific, Omaha, NE, USA) were used as the sample introduction system. Optimal tuning parameters for signal sensitivity and stability were determined using a $0.1 \text{ ng}\cdot\text{g}^{-1}$ ^{205}Tl standard.

Sample preparation and analysis involved dissolving three weighed qubits individually in a mixture of Optima grade nitric and hydrofluoric acids in the presence of a known amount of non-natural ^{229}Th and ^{233}U tracer. Once dissolved, samples were dried down and resuspended in 2% nitric acid before being introduced into the ICP-MS. Measurements of each sample were conducted as a triplicate scan, and the instrumental error was derived from one standard deviation of the three scans. Sample quantitation was conducted using standard isotope dilution methods described elsewhere [39, 40], and detection limits were determined as 3 times the standard deviation of the procedural blanks that were carried through the same process as the samples. All chemistry was conducted in a Class 10 laminar flow hood using acid leached and validated PFA vials to prevent contamination during the assay. All reagents were made with $18.2 \text{ M}\Omega\cdot\text{cm}$ deionized water.

References

- [1] John Preskill. Quantum Computing in the NISQ era and beyond. *Quantum*, 2:79, August 2018. doi:[10.22331/q-2018-08-06-79](https://doi.org/10.22331/q-2018-08-06-79).
- [2] Douglas Beck, et al. Nuclear Physics and Quantum Information Science, 2019.
- [3] Ian C. Cloët, et al. Opportunities for Nuclear Physics & Quantum Information Science. *arXiv:1903.05453 [hep-ex, physics:nucl-ex, physics:nucl-th, physics:physics, physics:quant-ph]*, July 2019.
- [4] Joseph Carlson, et al. Quantum Computing for Theoretical Nuclear Physics, A White Paper prepared for the U.S. Department of Energy, Office of Science, Office of Nuclear Physics. Technical Report 1631143, USDOE Office of Science (SC), Nuclear Physics (NP), January 2018.
- [5] C. L. Degen, F. Reinhard, and P. Cappellaro. Quantum sensing. *Reviews of Modern Physics*, 89(3):035002, July 2017. doi:[10.1103/RevModPhys.89.035002](https://doi.org/10.1103/RevModPhys.89.035002).
- [6] F. Hassler, A. R. Akhmerov, and C. W. J. Beenakker. The top-transmon: A hybrid superconducting qubit for parity-protected quantum computation. *New Journal of Physics*, 13(9):095004, September 2011. ISSN 1367-2630. doi:[10.1088/1367-2630/13/9/095004](https://doi.org/10.1088/1367-2630/13/9/095004).
- [7] William D. Oliver and Paul B. Welander. Materials in superconducting quantum bits. *MRS Bulletin*, 38(10):816–825, October 2013. ISSN 0883-7694, 1938-1425. doi:[10.1557/mrs.2013.229](https://doi.org/10.1557/mrs.2013.229).
- [8] Morten Kjaergaard, et al. Superconducting Qubits: Current State of Play. *Annual Review of Condensed Matter Physics*, 11(1):369–395, 2020. doi:[10.1146/annurev-conmatphys-031119-050605](https://doi.org/10.1146/annurev-conmatphys-031119-050605).
- [9] Antti P. Vepsäläinen, et al. Impact of ionizing radiation on superconducting qubit coherence. *Nature*, 584(7822):551–556, August 2020. ISSN 1476-4687. doi:[10.1038/s41586-020-2619-8](https://doi.org/10.1038/s41586-020-2619-8).
- [10] L. Cardani, et al. Reducing the impact of radioactivity on quantum circuits in a deep-underground facility. *Nature Communications*, 12(1):2733, May 2021. ISSN 2041-1723. doi:[10.1038/s41467-021-23032-z](https://doi.org/10.1038/s41467-021-23032-z).
- [11] Zijun Chen, et al. Exponential suppression of bit or phase errors with cyclic error correction. *Nature*, 595(7867):383–387, Jul 2021. ISSN 1476-4687. doi:[10.1038/s41586-021-03588-y](https://doi.org/10.1038/s41586-021-03588-y). URL <https://doi.org/10.1038/s41586-021-03588-y>.
- [12] C. D. Wilen, et al. Correlated charge noise and relaxation errors in superconducting qubits. *Nature*, 594(7863):369–373, June 2021. ISSN 1476-4687. doi:[10.1038/s41586-021-03557-5](https://doi.org/10.1038/s41586-021-03557-5).
- [13] Matt McEwen, et al. Resolving catastrophic error bursts from cosmic rays in large arrays of superconducting qubits. *Nature Physics*, 18(1):107–111, January 2022. ISSN 1745-2481. doi:[10.1038/s41567-021-01432-8](https://doi.org/10.1038/s41567-021-01432-8).
- [14] Rajeev Acharya, et al. Suppressing quantum errors by scaling a surface code logical qubit. *Nature*, 614(7949):676–681, February 2023. ISSN 1476-4687. doi:[10.1038/s41586-022-05434-1](https://doi.org/10.1038/s41586-022-05434-1).
- [15] Ted Thorbeck, et al. Two-Level-System Dynamics in a Superconducting Qubit Due to Background Ionizing Radiation. *PRX Quantum*, 4(2):020356, June 2023. doi:[10.1103/PRXQuantum.4.020356](https://doi.org/10.1103/PRXQuantum.4.020356).
- [16] Patrick M. Harrington, et al. Synchronous detection of cosmic rays and correlated errors in superconducting qubit arrays. *arXiv:2402.03208 [quant-ph]*, 2024. doi:[10.48550/arXiv.2402.03208](https://doi.org/10.48550/arXiv.2402.03208).
- [17] Xue-Gang Li, et al. Direct evidence for cosmic-ray-induced correlated errors in superconducting qubit array. 2024. doi:[10.48550/arXiv.2402.04245](https://doi.org/10.48550/arXiv.2402.04245).

- [18] Peter W. Shor. Scheme for reducing decoherence in quantum computer memory. *Physical Review A*, 52(4):R2493–R2496, October 1995. doi:[10.1103/PhysRevA.52.R2493](https://doi.org/10.1103/PhysRevA.52.R2493).
- [19] A. M. Steane. Error Correcting Codes in Quantum Theory. *Physical Review Letters*, 77(5):793–797, July 1996. doi:[10.1103/PhysRevLett.77.793](https://doi.org/10.1103/PhysRevLett.77.793).
- [20] Rochus Klesse and Sandra Frank. Quantum Error Correction in Spatially Correlated Quantum Noise. *Physical Review Letters*, 95(23):230503, November 2005. doi:[10.1103/PhysRevLett.95.230503](https://doi.org/10.1103/PhysRevLett.95.230503).
- [21] Austin G. Fowler, Matteo Mariantoni, John M. Martinis, and Andrew N. Cleland. Surface codes: Towards practical large-scale quantum computation. *Physical Review A*, 86(3):032324, September 2012. doi:[10.1103/PhysRevA.86.032324](https://doi.org/10.1103/PhysRevA.86.032324).
- [22] R.-P. Riwar, et al. Normal-metal quasiparticle traps for superconducting qubits. *Physical Review B*, 94(10):104516, September 2016. doi:[10.1103/PhysRevB.94.104516](https://doi.org/10.1103/PhysRevB.94.104516).
- [23] V. Iaiia, et al. Phonon downconversion to suppress correlated errors in superconducting qubits. *Nature Communications*, 13(1):6425, October 2022. ISSN 2041-1723. doi:[10.1038/s41467-022-33997-0](https://doi.org/10.1038/s41467-022-33997-0).
- [24] John L. Orrell and Ben Loer. Sensor-Assisted Fault Mitigation in Quantum Computation. *Physical Review Applied*, 16(2):024025, August 2021. doi:[10.1103/PhysRevApplied.16.024025](https://doi.org/10.1103/PhysRevApplied.16.024025).
- [25] S. Agostinelli, et al. Geant4—a simulation toolkit. *Nuclear Instruments and Methods in Physics Research Section A: Accelerators, Spectrometers, Detectors and Associated Equipment*, 506(3): 250–303, July 2003. ISSN 0168-9002. doi:[10.1016/S0168-9002\(03\)01368-8](https://doi.org/10.1016/S0168-9002(03)01368-8).
- [26] J. Allison, et al. Geant4 developments and applications. *IEEE Transactions on Nuclear Science*, 53 (1):270–278, February 2006. ISSN 1558-1578. doi:[10.1109/TNS.2006.869826](https://doi.org/10.1109/TNS.2006.869826).
- [27] J. Allison, et al. Recent developments in Geant4. *Nuclear Instruments and Methods in Physics Research Section A: Accelerators, Spectrometers, Detectors and Associated Equipment*, 835:186–225, November 2016. ISSN 0168-9002. doi:[10.1016/j.nima.2016.06.125](https://doi.org/10.1016/j.nima.2016.06.125).
- [28] D. W. Amaral, et al. Constraints on low-mass, relic dark matter candidates from a surface-operated SuperCDMS single-charge sensitive detector. *Physical Review D*, 102(9):091101, November 2020. doi:[10.1103/PhysRevD.102.091101](https://doi.org/10.1103/PhysRevD.102.091101).
- [29] M. H. Kelsey, et al. G4CMP: Condensed matter physics simulation using the Geant4 toolkit. *Nuclear Instruments and Methods in Physics Research Section A: Accelerators, Spectrometers, Detectors and Associated Equipment*, 1055:168473, October 2023. ISSN 0168-9002. doi:[10.1016/j.nima.2023.168473](https://doi.org/10.1016/j.nima.2023.168473).
- [30] P. K. F. Grieder. *Cosmic Rays at Earth: Researcher’s Reference Manual and Data Book*. Elsevier Science Ltd, Amsterdam New York, 1st ed edition, 2001. ISBN 978-0-444-50710-5.
- [31] Chris Hagmann, David Lange, and Douglas Wright. Cosmic-ray shower generator (CRY) for Monte Carlo transport codes. In *2007 IEEE Nuclear Science Symposium Conference Record*, volume 2, pages 1143–1146, 2007. doi:[10.1109/NSSMIC.2007.4437209](https://doi.org/10.1109/NSSMIC.2007.4437209).
- [32] C. E. Aalseth, et al. A shallow underground laboratory for low-background radiation measurements and materials development. *Review of Scientific Instruments*, 83(11):113503, November 2012. ISSN 0034-6748. doi:[10.1063/1.4761923](https://doi.org/10.1063/1.4761923).
- [33] Osprey® Universal Digital MCA Tube Base for Scintillation Spectrometry. URL <https://www.mirion.com/products/technologies/spectroscopy-scientific-analysis/gamma-spectroscopy/detector-electronics/osprey-universal-digital-mca-tube-base-for-scintillation-spectrometry>.

- [34] Steffen Hauf, et al. Radioactive decays in Geant4. *IEEE Transactions on Nuclear Science*, 60(4): 2966–2983, 2013. doi:[10.1109/TNS.2013.2270894](https://doi.org/10.1109/TNS.2013.2270894).
- [35] Steffen Hauf, et al. Validation of Geant4-based radioactive decay simulation. *IEEE Transactions on Nuclear Science*, 60(4):2984–2997, 2013. doi:[10.1109/TNS.2013.2271047](https://doi.org/10.1109/TNS.2013.2271047).
- [36] Ben Loer, Brian Archambault, Erin Fuller, and Bruce Pierson. A radiation-shielded, shallow underground, long-coherence time quantum qubit concept. Technical Report PNNL-31996, Pacific Northwest National Laboratory, September 2021.
- [37] Jay W. Grate, et al. Mass spectrometric analyses of high performance polymers to assess their radiopurity as ultra low background materials for rare event physics detectors. *NUCLEAR INSTRUMENTS & METHODS IN PHYSICS RESEARCH SECTION A-ACCELERATORS SPECTROMETERS DETECTORS AND ASSOCIATED EQUIPMENT*, 985, JAN 1 2021. ISSN 0168-9002. doi:[10.1016/j.nima.2020.164685](https://doi.org/10.1016/j.nima.2020.164685).
- [38] Isaac J. Arnquist, et al. Mass spectrometric assay of high radiopurity solid polymer materials for parts in radiation and rare event physics detectors. *NUCLEAR INSTRUMENTS & METHODS IN PHYSICS RESEARCH SECTION A-ACCELERATORS SPECTROMETERS DETECTORS AND ASSOCIATED EQUIPMENT*, 943, NOV 1 2019. ISSN 0168-9002. doi:[10.1016/j.nima.2019.162443](https://doi.org/10.1016/j.nima.2019.162443).
- [39] B. D. LaFerriere, T. C. Maiti, I. J. Arnquist, and E. W. Hoppe. A novel assay method for the trace determination of Th and U in copper and lead using inductively coupled plasma mass spectrometry. *NUCLEAR INSTRUMENTS & METHODS IN PHYSICS RESEARCH SECTION A-ACCELERATORS SPECTROMETERS DETECTORS AND ASSOCIATED EQUIPMENT*, 775:93–98, MAR 1 2015. ISSN 0168-9002. doi:[10.1016/j.nima.2014.11.052](https://doi.org/10.1016/j.nima.2014.11.052).
- [40] Khadouja Harouaka, Eric W. Hoppe, and Isaac J. Arnquist. A novel method for measuring ultra-trace levels of U and Th in Au, Pt, Ir, and W matrices using ICP-QQQ-MS employing an O-2 reaction gas. *JOURNAL OF ANALYTICAL ATOMIC SPECTROMETRY*, 35(12), DEC 1 2020. ISSN 0267-9477. doi:[10.1039/d0ja00220h](https://doi.org/10.1039/d0ja00220h).
- [41] Isaac J. Arnquist, Eric J. Hoppe, Mary Bliss, and Jay W. Grate. Mass Spectrometric Determination of Uranium and Thorium in High Radiopurity Polymers Using Ultra Low Background Electroformed Copper Crucibles for Dry Ashing. *ANALYTICAL CHEMISTRY*, 89(5):3101–3107, MAR 7 2017. ISSN 0003-2700. doi:[10.1021/acs.analchem.6b04854](https://doi.org/10.1021/acs.analchem.6b04854).
- [42] Isaac J. Arnquist, et al. Ultra-low radioactivity Kapton and copper-Kapton laminates. *NUCLEAR INSTRUMENTS & METHODS IN PHYSICS RESEARCH SECTION A-ACCELERATORS SPECTROMETERS DETECTORS AND ASSOCIATED EQUIPMENT*, 959, APR 11 2020. ISSN 0168-9002. doi:[10.1016/j.nima.2020.163573](https://doi.org/10.1016/j.nima.2020.163573).
- [43] A. Aguilar-Arevalo, et al. Measurement of the bulk radioactive contamination of detector-grade silicon with DAMIC at SNOLAB. *Journal of Instrumentation*, 16(06):P06019, jun 2021. doi:[10.1088/1748-0221/16/06/p06019](https://doi.org/10.1088/1748-0221/16/06/p06019).
- [44] nEXO Collaboration, et al. Sensitivity and discovery potential of the proposed nEXO experiment to neutrinoless double- β decay. *Physical Review C*, 97(6):065503, June 2018. doi:[10.1103/PhysRevC.97.065503](https://doi.org/10.1103/PhysRevC.97.065503).
- [45] N. Abgrall, et al. The Majorana Demonstrator radioassay program. *Nuclear Instruments and Methods in Physics Research Section A: Accelerators, Spectrometers, Detectors and Associated Equipment*, 828:22–36, August 2016. ISSN 0168-9002. doi:[10.1016/j.nima.2016.04.070](https://doi.org/10.1016/j.nima.2016.04.070).
- [46] E Aprile, et al. Material screening and selection for XENON100. *Astroparticle Physics*, 35(2):43–49, September 2011. doi:[10.1016/j.astropartphys.2011.06.001](https://doi.org/10.1016/j.astropartphys.2011.06.001).

- [47] E. Aprile, et al. Material radioassay and selection for the XENON1T dark matter experiment. *The European Physical Journal C*, 77(12):890, December 2017. ISSN 1434-6052. doi:[10.1140/epjc/s10052-017-5329-0](https://doi.org/10.1140/epjc/s10052-017-5329-0).
- [48] L. Cardani, et al. Disentangling the sources of ionizing radiation in superconducting qubits. *The European Physical Journal C*, 83(1):94, January 2023. ISSN 1434-6052. doi:[10.1140/epjc/s10052-023-11199-2](https://doi.org/10.1140/epjc/s10052-023-11199-2).
- [49] E. Armengaud, et al. Background studies for the edelweiss dark matter experiment. *Astroparticle Physics*, 47:1–9, 2013. ISSN 0927-6505. doi:[10.1016/j.astropartphys.2013.05.004](https://doi.org/10.1016/j.astropartphys.2013.05.004).
- [50] K. Abe, et al. Identification of ^{210}pb and ^{210}po in the bulk of copper samples with a low-background alpha particle counter. *Nuclear Instruments and Methods in Physics Research Section A: Accelerators, Spectrometers, Detectors and Associated Equipment*, 884:157–161, March 2018. ISSN 0168-9002. doi:[10.1016/j.nima.2017.12.015](https://doi.org/10.1016/j.nima.2017.12.015).
- [51] M. Laubenstein and G. Heusser. Cosmogenic radionuclides in metals as indicator for sea level exposure history. *Applied Radiation and Isotopes*, 67(5):750–754, May 2009. ISSN 0969-8043. doi:[10.1016/j.apradiso.2009.01.029](https://doi.org/10.1016/j.apradiso.2009.01.029).
- [52] J.L. Orrell, et al. Assay methods for ^{238}U , ^{232}Th , and ^{210}Pb in lead and calibration of ^{210}Bi bremsstrahlung emission from lead. *Journal of Radioanalytical and Nuclear Chemistry*, 309(3): 1271–1281, 2016. doi:[10.1007/s10967-016-4732-6](https://doi.org/10.1007/s10967-016-4732-6).
- [53] M.E. Keillor, et al. Recent bremsstrahlung-based assays of ^{210}Pb in lead and comments on current availability of low-background lead in north america. *Applied Radiation and Isotopes*, 126:185–187, 2017. doi:[10.1016/j.apradiso.2017.03.001](https://doi.org/10.1016/j.apradiso.2017.03.001).
- [54] D. S. Leonard, et al. Systematic study of trace radioactive impurities in candidate construction materials for EXO-200. *Nuclear Instruments and Methods in Physics Research Section A: Accelerators, Spectrometers, Detectors and Associated Equipment*, 591(3):490–509, July 2008. ISSN 0168-9002. doi:[10.1016/j.nima.2008.03.001](https://doi.org/10.1016/j.nima.2008.03.001).
- [55] E. Armengaud, et al. Performance of the EDELWEISS-III experiment for direct dark matter searches. *Journal of Instrumentation*, 12(08):P08010, August 2017. ISSN 1748-0221. doi:[10.1088/1748-0221/12/08/P08010](https://doi.org/10.1088/1748-0221/12/08/P08010).
- [56] ILIAS database on radiopurity of materials, 2011.
- [57] L. Balogh, et al. Copper electroplating for background suppression in the NEWS-G experiment. *Nuclear Instruments and Methods in Physics Research Section A: Accelerators, Spectrometers, Detectors and Associated Equipment*, 988:164844, February 2021. ISSN 0168-9002. doi:[10.1016/j.nima.2020.164844](https://doi.org/10.1016/j.nima.2020.164844).
- [58] R. Agnese, et al. First Dark Matter Constraints from a SuperCDMS Single-Charge Sensitive Detector. *Physical Review Letters*, 121(5):051301, August 2018. doi:[10.1103/PhysRevLett.121.051301](https://doi.org/10.1103/PhysRevLett.121.051301).
- [59] R. Agnese, et al. Projected sensitivity of the SuperCDMS SNOLAB experiment. *Physical Review D*, 95(8), April 2017. ISSN 2470-0010, 2470-0029. doi:[10.1103/PhysRevD.95.082002](https://doi.org/10.1103/PhysRevD.95.082002).
- [60] M Laubenstein, et al. Underground measurements of radioactivity. *Applied Radiation and Isotopes*, 61(2):167–172, August 2004. ISSN 0969-8043. doi:[10.1016/j.apradiso.2004.03.039](https://doi.org/10.1016/j.apradiso.2004.03.039).
- [61] L. N. Kalousis, et al. Cosmic muon flux measurements at the Kimballton Underground Research Facility. *Journal of Instrumentation*, 9(08):P08010, August 2014. ISSN 1748-0221. doi:[10.1088/1748-0221/9/08/P08010](https://doi.org/10.1088/1748-0221/9/08/P08010).

- [62] E. I. Esch, et al. The cosmic ray muon flux at WIPP. *Nuclear Instruments and Methods in Physics Research Section A: Accelerators, Spectrometers, Detectors and Associated Equipment*, 538(1): 516–525, February 2005. ISSN 0168-9002. doi:[10.1016/j.nima.2004.09.005](https://doi.org/10.1016/j.nima.2004.09.005).
- [63] Glenn F. Knoll. *Radiation Detection and Measurement*. Wiley, Hoboken, NJ, 4th ed edition, 2010. ISBN 978-0-470-13148-0.
- [64] M. Busch, et al. Low background materials and fabrication techniques for cables and connectors in the Majorana Demonstrator. *AIP Conference Proceedings*, 1921(1):070002, January 2018. ISSN 0094-243X. doi:[10.1063/1.5019005](https://doi.org/10.1063/1.5019005).
- [65] Isaac J. Arnquist, et al. Ultra-low radioactivity flexible printed cables. *EPJ Techniques and Instrumentation*, 10(1):1–17, December 2023. ISSN 2195-7045. doi:[10.1140/epjti/s40485-023-00104-6](https://doi.org/10.1140/epjti/s40485-023-00104-6).
- [66] E. W. Hoppe, et al. Reduction of radioactive backgrounds in electroformed copper for ultra-sensitive radiation detectors. *Nuclear Instruments and Methods in Physics Research Section A: Accelerators, Spectrometers, Detectors and Associated Equipment*, 764:116–121, November 2014. ISSN 0168-9002. doi:[10.1016/j.nima.2014.06.082](https://doi.org/10.1016/j.nima.2014.06.082).
- [67] J. Hakenmüller and W. Maneschg. Identification of radiopure tungsten for low background applications. *Journal of Physics G: Nuclear and Particle Physics*, 49(11):115201, October 2022. ISSN 0954-3899. doi:[10.1088/1361-6471/ac9249](https://doi.org/10.1088/1361-6471/ac9249).
- [68] R. Agnese, et al. Projected sensitivity of the SuperCDMS SNOLAB experiment. *Phys. Rev. D*, 95: 082002, Apr 2017. doi:[10.1103/PhysRevD.95.082002](https://doi.org/10.1103/PhysRevD.95.082002).
- [69] John L. Orrell, et al. Naturally occurring ^{32}Si and low-background silicon dark matter detectors. *Astroparticle Physics*, 99:9–20, 2018. ISSN 0927-6505. doi:[10.1016/j.astropartphys.2018.02.005](https://doi.org/10.1016/j.astropartphys.2018.02.005).
- [70] Alexis Aguilar-Arevalo, et al. The Oscura Experiment. (arXiv:2202.10518), February 2022. doi:[10.48550/arXiv.2202.10518](https://doi.org/10.48550/arXiv.2202.10518).
- [71] A. Aguilar-Arevalo, et al. Measurement of radioactive contamination in the high-resistivity silicon CCDs of the DAMIC experiment. *Journal of Instrumentation*, 10(08):P08014–P08014, aug 2015. doi:[10.1088/1748-0221/10/08/p08014](https://doi.org/10.1088/1748-0221/10/08/p08014).
- [72] D.-M. Mei and A. Hime. Muon-induced background study for underground laboratories. *Phys. Rev. D*, 73(5):053004, March 2006. doi:[10.1103/PhysRevD.73.053004](https://doi.org/10.1103/PhysRevD.73.053004).
- [73] A. P. M. Place, et al. New material platform for superconducting transmon qubits with coherence times exceeding 0.3 milliseconds. *Nature Communications*, 12(1), 2021.
- [74] Chenlu Wang, et al. Towards practical quantum computers: Transmon qubit with a lifetime approaching 0.5 milliseconds. *npj Quantum Information*, 8(1):1–6, January 2022. ISSN 2056-6387. doi:[10.1038/s41534-021-00510-2](https://doi.org/10.1038/s41534-021-00510-2).
- [75] G. Battistoni, et al. Monte carlo simulation of underground muon events in a finite size detector. *Astroparticle Physics*, 7(1):101–108, 1997. ISSN 09276505. doi:[10.1016/S0927-6505\(97\)00010-8](https://doi.org/10.1016/S0927-6505(97)00010-8).
- [76] M. Hatlo, et al. Developments of mathematical software libraries for the LHC experiments. *IEEE Trans. Nucl. Sci.*, 52:2818–2822, 2005. doi:[10.1109/TNS.2005.860152](https://doi.org/10.1109/TNS.2005.860152).
- [77] R. Brun and F. Rademakers. ROOT: An object oriented data analysis framework. *Nucl. Instrum. Meth. A*, 389:81–86, 1997. doi:[10.1016/S0168-9002\(97\)00048-X](https://doi.org/10.1016/S0168-9002(97)00048-X).
- [78] G. J. Dolan. Offset masks for lift-off photoprocessing. *Applied Physics Letters*, 31(5):337–339, September 1977. ISSN 0003-6951. doi:[10.1063/1.89690](https://doi.org/10.1063/1.89690).

A Light-Front Model for the Transition Distribution Amplitudes for Backward Timelike Compton Scattering

Barbara Pasquini^{1,2,*} and Andrea Schiavi^{b1,‡}

¹*Dipartimento di Fisica, Università degli Studi di Pavia, I-27100 Pavia, Italy*

²*Istituto Nazionale di Fisica Nucleare, Sezione di Pavia, I-27100 Pavia, Italy*

(Dated: March 4, 2024)

To access information on the internal structure of the nucleon, data from a variety of scattering experiments can be analyzed, in regimes where the information factorizes from an otherwise known scattering amplitude. A recent development, promising new insight, is the study of exclusive reactions in the backward kinematical region, where the information can be encoded in Transition Distribution Amplitudes (TDAs). We model the photon-to-nucleon TDAs, entering the factorized description of backward Timelike Compton Scattering, using techniques of light-front dynamics to integrate information from a quark model for the photon and the nucleon. We include the results of numerical predictions that could inform further experiments at Jefferson Lab and the future Electron–Ion Collider.

I. INTRODUCTION

Hard exclusive processes offer invaluable insight into unraveling the parton structure of hadrons. Notable examples include Deeply-Virtual Compton Scattering (DVCS) and its time-reversal conjugate process, Timelike Compton Scattering (TCS). The former is the scattering of a high-virtuality spacelike photon off a nucleon target, resulting in the production of a real photon and the recoiling nucleon, while the latter sees a real photon scatter off the nucleon target into a high-virtuality timelike photon. In the forward kinematical region, characterized by small absolute values of the Mandelstam variable t and large absolute values of the Mandelstam variable u , information on the internal structure of the nucleon is encoded in Generalized Parton Distributions (GPDs) [1–11]. These are related to matrix elements of a bilocal operator between the initial and final nucleon states, and represent the amplitude of transferring momentum to the hadron through the exchange of two partons.

The situation is more complex in the backward kinematical region, where $|u|$ is small and $|t|$ is large. However, the analogy with forward DVCS and TCS suggests a description in terms of a soft amplitude factorized from the hard scattering of the partons with the probe. The variable u characterizes the transition between a real photon and a nucleon, which can be encoded in Transition Distribution Amplitudes (TDAs) [12, 13]. These are related to matrix elements of a trilocal operator between the photon and nucleon states, and represent the amplitude of transferring momentum and one unit of baryon number through the exchange of three partons.

The focus of the present work is on backward TCS, which remains relatively unexplored compared to other processes involving TDAs [14–18]. The experimental study of TCS is a recent development, with data published for the first time in 2021 by the CLAS collaboration at Jefferson Lab for the forward region [19]. Moreover, backward TCS is especially appealing, since the electromagnetic Bethe–Heitler background, where the initial photon directly couples to a lepton–antilepton pair in the final state, is significantly suppressed (except for very narrow regions of solid angle for the produced lepton) [13]. To compare the factorized description against experimental results and to guide further phenomenological studies, a model for the photon-to-nucleon TDAs is required, beginning with the leading contributions.

The model developed in this work is based on the framework of light-front dynamics (LFD) [20–23], where the interacting particles are described in the Fock space in terms of light-front wave functions (LFWFs). In Sec. II, the backward kinematical region of TCS is analyzed, and the factorized description of the scattering amplitude is introduced. The photon-to-nucleon TDAs are defined, and their expressions in terms of matrix elements of a trilocal operator between the initial photon and the final nucleon states are derived. Section III is dedicated to modelling the photon-to-nucleon TDAs, specifically in the support region where the description in terms of the leading Fock-components of the photon and nucleon LFWFs is suitable. The photon is treated as a light quark–antiquark pair, while the Fock representation of the nucleon is truncated to the three valence quarks in a constituent quark model that has already been applied to GPDs [24–29] and to nucleon-to-neutral-pion TDAs [18]. Given the impracticality of

^b Currently employed in high-school teaching.

* Electronic address: barbara.pasquini@unipv.it

‡ Electronic address: andrearschiavi@gmail.com

the complete formulas, the analytical results of the model calculation are illustrated schematically, giving the various components alongside instructions for combining them into the final formulas. Numerical predictions for a selected set of TDAs and their first Mellin moments are discussed in Sec. III C. Concluding remarks and an outlook on further developments are given in the final Section IV.

II. BACKWARD TIMELIKE COMPTON SCATTERING

A. The Backward Kinematical Region

Timelike Compton Scattering refers to the scattering of a photon (γ) off a nucleon (N) into a virtual photon (γ^*) and the recoiling nucleon (N'), schematically

$$\gamma(q) + N(p_N) \rightarrow \gamma^*(q') + N'(p'_N), \quad (1)$$

where in brackets are the four-momenta of the particles. The virtual photon is timelike and produces a lepton-antilepton pair in the final state. The Mandelstam variables of the process are defined as

$$s = (q + p_N)^2 = (q' + p'_N)^2, \quad (2)$$

$$t = (p'_N - p_N)^2 = (q' - q)^2, \quad (3)$$

$$u = (p'_N - q)^2 = (q' - p_N)^2. \quad (4)$$

We are interested in the kinematical region where

$$(q')^2, s, |t| \gg |u|, m_N^2, \quad (5)$$

where m_N is the mass of the nucleon.

Introducing light-cone (LC) coordinates, for an arbitrary four-vector v we write $v^\pm = (v^0 \pm v^3)$ and $\vec{v}_\perp = (v^1, v^2)$, and give all components as $v^\mu = (v^+, v^-, \vec{v}_\perp)$. Furthermore, we adopt the T subscript for the transverse part of the four-vector, i.e., $v_T = (0, 0, \vec{v}_\perp)$. The LC decomposition of a four-vector can be written in a Lorentz covariant fashion using two light-like vectors $p = (1, 0, \vec{0}_\perp)$ and $n = (0, 1, \vec{0}_\perp)$. We have

$$v^\mu = v^+ p^\mu + v^- n^\mu + v_T^\mu, \quad v_T \cdot p = v_T \cdot n = 0, \quad (6)$$

where $v^+ = 2(n \cdot v)$, $v^- = 2(p \cdot v)$ and $p \cdot v_T = n \cdot v_T = 0$.

In a reference frame where the z -axis is along the direction of the colliding real photon and proton, the momenta involved in the process are

$$q = (1 + \xi)p, \quad (7)$$

$$p_N = \frac{m_N^2(1 + \xi)}{s - m_N^2}p + \frac{s - m_N^2}{(1 + \xi)}n, \quad (8)$$

$$p'_N = (1 - \xi)p + \frac{m_N^2 - \Delta_T^2}{(1 - \xi)}n + \Delta_T, \quad (9)$$

$$\Delta = p'_N - q = -2\xi p + \frac{m_N^2 - \Delta_T^2}{(1 - \xi)}n + \Delta_T, \quad (10)$$

$$q' = p_N - \Delta, \quad (11)$$

where ξ is the skewness variable, with $0 \leq \xi < 1$. It will also be useful to define the mean momentum

$$P = \frac{p'_N + q}{2} = p + \frac{m_N^2 - \Delta_T^2}{2(1 - \xi)}n + \frac{\Delta_T}{2}, \quad (12)$$

so that

$$p^+ = P^+, \quad (13)$$

and

$$\xi = -\frac{(p'_N - q) \cdot n}{(p'_N + q) \cdot n} = -\frac{\Delta \cdot n}{2P \cdot n}. \quad (14)$$

We also have

$$u = \Delta^2 = -2\xi \frac{m_N^2 - \Delta_T^2}{(1 - \xi)} + \Delta_T^2, \quad (15)$$

so $|u|$ is smaller for $\Delta_T = 0$, i.e., when the trajectories of the outgoing particles are aligned with the incoming particles, and for ξ close to zero.

B. Interpretation of the Photon-to-Nucleon Transition Distribution Amplitudes

Following Refs. [12, 13], we apply a collinear factorized description of the backward TCS in the kinematical region (5). Owing to the high-energy scale of the final photon and the low-energy scale $|u| = |p'_N - q|^2$, we can isolate from the rest of the scattering amplitude a transition from the initial photon to the final nucleon. We can imagine this transition happening through an exchange of partons between the initial photon and the initial nucleon, which, once extracted, take part in a perturbative subprocess that produces the final photon. This elementary scattering is described by coefficient functions (CFs). The splitting of the initial nucleon into its constituent quarks is described by non-perturbative objects called nucleon Distribution Amplitudes (DAs), while the transition from the initial photon to the final nucleon is encoded in photon-to-nucleon ($N\gamma$) TDAs. This factorized description of the amplitude of backward TCS is sketched in Fig. 1.

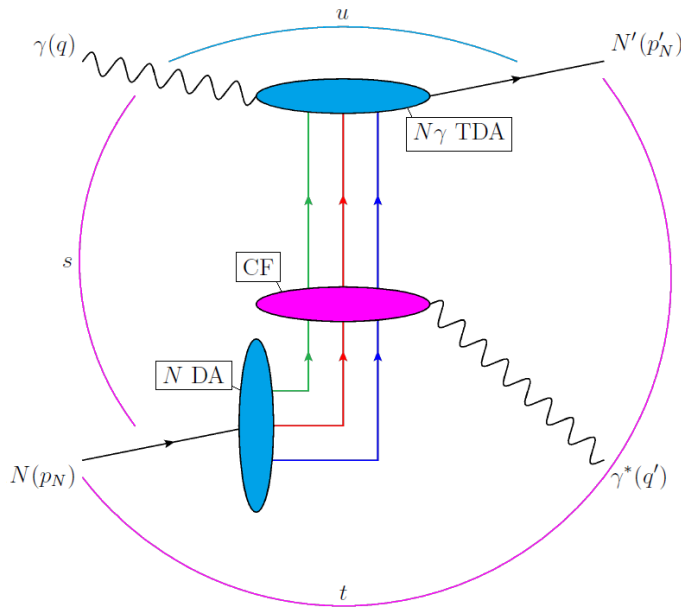


Figure 1. (Color online.) Sketch of the factorized amplitude of backward TCS. The central (pink) oval shape represents the high-energy elementary scattering, described by CFs. The upper and lower (light blue) oval shapes represent the non-perturbative subprocesses, encoded in photon-to-nucleon TDAs and nucleon DAs, respectively.

In the context of collinear factorization, there are three fundamental ways in which the photon-to-nucleon transition can happen, schematically illustrated in Figs. 2a–2c, where the photon is represented by the left (orange) oval shape and the nucleon by the right (violet) one. If the photon splits into a light (up or down) quark–antiquark pair, the antiquark is emitted and two absorbed quarks take its place (so that the result is a color singlet) to make up the nucleon (Fig. 2a). The photon could also split into two quark–antiquark pairs, with a quark taking the place of the antiquarks in the final nucleon (Fig. 2b), or into three pairs, the emitted antiquarks leaving behind the nucleon (Fig. 2c). Additional quark–antiquark pairs (of any flavor) or gluons can be directly absorbed by the nucleon, and should give rise to higher-order corrections to the three fundamental contributions. The three classes of contributions are characterized by different values of the fractions of longitudinal mean momentum (12) carried by the exchanged partons, with

positive values corresponding to emitted antiquarks and negative values interpreted as absorbed quarks. The first and second support regions are called DGLAP I and DGLAP II, respectively, as they are governed by a generalization of the Dokshitzer–Gribov–Lipatov–Altarelli–Parisi evolution equations [30–32]. The third region is called ERBL, being controlled by a generalization of the Efremov–Radyushkin–Brodsky–Lepage evolution equations [33–37].

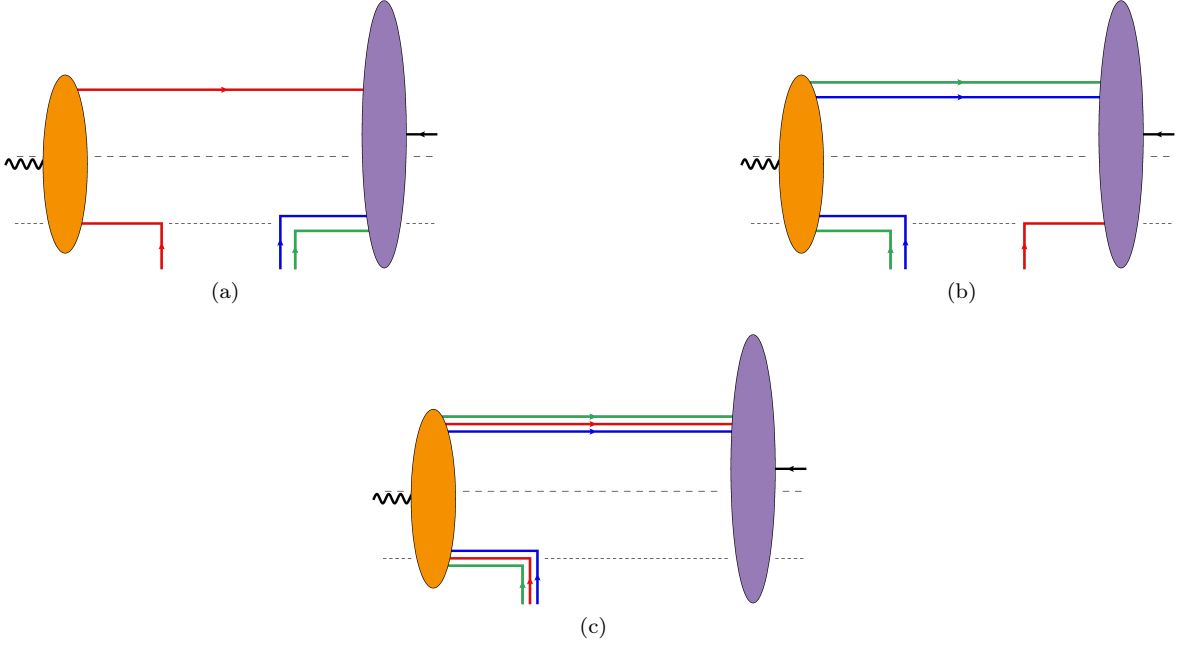


Figure 2. Sketch of the leading contribution to photon-to-nucleon TDAs in the DGLAP I (a), DGLAP II (b), and ERBL (c) support regions.

C. Definition of the Photon-to-Nucleon Transition Distribution Amplitudes

In order to define the photon-to-nucleon TDAs, we start by considering the matrix element of the trilocal operator that allows the transition between the initial photon and final nucleon, i.e.,

$$\langle p'_N, s'_N | \widehat{O}_{ABC}(\lambda_1 n, \lambda_2 n, \lambda_3 n) | q, \lambda \rangle, \quad (16)$$

where λ, s'_N are the LC helicities of the photon and the proton, respectively, and the operator \widehat{O}_{ABC} is defined as

$$\widehat{O}_{ABC}(\lambda_1 n, \lambda_2 n, \lambda_3 n) = \epsilon_{jkl} \bar{\psi}_{u,jA}(\lambda_1 n) \bar{\psi}_{u,kB}(\lambda_2 n) \bar{\psi}_{d,lC}(\lambda_3 n). \quad (17)$$

In Eq. (17), $\bar{\psi}_u, \bar{\psi}_d$ are the Dirac adjoints of the field operators for up and down quarks, respectively, A, B, C are Dirac indices, j, k, l are summed (anti)quark-color indices, and ϵ_{jkl} is the antisymmetric Levi-Civita symbol. For a final neutron, we just need to switch all up and down quarks, so we will only perform the calculations for the proton case. In general, we would have to insert Wilson lines between the local operators to ensure gauge invariance. However, choosing the LC gauge $A^+ = 0$, these lines become trivial along the direction of n .

We Fourier transform the matrix element of the trilocal operator with the transformation

$$\mathcal{F}[\dots] = (p \cdot n)^3 \int \left(\prod_{a=1}^3 \frac{d\lambda_a}{2\pi} \right) [\dots] e^{i \sum_{b=1}^3 x_b \lambda_b (p \cdot n)}. \quad (18)$$

In the LC decomposition of Eqs. (7)–(14), the result has the following structure:

$$\mathcal{F} \langle p'_N, s'_N | \widehat{O}_{ABC}(\lambda_1 n, \lambda_2 n, \lambda_3 n) | q, \lambda \rangle = \delta(x_1 + x_2 + x_3 - 2\xi) \frac{m_N}{4}$$

$$\times \sum_{\mathcal{I}} \left(s_{\mathcal{I}}^{N\gamma} \right)_{ABC} (q, \lambda, p'_N, s'_N) S_{\mathcal{I}}^{N\gamma} (x_1, x_2, x_3, \xi, u), \quad (19)$$

where the factor of $m_N/4$ is for convenience. The fractions of longitudinal momentum of the exchanged partons are in the following range:

$$\xi - 1 \leq x_b \leq \xi + 1, \quad b = 1, 2, 3. \quad (20)$$

When x_b is positive, it corresponds to the fraction of released longitudinal momentum in the photon-to-proton transition carried by an emitted antiquark, while, when negative, its absolute value is the fraction carried by an absorbed quark. In agreement with this interpretation, the x s are constrained to add up to 2ξ . When one x variable is positive and two are negative, we are in the DGLAP I support region (Fig. 2a), when two are positive and one is negative in the DGLAP II region (Fig. 2b), and when all three are positive in the ERBL region (Fig. 2c). The sum in Eq. (19) is over a set of independent Dirac structures, and the coefficients are the photon-to-nucleon TDAs, which turn out to be dimensionless and real, and also depend on a collinear factorization scale. We will only consider the leading-twist TDAs, i.e., the contribution to the matrix element (19) with the highest power of P^+ . It comes from the LC good components of the spinors (A8), and has a twist of three.

The Dirac structures are related to the ones for the nucleon-to-photon (γN) transition of DVCS, listed in Appendix B of Ref. [13], by

$$\left(s^{N\gamma} \right)_{ABC} = - \left(\gamma^{0\top} \right)_{AA'} \left(s^{\gamma N\top} \right)_{A'B'C'} \gamma_{B'B}^0 \gamma_{C'C}^0. \quad (21)$$

Note that our formula corrects the analogous Eq. (17) of Ref. [13], which misses a minus sign. In exactly backward TCS, where $\Delta_T = 0$, only four Dirac structures are nonzero. For convenience, we reproduce them below

$$\left(v_{1\mathcal{E}}^{\gamma N} \right)_{ABC} = (\hat{p}\mathcal{C})_{AB} (\gamma^5 \hat{\epsilon}^* U_+)_C, \quad (22)$$

$$\left(a_{1\mathcal{E}}^{\gamma N} \right)_{ABC} = (\hat{p}\gamma^5 \mathcal{C})_{AB} (\hat{\epsilon}^* U_+)_C, \quad (23)$$

$$\left(t_{1\mathcal{E}}^{\gamma N} \right)_{ABC} = (\sigma_{p\mu} \mathcal{C})_{AB} (\gamma^5 \sigma^{\mu\epsilon^*} U_+)_C, \quad (24)$$

$$\left(t_{2\mathcal{E}}^{\gamma N} \right)_{ABC} = (\sigma_{p\epsilon^*} \mathcal{C})_{AB} (\gamma^5 U_+)_C, \quad (25)$$

where \mathcal{C} is the charge conjugation matrix (A2), ϵ^μ is the photon polarization vector (41), U_+ is the good component of the nucleon spinor, and

$$\hat{p} = p_\nu \gamma^\nu, \quad (26)$$

$$\sigma^{\nu\mu} = \frac{1}{2} [\gamma^\nu, \gamma^\mu], \quad (27)$$

$$\sigma_{p\mu} = \hat{p}^\nu \sigma_{\nu\mu}, \quad (28)$$

$$\sigma_{p\epsilon^*} = \hat{p}^\nu \epsilon^{*\mu} \sigma_{\nu\mu}. \quad (29)$$

If we define the helicity amplitudes

$$T_{ABC}^{s'_N, \lambda} = \frac{m_N}{4} \left(\left(v_{1\mathcal{E}}^{N\gamma} \right)_{ABC} V_{1\mathcal{E}}^{N\gamma} + \left(a_{1\mathcal{E}}^{N\gamma} \right)_{ABC} A_{1\mathcal{E}}^{N\gamma} + \left(t_{1\mathcal{E}}^{N\gamma} \right)_{ABC} T_{1\mathcal{E}}^{N\gamma} + \left(t_{2\mathcal{E}}^{N\gamma} \right)_{ABC} T_{2\mathcal{E}}^{N\gamma} \right), \quad (30)$$

we can express the TDAs as linear combinations of the helicity amplitudes, i.e.,

$$V_{1\mathcal{E}}^{N\gamma} = \frac{\sqrt{2}}{\sqrt{1-\xi} (P^+)^{\frac{3}{2}} m_N} \left(T_{322}^{\uparrow,+1} + T_{232}^{\uparrow,+1} \right), \quad (31)$$

$$A_{1\mathcal{E}}^{N\gamma} = \frac{\sqrt{2}}{\sqrt{1-\xi} (P^+)^{\frac{3}{2}} m_N} \left(T_{322}^{\uparrow,+1} - T_{232}^{\uparrow,+1} \right), \quad (32)$$

$$T_{1\mathcal{E}}^{N\gamma} = \frac{\sqrt{2}}{\sqrt{1-\xi} (P^+)^{\frac{3}{2}} m_N} \left(T_{223}^{\uparrow,+1} - T_{333}^{\uparrow,-1} \right), \quad (33)$$

$$T_{2\mathcal{E}}^{N\gamma} = \frac{\sqrt{2}}{\sqrt{1-\xi}(P^+)^{\frac{3}{2}}m_N} \left(T_{223}^{\uparrow,+1} + T_{333}^{\uparrow,-1} \right). \quad (34)$$

The choice of Dirac indices in the above equations fixes the components of the Dirac adjoints of the spinors in the expansions of the local fields in the triloal operator (17). Since we are focusing on the good components (A8), an index value of 2 gives a nonzero contribution from a quark with spin $-1/2$ or antiquark with spin $+1/2$, while a quark with spin $+1/2$ or an antiquark with spin $-1/2$ contribute when the index is 3. Therefore, the helicity amplitudes in Eqs. (31)–(34) correspond to transitions where the total LC helicity is conserved without any transfer of orbital angular momentum between the photon and the proton, which is compatible with $\Delta_T = 0$. For example, considering $T_{322}^{\uparrow,+1}$ and the photon splitting into a down-antidown pair, we have a photon and two up quarks of LC helicity $+1, +1/2, -1/2$, respectively, transitioning into a proton and an antidown both of helicity $+1/2$, for a conserved total helicity of $+1$. Note that the down quark could have helicity $+1/2$, corresponding to no orbital angular momentum between the partons in the photon nor in the proton, or it could have helicity $-1/2$, for a third component of orbital angular momentum of $+1$ both in the photon and in the proton. We can interpret the other cases in an analogous fashion.

III. MODELING PHOTON-TO-NUCLEON TRANSITION DISTRIBUTION AMPLITUDES

In the following, we focus on the study of the leading contribution to the TDAs in the DGLAP I region, corresponding to the probing of the $q\bar{q}$ and qqq components of the photon and proton states, respectively, as represented in Fig. 2a. We first introduce a model for the LFWFs of the photon and proton states, and then give the structure of the analytical results for the TDAs in the model calculation. We conclude with numerical predictions for a selected set of TDAs and their first Mellin moments.

A. A Light-Front Dynamical Model for the Photon and the Nucleon

In LFD, we can represent interacting states on a basis of Fock states, provided that we avoid particles with zero longitudinal momentum (see, e.g., Refs. [22, 38]). If A labels a strongly interacting particle with on-shell four-momentum P and LC helicity Λ , we can write

$$|A; P, \Lambda\rangle = \sum_{N,\beta} \int \left[\frac{dx}{\sqrt{x}} \right]_N [d^2k_\perp]_N \Psi_{N,\beta}^{A,\Lambda}(\{x_i, \vec{q}_{i\perp}\}) |N; p_1, \dots, p_N, \beta\rangle, \quad (35)$$

where $N = n_q + n_{\bar{q}} + n_{\bar{q}}$ labels the number of partons with discrete quantum numbers collectively denoted by β . In Eq. (35), the integration measures are defined as

$$\left[\frac{dx}{\sqrt{x}} \right]_N = \prod_{i=1}^N \frac{dx_i}{\sqrt{x_i}} \delta \left(1 - \sum_{j=1}^N x_j \right), \quad (36)$$

$$[d^2k_\perp]_N = \frac{1}{(2(2\pi)^3)^{N-1}} \prod_{i=1}^N d^2k_{i\perp} \delta^{(2)} \left(\sum_{j=1}^N \vec{k}_{j\perp} \right), \quad (37)$$

where, for every parton with four-momentum p_i , we defined the fraction x_i of longitudinal momentum with respect to P^+ and the transverse momentum $\vec{k}_{i\perp}$ with respect to \vec{P}_\perp , i.e.,

$$p_i^+ = x_i P^+, \quad (38)$$

$$\vec{p}_{i\perp} = x_i \vec{P}_\perp + \vec{k}_{i\perp}. \quad (39)$$

The coefficients $\Psi_{N,\beta}^{A,\Lambda}$ in Eq. (35) are LFWFs that give the probability amplitude to find the N -parton Fock state in the hadron A . They only depend on the relative variables $(x_i, \vec{k}_{i\perp})$ and are thus Lorentz invariant.

We model the initial photon as a quark–antiquark pair, with flavor either up (u) or down (d). The corresponding LFWF can be obtained by the tree level diagram of Fig. 3 (see, e.g., Ref. [23]). We have

$$\Psi_{f\bar{f},78}^{\gamma,\lambda} = -e_f e \sqrt{2} \left(\frac{m^2 + k_{7\perp}^2}{x_7} + \frac{m^2 + k_{8\perp}^2}{x_8} \right)^{-1}$$

$$\times \left(\frac{m}{x_7 x_8} \delta_{\lambda s_7} \delta_{s_7 s_8} + \sqrt{2} \vec{\epsilon}_{\lambda \perp} \cdot \left(\frac{\vec{k}_{7\perp}}{x_7} \delta_{\lambda - s_7} \delta_{-s_7 s_8} + \frac{\vec{k}_{8\perp}}{x_8} \delta_{\lambda s_7} \delta_{s_7 - s_8} \right) \right), \quad (40)$$

where the subscripts 7, 8 collectively denote the LC helicity and the momentum of quark and antiquark, respectively, the Kronecker deltas only check the sign of the parton helicities, e_f is the charge of quark flavor f in units of the positron charge e , and m is the quark mass. In Eq. (40), $\vec{\epsilon}_{\lambda \perp}$ is the transverse part of the photon polarization vector, i.e.,

$$\epsilon_{\lambda}^{\mu}(q) = \left(0, \frac{2\vec{q}_{\perp} \cdot \vec{\epsilon}_{\lambda \perp}}{q^+}, \vec{\epsilon}_{\lambda \perp} \right), \quad \vec{\epsilon}_{\lambda \perp} = -\frac{1}{\sqrt{2}} (\lambda, i), \quad (41)$$

with $\lambda = +1, -1$ corresponding to counterclockwise and clockwise polarization, respectively.

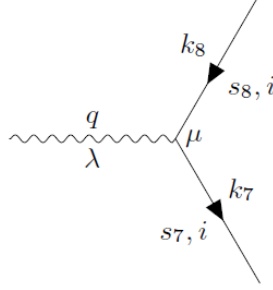


Figure 3. Photon to quark-antiquark pair at tree level.

For the proton, we use the constituent-quark LFWFs introduced in Ref. [24] and expanded in terms of eigenstates of orbital angular momentum in Ref. [39]. The model was applied to calculate the orbital-angular-momentum content of transverse-momentum-dependent distributions [39, 40], and to predict the spin asymmetries in semi-inclusive deep-inelastic scattering [41, 42]. The energy scale at which the nucleon is well represented by the constituent valence quarks was derived in Ref. [42], and is about 0.5 GeV.

For convenience, we report below the results for a proton with LC helicity $+1/2$, the only needed for Eqs. (31)–(34), numbering the three valence quarks as 4, 5, 6. The proton state is given by

$$|p'_N, \uparrow\rangle = |p'_N, \uparrow\rangle_{L_z=0} + |p'_N, \uparrow\rangle_{L_z=+1} + |p'_N, \uparrow\rangle_{L_z=-1} + |p'_N, \uparrow\rangle_{L_z=+2}, \quad (42)$$

where L_z is the third component of the total orbital angular momentum of the three valence quarks. Every orbital-angular-momentum component corresponds to one of the possible combinations of LC helicities of the quarks, so that the third component of total angular momentum $L_z + \sum_{i=4,5,6} s_i = +1/2$. They are given by

$$\begin{aligned} |p'_N, \uparrow\rangle_0 &= \int \left[\frac{dx}{\sqrt{x}} \right]_3 [d^2 k_{\perp}]_3 \left(\psi^{(1)}(4, 5, 6) + i (k_4^1 k_5^2 - k_4^2 k_5^1) \psi^{(2)}(4, 5, 6) \right) \\ &\times \frac{1}{\sqrt{6}} \epsilon_{xyz} u_{\uparrow x}^{\dagger}(4) \left(u_{\downarrow y}^{\dagger}(5) d_{\uparrow z}^{\dagger}(6) - d_{\downarrow y}^{\dagger}(5) u_{\uparrow z}^{\dagger}(6) \right) |0\rangle, \end{aligned} \quad (43)$$

$$\begin{aligned} |p'_N, \uparrow\rangle_{+1} &= \int \left[\frac{dx}{\sqrt{x}} \right]_3 [d^2 k_{\perp}]_3 \left(k_{4\perp}^+ \psi^{(3)}(4, 5, 6) + k_{5\perp}^+ \psi^{(4)}(4, 5, 6) \right) \\ &\times \frac{1}{\sqrt{6}} \epsilon_{xyz} \left(u_{\uparrow x}^{\dagger}(4) u_{\downarrow y}^{\dagger}(5) d_{\downarrow z}^{\dagger}(6) - d_{\uparrow x}^{\dagger}(4) u_{\downarrow y}^{\dagger}(5) u_{\downarrow z}^{\dagger}(6) \right) |0\rangle, \end{aligned} \quad (44)$$

$$\begin{aligned} |p'_N, \uparrow\rangle_{-1} &= \int \left[\frac{dx}{\sqrt{x}} \right]_3 [d^2 k_{\perp}]_3 (-1) k_{5\perp}^- \psi^{(5)}(4, 5, 6) \\ &\times \frac{1}{\sqrt{6}} \epsilon_{xyz} u_{\uparrow x}^{\dagger}(4) \left(u_{\uparrow y}^{\dagger}(5) d_{\uparrow z}^{\dagger}(6) - d_{\uparrow y}^{\dagger}(5) u_{\uparrow z}^{\dagger}(6) \right) |0\rangle, \end{aligned} \quad (45)$$

$$\begin{aligned} |p'_N, \uparrow\rangle_{+2} &= \int \left[\frac{dx}{\sqrt{x}} \right]_3 [d^2 k_{\perp}]_3 (-1) k_{4\perp}^+ k_{6\perp}^+ \psi^{(6)}(4, 5, 6) \\ &\times \frac{1}{\sqrt{6}} \epsilon_{xyz} u_{\downarrow x}^{\dagger}(4) \left(u_{\downarrow y}^{\dagger}(5) d_{\downarrow z}^{\dagger}(6) - d_{\downarrow y}^{\dagger}(5) u_{\downarrow z}^{\dagger}(6) \right) |0\rangle, \end{aligned} \quad (46)$$

where $k_i^\pm = k_i^1 \pm k_i^2$. In Eqs. (43)–(46), $u_{sx}^\dagger(i)$ ($d_{sx}^\dagger(i)$) is the creation operator for on-shell u (d) quarks, with LC helicity $s = \uparrow, \downarrow$ corresponding to $+1/2, -1/2$, respectively, x is the color, and the argument (i) stands for $(x_i, k_{i\perp})$. The functions $\psi^{(j)}$, with $j = 1, 2, \dots, 6$, are given by (see Ref. [39])

$$\psi^{(1)}(4, 5, 6) = \frac{1}{\sqrt{3}} \tilde{\psi}(\{x_i, \vec{k}_{i\perp}\}) \prod_i \frac{1}{\sqrt{N_i}} \left(-a_4 a_5 a_6 + (2a_4 + a_6) \vec{k}_{4\perp} \cdot \vec{k}_{5\perp} + 2a_4 k_{5\perp}^2 \right), \quad (47)$$

$$\psi^{(2)}(4, 5, 6) = \frac{1}{\sqrt{3}} \tilde{\psi}(\{x_i, \vec{k}_{i\perp}\}) \prod_i \frac{1}{\sqrt{N_i}} (2a_4 + a_6), \quad (48)$$

$$\psi^{(3)}(4, 5, 6) = \frac{1}{\sqrt{3}} \tilde{\psi}(\{x_i, \vec{k}_{i\perp}\}) \prod_i \frac{1}{\sqrt{N_i}} (-a_4 a_5 - k_{5\perp}^2), \quad (49)$$

$$\psi^{(4)}(4, 5, 6) = \frac{1}{\sqrt{3}} \tilde{\psi}(\{x_i, \vec{k}_{i\perp}\}) \prod_i \frac{1}{\sqrt{N_i}} \left(-a_4 a_5 - 2a_4 a_6 + k_{4\perp}^2 + 2\vec{k}_{4\perp} \cdot \vec{k}_{5\perp} \right), \quad (50)$$

$$\psi^{(5)}(4, 5, 6) = \frac{1}{\sqrt{3}} \tilde{\psi}(\{x_i, \vec{k}_{i\perp}\}) \prod_i \frac{1}{\sqrt{N_i}} a_4 a_6, \quad (51)$$

$$\psi^{(6)}(4, 5, 6) = \frac{1}{\sqrt{3}} \tilde{\psi}(\{x_i, \vec{k}_{i\perp}\}) \prod_i \frac{1}{\sqrt{N_i}} a_5, \quad (52)$$

where $N_i = a_i^2 + k_{i\perp}^2$ and $a_i = m + x_i M_0$, with M_0 the mass of the non-interacting three quark system, i.e., $M_0 = \sqrt{\sum_{i=4}^6 (m^2 + k_{i\perp}^2)}/x_i$. For the function $\tilde{\psi}$, we use

$$\tilde{\psi}(\{x_i, \vec{k}_{i\perp}\}) = 2(2\pi)^3 \sqrt{\frac{1}{M_0} \prod_{i=4}^6 \frac{\omega_i}{x_i} \frac{N'}{(M_0^2 + \tilde{\beta}^2)^{\tilde{\gamma}}}}, \quad (53)$$

where N' is a normalization and $\omega_i = (m^2 + k_{i\perp}^2)/x_i$ is the free-quark energy. The parameters $\tilde{\beta}, \tilde{\gamma}$, as well as the light-quarks mass m , are taken from Ref. [43], and are the result of a fit to the electromagnetic form factors. We have

$$m = 0.263 \text{ GeV}, \quad \tilde{\beta} = 0.607 \text{ GeV}, \quad \tilde{\gamma} = 3.5, \quad \tilde{N} = 0.047 \text{ GeV}^{-4}. \quad (54)$$

B. Structure of the Transition Distribution Amplitudes

We can now calculate the matrix elements of the triloal operator in Eq. (17) by inserting the model for the photon and proton LFWFs described in Sec. III A. Taking into account the quark-antiquark pair in the initial photon and the three valence quarks of the final nucleon, we end up evaluating matrix elements of the form

$$\langle q_{4x} q_{5y} q_{6z} | \frac{1}{\sqrt{6}} \epsilon_{xyz} \epsilon_{jkl} \bar{\psi}_{u,jA}(\lambda_1 n) \bar{\psi}_{u,kB}(\lambda_2 n) \bar{\psi}_{d,lC}(\lambda_3 n) | q_{7i} \bar{q}_{8i} \rangle, \quad (55)$$

where x, y, z are summed color indices and the index i runs over color for the quark or the corresponding anticolor for the antiquark. Each number in the sets 4, 5, 6 and 7, 8 collectively denotes the other quantum numbers of a quark in the color-antisymmetric three-quark Fock component of the proton and in the quark-antiquark-pair Fock component of the photon, respectively. Focusing on the leading twist three and expanding the fields in terms of ladder operators, the only nonzero contributions come from annihilating an antiquark and creating two quarks between the initial and final states. We have two possibilities: the photon splits into a down-antidown pair ($d\bar{d}$) or into an up-antiup pair ($u\bar{u}$). In the first case, we annihilate the \bar{d} and create two u and we are left with

$$\begin{aligned} & \langle q_{4x} q_{5y} q_{6z} | \frac{1}{\sqrt{6}} \epsilon_{xyz} \hat{O}_{ABC}(\lambda_1 n, \lambda_2 n, \lambda_3 n) | d_{7i} \bar{d}_{8i} \rangle \\ &= -\sqrt{6} \left(\bar{u}_{u,s_4 A}(k_4) \bar{u}_{u,s_5 B}(k_5) e^{i(\lambda_1 n \cdot k_4 + \lambda_2 n \cdot k_5)} + \bar{u}_{u,s_5 A}(k_5) \bar{u}_{u,s_4 B}(k_4) e^{i(\lambda_1 n \cdot k_5 + \lambda_2 n \cdot k_4)} \right) \\ & \times \bar{v}_{d,s_8 C}(k_8) e^{-i\lambda_3 n \cdot k_8} (2\pi)^3 2k_7^+ \delta_{s_6 s_7} \delta(k_6^+ - k_7^+) \delta^{(2)}(\vec{k}_{6\perp} - \vec{k}_{7\perp}). \end{aligned} \quad (56)$$

In the second case, we annihilate the \bar{u} and create u, d , so that

$$\langle q_{4x} q_{5y} q_{6z} | \frac{1}{\sqrt{6}} \epsilon_{xyz} \hat{O}_{ABC}(\lambda_1 n, \lambda_2 n, \lambda_3 n) | u_{7i} \bar{u}_{8i} \rangle$$

$$\begin{aligned}
&= -\sqrt{6} \left(\bar{v}_{u,s_8A}(k_8) \bar{u}_{u,s_5B}(k_5) e^{-i(\lambda_1 n \cdot k_8 - \lambda_2 n \cdot k_5)} + \bar{u}_{u,s_5A}(k_5) \bar{v}_{u,s_8B}(k_8) e^{+i(\lambda_1 n \cdot k_5 - \lambda_2 n \cdot k_8)} \right) \\
&\times \bar{u}_{d,s_6C}(k_6) e^{i\lambda_3 n \cdot k_6} (2\pi)^3 2k_7^+ \delta_{s_4 s_7} \delta(k_4^+ - k_7^+) \delta^{(2)}(\vec{k}_{4\perp} - \vec{k}_{7\perp}) \\
&- \sqrt{6} \left(\bar{v}_{u,s_8A}(k_8) \bar{u}_{u,s_4B}(k_4) e^{-i(\lambda_1 n \cdot k_8 - \lambda_2 n \cdot k_4)} + \bar{u}_{u,s_4A}(k_4) \bar{v}_{u,s_8B}(k_8) e^{+i(\lambda_1 n \cdot k_4 - \lambda_2 n \cdot k_8)} \right) \\
&\times \bar{u}_{d,s_6C}(k_6) e^{i\lambda_3 n \cdot k_6} (2\pi)^3 2k_7^+ \delta_{s_5 s_7} \delta(k_5^+ - k_7^+) \delta^{(2)}(\vec{k}_{5\perp} - \vec{k}_{7\perp}) \Big). \tag{57}
\end{aligned}$$

For the contribution from the proton LFWFs, we introduce the following notation for the a proton with LC helicity $+1/2$ (\uparrow) made up of three quarks:

$$\uparrow \rightarrow \uparrow \downarrow \uparrow + 0 = \psi^{(1)}(4, 5, 6) + i(k_4^1 k_5^2 - k_4^2 k_5^1) \psi^{(2)}(4, 5, 6), \tag{58}$$

$$\uparrow \rightarrow \uparrow \downarrow \downarrow + 1 = k_{4\perp}^+ \psi^{(3)}(4, 5, 6) + k_{5\perp}^+ \psi^{(4)}(4, 5, 6), \tag{59}$$

$$\uparrow \rightarrow \uparrow \uparrow \uparrow - 1 = (-1) k_{5\perp}^- \psi^{(5)}(4, 5, 6), \tag{60}$$

$$\uparrow \rightarrow \downarrow \downarrow \downarrow + 2 = (-1) k_{4\perp}^+ k_{6\perp}^+ \psi^{(6)}(4, 5, 6), \tag{61}$$

where we have explicitly specified the total quark orbital angular momentum $L_z = 0, \pm 1, +2$, which combines with the quark LC helicities to give the proton's LC helicity.

To obtain the final expressions for the photon-to-nucleon TDAs, we need to combine Eqs. (56) or (57) and Eq. (40) with Eqs. (58)–(61), and to sum and integrate over the quantum numbers of intermediate partons. Depending on the helicity amplitude (30) that we want to calculate, the result is a sum of many terms, and we do not find it impractical to write it out in full. Instead, we schematically represent all the terms for a generic helicity amplitude in Figs. 4–6, and we list below the steps to reconstruct the photon-to-proton TDAs of backward TCS.

1. A term of an helicity amplitude is given by a path in Figs. 4–6 by multiplying the nodes in the first and third columns with the complex conjugate of the fourth-column one. The triplet of arrows in a fourth-column node represents the LC helicities of the three quarks in the final proton, in the order of the corresponding second-column node. We add a third component of orbital angular momentum to the LC helicities of the quarks, so that the total is the $+1/2$ LC helicity of the proton. The third-column nodes with flavor order duu and udu have been obtained from Eqs. (56), (57) by the appropriate exchange of indices. Note that we are only considering the Dirac adjoint of the good components of the LC spinors (A8).
2. Fix the Dirac indices A, B, C . In the chiral representation (A1), the Dirac adjoints of the good components of the LC spinors (A8) are nonzero only for Dirac indices equal to 2, 3, corresponding to LC helicity $-1/2, +1/2$ for particles, respectively, and helicity $+1/2, -1/2$ for antiparticles, respectively.
3. We multiply by a factor of $\prod_{i=1}^3 \exp[\pm i((\lambda_i/2)x)]$, with $\lambda_1, \lambda_2, \lambda_3$ associated with a spinor in the third-column node, in the order of the node, and with the plus sign for particles and the minus sign for antiparticles. We also multiply by a factor of the form

$$(2\pi)^3 2k_7^+ \delta_{s_j s_7} \delta(k_j^+ - k_7^+) \delta^{(2)}(\vec{k}_{j\perp} - \vec{k}_{7\perp}), \tag{62}$$

with j equal to the value between 4, 5, 6 that does not appear in the third-column node that we are considering.

4. We introduce a sum over the LC helicities of the quark–antiquark pair in the initial photon, and integrate over the three quark momenta in the proton and the quark–antiquark momenta in the photon with the measures (36)–(37). We then Fourier transform with the transformation (18), which results in three Dirac delta distributions for the x variables (see the following item).
5. We use all the Dirac delta distributions and Kronecker deltas to fix all but two longitudinal momenta, that we always choose to be index 4 and 5. For every term of an helicity amplitude, we have

$$\vec{k}_{6\perp} = -\vec{k}_{4\perp} - \vec{k}_{5\perp}, \quad x_7 = 1 - x_8, \quad \vec{k}_{8\perp} = -\vec{k}_{7\perp}. \tag{63}$$

The other variables for every surviving path of the helicity amplitudes that we are interested in are given by the rows of Tabs. I–V. Note that, by Eq. (40), the photon cannot split into two partons whose helicities are both of the opposite sign of the original helicity, which would correspond to the $L_z = \pm 2$ components for the photon state. Therefore, the configurations with $s_7 = s_8 = -1/2$ do not appear in Tabs. I–III, and the entries with $s_7 = s_8 = +1/2$ do not appear in Tabs. IV, V. Also note that the $L_z = +1$ component only contributes to $T_{322}^{\uparrow,+1}, T_{232}^{\uparrow,+1}, T_{223}^{\uparrow,+1}$, while the $L_z = -1$ component only contributes to $T_{333}^{\uparrow,-1}$.

6. For every term, we have a factor of

$$\delta(x_1 + x_2 + x_3 - 2\xi), \quad (64)$$

which is consistent with the fact that we have to extract a total of 2ξ in going from the initial photon with momentum (7) to the final proton with momentum (9). This Dirac delta distribution is not included in the definition of the helicity amplitudes.

7. We add all the terms for an helicity amplitude, we add or subtract the helicity amplitudes according to Eqs. (31)–(34), and multiply by the remaining factor of

$$\frac{-\sqrt{6}\sqrt{2}(1+\xi)\sqrt{1-\xi^2}}{m_N(P^+)^{\frac{3}{2}}}, \quad (65)$$

with P^+ as in Eq. (12) (Note that the factors of P^+ cancel overall).

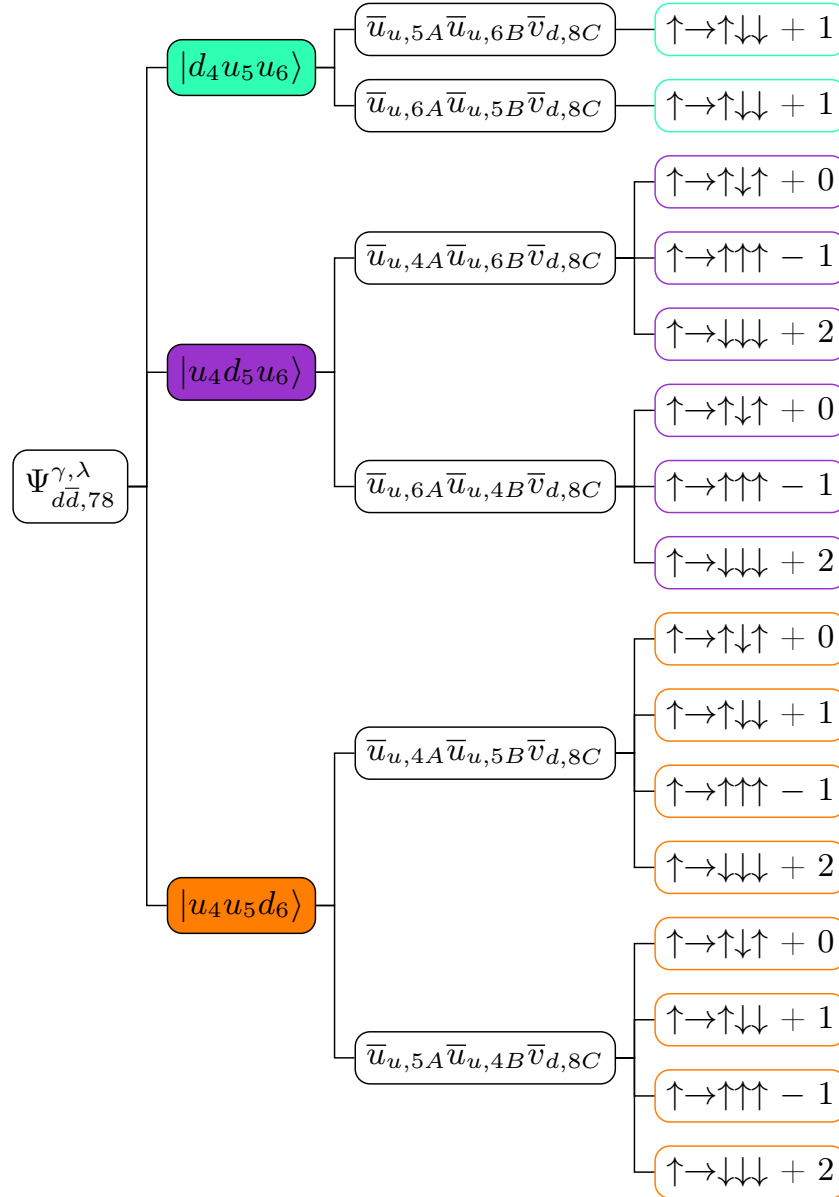


Figure 4. (Color online.) Structure of the helicity amplitude $T_{ABC}^{\uparrow,\lambda}$ with $\gamma \rightarrow d\bar{d}$.

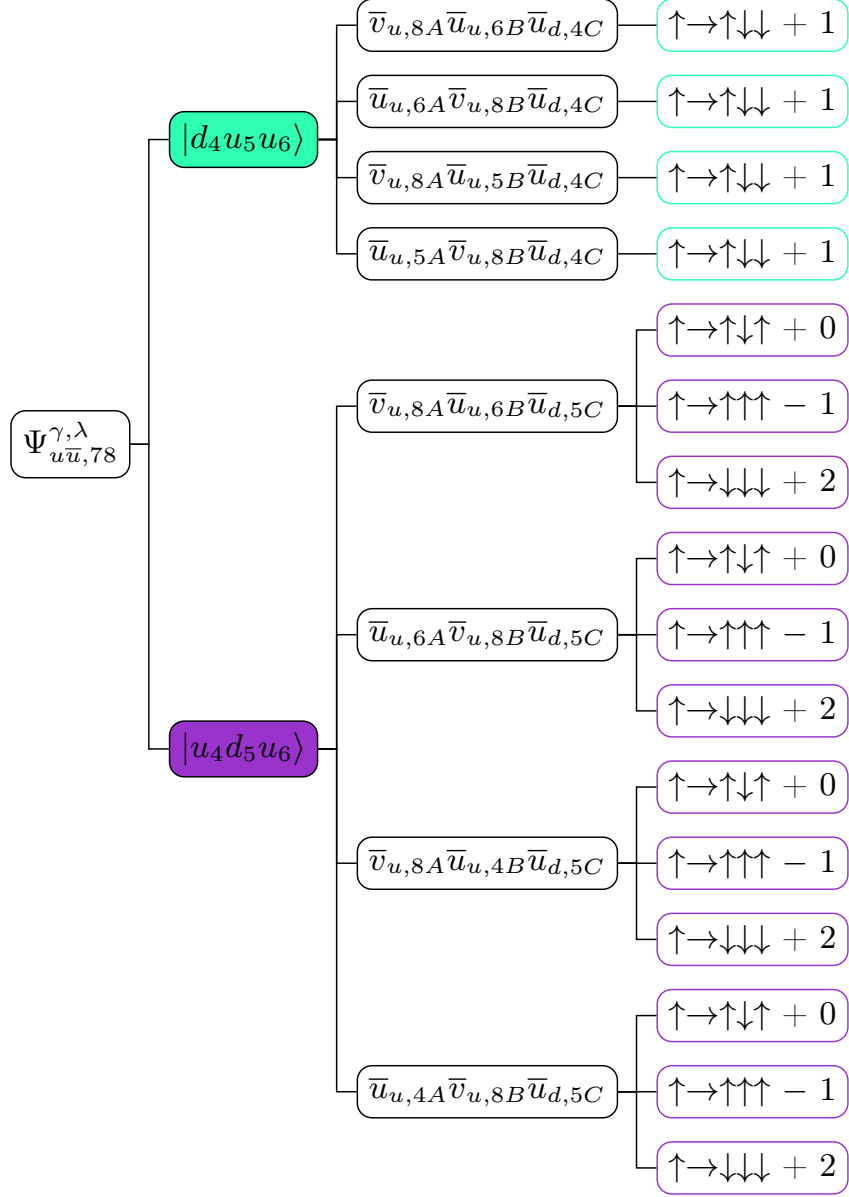


Figure 5. (Color online.) Structure of the helicity amplitude $T_{ABC}^{\uparrow,\lambda}$ with $\gamma \rightarrow u\bar{u}$, part I.

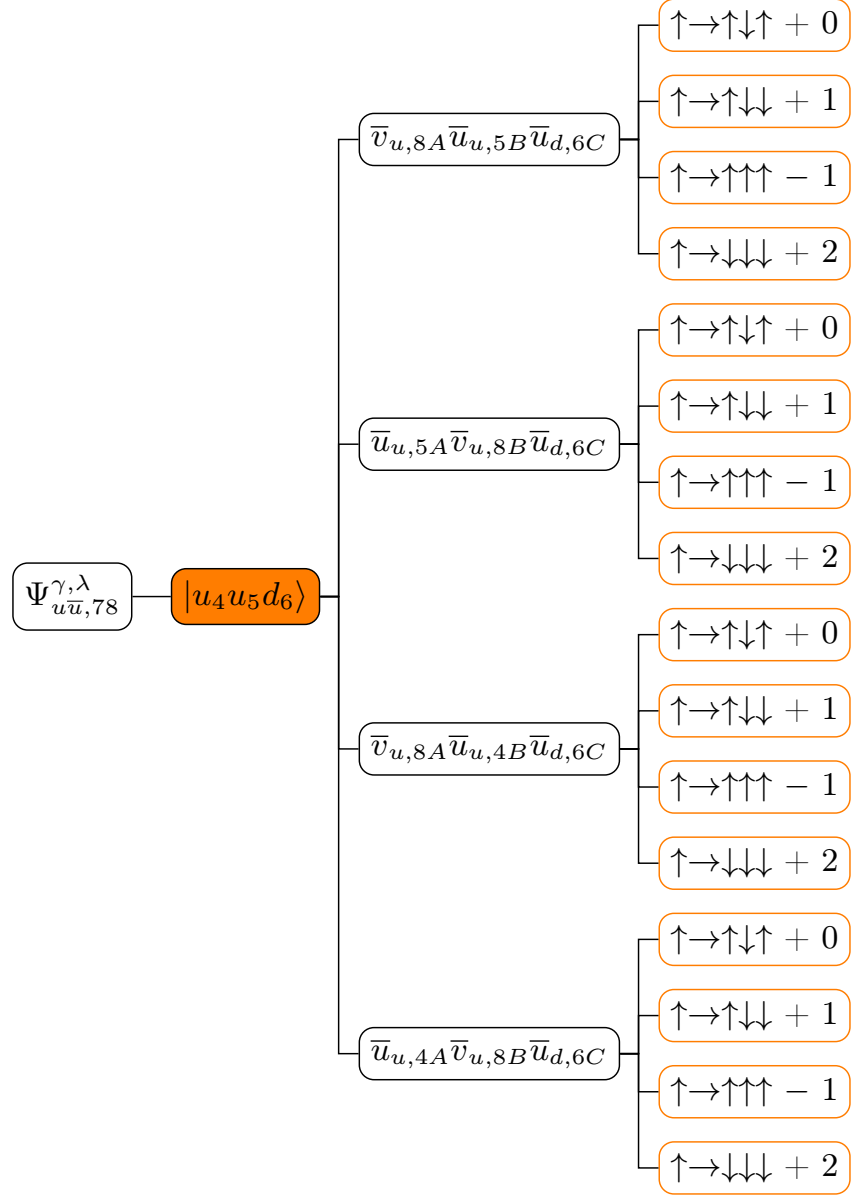


Figure 6. (Color online.) Structure of the helicity amplitude $T_{ABC}^{\uparrow,\lambda}$ with $\gamma \rightarrow u\bar{u}$, part II.

$T_{322}^{\uparrow,+1}$						
x_4	x_5	x_6	s_7	$\vec{k}_{7\perp}$	s_8	x_8
$-\frac{x_1}{1-\xi}$	$-\frac{x_2}{1-\xi}$	$\frac{1+\xi}{1-\xi} - \frac{x_3}{1-\xi}$	$+\frac{1}{2}$	$\vec{k}_{6\perp}$	$+\frac{1}{2}$	$\frac{x_3}{1+\xi}$
$-\frac{x_1}{1-\xi}$	$-\frac{x_2}{1-\xi}$	$\frac{1+\xi}{1-\xi} - \frac{x_3}{1-\xi}$	$-\frac{1}{2}$	$\vec{k}_{6\perp}$	$+\frac{1}{2}$	$\frac{x_3}{1+\xi}$
$\frac{1+\xi}{1-\xi} - \frac{x_1}{1-\xi}$	$-\frac{x_2}{1-\xi}$	$-\frac{x_3}{1-\xi}$	$+\frac{1}{2}$	$\vec{k}_{4\perp}$	$-\frac{1}{2}$	$\frac{x_1}{1+\xi}$
$-\frac{x_1}{1-\xi}$	$\frac{1+\xi}{1-\xi} - \frac{x_2}{1-\xi}$	$-\frac{x_3}{1-\xi}$	$-\frac{1}{2}$	$\vec{k}_{5\perp}$	$+\frac{1}{2}$	$\frac{x_2}{1+\xi}$
$\frac{1+\xi}{1-\xi} - \frac{x_2}{1-\xi}$	$-\frac{x_3}{1-\xi}$	$-\frac{x_1}{1-\xi}$	$+\frac{1}{2}$	$\vec{k}_{4\perp}$	$+\frac{1}{2}$	$\frac{x_2}{1+\xi}$
$-\frac{x_1}{1-\xi}$	$-\frac{x_3}{1-\xi}$	$\frac{1+\xi}{1-\xi} - \frac{x_2}{1-\xi}$	$+\frac{1}{2}$	$\vec{k}_{6\perp}$	$+\frac{1}{2}$	$\frac{x_2}{1+\xi}$

Table I. Constrained variables for the nonzero terms of $T_{322}^{\uparrow,+1}$. Contributions from the initial photon splitting into $d\bar{d}$ and into $u\bar{u}$ are above and below the dark line, respectively.

$T_{232}^{\uparrow,+1}$						
x_4	x_5	x_6	s_7	$\vec{k}_{7\perp}$	s_8	x_8
$-\frac{x_2}{1-\xi}$	$-\frac{x_1}{1-\xi}$	$\frac{1+\xi}{1-\xi} - \frac{x_3}{1-\xi}$	$+\frac{1}{2}$	$\vec{k}_{6\perp}$	$+\frac{1}{2}$	$\frac{x_3}{1+\xi}$
$-\frac{x_2}{1-\xi}$	$-\frac{x_1}{1-\xi}$	$\frac{1+\xi}{1-\xi} - \frac{x_3}{1-\xi}$	$-\frac{1}{2}$	$\vec{k}_{6\perp}$	$+\frac{1}{2}$	$\frac{x_3}{1+\xi}$
$\frac{1+\xi}{1-\xi} - \frac{x_2}{1-\xi}$	$-\frac{x_1}{1-\xi}$	$-\frac{x_3}{1-\xi}$	$+\frac{1}{2}$	$\vec{k}_{4\perp}$	$-\frac{1}{2}$	$\frac{x_2}{1+\xi}$
$-\frac{x_2}{1-\xi}$	$\frac{1+\xi}{1-\xi} - \frac{x_1}{1-\xi}$	$-\frac{x_3}{1-\xi}$	$-\frac{1}{2}$	$\vec{k}_{5\perp}$	$+\frac{1}{2}$	$\frac{x_1}{1+\xi}$
$\frac{1+\xi}{1-\xi} - \frac{x_1}{1-\xi}$	$-\frac{x_3}{1-\xi}$	$-\frac{x_2}{1-\xi}$	$+\frac{1}{2}$	$\vec{k}_{4\perp}$	$+\frac{1}{2}$	$\frac{x_1}{1+\xi}$
$-\frac{x_2}{1-\xi}$	$-\frac{x_3}{1-\xi}$	$\frac{1+\xi}{1-\xi} - \frac{x_1}{1-\xi}$	$+\frac{1}{2}$	$\vec{k}_{6\perp}$	$+\frac{1}{2}$	$\frac{x_1}{1+\xi}$

Table II. Constrained variables for the nonzero terms of $T_{232}^{\uparrow,+1}$. Contributions from the initial photon splitting into $d\bar{d}$ and into $u\bar{u}$ are above and below the dark line, respectively.

$T_{223}^{\uparrow,+1}$						
x_4	x_5	x_6	s_7	$\vec{k}_{7\perp}$	s_8	x_8
$\frac{1+\xi}{1-\xi} - \frac{x_3}{1-\xi}$	$-\frac{x_1}{1-\xi}$	$-\frac{x_2}{1-\xi}$	$+\frac{1}{2}$	$\vec{k}_{4\perp}$	$-\frac{1}{2}$	$\frac{x_3}{1+\xi}$
$\frac{1+\xi}{1-\xi} - \frac{x_3}{1-\xi}$	$-\frac{x_2}{1-\xi}$	$-\frac{x_1}{1-\xi}$	$+\frac{1}{2}$	$\vec{k}_{4\perp}$	$-\frac{1}{2}$	$\frac{x_3}{1+\xi}$
$\frac{1+\xi}{1-\xi} - \frac{x_1}{1-\xi}$	$-\frac{x_2}{1-\xi}$	$-\frac{x_3}{1-\xi}$	$+\frac{1}{2}$	$\vec{k}_{4\perp}$	$+\frac{1}{2}$	$\frac{x_1}{1+\xi}$
$\frac{1+\xi}{1-\xi} - \frac{x_2}{1-\xi}$	$-\frac{x_1}{1-\xi}$	$-\frac{x_3}{1-\xi}$	$+\frac{1}{2}$	$\vec{k}_{4\perp}$	$+\frac{1}{2}$	$\frac{x_2}{1+\xi}$
$-\frac{x_3}{1-\xi}$	$\frac{1+\xi}{1-\xi} - \frac{x_1}{1-\xi}$	$-\frac{x_2}{1-\xi}$	$-\frac{1}{2}$	$\vec{k}_{5\perp}$	$+\frac{1}{2}$	$\frac{x_1}{1+\xi}$
$-\frac{x_3}{1-\xi}$	$\frac{1+\xi}{1-\xi} - \frac{x_2}{1-\xi}$	$-\frac{x_1}{1-\xi}$	$-\frac{1}{2}$	$\vec{k}_{5\perp}$	$+\frac{1}{2}$	$\frac{x_2}{1+\xi}$
$-\frac{x_3}{1-\xi}$	$-\frac{x_2}{1-\xi}$	$\frac{1+\xi}{1-\xi} - \frac{x_1}{1-\xi}$	$-\frac{1}{2}$	$\vec{k}_{6\perp}$	$+\frac{1}{2}$	$\frac{x_1}{1+\xi}$
$-\frac{x_3}{1-\xi}$	$-\frac{x_1}{1-\xi}$	$\frac{1+\xi}{1-\xi} - \frac{x_2}{1-\xi}$	$-\frac{1}{2}$	$\vec{k}_{6\perp}$	$+\frac{1}{2}$	$\frac{x_2}{1+\xi}$

Table III. Constrained variables for the nonzero terms of $T_{223}^{\uparrow,+1}$. Contributions from the initial photon splitting into $d\bar{d}$ and into $u\bar{u}$ are above and below the dark line, respectively.

$T_{333}^{\uparrow,-1} (\gamma \rightarrow d\bar{d})$						
x_4	x_5	x_6	s_7	$\vec{k}_{7\perp}$	s_8	x_8
$-\frac{x_1}{1-\xi}$	$-\frac{x_2}{1-\xi}$	$\frac{1+\xi}{1-\xi} - \frac{x_3}{1-\xi}$	$+\frac{1}{2}$	$\vec{k}_{6\perp}$	$-\frac{1}{2}$	$\frac{x_3}{1+\xi}$
$-\frac{x_2}{1-\xi}$	$-\frac{x_1}{1-\xi}$	$\frac{1+\xi}{1-\xi} - \frac{x_3}{1-\xi}$	$+\frac{1}{2}$	$\vec{k}_{6\perp}$	$-\frac{1}{2}$	$\frac{x_3}{1+\xi}$
$-\frac{x_1}{1-\xi}$	$\frac{1+\xi}{1-\xi} - \frac{x_3}{1-\xi}$	$-\frac{x_2}{1-\xi}$	$-\frac{1}{2}$	$\vec{k}_{5\perp}$	$-\frac{1}{2}$	$\frac{x_3}{1+\xi}$
$-\frac{x_2}{1-\xi}$	$\frac{1+\xi}{1-\xi} - \frac{x_3}{1-\xi}$	$-\frac{x_1}{1-\xi}$	$-\frac{1}{2}$	$\vec{k}_{5\perp}$	$-\frac{1}{2}$	$\frac{x_3}{1+\xi}$
$-\frac{x_1}{1-\xi}$	$\frac{1+\xi}{1-\xi} - \frac{x_3}{1-\xi}$	$-\frac{x_2}{1-\xi}$	$+\frac{1}{2}$	$\vec{k}_{5\perp}$	$-\frac{1}{2}$	$\frac{x_3}{1+\xi}$
$-\frac{x_2}{1-\xi}$	$\frac{1+\xi}{1-\xi} - \frac{x_3}{1-\xi}$	$-\frac{x_1}{1-\xi}$	$+\frac{1}{2}$	$\vec{k}_{5\perp}$	$-\frac{1}{2}$	$\frac{x_3}{1+\xi}$

Table IV. Constrained variables for the nonzero terms of $T_{333}^{\uparrow,-1}$ from the initial photon splitting into $d\bar{d}$.

$T_{333}^{\uparrow,-1}(\gamma \rightarrow u\bar{u})$						
x_4	x_5	x_6	s_7	$\vec{k}_{7\perp}$	s_8	x_8
$\frac{1+\xi}{1-\xi} - \frac{x_1}{1-\xi}$	$-\frac{x_2}{1-\xi}$	$-\frac{x_3}{1-\xi}$	$+\frac{1}{2}$	$\vec{k}_{4\perp}$	$-\frac{1}{2}$	$\frac{x_1}{1+\xi}$
$\frac{1+\xi}{1-\xi} - \frac{x_2}{1-\xi}$	$-\frac{x_1}{1-\xi}$	$-\frac{x_3}{1-\xi}$	$+\frac{1}{2}$	$\vec{k}_{4\perp}$	$-\frac{1}{2}$	$\frac{x_2}{1+\xi}$
$-\frac{x_2}{1-\xi}$	$\frac{1+\xi}{1-\xi} - \frac{x_1}{1-\xi}$	$-\frac{x_3}{1-\xi}$	$-\frac{1}{2}$	$\vec{k}_{5\perp}$	$-\frac{1}{2}$	$\frac{x_1}{1+\xi}$
$-\frac{x_1}{1-\xi}$	$\frac{1+\xi}{1-\xi} - \frac{x_2}{1-\xi}$	$-\frac{x_3}{1-\xi}$	$-\frac{1}{2}$	$\vec{k}_{5\perp}$	$-\frac{1}{2}$	$\frac{x_2}{1+\xi}$
$-\frac{x_2}{1-\xi}$	$\frac{1+\xi}{1-\xi} - \frac{x_1}{1-\xi}$	$-\frac{x_3}{1-\xi}$	$+\frac{1}{2}$	$\vec{k}_{5\perp}$	$-\frac{1}{2}$	$\frac{x_1}{1+\xi}$
$-\frac{x_1}{1-\xi}$	$\frac{1+\xi}{1-\xi} - \frac{x_2}{1-\xi}$	$-\frac{x_3}{1-\xi}$	$+\frac{1}{2}$	$\vec{k}_{5\perp}$	$-\frac{1}{2}$	$\frac{x_2}{1+\xi}$
$\frac{1+\xi}{1-\xi} - \frac{x_1}{1-\xi}$	$-\frac{x_3}{1-\xi}$	$-\frac{x_2}{1-\xi}$	$+\frac{1}{2}$	$\vec{k}_{4\perp}$	$-\frac{1}{2}$	$\frac{x_1}{1+\xi}$
$\frac{1+\xi}{1-\xi} - \frac{x_2}{1-\xi}$	$-\frac{x_3}{1-\xi}$	$-\frac{x_1}{1-\xi}$	$+\frac{1}{2}$	$\vec{k}_{4\perp}$	$-\frac{1}{2}$	$\frac{x_2}{1+\xi}$
$-\frac{x_2}{1-\xi}$	$-\frac{x_3}{1-\xi}$	$\frac{1+\xi}{1-\xi} - \frac{x_1}{1-\xi}$	$+\frac{1}{2}$	$\vec{k}_{6\perp}$	$-\frac{1}{2}$	$\frac{x_1}{1+\xi}$
$-\frac{x_1}{1-\xi}$	$-\frac{x_3}{1-\xi}$	$\frac{1+\xi}{1-\xi} - \frac{x_2}{1-\xi}$	$+\frac{1}{2}$	$\vec{k}_{6\perp}$	$-\frac{1}{2}$	$\frac{x_2}{1+\xi}$

Table V. Constrained variables for the nonzero terms of $T_{333}^{\uparrow,-1}$ from the initial photon splitting into $u\bar{u}$.

C. Numerical Results

In this section, we present numerical predictions for the photon-to-proton TDAs within the light-front model presented in Sec. III A. We work in the backward kinematical region, corresponding to transverse momentum Δ_T of the proton with respect to the photon equal to zero, and to values of the skewness variable ξ close to zero. As an example, we chose $\xi = 0.1$, which, by Eq. (15), corresponds to $|u| = 0.196 \text{ GeV}^2$. The results are shown in Figs. 7–10. Making use of the constraint (64), we present 3D plots for the TDAs as functions of x_1 and x_2 in Figs. 7a–10a, while Figs. 7b–10b are the corresponding density plots. The density plots have been divided in various regions according to the value of x_3 . On the (white) diagonal, we have $x_3 = 0$, and the momentum fraction is positive below the line and negative above the line. It decreases moving towards the upper slanted (blue) line, where it reaches its minimal value of $\xi - 1$, while it increases towards the lower slanted (red) line, where we have the maximum value of $\xi + 1$. Since we are truncating the Fock expansion of the initial photon to the leading light-quark-antiquark-pair component, the soft transition into the final nucleon is schematically represented in Fig. 2a. The extracted antiquark corresponds to positive values of one of the variables x_1, x_2, x_3 , while the absorbed quarks to negative values of the remaining two. We can check from the figures that the model has the correct support. Furthermore, $V_{1\mathcal{E}}$ appears to be symmetric under the exchange of x_1 and x_2 , while $A_{1\mathcal{E}}$ is antisymmetric, as expected from Eqs. (31), (32). This is true even for the support region where both variables are negative, where an antiquark down is extracted from the photon, even though it is difficult to see, since the contribution is highly suppressed. We can also see that the absolute value of $T_{1\mathcal{E}}, T_{2\mathcal{E}}$ is smaller by approximately an order of magnitude with respect to $V_{1\mathcal{E}}, A_{1\mathcal{E}}$.

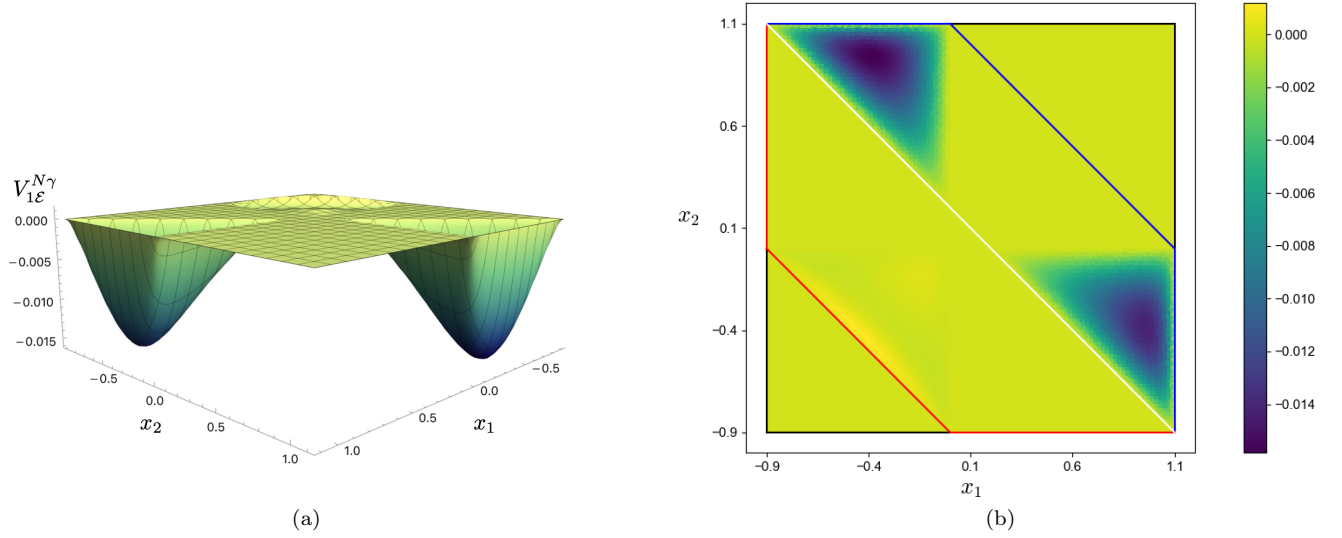


Figure 7. (Color online.) Results for the photon-to-proton $V_{1\epsilon}$ TDA for $\xi = 0.1$. (a) 3D plot as function of x_1 and x_2 . (b) Density plot as function of x_1 and x_2 . On the (white) diagonal, $x_3 = 0$. Inside the upper trapezoid, $\xi - 1 < x_3 < 0$, with $x_3 = \xi - 1$ on the upper slanted (blue) line. Inside the lower trapezoid, $0 < x_3 < \xi + 1$, with $x_3 = \xi + 1$ on the lower slanted (red) line.

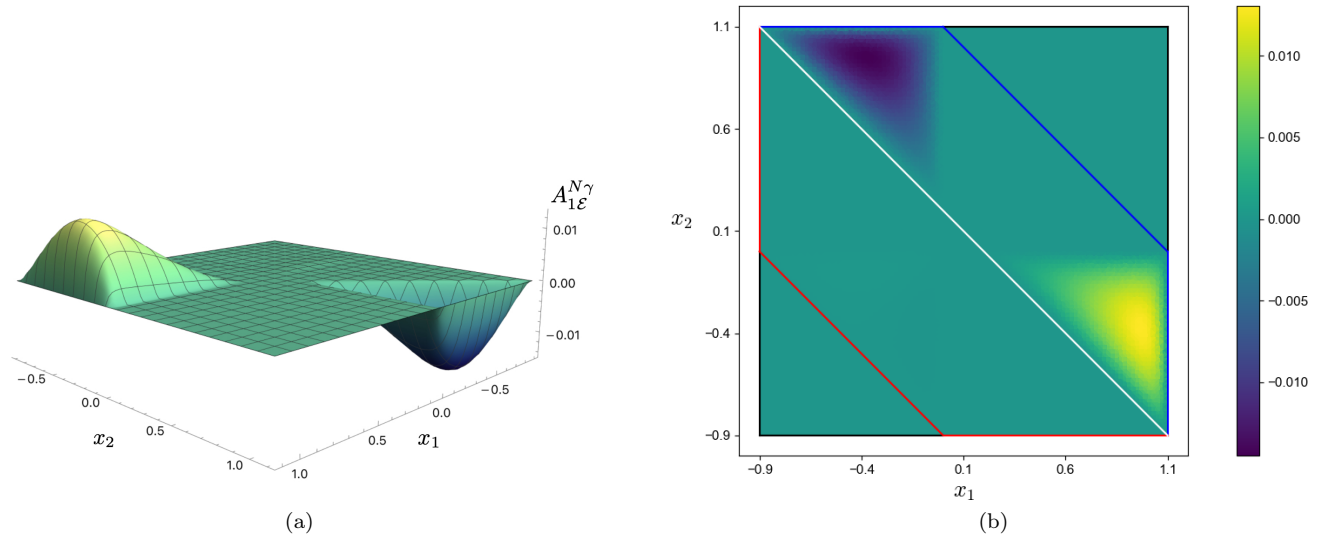


Figure 8. The same as in Fig. 7 for the photon-to-proton $A_{1\epsilon}$ TDA for $\xi = 0.1$.

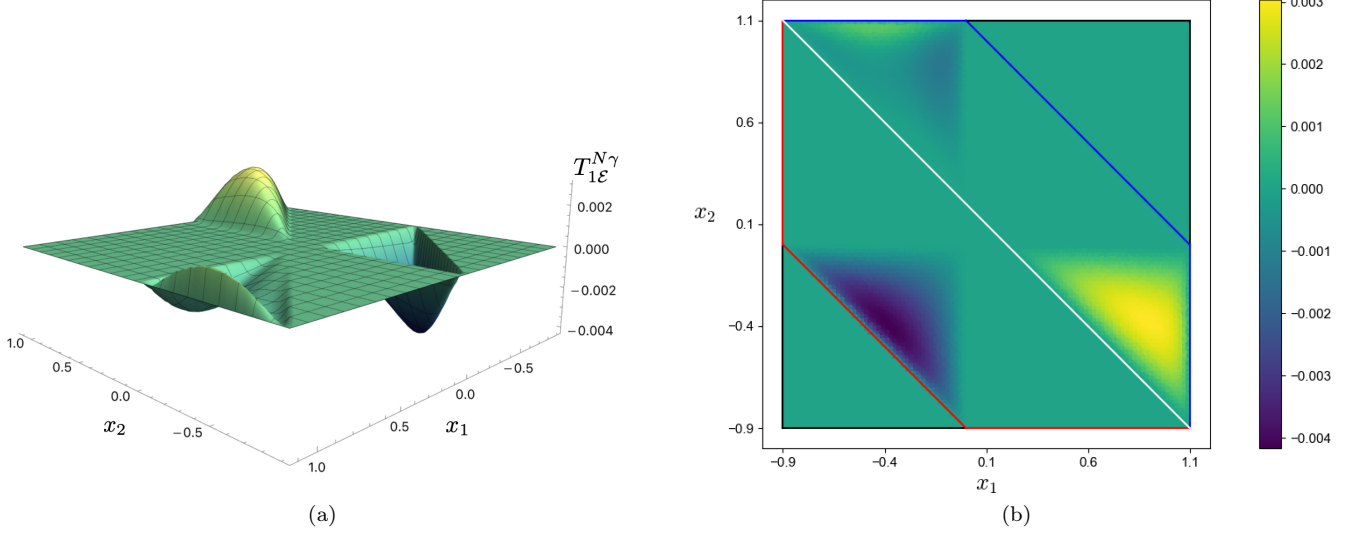


Figure 9. The same as in Fig. 7 for the photon-to-proton $T_{1\mathcal{E}}$ TDA for $\xi = 0.1$.

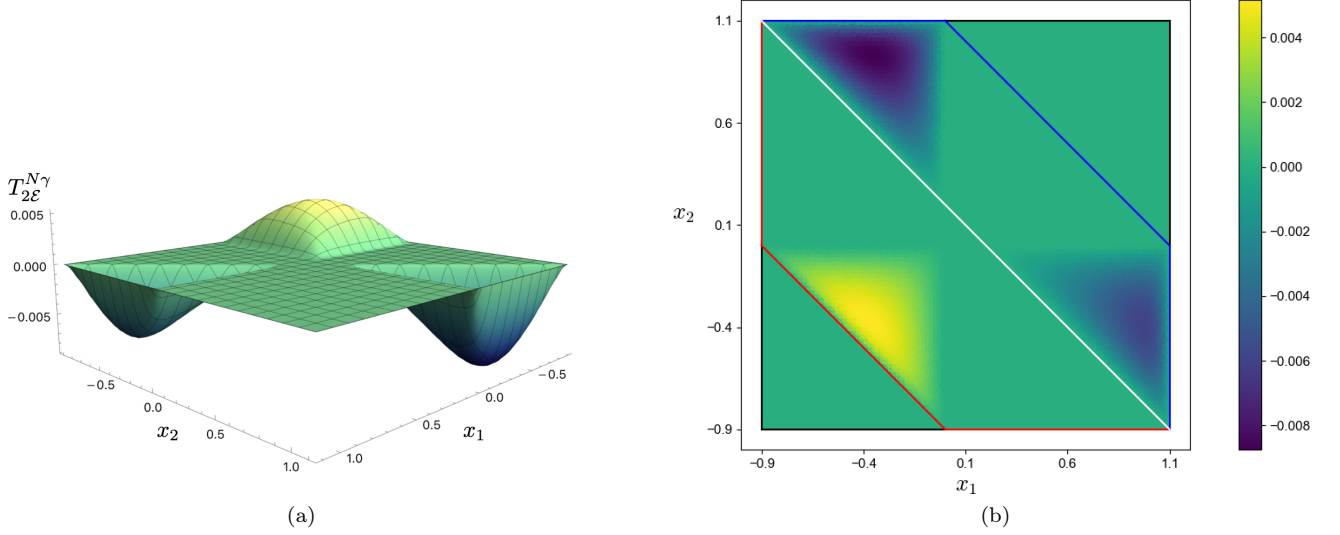


Figure 10. The same as in Fig. 7 for the photon-to-proton $T_{2\mathcal{E}}$ TDA for $\xi = 0.1$.

The Mellin moments of the TDAs are defined as

$$S^{(a,b,c)} = \int dx_1 dx_2 dx_3 \delta(x_1 + x_2 + x_3 - 2\xi) x_1^a x_2^b x_3^c S(x_1, x_2, x_3), \quad (66)$$

where S is one of the TDAs. To give a more quantitative representation of the backward photon-to-proton TDAs, we evaluated the $(0, 0, 0)$ -moments $S^{(0,0,0)}$. The results are given in Tab. VI, alongside the separate contributions from every possible orbital-angular-momentum component of the three-quark system in the proton. The non-admissible terms are denoted with a slash. We already know that the integral of the antisymmetric $A_{1\mathcal{E}}$ should be exactly zero, while it turns out to be negligible for $L_z = -1$ in $T_{1\mathcal{E}}, T_{2\mathcal{E}}$. Since this component only contributes to the helicity amplitude $T_{333}^{\uparrow,-1}$, the only one where the LC helicity changes sign between the photon and the proton, the result seems to suggest that such helicity flip is, on average, highly unlikely. The $L_z = 0, +1$ components give contributions of the same order of magnitude to the moments of $V_{1\mathcal{E}}$, while they dominate with respect to $L_z = -1$ in the case of $T_{1\mathcal{E}}, T_{2\mathcal{E}}$.

	L_z					
	Total	0	+1	-1	+2	
$V_{1\varepsilon}^{(0,0,0)}$	-5.2388(27)	-2.3415(24)	-2.8959(11)	/	/	$\times 10^{-3}$
$A_{1\varepsilon}^{(0,0,0)}$	0	0	0	/	/	
$T_{1\varepsilon}^{(0,0,0)}$	-0.6750(13)	+0.1100(05)	-0.7870(10)	~ 0	/	
$T_{2\varepsilon}^{(0,0,0)}$	-2.2842(18)	-1.4967(07)	-0.7870(10)	~ 0	/	

Table VI. Mellin moments $(0, 0, 0)$ of photon-to-proton TDAs for $\xi = 0.1$. The total results are shown in the second column, while columns 3–5 show the results from the individual partial waves of the proton LFWF. The entries with a slash are forbidden by angular momentum conservation.

IV. CONCLUSIONS

A factorization of the scattering amplitude of TCS in the backward kinematical region has been proposed in Ref. [13]. Analogously to other backward exclusive reactions, the low-energy subprocess that splits the initial nucleon into its parton content is represented by nucleon DAs, while the soft transition from the initial real photon to the final nucleon is encoded in photon-to-nucleon TDAs. A natural framework to study these non-perturbative objects is LFD, where the interacting states can be expanded in the Fock space, and a clear partonic interpretation emerges. Nucleon distribution amplitudes have already been investigated taking advantage of these techniques in Ref. [18]. This work follows in those steps, aiming for a phenomenologically solid model of the photon-to-nucleon TDAs. Currently, there is no formal proof of the factorization for backward TCS, but the hypothesis is supported by the analogy with the well-established case of forward scattering. The analysis of existing data from Jefferson Lab is also in agreement with the outset of factorization through TDAs in the backward region of exclusive reactions involving mesons [44–46].

The study of backward exclusive reactions is a promising subject, hence the request for effective models, also for the planning of experiments at the, currently under construction, Electron-Ion Collider [47]. This work begins the endeavour for modeling the photon-to-nucleon TDAs, focusing on the leading contribution where two light quarks take the place of a light antiquark in the parton configuration of the initial photon, in order to make up the final nucleon. The results exhibit the basic features that are to be expected, and the first Mellin moments have been numerically evaluated, separating the individual contribution from the possible orbital-angular-momentum components of the proton LFWFs. In the future, the same techniques could be used to investigate the other fundamental ways in which the transition can happen, involving higher-order Fock states of the photon and the proton. The scale of the model, about 0.5 GeV, is dictated by the effective description of the nucleon as three constituent valence quarks. Understanding the scale evolution will be key to compare theoretical predictions against the experimental data expected for the near future and work in this direction is in progress.

ACKNOWLEDGMENTS

We thank K. Semenov and B. Pire for useful discussions and for their continuous interest and motivation in pursuing this work.

Appendix A: Conventions for Light-Front Dynamics

The Dirac gamma matrices in the chiral representation are

$$\gamma^0 = \begin{pmatrix} 0_{2 \times 2} & I_{2 \times 2} \\ I_{2 \times 2} & 0_{2 \times 2} \end{pmatrix}, \quad \gamma^j = \begin{pmatrix} 0_{2 \times 2} & -\sigma^j \\ \sigma^j & 0_{2 \times 2} \end{pmatrix}, \quad \gamma^5 = \begin{pmatrix} I_{2 \times 2} & 0_{2 \times 2} \\ 0_{2 \times 2} & -I_{2 \times 2} \end{pmatrix}, \quad (\text{A1})$$

where $j = 1, 2, 3$, $I_{2 \times 2}$ is the 2×2 identity matrix, $0_{2 \times 2}$ is the 2×2 matrix of all zeros, and σ^j are the usual Pauli matrices. The charge conjugation matrix is

$$\mathcal{C} = i\gamma^2\gamma^0 = \begin{pmatrix} -i\sigma^2 & 0 \\ 0 & i\sigma^2 \end{pmatrix}, \quad (\text{A2})$$

and the change of basis matrix to the usual Dirac representation is

$$U = \frac{1}{\sqrt{2}} \begin{pmatrix} I_{2 \times 2} & I_{2 \times 2} \\ I_{2 \times 2} & -I_{2 \times 2} \end{pmatrix}. \quad (\text{A3})$$

We define the following operators on Dirac-spinor space:

$$\Lambda_{\pm} = \frac{1}{2}\gamma^0\gamma^{\pm}, \quad (\text{A4})$$

which have all the properties of a complete set of orthogonal projectors. The projections with Λ_+ are called good or large components, and the projections with Λ_- are called bad or small components. In the chiral representation (A1), they are already in diagonal form:

$$\Lambda_+ = \begin{pmatrix} 1 & 0 & 0 & 0 \\ 0 & 0 & 0 & 0 \\ 0 & 0 & 0 & 0 \\ 0 & 0 & 0 & 1 \end{pmatrix}, \quad \Lambda_- = \begin{pmatrix} 0 & 0 & 0 & 0 \\ 0 & 1 & 0 & 0 \\ 0 & 0 & 1 & 0 \\ 0 & 0 & 0 & 0 \end{pmatrix}. \quad (\text{A5})$$

The LC helicity spinors are

$$u_{\uparrow}^{\text{LC}}(p) = \frac{1}{\sqrt{p^+}} \begin{pmatrix} p^+ \\ p^1 + ip^2 \\ m \\ 0 \end{pmatrix}, \quad u_{\downarrow}^{\text{LC}}(p) = \frac{1}{\sqrt{p^+}} \begin{pmatrix} 0 \\ m \\ -p^1 + ip^2 \\ p^+ \end{pmatrix}, \quad (\text{A6})$$

$$v_{\uparrow}^{\text{LC}}(p) = \frac{1}{\sqrt{p^+}} \begin{pmatrix} 0 \\ -m \\ -p^1 + ip^2 \\ p^+ \end{pmatrix}, \quad v_{\downarrow}^{\text{LC}}(p) = \frac{1}{\sqrt{p^+}} \begin{pmatrix} p^+ \\ p^1 + ip^2 \\ -m \\ 0 \end{pmatrix}. \quad (\text{A7})$$

Therefore, the Dirac adjoints of the good components of the LC spinors are

$$\bar{u}_{\uparrow}(p) = \frac{1}{\sqrt{p^+}} (0 \ 0 \ p^+ \ 0) = \bar{v}_{\downarrow}(p), \quad \bar{u}_{\downarrow}(p) = \frac{1}{\sqrt{p^+}} (0 \ p^+ \ 0 \ 0) = \bar{v}_{\uparrow}(p). \quad (\text{A8})$$

-
- [1] D. Müller, D. Robaschik, B. Geyer, F. M. Dittes, and J. Hořejši, Fortsch. Phys. **42**, 101 (1994), arXiv:hep-ph/9812448.
[2] X.-D. Ji, Phys. Rev. D **55**, 7114 (1997), arXiv:hep-ph/9609381.
[3] A. V. Radyushkin, Phys. Rev. D **56**, 5524 (1997), arXiv:hep-ph/9704207.
[4] K. Goeke, M. V. Polyakov, and M. Vanderhaeghen, Prog. Part. Nucl. Phys. **47**, 401 (2001), arXiv:hep-ph/0106012.
[5] M. Diehl, Physics Reports **388**, 41 (2003), arXiv:hep-ph/0307382v2.
[6] A. V. Belitsky and A. V. Radyushkin, Phys. Rept. **418**, 1 (2005), arXiv:hep-ph/0504030.
[7] S. Boffi and B. Pasquini, Riv. Nuovo Cim. **30**, 387 (2007), arXiv:0711.2625 [hep-ph].
[8] E. R. Berger, M. Diehl, and B. Pire, Eur. Phys. J. C **23**, 675 (2002), arXiv:hep-ph/0110062.
[9] B. Pire, L. Szymanowski, and J. Wagner, Phys. Rev. D **83**, 034009 (2011), arXiv:1101.0555 [hep-ph].
[10] D. Mueller, B. Pire, L. Szymanowski, and J. Wagner, Phys. Rev. D **86**, 031502 (2012), arXiv:1203.4392 [hep-ph].
[11] H. Moutarde, B. Pire, F. Sabatie, L. Szymanowski, and J. Wagner, Phys. Rev. D **87**, 054029 (2013), arXiv:1301.3819 [hep-ph].
[12] B. Pire, K. Semenov-Tian-Shansky, and L. Szymanowski, Phys. Rept. **940**, 1 (2021), arXiv:2103.01079 [hep-ph].
[13] B. Pire, K. M. Semenov-Tian-Shansky, A. A. Shaikhutdinova, and L. Szymanowski, Eur. Phys. J. C **82**, 656 (2022), arXiv:2201.12853 [hep-ph].
[14] J. P. Lansberg, B. Pire, K. Semenov-Tian-Shansky, and L. Szymanowski, Phys. Rev. D **85**, 054021 (2012), arXiv:1112.3570 [hep-ph].

- [15] J. P. Lansberg, B. Pire, K. Semenov-Tian-Shansky, and L. Szymanowski, Phys. Rev. D **86**, 114033 (2012), [Erratum: Phys.Rev.D 87, 059902 (2013)], arXiv:1210.0126 [hep-ph].
- [16] B. Pire, K. Semenov-Tian-Shansky, and L. Szymanowski, Phys. Lett. B **724**, 99 (2013), [Erratum: Phys.Lett.B 764, 335–335 (2017)], arXiv:1304.6298 [hep-ph].
- [17] B. Pire, K. Semenov-Tian-Shansky, and L. Szymanowski, Phys. Rev. D **91**, 094006 (2015), [Erratum: Phys.Rev.D 106, 099901 (2022)], arXiv:1503.02012 [hep-ph].
- [18] B. Pasquini, M. Pincetti, and S. Boffi, Phys. Rev. D **80**, 014017 (2009), arXiv:0905.4018 [hep-ph].
- [19] P. Chatagnon *et al.* (CLAS), Phys. Rev. Lett. **127**, 262501 (2021), arXiv:2108.11746 [hep-ex].
- [20] P. A. M. Dirac, Rev. Mod. Phys. **21**, 392 (1949).
- [21] S. J. Brodsky and G. P. Lepage, Adv. Ser. Direct. High Energy Phys. **5**, 93 (1989).
- [22] S. J. Brodsky, H.-C. Pauli, and S. S. Pinsky, Phys. Rept. **301**, 299 (1998), arXiv:hep-ph/9705477.
- [23] Y. V. Kovchegov and E. Levin, *Quantum Chromodynamics at High Energy*, Vol. 33 (Oxford University Press, 2013).
- [24] S. Boffi, B. Pasquini, and M. Traini, Nucl. Phys. B **649**, 243 (2003), arXiv:hep-ph/0207340.
- [25] S. Boffi, B. Pasquini, and M. Traini, Nucl. Phys. B **680**, 147 (2004), arXiv:hep-ph/0311016.
- [26] B. Pasquini, M. Traini, and S. Boffi, Phys. Rev. D **71**, 034022 (2005), arXiv:hep-ph/0407228.
- [27] B. Pasquini, M. Pincetti, and S. Boffi, Phys. Rev. D **72**, 094029 (2005), arXiv:hep-ph/0510376.
- [28] B. Pasquini and S. Boffi, Phys. Rev. D **73**, 094001 (2006), arXiv:hep-ph/0601177.
- [29] B. Pasquini and S. Boffi, Phys. Lett. B **653**, 23 (2007), arXiv:0705.4345 [hep-ph].
- [30] V. N. Gribov and L. N. Lipatov, Sov. J. Nucl. Phys. **15**, 438 (1972).
- [31] G. Altarelli and G. Parisi, Nucl. Phys. B **126**, 298 (1977).
- [32] Y. L. Dokshitzer, Sov. Phys. JETP **46**, 641 (1977).
- [33] A. V. Efremov and A. V. Radyushkin, Theor. Math. Phys. **42**, 97 (1980).
- [34] A. V. Efremov and A. V. Radyushkin, Phys. Lett. B **94**, 245 (1980).
- [35] G. P. Lepage and S. J. Brodsky, Phys. Lett. B **87**, 359 (1979).
- [36] G. P. Lepage and S. J. Brodsky, Phys. Rev. Lett. **43**, 545 (1979), [Erratum: Phys.Rev.Lett. 43, 1625–1626 (1979)].
- [37] G. P. Lepage and S. J. Brodsky, Phys. Rev. D **22**, 2157 (1980).
- [38] B. D. Keister and W. N. Polyzou, Adv. Nucl. Phys. **20**, 225 (1991).
- [39] B. Pasquini, S. Cazzaniga, and S. Boffi, Phys. Rev. D **78**, 034025 (2008), arXiv:0806.2298 [hep-ph].
- [40] B. Pasquini and F. Yuan, Phys. Rev. D **81**, 114013 (2010), arXiv:1001.5398 [hep-ph].
- [41] S. Boffi, A. V. Efremov, B. Pasquini, and P. Schweitzer, Phys. Rev. D **79**, 094012 (2009), arXiv:0903.1271 [hep-ph].
- [42] B. Pasquini and P. Schweitzer, Phys. Rev. D **83**, 114044 (2011), arXiv:1103.5977 [hep-ph].
- [43] F. Schlumpf, J. Phys. G **20**, 237 (1994), arXiv:hep-ph/9301233.
- [44] K. Park *et al.* (CLAS), Phys. Lett. B **780**, 340 (2018), arXiv:1711.08486 [nucl-ex].
- [45] W. B. Li *et al.* (Jefferson Lab F π), Phys. Rev. Lett. **123**, 182501 (2019), arXiv:1910.00464 [nucl-ex].
- [46] S. Diehl *et al.* (CLAS), Phys. Rev. Lett. **125**, 182001 (2020), arXiv:2007.15677 [nucl-ex].
- [47] R. Abdul Khalek *et al.*, Nucl. Phys. A **1026**, 122447 (2022), arXiv:2103.05419 [physics.ins-det].

Five-dimensional collective Hamiltonian with improved inertial functions

Kouhei Washiyama,^{1,2,*} Nobuo Hinohara,^{1,3} and Takashi Nakatsukasa^{1,3,4}

¹Center for Computational Sciences, University of Tsukuba, Tsukuba 305-8577, Japan

²Research Center for Superheavy Elements, Kyushu University, Fukuoka 819-0395, Japan

³Faculty of Pure and Applied Sciences, University of Tsukuba, Tsukuba 305-8571, Japan

⁴RIKEN Nishina Center, Wako 351-0198, Japan

(Dated: March 4, 2024)

Background: To describe shape fluctuations associated with large-amplitude collective motion in the quadrupole degrees of freedom, the five-dimensional collective Hamiltonian (5DCH) has been widely used. The inertial functions in the 5DCH are microscopically calculated with the energy density functional (EDF) theory employing the cranking formula. However, since the cranking formula ignores dynamical residual effects, it is known to fail to reproduce the correct inertial functions, for instance, the total mass for the translational motion.

Purpose: We aim to resolve problems of the insufficient description of the inertial functions in the 5DCH. We provide a practical method to include the dynamical residual effects in the inertial functions that depend on the quadrupole deformation parameters β and γ .

Methods: We use the local quasiparticle random-phase approximation (LQRPA) based on the constrained Hartree-Fock-Bogoliubov states in the β - γ plane with the Skyrme EDF. The finite-amplitude method is used for efficient computations of the LQRPA.

Results: The inertial functions evaluated with the LQRPA significantly increase from the ones with the cranking formula due to the dynamical residual effects. This increase also shows a strong β - γ dependence. We show an application of the present method to a transitional nucleus ^{110}Pd . The low-lying positive-parity spectra are well reproduced with the LQRPA inertial functions.

Conclusions: We clarify the importance of the dynamical residual effects in the inertial functions of the 5DCH for the description of the low-lying spectra. The 5DCH with the improved inertial functions provides a reliable and efficient description of low-lying spectra in nuclei associated with the quadrupole shape fluctuation.

Introduction. A proper and feasible description of the shape dynamics in the ground and the excited states is one of the important subjects in nuclear physics. Observations of spectroscopic properties in nuclei suggest the existence of shape fluctuations and shape coexistence phenomena in low-lying states in nuclei, particularly in the so-called transitional regions from spherical to deformed shapes in the nuclear chart [1].

The self-consistent nuclear energy density functional (EDF) theory has often been employed to describe ground-state properties of nuclei [2, 3]. To describe shape fluctuations and shape coexistence phenomena associated with large-amplitude collective motion, it is necessary to use beyond-mean-field methods. The generator-coordinate method (GCM) with the quadrupole deformation parameters β and γ as generator coordinates [4–9] has been developed and shown the importance of including the triaxial degree of freedom, γ . Recently, the standard GCM was extended to construct the basis states stochastically [10, 11] and variationally [12]. Although the GCM is a fully quantum theory, in practice, we need to combine the GCM with the projection method to recover the broken symmetries. The GCM with the projection method requires a large amount of numerical computations. In addition, there remain many unsolved issues with realistic EDFs [3]. For instance, the discontinuities

and divergences are caused by the fractional powers of the density dependence in EDFs [13, 14].

As an alternative approach to the GCM, the five-dimensional collective Hamiltonian (5DCH) method [15, 16] with the intrinsic quadrupole deformation parameters (β, γ) and the three Euler angles has been extensively used based on the EDF [16–20]. In most of the EDF-based 5DCH studies, the inertial functions in the vibrational and rotational kinetic energies are calculated according to the formula in the adiabatic perturbation [21], which is identical to the well-known Inglis-Belyaev (IB) formula for the rotational moment of inertia [22, 23]. The vibrational masses are further approximated by the so-called perturbative cranking formula [24]. The cranking formula ignores variation of the self-consistent potential induced by the collective motion, known as the dynamical residual effects, thus, giving an insufficient description of the inertial functions [25]. In particular, the absence of the time-odd terms of the dynamical mean field leads to the violation of the Galilean symmetry and is known to produce the wrong translational mass [26]. Despite such drawbacks, the cranking formula has been widely used [16–20], because the full inclusion of the dynamical residual effects in the inertial functions requires a huge computational cost. Some recent 5DCH studies [20, 27] evaluate the rotational moments of inertia within the cranked Hartree-Fock-Bogoliubov (HFB) framework that are equivalent to the Thouless-Valatin inertia [28] to include the dynamical residual effects in the rotational kinetic energy. In many of the former studies, a phe-

* E-mail: washiyama@nucl.ph.tsukuba.ac.jp

nomenological enhancement factor of 1.2–1.4 is adopted for the inertial functions evaluated with the cranking formula.

To properly include the dynamical residual effects in the inertial functions, the constrained HFB (CHFb) plus local quasiparticle random-phase approximation (LQRPA) was proposed in Ref. [29]. Practical applications of the CHFb + LQRPA in the β - γ plane were performed only with the semi-realistic pairing-plus-quadrupole (P + Q) Hamiltonian [29–33]. Note that, for axially symmetric shapes without the γ degree of freedom, there have been a few attempts with the Skyrme EDF [34, 35]. These studies showed the importance of the dynamical residual effects in the inertial functions.

Our goal is to construct the 5DCH for the Skyrme EDF with the inertial functions including the dynamical residual effects. To overcome the numerical difficulties, we employ the finite-amplitude method (FAM) [36] that gives the response to an external one-body field. The result of the FAM is equivalent to that of the QRPA linear-response calculation, while the computational cost of the FAM is significantly lower than that of the QRPA. The FAM has been applied to various objectives [37–52]. The formulation with the FAM for the inertia associated with zero-energy modes was given in Ref. [46], and applied to the inertia for pairing rotations [46, 47] and that for spatial rotations [53, 54]. The present study is an extension of the methods developed in Refs. [35, 46] to the inertial functions in the 5DCH with β and γ .

5DCH method. The five-dimensional quadrupole collective Hamiltonian is given as [15]

$$H_{\text{coll}} = T_{\text{vib}} + T_{\text{rot}} + V(\beta, \gamma), \quad (1)$$

$$T_{\text{vib}} = \frac{1}{2} D_{\beta\beta}(\beta, \gamma) \dot{\beta}^2 + D_{\beta\gamma}(\beta, \gamma) \dot{\beta} \dot{\gamma} + \frac{1}{2} D_{\gamma\gamma}(\beta, \gamma) \dot{\gamma}^2, \quad (2)$$

$$T_{\text{rot}} = \frac{1}{2} \sum_{k=1}^3 \mathcal{J}_k(\beta, \gamma) (\omega_k^{\text{rot}})^2, \quad (3)$$

where the collective potential V and all the inertial functions appearing in the vibrational T_{vib} and rotational T_{rot} kinetic energies depend on β and γ . The inertial functions $D_{\beta\beta}$, $D_{\beta\gamma}$, $D_{\gamma\gamma}$, and $\mathcal{J}_k(\beta, \gamma) = 4\beta^2 D_k(\beta, \gamma) \sin^2(\gamma - 2\pi k/3)$ denote the vibrational masses and the rotational moments of inertia, respectively. ω_k^{rot} are the rotational angular velocities in the body-fixed frame. We use the Pauli prescription to quantize the Hamiltonian (1) and obtain the excitation energies and collective wave functions. More details of the 5DCH method can be found in Refs. [16, 29, 55].

The collective potential is given by the energy at the state $|\phi(\beta, \gamma)\rangle$ obtained by solving the CHFb equation with constraints on the mass quadrupole operators $\hat{Q}_{20} = \sum_{i=1}^A r_i^2 Y_{20}(\hat{r}_i)$ and $\hat{Q}_{22} = \sum_{i=1}^A r_i^2 [Y_{22}(\hat{r}_i) + Y_{2-2}(\hat{r}_i)]/\sqrt{2}$. The quadrupole deformation parameters are written as $\beta \cos \gamma = \eta Q_{20} = \eta \langle \phi(\beta, \gamma) | \hat{Q}_{20} | \phi(\beta, \gamma) \rangle$ and $\beta \sin \gamma = \eta Q_{22} = \eta \langle \phi(\beta, \gamma) | \hat{Q}_{22} | \phi(\beta, \gamma) \rangle$ with $\eta =$

$4\pi/(3R^2 A)$ and $R = 1.2A^{1/3}$ fm of the mass number A .

Inertial functions. The CHFb+LQRPA inertial functions in the β - γ plane are given in Ref. [29]. Although the LQRPA are defined at each CHFb state $|\phi(\beta, \gamma)\rangle$, for simplicity, we abbreviate $|\phi(\beta, \gamma)\rangle$ as $|\phi\rangle$ in the following.

We employ the FAM [36] for a solution of the LQRPA equation for the Skyrme EDF, which provides the X and Y amplitudes induced by an external field \hat{F} at a given frequency ω . Following Refs. [35, 46], the relation between the amplitudes (X, Y) and the local generators (\hat{Q}_i, \hat{P}_i) for the i th normal mode with the eigenfrequency Ω_i is given in their two-quasiparticle (2qp) components as

$$X_{\mu\nu}(\omega; \hat{F}) = \sum_i \frac{1}{\omega^2 - \Omega_i^2} (P_{\mu\nu}^i + i\omega Q_{\mu\nu}^i) p_i(\hat{F}), \quad (4a)$$

$$Y_{\mu\nu}(\omega; \hat{F}) = \sum_i \frac{1}{\omega^2 - \Omega_i^2} (-P_{\mu\nu}^{i*} - i\omega Q_{\mu\nu}^{i*}) p_i(\hat{F}), \quad (4b)$$

where we fix the normalization of (\hat{Q}_i, \hat{P}_i) to make the local inertial mass $M_i = 1$ [35]. Here, \hat{F} , \hat{Q}_i , and \hat{P}_i are all Hermitian. Their 2qp components $F_{\mu\nu}$ and $Q_{\mu\nu}^i$ are chosen to be real, while $P_{\mu\nu}^i$ are pure imaginary. In Eq. (4), the pure imaginary quantities $p_i(\hat{F})$ are given by

$$p_i(\hat{F}) \equiv \langle \phi | [\hat{P}_i, \hat{F}] | \phi \rangle = \sum_{\mu < \nu} (P_{\mu\nu}^{i*} - P_{\mu\nu}^i) F_{\mu\nu}. \quad (5)$$

The FAM response function, $S_{\hat{F}', \hat{F}}(\omega)$, for Hermitian and real operators, \hat{F} and \hat{F}' , is defined as

$$S_{\hat{F}', \hat{F}}(\omega) \equiv \sum_{\mu < \nu} \left[F_{\mu\nu}'^{20*} X_{\mu\nu}(\omega; \hat{F}) + F_{\mu\nu}^{02*} Y_{\mu\nu}(\omega; \hat{F}) \right] \quad (6)$$

$$= \sum_i \frac{1}{\omega^2 - \Omega_i^2} p_i(\hat{F}) p_i^*(\hat{F}'). \quad (7)$$

Then, a contour integration of Eq. (7) with a contour C_i that encloses the pole $\omega = \Omega_i$ in the complex energy plane,

$$\frac{1}{2\pi i} \oint_{C_i} \omega S_{\hat{F}', \hat{F}}(\omega) d\omega = \frac{1}{2} p_i(\hat{F}) p_i^*(\hat{F}') \quad (8)$$

gives $p_i(\hat{Q}_{20})$ and $p_i(\hat{Q}_{22})$ by proper choices of the operators F and F' .

We select two LQRPA normal modes for the collective coordinates q_i ($i = 1, 2$). The prescription for this selection is given in Ref. [29] (see also *Numerical procedure* below). The kinetic energy of the LQRPA normal modes in the diagonal form is rewritten in terms of the collective variables Q_{2m} ($m = 0, 2$) as

$$T_{\text{vib}} = \frac{1}{2} \sum_{i=1,2} \dot{q}_i^2 = \frac{1}{2} \sum_{m,n=0,2} \mathcal{M}_{mn} \dot{Q}_{2m} \dot{Q}_{2n}, \quad (9)$$

where the vibrational inertia tensor \mathcal{M}_{mn} is obtained by

$$\mathcal{M}_{mn} = \sum_{i=1,2} \frac{\partial q_i}{\partial Q_{2m}} \frac{\partial q_i}{\partial Q_{2n}}. \quad (10)$$

The inverses of these partial derivatives are evaluated as

$$\begin{aligned} \frac{\partial Q_{2m}}{\partial q_i} &= \frac{\partial}{\partial q_i} \langle \phi | \hat{Q}_{2m} | \phi \rangle \\ &= \langle \phi | [\hat{Q}_{2m}, \frac{1}{i} \hat{P}_i] | \phi \rangle = ip_i(\hat{Q}_{2m}). \end{aligned} \quad (11)$$

Thus, the inertia tensor (10) is obtained by the FAM calculation of $p_i(\hat{Q}_{2m})$ in Eq. (7) through Eq. (11).

With the relation between (β, γ) and (Q_{20}, Q_{22}) , the vibrational masses $D_{\beta\beta}$, $D_{\beta\gamma}$, and $D_{\gamma\gamma}$ are obtained from \mathcal{M}_{00} , \mathcal{M}_{02} , and \mathcal{M}_{22} in Eq. (10) [29]. Note that the formulation given above can be extended to cases with more than two collective variables.

For the rotational moments of inertia, the Thouless-Valatin rotational moment of inertia \mathcal{J}_k at the CHFB state $|\phi\rangle$ is evaluated from the FAM strength function at zero energy as $S_{\hat{J}_k, \hat{J}_k}(\omega = 0) = -\mathcal{J}_k$, where \hat{J}_k is the angular momentum operator [46].

Numerical procedure. We solve the CHFB + LQRPA equations following Ref. [35]. We calculate the vibrational masses with the FAM-LQRPA in two steps. First, to find peaks in the strength distribution, we solve the FAM equations with the external fields \hat{Q}_{20} and \hat{Q}_{22} at $0 \leq |\omega| \leq 4$ MeV, in both real and imaginary ω with a smearing width of 0.01 MeV. The peak position should correspond to the LQRPA poles Ω_i . Second, for each pole, we perform the contour integration (8) with a circle of radius 0.02 MeV discretized to eight points. Then, we select the two most collective LQRPA modes following the prescription [29] that a pair of LQRPA solutions that give the minimum value of $W = (D_{\beta\beta}D_{\gamma\gamma} - D_{\beta\gamma}^2)/\beta^2$ is selected from many LQRPA solutions. In practice, we select several peaks with large strengths and calculate Eq. (8) with all the combinations from the selected peaks to find the minimum W .

We solve the CHFB equations with the two-basis method [56, 57] in the three-dimensional Cartesian mesh with a $(13.2 \text{ fm})^3$ box with a mesh size of 0.8 fm. The reflection symmetries about $x = 0$, $y = 0$, and $z = 0$ planes lead to the single-particle states as eigenstates of the parity, z signature, and y -time simplex [58–61]. The single-particle basis consists of 1400 neutron and 1120 proton HF-basis states, which approximately correspond to the maximum quasiparticle energy of 60 MeV for ^{110}Pd and give a good convergence in the CHFB and LQRPA calculations [35]. We employ the SkM* EDF [62] and the contact volume-type pairing with a pairing window of 20 MeV above and below the Fermi level as described in Ref. [60]. The pairing strengths are adjusted to reproduce the empirical neutron and proton gaps in ^{106}Pd . We use an equilateral triangular mesh of $\Delta\beta \approx 0.05$ in $0 < \beta < 0.6$ and $0^\circ < \gamma < 60^\circ$ in the β - γ plane, consisting of 93 deformation points.

The numerical calculations of the FAM are performed with hybrid parallelization (MPI + OpenMP). For the vibrational masses, it takes about 480 core hours to select several peaks in the strength distributions and

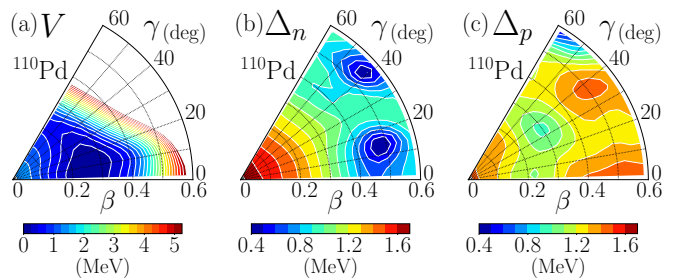


FIG. 1. Potential energy surface (a) and pairing gaps for neutrons (b) and protons (c) in the β - γ plane in ^{110}Pd .

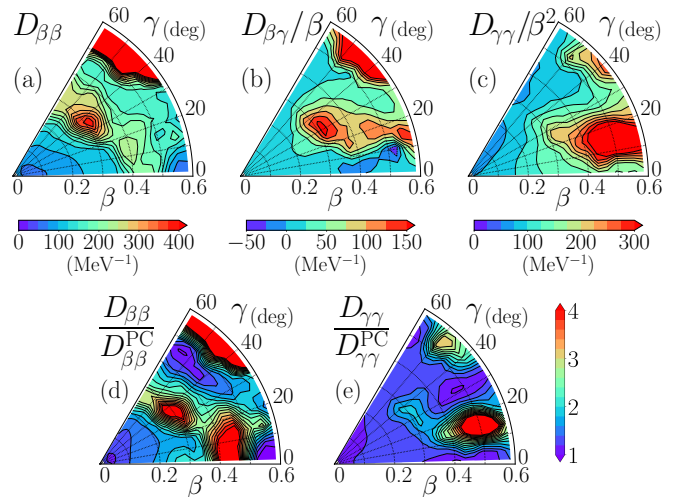


FIG. 2. Vibrational masses of the LQRPA in ^{110}Pd : (a) $D_{\beta\beta}$, (b) $D_{\beta\gamma}/\beta$, and (c) $D_{\gamma\gamma}/\beta^2$. The ratio of the LQRPA to the PC vibrational masses: (d) $D_{\beta\beta}/D_{\beta\beta}^{\text{PC}}$ and (e) $D_{\gamma\gamma}/D_{\gamma\gamma}^{\text{PC}}$.

150 core hours for a contour integration for each deformation point. For the three rotational moments of inertia, it takes about 3 core hours for each deformation point. Computing the LQRPA inertial functions is feasible in currently available computational resources.

Results and discussions. Figure 1(a) shows the calculated potential energy surface (PES) measured from the energy minimum in the β - γ plane in ^{110}Pd . The shallow energy minimum is found at $\beta \approx 0.25$ and $\gamma \approx 0^\circ$. The PES is flat in both the β and γ directions with $V(\beta, \gamma) < 1$ MeV in a wide region of $0.1 < \beta < 0.4$ and $0^\circ < \gamma < 60^\circ$. Figures 1(b) and 1(c) show the pairing gaps for neutrons Δ_n and protons Δ_p , respectively, in ^{110}Pd . The pairing gap in neutrons has local minima at $\beta \approx 0.5, \gamma \approx 15^\circ$ and $\beta \approx 0.6, \gamma \approx 40^\circ$.

Figure 2 shows the vibrational masses $D_{\beta\beta}$ (a), $D_{\beta\gamma}/\beta$ (b), and $D_{\gamma\gamma}/\beta^2$ (c) calculated with the CHFB + LQRPA in the β - γ plane for ^{110}Pd . A remarkable feature is a strong variation of the vibrational masses in the β - γ plane. In particular, the vibrational masses become locally large at around $\beta = 0.5$ and $\gamma = 15^\circ$, $\beta = 0.3$ and $\gamma = 40^\circ$, and $\beta > 0.4$ and $\gamma > 40^\circ$, at which the pairing gaps in neutrons and protons become locally small. A

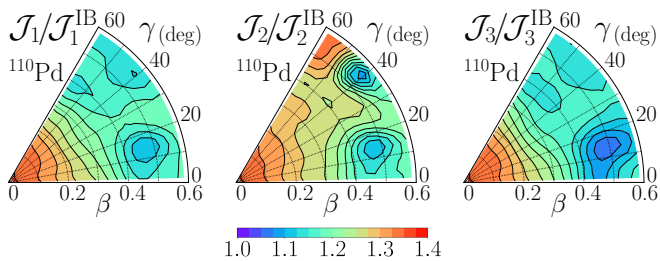


FIG. 3. Ratio of the LQRPA moments of inertia to the Inglis-Beljaev (IB) ones ($\mathcal{J}_k/\mathcal{J}_k^{\text{IB}}$) in the β - γ plane in ^{110}Pd .

correlation between the vibrational mass and pairing gap was also observed in the collective inertia in spontaneous fission [35].

It is of significant importance to compare the vibrational masses obtained by the LQRPA with those obtained by the perturbative cranking (PC) formula [24], denoted as $D_{\beta\beta}^{\text{PC}}$, $D_{\beta\gamma}^{\text{PC}}$, and $D_{\gamma\gamma}^{\text{PC}}$. Those of the PC formula have been extensively employed in the EDF-based 5DCH studies [17, 19, 20]. Figures 2(d) and (e) show the ratio of the LQRPA vibrational mass to the PC one. At a region near the minimum of the PES ($\beta \approx 0.25$ and $\gamma \approx 0^\circ$), the ratio is 1.0–2.0. However, the ratio exceeds 3.0 at the regions at which $D_{\beta\beta}$ and $D_{\gamma\gamma}$ take large values. Furthermore, the ratio shows a strong β - γ dependence and different properties in $D_{\beta\beta}$ and $D_{\gamma\gamma}$. Former EDF-based 5DCH studies have often employed the cranking inertial functions multiplied by a constant enhancement factor to include the dynamical residual effects. However, our findings clearly show that the use of the constant enhancement factor cannot be justified in the description of the vibrational masses. Similar enhancement is observed in the former LQRPA studies with the P + Q model [29, 30, 32] and in those with the axial symmetric restriction [34, 35].

Figure 3 shows the ratios of the LQRPA to the IB cranking moments of inertia $\mathcal{J}_k^{\text{IB}}$ [22, 23] in the β - γ plane for ^{110}Pd . The ratios are in a range of 1.0–1.4 and increase as β decreases; the dynamical residual effects become larger toward the spherical shape. The ratios become small where the pairing gap is small, which is opposite to the case of the vibrational masses. The enhancement is less pronounced than that in the vibrational masses; this indicates the larger dynamical residual effects in the vibrational masses than in the moments of inertia. This is consistent with the LQRPA studies with the P + Q model [29, 30, 32].

Figure 4 shows excitation spectra of the 5DCH for positive-parity I_α^+ states with I being the total angular momentum and α distinguishing the states with the same I and $B(E2)$ values in Weisskopf units in ^{110}Pd . Those of the cranking inertial functions indicate the results obtained with the PC vibrational masses and IB moments of inertia. In the spectra, we show the states with $I \leq 8$ and the excitation energies $E < 2.6$ MeV and the $B(E2)$ values of all the intraband transitions and of the inter-

band ones whose experimental data are available. It is clearly seen that the excitation energies calculated with the LQRPA inertial functions are lower than those calculated with the cranking ones. The enhancement of the LQRPA inertial functions lowers the ground-state rotational energies as well as the excited band-head energies. The low-lying spectra of the LQRPA are in good agreement with the experimental data, showing a clear advantage over those with the cranking inertial functions. However, some discrepancies from the experimental spectra remain particularly at excited bands. For instance, we overestimate the level spacing between 0^+ and 2^+ for the 0_2^+ and the 0_3^+ bands.

The $B(E2)$ values in the ground-state rotational band and $B(E2; 0_2^+ \rightarrow 2_1^+)$ and $B(E2; 2_2^+ \rightarrow 2_1^+)$ agree well with the experimental ones. The $B(E2; 2_3^+ \rightarrow 0_2^+)$ value with the LQRPA underestimates the experimental data, which is related to the overestimation of the level spacing of the 0_2^+ and the 2_3^+ bands. Overall, the dynamical residual effects lead to a better agreement in the property of the low-lying spectra. In contrast to the excitation energies, the $B(E2)$ values calculated with the LQRPA and the cranking inertial functions are similar to each other. It may suggest that the contribution of the dynamical residual effects is more important for the energy properties than for the wave functions, although it is dangerous to generalize the results for other nuclei.

Finally, we discuss the property of shape fluctuations in the low-lying spectra. Figure 5 shows the vibrational wave functions of I_α^+ states as $|\Phi_{\alpha I}(\beta, \gamma)|^2 \equiv \sum_K |\Phi_{\alpha IK}(\beta, \gamma)|^2$ with K being the z component of I in the body-fixed frame. We multiply the wave functions by $\beta^4 \sqrt{W(\beta, \gamma)R(\beta, \gamma)}$ with $W = (D_{\beta\beta}D_{\gamma\gamma} - D_{\beta\gamma}^2)/\beta^2$ and $R = D_1D_2D_3$ from the volume element in the normalization of the vibrational wave functions. The 0_1^+ wave function has a broad peak around $\beta \approx 0.3$, $\gamma \approx 0^\circ$, which is close to the minimum of the PES, and spreads over along both the β and γ directions. This shows that the ground state has a large-amplitude shape fluctuation in the β - γ plane. The 2_1^+ state shows a similar structure but is more localized around $\beta \approx 0.3$, $\gamma \approx 0^\circ$ than the 0_1^+ state is. The 2_2^+ wave function has a broad peak at a triaxial shape $\beta \approx 0.3$ and $\gamma \approx 30^\circ$ and spreads over along the γ direction. The 4_2^+ wave function has a feature similar to the 2_2^+ one, which indicates that the 4_2^+ state is a member of the 2_2^+ band and is localized more in the prolate side. The 0_2^+ and 2_3^+ wave functions show a feature of the β vibration, which has a node along the β direction. However, the component at around $\beta \approx 0.2$ spreads along the γ direction. This reflects a γ -soft character. These collective wave functions clearly show the importance of including the triaxial degree of freedom in the 5DCH for a transitional nucleus ^{110}Pd .

Summary. We have developed a method of calculating the inertial functions of the 5DCH, the vibrational masses and the rotational moments of inertia, by the LQRPA with the Skyrme EDF in the β - γ plane. The method can take into account the time-odd mean fields

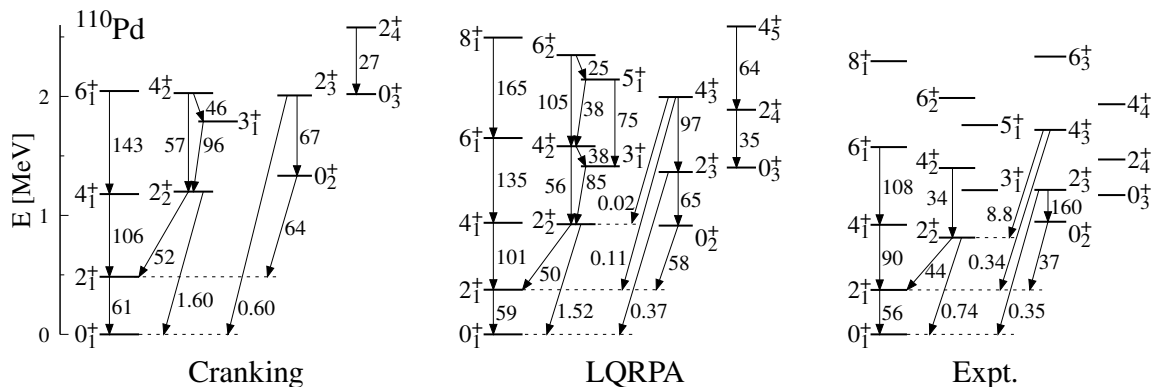


FIG. 4. Low-lying excitation spectra and $B(E2)$ values in Weisskopf units in ^{110}Pd obtained with the cranking inertial functions (left), with the LQRPA ones (middle), compared with the experimental data (right) [63]. See text for details.

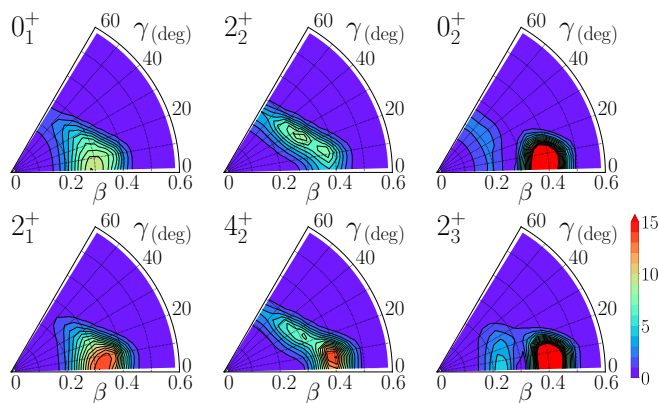


FIG. 5. Vibrational wavefunctions $|\Phi_{\alpha I}(\beta, \gamma)|^2$ of I_{α}^{+} states multiplied by $\beta^4 \sqrt{W(\beta, \gamma)R(\beta, \gamma)}$ in ^{110}Pd .

as the dynamical residual effects in the inertial functions. We constructed the 5DCH with the LQRPA inertial functions and described low-lying states in a transitional nucleus ^{110}Pd . The dynamical residual effects increase both the vibrational masses and rotational moments of inertia, compared with those within the cranking formula. This enhancement strongly depends on both β and γ , which indicates an insufficient treatment of the constant

enhancement factor to the cranking inertial functions employed in former EDF-based 5DCH studies. A good agreement with the experimental data is achieved for low-lying spectra. The vibrational wave functions in the low-lying states show significant shape fluctuations in the β - γ plane.

The present study shows the feasibility of performing computations of the LQRPA for the inertial functions with the present computational resources. However, systematic calculations of the 5DCH method across the nuclear chart will need huge computational costs. Computational costs are expected to be further reduced by using a recent development of the reduced basis method for the FAM [64].

Acknowledgments. The authors thank K. Yaoita for providing his numerical code for solving the collective Schrödinger equation. This work was supported in part by the JSPS KAKENHI (Grant No. JP19KK0343, No. JP20K03964, No. JP22H04569, and No. JP23H01167). Numerical calculations were performed using computational resources of Wisteria/BDEC-01 Odyssey (the University of Tokyo), provided by the Multidisciplinary Cooperative Research Program in the Center for Computational Sciences, University of Tsukuba.

-
- [1] K. Heyde and J. L. Wood, Shape coexistence in atomic nuclei, *Rev. Mod. Phys.* **83**, 1467 (2011).
 - [2] M. Bender, P.-H. Heenen, and P.-G. Reinhard, Self-consistent mean-field models for nuclear structure, *Rev. Mod. Phys.* **75**, 121 (2003).
 - [3] T. Nakatsukasa, K. Matsuyanagi, M. Matsuo, and K. Yabana, Time-dependent density-functional description of nuclear dynamics, *Rev. Mod. Phys.* **88**, 045004 (2016).
 - [4] M. Bender and P.-H. Heenen, Configuration mixing of angular-momentum and particle-number projected triaxial Hartree-Fock-Bogoliubov states using the Skyrme energy density functional, *Phys. Rev. C* **78**, 024309 (2008).
 - [5] J. M. Yao, J. Meng, P. Ring, and D. Vretenar, Configuration mixing of angular-momentum-projected triaxial relativistic mean-field wave functions, *Phys. Rev. C* **81**, 044311 (2010).
 - [6] T. R. Rodríguez and J. L. Egido, Triaxial angular momentum projection and configuration mixing calculations with the Gogny force, *Phys. Rev. C* **81**, 064323 (2010).
 - [7] J. M. Yao, K. Hagino, Z. P. Li, J. Meng, and P. Ring, Microscopic benchmark study of triaxiality in low-lying states of ^{76}Kr , *Phys. Rev. C* **89**, 054306 (2014).
 - [8] M. Kimura, R. Yoshida, and M. Isaka, Excitation and structure change of ^{24}Mg . I: -Triaxial deformed mean

- field in low-lying states–, *Prog. Theor. Phys.* **127**, 287 (2012).
- [9] Y. Suzuki and M. Kimura, Triaxial deformation and the disappearance of the $N = 28$ shell gap, *Phys. Rev. C* **104**, 024327 (2021).
- [10] S. Shinohara, H. Ohta, T. Nakatsukasa, and K. Yabana, Configuration mixing calculation for complete low-lying spectra with a mean-field Hamiltonian, *Phys. Rev. C* **74**, 054315 (2006).
- [11] Y. Fukuoka, S. Shinohara, Y. Funaki, T. Nakatsukasa, and K. Yabana, Deformation and cluster structures in ^{12}C studied with configuration mixing using Skyrme interactions, *Phys. Rev. C* **88**, 014321 (2013).
- [12] M. Matsumoto, Y. Tanimura, and K. Hagino, Extension of the generator coordinate method with basis optimization, *Phys. Rev. C* **108**, L051302 (2023).
- [13] M. Anguiano, J. L. Egido, and L. M. Robledo, Particle number projection with effective forces, *Nucl. Phys. A* **696**, 467 (2001).
- [14] J. Dobaczewski, M. V. Stoitsov, W. Nazarewicz, and P.-G. Reinhard, Particle-number projection and the density functional theory, *Phys. Rev. C* **76**, 054315 (2007).
- [15] A. Bohr and B. R. Mottelson, *Nuclear Structure* (Benjamin, New York, 1975) Vol. II.
- [16] L. Próchniak and S. G. Rohoziński, Quadrupole collective states within the Bohr collective Hamiltonian, *J. Phys. G* **36**, 123101 (2009).
- [17] J. Libert, M. Girod, and J.-P. Delaroche, Microscopic descriptions of superdeformed bands with the Gogny force: Configuration mixing calculations in the $A \sim 190$ mass region, *Phys. Rev. C* **60**, 054301 (1999).
- [18] L. Próchniak, P. Quentin, D. Samsen, and J. Libert, A self-consistent approach to the quadrupole dynamics of medium heavy nuclei, *Nucl. Phys. A* **730**, 59 (2004).
- [19] T. Nikšić, Z. P. Li, D. Vretenar, L. Próchniak, J. Meng, and P. Ring, Beyond the relativistic mean-field approximation. III. Collective Hamiltonian in five dimensions, *Phys. Rev. C* **79**, 034303 (2009).
- [20] J.-P. Delaroche, M. Girod, J. Libert, H. Goutte, S. Hilaire, S. Péru, N. Pillet, and G. F. Bertsch, Structure of even-even nuclei using a mapped collective Hamiltonian and the DIS Gogny interaction, *Phys. Rev. C* **81**, 014303 (2010).
- [21] P. Ring and P. Schuck, *The Nuclear Many-Body Problem* (Springer-Verlag, New York, 1980).
- [22] D. R. Inglis, Nuclear moments of inertia due to nucleon motion in a rotating well, *Phys. Rev.* **103**, 1786 (1956).
- [23] S. T. Beliaev, Concerning the calculation of the nuclear moment of inertia, *Nucl. Phys.* **24**, 322 (1961).
- [24] M. Girod and B. Grammaticos, The zero-point energy correction and its effect on nuclear dynamics, *Nucl. Phys. A* **330**, 40 (1979).
- [25] J. Dobaczewski and J. Skalski, The quadrupole vibrational inertial function in the adiabatic time-dependent Hartree-Fock-Bogolyubov approximation, *Nucl. Phys. A* **369**, 123 (1981).
- [26] K. Wen and T. Nakatsukasa, Microscopic collective inertial masses for nuclear reaction in the presence of nucleonic effective mass, *Phys. Rev. C* **105**, 034603 (2022).
- [27] J.-P. Delaroche, J. Libert, M. Girod, I. Deloncle, and M. Dupuis, Investigations of electric monopole transitions in medium-mass to heavy nuclei: Beyond mean field calculations with the Gogny force, *Phys. Rev. C* **109**, 014320 (2024).
- [28] D. J. Thouless and J. G. Valatin, Time-dependent Hartree-Fock equations and rotational states of nuclei, *Nucl. Phys.* **31**, 211 (1962).
- [29] N. Hinohara, K. Sato, T. Nakatsukasa, M. Matsuo, and K. Matsuyanagi, Microscopic description of large-amplitude shape-mixing dynamics with inertial functions derived in local quasiparticle random-phase approximation, *Phys. Rev. C* **82**, 064313 (2010).
- [30] K. Sato and N. Hinohara, Shape mixing dynamics in the low-lying states of proton-rich Kr isotopes, *Nucl. Phys. A* **849**, 53 (2011).
- [31] N. Hinohara, K. Sato, K. Yoshida, T. Nakatsukasa, M. Matsuo, and K. Matsuyanagi, Shape fluctuations in the ground and excited 0^+ states of $^{30,32,34}\text{Mg}$, *Phys. Rev. C* **84**, 061302(R) (2011).
- [32] N. Hinohara, Z. P. Li, T. Nakatsukasa, T. Nikšić, and D. Vretenar, Effect of time-odd mean fields on inertial parameters of the quadrupole collective Hamiltonian, *Phys. Rev. C* **85**, 024323 (2012).
- [33] K. Sato, N. Hinohara, K. Yoshida, T. Nakatsukasa, M. Matsuo, and K. Matsuyanagi, Shape transition and fluctuations in neutron-rich Cr isotopes around $N = 40$, *Phys. Rev. C* **86**, 024316 (2012).
- [34] K. Yoshida and N. Hinohara, Shape changes and large-amplitude collective dynamics in neutron-rich Cr isotopes, *Phys. Rev. C* **83**, 061302(R) (2011).
- [35] K. Washiyama, N. Hinohara, and T. Nakatsukasa, Finite-amplitude method for collective inertia in spontaneous fission, *Phys. Rev. C* **103**, 014306 (2021).
- [36] T. Nakatsukasa, T. Inakura, and K. Yabana, Finite amplitude method for the solution of the random-phase approximation, *Phys. Rev. C* **76**, 024318 (2007).
- [37] T. Inakura, T. Nakatsukasa, and K. Yabana, Self-consistent calculation of nuclear photoabsorption cross sections: Finite amplitude method with Skyrme functionals in the three-dimensional real space, *Phys. Rev. C* **80**, 044301 (2009).
- [38] P. Avogadro and T. Nakatsukasa, Finite amplitude method for the quasiparticle random-phase approximation, *Phys. Rev. C* **84**, 014314 (2011).
- [39] M. Stoitsov, M. Kortelainen, T. Nakatsukasa, C. Losa, and W. Nazarewicz, Monopole strength function of deformed superfluid nuclei, *Phys. Rev. C* **84**, 041305(R) (2011).
- [40] H. Liang, T. Nakatsukasa, Z. Niu, and J. Meng, Feasibility of the finite-amplitude method in covariant density functional theory, *Phys. Rev. C* **87**, 054310 (2013).
- [41] T. Nikšić, N. Kralj, T. Tutiš, D. Vretenar, and P. Ring, Implementation of the finite amplitude method for the relativistic quasiparticle random-phase approximation, *Phys. Rev. C* **88**, 044327 (2013).
- [42] N. Hinohara, M. Kortelainen, and W. Nazarewicz, Low-energy collective modes of deformed superfluid nuclei within the finite-amplitude method, *Phys. Rev. C* **87**, 064309 (2013).
- [43] M. T. Mustonen, T. Shafer, Z. Zenginerler, and J. Engel, Finite-amplitude method for charge-changing transitions in axially deformed nuclei, *Phys. Rev. C* **90**, 024308 (2014).
- [44] J. C. Pei, M. Kortelainen, Y. N. Zhang, and F. R. Xu, Emergent soft monopole modes in weakly bound deformed nuclei, *Phys. Rev. C* **90**, 051304(R) (2014).
- [45] M. Kortelainen, N. Hinohara, and W. Nazarewicz, Multipole modes in deformed nuclei within the finite amplitude

- method, *Phys. Rev. C* **92**, 051302(R) (2015).
- [46] N. Hinohara, Collective inertia of the Nambu-Goldstone mode from linear response theory, *Phys. Rev. C* **92**, 034321 (2015).
- [47] N. Hinohara and W. Nazarewicz, Pairing Nambu-Goldstone modes within nuclear density functional theory, *Phys. Rev. Lett.* **116**, 152502 (2016).
- [48] K. Wen and T. Nakatsukasa, Self-consistent collective coordinate for reaction path and inertial mass, *Phys. Rev. C* **94**, 054618 (2016).
- [49] K. Washiyama and T. Nakatsukasa, Multipole modes of excitation in triaxially deformed superfluid nuclei, *Phys. Rev. C* **96**, 041304(R) (2017).
- [50] X. Sun and D. Lu, Implementation of a finite-amplitude method in a relativistic meson-exchange model, *Phys. Rev. C* **96**, 024614 (2017).
- [51] N. Hinohara and J. Engel, Global calculation of two-neutrino double- β decay within the finite amplitude method in nuclear density functional theory, *Phys. Rev. C* **105**, 044314 (2022).
- [52] H. Sasaki, T. Kawano, and I. Stetcu, Noniterative finite amplitude methods for $E1$ and $M1$ giant resonances, *Phys. Rev. C* **105**, 044311 (2022).
- [53] K. Petřík and M. Kortelainen, Thouless-Valatin rotational moment of inertia from linear response theory, *Phys. Rev. C* **97**, 034321 (2018).
- [54] K. Washiyama and T. Nakatsukasa, Multipole modes for triaxially deformed superfluid nuclei, *JPS Conf. Proc.* **23**, 013012 (2018).
- [55] K. Matsuyanagi, M. Matsuo, T. Nakatsukasa, K. Yoshida, N. Hinohara, and K. Sato, Microscopic derivation of the Bohr-Mottelson collective Hamiltonian and its application to quadrupole shape dynamics, *Phys. Scr.* **91**, 063014 (2016).
- [56] B. Gall, P. Bonche, J. Dobaczewski, H. Flocard, and P.-H. Heenen, Superdeformed rotational bands in the mercury region. A cranked Skyrme-Hartree-Fock-Bogoliubov study, *Z. Phys. A* **348**, 183 (1994).
- [57] J. Terasaki, P.-H. Heenen, P. Bonche, J. Dobaczewski, and H. Flocard, Superdeformed rotational bands with density dependent pairing interactions, *Nucl. Phys. A* **593**, 1 (1995).
- [58] P. Bonche, H. Flocard, P.-H. Heenen, S. J. Krieger, and M. S. Weiss, Self-consistent study of triaxial deformations: Application to the isotopes of Kr, Sr, Zr and Mo, *Nucl. Phys. A* **443**, 39 (1985).
- [59] P. Bonche, H. Flocard, and P.-H. Heenen, Solution of the Skyrme HF+BCS equation on a 3D mesh, *Comput. Phys. Commun.* **171**, 49 (2005).
- [60] W. Ryssens, V. Hellemans, M. Bender, and P.-H. Heenen, Solution of the Skyrme-HF+BCS equation on a 3D mesh, II: A new version of the ev8 code, *Comput. Phys. Commun.* **187**, 175 (2015).
- [61] V. Hellemans, P.-H. Heenen, and M. Bender, Tensor part of the Skyrme energy density functional. III. Time-odd terms at high spin, *Phys. Rev. C* **85**, 014326 (2012).
- [62] J. Bartel, P. Quentin, M. Brack, C. Guet, and H.-B. Håkansson, Towards a better parametrisation of Skyrme-like effective forces: A critical study of the SkM force, *Nucl. Phys. A* **386**, 79 (1982).
- [63] National Nuclear Data Center, Brookhaven National Laboratory, <https://www.nndc.bnl.gov/nudat3/>.
- [64] N. Hinohara, X. Zhang, and J. Engel, in preparation.

Electroproduction of the Λ/Σ^0 hyperons at $Q^2 \simeq 0.5$ (GeV/c)² in forward angles

K. Okuyama,¹ K. Itabashi,² S. Nagao,³ S.N. Nakamura,^{1,3} K.N. Suzuki,⁴ T. Gogami,⁴ B. Pandey,^{5,6} L. Tang,^{5,7} P. Bydžovský,⁸ D. Skoupil,⁸ T. Mart,⁹ D. Abrams,¹⁰ T. Akiyama,¹ D. Androic,¹¹ K. Aniol,¹² C. Ayerbe Gayoso,¹³ J. Bane,¹⁴ S. Barcus,¹³ J. Barrow,¹⁴ V. Bellini,¹⁵ H. Bhatt,¹⁶ D. Bhetuwal,¹⁶ D. Biswas,⁵ A. Camsonne,⁷ J. Castellanos,¹⁷ J-P. Chen,⁷ J. Chen,¹³ S. Covrig,⁷ D. Chrisman,^{18,19} R. Cruz-Torres,²⁰ R. Das,²¹ E. Fuchey,²¹ K. Gnanvo,¹⁰ F. Garibaldi,^{15,22} T. Gautam,⁵ J. Gomez,⁷ P. Gueye,^{5,19} T.J. Hague,²³ O. Hansen,⁷ W. Henry,⁷ F. Hauenstein,²⁴ D.W. Higinbotham,⁷ C.E. Hyde,²⁴ M. Kaneta,¹ C. Keppel,⁷ T. Kutz,²¹ N. Lashley-Colthirst,⁵ S. Li,^{25,26} H. Liu,²⁷ J. Mammei,²⁸ P. Markowitz,¹⁷ R.E. McClellan,⁷ F. Meddi,^{15,29} D. Meekins,⁷ R. Michaels,⁷ M. Mihovilovic,^{30,31,32} A. Moyer,³³ D. Nguyen,^{20,34} M. Nycz,²³ V. Owen,¹³ C. Palatchi,¹⁰ S. Park,²¹ T. Petkovic,¹¹ S. Premathilake,¹⁰ P.E. Reimer,³⁵ J. Reinhold,¹⁷ S. Riordan,³⁵ V. Rodriguez,³⁶ C. Samanta,⁶ S.N. Santiesteban,²⁵ B. Sawatzky,⁷ S. Širca,^{30,31} K. Slifer,²⁵ T. Su,²³ Y. Tian,³⁷ Y. Toyama,¹ K. Uehara,¹ G.M. Urciuoli,¹⁵ D. Votaw,^{18,19} J. Williamson,³⁸ B. Wojtsekhowski,⁷ S.A. Wood,⁷ B. Yale,²⁵ Z. Ye,³⁵ J. Zhang,¹⁰ and Z. Zhang¹⁰

(JLab Hypernuclear Collaboration)

¹Department of Physics, Graduate School of Science,
Tohoku University, Sendai, Miyagi 980-8578 Japan

²WPI-QUP, KEK, Oho 1-1, Tsukuba, Ibaraki 305-0801, Japan

³Department of Physics, Graduate School of Science,
The University of Tokyo, Hongo, Tokyo 113-0033 Japan

⁴Department of Physics, Graduate School of Science,
Kyoto University, Kyoto, Kyoto 606-8502 Japan

⁵Department of Physics, Hampton University, Hampton, Virginia 23668, USA

⁶Department of Physics & Astronomy, Virginia Military Institute, Lexington, Virginia 24450, USA

⁷Thomas Jefferson National Accelerator Facility, Newport News, Virginia 23606, USA

⁸Nuclear Physics Institute, ASCR, 25068 Řež/Prague, Czech Republic

⁹Departemen Fisika, FMIPA, Universitas Indonesia, Depok 16424, Indonesia

¹⁰Department of Physics, University of Virginia, Charlottesville, Virginia 22904, USA

¹¹Department of Physics & Department of Applied Physics, University of Zagreb, HR-10000 Zagreb, Croatia

¹²Physics and Astronomy Department, California State University, Los Angeles, California 90032, USA

¹³Department of Physics, The College of William and Mary, Virginia 23185, USA

¹⁴Department of Physics, University of Tennessee, Knoxville, Tennessee 37996, USA

¹⁵Istituto Nazionale di Fisica Nucleare, Sezione di Roma, 00185, Rome, Italy

¹⁶Department of Physics, Mississippi State University, Mississippi State, Mississippi 39762, USA

¹⁷Department of Physics, Florida International University, Miami, Florida 33199, USA

¹⁸Department of Physics and Astronomy, Michigan State University, East Lansing, Michigan 48824, USA

¹⁹National Superconducting Cyclotron Laboratory,
Michigan State University, East Lansing, MI 48824, USA

²⁰Department of Physics, Massachusetts Institute of Technology, Cambridge, Massachusetts 02139, USA

²¹Department of Physics, State University of New York, Stony Brook, New York 11794, USA

²²Istituto Superiore di Sanità, 00161, Rome, Italy

²³Department of Physics, Kent State University, Kent, Ohio 44242 USA

²⁴Department of Physics, Old Dominion University, Norfolk, Virginia 23529, USA

²⁵Department of Physics, University of New Hampshire, Durham, New Hampshire 03824, USA

²⁶Nuclear Science Division, Lawrence Berkeley National Laboratory, Berkeley, CA 94720, USA

²⁷Department of Physics, Columbia University, New York, New York 10027, USA

²⁸Department of Physics and Astronomy, University of Manitoba, Winnipeg, Manitoba R3T 2N2, Canada

²⁹Sapienza University of Rome, I-00185, Rome, Italy

³⁰Faculty of Mathematics and Physics, University of Ljubljana, 1000 Ljubljana, Slovenia

³¹Jožef Stefan Institute, Ljubljana, Slovenia

³²Institut für Kernphysik, Johannes Gutenberg-Universität Mainz, DE-55128 Mainz, Germany

³³Department of Physics, Christopher Newport University, Newport News, Virginia 23606, USA

³⁴University of Education, Hue University, Hue City, Vietnam

³⁵Physics Division, Argonne National Laboratory, Lemont, Illinois 60439, USA

³⁶División de Ciencias y Tecnología, Universidad Ana G. Méndez,
Recinto de Cupey, San Juan 00926, Puerto Rico

³⁷Department of Physics, Syracuse University, New York, New York 10016, USA

³⁸School of Physics & Astronomy, University of Glasgow, Glasgow, G12 8QQ, Scotland, UK

In 2018, the E12-17-003 experiment was conducted at the Thomas Jefferson National Accelerator Facility (JLab) to explore the possible existence of an $nn\Lambda$ state in the reconstructed missing mass distribution from a tritium gas target. As part of this investigation, data was also collected using

a gaseous hydrogen target, not only for a precise absolute mass scale calibration but also for the study of Λ/Σ^0 electroproduction. This dataset was acquired at $Q^2 \simeq 0.5$ (GeV/c) 2 , $W = 2.14$ GeV, and $\theta_{\gamma K}^{c.m.} \simeq 8$ deg. It covers forward angles where photoproduction data is scarce and a low- Q^2 region that is of interest for hypernuclear experiments. On the other hand, this kinematic region is at a slightly higher Q^2 than previous hypernuclear experiments, thus providing crucial information for understanding the Q^2 dependence of the differential cross sections for Λ/Σ^0 hyperon electroproduction. This paper reports on the Q^2 dependence of the differential cross section for the $e + p \rightarrow e' + K^+ + \Lambda/\Sigma^0$ reaction in the $0.2 - 0.8$ (GeV/c) 2 , and provides comparisons with the currently available theoretical models.

I. INTRODUCTION

Studying the production of hyperons and hypernuclei provides invaluable insights into baryon-baryon interactions with an extended flavor, strangeness. Due to the short lifetime of the Λ hyperon/hypernucleus ($\sim 10^{-10}$ s), it cannot be observed as a stable state naturally. However, one can consider a Λ -hypernucleus as a stable object in view of the strong interaction. The development of accelerator facilities and detection techniques has made it possible to produce and study hyperons and hypernuclei in laboratories.

The study of hyperons and hypernuclei systems via the $(e, e'K^+)$ reaction at the Thomas Jefferson National Accelerator Facility (JLab) has been one its cornerstone program since the mid 90s. Understanding (un)polarized differential cross section for hyperon electroproduction is a fundamental observable to estimate the production yield of hypernuclei. However, experimental data on hyperon electroproduction under various kinematic settings is far from satisfactory. Therefore, predictions from theoretical models have become vital to supplement the data, in particular, at low- Q^2 and forward angles.

Isobaric models, based on effective Lagrangian using hadron degrees of freedom, play an important role: Kaon-Maid [1, 2], Saclay-Lyon A [3, 4], and other [5–9] models describe kaon-hyperon production with reasonable agreement compared to the existing experimental data.

In these isobaric models, background contribution from t-channel and/or u-channel often becomes problematic when describing the kaon-hyperon channel. As a countermeasure, Regge-plus-resonance (RPR) models, which introduces Regge pole exchange, have been recently applied to strangeness electroproduction with good results [10–12].

In the One-Photon-Exchange-Approximation (OPEA), the electroproduction process $p(e, e'K^+)\Lambda/\Sigma^0$ can be related to the photoproduction one via a virtual photon $p(\gamma^*, K^+)\Lambda/\Sigma^0$ as shown in Fig. 1. This relation is given by [13],

$$\frac{d^3\sigma}{dE_{e'}d\Omega_{e'}d\Omega_K^{c.m.}} = \Gamma \frac{d\sigma_{\gamma^*}}{d\Omega_K^{c.m.}}, \quad (1)$$

where Γ is the so-called virtual photon flux. $d\sigma_{\gamma^*}/d\Omega_K^{c.m.}$ is regarded as a differential cross section for the kaon-hyperon production from a virtual photon. The four-momentum of a virtual photon is denoted as $q^\mu :=$

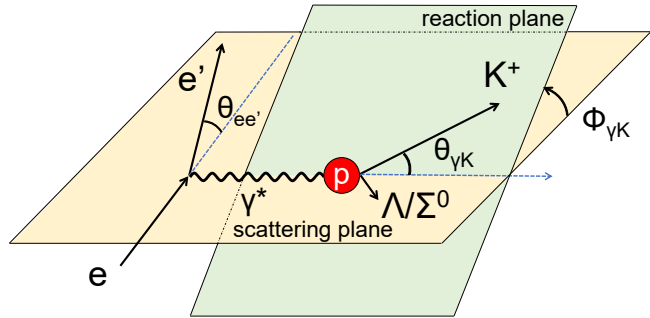


FIG. 1. Schematic drawing of the $p(e, e'K^+)\Lambda/\Sigma^0$ reaction. This shows the $\Lambda/\Sigma^0 - K^+$ production under One-Photon-Exchange-Approximation.

$(\omega/c, \mathbf{q}) = (E_e/c - E_{e'}/c, \mathbf{P}_e - \mathbf{P}_{e'})$. The difference between photoproduction and electroproduction can be related using the four-momentum transfer, $Q^2 := -q^2 = -\omega^2/c^2 + |\mathbf{q}|^2$, i.e., $Q^2 = 0$ for photoproduction and $Q^2 > 0$ for electroproduction.

The differential cross section for virtual photoproduction can be decomposed into 4 terms when polarization observables are not measured in either the initial or the final state as in the present experiment,

$$\begin{aligned} \frac{d\sigma_{\gamma^*}}{d\Omega_K^{c.m.}} &= \frac{d\sigma_T}{d\Omega_K^{c.m.}} + \varepsilon \frac{d\sigma_{TT}}{d\Omega_K^{c.m.}} \cos 2\phi_{\gamma K} \\ &+ \varepsilon \frac{d\sigma_L}{d\Omega_K^{c.m.}} + \sqrt{2\varepsilon(\varepsilon + 1)} \frac{d\sigma_{LT}}{d\Omega_K^{c.m.}} \cos \phi_{\gamma K}. \quad (2) \end{aligned}$$

Each term can be calculated using theoretical models and subsequently combined as in Eq. (2) to obtain $d\sigma_{\gamma^*}/d\Omega_K^{c.m.}$. In section V, comparison of our experimental results to theoretical calculations will be discussed.

Hyperon electroproduction has been performed primarily at JLab, while hyperon photoproduction experiments have been performed by CLAS at JLab [14–17], SAPHIR at ELSA [18], LEPS at SPring-8 [19], and GRAAL at ESRF [20]. Experimentally, the photoproduction process has been well investigated providing abundant data for a wide range of angles to test theoretical models. However, there are still large amounts of disagreements among the models due to the lack of data on photoproduction at forward and backward angles. The electroproduction process has the advantage of

TABLE I. Kinematic settings and experimental performance for the $p(e, e'K^+)\Lambda/\Sigma^0$ reaction using hydrogen target in the E12-17-003 experiment

Electron Beam (e)	
Beam Energy	4.326 GeV
Energy Spread ($\Delta E/E$ in FWHM)	$\leq 1.0 \times 10^{-4}$
Scattered Electron (e')	
Central Momentum	2.100 GeV/ c
Momentum Acceptance	4.5%
Momentum Resolution ($\Delta p/p$ in FWHM)	1.0×10^{-4}
Kaon (K^+)	
Central Momentum	1.823 GeV/ c
Momentum Acceptance	4.5%
Momentum Resolution ($\Delta p/p$ in FWHM)	1.0×10^{-4}

TABLE II. Electron beams irradiated to the targets

Target	Beam Current [μA]	Beam Charge [C]	N_e
Tritium	22.5	16.9	1.1×10^{20}
Hydrogen	22.5	4.7	2.9×10^{19}

acquiring data at forward angles, along the direction of virtual photons.

The present paper is organized as follows. In section II, an outline of our experiment is given. In section III, event selection and derivation of the differential cross sections are explained. In section IV, the results for our Q^2 dependence are presented followed by a discussion in section V. A conclusion is provided in section VI.

II. EXPERIMENT

In the present paper, the data using the gaseous hydrogen target in the E12-17-003 experiment ($Q^2 \simeq 0.5$ (GeV/ c) 2 , $W = 2.14$ GeV, and $\theta_{\gamma K}^{c.m.} \simeq 8$ deg) was analyzed, and the differential cross sections for the $p(e, e'K^+)\Lambda/\Sigma^0$ reaction were obtained.

The data was collected in Experimental Hall A using its two large magnetic spectrometers (HRS: High Resolution Spectrometer [21]) as shown in Fig. 2. One of the HRSs was used to detect the scattered electrons (HRS-L), the other was used to detect the produced kaons (HRS-R). Our experiment ran from October 31th to November 26th in 2018. We performed the experiment using an electron beam set at an energy of 4.326 GeV. However, a more accurate beam energy of ~ 4.313 GeV was measured periodically in front of the target, which was used in the present analysis. The kinematic settings of our experiment are summarized in Table I.

We dedicated about 25% of total beamtime into calibration runs using the hydrogen target (see Table II).

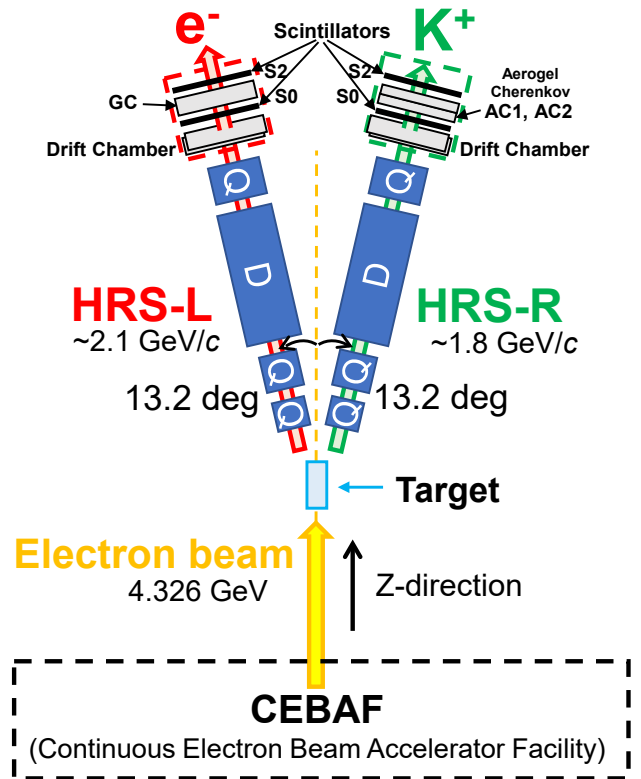


FIG. 2. Overall experimental setup (not to scale) of the E12-17-003 experiment at JLab Hall A. Quadrupole magnet (Q) and dipole magnet (D) are combined as QQDQ. Z-direction is defined as the electron beam direction.

III. ANALYSIS

The missing mass technique was used to reconstruct the mass of the hyperon (M_X) from the measured four-momenta of the electrons ($E_{e'}/c, \mathbf{P}_{e'}$) and kaons ($E_K/c, \mathbf{P}_K$). In the case of the proton target, the missing masses correspond to masses of produced hyperons,

$$\begin{aligned}
 M_X c^2 &= [E_X^2 - \mathbf{P}_X^2 c^2]^{1/2} \\
 &= [(E_e - E_{e'} + M_p c^2 - E_K)^2 \\
 &\quad - (\mathbf{P}_e - \mathbf{P}_{e'} - \mathbf{P}_K)^2 c^2]^{1/2}. \quad (3)
 \end{aligned}$$

To obtain a background free missing mass spectrum, event selection procedures are necessary. As a first step, we selected the reaction point (Z-vertex) to reject events originating from the aluminum alloy of the gas cell end caps. A next step was to identify kaons among positively charged particles detected in the HRS-R. Kaon identification was successfully accomplished using the detector packages of the HRS-R, such as the two aerogel Cherenkov detectors with refractive indices of 1.015 and 1.055, respectively. Furthermore, time-of-flight measurements were performed with a simultaneous use of plastic scintillators behind both spectrometers (see Fig. 2).

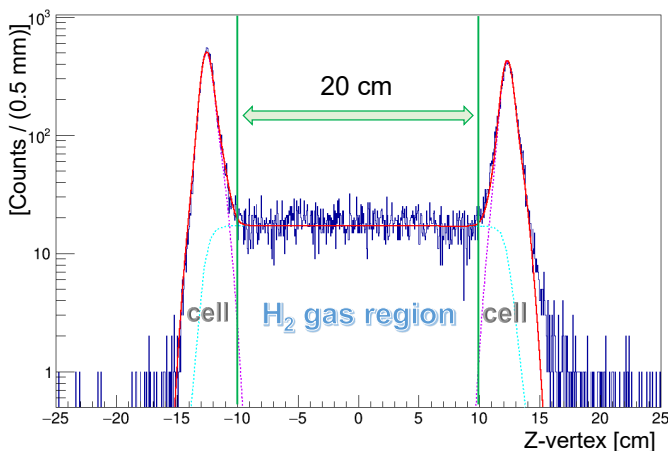


FIG. 3. The average Z -vertex distribution reconstructed by using the two HRSs. The green line shows the cut $|Z| < 10$ cm where events were selected. See text for details.

A. Vertex selection

Electron scattering occurs along the electron beam, Z -direction inside the gas target region. The Z -vertex position was reconstructed using both HRSs independently. Each spectrometer bends charged particles vertically along the momentum dispersive plane leading to distinct positions and angles at respective their focal planes. Meanwhile, the horizontal components at the focal planes have information of the Z -vertex because it is independent of the momentum dispersion. The Z -vertex reconstruction was found to be 5 mm for 1σ using one of the HRSs.

The average Z -vertex distribution obtained from the HRSs and its fitting functions are shown in Fig. 3: the two peaks at -12.5 cm (front) and +12.5 cm (rear) come from the target cell made of aluminum alloy [22]. Although the cell was designed to be 25 cm long, only events within $|Z| < 10$ cm were selected to avoid contamination.

In Fig. 3, the fitting functions consisted of double Gaussians for the cell end caps and are shown in purple lines. A 2nd-order polynomial function convoluted by a gaussian to include the gas region is shown as a cyan line. The aluminum contamination within the selected gas region was found to be about 0.3%. The fitting worked well for $|Z| < 15$ cm, however, some events can be seen outside of the range. These events contribute to as much as 0.84% of total counts and were taken into account as a systematic error. Thus, the estimated Al contamination ratio within the selected region was,

$$(\text{Al contami. ratio}) = 0.30 \pm 0.05(\text{Stat.})_{-0.00}^{+0.84}(\text{Syst.}) [\%].$$

B. Kaon identification

Cherenkov detectors were used to separate K^+ from π^+ and p based on their velocities in the HRS-R. The

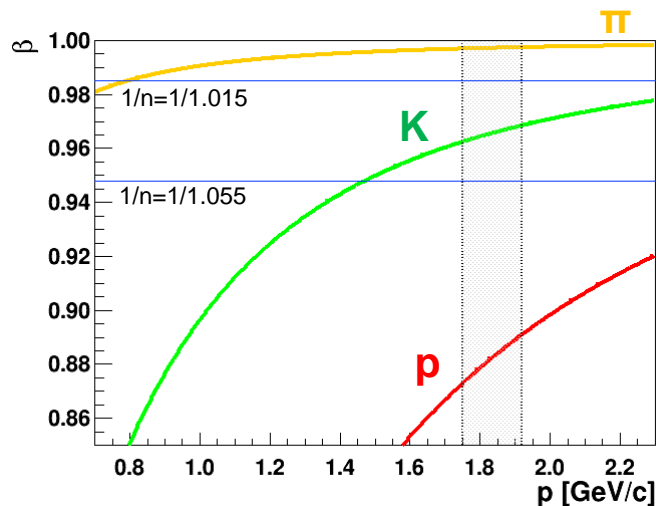


FIG. 4. $K/\pi/p$ discrimination using the Cherenkov detectors for this experiment (shaded band)

threshold for the Cherenkov light emission is $\beta_{\text{thres}} = pc/\sqrt{m^2c^4 + p^2c^2} > 1/n$. In this experiment, ~ 1.8 -GeV/ c particles passed through the aerogels located between the timing scintillators (see Fig. 2). Figure 4 shows the relationship between momentum p and the relative velocity β for π^+/K^+ and K^+/p separation performed using the two aerogel detectors in the off-line analysis. However, large amount of contamination from pions and protons still remain after applying the Cherenkov cut as indicated in Fig. 5. In both spectrometers, the S2 plastic scintillators measure the time-of-flight from the target position,

$$\begin{aligned} t(\text{Target}) &= t(\text{S2}) - \frac{\text{Path Length}}{\beta c} \\ &= t(\text{S2}) - \frac{\sqrt{p^2c^2 + m^2c^4} \times \text{Path Length}}{pc^2} \end{aligned} \quad (4)$$

with Path Length of about 27 m. The coincidence time $t_{\text{Coin.}}$ was defined as,

$$t_{\text{Coin.}} := t_{\text{HRS-L}}(\text{Target}) - t_{\text{HRS-R}}(\text{Target}). \quad (5)$$

If we assume the mass m is that of K^+ for HRS-R and that of e for HRS-L, then $t_{\text{Coin.}} = 0$ for true $(e, e'K^+)$ events. The coincidence time distribution obtained from the hydrogen data is shown in Fig. 5. Three distinct peaks corresponding to π^+ , K^+ , and p are clearly seen. The underlying accidental background had a 2-ns bunch structure corresponding to the RF of the accelerator; however, it cannot be seen due to the strict cut of the aerogel Cherenkov detectors. This accidental background will be discussed later in section III C. The cut condition for the coincidence time was chosen to be $|t_{\text{Coin.}}| < 1$ ns.

Figure 5 also shows the fitting functions used in the analysis taken to be a Voigt function for pions and kaons, and a double gaussian for protons. By definition, accidentals are periodic superposition of these distributions

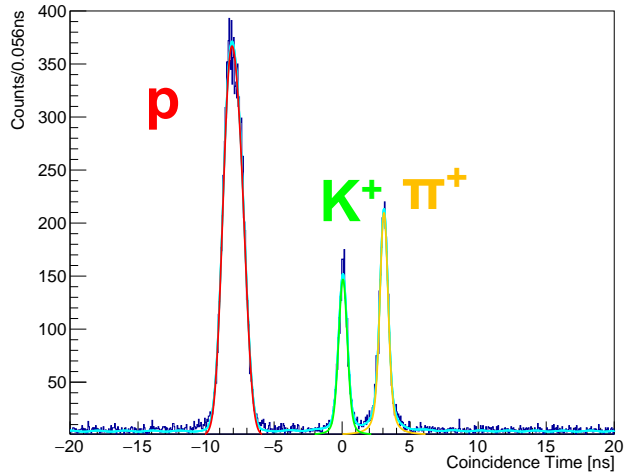


FIG. 5. Coincidence time distribution obtained from Eq. (5). The kaon region is selected as $|t_{\text{Coin.}}| < 1$ ns.

functions. As a result of this fitting, the estimated pion contamination ratio within the selected region was,

$$(\pi^+ \text{ contami. ratio}) = 1.77^{+0.32}_{-0.28}(\text{Stat.})^{+0.40}_{-0.04}(\text{Syst.}) [\%].$$

C. Missing mass spectrum

The missing mass spectrum obtained from the hydrogen target is shown in Fig. 6. Kaon identification was successfully accomplished using the detector packages of HRS-R. As already shown in Fig. 5, under such a high-rate continuous electron beam condition, background events due to accidental coincidences of scattered electrons in HRS-L and positively charged hadrons in HRS-R were unavoidable.

However, the accidentals contribution can be deduced by making a distribution with artificially mixed events corresponding to random coincidences between the two HRS spectrometers. This analysis technique was applied and the result is shown in Fig. 6 by the green line.

In Fig. 6, tail structures can be seen on the right side of both peaks corresponding to the radiative tails. To derive the differential cross sections for the Λ/Σ^0 production, these radiative tails should be taken into account properly. Two techniques were used for this purpose; one was to fit the spectrum by using only the real data, the other was to use a Monte-Carlo simulation (e.g. SIMC code [23]). Both techniques are discussed in the following subsection.

D. Radiative tail

The background subtracted missing mass spectrum is shown in Fig. 7. Other sources of background include

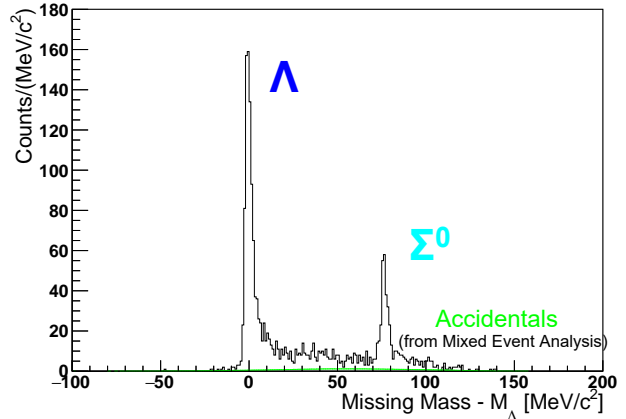


FIG. 6. Missing mass spectrum obtained from the $p(e, e' K^+)X$ reaction.

events originating from the target cell windows in the Z-vertex cut (Fig. 3), and pion contamination in the coincidence time cut (Fig. 5). Proton contamination in the coincidence time cut was found to be negligible. Sum of those contributions were estimated to be $\sim 2\%$. Radiative tail can be seen on the right sides of the Λ and Σ^0 peaks coming from both incoming and outgoing electrons (dominant contribution).

The numbers of Λ and Σ^0 events included in the radiative tails can be obtained from the fit of the tails for both Λ (blue) and Σ^0 (cyan) as shown in Fig. 7, respectively.

Each fit functions consisted of a sum of a Landau distribution $h(x)$ and exponential function $f(x)$ convoluted by a Gaussian $g(x)$, namely,

$$((f + h) * g)(x) = (f * g)(x) + (h * g)(x) \quad (6)$$

$$\begin{cases} f(x) & : \text{exponential function} \\ g(x) & : \text{gaussian} \\ h(x) & : \text{Landau distribution} \end{cases}$$

Background contributions from the target cell and pion contamination are shown as the orange line originating from a fit with double Voigt functions. Scaling factors were determined based on the contamination ratios and the total fitting function is shown in a red line. The fitting result reproduced the data well.

Radiative tails are dominated by events from the incoming and outgoing electrons and were estimated using the in-house SIMC Monte Carlo simulation tool [23]. The full target geometry including its aluminum end caps as described in section III A was included in the simulation. Radiation effects from both internal [24] and external [25] contributions were taken into account. Because of the limited solid angle of the HRS (~ 5.5 msr), particles were generated uniformly assuming a negligible angular dependence across the spectrometer acceptance. The results of the simulation that includes radiative effects are shown in Fig. 8.

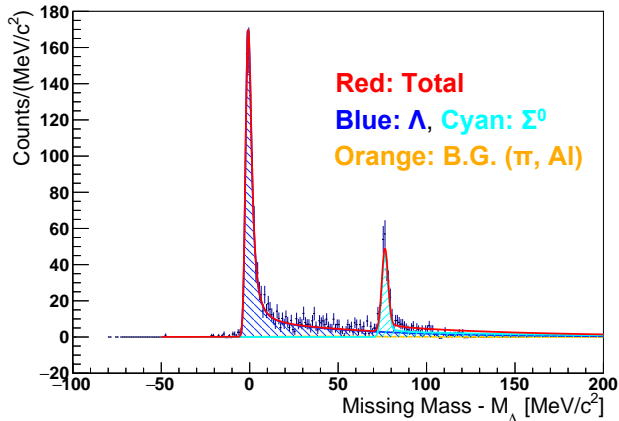


FIG. 7. Fitting result of the missing mass spectrum after accidentals subtraction. Blue and cyan line are functions corresponding to the Λ and Σ^0 production, respectively. The background and total fit function are shown in orange and red, respectively.

While the fitting result of Fig. 7 seems to overestimate the number of radiative tail events, the distribution reproduced by SIMC seems to underestimate it. This is because the data contains possible other unknown background. In the present analysis, the number of detected hyperons obtained from the fit of Fig. 7 was chosen as the most faithful value based on the experimental data. Besides, the variations of the fitting results by changing the fit conditions and the integral ranges, as well as those reflecting the distribution reproduced by SIMC, were taken into account as systematic errors. The largest value was added as an upper error and the smallest value was added as a lower error.

E. Derivation of the differential cross section

The extracted differential cross section was calculated from

$$\begin{aligned} & \left(\frac{d\sigma_{\gamma^* p \rightarrow K^+ \Lambda(\Sigma^0)}}{d\Omega_{K^+}} \right)_{\text{HRS-R}, i} \\ &= \frac{1}{N_T} \cdot \frac{1}{N_{\gamma^*}} \cdot \frac{1}{\bar{\epsilon}} \cdot \sum_{i=1}^{N_{\Lambda(\Sigma^0)}} \frac{1}{\epsilon_i^{\text{DAQ}} \cdot \epsilon_i^{\text{Decay}} \cdot \Delta\Omega_{\text{HRS-R}, i}} \quad (7) \end{aligned}$$

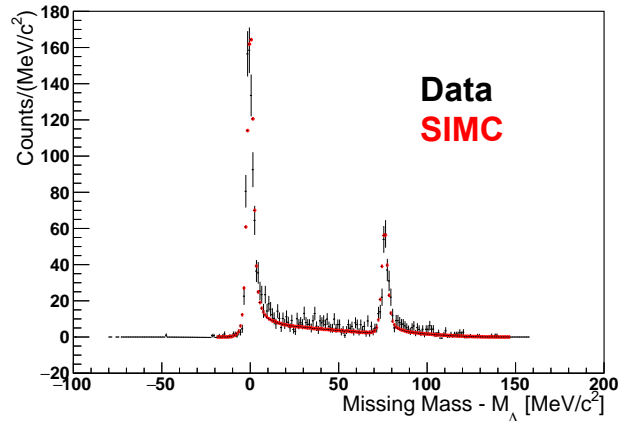


FIG. 8. Experimentally reconstructed missing mass spectrum (black points) compare to our SIMC Monte Carlo simulation (red points).

where

- $N_{\Lambda(\Sigma^0)}$: Number of $\Lambda(\Sigma^0)$ events
- N_T : Number of proton targets [b^{-1}]
- N_{γ^*} : Number of virtual photons
- $\bar{\epsilon}$: Average event cut efficiency
- ϵ_i^{DAQ} : DAQ efficiency when taking i -th event
- $\epsilon_i^{\text{Decay}}$: Survival ratio of K^+
- $\Delta\Omega_{\text{HRS-R}, i}$: Solid angle with HRS-R for i -th event [sr]

Since the target thickness of the gaseous hydrogen was 70.8 mg/cm^2 , the number of target is $N_T = 0.0375 \text{ b}^{-1}$. The efficiencies, survival ratio ($\epsilon^{\text{Decay}} \sim 14\%$) and solid angle ($\Delta\Omega_{\text{HRS-R}} \sim 5.5 \text{ msr}$) should be considered on an event by event basis, however, the cut efficiencies can be replaced by the average value $\bar{\epsilon}$ obtained from the data. All components of the efficiency and the average value are summarized in Table III. The kaon survival ratio ϵ^{Decay} and solid angle $\Delta\Omega_{\text{HRS-R}}$ had a momentum dependence. Thus, these components were explicitly separated from $\bar{\epsilon}$ and evaluated on an event by event basis. The data acquisition efficiency $\epsilon^{\text{DAQ}} \sim 96\%$ was evaluated on a run by run basis. Additionally, Table IV summarizes the estimated systematic errors.

IV. RESULT

The measured differential cross sections for Λ and Σ^0 are summarized in Table V including an analysis of our data using two regions: $Q^2 < 0.5 \text{ (GeV/c)}^2$ and $Q^2 \geq 0.5 \text{ (GeV/c)}^2$ shown to provide a Q^2 dependence. These results correspond to $Q^2 \simeq 0.5 \text{ (GeV/c)}^2$, $W = 2.14 \text{ GeV}$, and $\theta_{\gamma K}^{\text{c.m.}} \simeq 8 \text{ deg}$. We compare our results to past ex-

TABLE III. Efficiencies used for the cross section estimation

Item	$\bar{\varepsilon}(\Lambda)$ [%]	$\bar{\varepsilon}(\Sigma^0)$ [%]	Description
ε^Z	82.5	76.2	Z-vertex cut for hydrogen target selection
ε^{AC}	60.2	59.1	Aerogel Cherenkov cut for kaon identification
ε^{CT}	98.8	97.0	Coincidence Time cut for kaon identification
$\varepsilon^{\text{Single}}$	97.0	97.0	Percentage of single-hit events in HRS-L (excluding multi-hit)
ε^{FP}	96.2	96.2	Focal Plane cut for removing unphysical events
$\varepsilon^{\text{Track}}$	98.1	98.1	Percentage of successful track reconstructions
ε^{χ^2}	> 99.9	> 99.9	χ^2 cut for the reconstructed tracks
$\varepsilon^{\text{Total}}$	44.9	40.0	Total efficiencies of the above

TABLE IV. Summary of the estimated systematic errors

Item	Λ		Σ^0	
	Lower	Upper	Lower	Upper
B.G. from Al Cell	0.89%	0.05%	0.89%	0.05%
Pion Contamination	0.72%	0.32%	0.72%	0.32%
Radiative tail	9.43%	4.30%	25.2%	47.6%
Kaon Survival Ratio	4.13%	0.76%	4.13%	0.76%
Number of Target Centers	0.83%	0.83%	0.83%	0.83%
Number of Beam Particles	1.00%	1.00%	1.00%	1.00%
Number of Virtual Photons	1.40%	2.30%	1.76%	1.11%
Mixed Event Analysis	0.20%	0.20%	0.30%	0.30%
All	10.53%	5.11%	25.7%	47.6%

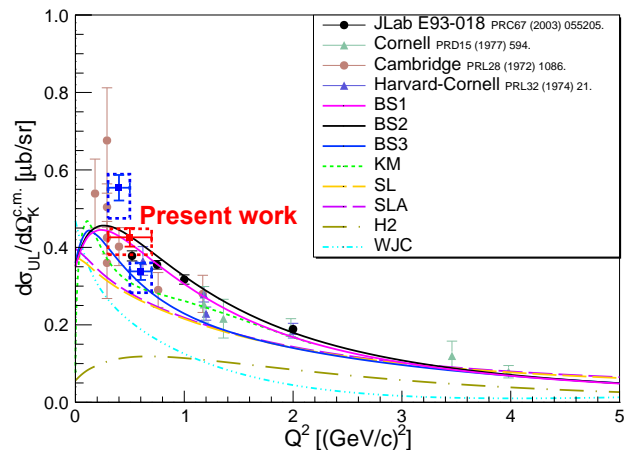
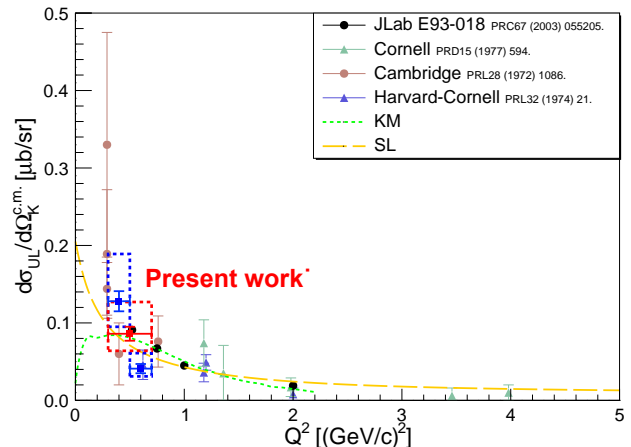
periments and theoretical predictions in Figs. 9 and 10. The results with the full dataset are shown in red and the those with the divided dataset are shown in blue. Statistical errors are represented by solid error bars, while systematic errors are depicted as dashed boxes.

For comparison, other experimental data and theoretical predictions based on the isobaric approach are shown in the figures. It should be noted that the other data and the theoretical calculations correspond to unpolarized differential cross sections defined as

$$\frac{d\sigma_{UL}}{d\Omega_K^{c.m.}} := \frac{d\sigma_T}{d\Omega_K^{c.m.}} + \varepsilon \frac{d\sigma_L}{d\Omega_K^{c.m.}} \quad (8)$$

which is obtained by averaging Eq. (2) over 360 deg with respect to $\phi_{\gamma K}$.

The other experimental data correspond to different kinematics [26–28]: a scaling method was used following the procedure described by Moring *et al.* [29] to compare the various data points. All of the experimental data shown in the figures were taken at forward angles, $\theta_{\gamma K}^{c.m.} < 15$ deg. Also, major isobaric models, BS1 [6], BS2 [6], BS3 [7], Kaon-Maid (KM) [1, 2], Saclay-Lyon (SL) [3], Saclay-Lyon A (SLA) [4], H2 [8], Williams-Ji-Cotanch (WJC) [9] are shown for $W = 2.14$ GeV, $\theta_{\gamma K}^{c.m.} = 8$ deg, and $\varepsilon = 0.8$. The KM model is displayed up to its maximum computational range, $Q^2 = 2.2$ (GeV/c) 2 . Our results do not deviate significantly from the existing experimental data and the theoretical calculations.

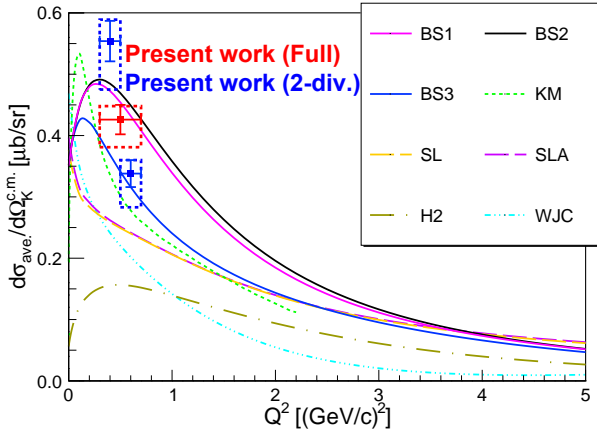
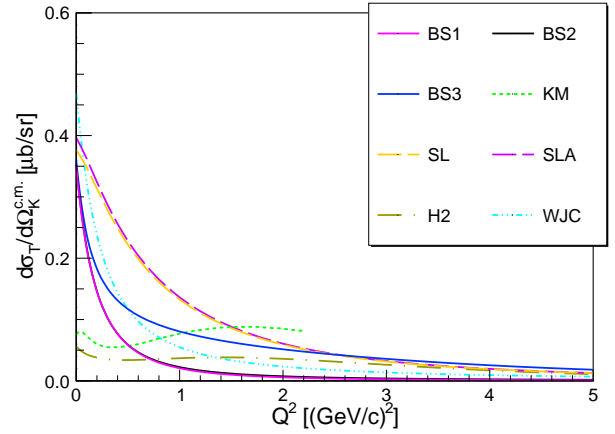
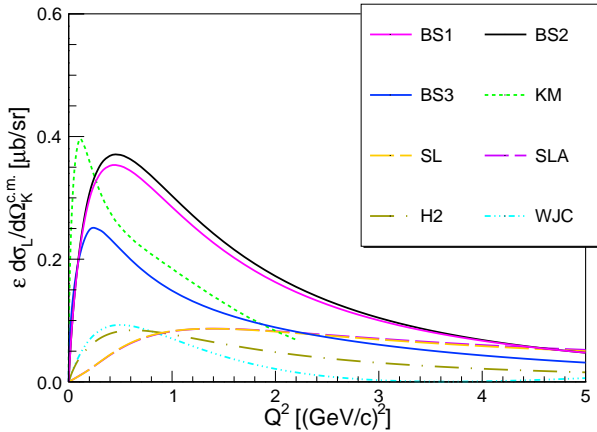
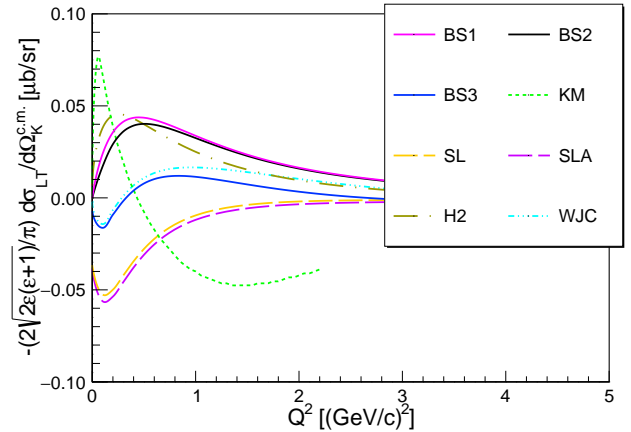
FIG. 9. Q^2 -dependence of the differential cross section for the $p(\gamma^*, K^+)\Lambda$ reaction.FIG. 10. Q^2 -dependence of the differential cross section for the $p(\gamma^*, K^+)\Sigma^0$ reaction.

V. DISCUSSION

The unpolarized differential cross section is valid only if the acceptance covers the whole azimuthal angular range

TABLE V. Summary of the obtained differential cross sections

$\gamma^*p \rightarrow K^+\Lambda$		
Full	$0.426^{+0.024}_{-0.023}(\text{Stat.})^{+0.022}_{-0.045}(\text{Syst.}) \mu\text{b/sr}$	at $Q^2 = 0.2 - 0.8 \text{ (GeV/c)}^2$
Divided-1	$0.554^{+0.033}_{-0.032}(\text{Stat.})^{+0.035}_{-0.079}(\text{Syst.}) \mu\text{b/sr}$	at $Q^2 = 0.2 - 0.5 \text{ (GeV/c)}^2$
Divided-2	$0.338 \pm 0.022(\text{Stat.})^{+0.022}_{-0.055}(\text{Syst.}) \mu\text{b/sr}$	at $Q^2 = 0.5 - 0.8 \text{ (GeV/c)}^2$
$\gamma^*p \rightarrow K^+\Sigma^0$		
Full	$0.086^{+0.009}_{-0.008}(\text{Stat.})^{+0.041}_{-0.022}(\text{Syst.}) \mu\text{b/sr}$	at $Q^2 = 0.2 - 0.8 \text{ (GeV/c)}^2$
Divided-1	$0.128 \pm 0.013(\text{Stat.})^{+0.061}_{-0.033}(\text{Syst.}) \mu\text{b/sr}$	at $Q^2 = 0.2 - 0.5 \text{ (GeV/c)}^2$
Divided-2	$0.041 \pm 0.006(\text{Stat.})^{+0.020}_{-0.010}(\text{Syst.}) \mu\text{b/sr}$	at $Q^2 = 0.5 - 0.8 \text{ (GeV/c)}^2$

FIG. 11. Q^2 dependence of the average differential cross section for the $p(\gamma^*, K^+)\Lambda$ reaction. Comparison in Q^2 dependence between our results and the isobaric models is shown.FIG. 12. Q^2 dependence of the transverse differential cross section for the $p(\gamma^*, K^+)\Lambda$ reaction.FIG. 13. Q^2 dependence of the longitudinal differential cross section for the $p(\gamma^*, K^+)\Lambda$ reaction.FIG. 14. Q^2 dependence of the transverse-longitudinal differential cross section for the $p(\gamma^*, K^+)\Lambda$ reaction.

of 360 deg. However, our experimental apparatus covered an angle approximately from 90 deg to 270 deg. Therefore, in our dataset, averaging over $\phi_{\gamma K}$ within our experimental acceptance cancels the contribution of $d\sigma_{TT}$

but retains that of $d\sigma_{LT}$ with a numerical factor,

$$\frac{d\sigma_{\text{ave.}}}{d\Omega_K^{\text{c.m.}}} := \frac{d\sigma_T}{d\Omega_K^{\text{c.m.}}} + \epsilon \frac{d\sigma_L}{d\Omega_K^{\text{c.m.}}} - \frac{2}{\pi} \sqrt{2\epsilon(\epsilon+1)} \frac{d\sigma_{LT}}{d\Omega_K^{\text{c.m.}}}. \quad (9)$$

This average differential cross section corresponds to the obtained results in Table V. A comparison with predictions of the isobaric models calculated according to Eq. (9) is shown in Fig. 11 for Λ electroproduction. Similarly, contributions from the separate terms, the transverse $d\sigma_T$, longitudinal $d\sigma_L$, and longitudinal-transverse interference $d\sigma_{LT}$ are compared for the isobaric models in Figs. 12, 13, and 14, respectively.

The average differential cross sections obtained in this experiment are reproduced by the BS1 and BS2 models [6] as seen in Fig. 11. These models were developed recently using also the new data from the CLAS [15] and LEPS [19] collaborations and they were proven to reproduce well the photoproduction data at forward angles [6]. Based on our new results, these models also reproduce the electroproduction data in our kinematic region. The BS3 model also reproduces our results relatively well. It is an extended version of the BS1 and BS2 models to electroproduction by adding couplings of the nucleon resonances to the longitudinal component of the virtual photon [7]. This is also why the BS3 model predicts different Q^2 dependence of the longitudinal terms, $d\sigma_L$ and $d\sigma_{LT}$, observed in Figs. 13 and 14.

The KM model [1, 2] has a steep rise at the average differential cross section at low Q^2 due to its strong $d\sigma_L$ term as shown in Fig. 13, and seems to reproduce our results. However, the behavior in low- Q^2 region was found to be inconsistent with the new electroproduction data of MAMI at $Q^2 = 0.055$ (GeV/c) 2 [30]. In particular, the longitudinal component was shown to be too large below $Q^2 = 0.055$ (GeV/c) 2 . While the KM model is known to reproduce well photoproduction data, there is deviation from experimental data for electroproduction especially at low Q^2 . This discrepancy is due to the poor knowledge of the longitudinal couplings since experimental data were scarce in the 1990s when it was developed. Furthermore, the number of resonances used in the KM model is only moderate similarly as in the older models like SL, SLA, H2, and WJC. In the $K\Lambda$ channel, the KM model utilizes only the $S_{11}(1650)$, $P_{11}(1710)$, $P_{13}(1720)$, and missing $D_{13}(1895)$ nucleon resonances, whereas in the $K\Sigma$ channels, the KM model makes use of only the $S_{11}(1650)$, $P_{11}(1710)$, $P_{13}(1720)$, $S_{31}(1900)$, and $P_{31}(1910)$ states. Therefore, in the $K\Lambda$ channel, contribution to the longitudinal terms from other resonances seems to be important to describe the small discrepancy between the KM model and the present data as indicated in Figs. 13 and 14.

Next, the SL model [3] and the SLA model [4] also can reproduce our results to some extent. Note that predictions of these Saclay-Lyon models shown in the figures almost overlap each other. Even though these models do not include any couplings of the nucleon resonances with the longitudinal component of the virtual photon and they could not use the recent experimental data in their construction, they provide results which are close to ours in this kinematic condition.

Finally, the H2 [8] and WJC model [9] are also rela-

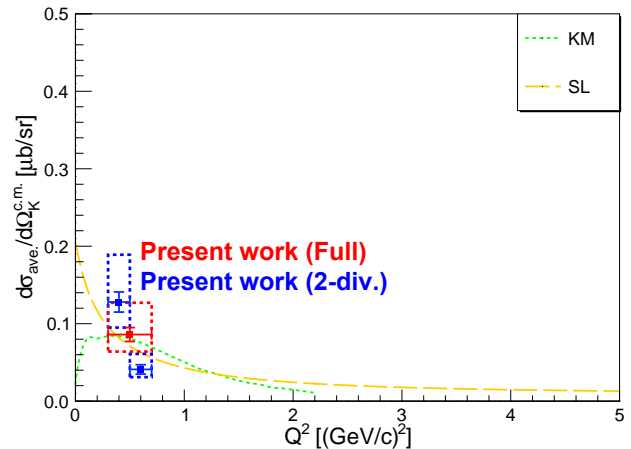


FIG. 15. Q^2 dependence of the average differential cross section for the $p(\gamma^*, K^+)\Sigma^0$ reaction.

tively old models but their results were shown here for comparison. These models reveal similar Q^2 dependence as the other models but they do not reproduce the magnitude of the average differential cross section due to missing strength both in the transverse and longitudinal terms. The H2 model was fitted only to photoproduction data taken at CLAS in 2003 [16], and therefore it was not expected to show great results for electroproduction at other kinematic conditions.

The Q^2 dependence of the response functions in Eq. (9) is determined by a competition between their genuine dependence on Q^2 stemming from dynamics of an isobaric model given by included Feynman diagrams [6, 7], and dumping effects due to the electromagnetic form factors which mimic an internal structure of the hadrons included in the models. In Figs. 12 and 13, we show contributions from the transverse and the longitudinal terms in Eq. (9), respectively. We see that the overall Q^2 dependence of the BS models observed in Fig. 11 at $Q^2 < 0.5$ (GeV/c) 2 is given by the longitudinal contribution. The peak observed in Fig. 13 dominates the average differential cross sections and hence the BS models can reproduce our results at $Q^2 \simeq 0.5$ (GeV/c) 2 . On the contrary, the SL model predicts large values of $d\sigma_T$ but the $d\sigma_L$ gives only small contributions which makes the difference between the SL and BS models.

The longitudinal-transverse interference term is shown in Fig. 14. This term has a relatively small effect on the average differential cross section, hence the similarities for the average differential cross section in Fig. 11 and unpolarized differential cross section in Fig. 9.

For Σ^0 electroproduction, the KM model and the SL model are the only available isobaric models to compare with our results. The average differential cross section for Σ^0 is shown in Fig. 15. Similarly, the longitudinal-transverse interference term has a small contribution. Both the KM and SL models show similar results at

our kinematic conditions. However, the SL model can reproduce our results of steep Q^2 dependence more accurately, although having large systematic errors due to the difficulties of the estimation of the radiative tail. For Σ^0 electroproduction, both experimental and theoretical updates are needed to clarify the differential cross section.

VI. CONCLUSION

In the present paper, the differential cross sections for Λ/Σ^0 electroproduction at forward angles were reported. Despite of the fact that there is abundant experimental data for photoproduction in a wide range of kinematics by CLAS, SAPHIR, LEPS, and GRAAL collaborations, understanding of production dynamics at forward angles has been limited because of the lack of experimental data at forward angles due to experimental difficulties. On the other hand, electroproduction data can be taken at forward angles but available data is still limited.

The results of the differential cross sections for Λ/Σ^0 electroproduction obtained in this experiment were compared with the theoretical predictions using the isobaric models. Our results provided new data at forward angles not covered by photoproduction so far. The best agreements of Λ electroproduction are with the BS models, which are also in good agreement with the new results of CLAS.

In the BS3 model, the longitudinal couplings of the virtual photon to nucleon fields play an important role in obtaining satisfactory results as shown in Ref. [7]. At $Q^2 \simeq 0.5$ (GeV/c)² contributions from these couplings enhance the longitudinal cross section making a peak. The contribution from the longitudinal couplings

cannot be investigated by photoproduction, but can be approached only by electroproduction. Therefore our new data is an important input to the theoretical models in determining the magnitudes of the longitudinal couplings. This study is expected not only to advance our comprehension of fundamental aspects of hyperon electroproduction and photoproduction but also to extend its relevance to applied studies, such as hypernuclear physics.

ACKNOWLEDGMENTS

We thank the JLab staff of the Division of Physics, Division of Accelerator, and the Division of Engineering for providing support for conducting the experiment. This work was supported by U.S. Department of Energy (DOE) grant DE-AC05-06OR23177 under which Jefferson Science Associates, LLC, operates the Thomas Jefferson National Accelerator Facility. The work of the Argonne National Laboratory group member is supported by DOE grant DE-AC02-06CH11357. The Kent State University contribution is supported under grant no. PHY-1714809 from the U.S. National Science Foundation. The hypernuclear program at JLab is supported by U.S. DOE grant DE-FG02-97ER41047. This work was supported by the Grant-in-Aid for Scientific Research on Innovative Areas “Toward new frontiers Encounter and synergy of state-of-the-art astronomical detectors and exotic quantum beams.” This work was supported by JSPS KAKENHI grants nos. 18H05459, 18H05457, 18H01219, 17H01121, 19J22055, 18H01220, and Grant-in-Aid for JSPS Research Fellow 23KJ0100. This work was also supported by the Graduate Program on Physics for the Universe, Tohoku University (GP-PU), and SPIRITS 2020 of Kyoto University.

-
- [1] T. Mart and C. Bennhold, Phys. Rev. C **61**, 012201 (1999).
 - [2] F. Lee, T. Mart, C. Bennhold, H. Haberzettl, and L. Wright, Nucl. Phys. A **695**, 237 (2001).
 - [3] J. C. David, C. Fayard, G. H. Lamot, and B. Saghai, Phys. Rev. C **53**, 2613 (1996).
 - [4] T. Mizutani, C. Fayard, G.-H. Lamot, and B. Saghai, Phys. Rev. C **58**, 75 (1998).
 - [5] P. Bydžovský, F. Cusanno, S. Frullani, F. Garibaldi, M. Iodice, M. Sotona, and G. M. Urciuoli, arXiv:nucl-th/0305039 (2003).
 - [6] D. Skoupil and P. Bydžovský, Phys. Rev. C **93**, 025204 (2016).
 - [7] D. Skoupil and P. Bydžovský, Phys. Rev. C **97**, 025202 (2018).
 - [8] P. Bydžovský and M. Sotona, Nucl. Phys. A **754**, 243c (2005).
 - [9] R. A. Williams, C.-R. Ji, and S. R. Cotanch, Phys. Rev. C **46**, 1617 (1992).
 - [10] T. Corthals, J. Ryckebusch, and T. V. Cauteren, Phys. Rev. C **73**, 045207 (2006).
 - [11] L. De Cruz, T. Vranckx, P. Vancraeyveld, and J. Ryckebusch, Phys. Rev. Lett. **108**, 182002 (2012).
 - [12] P. Bydžovský and D. Skoupil, Phys. Rev. C **100**, 035202 (2019).
 - [13] E. Amaldi, S. Fubini, and G. Furlan, *Pion Electroproduction. Electroproduction at Low-Energy and Hadron Form-Factors*, Vol. 83 (Springer Tracts in Modern Physics, 1979).
 - [14] R. Bradford, R. A. Schumacher, J. W. C. McNabb, L. Todor, G. Adams, P. Ambrozewicz, E. Anciant, M. Anghinolfi, B. Asavapibhop, G. Asryan, G. Audit, H. Avakian, H. Bagdasaryan, N. Baillie, J. P. Ball, *et al.*, Phys. Rev. C **73**, 035202 (2006).
 - [15] M. E. McCracken, M. Bellis, C. A. Meyer, M. Williams, K. P. Adhikari, M. Anghinolfi, J. Ball, M. Battaglieri, B. L. Berman, A. S. Biselli, D. Branford, W. J. Briscoe, W. K. Brooks, V. D. Burkert, S. L. Careccia, *et al.*, Phys. Rev. C **81**, 025201 (2010).
 - [16] J. W. C. McNabb, R. A. Schumacher, L. Todor,

- G. Adams, E. Anciant, M. Anghinolfi, B. Asavapibhop, G. Audit, T. Auger, H. Avakian, H. Bagdasaryan, J. P. Ball, S. Barrow, M. Battaglieri, K. Beard, *et al.*, Phys. Rev. C **69**, 042201 (2004).
- [17] B. Dey, C. A. Meyer, M. Bellis, M. E. McCracken, M. Williams, K. P. Adhikari, M. Aghasyan, M. Anghinolfi, J. Ball, M. Battaglieri, V. Batourine, I. Bedlinskiy, B. L. Berman, A. S. Biselli, D. Branford, *et al.*, Phys. Rev. C **82**, 025202 (2010).
- [18] K.-H. Glander, J. Barth, W. Braun, J. Hannappel, N. Jöpen, F. Klein, E. Klempt, R. Lawall, J. Link, D. Menze, W. Neuerburg, M. Ostrick, E. Paul, I. Schulday, W. J. Schwille, H. v. Pee, F. W. Wieland, J. Wißkirchen, and C. Wu, Eur. Phys. J. A **19**, 251 (2004).
- [19] M. Sumihama, J. K. Ahn, H. Akimune, Y. Asano, C. Bennhold, W. C. Chang, T. Corthals, S. Daté, H. Ejiri, H. Fujimura, M. Fujiwara, M. Guidal, K. Hicks, T. Hotta, K. Imai, *et al.*, Phys. Rev. C **73**, 035214 (2006).
- [20] A. Lleres, O. Bartalini, V. Bellini, J. P. Bocquet, P. Calvat, M. Capogni, L. Casano, M. Castoldi, A. D'Angelo, J. P. Didelez, R. Di Salvo, A. Fantini, C. Gaulard, G. Gervino, F. Ghio, *et al.*, Eur. Phys. J. A **31**, 79 (2007).
- [21] J. Alcorn, B. Anderson, K. Aniol, J. Annand, L. Auerbach, J. Arrington, T. Averett, F. Baker, M. Baylac, E. Beise, J. Berthot, P. Bertin, W. Bertozzi, L. Bimbot, T. Black, *et al.*, Nucl. Instrum. Methods, Phys. Res. Sect. A **522**, 294 (2004).
- [22] S. Santiesteban, S. Alsalmi, D. Meekins, C. A. Gayoso, J. Bane, S. Barcus, J. Campbell, J. Castellanos, R. Cruz-Torres, H. Dai, T. Hague, F. Hauenstein, D. Higinbotham, R. Holt, T. Kutz, *et al.*, Nucl. Instrum. Methods, Phys. Res. Sect. A **940**, 351 (2019).
- [23] https://hallweb.jlab.org/wiki/index.php/SIMC-Monte_carlo.
- [24] M. Vanderhaeghen, J. M. Friedrich, D. Lhuillier, D. Marchand, L. Van Hoorebeke, and J. Van de Wiele, Phys. Rev. C **62**, 025501 (2000).
- [25] Y.-S. Tsai, Rev. Mod. Phys. **46**, 815 (1974).
- [26] C. J. Bebek, C. N. Brown, P. Bucksbaum, M. Herzlinger, S. D. Holmes, C. A. Lichtenstein, F. M. Pipkin, S. W. Raither, and L. K. Sistrerson, Phys. Rev. D **15**, 594 (1977).
- [27] C. N. Brown, C. R. Canizares, W. E. Cooper, A. M. Eisner, G. J. Feldman, C. A. Lichtenstein, L. Litt, W. Lockert, V. B. Montana, F. M. Pipkin, and N. Hicks, Phys. Rev. Lett. **28**, 1086 (1972).
- [28] C. J. Bebek, C. N. Brown, M. Herzlinger, S. Holmes, C. A. Lichtenstein, F. M. Pipkin, L. K. Sistrerson, D. Andrews, K. Berkelman, D. G. Cassel, D. L. Hartill, and N. Hicks, Phys. Rev. Lett. **32**, 21 (1974).
- [29] R. M. Moring, D. Abbott, A. Ahmidouch, T. A. Amatuni, P. Ambrozewicz, T. Angelescu, C. S. Armstrong, J. Arrington, K. Assamagan, S. Avery, K. Bailey, K. Beard, S. Beedoe, E. J. Beise, H. Breuer, *et al.*, Phys. Rev. C **67**, 055205 (2003).
- [30] A1 Collaboration, P. Achenbach, C. Ayerbe Gayoso, J. C. Bernauer, S. Bianchin, R. Böhm, O. Borodina, D. Bosnar, M. Bösz, V. Bozkurt, P. Bydžovský, L. Debenjak, M. O. Distler, A. Esser, I. Friščić, *et al.*, Eur. Phys. J. A **48**, 14 (2012).

Review

Recent Findings from Heavy-Flavor Angular Correlation Measurements in Hadronic Collisions

Deepa Thomas ^{1,*}  and Fabio Colamaria ^{2,*} ¹ The University of Texas at Austin, Department of Physics, 2515 Speedway, Austin, TX 78712, USA² Istituto Nazionale di Fisica Nucleare, Sezione di Bari, Via E. Orabona, 4 - 70125 Bari, Italy* Correspondence: deepa.thomas@utexas.edu (D.T.); fabio.colamaria@ba.infn.it (F.C.)

Abstract: The study of angular correlations of heavy-flavor particles in hadronic collisions can provide crucial insight into the heavy quark production, showering, and hadronization processes. The comparison with model predictions allows us to discriminate among different approaches for heavy quark production and hadronization, as well as different treatments of the underlying event employed by the models to reproduce correlation observables. In ultra-relativistic heavy-ion collisions, where a deconfined state of matter, the quark–gluon plasma (QGP), is created, heavy-flavor correlations can shed light on the modification of the heavy quark fragmentation due to the interaction between charm and beauty quarks with the QGP constituents, as well as characterize their energy loss processes while traversing the medium. Insight into the possible emergence of collective-like mechanisms in smaller systems, resembling those observed in heavy-ion collisions, can also be obtained by performing correlation studies in high-multiplicity proton–proton and proton–nucleus collisions. In this review, the most recent and relevant measurements of heavy-flavor correlations performed in all collision systems at the LHC and RHIC will be presented, and the new understandings that they provide will be discussed.

Keywords: heavy quarks; correlations; jet fragmentation; energy loss; collectivity in small systems; heavy quark production; hadronization



Citation: Thomas, D.; Colamaria, F. Recent Findings from Heavy-Flavor Angular Correlation Measurements in Hadronic Collisions. *Universe* **2024**, *10*, 0. <https://doi.org/>

Academic Editor: Firstname
Lastname

Received: 15 January 2024

Revised: 6 February 2024

Accepted: 7 February 2024

Published:



Copyright: © 2024 by the authors. Licensee MDPI, Basel, Switzerland. This article is an open access article distributed under the terms and conditions of the Creative Commons Attribution (CC BY) license (<https://creativecommons.org/licenses/by/4.0/>).

1. Introduction

The study of heavy quark (charm and beauty quarks) production in high-energy hadronic collisions is an important tool to test and validate perturbative quantum chromodynamics (pQCD) calculations [1–4], as they are produced in hard parton scattering processes. The production cross-section of several heavy-flavor hadrons and their decay products has been measured at different centers of mass energies at RHIC [5–7], Tevatron [8–10], and at the LHC [11–32], and are compared with pQCD calculations [3,33–37]. The correlated production of heavy flavors, studied as a function of variables such as the azimuthal angle between heavy-flavor particles, either by direct reconstruction of heavy-flavor hadrons or from their decay products, can provide a significantly larger amount of information than single-particle inclusive heavy-flavor production.

In ultra-relativistic heavy-ion collisions, heavy quarks play an important role in the study of the deconfined phase of strongly interacting matter, the quark–gluon plasma (QGP), created in these collisions. Traditional observables of heavy quarks, such as the nuclear modification factor (R_{AA}) and the elliptic flow coefficient (v_2), have been extensively studied at RHIC [38–40] and at the LHC [12,41–44]. These measurements indicate that heavy quarks experience significant in-medium energy loss at large transverse momentum (p_T), and that charm quarks partially thermalize within the medium at smaller p_T . These effects are induced by the interaction of heavy quarks with the medium constituents, mainly made up of light partons. The interaction has two main contributions, the purely elastic process, resulting in a collisional energy loss [45–47], and gluon bremsstrahlung, producing

arXiv:2403.01035v1 [nucl-ex] 1 Mar 2024

a radiative energy loss [48–53]. Both of these processes depend on the parton mass; thus, studies of heavy quark in heavy-ion collisions provide important information about the properties of the QGP. Currently, it remains a challenge to describe R_{AA} and v_2 simultaneously from a low to high range of transverse momentum in a given theoretical framework. More differential observables, such as angular correlations between heavy-flavor particles, are more sensitive to the specific interaction processes between heavy quarks and the QGP constituents, and can thus provide further information on the propagation of heavy quarks in the QGP medium [54,55].

In proton–nucleus (p–A) collisions, due to the presence of the nucleus in the initial state, several cold-nuclear-matter effects can influence the production, fragmentation, and hadronization of heavy quarks, such as the impact of the nuclear parton distribution function (nPDF) [56–58], the presence of a coherent and saturated gluonic system dominated by gluons at low Bjorken- x [59–62], and partons undergoing multiple elastic, inelastic, and coherent scatterings [63,64]. These effects can also modify the heavy-flavor correlation distribution [65–67], and their understanding is crucial for the interpretation of any modification of the correlation distributions in the presence of a QGP, produced in heavy-ion collisions.

In this article, we review and summarize the latest measurements of angular correlations of heavy-flavor particles in proton–proton (pp), proton–nucleus (p–A), and nucleus–nucleus (A–A) collisions at the LHC and RHIC energies. The article is structured as follows. In Section 2, studies of heavy-flavor production mechanisms in pp and p–A collisions using angular correlation techniques are discussed. The fragmentation of heavy quarks into final-state jets in pp and p–A collisions was studied using angular correlations of heavy-flavor hadrons and charged particles, as discussed in Section 3. In Section 4, new insight into heavy quark propagation and energy loss in the QGP obtained using correlations of heavy quarks is discussed. In recent years, questions have been raised about the possible formation of a QGP in smaller collision systems, such as in pp and p–A collisions, due to the observation of a “long-range ridge structure” in two-particle azimuthal correlations of light-flavor particles. To further investigate this possibility, measurements of azimuthal correlations of heavy-flavor particles and charged hadrons were performed, from which the azimuthal anisotropy of heavy-flavor particles was extracted. These studies are reviewed in Section 5.

2. Study of Heavy Quark Production Mechanisms

In high-energy hadronic collisions, heavy quarks (charm and beauty) are mainly produced in hard parton scattering processes. An inclusive production of several heavy-flavor hadrons has been measured in experiments at the LHC and at lower energies, and is compared with pQCD calculations such as FONLL and GM-VFNS [3,33–37]. Exclusive measurements of heavy-flavor correlations, e.g., as a function of the azimuthal angle between heavy-flavor hadrons, φ , are a stronger test of the heavy quark pair (QQ) production mechanisms than single-particle inclusive distributions. At leading order (LO), $2 \rightarrow 2$ in α_s for the parton interaction sub-processes, the heavy quark pairs will be emitted with a back-to-back topology in azimuth due to momentum conservation. At next-to-leading order (NLO), $2 \rightarrow 2 + n$ ($n \geq 1$), additional partons are emitted, resulting in different topologies of the produced heavy quarks [65,66]. Experimentally, correlation patterns of heavy quarks can be assessed with measurements of angular correlations of heavy-flavor particle pairs, as discussed below.

Measurements of angular correlations of heavy-flavor particles in proton–proton (pp) collisions that fit this context were performed by the PHENIX Collaboration at RHIC at $\sqrt{s} = 200$ GeV [68], and by ATLAS [69], CMS [70], and LHCb [71,72] Collaborations at the LHC at $\sqrt{s} = 7$ and 8 TeV, and in proton–lead (p–Pb) collisions at $\sqrt{s_{NN}} = 8.16$ TeV by the LHCb Collaboration [73]. The goal of these measurements is to understand the correlated production of heavy quark pairs, and to test theoretical calculations at higher orders.

The PHENIX Collaboration performed a study of azimuthal correlations of $\mu\mu$ pairs from heavy-flavor hadron decays in pp collisions at $\sqrt{s} = 200$ GeV at forward and backward rapidity ($1.2 < |\eta| < 2.2$) [68]. The $\mu\mu$ pairs have contributions from $c\bar{c}$, $b\bar{b}$, Drell–Yan, and hadronic pairs (kaons and pions), which are distinguished using template fits to opposite- and like-sign spectra in mass and transverse momentum, p_T . While the decays from $c\bar{c}$ and Drell–Yan mechanisms contribute to opposite-sign pairs only ($\mu^+\mu^-$), decays from $b\bar{b}$ pairs populate the like-sign distribution ($\mu^\pm\mu^\pm$) as well, either because of combination of $B \rightarrow \mu$ and $B \rightarrow D \rightarrow \mu$ decay chains or decays following $B^0\bar{B}^0$ oscillations. Different components contribute with different relative abundances to the muon pair continuum in different mass regions of $\mu^+\mu^-$ and $\mu^\pm\mu^\pm$ pairs. The contributions from $c\bar{c}$ and $b\bar{b}$ are separated considering mass regions where they dominate. This corresponds to $1.5 < m_{\mu^+\mu^-} < 2.5$ GeV/ c^2 for charm, and $3.5 < m_{\mu^\pm\mu^\pm} < 10$ GeV/ c^2 for beauty. The azimuthal opening angle distributions for $\mu\mu$ pairs from $c\bar{c}$ and $b\bar{b}$ decays, for muons with $p > 3$ GeV/ c and $1.2 < |\eta| < 2.2$, are shown in Figure 1. The measurements are compared with model calculations based on PYTHIA [74] and POWHEG [75]. The distribution from PYTHIA describes the data in the probed kinematic range for both $c\bar{c}$ and $b\bar{b}$. While the distribution from POWHEG simulations for $c\bar{c}$ are wider compared to the one from PYTHIA, they are more similar for $b\bar{b}$. Both PYTHIA and POWHEG use the PYTHIA fragmentation scheme and very similar parton distribution functions. The differences between the model calculation for charm–origin correlations could originate from the different underlying correlation between c and \bar{c} quarks emerging from the hard process. While POWHEG implements NLO calculations for evaluating the hard parton scattering matrix elements, PYTHIA evaluates them at LO and mimics the NLO processes in the parton shower.

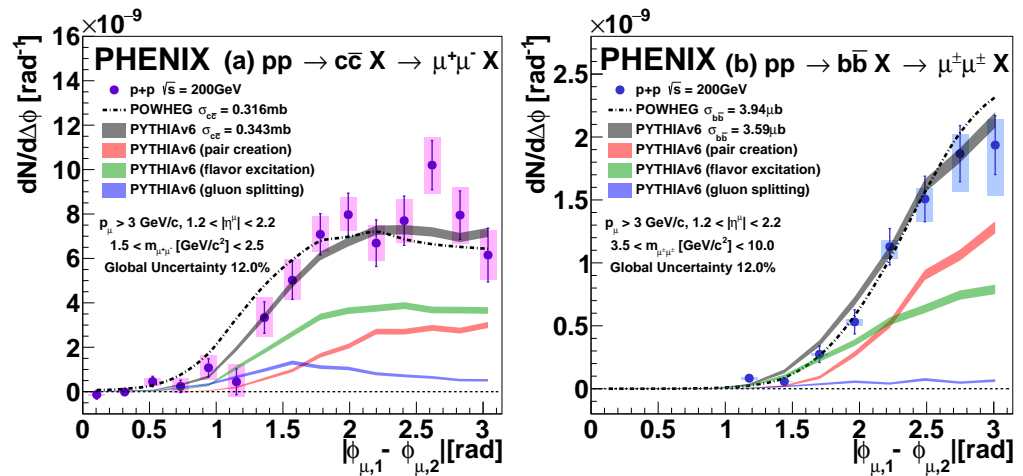


Figure 1. The azimuthal opening angle distribution of $\mu\mu$ pairs from $c\bar{c}$ (a) and $b\bar{b}$ (b) decays, measured by the PHENIX Collaboration in pp collisions at $\sqrt{s} = 200$ GeV. The data are compared with the distributions calculated with POWHEG and PYTHIA event generators, where the different production mechanisms are also shown separately [68].

To study the multiple production of charm states in a single pp collision, and understand contributions from double parton scattering (DPS) [76–79], the LHCb Collaboration performed measurements of J/ψ production with an associated open-charm hadron (either D^0 , D^+ , D_s^+ or Λ_c^+), and of double open-charm hadron production in pp collisions at $\sqrt{s} = 7$ TeV [71]. These measurements can probe the quarkonium production mechanism [80] and contributions from the intrinsic charm content of the proton [81] to the total cross-section. The J/ψ and open-charm hadron production is denoted as $J/\psi C$ and the double open-charm hadron production as CC , with a control channel using $c\bar{c}$ events denoted as $C\bar{C}$. The measurements are performed in the LHCb fiducial region ($2 < y^{J/\psi} < 4.5$, $p_T^{J/\psi} < 10$ GeV/ c). The azimuthal angle and rapidity distributions between J/ψ and charm

hadrons in $J/\psi C$ events are shown in Figure 2. No significant azimuthal correlation is observed and the Δy distribution shows a triangular shape consistent with what is expected when the rapidity distribution for single-charm hadrons is flat and in the absence of physical correlations between the two particles. A similar trend in $\Delta\phi$ and Δy is observed for CC pairs, with a slightly enhanced back-to-back configuration in $\Delta\phi$, visible for CC pairs compared to $J/\psi C$ pairs. The absence of significant azimuthal or rapidity correlations for $J/\psi C$ pairs could support the DPS hypothesis, but no comparison with model predictions are provided in the publication. In contrast, $C\bar{C}$ pairs show a clear enhancement in the $\Delta\phi$ distribution at small $|\Delta\phi|$, consistent with $c\bar{c}$ production via the gluon splitting mechanism at NLO [82], together with a significant contribution of back-to-back correlations, consistent with the topology of an LO production, as shown in Figure 3. This figure also shows a small enhancement at small Δy , which is also consistent with gluon splitting topologies, unlike the distributions for CC and $J/\psi C$ pairs.

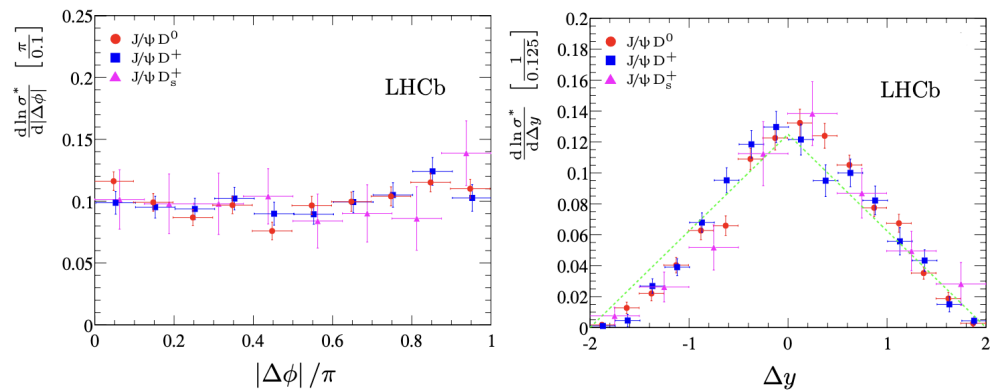


Figure 2. Distributions of the azimuthal angle (left) and rapidity (right) differences between J/ψ and different charm mesons (C) for $2 < y^{J/\psi}, y^C < 4$, $p_T^{J/\psi} < 12 \text{ GeV}/c$, and $3 < p_T^C < 12 \text{ GeV}/c$, in pp collisions at $\sqrt{s} = 7 \text{ TeV}$, measured by the LHCb Collaboration. The dashed line in the right plot shows the expected Δy distribution for uncorrelated pairs [71].

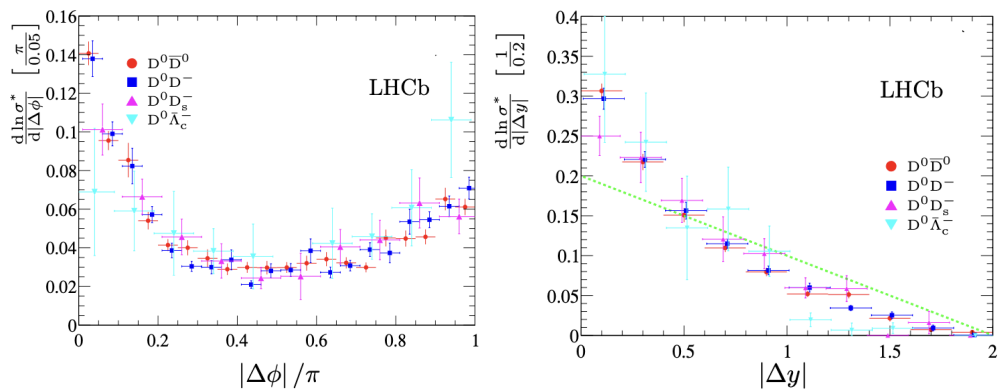


Figure 3. Distributions of the azimuthal angle (left) and rapidity (right) differences between charm and anti-charm mesons ($C\bar{C}$), for $2 < y^C < 4$ and $3 < p_T^C < 12 \text{ GeV}/c$ in pp collisions at $\sqrt{s} = 7 \text{ TeV}$, measured by the LHCb Collaboration. The dashed line in the right plot shows the expected Δy distribution for uncorrelated pairs [71].

The production of heavy quarks via single parton scattering (SPS) or via DPS can be affected by cold-nuclear-matter effects [56–66] in proton–ion collisions. In particular, DPS production can be very sensitive to the nuclear PDF in p – A as it involves two parton pairs, including possible dependence on the position of the partons inside the nucleus [83]. Based on the Glauber model [84], in the absence of nuclear effects, the SPS production cross-section is expected to scale with the ion mass number. DPS production, on the other hand, is enhanced compared to a mass number scaling due to collisions of partons from

two different nucleons in the ion, and the enhancement factor is about three in proton–lead (p–Pb) collisions [79,85,86]. This feature was studied by the LHCb Collaboration by measuring the production of D meson pairs (D^0, D^+, D_s^+ mesons), as well as J/ψ D meson pairs in p–Pb collisions at $\sqrt{s_{NN}} = 8.16$ TeV [73]. Like-sign (LS) pairs, where two hadrons have the same charm quark charge, and opposite-sign (OS) pairs, where they have opposite charm charge, are considered. Pairs of OS charm hadrons are dominantly produced from a $c\bar{c}$ pair via SPS; thus, the kinematics of the two hadrons are correlated, while DPS leads to both correlated and uncorrelated OS pairs. The kinematic correlation between the two charm hadrons was investigated using the two-charm invariant mass (m_{DD}) and their relative azimuthal angle $\Delta\phi$. The $\Delta\phi$ distribution for LS D^0D^0 pairs and OS $D^0\bar{D}^0$ pairs for all p_T and when requiring a $p_T^{D^0} > 2$ GeV/c condition is shown in Figure 4. Without the p_T condition, the $\Delta\phi$ distribution is almost uniform for both LS and OS pairs, similar to that predicted by PYTHIA8 simulation. However, with the $p_T^{D^0} > 2$ GeV/c condition, the $D^0\bar{D}^0$ pair distribution shows an enhancement at $\Delta\phi \sim 0$, while the D^0D^0 distribution is consistent with being flat; both are inconsistent with the predictions from PYTHIA8 simulations. The flat $\Delta\phi$ behavior for D^0D^0 is qualitatively consistent with a large DPS contribution in LS pair production. The effective cross-section and nuclear modification factor for LS charm hadron pairs were also measured and were reported to be compatible with the expected enhancement by a factor of 3 for a DPS-over-SPS production ratio from pp to p–Pb collisions [73].

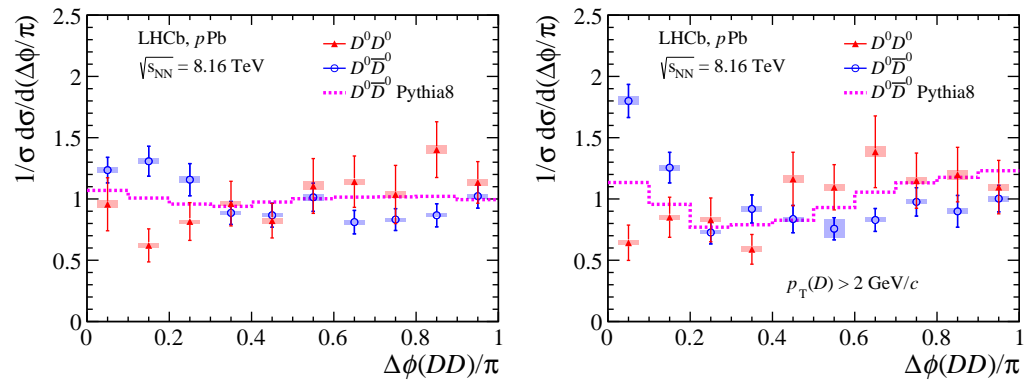


Figure 4. The $\Delta\phi$ distribution for D^0D^0 (red) and $D^0\bar{D}^0$ (blue) pairs measured by the LHCb Collaboration in p–Pb collisions at $\sqrt{s_{NN}} = 8.16$ TeV, compared with PYTHIA8 simulations (magenta dashed line), without (left) and with (right) a $p_T^{D^0} > 2$ GeV/c requirement. Vertical bars (filled box) represent statistical (systematic) uncertainties [73].

The production of beauty quark pairs was studied by the ATLAS [69], CMS [70], and LHCb [72] Collaborations by measuring correlations of particles with beauty content. The ATLAS experiment measured the production of two b-hadrons, where one decays to $J/\psi(\rightarrow \mu\mu) + X$ and the other to $\mu + Y$, resulting in three muons in the final state in pp collisions at $\sqrt{s} = 8$ TeV [69]. To probe the b-hadron production, several differential cross-sections were measured, such as $\Delta\phi(J/\psi, \mu)$, $\Delta y(J/\psi, \mu)$, separation between the J/ψ and the third muon in azimuth–rapidity plane $\Delta R(J/\psi, \mu)$, mass of the three muon system $m(J/\psi, \mu)$, etc. Since this review focuses on the angular correlation measurements, the $\Delta\phi$ and Δy distributions compared with predictions from PYTHIA8.2 [87], HERWIG++ [88], MADGRAPH5-AMC@NLO+PYTHIA8 [89], and SHERPA [90,91] Monte Carlo generators are shown in Figure 5. The $\Delta\phi$ prediction from HERWIG++ provides the best description of the data compared to others. The trends seen in $\Delta R(J/\psi, \mu)$ are similar to $\Delta\phi(J/\psi, \mu)$. For $\Delta y(J/\psi, \mu)$ distribution, the MADGRAPH5-AMC@NLO+PYTHIA8 and SHERPA predictions provide a good description of the data, while PYTHIA8 and HERWIG++ fail to describe data at high $\Delta y(J/\psi, \mu)$. Different kinematic correlation observables can thus provide enhanced sensitivity to the underlying model differences and allow us to discriminate among them.

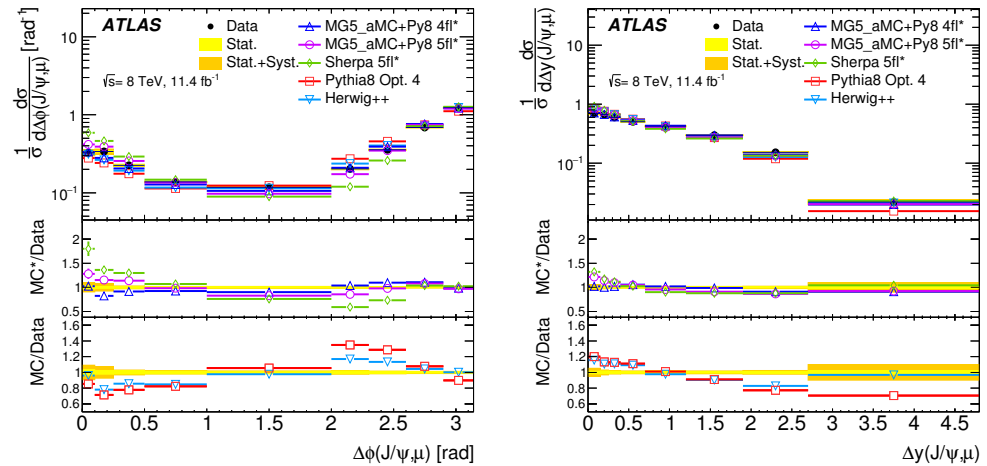


Figure 5. Normalized differential cross-section of J/ψ and μ pairs as a function of $\Delta\phi(J/\psi, \mu)$ (left) and $\Delta y(J/\psi, \mu)$ (right) in pp collisions at $\sqrt{s} = 8$ TeV, measured by the ATLAS Collaboration. Data are compared with predictions from PYTHIA8.2, HERWIG++, MADGRAPH5-AMC@NLO+PYTHIA8, and SHERPA Monte Carlo generators. The model-to-data ratios are shown in the bottom panels [69].

The azimuthal angular correlations between beauty hadron pairs, called here “B hadrons”, were measured by the CMS Collaboration in pp collisions at $\sqrt{s} = 7$ TeV, where the B hadrons were identified by the presence of displaced secondary vertices (SVs) from their decays [70]. The flight direction of the B hadron is defined by the direction connecting the primary and the secondary vertices. The angular correlation variables between B and \bar{B} hadrons, in events with two SVs, are calculated using their flight directions. While a back-to-back configuration is expected for LO processes, the $B\bar{B}$ production at small opening angles directly relates to collinear emission processes at higher order ($g \rightarrow b\bar{b}$). The $B\bar{B}$ pair production cross-section as a function of $\Delta\phi$ for three different energy scales, characterized by the leading jet p_T , is presented in Figure 6 (left plot). A significantly large cross-section is observed at small angles, with values higher than at large angles, whose relative contribution increases with increasing jet p_T . At higher energy scales, larger contributions from higher-order processes, for example, gluon radiation, are expected, resulting in more gluon splitting into $B\bar{B}$ pairs. PYTHIA predictions [74] are normalized to the region $\Delta\phi > 3/4\pi$, where the theoretical calculation is more reliable as the cross-section is expected to be dominated by the LO diagrams. Data and theory predictions from MADGRAPH [92,93], MC@NLO [94–96], and CASCADE [97] models are compared, with respect to the PYTHIA prediction, as shown in Figure 6 (right plot). It is observed that none of the predictions describe the data particularly well, in particular for the collinear region. The data lie between MADGRAPH and PYTHIA curves.

The azimuthal and rapidity correlations in $b\bar{b}$ production in the forward rapidity region were investigated by LHCb experiment in pp collisions at $\sqrt{s} = 7$ and 8 TeV by correlating pairs of beauty hadrons [72]. The beauty hadrons were reconstructed via their inclusive decays into J/ψ mesons ($b \rightarrow J/\psi X$). The $|\Delta\phi^*|$ and $|\Delta\eta^*|$ variables, i.e., the difference in azimuthal angle ϕ^* and pseudorapidity η^* between the two beauty hadrons, estimated from the direction of the vector from the primary vertex to the decay vertex of the J/ψ meson, were measured. The normalized differential production cross-sections as a function of $|\Delta\phi^*|$ for $p_T^{J/\psi} > 3$ and > 7 GeV/c are shown in Figure 7. No significant enhancement is observed at small $|\Delta\phi^*|$ at low $p_T^{J/\psi}$, but a peak starts to appear in that region at higher $p_T^{J/\psi}$, due to higher contribution from NLO processes. This observation is similar to the CMS measurement [70] from B hadron pairs. Compared to open-charm mesons [71], the small angle enhancement is observed at higher p_T since the contribution from processes like gluon splitting requires higher energy scales to produce higher-mass b quarks. The $|\Delta\phi^*|$ distributions are compared with LO and NLO expectations from PYTHIA [87] and POWHEG [98] MC simulations, respectively. The prediction from an

artificial data-driven model assuming uncorrelated $b\bar{b}$ production is also shown. At lower p_T^J/ψ , the PYTHIA prediction describes the data well, suggesting that NLO effects in $b\bar{b}$ production in this kinematic region are small compared with the experimental precision. At higher p_T^J/ψ , data are instead better described by POWHEG calculations.

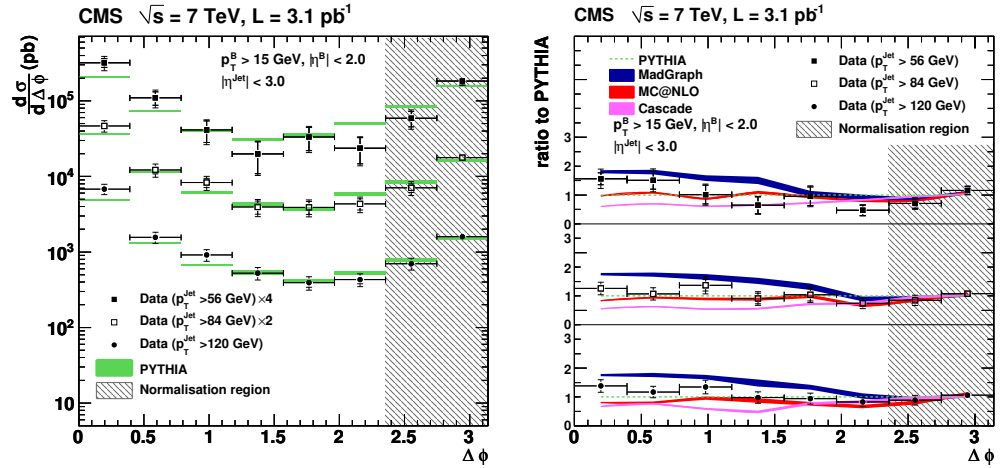


Figure 6. (Left) Differential $B\bar{B}$ production cross-section as a function of $\Delta\phi$ for three leading jet p_T regions in pp collisions at $\sqrt{s} = 7$ TeV, measured by the CMS Collaboration, and compared to PYTHIA predictions. For the data points, the error bars show the statistical (inner bars) and the total (outer bars) uncertainties. (Right) Ratio of the cross-section as a function of $\Delta\phi$ for data, MADGRAPH, MC@NLO, and CASCADE models, with respect to PYTHIA predictions, for the three leading jet p_T regions. The simulations (shaded bands) are normalized to the region $\Delta\phi > \frac{3}{4}\pi$. The widths of the shaded bands indicate the statistical uncertainties of the predictions [70].

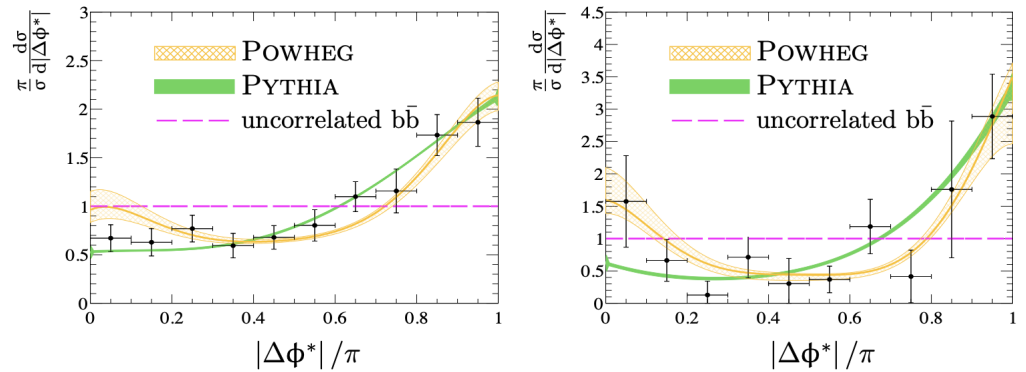


Figure 7. Normalized differential production cross-sections of B hadron pairs as a function of $|\Delta\phi^*|$ for $p_T^J/\psi > 3$ GeV/c (left) and $p_T^J/\psi > 7$ GeV/c (right) in pp collisions at $\sqrt{s} = 7$ and 8 TeV, measured by the LHCb Collaboration. The data are compared with POWHEG and PYTHIA predictions. The expectations for uncorrelated $b\bar{b}$ production are shown by the dashed magenta line. The uncertainties in the model predictions due to the choice of factorization and re-normalization scales are shown as solid bands [72].

3. Characterizing the Fragmentation of Heavy Quarks into Jets

In the absence of a surrounding nuclear medium, the process of hadronization of a heavy quark into colorless hadrons is generally described as a non-perturbative fragmentation of the quark into lower-momentum partons that, in the final state, are converted into colorless hadrons. At high p_T , this process produces a spray of particles traveling in a similar direction, called “jet”. A thorough characterization of the in-vacuum heavy quark fragmentation process can be obtained by measuring the angular correlation distribution between heavy-flavor “trigger” particles and other “associated” charged particles produced

in the same event, in pp collisions. Under the assumption of a leading-order production process of the quark–anti quark pair, two peaks can be observed in the correlation distribution for $\Delta\varphi \approx 0$ (“near-side” peak) and $\Delta\varphi \approx \pi$ (“away-side” peak). These peaks are produced by particles in the jets emerging from the heavy quark pair fragmentation, which are approximately collinear with the quark’s directions. While the presence of next-to-leading-order heavy quark production processes—that are quite significant at LHC energies—breaks this picture for the away-side peak, the features of the near-side peak retains a clear connection to the original parton shower features. In particular, studying the peak shape, its particle content and composition, and the p_T distribution of its constituents for different kinematic regimes allows us to retrieve information about the heavy quark fragmentation process. By comparing the features of the near-side peak with predictions from theoretical models or Monte Carlo simulations that implement different techniques to model the heavy quark fragmentation (and, in general, for the description of processes involving heavy quarks), it becomes possible to discriminate models and to validate those that yield the most accurate description of the data. In general, these comparisons allow us to determine constraints on the model configuration, parameters, and tuning.

In the presence of a deconfined medium, like the quark–gluon plasma produced in ultra-relativistic heavy-ion collisions, the hadronization process can be modified with respect to in-vacuum fragmentation. In particular, an additional hadronization mechanism, the coalescence, is expected to play a prominent role, where neighboring quarks in phase space recombine into higher-momentum bound hadrons [99–101]. The role of coalescence, as a competing mechanism to the quark fragmentation, is already hinted from studies of charm/hadron production ratios in heavy-ion collisions [42,102,103]. The modified hadronization should result in a significant modification of the final-state jet produced by the heavy quark. Such a modification can be evidenced and quantified by comparing the properties of the near-side peak of angular correlations between heavy-flavor particles and other particles, in Pb–Pb collisions to the reference system of pp collisions.

In this context, the ALICE Collaboration measured the azimuthal correlation distribution between D mesons and charged particles in pp collisions at $\sqrt{s} = 13$ TeV [104]. A weighted average of the correlation distributions of D^0 , D^+ , and D^{*+} mesons was considered, at central rapidity ($|y| < 0.5$) in the transverse momentum range $3 < p_T^D < 36$ GeV/c, while the associated particles were reconstructed in $\eta < 0.8$ for $p_T^{\text{assoc}} > 0.3$ GeV/c. Only pairs with $|\Delta\eta| < 1$ were considered. The correlation distribution was fitted with a function composed of a generalized Gaussian, describing the near-side peak, a Gaussian describing the away-side peak, and a constant, accounting for the physically uncorrelated pairs, assumed to be flat along $\Delta\varphi$. This model allowed for obtaining a quantitative description of the properties of the peaks in terms of their integral (peak yield) and width for the different kinematic ranges studied. The correlation distributions and the near- and away-side peak properties were found to be consistent with the results obtained for lower center-of-mass energies ($\sqrt{s} = 5.02$ TeV [105] and $\sqrt{s} = 7$ TeV [106]). The similarity of the near-side features implies that the charm quark fragmentation process is independent of the collision energy, at least for the energy ranges studied at the LHC.

Focusing further on the near-side correlation peak properties, a significant increase in its yield with increasing values of p_T^D was observed. This can be explained by the corresponding increase in charm quark p_T , on average, which implies that a larger amount of energy is available for the production of associated particles during its fragmentation. At the same time, a narrowing of the peak width can be observed when probing larger D meson p_T . Such an effect is related to the increased Lorentz boost of the charm quark, leading to a more collimated spray of particles produced by the fragmentation in the laboratory frame.

A comparison of the ALICE results with several model predictions, including PYTHIA8 [87] with 4C tune, POWHEG+PYTHIA8 [107,108] using hard parton scattering matrix elements at LO or at NLO accuracy, HERWIG 7 [109], and EPOS 3.117 [110,111], is shown in Figure 8. In particular, the near-side yields (widths) are shown in the first (third) row,

and their model-to-data ratios are reported in the second (fourth) row. Although all the models are able to reproduce the increase in peak yields for increasing D meson p_T , the strength of such a dependence, and the absolute values of the yields differ substantially among the various models. In particular, an ordering is found for the predicted near-side yields, with the lowest values observed for HERWIG (which tends to underestimate the data for $p_T^D < 16$ GeV/c), followed by PYTHIA, POWHEG+PYTHIA, and EPOS, which overestimates the yield values in most of the p_T intervals. Among the tested predictions, POWHEG+PYTHIA8 and PYTHIA generators are those that better reproduce the measured data and are thus more suited to quantify the number of particles emerging from charm quark fragmentation in association with the D meson. The various model predictions for the near-side widths show instead similar values in all the studied kinematic ranges, and overall, all models are consistent with the ALICE measurements within the uncertainties.

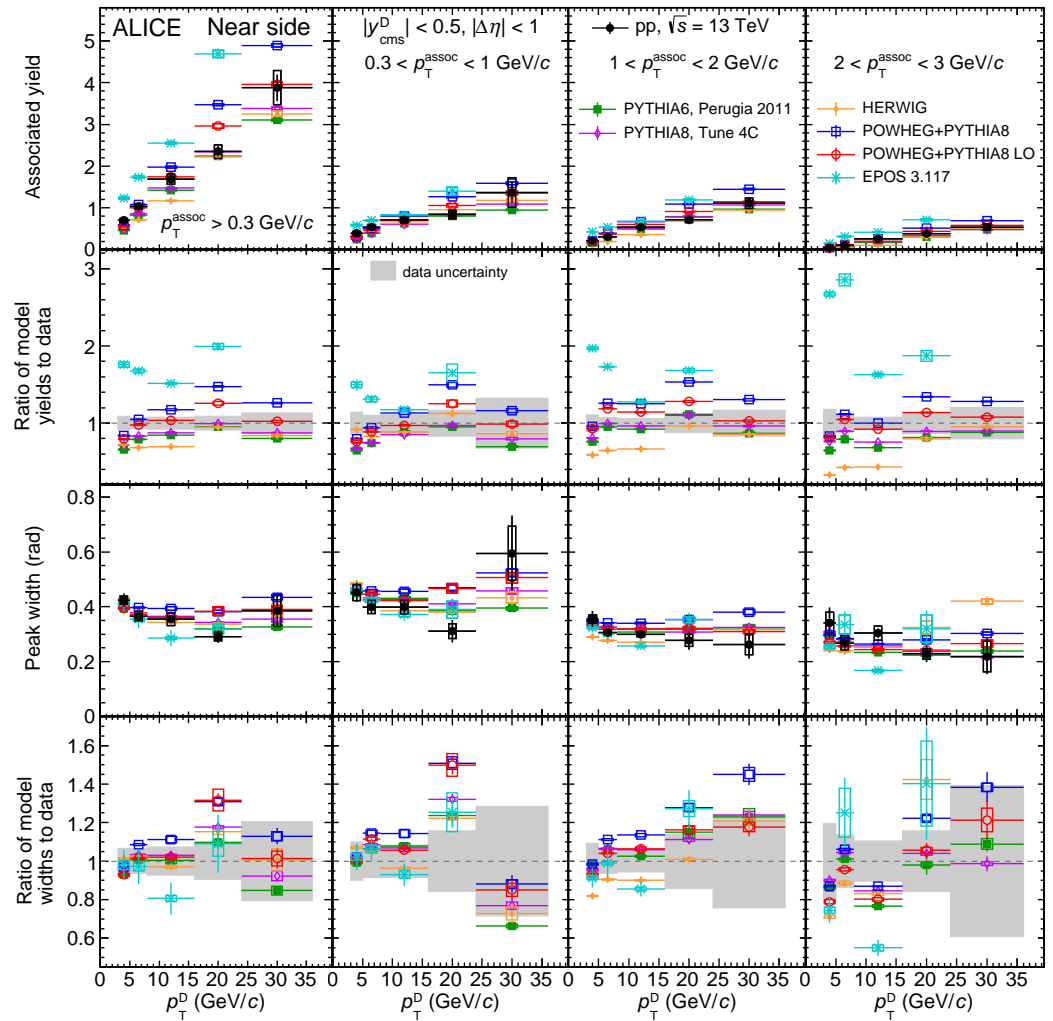


Figure 8. First (third) row: near-side associated yields (widths) of azimuthal correlation distributions between D mesons and charged particles in pp collisions at $\sqrt{s} = 13$ TeV, measured by the ALICE Collaboration and predicted by several models, as a function of p_T^D , for different p_T^{assoc} intervals. Second (fourth) row: model-to-data ratios of near-side associated yields (widths) of D meson and charged particle correlation distributions [104].

The in-vacuum behavior of heavy quarks, including their parton shower and hadronization, can be altered in the presence of a nuclear medium. Measurements in p–Pb collisions are sensitive to the influence of cold-nuclear-matter effects on the heavy quarks, and can thus act as a reference to help disentangle and understand those modifications that are instead induced by the quark–gluon plasma environment in heavy-ion collisions. To probe

whether cold-nuclear-matter effects play a role in the charm quark fragmentation process, the ALICE Collaboration has measured the azimuthal correlation distribution of D mesons and charged particles at mid-rapidity in multiplicity-integrated p–Pb collisions at $\sqrt{s_{NN}} = 5.02$ TeV. The same analysis technique used in the pp collision results discussed above [104] was exploited, with the same kinematic coverage. The shape of the correlation distribution and its evolution with transverse momenta of D mesons and associated charged particles were compared, and found to be fully consistent, with those obtained in pp collisions at the same center-of-mass energy, as shown in Figure 9. Specifically, the comparison of the near-side peak yields and widths in the two collision systems is shown in Figure 10. No modification of the near-side yield values, and the same increase in D meson p_T measured in pp collisions were observed. For the near-side widths, the tendency for a collimation of the peak at larger p_T^D is possibly less pronounced, but pp and p–Pb results are similar within uncertainties. From these results, no indications for a modified fragmentation process of charm quarks due to cold-nuclear-matter effects, or for any alteration of the charm hadronization mechanism, are observed.

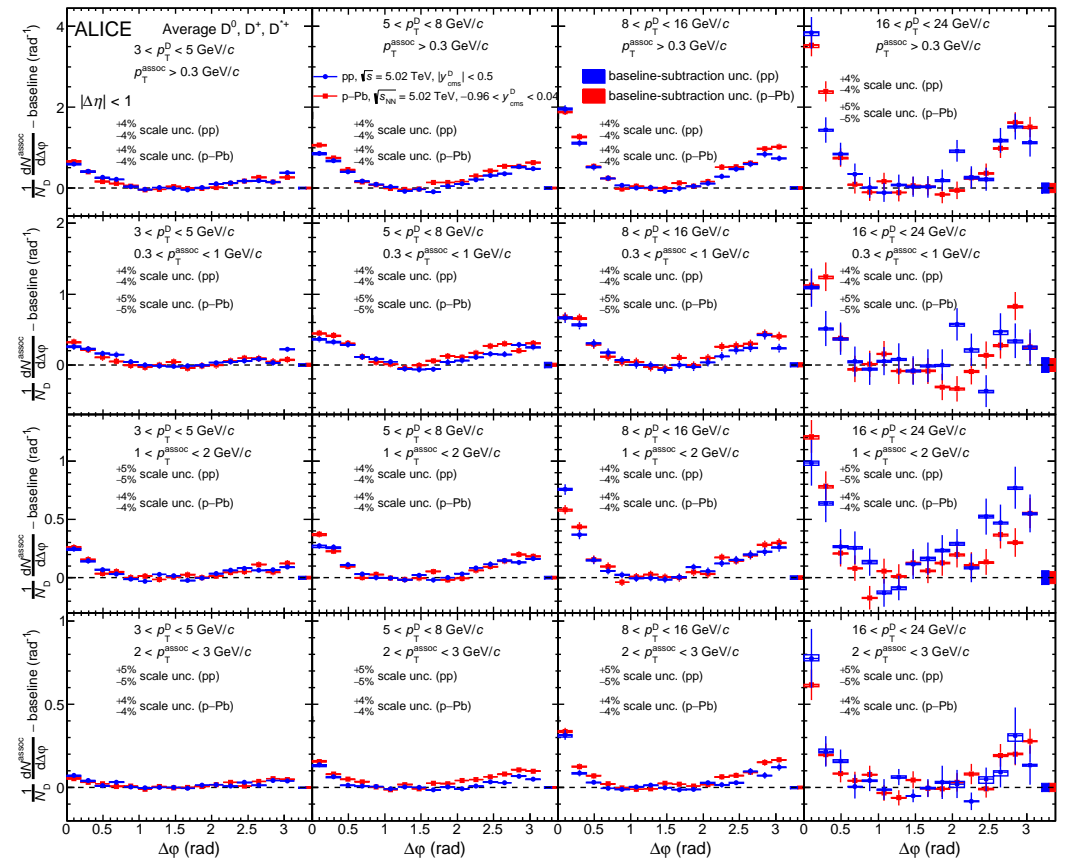


Figure 9. Comparison of the azimuthal correlation distributions between D mesons and charged particles in pp and p–Pb collisions at $\sqrt{s_{NN}} = 5.02$ TeV, for the kinematic ranges studied by the ALICE Collaboration [105].

In recent years, the high-energy nuclear physics community’s interest in the dynamics of partons produced in small collision systems at very high multiplicities has grown. Although no clear modifications of high- p_T particle production yields (beyond what is expected from nuclear modification of the parton distribution functions) have been measured, several indications of collective-like effects have been observed at the LHC in the recent past, including measurements in the heavy-flavor sector [112–115] as discussed in more detail in Section 5. In general, the evaluation of flow coefficients in small collision systems is based on two- or multi-particle correlation techniques, and relies on the assumption that the contribution of jet peaks to the correlation distribution has negligible dependence on

the event multiplicity, and can be removed from the high-multiplicity correlation distribution by measuring it in low-multiplicity collisions, where no collective effects are present. Such an assumption can be tested by studying the jet fragmentation properties at different event multiplicities in small collision systems. In this regard, the ALICE experiment has studied the dependence of the azimuthal correlation distribution of D mesons and charged particles, and of its near-side peak features on the event multiplicity in pp collisions at $\sqrt{s} = 13$ TeV [104] and p–Pb collisions at $\sqrt{s_{NN}} = 5.02$ TeV [105]. The results show that, within the experimental uncertainties, the near-side peak yields and widths are consistent for all the multiplicity ranges studied, suggesting a similar fragmentation of charm quark into final-state D mesons and other associated particles that is independent of the surrounding event activity.

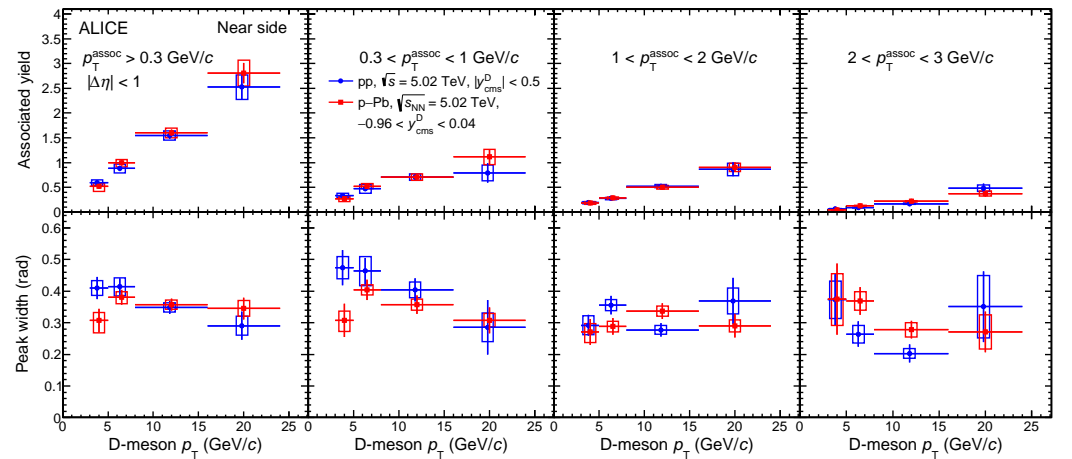


Figure 10. Comparison of near-side associated yields (**first row**) and widths (**second row**) of D meson and charged-particle azimuthal correlation distributions in pp and p–Pb collisions at $\sqrt{s_{NN}} = 5.02$ TeV, measured by the ALICE Collaboration, as a function of p_T^D , for different p_T^{assoc} intervals [105].

As an alternate approach for investigating the in-vacuum heavy quark fragmentation and possible impact of cold-nuclear-matter effects, the ALICE Collaboration has measured angular correlations between electrons produced from decays of heavy-flavor hadrons (called herein “heavy-flavor decay electrons” for simplicity) and charged particles in pp and p–Pb collisions at $\sqrt{s_{NN}} = 5.02$ TeV [116]. Compared to correlations with D mesons as heavy-flavor trigger particles, heavy-flavor decay electrons have a looser connection with the direction and momentum of the original heavy quark because of the hadron decay kinematics. On the other hand, such an analysis profits from a larger statistical sample, which allows for the transverse momentum range of the associated charged particles to be significantly extended (up to 7 GeV/c). Additionally, at high p_T , the sample of heavy-flavor decay electrons is dominated by those from beauty quarks, which enables the study of beauty quark fragmentation when focusing in the p_T region above 7 GeV/c. The study is performed at mid-rapidity, in the electron p_T range $4 < p_T < 16$ GeV/c, considering pairs with pseudorapidity displacement $|\Delta\eta| < 1$. Also, in this case, a quantitative assessment of the quark-into-jet fragmentation is performed by fitting the correlation distribution with a function, composed as the sum of two von Mises functions, to model the near- and away-side peaks, plus a constant term.

In Figure 11, the near-side peak yields and widths measured by ALICE in pp collisions are compared with predictions from the PYTHIA8 event generator [87] with the Monash tune and from the EPOS3 event generator [110,111]. Two transverse momentum ranges are considered for the electrons, i.e., $4 < p_T^e < 7$ GeV/c, with a balanced contribution between charm and beauty origins, and $7 < p_T^e < 16$ GeV/c, where the large majority of electrons are produced by beauty hadron decays. For both p_T^e ranges, the largest contribution of charged particles produced in the fragmentation is present below 2 GeV/c, pointing to a dominance of soft particle production from the quark fragmentation. The fraction of high-

p_T -associated particles significantly increases when probing the high- p_T^e range, despite remaining subdominant. In addition, the absolute value of the yields is substantially larger in the $7 < p_T^e < 16$ GeV/ c range compared to the $4 < p_T^e < 7$ GeV/ c interval. This is similar to what was observed for the D meson correlation with charged particles, and can be ascribed to the larger average energy of heavy quarks producing higher- p_T electrons, which generally leads to an increased multiplicity of fragmenting particles. The values of the near-side widths are fully consistent between the two p_T^e ranges, and point towards an emission of harder particles more collinear with the electron, while softer particles are emitted at larger angles. Both PYTHIA8 and EPOS3 generators can successfully describe the near-side yield values, with EPOS3 predicting larger values for high p_T of the associated tracks. While PYTHIA8 also correctly reproduces the near-side widths, EPOS3 tends to overestimate them at high p_T^{assoc} , predicting a flatter trend than what is observed in the data. The away-side peak yields and widths are also shown in the same figure. The away-side peak has a connection to the fragmentation of the heavy quark that did not lead to the production of the trigger particle, though such a connection is less direct than that of the near-side peak. In contrast, the away-side peak features are sensitive to the production mechanisms of the heavy quark pairs, which induce different angular topologies, as discussed in Section 2. Very similar considerations as for the near-side can be drawn for the away-side peak yield values. The away-side peak widths are about a factor 2 larger than those measured for the near-side, with significantly larger uncertainties. This is mainly due to the NLO production processes of heavy quarks, which break the back-to-back topology of the quark pairs, and to the additional smearing with respect to the original quark-anti-quark correlation distribution induced by the hadronic decays.

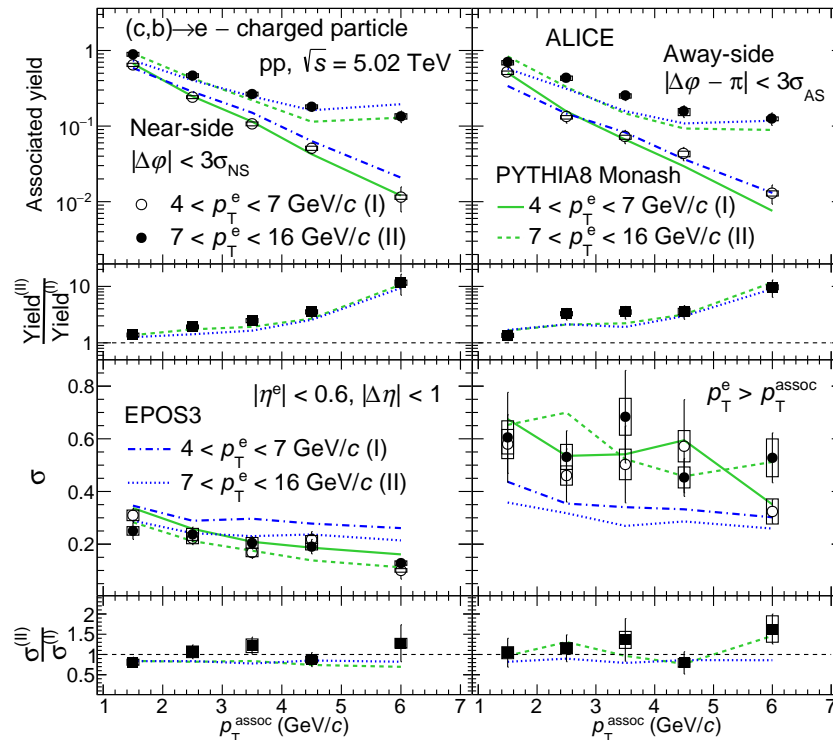


Figure 11. Near- (left) and away-side (right) associated peak yields (top) and widths (bottom) of correlation distributions between heavy-flavor hadron decay electrons and charged particles in pp collisions at $\sqrt{s_{NN}} = 5.02$, measured by the ALICE Collaboration and predicted by PYTHIA8 and EPOS3. The results are reported for two p_T ranges, and the insets show the ratios of the observable distributions in higher to lower p_T ranges considered [116].

In the same publication, the near- and away-side peak properties of the azimuthal correlation between heavy-flavor decay electrons and charged particles in pp and p-Pb

collisions at $\sqrt{s_{NN}} = 5.02$ TeV are compared for $4 < p_T^e < 12$ GeV/c and various charged-particle transverse momentum intervals. From the comparison, shown in Figure 12, fully compatible peak yields and widths are found in the two collision systems. This observation holds also for the high p_T^{assoc} intervals not covered by previous D-hadron and charged particle correlation measurements [105]. These results thus complement the findings observed for that analysis, and confirm that the charm quark fragmentation is unaffected by the presence of cold-nuclear-matter effects. No strong conclusions can be drawn for the beauty, given the lack of a specific comparison in a high- p_T^e interval.

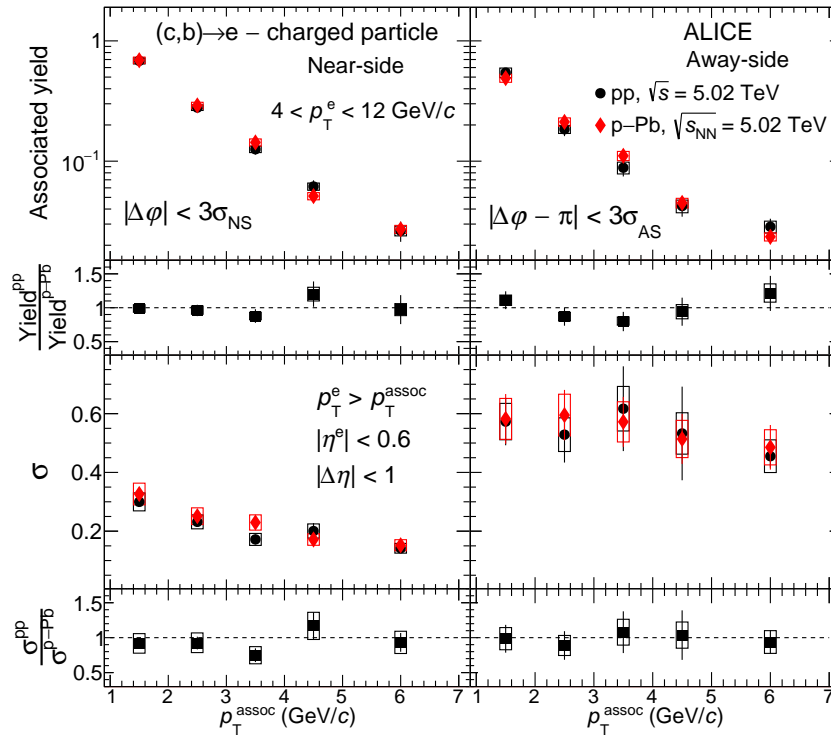


Figure 12. Comparison of near- (left) and away-side (right)-associated peak yields (top) and widths (bottom) from the azimuthal correlation distributions of heavy-flavor hadron decay electrons and charged particles in pp and p–Pb collisions at $\sqrt{s_{NN}} = 5.02$ TeV, measured by the ALICE Collaboration. The insets show the ratios of the observable distribution in pp to p–Pb collisions [116].

4. Heavy Quark Energy Loss and Redistribution

In the presence of the quark–gluon plasma, produced in ultra-relativistic heavy-ion collisions, high- p_T partons produced in hard scatterings with high Q^2 lose energy via medium-induced gluon radiation and collisions with the medium constituents [41,42,117–120]. The processes by which quarks and gluons lose energy in the QGP can modify the internal structure and energy of the jet they produce, a phenomenon known as jet quenching. Through the passage of a jet, the QGP can itself be modified, due to the injection of energy and momentum lost by the jet into the plasma. Because of momentum conservation, a “wake” is induced in the medium as the jet loses energy and momentum, giving the medium a net momentum in the jet direction, yielding a correlation between the bulk dynamics of the medium and the jet direction [121].

Measurements of heavy-flavor jets and particle distributions within jets can be used to constrain parton energy loss mechanisms and to probe how the “lost” energy is redistributed to other partons and the subsequent particles emerging from the collision. In general, these measurements and analyses may lead to a better understanding of heavy quark propagation inside the medium [54,55,122,123]. Such measurements can provide complementary information to the measurements of inclusive heavy-flavor mesons [124], such as the nuclear modification factor [12,125–128] and azimuthal anisotropy [40,43,128–130].

Experiments at RHIC and at the LHC have been performed to investigate the angular correlations of particles associated with heavy-flavor jets. In this section, a brief overview of these measurements is presented.

The PHENIX and STAR Collaborations at RHIC performed studies of angular correlations of electrons from heavy-flavor hadron decays with charged hadrons [131], and angular correlations of D mesons with charged hadrons [132], respectively. In pp collisions, such a correlation distribution is characterized by a jet peak at small $\Delta\phi$ due to particle pairs from the same fragmenting jet, and a jet peak at $\Delta\phi \sim \pi$ due to particle pairs from the fragmenting partons in back-to-back di-jet. Angular correlation measurements in pp collisions are discussed in much detail in the previous Section 3. In nucleus–nucleus collisions, these correlations can provide information about the pattern of energy loss for the back-to-back di-jet system as well as interaction between the fast partons and the medium. The STAR Collaboration performed a study of the centrality dependence of 2D angular correlations ($\Delta\eta, \Delta\phi$) of D^0 mesons ($2 < p_T^{D^0} < 10$ GeV/c), produced by charm quark hadronization after it traverses the medium, and associated charged hadrons (p_T integrated) in Au–Au collisions at $\sqrt{s_{NN}} = 200$ GeV [132]. The main focus of this analysis was the near-side correlation distribution, within $\Delta\phi \leq \pi/2$, measuring the 2D widths of the jet-like peak, and the number of associated charged hadrons associated with the triggered D^0 meson. The near-side yield and peak widths as a function of the collision centrality are shown in Figure 13. The expectations from PYTHIA Monte Carlo simulations [133,134], as a proxy for pp collisions, are also included. The yields and widths in 50–80% central Au–Au collisions are consistent with the PYTHIA predictions within the measured uncertainties. The near-side yields and the widths are observed to increase towards more central Au–Au collisions, similar to what was measured for unidentified di-hadron correlations [135]. The increase in the near-side yields and widths in most central collisions is observed for the same p_T range, where a strong suppression in D^0 meson yield is observed [132], thus bringing complementary information about charm quark propagation in the QGP medium. The measurement could indicate that the energy lost by the charm quark results in the production of new particles accompanying the D meson. The PHENIX Collaboration measured angular correlations of electrons from heavy-flavor hadron decays and charged particles in Au–Au collisions at $\sqrt{s_{NN}} = 200$ GeV in 0–60% centrality, for two trigger electron p_T intervals, $2 < p_T^e < 3$ GeV/c and $3 < p_T^e < 4$ GeV/c, and for different associated charged-particle p_T intervals [131]. To investigate the possible modification of the jet produced by the opposite heavy quark with respect to one producing the trigger electron, the away-side ($1.25 < \Delta\phi < \pi$ rad) yield was obtained. The ratio of the away-side yields in Au–Au collisions to pp collisions is shown in Figure 14. The I_{AA} is the largest and above unity for low associated-particle p_T , and decreases with increasing associated particle p_T . The I_{AA} obtained for correlations of electrons from heavy-flavor hadron decays is compared with the one obtained for unidentified di-hadron correlations with similar average triggered hadron p_T . The I_{AA} for heavy-flavor trigger particles is consistent with that of unidentified charged particles [136], though within large uncertainties, which could indicate similar modifications of charged particles inside light-flavor and heavy-flavor jets due to interaction with the QGP medium.

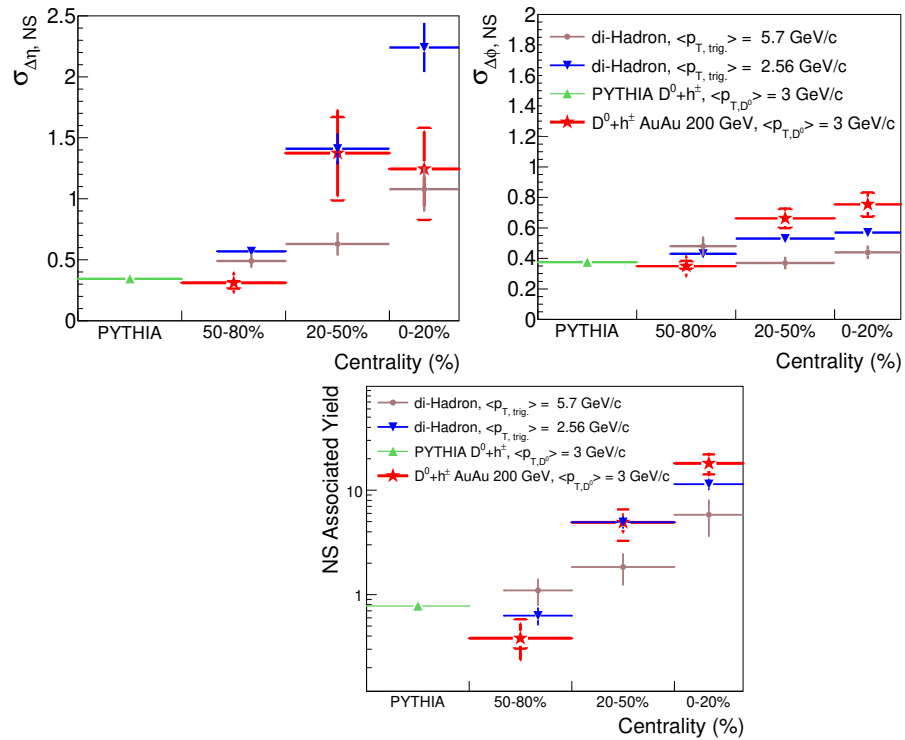


Figure 13. Near-side jet-like peak properties of D^0 meson and hadron correlation distribution in Au–Au collisions at $\sqrt{s_{\text{NN}}} = 200$ GeV, measured by the STAR Collaboration. The near-side peak width along $\Delta\eta$ (top left), width along $\Delta\phi$ (top right), and correlated hadron yield per D^0 trigger (bottom) are shown. PYTHIA predictions and di-hadron results [135] are also included. Vertical bars show the statistical errors, and cross-bars show the systematic uncertainties [132].

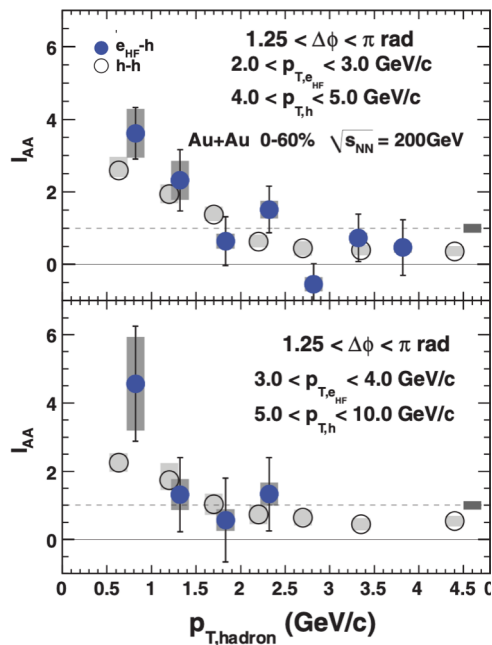


Figure 14. I_{AA} determined from the per-trigger yield of away-side $\Delta\phi$ distribution of electrons from heavy-flavor hadron decays and charged particles in Au–Au collisions at $\sqrt{s_{\text{NN}}} = 200$ GeV, measured by the PHENIX Collaboration. The $\Delta\phi$ range used is $1.25 < \Delta\phi < \pi$ rad. For comparison, the di-hadron I_{AA} values [136] are also shown for trigger p_T selections where the parent heavy meson has similar p_T as the trigger light hadron [131].

Measurements of angular correlations between heavy-flavor mesons and jets can be used to constrain parton energy loss mechanisms and to better understand the heavy quark diffusion (i.e., propagation) inside the QGP medium [122]. The charm quark diffusion with respect to the jet axis was measured by the CMS Collaboration [137] in pp and Pb–Pb collisions, for two D^0 meson p_T intervals, a lower p_T interval of $4 < p_T^{D^0} < 20$ GeV/ c and high $p_T > 20$ GeV/ c , for $p_T^{\text{jet}} > 60$ GeV/ c . The measured observable is the radial distribution of the D^0 mesons with respect to the jet axis, $r = \sqrt{\Delta\phi^2 + \Delta\eta^2}$, defined as the quadratic sum of the differences in pseudorapidity and azimuth between the D^0 meson and the jet axis direction, shown in Figure 15 for $4 < p_T^{D^0} < 20$ GeV/ c . The average value of r for low- p_T D^0 mesons was measured to be 0.198 ± 0.015 (stat) ± 0.005 (sys) and 0.160 ± 0.007 (stat) ± 0.009 (sys) for Pb–Pb and pp collisions, respectively. This indicates that D^0 mesons at low p_T are farther away from the jet axis in Pb–Pb compared to pp collisions. At higher p_T , the radial distribution of D^0 mesons is more similar in Pb–Pb and pp collisions. The pp results are compared with PYTHIA [138] and SHERPA [90] event generators, which capture the data trend well within the measured uncertainties. The Pb–Pb distribution is compared to an energy loss model, CCNU [122], which includes in-medium elastic (collisional) and inelastic (radiative) interactions for both the heavy and the light quarks. The model predicts a small depletion of the D^0 meson yield at small r and an enhancement of yield at larger r compared to pp collisions, which is consistent with the trend seen in the data, as can be seen in the ratio plot of Figure 15. This measurement hints at a modification of the D^0 meson radial profile in Pb–Pb collisions at low p_T , possibly induced by interactions of the charm quark with the medium constituents, which alter the original quark direction. This modification vanishes at higher p_T .

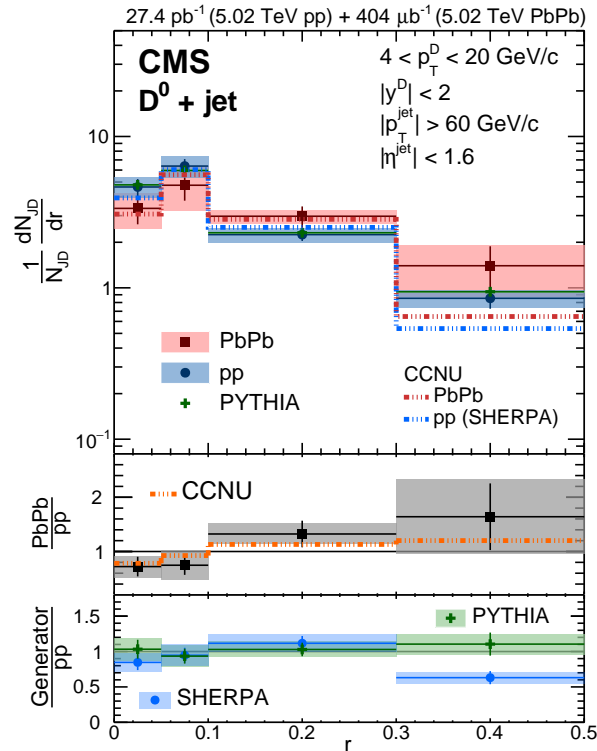


Figure 15. Distribution of D^0 mesons ($4 < p_T^{D^0} < 20$ GeV/ c) in jets, as a function of the distance from the jet axis (r) for $p_T^{\text{jet}} > 60$ GeV/ c and $|\eta^{\text{jet}}| < 1.6$ in pp and Pb–Pb collisions at $\sqrt{s_{\text{NN}}} = 5.02$ TeV from the CMS Collaboration. The Pb–Pb spectra are compared to the CCNU energy loss model, while the pp spectra are compared with predictions from the PYTHIA and SHERPA pp MC event generators. The ratios of the D^0 meson radial distributions in Pb–Pb to the pp data are shown in the middle panel. In the bottom panel, the ratios of the D^0 meson radial distributions predicted by the two MC event generators to the CMS results in pp collisions are presented [137].

Similarly, correlation measurements can be used to study the modification of jet shapes in heavy-ion collisions, using charged hadron constituents as a function of their radial distance from the jet axis, as performed by the CMS experiment [139]. These measurements can give insight into details of jet quenching and medium response to the evolving jet. The CMS experiment used jets initiated by beauty quarks (b-jets) to provide unique experimental means to investigate the mass dependence of quenching effects and parton shower evolution. The transverse momentum profile $P(\Delta r)$ of charged particles in the jets, defined as $P(\Delta r) = \frac{1}{\Delta r_b - \Delta r_a} \frac{1}{N_{\text{jet}}} \sum_{\text{jets}} \sum_{\text{trk} \in (\Delta r_a, \Delta r_b)} p_T^{\text{trk}}$, was measured, where $\Delta r = \sqrt{\Delta\phi^2 + \Delta\eta^2}$ is the radial distance between a track and the jet axis defined in pseudorapidity and azimuthal angle, Δr_a and Δr_b are the edges of rings in Δr , and p_T^{trk} is the charged particle's transverse momentum. The $P(\Delta r)$ distribution is normalized to unity within $\Delta r < 1$ to produce the jet shape distribution, $\rho(\Delta r)$, that indicates how the momentum of charged particles is distributed with respect to the jet axis. The shapes of b-jets and inclusive jets of $p_T > 120$ GeV/c for charged particles with $p_T > 1$ GeV/c was measured for Pb–Pb and pp collisions, as shown in Figure 16. The b-jets are found to be broader than inclusive jets. The ratio of $\rho(\Delta r)$ distribution in Pb–Pb to pp collisions (2nd row panels) shows a depletion of particles for low Δr and a strong enhancement at large Δr , indicating redistribution of p_T of jet constituents from small to large distances from the jet axis. The large Δr enhancement in Pb–Pb collisions is centrality-dependent and is most significant in central collisions, indicating a modification of energy flow around the jet axis in the presence of the QGP medium. The large Δr enhancement in Pb–Pb collisions is more pronounced for b-jets than inclusive jets, showing mass dependent interactions in the QGP. The difference in the transverse momentum profile between Pb–Pb and pp collisions characterizes the magnitude of the measured excess momentum as shown in the third row of the figure. A more significant transverse momentum excess in Pb–Pb collisions at intermediate and high Δr is found for b-jets than for inclusive jets. A comparison of b-jet shapes to those of inclusive jets is shown in the bottom panel for pp and Pb–Pb collisions. In pp collisions, b-jets show a depletion for $\Delta r < 0.05$, with respect to inclusive jets, that could be interpreted as being due to the dead-cone effect [140] (suppression of collinear parton radiation from a massive emitter such as a heavy quark). In Pb–Pb collisions, the depletion at small Δr is similar to pp collisions. For higher Δr , b-jet shapes are broader than inclusive jet shapes in pp and Pb–Pb collisions, with a significant enhancement in the most central Pb–Pb collisions. This measurement provides new constraints for theoretical calculations of parton flavor dependence of energy loss and jet–medium interactions in the quark–gluon plasma.

At momenta comparable to or smaller than the quark mass, heavy quarks are thought to undergo Brownian-like motion in the quark–gluon plasma, with their transport characterized by a diffusion coefficient [141]. The process of losing energy via gluon radiation is referred to as radiative energy loss [142]. Heavy quarks, when produced at LO, will have a back-to-back correlation in azimuthal angle between the quark and anti-quark, due to momentum conservation. As a consequence of the multiple interactions with the medium, this initial correlation can broaden around $\Delta\phi = \pi$. Energy loss via a radiative mechanism may dampen this broadening [143]. Angular correlations of heavy quarks can thus be sensitive to the relative contribution of collisional and radiative energy loss processes [54,55]. The ATLAS Collaboration performed measurements of angular correlations between muon pairs in pp and Pb–Pb collisions at $\sqrt{s_{\text{NN}}} = 5.02$ TeV [144]. Muon pairs from beauty hadron decays were selected by considering muons with the same charge with both muons having $p_T > 4$ GeV/c. The $\Delta\phi$ distribution of muon pairs shows a clear peak on the away-side, consistent with the back-to-back configuration of beauty quark pair production from hard scattering processes. The width of the away-side peaks was characterized by fitting the $\Delta\phi$ distribution with a Cauchy–Lorentz function. The centrality dependence of the away-side width was measured, as shown in Figure 17. The widths obtained for different centralities in Pb–Pb collisions are consistent with the value measured in pp collisions, with a slightly reduced value observed for the 0–10% centrality interval. To further investigate the mechanisms by which a heavy quark interacts with the QGP constituents, this measurement can

be extended to different p_T regions of muon pairs. Comparison with model calculations including collisional and/or radiative energy loss would help with the interpretation of the current observation. The measurement will provide important constraints on theoretical descriptions of the dynamics of heavy quarks inside the quark–gluon plasma.

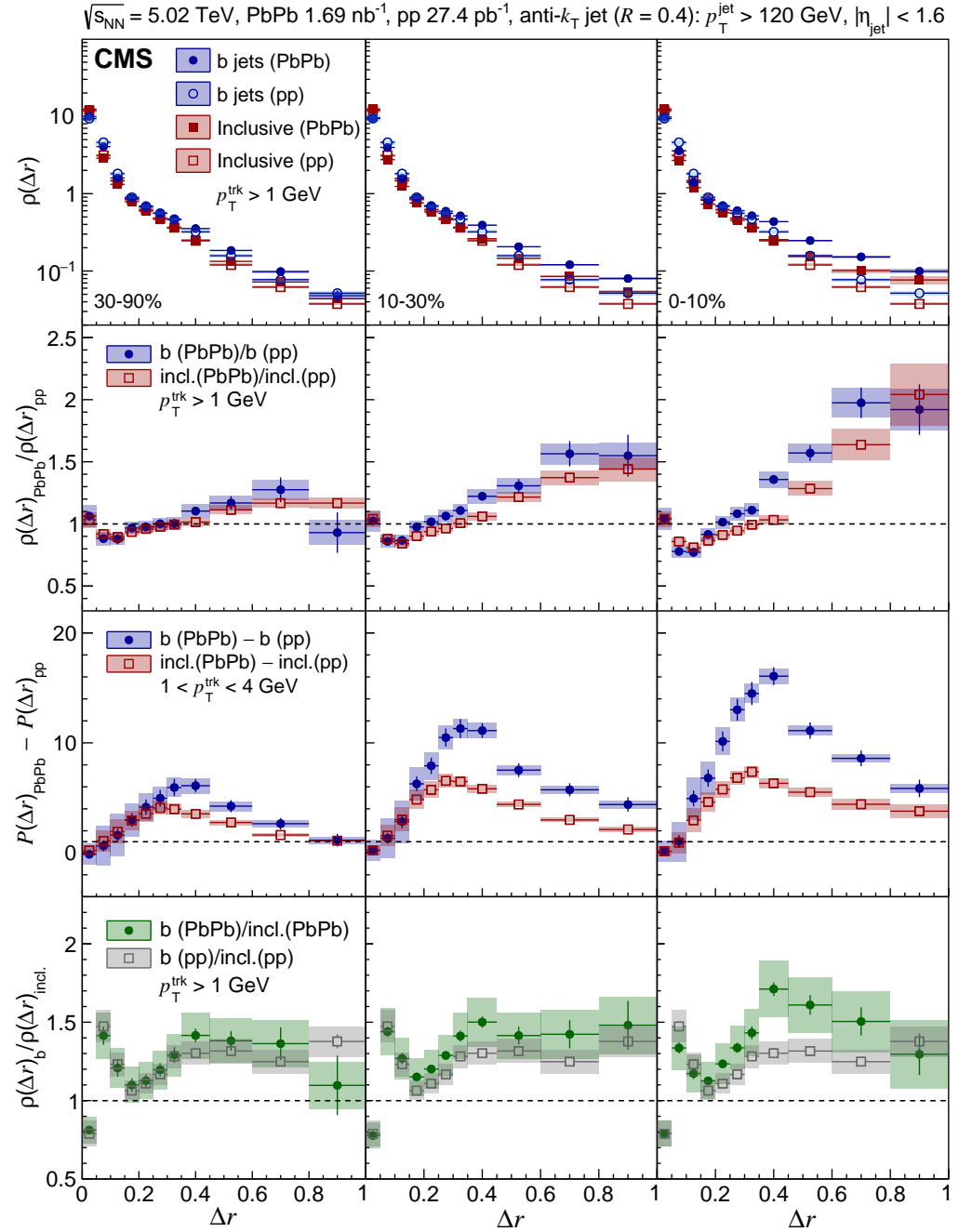


Figure 16. **First row:** jet shape distributions $\rho(\Delta r)$ for inclusive and b-jets with $p_T > 120 \text{ GeV}/c$ in three centrality bins (left to right) for Pb–Pb collisions at $\sqrt{s_{NN}} = 5.02 \text{ TeV}$, and in pp collisions, both measured by the CMS Collaboration. **Second row:** ratio of Pb–Pb to pp jet shape results for inclusive jets (red) and b-jets (blue). **Third row:** difference between the charged-particle transverse momentum profile between Pb–Pb and pp collisions for inclusive and b-jets. **Fourth row:** ratio of b- to inclusive jet shapes for several Pb–Pb centrality bins (green), as well as pp collisions (identical in all three panels). In all panels, the vertical bars and shaded boxes represent the statistical and systematic uncertainties, respectively [139].

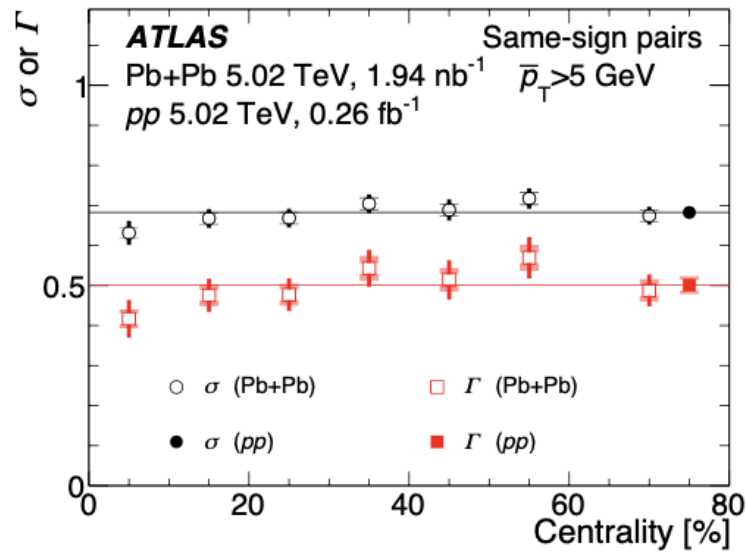


Figure 17. The measured widths of the away-side peak of the angular correlations between same-sign muon pairs in pp and Pb–Pb collisions at $\sqrt{s_{\text{NN}}} = 5.02$ TeV from the ATLAS Collaboration. The vertical bars and shaded bands on the data points represent the statistical uncertainties, and systematic uncertainties, respectively. The horizontal lines indicate the nominal pp values plotted across the full centrality range [144].

5. Small-System Collective-Like Effects for Heavy Quarks

As discussed in the previous section, Section 4, the properties of the QGP are studied by analyzing high-energy heavy-ion collisions [145–150]. One of the key signatures of the formation of the QGP in these collision systems is the azimuthal anisotropy of the produced particles [151], due to the onset of collective motion of the system that is driven by the specific geometrical structure of the overlap region of the two colliding nuclei. During the medium expansion, the initial-state spatial anisotropy is translated into a momentum anisotropy of the particles emerging from the medium [152]. The magnitude of the azimuthal anisotropies is quantified via a Fourier decomposition of the particle azimuthal distribution [153], where the Fourier coefficients v_n characterize the strength of the anisotropy. For non-central A–A collisions, where the overlap region typically has an almond shape, the largest contribution to the azimuthal anisotropy is provided by the second-order Fourier coefficient v_2 , referred to as the elliptic flow coefficient. Its value is used to characterize the strength of the collective motion of the system. In two-particle angular correlation distributions measured in non-central A–A collisions, the effect of the elliptic flow can be seen as pronounced structures on the near and away sides along $\Delta\phi$, extending over a large $\Delta\eta$ region, which are commonly referred to as “ridges” [154]. The measurements are well described by models invoking a hydrodynamic expansion of the hot and dense asymmetrical medium produced in the collision. Surprisingly, similar long-range ridge structures and a positive v_2 coefficient were also observed for light-flavor particles in high-multiplicity pp and p–Pb collisions at the LHC [155–160], and in high-multiplicity d –Au and ^3He –Au collisions at RHIC [161,162]. The interpretation of the positive v_2 in these small systems is currently highly debated [163]. It has raised the question of whether a fluid-like QGP medium with a size smaller than that produced in A–A collisions is created [164,165]. Alternate explanations foresee mechanisms involving initial-state effects, such as gluon saturation within the color glass condensate effective field theory [166,167], or final-state color–charge exchanges [168,169].

Heavy quarks, produced during the early stages of hadronic collisions [1–4], can be used to probe both initial- and final-state effects of the collision dynamics [124,170–173]. In A–A collisions, strong elliptic flow signals were observed for leptons from the decay of heavy-flavor hadrons and open-charm D mesons [129,130,150,174–176], suggesting

that charm quarks develop significant collective behavior via their strong interactions with the bulk of the QGP medium. Measurements of elliptic flow of hidden-charm J/ψ mesons provide further evidence for strong rescatterings of charm quarks [178]. Recent measurements of positive v_2 for non-prompt D mesons (i.e., D mesons produced from the decays of beauty hadrons), though with smaller values than prompt D meson v_2 , were released by the CMS [179] and ALICE Collaborations [180], suggesting that beauty quarks could also participate in the medium collective motion, though with lesser extent than charm quarks.

In small colliding systems, the study of heavy-flavor hadron collectivity has the potential to disentangle possible contributions from both initial- and final-state effects [172,173,181]. In particular, heavy-flavor hadrons may be more sensitive to possible initial-state gluon saturation effects. The Collaboration at the LHC performed several measurements to evaluate the v_2 of charm and beauty hadrons in pp and p–Pb collisions, using two-particle angular correlation techniques [112,113,115,182–184]. The general procedure performed was to obtain the angular correlations of heavy-flavor trigger particles with charged particles [112] in events with high multiplicity. The correlation distribution in these events contains contributions related to collectivity and jet fragmentation, with the latter being referred to as non-flow effects. These non-flow contributions can be suppressed by requiring a pseudorapidity separation ($\Delta\eta$) between heavy-flavor particles and charged particles. The azimuthal correlation distribution normalized to the number of trigger particles is obtained. While a large $\Delta\eta$ separation largely reduces non-flow contributions, especially for the near-side region, a significant contribution from recoil jet fragmentation still remains on the away-side of the $\Delta\phi$ distribution. This can be subtracted by using the azimuthal correlation distributions measured in low-multiplicity events. The subtraction method relies on the assumptions that the jet correlations on the away side remain unmodified as a function of the event multiplicity and that there are no significant correlations due to collective effects in low-multiplicity collisions. The non-flow subtracted $\Delta\phi$ distribution is fit with a Fourier decomposition, $a[1 + 2V_{1\Delta}^{\text{HF}-\text{ch}} \cos(\Delta\phi) + 2V_{2\Delta}^{\text{HF}-\text{ch}} \cos(2\Delta\phi)]$. The second-order coefficient $2V_{2\Delta}^{\text{HF}-\text{ch}}$, which is the dominant term, is obtained. Using the assumption that $V_{2\Delta}^{\text{HF}-\text{ch}}$ can be factorized as a product of single-particle v_2 coefficients, the elliptic flow coefficient of the heavy-flavor particle, v_2^{HF} , is extracted from the equation $v_2^{\text{HF}} = V_{2\Delta}^{\text{HF}-\text{ch}}/v_2^{\text{ch}-\text{ch}}$. The v_2 values of several heavy-flavor particle species in small systems were measured by the ALICE Collaboration using leptons from heavy-flavor hadron decays [112,184] and J/ψ [182], by the ATLAS Collaboration using muons from charm and beauty hadron decays [113], and by the CMS Collaboration using prompt D^0 [114], non-prompt D^0 mesons [115], and J/ψ [183] mesons.

The v_2 of prompt D^0 mesons [114], non-prompt D^0 mesons [115], and prompt J/ψ [183] as a function of p_T for p–Pb collisions at $\sqrt{s_{\text{NN}}} = 8.16$ TeV, measured by the CMS Collaboration, is shown in Figure 18 (left panel). The v_2 of strange hadrons [114] is also shown. A positive v_2 value for prompt D^0 and J/ψ is observed, with a rising and then a decreasing trend with p_T , peaking at about 3–4 GeV/c. A clear ordering in the v_2 values is observed for the low- p_T region ($p_T < 3$ GeV/c), where heavier particles have smaller v_2 at a given p_T value. A similar mass ordering for the v_2 of D^0 mesons and strange hadrons in semi-central Pb–Pb collisions is observed, although the multiplicity range in Pb–Pb collisions is much larger [130]. In Pb–Pb collisions, this behavior is understood to be due to particle emission from a collectively expanding source with a common velocity field. This might indicate a significant collective behavior of charm quarks in high-multiplicity p–Pb systems at LHC energies. For non-prompt D^0 mesons, the v_2 values are consistent with zero at low p_T , while at high p_T , a hint of a positive v_2 value is observed, but it is not significant within statistical and systematic uncertainties. The non-prompt D^0 v_2 is observed to be smaller than that of prompt D^0 mesons with a significance of 2.7 standard deviations. This also indicates a mass hierarchy of the original quark participating in the collective-like dynamics. In Pb–Pb collisions, a similar mass ordering for muon v_2 from charm and beauty decay at low p_T was observed [185], and is understood as being due to final-state scattering mech-

anisims [186–188]. The values of v_2 from a calculation within the color glass condensate (CGC) framework [171–173] for prompt J/ψ mesons, prompt and non-prompt D^0 mesons in p–Pb collisions are compared with the data in Figure 18 (left panel). Within the CGC framework, correlations in the initial stage of the collision between partons originating from projectile protons and dense gluons in the lead nucleus can generate a sizable elliptic flow. The model qualitatively describes the data, suggesting that initial-state effects may play an important role in the generation of collectivity for these particles in p–Pb collisions. The CGC framework also predicts a mass hierarchy between prompt and non-prompt D^0 mesons for $p_T \sim 2\text{--}5\text{ GeV}/c$, consistent with the data within uncertainties.

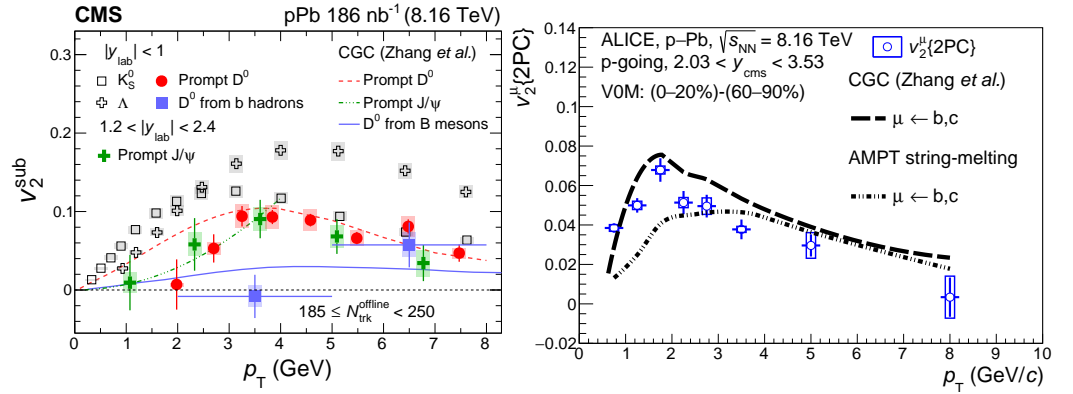


Figure 18. (Left) v_2 of prompt [114] and non-prompt D^0 mesons [115], K_s^0 mesons and Λ baryons at mid-rapidity [114], and prompt J/ψ mesons at forward rapidity [183], measured by the CMS Collaboration as a function of p_T in high-multiplicity p–Pb collisions at $\sqrt{s_{\text{NN}}} = 8.16\text{ TeV}$. (Right) The p_T differential v_2^{μ} of inclusive muons measured by the ALICE Collaboration at forward rapidity in high-multiplicity p–Pb collisions at $\sqrt{s_{\text{NN}}} = 8.16\text{ TeV}$ [184], compared with predictions of v_2 of muons from heavy-flavor hadron decays from CGC and AMPT models. The vertical bars correspond to the statistical uncertainties, while the boxes denote the systematic uncertainties.

The ALICE Collaboration measured the v_2 of muons at forward ($2.03 < y_{\text{cms}} < 3.53$) and backward rapidity ($-4.46 < y_{\text{cms}} < -2.96$) in high-multiplicity p–Pb collisions at $\sqrt{s_{\text{NN}}} = 8.16\text{ TeV}$ [184]. For $p_T > 2\text{ GeV}/c$, a dominant contribution of muons is produced from heavy-flavor hadron decays. A positive v_2 was measured at both rapidities. To better understand the source of the observed azimuthal anisotropies in small collision systems, the measurement was compared with a multi-phase transport (AMPT) model [181,189,190] and CGC [171–173] model calculations for muons from heavy-flavor hadron decays. The results for muons measured at forward rapidity are shown in the right panel of Figure 18. The AMPT model provides a microscopic evolution of parton interactions, including a parton escape mechanism described via a parton cascade model [191]. The AMPT model generates a positive v_2 , mainly driven by the anisotropic parton escape mechanism, where partons have a higher probability to escape the interaction region along its shorter axis [192]. In the CGC calculations, the correlations in the initial stage of the collision between partons in the colliding proton and gluons in the dense Pb ion generate a significant v_2 signal that persists till the final state and is observed in the heavy-flavor hadron decay muon measurement. The CGC-based calculations provide a larger v_2 compared to AMPT calculations at low p_T , up to $3\text{ GeV}/c$, while the two models provide similar results and describe the data at high p_T , where heavy-flavor hadron decays dominate the muon sample. This comparison indicates that both initial- and final-state effects can explain the azimuthal anisotropies observed in small collision systems.

The v_2 of J/ψ at forward and backward rapidity in high-multiplicity p–Pb collisions was compared with measurements in non-central Pb–Pb collisions by the ALICE experiment [182]. The p_T -dependent v_2 values in p–Pb collisions are consistent with those measured in Pb–Pb collision within uncertainties. In Pb–Pb collisions, at low p_T , the v_2 coefficient is believed to originate from the recombination of charm quarks thermalized in

the medium, which is described by thermal models [193]. In p–Pb collisions, the amount of produced charm quarks is small and, therefore, the contribution from recombination should be negligible. For $p_T > 4$ GeV/ c , the v_2 in Pb–Pb collisions is expected to come from path length-dependent suppression inside the QGP medium. In p–Pb collisions, the medium, if any, is expected to have a much smaller size, and hence, very feeble path length-dependent effects are expected.

The v_2 of prompt D^0 mesons as a function of p_T in pp collisions at $\sqrt{s} = 13$ TeV, measured by the CMS Collaboration [115], is shown in Figure 19 (left panel). A positive v_2 signal for prompt charm hadrons over a p_T range up to 6 GeV/ c is observed, with a decreasing trend towards higher p_T values. The v_2 for prompt D^0 mesons is found to be comparable, within uncertainties, with that of light-flavor hadron species, i.e., unidentified charged particles (dominated by pions), K_S^0 mesons and Λ baryons [194], that are also presented in the same figure. At similar event multiplicities, the prompt D^0 meson v_2 values are found to be comparable within uncertainties in pp and p–Pb systems.

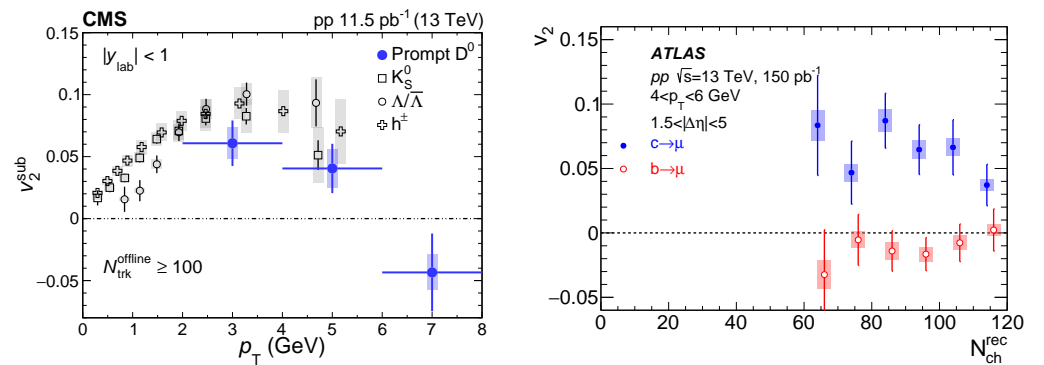


Figure 19. (Left) v_2 of prompt D^0 mesons measured as a function of p_T at mid-rapidity in high-multiplicity pp collisions at $\sqrt{s} = 13$ TeV [115], measured by the CMS Collaboration. The prompt D^0 meson measurement is compared with those of charged particles, K_S^0 mesons and Λ baryons [194]. (Right) v_2 of muons from charm and beauty hadron decays as a function of track multiplicity for muons with $4 < p_T < 6$ GeV/ c in pp collisions at $\sqrt{s} = 13$ TeV [113], measured by the ATLAS Collaboration. The vertical bars correspond to the statistical uncertainties, while the shaded areas denote the systematic uncertainties.

The elliptic flow of muons from the decay of charm and beauty hadrons in pp collisions at $\sqrt{s} = 13$ TeV was measured by the ATLAS Collaboration [113] for $4 < p_T < 7$ GeV/ c and $|\eta| < 2.4$. It is shown as a function of reconstructed track multiplicity in Figure 19 (right panel). A significant non-zero v_2 is observed for muons from charm hadron decays, without significant dependence on multiplicity. The v_2 of muons from charm hadron decays decreases with increasing p_T , and is consistent with zero for $p_T \gtrsim 6$ GeV/ c . The v_2 for muons from beauty hadron decays was measured to be consistent with zero within uncertainties through all the multiplicity ranges measured, and also shows no p_T dependence. These results also indicate a mass hierarchy of the v_2 signal at the partonic level.

The presented measurements of heavy-flavor v_2 in high-multiplicity pp and p–Pb collisions, the indication of mass dependence of v_2 in p–Pb collisions, and the comparison with models capable of describing the measurements, can provide insights into the origin of heavy-flavor quark collectivity in small colliding systems. However, the identification of the source of the observed collective-like effects remains a topic of debate.

6. Summary

This article reviews the most recent experimental measurements of correlated heavy-flavor particle production as a function of the relative azimuthal angle and/or rapidity. Angular correlation techniques are used to study the production, fragmentation, and hadronization of heavy quarks in pp collisions and to understand how these processes are modified in the presence of a strongly interacting quark–gluon plasma in heavy-ion

collisions. Azimuthal anisotropy observations in high-multiplicity pp and p–A collisions and their possible origin are also reviewed.

In pp collisions, angular correlations of heavy-flavor particle pairs allow for testing pQCD calculations at different order in α_s . Such correlation distributions were measured at RHIC and at the LHC through different experiments, and were compared with predictions from different Monte Carlo generators, such as PYTHIA, POWHEG, HERWIG, MADGRAPH, and SHERPA. It is challenging for these models to provide an optimal description of the data. These kinematic correlation observables provide sensitivity to the underlying differences within the models. The shape of the correlation distribution is also used to study the multiple production of heavy quarks in a single pp and p–A collision. The angular separation between heavy-flavor particle pairs shows distinct structural differences when produced in single or double parton scattering processes.

A thorough characterization of the in-vacuum heavy quark fragmentation process can be performed by measuring the angular correlation distribution between a trigger heavy-flavor particle and associated charged particles, as performed by the ALICE Collaboration. The angular correlation distribution and more quantitative observables extracted from it, such as the near- and away-side peak yields and widths measured in pp and p–Pb collisions, were compared with different Monte Carlo generators such as PYTHIA, POWHEG+PYTHIA, HERWIG, and EPOS. The first two models provide predictions that are closest to the data, but further configuration and parameter tuning could be helpful for a better reproduction of the properties of the correlation distribution. By comparing the correlation distributions in pp and p–Pb collisions, effects from cold nuclear matter on the heavy quark fragmentation process can be studied. No significant impact was observed in the kinematic ranges measured in the experiments. It is also important that the fragmentation studies can be performed as a function of event multiplicity, as correlation techniques used to evaluate flow coefficients in small systems rely on the assumption that jet fragmentation is independent of event multiplicity. Results of correlation measurements as a function of charged-particle multiplicity in pp and p–Pb collisions indicate that, within the experimental uncertainties, the correlation distributions and their properties are consistent for all multiplicity ranges studied, implying a similar fragmentation of charm quarks into final-state mesons.

In ultra-relativistic heavy-ion collisions, heavy-flavor jets and particle distributions within jets are excellent tools for characterizing heavy quark propagation and to constrain energy loss mechanisms affecting partons traversing the quark–gluon plasma. The STAR and PHENIX experiments at RHIC examined the angular correlations between a trigger heavy-flavor particle and associated charged particles in Au–Au collisions and compared the results with those obtained in pp collisions and with predictions from the PYTHIA event generator. The trigger-particle p_T -integrated near-side yields and widths were observed to increase towards more central Au–Au collisions. The measurement indicates that charm quarks lose energy in the QGP, and the lost energy is converted into additional low- p_T particles accompanying the charm meson. On the away side, a higher yield of low- p_T -associated particles was observed in Au–Au collision compared to pp, which decreased and hinted towards a suppression for increasing the associated particle p_T . The charm quark diffusion inside the QGP medium, studied at the LHC by the CMS Collaboration, implies that low- p_T D mesons in Pb–Pb collisions tend to be further displaced from the jet axis compared to pp collisions, due to interaction with the medium constituents. Studies of the modification of jet shapes using correlation techniques, by measuring the distribution of charged particles inside a jet as a function of their radial distance from the jet axis, was performed by the CMS Collaboration for jets initiated by beauty quarks (b-jets). The measurement indicates a redistribution of the momentum of jet constituents from smaller to larger radial distances from the jet axis in the presence of the QGP medium. These measurements provide new constraints for theoretical calculations of parton-flavor dependence of energy loss and jet–medium interactions in the QGP.

To understand the long-range ridge structures and the positive v_2 values observed for light-flavor particles in high-activity collisions of smaller systems as pp, p–Pb, and d–Au, the experiments also searched for non-zero v_2 signals in the heavy-flavor sector with the aim to provide insights whether the observed collectivity originates from initial- or final-state effects, or both. Experiments at the LHC performed several measurements to evaluate the v_2 of charm and beauty hadrons in pp and p–Pb collisions, using two-particle correlation techniques. A positive v_2 value for charm hadrons was measured, showing a rising and then decreasing trend with p_T , and a mass ordering in the low- p_T region where heavier particles have smaller v_2 at a given p_T . These trends are similar to those observed in Pb–Pb collisions, where they originate from parton interactions with the medium constituents described by hydrodynamic laws. The measurements in p–Pb collisions were compared with AMPT model calculations that generate positive v_2 via an anisotropic parton escape mechanism, and with CGC calculations that predict correlations in the initial stage of the collision between partons originating from projectile protons and gluons in the dense lead nucleus, resulting in a sizable v_2 . Both models qualitatively provide compatible results and are able to describe the data, indicating that both initial- and final-state effects could explain the azimuthal anisotropies observed in small systems, while leaving the question of the exact origin of these effects still open.

The measurements presented in this review were performed by the STAR and PHENIX Collaborations at RHIC, and by the ALICE, ATLAS, CMS, and LHCb Collaborations at the LHC, using data collected in 2018. While the current measurements have provided important information about various aspects of heavy-flavor production in hadronic collisions as discussed above, the uncertainties in several of these measurements are high, and extension to different kinematic regions are required to achieve the goals intended with these measurements. With the ongoing Run 3 data collection at the LHC, and the new sPHENIX experiment at RHIC, we can expect additional correlation measurements with improved precision, as well as access to further, more differential observables. These ongoing and future efforts will help to improve our knowledge of the abovementioned topics, and to shed further light on some of the open questions in the field.

Author Contributions: Conceptualization, F.C. and D.T.; investigation, F.C. and D.T.; writing—original draft preparation, F.C. and D.T.; writing—review and editing, F.C. and D.T. All authors have read and agreed to the published version of the manuscript.

Funding: This work was supported by U.S. Department of Energy Office of Science under contract number DE-SC0013391.

Conflicts of Interest: The authors declare no conflicts of interest.

References

1. Cacciari, M.; Greco, M.; Nason, P. The p_T spectrum in heavy-flavour hadroproduction. *J. High Energy Phys.* **1998**, *05*, 007. <https://doi.org/10.1088/1126-6708/1998/05/007>.
2. Cacciari, M.; Frixione, S.; Nason, P. The p_T spectrum in heavy flavor photoproduction. *J. High Energy Phys.* **2001**, *03*, 006. <https://doi.org/10.1088/1126-6708/2001/03/006>.
3. Kniehl, B.A.; Kramer, G.; Schienbein, I.; Spiesberger, H. Reconciling open charm production at the Fermilab Tevatron with QCD. *Phys. Rev. Lett.* **2006**, *96*, 012001. <https://doi.org/10.1103/PhysRevLett.96.012001>.
4. Kniehl, B.A.; Kramer, G.; Schienbein, I.; Spiesberger, H. Finite-mass effects on inclusive B meson hadroproduction. *Phys. Rev. D* **2008**, *77*, 014011. <https://doi.org/10.1103/PhysRevD.77.014011>.
5. Aggarwal, M.M.; et al. (STAR Collaboration) Measurement of the Bottom contribution to non-photon electron production in $p + p$ collisions at $\sqrt{s} = 200$ GeV. *Phys. Rev. Lett.* **2010**, *105*, 202301. <https://doi.org/10.1103/PhysRevLett.105.202301>.
6. Adare, A.; et al. (PHENIX Collaboration) Measurement of Bottom versus Charm as a Function of Transverse Momentum with Electron-Hadron Correlations in $p + p$ Collisions at $\sqrt{s} = 200$ GeV. *Phys. Rev. Lett.* **2009**, *103*, 082002. <https://doi.org/10.1103/PhysRevLett.103.082002>.
7. Adare, A.; et al. (PHENIX Collaboration) Measurement of high- p_T single electrons from heavy-flavor decays in $p + p$ collisions at $\sqrt{s} = 200$ GeV. *Phys. Rev. Lett.* **2006**, *97*, 252002. <https://doi.org/10.1103/PhysRevLett.97.252002>.
8. Acosta, D.; et al. (CDF II Collaboration) Measurement of prompt charm meson production cross sections in $p\bar{p}$ collisions at $\sqrt{s} = 1.96$ TeV. *Phys. Rev. Lett.* **2003**, *91*, 241804. <https://doi.org/10.1103/PhysRevLett.91.241804>.

9. Cacciari, M.; Nason, P. Charm cross-sections for the Tevatron Run II. *J. High Energy Phys.* **2003**, *09*, 006. <https://doi.org/10.1088/1126-6708/2003/09/006>.
10. Acosta, D.; et al. (CDF Collaboration) Measurement of the J/ψ meson and b -hadron production cross sections in $p\bar{p}$ collisions at $\sqrt{s} = 1960$ GeV. *Phys. Rev. D* **2005**, *71*, 032001. <https://doi.org/10.1103/PhysRevD.71.032001>.
11. Acharya, S.; et al. (ALICE Collaboration) Measurement of electrons from semileptonic heavy-flavour hadron decays at midrapidity in pp and Pb–Pb collisions at $\sqrt{s_{NN}} = 5.02$ TeV. *Phys. Lett. B* **2020**, *804*, 135377. <https://doi.org/10.1016/j.physletb.2020.135377>.
12. Sirunyan, A.M.; et al. (CMS Collaboration) Nuclear modification factor of D^0 mesons in PbPb collisions at $\sqrt{s_{NN}} = 5.02$ TeV. *Phys. Lett. B* **2018**, *782*, 474–496. <https://doi.org/10.1016/j.physletb.2018.05.074>.
13. Aaij, R.; et al. (LHCb Collaboration) Measurements of prompt charm production cross-sections in pp collisions at $\sqrt{s} = 13$ TeV. *J. High Energy Phys.* **03**, 2016, 159; Erratum in *J. High Energy Phys.* **2016**, *09*, 13; Erratum in *J. High Energy Phys.* **2017**, *05*, 74. [https://doi.org/10.1007/JHEP03\(2016\)159](https://doi.org/10.1007/JHEP03(2016)159).
14. Acharya, S.; et al. (ALICE Collaboration) Measurement of inclusive charged-particle b-jet production in pp and p–Pb collisions at $\sqrt{s_{NN}} = 5.02$ TeV. *J. High Energy Phys.* **2022**, *01*, 178. [https://doi.org/10.1007/JHEP01\(2022\)178](https://doi.org/10.1007/JHEP01(2022)178).
15. Acharya, S.; et al. (ALICE Collaboration) Measurement of the production of charm jets tagged with D^0 mesons in pp collisions at $\sqrt{s} = 5.02$ and 13 TeV. *arXiv* **2022**, arXiv:2204.10167.
16. Acharya, S.; et al. (ALICE Collaboration) Measurement of D^0 , D^+ , D^{*+} and D_s^+ production in pp collisions at $\sqrt{s} = 5.02$ TeV with ALICE. *Eur. Phys. J. C* **2019**, *79*, 388. <https://doi.org/10.1140/epjc/s10052-019-6873-6>.
17. Acharya, S.; et al. (ALICE Collaboration) Production of muons from heavy-flavour hadron decays in pp collisions at $\sqrt{s} = 5.02$ TeV. *J. High Energy Phys.* **2019**, *09*, 008. [https://doi.org/10.1007/JHEP09\(2019\)008](https://doi.org/10.1007/JHEP09(2019)008).
18. Acharya, S.; et al. (ALICE Collaboration) Measurement of beauty and charm production in pp collisions at $\sqrt{s} = 5.02$ TeV via non-prompt and prompt D mesons. *J. High Energy Phys.* **2021**, *005*, 220. [https://doi.org/10.1007/JHEP05\(2021\)220](https://doi.org/10.1007/JHEP05(2021)220).
19. Abelev, B.; et al. (ALICE Collaboration) Heavy flavour decay muon production at forward rapidity in pp collisions at $\sqrt{s} = 7$ TeV. *Phys. Lett. B* **2012**, *708*, 265–275. <https://doi.org/10.1016/j.physletb.2012.01.063>.
20. Abelev, B.; et al. (ALICE Collaboration) Measurement of charm production at central rapidity in pp collisions at $\sqrt{s} = 2.76$ TeV. *J. High Energy Phys.* **2012**, *007*, 191. [https://doi.org/10.1007/JHEP07\(2012\)191](https://doi.org/10.1007/JHEP07(2012)191).
21. Abelev, B.; et al. (ALICE Collaboration) Measurement of electrons from semileptonic heavy-flavour hadron decays in pp collisions at $\sqrt{s} = 7$ TeV. *Phys. Rev. D* **2012**, *86*, 112007. <https://doi.org/10.1103/PhysRevD.86.112007>.
22. Aaij, R.; et al. (LHCb collaboration) Measurements of prompt charm production cross-sections in pp collisions at $\sqrt{s} = 5$ TeV. *J. High Energy Phys.* **2017**, *006*, 147. [https://doi.org/10.1007/JHEP06\(2017\)147](https://doi.org/10.1007/JHEP06(2017)147).
23. Abelev, B.; et al. (ALICE Collaboration) Measurement of electrons from beauty hadron decays in pp collisions at $\sqrt{s} = 7$ TeV. *Phys. Lett. B* **2013**, *721*, 13–23; Erratum in *Phys. Lett. B* **2016**, *763*, 507–509. <https://doi.org/10.1016/j.physletb.2013.01.069>.
24. Abelev, B.; et al. (ALICE Collaboration) Measurement of electrons from semileptonic heavy-flavor hadron decays in pp collisions at $\sqrt{s} = 2.76$ TeV. *Phys. Rev. D* **2015**, *91*, 012001. <https://doi.org/10.1103/PhysRevD.91.012001>.
25. Aaij, R.; et al. (LHCb collaboration) Measurement of the B^{\pm} production cross-section in pp collisions at $\sqrt{s} = 7$ TeV. *J. High Energy Phys.* **2012**, *004*, 093. [https://doi.org/10.1007/JHEP04\(2012\)093](https://doi.org/10.1007/JHEP04(2012)093).
26. Aad, G.; et al. (ATLAS collaboration) Measurement of the b-hadron production cross section using decays to $D^* \mu^- X$ final states in pp collisions at $\sqrt{s} = 7$ TeV with the ATLAS detector. *Nucl. Phys. B* **2012**, *864*, 341–381. <https://doi.org/10.1016/j.nuclphysb.2012.07.009>.
27. Aad, G.; et al. (ATLAS collaboration) Measurement of the differential cross-section of B^+ meson production in pp collisions at $\sqrt{s} = 7$ TeV at ATLAS. *J. High Energy Phys.* **2013**, *010*, 042. [https://doi.org/10.1007/JHEP10\(2013\)042](https://doi.org/10.1007/JHEP10(2013)042).
28. Chatrchyan, S.; et al. (ATLAS collaboration) Measurement of the cross section for production of $b\bar{b}X$, decaying to muons in pp collisions at $\sqrt{s} = 7$ TeV. *J. High Energy Phys.* **2012**, *006*, 110. [https://doi.org/10.1007/JHEP06\(2012\)110](https://doi.org/10.1007/JHEP06(2012)110).
29. Khachatryan, V.; et al. (CMS Collaboration) Measurement of the B^+ Production Cross Section in pp collisions at $\sqrt{s} = 7$ TeV. *Phys. Rev. Lett.* **2011**, *106*, 112001. <https://doi.org/10.1103/PhysRevLett.106.112001>.
30. Chatrchyan, S.; et al. (CMS Collaboration) Measurement of the B^0 production cross section in pp collisions at $\sqrt{s} = 7$ TeV. *Phys. Rev. Lett.* **2011**, *106*, 252001. <https://doi.org/10.1103/PhysRevLett.106.252001>.
31. Chatrchyan, S.; et al. (CMS Collaboration) Measurement of the B_s^0 Production Cross Section with $B_s^0 \rightarrow J/\psi\phi$ Decays in pp collisions at $\sqrt{s} = 7$ TeV. *Phys. Rev. D* **2011**, *84*, 052008. <https://doi.org/10.1103/PhysRevD.84.052008>.
32. Khachatryan, V.; et al. (CMS Collaboration) Measurement of the total and differential inclusive B^+ hadron cross sections in pp collisions at $\sqrt{s} = 13$ TeV. *Phys. Lett. B* **2017**, *771*, 435–456. <https://doi.org/10.1016/j.physletb.2017.05.074>.
33. Cacciari, M.; Frixione, S.; Houdeau, N.; Mangano, M.L.; Nason, P.; Ridolfi, G. Theoretical predictions for charm and bottom production at the LHC. *J. High Energy Phys.* **2012**, *010*, 137. [https://doi.org/10.1007/JHEP10\(2012\)137](https://doi.org/10.1007/JHEP10(2012)137).
34. Kniehl, B.A. Inclusive production of heavy-flavored hadrons at NLO in the GM-VFNS. In Proceedings of the 16th International Workshop on Deep Inelastic Scattering and Related Subjects (DIS 2008), London, UK, 7–11 April 2008; p. 195. <https://doi.org/10.3360/dis.2008.195>.
35. Kniehl, B.A.; Kramer, G.; Schienbein, I.; Spiesberger, H. Inclusive B-Meson Production at the LHC in the GM-VFN Scheme. *Phys. Rev. D* **2011**, *84*, 094026. <https://doi.org/10.1103/PhysRevD.84.094026>.
36. Bolzoni, P.; Kramer, G. Inclusive lepton production from heavy-hadron decay in pp collisions at the LHC. *Nucl. Phys. B* **2013**, *872*, 253–264; Erratum in *Nucl. Phys. B* **2013**, *876*, 334–337. <https://doi.org/10.1016/j.nuclphysb.2013.04.002>.

37. Bolzoni, P.; Kramer, G. Inclusive charmed-meson production from bottom hadron decays at the LHC. *J. Phys. G Nucl. Part. Phys.* **2014**, *41*, 075006. <https://doi.org/10.1088/0954-3899/41/7/075006>.
38. Adare, A.; et al. (PHENIX Collaboration) Heavy Quark Production in $p + p$ and Energy Loss and Flow of Heavy Quarks in Au+Au Collisions at $\sqrt{s_{NN}} = 200$ GeV. *Phys. Rev. C* **2011**, *84*, 044905. <https://doi.org/10.1103/PhysRevC.84.044905>.
39. Abelev, B.I.; et al. (STAR Collaboration) Transverse momentum and centrality dependence of high- p_T non-photon electron suppression in Au+Au collisions at $\sqrt{s_{NN}} = 200$ GeV. *Phys. Rev. Lett.* **2007**, *98*, 192301; Erratum in *Phys. Rev. Lett.* **2011**, *106*, 159902. <https://doi.org/10.1103/PhysRevLett.98.192301>.
40. Adamczyk, L.; et al. (STAR Collaboration) Elliptic flow of electrons from heavy-flavor hadron decays in Au + Au collisions at $\sqrt{s_{NN}} = 200, 62.4, \text{ and } 39$ GeV. *Phys. Rev. C* **2017**, *95*, 034907. <https://doi.org/10.1103/PhysRevC.95.034907>.
41. Acharya, S.; et al. (ALICE Collaboration) Prompt $D^0, D^+, \text{ and } D^{*+}$ production in Pb–Pb collisions at $\sqrt{s_{NN}} = 5.02$ TeV. *J. High Energy Phys.* **2022**, *001*, 174. [https://doi.org/10.1007/JHEP01\(2022\)174](https://doi.org/10.1007/JHEP01(2022)174).
42. Acharya, S.; et al. (ALICE Collaboration) Measurement of prompt D_s^+ -meson production and azimuthal anisotropy in Pb–Pb collisions at $\sqrt{s_{NN}} = 5.02$ TeV. *Phys. Lett. B* **2022**, *827*, 136986. <https://doi.org/10.1016/j.physletb.2022.136986>.
43. Acharya, S.; et al. (ALICE Collaboration) D -meson azimuthal anisotropy in midcentral Pb-Pb collisions at $\sqrt{s_{NN}} = 5.02$ TeV. *Phys. Rev. Lett.* **2018**, *120*, 102301. <https://doi.org/10.1103/PhysRevLett.120.102301>.
44. Acharya, S.; et al. (ALICE Collaboration) Transverse-momentum and event-shape dependence of D -meson flow harmonics in Pb–Pb collisions at $\sqrt{s_{NN}} = 5.02$ TeV. *Phys. Lett. B* **2021**, *813*, 136054. <https://doi.org/10.1016/j.physletb.2020.136054>.
45. Braaten, E.; Thoma, M.H. Energy loss of a heavy fermion in a hot plasma. *Phys. Rev. D* **1991**, *44*, 1298–1310. <https://doi.org/10.1103/PhysRevD.44.1298>.
46. Peshier, A. The QCD collisional energy loss revised. *Phys. Rev. Lett.* **2006**, *97*, 212301. <https://doi.org/10.1103/PhysRevLett.97.212301>.
47. Peigne, S.; Peshier, A. Collisional energy loss of a fast heavy quark in a quark-gluon plasma. *Phys. Rev. D* **2008**, *77*, 114017. <https://doi.org/10.1103/PhysRevD.77.114017>.
48. Gyulassy, M.; Wang, X.N. Multiple collisions and induced gluon Bremsstrahlung in QCD. *Nucl. Phys. B* **1994**, *420*, 583–614. [https://doi.org/10.1016/0550-3213\(94\)90079-5](https://doi.org/10.1016/0550-3213(94)90079-5).
49. Baier, R.; Dokshitzer, Y.L.; Peigne, S.; Schiff, D. Induced gluon radiation in a QCD medium. *Phys. Lett. B* **1995**, *345*, 277–286. [https://doi.org/10.1016/0370-2693\(94\)01617-L](https://doi.org/10.1016/0370-2693(94)01617-L).
50. Gyulassy, M.; Levai, P.; Vitev, I. NonAbelian energy loss at finite opacity. *Phys. Rev. Lett.* **2000**, *85*, 5535–5538. <https://doi.org/10.1103/PhysRevLett.85.5535>.
51. Dokshitzer, Y.L.; Kharzeev, D.E. Heavy quark colorimetry of QCD matter. *Phys. Lett. B* **2001**, *85*, 199–206. [https://doi.org/10.1016/S0370-2693\(01\)01130-3](https://doi.org/10.1016/S0370-2693(01)01130-3).
52. Armesto, N.; Salgado, C.A.; Wiedemann, U.A. Low- p_T collective flow induces high- p_T jet quenching. *Phys. Rev. C* **2005**, *72*, 064910. <https://doi.org/10.1103/PhysRevC.72.064910>.
53. Zhang, B.W.; Wang, E.; Wang, X.N. Heavy quark energy loss in nuclear medium. *Phys. Rev. Lett.* **2004**, *93*, 072301. <https://doi.org/10.1103/PhysRevLett.93.072301>.
54. Nahrgang, M.; Aichelin, J.; Gossiaux, P.B.; Werner, K. Azimuthal correlations of heavy quarks in Pb + Pb collisions at $\sqrt{s} = 2.76$ TeV at the CERN Large Hadron Collider. *Phys. Rev. C* **2014**, *90*, 024907. <https://doi.org/10.1103/PhysRevC.90.024907>.
55. Cao, S.; Qin, G.Y.; Bass, S.A. Modeling of heavy-flavor pair correlations in Au-Au collisions at 200A GeV at the BNL Relativistic Heavy Ion Collider. *Phys. Rev. C* **2015**, *92*, 054909. <https://doi.org/10.1103/PhysRevC.92.054909>.
56. Eskola, K.J.; Paukkunen, H.; Salgado, C.A. EPS09: A New Generation of NLO and LO Nuclear Parton Distribution Functions. *J. High Energy Phys.* **2009**, *04*, 65. <https://doi.org/10.1088/1126-6708/2009/04/065>.
57. de Florian, D.; Sassot, R. Nuclear parton distributions at next-to-leading order. *Phys. Rev. D* **2004**, *69*, 074028. <https://doi.org/10.1103/PhysRevD.69.074028>.
58. Hirai, M.; Kumano, S.; Nagai, T.H. Determination of nuclear parton distribution functions and their uncertainties in next-to-leading order. *Phys. Rev. C* **2007**, *76*, 065207. <https://doi.org/10.1103/PhysRevC.76.065207>.
59. Fujii, H.; Watanabe, K. Heavy quark pair production in high energy pA collisions: Open heavy flavors. *Nucl. Phys. A* **2013**, *920*, 78–93. <https://doi.org/10.1016/j.nuclphysa.2013.10.006>.
60. Tribedy, P.; Venugopalan, R. QCD saturation at the LHC: Comparisons of models to $p + p$ and $A + A$ data and predictions for $p + Pb$ collisions. *Phys. Lett. B* **2012**, *710*, 125–133; Erratum in *Phys. Lett. B* **2013**, *718*, 1154. <https://doi.org/10.1016/j.physletb.2012.02.047>.
61. Albacete, J.L.; Dumitru, A.; Fujii, H.; Nara, Y. CGC predictions for $p + Pb$ collisions at the LHC. *Nucl. Phys. A* **2013**, *897*, 1–27. <https://doi.org/10.1016/j.nuclphysa.2012.09.012>.
62. Rezaeian, A.H. CGC predictions for $p+A$ collisions at the LHC and signature of QCD saturation. *Phys. Lett. B* **2013**, *718*, 1058–1069. <https://doi.org/10.1016/j.physletb.2012.11.066>.
63. Accardi, A.; Arleo, F.; Brooks, W.K.; D’Enterria, D.; Muccifora, V. Parton Propagation and Fragmentation in QCD Matter. *Riv. Nuovo Cim.* **2009**, *32*, 439–554. <https://doi.org/10.1393/ncr/i2009-10048-0>.
64. et al. C A Salgado; J Alvarez-Muñiz; F Arleo; N Armesto; M Botje; M Cacciari; J Campbell; C Carli; B Cole; D D’Enterria; Proton-Nucleus Collisions at the LHC: Scientific Opportunities and Requirements. *J. Phys. G* **2012**, *39*, 015010. <https://doi.org/10.1088/0954-3899/39/1/015010>.

65. Vogt, R. Heavy Flavor Azimuthal Correlations in Cold Nuclear Matter. *Phys. Rev. C* **2018**, *98*, 034907. <https://doi.org/10.1103/PhysRevC.98.034907>.
66. Vogt, R. $b\bar{b}$ kinematic correlations in cold nuclear matter. *Phys. Rev. C* **2020**, *101*, 024910. <https://doi.org/10.1103/PhysRevC.101.024910>.
67. Marquet, C.; Roiesnel, C.; Tael, P. Linearly polarized small- x gluons in forward heavy-quark pair production. *Phys. Rev. D* **2018**, *97*, 014004. <https://doi.org/10.1103/PhysRevD.97.014004>.
68. Aidala, C.; et al. (PHENIX Collaboration) Measurements of $\mu\mu$ pairs from open heavy flavor and Drell-Yan in $p + p$ collisions at $\sqrt{s} = 200$ GeV. *Phys. Rev. D* **2019**, *99*, 072003. <https://doi.org/10.1103/PhysRevD.99.072003>.
69. Aaboud, M.; et al. (ATLAS Collaboration) Measurement of b -hadron pair production with the ATLAS detector in proton-proton collisions at $\sqrt{s} = 8$ TeV. *J. High Energy Phys.* **2017**, *011*, 62. [https://doi.org/10.1007/JHEP11\(2017\)062](https://doi.org/10.1007/JHEP11(2017)062).
70. Khachatryan, V.; et al. (CMS Collaboration) Measurement of $B\bar{B}$ Angular Correlations based on Secondary Vertex Reconstruction at $\sqrt{s} = 7$ TeV. *J. High Energy Phys.* **2011**, *003*, 136. [https://doi.org/10.1007/JHEP03\(2011\)136](https://doi.org/10.1007/JHEP03(2011)136).
71. Aaij, R.; et al. (LHCb Collaboration) Observation of double charm production involving open charm in pp collisions at $\sqrt{s} = 7$ TeV. *J. High Energy Phys.* **2012**, *006*, 141; Addendum in *J. High Energy Phys.* **2014**, *003*, 108. [https://doi.org/10.1007/JHEP06\(2012\)141](https://doi.org/10.1007/JHEP06(2012)141).
72. Aaij, R.; et al. (LHCb Collaboration) Study of $b\bar{b}$ correlations in high energy proton-proton collisions. *J. High Energy Phys.* **2017**, *011*, 30. [https://doi.org/10.1007/JHEP11\(2017\)030](https://doi.org/10.1007/JHEP11(2017)030).
73. Aaij, R.; et al. (LHCb Collaboration) Observation of Enhanced Double Parton Scattering in Proton-Lead Collisions at $\sqrt{s_{NN}} = 8.16$ TeV. *Phys. Rev. Lett.* **2020**, *125*, 212001. <https://doi.org/10.1103/PhysRevLett.125.212001>.
74. Sjostrand, T.; Mrenna, S.; Skands, P.Z. PYTHIA 6.4 Physics and Manual. *J. High Energy Phys.* **2006**, *05*, 26. <https://doi.org/10.1088/1126-6708/2006/05/026>.
75. Frixione, S.; Nason, P.; Ridolfi, G. A Positive-weight next-to-leading-order Monte Carlo for heavy flavour hadroproduction. *J. High Energy Phys.* **2007**, *09*, 126. <https://doi.org/10.1088/1126-6708/2007/09/126>.
76. Kom, C.H.; Kulesza, A.; Stirling, W.J. Pair Production of J/ψ as a Probe of Double Parton Scattering at LHCb. *Phys. Rev. Lett.* **2011**, *107*, 082002. <https://doi.org/10.1103/PhysRevLett.107.082002>.
77. Baranov, S.P.; Snigirev, A.M.; Zotov, N.P. Double heavy meson production through double parton scattering in hadronic collisions. *Phys. Lett. B* **2011**, *705*, 116–119. <https://doi.org/10.1016/j.physletb.2011.09.106>.
78. Novoselov, A. Double parton scattering as a source of quarkonia pairs in LHCb. *arXiv* **2011**, arXiv:1106.2184.
79. Luszczak, M.; Maciula, R.; Szczurek, A. Production of two $c\bar{c}$ pairs in double-parton scattering. *Phys. Rev. D* **2012**, *85*, 094034. <https://doi.org/10.1103/PhysRevD.85.094034>.
80. Brodsky, S.J.; Lansberg, J.P. Heavy-Quarkonium Production in High Energy Proton-Proton Collisions at RHIC. *Phys. Rev. D* **2010**, *81*, 051502. <https://doi.org/10.1103/PhysRevD.81.051502>.
81. Brodsky, S.J.; Hoyer, P.; Peterson, C.; Sakai, N. The Intrinsic Charm of the Proton. *Phys. Lett. B* **1980**, *93*, 451–455. [https://doi.org/10.1016/0370-2693\(80\)90364-0](https://doi.org/10.1016/0370-2693(80)90364-0).
82. Norrbin, E.; Sjostrand, T. Production and hadronization of heavy quarks. *Eur. Phys. J. C* **2000**, *17*, 137–161. <https://doi.org/10.1007/s100520000460>.
83. Shao, H.S. Probing impact-parameter dependent nuclear parton densities from double parton scatterings in heavy-ion collisions. *Phys. Rev. D* **2020**, *101*, 054036. <https://doi.org/10.1103/PhysRevD.101.054036>.
84. Miller, M.L.; Reygers, K.; Sanders, S.J.; Steinberg, P. Glauber modeling in high energy nuclear collisions. *Ann. Rev. Nucl. Part. Sci.* **2007**, *57*, 205–243. <https://doi.org/10.1146/annurev.nucl.57.090506.123020>.
85. Cazaroto, E.R.; Goncalves, V.P.; Navarra, F.S. Heavy quark production in pA collisions: the double parton scattering contribution. *Mod. Phys. Lett. A* **2018**, *33*, 1850141. <https://doi.org/10.1142/S0217732318501419>.
86. Helenius, I.; Paukkunen, H. Double D-meson production in proton-proton and proton-lead collisions at the LHC. *Phys. Lett. B* **2020**, *800*, 135084. <https://doi.org/10.1016/j.physletb.2019.135084>.
87. Sjostrand, T.; Mrenna, S.; Skands, P.Z. A Brief Introduction to PYTHIA 8.1. *Comput. Phys. Commun.* **2008**, *178*, 852–867. <https://doi.org/10.1016/j.cpc.2008.01.036>.
88. Bahr, M.; et al. Herwig++ Physics and Manual. *Eur. Phys. J. C* **2008**, *58*, 639–707. <https://doi.org/10.1140/epjc/s10052-008-0798-9>.
89. Alwall, J.; Frederix, R.; Frixione, S.; Hirschi, V.; Maltoni, F.; Mattelaer, O.; Shao, H.S.; Stelzer, T.; Torrielli, P.; Zaro, M. The automated computation of tree-level and next-to-leading order differential cross sections, and their matching to parton shower simulations. *J. High Energy Phys.* **2014**, *007*, 79. [https://doi.org/10.1007/JHEP07\(2014\)079](https://doi.org/10.1007/JHEP07(2014)079).
90. Gleisberg, T.; Hoeche, S.; Krauss, F.; Schonherr, M.; Schumann, S.; Siegert, F.; Winter, J. Event generation with SHERPA 1.1. *J. High Energy Phys.* **2009**, *02*, 7. <https://doi.org/10.1088/1126-6708/2009/02/007>.
91. Schumann, S.; Krauss, F. A Parton shower algorithm based on Catani-Seymour dipole factorisation. *J. High Energy Phys.* **2008**, *03*, 38. <https://doi.org/10.1088/1126-6708/2008/03/038>.
92. Maltoni, F.; Stelzer, T. MadEvent: Automatic event generation with MadGraph. *J. High Energy Phys.* **2003**, *02*, 27. <https://doi.org/10.1088/1126-6708/2003/02/027>.
93. Alwall, J.; Demin, P.; de Visscher, S.; Frederix, R.; Herquet, M.; Maltoni, F.; Plehn, T.; Rainwater, D.L.; Stelzer, T. MadGraph/MadEvent v4: The New Web Generation. *J. High Energy Phys.* **2007**, *09*, 28. <https://doi.org/10.1088/1126-6708/2007/09/028>.

94. Frixione, S.; Webber, B.R. Matching NLO QCD computations and parton shower simulations. *J. High Energy Phys.* **2002**, *06*, 29. <https://doi.org/10.1088/1126-6708/2002/06/029>.
95. Frixione, S.; Nason, P.; Webber, B.R. Matching NLO QCD and parton showers in heavy flavor production. *J. High Energy Phys.* **2003**, *08*, 7. <https://doi.org/10.1088/1126-6708/2003/08/007>.
96. Frixione, S.; Webber, B.R. The MC and NLO 3.4 Event Generator. *arXiv* **2008**, arXiv:0812.0770.
97. Jung, H.; Salam, G.P. Hadronic final state predictions from CCFM: The Hadron level Monte Carlo generator CASCADE. *Eur. Phys. J. C* **2001**, *19*, 351–360. <https://doi.org/10.1007/s100520100604>.
98. Gauld, R.; Rojo, J.; Rottoli, L.; Talbert, J. Charm production in the forward region: constraints on the small-x gluon and backgrounds for neutrino astronomy. *J. High Energy Phys.* **2015**, *011*, 9. [https://doi.org/10.1007/JHEP11\(2015\)009](https://doi.org/10.1007/JHEP11(2015)009).
99. Fries, R.J.; Muller, B.; Nonaka, C.; Bass, S.A. Hadronization in heavy ion collisions: Recombination and fragmentation of partons. *Phys. Rev. Lett.* **2003**, *90*, 202303. <https://doi.org/10.1103/PhysRevLett.90.202303>.
100. Greco, V.; Ko, C.M.; Levai, P. Parton coalescence at RHIC. *Phys. Rev. C* **2003**, *68*, 034904. <https://doi.org/10.1103/PhysRevC.68.034904>.
101. Ravagli, L.; Rapp, R. Quark Coalescence based on a Transport Equation. *Phys. Lett. B* **2007**, *655*, 126–131. <https://doi.org/10.1016/j.physletb.2007.07.043>.
102. Adam, J.; et al. (STAR Collaboration) Observation of D_s^\pm/D^0 enhancement in Au+Au collisions at $\sqrt{s_{NN}} = 200$ GeV. *Phys. Rev. Lett.* **2021**, *127*, 092301. <https://doi.org/10.1103/PhysRevLett.127.092301>.
103. Acharya, S.; et al. (ALICE Collaboration) Constraining hadronization mechanisms with $\Lambda_c^+/D0$ production ratios in Pb–Pb collisions at $s_{NN}=5.02$ TeV. *Phys. Lett. B* **2023**, *839*, 137796. <https://doi.org/10.1016/j.physletb.2023.137796>.
104. Acharya, S.; et al. (ALICE Collaboration) Investigating charm production and fragmentation via azimuthal correlations of prompt D mesons with charged particles in pp collisions at $\sqrt{s} = 13$ TeV. *Eur. Phys. J. C* **2022**, *82*, 335. <https://doi.org/10.1140/epjc/s10052-022-10267-3>.
105. Acharya, S.; et al. (ALICE Collaboration) Azimuthal correlations of prompt D mesons with charged particles in pp and p–Pb collisions at $\sqrt{s_{NN}} = 5.02$ TeV. *Eur. Phys. J. C* **2020**, *80*, 979. <https://doi.org/10.1140/epjc/s10052-020-8118-0>.
106. Adam, J.; et al. (ALICE Collaboration) Measurement of azimuthal correlations of D mesons and charged particles in pp collisions at $\sqrt{s} = 7$ TeV and p–Pb collisions at $\sqrt{s_{NN}} = 5.02$ TeV. *Eur. Phys. J. C* **2017**, *77*, 245. <https://doi.org/10.1140/epjc/s10052-017-4779-8>.
107. Nason, P. A New method for combining NLO QCD with shower Monte Carlo algorithms. *J. High Energy Phys.* **2004**, *11*, 40. <https://doi.org/10.1088/1126-6708/2004/11/040>.
108. Frixione, S.; Nason, P.; Oleari, C. Matching NLO QCD computations with Parton Shower simulations: the POWHEG method. *J. High Energy Phys.* **2007**, *11*, 70. <https://doi.org/10.1088/1126-6708/2007/11/070>.
109. Johannes Bellm; Stefan Gieseke; David Grellscheid; Simon Plätzer; Michael Rauch; Christian Reuschle; Peter Richardson; Peter Schichtel; Michael H. Seymour; Andrzej Siódmok; Alexandra Wilcock; Nadine Fischer; Marco A. Harrendorf; Graeme Nail; Andreas Papaefstathiou & Daniel Rauch. Herwig 7.0/Herwig++ 3.0 release note. *Eur. Phys. J. C* **2016**, *76*, 196. <https://doi.org/10.1140/epjc/s10052-016-4018-8>.
110. Drescher, H.J.; Hladik, M.; Ostapchenko, S.; Pierog, T.; Werner, K. Parton based Gribov-Regge theory. *Phys. Rept.* **2001**, *350*, 93–289. [https://doi.org/10.1016/S0370-1573\(00\)00122-8](https://doi.org/10.1016/S0370-1573(00)00122-8).
111. Werner, K.; Karpenko, I.; Pierog, T.; Bleicher, M.; Mikhailov, K. Event-by-Event Simulation of the Three-Dimensional Hydrodynamic Evolution from Flux Tube Initial Conditions in Ultrarelativistic Heavy Ion Collisions. *Phys. Rev. C* **2010**, *82*, 044904. <https://doi.org/10.1103/PhysRevC.82.044904>.
112. Acharya, S.; et al. (ALICE Collaboration) Azimuthal Anisotropy of Heavy-Flavor Decay Electrons in p–Pb Collisions at $\sqrt{s_{NN}} = 5.02$ TeV. *Phys. Rev. Lett.* **2019**, *122*, 072301. <https://doi.org/10.1103/PhysRevLett.122.072301>.
113. Aad, G.; et al. (ATLAS Collaboration) Measurement of azimuthal anisotropy of muons from charm and bottom hadrons in pp collisions at $\sqrt{s} = 13$ TeV with the ATLAS detector. *Phys. Rev. Lett.* **2020**, *124*, 082301. <https://doi.org/10.1103/PhysRevLett.124.082301>.
114. Sirunyan, A.M.; et al. (CMS Collaboration) Elliptic flow of charm and strange hadrons in high-multiplicity pPb collisions at $\sqrt{s_{NN}} = 8.16$ TeV. *Phys. Rev. Lett.* **2018**, *121*, 082301. <https://doi.org/10.1103/PhysRevLett.121.082301>.
115. Sirunyan, A.M.; et al. (CMS Collaboration) Studies of charm and beauty hadron long-range correlations in pp and pPb collisions at LHC energies. *Phys. Lett. B* **2021**, *813*, 136036. <https://doi.org/10.1016/j.physletb.2020.136036>.
116. Acharya, S.; et al. (ALICE Collaboration) Azimuthal correlations of heavy-flavor hadron decay electrons with charged particles in pp and p–Pb collisions at $\sqrt{s_{NN}} = 5.02$ TeV. *Eur. Phys. J. C* **2023**, *83*, 741. <https://doi.org/10.1140/epjc/s10052-023-11835-x>.
117. Gyulassy, M.; Plumer, M. Jet Quenching in Dense Matter. *Phys. Lett. B* **1990**, *243*, 432–438. [https://doi.org/10.1016/0370-2693\(90\)91409-5](https://doi.org/10.1016/0370-2693(90)91409-5).
118. Baier, R.; Dokshitzer, Y.L.; Mueller, A.H.; Peigne, S.; Schiff, D. Radiative energy loss and p_T broadening of high-energy partons in nuclei. *Nucl. Phys. B* **1997**, *484*, 265–282. [https://doi.org/10.1016/S0550-3213\(96\)00581-0](https://doi.org/10.1016/S0550-3213(96)00581-0).
119. Thoma, M.H.; Gyulassy, M. Quark Damping and Energy Loss in the High Temperature QCD. *Nucl. Phys. B* **1991**, *351*, 491–506. [https://doi.org/10.1016/S0550-3213\(05\)80031-8](https://doi.org/10.1016/S0550-3213(05)80031-8).
120. Braaten, E.; Thoma, M.H. Energy loss of a heavy quark in the quark-gluon plasma. *Phys. Rev. D* **1991**, *44*, R2625. <https://doi.org/10.1103/PhysRevD.44.R2625>.

121. Casalderrey-Solana, J.; Milhano, J.G.; Pablos, D.; Rajagopal, K.; Yao, X. Jet Wake from Linearized Hydrodynamics. *J. High Energy Phys.* **2021**, *005*, 230. [https://doi.org/10.1007/JHEP05\(2021\)230](https://doi.org/10.1007/JHEP05(2021)230).
122. Wang, S.; Dai, W.; Zhang, B.W.; Wang, E. Diffusion of charm quarks in jets in high-energy heavy-ion collisions. *Eur. Phys. J. C* **2019**, *79*, 789. <https://doi.org/10.1140/epjc/s10052-019-7312-4>.
123. Hambrock, R.; Horowitz, W.A. AdS/CFT predictions for azimuthal and momentum correlations of $b\bar{b}$ pairs in heavy ion collisions. *Nucl. Part. Phys. Proc.* **2017**, 289–290, 233–236. <https://doi.org/10.1016/j.nuclphysbps.2017.05.052>.
124. Dong, X.; Lee, Y.J.; Rapp, R. Open Heavy-Flavor Production in Heavy-Ion Collisions. *Ann. Rev. Nucl. Part. Sci.* **2019**, *69*, 417–445. <https://doi.org/10.1146/annurev-nucl-101918-023806>.
125. Adam, J.; et al. (ALICE Collaboration) Transverse momentum dependence of D-meson production in Pb-Pb collisions at $\sqrt{s_{NN}} = 2.76$ TeV. *J. High Energy Phys.* **2016**, *003*, 81. [https://doi.org/10.1007/JHEP03\(2016\)081](https://doi.org/10.1007/JHEP03(2016)081).
126. Adam, J.; et al. (ALICE Collaboration) Centrality dependence of high- p_T D meson suppression in Pb-Pb collisions at $\sqrt{s_{NN}} = 2.76$ TeV. *J. High Energy Phys.* **2015**, *011*, 205; Addendum in *J. High Energy Phys.* **2017**, *06*, 32. [https://doi.org/10.1007/JHEP11\(2015\)205](https://doi.org/10.1007/JHEP11(2015)205).
127. Sirunyan, A.M.; et al. (CMS Collaboration) Measurement of the B^\pm Meson Nuclear Modification Factor in Pb-Pb Collisions at $\sqrt{s_{NN}} = 5.02$ TeV. *Phys. Rev. Lett.* **2017**, *119*, 152301. <https://doi.org/10.1103/PhysRevLett.119.152301>.
128. Khachatryan, V.; et al. (CMS Collaboration) Suppression and azimuthal anisotropy of prompt and nonprompt J/ψ production in PbPb collisions at $\sqrt{s_{NN}} = 2.76$ TeV. *Eur. Phys. J. C* **2017**, *77*, 252. <https://doi.org/10.1140/epjc/s10052-017-4781-1>.
129. Abelev, B.B.; et al. (ALICE Collaboration) Azimuthal anisotropy of D meson production in Pb-Pb collisions at $\sqrt{s_{NN}} = 2.76$ TeV. *Phys. Rev. C* **2014**, *90*, 034904. <https://doi.org/10.1103/PhysRevC.90.034904>.
130. Sirunyan, A.M.; et al. (CMS Collaboration) Measurement of prompt D^0 meson azimuthal anisotropy in Pb-Pb collisions at $\sqrt{s_{NN}} = 5.02$ TeV. *Phys. Rev. Lett.* **2018**, *120*, 202301. <https://doi.org/10.1103/PhysRevLett.120.202301>.
131. Adare, A.; et al. (PHENIX Collaboration) Azimuthal correlations of electrons from heavy-flavor decay with hadrons in p^+p and Au+Au collisions at $\sqrt{s_{NN}} = 200$ GeV. *Phys. Rev. C* **2011**, *83*, 044912. <https://doi.org/10.1103/PhysRevC.83.044912>.
132. Adam, J.; et al. (STAR Collaboration) Measurement of D^0 -meson + hadron two-dimensional angular correlations in Au+Au collisions at $\sqrt{s_{NN}} = 200$ GeV. *Phys. Rev. C* **2020**, *102*, 014905. <https://doi.org/10.1103/PhysRevC.102.014905>.
133. Sjostrand, T.; van Zijl, M. A Multiple Interaction Model for the Event Structure in Hadron Collisions. *Phys. Rev. D* **1987**, *36*, 2019. <https://doi.org/10.1103/PhysRevD.36.2019>.
134. Shi, S.; Dong, X.; Mustafa, M. A study of charm quark correlations in ultra-relativistic $p + p$ collisions with PYTHIA. *arXiv* **2015**, arXiv:1507.00614.
135. Agakishiev, G.; et al. (STAR Collaboration) Anomalous centrality evolution of two-particle angular correlations from Au-Au collisions at $\sqrt{s_{NN}} = 62$ and 200 GeV. *Phys. Rev. C* **2012**, *86*, 064902. <https://doi.org/10.1103/PhysRevC.86.064902>.
136. Adare, A.; et al. (PHENIX Collaboration) Dihadron azimuthal correlations in Au+Au collisions at $\sqrt{s_{NN}} = 200$ GeV. *Phys. Rev. C* **2008**, *78*, 014901. <https://doi.org/10.1103/PhysRevC.78.014901>.
137. Sirunyan, A.M.; et al. (CMS Collaboration) Studies of charm quark diffusion inside jets using PbPb and pp collisions at $\sqrt{s_{NN}} = 5.02$ TeV. *Phys. Rev. Lett.* **2020**, *125*, 102001. <https://doi.org/10.1103/PhysRevLett.125.102001>.
138. Sjöstrand, T.; Ask, S.; Christiansen, J.R.; Corke, R.; Desai, N.; Ilten, P.; Mrenna, S.; Prestel, S.; Rasmussen, C.O.; Skands, P.Z. An introduction to PYTHIA 8.2. *Comput. Phys. Commun.* **2015**, *191*, 159–177. <https://doi.org/10.1016/j.cpc.2015.01.024>.
139. Tumasyan, A.; et al. (CMS Collaboration) Search for medium effects using jets from bottom quarks in PbPb collisions at $\sqrt{s_{NN}} = 5.02$ TeV. *Phys. Lett. B* **2023**, *844*, 137849. <https://doi.org/10.1016/j.physletb.2023.137849>.
140. Dokshitzer, Y.L.; Khoze, V.A.; Troian, S.I. On specific QCD properties of heavy quark fragmentation ('dead cone'). *J. Phys. G* **1991**, *17*, 1602–1604. <https://doi.org/10.1088/0954-3899/17/10/023>.
141. Casalderrey-Solana, J.; Teaney, D. Heavy quark diffusion in strongly coupled $N = 4$ Yang-Mills. *Phys. Rev. D* **2006**, *74*, 085012. <https://doi.org/10.1103/PhysRevD.74.085012>.
142. Djordjevic, M.; Gyulassy, M. Heavy quark radiative energy loss in QCD matter. *Nucl. Phys. A* **2004**, *733*, 265–298. <https://doi.org/10.1016/j.nuclphysa.2003.12.020>.
143. Zakharov, B.G. Radiative p_\perp -broadening of fast partons in an expanding quark-gluon plasma. *Eur. Phys. J. C* **2021**, *81*, 57. <https://doi.org/10.1140/epjc/s10052-021-08847-w>.
144. Aad, G.; et al. (ATLAS Collaboration) Azimuthal angle correlations of muons produced via heavy-flavor decays in 5.02 TeV Pb+Pb and pp collisions with the ATLAS detector. *arXiv* **2023**, arXiv:2308.16652.
145. Adcox, K.; et al. (PHENIX Collaboration) Formation of dense partonic matter in relativistic nucleus-nucleus collisions at RHIC: Experimental evaluation by the PHENIX collaboration. *Nucl. Phys. A* **2005**, *757*, 184–283. <https://doi.org/10.1016/j.nuclphysa.2005.03.086>.
146. Adams, J.; et al. (STAR Collaboration) Experimental and theoretical challenges in the search for the quark gluon plasma: The STAR Collaboration's critical assessment of the evidence from RHIC collisions. *Nucl. Phys. A* **2005**, *757*, 102–183. <https://doi.org/10.1016/j.nuclphysa.2005.03.085>.
147. Back, B.B.; et al. (PHOBOS Collaboration) The PHOBOS perspective on discoveries at RHIC. *Nucl. Phys. A* **2005**, *757*, 28–101. <https://doi.org/10.1016/j.nuclphysa.2005.03.084>.
148. Arsene, I.; et al. (BRAHMS Collaboration) Quark gluon plasma and color glass condensate at RHIC? The Perspective from the BRAHMS experiment. *Nucl. Phys. A* **2005**, *757*, 1–27. <https://doi.org/10.1016/j.nuclphysa.2005.02.130>.

149. Aamodt, K.; et al. (ALICE Collaboration) Suppression of Charged Particle Production at Large Transverse Momentum in Central Pb-Pb Collisions at $\sqrt{s_{NN}} = 2.76$ TeV. *Phys. Lett. B* **2011**, *696*, 30–39. <https://doi.org/10.1016/j.physletb.2010.12.020>.
150. ALICE Collaboration. The ALICE experiment—A journey through QCD. *arXiv* **2022**, arXiv:2211.04384.
151. Voloshin, S.A.; Poskanzer, A.M.; Snellings, R. Collective phenomena in non-central nuclear collisions. *Landolt-Bornstein* **2010**, *23*, 293–333. https://doi.org/10.1007/978-3-642-01539-7_10.
152. Qin, G.Y.; Petersen, H.; Bass, S.A.; Muller, B. Translation of collision geometry fluctuations into momentum anisotropies in relativistic heavy-ion collisions. *Phys. Rev.* **2010**, *C82*, 064903. <https://doi.org/10.1103/PhysRevC.82.064903>.
153. Voloshin, S.; Zhang, Y. Flow study in relativistic nuclear collisions by Fourier expansion of Azimuthal particle distributions. *Z. Phys. C* **1996**, *70*, 665–672. <https://doi.org/10.1007/s002880050141>.
154. Abelev, B.I.; et al. (STAR Collaboration) Long range rapidity correlations and jet production in high energy nuclear collisions. *Phys. Rev.* **2009**, *C80*, 064912. <https://doi.org/10.1103/PhysRevC.80.064912>.
155. Abelev, B.; et al. (ALICE Collaboration) Long-range angular correlations on the near and away side in p-Pb collisions at $\sqrt{s_{NN}} = 5.02$ TeV. *Phys. Lett.* **2013**, *B719*, 29–41. <https://doi.org/10.1016/j.physletb.2013.01.012>.
156. Aaboud, M.; et al. (ATLAS Collaboration) Measurements of long-range azimuthal anisotropies and associated Fourier coefficients for pp collisions at $\sqrt{s} = 5.02$ and 13 TeV and $p+Pb$ collisions at $\sqrt{s_{NN}} = 5.02$ TeV with the ATLAS detector. *Phys. Rev.* **2017**, *C96*, 024908. <https://doi.org/10.1103/PhysRevC.96.024908>.
157. Chatrchyan, S.; et al. (CMS Collaboration) Multiplicity and transverse momentum dependence of two- and four-particle correlations in pPb and PbPb collisions. *Phys. Lett.* **2013**, *B724*, 213–240. <https://doi.org/10.1016/j.physletb.2013.06.028>.
158. Abelev, B.B.; et al. (ALICE Collaboration) Long-range angular correlations of β , K and p in p-Pb collisions at $\sqrt{s_{NN}} = 5.02$ TeV. *Phys. Lett.* **2013**, *B726*, 164–177. <https://doi.org/10.1016/j.physletb.2013.08.024>.
159. Khachatryan, V.; et al. (CMS Collaboration) Long-range two-particle correlations of strange hadrons with charged particles in pPb and PbPb collisions at LHC energies. *Phys. Lett.* **2015**, *B742*, 200–224. <https://doi.org/10.1016/j.physletb.2015.01.034>.
160. Khachatryan, V.; et al. (CMS Collaboration) Observation of Long-Range Near-Side Angular Correlations in Proton-Proton Collisions at the LHC. *J. High Energy Phys.* **2010**, *09*, 91. [https://doi.org/10.1007/JHEP09\(2010\)091](https://doi.org/10.1007/JHEP09(2010)091).
161. Adare, A.; et al. (PHENIX Collaboration) Quadrupole Anisotropy in Dihadron Azimuthal Correlations in Central $d+Au$ Collisions at $\sqrt{s_{NN}} = 200$ GeV. *Phys. Rev. Lett.* **2013**, *111*, 212301. <https://doi.org/10.1103/PhysRevLett.111.212301>.
162. Adamczyk, L.; et al. (STAR Collaboration) Long-range pseudorapidity dihadron correlations in $d+Au$ collisions at $\sqrt{s_{NN}} = 200$ GeV. *Phys. Lett.* **2015**, *B747*, 265–271. <https://doi.org/10.1016/j.physletb.2015.05.075>.
163. Loizides, C. Experimental overview on small collision systems at the LHC. *Nucl. Phys.* **2016**, *A956*, 200–207. <https://doi.org/10.1016/j.nuclphysa.2016.04.022>.
164. Werner, K.; Karpenko, I.; Pierog, T. The ‘Ridge’ in Proton-Proton Scattering at 7 TeV. *Phys. Rev. Lett.* **2011**, *106*, 122004. <https://doi.org/10.1103/PhysRevLett.106.122004>.
165. Deng, W.T.; Xu, Z.; Greiner, C. Elliptic and Triangular Flow and their Correlation in Ultrarelativistic High Multiplicity Proton Proton Collisions at 14 TeV. *Phys. Lett.* **2012**, *B711*, 301–306. <https://doi.org/10.1016/j.physletb.2012.04.010>.
166. Dusling, K.; Venugopalan, R. Comparison of the color glass condensate to dihadron correlations in proton-proton and proton-nucleus collisions. *Phys. Rev.* **2013**, *D87*, 094034. <https://doi.org/10.1103/PhysRevD.87.094034>.
167. Bzdak, A.; Schenke, B.; Tribedy, P.; Venugopalan, R. Initial state geometry and the role of hydrodynamics in proton-proton, proton-nucleus and deuteron-nucleus collisions. *Phys. Rev.* **2013**, *C87*, 064906. <https://doi.org/10.1103/PhysRevC.87.064906>.
168. Dumitru, A.; Lappi, T.; McLerran, L. Are the angular correlations in pA collisions due to a Glasma or Bose condensation? *Nucl. Phys.* **2014**, *A922*, 140–149. <https://doi.org/10.1016/j.nuclphysa.2013.12.001>.
169. Wong, C.Y. Momentum Kick Model Description of the Ridge in $(\Delta\phi)$ - $(\Delta\eta)$ Correlation in pp Collisions at 7 TeV. *Phys. Rev.* **2011**, *C84*, 024901. <https://doi.org/10.1103/PhysRevC.84.024901>.
170. Bierlich, C.; Gustafson, G.; Lönnblad, L.; Shah, H. The Angantyr model for Heavy-Ion Collisions in PYTHIA8. *J. High Energy Phys.* **2018**, *10*, 134. [https://doi.org/10.1007/JHEP10\(2018\)134](https://doi.org/10.1007/JHEP10(2018)134).
171. Dusling, K.; Li, W.; Schenke, B. Novel collective phenomena in high-energy proton-proton and proton-nucleus collisions. *Int. J. Mod. Phys. E* **2016**, *25*, 1630002. <https://doi.org/10.1142/S0218301316300022>.
172. Zhang, C.; Marquet, C.; Qin, G.Y.; Wei, S.Y.; Xiao, B.W. Elliptic Flow of Heavy Quarkonia in pA Collisions. *Phys. Rev. Lett.* **2019**, *122*, 172302. <https://doi.org/10.1103/PhysRevLett.122.172302>.
173. Zhang, C.; Marquet, C.; Qin, G.Y.; Shi, Y.; Wang, L.; Wei, S.Y.; Xiao, B.W. Collectivity of heavy mesons in proton-nucleus collisions. *Phys. Rev. D* **2020**, *102*, 034010. <https://doi.org/10.1103/PhysRevD.102.034010>.
174. Adam, J.; et al. (ALICE Collaboration) Elliptic flow of muons from heavy-flavour hadron decays at forward rapidity in Pb–Pb collisions at $\sqrt{s_{NN}} = 2.76$ TeV. *Phys. Lett.* **2016**, *B753*, 41–56. <https://doi.org/10.1016/j.physletb.2015.11.059>.
175. Adam, J.; et al. (ALICE Collaboration) Elliptic flow of electrons from heavy-flavour hadron decays at mid-rapidity in Pb–Pb collisions at $\sqrt{s_{NN}} = 2.76$ TeV. *J. High Energy Phys.* **2016**, *09*, 28. [https://doi.org/10.1007/JHEP09\(2016\)028](https://doi.org/10.1007/JHEP09(2016)028).
176. Acharya, S.; et al. (ALICE Collaboration) D-meson azimuthal anisotropy in mid-central Pb–Pb collisions at $\sqrt{s_{NN}} = 5.02$ TeV. *arXiv* **2017**, arXiv:1707.01005.
177. Abelev, B.B.; et al. (ALICE Collaboration) Azimuthal anisotropy of D meson production in Pb–Pb collisions at $\sqrt{s_{NN}} = 2.76$ TeV. *Phys. Rev. C* **2014**, *90*, 034904. <https://doi.org/10.1103/PhysRevC.90.034904>.

178. Acharya, S.; et al. (ALICE Collaboration) J/ψ elliptic flow in Pb-Pb collisions at $\sqrt{s_{NN}} = 5.02$ TeV. *Phys. Rev. Lett.* **2017**, *119*, 242301. <https://doi.org/10.1103/PhysRevLett.119.242301>.
179. Measurements of azimuthal anisotropy of nonprompt D^0 mesons in PbPb collisions at $\sqrt{s_{NN}} = 5.02$ TeV. *arXiv* **2022**, arXiv:2212.01636.
180. Acharya, S.; et al. (ALICE Collaboration) Measurement of Non-prompt D^0 -meson Elliptic Flow in Pb-Pb Collisions at $\sqrt{s_{NN}} = 5.02$ TeV. *arXiv* **2023**, arXiv:2307.14084.
181. Li, H.; Lin, Z.W.; Wang, F. Charm quarks are more hydrodynamic than light quarks in final-state elliptic flow. *Phys. Rev. C* **2019**, *99*, 044911. <https://doi.org/10.1103/PhysRevC.99.044911>.
182. Acharya, S.; et al. (ALICE Collaboration) Search for collectivity with azimuthal J/ψ -hadron correlations in high multiplicity p-Pb collisions at $\sqrt{s_{NN}} = 5.02$ and 8.16 TeV. *Phys. Lett. B* **2018**, *780*, 7–20. <https://doi.org/10.1016/j.physletb.2018.02.039>.
183. Sirunyan, A.M.; et al. (CMS Collaboration) Observation of prompt J/ψ meson elliptic flow in high-multiplicity pPb collisions at $\sqrt{s_{NN}} = 8.16$ TeV. *Phys. Lett. B* **2019**, *791*, 172–194. <https://doi.org/10.1016/j.physletb.2019.02.018>.
184. Acharya, S.; et al. (ALICE Collaboration) Measurements of azimuthal anisotropies at forward and backward rapidity with muons in high-multiplicity p-Pb collisions at $\sqrt{s_{NN}} = 8.16$ TeV. *Phys. Lett. B* **2023**, *846*, 137782. <https://doi.org/10.1016/j.physletb.2023.137782>.
185. Aad, G.; et al. (ATLAS Collaboration) Measurement of azimuthal anisotropy of muons from charm and bottom hadrons in Pb+Pb collisions at $\sqrt{s_{NN}} = 5.02$ TeV with the ATLAS detector. *Phys. Lett. B* **2020**, *807*, 135595. <https://doi.org/10.1016/j.physletb.2020.135595>.
186. Nahrgang, M.; Aichelin, J.; Gossiaux, P.B.; Werner, K. Influence of hadronic bound states above T_c on heavy-quark observables in Pb + Pb collisions at the CERN Large Hadron Collider. *Phys. Rev. C* **2014**, *89*, 014905. <https://doi.org/10.1103/PhysRevC.89.014905>.
187. Ke, W.; Xu, Y.; Bass, S.A. Modified Boltzmann approach for modeling the splitting vertices induced by the hot QCD medium in the deep Landau-Pomeranchuk-Migdal region. *Phys. Rev. C* **2019**, *100*, 064911. <https://doi.org/10.1103/PhysRevC.100.064911>.
188. Katz, R.; Prado, C.A.G.; Noronha-Hostler, J.; Noronha, J.; Suaide, A.A.P. Sensitivity study with a D and B mesons modular simulation code of heavy flavor RAA and azimuthal anisotropies based on beam energy, initial conditions, hadronization, and suppression mechanisms. *Phys. Rev. C* **2020**, *102*, 024906. <https://doi.org/10.1103/PhysRevC.102.024906>.
189. Lin, Z.W.; Ko, C.M.; Li, B.A.; Zhang, B.; Pal, S. A Multi-phase transport model for relativistic heavy ion collisions. *Phys. Rev. C* **2005**, *72*, 064901. <https://doi.org/10.1103/PhysRevC.72.064901>.
190. Lin, Z.W.; Zheng, L. Further developments of a multi-phase transport model for relativistic nuclear collisions. *Nucl. Sci. Tech.* **2021**, *32*, 113. <https://doi.org/10.1007/s41365-021-00944-5>.
191. Zhang, B. ZPC 1.0.1: A Parton cascade for ultrarelativistic heavy ion collisions. *Comput. Phys. Commun.* **1998**, *109*, 193–206. [https://doi.org/10.1016/S0010-4655\(98\)00010-1](https://doi.org/10.1016/S0010-4655(98)00010-1).
192. He, L.; Edmonds, T.; Lin, Z.W.; Liu, F.; Molnar, D.; Wang, F. Anisotropic parton escape is the dominant source of azimuthal anisotropy in transport models. *Phys. Lett. B* **2016**, *753*, 506–510. <https://doi.org/10.1016/j.physletb.2015.12.051>.
193. Du, X.; Rapp, R. Sequential Regeneration of Charmonia in Heavy-Ion Collisions. *Nucl. Phys. A* **2015**, *943*, 147–158. <https://doi.org/10.1016/j.nuclphysa.2015.09.006>.
194. Khachatryan, V.; et al. (CMS Collaboration) Evidence for collectivity in pp collisions at the LHC. *Phys. Lett. B* **2017**, *765*, 193–220. <https://doi.org/10.1016/j.physletb.2016.12.009>.

Disclaimer/Publisher's Note: The statements, opinions and data contained in all publications are solely those of the individual author(s) and contributor(s) and not of MDPI and/or the editor(s). MDPI and/or the editor(s) disclaim responsibility for any injury to people or property resulting from any ideas, methods, instructions or products referred to in the content.